

Fundamental and Applied Catalysis

Isabella Nova
Enrico Tronconi *Editors*

Urea-SCR Technology for deNO_x After Treatment of Diesel Exhausts

 Springer

Fundamental and Applied Catalysis

Series editors

Martyn Twigg, Royston, UK

Michael Spencer, Cardiff, UK

For further volumes:

<http://www.springer.com/series/5964>

Isabella Nova · Enrico Tronconi
Editors

Urea-SCR Technology for deNO_x After Treatment of Diesel Exhausts

 Springer

Editors
Isabella Nova
Enrico Tronconi
Politecnico di Milano
Milan
Italy

ISSN 1574-0447
ISBN 978-1-4899-8070-0 ISBN 978-1-4899-8071-7 (eBook)
DOI 10.1007/978-1-4899-8071-7
Springer New York Heidelberg Dordrecht London

Library of Congress Control Number: 2014934157

© Springer Science+Business Media New York 2014

This work is subject to copyright. All rights are reserved by the Publisher, whether the whole or part of the material is concerned, specifically the rights of translation, reprinting, reuse of illustrations, recitation, broadcasting, reproduction on microfilms or in any other physical way, and transmission or information storage and retrieval, electronic adaptation, computer software, or by similar or dissimilar methodology now known or hereafter developed. Exempted from this legal reservation are brief excerpts in connection with reviews or scholarly analysis or material supplied specifically for the purpose of being entered and executed on a computer system, for exclusive use by the purchaser of the work. Duplication of this publication or parts thereof is permitted only under the provisions of the Copyright Law of the Publisher's location, in its current version, and permission for use must always be obtained from Springer. Permissions for use may be obtained through RightsLink at the Copyright Clearance Center. Violations are liable to prosecution under the respective Copyright Law. The use of general descriptive names, registered names, trademarks, service marks, etc. in this publication does not imply, even in the absence of a specific statement, that such names are exempt from the relevant protective laws and regulations and therefore free for general use.

While the advice and information in this book are believed to be true and accurate at the date of publication, neither the authors nor the editors nor the publisher can accept any legal responsibility for any errors or omissions that may be made. The publisher makes no warranty, express or implied, with respect to the material contained herein.

Printed on acid-free paper

Springer is part of Springer Science+Business Media (www.springer.com)

Preface

It is widely recognized that Diesel vehicles are sure to significantly increase their worldwide penetration, particularly in countries like the United States where the present market share is not remarkable in comparison to that of vehicles with gasoline engines. This is mainly due to Diesel engines being inherently more thermodynamically efficient than spark-ignition engines, thus offering the prospect of reducing emissions of carbon dioxide.

Diesels produce, however, higher emissions of nitrogen oxides (NO_x) and particulate matter (PM). The emissions levels which can be achieved depend on both the engine-out emissions and the performance of the emissions control system. For the engine-out emissions, there is a well-known trade-off between PM and NO_x. Such a trade-off is not, however, a constant relationship between the two pollutants. Developments in combustion systems, fuel injection equipment, turbocharging, and associated control systems have allowed and continue to allow the trade-off curve to move to lower values of both NO_x and PM. The trade-off thus gives engine developers the opportunity to combine the optimization of 'raw' emissions and fuel economy with the optimization of the emissions control system.

Improvements in combustion and/or alternative fuels can lead to lower NO_x emissions, but it is generally recognized by now that, in order to meet the current and forthcoming legislative emissions standards both in Europe and in the USA, the application of after treatment systems is required. Indeed, Diesel particulate filters (DPFs) are needed to achieve the PM emission levels regardless of the system used to reduce NO_x. But, most importantly, the significant CO₂ reduction (i.e., the improved fuel consumptions), that is also dictated by the upcoming regulations, are forcing a drastic decrease in the average temperature profile of the exhaust gases; in such conditions, the catalytic removal of NO_x becomes extremely challenging. In fact, a significant portion of the present test cycles (e.g., the NEDC, New European Driving Cycle, and the WHTC, World Harmonized Transient Cycle) is characterized by very low exhaust temperatures. This makes very difficult the fulfillment of NO_x emission limits.

Currently, the major deNO_x after-treatment technologies under consideration include the so-called Lean-NO_x Traps (LNT), which are used with direct injection gasoline and Diesel engines, and the Selective Catalytic Reduction (urea-SCR) process.

Urea-SCR was the European motor industry's technology of choice to meet Euro 4 and Euro 5 emissions requirements for heavy-duty Diesel engines and more recently was also applied to light-duty vehicles and passenger cars in the USA and in Europe, as well. An SCR system is designed to catalytically reduce NO_x emissions in the oxygen-rich environment of Diesel exhausts. To this purpose, the SCR system needs a chemical reagent, or reductant, to help convert the NO_x to nitrogen: in mobile applications, the preferred reductant is typically an aqueous solution of nontoxic urea, which is used as an ammonia source. In fact, the so-called Adblue[®] solution (or DEF, Diesel Emission Fluid) is injected into the exhaust system where it is decomposed to NH₃.

Usually, a Diesel Oxidation Catalyst is also present in the system configuration, upstream of the SCR converter, to partially convert NO to NO₂; this enriches the stream entering the SCR reactor with significant amounts of NO₂ in addition to NO, and thus enables the onset of the SCR deNO_x reactions at lower temperature in comparison to the case where most of the NO_x is composed of NO alone.

Urea-SCR was first brought to the market in 2005 for heavy-duty vehicle applications by Daimler AG (DaimlerChrysler at the time) under the trade mark BLUETEC[®], based on the use of extruded honeycomb monolith catalysts consisting of V₂O₅-WO₃-TiO₂, similar to those extensively used worldwide for the control of NO_x emissions from power stations and other stationary sources. Subsequently, we have seen a trend in the automobile industry to replace Vanadium-based SCR catalysts with a new generation of metal-exchanged zeolite-based systems in order to expand the operating temperature window and to solve the high temperature deactivation problems typical of the anatase-rutile TiO₂ transition. A variety of zeolites have been proposed for this purpose (e.g., ZSM-5, mordenite, beta, ferrierite, Y-zeolite, and more recently chabazite). Zeolites are generally promoted by transition metals, such as iron and copper: the resulting catalytic systems are associated with an excellent deNO_x activity, particularly in the case of the Cu-zeolites. Indeed, metal-promoted zeolites have rapidly become the class of automotive SCR catalysts of choice, making urea-SCR the leading deNO_x technology nowadays. In the last few years, the improvement of the critical low-temperature deNO_x activity has been impressive, primarily due to the development of a new generation of Cu-promoted catalysts based on small pore zeolites, which also exhibit unparalleled stability with time-on-stream. The fundamental reasons for such enhanced performance, however, are not fully understood yet: they currently represent the objective of many academic and industrial research efforts.

There are several additional complications in using urea-SCR, including for example. The need for efficient ammonia release from the urea solution, and the related risks of deposits in the exhaust system due to by-products formation. Another issue is the accurate ammonia dosage: there should be enough ammonia present on the catalyst to reduce all NO_x, but at the same time there must be no excess of ammonia, to prevent its slippage from the vehicle. In order to realize this balance, a deep understanding of the influence of the operating conditions on the amount of ammonia stored on the catalyst, and on the rates of ammonia

adsorption/desorption, is crucial for the design and particularly for the control of SCR catalytic converters for vehicles. Ammonia slip catalysts represent a recent development in this area. Another area of current development is related to the fact that the SCR catalyst is often placed downstream of the Diesel Particulate Filter (DPF), in order to meet the requirements on soot particle emissions. On one hand, this configuration exposes the SCR catalyst to very high temperatures during DPF regeneration, so that its hydrothermal stability is a major concern. On the other hand, the multifunctional combination of DPF and SCR in a single device (SCR catalyst coated onto the DPF) presents several advantages, and is receiving considerable attention.

Finally, mathematical modeling has been recognized since the early days as a critical tool for timely and cost-effective development of urea-SCR technology for vehicles. This has resulted in a significant evolution, wherein the initial simple empirical models have been progressively replaced by the present sophisticated, chemically and physically consistent models, used in many companies to generate reliable simulations of NO_x emissions in highly transient test cycles for a wide range of conditions and parameters. Further efforts are being devoted to incorporate more details of the SCR catalytic chemistry, and to relate them to the catalyst features.

Several years after its first commercial applications, the development of urea-SCR has now clearly turned into a success story, with positive and promising perspectives and still many opportunities for further improvements and breakthroughs in a number of areas. So now, it is probably a good time to review the status of the technology, and highlight the next challenges.

This book provides a complete overview of the selective catalytic reduction of NO_x by ammonia/urea (urea-SCR), drawing from the know-how of many leading experts in the field. The book begins with a discussion of the technology in the framework of the current context (legislation, market, system configurations), covers the fundamental aspects of the SCR process (catalysts, chemistry, mechanism, and kinetics) and eventually analyses its application to the real scale (modeling of full scale monolith catalysts, control aspects, ammonia/urea delivery systems and strategies, integration with other devices for combined removal of pollutants). The book concludes with case histories presented by two companies which have greatly and creatively contributed to make urea-SCR a well-established and crucial technology for the automotive industry.

The book is aimed primarily at researchers in industry and academia working on exhaust gas aftertreatment systems. Several chapters however provide reference material that will be useful for teaching general courses on catalytic processes for environmental protection, or dedicated courses on the Selective Catalytic Reduction of NO_x.

Finally, this book is the result of the work of a number of industrial and academic experts: all of these persons are to be congratulated for devoting their time and effort to the present volume.

Contents

Part I Selective Catalytic Reduction Technology

1	Review of Selective Catalytic Reduction (SCR) and Related Technologies for Mobile Applications	3
	Timothy V. Johnson	
1.1	Introduction	3
1.2	Regulatory Overview	4
	1.2.1 Heavy-Duty Truck Regulations	4
	1.2.2 Light-Duty Regulations	5
1.3	Engine Developments	6
	1.3.1 Heavy-Duty Engines	6
	1.3.2 Light-Duty Diesel Engines	8
1.4	SCR Technologies	10
	1.4.1 SCR System Introduction	10
	1.4.2 Urea Delivery System	12
	1.4.3 Alternative Sources for Ammonia and Systems	13
	1.4.4 DOC Overview	14
	1.4.5 SCR Catalysts	15
	1.4.6 Ammonia Slip Catalysts	19
1.5	SCR System Design	20
1.6	Onboard Generation of Ammonia Using Lean NOx Traps	23
1.7	Outlook	25
1.8	Conclusions	26
	1.8.1 Regulations and Engine Technologies	26
	1.8.2 Onboard Ammonia Delivery Systems and SCR Catalyst Systems	26
	1.8.3 Outlook	27
	References	27
2	SCR Technology for Off-highway (Large Diesel Engine) Applications	33
	Daniel Chatterjee and Klaus Rusch	
2.1	Introduction	33
2.2	Off-highway Emission Legislation	36

2.3	SCR Systems for High-Speed Engines	38
2.3.1	Small Ship Applications	39
2.3.2	Rail Applications	39
2.3.3	Gensets	40
2.4	Medium and Low-Speed Engines	42
2.4.1	Fuels and Sulfur	42
2.4.2	SCR Technology for Marine Applications	45
2.4.3	Low-Speed Engine Genset	45
2.5	Combined Systems	47
2.5.1	DPF + SCR	47
2.5.2	Combination of DeNoxiation and DeSulfurization	51
2.6	System Integration	51
2.6.1	Reductant Supply	51
2.6.2	Canning Concepts	55
2.7	Control Strategies	56
2.8	Outlook	58
	References	59

Part II Catalysts

3	Vanadia-Based Catalysts for Mobile SCR	65
	Jonas Jansson	
3.1	Introduction	65
3.2	Legislation	66
3.3	Main SCR Reactions	67
3.4	Urea Injection	68
3.5	Properties of Vanadia SCR Catalyst	68
3.6	Reaction Mechanism	71
3.7	Function/Principle Design	73
3.8	Dimensioning of SCR System	76
3.9	Effect of NO ₂	81
3.10	Aging of Vanadia SCR Catalysts	83
3.10.1	Thermal Aging	83
3.10.2	Impact of Sulfur	85
3.10.3	Alkali Metals and Alkaline Earth Metals	87
3.10.4	Oil Poisons	88
3.10.5	Hydrocarbons	90
3.10.6	Arsenic and Lead	91
3.10.7	Biofuel	91
3.10.8	In-use Aging Evaluation	92
3.11	Summary and Conclusions	92
	References	93

4	Fe-Zeolite Functionality, Durability, and Deactivation Mechanisms in the Selective Catalytic Reduction (SCR) of NO_x with Ammonia	97
	Todd J. Toops, Josh A. Pihl and William P. Partridge	
4.1	Introduction	97
4.2	Experimental Considerations in Evaluating and Aging Catalysts	99
4.3	Fe-Zeolite NO _x Reduction Characteristics	104
4.4	Durability, Aging Techniques, and Deactivation Mechanism Affecting Performance	111
4.5	Summary	118
	References	119
5	Cu/Zeolite SCR Catalysts for Automotive Diesel NO_x Emission Control	123
	Hai-Ying Chen	
5.1	Introduction	123
5.2	Chemistry and Functionality of Cu/Zeolite SCR Catalysts	124
5.3	Deactivation Mechanisms of Cu/Zeolite SCR Catalysts	126
5.3.1	Hydrothermal Deactivation	126
5.3.2	Hydrocarbon Storage, Inhibition, and Poisoning	132
5.3.3	Sulfur Poisoning	133
5.3.4	Urea and Urea Deposit Related Catalyst Deactivation	133
5.3.5	Chemical Poisoning	134
5.4	Development of Small-Pore Zeolite Supported Cu SCR Catalysts	135
5.5	Investigation on the Superior Hydrothermal Stability of Small-Pore Zeolite Supported Cu SCR Catalyst	140
5.6	Investigation on the Active Cu Sites in Small-Pore Zeolite Supported Cu SCR Catalysts	142
5.7	Summary	143
	References	144
6	Low-Temperature Selective Catalytic Reduction (SCR) of NO_x with NH₃ Over Zeolites and Metal Oxide-Based Catalysts and Recent Developments of H₂-SCR	149
	Gongshin Qi, Lifeng Wang and Ralph T. Yang	
6.1	Ammonia-SCR	149
6.1.1	Introduction	149
6.1.2	Catalysts and Mechanistic Aspects of the Low-Temperature Ammonia-SCR	151

6.2	H ₂ -SCR	163
6.2.1	Introduction	163
6.2.2	Catalysts and Mechanistic Aspects of H ₂ -SCR	165
6.3	Challenges and Prospective	171
	References	172
Part III Mechanistic Aspects		
7	Active Sites for Selective Catalytic Reduction	181
	Wolfgang Grünert	
7.1	Introduction	181
7.2	Strategies and Methods for the Identification of Active Sites.	182
7.3	Supported Vanadia Catalysts	193
7.4	Zeolite-Based Catalysts	198
7.4.1	Fe Zeolites.	198
7.4.2	Cu Zeolites	206
7.5	Recent Catalyst Development.	208
7.6	Concluding Remarks	210
	References	211
8	Mechanistic Aspect of NO–NH₃–O₂ Reacting System.	221
	Masaoki Iwasaki	
8.1	Introduction	221
8.2	Steady-State Reaction Analysis	221
8.2.1	NH ₃ /NO/O ₂ , NH ₃ /O ₂ , and NO/O ₂ Reactions	221
8.2.2	Apparent Activation Energy.	223
8.2.3	Apparent Reaction Orders	224
8.2.4	Relationship with NO Oxidation Activity	227
8.2.5	Effect of Coexisting Gases and Poisoning	230
8.3	Transient Reaction Analysis.	233
8.3.1	Periodic NH ₃ Supply.	233
8.3.2	NO Pulse Reaction	237
8.3.3	In Situ FT-IR Analysis	238
8.4	Reaction Mechanisms	240
8.4.1	Vanadium-Based Catalysts.	240
8.4.2	Fe- or Cu-Exchanged Zeolite Catalysts	242
8.5	Conclusions	244
	References	244
9	The Role of NO₂ in the NH₃–SCR Catalytic Chemistry	247
	Enrico Tronconi and Isabella Nova	
9.1	Introduction	247
9.2	Experimental	248

9.3	Surface Storage of NO _x	249
9.3.1	NO ₂ Adsorption/Desorption	249
9.3.2	FTIR in Situ Study of NO ₂ Adsorption	250
9.3.3	Effect of the Catalyst Redox State on NO ₂ Adsorption	251
9.4	The Role of Surface Nitrates in the Fast SCR Mechanism.	253
9.4.1	NH ₃ + NO _x Temperature Programmed Reaction (TPR) Runs	253
9.4.2	Role of Nitrates in the NO/NO ₂ -NH ₃ SCR Mechanism.	255
9.5	Mechanistic Studies by Transient Response Methods	255
9.5.1	Reactivity of Surface Nitrates with NO and with NH ₃	256
9.5.2	The Role of Nitrites	257
9.5.3	Overall Mechanistic Scheme	258
9.5.4	Ammonia Blocking of Nitrates Reduction	259
9.5.5	Considerations on the Red-ox Nature of the NH ₃ -SCR Mechanisms	260
9.5.6	Higher Temperatures: The NO ₂ -SCR Reaction	261
9.5.7	Selectivity Issues: The Formation of NH ₄ NO ₃ , N ₂ O	262
9.6	Feeding Nitrates: The Enhanced SCR Reaction	263
9.6.1	The Boosting Action of Ammonium Nitrate	263
9.6.2	Analysis of the Enhanced SCR Chemistry	267
9.7	Summary and Conclusions.	268
	References	269

Part IV Reaction Kinetics

10 Kinetics of NH₃-SCR Reactions Over

	V₂O₅-WO₃/TiO₂ Catalyst	273
	Isabella Nova and Enrico Tronconi	
10.1	Introduction	273
10.2	Methods	274
10.2.1	Experimental Rig and Procedures	274
10.2.2	Mathematical Model of the Microreactor for Kinetic Tests.	275
10.3	NH ₃ /O ₂ Reacting System.	276
10.4	NH ₃ -NO/O ₂ Reacting System	282
10.5	NH ₃ -NO/NO ₂ Reacting System	294
10.6	Conclusions	308
	References	308

11 Lean NO_x Reduction by NH₃ on Fe-Exchanged Zeolite and Layered Fe/Cu Zeolite Catalysts: Mechanisms, Kinetics, and Transport Effects.	311
Michael P. Harold and Pranita Metkar	
11.1 Introduction	311
11.2 Reaction System Performance Features	312
11.2.1 NO Oxidation and NO ₂ Decomposition.	315
11.2.2 NH ₃ Oxidation	316
11.2.3 Selective Catalytic Reduction of NO _x	317
11.3 Kinetics and Mechanistic Considerations.	324
11.3.1 NO Oxidation	325
11.3.2 Standard SCR Reaction.	331
11.3.3 Ammonia Inhibition	333
11.3.4 Selective Catalytic Reaction with NO and NO ₂	334
11.4 Reaction and Transport Interactions	343
11.5 Reactor Modeling Developments	348
11.6 Concluding Remarks.	353
References	354
12 Kinetic Modeling of Ammonia SCR for Cu-Zeolite Catalysts	357
Louise Olsson	
12.1 Introduction	357
12.2 Kinetic Models for Ammonia and Water Storage Over Cu-Zeolites	358
12.2.1 Global Kinetic Model for Ammonia Storage and Desorption.	361
12.2.2 Detailed Kinetic Model for Ammonia and Water Storage	362
12.3 Kinetic Models for Ammonia Oxidation Over Cu-Zeolites	364
12.3.1 Global Kinetic Model for Ammonia Oxidation	364
12.3.2 Detailed Kinetic Model for Ammonia Oxidation	364
12.4 Kinetic Models for NO _x Storage and NO Oxidation Over Cu-Zeolites	365
12.4.1 Detailed Kinetic Model for NO Oxidation.	365
12.4.2 Global Kinetic Model for NO Oxidation	369
12.5 Kinetic Models for SCR Reactions Over Cu-Zeolites	371
12.5.1 Global Kinetic Models for SCR Over Cu-Zeolites	371
12.5.2 Detailed Kinetic Models for SCR Over Cu-Zeolites	376
12.6 Conclusions	381
References	381

Part V Modeling and Control

13 SCR Reactor Models for Flow-Through and Wall-Flow Converters 385
 Dimitrios Karamitros and Grigorios Koltsakis

13.1 Introduction 385

13.2 Fundamentals of Flow-Through Catalyst Modeling. 386

 13.2.1 Balance Equations 387

 13.2.2 Washcoat Internal Diffusion Modeling 389

 13.2.3 Multidimensional Model Extension. 391

13.3 Reaction Modeling 392

 13.3.1 Adsorption Model. 392

 13.3.2 de-NO_x Reactions. 394

 13.3.3 Parameter Calibration 397

13.4 Importance of Washcoat Diffusion Modeling. 397

 13.4.1 Experimental Results 398

 13.4.2 Simulation Study and Effective Diffusivity Investigation 398

13.5 From Lab Reactor Tests to Real-World System Modeling. 400

 13.5.1 Overview of Model Parameterization Approaches 400

 13.5.2 Microreactor and Monolith Reactor Tests 400

 13.5.3 Real-World Full-Scale Applications 402

13.6 Fundamentals of SCR on DPF Modeling. 403

 13.6.1 Wall-Flow Filter Model. 403

 13.6.2 SCR Kinetic Model and Soot Oxidation Kinetics 406

 13.6.3 Wall-Flow Versus Flow-Through Monoliths 407

 13.6.4 Interactions Between Soot and de-NO_x Activity. 408

13.7 Integrated Exhaust System Modeling 412

 13.7.1 Model-Based DPF + SCR System Optimization 413

 13.7.2 Combined LNT-SCR Concepts. 416

 13.7.3 Combined SCR-ASC Concept 418

13.8 Conclusion: Perspectives 419

References 422

14 Diesel Engine SCR Systems: Modeling, Measurements, and Control 425
 Ming-Feng Hsieh and Junmin Wang

14.1 Introduction 425

14.2 SCR Control-Oriented Modeling 426

 14.2.1 Introduction 426

 14.2.2 Main SCR Reactions. 426

 14.2.3 Control-Oriented SCR Model. 427

14.3 SCR Sensing and Estimation Systems. 430

 14.3.1 NO_x Sensor NH₃ Cross-Sensitivity 431

14.3.2	SCR Catalyst Ammonia Coverage Ratio Estimation	437
14.4	SCR Control	441
14.4.1	Control-Oriented SCR Model	442
14.4.2	Controller Design and Architecture	443
14.4.3	Experimental Setup	444
14.4.4	Experimental Results of US06 Test Cycle	446
14.5	Conclusions	448
	References	449

Part VI Ammonia Supply

15	DEF Systems and Aftertreatment Architecture Considerations. . .	455
	Ryan Floyd, Levin Michael and Zafar Shaikh	
15.1	Role of Engine and Dosing Calibration	459
15.2	Overview of Injection Technology and Spray Quality	461
15.3	Overview of SCR System Mixing Devices	467
15.4	SCR System Mixing Devices: Ford Practical Example	471
15.5	Aftertreatment Architecture	474
15.6	Deposit Mitigation: Practical Example	479
15.7	Concluding Remarks	483
	References	483
16	Ammonia Storage and Release in SCR Systems for Mobile Applications	485
	Daniel Peitz, Andreas Bernhard and Oliver Kröcher	
16.1	Introduction	485
16.2	Urea as Ammonia Precursor Compound	486
16.2.1	Solid Urea	486
16.2.2	Urea Solution	487
16.2.3	Urea Thermolysis and Evaporation	487
16.2.4	Urea Decomposition Byproducts and Catalyst Deactivation	489
16.2.5	Catalytic Urea Decomposition	491
16.3	Alternative Ammonia Precursor Compounds	493
16.3.1	Cyanuric Acid	493
16.3.2	Ammonium Formate	494
16.3.3	Ammonium Carbamate	495
16.3.4	Metal Ammine Chlorides	496
16.3.5	Methanamide	498
16.3.6	Guanidinium Salts	499
16.3.7	Catalytic Decomposition of Alternative NH ₃ Precursor Compounds	499
	References	501

17 Modeling the Gas Flow Process Inside Exhaust Systems: One Dimensional and Multidimensional Approaches	507
Gianluca Montenegro and Angelo Onorati	
17.1 Introduction	507
17.2 1D Models for the Prediction of Gas Flows.	508
17.2.1 Modeling the Thermal Aspects.	510
17.2.2 Thermal and Hydrolytic Decomposition of Urea	516
17.2.3 Kinetic Model	517
17.3 Multidimensional Models	521
17.3.1 Governing Equations.	521
17.3.2 Modeling the UWS Injection	526
17.3.3 Modeling the Formation of Liquid Film	532
17.3.4 Discretization of Source Terms and Equations	535
17.3.5 Examples of CFD Application	538
References	547

Part VII Integrated Systems

18 Dual-Layer Ammonia Slip Catalysts for Automotive SCR Exhaust Gas Aftertreatment: An Experimental and Modeling Study	553
Isabella Nova, Massimo Colombo, Enrico Tronconi, Volker Schmeißer, Brigitte Bandl-Konrad and Lisa Zimmermann	
18.1 Introduction	554
18.2 Methods	556
18.2.1 Experimental	557
18.2.2 Modeling.	558
18.3 Derivation and Validation of the SCR Model.	561
18.3.1 Reaction Network and Kinetic Scheme Over the SCR Component	561
18.3.2 Kinetic Fit	566
18.3.3 Model Validation	567
18.4 Derivation and Validation of the PGM Catalyst Model	567
18.4.1 Reaction Network and Kinetic Scheme Over the PGM Component	567
18.4.2 Model Fit	573
18.4.3 Model Validation	573
18.5 Analysis and Modeling of SCR/PGM Interactions	575
18.5.1 Experimental Study of SCR/PGM Interactions.	575
18.5.2 Predictive Simulations of the SCR/PGM Combined Systems	577

18.6	Modeling of Dual-Layer Monolith ASC	579
18.6.1	Development of a Dual-Layer Monolith Model	579
18.6.2	Validation of the Dual-Layer Monolith ASC Model	581
18.7	Conclusions	583
	References	584
19	NSR–SCR Combined Systems: Production and Use of Ammonia	587
	Fabien Can, Xavier Courtois and Daniel Duprez	
19.1	Introduction	587
19.2	NH ₃ Emission from NSR Catalysts	588
19.2.1	The NSR Process	588
19.2.2	Ammonia Formation Pathways	589
19.2.3	Influencing Parameters/Ammonia Reactivity	591
19.2.4	Conclusion	596
19.3	Coupling of NO _x Trap and NH ₃ –SCR Catalysts	596
19.3.1	Emergence and Development of the NSR–SCR Coupling Concept	596
19.3.2	Coupling of Pt Catalysts with Zeolites	598
19.3.3	Coupling of Pt(RhPd)/BaO/Al ₂ O ₃ with Cu–Zeolite Catalysts	598
19.3.4	Coupling of Pt(RhPd)/BaO/Al ₂ O ₃ with Fe–Zeolite Catalysts	603
19.3.5	Other Systems Including Tungsten-Based Catalysts	606
19.4	Selective Catalytic Reduction of NO _x by Ammonia (NH ₃ –SCR)	608
19.4.1	Mechanistic Aspects of the SCR Reaction	608
19.4.2	Effect of Zeolite Framework	610
19.4.3	Role of Acidic Sites	611
19.4.4	Active Sites and Performances of Cu–Zeolite, Fe–Zeolite, and Other Systems in NH ₃ –SCR	612
19.5	Conclusion and Perspective	614
	References	615
20	Integration of SCR Functionality into Diesel Particulate Filters	623
	Thorsten Boger	
20.1	Introduction	624
20.2	Diesel Particulate Filter Technologies	626
20.2.1	Diesel Particulate Filter Designs and Materials	626
20.2.2	Catalyst Coatings for Diesel Particulate Filters	629

- 20.3 Performance Considerations for SCR Integrated Diesel
 - Particulate Filters 630
 - 20.3.1 Pressure Drop and Permeability 630
 - 20.3.2 Filtration 636
 - 20.3.3 Filter Regeneration, Thermal Management,
and Durability 640
 - 20.3.4 DeNOx Efficiency 643
- 20.4 Modeling of SCR Integrated Particulate Filters 645
- 20.5 Application Examples 648
 - 20.5.1 Light Duty 648
 - 20.5.2 Heavy Duty 650
- 20.6 Summary 651
- References 652

Part VIII Case Histories

- 21 Development of the 2010 Ford Diesel Truck Catalyst System 659**
 - Christine Lambert and Giovanni Cavataio
 - 21.1 Introduction 660
 - 21.2 Early Research at Ford on Lean NOx Control
for Diesel Vehicles 661
 - 21.3 Ford’s Research Program on a Prototype Light-Duty
Diesel Truck 663
 - 21.3.1 SCR System Design 663
 - 21.3.2 DOC Development for SCR Systems 664
 - 21.3.3 SCR Catalyst Formulations 666
 - 21.3.4 Vehicle System Results 666
 - 21.4 Migration of Research into a Production Vehicle Program 668
 - 21.4.1 Vehicle Program Needs for Lean NOx Control 668
 - 21.4.2 Catalyst and System Design Options 669
 - 21.5 Development Challenges Associated with SCR
Catalyst Systems 670
 - 21.5.1 Thermal Stability of the DOC 670
 - 21.5.2 Thermal Stability of the SCR Catalyst 671
 - 21.5.3 Ammonia Storage Management 674
 - 21.5.4 HC Poisoning/Coking of Zeolitic SCR Catalysts 676
 - 21.5.5 Precious Metal Poisoning 679
 - 21.5.6 Sulfur Effects on Catalysts 681
 - 21.5.7 Urea Injection/Mixing 682
 - 21.5.8 Urea Specifications and Refill 682

21.6	Environmental Impact of Medium-Duty Diesels:	
	Current and Future	683
21.6.1	NO _x Emissions	683
21.6.2	Greenhouse Gas Footprint (CO ₂ , CH ₄ , N ₂ O)	684
21.6.3	Use of Base Metals, Pd Rich Catalysts	684
21.7	Conclusion.	686
	References	687
22	Model-Based Approaches to Exhaust Aftertreatment	
	System Development.	691
	Michel Weibel, Volker Schmeißer and Frank Hofmann	
22.1	Introduction	692
22.2	Modeling of the Exhaust Gas Aftertreatment System	693
	22.2.1 Total System Simulation	693
	22.2.2 Model Structure	694
	22.2.3 Kinetics and Parameterization	695
22.3	Simulation Methods in the Development Process	696
	22.3.1 Demands of the Development Process.	696
	22.3.2 The Virtual Testbench Concept	697
	22.3.3 Development of an AdBlue [®] Dosing Control Strategy	697
22.4	Outlook: On-board Model-Based SCR Control.	704
22.5	Summary	705
	References	706
	About the Editors	709
	Index	711

Part I
Selective Catalytic Reduction Technology

Chapter 1

Review of Selective Catalytic Reduction (SCR) and Related Technologies for Mobile Applications

Timothy V. Johnson

1.1 Introduction

NO_x is formed when air is heated to very high temperatures, and is thus emitted from combustion and engines. The most prevalent NO_x species from engines is NO. It will oxidize in the atmosphere to form NO₂, and also react with many hydrocarbons (HCs) to form ozone; both ozone and NO₂ are toxic and strong oxidants. Thus, NO_x is a criteria pollutant and is regulated. NO_x is very effectively controlled from gasoline engines with three-way catalysts (TWCs) (CO, HCs, NO_x), but they only operate under stoichiometric conditions. For lean diesel conditions, selective catalytic reduction (SCR) is the leading method of remediation. The reductant, ammonia (NH₃), which needs to be added to the exhaust, selectively reduces the NO_x rather than being oxidized by the excess oxygen, as do the innate exhaust reductants, CO and HCs.

This chapter will set the stage for the other chapters in the book by providing a representative review of the regulations, general engine trends, and key developments in SCR catalyst technology. It is not intended to be all-encompassing and comprehensive. Representative papers and presentations were chosen here that provide examples of new, key developments, and direction. For a more detailed review of SCR technologies, and diesel emission control technology trends and developments in general, the reader is referred to Johnson [1–3].

T. V. Johnson (✉)

Emerging Technologies and Regulations, Corning Environmental Technologies, Corning Incorporated, HP-CB-3-1, Corning, NY 14831, USA
e-mail: JohnsonTV@Corning.com

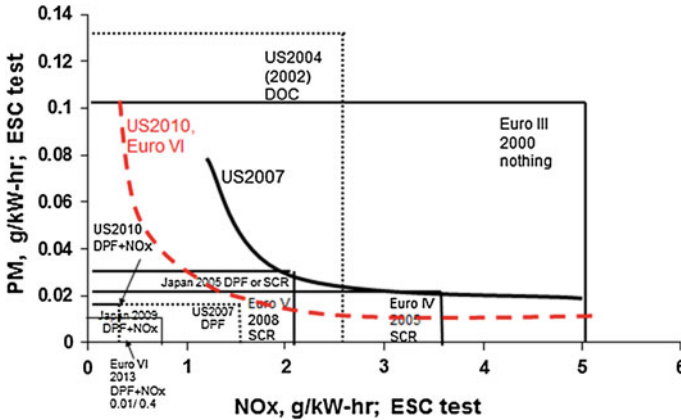


Fig. 1.1 Overview of key HD tailpipe regulations as measured on the ESC. The *dashed* and *solid lines* represent an estimate of the best commercially viable engine-out emissions for engines in 2007 and 2010

1.2 Regulatory Overview

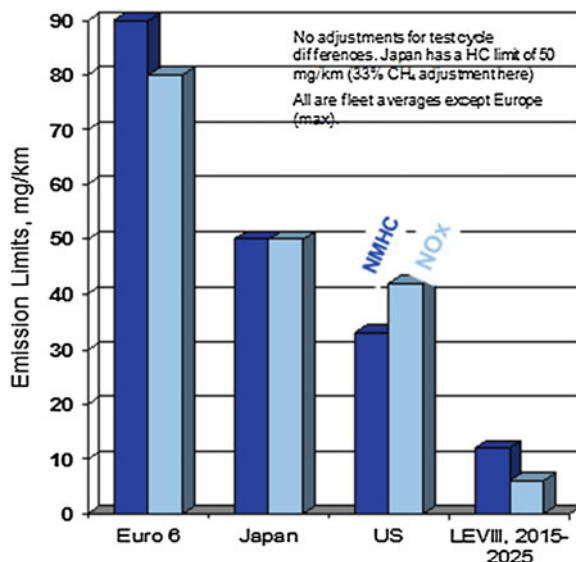
Although the first commercial lean deNO_x system was a lean NO_x trap (LNT) on the European Toyota Avensis in the early 2000s, and then on the US Dodge Ram truck (Cummins engine) in 2007, the first wide-scale use of deNO_x was the implementation of SCR for heavy-duty (HD) truck applications in Europe in 2005. The US Tier 2 and California Low Emission Vehicle (LEVII) regulations were the first to force SCR on light-duty (LD) applications in 2007. SCR did not make its way into NR applications until 2011 in both the US and Europe.

Following is a general overview of the HD, LD, and NR regulations pertinent to understanding the main drivers for SCR systems.

1.2.1 Heavy-Duty Truck Regulations

Figure 1.1 shows a summary of the key HD truck regulations in the world, along with estimates of the best commercially viable engine-out NO_x and particulate matter (PM) capabilities, as measured on the European Steady-State Cycle (ESC). The first vehicle regulation in the world that was attained with SCR systems was the Japan 2005 HD truck regulation in October 2004, shortly followed by Euro IV in January 2005. Although Euro IV was only a 30 % NO_x tightening from Euro III (2000), the PM regulation dropped ~80 %, and truck manufacturers generally elected to tune their engines for higher NO_x and lower PM and fuel consumption, and then use SCR to drop the tailpipe levels to within the NO_x (and PM) requirements. It is interesting to note that although the US2007 NO_x regulations

Fig. 1.2 Leading light-duty diesel NOx and non-methane hydrocarbon emissions



were 60 % lower than for Euro IV, and the PM regulations were about 35–55 % tighter (steady state and transient testing, respectively), the US manufacturers chose to meet the NOx regulations with engine technology (mainly exhaust gas recirculation (EGR)), and the PM regulations with diesel particulate filters (DPFs). The Japan 2005 regulation is intermediate between Europe and the US for both NOx and PM, and there was a split of approaches used in Japan, with trucks in high fuel consumption applications generally using a European SCR-only approach, and all others using a EGR + DPF approach.

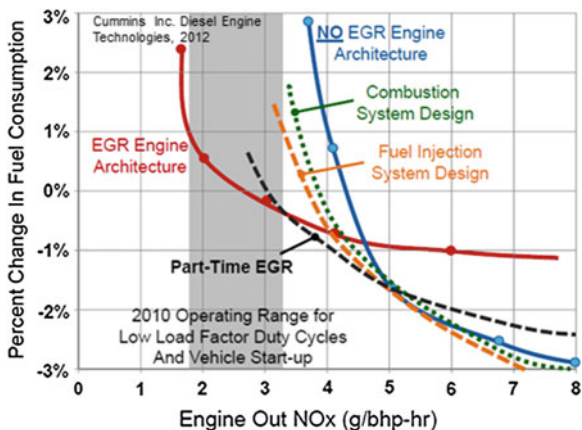
In the 2009+ time frame, Japan 2009, US2010, and Euro VI (2013) all require both SCR and DPF solutions. These regulations range from 0.26 to 0.7 g NOx/kW-h and 0.010 to 0.013 g PM/kW-h.

1.2.2 Light-Duty Regulations

The leading LD diesel non-methane HC and NOx regulations are graphically shown in Fig. 1.2. Only the US (Federal and California LEV VIII) has the test-cycle and limit value combination to force NOx aftertreatment. All require a DPF (regulations not shown). By 2013, perhaps a dozen diesel models will be on the US market. However, the majority of Euro 6 applications will have NOx aftertreatment to minimize NO₂ emissions and fuel consumption.

One regulatory development that will drive SCR system design in Europe and elsewhere is emerging now in Europe: Real-World Driving Emissions (RDE). Investigators have found that NOx emissions from LD diesels can be 3–4X higher

Fig. 1.3 EGR can have fuel consumption benefits at low engine-out NO_x levels (<4 g/bhp-h or 5.2 g/kW-h), but at higher levels there is a fuel penalty versus SCR approaches with high deNO_x efficiency [4]



than the laboratory certification level. It is too early to note the details of these regulations, but they are likely to include portable emissions monitoring systems (PEMS) and require advance controls for cold start, high speed, and load conditions.

The regulatory trend in the US, Europe, and Japan is for very low-NO_x emissions. All HD trucks in these markets will have SCR systems by early 2014. These regulations are migrating into the NR machine sector, wherein most engines >70 kW will have SCR systems in 2014+. For passenger cars, all but the smaller diesels will have SCR systems in the three markets. Tighter regulations are foreseen for the developing markets, with Brazil leading the way, followed by China and India.

1.3 Engine Developments

This section will summarize HD and LD diesel engine technologies. We may see lean-burn gasoline engines in the market, and SCR is a viable option for these engines, but this is beyond the scope of this summary.

1.3.1 Heavy-Duty Engines

HD engine technology is in development to meet the next round of OBD (onboard diagnostics) tightening in the US for 2013 and the new CO₂ regulations in 2014. Concurrent with this, the Euro VI regulations come into play in 2013–2014.

Stanton [4] shows in Fig. 1.3 that the most effective engine means for reducing NO_x, EGR is an efficient approach and can have fuel consumption benefits if SCR

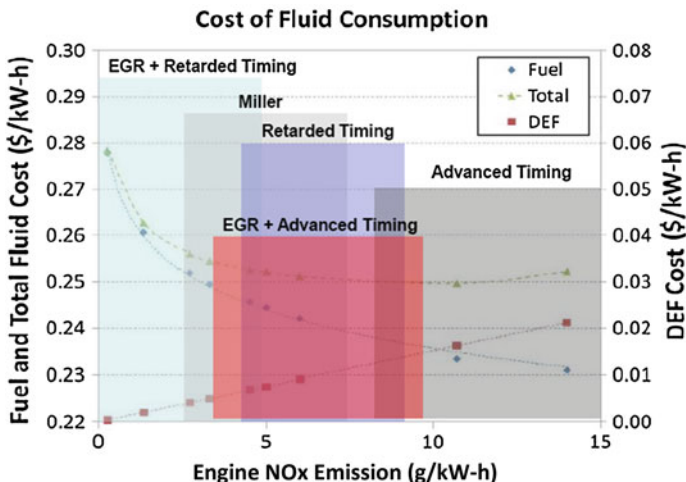


Fig. 1.4 General advance HD engine technologies and the resultant urea (DEF) and fuel cost curves, assuming DEF costs \$2.56 per gallon (\$0.69/l) and diesel fuel cost \$3.89/gallon (\$1.05/l). Fluid costs are minimized at 8–11 g/kW-h NOx [5]

efficiency requires low engine-out NOx levels (<2.5–5 g/kW-h NOx) in low-load operating regimes. However, if increased SCR deNOx efficiency allows higher NOx levels, EGR results in a fuel penalty. Given this, Stanton estimates that if SCR can attain a 98 % cycle-average deNOx efficiency, EGR can be eliminated. Furthermore, as shown in Fig. 1.3, running at higher engine-out NOx can return substantial fuel consumption benefits. In the high-NOx regimes, about 1 % fuel can be saved for every 1.2–1.5 % urea consumed (relative to fuel) to drop the NOx. This is beneficial for both CO₂ reductions and fluid cost savings (urea plus fuel).

Roberts [5] described some HD technologies for both high- and low-engine-out NOx approaches. A summary is shown in Fig. 1.4, wherein each point represents an engine hardware configuration that is optimized for low fuel consumption. As with previous such descriptions of advance engine technology packages [6], fuel consumption decreases as NOx increases, even out at >5 g NOx/kW-h. Roberts shows minimum fluid operating costs (top line) at 8–11 g/kW-h engine-out NOx. He assumes here that the urea (Diesel Exhaust Fluid (DEF)) is 65 % the cost of fuel. Emission control technologies (like SCR) would be needed to achieve at least 97–98 % efficiency to achieve this minimum fluid-consumption-cost calibration range, to meet the US 2010 regulations.

Zybell [7] also described some HD technology packages for meeting low emissions and fuel consumption, but mainly in the context of fuel injection technology. His slopes of fuel consumption versus NOx are not as steep as shown in Figs. 1.3 and 1.4, so his minimum cost range is in the 3–5 g/kW-h NOx range. However, when fuel injection pressure is increased from 1,800 to 2,400 bar, the fluid consumption drops about 0.6 % and the minimum calibration shifts to

2.5–4.0 g/kW-h NO_x. Continuing the trend, if injection pressure is increased to 3,000 bar, fluid consumption drops another 0.1 % and the minimum point shifts to 2.0–3.0 g/kW-h NO_x.

Kobayashi et al. [8] gave a detailed account of their attempt to drop engine-out NO_x to 0.2 g/kW-h on a 10.5 l engine with the following features: 2,000 bar common rail fuel injection system, low-pressure (LP) and high-pressure (HP) EGR, variable valve actuation, 300 bar peak cylinder pressure, variable swirl, and advanced combustion chamber design. With a DPF, the engine achieved 0.8 g/kW-h NO_x on the JE05 Japanese HD transient cycle. At 1,200 RPM and 8 bar BMEP, substituting about 40–70 % LP-EGR instead of HP-EGR results in similar NO_x levels, despite 5–10 % higher total EGR rates, but with greatly reduced PM and fuel consumption. Also striving for high-efficiency and low-NO_x, Ojeda [9] reported that a prototype 13-l engine with 2-stage EGR cooling, 2-stage turbocharging, a 2,200 bar injection system, and optimized combustion system achieved 45 % BTE at road loads, with a 0.5 g/bhp-h NO_x (0.65 g/kW-h) NO_x level. This is higher efficiency than some 2,010 engines running with SCR at much higher NO_x levels. Although impressive, these studies show that achieving the engine-out NO_x levels required to meet the emerging tailpipe regulations, without NO_x after-treatment is quite difficult and could be very expensive.

Improved thermal management is increasing in importance, especially as it pertains to reducing urban NO_x from engines with SCR. The first evidence that this issue is being addressed on Euro VI engines was reported by Vermeulen et al. [10]. The 13-l prototype Scania engine had cooled-EGR to reduce low-load NO_x and intake throttling for thermal management. NO_x in-service conformity (ISC) was well below the 1.5X limit after allowable calibration adjustments, and NO_x emissions generally vary from 0.35 to 0.76 g/kW-h for most trips and segments. The SCR system was fully functional after 500 s of operation after a cold start at 3 °C.

Finally, US HD engine manufacturers described their future approaches to meeting the US Department of Energy (DOE) goal of demonstrating 50 % BTE (break thermal efficiency) on a HD engine [1]. All four US HD truck engine manufacturers get much of their efficiency improvements from combustion (chamber design, control, mixing, etc.), reduction of friction and parasitic losses, and Rankine cycle waste heat recovery (WHR). Improved SCR performance is also mentioned commonly (for higher NO_x calibrations).

Although HD NO_x regulations might be met by further advancements in engine technology, the best balance of low fuel consumption and low tailpipe NO_x emissions requires about 98+ % efficient SCR.

1.3.2 Light-Duty Diesel Engines

LD diesel engines are also improving to keep the efficiency advantage over gasoline. Pischinger [11] described future technologies for both diesel and gasoline engines to achieve 35 % CO₂ reductions. Major improvements in both platforms

include 25 % downsizing (7 % reductions), stop–start system (6 %), LP-EGR (3 %), and down-speeding (3 %). The approach can result in lower exhaust temperatures due to more turbocharging, and higher NO_x as the result of the same fuel amount burned in a smaller cylinder. However, for gasoline vehicles to meet the 95 g/km fleet average CO₂ emission requirement in Europe in 2020, Pischinger projects significant hybridization is needed. Diesel engines can meet the regulation with standard drivetrains.

In the US, to meet the tight LEV_{III} emissions, reduced cold start emissions are the key, requiring significant thermal management methods. Popuri et al. [12] use an intake throttle, bypass valves for the EGR, turbine, and LP-VGT (variable gate turbocharger), idle speed modulation, late cycle fuel injections, cylinder deactivation (fueling cut off), and an exhaust-manifold integrated diesel oxidation catalyst (DOC) to allow urea injection 125 s, earlier than for a baseline engine. Despite that the engine-out NO_x increased 20 %, and fuel consumption increased 5–7 % when the methods are used, Federal Test Procedure (FTP) Bag 1 deNO_x was an impressive 70 % and overall fuel efficiency increased 25 % compared to their baseline engine. A 4.5 l engine in a 5,000 pound (2,270 kg) vehicle achieved US Tier 2 Bin 5 standards at 25.5 MPG (9.1 l/100 km). Ruth [13] reported significant progress in the same program that reduces thermal management requirements and is now targeted to meet the LEV_{III} fleet average requirements (–70 % vs. Tier 2 Bin 5) by using a passive NO_x adsorber (PNA) that adsorbs NO_x at low temperature and releases it passively as temperature increases, a combination SCR + DPF (SCR catalyst coated onto a DPF), and gaseous NH₃ injection. The progress shows how critical advanced SCR technology is to improve feasibility of clean LD diesel engines.

Another LEV_{III} approach was reported by Balland et al. [14]. To address the challenge SCR and other deNO_x systems have in reducing high-load NO_x, the investigators report that a standard DOC can efficiently remove NO_x at stoichiometry, and thus run the engine in that mode during accelerations. The approach requires tight control of EGR, the turbocharger, and other engine parameters, and uses an “air-based control” approach similar to that of gasoline engines, rather than a fuel-based approach typical of diesel engines. Exhaust temperatures also increase substantially in the accelerations and the strategy is part of cold start thermal management.

Diesel engine costs have been a problem in competing with modern gasoline engines. Regner et al. [15] are updating the opposed-piston diesel engine, solving the historic problems using new materials and modern analytical techniques. Because it has no head or valve train, compared to a standard diesel engine, it has 40 % fewer parts, is 30 % lighter, and costs about 10 % less. Fuel consumption is 15–20 % lower than a state of the art 6.7 l diesel engine, but lube oil consumption and NO_x emissions are about double.

Contrary to HD applications, wherein deNO_x improvements are used to reduce fuel consumption and 98 % deNO_x is desired, modern LD diesel engines do not have as strong a relationship between NO_x and fuel consumption at the higher NO_x levels. In the US, all of the available deNO_x efficiency will be used to meet

the LD NO_x regulations. In Europe, deNO_x efficiencies of 50–70 % are needed to meet the regulations in the most efficient means.

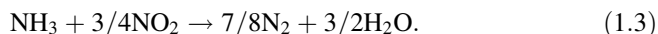
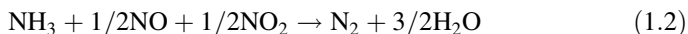
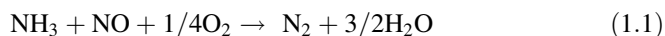
Lean NO_x control (lean deNO_x) technologies will be integral to meeting the emerging HD criteria pollutant regulations for diesel engines. Minimum removal efficiencies on the order of 85 % will be needed, but levels up to 97–98 % are desired to allow engines to operate in high-NO_x low-fuel consumption regimes. For LD applications, the efficiency is as important in the US, but light-off or low-temperature performance characteristics are even more so.

1.4 SCR Technologies

1.4.1 SCR System Introduction

The TWC is the most effective NO_x reduction system on vehicles but requires the absence of oxygen. It has been in production for more than 30 years and is removing more than 99 % of the NO_x from modern engines. In this system, unburned CO and HCs are used to reduce NO_x on a rhodium catalyst. The key to this technology is the gas mixture control. It is critical to have a near-stoichiometric mixture, wherein the mixture of air and fuel are near-ideal and there is very little excess oxygen. If oxygen is present in the exhaust, the CO and HCs will react with it rather than with the NO_x. Diesel engines are lean-burn with plenty of excess oxygen. Practical and effective catalysts for selectively reducing NO_x with CO or HCs in a lean environment are not yet available, but selective catalysts using ammonia as the reductant have been commercialized in the stationary sector for decades.

The key SCR catalyst reactions are shown as



Reaction (1.1) is generally the “standard SCR reaction”. As NO₂ is always present in the exhaust to some extent (maybe 10 % of NO_x), Reaction (1.2) is also pertinent, and is in fact the fastest and preferred NO_x reduction reaction. To promote this “fast SCR reaction” a DOC is commonly used to form more NO₂ over platinum by the following reaction:



If too much NO₂ is produced in the DOC, more than 1:1 = NO:NO₂, then Reaction (1.3) becomes operative. This is undesirable because the “excess” NO₂ can yield N₂O, which is a strong greenhouse gas:

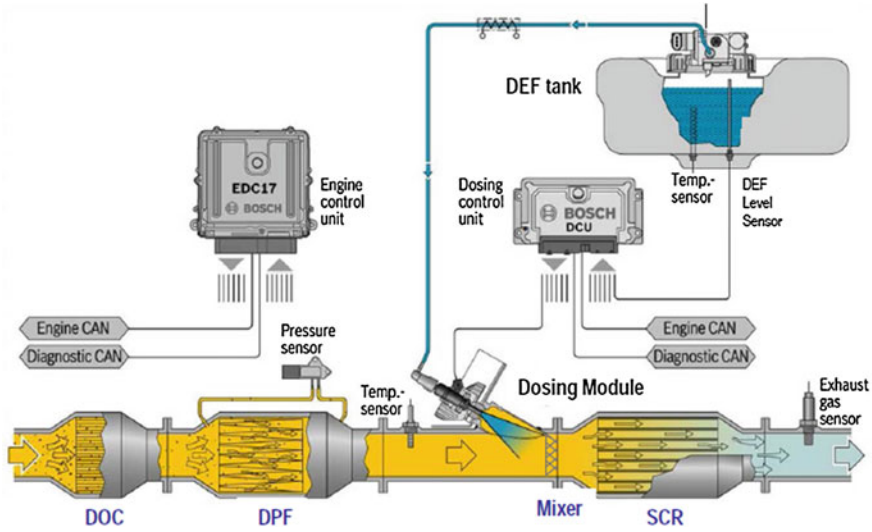
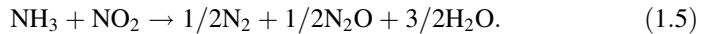
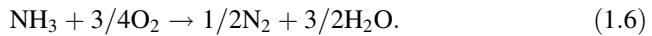


Fig. 1.5 Layout of a DPF + SCR system [16]



If the reactants are not well-mixed, if excess ammonia is injected to obtain high deNO_x efficiencies, or if ammonia stored on the SCR catalyst is released too fast, ammonia emissions can occur. To remediate this, an ASC is utilized:



SCR technology is entering its third or fourth generation since commercial introduction in Europe in 2003. Then, systems were removing upwards of 75 % NO_x over the European HD Transient Cycle to meet Euro IV regulations. To meet the US2010 and emerging Euro VI regulations in 2013, cycle-average deNO_x efficiencies approaching 95 % is realized. Work is continuing in the US to go even higher in efficiency to meet the current and emerging LD NO_x regulations. In both HD and LD applications, targets of 98 % test-cycle deNO_x efficiency are in the scope for future systems.

To achieve this high level of efficiency, all aspects of the system need to be optimized. An SCR system will generally comprise an ammonia delivery system, and the catalyst system itself comprises the DOC (and typically DPF), SCR catalyst, and the ammonia slip catalyst.

Casarella [16] shows the layout of a typical diesel emission control system incorporating the DPF, Fig. 1.5. In the US, the urea solution is referred to as DEF. In Europe, it is referred to as “AdBlue”.

In addition to the SCR catalyst system (DOC, SCR, ASC, mixer) and the DPF, the other main components of the system are the urea delivery system, comprising the storage tank (DEF tank) and sensors, the heated delivery line, pump, and

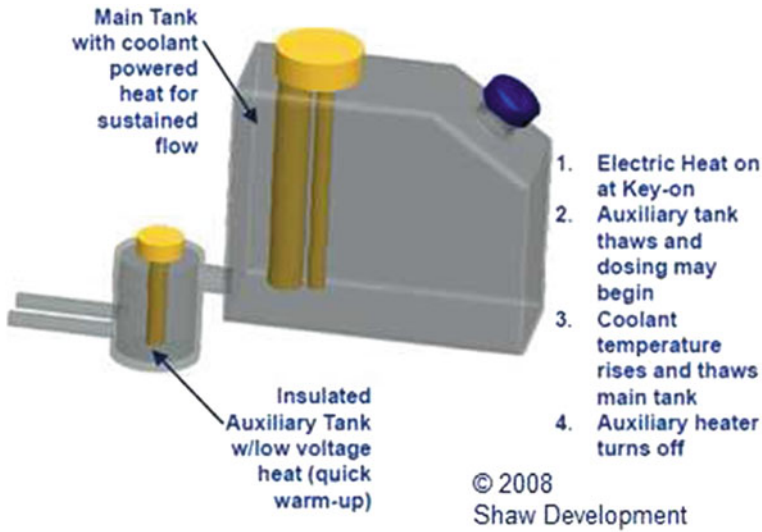


Fig. 1.6 Basic features of the heating system of a urea storage tank [17]

dosing module, including the injector and mixer; and the control system, comprising the sensors, dosing control module, engine control module, and controller area network (CAN) buses.

The following sections will provide more details on these subsystems.

1.4.2 Urea Delivery System

The urea tank, injector, controls, and mixer are significantly engineered systems. Ostertag [17] provides an example of the tank design alone. Figure 1.6 shows the heat-up features and basic designs. Urea is corrosive, so material selection is limited to stainless steel and plastic. Because urea solution (32.5 % urea, balance deionized water) will freeze at $-11\text{ }^{\circ}\text{C}$, the design has to allow for the 7 % expansion upon freezing and for rapid thawing to enable prompt use of the system. Further, internal components like heaters, level and temperature sensors, and fill and extraction lines need to be designed to withstand impact by solids in partially thawed systems. The design shown in Fig. 1.6 has all these components integrated into one unit (in yellow). Finally, and especially for NR applications, the draw point for liquid urea needs to accommodate different vehicle angles of operation.

The urea pump, dosing module, and injectors play a critical role. Designs have migrated from separate pumps and dosing modules to integrated designs [18]; from air-assisted to airless injection; and to systems with no return line. Injectors are designed to disperse fine droplets (20–100 μm mean size) into the exhaust, while minimizing contact with the exhaust pipe to minimize solid by-product formation.

Currently, good extended low-temperature (<200 °C) SCR performance is limited by urea injection issues (evaporation and hydrolysis). Much of this is dependent on good mixing. Improved mixers allow urea injections at temperatures as low as 180 °C, and can result in NO_x reductions of ~30 % over the US cold HD transient cycle relative to no mixer [19]. Alano et al. [20], describe a compact mixer that needs only 75 mm of urea mixing length, compared to 350 mm in some commercial LD SCR systems, enabling the SCR catalyst to be placed closer to the engine for faster heat-up. The mixer achieves a urea mixing index of 0.95 (all cross-section NH₃ measurements are within 5 % of one another) over a range of gas flows, with a maximum increase in back pressure of 0.4 kPa (4 mbar) during accelerations relative to a conventional system. In the closer position, the SCR catalyst got up to 25 °C hotter and achieved 67 % deNO_x efficiency on the NEDC versus 37 % for a catalyst placed further back.

To accomplish the same objective, urea hydrolysis catalysts are emerging. Kröcher et al. [21] show that upwards of eight different decomposition products are emitted from urea upon heating, but with a titania decomposition catalyst, ammonia is produced at temperatures as low as 150–160 °C in model gas with no other unexpected decomposition products.

Urea injection control can be quite complex, but it is migrating from open-loop control based on engine operating parameters and engine-out NO_x predictions, to closed-loop control based on NO_x or urea and temperature sensors. Good urea control also needs to consider the ammonia stored on the catalyst. This will be discussed in detail later.

1.4.3 Alternative Sources for Ammonia and Systems

Although the urea infrastructure is well developed in Europe, Japan, and the US, finding alternative sources for ammonia is still of significant interest to enable SCR catalysts to function better at low exhaust temperatures, decrease the size and cost of the system, and to enable use of the system at very low ambient temperatures. Johannessen [22] updated the developments on a gaseous ammonia system using chloride-based adsorbents. Both HD and LD systems were described showing 100X dosing ranges within 5 % accuracy and <1.5 % deviation in set-point, under a range of exhaust conditions. Start-up units initially draw 550 W in HD, and 250 W in LD applications, but go down to the 100 W range during normal operation. Safety and durability issues appear addressed, and system optimization through testing and simulation is continuing. A European consortia of automotive companies was recently formed to begin standardizing the system and exploring gaps [23]. In tests on the system in challenging low-load urban driving conditions, gaseous ammonia injections started at 100 °C, and 25–83 % deNO_x efficiency was obtained, depending on the amount of ammonia stored in the catalyst. In other reagent studies, Thomas and Highfield [24] describe some early performance data with an ammonium formate and urea system containing 54 % water, versus

67.5 % for standard urea solutions. Advantages include reduced freezing point ($-30\text{ }^{\circ}\text{C}$), better high-temperature storage stability, lower hydrolysis temperature, no polymerization like with urea (fewer or no deposits), and they demonstrated full “drop-in” capability in a urea system on a new diesel pickup truck with an SCR system.

1.4.4 DOC Overview

DOCs play two primary roles in commercial emission control systems:

- (1) Oxidize HCs and CO, either to reduce emissions coming from the engine, or to create exothermic heat used to regenerate a DPF.
- (2) Oxidize NO to NO₂ (Reaction (1.4), above), which is used to continuously oxidize soot on a DPF, and for enhancing the fast SCR deNO_x reactions (Reaction 1.2), particularly at low temperatures.

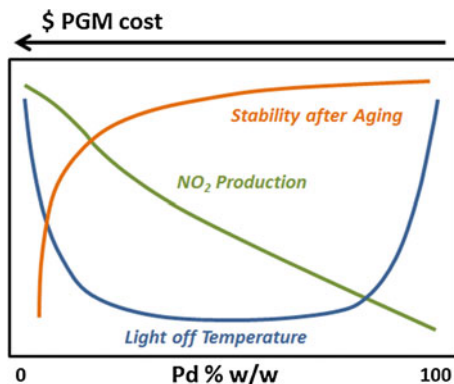
This section will focus on the role of DOCs in SCR systems.

Henry et al. [25] looked at the interplay of the above two functions by using a series of iterative reaction-decoupling experiments to explain interactions between HC and NO oxidation. They show that NO oxidation is inhibited on Pt/Pd due to the reduction reaction with NO₂ by HCs. Long chain alkanes had a more adverse effect than short chain alkenes due to slower oxidation rate with oxygen. Decreasing space velocity was shown to help NO₂ formation in the presence of HCs. Prestoring HCs on the DOC improved NO oxidation up to 300 °C. The interplay of CO and HC removal and NO₂ generation takes another tack as well. Spurk et al. [26] investigated NO₂ coming from a catalyzed DPF for use in a downstream SCR system. Surprisingly, they found the NO₂ coming out of the DOC and going into the DPF is not as important as the HCs coming from the DOC. Essentially, the HCs going into the DPF can interfere with the NO₂ formation in the DPF. The total DPF platinum loading is more important to NO₂ formation than total precious metal loading on the DPF.

Jen et al. [27] showed that platinum can migrate from DOCs (or presumable DPFs) to SCR catalysts, if they are exposed to temperature greater than 670 °C for extended periods of time (16 h). SCR efficiencies can decrease, especially if the DOC is exposed to temperatures greater than 750 °C, as even minute quantities of platinum can cause oxidation of ammonia. These temperatures might be experienced during DPF thermal regenerations. Later, Cavataio et al. [28] showed that if palladium replaces some of the platinum in the DOC, less migration can occur. Although the 2:1 Pt:Pd mixture shows some deterioration in SCR deNO_x efficiency, it is much worse for the Pt-only formulation. Washcoat formulation and/or processing can make a difference, and NO, HC, or CO oxidation is unaffected or enhanced with the Pd additions.

Kim et al. [29] did a systematic study on the effects of varying the Pt:Pd ratio on DOC HC and NO oxidation and durability in a variety of conditions. All bimetallic

Fig. 1.7 Effect of increasing Pd mass fraction respect to Pt content in DOCs. Low Pd % does not significantly affect NO oxidation, but improves catalyst durability and HC oxidation (adapted from Kim et al. [29])



Pt–Pd catalysts show better HC light-off activity and thermal stability than the Pt- or Pd-only catalyst. NO oxidation to NO₂ was found to always depend directly on platinum content, with similar durability trends as with HCs. Figure 1.7 shows a schematic representation of these findings. They found that HC–CO mixtures synergistically have ~20 °C lower light-off temperatures than either one alone.

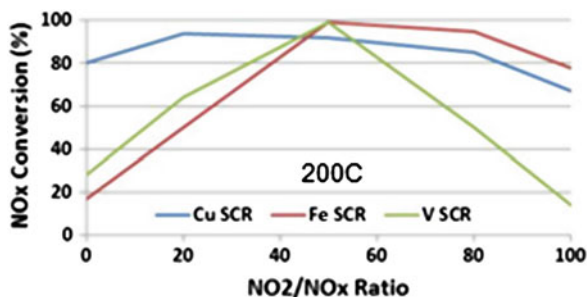
Going further in catalyst cost reduction, Wang et al. [30] developed an NO oxidation catalyst that does not use any precious metal. The manganite-based catalyst drops the optimum NO:NO₂ = 1:1 oxidation temperature about 50–250 °C versus a platinum catalyst. Other manganite catalysts also exhibit CO and HC oxidation characteristics [31].

DOCs can be a major source of the strong greenhouse gas N₂O. Glover and coworkers [32] also did a study on Pt:Pd effects on DOC properties, adding N₂O formation and looking more at fundamentals. CO plays a key role on the overall catalyst performance by its positive effect on propylene oxidation which, in turn, is responsible for NO reduction to N₂O and the onset of NO₂ formation. On the Pt:Pd = 4:1 catalyst, propylene partially reduces NO to form N₂O at about 200 °C, but this temperature shifts to 250 °C when CO is added. The effect of higher Pd concentration on NO conversion is detrimental for NO oxidation to NO₂, but is positive for producing less N₂O, especially at high oxygen concentrations. NO_x storage and release may play an important role in NO₂ formation over the lightly loaded full Pt DOC formulation studied. A 40 g/ft³ (1.4 g/l) bimetal formulation (Pt:Pd = 4:1) is comparable on CO and HC light-off to a 113 g/ft³ Pt formulation. Closing on N₂O formation, Kamasamudram et al. [33] show propylene forms much more N₂O than dodecane (C₁₂H₂₆).

1.4.5 SCR Catalysts

The heart of the SCR system is the SCR catalyst. Three general families of SCR catalysts are in commercial use today: Vanadia, tungsten, copper zeolite, and iron

Fig. 1.8 Sensitivity of SCR catalyst deNO_x performance inlet NO₂ content at 200 °C [34]



zeolite. Walker [34] recently summarized the main characteristics of each of these catalysts.

Copper zeolite has the best low-temperature performance and its steady-state performance shows very little sensitivity to NO₂ concentration. However, it is susceptible to sulfur poisoning and requires an occasional high-temperature cleaning step (>500 °C; Tang et al. [35]) to thermally remove the contaminants. Copper zeolites have markedly improved in the last couple of years, making them the preferred catalyst for high-performing systems.

Iron zeolite has the best HT temperature performance, but NO₂ management of the inlet gas is needed for improved LT performance. As such, system precious metal usage on the DOC is higher. Fe-zeolites show no sulfur poisoning but moderate HC poisoning is observed, minimizing the HT cleaning step.

Vanadia is the cheapest of the catalysts, but has poor HT durability (deteriorates at 550–600 °C), and thus cannot be utilized in systems that have a DPF that requires active regeneration ($T > 650$ °C). As with iron zeolites, the LT performance strongly depends on NO₂ availability.

Figure 1.8 shows the sensitivity of the three types of catalysts to the inlet NO₂/NO_x ratio at 200 °C, wherein copper zeolite shows superior LT deNO_x performance with no or little NO₂ in the gas. However, in a standard system with a DOC for HC control that will also oxidize NO to NO₂ for optimum performance, vanadia performs similarly to copper zeolite in the temperature range of 225–275 °C, but iron zeolite is inferior. Copper zeolite almost as well as Fe zeolite are at temperatures higher than this.

SCR catalyst formulations and design are improving both low- and high-temperature performance through better dispersion of the cation in the zeolite and with much more durable zeolite structures. HC and sulfur poisoning effects are becoming better understood and controlled, for example, through better modeling of deterioration and more restrictive zeolite cages that keep most HCs from entering the catalyst structure.

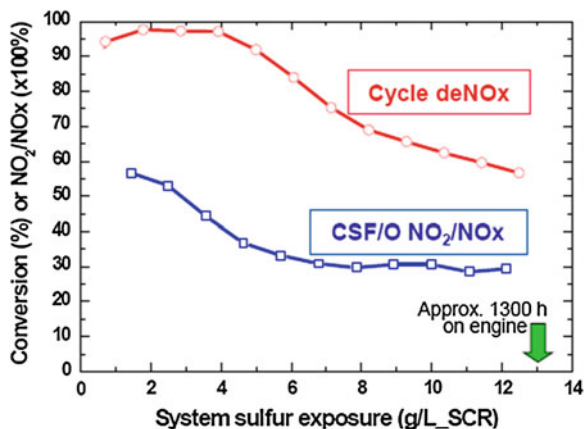
Vanadia SCR catalysts are used in Europe, the emerging markets, and in some agricultural applications in the US, but not in Japan due to durability issues related to thermal exposure when DPFs are regenerated. Advances are now reported [36] on vanadate SCR catalysts that have no volatility up to 750 °C or higher, versus 550–600 °C for some commercial catalysts, giving them similar HT durability to

zeolites. DeNOx performance at 250 and 350 °C is 5–10 points better after HT aging (>700 °C) than for a benchmarked commercial catalyst, but less severely aged catalysts have lower efficiencies than the base catalyst. Walker [37] reports that new Cu-zeolite formulations now sustain aging to 900 °C and form less N₂O. Narula et al. [38] show that it is possible to modify zeolite structures systematically to influence the electron density at metal centers, and to provide ammonia bonding sites in the vicinity of the metal centers. They replaced alumina in the structure with several trivalent cations. In another contribution [39], they showed that chemical mixtures of copper and iron zeolites can improve LT performance over than copper alone, and when lanthanum is added to the binary formulation performance is improved further.

HC poisoning is an issue for both Cu- and Fe-zeolites. HCs can accumulate at the lower temperatures, and then ignite at the higher temperatures, causing thermal deterioration of the catalyst. Prikhodko et al. [40] quantified HC adsorption for state of the art Cu- and Fe-zeolites. They show that Fe-zeolite adsorb upwards of 5–10 times more HCs than Cu-zeolite, but the Cu-zeolite oxidizes a higher percentage upon release. The authors show that both types adsorb more HCs in PCCI combustion mode (premixed charge compression ignition) than in conventional diesel combustion mode due to changes in HC speciation. Cu-zeolites are more susceptible to both HC uptake and generation of oxidation exotherms. This is more significant for LD applications wherein PCCI mode is used more, and more time is spent at lower temperatures. Luo et al. [41] studied the effects of propylene (C₃H₆) and dodecane (n-C₁₂H₂₆) exposure on the SCR performance of two Cu-exchanged zeolite catalysts, one was a state of the art Cu-zeolite with relatively small pores (unspecified type), and the other was a standard Cu-BEA zeolite with somewhat larger pores. The small-pored sample was completely unaffected by dodecane at temperatures lower than 300 °C, and only slightly inhibited (less than 5 % conversion loss) by propylene. With the standard catalyst at 150 °C, no propylene inhibition was noted due to oxidation of the HC; but at 300 °C, both oxidation intermediates and coke formation led to deactivation. Dodecane inhibition was observed over the whole temperature range by strong HC adsorption blocking of pores and active catalyst sites. The small pores in the state of the art sample do not allow the diffusion of large HC molecules into the pores that hinder adsorption onto active sites. Han et al. [42] showed that low-temperature performance and reduced HC effects can be achieved if a ceria oxygen storage catalyst is layered on top of an iron zeolite catalyst. The catalyst helps urea decomposition, thus improving the low-temperature deNOx capability from 32 to 58 % at 200 °C an LD steady-state test. After 8 h of exposure to high HC levels from a burner, the layered catalyst maintained a deNOx efficiency of 80 % at 240 °C, while the original version was only at 60 % under the same conditions due to HC poisoning.

On sulfur poisoning, Tang et al. [35], used SO₂ exposure levels equal to those obtained with ultra-low sulfur diesel fuel (<15 ppm sulfur), and show that copper zeolite catalyst started losing deNOx efficiency after about 400 h of operation at temperatures of 200–300 °C. These results are shown in Fig. 1.9. Through 1,300 h of operation, the catalyst had deteriorated continuously from 98 % deNOx

Fig. 1.9 DOC + CSF begins deteriorating after about 250 h of operation in “deratd FTP” testing (200–350 °C) simulating fuel with 15 ppm sulfur. Four g/l sulfur is roughly 400 h of operation in the simulation that uses 35 ppm SO₂. Cu-zeolite deteriorates after 400 h [35]



efficiency to 60 % efficiency. Also, the NO₂:NO_x ratio from the filter deteriorated from 0.60 to 0.30 during the first 600 h, but then remained the same. They found that most of the sulfur was in the top layer of washcoat in the first third of the catalyst. Most of the poisoning was attributed to ammonium sulfate, which comes off at 400–500 °C, and to a much lesser extent, copper sulfate, which comes off at 500–850 °C. When heated to 500 °C, the SCR catalyst performance recovered, and this was done every 700 h of operation at the lower temperatures.

Regarding the SCR catalyst substrate support, today, SCR substrates generally have 300 and 400 cells/square inch (300- and 400-csi). Heibel [43] showed that in the mass transfer controlled regime (230–350 °C), 600-csi substrates react 35 % faster than 400-csi catalysts. Substrates with higher cell densities are being evaluated in advanced programs for improved deNO_x performance.

SCR catalyst systems will age, and this needs to be understood for good performance over the full useful life of the catalysts. Bartley et al. [44] describe NH₃ storage capacity measurement data as a function of SCR catalyst aging time and temperature. The researchers modeled the aging using first principle Langmuir adsorption isotherms. These data can be used in model-based control algorithms to calculate the current NH₃ storage capacity of an SCR catalyst operating in the field, based on time and temperature history.

The US Environmental Protection Agency (EPA) capped nitrous oxide (N₂O) emissions in both the LD and HD greenhouse gas rules, so much work is being done to understand its sources. Kamasamudram et al. [33] show that N₂O is very stable, and forms by three mechanisms in an SCR catalyst:

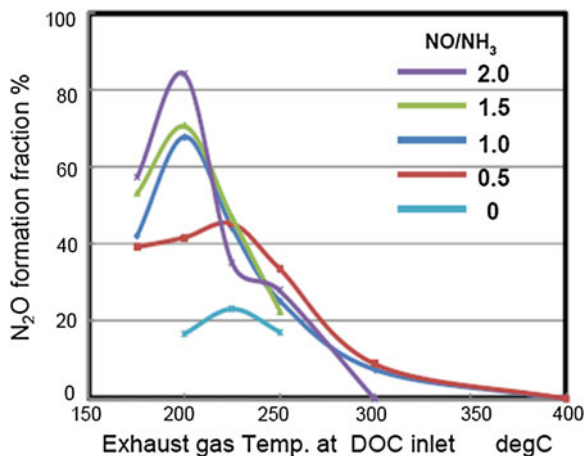
- LT ($T < 250$ °C) decomposition of ammonium nitrate by the reaction:



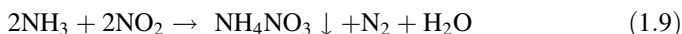
- HT oxidation of ammonia by copper zeolites by the reaction:



Fig. 1.10 Nitrous oxide formation in ammonia slip catalysts is promoted by high NO:NH₃ ratios coming out of the SCR catalyst [45]



- Reaction of excess NO₂ (>50 % of NO_x) to form ammonium nitrate by the reaction:

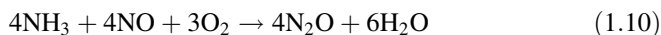


Ammonium nitrate then immediately decomposes by Reaction (1.7) at temperatures greater than 200 °C.

Kamasamudram et al. [33] show that increasing copper loading in the Cu-zeolite SCR catalyst can decrease N₂O formation by the first two mechanisms, and better DOC design and control can prevent the third mechanism. The investigators show that it is possible to reduce N₂O to nitrogen, but these reactions occur at much higher temperatures than those at which they are formed.

1.4.6 Ammonia Slip Catalysts

In high performing SCR systems, excess ammonia is injected to make sure ammonia and NO_x are present together at the catalyst for high conversion efficiency. Some unreacted ammonia may pass through the catalyst, so ammonia slip catalysts are needed. The catalysts can have good selectivity to nitrogen, but these catalysts can also form N₂O. Matsui et al. [45] show in Fig. 1.10 that upto 80 % of the ammonia going into the slip catalyst can convert into N₂O if there is also a relatively high amount of NO (2X vs. NH₃); the reaction is,



A high NO:NH₃ ratio coming out of the SCR catalyst can occur, for example, if there is poor urea mixing prior to entering the SCR catalyst, and urea is injected at less than stoichiometric requirements, or if ammonia is partially oxidized

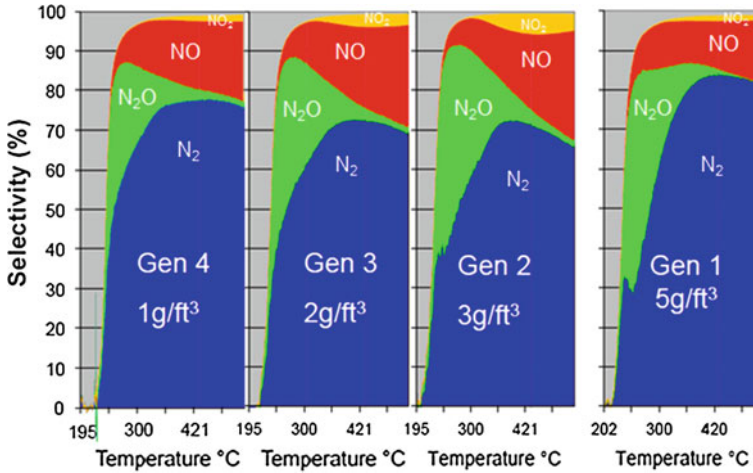


Fig. 1.11 Generational improvements in ammonia slip catalysts. Early improvements dropped cost with minor compromise in selectivity. The latest generation recovers the performance with greatly reduced precious metal loading [34]

(by Cu-zeolite, for example) to form NO. Kamasamudram et al. [33] show that slip catalysts with lower precious metal content minimize N_2O formation.

Ammonia slip catalysts are improving in terms of cost and selectivity to nitrogen. Figure 1.11 from Walker [34] shows modern catalysts have similar performance to the first generation catalysts, but with only 20 % of the platinum loading. The latest catalyst has much better selectivity to nitrogen with less undesirable by-products, yet with half the precious metal of its predecessor. Formation of NO and NO_2 is still an issue but improving.

1.5 SCR System Design

Many new SCR systems designs are emerging to meet the tightening cold start and deNOx efficiency requirements under low-load urban driving conditions.

For LD applications, Holderbaum and Kwee [46] evaluated the placement of the SCR relative to the DPF. Considering the added fuel needed to heat the SCR system for cold start, and to regenerate the DPF with different frequencies due to changes in passive NO_2 regeneration, the authors conclude that for an 1,800 kg car with a 2-l engine, if cold starts occur more frequently than once every 60 km, it is better to place the SCR in front of the DPF. Figure 1.12 shows some results. Note that the 60 km threshold is greater than the distance used in certification cycles, wherein placing the SCR behind the DPF incurs a 2 % fuel penalty versus a front placement. The forward SCR placement aids European certification for both CO_2 and NOx emissions.

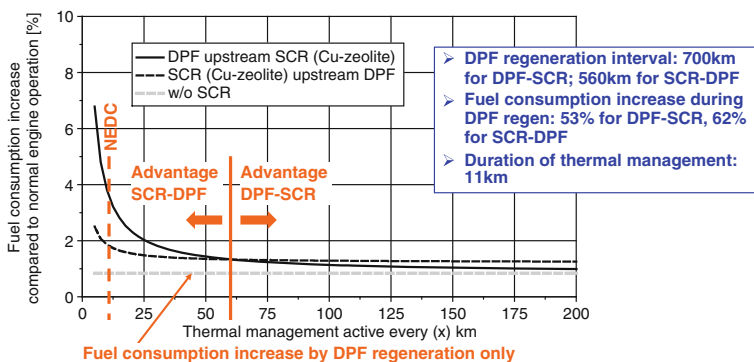
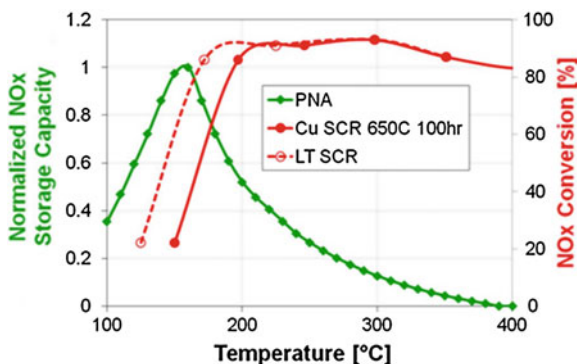


Fig. 1.12 Considering fuel consumption for heating and regenerating the system, placing the SCR in front of the DPF in light-duty applications is beneficial if there is less than 60 km between cold starts [46]

Fig. 1.13 An upstream passive NOx adsorber (PNA) captures NOx generated at $T < 150$ °C. A LT urea-SCR catalyst can then convert this NOx upon release at $T > 150$ °C [47]



For US LD diesels, removing cold start NOx emissions are key to meeting the tailpipe emissions regulations. A new combination NOx adsorber and SCR catalyst configuration was shown by Henry et al. [47, 48]. Figure 1.13 shows some performance characteristics and the concept when coupled with an SCR catalyst. The system consists of an upstream PNA that might capture 65 % of the NOx at temperatures less than 150 °C, and then passively releases it at temperatures greater the 150 °C. At these temperatures, a copper zeolite is just becoming active and can reduce some of this released NOx. The technology enables NOx reductions of about 15 mg/mile (24 mg/km) on the US LD FTP cycle. Walker [34] reported on improvements in the PNA wherein stored NOx is held up to 250–300 °C.

Work is continuing on the combination SCR + DPF system, wherein SCR catalyst is coated onto the DPF. This allows SCR catalyst to be placed on the vehicle without using an added component, and can get the SCR catalyst closer to the engine for faster light-off. Numerous reports dating to 2008 show that total NOx removal efficiency is thus improved, with little to no compromise in DPF

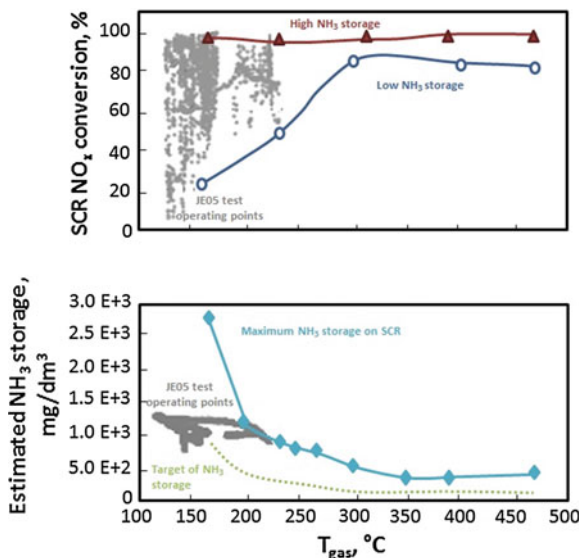
regeneration. Walker [34] and Folic and Johansen [49] show that passive DPF regeneration with NO_2 is adversely impacted by adding SCR catalyst to the DPF, but still occurs and can be managed. Tan et al. [50] found that DPF regeneration calibration needs to be adjusted to longer times or higher temperatures to get the same cleaning performance as the base DPF system. They also showed a new issue when soot is accumulated on the DPF + SCR: Ammonia storage capacity decreases for fresh samples at all temperatures and soot loadings tested (200–350 °C, 1.0–2.5 g/l), but is not affected by soot loading for aged samples (except at 200 °C). Loss of ammonia storage capacity impacts SCR performance at 200 °C, but not at 300 °C at a soot load of 2 g/l. Schrade et al. [51] demonstrated the opposite effect of soot on ammonia storage capacity, so this is still an open question. They also report that soot on the DPF can help deNOx functionality if the NO_2 content is higher than optimal, but hinders it if the NO_2 is lower. The soot will be oxidized by NO_2 , resulting in lower levels getting to the underlying SCR catalyst. Folic and Johansen [49] also looked at the relationship between filter porosity, SCR catalyst deNOx efficiency, and back pressure. With all filters, there was an optimum back pressure versus deNOx performance, wherein generally they both increase together, but at higher catalyst loadings, the deNOx efficiency can decrease with increasing back pressure. Filters with >60–65 % porosity have better deNOx performance at a given back pressure than filters with <60 % porosity.

Urea injection parameters are determined by NOx quantity in the exhaust (concentration and flow rate), temperature, and the amount of ammonia stored in the catalyst. There is normally closed-loop feedback control using an NOx sensor at the SCR exit, and in many applications, an NOx sensor is used upstream to determine inlet NOx levels.

As urea generally cannot be injected at temperatures less than 180 °C due to evaporation and hydrolysis kinetics, it is important to properly manage ammonia storage in the catalyst for low-load applications. Murata et al. [52] show that SCR efficiency at temperatures <265 °C is strongly dependent on the amount of ammonia that is stored in the catalyst. They developed an algorithm that kept stored urea within control limits, resulting in improved deNOx efficiency, from nominally 50–75 % in the Japanese HD transient cycle with an average temperature of only 160 °C. The concept is shown in Fig. 1.14.

Another approach to managing the stored ammonia for improved low-temperature performance is described by Yasui et al. [53] and illustrated in Fig. 1.15. They use two Fe-zeolite SCR catalysts placed downstream from the DPF system. An ammonia sensor is placed between the two SCR catalysts, and ammonia is generously injected to keep the first catalyst loaded at all times, as conditions allow. This accomplishes two goals. First, the efficiency of the SCR system is improved as there is plentiful ammonia present in the system. More importantly, the strategy helps cold start management. In traditional cold start thermal management, the SCR catalyst is heated as fast as possible to get it . Here, the catalyst is always loaded with ammonia, and the catalyst is heated slowly to prevent rapid release of ammonia during this period.

Fig. 1.14 Key controlling parameters in algorithm for the use of stored ammonia. An adsorption model is used to define a desired range of stored ammonia. Ammonia release is conveniently predicted for SCR NO_x conversion (Adapted from Murata et al. [52])



1.6 Onboard Generation of Ammonia Using Lean NO_x Traps

LNT is a very different deNO_x concept from SCR, and is a favored approach for smaller vehicles. But it is also being used in conjunction with SCR catalysts, so a few comments are warranted here. The LNT adsorbs NO_x as an alkaline earth nitrate (baria, potassia) during lean operation. Eventually the capacity to efficiently adsorb NO_x is reached, and the LNT is regenerated with a periodic migration to a rich exhaust gas. The nitrate decomposes, and the released NO_x is reduced by CO and HCs on a rhodium catalyst in the absence of oxygen, as in a three-way catalyst. The lean-rich periods are nominally 30–90 s lean and 2–6 s rich, but this can vary tremendously depending on driving conditions. During the brief rich period, ammonia is formed and can be captured in a downstream SCR catalyst, and used for additional NO_x reduction during the lean period.

The first LD diesel sold in the US to meet recent tailpipe regulations had the BlueTec™ 1 emission control system, utilizing an LNT followed by an SCR catalyst. The unique system used the rich cycle of the LNT to generate ammonia, which was captured and used by the downstream SCR for lean NO_x reduction. Weibel et al. [54] reported that ammonia selectivity increases with aging and rich period, and decreases with increasing the air/fuel ratio (λ). Under conditions of $\lambda = 0.88$ and rich periods of 5 s (180 s lean), ammonia selectivity is greater than 70 % in the temperature range of 225–350 °C for all aging tests temperatures greater than 600 °C and 50,000 miles. The SCR adds about 20 % deNO_x efficiency over an LNT-only configuration.

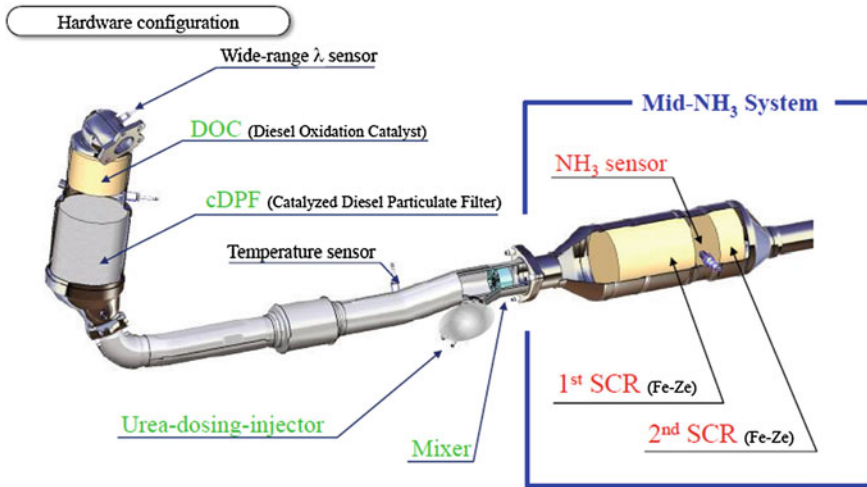


Fig. 1.15 Layout of a new LD SCR system incorporating two SCR catalysts with an ammonia sensor in between. The first catalyst is kept loaded with ammonia, as indicated by the sensor [53]

Theis et al. [55] reported on an interesting study whereby they alternated LNT and SCR slices in one can to check the effect of NO_x, ammonia, and HC distribution on deNO_x performance. The system performance improved as the number of alternating slices of the LNT and SCR increased, keeping the total volume constant. The deNO_x efficiency for the eight segment system (four pairs of LNT and SCR catalysts) was 81 % in a reference test at 275 °C, versus 78 % for four segments and 60 % for two segments. The reference single LNT with no SCR catalyst had only 30 % deNO_x efficiency. The authors also show reduced N₂O, NH₃, HC, and CO emissions with the segmented systems. Various dynamics are operative, but the segmented systems tend to better-match the NO and ammonia concentrations in the SCR, and alternating SCR slices better-adsorb HCs for enhanced utility. Harold et al. [56] went a step further, and layered the SCR catalyst on top of the LNT catalyst. Relative to an LNT alone, the layered combination reduced 25 % (absolute) more NO at 200 and 250 °C with very high selectivity to nitrogen (95 %+) compared to 30–75 % for the LNT alone. Further, they added ceria to the LNT formulation in the back zone of the catalyst to achieve better low-temperature performance due mainly to improved water–gas shift reaction and additional LT NO_x storage.

Xu et al. [57] reported vehicle and laboratory testing on a second-generation LNT + SCR system. The DOC + LNT + SCR + DPF system was installed on a prototype F-150 pickup truck (2,610 kg, 4.4 l V8, turbo-diesel). The aged system (64 h, 750 °C) reduced NO_x by 96 % to 13.5 mg/mile, and HC emissions were 14 mg/mile (–99 %), bringing the vehicle to within the emerging California Low Emission Vehicle 3 (LEVIII) limit values (30 mg/mile HC + NO_x) on the standard certification test cycle. The laboratory work focused on HC reductions from

the system. The SCR component reduced HCs about 75 %, mainly by adsorption under rich conditions and oxidation under lean conditions. Cavataio et al. [58] compared this capability to that of a urea-SCR system for meeting the US EPA Tier 2 Bin 2 (or California LEVIII fleet average) standards. Although the LNT + SCR system is 18 % smaller it had met the target emissions, while the SCR system fell short. Further, the LNT + SCR system is estimated to be slightly cheaper, but has most of the cost tied up in precious metal (with its inherent price volatility). On the downside, the fuel penalty was high at 10 %, versus 2 % for the SCR system. Also, sulfur management of the LNT + SCR system was not considered.

Although the LNT + SCR system has not been commercialized since being used on the 2009 Mercedes Benz E320 in the US, it is still generating significant interest and we may see its renewed adaption as understanding and performance improves. It is quite possible that lean-gasoline applications will use a version of the technology, perhaps with a TWC instead of an LNT. NO_x emissions are too high to make urea-based SCR as attractive as it is for diesel, and reports are surfacing that are attractive [59, 60].

1.7 Outlook

SCR is the leading lean deNO_x technology today. SCR was first introduced tested on trucks in the mid-1990s. The deNO_x efficiency was about 50–60 % and the swept volume ratio (SCR catalyst/engine displacement) was about 6:1. Today, we are entering the fourth generation of commercialized SCR catalysts, and NO_x emissions dropped 90 % using a system half the size. An analogy might be used for the three-way catalyst in the mid-1990s. At that time it was in its third or fourth generation. Today, 15 years later, modern TWCs have 95 % lower emissions and 70 % less precious metal. There is still plenty of opportunity for improvement in the SCR system.

One significant opportunity is improving low-temperature performance. Areas for improvement are delivering ammonia at temperatures down to 100 °C, understanding and improving ammonia storage in the catalysts, and improving the low-temperature NO_x reduction activity of the catalyst.

Another opportunity is in understanding and improving how SCR catalyst systems age. In HD applications the catalyst may need to operate for a million kilometers. Thermal aging and poisoning need to be better understood to allow tighter control and high deNO_x efficiency throughout the useful life.

There is much emerging opportunity in size reduction through consolidation of components. Engines in all applications will go lean and need deNO_x. Many of these, such as smaller cars and NR applications (tractors, small construction equipment), do not have much space for large systems. Illustrated above, consolidation of the SCR and DPF can save space and cost with little compromise in

performance. TWCs today are layered and zoned, and Harold et al. [56] show the potential of extending this approach to SCR systems.

Perhaps the most significant consideration going forward will be on CO₂ reductions. New fuels and combinations will be used, exhaust temperatures will drop, and the charges will be lean. NO_x emissions regulations will not loosen, and are showing signs of tightening again. SCR will be a vital technology to address these future challenges.

1.8 Conclusions

1.8.1 Regulations and Engine Technologies

Tightening mobile NO_x regulations are driving lean deNO_x control, especially in the HD sector, but also in the US and Japanese LD diesel market, and soon in Europe. HD engine fuel consumption can benefit significantly by running at high engine-out NO_x. DeNO_x efficiencies of 98+ % can have significant advantages in fuel consumption and less engine hardware (EGR). In the LD sector, this level of deNO_x efficiency is needed to meet the US regulations, with the main opportunity in reducing cold start emissions. Although most European LD diesels can meet the emerging Euro 6 regulation without NO_x aftertreatment, it is desired to reduce NO₂ emissions and save fuel through higher NO_x engine calibrations. Urea-SCR is the leading approach in all segments, and is accomplishing deNO_x efficiencies of 95 % with reasonable systems and temperature ranges.

1.8.2 Onboard Ammonia Delivery Systems and SCR Catalyst Systems

Urea-water solutions are the only commercialized source for ammonia for SCR systems. This requires an onboard urea storage and injection system. These are highly engineered systems to provide for the freezing of urea, and monitoring and pumping it for injection. Injection temperatures are limited to about 180 °C due to deposit formation, but hydrolysis catalysts are evolving to drop this temperature. Urea-exhaust mixers are critical to get good SCR performance. Gaseous ammonia systems are in development, enabling ammonia injection down to 100 °C.

Much of the new reports on DOCs concern the interplay of precious metal formulations on cost reduction, HC oxidation, NO oxidation to NO₂, and the formation of N₂O. HC and CO oxidation is promoted by replacement of platinum with palladium, but NO₂ formation is compromised. NO₂ cannot form if HCs are present, as the HCs will reduce any NO₂ back to NO. HCs are also instrumental in reducing NO to N₂O, particularly at ~200–250 °C if CO is not present.

Commercial SCR catalysts fall into three types: vanadia, copper zeolite, and iron zeolite. Copper zeolite is the best performing across the temperature range and has excellent thermal durability. Vanadia catalysts are the lowest cost, and can perform well at low temperatures but need good NO₂ management, as do iron zeolites. Iron zeolites have the best high-temperature performance. Much effort is being put on understanding and improving durability. Vanadia systems deteriorate at high temperature (>550 °C), but are not sensitive to sulfur poisoning. Copper zeolite needs to be periodically desulfated at >500 °C, and both copper and iron zeolites are susceptible to HC poisoning. N₂O formation in the SCR system is under much investigation now. Ammonia storage and management is critically important for good low-temperature performance and much progress is being made in this regard.

Emerging systems design includes consolidation of the SCR and DPF into one unit. Impacts on deNO_x efficiency are minimal, but passive DPF regeneration with NO₂ is reduced. PNA are emerging. They adsorb NO_x at low temperatures and then passively release the NO_x, upon further heating. They can be coupled with appropriate SCR catalysts for much-improved LT performance. Some effort is being made on generating ammonia onboard using lean NO_x traps (LNTs), with preferences migrating to putting the LNT and SCR in closer proximity to one another (sequential slices or layering on the same catalyst).

1.8.3 Outlook

The outlook is optimistic that SCR systems will achieve 98+ % deNO_x efficiency. Emerging issues are related to improved low-temperature performance, enhanced durability, and reduced size and cost.

References

1. Johnson, T. V. (2012) Diesel Emissions in Review, SAE Int. J. Engines, May 2012 5:216–234; doi:[10.4271/2012-01-0368](https://doi.org/10.4271/2012-01-0368).
2. Johnson, T. V. (2011) Diesel Emissions in Review, SAE Int. J. Engines, June 2011 4:143–157; doi:[10.4271/2011-01-0304](https://doi.org/10.4271/2011-01-0304).
3. Johnson, T. V. (2010) Review of Diesel Emissions and Control, SAE Int. J. Fuels Lubr. August 2010 3:16–29; doi:[10.4271/2010-01-0301](https://doi.org/10.4271/2010-01-0301).
4. Stanton, D. (2012) Diesel Engine Technologies to Meet Future On-Road and Off-Road US EPA Regulations, presentation at 4th CTI International Conference, NO_x Reduction, Current and Future Solutions for On-Road and Off-Road Applications, Detroit, June 19–20, 2012.
5. Roberts, C. (2011) The Pursuit of High Efficiency Engines-SwRI Programs, presentation at the Emissions 2011 Conference, Ann Arbor, MI, June 2011.
6. Stanton, D. (2009) Technology Development for High Efficiency Clean Diesel Engines and a Pathway to 50% Thermal Efficiency”, presentation at US Department of Energy, Directions in Engine Efficiency and Emissions Research (DEER) Conference, September 2009, Detroit.

7. Zybell, J. G. (2011) Technology Path to Meet Future Fuel Economy Targets in the CV Segment, presentation at Integer Diesel Emissions Conference and DEF Forum, Atlanta, October 2011.
8. Kobayashi, M., Aoyagi, Y., Adachi, T., Murayama, T., Hashimoto, M., Goto, Y., Suzuki, H. (2011) Effective BSFC and NO_x Reduction on Super Clean Diesel of Heavy Duty Diesel Engine by High Boosting and High EGR Rate, SAE Technical Paper 2011-01-0369, doi:[10.4271/2011-01-0369](https://doi.org/10.4271/2011-01-0369).
9. de Ojeda, W. (2011) Development and Demonstration of a Fuel-Efficient HD Engine (Dept of Energy Supertruck Program), presentation at US Department of Energy, Directions in Engine Efficiency and Emissions Research (DEER) Conference, October 3–6, 2011, Detroit.
10. Vermeulen, R., Vonk, W., and Dekker, H. (2011) Real-World Exhaust Gas Emissions of a Prototype N3 Heavy Duty Vehicle with Euro VI Technology, TNO Technical Report TNO-RPT-2011-00076, 27 October 2011.
11. Pischinger, S. (2011) Efficient Powertrain Technology for the Future, keynote presentation at the Symposium on International Automotive Technology 2011, Pune, India, January 2011.
12. Popuri, S., Langenderfer, D., Cunningham, M., Vajapeyazula, P., Garimella, P., Joshi, A., Cecil, A., Frazier, T., and Stanton, D. (2011) Demonstration of > 10% FTP75 Cycle Efficiency Improvement for a Light-Duty Diesel Engine System at T2B5 Tailpipe Emissions Levels, presentation at SAE Light-Duty Diesel Emissions Symposium, Detroit, November 2011.
13. Ruth, M. (2012) Cummins' Next Generation Tier 2, Bin 2 Light Truck Diesel Engine, presentation at the US Department of Energy Directions in Engine Efficiency and Emissions Research (DEER), Dearborn, MI, October 2012.
14. Balland, J., Schreurs, B., Hardam, H., Yasui, Y. (2012) A New Clean Diesel Concept for US LEV III SULEV - Advanced Air/Fuel Control for NO_x Reduction and for SCR Heat Up, presentation at 4th IAV MinNO_x Conference 12–13 June 2012, Berlin.
15. Regner, G., Herold, R. E., Wahl, M. H., Dion, E., Redon, F., Johnson, D., Callahan, B. J., and McIntyre, S. (2011) The Achates Power Opposed-Piston Two-Stroke Engine: Performance and Emissions Results in a Medium-Duty Application, SAE Technical Paper 2011-01-2221, doi:[10.4271/2011-01-2221](https://doi.org/10.4271/2011-01-2221).
16. Casarella, M. (2011) Urea Dosing Systems and Controls for Light Duty Diesel Applications, presentation at SAE Light-Duty Diesel Emissions Symposium, Ypsilanti, MI, November 2011.
17. Ostertag, M. (2008) Urea Reservoir Systems for Off-Highway and Heavy Duty Market, presentation at CTI NO_x Reduction Forum, December 2008, Detroit.
18. Needham, D., Spadafora, P., Schiffgens, H. J., Kirwan, J. E., Cabush, D. D., Kalina, A. (2012) Delphi SCR Dosing System – An Alternative Approach for Close-Coupled SCR Catalyst Systems, proceedings of 21st Aachen Colloquium Automobile and Engine Technology October 2012, Aachen, Germany.
19. Zhan, R., Li, W., Eakle S. T., Weber, P. A. (2010) Development of a Novel Device to Improve Urea Evaporation, Mixing and Distribution to Enhance SCR Performance, SAE Technical Paper 2010-01-1185, doi:[10.4271/2010-01-1185](https://doi.org/10.4271/2010-01-1185).
20. Alano, E., Jean, E., Perrot, Y., Brunel, J.-P., Ferrand, N., Ferhan, M., Chapel, J., and Pajot, K (2011) Compact SCR for Passenger Cars, SAE Technical Paper 2011-01-1318 doi:[10.4271/2011-01-1318](https://doi.org/10.4271/2011-01-1318).
21. Kröcher, O., Elsener, M., Mehring, M., Bernhard, A. (2010) Highly-Developed Thermal Analysis Methods for the Characterization of Soot and Deposits in Urea-SCR Systems, in AVL 6th International Exhaust Gas and Particulate Emissions Forum, March 2010, Ludwigsburg, Germany.
22. Johannessen, T. Next Generation SCR System for Fuel-Efficient NO_x Reduction, presentation at SAE Light-Duty Diesel Emissions Symposium, Detroit, November 2011.
23. Hansen, K. F., Hägg, A., Stenfeldt, M., Lepage, M., Lafossas, F. A., Yasui, Y., Fischer, M. (2012) Solid Ammonia Storage for Third Generation SCR, presentation at the IAV MinNO_x Symposium, June 2012, Berlin.

24. Thomas, D., and Highfield, T. (2011) Ammonium Formate/Urea Based Diesel Exhaust Fluid for Superior Low Temperature SCR Performance, presentation at SAE Light-Duty Diesel Emissions Symposium, Detroit, November 2011.
25. Henry, C., Currier, N., Ottinger, N., Yezerets, A., Castagnola, M., Chen, H.-Y., and Hess, H. (2011b) Decoupling the Interactions of Hydrocarbons and Oxides of Nitrogen over Diesel Oxidation Catalysts, SAE paper 2011-01-1137, doi:[10.4271/2011-01-1137](https://doi.org/10.4271/2011-01-1137).
26. Spurk, P., Frantz, S., Schütze, F. W., Noack, H. D., Müller, W. (2010) NO₂ Formation on the DOC/DPF System – A System Thought, in AVL 6th International Exhaust Gas and Particulate Emissions Forum, March 2010, Ludwigsburg, Germany.
27. Jen, H.-W., Girard, J. W., Cavataio, G., Jagner, M. J. (2008) Detection, Origin and Effect of Ultra-Low Platinum Contamination on Diesel-SCR Catalysts, SAE paper 2008-01-2488, doi:[10.4271/2008-01-2488](https://doi.org/10.4271/2008-01-2488).
28. Cavataio, G., Jen, H.-W., Girard, J. W., Dobson, D., Warner, J. R., Lambert, C. K. (2009) Impact and Prevention of Ultra-Low Contamination of Platinum Group Metals on SCR Catalysts Due to DOC Design, SAE Technical Paper 2009-01-0627, doi:[10.4271/2009-01-0627](https://doi.org/10.4271/2009-01-0627).
29. Kim, C. H., Schmid, M., Schmiege, S. J., Tan J., and Li, W. (2011) The Effect of Pt-Pd Ratio on Oxidation Catalysts Under Simulated Diesel Exhaust, SAE paper 2011-01-1134, doi:[10.4271/2011-01-1134](https://doi.org/10.4271/2011-01-1134).
30. Wang, W., McCool, G., Kapur, N., Yuan, G., Shan, B., Nguyen, M., Graham, U. M., Davis, B. H., Jacobs, G. Cho, K., Hao, X. (2012) Mixed-Phase Oxide Catalyst Based on Mn-Mullite (Sm, Gd)Mn₂O₅ for NO Oxidation in Diesel Exhaust, *Science* 337, 832 (2012), doi:[10.1126/science.122509](https://doi.org/10.1126/science.122509).
31. Ishizaki, K., Mitsuda, N., Ohya, N., Ohno, H., Naka, T., Abe, A., Takagi, H., Sugimoto, A. (2012) A Study of PGM-Free Oxidation Catalyst YMnO₃ for Diesel Exhaust Aftertreatment, SAE Technical Paper 2012-01-0365, doi:[10.4271/2012-01-0365](https://doi.org/10.4271/2012-01-0365).
32. Glover, L., Douglas, R., McCullough, G., Keenan, M., Revereault, P., and McAtee, C. (2011) Performance Characterization of a Range of Diesel Oxidation Catalysts: Effect of Pt:Pd Ratio on Light Off Behavior and Nitrogen Species Formation, SAE Technical Paper 2011-24-0193, doi:[10.4271/2011-24-0193](https://doi.org/10.4271/2011-24-0193).
33. Kamasamudram, K., Henry, C., Currier, N., and Yezerets, A., (2012) N₂O Formation and Mitigation in Diesel Aftertreatment Systems, *SAE Int. J. Engines* 5: doi [10.4271/2012-01-1085](https://doi.org/10.4271/2012-01-1085).
34. Walker, A. (2012) Current and Future Trends in Catalyst-Based Emission Control System Design”, presentation at the SAE Heavy-Duty Diesel Emission Control Symposium, September 2012, Gothenburg.
35. Tang, W., Huang, X., and Kumar, S. (2011) Sulfur Effect and Performance Recovery of a DOC + CSF + Cu-Zeolite SCR System, presentation at US Department of Energy, Directions in Engine Efficiency and Emissions Research (DEER) Conference, October 3–6, 2011, Detroit.
36. Chapman, D.M., Fu, G., Augustine S., Crouse, J., Zavalij, L., Watson, M., Perkins-Banks, D. (2010) New Titania Materials with Improved Stability and Activity for Vanadia-Based Selective Catalytic Reduction of NO_x, SAE Technical Paper 2010-01-1179, doi:[10.4271/2010-01-1179](https://doi.org/10.4271/2010-01-1179).
37. Walker, A. (2010) Optimising Future Catalyst Systems, presentation at SAE Heavy-Duty Diesel Emissions Control Symposium, Gothenburg, September 2010.
38. Narula, C., Yang, X., Bonnesen, P., and Hagaman, E., (2011) High Performance NH₃ SCR Zeolite Catalysts for Treatment of NO_x in Emissions from Off-Road Diesel Engine, SAE Technical Paper 2011-01-1330, doi:[10.4271/2011-01-1330](https://doi.org/10.4271/2011-01-1330).
39. Yang, X., Narula, C. (2010) Simple Approach to Tuning Catalytic Activity of MFI-Zeolites for Low Temperature SCR of NO_x, poster at US Department of Energy Directions in Engine Efficiency and Emissions Research (DEER) Conference, September 27–30, 2010, Detroit.
40. Prikhodko, V., Pihl, J., Lewis, S. and Parks, J. (2012) Hydrocarbon Fouling of SCR During PCCI Combustion, *SAE Int. J. Engines* 5(3):2012, doi:[10.4271/2012-01-1080](https://doi.org/10.4271/2012-01-1080).

41. Luo, J-Y, Yezerets, A., Henry, C., Hess, H., Kamasamudram, K., Chen, H-Y, Epling, W. S. (2012), Hydrocarbon Poisoning of Cu-Zeolite SCR Catalysts, SAE Technical Paper 2012-01-1096, doi:[10.4271/2012-01-1096](https://doi.org/10.4271/2012-01-1096).
42. Han, J., Kim, E., Lee, T., Kim, J., Ahn, N, and Han, H.-S. (2011) Urea-SCR Catalysts with Improved Low Temperature Activity, SAE Technical Paper 2011-01-1315, doi:[10.4271/2011-01-1315](https://doi.org/10.4271/2011-01-1315).
43. Heibel, A. (2010) Advances in Substrate Technology, presentation at SAE Heavy-Duty Diesel Emissions Control Symposium, Gothenburg, September 2010.
44. Bartley, G. J., Chadwell, C. J., Kostek, T. W., Zhan, R. (2012) SCR Deactivation Kinetics for Model-Based Control and Accelerated Aging Applications, SAE paper 2012-01-1077, Published 04/16/2012, SAE International, doi:[10.4271/2012-01-1077](https://doi.org/10.4271/2012-01-1077).
45. Matsui, W., Suzuki, T., Ohta, Y., Daisho, Y., Suzuki, H., and Ishii, H. (2011) A Study on the Improvement of NO_x Reduction Efficiency for a Urea-SCR System (Sixth Report) - Clarifying N₂O formation mechanism, JSAE Technical Paper 20115720, October 2011.
46. Holderbaum, B., and Kwee (2009) Integration of DPF and SCR - Interfaces and Interactions, presentation at the 5th International CTI Forum, SCR Systems, Fellbach, Germany, April 2009.
47. Henry, C., Langenderfer, D., Yezerets, A., Ruth, M., Chen, H.-Y., Hess, H., and Naseri, M. (2011a) Passive Catalytic Approach to Low Temperature NO_x Emission Abatement, presentation at US Department of Energy, Directions in Engine Efficiency and Emissions Research (DEER) Conference, October 3–6, 2011, Detroit.
48. Henry, C., Gupta, A., Currier, N., Ruth, M., Hess, H., Naseri, M., Cumaranatunge, L., Chen (2012) Advanced Technology Light Duty Diesel Aftertreatment System, presentation at the US Department of Energy Directions in Engine Efficiency and Emissions Research (DEER), Dearborn, MI, October 2012.
49. Folić, M., Johansen, K. (2012) SCR-DPF Integrations for Diesel Exhaust Performance and Perspectives for High SCR Loadings, presentation at the US Department of Energy Directions in Engine Efficiency and Emissions Research (DEER), Dearborn, MI, October 2012.
50. Tan, J., Solbrig, C., and Schmiege, S. J. (2011) The Development of Advanced Two-Way SCR/DPF Systems to Meet Future Heavy-Duty Diesel Emissions, SAE Technical Paper 2011-01-1140, doi:[10.4271/2011-01-1140](https://doi.org/10.4271/2011-01-1140).
51. Schrade, F., Brammer, M., Schaeffner, J., Langeheinecke, K., Kraemer, L. (2012) Physico-Chemical Modeling of an Integrated SCR on DPF (SCR/DPF) System, SAE Int. J. Engines 5(3):2012, doi:[10.4271/2012-01-1083](https://doi.org/10.4271/2012-01-1083).
52. Murata, Y., Tokui, S., Watanabe, S., Daisho, Y., Suzuki, H., Ishii, H., (2008) Improvement of NO_x Reduction Rate of Urea-SCR System by NH₃ Adsorption Quantity Control, SAE Technical Paper 2008-01-2498, doi:[10.4271/2008-01-2498](https://doi.org/10.4271/2008-01-2498).
53. Yasui, Y., Matsunaga, H., Hashimoto, E., Satoh, N., Hardam, H., Balland, J., Yamada, M., Takahashi, T. (2012) A New Clean Diesel Concept for US LEV-III SULEV - First Report - A New Emission Strategy and Aftertreatment Management Control, presentation at the IAV MinNO_x Conference, June 2012, Berlin.
54. Weibel, W., Waldbüßer, N., Wunsch, R., Chatterjee, D., Bandl-Konrad, B., Krutzsch, B. (2009) A Novel Approach to Catalysis for NO_x Reduction in Diesel Exhaust Gas, presentation at 8th International Catalysis for Automotive Pollution Control, Brussels, April 2009.
55. Theis, J. R., Dearth, M., and McCabe, R. (2011) LNT + SCR Catalyst Systems Optimized for NO_x Conversion on Diesel Applications, SAE Technical Paper 2011-01-0305, doi:[10.4271/2011-01-0305](https://doi.org/10.4271/2011-01-0305).
56. Harold, M., Luss, D., Liu, Yi (2012) Dual Layered Catalysts for Lean Reduction of NO_x by In Situ Generation of Ammonia, presentation at the Catalysts for Automotive Pollution Control 9 (CAPoC9), September 2012, Brussels.

57. Xu, L., McCabe, R., Tennison, P., and Jen, H-W. (2011) Laboratory and Vehicle Demonstration of “2nd-Generation” LNT + in situ SCR Diesel Emission Control Systems, SAE Technical Paper 2011-01-0308, doi:[10.4271/2011-01-0308](https://doi.org/10.4271/2011-01-0308).
58. Cavataio, G., Guo, K., Xu, L., Dobson, D., Warner, J., Dearth, M., Theis, J., Ruona, W., McCabe, R., Lambert, C., (2011) Comparing Urea SCR to In-situ LNT+SCR After Treatment Systems for Light Duty Vehicles, SAE 2011 Light Duty Diesel Emissions Control Symposium, November 2–3, 2011, Ann Arbor.
59. Guralp, O., Qi, Q., Li, W., and Najt, P. (2011) Experimental Study of NO_x Reduction by Passive Ammonia-SCR for Stoichiometric SIDI Engines, SAE Technical paper 2011-01-0307, doi:[10.4271/2011-01-0307](https://doi.org/10.4271/2011-01-0307).
60. Toops, T. J., Parks II, J. E., Pihl, J. A., DiGiulio, C. D., Amiridis, M. D. (2012) Lean Gasoline Emissions Control: NH₃ Generation Over Commercial Three-Way Catalysts and Lean-NO_x Traps, presentation at US Department of Energy, Directions in Engine Efficiency and Emissions Research (DEER) Conference, October 2012, Detroit.

Chapter 2

SCR Technology for Off-highway (Large Diesel Engine) Applications

Daniel Chatterjee and Klaus Rusch

Abbreviations

BMEP	Break Mean Effective Pressure
BSO	Bodensee-Schiffahrts-Ordnung (local regulation for ships on Lake Constance)
CPSI	Cells per Square Inch
DOC	Diesel Oxidation Catalyst
DPF	Diesel Particulate Filter
EPA	Environmental Protection Agency
EU	European Union
HFO	Heavy Fuel Oil
IMO	International Maritime Organization
NRTC	Non-Road Transient Cycle
PGM	Precious Group Metals
PLC	Programmable Logic Controller
PM	Particulate Matter
SCR	Selective Catalytic Reduction

2.1 Introduction

The term *Off-highway* includes a great variety of diesel engine applications like propulsion of ships, mining trucks, harvesters, trains, power generation and pump drives, e.g. for hydraulic fracturing (see Fig. 2.1). In a broader sense, even power generation and pump drives need to be considered *mobile*, as they are often mounted into containers or onto trailers.

D. Chatterjee (✉) · K. Rusch
MTU Friedrichshafen GmbH, Maybachplatz 1 88045 Friedrichshafen, Germany
e-mail: daniel.chatterjee@mtu-online.com



Marine	Industrial	Defense	Oil Gas	Power
<ul style="list-style-type: none"> • Yachts • Commercial 	<ul style="list-style-type: none"> • Rail • Agriculture • C&I • Mining 	<ul style="list-style-type: none"> • Vehicles • Navy 	<ul style="list-style-type: none"> • Onshore • Offshore 	<ul style="list-style-type: none"> • Emergency Power • Prime Power • Continuous Power
				

Fig. 2.1 Off-highway applications for diesel engines (Pictures MTU)

Diesel engines for off-highway applications can be heavy-duty derivatives, mainly for the power range below 560 kW, or special designed diesel engines. Engines with a power output of more than 560 kW are referred as *large diesel engines*. The power output of these large engines reaches up to 100 MW. Based on their speed of rotation, large diesel engines are divided into high-speed engines (>1,000 rpm), medium-speed engines (400–1,000 rpm) and low-speed engines (<400 rpm). Typically, the displacement increases as the rotating speed of the engines decreases. Usually, medium- and low-speed engine displacements range from 30 to 2,000 L/cylinder (e.g. large two stroke engines), whereas those for high-speed engines typically lie between 0.2 and 20 L/cylinder. An example of a high-speed engine and a medium-speed engine can be found in Figs. 2.2 and 2.3.

A further differentiation is the fuel. Most high-speed engines are using high-quality standard diesel fuel like trucks or passenger cars. However, heavy fuel oil (HFO), which can contain a significant amount of sulfur (up to 5 %) [1], is the preferred fuel for medium- and low-speed engines.

Exhaust emissions from off-highway diesel engines have to comply with more and more stringent emission regulation. Similar to diesel engines used in heavy-duty trucks or passenger cars, the reduction of exhaust emissions requires a combination of engine-internal measures and aftertreatment technology. Corresponding to the engine size and application, exhaust gas aftertreatment technologies for off-highway diesel engines combine on-highway as well as power plant technology (see Fig. 2.4).

The dimensions can range from SCR boxes well known from on-highway trucks up to house-like industrial systems for diesel engine power plants (see Fig. 2.5).

Engine Configuration	
cylinder numbers	8V,12V, 16V, 20V
displacement per cylinder	4.77 l
power range	1 to 3 MW
max. power per cylinder	150 kW
rated speed	1800 rpm
rated BMEP	21.0 bar

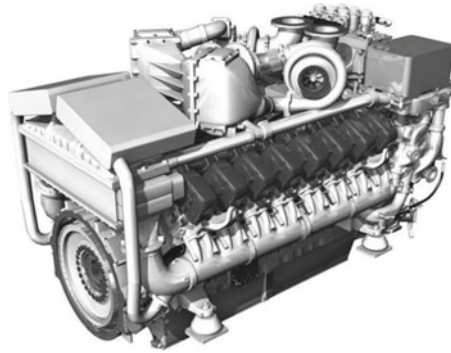


Fig. 2.2 Example of a large high-speed engine (MTU S4000) (Picture MTU)

Engine Configuration	
cylinder numbers	6,8, 9, 12, 16
displacement per cylinder	32 l
power range	3 to 8 MW
max. power per cylinder	500 kW
rated speed	750 rpm
rated BMEP	24.9 bar

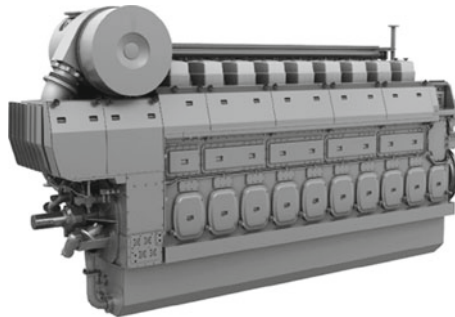


Fig. 2.3 Example of a large medium-speed engine (Bergen B32:40) (Picture Bergen Engines AS)

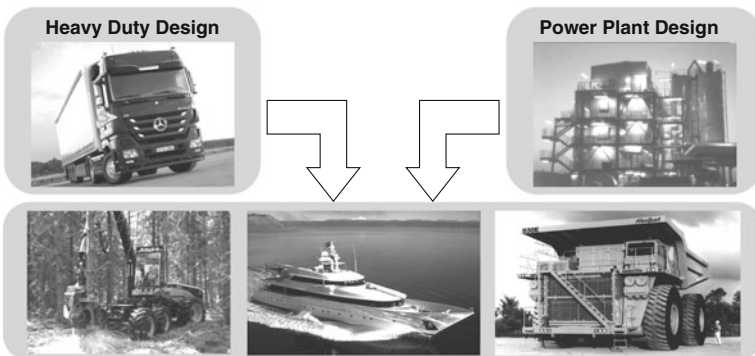


Fig. 2.4 Influences and roots of off-highway exhaust gas aftertreatment systems (Pictures MTU)

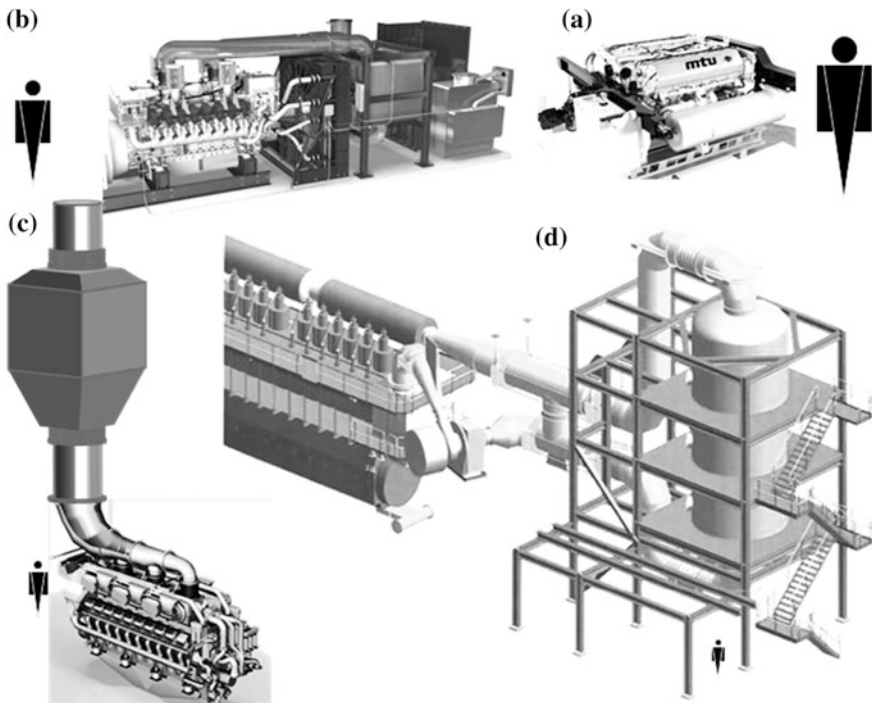


Fig. 2.5 Off-highway diesel engines with SCR range from truck-like mobile systems up to stationary power plants: **a** Railcar 700 kW, **b** Container Genset 3 MW, **c** Ship Propulsion 7 MW, **d** Stationary Two-Stroke Engine 50 MW (*Pictures MTU and Johnson Matthey*)

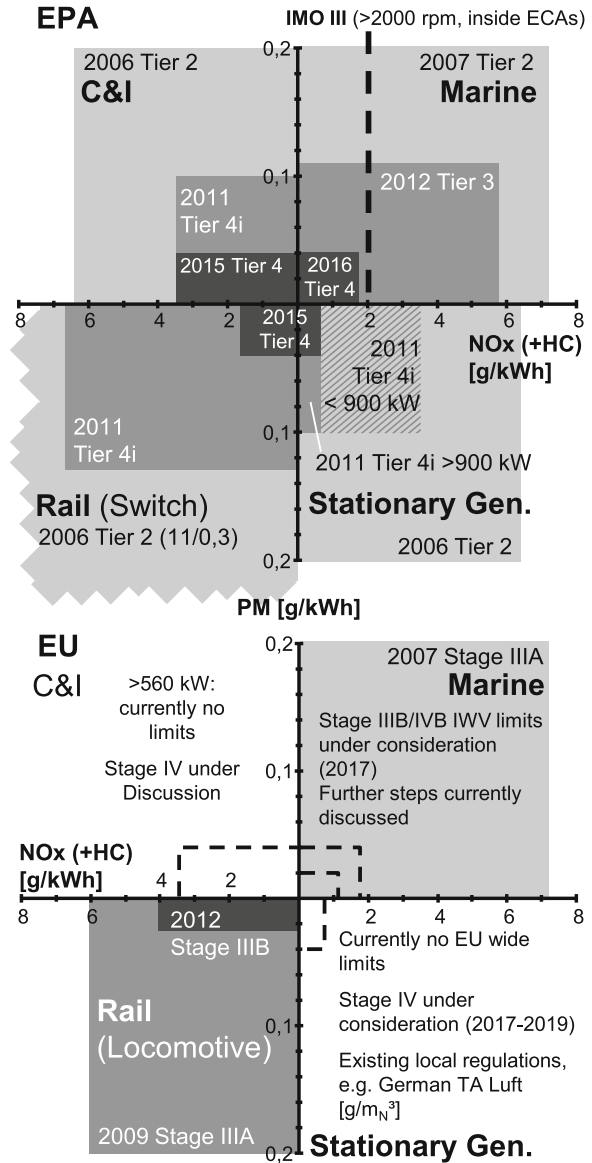
Because the SCR technology for smaller engines can directly be derived from available on-highway technologies, this chapter will focus mainly on the specific requirements of large diesel engines with a power output larger than 560 kW.

2.2 Off-highway Emission Legislation

Due to the increasing awareness of air quality, stricter emission limits have been introduced, which will be even further tightened for off-highway diesel engines in the coming years. Depending on the application and the location, different emission limits apply. The most stringent emission regulations are currently imposed by the European Union (EU) and the Environmental Protection Agency (EPA) in USA. Off-highway diesel engines have to fulfill different emission standards, depending on the application.

Nitrogen oxides (NO_x) and particulate matter (PM) are the main pollutants, which are in the focus of the current emission legislations. Figure 2.6 gives an overview of emission limits for engines with a power output higher than 560 kW. It should be noted, that especially EPA Tier 4 will require very low exhaust emissions.

Fig. 2.6 EPA and EU emission legislation for engines >560 kW (Emission limits taken from [2])



An additional challenge arises from the fact that, depending on the application, different test cycles have to be used for the certification of engines. The test cycles shown in Fig. 2.7 reveal that engines are operated only in selected areas of the engine map during respective certification runs. Only steady state test cycles are used for off-highway engines with a power output greater than 560 kW. For mobile machinery engines with a power output below 560 kW, the NRTC is added

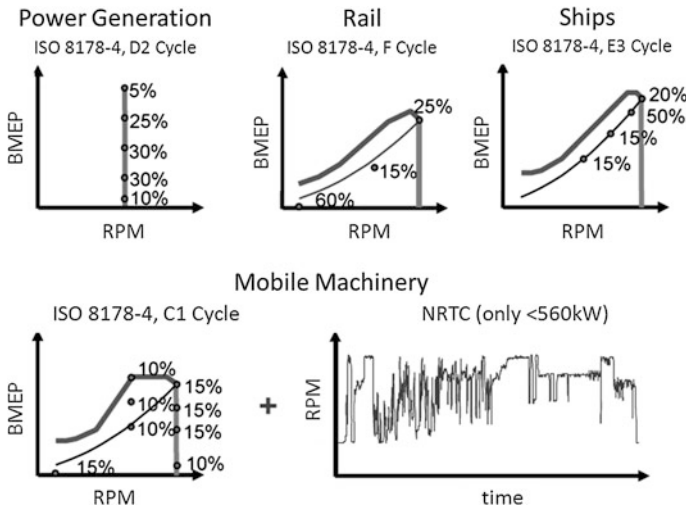


Fig. 2.7 Engine operating points of different off-highway test cycles (Data taken from [3])

as a transient test cycle. On-highway heavy-duty engines with SCR exhaust gas aftertreatment always have to pass a transient and mostly additionally a steady state test cycle.

During the steady state test cycle, the engine is operated at constant speed and load while the emission measurement is conducted. After each emission measurement, the operating point is changed and the next measurement will be performed. Finally, the overall test cycle result is calculated by a weighted sum of all measurements. During the NRTC test, the engine is operated fully transient, with a continuous measurement of the emissions. Therefore, the aftertreatment system has also to be able to perform under transient conditions. This fact leads to specific requirements, e.g. highly accurate urea dosing. More details on emission legislation and certification procedures can be found in [2].

As a consequence, different engine and aftertreatment calibrations are required with respect to the corresponding application. Furthermore, depending on the application and the required emission limits, different exhaust gas aftertreatment technologies have to be used. Examples are DPF only, SCR only and combined DPF + SCR aftertreatment systems.

2.3 SCR Systems for High-Speed Engines

Up to a few hundred kW of power output, on-highway engines or derivatives are used also for off-road applications. For most of these applications, the exhaust technology is very similar if not equal to on-highway systems. Yet, engines with a higher power output or applications with special regulations require different solutions.

2.3.1 *Small Ship Applications*

Due to worldwide-applicable IMO III regulation coming into force within the next few years, aftertreatment will come into focus for ocean going vessels. Local regulations have also led to the development of NO_x reduction systems for smaller ships. For example, the Bodensee-Schiffahrts-Ordnung (BSO) is setting NO_x-limits for ships on Lake Constance in Germany, Switzerland and Austria. In addition to the specific emissions in [g/kWh], the absolute amount of emitted NO_x in [g/h] is limited, too, requiring sport boats to use exhaust gas aftertreatment. For such small applications on-highway SCR-technology is suitable. While urea dosing and catalyst systems can be sourced from mass produced on-highway components, catalyst housing and insulation have to be adapted to the available space on board as well as to other requirements, such as maximum surface temperature and thermal protection.

As the necessary storage capacity for reducing agent is small, it might be reasonable to use NH₃ gas as reducing agent instead of aqueous urea. Figure 2.8 shows a system realized by H+H Umwelt und Industrietechnik for a 300 kW engine. The reducing agent dosing system consists of a mass flow controller and a shut-off valve only. While the local authorities have allowed this kind of solution for the Lake Constance, NH₃ gas bottles are not allowed for most applications due to safety reasons. Solutions for solid storage of NH₃ are being developed and allow direct dosing of gas without the inherent danger of compressed ammonia [4]. Reductant supply systems are discussed in detail in Part VI of this book.

2.3.2 *Rail Applications*

Stringent emission limits for EU and US railroads have forced the introduction of exhaust gas aftertreatment for rail diesel engines. While the most complete pollutant reduction could be achieved with a combined particulate filter and SCR system, an alternative way to meet legislation could be through tuning the engine to meet PM emission limits without a particulate filter and use SCR for NO_x reduction.

Severe packaging constraints force a high integration of engine and exhaust gas aftertreatment. For railcars, for example, engines, aftertreatment including urea tank, generators and coolers are combined into so called power-packs. Figure 2.9 shows an MTU power pack with a 700 kW diesel engine. The SCR system is replacing the silencers mounted left and right to the engine. Figure 2.10 depicts the integration of urea dosing and mixing, as well as the silencing function into the aftertreatment box [5]. On-highway technology is used for urea dosing as well as for catalyst and canning. Power-packs with derivatives of truck engines even use truck silencers with minor modifications.

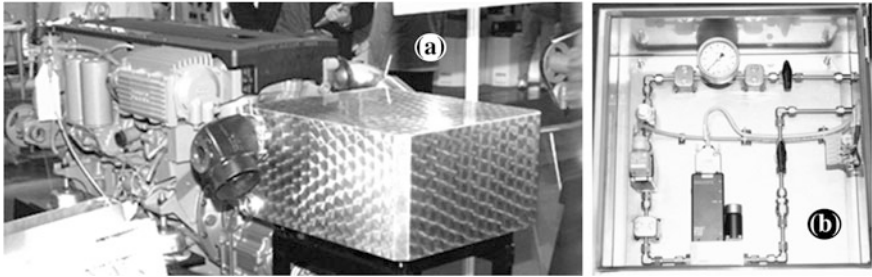


Fig. 2.8 SCR system for a 300 kW engine with **a** engine and catalytic reactor and **b** gaseous NH_3 -dosing from a compressed gas cylinder (Pictures H+H Umwelt und Industrietechnik)

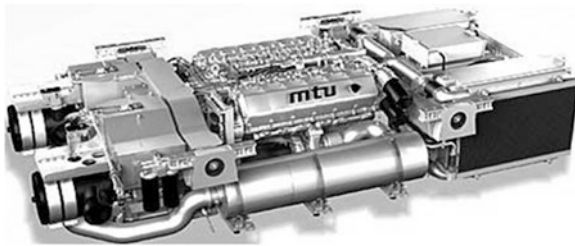


Fig. 2.9 Diesel-electric power-pack with MTU 12 V 1600 R80L and SCR aftertreatment. Diesel engine, generator, exhaust-system, tanks and other auxiliary systems are packaged on a frame for under-floor mounting on railcars (Picture MTU)

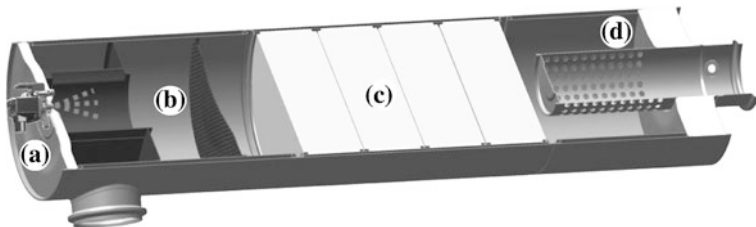


Fig. 2.10 SCR system for the EU III B certified MTU 12 V 1600 R80L engine for railcars with **a** urea dosing and **b** mixing section, **c** catalyst and **d** silencing integrated into a compact housing (Picture MTU)

2.3.3 Gensets

With high-speed engines up to a power output of a few MW, electrical power generation is available as containerized systems [6]. Figure 2.11 gives an example of such a genset. Mostly used as emergency and peak power systems, such engines are characterized by fast load response. The dynamic of exhaust temperature and

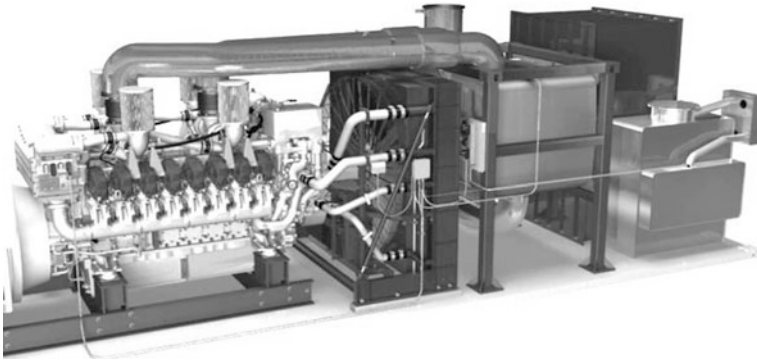
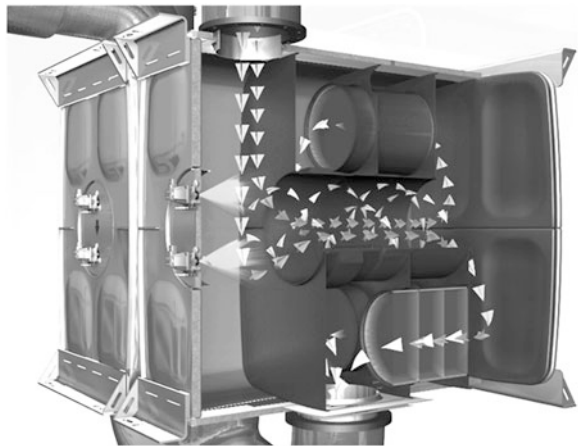


Fig. 2.11 MTU 16 V 4000 genset with SCR aftertreatment integrated into a container (Picture MTU)

Fig. 2.12 SCR System for a containerized genset with MTU 16 V 4000 engine, using on-highway-derived technology for dosing, canning and catalyst (Picture MTU)



flow is comparable to on-highway applications or mobile machinery. Aftertreatment systems have to be highly integrated in order to fulfill the space requirements. Since these demands are similar to on-highway applications, technology derived from heavy-duty trucks is used for pumping and dosing of reductant fluid, most commonly a 32.5 % urea solution.

Catalyst canning and housing technology have their roots in heavy-duty truck-systems, preferably with a mixing section integrated into the catalyst housing as shown in Fig. 2.12. Depending on the allowable pressure drop, the catalyst cell density can go up to 400 cpsi and the space velocity can reach 50,000 1/h.

For engines with very high power density, the temperatures downstream of the turbo charger may exceed 550 °C. The usage of on-highway vanadium-type catalysts is limited by the maximum exhaust temperatures and has to be evaluated carefully. For temperatures above 450 to 500 °C, ammonia oxidation as an undesired side reaction may reduce the NO_x conversion capacity. At temperatures

above 550 °C, the catalyst formulation has to be tested to guarantee that the catalyst possesses sufficient aging resistance [7]. The optimum vanadium content of a catalyst for those engines may therefore be lower than for an on-highway application where low temperature activity is more important. Also zeolite-type catalysts may be an alternative. However, sulfur free fuels are mandatory to allow the use of zeolite technologies as well as PGM catalysts for pre-oxidation and for reduction of NH₃ slip. Systems run for emergency-power or peak-shaving will in general have lower temperature profiles than systems for continuous power. This may lead to a different catalyst and system design depending on the exhaust temperature profile. Details about different catalyst formulations and their application range are discussed in Part II of this book.

2.4 Medium and Low-Speed Engines

Derived from power plant technology, first medium- and low-speed diesel engines for gensets were equipped with SCR technology in the late 1980s. Cell density of power plant catalysts is normally given in cells per 150 mm edge length while for automotive catalysts cells per square inch (CPSI) is used. Power plant catalysts usually are square-type honeycombs with 150 mm edge length and less than 40 × 40 cells (≈46 cpsi). Since the introduction of NO_x aftertreatment for heavy-duty vehicles, round-shaped catalysts with up to 15 inch in diameter and higher cell densities are available, which are also used for small stationary engines.

2.4.1 Fuels and Sulfur

An important difference between high-speed and low- or medium-speed engines with respect to the exhaust system is the fuel.

Medium-speed engines can run with lower-quality fuels than high-speed engines. Lower-grade distillates as well as residual fuels (HFO) are used. As described in Table 2.1, for the SCR technology, important fuel characteristics are the content of ash, sulfur and for residual fuels also vanadium.

Zeolite-type catalysts will deactivate very rapidly with high-sulfur fuels. Vanadium-type catalysts are sulfur tolerant. To a certain degree, the SCR activity is increased by the presence of sulfur-oxides as the catalyst surface will be acidified. But two other mechanisms are limiting: Possible formation of ammonium salts and oxidation of SO₂ to SO₃ [8].

The following equations describe the sum of possible reactions with ammonia and SO₃ leading to ammonium sulfate (Eq. 2.1) and ammonium hydrogen sulfate (Eq. 2.2):

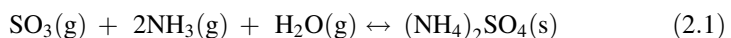
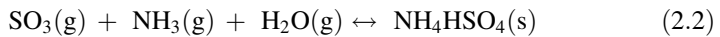


Table 2.1 Fuel characteristics with importance to SCR technology

Ash	Catalyst pitch to be adapted: Residual fuels: ≤ 35 cells / 150 mm (35 cpsi) + installation of soot-blowers On-highway quality: ≥ 300 cpsi (≈ 100 cells / 150 mm)
Sulfur	Minimum temperature for reductant dosing depends on SO_3 -concentration in the exhaust gas (see Fig. 2.14) Catalyst partly converts SO_2 into SO_3 . Dew-point of exhaust and acidity of condensate are changed Low-sulfur fuel enables the use of oxidation catalysts and the use of zeolite-type SCR-catalysts
Vanadium	Vanadium from residual fuels is captured in the catalyst. Catalyst activity increases with time also for undesired reactions: SO_2 conversion, risk of ammonia salt formation and NH_3 oxidation increase



Ammonium hydrogen sulfate is highly hygroscopic and leads to sticky deposits which will not only block the catalyst pores but also the channels. Ammonium sulfate is not as dangerous as it builds a dry ash-like salt and will decompose before melting [9]. Small quantities of pure ammonium sulfate can be handled by soot blowers. Figure 2.13 shows the gas phase conditions at which ammonium sulfate or ammonium hydrogen sulfate will form.

Due to capillary condensation, salts may form on the catalyst up to 350 °C [8]. For exact calculations, the local gas-phase concentration of SO_3 , NH_3 and H_2O along the catalyst and the pore distribution of the catalyst are necessary [11]. The dew-point of sulfuric acid calculated according to [12] is shown in Fig. 2.14.

While NH_3 is consumed by the SCR-reaction over the length of the catalyst, the SO_3 concentration increases as the catalyst enhances the oxidation of SO_2 to SO_3 according to Eq. (2.3):



The risk of salt formation depends on the local maximum of the product of NH_3 * SO_3 along the catalyst. Higher vanadium content of the catalyst increases the SCR activity but also the SO_x conversion. Therefore, the sulfur content of the fuel limits the minimum dosing temperature as well as the low temperature SCR activity. Figure 2.15 is an estimate of the minimum temperature before catalyst for reductant dosing with regard to fuel sulfur content.

To control the catalyst bed temperature in high sulfur fuel applications, as shown in Fig. 2.16 a bypass is often installed for the SCR catalyst as well as for the boiler [14]. This keeps the catalyst at high temperatures even during low-load operation or idling and avoids condensation of sulfuric acid in the catalyst during start-up.

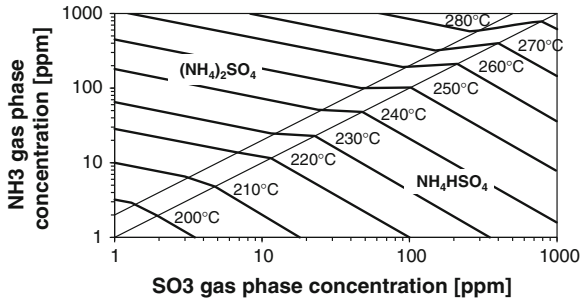


Fig. 2.13 Conditions for ammonium sulfate salt build-up on the catalyst (Data according to [10]). With a NH₃ to SO₃ ratio with less than 1:1, formation of NH₄HSO₄ (ammonium hydrogen sulfate) will dominate. Whereas with a ratio of greater than 2:1 preferably (NH₄)₂SO₄ (ammonium sulfate) and with a ratio between 1:1 and 2:1 a mixture of both will form. With increasing temperature higher concentrations of NH₃ and SO₃ are necessary for salt formation

Fig. 2.14 Dew-point temperature of sulfuric acid as function of SO₃ and H₂O concentration in the exhaust gas (Calculated according to [12])

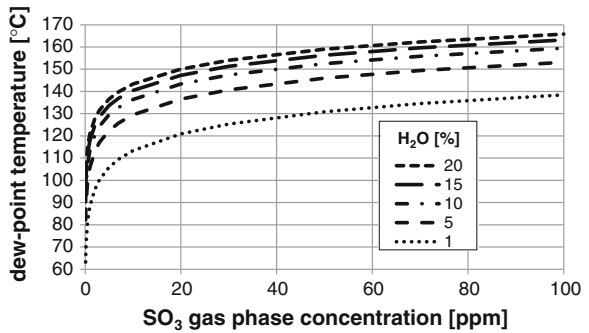


Fig. 2.15 Minimum exhaust temperature before catalyst for NH₃-dosing as function of fuel sulfur content based on empirical data according to [13]

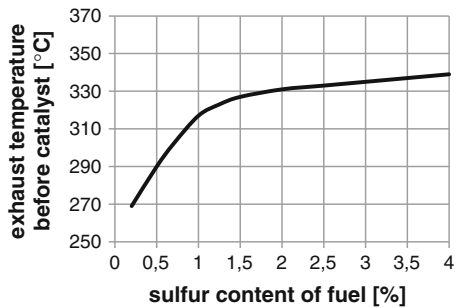
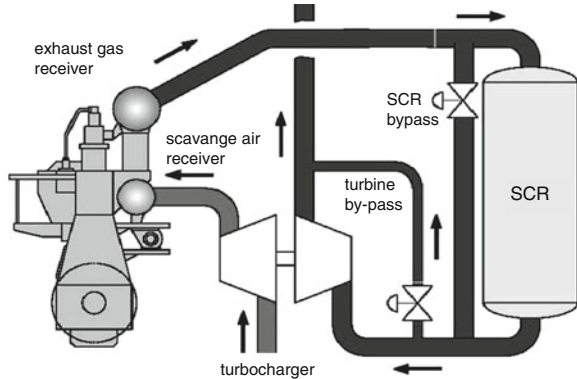


Fig. 2.16 Typical arrangement of pre-turbo SCR for a two stroke engine with an exhaust bypass around the catalytic reactor (Picture Johnson Matthey)



2.4.2 SCR Technology for Marine Applications

First commercial ships were equipped with SCR technology in the early 1990s (e.g. MS Aurora 1992 by ABB/HUG and RoRo Ferry Nils-Dacke of TT-Line in 1995 by Siemens [15, 16]).

Since then, the introduction of local emission regulations have led to the development of SCR technology for ships of various sizes and with various engines [17, 18].

NO_x -tax in Norway and emission-dependent fairway, as well as port dues in Sweden [19] have led to numerous installations of exhaust cleaning systems on commercial ocean going ships, especially in the Baltic Sea and North Sea. Thus, NO_x levels of ships with SCR installation are below the limits of IMO III and are therefore realized far earlier than when this worldwide regulation will go in effect.

For low-speed and medium-speed engines the main technology is derived from diesel engine power plant systems. Whereas in power plants the reducing agent can also be ammonia-water, on bigger ships only urea-water solution is used for safety reasons. In marine applications, special care has to be taken regarding the vibration resistance of urea tubing. Pumping and dosing systems, as well as urea supply tubes should use welding connections wherever possible to avoid urea leakage. A second difference to land-based applications is the demand for classified systems. Classification societies, e.g. Germanischer Lloyd, have included exhaust gas aftertreatment in their rules [20].

Figures 2.17 and 2.18 show a typical setup and details of a SCR exhaust gas aftertreatment system for a HFO-fueled vessel. The SCR catalyst is placed before the boiler as close to the engine as possible to allow high temperatures at the catalyst for high NO_x conversion and to avoid building of ammonium sulfates.

2.4.3 Low-Speed Engine Genset

The high efficiency of low-speed two stroke engines is coupled with low exhaust temperatures. Big stationary or marine engines have temperatures downstream of

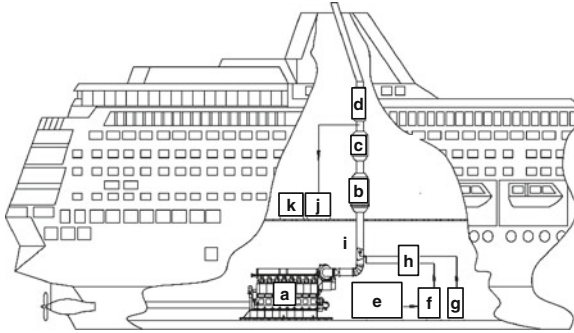


Fig. 2.17 Overview of an SCR installation on an ocean going ship with a heavy fuel engine. The SCR is installed before the boiler to allow high temperatures at the catalyst for high NO_x conversion and to avoid building of ammonium sulfates. **a** Diesel engine, **b** SCR reactor, **c** boiler, **d** silencer, **e** urea tank, **f** urea pump skid, **g** compressor (working air), **h** dosing unit, **i** two-phase nozzle, **j** NO_x -analyzer (optional), **k** PLC control cabinet (Pictures H+H Umwelt und Industrietechnik)

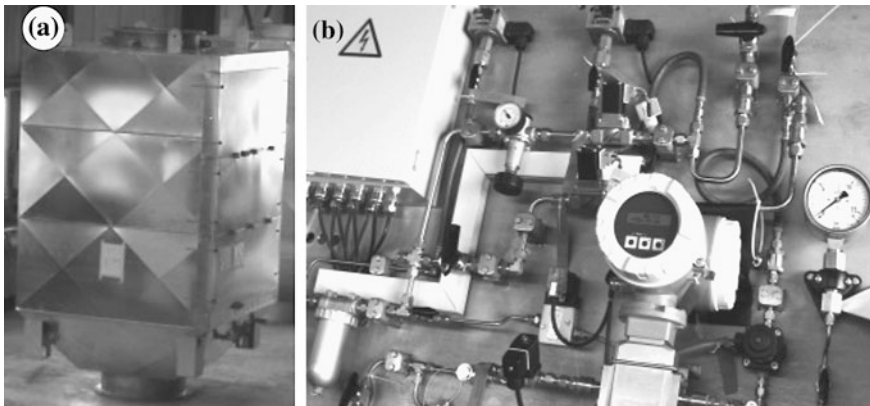
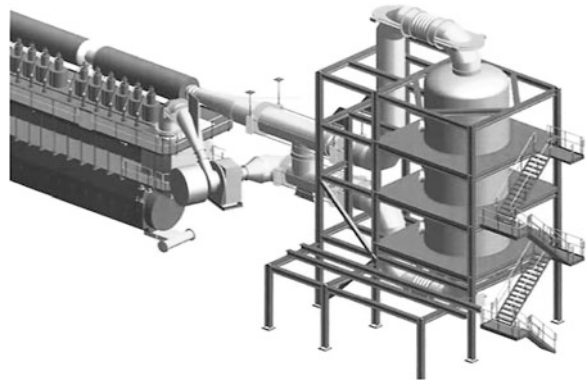


Fig. 2.18 **a** Catalyst housing and **b** urea dosing panel for a medium-speed engine ship application (Pictures H+H Umwelt und Industrietechnik)

the turbine all the way down to $150\text{ }^\circ\text{C}$, making catalytic exhaust gas aftertreatment impossible. To apply SCR with such engines, the catalyst has to be placed upstream of the turbo charger where temperatures are high enough for exhaust gas aftertreatment. Figure 2.19 shows such an installation with a stationary two stroke engine. The design of the catalyst housing has to regard the exhaust pressure of several bar above ambient [14, 21]. A positive side effect is that this higher pressure is increasing the catalytic reaction but it also enhances the undesired side reactions. As low-speed engines normally run with bunker fuels containing higher amounts of sulfur and vanadium, an important criterion for the catalyst layout is

Fig. 2.19 SCR pre-turbo in a pressurized vessel installed at a 50 MW two stroke engine (Picture Johnson Matthey)



the allowed conversion of SO_2 to SO_3 . Even with the SCR catalyst's very low initial vanadium concentration, vanadium from the fuel loads the catalyst and the SO_x conversion will rise over time until the catalyst has to be exchanged due to its increasing activity. As for medium-speed engines, a bypass can control the catalyst temperature. In contrast to low-load temperature control for SCR installations after turbo, for pre-turbo installations the maximum catalyst temperature has to be controlled as the SO_2 oxidation significantly increases at higher temperatures.

2.5 Combined Systems

2.5.1 DPF + SCR

The combination of a DPF and a SCR aims at the reduction of NO_x and PM simultaneously. The combination of both technologies (SCR + DPF) is already used in modern Euro 6, JP09, and US EPA 2010 certified heavy-duty trucks and has undergone comprehensive examination [22–27]. However, for the off-highway application it cannot be considered a standard technology, yet.

An example of a prototype installation on a shunting locomotive, see Fig. 2.20 [22], is presented in this section. Because of the highly variable operating conditions and frequent idling of a shunting locomotive, this example represents a very critical and challenging application for an aftertreatment system.

2.5.1.1 Reactor Concept

As space is limited in a locomotive, especially if it is not designed for the integration of an aftertreatment system, the reactor has to be fitted in place of the silencer. Hence, a very compact reactor, which is able to act as a silencer too, is required. A further challenge arises for aftertreatment systems that are combined

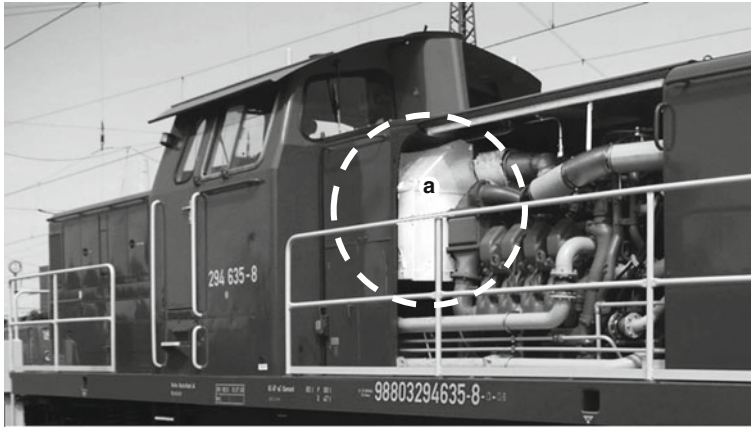


Fig. 2.20 Shunting locomotive from Deutsche Bahn AG with **a** combined DPF + SCR installation (Picture MTU)

with older engines. This poses some limitations on the backpressure in order to prevent an excessive increase in fuel consumption. In the presented example, 130 mbar were set as the maximum backpressure for the total aftertreatment system, which mainly determines the required DPF volume and the design of the exhaust flow paths in the reactor.

Figure 2.21 shows the cross-section of the installed DPF + SCR reactor. After entering the inlet chamber, the exhaust flow is divided into a right and a left path. First, the exhaust flows through a diesel oxidation catalyst (DOC) to convert some NO to NO₂, which is a prerequisite for a continuous soot oxidation within the diesel particulate filter (DPF) and which additionally improves the SCR conversion rate, (see Fig. 2.22) [22]. The DPF placed behind the DOC reduces particulate matter (PM) with high efficiency. Downstream of the DPF, a special designed mixing chamber gives the injected urea solution sufficient time for evaporation, mixing and thermolysis before entering the SCR catalyst. Finally, an ammonia slip catalyst is used to prevent any NH₃ slip to the environment.

Due to the required low backpressure, rectangular DPF substrates are used to optimize the exhaust flow cross-section. The utilization of rectangular substrates is not common in mobile applications. Hence, no “mobile” canning technology is available and the canning known from power plant systems (see Sect. 2.6) does not meet the requirements. Therefore, a dedicated canning technology had to be developed. Further details on this can be found in [22]. The integration of round and rectangular substrates is a good example of how heavy-duty vehicle technology and industrial design are combined in aftertreatment systems for off-highway applications.

Fig. 2.21 Combined aftertreatment system for a shunting locomotive: **a** DPF + SCR installed in one reactor housing, **b** gas flow (Picture MTU) with A exhaust gas inlet, 1 diesel oxidation catalyst (DOC), 2 diesel particulate filter (DPF), 3 urea solution Injection, 4 SCR catalyst, 5 ammonia slip catalyst (ASC), 6 urea mixing area, B exhaust gas outlet

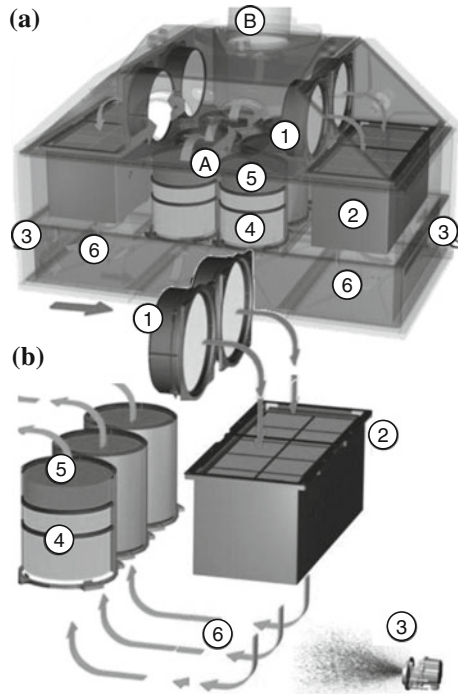
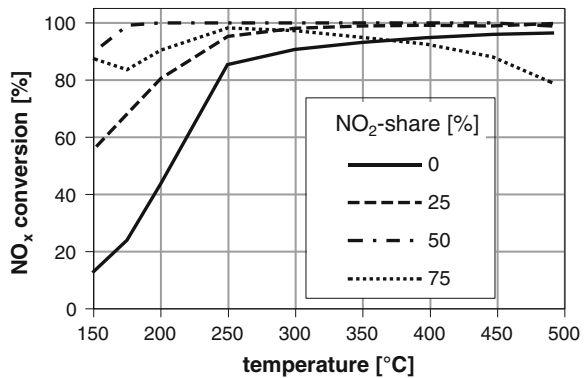


Fig. 2.22 NO_x conversion as a function of temperature and NO₂/NO_x ratio (synthetic gas test bench measurements) (Data MTU)



2.5.1.2 Field Experience

In the ISO-F acceptance test the system revealed an overall NO_x conversion efficiency of more than 70 %. Based on the engine out emissions the NO_x emissions after the aftertreatment system stayed well below 3.5 g/kWh required by the EU-IIIIB legislation. At the same time NH₃ emissions were kept at an absolute minimum.

Fig. 2.23 Measured temperature distribution in front of the DPF + SCR Reactor (Data MTU)

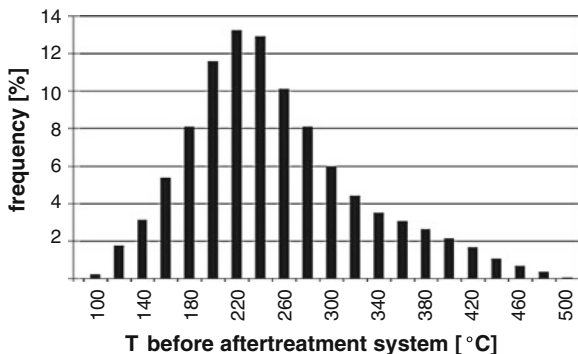
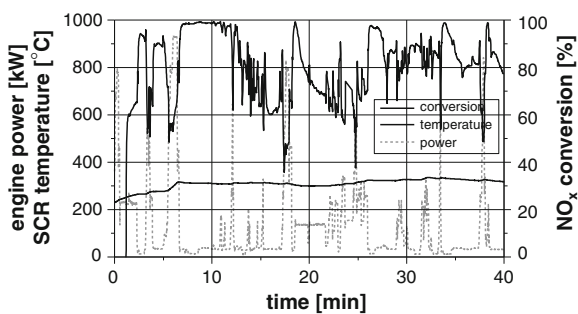


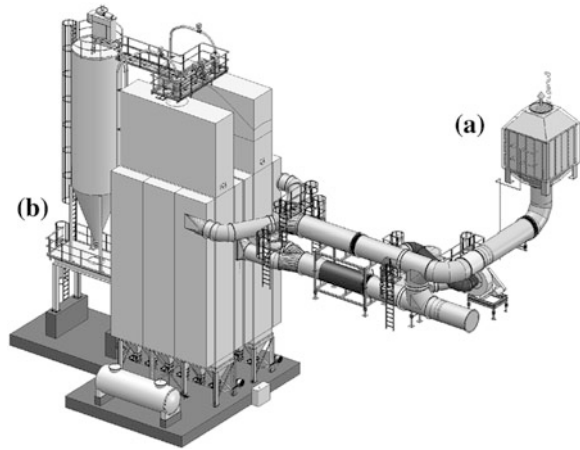
Fig. 2.24 NO_x conversion during field operation of the shunting locomotive (Data MTU)



Because the typical operating conditions in the field includes 70 % idling, the aftertreatment system is exposed a significant amount of time to low temperatures. Figure 2.23 displays a representative exhaust temperature distribution in front of the exhaust gas aftertreatment system. It is revealed that the average inflowing exhaust gas temperature typically is in the range of 250 °C, which seems quite low, because for this system urea dosing is enabled only for temperatures higher than 250 °C (many on-highway applications are using already 200 °C as threshold). However, due to the high thermal mass of the DOC and the DPF, the temperature before the SCR catalyst is significantly higher. The transient measurements of NO_x conversion and temperature of the SCR catalyst during operation, displayed in Fig. 2.24, reveal an average SCR operating temperature around 300 °C. The NO_x conversion efficiency is typically in the range of 80 % or higher, which confirms the efficiency of such a system even under transient conditions. A prerequisite for this performance is also a precise control of the amount of injected urea solution.

It has to be noted, that a combined aftertreatment system requires a high engineering and integration effort and cannot directly be derived from available on-highway technology.

Fig. 2.25 Combined exhaust gas aftertreatment system for a low-speed engine with **a** SCR and **b** dry DeSO_x (DryEGCS) (Picture Couple Systems GmbH)



2.5.2 Combination of DeNoxation and DeSulfurization

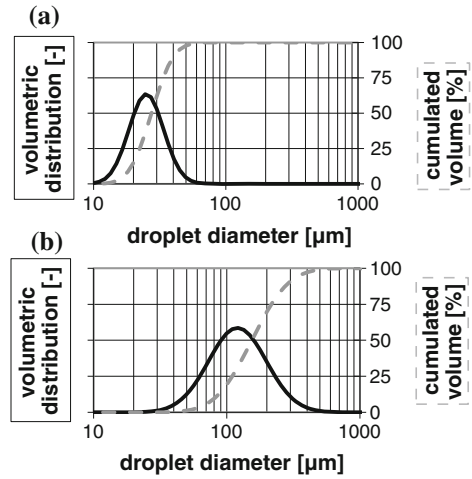
For bunker fuels with high sulfur levels, a combined system would mean to consolidate the NO_x and SO_x aftertreatment. For SO_x reduction wet systems are known from stationary coal and diesel power plants. Wet scrubbers are further developed for exhaust gas aftertreatment on ships [28, 29]. With those systems the SCR is normally installed upstream of the SO_x-reduction system. Recently, also systems where the desulfurization is done with a dry absorption process have been successfully installed on ships [30]. Figure 2.25 shows a combined system for a stationary engine. Beneficial for dry systems is the smaller heat loss compared to wet systems. This enables the placement of the SCR downstream of the DeSO_x without the need of heating up the exhaust again. Without SO₂ present in the exhaust gas, the V-content as well as the cell density of the SCR-catalyst can be increased. A SCR system installed downstream of a desulfurization will therefore be smaller than it has to be for the engine out SO₂ concentration. Additionally problems with ammonium-salt formation will not occur and the overall NO_x-conversion can be higher due to a lower minimum allowed urea dosing temperature. The downside of dry desulfurization is the much higher space requirement needed for this installations compared to wet systems.

2.6 System Integration

2.6.1 Reductant Supply

One precondition for high NO_x reduction with NH₃-SCR-Systems is proper mixing of the reducing agent with the exhaust gas, as well as a good thermolysis of urea.

Fig. 2.26 Droplet diameter of different spray systems (based on [31]): **a** hollow cone nozzles (airless) and industrial two phase nozzles (air assisted), **b** spray systems derived from gasoline injectors (airless)



Spray systems and mixing devices build a closely coupled system which has to be designed carefully.

2.6.1.1 Spray Systems

First for on-highway truck applications and later also for passenger cars, several airless systems have been developed. Up to now, the maximum amount of reducing agent per dosing system is around 10 to 20 L/h. Above this, industrial spray systems are customized and available to deliver much larger quantities. Air assisted nozzles or airless nozzles with good atomization (e.g. hollow cone nozzles) lead to droplet diameters below 100 μm and volumetric mean diameters down to 20 μm . Spray systems derived from gasoline injection valves are characterized by a rather coarse spray (see Fig. 2.26).

2.6.1.2 Mixing Concepts

In analogy to the flow uniformity which has first been defined in [32], a uniformity index γ is commonly used also to describe the ammonia distribution across the exhaust pipe or the catalyst cross section. The concentration distribution is defined according to Eq. (2.4):

$$\gamma = 1 - \frac{1}{2A \cdot \bar{c}} \cdot \int_A \sqrt{(c - \bar{c})^2} dA \quad (2.4)$$

with c and \bar{c} being the local and average NH_3 -concentration respectively, and A being the cross-section of the relevant plane, e.g. the front face of the catalyst.

Table 2.2 Functionalities included in mixing devices

Measure	Effect
Generation of small scale turbulence	Enhancement of evaporation
Generation of large scale turbulence	Mixing across entire pipe diameter
Droplet catching	Avoiding wall wetting
Providing a hot surface	Heat exchange for evaporation and urea decomposition
Providing surface by a baffle plate	Secondary atomization of droplets

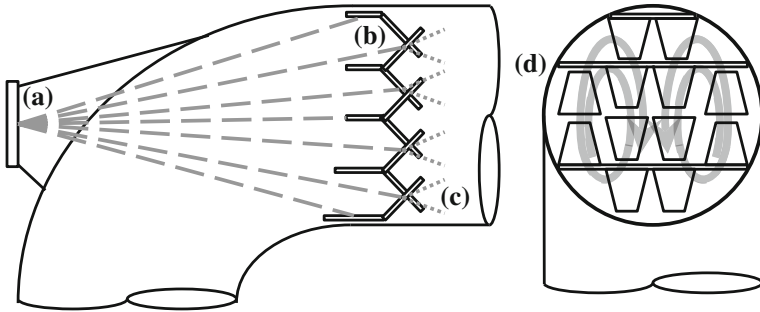


Fig. 2.27 Baffle plate mixing element for coarse urea spray with the main functionalities **a** spray generation, **b** droplet catching and heat exchange, **c** secondary atomization, **d** large scale mixing (Drawings based on [34])

For discrete measurement points with concentration c_i representing an area A_i the uniformity index is defined as

$$\gamma = 1 - \frac{1}{2A \cdot \bar{c}} \cdot \sum_{i=1}^n A_i |c_i - \bar{c}| \quad (2.5)$$

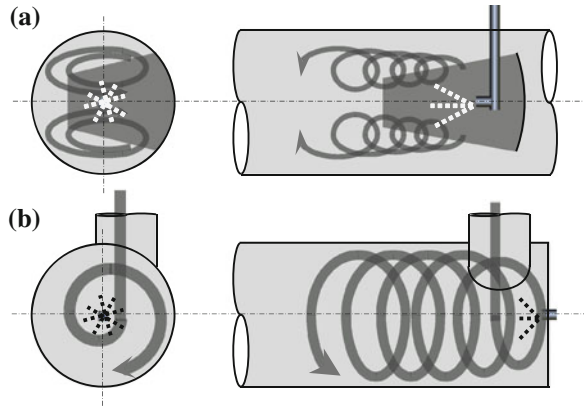
NO_x reduction of more than 95 % with NH_3 slip below 10 ppm needs a NH_3 -distribution of $\gamma > 95$ %. Good mixing systems for passenger cars and trucks are able to achieve $\gamma > 99$ %.

Functions included in mixing devices are shown in Table 2.2.

Several mixing technologies are commercially available. Depending on the reductant injection, two general types of mixers can be defined: (a) Mixers for secondary atomization combined with small scale turbulence for droplet breakup and (b) swirl or vortex generators for large scale distribution [31, 33].

For droplets with diameters $\gg 50 \mu\text{m}$, a secondary atomization is necessary as such large droplets would otherwise not evaporate properly and would lead to wall wetting downstream of the injection point. Therefore, mixing concepts for coarse spray primarily consist of small-scale turbulence generators and baffle plates for droplet breakup and evaporation (see Fig. 2.27) and have to be installed downstream of the injection location [31]. Additionally large-scale turbulence generators may be integrated for mixing.

Fig. 2.28 Working principle of **a** vortex mixer and **b** swirl generator



Droplets smaller than $50\ \mu\text{m}$ easily follow the exhaust flow. As the evaporation of small droplets is fast enough, secondary atomization is not necessary, i.e. mixers for fine spray (and self-evident for gaseous reductant) can be installed directly upstream of the injection location. Literature describes several geometric forms, which can be classified into two general groups shown in Fig. 2.28: (a) turbulence wings, mostly delta-wings [33, 35], or round plates installed into the exhaust pipe generating a pair of counter-rotating vortices. (b) swirl generators, which induce one single swirl over the entire exhaust pipe or mixing chamber.

Vortex mixers are well known from power plant systems where they are used with grids of injection nozzles for gaseous ammonia or aqueous ammonia solutions. The mixer is installed upstream of the injection point and the reducing agent is sprayed into the vortex system. The nozzle itself can be placed directly behind the mixer in a zone with low flow in order to have an optimum initial breakup of the spray. Adapted to the exhaust flow of a diesel engine, vortex mixer can be placed together with a single air assisted nozzle in the center of the exhaust pipe. The vortices as a result of large scale turbulence, distribute the reducing agent across the entire exhaust cross section.

In combination with airless on-highway dosing systems which produce a fine spray, vortex mixers allow placement of the nozzle close to the wall of the exhaust pipe from where the droplets are transported away from the wall into the exhaust flow. Without mixer, the impulse of the fine droplets would not be enough to penetrate into the center of the exhaust stream.

Instead of two or more vortices a single swirl is often used for applications where the dosing system is placed at a front face of a catalytic reactor or at a 90° bow of the exhaust pipe. The reductant is sprayed in the center of the swirl.

For both types care has to be taken that centrifugal forces are not too high to avoid wall wetting downstream of a urea dosing system.

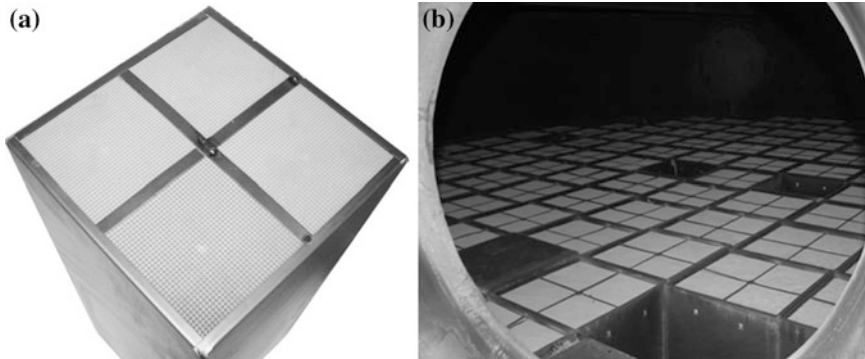


Fig. 2.29 **a** Canning of square catalyst bricks into metal frames and **b** loading of a catalytic reactor (*Pictures Johnson Matthey*)

2.6.2 Canning Concepts

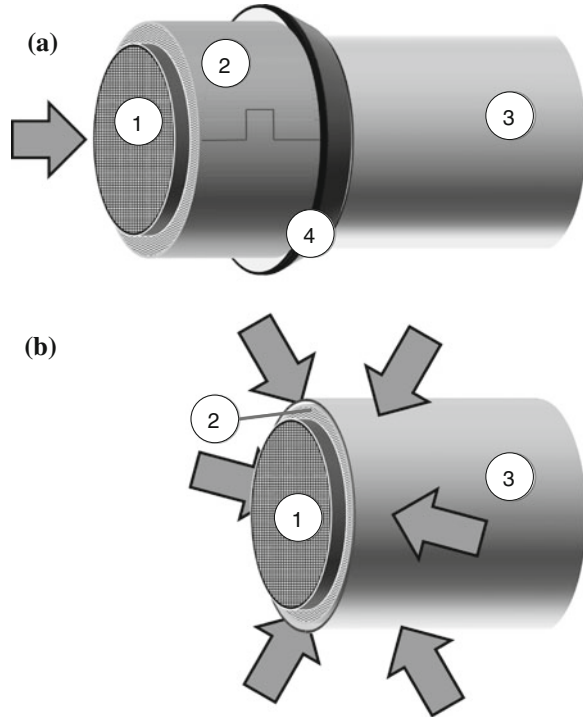
Depending on the exhaust mass flow, which first of all is related to the engine size, two completely different technologies are applied for mounting the catalyst bricks into the exhaust system. For exhaust flows higher than 10,000 to 20,000 Nm³/h, the technology is derived from power plant applications. Square catalyst bricks are grouped into metal frames. The catalysts are held in place by the geometric structure of these metal frames. The frames are packed into the catalytic reactor through a manhole and are supported by a metallic structure within the reactor (see Fig. 2.29). To avoid mechanical damage of the catalyst bricks, a fiber mat is packed between catalyst and metal frame. But in contrast to automotive canning technologies, the mats do not have to hold in place the catalyst.

An advantage of this technology is the optimal usage of the available cross-section and the possibility of exchanging the catalysts or reloading catalysts if a spare layer is foreseen in the reactor. For large engines being built and commissioned on site, catalysts are normally put in place just after the engine is running properly, in order to avoid catalysts deterioration due to excess temperature or other exceptional conditions during commissioning of the engine.

Because of the rectangular geometry, the holding forces between canning and catalyst are low and systems with this power plant-like canning can withstand only small g-forces. The technology is appropriate for stationary or quasi-stationary applications like big ships.

For smaller engines and mobile applications, canning technologies known from on-highway systems are preferred. Most of the time, the catalyst bricks are canned into round metal cans. Stüttem [36] describes the principle technologies used for automotive catalysts. Stuffing and shrinking are the typical processes. First, the size of the catalyst substrates is measured and the support mats are weighed. Second the necessary diameter of the metallic canning is then calculated to reach the optimum pressure within the support mat. The target is to guarantee the

Fig. 2.30 Principle of the canning technologies
a stuffing and **b** shrinking
 with 1 catalyst, 2 support mat,
 3 metal canning, 4 stuffing
 cone



necessary holding force over the lifetime without over-pressing either the mat or the catalyst brick. In the final step with the stuffing process, the catalyst and the support mat are pressed into a readily sized canning. With the alternative shrinking process, the catalyst and mat are put into an oversized canning which than is shrunk to the demanded size (see Fig. 2.30).

2.7 Control Strategies

Depending on the dynamic behavior of the engine exhaust as well as the size of the SCR system and the necessary NO_x -conversion, different control strategies are used for correct urea dosing.

Systems for low- or medium-speed diesel engines used as gendrive or for propulsion of ships with fixed propellers often work with look-up tables or a characteristic curve as input for an open-loop reductant dosing control (Fig. 2.31). As the engines only use a small band within the engine map (Fig. 2.32) the NO_x -emission and thus the reductant dosing rate has a fixed correlation to either engine speed or load.

Fig. 2.31 Feed forward reductant dosing control based on a lookup table

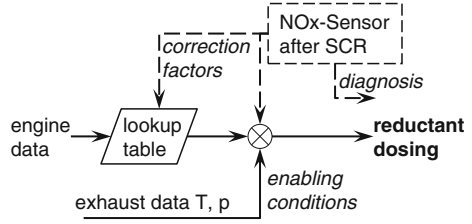


Fig. 2.32 Diesel engines used as gendrive or for propulsion ships with a fixed propeller use only a narrow band within the engine map. This enables the use of look-up tables for reductant dosing control

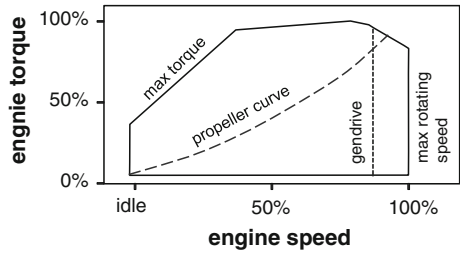


Fig. 2.33 Temperature dependency of possible reductant dosing control strategies

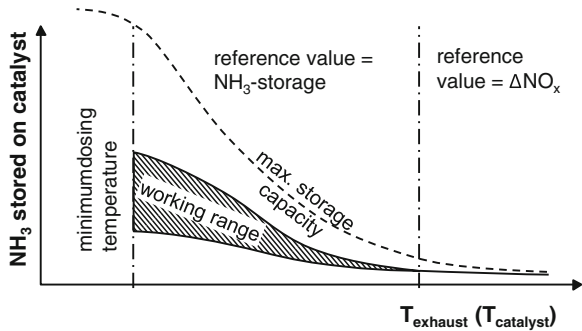
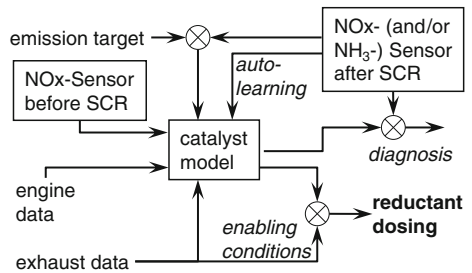


Fig. 2.34 Reductant dosing control scheme for transient systems with high NO_x-conversion including exhaust sensors and catalyst model



For applications which demand a high NO_x-reduction but which have slow changes in exhaust temperature and massflow, a feed-back control based on NO_x-measurement downstream of the SCR is additionally used. Depending on the volume of catalyst installed and on the operating temperature, the response time of

the SCR-system may be too slow for a closed-loop control. In such applications the NO_x -signal may be used to adapt the lookup tables and to improve the feed-forward control (see Fig. 2.31).

To allow high NO_x -reduction and fast transient response within the entire engine map, a model based control strategy as outlined in Fig. 2.34 has to be applied [37]. A common way is to operate with the ammonia storage level on the catalyst as reference value [38]. Provided that the system is tuned to negligible NH_3 -slip the actual NH_3 -storage level on the catalyst surface can be calculated from NO_x -input, NO_x -conversion and urea dosing. Depending on the transience of a given application a certain safety margin is set between the physical storage capacity of the catalyst and the target value. The reductant dosing rate is then controlled to keep the NH_3 filling level as high as possible for maximum NO_x -conversion efficiency. Only for high temperatures where the NH_3 storage capacity of the SCR catalyst is low, the demanded NO_x -conversion can be directly used as reference value for the reductant dosing (Fig. 2.33).

For truck-like systems with an electronic engine control providing a lot of emission relevant data, e.g. the actual exhaust massflow, the control algorithm from on-highway trucks can directly be applied also for off-highway applications. In addition to the above mentioned feed-back signal, literature describes other possibilities to include exhaust concentration sensors into the control algorithm [39, 40]. Instead of calculating the NO_x -input from engine data it can directly be measured with a NO_x -sensor upstream of the catalyst. A NH_3 -sensor for slip control allows to reduce the safety margin between physical ammonia storage storagecapacity and the actual storage level [41]. Detailed discussion on control strategies can be found in Chap. 14 of this book.

2.8 Outlook

It is expected that despite of further engine optimizations, even stricter future emission limits worldwide will lead to an increase in exhaust gas aftertreatment applications for off-highway engines. SCR is currently considered as the main path of technology for NO_x aftertreatment in this market. However, development work has still to be done to adapt this technology further to meet all off-highway conditions and requirements. Especially in the mid-power range, where neither on-highway nor power plant technologies meet the constraints of operating temperature, as well as packaging and mechanical durability. Off-highway engines can run up to 35 years, which is far beyond the typical operating life-time of on-highway vehicles. Therefore, a specific challenge is the prevention of aging of the catalyst technology. Due to the great variety of applications, modular and compact packaging concepts are needed to adjust the aftertreatment system in regards to the application-specific requirements in a cost effective way. These challenges have to be addressed and solved, because it is expected that in the future many off-highway diesel engines will be equipped with an SCR system.

Acknowledgments Marc Hehle and Klaus Wehler are acknowledged for supporting our work at MTU Friedrichshafen GmbH. Enrico Tronconi, Isabella Nova, for their fruitful scientific collaboration over the last 12 years.

References

1. United States Environmental Protection Agency (1999) In-Use Marine Diesel Fuel. EPA420-R-99-027
2. DieselNet (2012) Emission Standards <http://www.dieselnet.com/standards> Accessed 25 Jul 2013
3. DieselNet (2012) Emission Test Cycles <http://www.dieselnet.com/standards/cycles> Accessed 25 Jul 2013
4. Johannessen, T (2011) Next generation SCR system for fuel-efficient NO_x reduction. Paper presented at the Conference Selective Catalytic Reduction, IQPC, Wiesbaden, Germany, 26-28 Sep 2011
5. Rusch K, Maletic B, Chatterjee D, Bauknecht M, Kneifel A, Niemeyer J (2012) Model-Based Development of an SCR System for Railcars. Paper presented at the 5th International CTI Conference Emission Reduction for Off-Highway Applications, Lindau, Germany, 26-27 Sep 2012
6. Sinzenich H, Wehler K, Müller R (2011) Selective Catalytic Reduction: Exhaust aftertreatment for reducing nitrogen oxide emissions. <http://www.mtu-online.com/mtu/technical-info>. Accessed 24 Jul 2013
7. Schildhauer T, Elsener M, Kröcher O, Moser J, Begsteiger I, Chatterjee D, Rusch K (2012) Measurement of vanadium emissions from SCR catalysts: Method development and temperature dependency. Paper presented at the 7th International Exhaust Gas and Particulate Forum, Ludwigsburg, Germany, 6-7 Mar 2012
8. Huang Z, Zhu Z, Liu Z, Liu Q (2003) Formation and reaction of ammonium sulfate salts on V₂O₅/AC catalyst during selective catalytic reduction of nitric oxide by ammonia at low temperatures. *Journal of Catalysis* 214: 213–219
9. Wilmes A (2007) Taschenbuch chemischer Substanzen. Wissenschaftlicher Verlag Harry Deutsch, Frankfurt a.M
10. Willi R (1996) Low-Temperature Selective Catalytic Reduction of NO_x—Catalytic Behavior and Kinetic Modeling. Dissertation, ETH Zürich
11. Matsuda S, Kamo T, Kato A, Nakajima F, Kumura T, Kuroda H (1982) Deposition of Ammonium Bisulfate in the Selective Catalytic Reduction of Nitrogen Oxides with Ammonia. *Ind. Eng. Chem. Prod. Res. Dev.* 21(1):48–52
12. ZareNezhad B (2009) New correlation predicts flue gas sulfuric acid dewpoints. *Oil&Gas Journal* 107(35)
13. Aabo K (2008) MAN Diesel forward technology design as response to maritime emission control regulations, specifically the IMO MARPOL Annex VI Update and EPA's Final Rule for Control of Emissions of Air Pollution from Marine Compression Ignition Engines. Paper presented at the conference Faster Freight Cleaner Air East Coast, New York, 10 Jul 2008
14. Johnson Matthey (2009) SINOx[®] SCR System for 2-stroke Diesel Engine Power Plant. <http://jmsec.com/cm/Downloads/Application-Fact-Sheets.html>. Accessed 24 Jul 2013
15. Mathes W, Züribig J, Witzel F, Müller R (1996) SINOX-catalysts on TT-Line RoRo Nils-Dacke for a more economical and cleaner mode of operation. Paper presented at the 13th Intl Conf on Marine Transport Using Roll-on/Roll-off and Horizontal Handling Methods, Luebeck, Germany, 21-23 May 1996

16. Hug HT, Mayer A, Hartenstein A (1993) Off-Highway Exhaust Gas Aftertreatment: Combining Urea-SCR, Oxidation Catalysis and Traps. SAE Technical Paper 930363
17. IMO Marine Environmental Protection Committee (2012) Air Pollution and Energy Efficiency, Supplementary information to the Interim Report of the Correspondence Group on Assessment of Technological Developments to Implement the Tier III NO_x Emission Standards under MARPOL Annex VI, Submitted by the United States of America
18. Hefazi H, Rahai H R (2008) Emission Control Technologies for Ocean Going Vessels, Final Report Submitted to State of California Air Resources Board
19. Kågeson P (2009) Market-based instruments for NO_x abatement in the Baltic Sea. Air Pollution & Climate Secretariat, Göteborg
20. GL Group (2013) GL Rules & Guidelines. <http://www.gl-group.com/en/gltools/18880.php>. Accessed 14 Jan 2013
21. Leng J, Meylemans L, Müller R, Meier KE (2004) SCR retrofit for large 2-stroke diesels. Paper presented at the 15th Conference on Electric Power Supply Industry, Shanghai, China, 18-22 Oct 2004
22. Weigel C, Schäffner G, Kattwinkel P, Viehweg P, Hehle M., Bergmann D (2010) Technologies for Exhaust Aftertreatment: Testing Under Real Conditions. MTZ 71(11): 808–813
23. Conway R, Chatterjee S, Beavan A, Goersmann C et al. (2005) NO_x and PM Reduction Using Combined SCR and DPF Technology in Heavy Duty Diesel Applications. SAE Technical Paper 2005-01-3548
24. Hinz A, Jarvis T, Abul-Milh M, Amar P et al. (2006) Field Test Trucks Fulfilling EPA'07 Emission Levels On-Road by Utilizing the Combined DPF and Urea-SCR System SAE Technical Paper 2006-01-0421
25. Soeger N, Mussmann L, Sesselmann R, Leippe G, Giezelt C, Bailey O, Hori (2005) Impact of Aging and NO_x/Soot Ratios on the Performance of a Catalyzed Particulate Filter for Heavy Duty Diesel Applications. SAE Paper 2005-01-0663
26. Mussmann L, Müller W, Soeger N, Spurk P (2007) Combined DPF/SCR Concepts for Future Heavy Duty Emission Limits. Paper presented at the 1st MinNox Conference, Berlin, Germany, 1-7 Feb 2007
27. Lappas I, Geisselmann A, Reith C, Müller W (2009) Catalyst Technologies for Heavy Duty Vehicles in On Road and Off Road Applications. Paper presented at the 7th FAD Conference, Dresden, Germany 4-5 Nov 2009
28. Kircher D, Stotz T (2008) Holland America Line sea water scrubber demonstration project. Paper presented at Faster Freight, Cleaner Air, Seattle, Washington, USA 17 Sep 2008
29. Caiazzo G, Langella G, Miccio F, Scala F (2012) Seawater SO₂ Scrubbing in a Spray Tower for Marine Application. Paper presented at the 35th Meeting of the Italian Section of the Combustion Institute, Milano, Italy, 10-12 Oct 2012
30. Jürgens R (2012) Exhaust Aftertreatment for Ship Engines Running on Heavy Fuel Oil—Requirements and Experience. Paper presented at the 5th International CTI Conference Emission Reduction for Off-Highway Applications, Lindau, Germany, 26-27 Sep 2012
31. Kaiser R, Rusch K (2007) Designing of SCR Systems for reducing Nitrogen Oxide in Diesel Engines. MTZ 68(12):1062–1070
32. Weltens H, Bressler H, Terres F, Neumaier H, Rammoser D (1993) Optimization of Catalytic Converter Gas Flow Distribution by CFD Prediction. SAE Technical Paper 930780
33. Grünwald JD (2007) Verbesserung der Reduktionsmitteldispersion und -verdunstung in SCR-Abgasanlagen. Dissertation, TU München
34. Forster E, Kaiser R, Regenold K, Rusch K (2008) Static Mixing Element and Method of Producing a Static Mixing element. US patent 8,375,708
35. Berner G, Pröbstle G, Herr W, Balling L (1991) Static Mixer. European patent EP0594657
36. Stüttem M (2005) Abgasanlagen. In Braess H, Seiffert U (eds) Vieweg Handbuch Kraftfahrzeugtechnik, 4th edn. Vieweg, Wiesbaden

37. Willems F, Cloudt R, van den Eijnden E, van Genderen M, Verbeek R, de Jaeger B, Boomsma W, van den Heuvel I (2007) Is closed-loop SCR control required to meet future emission targets? SAE Technical Paper 2007-01-1574
38. Schär C, Onder C, Geering H, Elsener M (2003) Control of a Urea SCR Catalytic Converter System for a Mobile Heavy Duty Diesel Engine. SAE Technical Paper 2003-01-0776
39. Hofmann L, Rusch K, Fischer S (2004) Onboard Emissions Monitoring on a HD truck with an SCR system using NO_x sensors. SAE Technical Paper 2004-01-1290
40. Song Q, Zhu G (2002) Model-based Closed-loop Control of Urea SCR Exhaust Aftertreatment System for Diesel Engine. SAE Technical Paper 2002-01-0287
41. Herman A, Wu MC, Cabush D, Shost M (2009) Model Based Control of SCR Dosing and OBD Strategies with Feedback from NH₃ Sensors. SAE Technical Paper 2009-01-0911

Part II

Catalysts

Chapter 3

Vanadia-Based Catalysts for Mobile SCR

Jonas Jansson

3.1 Introduction

NH₃-based SCR has been used for stationary applications since the 1970s. SCR systems were first installed in Japan for gas, coal, and oil-fired utility boilers. These applications were equipped with SCR catalysts in order to reduce NO_x in response to the more stringent ambient NO_x standard set by the Japanese government in 1973 [1, 2]. These applications typically used stacks of vanadia/titania-based SCR catalysts as honeycomb monoliths, tubes, or plates, using ammonia as reductant [3]. The efficiency of these systems were quite high, in the range of 90–95 % NO_x conversion and relatively robust in maintaining NO_x conversion over time [3]. In the mid 1980s, SCR systems were introduced in Europe on stationary applications.

In the 1990s, it was investigated whether the SCR technology used for reducing NO_x in stationary applications could be transferred to mobile applications, more specifically to heavy-duty diesel engines used for truck applications [4]. Koebel et al. [5] studied the reduction of NO_x from a 117 kW diesel engine by means of urea-SCR. They showed the potential of high NO_x conversion and outlined the challenges of transient control of urea dosing when running the engine in mobile applications. Havenith et al. [6] used a 12 l, 315 kW heavy-duty diesel engine complying with Euro2 emission standard. Different transient urea dosing strategies were used and the authors showed that Euro4 NO_x emission levels could be achieved in FIGE (ETC) transient cycle. Fritz et al. [7] made an on-road demonstration of a mobile SCR system based on an extruded vanadia SCR catalyst, which was started to be developed in 1992. In engine test bench, the SCR system was shown to meet Euro4 NO_x emission levels. Two on-road demonstration programs were run. The first started in 1995 and consisted of eight heavy-duty

J. Jansson (✉)

Department BF66330, BC2, Volvo Group Trucks Technology, SE-405 08 Gothenburg, Sweden

e-mail: jonas.jansson@volvo.com

diesel vehicles. The second demonstration started in 1998 and consisted of 13 heavy-duty diesel vehicles. Similar studies were also done in the US [8].

The driver for introduction of SCR on mobile applications was the introduction of Euro4 and Euro5 legislations, which called for a reduction in tail-pipe NO_x. The mobile applications would make use of an aqueous urea solution as reductant, which needs to be carried in a separate tank on the vehicle. This would also mean a need for a urea infrastructure [9]. Competing technologies were HC-SCR [10] and lean NO_x adsorbers [11], which could make use of diesel fuel as the reductant, eliminating the need for a separate urea tank. However, the higher NO_x conversions and lower sensitivity to poisons for ammonia-SCR over vanadia catalysts spoke in favor of urea-SCR. For the development of the SCR catalyst technology for mobile applications, the choice of vanadia-SCR was natural due to the experience that existed for using this together with stationary diesel engines. Vanadia-SCR for mobile applications was introduced on a large scale in Europe in 2005/2006 with the introduction of the Euro4 legislation. Urea infrastructure was also proven not to be such a large issue as first anticipated due to early consensus in the market to go for the urea-SCR technology, allowing the distributors to adapt using the existing fuel infrastructure.

3.2 Legislation

An overview of emission legislation for heavy-duty trucks in Europe is shown in Fig. 3.1. Up to Euro3 legislation (introduction in 2000), it had been possible to meet newer emission legislation with refined engine technology leading to less NO_x and PM (particulate mass) being produced in the combustion chamber. However, starting with Euro4 (3.5 g/kWh NO_x, 0.02 g/kWh PM steady state), manufacturers were looking into using exhaust aftertreatment in combination with engine technology in order to meet the emission legislation [4, 9].

With the state-of-the-art engine technology in the beginning of the 2000s, two different strategies could be used for meeting Euro4 NO_x and PM levels. One is to tune the engine to low PM, so that the emission limit for PM was fulfilled. This was done by using early injection timing and other engine means which lowered the soot from the combustion so PM level was met. This leads to improved fuel consumption of the engine, however, also to higher NO_x emissions. The NO_x emissions are then reduced by means of SCR [4], see Fig. 3.2.

The other path would be to lower the engine-out NO_x to the legislated value with later injection timing and cooled EGR. This would lead to higher soot from the combustion and higher fuel consumption. A DOC (diesel oxidation catalyst) and/or a DPF (diesel particulate filter) are then used in order to reduce the particulates to the legislated value (Fig. 3.2).

The choice of system is not obvious. The SCR system has the advantage of a simpler engine design leading to less complexity and lower engine product cost. Since the SCR system does not require cooled EGR, higher engine power output

Fig. 3.1 NO_x and PM legislation for heavy-duty vehicles in Europe

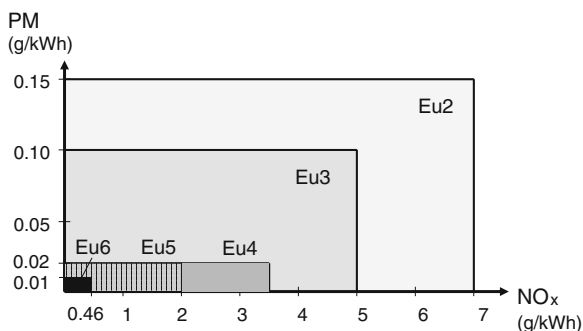
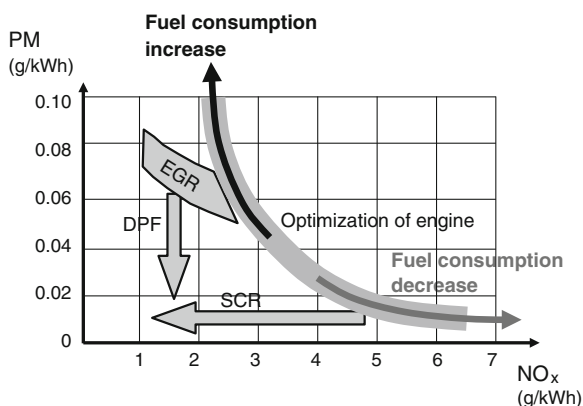


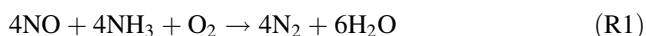
Fig. 3.2 Optimization of engine for either NO_x reduction by SCR or PM reduction by DPF

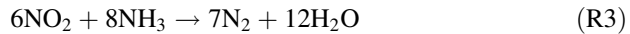
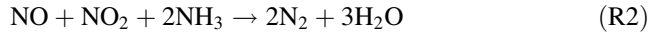


could be achieved compared to an EGR solution, given a specific cooling capacity in the vehicle. The cost of the vanadia SCR catalyst raw materials are also lower compared to a DOC/DPF using expensive precious metals. In addition, the SCR system has a better fuel consumption compared to the cooled EGR system. However, the disadvantages of the SCR system are the added cost and complexity of the urea dosing pump, additional storage tank for urea, and the need for the driver to regularly refill urea. Some manufacturers went for EGR/DOC/DPF and some with SCR for Euro4. However, with the introduction of Euro5, the after-treatment technology converged more and more toward SCR, due to the increased fuel penalty for reducing NO_x with engine means.

3.3 Main SCR Reactions

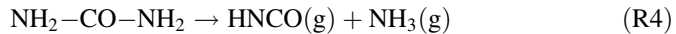
If NH₃ is used as a reductant, the main reactions between NO_x and NH₃ are:



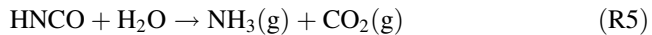


Since the NO_x emissions from the diesel engine consist of approximately 90 % NO and only 5–10 % NO₂, reaction (R1) will be the main reaction.

If aqueous urea solution is used as reductant, the urea droplets decompose to ammonia in the hot exhaust gases. This proceeds through first evaporating water in the urea droplets. After this, the urea decomposes thermally via the reaction (R4) forming one molecule of NH₃.



After this, isocyanic acid, HNCO can undergo hydrolysis via reaction (R5) giving another NH₃ molecule.



3.4 Urea Injection

The reductant for the SCR reaction needs to be added in proportion to the NO_x coming from the engine. For the SCR reaction over a vanadia SCR catalyst, the desired reductant is NH₃. Carrying the reductant onto the vehicle could be done in several ways. Installations with NH₃(g) and NH₃(aq) are not preferred due to the hazards with dealing with such fluids in vehicles being on the road. NH₃ could be stored in a metal salt, for example, MgCl₂ or SrCl₂ [12]. NH₃ is chemically bound to the metal salt and is released by heating the salt. The salt can after having released all NH₃, be refilled by NH₃ gas again [13]. The SCR reaction over vanadia SCR catalysts could also use ammonium formate as reductant [14]. The advantage with this reductant is its low freezing point. Using ammonia salts like ammonium carbonate or ammonium carbamate has also been suggested [13]. The most widely used carrier for the reductant is an aqueous solution of urea (NH₂—CO—NH₂). The solution is 32.5 % urea in water with the generic name AdBlue.

3.5 Properties of Vanadia SCR Catalyst

Vanadia SCR catalysts contain V₂O₅ as the active component. V₂O₅ is typically impregnated on an anatase TiO₂ support together with WO₃ to stabilize the vanadia and increase thermal durability. Typical compositions are 1–3 % V₂O₅ and ~10 % WO₃ on the TiO₂ support [2, 15].

For mobile applications, the SCR catalyst material is either washcoated onto an inert monolith substrate or the catalyst material is extruded or produced in a way

that the monolith walls consist of active catalyst material throughout the complete wall (see Fig. 3.3). The monolith is a structure with several small channels through which the exhaust gas passes. The monolith is characterized by the cell density and the substrate wall thickness. The cell density is the number of cells per unit area. In the automotive industry, this is often measured in the unit of cells per square inch (cpsi). The wall thickness is commonly measured in μm or milli-inch (mil), where $1 \text{ mil} = 25.4 \mu\text{m}$. The purpose of the monolith type of structure is to enhance the contact area between the exhaust gas and the SCR coating while still maintaining a moderate pressure drop over the system. In a washcoated SCR catalyst (Fig. 3.3 top), the monolith structure consists of an inert material. The inert monolith material needs to have enough mechanical strength and integrity to withstand the forces and vibrations the SCR catalyst will be exposed to in the vehicle. Common monolith materials are cordierite and steel. The active catalyst material is then applied as a thin layer on the walls of the inert monolith substrate. In the fully extruded SCR catalyst or full body SCR catalyst (Fig. 3.3 bottom), the whole catalyst monolith consists of active material. The catalyst material thus not only needs to maintain the SCR reaction but also has enough mechanical integrity.

The shape of the cross-section of the monolith channels may be of different geometry for both coated and extruded SCR catalysts. A very common shape is the square geometry as in Fig. 3.3, however, other forms like triangular are also existing.

In addition to the above-mentioned designs, it is principally possible to apply SCR catalyst coating on a DPF (diesel particulate filter) substrate as well, thus combining NO_x reducing and particulate trapping function in the same unit [16, 17]. However, since the SCR catalysts coated on DPF need to withstand the soot regeneration of the filter, high thermal durability for the SCR catalyst is needed. This means that zeolite SCR materials with high thermal stability are more suited for this type of SCR design compared to vanadia SCR catalysts.

Vanadia SCR catalysts have typically a window of maximum NO_x conversion between ca 250 °C and ca 450–500 °C. An example is shown in Fig. 3.4 where steady-state NO_x conversion is measured on a heavy-duty engine at constant engine speed. This result is well known both from testing on an engine [18] and in synthetic gas testing [19]. At low temperatures, below the light-off temperature, the reaction rate for the NO + NH₃ reaction is low, leading to the low NO_x conversion seen below ca 250 °C. At temperatures above ca 450–500 °C, the selectivity of the SCR reaction is lowered since NH₃ is being oxidized by O₂ instead of reacting with NO. This higher rate of oxidation of NH₃ leads to the loss in NO_x conversion at high temperatures [20].

The activity window of vanadia-based SCR catalysts can be changed by modifying the vanadia concentration. Increasing the vanadia concentration will increase the low-temperature activity of the SCR catalyst. Increasing the V₂O₅ concentration from 0.78 to 1.4 % decreased the NO conversion light-off from ca 267 to ca 207 °C [2]. Similar result is obtained in [21]. However, the surface area of the catalyst decreases with increasing V₂O₅ concentration. Increasing the V₂O₅ concentration from 0.78 to 1.4 % decreased the Specific Surface Area (SSA) from

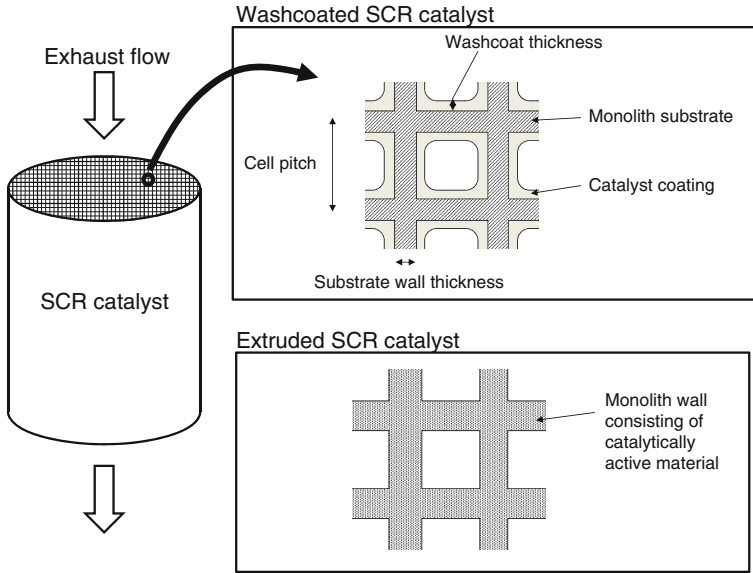


Fig. 3.3 Principal design of an SCR catalyst for mobile applications. SCR catalyst with catalytic material coated on a monolith substrate and an SCR catalyst consisting of a fully extruded substrate

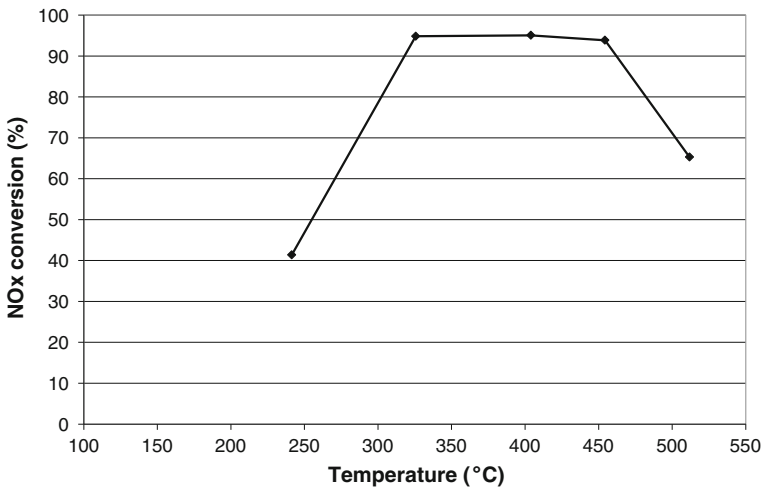


Fig. 3.4 NOx conversion as a function of temperature measured at constant engine speed on a heavy-duty engine. Maximum space velocity is 55,000 h⁻¹

87 to 80 m²/g [2]. Further increase of V₂O₅ concentration to 3.56 % reduced the SSA to 64 m²/g. High V₂O₅ concentration also promotes the anatase to rutile phase transition, which will lead to lower thermal stability of the catalyst [2]. Vanadia concentrations above ca 3 % will also lead to loss in selectivity of the catalyst and increased formation of N₂O [15, 22, 23].

In order to improve catalyst performance, WO₃ or MoO₃ is added to the V₂O₅/TiO₂ system. Addition of 9 % WO₃ increases the activity of the SCR catalyst [21] leading to lower light-off temperature for the NO conversion by NH₃ [2]. WO₃ also improves thermal durability of the catalyst by stabilizing the TiO₂ from phase change from anatase to rutile [2, 24]. Forzatti et al. [2] noted that for TiO₂ without WO₃, rutile formation was starting to be seen at 700 °C while for 9 % WO₃/TiO₂, rutile formation was seen first at 900 °C.

3.6 Reaction Mechanism

The most acknowledged reaction mechanism for the NO + NH₃ reaction (R1) over the vanadia SCR catalyst is a dual-site Eley-Rideal mechanism proposed by Inomata et al. [25] and Miyamoto et al. [20]. A simplified description of the mechanism is shown in Fig. 3.5.

The active site consists of an acid site associated with V–OH adjacent to V⁵⁺ = O. NH₃ is first strongly adsorbed as NH₄⁺ to the V⁵⁺ = O–V–OH site (Fig. 3.5a). Gas-phase NO then reacts with the adsorbed NH₄⁺ (Fig. 3.5b) to form the activated complex shown in (Fig. 3.5c). N₂ and H₂O split from the activated complex and desorb, leaving two V–OH groups (Fig. 3.5d). One of the V–OH is oxidized by gas-phase oxygen to form V⁵⁺ = O and water (Fig. 3.5e and f) thus closing the catalytic cycle.

The Eley-Rideal mechanism shown in Fig. 3.5 describes well the reaction (R1) at operating temperatures T > 280 °C [26]. At lower temperatures, however (T < 250 °C), NH₃ can inhibit the SCR-reaction [26, 27], an effect that cannot be explained by the mechanism in Fig. 3.5. Nova et al. [26, 27] proposed that at low temperatures the reaction proceed through a modified redox kinetics: NH₃ can adsorb to two types of sites, one redox site associated with vanadyl species and one nonreducible strongly acidic site. The inhibition of the SCR reaction can occur by NH₃ blocking part of the active catalyst sites from the redox cycle.

For the NO + NH₃ reaction (R1), the reaction rate could be approximated with

$$r = k(T) \cdot c_{\text{NO}} \cdot \theta_{\text{NH}_3} \quad (3.1)$$

That is, the reaction order is one with regard to NO [2, 25]. This is a good assumption in many cases, however, as shown by Nova et al. [26] a more detailed study of the reaction using transient step changes in NH₃ with different O₂ concentration and at different reaction temperatures, revealed a more complex reaction rate expression:

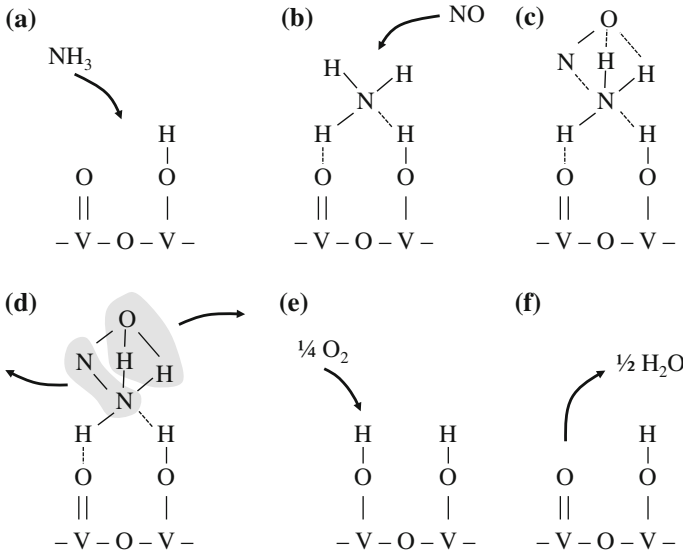
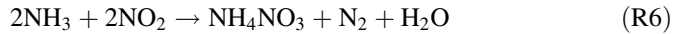


Fig. 3.5 Mechanism for the NO reduction by NH₃ over V₂O₅

$$r = \frac{k(T) \cdot c_{\text{NO}} \cdot \theta_{\text{NH}_3}}{\left(1 + K_{\text{NH}_3} \frac{\theta_{\text{NH}_3}}{1 - \theta_{\text{NH}_3}}\right) \left(1 + k_{\text{O}_2} \frac{c_{\text{NO}} \theta_{\text{NH}_3}}{p_{\text{O}_2}^{1/4}}\right)} \quad (3.2)$$

However, this equation could approximately be reduced to Eq. (3.1) under condition that O₂ > 1–2 %, T > 280 °C. This is in line with the result of Inomata et al. [25] who showed that the rate of reaction at 250 °C was independent of O₂ concentration above 1 % O₂.

For the reaction of NO + NO₂ with NH₃ (R2), Ciardelli et al. [28] proposed a mechanism involving nitrate species as an intermediate. NO₂ and NH₃ first react to form NH₄NO₃ and N₂ in a fast reaction:

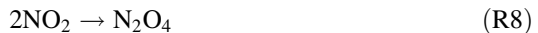


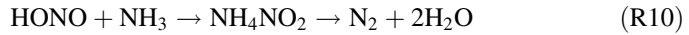
The nitrate species may then react with NO in a redox reaction to form NO₂:



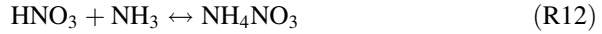
The NO₂ formed in reaction (R7) may be reused in (R6) to form another N₂. The overall reaction, combining the steps in (R6) and (R7) will be the overall NO + NO₂ reaction (R2).

The reaction scheme was further developed in [27, 29, 30] as broken down into the following steps:





HONO formed in (R11) can then react according to (R10) and form another N_2 . In parallel, there is the equilibrium reaction



This reaction scheme also explained the low performance and low selectivity in the $\text{NO}_2 + \text{NH}_3$ reaction (R3). In the absence of NO, reaction (R11) (or reaction (R7) in the simple scheme) cannot take place. This will lead to accumulation of HNO_3 or NH_4NO_3 instead of forming N_2 . At high temperature the accumulated NH_4NO_3 can also decompose to N_2O according to



3.7 Function/Principle Design

The principle layout for a mobile vanadia SCR system meeting Euro4 or Euro5 emission legislation is shown in Fig. 3.6. The principal components are a unit containing the SCR catalyst elements (5), a urea tank (8), a urea dosing module (9), different sensors (10) (11) (12) (13), and hardware and software for controlling the system (14) (15).

The exhaust from the diesel engine (1) is directed in an exhaust pipe (2) toward the unit containing the SCR catalyst (5). The SCR catalyst monoliths (6) are typically installed inside the silencer. The unit (5) has thus the function of both containing the catalytic monolith elements (6) and reducing noise from the engine. In order to maintain as high as possible the reaction temperature for the SCR reaction, the distance between the engine exhaust outlet to the SCR catalyst inlet is minimized. In case this is not possible to do due to packaging constraint in the vehicle, the exhaust piping (2) could be isolated. The AdBlue (urea solution) is stored in a urea tank (8) mounted on the vehicle. Tank sizes can be of different sizes depending on the specific need of the driver, in the same way as diesel tanks can be of different sizes. Normal urea tank sizes ranges between 50 L and 150 L. The urea is entered into the exhaust stream by means of a urea dosing pump (9). The pump is spraying the urea liquid in the form of small droplets into the exhaust stream at the urea injection point in the exhaust pipe (3). The injected urea droplets decompose to ammonia in the hot exhaust gases. Water is first evaporated from the urea droplets and the solid urea is then decomposed to NH_3 via the reactions (R4) and (R5).

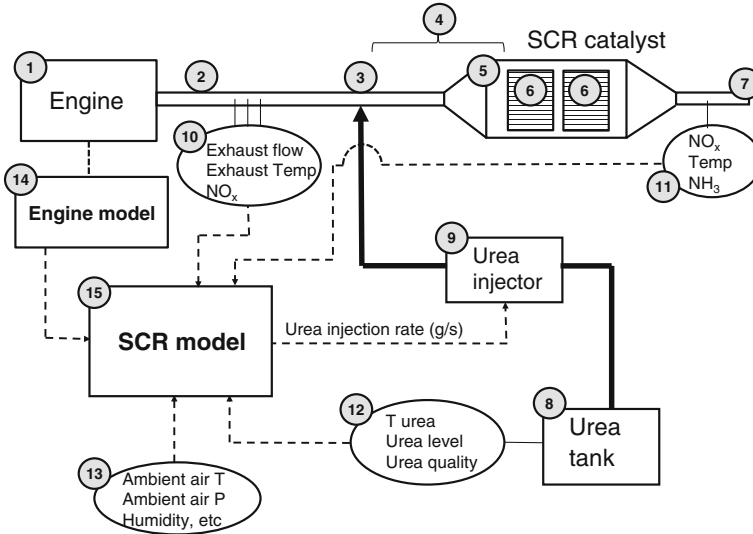


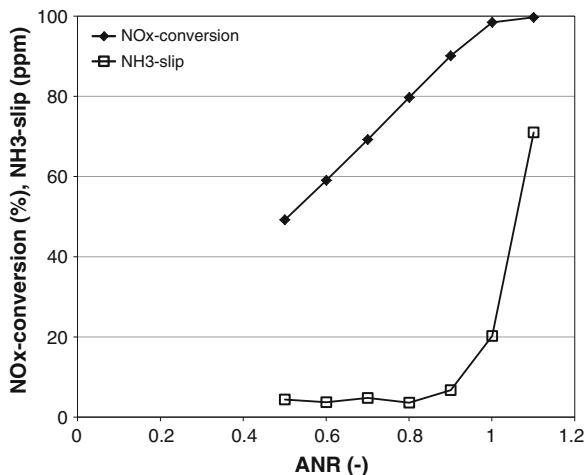
Fig. 3.6 Principle layout of installation of an SCR system in a mobile application. (1) Engine (2) Exhaust pipe carrying the exhaust from the engine (3) Urea injection point in exhaust pipe (4) Urea mixing zone (5) Silencer containing the (6) SCR catalyst elements (7) Exhaust outlet (8) AdBlue (urea) tank (9) Urea pump/injector (10) Sensors for measuring exhaust conditions upstream the SCR catalyst (11) Sensors for measuring exhaust conditions downstream the SCR catalyst (12) Sensors for measuring conditions inside the urea tank (13) Ambient sensors (14) Engine model/Engine ECU (15) SCR model/SCR control unit

The mixing of the urea droplets with the exhaust gas and the decomposition through reactions (R4) and (R5) take place in the urea mixing zone (4) in Fig. 3.6. This can be realized through a pipe between the urea injection point and the catalyst inlet surface or by internal piping or tubes inside the silencer unit. In the case where the mixing zone (4) is integrated in the SCR unit (5), the urea injection point (3) would appear to be at the inlet of the SCR unit. It is important to design the urea mixing zone (4) to have sufficient residence time or length from the urea injection point to the SCR monolith entrance in order for the decomposition reactions to take place. It is also important to verify that sufficient mixing between the urea droplets and the exhaust gas is taking place. Typically, CFD-analysis needs to be done in order to ensure that a homogenous mixture of NO_x and NH₃ is entering the catalyst monoliths.

When entering the SCR catalysts, NO_x and NH₃ are reacting through the SCR reactions (R1), (R2), and (R3). NO_x from the diesel engine consist to ca 90 % of NO. This means that for a vanadia SCR system layout according to Fig. 3.6, it will be the NO-only reaction (R1) which is the most important.

In order to get the desired NO_x conversion and avoid NH₃ slip in the exhaust gases leaving the system, an appropriate urea injection rate is needed. Figure 3.7 shows the effect on NO_x conversion and NH₃ slip as a function of ammonia-NO_x

Fig. 3.7 Example of NO_x conversion and NH₃ slip as a function of Ammonia NO_x ratio (ANR)



ratio (ANR) in a steady-state engine point. ANR = 1 is defined as the theoretical flow of urea solution (g/s) required for converting 100 % of the incoming NO_x flow (g/s). For reactions according to (R1) and a urea concentration of 32.5 %:

$$ANR \approx \text{urea flow(g/s)} / (2 \times \text{NO}_x\text{flow(g/s)})$$

As can be seen in Fig. 3.7, at low ANR, the NH₃ slip is close to zero and NO_x conversion is close to proportional to ANR. At higher ANR (closer to 1), NH₃ slip is increasing rapidly as the NO_x conversion approaches 100 %. Since NH₃ slip in the exhaust outlet needs to be minimized, this puts a limit to what NO_x conversion can be achieved. By adding an ammonia slip catalyst (ASC) after the SCR catalyst, the NH₃ slip can be lowered allowing for extra margin in the control [18].

Figure 3.7 shows a steady-state case. In real-world transient operation, the NO_x flow varies continuously. This means that good control of the urea injection rate is needed in order to achieve high NO_x conversions while avoiding NH₃ slip. The urea injection rate is calculated by a control software, depicted as (15) in Fig. 3.6. The software/SCR model can make use of different sensors. Sensors (10) to determine the state of the exhaust gases to be treated (e.g., NO_x flow and temperature), sensors (11) to quantify the outlet gas conditions, sensors (12) to determine the state and quality of the reductant (urea) and sensors (13) for determining ambient conditions. The sensors may be physical sensors or virtual sensors. Virtual sensors are models that calculate the sensor value based on a theoretical or empirical model, thus eliminating the need for a physical component. An example of result from a transient control taken from the ETC cycle on a Euro4 engine is shown in Fig. 3.8.

Control of the SCR system could be either open-loop or closed-loop [31, 32]. Basic open-loop control will be robust and not have any stability problems [32]; however, it will be difficult to achieve very high NO_x conversions. Song and Zhu [32] estimated that maximum ca 75 % NO_x conversion would be possible with

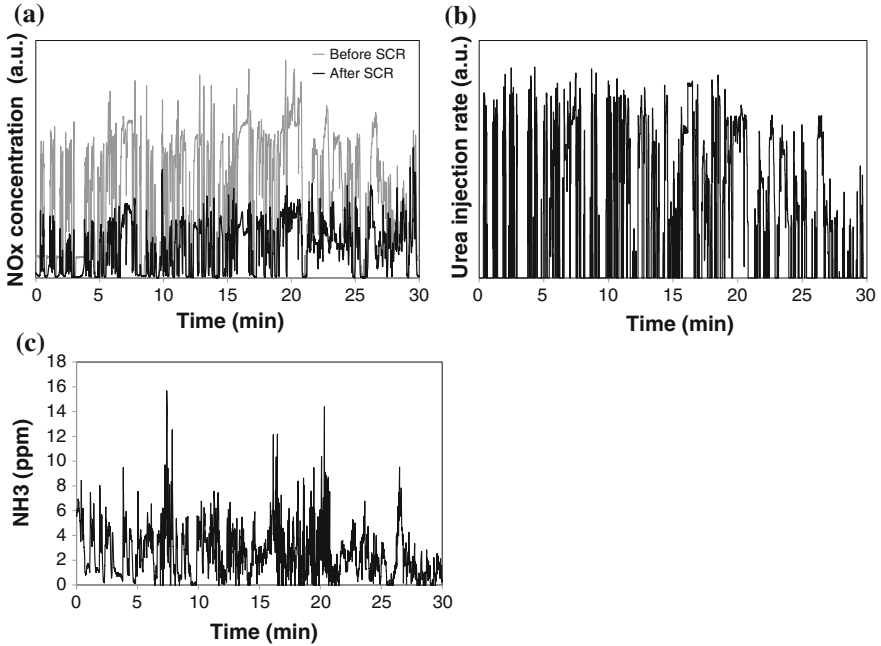


Fig. 3.8 Example of control of a Euro4 SCR system. **a** NO_x concentration before SCR catalyst (gray) and resulting NO_x concentration after SCR catalyst (black), **b** urea injection rate calculated from the controller, **c** resulting NH₃ slip

open-loop control while ca 90 % could be achieved with closed-loop control. van Helden et al. [31] estimated maximum 70–80 % ANR for open-loop control while 85–95 % NO_x conversion was estimated for close-loop control.

An example of how to construct a control strategy for an SCR system meeting Euro4 emission level is described by Schär et al. [33]. With a combination of feed-forward and feedback control, they obtained 82 % NO_x conversion in ETC while maintaining average NH₃ slip below 10 ppm.

3.8 Dimensioning of SCR System

Figure 3.9 shows the NO_x conversion measured at constant engine speed for a vanadia SCR system tested on a heavy-duty diesel engine. Three different SCR catalyst volumes were used giving maximum system space velocities of 55,000, 80,000, and 140,000 h⁻¹, respectively. Maximum space velocity is defined as the space velocity in the engine operating point with highest exhaust mass flow. It can be seen in Fig. 3.9 that increasing the space velocity will decrease the possible NO_x conversion for the system. This is well known and due to the fact that a high

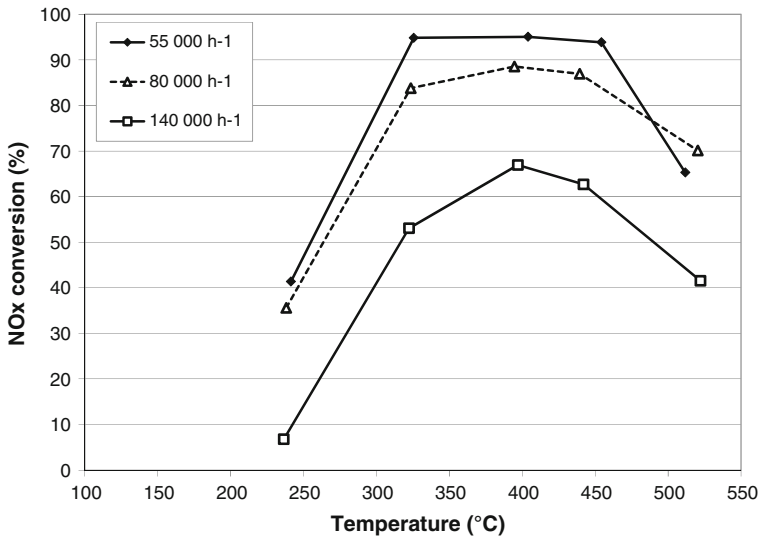


Fig. 3.9 NOx conversion as a function of temperature measured at constant engine speed on a heavy-duty engine using different SCR catalyst volumes corresponding to maximum space velocities of 55,000 h⁻¹ (◆), 80,000 h⁻¹ (Δ), 140,000 h⁻¹ (□)

space velocity means that the residence time in the SCR catalyst is shorter. Similar result was presented for example by Blakeman et al. [18]. They tested three different maximum space velocities, 35,000, 46,000, and 70,000 h⁻¹, and showed gradually lower NOx conversion for the increased space velocities.

Figure 3.10 shows NOx conversion in several engine operating points covering a large range of exhaust mass flows and with three different SCR catalyst volumes for a vanadia SCR catalyst. The data are thus covering space velocities ranging from ca 18,000 up to 140,000 h⁻¹. NOx conversion in each point is plotted against space velocity. Engine points with temperatures below 300 °C are removed from the plot, since in they are in the light-off region of the catalyst.

A clear dependence of NOx conversion on space velocity is seen in Fig. 3.10. For the lowest space velocities (<30,000 h⁻¹) and exhaust temperatures >300 °C, NOx conversions >90 % were achievable while at the highest space velocity (140,000 h⁻¹) merely 40 % NOx conversion was obtained. When designing the appropriate SCR catalyst volume for an engine the required NOx conversion will limit the maximum space velocity that can be allowed. Taking the data in Fig. 3.10, if a NOx conversion of 80 % is required, the maximum space velocity needs to be around 50,000–60,000 h⁻¹ for this specific system.

Although the data in Fig. 3.10 indicate that the space velocity should be as low as possible in order to maximize NOx conversion, in practical application this may not be feasible. A very low maximum space velocity will mean a large SCR catalyst volume, which will add weight to the truck and the SCR catalyst will occupy a larger space on the truck, meaning that the available space on the truck

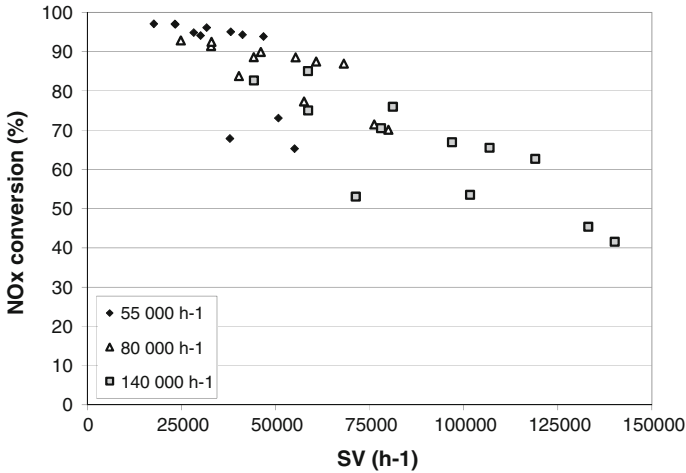


Fig. 3.10 NO_x conversion as a function of space velocity for a vanadia SCR system tested on a heavy-duty diesel engine

will decrease. Since it is desired to minimize both packaging space and weight from the SCR muffler, careful choice of the trade-off between NO_x conversion and space velocity is needed.

Examples of space velocities used for heavy-duty diesel applications with vanadia SCR catalysts are in the range 20,000–70,000 h⁻¹ [6, 18, 34, 35]. Havenith et al. [6] used 51 dm³ of washcoated vanadia/alumina SCR catalyst volume, corresponding to a space velocity of 28,000 h⁻¹ for a 12 l heavy-duty engine. van Helden et al. [35] used 34 dm³ of washcoated vanadia SCR catalyst volume (space velocity 45,000 h⁻¹) for a 12.0 and a 12.6 l heavy-duty engine. Hofmann et al. [36] used the same SCR catalyst volume (34 dm³), but with a fully extruded vanadia SCR catalyst for a 12 l heavy-duty diesel engine.

In the light-off region of the catalyst (ca 200–300 °C, see also Fig. 3.11) the performance of the system will depend on the activity of the SCR catalyst (light-off temperature). As discussed above, the activity window of the vanadia SCR catalyst could be tuned by the catalyst composition, mainly the vanadia concentration. Increasing the low-temperature activity could allow to make a smaller SCR catalyst while still having the same NO_x conversion. The low-temperature performance of a washcoated SCR catalyst could also of course be modified by changing the washcoat loading (changing the number of catalytic sites). Tao et al. [37] showed that the SCR catalyst activity at low temperature was increased with increasing washcoat loading. Increasing the washcoat loading from 180 g/L to 240 g/L decreased the temperature for 70 % NO_x conversion from 275 to 250 °C. A further increase of the washcoat loading to 540 g/L decreased the temperature for 70 % NO_x conversion to approximately 220 °C. However, increasing the washcoat loading will increase the washcoat thickness, leading to higher back-pressure as discussed below.

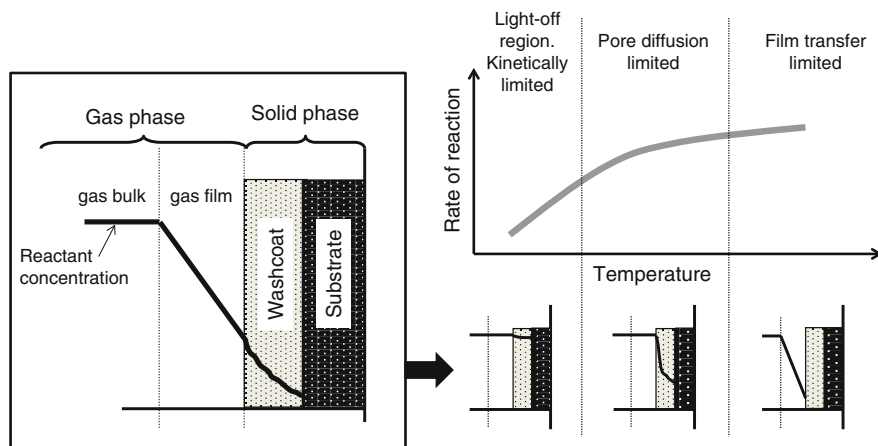
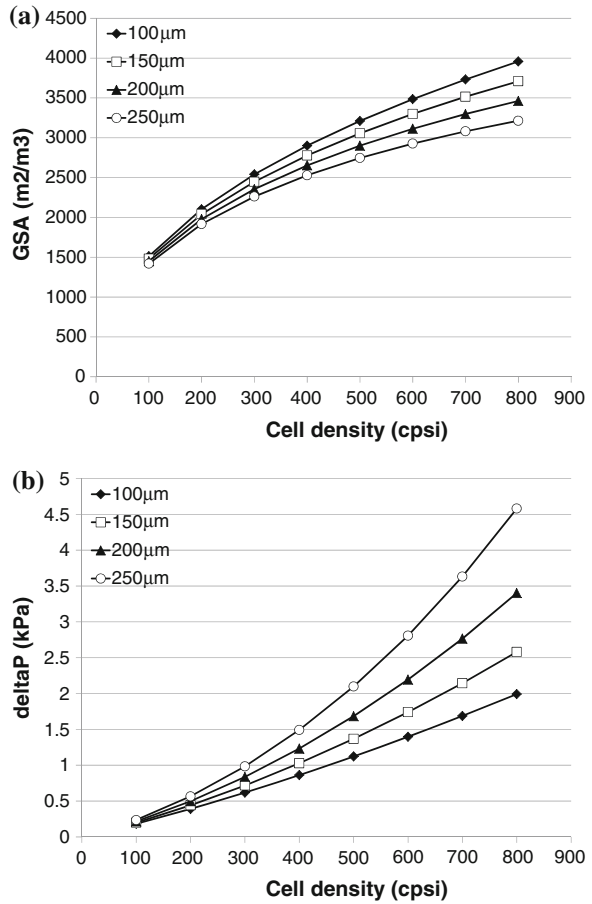


Fig. 3.11 Principal figure of mass transfer in a washcoated catalyst

In the pore diffusion limited region of the catalyst (see Fig. 3.11), the pore structure of the washcoat or extruded substrate will be important. Especially for high washcoat loadings with large washcoat thickness, the diffusion of reactants into the washcoat will limit the access to the active sites. Large pores will allow for a higher diffusion rate into the washcoat but will reduce the specific surface area of the catalyst. Smaller pores will increase the specific surface area but limit the diffusion rate. For a typical vanadia/titania SCR catalyst a compromise is found at a specific surface area of approximately $75 \text{ m}^2/\text{g}$ and pore sizes of the order of 10 nm [38]. The rate of diffusion could also be improved by introducing macropores into the washcoat, allowing for faster diffusion of reactants while maintaining the specific surface area provided by the micropores.

In the film transfer limited region (see Fig. 3.11), the performance of the SCR system can be increased by increasing the area for gas–solid mass transfer by increasing the geometrical surface area (GSA) of the catalyst. As discussed above, SCR catalysts for mobile applications are in the form of monolith units (see Fig. 3.3). Increasing the geometrical surface area can be done by increasing the cell density. Figure 3.12a shows the relation between GSA and cell density. When increasing the cell density, the rate of mass transfer is increased due to the higher contact area (GSA) between the gas-phase and the monolith walls, and this will increase the NO_x conversion in the film transfer limited region. This is well known and has for example been demonstrated in [39]. However, as can be seen in Fig. 3.12b, increasing the number of cells per unit area (increasing the cell density) will also increase the pressure loss over the system. This is not a wanted situation since higher pressure loss over the system means higher fuel consumption for the engine. As can be seen in Fig. 3.12, the pressure loss is increasing more rapidly as the cell density is increased compared to the increase in geometrical surface area. This means that there is an optimum cell density where the increase in GSA if the

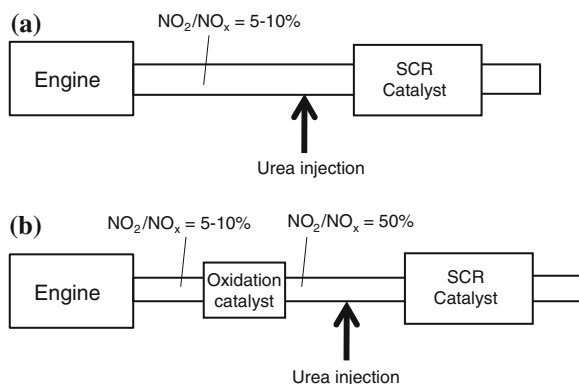
Fig. 3.12 a Geometric surface area (GSA) as a function of cell density and wall thickness. **b** Pressure loss at ambient temperature in kPa over a 5.66'' x 6'' substrate at 10 Nm³/min. Wall thickness including coating in **a** and **b**: \blacklozenge 100 μm , \square 150 μm , \blacktriangle 200 μm , \circ 250 μm



cell density was further increased is not motivated by the more rapidly increasing pressure loss. One way to partly resolve this is to reduce the thickness of the monolith walls, thus increasing the open frontal area and reducing the pressure loss.

Common cell densities used for heavy-duty diesel applications with vanadia SCR catalysts are 300 cps [19, 36] and 400 cps [6, 18, 35, 37, 40]. For these cell densities, the wall thicknesses for cordierite substrates range typically from 4 mil (100 μm) to 8 mil (200 μm) [18, 19, 37, 41]. In Fig. 3.12, with wall thickness is here considered the total wall thickness resulting from the substrate including the catalyst washcoat. The washcoat thickness for a coated vanadia SCR catalyst depends on the washcoat loading and could range from 20 to 100 μm [37]. For a washcoated SCR catalyst, the wall thickness could of course be reduced either by decreasing the inert substrate wall thickness or reduce the washcoat thickness as long as this does not effect the catalyst performance.

Fig. 3.13 Principal layout of (a) SCR system without upstream oxidation catalyst, (b) SCR system with NO_2 forming oxidation catalyst upstream the SCR catalyst



3.9 Effect of NO_2

As mentioned above, the NO_x from the diesel engine exhaust consists to ca 90 % of NO , which means that the reaction will proceed to the largest extent via the $\text{NO} + \text{NH}_3$ reaction (R1). However, reaction with equimolar $\text{NO} + \text{NO}_2$, reaction (R2), has a higher reaction rate compared to reaction (R1) [42]. This means that if a part of the NO in the engine exhaust could be converted to NO_2 , the rate of the SCR reaction would increase. A way of doing this is to add an oxidation catalyst that oxidizes NO to NO_2 upstream the SCR catalyst. The layout of this is shown in Fig. 3.13.

The effect of adding an upstream oxidation catalyst to the SCR system is demonstrated in Fig. 3.14. By oxidizing part of the NO to NO_2 , the light-off for the SCR reaction could be shifted from ca 250 to ca 225 °C. The low-temperature activity of the SCR system is thus improved by adding the oxidation catalyst upstream. Since the optimum NO_2/NO_x ratio is 50 % for reaction (R2) even further improvement of the low-temperature performance of the system could be done by increasing the NO_2 make over the oxidation catalyst (for example by increasing the PGM loading). However, the peak NO_2/NO_x ratio will then exceed 50 % and the reaction will partly proceed via the $\text{NO}_2 + \text{NH}_3$ reaction (R3). Since this reaction is slower compared to (R2) the NO_x conversion will decrease for the points where NO_2/NO_x exceeds 50 % compared to points with lower NO_2/NO_x ratios. This was clearly shown by Walker et al. [43] where the use of an oxidation catalyst creating optimal NO_2/NO_x ratio improved the NO_x conversion at all temperatures, while an oxidation catalyst forming higher NO_2/NO_x indeed further improved the low-temperature SCR performance, but at the temperatures where NO_2 formation was exceeding 50 %, the NO_x conversion was drastically decreased and showed even lower NO_x conversion compared to a system without any oxidation catalyst.

Disadvantages of adding an upstream oxidation catalyst is of course the added cost and complexity for this component and the increased sensitivity for fuel sulfur

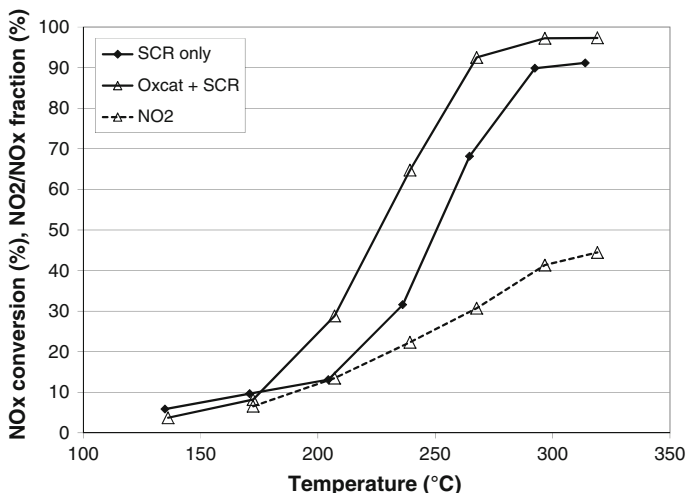


Fig. 3.14 Effect of introducing an oxidation catalyst upstream the SCR catalyst. NO_x conversion with (Δ) and without (◆) an oxidation catalyst upstream the SCR catalyst

for a PGM-containing system compared to an SCR-only system. Fuel sulfur will both deactivate the PGM sites on the DOC, but the DOC will also oxidize SO₂ to SO₃, which will lead to risk of sulfur deactivation of the SCR catalyst due to ammonium sulfate formation.

It should be mentioned that a similar reasoning as for the oxidation catalyst above applies also if a diesel particulate filter (DPF) is incorporated to the system. The DPF is then normally mounted as in Fig. 3.15. It must then be assured that the NO₂/NO_x ratio downstream the DPF stays at an optimum level and not exceeds 50 % leading to loss in NO_x conversion.

Adding a DPF also requires careful consideration of the particulate regeneration of the DPF. Since NO₂/NO_x needs to be limited to less than 50 % in order not to affect the NO_x conversion over the vanadia SCR catalyst, the passive NO₂ oxidation of soot in the particulate filter will be constrained, leading to risk of accumulation of soot in the DPF. A DPF could be regenerated actively from soot by means of hydrocarbon injection before the DOC with a 7th injector or in-cylinder late post injection. This will, however, create high temperatures in the DPF (approximately in the range of 600 °C) which will accelerate the thermal aging of the vanadia SCR. There is also a risk that accumulation of soot in the DPF could result in spontaneous start of soot oxidation leading to catastrophic thermal failure of the downstream vanadia SCR catalyst. Also in the case of only a DOC upstream the SCR catalyst, the risk of thermal deactivation due to oxidation of hydrocarbons over the DOC needs to be considered.

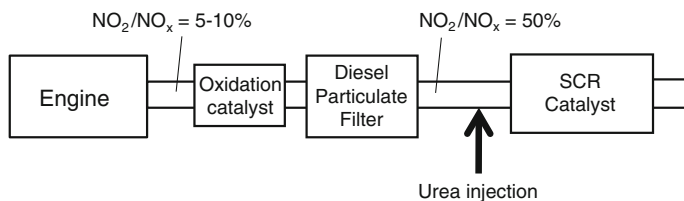


Fig. 3.15 Combining an oxidation catalyst and a diesel particulate filter with a downstream SCR catalyst

3.10 Aging of Vanadia SCR Catalysts

3.10.1 Thermal Aging

Exposure of vanadia SCR catalysts to elevated temperatures will lead to thermal deactivation of the catalyst and gradual loss in NO_x conversion. Cavataio et al. [44] showed that after exposing a vanadia-based SCR catalyst to 64 h hydrothermal aging at 670°C the activity was to a large degree lost. The maximum NO_x conversion after this treatment was only about 20 %, while for Fe and Cu-exchanged zeolite SCR catalysts, maximum NO_x conversions $>90\%$ were found after the same hydrothermal treatment. In Fig. 3.16, the effect on NO_x conversion in the ESC cycle after thermal aging at different exhaust temperatures is shown. The data was obtained on a Euro4 heavy-duty engine equipped with a vanadia SCR catalyst. A gradual decrease in NO_x conversion performance is seen with increasing aging temperature, with a steeper drop in performance when the aging temperature exceeded about 600°C . After prolonged exposure at temperatures around 600°C further gradual decrease of NO_x conversion was seen (see Fig. 3.20).

Similar result was obtained by Maunula et al. [45]. They found a significant drop in NO_x conversion after 8–20 h hydrothermal aging of a $\text{V}_2\text{O}_5/\text{TiO}_2\text{-WO}_3$ catalyst between $650\text{--}700^\circ\text{C}$ both when testing in synthetic gas and on an engine.

The loss in catalytic activity after thermal exposure has been related to loss in surface area of the TiO_2 . V_2O_5 promotes the sintering of anatase TiO_2 and at higher temperatures catalyzes the phase transition of the high surface area anatase to low surface area rutile [2, 46]. Nova et al. [47] found that the BET surface area of a $\text{V}_2\text{O}_5/\text{WO}_3/\text{TiO}_2$ catalyst was gradually decreased upon increasing calcination temperature. Already upon calcining for 2 h at 550°C , a small loss in BET area was seen (from 63 to $54\text{ m}^2/\text{g}$). At higher calcination temperatures, severe loss in surface area was seen ($37\text{ m}^2/\text{g}$ at 700°C and $17\text{ m}^2/\text{g}$ at 800°C). At 850°C , phase change from anatase to rutile was seen with further loss in surface area. The low-temperature activity for NO_x reduction was improved after calcining for 2 h at 800°C while a loss in selectivity to N_2 at temperatures above ca 380°C was seen. The result was that the activity window for the SCR reaction was reduced after the

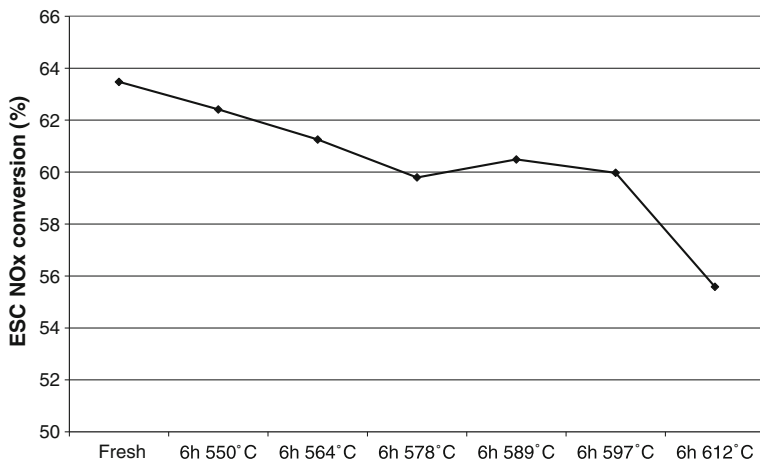


Fig. 3.16 Effect of thermal aging on NOx conversion over a vanadia SCR catalyst for a Euro4 heavy-duty engine

thermal treatment. The result was interpreted as an aggregation of isolated vanadium ions due to the sintering of the TiO_2 support.

More recently, the stability of vanadia SCR catalysts has been improved. Girard et al. [19] showed that a previous generation vanadia SCR catalyst lost a significant part of NOx conversion after hydrothermal treatment for 75 h at 550 °C (only maximum 60 % NOx conversion was achieved at $80,000 \text{ h}^{-1}$ space velocity), while two more recent formulations had significantly better activity after the same treatment (max 90 % NOx conversion and better selectivity at high temperatures). One of the newer vanadia SCR formulations also withstood hydrothermal aging for 50 h at 600 °C without significant loss in performance.

The loss in NOx conversion for vanadia catalysts after high temperature exposure has raised concerns of vanadia volatilization from SCR catalysts. Chapman [48] showed a small loss of vanadia from a $\text{V}_2\text{O}_5/\text{TiO}_2\text{-WO}_3$ sample after hydrothermal treatment for 1 h at 750 °C. Similar results were found by Liu et al. [49]. Girard et al. [19] found a possible loss of vanadia after hydrothermal treatment for 75 h at 550 °C for an older vanadia SCR catalyst technology, although they questioned the significance of the measurement compared to catalyst variation. However, for a more stable vanadia SCR catalyst technology, no loss of vanadia was found. Maunula et al. [45] found no loss of vanadia even after exposure to 1,000 °C.

3.10.2 Impact of Sulfur

V_2O_5/TiO_2 -based SCR catalysts are generally relatively robust against sulfur poisoning. Several studies have been made with sulfur on vanadia-based SCR catalysts. Walker et al. [50] aged a coated vanadia SCR system on a 12 l engine running at 240 °C for 50 h with 350 ppm sulfur in the fuel. They saw no deactivation when testing the NO_x conversion performance of the SCR catalyst in the ESC legislative cycle. Ura et al. [51] exposed an extruded vanadia catalyst to 600 ppm SO₂ at 200 °C for 29 h. The activity was then measured in synthetic gas rig. There was very little impact of this treatment when comparing NO_x conversion before and after this treatment, showing that the NO_x conversion was very little impacted by this sulfur treatment. The high robustness for the V_2O_5/TiO_2 system to sulfur has been attributed to the fact that the TiO₂ support is very weakly and reversibly sulfated [24].

However, at low-temperature conditions, vanadia SCR catalysts will be deactivated when running on high sulfur fuel due to blocking by sulfate species. This can be seen when operating an engine at exhaust temperatures below ca 300 °C. Figure 3.17 shows the decrease in NO_x conversion when operating a heavy-duty diesel engine in a low-temperature cycle using fuel with 350 ppm sulfur. The maximum exhaust temperature was 280 °C in this cycle. The NO_x conversion decreases from 66 % initially to only 14 % after 45 h of engine operation. This loss in conversion is due to condensation of ammonium sulfate leading to blocking of the SCR catalyst [2, 15, 52–54]. The formation of ammonium sulfate occurs at exhaust temperatures below 250–320 °C depending on NH₃ and SO₂ concentration [2, 15, 52]. When operating at higher concentrations of sulfur in the fuel, the rate of deactivation will be higher. This is seen in Fig. 3.18 where a more rapid decline in NO_x conversion is seen when running with 1,620 ppm sulfur in the fuel compared to 350 ppm in Fig. 3.17.

The formation of ammonium sulfate is a reversible process and at temperatures above ca 350 °C decomposition will occur. This is seen in Fig. 3.17, where after operating at 350 °C for 60 min, the activity was regained almost to the initial value and after 40 min at 400 °C full recovery to the initial activity was seen.

Similar results have been reported by Blakeman et al. [18]. They exposed a coated vanadia SCR catalyst to low-temperature engine operation (260 °C exhaust temperature) for 40 h with 3,600 ppm sulfur in the fuel. A large loss in NO_x conversion was seen for temperatures below 375 °C. However, above 375 °C, high NO_x conversion was achieved. When repeating performance testing after exposing the catalyst to temperatures above 375 °C, almost full recovery of the initial performance before the sulfur poisoning was seen. The authors found that the reason for the deactivation was sulfates and heavy hydrocarbons physically blocking the catalyst surface. When regenerating the catalyst at 375 °C, desorption of large amounts of sulfate and heavy VOF was seen [18]. The peak temperature for the desorption was 350 °C which corresponded well to the temperature for start

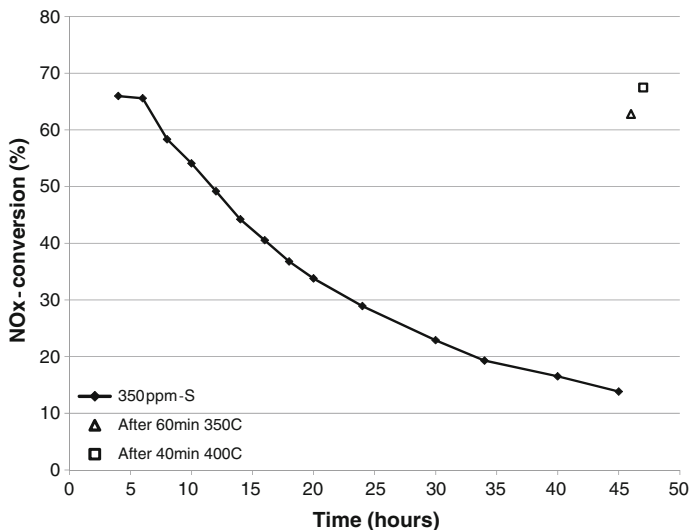


Fig. 3.17 Decrease in NOx conversion as a function of time when operating a heavy-duty diesel engine with 350 ppm sulfur in the fuel (*solid line*) in a low-temperature cycle. Regain in NOx conversion after 60 min at 350 °C (Δ) and 40 min at 400 °C (\square)

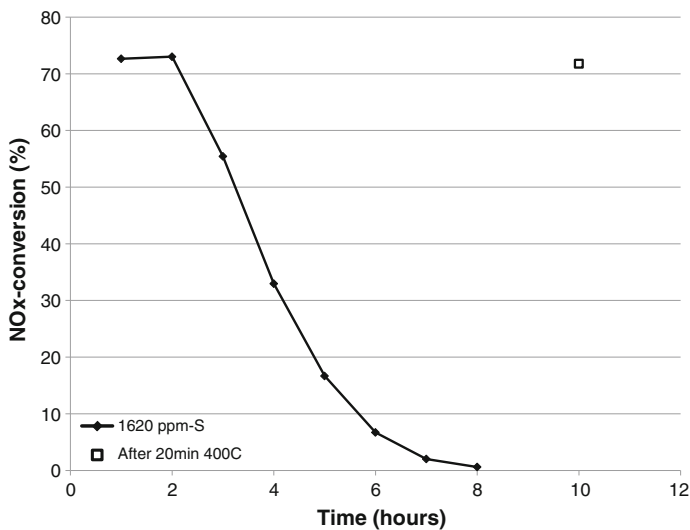


Fig. 3.18 Decrease in NOx conversion as a function of time when operating a heavy-duty diesel engine with 1,620 ppm sulfur in the fuel (*solid line*) in a low-temperature cycle. Regain in NOx conversion after 20 min at 400 °C (\square)

of recovery of the NO_x conversion. This also correlates well with the result in Fig. 3.17.

The implications of these results are that for engines/vehicles operating at high exhaust temperatures (above ca 350–375 °C) or where the exhaust temperature exceeds 350–375 °C frequently enough to desorb sulfates having been formed in low-temperature operation, very low effect of sulfur poisoning will be seen for vanadia SCR catalysts. However, when operating engines/vehicles with no or very little time above ca 300 °C exhaust temperature, deactivation of the vanadia SCR catalyst will be seen due to sulfate formation. The rate of this deactivation will be faster the higher the sulfur content in the fuel is.

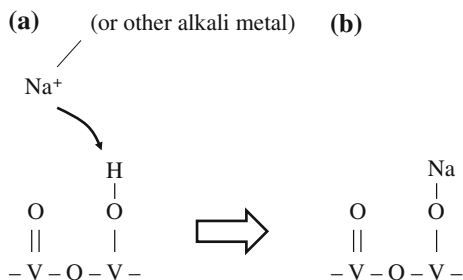
A related problem when it comes to fuel with high sulfur content, which is not directly connected to the NO_x conversion, is the high particulate mass that is formed when operating an engine with high sulfur content in the fuel. Chen et al. [55] showed that with 350 ppm sulfur in the fuel, the sulfate contribution to the particulate mass will be half of the Euro4 legislative value. Blakeman et al. [18] showed that the particulate mass being desorbed after operating at low exhaust temperatures are more than an order of magnitude higher than the Euro4 legislative value.

3.10.3 Alkali Metals and Alkaline Earth Metals

Alkali metals are known poisons for vanadia SCR catalysts. Cavataio et al. [56] found very severe impact of potassium exposure. The NO_x conversion activity was completely or almost completely lost after a 1 wt% exposure of K to both a washcoated and an extruded vanadia catalyst. Similar result was found by Kröcher et al. [57]. Exposure to 0.40 mol% potassium caused a very strong loss of activity to less than 10 % of the initial value and significant deactivation was seen already at 0.11 mol%K. The deactivation was suggested to be due to formation of potassium vanadates. A strong impact of Ca exposure was also observed, however, less compared to K exposure. The activity dropped to only 40 % of its original value when exposed to Ca. However, if SO_2 was present together with Ca, the loss in conversion from Ca was less severe due to formation of CaSO_4 [57]. Mg resulted in significant loss of NO_x conversion but less compared to Ca and K exposure. Exposure to K and Ca also resulted in loss of NH_3 adsorption capacity for vanadia SCR catalysts [57, 58]. Larger loss was seen for K exposure compared to Ca exposure, in line with the catalytic activity results. Nicosia et al. [58] used DRIFT spectroscopy and XPS to study the K and Ca poisoning of $\text{V}_2\text{O}_5/\text{WO}_3\text{-TiO}_2$. They concluded that K and Ca inhibited Brönsted acid sites and $\text{V}^{5+} = \text{O}$ sites and used a hole site deactivation model where one K or Ca atom could deactivate four neighboring vanadia centers.

Chen et al. [53] studied the poisoning effect of several alkali metals on $\text{V}_2\text{O}_5/\text{TiO}_2$ and found a strong deactivating effect on the NO reduction reaction for all of

Fig. 3.19 Simplified model for deactivation of V_2O_5 catalyst by Na



the elements Cs, Rb, K, Na, and Li. The strength of the poisoning was found to follow the order of basicity with Cs having the largest poisoning effect:



The effect of the alkaline earth metal Ca was also measured and was found to have a weaker poisoning effect than all the alkali metals. This is in line with Ca being less basic compared to Li [53]. However, since Ca still gives a significant impact on the NO_x conversion [53, 57] one can conclude that all alkali metals will have a strong negative impact on the NO_x conversion over V_2O_5 catalysts. Putting the results from [53, 57] together, the following order for the poisoning effect of alkali and alkaline earth metals can be summarized:



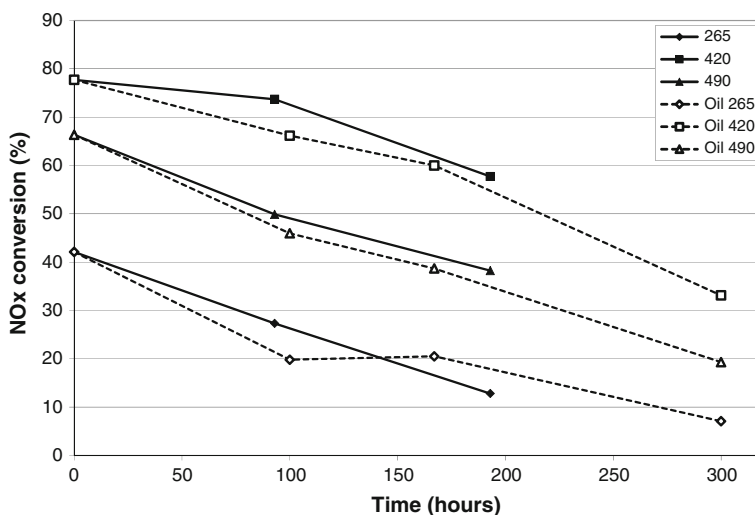
A simplified mechanism for the deactivation of V_2O_5 catalyst by alkali metal is shown in Fig. 3.19. The alkali metal ion (Na^+ in Fig. 3.19) reacts with the acid V-OH site and forms V-O-Na [59]. This blocks both the NH_3 adsorption and the $V^{5+} = O-V-OH$ site from the SCR catalytic cycle. This model is in line with the larger poisoning effect by metals with higher basicity.

3.10.4 Oil Poisons

Engine lubricant oil contains compounds that may enter the SCR catalyst and potentially deactivate the NO_x conversion function. Typical compounds, which could be present in engine lubricant oil due to oil additives are Zn, S, P, Ca, Mg, B, and Mo. Table 3.1 shows some typical values for these compounds. The effects of S, Ca and Mg were discussed above. The effect of Zn, P, B and Mo was studied in [57]. B was found to cause no deactivation of the SCR activity and Mo had only a minor impact. P had a moderate impact, decreasing the NO_x conversion by 3–4 % at high temperatures and 10 % at 300 °C. Zn reduced the NO_x conversion to 80–90 % of the original value at high temperatures. All of the elements Zn, P, B

Table 3.1 Some typical concentration of elements in lubricant oil. nd = not determined

	CJ-4 [60]	Multigrade 15W40 [61]	DH-1/CF-4 [62]	ACEA E3 [63]
Zn (ppm)	1,226	1,494	1,000	1,355
S (ppm)	3,200	nd	6,700	6,688
P (ppm)	985	1,201	890	1,227
Ca (ppm)	1,388	2,644	3,900	3,439
Mg (ppm)	355	310	nd	6
B (ppm)	586	nd	nd	nd
Mo (ppm)	77	nd	nd	nd

**Fig. 3.20** Aging of a vanadia SCR catalyst thermally (*solid lines*) and thermally with the addition of lubricant oil (*dotted lines*)

and Mo had less or much less impact on the SCR catalytic activity compared to the effect of alkali or alkaline earth metals.

In Fig. 3.20 is presented the result from a heavy-duty diesel engine where the effect of oil aging was studied. First, a vanadium SCR catalyst was aged in a high temperature cycle with exhaust temperatures >500 °C for 90 % of the time and 60 % of the time between 580–610 °C. As expected from this high temperature aging a gradual loss in NO_x conversion is seen as a function of aging time (solid lines in Fig. 3.20). After this, a second SCR catalyst was exposed to the same aging cycle, but with the difference that 1 % engine lubricant oil was added to the diesel fuel. Again, thermal deactivation was seen for the SCR catalyst. However, very little difference in the rate of deactivation was seen compared to the first run without oil addition. Under these conditions, the potential poisoning from oil components are much less important compared to the thermal aging.

The effect of oil poisoning at moderate exhaust temperatures can be seen in Fig. 3.21. In this study, a vanadia SCR catalyst was run 300 h on a heavy-duty diesel engine in a low load cycle. The exhaust temperature remained below 300 °C for the majority of the aging time, with only 3 % of the aging time at $T > 300$ °C and maximum temperature of 395 °C. During the aging, the oil consumption was accelerated so that during the 300 h, an equivalent amount of oil was consumed corresponding to a mileage of 500,000 km. The NO_x conversion before and after the aging was measured in the steady-state engine operating points denoted in Fig. 3.21.

It can be seen in Fig. 3.21 that there is no significant change in NO_x conversion after the 300 h aging. The NO_x conversion has only decreased moderately or not at all in spite of the fact that it has been exposed to oil corresponding to a mileage of 500,000 km. The vanadia SCR catalyst thus seems quite stable to the exposure of this amount of oil poisons. These results are in line with Walker et al. [50] who found moderate impact after exposing a coated vanadia catalyst to oil exposure corresponding to 1,230,000 km. Similar results were found by Bardasz et al. [63] who saw no measurable activity loss after 200 h on an engine with increased oil consumption.

3.10.5 Hydrocarbons

The effect of hydrocarbon poisoning on vanadia-based SCR catalysts is less pronounced compared to zeolite-based SCR catalysts [19]. Girard et al. [19] exposed three different vanadia SCR catalysts to 700 ppm C₃H₆ during the NO + NH₃ reaction at 300 °C. Only moderate effect was seen with about 5 % loss in NO_x conversion. The performance for one of the vanadia catalysts tested was almost not affected at all. The experiment was repeated at 200 °C with similar result. This was in contrast to an Fe-zeolite and a Cu-zeolite catalyst where significant impact was seen after exposure to 700 ppm C₃H₆. Schmiege and Lee [64] found a similar result. They measured NO_x conversion after exposure to n-octane or a propene/propane mixture for 1 hour. Exposures were made at 300 ppm C₁ and 900 ppm C₁. Exposure at 225 °C of both hydrocarbons had a very small impact on the vanadia SCR catalysts, and exposure at 450 °C had moderate impact (NO_x conversion dropping from ca 90 % to ca 85 % at 300 ppm C₁ and dropping to ca 75 % at 900 ppm C₁). The initial activity was recovered upon removal of the hydrocarbons at 450 °C. This indicates that the hydrocarbon poisoning was reversible.

Gieshoff et al. [46] reported that the low-temperature performance of a vanadia SCR catalyst was decreased by adding 10 ppm and 30 ppm n-decane to the inlet gas. The light-off temperature was shifted from ca 250 °C without hydrocarbon to ca 300 °C when 30 ppm n-decane was added. However, above 350–400 °C, no decrease in NO_x conversion was seen in the presence of hydrocarbon compared to without.

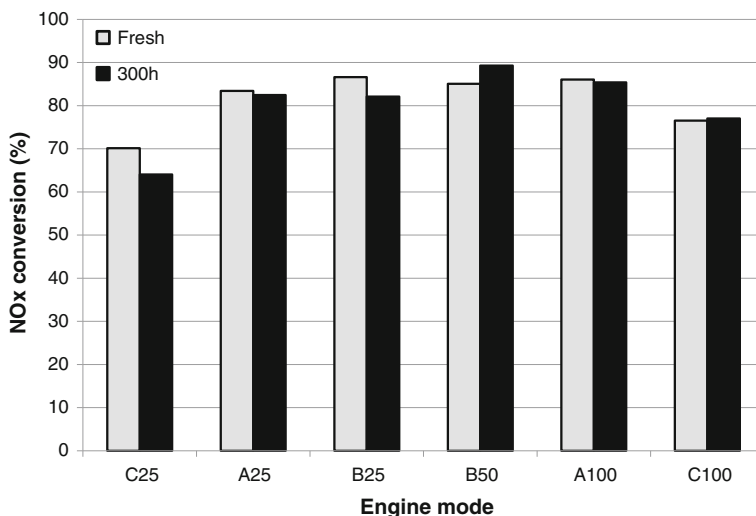


Fig. 3.21 Aging with accelerated oil consumption on a Euro4 heavy-duty diesel engine. 300 h aging correspond to an equivalent oil consumption for 500,000 km

3.10.6 Arsenic and Lead

Arsenic is a poison for vanadia SCR catalysts known from stationary power plants where it is present as As_2O_3 in gas-phase or in fly ashes [65]. As_2O_3 is captured irreversibly to the V_2O_5 surface causing deactivation of the catalyst [59]. However, since As is not a common compound in diesel exhaust, this type of poisoning is not seen in mobile SCR applications.

Lead (Pb) is a relatively strong poison for vanadia SCR catalysts [53]. However, since Pb is also not a common compound in diesel exhaust, this type of poisoning is not seen in mobile SCR applications.

3.10.7 Biofuel

Biodiesel (FAME) is a renewable fuel that is made by transesterification of vegetable oils or animal fat with methanol. Several different types of oils could be used, the most common are soybean oil, rapeseed oil, and palm oil [66]. The most widely used transesterification process for commercial biodiesel is alkali-catalyzed [67]. This process typically uses NaOH or KOH as a catalyst. Although the biodiesel is purified, residual amounts of Na or K can remain in the biodiesel [68]. Current standard is $Na + K < 5$ ppm for 100 % biodiesel (B100). Biodiesel also contains phosphorus that originates from phospholipids. The current standard is $P < 4$ ppm for B100.

Since it is known that Na, K, and P are poisons for the SCR reaction over vanadia-based SCR catalysts (see above), it is expected that running an engine with biodiesel could have some negative impact on a downstream SCR catalyst. Krahl et al. [69] exposed an extruded vanadia SCR catalyst to 1000 h aging on an engine running on biodiesel with 10 ppm phosphorus. They saw a drop in NO_x conversion after this treatment both when evaluating the performance with biodiesel and with standard diesel. They interpreted this as phosphorus poisoning. Cavataio et al. [56] exposed one washcoated and one extruded vanadia SCR catalyst to potassium levels corresponding to a mileage of 52,000 miles. After this exposure both the coated and extruded vanadia SCR catalyst had lost all or almost all activity.

3.10.8 In-use Aging Evaluation

Evaluation of durability of vanadia SCR catalysts after in-use testing in a vehicle has been performed in several studies. Fritz et al. [7] studied the performance of an extruded vanadia SCR catalyst mounted to a heavy-duty truck. They saw a slight drop in performance (from 92.1 % to 87.2 % NO_x conversion) after a mileage of 117,500 miles. Amon and Keefe [70] studied the performance of an extruded vanadia SCR catalyst mounted on two 40 ton long-distance transportation trucks. By taking out samples from the operating systems they could establish a gradual decline in catalyst activity with a more rapid decline initially and then leveling out. After 332,000 miles, the activity was still 90 % of the original performance. In a field trial in US, Block et al. [71] evaluated NO_x conversion on two high-way trucks and one refuse truck after 1 year and 2 years operation. After 1 year, the NO_x conversion was 79–95 % and after 2 years slightly lower (81–91 %).

3.11 Summary and Conclusions

Vanadia-based SCR catalysts have found broad use for reducing NO_x from diesel engines in mobile applications. The typical system uses AdBlue (32.5 % urea solution) which decomposes in the exhaust gases as a reductant. Current vanadia-based technology has proven to have good durability and resistance to sulfur, oil poisons, and hydrocarbons. However, the vanadia system is sensitive to exposure of alkali metals and very high temperatures. It is feasible to combine vanadia SCR technology with DOC or DOC/DPF technology, however careful design of the NO₂ level entering the vanadia SCR catalyst is needed as well as thermal management of the DOC/DPF.

References

1. Ando J, Tohata H, Isaacs G A (1976) NO_x Abatement for Stationary Sources in Japan. U.S. Environmental Protection Agency, EPA-600/2-76-013b, Cincinnati, Ohio
2. Forzatti P, Lietti L (1996) Recent Advances in DeNO_xing Catalysis for Stationary Applications. *Heterogeneous Chem Rev* 3:33–51
3. Jones G D, Johnson K L (1979) Technology Assessment Report for Industrial Boiler Applications: NO_x Flue Gas Treatment. U.S. Environmental Protection Agency, EPA-600/7-79-178 g, Austin, Texas
4. Scarnegie B, Miller W, Ballmert B, Doelling W, Fischer S (2003) Recent DPF/SCR Results Targeting US2007 and Euro 4/5 HD Emissions. SAE Technical Paper 2003-01-0774
5. Koebel M, Elsener M, Marti T (1996) NO_x-Reduction in Diesel Exhaust Gas with Urea and Selective Catalytic Reduction. *Combust Sci Tech* 121:85–102
6. Havenith C, Verbeek R P (1997) Transient Performance of a Urea deNO_x Catalyst for Low Emissions Heavy-Duty Diesel Engines. SAE Technical Paper 970185
7. Fritz N, Mathes W, Zuerbig J, Mueller R (1999) On-Road Demonstration of NO_x Emission Control for Diesel Trucks with SINO_x Urea SCR System. SAE Technical Paper 1999-01-0111
8. Brodrick C J, Farsh-chi M, Dwyer H A, Sperling D, Gouse S W, Doelling W, Hoelzer J, Jackson M (1999) Urea-SCR System Demonstration and Evaluation for Heavy-Duty Diesel Trucks. SAE Technical Paper 1999-01-3722
9. Müller W, Ölschlegel H, Schäfer A, Hakim N, Binder K (2003) Selective Catalytic Reduction - Europe's NO_x Reduction Technology. SAE Technical Paper 2003-01-2304
10. Schmiege S (2010) Aspects of HC-SCR Catalyst Durability for Lean-Burn Engine Exhaust Aftertreatment. *SAE Int J Fuels Lubr* 3(2):691–709. doi:10.4271/2010-01-2160
11. Stanglmaier R H, Roecker R C, Roberts Jr C E, Stewart D W (2004). US Patent 6732507B1
12. Elmøe T D, Sørensen R Z, Quaade U, Christensen C H, Nørskov J K, Johannessen T (2006) *Chem Eng Sci* 61:2618–2625
13. Fulks G, Fisher G, Rahmoeller K, Wu M, D'Herde E, Tan J (2009) A Review of Solid Materials as Alternative Ammonia Sources for Lean NO_x Reduction with SCR. SAE Technical Paper 2009-01-0907
14. Nissinen T, Kukkonen J (2009) US Patent 7595034B2
15. Koebel M, Elsener M, Kleemann M (2000) Urea-SCR - a promising technique to reduce NO_x emissions from automotive diesel engines. *Catal Today* 59:335–345
16. Lee J H, Paratore M J, Brown D B (2008) Evaluation of Cu-Based SCR/DPF Technology for Diesel Exhaust Emission Control. SAE Technical Paper 2008-01-0072
17. Ballinger T, Cox J, Konduru M, De D, Manning W, Andersen P (2009) Evaluation of SCR Catalyst Technology on Diesel Particulate Filters. SAE Technical Paper 2009-01-0910
18. Blakeman P, Arnyby K, Marsh P, Newman C, Smedler G (2008) Optimization of an SCR Catalyst System to Meet EU IV Heavy Duty Diesel Legislation. SAE Technical Paper 2008-01-1542
19. Girard J, Montreuil C, Kim J, Cavataio G, Lambert C (2009) Technical Advantages of Vanadium SCR Systems for Diesel NO_x Control in Emerging Markets. *SAE Int J Fuels Lubr* 1(1):488–494. doi:10.4271/2008-01-1029
20. Miyamoto A, Kobayashi K, Inomata M, Murakami Y (1982) Nitrogen-15 Tracer Investigation of the Mechanism of the Reaction of NO with NH₃ on Vanadium Oxide Catalysts. *J Phys Chem* 86:2945–2950
21. Lietti L, Nova I, Forzatti P (2000) Selective catalytic reduction (SCR) of NO by NH₃ over TiO₂-supported V₂O₅-WO₃ and V₂O₅-MoO₃ catalysts. *Topics in Catal* 11/12:111–122
22. Djerad S, Tifouti L, Crocoll M, Weisweiler W (2004) Effect of vanadia and tungsten loadings on the physical and chemical characteristics of V₂O₅-WO₃/TiO₂ catalysts. *J Mol Catal A* 208:257–265

23. Wachs I E, Deo G, Weckhuysen B M, Andreini A, Vuurman M A, de Boer M, Amiridis M D (1996) Selective Catalytic Reduction of NO with NH₃ over Supported Vanadia Catalysts. *J Catal* 161:211–221
24. Busca G, Lietti L, Ramis G, Berti F (1998) Chemical and mechanistic aspects of the selective catalytic reduction of NO_x by ammonia over oxide catalysts: A review. *Appl Catal B* 18:1–36
25. Inomata M, Miyamoto A, Murakami Y (1980) Mechanism of the Reaction of NO and NH₃ on Vanadium Oxide Catalyst in the Presence of Oxygen under Dilute Gas Condition. *J Catal* 62:140–148
26. Nova I, Ciardelli C, Tronconi E, Chatterjee D, Bandl-Konrad B (2006) NH₃-SCR of NO over a V-based Catalyst: Low-T Redox Kinetics with NH₃ Inhibition. *AIChE J* 52(9):3222–3233
27. Nova I, Ciardelli C, Tronconi E, Chatterjee D, Weibel M (2009) Unifying Redox Kinetics for Standard and Fast NH₃-SCR over a V₂O₅-WO₃/TiO₂ Catalyst. *AIChE J* 55(6):1514–1529
28. Ciardelli C, Nova I, Tronconi E, Chatterjee D, Bandl-Konrad B (2004) A “Nitrate Route” for the low temperature “Fast SCR” reaction over a V₂O₅-WO₃/TiO₂ commercial catalyst. *Chem Commun* 2004:2718–2719
29. Nova I, Ciardelli C, Tronconi E, Chatterjee D, Bandl-Konrad B (2006) NH₃-NO/NO₂ chemistry over V-based catalysts and its role in the mechanism of the Fast SCR reaction. *Catal Today* 114:3–12
30. Ciardelli C, Nova I, Tronconi E, Chatterjee D, Bandl-Konrad B, Weibel M, Krutzsch B (2007) Reactivity of NO/NO₂-NH₃ SCR system for diesel exhaust aftertreatment: Identification of the reaction network as a function of temperature and NO₂ feed content. *Appl Catal B* 70:80–90
31. van Helden R, Verbeek R, Willems F, van der Well R (2004) Optimization of Urea SCR deNO_x Systems for HD Diesel Engines. SAE Technical Paper 2004-01-0154
32. Song Q, Zhu G (2002) Model-based Closed-loop Control of Urea SCR Exhaust Aftertreatment System for Diesel Engine. SAE Technical Paper 2002-01-0287
33. Schär C M, Onder C H, Geering H P, Elsener M (2003) Control of a Urea SCR Catalytic Converter System for a Mobile Heavy Duty Diesel Engine. SAE Technical Paper 2003-01-0776
34. Winkler C, Flörchinger P, Patil M D, Gieshoff J, Spurk P, Pfeifer M (2003) Modeling of SCR DeNO_x Catalyst – Looking at the Impact of Substrate Attributes. SAE Technical Paper 2003-01-0845
35. van Helden R, van Genderen M, van Aken M, Verbeek R, Patchett J, Kruijthof J, Straten T, de Saluneaux C G (2002) Engine Dynamometer and Vehicle Performance of a Urea SCR-System for Heavy-Duty Truck Engines. SAE Technical Paper 2002-01-0286
36. Hofmann L, Rusch K, Fischer S, Lemire B (2004) Onboard Emissions Monitoring on a HD Truck with an SCR System Using Nox Sensors. SAE Technical Paper 2004-01-1290
37. Tao T, Xie Y, Dawes S, Melscoet-Chauvel I, Pfeifer M, Spurk P C (2004) Diesel SCR NO_x Reduction and Performance on Washcoated SCR Catalysts. SAE Technical Paper 2004-01-1293
38. Balling L, Sigling R, Schmelz H, Hums E, Spitznagel G (1991) Poisoning Mechanisms in Existing SCR Catalytic Converters and Development of a New Generation for Improvement of the Catalytic Properties. In: Proceedings of the Joint Symposium on Stationary Combustion NO_x Control, Washington, DC, 25–28 March 1991
39. Gekas I, Gabrielsson P, Johansen K, Nyengaard L, Lund T (2002) Urea-SCR Catalyst System Selection for Fuel and PM Optimized Engines and a Demonstration of a Novel Urea Injection System. SAE Technical Paper 2002-01-0289
40. Koebel M, Elsener M, Madia G (2001) Recent Advances in the Development of Urea-SCR for Automotive Applications. SAE Technical Paper 2001-01-3625
41. Aoki Y, Miyairi Y, Ichikawa Y, Abe F (2002) Product Design and Development of Ultra Thin Wall Ceramic Catalytic Substrate. SAE Technical Paper 2002-01-0350
42. Johnson T V (2004) Diesel Emission Control Technology – 2003 in Review. SAE Technical Paper 2004-01-0070
43. Walker A P, Cooper B J, McDonald A C, Sanchez M (2003) The Development and On-Road Performance and Durability of the Four-Way Emission Control SCRT System. US

- Department of Energy Diesel Engine Emission Reduction (DEER) Conference, Newport, August 2003
44. Cavataio G, Girard J, Patterson J E, Montreuil C, Cheng Y, Lambert C K (2007) Laboratory Testing of Urea-SCR Formulations to Meet Tier 2 Bin 5 Emissions. SAE Technical Paper 2007-01-1575
 45. Maunula T, Kinnunen T (2011) Design and Durability of Vanadium-SCR Catalyst Systems in Mobile Off-Road Applications. SAE Technical Paper 2011-01-1316
 46. Gieshoff J, Schäfer-Sindlinger A, Spurk P C, van den Tillaart J A A, Garr G (2000) Improved SCR Systems for Heavy Duty Applications. SAE Technical Paper Series 2000-01-0189
 47. Nova I, dall'Acqua L, Lietti L, Giamello E, Forzatti P (2001) Study of thermal deactivation of a de-NO_x commercial catalyst. *Appl Catal B* 35:31–42
 48. Chapman D M (2011). US Patent 2011/0138789 A1
 49. Liu Z, Ottinger N, Cremeens C (2012) Methods for Quantifying the Release of Vanadium from Engine Exhaust Aftertreatment Catalysts. *SAE Int J Engines* 5(2):663-671. doi:[10.4271/2012-01-0887](https://doi.org/10.4271/2012-01-0887)
 50. Walker A P, Blakeman P G, Ilkenhans T, Magnusson B, McDonald A C, Kleijwegt P, Stunnenberg F, Sanchez M (2004) The Development and In-Field Demonstration of Highly Durable SCR Catalyst Systems. SAE Technical Paper 2004-01-1289
 51. Ura J A, Girard J, Cavataio G, Montreuil C, Lambert C (2009) Cold Start Performance and Enhanced Thermal Durability of Vanadium SCR Catalysts. SAE Technical Paper 2009-01-0625
 52. Gibson J, Groene O (1991) Selective catalytic reduction on marine diesel engines. *Automotive Engineering*, October:18–22
 53. Chen J P, Buzanowski M A, Yang R T, Cichanowicz J E (1990) Deactivation of the Vanadia Catalyst in the Selective Catalytic Reduction Process. *J Air Waste Manage Assoc* 40:1403–1409
 54. Kijlstra W S, Komen N J, Andreini A, Poels E K, Blik A (1996) Promotion and Deactivation of V₂O₅/TiO₂ SCR catalysts by SO₂ at low Temperature. *Stud Surf Sci Catal* 101:951–960
 55. Chen W, Wang J, Shuai S, Wu F (2008) Effects of Fuel Quality on a Euro IV Diesel Engine with SCR After-Treatment. SAE Technical Paper 2008-01-0638
 56. Cavataio G, Jen H, Dobson, D, Warner, J (2009) Laboratory Study to Determine Impact of Na and K Exposure on the Durability of DOC and SCR Catalyst Formulations. SAE Technical Paper 2009-01-2823
 57. Kröcher O, Elsener M (2008) Chemical deactivation of V₂O₅/WO₃-TiO₂ SCR catalysts by additives and impurities from fuels, lubrication oils, and urea solution I. *Catalytic studies*. *Appl Catal B* 75:215–227
 58. Nicosia D, Czekaj I, Kröcher O (2008) Chemical deactivation of V₂O₅/WO₃-TiO₂ SCR catalysts by additives and impurities from fuels, lubrication oils and urea solution Part II. Characterization study of the effect of alkali and alkaline earth metals. *Appl Catal B* 77:228–236
 59. Pritchard S, DiFrancesco C, Kaneko S, Kobayashi N, Suyama K, Iida K (1995) Optimizing SCR Catalyst Design and Performance for Coal-Fired Boilers. EPRI/EPA 1995 Joint Symposium on Stationary Combustion NO_x Control, Kansas City, May 16–19, 1995
 60. Sappok A, Kamp C, Wong V (2012) Sensitivity Analysis of Ash Packing and Distribution in Diesel Particulate Filters to Transient Changes in Exhaust Conditions. *SAE Int J Fuels Lubr* 5(2):733–750. doi:[10.4271/2012-01-1093](https://doi.org/10.4271/2012-01-1093)
 61. Watson S, Huang W, Wong V (2007) Correlations among Ash-Related Oil Species in the Power Cylinder, Crankcase and the Exhaust Stream of a Heavy-Duty Diesel Engine. SAE Technical Paper 2007-01-1965
 62. Shibata M, Nagata H, Takeshima S, Hoshino K (2007) A Study of Engine Oil Composition Effects on Zeolite-type SCR Catalyst Durability. SAE Technical Paper 2007-01-1924
 63. Bardasz E, Mackney D, Britton N, Kleinschek G, Olofsson K, Murray I, Walker A P (2003) Investigations of the Interactions between Lubricant-derived Species and Aftertreatment

- Systems on a State-of-the-Art Heavy Duty Diesel Engine. SAE Technical Paper 2003-01-1963
64. Schmieg S, Lee J (2005) Evaluation of Supplier Catalyst Formulations for the Selective Catalytic Reduction of NO_x With Ammonia. SAE Technical Paper 2005-01-3881
 65. Valdés-Solís T, Marbán G, Fuertes A B (2003) *Appl Catal B* 46:261–271
 66. Hoekman S K, Broch A, Robbins C, Cenicerros E, Natarajan M (2012) Review of biodiesel composition, properties, and specifications. *Renew Sustain Energy Rev* 16:143–169
 67. Gerpen J V (2005) Biodiesel processing and production. *Fuel Proc Technol* 86:1097–1107
 68. Williams A, McCormick R, Luecke J, Brezny R, Geisselmann A, Voss K, Hallstrom K, Leustek M, Parsons J, Abi-Akar H (2011) Impact of Biodiesel Impurities on the Performance and Durability of DOC, DPF and SCR Technologies. *SAE Int J Fuels Lubr* 4(1):110–124. doi:[10.4271/2011-01-1136](https://doi.org/10.4271/2011-01-1136)
 69. Krahl J, Munack A, Ruschel Y, Schröder O, Schwarz S, Hofmann L, Bünger J (2006) Influence of the Phosphorus Content in Rapeseed Oil Methyl Esters During a 1000 Hours Endurance Test on the Function of a SCR-system Measured by Exhaust Gas Emissions and Health Effects. SAE Technical Paper 2006-01-3282
 70. Amon B, Keefe G (2001) On-Road Demonstration of NO_x Emission Control for Heavy-Duty Diesel Trucks using SINOx™ Urea SCR Technology—Long-term Experience and Measurement Results. SAE Technical Paper 2001-01-1931
 71. Block M, Clark N, Wayne S, Nine R, Miller W (2005) An Investigation into the Emissions Reduction Performance of an SCR System Over Two Years' In-Use Heavy-Duty Vehicle Operation. SAE Technical Paper 2005-01-1861

Chapter 4

Fe-Zeolite Functionality, Durability, and Deactivation Mechanisms in the Selective Catalytic Reduction (SCR) of NO_x with Ammonia

Todd J. Toops, Josh A. Pihl and William P. Partridge

4.1 Introduction

Since the introduction of the first emissions control regulations in the 1970s and 1980s [1], catalysis has been implemented extensively to maintain compliance and to dramatically reduce the harmful pollutants emitted from combustion engines. For stoichiometric exhaust, primarily from gasoline-powered vehicles, precious metals, or platinum-group metals (PGM), such as Pt, Pd, and Rh, have been the hallmark of three-way catalysis, e.g., [2–4], as they are highly active in oxidation of carbon monoxide (CO) and hydrocarbons (HCs) as well as the reduction of nitrogen oxides (NO_x). The chemistry behind these reactions is equilibrium driven, as the more benign products of CO₂, H₂O, and N₂ are thermodynamically favored. However, these catalysts only function properly if the exhaust is at or near stoichiometric conditions. As a result, gasoline vehicle manufacturers began designing their engine control systems to operate with stoichiometric air/fuel ratios to optimize catalyst performance and minimize emissions. The need for more fuel-efficient vehicles, both with respect to increasing fuel costs and future CO₂ emissions regulations, is driving vehicle manufacturers to investigate more efficient combustion strategies, such as lean-burn gasoline, or increase production of more fuel efficient diesel vehicles.

Both diesel-powered vehicles (mobile source) and industrial plants (stationary source) operate primarily under lean exhaust conditions; i.e., excess oxygen content. This lean operation results in improved efficiency compared to stoichiometric operation, and these conditions are favorable for the oxidation of CO and HCs; however, it results in a very challenging environment for the catalytic reduction of NO_x. It is this challenge that the diesel community has been actively studying as the

T. J. Toops (✉) · J. A. Pihl · W. P. Partridge
Fuels, Engines and Emissions Research Center, Oak Ridge National Laboratory, 1 Bethel
Valley Road, Oak Ridge, TN 37831, USA
e-mail: toopstj@ornl.gov

emissions regulations for these fuel-efficient vehicles have become more stringent [5]. Of the most common technologies for reducing NO_x from lean-burn engines—lean NO_x traps (LNT), hydrocarbon-based lean NO_x catalysis (LNC), and NH_3 -based selective catalytic reduction (SCR)—SCR has had the most commercial success [6–18].

Industrial plants have been relying on a form of SCR since the 1960s [19], however, the controlled and stable nature of industrial plant operation allows several degrees of freedom that are not possible on a vehicle. Industrial plants have relatively steady emissions output, are able to introduce gaseous NH_3 , can control the temperature of the catalyst to a very narrow window, and readily employ clean-up catalysts as the space constraints are not as limiting as on a vehicle. With these factors in mind, the low-cost vanadium and tungsten oxides supported on titania are the most widely used catalysts employed to selectively reduce NO_x from stationary sources [20]. These catalysts have also been implemented for diesel vehicles in Europe, but they have limited thermal durability as well as the potential to emit harmful gaseous vanadium [21–23].

The other catalysts that have found commercial success in SCR applications are zeolites exchanged with base metals, primarily Cu and Fe. These zeolite-based catalysts are particularly attractive because they do not rely on precious metals, have high tolerance to sulfur, and have good activity over a wide temperature range. Zeolites exchanged with Cu and Fe have been studied extensively, and much of the general chemistry and functionality is now known [24–28], although the detailed SCR mechanism is a matter of ongoing research [29–31]. These catalysts have improved hydrothermal stability over the previously discussed vanadia-based catalysts, and it is this improved durability that has led to the metal-exchanged zeolite being the predominant SCR system implemented in US-based commercial vehicles. However, durability is still a significant concern as several deactivation mechanisms are known to exist [17, 32–41]. A key limitation of many zeolites is their high temperature stability in the presence of steam. The SCR catalyst is exposed to high temperatures when the diesel particulate filter (DPF) required for particulate emissions control is regenerated and the trapped soot is oxidized at 600–700 °C. If uncontrolled, these thermal excursions, which are initiated over an upstream diesel oxidation catalyst (DOC), can lead to SCR catalyst degradation and loss of performance.

The primary difference between Fe- and Cu-exchanged zeolites lies in their respective operating windows for NO_x reduction: Fe-zeolites typically generate higher NO_x conversion efficiencies at higher temperatures, while Cu-zeolites work better at lower temperatures. This chapter will focus on Fe-exchanged zeolites; other chapters include detailed discussions of Cu-zeolites. Numerous zeolites have been studied for SCR applications, including MOR, FER, BEA, ZSM-5, CHA, SAPO-34 [24]. The zeolite structure and composition impact a variety of catalyst properties, including NO_x reduction activity, NH_3 storage capacity, and durability. Commercial systems have relied on zeolite beta (BEA) or one of the chabazite

structures (CHA or SAPO-34) due to their improved hydrothermal stability compared to other zeolites. Our prior work has focused on Fe-BEA samples provided by our industrial partners, so the discussions below will center on this class of materials.

This chapter will focus on the Fe-zeolite SCR system and will detail its functionality and durability and discuss the deactivation mechanisms that have been observed. The Cu-zeolite SCR system will be primarily discussed elsewhere in this book, but its reactivity and durability will be a source of comparison throughout.

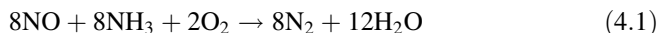
4.2 Experimental Considerations in Evaluating and Aging Catalysts

Before fully delving into the functionality of the Fe-zeolite SCR catalysts, a brief discussion on experimental considerations is warranted. To meet vehicle emissions regulations, these catalysts must be fully functional under a wide range of ‘conditions’, expected exhaust temperatures, compositions, and flow rates that must be considered in the development and evaluation of these catalysts. However, before integration into a vehicle emissions control systems, catalysts are typically evaluated and aged in lab-scale environments. Much of this work is done in synthetic exhaust gas flow reactors; microreactors for catalyst powders and bench-scale flow reactors for monolithic core samples. Additionally, the catalysts are studied on engine dynamometer-based systems that more closely replicate on-road conditions, yet offer significantly more control over exhaust conditions than can be achieved in a vehicle. Results generated in each of these systems will be discussed here, with specific focus on bench-scale flow reactor studies.

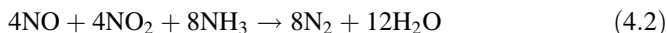
Evaluation of core samples from commercial-intent catalysts has been an important method for measuring and predicting the behavior of on-board systems. Sample core sizes can vary from very small samples, 5–8 mm OD, to large samples, 75 mm OD, with most researchers focusing on samples around 25 mm OD and anywhere from 16 to 100 mm in length. Using washcoated catalyst cores allows the researcher to evaluate the system as close to its commercial application as possible, while maintaining control over temperature and gas composition. There can be challenges in obtaining a uniform washcoat distribution and sample-to-sample, or even channel-to-channel variations can be significant; however, if the sample is large enough and carefully harvested from the full size catalyst these variations can be minimized.

In focusing on SCR catalysts, it is important to first briefly define the chemistry that is important for the reduction of NO_x . There are three primary global reactions to consider:

- Standard SCR:



- Fast SCR:



- NO₂ SCR:

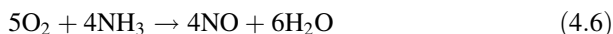
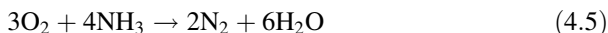


Many of the elementary reactions involved in these global reactions are discussed elsewhere, including several of the side reactions leading to non-desirable products, e.g., N₂O [24, 42–44]. Other key chemical reactions that occur on these catalysts and impact performance are the following:

- NH₃ storage:



- NH₃ oxidation:



- NO oxidation to NO₂:



It is with each of these reactions in mind that researchers probe the functionality of SCR catalysts with a goal of developing functional models that predict their behavior under a wide range of conditions.

To capture these processes in an efficient manner, experimental protocols are developed and employed. These typically rely on modelers and experimentalists working closely with each other to ensure that the protocol captures the key dynamics, and that the catalyst is in a well-known state before measuring reactivity. In SCR systems, this goes beyond de-greening or preconditioning, as the exchange metal can change oxidation states based on gas composition [27]. Two of these protocols will be introduced here. The first is a detailed approach that captures not only the key reactions but how reactivity changes at different NH₃ and NO ratios [45]. The second approach is more concise and only relies on four steps [46].

The detailed approach was developed to capture the key steady-state reactivity and the transient nature of SCR chemistry, specifically as it relates to NH₃ storage

capacity, NO_x reactivity with stored and gas-phase NH_3 , and the influence of NH_3/NO_x and NO_2/NO_x ratios. The protocol was developed for implementation in an automated bench-scale flow reactor using core samples cut from commercial catalyst monoliths. The protocol includes steps to measure the following catalyst properties:

1. NH_3 storage capacity by three independent techniques:
 - a. NH_3 uptake during adsorption,
 - b. NH_3 release during isothermal and temperature programmed desorptions, and
 - c. NO_x reduction by *stored* NH_3 , i.e., without NH_3 in the feed.
2. Steady-state SCR kinetics with varying reactant compositions:
 - a. NH_3/NO : 0.8, 0.9, 1.0, 1.1, 1.2,
 - b. NO_2/NO_x : 0.0, 0.25, 0.5, 0.7, 1.0,
3. NH_3 oxidation behavior, and
4. NO oxidation behavior.

The sequence of inlet gas compositions and how these changes in feed affect the effluent concentrations are shown in Fig. 4.1. Further analysis of these traces allows the calculation of steady-state conversions, NH_3 storage under three different conditions, as well as the stability of the stored NH_3 . Data generated from selected portions of the protocol using Fe-zeolite SCR catalysts will be discussed in the following section for the following conditions: 150–550 °C, 60–120 k hr^{-1} GHSV, and a total NO_x feed of 150–450 ppm.

Another commonly referenced experimental approach is a 4-step protocol that aims to understand NH_3 capacity utilization in SCR catalysts by resolving three types of capacity: total, dynamic, and unused [46]. Total NH_3 capacity represents the equilibrium coverage if the entire catalyst was exposed to the inlet NH_3 concentration and temperature, i.e., in the absence of SCR reactions. This value generally increases with increasing NH_3 concentration and decreases with increasing temperature and is akin to an adsorption isotherm-based measurement. Dynamic NH_3 capacity is the NH_3 capacity used under SCR conditions; this value is a fraction of the total NH_3 capacity, has a constant value at steady-state SCR conditions, and is dynamic in the sense that it varies with transient SCR conditions. The unused or vacant NH_3 capacity is the difference between the total and dynamic NH_3 capacity, and represents unused capacity if the entire catalyst was at the inlet conditions. It should be clear that there is a balance between the sum of the dynamic and unused capacity, and the total capacity; i.e., the dynamic capacity cannot exceed the total capacity. In practice there are differences between the various capacities that vary with location, correlate with other SCR operating parameters, and give insights into capacity utilization.

The 4-step protocol is illustrated in Fig. 4.2 for a case using 200 ppm NO and NH_3 feed; of course other concentrations, NO_2/NO_x and NH_3/NO_x ratios would be needed to fully characterize the performance and properties of a given catalyst.

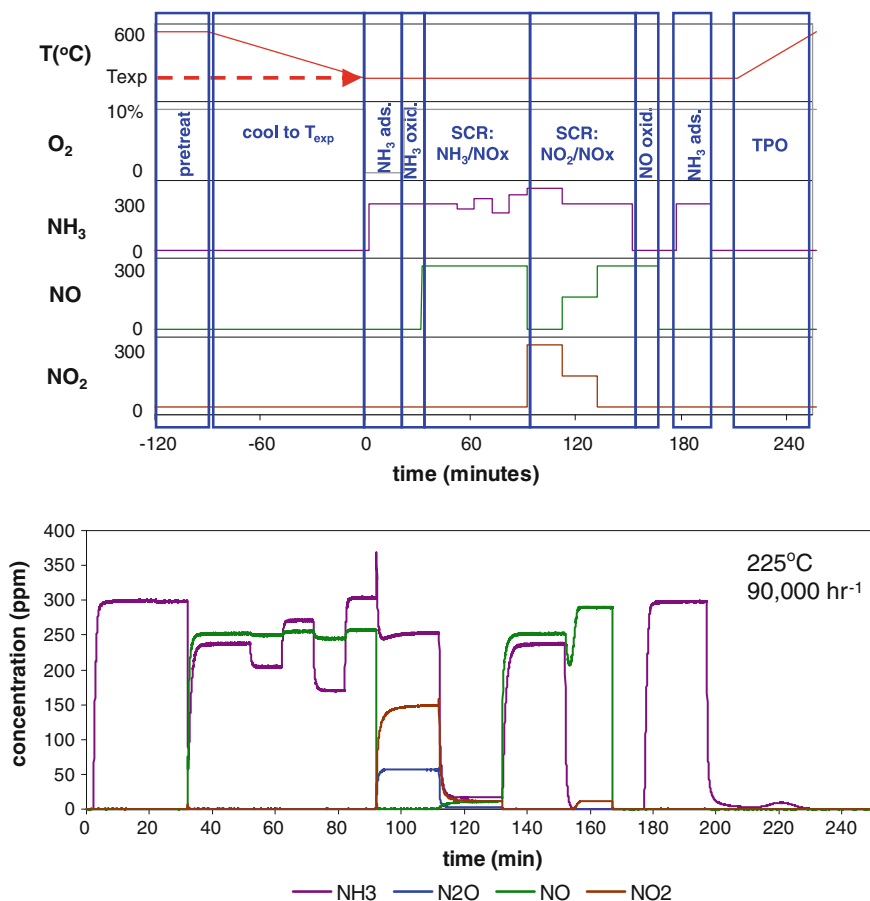


Fig. 4.1 Detailed SCR evaluation protocol with the feed sequence outlined on top (including the pretreatment) and an example effluent gas trace during the protocol of NH₃, N₂O, NO, and NO₂

Step 1 (200 ppm NO) is designed to fully clean the catalyst of stored NH₃, and quantify any NO oxidation. Step 2 continues the NO flow from step 1, but also introduces an equimolar flow of NH₃ and is used to measure transient and steady-state NO and NH₃ conversion and the dynamic NH₃ capacity during standard SCR operation. The area above the NO_x curve and below the NH₃ feed in step 2 (SCR in Fig. 4.2) represents the amount of NH₃ used for NO_x reduction, and the steady-state value is indicated by the green arrow. The area below the NH₃ curve represents the NH₃ slip, and the steady-state value is indicated by the orange arrow. Any difference between the steady-state NO_x and NH₃ curves represents NH₃ used for other reactions (e.g., NH₃ oxidation); these other reactions are assumed to be steady and continuous throughout the SCR step. The remaining step-2 area is the dynamic NH₃ capacity, which is determined by integrating between the NO_x and NH₃ curves and

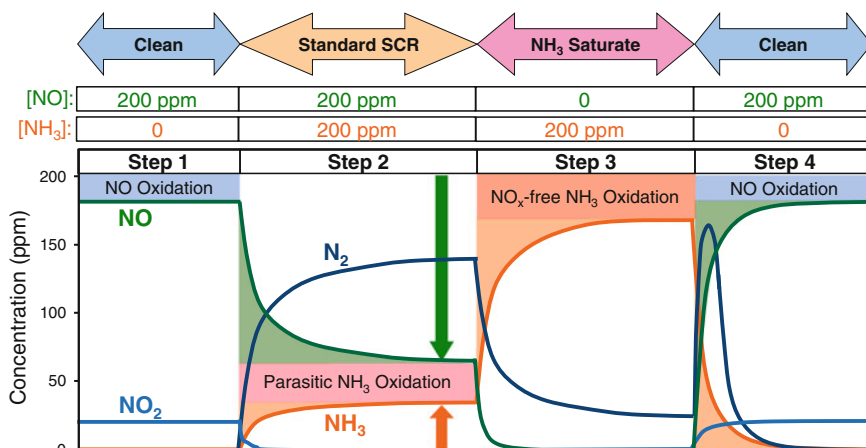


Fig. 4.2 4-step SCR evaluation protocol

subtracting the integrated NH₃ used for other reactions. Step 3 continues the NH₃ flow from step 2 at zero NO_x and is used to determine neat or NO_x-free NH₃ oxidation and the unused NH₃ capacity. It should be noted that NH₃ oxidation can differ in the presence and absence of NO, and specifically, can be enhanced by the presence of NO [13, 46–48]; these observations can be predicted and have been incorporated into SCR models [47, 49]. The unused NH₃ capacity is determined from integrating between the steady-state and instantaneous NH₃ curves, as indicated by the orange-shaded region in step 3 of Fig. 4.2. At the end of step 3 the total NH₃ capacity of the catalyst has been filled by sequentially filling the dynamic and unused capacity in steps 2 and 3, respectively; and the total NH₃ capacity can be independently measured in step 4 via its desorption and SCR reaction. Transitioning to step 4 the NH₃ flow is shut off and NO is reintroduced. The total NH₃ capacity is determined from the sum of the integrated NO_x reduction (green-shaded region in step 4 of Fig. 4.2) and the desorbed and unreacted NH₃ (orange-shaded region in step 4 of Fig. 4.2). Determining NH₃ capacity components from other protocols generally follows similar integrated analysis described here for the 4-step protocol.

Both of these protocols give a variety of parameters that are important in understanding the status and reactivity of a given catalyst. The detailed approach gives a more complete picture of more of the reactions, but it takes longer to run. The 4-step protocol targets the NH₃ storage behavior under specific conditions expected to occur in the vehicle and is more succinct, but lacks some the reactions necessary to develop a robust kinetic model. They are presented here to illustrate the range of approaches that can be taken in measuring the performance and properties of Fe-zeolite SCR catalysts, or other SCR catalysts for that matter. The remaining data will draw from results using both protocols.

4.3 Fe-Zeolite NO_x Reduction Characteristics

As discussed in the Introduction, Fe-zeolite SCR catalysts have similar properties to Cu-zeolites, but they do have distinct differences. To illustrate this, a protocol similar to the detailed one described above was used to evaluate Fe- and Cu-zeolite catalysts. Figure 4.3a shows the stoichiometric ($\text{NH}_3/\text{NO}_x = 1$) reactivity of both Fe- and Cu-zeolites when operated under standard SCR conditions ($\text{NO}_2/\text{NO}_x = 0$) at a space velocity of $30,000 \text{ h}^{-1}$. Significantly improved low-temperature reactivity of Cu is evident below $350 \text{ }^\circ\text{C}$, and the high temperature benefits of Fe-zeolite are apparent above this temperature. Furthermore, the ability of Cu-zeolite to store high quantities of NH_3 are evident in Fig. 4.3b, c, where up to 4x more NH_3 is stored in the same volume of catalyst (note the different y-axis scales). As discussed above, both these catalysts were supplied by commercial partners and the precise zeolite framework and Si:Al ratios are not known. However, a consistent trend reported in the SCR literature has been that Fe-zeolites have less NH_3 storage than Cu-zeolites [28, 46]. One explanation that has been proposed is that the differences can be ascribed to the presence of NH_3 adsorption sites with different strengths on the two catalysts and/or to a different coverage dependence of the activation energy for ammonia desorption [28]. Another possibility is that the NH_3 can readily store on the Cu sites in addition to the zeolite framework, but not on the Fe sites. An additional feature of note in Fig. 4.3b, c is the difference between lean and rich storage. Both Cu- and Fe-zeolite store more under the rich storage conditions (NH_3 in the absence of O_2) compared to the lean case (NH_3 storage in the presence of O_2). A significant contributor to the difference between lean and rich storage is the NH_3 oxidation activity of the catalysts. Cu-zeolite, which is much more active for NH_3 oxidation, shows a larger difference between lean and rich storage at low temperatures compared to Fe-zeolite. This oxidation behavior will be addressed again later in this section.

While Fig. 4.3 illustrates the behavior of the SCR catalyst at the reactor outlet, it is often important to investigate the behavior of the reactants inside the catalyst to see how the NH_3 is being utilized and where the NO_x is being reduced. This distributed NH_3 utilization in an Fe-zeolite (BEA) SCR catalyst was studied using the 4-step protocol shown in Fig. 4.2. The partitioning of NH_3 utilization between NO_x reduction, slip, dynamic capacity, and other reactions (NH_3 decomposition or NH_3 oxidation by O_2) can be determined from step 2 ($\text{NH}_3 + \text{NO}$). Figure 4.4 shows how this utilization varies in the front half of the catalyst. The green arrows indicate the amount of NH_3 used for NO_x reduction (1:1 $\text{NH}_3:\text{NO}$ stoichiometry) which is determined as the difference in the green curve and the 200-ppm feed value; this amount increases over the front half of the catalyst (0.5 L). The NH_3 slip (orange arrows) decreases along the catalyst axis, and NH_3 is fully consumed by the 0.5 L location; thus, with no remaining NH_3 slip there is no potential for further NH_3 storage or NO_x reduction. The other NH_3 reactions (light-blue boxes) are less at the catalyst front and approximately constant beyond the 0.25 L catalyst location. Figure 4.5 summarizes these results and shows the distribution of NH_3 utilization under steady-state SCR over the entire catalyst. Notably, 55–80 % of

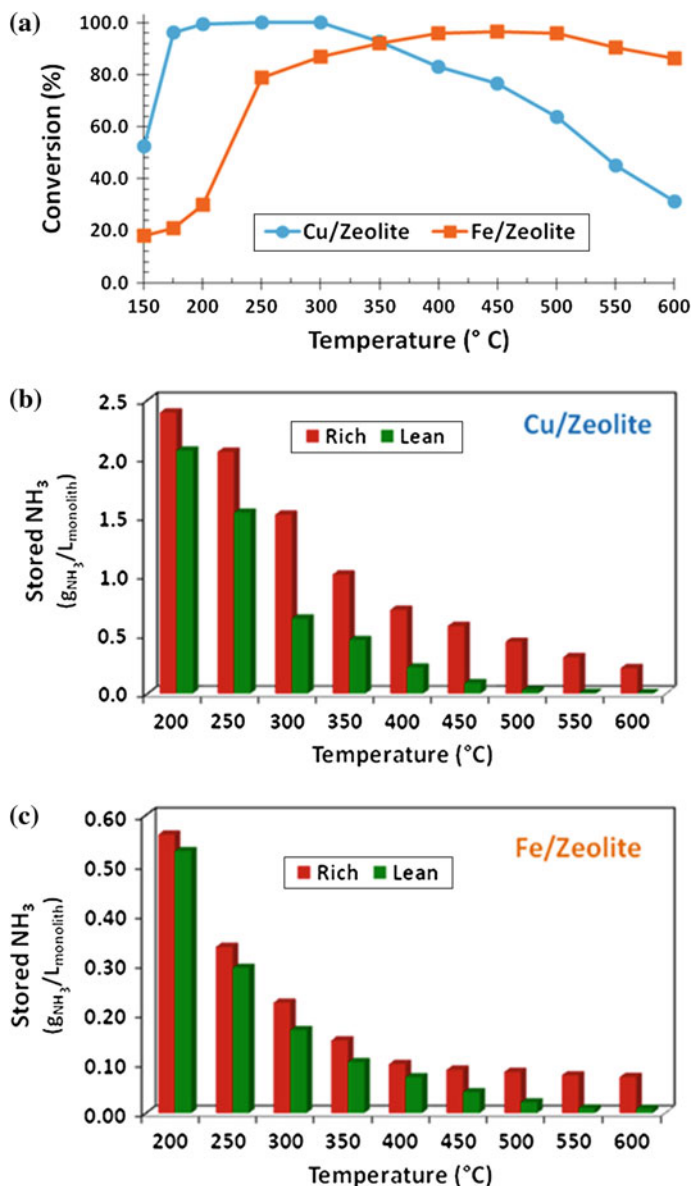


Fig. 4.3 a NO_x conversion comparison for Cu- and Fe-zeolite SCR catalysts; GHSV of 30,000 h⁻¹ under 500 ppm NO, 500 ppm NH₃, 10 % O₂, 5 % H₂O, and 5 % CO₂. NH₃ storage under both lean (with O₂) and rich (no O₂) conditions for **b** Cu-zeolite and **c** Fe-zeolite; GHSV of 30,000 h⁻¹, 500 ppm NH₃, 0 or 10 % O₂, 5 % H₂O, and 5 % CO₂

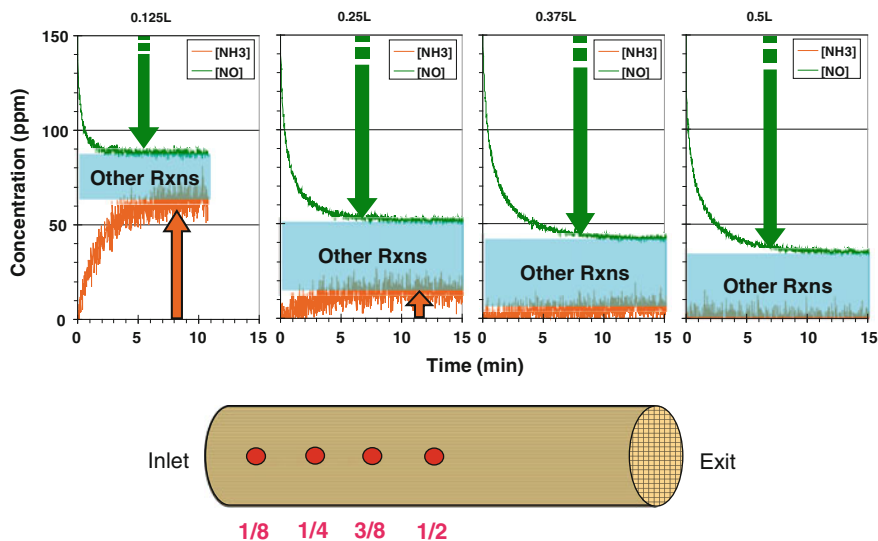
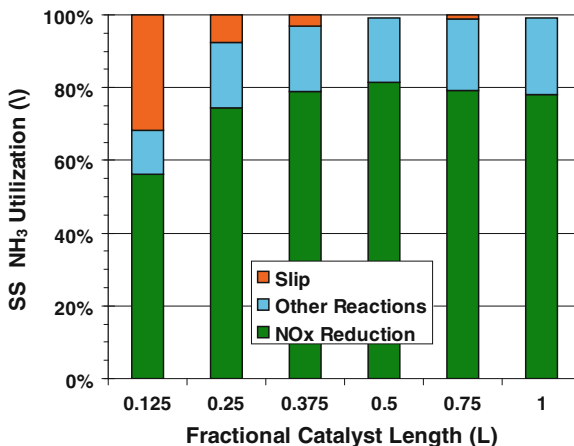


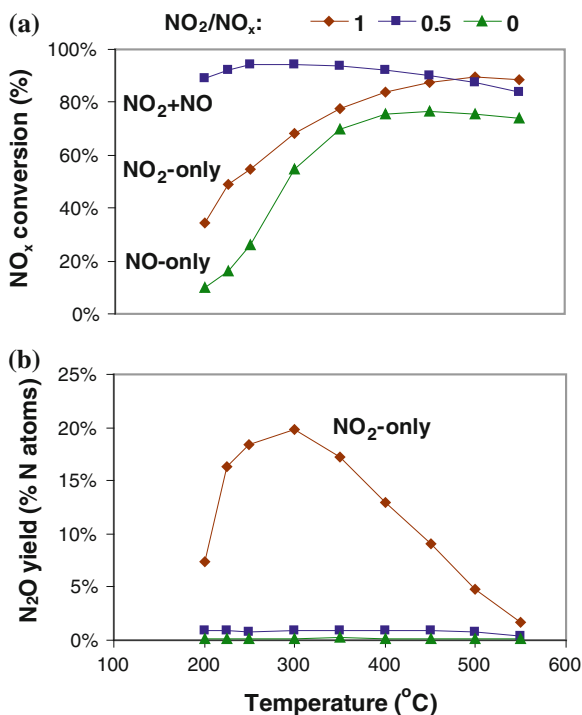
Fig. 4.4 Variation of NH_3 and NO concentrations in the front half of the Fe-zeolite catalyst during SCR reactivity. Space velocity of entire catalyst is $30,000 \text{ h}^{-1}$ (GHSV); 200 ppm NO , 200 ppm NH_3 , 10 % O_2 , 5 % H_2O , 325 °C

Fig. 4.5 Distributed NH_3 utilization throughout the Fe-zeolite SCR at steady state. Reaction conditions: 200 ppm NO , 200 ppm NH_3 , 10 % O_2 , 5 % H_2O , 325 °C, and $\text{GHSV} = 30,000 \text{ h}^{-1}$



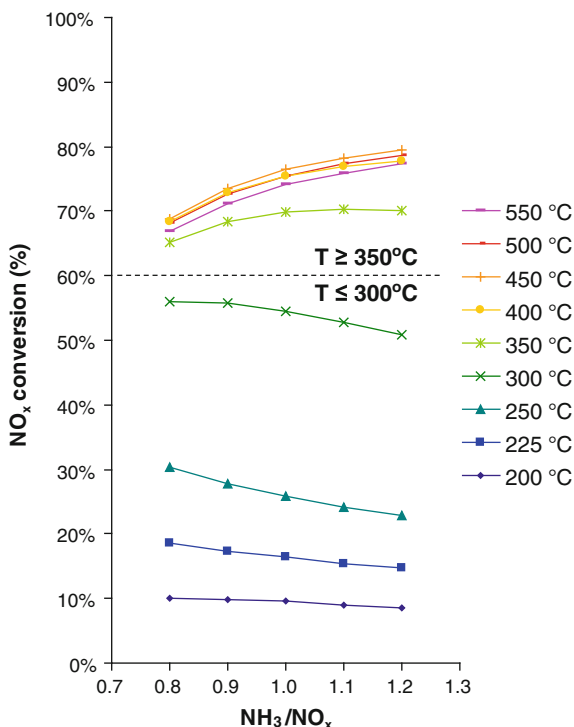
the NH_3 is used for NO_x reduction. However, a significant (15–20 %) amount of the NH_3 is consumed by other reactions and is not available for NO_x reduction use. Other results (not shown) indicate that the unused NH_3 capacity (step 3) increases linearly along the catalyst length, the dynamic NH_3 capacity (step 2) is concentrated in the front where SCR reactions occur, and the total capacity (step 4) balances with the dynamic and unused capacities. These types of catalyst insights improve kinetic and system models to design and control SCR catalysts for better efficiency and durability, e.g., how to reduce unwanted NH_3 oxidation by O_2 .

Fig. 4.6 SCR NO_x conversion and N_2O selectivity as a function of temperature for NO_2/NO_x ratios of 0.0, 0.5, and 1.0. Data collected with a fresh catalyst sample operated at a GHSV of $90,000 \text{ h}^{-1}$ with stoichiometric quantities of NO_x (300 ppm NO, 150 ppm NO + 150 ppm NO_2 , or 225 ppm NO_2 , respectively), 10 % O_2 , 5 % H_2O , and 5 % CO_2



As noted in Fig. 4.5, the NH_3 is consumed at approximately 0.375 L, or after $\sim 1/3$ of the catalyst at an SV of $30,000 \text{ h}^{-1}$. In studying the overall performance behavior, the data focused on this space velocity which is typical of vehicle applications. However, in implementing the protocols that do not rely on intra-catalyst measurements, higher space velocities, $90,000\text{--}120,000 \text{ h}^{-1}$ are typically employed to measure reactivity with less than 100 % conversion of the reactants, i.e., NH_3 beyond 0.375 L in Fig. 4.4. Figures 4.6 and 4.7 are examples of the types of steady-state data that can be extracted from the protocol runs. Figure 4.6 shows the NO_x conversion activity of the Fe-zeolite SCR catalyst as a function of temperature for three NO_2/NO_x ratios (0.0, 0.5, and 1.0) over a de-greened catalyst. As expected for Fe-zeolite SCR catalysts, 1:1 mixtures of NO and NO_2 (“fast” SCR) yield much higher SCR reaction rates than NO or NO_2 alone [24]; however, for this Fe-zeolite formulation, NO_2 -only is more reactive than NO alone. This appears to be a general characteristic of Fe-zeolites [24] and indicates that the “slow SCR” terminology used to describe NO_2 SCR is a misnomer. However, even though the overall NO_x reduction is improved with increasing NO_2 concentrations, the selectivity to the undesirable N_2O increases significantly for the NO_2 -only case and measurably for the $\text{NO}_2/\text{NO}_x = 0.5$ case, as noted in the bottom graph in Fig. 4.6. This increase in N_2O formation is an indicator of the formation and decomposition of an ammonium nitrate intermediate rather than the more desirable ammonium nitrite [47, 49–51]. The NO_x conversions were measured at steady state (which can take hours to achieve

Fig. 4.7 SCR NO_x conversion as a function of NH_3/NO_x ratio at various operating temperatures. Data collected with a fresh catalyst sample operated at a GHSV of $90,000 \text{ h}^{-1}$ under 300 ppm NO , 10 % O_2 , 5 % H_2O , and 5 % CO_2



at these low temperatures), so no further accumulation of ammonium nitrate was occurring (the rates of formation and decomposition were equal). Thus, the higher NO_x conversions observed with NO_2 SCR are due to conversion of NO_2 to N_2 and N_2O and not accumulation of ammonium nitrate on the surface.

Figure 4.7 summarizes NO_x conversion as a function of NH_3/NO ratio and temperature. At 300 °C and below, the NO_x conversion decreases with increasing NH_3 dose. This behavior indicates that NH_3 inhibits the NO SCR reaction at low temperatures. Above 300 °C, the trend reverses, and NO_x conversion improves with increasing NH_3 concentration. Interestingly, Fig. 4.8 shows that NH_3 oxidation becomes measurable at temperatures above 300 °C. The maximum observed conversion is only 15 % at 550 °C, which is much lower than the reported values of >90 % on Cu-zeolites [52]. The lower NH_3 oxidation activity over the Fe-zeolite is the underlying reason for its higher NO_x conversion activity at high temperatures. Interestingly, the selectivity on these catalysts favors N_2 formation with only 2 % NO yield and <1 % N_2O at 500 °C. This is an important consideration since it illustrates that models need to account for losses of NH_3 to oxidation, but not necessarily more NO formation.

In addition to the steady-state data typically collected for evaluation of SCR catalysts, the test protocols include well-defined transient steps that generate additional insights into the catalyst surface chemistry. Figure 4.9 shows the NH_3

Fig. 4.8 NH_3 oxidation behavior (*top*) and its associated yield (*bottom*). Data collected with a fresh catalyst sample operated at a GHSV of $90,000 \text{ h}^{-1}$ and a feed of 300 ppm NH_3 , 10 % O_2 , 5 % CO_2 , 5 % H_2O

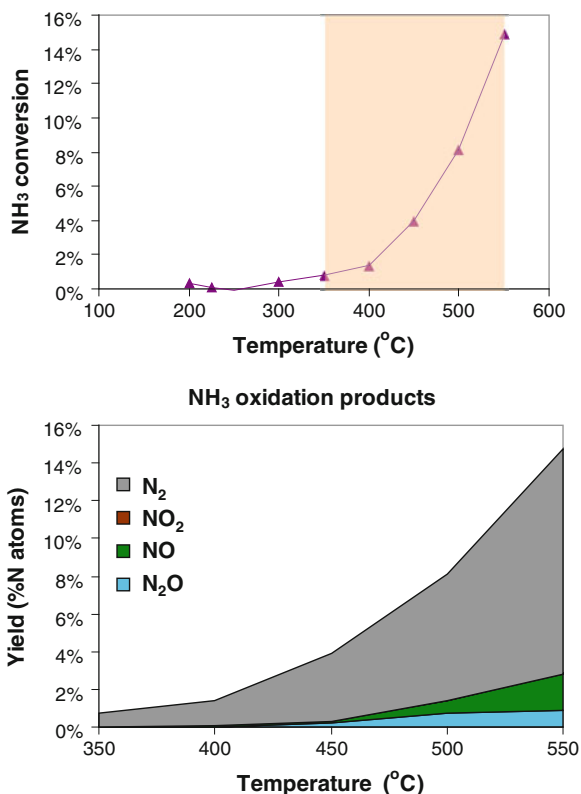


Fig. 4.9 Concentration of NH_3 released as a function of temperature during TPD portion of protocol. Data collected with a fresh catalyst sample operated at a GHSV of $120,000 \text{ h}^{-1}$ under 300 ppm NO , 10 % O_2 , 5 % H_2O , and 5 % CO_2

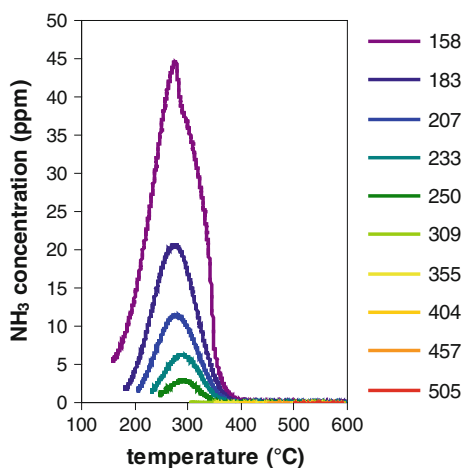
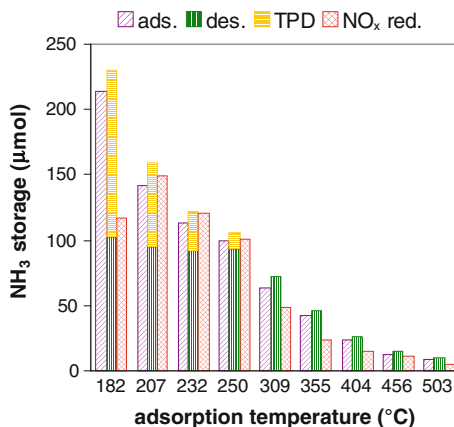


Fig. 4.10 Catalyst NH_3 storage capacity as a function of adsorption temperature as measured by uptake during adsorption (ads.), release during isothermal desorption (des.) and temperature programmed desorption (TPD), and NO_x converted by stored NH_3 after removing NH_3 from the feed gas (NO_x red.)



released from the catalyst during the temperature programmed desorption (TPD) at the end of the detailed protocol run. For adsorption temperatures above 300 °C, all of the NH_3 is released during the isothermal desorption step prior to the TPD (see Fig. 4.1). For adsorption temperatures below 300 °C, the amount of NH_3 desorbed during the TPD increases with decreasing adsorption temperature. For all but one of the TPD runs, there is a single NH_3 desorption feature centered at approximately 300 °C. Note that this temperature also represents the threshold for NH_3 inhibition of the NO SCR reaction. At 150 °C there is a second low temperature NH_3 desorption, likely due to formation of ammonium nitrates on the catalyst surface.

The detailed protocol includes several transient steps that provide independent measures of NH_3 storage capacity under various operating conditions. These include adsorption under inert conditions, isothermal, and temperature programmed desorption, and reactivity of NO with stored NH_3 after the NH_3 feed is shut off. Integrating the NH_3 stored, released, or reacted during each of these steps yields the capacities summarized in Fig. 4.10. The integrals from the two desorption steps are shown as stacked bars to indicate the total NH_3 desorbed. This plot yields two noteworthy insights. First, with the exception of the lowest temperature run, the three independent measurement techniques for determining storage capacities are fairly consistent. Based on this observation, we conclude that a measurement of NH_3 storage capacity can be achieved through any of the three techniques. The exception to this conclusion is for temperatures below 200 °C, where the slow SCR kinetics limit the NO_x reacted with stored NH_3 . At these low temperatures, the appropriate measure of NH_3 storage capacity will depend on the application of the measurement. The consistency between the various NH_3 storage measurements is due to the low NH_3 oxidation activity of the catalyst. Catalysts with higher NH_3 oxidation rates (such as Cu-zeolites) exhibit much larger differences between NH_3 stored under inert conditions as compared to NH_3 desorbed/ reacted under oxidizing conditions.

4.4 Durability, Aging Techniques, and Deactivation Mechanism Affecting Performance

Much of the research performed and publicly disseminated relies on fresh or degreened catalyst samples; however, aging can have a significant impact on the performance of these catalysts. It is critical to understand these impacts since vehicle emissions must be certified with the catalysts in an aged state. For light-duty vehicles this aged condition is 120,000–150,000 miles and for heavy-duty vehicles it is 435,000 miles. The primary factor that goes into aging is the thermal durability requirements, as the emissions control devices are expected to reach temperatures up to 800 °C under typical operating conditions. This high temperature is expected during the active regeneration of the DPF or under stoichiometric operation of lean gasoline engines. Additionally, reversible deactivation from hydrocarbons and sulfur can affect the SCR chemistry [32, 34, 39, 40], and there have been reports of irreversible contamination from metals originating from the fuel [53–56], lubricants [38], or even upstream catalysts [35–37]. Operating these catalyst systems to the end of full useful life, especially when evaluating several new catalysts and operating procedures, is often unreasonable and cost-prohibitive; therefore, accelerated aging protocols/routines are necessary. The remainder of this section will address the deactivation mechanisms observed in Fe-zeolite SCR catalysts as well as the accelerated aging protocols often used to produce the aged samples.

The majority of published research on the thermal durability of zeolite-based SCR catalysts utilize controlled furnace-based hydrothermal aging to accelerate the aging process [10, 57, 58]. This approach can adequately match the thermal strains that catalysts experience under engine or vehicle aging conditions, as has been elegantly demonstrated by Schmieg et al. on a Cu-zeolite (CHA) SCR catalyst [52]. An additional benefit of furnace aging is that it allows the isolation of thermal durability aspects of the catalyst. Generally, modern metal-exchanged zeolites have shown good durability under these controlled conditions, exhibiting less than a 10 % decrease in NO_x reduction activity. As an example, Fig. 4.11, shows the impact of aging an Fe-zeolite (BEA) SCR in the presence of H₂O, CO₂, O₂, and SO₂ in a furnace-based flow reactor for 64 h at 670 °C. As mentioned above, the NO_x conversion of the hydrothermally aged SCR catalyst was minimally affected. Devadas et al. obtained similar results after 50 h of hydrothermal aging with an Fe-zeolite (ZSM-5) SCR catalyst [57]. Even aged catalysts that maintain activity can experience a decrease in surface area and dealumination, which occurs when the Al³⁺ ions in the SiO₂–Al₂O₃ tetrahedral framework migrate out of the structure. This typically manifests itself as a decrease in NH₃ adsorption capacity and the loss of surface acidity [52, 59]. When aging above the mild temperatures shown in Fig. 4.11, i.e., >800 °C, many of the zeolites begin to dramatically breakdown structurally [52, 59].

For a more complete system-based durability evaluation, it is common to include the DOC and DPF in the aging protocol, and to rely on HC oxidation over

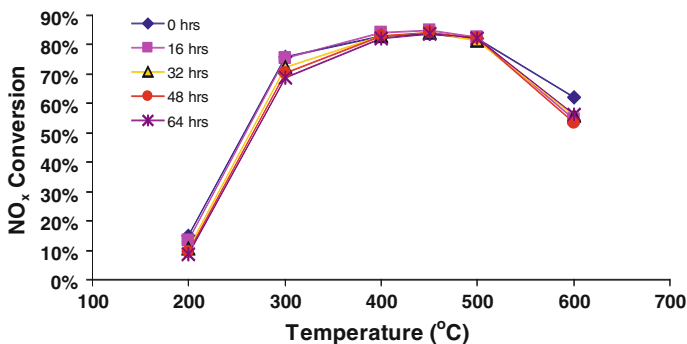


Fig. 4.11 Effect of aging time at 670 °C on NO_x conversion with Fe-zeolite SCR; evaluated with 5 % CO₂, 5 % H₂O, 14 % O₂, 350 ppm NO, 350 ppm NH₃, N₂ balance, GHSV = 30,000 h⁻¹

the DOC to generate the exotherm for inducing thermal aging. These approaches generally rely on engine-based systems, but in some instances could be performed with only flow reactors [60]. These more complex approaches can lead to several deactivation mechanisms occurring simultaneously, but can offer good insight into the potential limitations of the overall system. To illustrate this approach, an engine-based DOC-SCR-DPF accelerated aging approach will be discussed [37]. In the study, the aging of the SCR catalyst was achieved by increasing the exhaust temperature to replicate periodic DPF regenerations with target exhaust gas temperatures of 650, 750, and 850 °C at the SCR inlet. The activity of the engine-aged Fe-zeolite (BEA) SCR catalysts was then evaluated in a flow reactor to determine the extent of catalyst degradation, and material characterization was performed to ascertain the deactivation mechanisms associated with engine aging.

In implementing this engine and flow reactor systematic approach, it is possible to investigate different sections of the catalyst. Figure 4.12 shows the impact of aging temperature on the front and rear sections of the Fe-zeolite SCR catalysts. Very different activity is observed in these samples. Although there was an axial temperature gradient across the catalysts, ~100 °C when aging at 650 and 750 °C and ~50 °C at 850 °C, this cannot explain the dramatic difference in performance; the rear of the 750 °C-aged SCR reached 650 °C, but it outperforms the front of the 650 °C-aged SCR. More evidence of involvement of a different deactivation mechanism can be seen in BET-measured surface areas in Fig. 4.13. The front and rear sections of the SCR catalyst engine aged at 650 °C are 60 m²/g and 59 m²/g, respectively, which both approximate the fresh catalyst, 58 m²/g. At higher aging temperatures, surface areas begin to decrease and the thermal gradient is apparent as the front section is more adversely affected than the rear sample. Of course for this to be the sole cause of performance degradation there would have to be a notable surface area decrease in the front section of the sample aged at 650 °C to explain the results in Fig. 4.12. In examining the 850 °C results it is clear that both the front and rear sections have both significant activity losses and surface area losses.

Fig. 4.12 NO_x conversion of the accelerated engine-aged Fe-zeolite SCR catalysts **a** front and **b** rear sections; evaluated with 5 % CO₂, 5 % H₂O, 14 % O₂, 350 ppm NO, 350 ppm NH₃, N₂ balance, GHSV = 30,000 h⁻¹

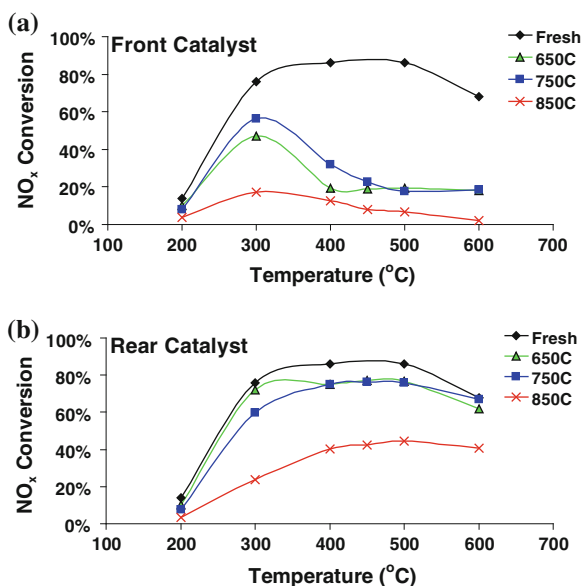
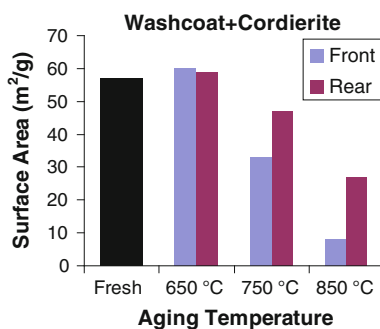


Fig. 4.13 BET surface area measurements of fresh and accelerated engine-aged Fe-zeolite SCR catalysts



The thermal aging effect on the zeolite structure is further evident in XRD and NMR studies shown in Figs. 4.14, 4.15, and 4.16. Figure 4.14 shows the XRD patterns of the fresh and accelerated engine-aged Fe-SCR catalysts; only the front sections are shown here. The clearest phase change that occurs is the gradual loss in the zeolite crystallinity at increasing aging temperatures. The primary zeolite peaks are visible at $2\theta = 8$ and 22.5° . The peaks are clear and predominant in the fresh sample, and also after aging at 650 °C. However, upon heating to 750 and 850 °C, the zeolite structure begins to diminish. This breakdown of the zeolite generally results in alumina formation with detectable peaks of alumina in the XRD patterns occurring at $2\theta = 43$ and 67° . These peaks are more discernible at 850 °C and to a lesser extent at 750 °C. Additionally, at higher aging temperatures, there is a minor growth in the Fe₂O₃ phase at $2\theta = 36$ and 54° . This indicates that active Fe cations in the fresh catalyst have formed Fe₂O₃ clusters in

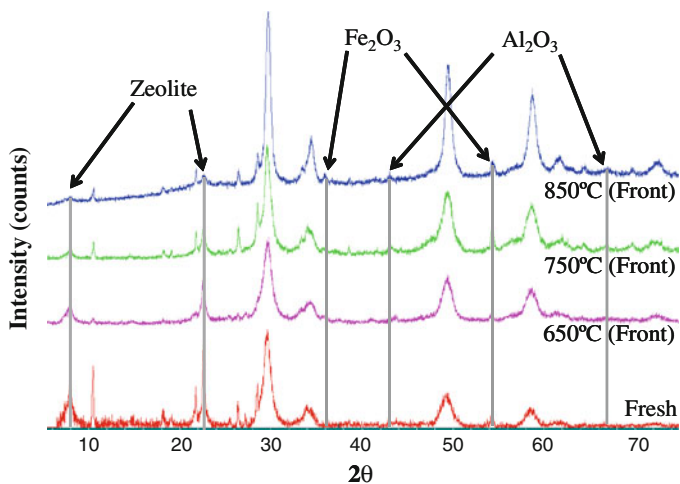
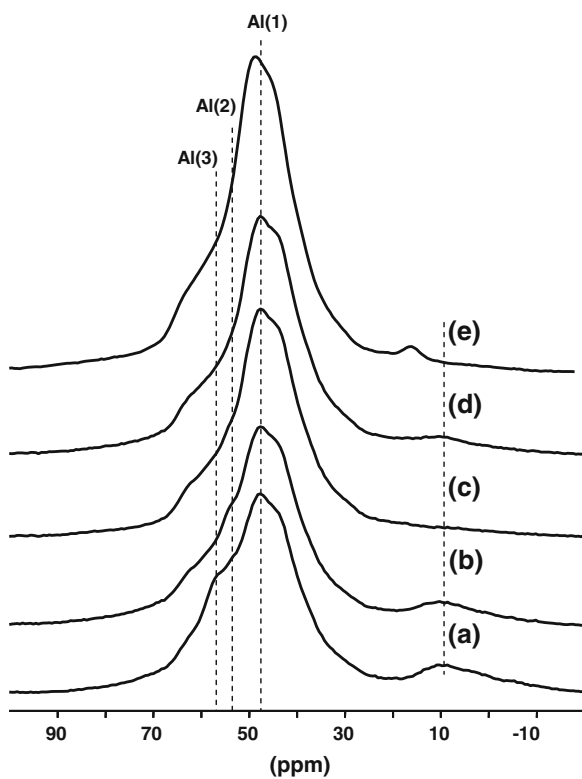


Fig. 4.14 X-ray diffraction patterns of fresh and accelerated engine-aged Fe-zeolite SCR catalysts

Fig. 4.15 One-dimensional ^{27}Al MAS spectra of the **a** fresh Fe-zeolite/cordierite, samples aged at **b** 650, **c** 750, and **d** 850 °C, and **e** cordierite



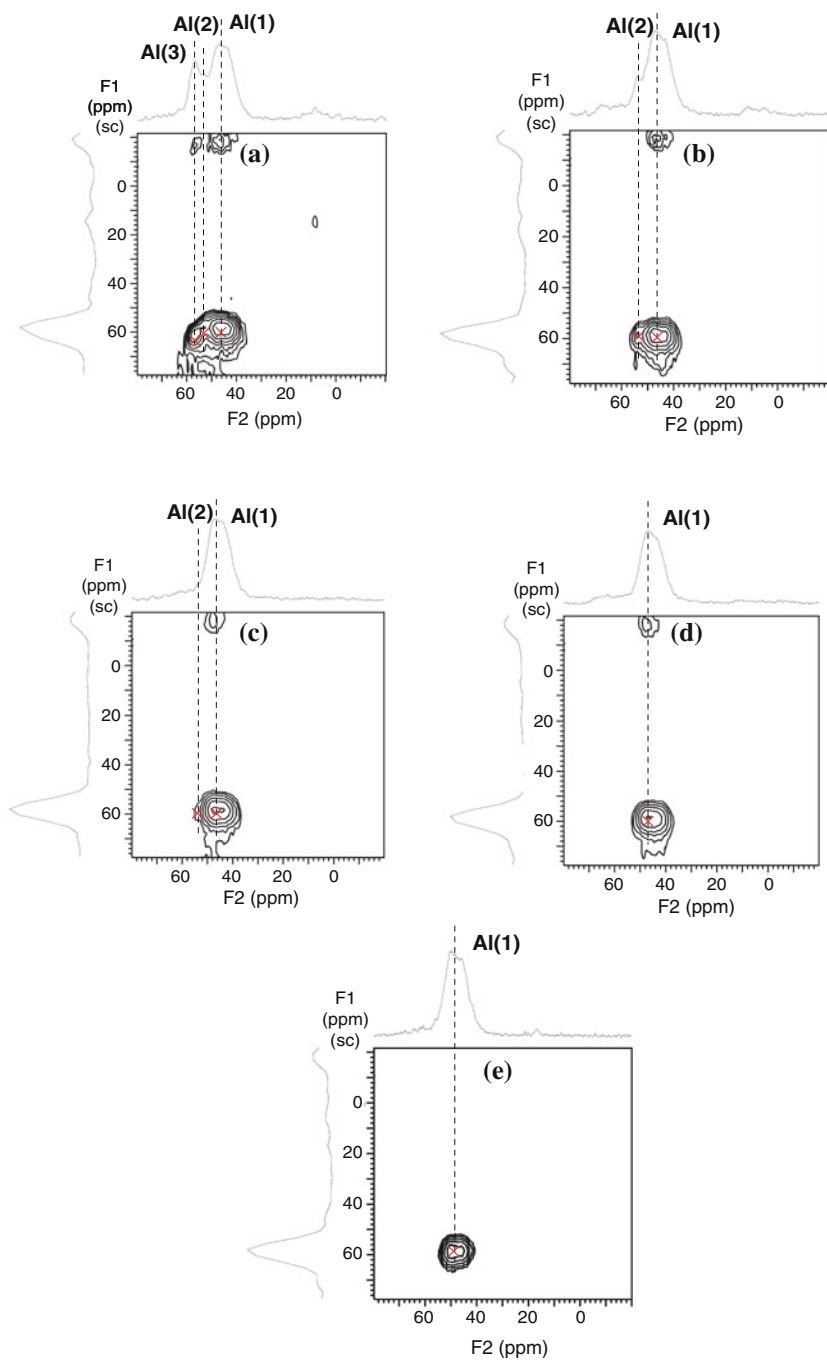


Fig. 4.16 Two-dimensional 3QMAS ^{27}Al -NMR spectra of **a** fresh Fe-zeolite SCR catalysts and samples aged at **b** 650, **c** 750, and **d** 850 °C, and **e** A cordierite spectrum was also recorded since it was present in each of the samples

the aged samples. As the zeolite structure collapses, active cations are freed and they can form oxide clusters such as Fe_2O_3 . As the zeolite structure begins to decompose, the surface area decreases, and there will be fewer available sites to bind the Fe cations, and thus the Fe_2O_3 phase will become more prevalent [14]. These results, especially combined with the performance evaluation, point to this zeolite failing when aged above 750 °C. The obvious Fe_2O_3 peak at 54° combined with the drop in surface area of the 850 °C-aged samples provide very strong evidence for zeolite collapse.

Solid-state ^{27}Al -NMR is sensitive to the local structure and bonding and provides a method to extend our description of aluminum bonding in these heterogeneous, amorphous materials [61]. In particular, the 2D experiment that employs triple quantum excitation/evolution and magic angle spinning (3QMAS) has shown great promise in resolving multiple tetrahedral and octahedral aluminum sites as well as penta-coordinate aluminum in zeolites [62]. The suite of stacked ^{27}Al MAS spectra in Fig. 4.15 are of the fresh Fe-zeolite/cordierite samples in the fresh state (a), and after aging at 650 (b), 750 (c), and 850 °C (d), as well as a cordierite blank (e). The same sample suite yields the 3QMAS spectra shown in Fig. 4.16. In both figures, the catalyst spectra are also compared with the spectrum of the cordierite support. Cordierite and Fe-zeolite are constructed of aluminum with tetrahedral coordination represented by the asymmetric resonance band centered at 50 ppm in the 1D spectrum (see Fig. 4.15). The number of distinct aluminum sites is difficult to assess from the 1D data. The 2D spectrum of the fresh Fe-zeolite/cordierite, Fig. 4.16a, clearly shows the broad tetrahedral resonance contains three partially resolved resonances. The Al(1) resonance is due to the support (see Fig. 4.16e). The Al(2) and Al(3) resonances near 55 ppm arise from the Fe-zeolite catalyst [63]. These signals diminish in the successively aged samples, as seen in both Figs. 4.15 and 4.16, and completely disappear in the 850 °C-aged sample. The loss of the signal is attributed to dislodgement of lattice aluminum species to extra-framework positions, perhaps yielding undefined resonances due to the presence of paramagnetic iron species.

Combining all of these characterization techniques and comparing the results to the performance data, it is clear that heating to 850 °C has the most significant impact on the structure and reactivity of the catalysts. These losses in zeolite structure are occurring at lower temperatures compared to the Cu-zeolite (CHA) discussed above [52], but this is essentially due to the difference in zeolite being used. To date there has not been a commercially produced catalyst that has demonstrated the ability to exchange Fe in the CHA zeolite, but there have been some recent academic reports that suggest it is possible and could lead to more thermally durable Fe-zeolite SCR catalysts [64, 65].

The materials characterization is clearly important to help understand and quantify some of the deactivation mechanisms occurring; however, it is not sufficient to explain the deactivation of the front section of the Fe-zeolite SCR, especially the one aged at 650 °C. For this, it is necessary to point to the findings of Jen et al. [35, 36], who illustrated that Pt and to a lesser extent Pd can volatilize from the upstream DOC and deposit on the front face of the SCR. This has a deleterious

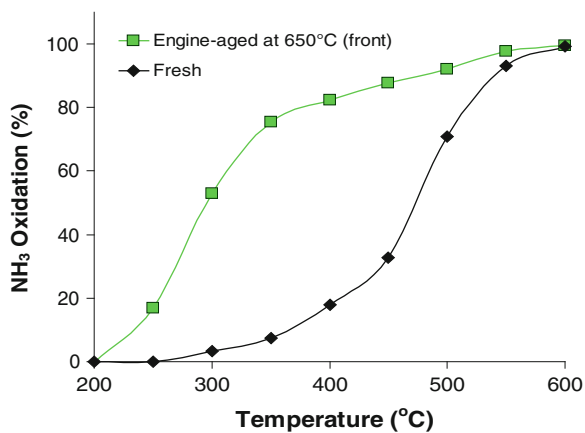


Fig. 4.17 NH₃ oxidation evaluated with 5 % CO₂, 5 % H₂O, 14 % O₂, 350 ppm NH₃, N₂ balance, and a GHSV = 30,000 h⁻¹

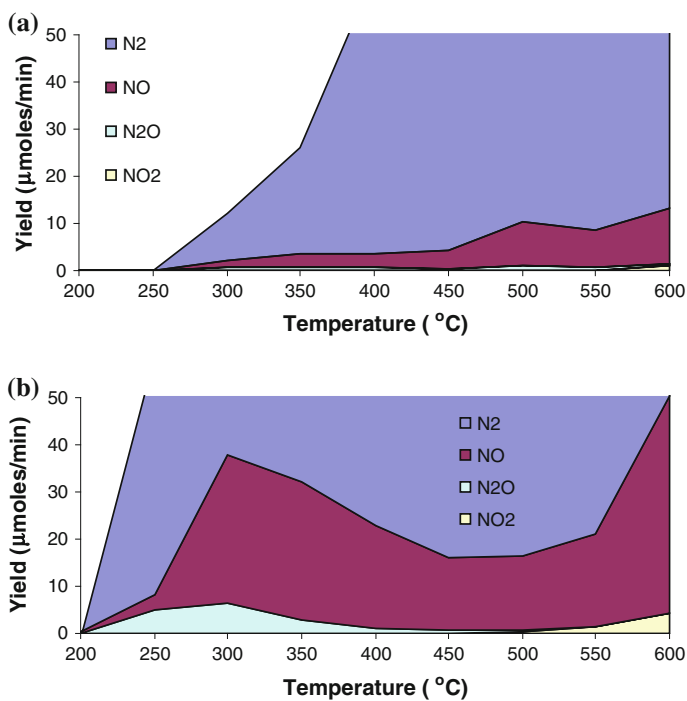


Fig. 4.18 Product yield during the NH₃ oxidation evaluation depicting N₂, NO, N₂O, and NO₂ in **a** fresh SCR catalyst and **b** SCR catalyst engine-aged at 650 °C

effect on NH_3 availability for NO_x SCR as it is easily oxidized over even trace quantities of Pt and Pd. This is clearly illustrated in Fig. 4.17 as the front of the 650 °C-aged sample shows NH_3 oxidation readily occurs above 250 °C, such that above 300 °C less than 80 % of the introduced NH_3 is available. This is coincident with the dramatic decrease in activity shown in Fig. 4.12. Furthermore, with PGM contamination it is expected that the amount of N_2O being made will increase with these catalysts, and Fig. 4.18 illustrates this rise in N_2O yield when comparing the fresh to the 650 °C-aged catalyst. Of course this deactivation mechanism is not unique to Fe-zeolites, and should be a consideration for each NH_3 -SCR-based system. Also to be considered are the findings of the follow-up study illustrating the reduced volatilization that occurs with Pt/Pd mixtures [36].

4.5 Summary

As is illustrated in this chapter, Fe-zeolites have a specific role in NH_3 -based SCR of NO_x , and provide reaction characteristics that are different from other SCR-based systems. Through application of an appropriate experimental protocol, it is possible to gain deep insight into the detailed workings of these catalysts. Although the chemistry is largely similar to that of Cu-zeolite SCR catalysts, there are key differences that differentiate the two systems:

- The operating window of Fe-zeolite is considerably higher, which is primarily attributed to its decreased activity for NH_3 oxidation by O_2 . This is one of the key differentiating attributes of the catalyst, and allows emissions control developers more flexibility when designing their systems. Additionally, a carefully designed system combining with Cu-zeolites and Fe-zeolites could allow a broader temperature window [66–68].
- The NH_3 storage capacity of Fe-zeolite is significantly lower than Cu-zeolite. While this feature is less desirable in a hybrid LNT + SCR system where NH_3 is generated over the LNT and stored on the SCR for later use, it can be preferred from a controls standpoint since there is less accumulation to account for on the catalyst. In fact, the very high storage of NH_3 at low temperatures significantly complicates the functionality of a Cu-only system during transient operation.
- Current model Fe-zeolites have shown hydrothermal stability up to 670 °C, but at higher temperatures there are significant concerns with durability. With further improvements in the zeolite framework, a durable Fe-SCR catalyst may have a role in automotive emissions control of NO_x .

These differences help illustrate the range of catalyst functionality in SCR chemistry, and the protocols outlined here offer guidance on practical methods of

measuring this functionality. Understanding the behavior of the system and how it changes during operation/aging is critically important to implementing and modeling these SCR systems for emissions control, and ultimately improving their functionality and durability.

References

1. U.S. Environmental Protection Agency, "Milestones in Auto Emissions Control", Fact Sheet OMS-12, EPA 400-F-92-014 (1994).
2. W.B. Williamson, J. C. Summers, J.A. Scaparo, ACS Symposium Series, 495 (1992) 26.
3. H. Tamaura, K. Tanaka, Langmuir 10:12 (1994) 4530.
4. W. Grunert, H. Papp, C. Rottlander, M. Baerns, Chemische Technik 47:4 (1995) 205.
5. U.S. Environmental Protection Agency, Federal Register 70:133 (2005) 40420.
6. X. Feng and W. K. Hall, J. Catal. 166 (1997) 368.
7. M. Koebel, M. Elsener, and M. Kleemann, J. Catal. 180 (1998) 171.
8. H.Y. Chen, and W.M.H. Sachtler, Catal. Lett. 50 (1998) 125.
9. H.Y. Chen, and W.M.H. Sachtler, Catal. Today 42 (1998) 73.
10. R.M. Heck, Catal. Today 53 (1999) 519.
11. R.Q. Long and R.T. Yang, J. Catal., 188 (1999) 332.
12. M. Koebel, M. Elsener, and M. Kleemann, Catal. Today 59 (2000) 33.
13. Q. Sun, Z.X. Gao, H.Y. Chen, and W.M.H. Sachtler, J. Catal. 201 (2001) 89.
14. R.Q. Long and R.T. Yang, Catal. Lett. 74 (2001) 201.
15. R.Q. Long and R.T. Yang, Catal. Lett. 207 (2002) 224.
16. B.R. Wood, J.A. Reimer, and A.T. Bell, J. Catal., 209 (2002) 151.
17. G. Cavataio, J. Girard, J.E. Patterson, C. Montreuil, Y. Cheng, C.K. Lambert, SAE Technical Paper Series 2007-01-1575 (2007) 1.
18. J.R. Theis, SAE Technical Paper Series 2008-01-0811 (2008) 1.
19. Manufacturers of Emission Controls Association, "Emission Control Technology for Stationary Internal Combustion Engines", Status report (1997) 1.
20. U.S. Environmental Protection Agency, "Summary of NOx Control Technologies and their Availability and Extent of Application", EPA 450/3-92-004 (1992).
21. D.M. Chapman, Applied Catalysis A: General 392:1-2 (2011) 143.
22. S. Hu, J.D. Herner, M. Schafer, W. Roberston, J.J. Schauer, H. Dwyer, J. Collins, T. Huai, A. Ayala, Atmos. Environ. 43 (2009) 2950.
23. Z.G. Liu, N.A. Ottinger, C.M. Creemeens, SAE Technical Paper Series 2012-01-0887 (2012) 1.
24. S. Brandenberger, O. Kröcher, A. Tissler, R. Althoff, Catal. Rev. Sci. Eng. 50 (2008) 492.
25. S. Brandenberger, O. Kröcher, A. Tissler, R. Althoff, Appl. Catal. B 95 (2010) 348.
26. S. Brandenberger, O. Kröcher, A. Tissler, R. Althoff, Appl. Catal. A 373 (2010) 168.
27. A. Grossale, I. Nova, E. Tronconi, Catalysis Today 136:1-2 (2008) 18.
28. M. Colombo, I. Nova, E. Tronconi, Catalysis Today 151:3-4 (2010) 223.
29. A. Grossale, I. Nova, E. Tronconi, Catalysis Letters 130:3-4 (2009) 525.
30. A. Grossale, I. Nova, E. Tronconi, J. Catal. 265:2 (2009) 141.
31. M.P. Ruggieri, A. Grossale, I. Nova, E. Tronconi, H. Jirglova, Z. Sobalik, Catal. Today 184:1 (2012) 107.
32. Y. Cheng, C. Montreuil, G. Cavataio, C.K. Lambert, SAE Technical Paper Series 2008-01-1023 (2008) 1.
33. G. Cavataio, H.-W. Jen, J.R. Warner, J.W. Girard, J.Y. Kim, C.K. Lambert, SAE Technical Paper Series 2008-01-1025 (2008) 1.
34. V.Y. Prikhodko, J.A. Pihl, S.A. Lewis, J.E. Parks, SAE Technical Paper Series 2012-01-1080 (2012) 1.

35. H.W. Jen, J.W. Girard, G. Cavataio, and M.J. Jagner, SAE Technical Paper Series 2008-01-2488 (2008).
36. G. Cavataio, H.W. Jen, J.W. Girard, and M.J. Jagner, SAE Technical Paper Series 2009-01-0627 (2009).
37. T. J. Toops, K. Nguyen, A.L. Foster, B.G. Bunting, N.A. Ottinger, J.A. Pihl, E.W. Hagaman, J. Jiao, *Catal. Today* 151 (2010) 257.
38. R.G. Silver, M.O. Stefanick, B.I. Todd, *Catal. Today* 136:1–2 (2008) 28.
39. J. Li, R.H. Zhu, Y.S. Cheng, C.K. Lambert, R.T. Yang, *Environmental Science & Technology* 44:5 (2010) 1799.
40. L. Ma, J. Li, Y.S. Cheng, C.K. Lambert, L.X. Fu, *Environmental Science & Technology* 46:3 (2012) 1747.
41. S. Brandenberger, O. Kröcher, *Chimia* 66 (2012) 687.
42. A. Grossale, I. Nova, E. Tronconi, D. Chatterjee, M. Weibel, *J. Catal.* 256:2 (2008) 312.
43. P.S. Metkar, V. Balakotaiah, M.P. Harold, *Catalysis Today* 184:1 (2012) 115.
44. L. Olsson, H. Sjövall, R.J. Blint, *Appl. Catal. B* 81:3–4 (2008) 203.
45. J.A. Pihl, “Development of a CLEERS transient experimental protocol for urea/ammonia SCR”, 2010 DOE Crosscut Workshop on Lean Emissions Reduction Simulation (CLEERS), Dearborn, MI, USA, April 20, 2010.
46. K. Kamasamudram, N.W. Currier, X. Chen, A. Yezerets, *Catalysis Today* 151 (2010) 212.
47. H. Sjövall, R.J. Blint, A. Gopinath, L. Olsson, *Ind. Eng. Chem. Res.* 49 (2010) 39.
48. A. Schuler, M. Votsmeier, P. Kiwic, J. Geisshoff, W. Hauptmann, A. Drochner, H. Vogel, *Chem. Eng. J.* 154:1–3 (2009) 333.
49. M. Colombo, I. Nova, E. Tronconi, V. Schmeisser, B. Bandl-Konrad, L. Zimmerman, *Appl. Catal. B: Environ.* 111 (2012) 106.
50. G. Madia, M. Koebel, M. Elsener, A. Wokaun, *Ind. Eng. Chem. Res.* 41:16 (2002) 4008.
51. G. Delahay, S. Kieger, B. Neveu, B. Coq, *Comptes Rendus de l'Académie des Sciences Serie II Fascicule C-Chimie* 1:4 (1998) 229.
52. S.J. Schmiege, S.H. Oh, C.H. Kim, D.B. Brown, J. H. Lee, C.H.F. Peden, D. H. Kim, *Catalysis Today* 184 (2012) 252.
53. G. Cavataio, H.-W. Jen, D.A. Dobson, J.R. Warner, SAE Technical Paper Series 2009-01-2823 (2009) 1.
54. D.W. Brookshear, K. Nguyen, T. J. Toops, B.G. Bunting, J. Howe, *Catalysis Today* 184 (2012) 205.
55. D.W. Brookshear, K. Nguyen, T. J. Toops, B.G. Bunting, *Topics in Catalysis* 56:1–8 (2013) 62.
56. A. Williams, J. Burton, R.L. McCormick, T.J. Toops, A.A. Wereszczak, E.E. Fox, M.J. Lance, G. Cavataio, D. Dobson, J. Warner, R. Brezny, D.W. Brookshear, K. Nguyen, SAE Technical Paper Series 2013-01-0513 (2013) 1.
57. M. Devadas, O. Krocher, A. Wokaun, *React. Kin. Catal. Lett.* 86:2 (2005) 347.
58. M. Devadas, O. Krocher, M. Elsener, A. Wokaun, G. Mitrikas, N. Soger, M. Pfeifer, Y. Demel, L. Mussmann, *Catal. Today* 119:1 (2007) 137.
59. K. Rahkamaa-Toloen, M.L. Maunula, M. Huuhtanen, R.L. Keiski, *Catal. Today* 100:3–4 (2005) 217.
60. N.A. Ottinger, K. Nguyen, B.G. Bunting, T.J. Toops, J. Howe, *SAE International Journal of Fuels and Lubricants* 2:1 (2009) 217.
61. M. E. Smith, *Appl. Magn. Reson.* 4 (1993) 1.
62. J. Huang, Y. Jiang, V. R. R. Marthala, B. Thomas, E. Romanova, M. Hunger, *J. Phys. Chem. C* 112 (2008) 3811.
63. J. Perez-Ramirez, J. C. Groen, A. Bruckner, M. S. Kumar, U. Bentrup, M. N. Debbagh, and L. A. Villaescusa, *J. Catal.* 232 (2005) 318.
64. Q. Ye, L. Wang, R.T. Yang, *Appl. Catal. A* 427–428 (2012) 24.

65. X.F. Yang, Z.L. Wu, M. Moses-Debusk, D.R. Mullins, S.M. Mahurin, R.A. Geiger, M. Kidder, C.K. Narula, *J. Phys. Chem. C* 116:44 (2012) 23322.
66. P.S. Metkar, M.P. Harold, V. Balakotaiah, *Chem. Engr. Sci.* 87 (2013) 51.
67. Y. Liu, M.P. Harold, D. Luss, *Appl. Catal. B* 121 (2012) 239.
68. P.S. Metkar, M.P. Harold, V. Balakotaiah, *Appl. Catal. B* 111 (2012) 67.

Chapter 5

Cu/Zeolite SCR Catalysts for Automotive Diesel NO_x Emission Control

Hai-Ying Chen

5.1 Introduction

Cu/zeolite catalysts have long been recognized to be highly active in the Selective Catalytic Reduction (SCR) of NO_x with NH₃ [1–16]. Compared to titania supported vanadia SCR catalysts, which have been successfully commercialized for stationary NO_x emission control since the 1970s and installed on certain Heavy Duty Diesel (HDD) vehicles to meet the NO_x emission regulations since the early 2000s, Cu/zeolite SCR catalysts exhibit higher NO_x conversion efficiency, particularly at low temperatures [11, 17]. In addition, Cu/zeolite SCR catalysts are more tolerant to high temperature excursions. For automotive applications, this is a critical requirement for the SCR component when it is combined with a Diesel Particulate Filter (DPF) in the emission control system. In order to effectively regenerate the DPF component, the entire system is exposed to temperatures above 600 °C periodically. Cu/zeolite SCR catalysts are significantly more stable than vanadium-based SCR catalysts at temperatures above 650 °C.

Fe/zeolite catalysts are another group of SCR catalysts that are durable to high temperature exposure and exhibit good SCR activity. Fe/zeolite catalysts even show higher NO_x reduction efficiency at temperatures above 350 °C compared to Cu/zeolite catalysts [11, 16–18]. However at temperatures between 200 and 300 °C, which are common to normal diesel engine operation conditions, Cu/zeolite catalysts are significantly more active than Fe/zeolite catalysts. Furthermore, their low temperature activity is less sensitive to the NO₂/NO_x ratio in the feed. Although Cu/zeolite catalysts are less selective than Fe/zeolite catalysts in utilizing NH₃ for NO_x reduction at high temperatures, this lower selectivity can be compensated by a slight NH₃ over-injection. All these features make Cu/zeolite SCR catalysts a preferred technology for automotive diesel NO_x emission control.

H.-Y. Chen (✉)

Johnson Matthey Inc., Wayne, PA 19087, USA

e-mail: chenh@jmus.com

Extensive investigations on the application of Cu/zeolite SCR catalysts on diesel vehicles began in the early 2000s when the US EPA introduced the Tier 2 emission regulations for light duty vehicles and the US EPA 2007/2010 emission standards for both light and heavy duty diesel trucks [9–14]. A US DOE funded project carried out by Ford Motor Company demonstrated that >90 % NO_x reduction efficiency could be achieved with an emission control system consisting of a Diesel Oxidation Catalyst (DOC), a Cu/zeolite SCR catalyst, followed by a diesel particulate filter (DPF) [11]. When the system was relatively fresh, the vehicle could easily achieve the US EPA Tier 2 Bin 5 emission standards despite the low temperature operation of the vehicle. When the system was aged to simulate the real road useful life, a gradual degradation of the NO_x reduction efficiency became obvious. At the end of its useful life, the systems could no longer meet the NO_x emission standard. Subsequent postmortem analysis of the Cu/zeolite SCR catalyst indicated that hydrothermal deactivation of the Cu/zeolite SCR catalyst, due to the accumulated exposure time at high temperatures, was the major cause of its performance degradation [19]. There were also indications that a portion of the Cu/zeolite SCR catalyst might have been exposed to temperatures substantially higher than 670 °C. These results clearly demonstrated that a significant improvement of the hydrothermal stability of Cu/zeolite SCR catalysts was needed for them to achieve real world durability requirements.

Small-pore zeolite supported Cu SCR catalysts have been discovered to exhibit improved hydrothermal stability [20–23]. At best, these catalysts can maintain high NO_x reduction efficiency with little degradation even after prolonged hydrothermal exposure at 800 °C and can tolerate short temperature excursions as high as 900 °C. In addition, the new class of Cu/zeolite SCR catalysts also exhibit improved N₂ selectivity with reduced N₂O formation and good HC tolerance. With all these improved properties, small-pore zeolite supported Cu SCR catalysts have been successfully implemented on diesel engine powered vehicles meeting the stringent US EPA 2010 or Europe EU5 emission regulations.

In this chapter, the chemistry and functionalities of Cu/zeolite SCR catalysts are discussed. Results on the investigation of the deactivation mechanisms of the previous generation of Cu/zeolite SCR catalysts, especially under hydrothermal aging conditions, are presented. Next, the development of small-pore zeolite supported Cu SCR catalysts will be reviewed. Finally, recent studies reported in the literature to understand the hydrothermal stability and performance of small-pore zeolite supported Cu SCR catalysts will be summarized.

5.2 Chemistry and Functionality of Cu/Zeolite SCR Catalysts

Extensive studies have been conducted by many research groups to understand the reaction mechanisms and kinetics of the SCR reaction of NO_x with NH₃, as well as to elucidate the active sites of SCR catalysts. These will be discussed by other

authors in [Chaps. 6 and 7](#) of this book. Excellent review articles are also available in the literature [[4](#), [15](#), [16](#)]. In this section, the chemistry and functionalities of Cu/zeolite SCR catalysts will be briefly reviewed.

Zeolites, or molecular sieves, are a group of materials with ordered crystalline lattice structures. Within the framework, regular-shaped pores (or cages) are formed. These pores are interconnected to each other through openings (or windows) of the framework. So far, more than 200 unique types of zeolite structures have been identified. Each of the structures is designated with a three-letter code. Details about the zeolite structures and the related materials can be found at the International Zeolite Association's website [[24](#)].

In this chapter, we characterize zeolites as containing small, medium, or large pores. The definition is based on the largest opening of the framework. As such, small-pore zeolites are defined by openings of eight tetrahedral atoms, such as Si and Al, linking to each other by eight oxygen atoms. This type of structure is also called an 8-membered ring structure or 8-ring structure. Similarly, medium- and large-pore zeolites are defined by 10-ring and 12-ring openings, respectively.

Many zeolites have been evaluated as supports for Cu in SCR catalysis. Almost all the earlier work, however, is limited to medium- and large-pore zeolites, such as ZSM-5 (MFI, 10-ring), ferrierite (FER, 10-ring), mordenite (MOR, 12-ring), Y (FAU, 12-ring), and beta (BEA, 12-ring). Among them, Cu/ZSM-5 and Cu/beta are the two most studied systems. Of the two, Cu/beta catalysts show better hydrothermal stability and were favored by industry, while Cu/ZSM-5 catalysts were primarily studied by academia. It was not until recently that both industry and academia shifted their interests to small-pore zeolites as supports of Cu SCR catalysts.

In an aluminosilicate zeolite, silicon and aluminum atoms are tetrahedrally coordinated with oxygen atoms and linked to each other through oxygen bonds. Since the aluminum atom carries only three valence charges, it creates a charge imbalance at the tetrahedral site. To compensate the additional charge, a positively charged cation is attracted and anchored near the aluminum site. If the cation is a proton, this site is called a Brønsted acid site and behaves like a Brønsted acid; if the cation is a metal ion, the site is generally called an exchange site since the metal ion can be replaced by other cations.

Both the framework structure and the acid/exchange sites of a zeolite support play important roles in the SCR reaction [[4](#), [16](#)]. The openings of the framework structure allow gases such as NO_x, NH₃, and O₂, to enter into the interconnected pores of the zeolite support. The intra-crystalline pores generate a large surface area for low concentrations of NO_x and NH₃ to condense on the surface and provide spatial confinement for these molecules to react. The acid sites are directly involved in the SCR reaction. They adsorb NH₃ forming NH₄⁺ ions, which is believed to be a key step in the SCR reaction mechanism. The exchange sites anchor Cu cations so that Cu ions are atomically dispersed inside the matrix of the zeolite.

The exact nature of the copper sites is still under investigation. Most of the literature agrees that highly dispersed Cu ions are the active sites that catalyze NO oxidation, whether they are isolated [Cu]²⁺ ions, Cu-hydroxo [Cu–OH]⁺ ions,

binuclear $[\text{Cu}-\text{O}-\text{Cu}]^{2+}$ ions, or multinuclear Cu-oxo ions. Oxidation of NO and the subsequent formation of NO_x surface adsorption complexes on Cu sites are in general believed to be another key step in the SCR reaction mechanism [25]. Depending on the catalyst preparation method, different levels of copper oxides or clusters of copper oxides may be formed on the external surface or even inside the pores of the zeolite support. These types of CuO are more active in catalyzing non-selective NH₃ oxidation than the SCR reaction, hence negatively affecting the selectivity of NH₃ for NO_x reduction. Such an effect is more pronounced at high temperatures.

In summary, Cu/zeolite SCR catalysts provide two functions in the SCR reaction. The zeolite support provides acid sites for NH₃ adsorption and activation. The Cu sites provide redox centers in catalyzing the oxidation of NO, which subsequently forms surface adsorption complexes and further reacts the adsorbed NH₄⁺ producing N₂ with very high selectivity. It should be noted that, for a high performing Cu/zeolite SCR catalyst, the two functions must be well balanced to achieve the optimum SCR activity and selectivity over a wide temperature region. In other words, the Cu loading has to be optimized. At a low Cu loading, there may be insufficient Cu sites to perform the redox function. At a high Cu loading, there may be insufficient acid sites for NH₃ adsorption and activation. Even if the number of acid sites is not a rate-determining factor, a high Cu loading can cause excessive NH₃ oxidation which reduces the selectivity of the catalyst. In addition, an excessive Cu loading may also negatively affect the hydrothermal stability of the catalyst. This will be discussed further in the following section.

5.3 Deactivation Mechanisms of Cu/Zeolite SCR Catalysts

5.3.1 Hydrothermal Deactivation

Zeolites are metastable materials because of the presence of intra-crystalline pores in their framework. When a zeolite is heated to high temperatures, its structure collapses forming denser crystalline phases, such as quartz [26]. Under hydrothermal conditions, water accelerates this phase transition by attacking the aluminum sites through a dealumination process, in which aluminum atoms are detached from their tetrahedrally coordinated framework positions creating defect sites at those locations [27, 28]. Depending on the chemical properties of the cations associated with those aluminum sites, extra framework aluminum oxide clusters, metal oxide clusters, or metal aluminates can be formed in the cavities of the zeolite during the dealumination process [29–32]. In its early stage, the dealumination process may not cause an obvious structural change of the zeolite, even though it significantly affects the acidity and the nature of the exchange sites. As Cu/zeolite SCR catalysts rely on all these functionalities for SCR reactions, any change of these properties can impact their catalytic performance.

Water is inevitable in the exhaust stream of diesel engines as it is a product from the fuel combustion process. The typical water content in diesel exhaust is in the range of 4–9 %. Under normal operation conditions however, the exhaust temperature is relatively low, in the range of 200–300 °C. This is not high enough to alter the properties of most Cu/zeolite SCR catalysts. The thermal stability requirement is mainly the result of the periodic regeneration events required to clean the DPF component of the emission control system. To effectively burn off the diesel particulate matter (or soot) trapped on the DPF component, the exhaust temperature has to be periodically raised to above 600 °C. During the DPF regeneration events, the temperature of the SCR component can be even higher. For example, with an emission control system consisting of (DOC + SCR + DPF), additional fuel is injected upstream of the DOC component during the DPF regeneration events to generate heat which increases the temperature of the downstream SCR and DPF components. Taking heat loss into consideration, the temperature of the SCR component has to be above 600 °C in order for the DPF component to reach that temperature. In another emission control configuration (DOC + DPF + SCR), the additional heat generated by soot oxidation on the DPF component during regeneration events may well exceed the heat loss between the DPF and the SCR components, increasing the exhaust temperature before the SCR component. Although the exposure time to high temperature lasts only several minutes in a typical DPF regeneration event, the accumulated time at high temperature over the useful life of the system is significantly longer. In fact for SCR catalyst development and screening purposes, it is a common practice to hydrothermally age the catalyst at a defined high temperature for a long period of time to assess its hydrothermal stability. For instance, Ford was using an aging condition of 670 °C/64 h with 4.5 % H₂O to assess the durability of SCR catalysts in the DOE funded SCR demonstration project [11].

Many properties of a zeolite support can affect its hydrothermal stability. The type of framework structure and the silica-to-alumina ratio (SAR) of the material have been well recognized to play important roles [26]. Of the medium- and large-pore zeolites studied in the previous generation of Cu/zeolite SCR catalysts, ZSM-5 (MFI) and beta (BEA) were found to be hydrothermally more durable. It is well known that a zeolite with a higher SAR is in general more durable to hydrothermal aging since it has less aluminum sites to attract water. With a high SAR, however, the zeolite may not have sufficient acid sites for the SCR reaction or enough exchange sites for the adequate amount of Cu loading and dispersion. This can result in a catalyst with overall low catalytic activity. For a balanced high performance and hydrothermal stability, the typical SAR of the zeolite supports used in Cu/zeolite catalysts is up to 50. Other factors, though less well recognized, also play important roles in governing hydrothermal stability. These include crystal size, morphology and phase purity [28, 33].

The presence of Cu (or other metal ions) at the exchange sites also influences the hydrothermal stability of the zeolite [13, 30, 34]. On one hand, Cu ions replace the protons at the exchange sites, making the adjacent tetrahedral aluminum sites less susceptible to H₂O interaction. This “shielding” effect hinders the dealumination

process and improves the hydrothermal stability of the catalyst. On the other hand, Cu is known to readily react with alumina forming stable copper aluminate at high temperatures. Such a chemical reaction accelerates the dealumination process and decreases the thermal stability of the catalyst. Therefore, an optimum Cu exchange level or Cu to aluminum ratio is also important for a Cu/zeolite catalyst to have good hydrothermal stability.

To further illustrate the hydrothermal deactivation mechanism of Cu/zeolite SCR catalysts, some of the results obtained on a Cu/beta SCR catalyst from our previous studies will be summarized below [35–37]. The Cu/beta SCR catalyst was prepared by ion exchange of Cu onto a beta zeolite with an SAR = 25. The Cu loading was 5 wt.%, corresponding to a Cu/Al ratio of 0.65, or 130 % ion-exchange level. Here, the exchange level is calculated by assuming that all Cu present in the sample are Cu^{2+} ions and that, simply from a charge balance point of view, each Cu^{2+} ion can occupy two tetrahedral aluminum sites. The fact that the Cu/Al ratio exceeded 0.5, or 100 % ion-exchange level in the sample, suggests that part of the Cu may exist as hydroxo- or oxo-ions, or copper oxides.

In-situ XRD was used to assess the thermal stability of the beta zeolite support and the Cu/beta catalyst. The powder samples were mounted on the hot-stage in the sample chamber under a flowing 20 % O_2 /80 % N_2 gas mixture. The temperature was increased from room temperature to 970 °C at a 10 °C/min ramping rate. Two dwells were included in the heating profile, each an hour long, at 900 and 970 °C. XRD data sets were collected at 55 °C increments, or ~5-min intervals. Finally, an XRD scan was recorded when the sample was cooled to room temperature.

The XRD scans of the parent beta zeolite support as a function of temperature/scan interval are compiled in Fig. 5.1. The initial increase of the intensity from room temperature to 253 °C (Scan numbers = 1–6 in Fig. 5.1) for the peak at $2\theta=7.5^\circ$ can be attributed to dehydration of water from the zeolite [38]. The peak maintains its intensity until 415 °C (Scan number = 9 in Fig. 5.1). Above this temperature, a slow decline in the peak intensity can be seen, suggesting a gradual loss of crystallinity. The trend is slightly different for the diffraction at $2\theta=22.8^\circ$ and other peaks. Their intensity remains relatively constant until the temperature reaches ~600 °C (Scan number = 13 in Fig. 5.1). Thereafter, a slow decrease in the intensity becomes noticeable. All these reflection peaks (including the one at $2\theta=7.5^\circ$) however, remain even after 1 h dwell at 970 °C. This indicates that the material still maintains its framework structure. Indeed, a final XRD scan of the sample when it is cooled to room temperature reveals that the zeolite structure remains relatively intact, although it does show about a 40 % loss in intensity compared to the XRD pattern before the heat treatment. Nevertheless, the beta zeolite sample used in this study has good thermal stability.

The XRD patterns of the Cu/beta catalyst as a function of temperature/time interval are plotted in Fig. 5.2. At temperatures below 800 °C (Scan number = 16 in Fig. 5.2), the change in intensity of all the diffraction peaks that correspond to the beta zeolite framework structure follows nearly the same trend as seen on the parent beta zeolite. Above this temperature however, the intensity of all peaks decreases rapidly. The zeolite crystalline structure completely collapses and

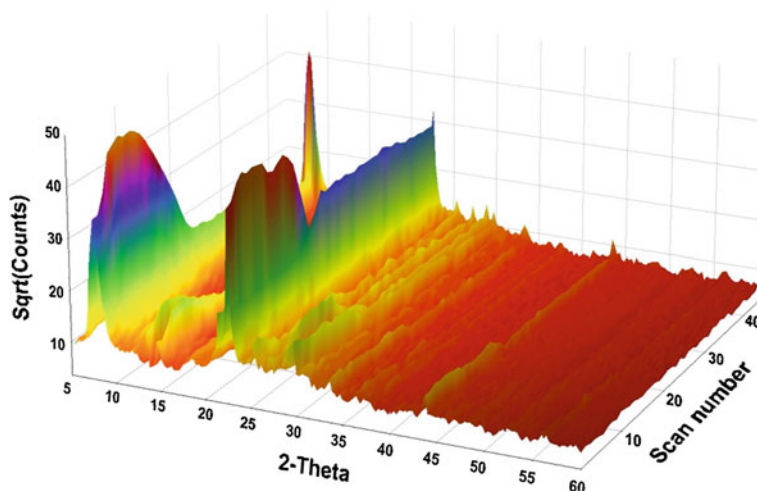


Fig. 5.1 In-situ XRD scans of a beta zeolite from room temperature to 970 °C. The temperature increases as the “Scan number” increases with two dwells at 900 °C (Scan number = 19–30) and 970 °C (Scan number = 32–43). The last scan is recorded when the sample is cooled to room temperature

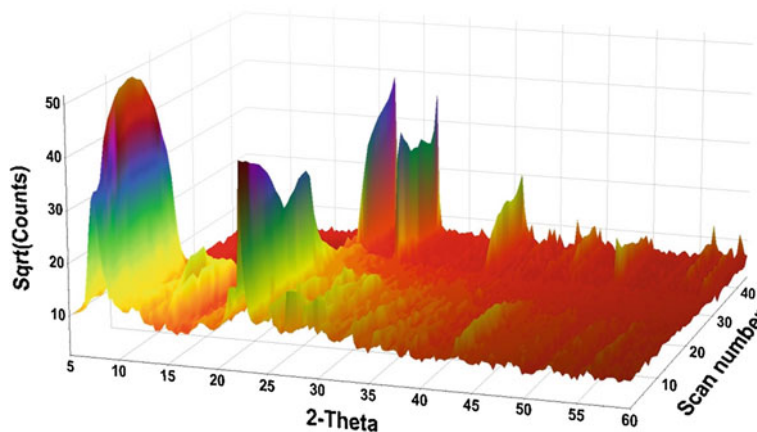
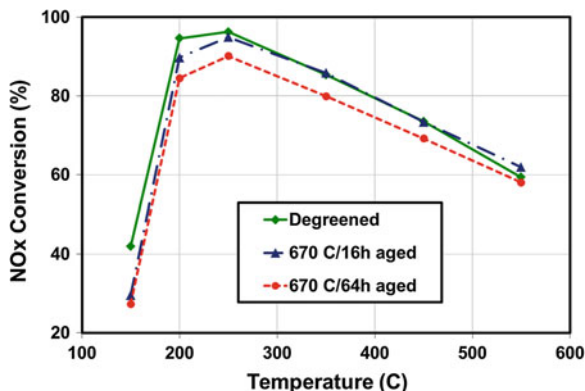


Fig. 5.2 In-situ XRD scans of a Cu/beta catalyst from room temperature to 970 °C. The temperature increases as the “Scan number” increases with two dwells at 900 °C (Scan number = 19–30) and 970 °C (Scan number = 32–43). The last scan is recorded when the sample is cooled to room temperature

becomes amorphous at 924 °C (Scan number = 31 in Fig. 5.2). When the temperature reaches 970 °C (Scan number = 32 in Fig. 5.2), new SiO₂-quartz and SiO₂-cristobalite crystalline phases appear in the diffraction patterns. In Fig. 5.2, very weak CuO diffraction peaks at 2θ -35.4 and 38.7° can be seen at room

Fig. 5.3 NO_x conversion efficiency as a function of reaction temperature on a Cu/ beta SCR catalyst before and after hydrothermal aging at 670 °C/4.5 % H₂O for 16 and 64 h. SCR reaction conditions: 350 ppm NO, 350 ppm NH₃, 14 % O₂, 4.6 % H₂O, 5 % CO₂, balanced with N₂, at a SV = 30,000 h⁻¹

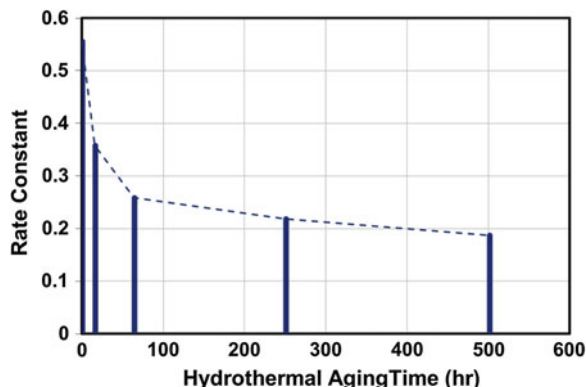


temperature (Scan number = 1 in Fig. 5.2). These peaks become weaker and weaker with the increase in temperature and completely disappear at 626 °C (Scan number = 13 in Fig. 5.3). Above this temperature, no diffraction peaks associated with any known Cu compounds can be identified. The presence of CuO on the sample is likely due to its relatively high Cu loading (130 % Cu exchange level). When the Cu loading was reduced to 3 wt.%, or 80 % Cu exchange level, no CuO diffraction peaks are apparent. However, a decrease in crystallinity and loss of zeolite framework structure are still observed at temperatures above 800 °C with the low loaded Cu/beta catalyst.

The results in Figs. 5.1 and 5.2 demonstrate that Cu accelerates the phase transition of the zeolite structure. As discussed earlier, this is likely due to the formation of more stable copper aluminate at high temperatures which facilitates the dealumination process. Although no diffraction peaks corresponding to bulk copper aluminate can be seen in Fig. 5.2, it is possible that once the CuAl₂O₄-like compound forms, it is highly dispersed in the matrix of the SiO₂. The relatively low concentration of aluminum in the material and the high stability of copper aluminate support this hypothesis. Since a redispersion of CuO at temperatures below 626 °C is observed in Fig. 5.2, it clearly suggests that CuO has high mobility in a beta zeolite.

Although the in-situ XRD study suggests that the Cu/beta SCR catalyst is thermally stable up to 800 °C, it deactivates noticeably when the catalyst is hydrothermally treated at lower temperatures but for a longer period of time. As shown in Fig. 5.3, the Cu/beta catalyst can achieve >90 % NO_x reduction efficiency under typical diesel application conditions with a temperature between 200 and 300 °C and a Space Velocity (SV) of 30,000 h⁻¹ when it is relatively fresh (labeled as “degreened” in Fig. 5.3). After being hydrothermally treated at 670 °C for 16 h in a flow of 4.5 % H₂O/air mixture, the catalyst starts to lose its NO_x conversion efficiency at temperatures below 350 °C. Further extending the aging time to 64 h, which could be considered as the end of useful life of the catalyst from a hydrothermal durability requirement point of view, the catalyst can barely reach 90 % NO_x conversion. Such an extent of catalyst deactivation is not acceptable for real-world applications.

Fig. 5.4 SCR reaction rate constant (k) on a Cu/beta SCR catalyst as a function of hydrothermal aging time at 670 °C/4.5 % H₂O. SCR reaction conditions: 350 ppm NO, 350 ppm NH₃, 14 % O₂, 4.6 % H₂O, 5 % CO₂, balanced with N₂, at 200 °C with a SV = 1,00,000 h⁻¹



To understand the deactivation trend of the Cu/beta catalyst as a function of exposure time to the 670 °C/4.5 %H₂O hydrothermal aging, SCR activities of the aged catalysts at 200 °C were measured at a very high space velocity (SV = 1,00,000 h⁻¹). This would render the overall NO_x conversions low enough for a SCR reaction rate constant (k) to be calculated based on pseudo first-order kinetics for NO [39]. The results are plotted in Fig. 5.4. The initial 64 h of hydrothermal exposure causes a rapid deactivation of the catalyst as demonstrated by a sharp decline in the SCR reaction rate constant. Extending the aging time beyond 64 h further reduces the activity of the catalyst but at a slower rate.

BET surface area measurement of the aged catalysts shows no reduction of surface area during the aging, suggesting that the zeolite support maintains its framework structure. However, a gradual decrease of the zeolite's crystallinity is noticeable based on the XRD analysis (see Fig. 5.5). The trend in the loss of crystallinity, however, does not correlate with that of the SCR activity degradation. Instead, the NH₃ storage capacity of the aged catalysts follows nearly the same profile as the SCR activity. Since the NH₃ storage capacity reported in Fig. 5.5 is determined by the amount of the NH₃ stored on the catalyst that participates in the SCR reaction, it is believed to be directly correlated to the number of Brønsted acid sites in the zeolite support [36]. Therefore, the results in Fig. 5.5 clearly demonstrate that the catalyst degradation after hydrothermal aging under 670 °C/4.5 % H₂O is mainly caused by the loss of acidity of the beta zeolite support through the dealumination process. The trend in the NH₃ storage capacity in Fig. 5.5 also suggests that the dealumination process occurs in two stages; with a rapid phase in the initial 64 h of hydrothermal aging, followed thereafter by a gradual phase.

During the initial 64 h of aging, Cu dispersion determined by NO uptake shows no noticeable change, suggesting that the exchanged Cu sites are less affected [36]. After additional aging hours, however, a gradual decline of Cu dispersion

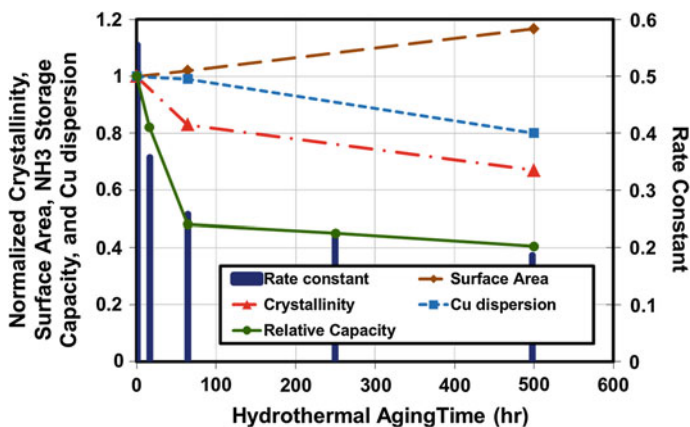


Fig. 5.5 Normalized BET surface, XRD crystallinity, NH_3 storage capacity, and Cu dispersion of the Cu/ β SCR catalyst with increasing hydrothermal aging time at 670 °C/4.5 % H_2O

following the same trend as the loss of NH_3 storage capacity is apparent (Fig. 5.5), indicating a reduction of exchanged Cu sites.

Comparing the trends between the loss of NH_3 storage capacity and the loss of Cu dispersion, it becomes obvious that, under typical hydrothermal aging conditions with a temperature of 670 °C, dealumination leading to the loss of acidity of the zeolite support is the major cause of the catalyst deactivation. At that temperature, the undesirable Cu/ Al_2O_3 interaction is a much slower process.

In real-world applications, the temperature distribution in an SCR catalyst component may vary drastically. This can introduce different levels of hydrothermal deactivation at different locations of the SCR catalyst. For example, with the simulated 1,20,000 miles engine-aged SCR catalyst, Cheng et al. found a significant loss of BET surface area with samples taken from the front section of the SCR catalyst but nearly no change of surface area with samples from the rear section [19]. This finding suggests a substantial temperature gradient along the length of the SCR catalyst. Therefore, a practical Cu/zeolite SCR catalyst has to be not only hydrothermally stable for a long period of time under normal operating conditions, but also able to withstand extreme temperatures well above the DPF regeneration temperature due to occasionally uncontrolled events [40].

5.3.2 Hydrocarbon Storage, Inhibition, and Poisoning

With a porous framework structure and large intra-crystalline surface area, zeolites can adsorb and store a considerable amount of hydrocarbons (HCs). At low temperatures, HCs may simply block the active sites for SCR reaction causing an HC inhibition effect. Such an effect is reversible; the SCR activity recovers once the HCs are removed from the stream. In addition, the acid sites and redox sites in

a Cu/zeolite catalyst can further interact with most of the HCs that enter the pores. At certain temperatures, some HCs may be catalyzed by the acid sites and the redox sites, leading to polymerization or partial oxidation, and the formation of carbonaceous deposits on the catalyst. This causes a poisoning effect since a high temperature exposure is needed to completely remove the deposits to regenerate the active sites [40, 41].

In a diesel emission control system, a diesel oxidation catalyst (DOC) is typically placed in front of the SCR component. Under normal operation conditions, the exhaust temperature is high enough that nearly all engine-out HCs can be completely oxidized by the DOC component. This significantly minimizes the HC inhibition and poisoning effects on the Cu/zeolite SCR catalyst. However, when the exhaust temperature is below the HC light-off temperature of the DOC, such as during extended vehicle idling, substantial amounts of HCs can pass through the DOC and store on the Cu/zeolite catalyst. The stored HCs will be oxidized and generate heat on the Cu/zeolite catalyst when the exhaust temperature subsequently rises above the ignition temperature. Depending on the amount of HCs stored on catalyst, this exothermal event can raise the SCR catalyst temperature high enough to cause severe thermal deactivation [42]. Obviously, minimizing HC storage on Cu/zeolite catalysts is highly desirable.

5.3.3 Sulfur Poisoning

Because of its high chemical binding strength and the oxidative conditions in the exhaust stream, sulfur can readily react with Cu in a Cu/zeolite SCR catalyst forming stable CuSO_4 -like compounds [6, 43–45]. This sulfur poisoning affects the redox properties of the Cu sites, severely inhibits NO oxidation and the subsequent formation of the adsorbed NO_x complex, and ultimately decreases the SCR activity of the catalyst at temperatures below 350 °C. Above this temperature, CuSO_4 -like compounds become less stable. Also, the remaining active Cu sites may provide sufficient redox function for the SCR reaction. As a result, Cu/zeolite catalysts are in general insensitive to sulfur at temperatures above 350 °C. To completely remove the sulfur poisoning effect from a Cu/zeolite catalyst, however, the catalyst has to be exposed to temperatures above 500 °C for CuSO_4 to be thermally decomposed. In practice, achieving those temperatures is not an issue, as the SCR catalyst will automatically exceed 500 °C during the periodic DPF regeneration events.

5.3.4 Urea and Urea Deposit Related Catalyst Deactivation

Urea, in the form of an aqueous solution, is used as the source of NH_3 for NO_x reduction in automotive diesel emission control systems. The solution is injected in front of the SCR component as fine droplets, which vaporize and are mixed with

the exhaust gas. In the gas phase, urea decomposes to NH_3 and isocyanic acid. The latter is subsequently hydrolyzed on the SCR catalyst generating a second molecule of NH_3 . Cu/zeolite SCR catalysts have been found to be extremely active in catalyzing the hydrolysis reaction of isocyanic acid [13, 46].

When the exhaust temperature is low ($<200\text{ }^\circ\text{C}$), heat transfer from gas to urea/water droplets may not be sufficient to completely evaporate the urea solution, especially the large droplets. When reaching the SCR catalyst surface, the droplets may only partially decompose and form deposits on the catalyst, causing catalyst deactivation [47, 48]. Although the majority of urea-related deposits can be decomposed once the catalyst temperature is above $350\text{ }^\circ\text{C}$, there is a small portion of the residue on the catalyst that is stable up to $450\text{ }^\circ\text{C}$. In addition to forming deposits, urea solution can also chemically react with Cu/zeolite catalysts causing Cu migration, sintering, and formation of metallic Cu nanoparticles [19]. It also accelerates dealumination of the zeolite support. All these contribute to irreversible catalyst deactivation.

To minimize urea solution droplets reaching the SCR catalyst, a mixing device is added between the urea injector and the SCR component to further break down the droplets and to facilitate the vaporization process. Engine calibrations to quickly raise exhaust temperature and thereafter maintain it above a set point are also critical for the SCR catalyst to achieve and maintain high NO_x reduction efficiency. With all these advanced engineering approaches, SCR catalyst deactivation caused by urea and urea-related deposits is usually less of a concern.

5.3.5 Chemical Poisoning

Chemical poisons from engine lubricant oil, such as Ca, Zn and P, have also been found to interact with Cu/zeolite SCR catalyst and cause catalyst deactivation [19, 49]. Since their concentration is very low in the exhaust stream and there are other catalyst components placed in front of the SCR catalyst which traps a significant portion of the chemicals, only a minor amount of lubricant oil derived chemical poisons will accumulate on the SCR catalysts. In addition, such chemical poisons tend to deposit on the very front section of the SCR catalysts. Therefore, adequate catalyst sizing to take this into account can mitigate the impact of chemical poisons from lubricant oil.

Alkali metals, even at a low level, can severely deactivate Cu/zeolite SCR catalysts [50]. Once reaching the Cu/zeolite SCR catalyst, the alkali metals may displace Cu from the exchange sites and lead to the formation of CuO. This reduces the low temperature activity of the catalyst and causes excessive NH_3 oxidation at high temperatures. Alkali metals can come from the impurities of urea solution or biodiesel fuel. Their levels have to be kept low enough to minimize their impact on the Cu/zeolite SCR catalysts.

Of all the deactivation modes discussed above, hydrothermal deactivation is the most challenging technical hurdle. Significant improvement on the hydrothermal

stability of the acid sites and the exchange sites in a Cu/zeolite catalyst has to be made for these types of catalysts to be practically useful for automotive applications.

5.4 Development of Small-Pore Zeolite Supported Cu SCR Catalysts

The demand for more hydrothermally stable Cu/zeolite SCR catalysts and the recognition of the limitations of the conventional zeolite supports drove researchers to evaluate other zeolite materials. In 1992, Ishihara et al. [20, 51] reported that copper-exchanged SAPO-34, a small-pore silicoaluminophosphate material having the CHA (8-ring) framework structure, exhibited superior hydrothermal stability and catalytic activity for the selective catalytic reduction of NO_x with propene, compared to Cu-exchanged beta, USY and ZSM-5. This type of catalyst was also found to be more hydrothermally stable and active in catalyzing N₂O decomposition compared to Cu/ZSM-5 [52–54]. In 2004, Zones et al. [21] synthesized a high silica chabazite (CHA) with a small particle size and proposed that it could be used as a support for transition metals, such as Cu, in catalyzing the selective reduction of NO_x in the exhaust of an internal combustion engine.

Since the HC-SCR reaction on transition-metal exchange zeolite catalysts involves NH₃ formation as an intermediate, which subsequently goes through NH₃-SCR reaction to reduce NO_x to N₂, it is reasonable to expect that a highly active and durable HC-SCR catalyst also exhibits excellent NH₃-SCR performance [55–57]. Indeed, Bull et al. [22] reported that catalysts with Cu supported on high silica chabazite, such as SSZ-13, exhibited good NH₃-SCR activity and hydrothermal stability. Andersen et al. [23] found that Cu/SAPO-34 showed significantly improved hydrothermal stability for NH₃-SCR applications. In addition, Andersen et al. [23] discovered that a wide range of small-pore zeolites could all significantly improve the hydrothermal stability of the Cu/zeolite catalysts.

Table 5.1 lists a few of the examples reported in the patent application by Andersen et al. [23]. For clarity, NO_x conversions at 250 °C on a series of Cu/zeolite SCR catalysts before and after different hydrothermal treatments, are summarized in the table. Data from two sets of hydrothermal aging conditions are included. The “750 °C/24 h” and “900 °C/1 h” each represents that the catalysts have been hydrothermally aged in a flow of 4.5 % H₂O/air mixture at 750 °C for 24 h or 900 °C for 1 h, respectively. These two conditions are used to assess the long-term hydrothermal durability and the upper temperature limit of these catalysts.

Cu/beta and Cu/ZSM-5 are included in Table 5.1 as references. The beta zeolite is a large-pore zeolite with 12-ring openings and a BEA framework structure. The ZSM-5 is a medium-pore zeolite with 10-ring openings and an MFI structure.

Table 5.1 Examples of small-pore zeolite supported Cu SCR catalysts and their NO_x conversion and N₂O yield at 250 °C

Catalysts	Zeolite structure	NO _x conversion at 250 °C (%)	N ₂ O yield at 250 °C (ppm)
Cu/beta (Fresh)	BEA (12-ring)	98	17
Cu/ZSM-5 (Fresh)	MFI (10-ring)	98	7
Cu/SAPO-34 (Fresh)	CHA (8-ring)	95	1
Cu/Nu-3 (Fresh)	LEV (8-ring)	97	1
Cu/beta (750 °C/24 h)	BEA (12-ring)	69	16
Cu/SAPO-34 (750 °C/24 h)	CHA (8-ring)	99	3
Cu/SSZ-13 (750 °C/24 h)	CHA (8-ring)	99	7
Cu/ZSM-34 (750 °C/24 h)	ERI (8-ring)	98	3
Cu/beta (900 °C/1 h)	BEA (12-ring)	58	22
Cu/ZSM-5 (900 °C/1 h)	MFI (10-ring)	28	0
Cu/SAPO-34 (900 °C/1 h)	CHA (8-ring)	97	2
Cu/Nu-3 (900 °C/1 h)	LEV (8-ring)	98	4
Cu/SSZ-13 (900 °C/1 h)	CHA (8-ring)	99	7
Cu/Sigma-1 (900 °C/1 h)	DDR (8-ring)	85	4

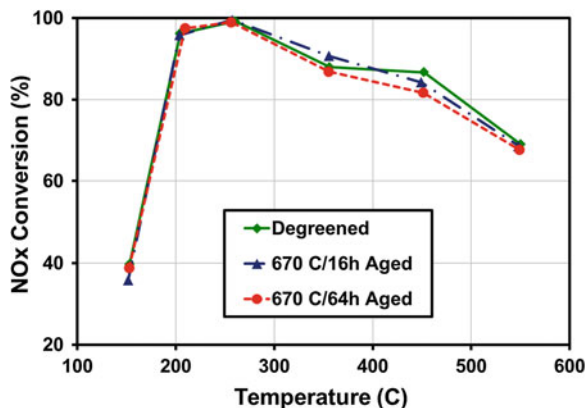
Both catalysts show very good SCR activity when they are fresh, but are severely deactivated after either 750 °C/24 h or 900 °C/1 h hydrothermal aging.

The rest of the catalysts shown in Table 5.1 all consist of small-pore zeolites with 8-ring openings but a variety of framework structures such as CHA, LEV, ERI, and DDR. When fresh, all the catalysts exhibit excellent SCR activity achieving nearly 100 % NO_x conversion at 250 °C similar to the Cu/beta and the Cu/ZSM-5 catalysts. These small-pore zeolite supported Cu SCR catalysts however, exhibit much higher hydrothermal stability. After 750 °C/24 h or 900 °C/1 h aging, they still achieve very high NO_x conversion efficiency. In fact, no obvious performance degradation occurs for most of the catalysts.

In Table 5.1, both SSZ-13 and SAPO-34 have the same crystallographic framework structure, CHA. Their compositions however, are different. SSZ-13 is a high silica chabazite containing a major amount of SiO₂ and a minor amount of Al₂O₃, whereas SAPO-34 is a silicoaluminophosphate containing nearly equimolar amounts of Al₂O₃ and P₂O₅, with a small amount of SiO₂ substituting some of the P₂O₅. Despite their composition differences, the two materials both show excellent hydrothermal stability and SCR activity, suggesting that the small-pore zeolite structure is the determining factor that contributes to the improved hydrothermal stability of this type of Cu SCR catalyst.

To further demonstrate the improved hydrothermal stability of the small-pore zeolite supported Cu SCR catalyst, the NO_x conversion efficiencies in the temperature range from 150 to 550 °C on a Cu/SAPO-34 catalyst, before and after hydrothermal aging at 670 °C in a flow of 4.5 % H₂O/air mixture for 16 and 64 h,

Fig. 5.6 NO_x conversion efficiency as a function of reaction temperature on a Cu/SAPO-34 SCR catalyst before and after hydrothermal aging at 670 °C/4.5 % H₂O for 16 and 64 h. SCR reaction conditions: 350 ppm NO, 350 ppm NH₃, 14 % O₂, 4.6 % H₂O, 5 % CO₂, balanced with N₂ at a SV = 30,000 h⁻¹



are plotted in Fig. 5.6. Almost no change in performance can be seen on the catalyst after aging. Compared to the similar sets of data generated on a Cu/beta catalyst (see Fig. 5.3), the improvement in the hydrothermal durability of the Cu/SAPO-34 catalyst is apparent.

A comprehensive study on the hydrothermal stability of a commercially available small-pore zeolite supported Cu SCR catalyst, Cu/SSZ-13, was reported by Schmiege et al. [49]. A series of catalysts were laboratory hydrothermally aged in the temperature range of 500–950 °C for different periods of time (1–240 h) and their catalytic functions (NO_x conversion, NO and NH₃ oxidation, NH₃ storage) and physical properties characterized. Schmiege et al. established that the catalyst could maintain its SCR performance as long as the hydrothermal aging temperature ($T_{\text{threshold}}$, in °C) and the exposure time (t_{aging} , in hour) were below the “borderline”:

$$T_{\text{threshold}} = -31.91 * \ln(t_{\text{aging}}) + 935.55 \quad (1)$$

Accordingly, the formula indicates that the small-pore zeolite supported Cu SCR catalyst can tolerate a short time (1 h) temperature excursion as high as 935 °C, or nearly 1606 h hydrothermal aging at 700 °C without showing noticeable SCR performance degradation.

In addition, Schmiege et al. analyzed a vehicle-aged SCR catalyst and found that, at the end of its useful life (1,35,000 miles vehicle operation), the hydrothermal exposure of the SCR catalyst was equivalent to the laboratory hydrothermal aging at 800 °C for 16 h. This is below the “borderline,” which predicts that the catalyst can still maintain its high SCR activity even if it is hydrothermally aged at 800 °C for 70 h. Clearly, the development of small-pore zeolite supported Cu SCR catalysts has overcome the hydrothermal stability requirement needed for real world applications.

The hydrothermal stability and catalytic activity of small-pore zeolite supported Cu SCR catalysts have also been confirmed by publications from academia. Besides the small-pore zeolites listed in Table 5.1, several others such as SSZ-16

(AFX), SAPO-18 (AEI), SSZ-39 (AEI), [Ga]SSZ-13 (CHA), ZK-5 (KFI), and STA-7 (SAV) have also been reported to exhibit the same properties [58–63]. In addition, catalysts with Cu being incorporated into the small-pore zeolite matrix during the zeolite synthesis step, instead of a post ion-exchange step, have also been found to show excellent SCR activity and hydrothermal stability [63–66].

Another highly desirable feature of the small-pore zeolite supported Cu SCR catalyst is low N₂O formation. As shown in Table 5.1, very low N₂O yield (in the level of a few ppm) is detected on any of the small-pore zeolite supported Cu SCR catalysts. A slight increase of N₂O formation is noticed on the hydrothermally aged catalysts, but the overall yield is still very low. In contrast, high levels of N₂O are generated over the Cu/beta and Cu/ZSM-5 catalysts. Although the N₂O formation mechanism under SCR reaction conditions over Cu/zeolite catalysts is not well understood at present, it is apparent that the dimension of the openings of the zeolite framework structure has a strong influence on N₂O production. The N₂O yield clearly follows the order of small < medium < larger pore zeolites. This trend matches well with the results reported by Kwak et al. [67, 68]. Because of its strong greenhouse effect, it is highly desirable to reduce N₂O formation in the diesel exhaust stream. Therefore, the small-pore zeolite supported Cu SCR catalysts offer another benefit with low N₂O formation.

The dimension of the openings in a zeolite also regulates which gas molecules can enter the intra-crystalline pores based on the kinetic diameter of the gas molecules. With 8-ring openings, the windows of a small-pore zeolite are large enough to allow small gas molecules such as O₂, NO_x and NH₃ to freely enter the pores, but are small enough to exclude most of the long chain HCs. For example, the size of the openings in a CHA zeolite is about 0.38 nm in diameter. It is larger than the kinetic diameter of O₂ (0.35 nm), NO (0.32 nm), NO₂ (0.34 nm), or NH₃ (0.26 nm) molecules, but smaller than that of any type of aromatic HCs such as toluene (0.59 nm). Since the kinetic diameter of short chain HCs such as C₃H₆ (0.45 nm) or C₃H₈ (0.43 nm) is only slightly larger than the size of the openings in a CHA zeolite, these gases can access the CHA pores but with restrictions. Although the kinetic diameter of other straight longer chain HCs is about the same as that of C₃H₆ or C₃H₈, their accessibility to the pores in a CHA zeolite is reduced significantly with the increase in chain length. As a comparison, the size of the openings in a beta zeolite is about 0.66–0.72 nm in diameter, and about 0.54–0.56 nm in a ZSM-5. These openings are wide enough to allow many HCs to enter the pores of the zeolites.

Because of this molecular sieving effect, small-pore zeolite supported Cu SCR catalysts show different HC tolerance behavior compared to other medium- or large-pore zeolite supported catalysts. Figure 5.7 compares NO_x conversion at 300 °C on a Cu/SAPO-34 and a Cu/beta catalyst before and after addition of three types of HCs. Before HC addition, both catalysts show nearly 90 % NO_x conversion. When propene (333 ppm C₃H₆, 1,000 ppm as C₁), a short chain HC, is added into the gas mixture, the NO_x conversion on both catalysts drops to ~75 %, showing a HC inhibition effect. When normal-octane (125 ppm n-C₈H₁₈, 1,000 ppm as C₁), a straight long-chain saturated HC, is injected into the gas

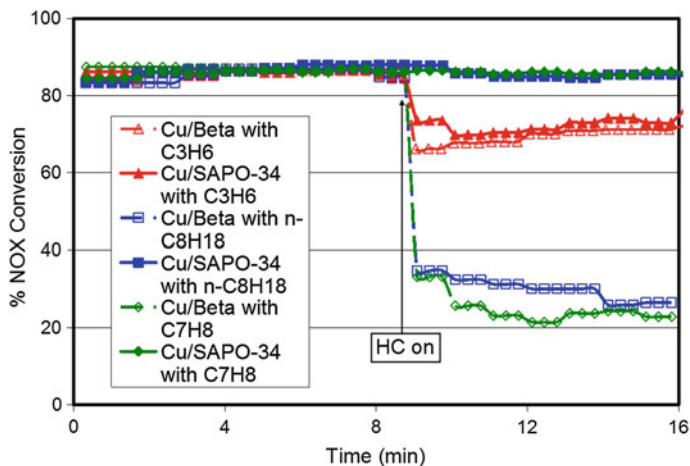


Fig. 5.7 NO_x conversion efficiency at 300 °C before and after HC addition. SCR reaction conditions: 350 ppm NO, 350 ppm NH₃, 14 % O₂, 4.6 % H₂O, 5 % CO₂, 1,000 ppm C₁ (when added) balanced with N₂ at a SV = 30,000 h⁻¹

stream, the NO_x conversion on the Cu/beta decreases to ~30 %, showing an even more severe HC inhibition effect. In contrast, no change of NO_x conversion is observed on the Cu/SAPO-34 catalyst. Apparently, n-C₈H₁₈ is excluded from entering the pores of the CHA structure in the SAPO-34 support, hence not affecting its SCR activity. The same trend holds true when toluene (143 ppm C₇H₈, 1,000 ppm as C₁), an aromatic HC, is added to the feed. Clearly, small-pore zeolite supports significantly minimize HC inhibition effects.

A detailed study carried out by Ye et al. [60] on the C₃H₆ inhibition effect over Cu/ZSM-5, Cu/SSZ-13, Cu/SAPO-34, and Cu/SAPO-18 SCR catalysts revealed that the presence of C₃H₆ only affects the SCR activity of the small-pore zeolite catalyst at the medium-temperature region (~300–350 °C). These temperatures are high enough for C₃H₆ to overcome the steric restriction to enter the pores and to react with the active sites forming carbonaceous deposits, but not high enough to achieve complete oxidation. At lower temperatures (<250 °C), although a low level of propene can still enter the pores, it shows negligible inhibition effects on the small-pore zeolite catalysts. In contrast, the propene inhibition effect is even more pronounced at low temperatures on Cu/ZSM-5, probably because of the higher HC storage on this catalyst.

As large HCs are excluded from entering the pores of small-pore zeolites, HC condensation and storage on small-pore zeolite supported Cu SCR catalysts is substantially reduced. Therefore, small-pore zeolite supports offer yet another advantage by reducing HC storage on the SCR catalyst. This substantially minimizes the risk of large exotherm generation.

Small-pore zeolite supported Cu SCR catalysts still face the challenges of sulfur poisoning and chemical poisoning that were discussed previously. Studies by Castagnola et al. [69] and by Tang et al. [70] both show that the new generation Cu/zeolite catalysts suffer from SCR activity loss at low temperatures after sulfur exposure. The SCR performance of the catalysts can be fully recovered, however, once the catalysts are exposed to temperatures above 500 °C. On a vehicle-aged Cu/SSZ-13 catalyst, mainly in the very front section of the SCR catalyst, Schmiege et al. [49] detected chemical poisons from lubricant oil, as well as a low level of Pt volatilized from the upstream DOC component. Although these poisons cause noticeable SCR activity degradation, the volume of the front section is relatively small compared to the entire catalyst volume. Therefore, they concluded that the impact of the chemical poisons to the overall performance of the entire system is small. Indeed, small-pore zeolite supported Cu SCR catalysts have been successfully implemented in the US on both pick-up trucks and heavy duty diesel vehicles meeting the stringent US EPA 2010 emission regulations. They have also been commercialized in Europe on light duty diesel passenger vehicles meeting the EU5 emission standards.

5.5 Investigation on the Superior Hydrothermal Stability of Small-Pore Zeolite Supported Cu SCR Catalyst

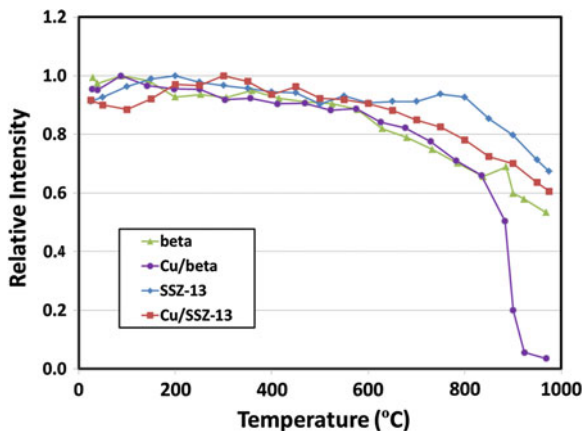
The discovery and the commercialization of small-pore zeolite supported Cu SCR catalysts raise a fundamental question: why can small-pore zeolites enhance the hydrothermal stability of the Cu/zeolite catalysts, while medium- and large-pore zeolites fail?

Small-pore molecular sieve SAPO-34 is known to exhibit exceptional thermal stability and maintain its crystalline structure up to 1,000 °C [71]. Since the acid/exchange sites in a SAPO-34 are associated with the Si tetrahedral sites, they are less susceptible than tetrahedral Al sites to H₂O interaction and hence are more stable to hydrothermal aging [72].

However, catalysts with Cu supported on SSZ-13, a material from the aluminosilicate family, also exhibit good hydrothermal stability. The acid/exchange sites in an SSZ-13 still originate from the aluminum sites, just like the other aluminosilicate medium- or large-pore zeolites. Under hydrothermal aging conditions, these sites are accessible to H₂O and are potentially still subject to the dealumination process and the undesirable Cu/Al₂O₃ interaction as discussed previously.

Such improved hydrothermal stability is not limited to the CHA structure, as catalysts with Cu supported on other types of small-pore zeolites all show superior hydrothermal stability. Apparently, the framework topology of a small-pore zeolite plays an important role in enhancing the hydrothermal stability of the Cu/zeolite catalyst.

Fig. 5.8 Relative XRD peak intensity as a function of temperature



Fickel et al. [59] studied the hydrothermal stability of a series of small-pore zeolite supported Cu catalysts, including Cu/SSZ-13 (CHA), Cu/SAPO-34 (CHA), Cu/SSZ-16 (AFX), Cu/Sigma-1 (DDR), Cu/Nu-3 (LEV), and a medium-pore zeolite catalyst Cu/ZSM-5 (MFI). They suggested that, during the dealumination process at high temperature, $\text{Al}(\text{OH})_3$ needs to exit the framework and pore system of a zeolite to cause structural defects. They estimated the kinetic diameter of $\text{Al}(\text{OH})_3$ as approximately 0.50 nm. This is clearly larger than the pore openings in a small-pore zeolite, thus aluminum hydroxide cannot exit the pores of the framework. Consequently, the $\text{Al}(\text{OH})_3$ stays inside the pore in which the aluminum ion is originally located. Furthermore they proposed that, when the temperature is low enough, the dislocated aluminum can reattach back to the framework and maintain the integrity of the structure and chemical environment. Therefore, they concluded that the constricting dimensions of the small openings in the small-pore zeolites are the most prominent reason for the exceptionally high hydrothermal stability of the small-pore zeolite supported Cu SCR catalysts.

Following this hypothesis, it is reasonable to assume that the undesirable Cu/ Al_2O_3 interaction at high temperature also involves Cu- and Al-related moieties migrating out of the pores of the zeolite framework to form stable CuAl_2O_4 -like compounds. The Cu- and Al-related moieties may be large enough that they cannot exit the small openings of the framework in a small-pore zeolite, while there appears to be no such steric restriction with medium- or large-pore zeolites. Therefore, the destructive Cu/ Al_2O_3 interaction seen on medium- or large-pore zeolite supported Cu catalysts is diminished with small-pore zeolite supported Cu catalysts.

The above theory seems to be supported by our XRD results. Similar to the experiments described in the previous section, in-situ XRD measurements were also conducted on a parent SSZ-13 zeolite and a Cu/SSZ-13 catalyst. Plotted in Fig. 5.8 are the relative intensities of the XRD diffraction peaks ($2\theta=21^\circ$) of the two samples as a function of the temperature when the diffraction patterns are

recorded. For comparison, similar data at 2θ – 22.5° from the beta and the Cu/beta samples discussed previously are also plotted in the figure. Although both the beta and the SSZ-13 samples used in the study have similar thermal stability, maintaining their framework structure even after 970°C exposure, the Cu containing samples show drastically different thermal stability. The presence of Cu clearly destabilizes the beta zeolite framework structure at temperatures above 800°C , but barely affects the SSZ-13 zeolite framework structure up to 970°C . This strongly supports the theory that the small openings in a small-pore zeolite may prevent the negative Cu/ Al_2O_3 interaction.

In summary, it appears that it is the narrow dimension of the openings in a small-pore zeolite that hinders the dealumination process and prevents the undesirable Cu/ Al_2O_3 interaction. This in turn results in the improved hydrothermal stability observed for small-pore zeolite supported Cu SCR catalysts.

5.6 Investigation on the Active Cu Sites in Small-Pore Zeolite Supported Cu SCR Catalysts

Although the discussions above were mostly focused on the zeolite supports, it should be pointed out that Cu plays an equally important role in contributing to the excellent SCR activity of the small-pore zeolite supported Cu catalysts. Studies to understand the active Cu sites in small-pore zeolites have emerged recently and almost all of them were based on the CHA type zeolites, SSZ-13, and SAPO-34.

Wang et al. [73] demonstrated that the H^+ form of SAPO-34 is inactive for the SCR reaction. Precipitating CuO on the external surface of the SAPO-34 support only slightly promotes the SCR reaction but leads to significant NH_3 oxidation. Ion-exchange of Cu into the cages of the SAPO-34 framework however, drastically enhances the SCR activity. They hypothesized that isolated Cu^{2+} ions located at the exchange sites inside the pores of SAPO-34 are the active sites for the SCR reaction. Subsequently, the same group characterized a series of Cu/SAPO-34 catalysts with a different number of exchange sites and confirmed their theory [74].

Using Rietveld refinement of variable-temperature synchrotron XRD data obtained on an ion-exchanged Cu/SSZ-13 catalyst, Fickel et al. [58] found that Cu^{2+} ions are located in the cages near the double six member rings of the CHA framework structure, with each Cu^{2+} ion being coordinated to three oxygen atoms of the six-member rings. This is further supported by their XAFS data [75]. Since they did not observe the NO decomposition reaction, which is believed to proceed on dimeric Cu^{2+} ions occurring on the Cu/SSZ-13 catalyst, they proposed that the Cu^{2+} ions in the Cu/SSZ-13 are isolated and that it is the isolated Cu^{2+} ions that contribute to the high SCR activity. Subsequently, an in-situ X-ray Absorption Fine Structure/X-ray Diffraction (XAFS/XRD) study was performed by Deka et al. [76] under SCR conditions but in the absence of water. They confirmed that isolated mononuclear Cu^{2+} ions located on the plane and slightly distorted from

the center of the six member rings are the active sites under typical SCR reaction conditions.

Also using the XAFS technique in combination with density functional theory (DFT) and first-principles thermodynamics models, McEween et al. [77] characterized a Cu/SSZ-13 catalyst under *operando* conditions representative of the SCR of NO_x with NH₃ in the presence of water vapor. They also detected only isolated Cu ions. Slightly different from that reported by Fickel et al., they found that each Cu²⁺ ion is fourfold coordinated to three lattice O of the zeolite framework and one H₂O ligand. Given that a much lower calcination temperature (200 °C) was used in the study by McEween et al., the presence of an additional H₂O ligand associated to the Cu ions is reasonable. In fact, they found that on a fully hydrated sample, the Cu coordination is indistinguishable from hexa-aqua Cu²⁺. A very important finding in the study by McEween et al., however, is that both Cu⁺ and Cu²⁺ coexist on the catalyst under “standard” SCR reaction conditions when there is no NO₂ in the feed. This is clear and direct evidence that Cu is undergoing redox cycles under SCR reaction conditions. Quantitatively comparing the percentage of Cu⁺ versus the SCR reaction kinetics on Cu/SSZ-13, Cu/SAPO-34, and Cu/ZSM-5 catalysts, Kirsperky et al. [78] found that there is no correlation, suggesting that the Cu⁺ and Cu²⁺ redox cycle is not necessarily the rate-determining step on these catalysts.

This highlights that, as discussed previously, Cu/zeolite SCR catalysts are bi-functional catalysts. For a good catalyst with high SCR performance and hydrothermal durability, both the acid function from the acid sites and the redox function from the Cu sites need to be well balanced.

5.7 Summary

Compared to the medium- or large-pore zeolite supported Cu catalysts, small-pore zeolite supported Cu catalysts exhibit superior hydrothermal stability, excellent SCR activity, and selectivity with very low N₂O formation. They are less susceptible to HC inhibition or poisoning. All of these desirable features can be attributed to the narrow openings in the framework structure of the small-pore zeolites. With all these improvements, small-pore zeolite supported Cu SCR catalysts have been successfully commercialized and applied on diesel powered vehicles meeting the stringent US EPA 2010 or European EU5 emission standards.

Acknowledgments I am very grateful to many of my colleagues at Johnson Matthey for their contributions to the work presented in this chapter. I also want to express my sincere gratitude to many collaborators across industry and academia for their valuable discussions. Finally, I thank Johnson Matthey for the permission of this publication.

References

1. Seiyama T, Arakawa T, Matsuda T et al (1977) Catalytic activity of transition metal ion exchanged Y zeolites in the reduction of nitric oxide with ammonia. *Journal of Catalysis* 48:1–7
2. Komatsu T, Nunokawa M, Moon IS et al (1994) Kinetic Studies of Reduction of Nitric Oxide with Ammonia on Cu²⁺-Exchanged Zeolites. *Journal of Catalysis* 148:427–437
3. Mizumoto M, Yamazoe N, Seiyama T (1979) Effects of coexisting gases on the catalytic reduction of NO with NH₃ over Cu(II) NaY. *Journal of Catalysis* 59:319–324
4. Centi G, Perathoner S (1995) Nature of active species in copper-based catalysts and their chemistry of transformation of nitrogen oxides. *Applied Catalysis A: General* 132:179–259
5. Andersson LAH, Brandin JGM, Odenbrand CUI (1989) Selective catalytic reduction of NOx over acid-leached mordenite catalysts. *Catalysis Today* 4:173–185
6. Palomares AE, Prato JG, Corma A (2002) A new active zeolite structure for the selective catalytic reduction (SCR) of nitrogen oxides, ITQ7 zeolite, the influence of NO₂ on this reaction. *Catalysis Today* 75:367–371
7. Delahay G, Coq B, Kieger S et al (1999) The origin of N₂O formation in the selective catalytic reduction of NOx by NH₃ in O₂ rich atmosphere on Cu-faujasite catalysts. *Catalysis Today* 54:431–438
8. Delahay G, Kieger S, Tanchoux N et al (2004) Kinetics of the selective catalytic reduction of NO by NH₃ on a Cu-faujasite catalyst. *Applied Catalysis B: Environmental* 52:251–257
9. Xu L, McCabe RW, Hammerle RH (2002) NOx self-inhibition in selective catalytic reduction with urea (ammonia) over a Cu-zeolite catalyst in diesel exhaust. *Applied Catalysis B: Environmental* 39:51–63
10. Tennison P, Lambert C, Levin M (2004) NOx Control Development with Urea SCR on a Diesel Passenger Car. SAE Technical Paper 2004–01–1292
11. Lambert C, Cavataio G, Cheng Y et al (2006) Urea SCR and DPF system for Tier 2 diesel light-duty trucks. DEER Conference 2006. [Online] Available: http://www1.eere.energy.gov/vehiclesandfuels/pdfs/deer_2006/session5/2006_deer_lambert.pdf.
12. Schmiege SJ, Lee J-H (2005) Evaluation of supplier catalyst formulations for the selective catalytic reduction of NOx with ammonia. SAE Technical Paper 2005–01–3881
13. Baik JH, Yim SD, Nam I-S et al (2004) Control of NOx emissions from diesel engine by selective catalytic reduction (SCR) with urea. *Topics in Catalysis* 30/31:37–41
14. Park J-H, Park HJ, Baik JH et al (2006) Hydrothermal stability of CuZSM5 catalyst in reducing NO by NH₃ for the urea selective catalytic reduction process. *Journal of Catalysis* 240:47–57
15. Pârvolescu VI, Grange P, Delmon B (1998) Catalytic removal of NO. *Catalysis Today* 46:233–316
16. Brandenberger S, Kröcher O, Tissler A et al (2008) The State of the art in selective catalytic reduction of NOx by ammonia using metal-exchanged zeolite catalysts. *Catalysis Reviews* 50:492–531
17. Kamasamudram K, Currier NW, Chen X et al (2010) Overview of the practically important behaviors of zeolite-based urea-SCR catalysts, using compact experimental protocol. *Catalysis Today* 151:212–222
18. Kamasamudram K, Currier NW, Szailer T et al (2010) Why Cu- and Fe-zeolite SCR catalysts behave differently at low temperatures. SAE Technical Paper 2010–01–1182
19. Cheng Y, Xu L, Hargas J et al (2007) Laboratory postmortem analysis of 120 k mi engine aged urea SCR catalyst. SAE Technical Paper 2007–01–1579
20. Ishihara T, Kagawa M, Hadama F et al (1997) Copper ion-exchanged SAPO-34 as a thermostable catalyst for selective reduction of NO with C₃H₆. *Journal of Catalysis* 169:93–102
21. Zones SI, Yuen LT, Miller SJ (2004) Small crystallite zeolite CHA. U.S. Patent US 6,709,644
22. Bull I, Xue WM, Burk P et al (2009) Copper CHA zeolite catalysts. U.S. Patent US 7,601,662

23. Andersen PJ, Bailie JE, Casci JL et al (2008) Transition metal/zeolite SCR catalysts. Patent application WO 2008/132452
24. Database of zeolite structures. [Online]. Available: <http://www.iza-structure.org/databases/>
25. Fedeyko JM, Chen B, Chen H-Y (2010) Mechanistic study of the low temperature activity of transition metal exchanged zeolite SCR catalysts. *Catalysis Today* 151:231–236
26. Cruciani G (2006) Zeolites upon heating: Factors governing their thermal stability and structural changes. *Journal of Physics and Chemistry of Solids* 67:1973–1994
27. Wang QL, Giannetto G, Torrealba M et al (1991) Dealumination of zeolites II, kinetic study of the dealumination by hydrothermal treatment of a NH_4NaY zeolite. *Journal of Catalysis* 130:459–470
28. Sano T, Ikeya H, Kasuno T et al (1997) Influence of crystallinity of HZSM-5 zeolite on its dealumination rate. *Zeolites* 19:80–86
29. Grinsted RA, Jen H-W, Montreuil CN et al (1993) The relation between deactivation of CuZSM-5 in the selective reduction of NO and dealumination of the zeolite. *Zeolites* 13:602–606
30. Yan JY, Sachtler WMH, Kung HH (1997) Effect of Cu loading and addition of modifiers on the stability of Cu/ZSM-5 in lean NO_x reduction catalysis. *Catalysis Today* 33:279–290
31. Wilken N, Wijayanti K, Kamasamudram K et al (2012) Mechanistic investigation of hydrothermal aging of Cu-Beta for ammonia SCR. *Applied Catalysis B: Environmental* 111–112:58–66
32. Kharas KCC, Robota HJ, Liu DJ (1993) Deactivation in Cu-ZSM-5 lean-burn catalysts. *Applied Catalysis B: Environmental* 2:225–237
33. Ding L, Zheng Y, Hong Y et al (2007) Effect of particle size on the hydrothermal stability of zeolite beta. *Microporous and Mesoporous Materials* 101:432–439
34. Kucherov AV, Hubbard CP, Shelef M (1995) Rearrangement of cationic sites in CuH-ZSM-5 and reactivity loss upon high-temperature calcination and steam aging. *Journal of Catalysis* 157:603–610
35. Chang HL, Chen H-Y, Fedeyko JM et al (2007) Thermal durability and deactivation of Cu-zeolite SCR catalyst. Paper presented at the 20th North American Catalysis Society Meeting
36. Fedeyko JM, Chen H-Y, Ballinger TH et al (2009) Development of thermally durable Cu/SCR catalysts. SAE Technical Paper 2009-01-0899
37. Andersen PJ, Casci JL, Chen H-Y et al (2011) Small pore molecular sieve supported transition metal catalysts for the selective catalytic reduction of NO_x with NH₃. Paper presented at the 22nd North American Society Meeting
38. Jardim PM, Marinkovic BA, Saavedra A et al (2004) A comparison between thermal expansion properties of hydrated and dehydrated orthorhombic HZSM-5 zeolite. *Microporous and Mesoporous Materials* 76:23–28
39. Long RQ, Yang RT (2002) Selective catalytic reduction of NO with ammonia over Fe³⁺-exchanged mordenite (Fe-MOR): catalytic performance, characterization, and mechanistic study. *Journal of Catalysis* 207:274–285
40. Cavataio G, Girard J, Patterson J et al (2007) Laboratory testing of urea-SCR formulations to meet Tier 2 Bin 5 emissions. SAE Technical Paper 2007-01-1575
41. Montreuil CN, Lambert C (2008) The effect of hydrocarbons on the selective catalyzed reduction of NO_x over low and high temperature catalyst formulations. SAE Technical Paper 2008-01-1030
42. Girard J, Snow R, Cavataio G et al (2008) Influence of hydrocarbon storage on the durability of SCR catalysts. SAE Technical Paper 2008-01-0767
43. Cheng Y, Montreuil CN, Cavataio G et al (2008) Sulfur tolerance and DeSO_x studies on diesel SCR catalysts. SAE Technical Paper 2008-01-1023
44. Cheng Y, Montreuil CN, Cavataio G et al (2009) The effects of SO₂ and SO₃ poisoning on Cu/zeolite SCR catalysts. SAE Technical Paper 2009-01-0898
45. Cheng Y, Lambert C, Kim DH et al (2010) The different impacts of SO₂ and SO₃ on Cu/zeolite SCR catalysts. *Catalysis Today* 151:266–270

46. Yim SD, Kim SJ, Baik JH et al (2004) Decomposition of Urea into NH_3 for the SCR Process. *Industrial & Engineering Chemistry Research* 43:4856–4863
47. Xu L, Watkins W, Snow R et al (2007) Laboratory and engine study of urea-related deposits in diesel urea-SCR after-treatment systems. *SAE Technical Paper* 2007-01-1582
48. Cheng Y, Hoard J, Lambert C et al (2008) NMR studies of Cu/zeolite SCR catalysts hydrothermally aged with urea. *Catalysis Today* 136:34–39
49. Schmiege SJ, Oh SH, Kim CH et al (2012) Thermal durability of Cu-CHA NH_3 -SCR catalysts for diesel NOx reduction. *Catalysis Today* 184:252–261
50. Cavataio G, Jen HW, Dobson D et al (2009) Laboratory study to determine impact of Na and K exposure on the durability of DOC and SCR catalyst formulations. *SAE Technical Paper* 2009-11-02
51. Ishihara T, Kagawa M, Mizuhara Y et al (1992) Selective reduction of nitrogen monoxide with propene over Cu-silicoaluminophosphate (SAPO) under oxidizing atmosphere. *Chemistry Letters* 2119–2122.
52. Akolekar DB, Bhargava SK, Foger K (1998) FTIR investigations of the adsorption and disproportionation of NO on Cu-exchanged silicoaluminophosphate of type 34. *Journal of Chem. Soc., Faraday Trans* 94:155–160
53. Frache A, Palella BI, Cadoni M et al (2003) CuAPSO-34 catalysts for N_2O decomposition in the presence of H_2O . *Topics in Catalysis* 22:53–57
54. Frache A, Palella B, Cadoni M et al (2002) Catalytic DeNOx activity of cobalt and copper ions in microporous MeALPO-34 and MeAPSO-34. *Catalysis Today* 75:359–365
55. Pognant F, Saussey J, Lavalley JC et al (1995) NH_3 formation during the reduction of nitrogen monoxide by propane on H-Cu-ZSM-5 in excess oxygen. *Journal of the Chemical Society, Chemical Communications* 1:89–90
56. Pognant F, Saussey J, Lavalley JC et al (1996) In situ FT-IR study of NH_3 formation during the reduction of NOx with propane on H/Cu-ZSM-5 in excess oxygen. *Catalysis Today* 29:93–97
57. Chen H-Y, Sun Q, Wen B et al (2004) Reduction over zeolite-based catalysts of nitrogen oxides in emissions containing excess oxygen: unraveling the reaction mechanism. *Catalysis Today* 96:1–10
58. Fickel DW, Lobo RF (2009) Copper coordination in Cu-SSZ-13 and Cu-SSZ-16 investigated by variable-temperature XRD. *The Journal of Physical Chemistry C* 114:1633–1640
59. Fickel DW, D'Addio E, Lauterbach JA et al (2011) The ammonia selective catalytic reduction activity of copper-exchanged small-pore zeolites. *Applied Catalysis B: Environmental* 102:441–448
60. Ye Q, Wang L, Yang RT (2012) Activity, propene poisoning resistance and hydrothermal stability of copper exchanged chabazite-like zeolite catalysts for SCR of NO with ammonia in comparison to Cu/ZSM-5. *Applied Catalysis A: General* 427/428:24–34
61. Moliner M, Franch C, Palomares E et al (2012) Cu-SSZ-39, an active and hydrothermally stable catalyst for the selective catalytic reduction of NOx, *Chemical Communications* 48:8264–8266
62. Erichinger M, Maletz G, Eisert K (2011) KFI-type copper-containing zeolite and use in SCR catalyst. Patent application WO 2011/098512
63. Lorena Picone A, Warrender SJ, Slawin AMZ et al (2011) A co-templating route to the synthesis of Cu SAPO STA-7, giving an active catalyst for the selective catalytic reduction of NO. *Microporous and Mesoporous Materials* 146: 36–47
64. Ren L, Zhu L, Yang C et al (2011) Designed copper-amine complex as an efficient template for one-pot synthesis of Cu-SSZ-13 zeolite with excellent activity for selective catalytic reduction of NOx by NH_3 . *Chemical Communications* 47:9789–9791
65. Deka U, Lezcano-Gonzalez I, Warrender SJ et al (2013) Changing active sites in Cu-CHA catalysts: deNOx selectivity as a function of the preparation method. *Microporous and Mesoporous Materials* 166:144–152

66. Martínez-Franco R, Moliner M, Franch C et al (2012) Rational direct synthesis methodology of very active and hydrothermally stable Cu-SAPO-34 molecular sieves for the SCR of NO_x. *Applied Catalysis B: Environmental* 127:273–280
67. Kwak JH, Tonkyn RG, Kim DH et al (2010) Excellent activity and selectivity of Cu-SSZ-13 in the selective catalytic reduction of NO_x with NH₃. *Journal of Catalysis* 275:187–190
68. Kwak JH, Tran D, Burton SD et al (2012) Effects of hydrothermal aging on NH₃-SCR reaction over Cu/zeolites. *Journal of Catalysis* 287:203–209
69. Castagnola M, Caserta J, Chatterjee S et al (2011) Engine performance of Cu- and Fe-based SCR emission control systems for heavy duty diesel applications. SAE Technical Paper 2011-01-1329
70. Tang W, Huang X, Kumar S (2011) Sulfur effect and performance recovery of a DOC + CSF + Cu-zeolite SCR system. Presented at DEER Conference 2011. [Online] Available: http://www1.eere.energy.gov/vehiclesandfuels/pdfs/deer_2011/tuesday/presentations/deer11_tang.pdf
71. Watanabe Y, Koiwai A, Takeuchi H et al (1993) Multinuclear NMR studies on the thermal stability of SAPO-34. *Journal of Catalysis* 143:430–436
72. Palella BI, Cadoni M, Frache A et al (2003) On the hydrothermal stability of CuAPSO-34 microporous catalysts for N₂O decomposition: a comparison with CuZSM-5. *Journal of Catalysis* 217:100–106
73. Wang L, Li W, Qi G et al (2012) Location and nature of Cu species in Cu/SAPO-34 for selective catalytic reduction of NO with NH₃. *Journal of Catalysis* 289:21–29
74. Wang J, Yu T, Wang X et al (2012) The influence of silicon on the catalytic properties of Cu/SAPO-34 for NO_x reduction by ammonia-SCR. *Applied Catalysis B: Environmental* 127:137–147
75. Korhonen ST, Fickel DW, Lobo RF et al (2011) Isolated Cu²⁺ ions: active sites for selective catalytic reduction of NO. *Chemical Communications* 47:800–802
76. Deka U, Juhin A, Eilertsen EA et al (2012) Confirmation of isolated Cu²⁺ Ions in SSZ-13 zeolite as active sites in NH₃-selective catalytic reduction. *The Journal of Physical Chemistry C* 116:4809–4818
77. McEwen J-S, Anggara T, Schneider WF et al (2012) Integrated operando X-ray absorption and DFT characterization of Cu-SSZ-13 exchange sites during the selective catalytic reduction of NO_x with NH₃. *Catalysis Today* 184:129–144
78. Kispersky VF, Kropf AJ, Ribeiro FH et al (2012) Low absorption vitreous carbon reactors for operando XAS: a case study on Cu/Zeolites for selective catalytic reduction of NO_x by NH₃. *Physical Chemistry Chemical Physics* 14:2229–2238

Chapter 6

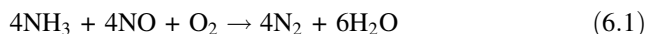
Low-Temperature Selective Catalytic Reduction (SCR) of NO_x with NH₃ Over Zeolites and Metal Oxide-Based Catalysts and Recent Developments of H₂-SCR

Gongshin Qi, Lifeng Wang and Ralph T. Yang

6.1 Ammonia-SCR

6.1.1 Introduction

The 1990 Clean Air Act amendments require major sources of air emissions to limit the discharge of nitrogen oxides (NO_x). They are a major cause for photochemical smog, acid rain, ozone depletion, and greenhouse effects. NO_x is present in the flue gas emitted from combustion processes. Therefore, cost-effective methods for controlling NO_x are of significant interest. To abate nitrogen oxides, many methods have been studied, such as fuel-gas treatment, combustion control, NO decomposition, NO sorption, non-catalytic reduction, selective catalytic reduction (SCR) with ammonia and hydrocarbon, and NO_x trapping/catalytic reduction. Among these various technologies, the ammonia-SCR has been considered the most reliable method due to the proved successful implementation, and several excellent review papers have been published during the past 20 years [1–6]. Since NO_x in lean combustion exhaust is usually composed of more than 90 % NO, the main reaction of SCR of NO with ammonia will be



This reaction indicates a 1:1 stoichiometry for NH₃ and NO along with the consumption of oxygen. The reaction without oxygen is much slower and is not

G. Qi (✉)

General Motors Global Research and Development, Warren, MI 48090, USA
e-mail: gongshin.qi@gm.com

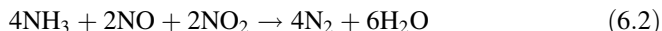
L. Wang · R. T. Yang

Department of Chemical Engineering, University of Michigan, Ann Arbor, MI 48109, USA
e-mail: lfwang@umich.edu

R. T. Yang

e-mail: yang@umich.edu

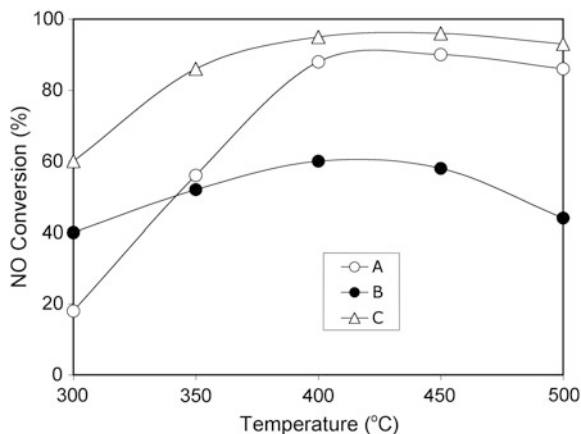
applicable for lean exhaust aftertreatment. On the other hand, the reaction rate with equimolar amounts of NO and NO₂ (Reaction 6.2) is much faster than that of Reaction (6.1) and this reaction will become more important in diesel engine aftertreatment since SCR catalysts are usually located downstream of diesel oxidation catalysts which can oxidize NO to NO₂.



For the automotive industry, in order to meet the stringent regulations, many efforts have been made to reduce NO_x emission by using advanced combustion technologies, or by using aftertreatment technologies, such as urea-SCR and lean NO_x trap catalysts. Urea-SCR has been considered as the most efficient and reliable technology for automobile application. In order to improve fuel economy and reduce CO₂ emission, fuel-efficient diesel and lean-burn gasoline vehicles are desirable, relative to the traditional gasoline-powered vehicles. Advanced engines and related technologies have been implemented to reduce NO_x from engine exhaust gas, which have also resulted in lower exhaust temperatures. In addition, cold start emissions reduction has become critical in light-duty diesel applications and improved deNO_x performance in urban driving or other low load conditions have been required even for heavy-duty applications.

Questions may be raised as to why a low-temperature (<200 °C) SCR catalyst is needed for SCR system for vehicle application where urea would be injected below 200 °C. This would be true for the urea-SCR system, but some alternative technologies to urea-SCR have emerged recently. For example, FEV, Inc. has invested significant resources in the development of the so-called solid SCR technology. The basic principle of the solid SCR is the same as the urea-SCR; the difference is the source of ammonia. Instead of an aqueous urea solution, the solid SCR system uses a solid ammonia precursor, known as ammonium carbamate. Ammonium carbamate can sublime directly into gaseous ammonia when the temperature is above 60 °C and the generated ammonia is injected into the exhaust to react with the NO_x. This technology can provide an opportunity to inject ammonia at a much lower temperature compared to the urea-SCR. Another solid SCR technology developed by Amminex (a Danish company) uses metal chloride amines, such as strontium chloride amine, as the ammonia precursor which can release ammonia at 150 °C. Both solid SCR systems can provide high NO_x reduction efficiencies, even at a low exhaust temperature. As a result, high SCR activity at low temperature is needed and is crucial for meeting emission regulations and improving fuel economy [7]. In the past, extensive studies on the development of the advanced low-temperature NH₃-SCR catalysts have been made. Here, Fe, Cu-exchanged zeolite catalysts, and base metal oxide catalysts are reviewed, and aspects of possible reaction mechanism over different catalysts are discussed.

Fig. 6.1 NO conversions on different catalysts as a function of temperatures



6.1.2 Catalysts and Mechanistic Aspects of the Low-Temperature Ammonia-SCR

6.1.2.1 Zeolite-Based Catalysts

Fe-Zeolite-based catalysts

The base metals (especially Fe and Cu) exchanged zeolite catalysts have been extensively studied since the 1990s and several excellent reviews have been published recently [8, 9]. Among all the zeolite-based catalysts, Fe-ZSM-5 and Cu-ZSM-5 are the most extensively investigated in the past 20 years. Generally speaking, Fe-ZSM-5 shows better SCR performance at higher temperatures, while Cu-ZSM-5 shows better performance at lower temperatures, although its hydrothermal durability and sulfur poisoning resistance are relatively poor compared to the Fe-ZSM-5 catalysts [10]. A variety of ion-exchange methods have been used to prepare Fe-ZSM-5 catalysts, including ion-exchange method [11, 12, 14], vapor phase ion-exchange methods [13, 15] and solid-state exchange method [16–19]. However, the preparation of Fe-ZSM-5 has proven to be especially difficult because the iron (III) compounds can barely penetrate into the pores of ZSM-5 due to the large hydration cell [9]. Long and Yang [11, 14, 20] successfully synthesized highly active Fe-ZSM-5 by an ion-exchange method using FeCl_2 as iron sources; its activity is much higher than the well-known $\text{V}_2\text{O}_5/\text{TiO}_2$ catalyst.

Qi and Yang developed a new method for preparing the Fe/ZSM-5 catalyst by the conventional incipient-wetness impregnation method using $\text{NH}_4\text{-ZSM-5}$ and FeCl_2 as the iron precursor [21]. The resulting catalyst prepared from FeCl_2 yielded significantly higher activities than catalysts prepared by using other methods or precursors. The results of NO conversions with different catalysts are shown in Fig. 6.1. At temperatures over 350 °C on 2.5 % Fe/ZSM-5, the NO conversion reached nearly 90 % and also with a wide temperature window similar

Table 6.1 Comparison of catalytic performance of Fe-ZSM-5 prepared by different methods

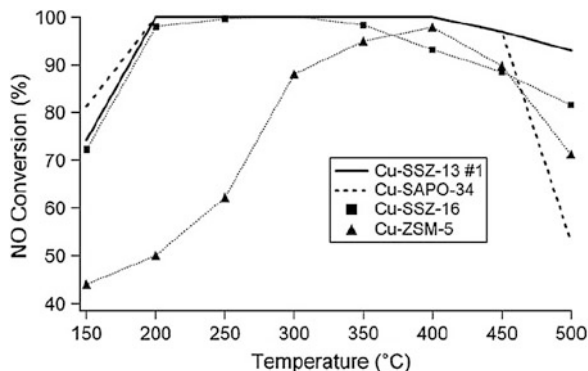
Catalysts	Fe content (wt.%)	Temperature (°C)	NO conversion (%)	TOF $\times 10^3$ (s ⁻¹)	Reference
Fe-ZSM-5	3.6	300	89	10.30	[21]
Fe/ZSM-5	2.5	300	65	13.54	[22]
Fe/ZSM-5	1.6	300	25	5.20	[14]
Fe/ZSM-5	1.0	300	35	18.23	[22]
Fe/MFI	–	300	80	12.8	[15]
Fe-ZSM-5	1.7	300	19	11.64	[20]
Fe-ZSM-5	1.7	300	9	5.51	[20]
Fe _{sub} ZSM-5	3.8	300	70	10.58	[23]

to the Fe-ZSM-5 prepared by aqueous ion-exchange method. Compared to the Fe-ZSM-5 catalyst prepared by aqueous ion-exchange method, the new Fe/ZSM-5 catalyst has superior activities, especially in the lower temperature range. In comparison, the commercial catalyst 4.4 % V₂O₅–8.2 % WO₃/TiO₂ showed substantially lower activities in NO reduction under the same conditions, and the NO conversion dropped more rapidly when the temperature was over 450 °C.

Reaction conditions: 40 mg catalyst, 1,000 ppm NO, 1,000 ppm NH₃, 2 % O₂, balance He, and GHSV = 5.7×10^5 h⁻¹. (A) Fe-ZSM-5, prepared by ion-exchange in FeCl₂ solution; (B) 4.4 % V₂O₅–8.2 % WO₃/TiO₂ prepared by impregnation; (C) 2.5 % Fe/ZSM-5, prepared by incipient-wetness impregnation with FeCl₂ as precursor [21].

A comparison of several Fe-ZSM-5 catalysts reported in the literature is also shown in Table 6.1. The rates in Table 6.1 are expressed in terms of TOF number. The TOF was calculated based on the total number of Fe ions in the zeolites. This was done in order to have a uniform comparison for rates that were obtained under different conditions. It is very clear that the catalyst prepared by the impregnation method is the most active catalyst among the catalysts. Based on the catalytic activity and characterization results, Qi and Yang [21] concluded that the Fe²⁺, Fe³⁺ and highly dispersed iron oxide species may contribute to the high activities. Despite the extensive research on the chemistry of Fe-ZSM-5, different types of active sites have been proposed, such as small Fe_xO_y(OH)_z clusters and oxygen-bridged binuclear iron species [15, 33–35]; monomeric Fe²⁺ and Fe³⁺ ions [20, 24, 36], and extra-framework Fe–O–Al [37]. Schwidder et al. [24] studied Fe-ZSM-5 catalysts (0.2–1.2 wt.% Fe) prepared by exchanging Na⁺ in Na-ZSM-5 with Fe²⁺ for SCR of NO by isobutane and by NH₃. The catalysts were highly active in both reactions compared to the catalyst prepared by chemical vapor deposition of FeCl₃ into H-ZSM-5. It was concluded that mononuclear Fe ions are active sites for both SCR reactions, but oligomers (and aggregate surfaces) are more active in NH₃-SCR reaction. The higher SCR reaction rate over Fe-ZSM-5 with oligomers is possibly due to the high activity for NO oxidation to NO₂ since it is believed that NO oxidation to NO₂ is the rate-determining step for ammonia-SCR over Fe-Zeolite-based catalysts [25–32]. Recently, Brandenberger et al. [38] investigated the

Fig. 6.2 NH_3 -SCR activity as a function of temperature over hydrothermally pretreated Cu-SSZ-13, Cu-SAPO-34, Cu-SSZ-16, and Cu-ZSM-5 [53]



activities of different iron species in Fe-ZSM-5 for SCR of NO by ammonia. Their results suggest that the SCR of NO by ammonia is catalyzed by different active sites with different activation energies. At temperature below 300 °C, the SCR activity was primarily obtained from monomeric iron sites; however, at $T > 300$ °C, $T > 400$ °C, and $T > 500$ °C, the contribution of dimeric iron species, oligomeric species, and partially uncoordinated iron sites in the outmost layer of iron oxide particles, respectively, become important.

Cu-Zeolite-based catalysts

Cu ion-exchanged ZSM-5 zeolites exhibit high NO decomposition rates and SCR activities, but ZSM-5 zeolite possesses poor hydrothermal stability due to dealumination and Cu migration. Consequently, other types of zeolites have been explored for improving the activity and durability of the SCR catalysts. Cu-exchanged beta zeolite [48, 49] has been shown to have excellent activity with better hydrothermal stability than ZSM-5 catalysts. Recently, it was reported that Cu ion-exchanged SSZ-n [50, 51] showed higher NO_x conversions over a broad temperature range with higher N_2 selectivity and hydrothermal stability compared with Cu/ZSM-5 and Cu/beta. Silico-alumino-phosphate (SAPO) zeolites possess ion-exchange properties as a result of the isomorphous substitution of P in AlPO_4 by Si, and SAPO-34, with a small-pore chabazite structure, exhibits extremely high thermal stability even in the presence of water. Cu ion-exchanged SAPO-34 has been investigated for hydrocarbon-SCR [52] and more recently for NH_3 -SCR [53, 54].

Figure 6.2 shows NH_3 -SCR activity over the hydrothermally pretreated copper-exchanged small-pore zeolites (Cu-SSZ-13, Cu-SSZ-16 and Cu-SAPO-34) and the medium-pore Cu-ZSM-5. It can be concluded that after hydrothermal treatment at 750 °C the copper-exchanged small-pore zeolites can still maintain the high SCR activity, while the activity of Cu-ZSM-5 deteriorates significantly [53]. The restricting dimension of the small-pores in Cu-SSZ-13, Cu-SSZ-16, and Cu-SAPO-34 is the most prominent reason for the high hydrothermal stability of these materials as well as their exceptional NH_3 -SCR activity [53].

Reaction mechanism over zeolite-based catalysts

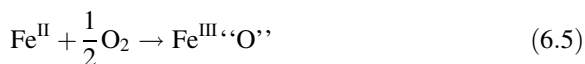
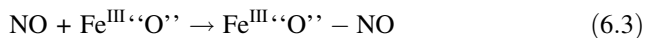
Isotopic experiments on a Ba–Na–Y zeolite catalyst [15] have shown that the formation of N_2 takes one nitrogen atom from NO_x and another nitrogen atom from ammonia. One important reaction for ammonia-SCR over Fe-zeolite is the NO oxidation to NO_2 , because the presence of NO_2 can significantly improve the SCR performance, especially at low temperature [25, 39–41]. The reaction rate of the ammonia-SCR can be described by the following simple power law:

$$\text{Rate of NO conversion} = k[NO]^x[NH_3]^y[O_2]^z$$

The reaction order with respect to NO has been measured by many research groups to be around 1.0 on the Fe-exchanged zeolite with activation energies ranging between 44 and 61 kJ/mol [25, 42–46]. According to many reports the reaction order with respect to NH_3 is about zero and slightly negative at low temperatures, which is typical for inhibition of the SCR reaction by NH_3 over Fe-zeolite catalysts, and this inhibition effect was explained by competitive adsorption of NH_3 and NO on the same active sites. Under real application for diesel aftertreatment, O_2 and H_2O are present in large excess at 5–10 % by volume, so their rate dependences can be neglected. Based on the above discussion, the SCR kinetics can be simplified as the rate law as follows:

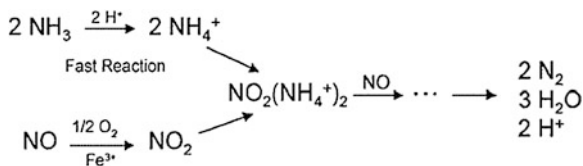
$$\text{Rate of NO conversion} \approx k[NO]$$

The exact reaction mechanism is still under investigation. But in general, it is believed that in order to reduce NO_x efficiently, the catalyst must exhibit dual active sites; the zeolite support provide acid sites to adsorb ammonia and form ammonium (NH_4^+); the exchanged metal sites oxidize NO to NO_2 , and NO oxidation to NO_2 is the rate-determining step for ammonia-SCR over Fe-zeolite catalysts. The mechanism of NO oxidation to NO_2 over iron was proposed based on the following equations [23]:



And this proposal suggested that the rate of NO oxidation reaction is controlled by the NO_2 desorption step (Eq. 6.4) and a redox cycle of Fe^{3+}/Fe^{2+} was also involved. Figure 6.3 shows an extensively studied and widely accepted mechanism of NO_x reduction by ammonia over Fe-ZSM-5 [46, 47]. During the SCR reaction, gaseous NH_3 molecules are adsorbed quickly onto the Bronsted acid sites to form NH_4^+ ions, and NO molecules are oxidized to NO_2 over Fe^{3+} sites by oxygen. Then one molecule of the formed NO_2 diffuses to two adjacent NH_4^+ ions to form an active complex $NO_2(NH_4^+)_2$. The active complex reacts with one molecule of NO to produce N_2 and H_2O , thus completing the catalytic cycle. The overall reaction is the same as Reaction (6.2).

Fig. 6.3 Reaction mechanism of SCR of NO_x with NH_3 over Fe-ZSM-5 [46, 47]



6.1.2.2 Metal Oxide-Based Catalysts

Single metal oxide-based catalysts

Many SCR catalysts containing transition metals, such as Fe, Mn, Cr, Cu, have shown good activities for low-temperature SCR [2, 3, 6, 55–68]. Among these catalysts, manganese-based oxides have been extensively studied due to their excellent low-temperature SCR performance. Here, the pure manganese oxides, manganese-based mixed oxides (composite oxides), and supported manganese oxide catalysts are reviewed.

Manganese oxides of different crystallinity, oxidation state, and specific surface area were first investigated by Kapteijn et al. [68]. MnO_2 appears to have the highest activity based on per unit surface area, followed by Mn_5O_8 , Mn_2O_3 , Mn_3O_4 , and MnO . The specific SCR activity generally increased with the increase the oxidation state of Mn. Although the activity is higher on MnO_2 , the N_2 selectivity is lower than that on Mn_2O_3 [68]. Recently, Tan et al. [69] confirmed that β - MnO_2 achieved higher conversion of NO, higher generation rate of N_2O per unit surface area with respect to α - Mn_2O_3 . The higher N_2O selectivity over β - MnO_2 is due to the higher activation capability to NH_3 molecules caused by a lower Mn–O bond energy; consequently, there are more adsorbed nitrogen atom species formed, which reacted with NO to form N_2O on β - MnO_2 . Kang et al. [55] evaluated the SCR performance over pure MnO_x prepared by a precipitation method with various precipitants such as ammonium carbonate (AC), potassium carbonate (PC), sodium carbonate (SC), ammonium hydroxide (AH), potassium hydroxide (PH), and sodium hydroxide (SH). Figure 6.4 shows the catalytic NO_x conversions and N_2 selectivities of the MnO_x catalysts prepared with different precipitants and calcined at 623 K. The catalysts precipitated with precipitants containing carbonate as anion showed higher NO_x conversions than those prepared with alkali or ammonium hydroxides, and the former catalysts also showed better N_2 selectivities based on the results shown in Fig. 6.4. The MnO_x catalysts prepared with SC have higher surface area, more Mn^{4+} species and the higher concentration of surface oxygen, which is believed to be critical for SCR reactions [55].

The presence of carbonate species may help the adsorption of NH_3 , which resulted in the high catalytic activity. The value of the $\text{Mn}^{4+}/\text{Mn}^{3+}$ ratio was considered as a parameter characterizing the intrinsic oxidation properties of metal oxide catalysts. The oxidation activity increased with the increasing $\text{Mn}^{4+}/\text{Mn}^{3+}$ ratio. It can be inferred that the higher SCR activity over the MnO_x prepared by SC is probably due to the higher amount of NO_2 produced from NO oxidation. On the

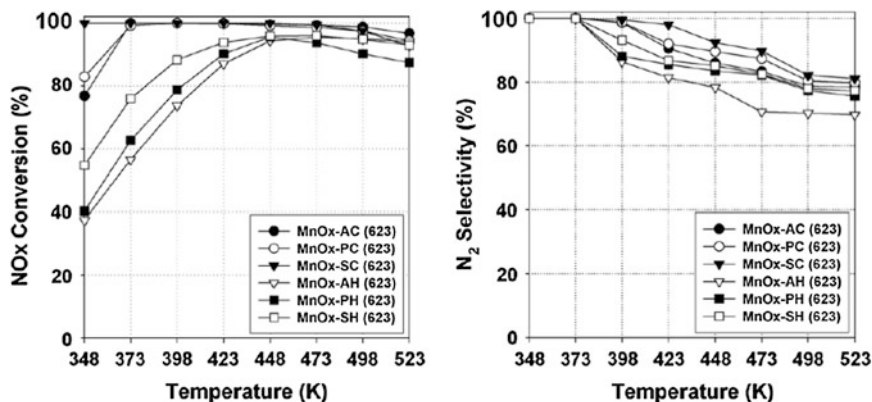


Fig. 6.4 NO_x conversions and N₂ selectivities as a function of temperatures over various MnO_x catalysts (see text). All catalysts were calcined at 623 K. Reaction conditions: 500 ppm NO, 500 ppm NH₃ and 5 % O₂ in N₂ with GHSV = 50,000 h⁻¹ [55]

other hand, the higher surface oxygen concentration was found to be preferable for SCR reactions over manganese-containing catalysts because higher surface oxygen concentration facilitates the $-\text{NH}_2$ formation [69], and the formed $-\text{NH}_2$ species would then react with gas-phase NO or nitrite intermediates on the catalysts surface to form nitrogen and water.

Mixed oxide-based catalysts

Since the pure MnO_x catalysts are generally low in surface area and suffer from sintering, many studies have been conducted in the past to improve the catalyst surface area, stability, and sulfur/water poison resistance by either adding other metal oxides to form mixed oxides or using different supports such as TiO₂, Al₂O₃, SiO₂, and zeolites. Long and Yang [70] investigated Fe–Mn-based transition metal oxides (Fe–Mn, Fe–Mn–Zr and Fe–Mn–Ti) and found nearly 100 % NO conversion at 100–180 °C for SCR of NO with ammonia at a space velocity of 15000 h⁻¹. The higher activity over the mixed oxides was due to the higher NO oxidation to NO₂. Qi and Yang [62–64, 66] studied the MnO_x–CeO₂ mixed oxides and observed that the best MnO_x–CeO₂ catalyst with a molar Mn/(Mn + Ce) ratio of 0.3 yielded nearly 100 % NO conversion at 120 °C at a space velocity of 42,000 h⁻¹ which are shown in Fig. 6.5. The catalytic performance for SCR reaction over MnO_x–CeO₂ catalysts prepared by different methods is also shown in Fig. 6.5. Under a very high space velocity (GHSV = 210,000 h⁻¹), these catalysts still show high NO conversions, especially the catalysts prepared by citric acid method. The maximum NO conversion decreased in the sequence of MnO_x–CeO₂ (CA) > MnO_x–CeO₂ (CP) > MnO_x–CeO₂ (IM). The order of the surface area for these catalysts is MnO_x–CeO₂ (CP) > MnO_x–CeO₂ (CA) > MnO_x–CeO₂ (IM). As mentioned above, the MnO_x–CeO₂ (CA) catalyst showed much higher NO

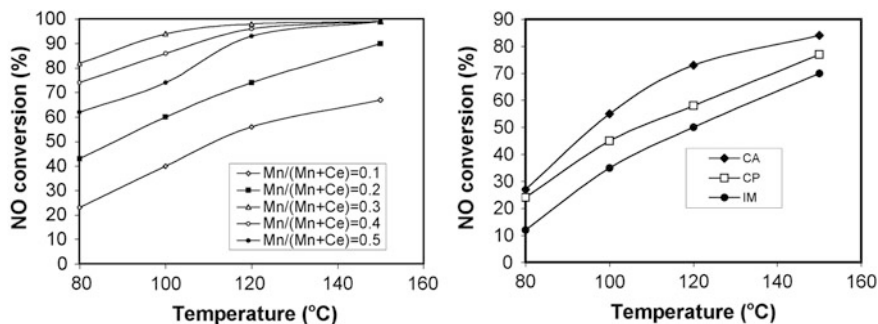
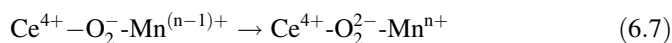
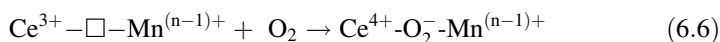


Fig. 6.5 Right NO conversion on $\text{MnO}_x\text{-CeO}_2$ mixed oxide catalysts with different Mn/Ce mole ratios. Reaction conditions: $[\text{NO}] = [\text{NH}_3] = 1,000$ ppm, $[\text{O}_2] = 2\%$, $\text{GHSV} = 42,000$ h^{-1} ; left NO conversion on $\text{MnO}_x\text{-CeO}_2$ mixed oxide catalysts prepared by different methods. Reaction conditions: $[\text{NO}] = [\text{NH}_3] = 1,000$ ppm, $[\text{O}_2] = 2\%$, He balance, 0.2 g catalyst, total flow rate = 500 ml/min, $\text{GHSV} = 210,000$ h^{-1} . CA: Citric acid method; CP: Coprecipitation method; IM: Impregnation by incipient wetness [64]

conversions than $\text{MnO}_x\text{-CeO}_2$ (CP) and $\text{MnO}_x\text{-CeO}_2$ (IM); hence, it seems that the SCR activity does not correlate with the surface area.

The structure and physicochemical properties of the $\text{MnO}_x\text{-CeO}_2$ mixed oxides have been studied extensively due to their high oxidation activity [71–75]. Many researchers have reported that the higher oxidation activity of the $\text{MnO}_x\text{-CeO}_2$ mixed oxides is due to the formation of solid solution and oxygen vacancy upon combination of Mn and Ce by sol–gel or co-precipitation method based on the change of the lattice parameters [64, 71–73, 76, 77]. The lattice parameter of ceria decreases with the addition of Mn, suggesting that Mn^{3+} ions are incorporated into the ceria lattice to form a solid solution, since the radius of Mn^{3+} ion (0.065 nm) is smaller than that of the Ce^{4+} ion (0.094 nm) and generates oxygen vacancies due to charge compensation. The higher NO oxidation activity is not a result of the higher surface area of the mixed oxides, but due to the formation of the active oxygen upon the incorporation of Mn into the CeO_2 lattice, which readily converts the adsorbed NO to form NO_2 . Oxygen species such as O_2^- (superoxide) and O_2^{2-} (peroxide) can be formed by adsorbing O_2 at the anion vacancy (\square) through the following Reactions (6.6) and (6.7) [76], and the oxygen species reacts with NO readily to form NO_2 , then facilitates the overall SCR reaction at low temperature through fast SCR (i.e., Reaction 6.2).



Many other transition metals were added to further improve the low-temperature SCR performance on $\text{MnO}_x\text{-CeO}_2$ mixed oxides. Qi and Yang [66] found that the addition of Fe and Zr increased the low-temperature activity and N_2 selectivity as well as the resistance to water and SO_2 poisoning. Casapu et al. [75] reported that by

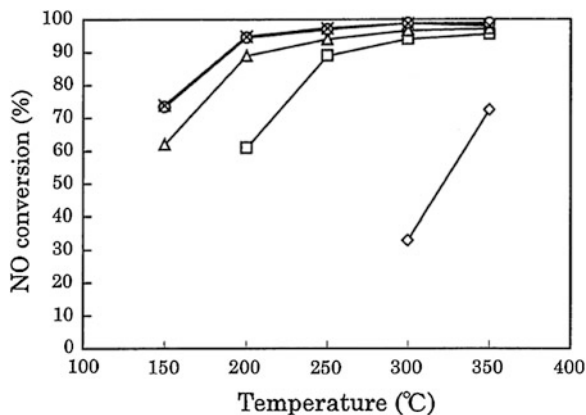
doping the $\text{MnO}_x\text{-CeO}_2$ catalyst with niobium oxides, a significant improvement of the SCR performance was achieved. The acidity and the strength of NH_3 adsorption on the catalyst surface were remarkably enhanced due to the addition of niobium. Besides, it was shown that the formation of MnNb_2O_6 decreased the oxidation activity of manganese species; as a consequence, the unselective NH_3 oxidation is avoided at high temperature [75].

Other than $\text{MnO}_x\text{-CeO}_2$ mixed oxides, Cu-Mn [78] and Cr-Mn mixed oxides [79] have also been studied for low-temperature SCR of NO with ammonia. Similar to $\text{MnO}_x\text{-CeO}_2$ mixed oxides, the mixed oxides have higher SCR activities than that of the single oxides; the mole ratio of the Mn and the doped metal, calcination temperature, and preparation methods are very important to the structure, dispersion of Mn, and the SCR activity. Although the manganese-based mixed oxides as low-temperature SCR catalysts have been studied extensively, the mechanism of the effect of the doped metals on the electronic dispersion and the crystal structure of Mn is still under investigation. Ding et al. [16] further developed a chain of reactions to explain this synergistic effect, and suggested a mechanism via a process of oxygen activation and oxygen transfer through the redox cycles of $\text{Mn}^{4+}/\text{Mn}^{3+}$ and $\text{Ce}^{4+}/\text{Ce}^{3+}$, briefly explained as follows [66, 80, 81]. The oxygen transfers from molecular oxygen to active sites of MnO_2 through an oxygen reservoir, CeO_2 , leading to effective activation of molecular oxygen in the feed stream. Normally, the adsorbed oxygen on manganese would be expected to participate in the oxidation reaction. Additional oxygen generated may be more active and easier to access.

Supported metal oxides based catalysts

Among the catalysts studied for low-temperature SCR of NO_x with ammonia, transition metal oxides, such as MnO_x , CrO_x , CuO , V_2O_5 , MoO_3 , Fe_2O_3 , supported on TiO_2 , Al_2O_3 , SiO_2 , active carbon, and zeolite have been studied extensively. The Shell company has developed $\text{V}_2\text{O}_5/\text{TiO}_2$ -based catalyst operated in the temperature range of 140–250 °C and can provide over 90 % NO_x conversion. The excellent low-temperature performance is attributed to the better reactor design and improved catalysts formulation with dopant such as Fe, Mo, and Co [82]. Wong and Nobe [83] reported various transition metal oxides supported on TiO_2 and Al_2O_3 , SiO_2 for the SCR of NO with ammonia and concluded that metal oxides supported on TiO_2 are more active. The V_2O_5 catalysts supported on $\text{TiO}_2\text{-SiO}_2\text{-MoO}_3$ (TSM) prepared by the co-precipitation method were investigated for low-temperature SCR of NO with ammonia by Kobayashi et al. [84]. The $\text{V}_2\text{O}_5/\text{TSM}$ catalyst with 7–13 wt.% SiO_2 was found to possess a superior SCR activity and a good sulfur tolerance at low temperatures. The effect of V_2O_5 loading on the NO conversion was examined over the $\text{V}_2\text{O}_5/\text{TSM}$ catalysts. As shown in Fig. 6.6, NO conversion increases significantly with the V_2O_5 loading, especially at low temperatures (<250 °C) and shows a maximum around a loading of 8 wt.%. The presence of highly active polymeric vanadates formed by the incorporation of MoO_3 to $\text{TiO}_2\text{-SiO}_2$ and superior redox properties seems to increase the SCR activity; and the lower SO_2 oxidation to SO_3 activity leads to a remarkable improvement in sulfur tolerance at low temperatures.

Fig. 6.6 SCR activity of V_2O_5 /TSM with V_2O_5 loadings of 0 (\diamond), 2 (\square), 4 (\triangle), 8 (\circ) and 12 wt.% (\times). SiO_2 contents are all 7 wt.%. Reaction conditions: 200 ppm NO, 200 ppm NH_3 , 10 % O_2 , 10 % H_2O , N_2 balance, $SV = 11,000 \text{ h}^{-1}$ [84]



The formation of N_2O is still a problem with V_2O_5/TiO_2 catalysts. It was reported that N_2O generation over V_2O_5/TiO_2 catalysts at low temperature was due to the formation of surface V-ON species that came from partial oxidation of adsorbed ammonia species with $NO + O_2$; N_2O could form when these active sites were close enough, so the high active site density caused by increasing in vanadium loading would enhance the formation of N_2O [85].

Manganese oxide supported catalysts have been examined by many researchers. Singoredjo and Moulijn [86] reported alumina-supported manganese oxides exhibited a high and selective activity for the low-temperature ammonia-SCR of NO. Acetate and nitrate were used as the precursor for manganese. Based on their study, the manganese acetate resulted in a better dispersion of manganese oxide on the alumina support and hence a higher specific catalytic activity than manganese nitrate as precursor. A same trend was observed on the TiO_2 -supported manganese oxide catalysts [87] and the activity of the MnO_x/TiO_2 catalyst could be adjusted by doping other transition metals such as Fe, Ni, Cu, and Ce [65, 67, 88]. Low-temperature ammonia-SCR on the oxides of V, Cr, Mn, Fe, Co, Ni, and Cu supported on anatase TiO_2 have been studied [89]. The catalytic performance on these transition metal oxides supported on TiO_2 decreased in the following order: $Mn > Cu > Cr > Co > Fe > V > Ni$. There was no conversion when TiO_2 was used as a catalyst for SCR of NO. Therefore, Mn species must play a significant role in this catalytic reaction. Figure 6.7 shows the results of different MnO_x/TiO_2 for SCR of NO by ammonia as a function of manganese loading. It is clear that the addition of manganese on TiO_2 caused enhancement of the catalytic activity. Increasing manganese loading increased NO conversion until the manganese loading reached 10 %. After this level, a further increase in manganese loading did not increase the activity. The N_2 product selectivities as functions of the temperature for these catalysts are also shown in Fig. 6.7. The effect of loading on the selectivity was quite significant. The higher the loading, the more the N_2O formed. With increasing temperature the selectivity decreased considerably for all samples. To reduce sintering of manganese oxide, a series of transition metals (Fe, Cu, Ni Cr) were added to the Mn/TiO_2 catalyst, and the activity and the characterization

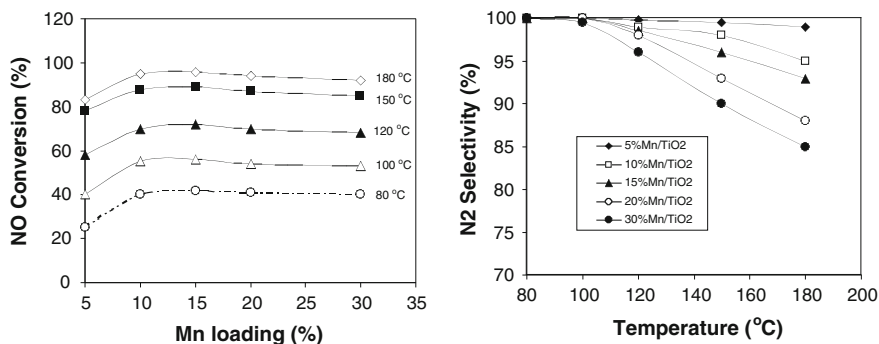


Fig. 6.7 NO conversion (right) and N₂ selectivity (left) on the MnO_x/TiO₂ catalysts with various MN loadings. Reaction conditions: [NO] = [NH₃] = 1,000 ppm, [O₂] = 2 %, He balance, total flow rate 100 ml/min, catalyst 0.25 g [65]

of the catalysts were investigated. With the addition of transition metal, the activity of the catalysts increased greatly and the Fe had the most favorable effect on the activity. A model (Fig. 6.8) had been proposed to interpret the effect of the transition metals on the activity of MnO_x/TiO₂. From the model, the behavior of transition metals was simulated. The addition of transition metals could segregate the particles of manganese oxides and titania. And the particles were prevented from sintering so that the manganese oxides were kept in amorphous phase; therefore, the catalytic activity was significantly improved.

Recently, Nam et al. [90] reported that an Mn–Fe/ZSM-5 prepared by impregnation method demonstrated excellent low-temperature SCR activities and N₂ selectivity. The well-dispersed MnO₂ and the high NH₃ adsorption capacity of the Mn–Fe/ZSM-5 catalyst have been identified as the primary reasons for its high deNO_x activity for ammonia-SCR. The increased dispersion of MnO₂ upon the addition of Fe has been confirmed by the TEM image shown in Fig. 6.9. The dark colored particles showing MnO₂ and the bright ones are ZSM-5 support. Large particles of MnO₂ are localized on the surface of Mn/ZSM-5, whereas small ones are well dispersed on the surface of the Mn–Fe/ZSM-5 catalyst.

The manganese-based catalysts have been demonstrated to have good low-temperature activity for ammonia-SCR; however, these catalysts are prone to be easily deactivated by SO₂ present in the exhaust gas. Development of the highly active catalysts with sulfur tolerance at low temperatures is still a challenge. Qi and Yang [64, 66] studied the sulfur effect on the low-temperature SCR over MnO_x–CeO₂ mixed oxides and found that, when 100 ppm SO₂ and 2.5 % H₂O were added at 150 °C the conversion of NO decreased 15 % in 3 h. After adding Pr or Fe into the mixed oxides, the conversion of NO decreased less than 5 % in the same conditions. Casapu et al. [91] conducted the effect of SO₂ and H₂O on the MnO_x–CeO₂-based monolithic catalysts and indicated that irreversible loss of the low-temperature SCR activity was observed. However, the SO₂ tolerance was increased by adding Fe, V to Mn-based catalysts monolithic catalysts, although the

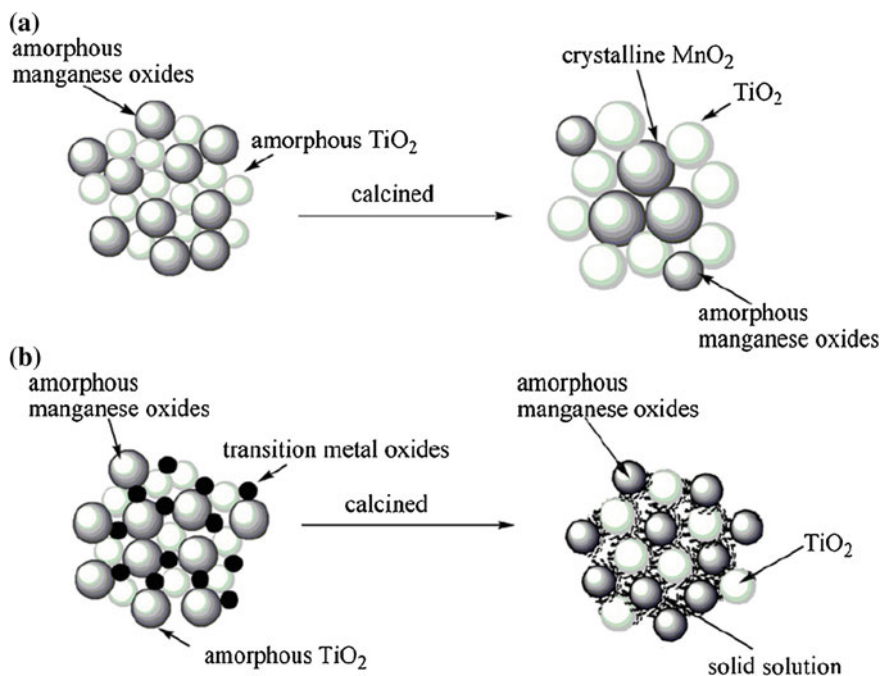


Fig. 6.8 A model for **a** Mn/TiO₂ and **b** metal-Mn/TiO₂ before and after calcination [88]

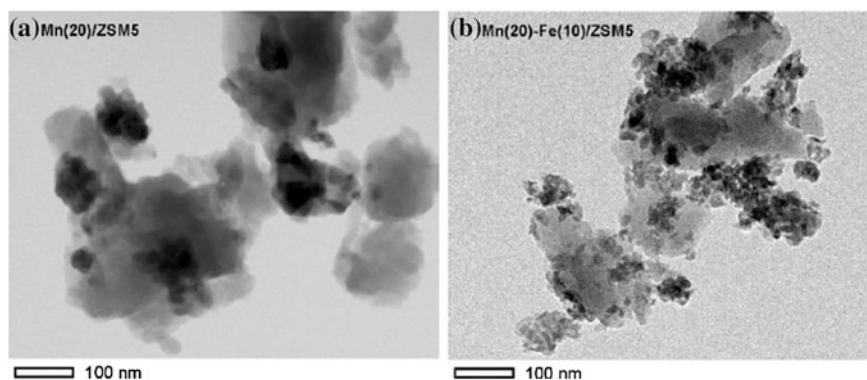
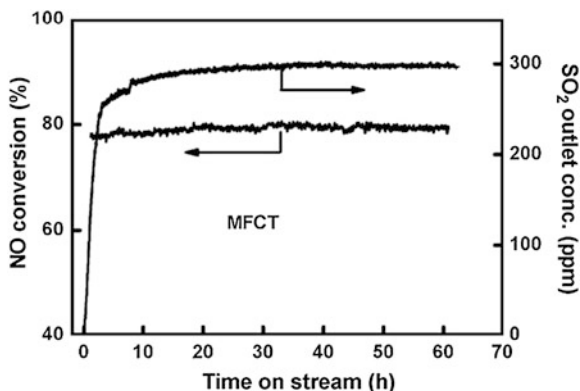


Fig. 6.9 TEM images of the Mn(20)/ZSM-5 (a) and, Mn(20)-Fe(10)/ZSM-5, (b) catalysts [90]

low-temperature NO conversion decreased [60]. Yu et al. [92] investigated the sulfur poisoning resistance on mesoporous MnO₂-Fe₂O₃-CeO₂-TiO₂ (MFCT) prepared with sol-gel method and impregnated MnO₂-Fe₂O₃-CeO₂-TiO₂ (IMP-MFCT) catalysts for low-temperature SCR. Comparing with the IMP-MFCT catalyst, the MFCT catalyst exhibited better SCR performance, higher N₂ selectivity and SO₂ tolerance. Figure 6.10 shows a 60-h test result of SCR of NO with

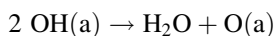
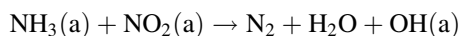
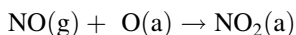
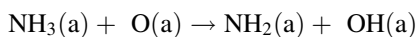
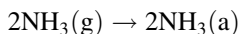
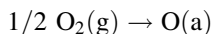
Fig. 6.10 Stability of a 60-h test for SO₂-poisoning resistance of Mn-Fe-Ce-TiO₂ (MFCT) catalyst prepared with sol-gel method. (SO₂: 300 ppm, NO; 600 ppm, NH₃/NO = 0.8, O₂: 2 %, N₂: balance gas, temperature: 240 °C, GHSV: 24000 h⁻¹)



ammonia on the MFCT catalyst in the presence of 300 ppm SO₂ at 240 °C with a NH₃/NO ratio = 0.8 and clearly a nearly 80 % of NO conversion was reached and maintained during the 60 h test. The high SO₂ tolerance was due to the lower decomposition of ammonium sulfate and almost no metal sulfates formation on this catalyst based on the characterization of the catalyst.

Reaction mechanism over metal oxides-based catalysts for ammonia-SCR of NO_x

The mechanism of surface reaction of NO_x on metal oxides catalysts has been studied extensively [1]. Different hypotheses have been proposed for the mechanism including the reaction between ammonium ion and adsorbed NO₂; the reaction between an amide and gaseous NO; and the reaction between coordinated ammonia and a species generated by spillover of NO on the support. Kijlstra et al. [93] studied the mechanism of SCR of NO with ammonia at low temperatures on MnO_x/Al₂O₃ catalyst. They proposed that the reaction starts with the adsorption of NH₃ on Lewis acid and subsequently transforms into NH₂; the NH₂ would then react with gas phase NO (an E-R mechanism) and nitrite intermediates on the surface (an L-H mechanism). Similar to the mechanism proposed by Kijlstra et al., Qi and Yang [62] proposed the following reaction pathway over MnO_x-CeO₂ catalyst:



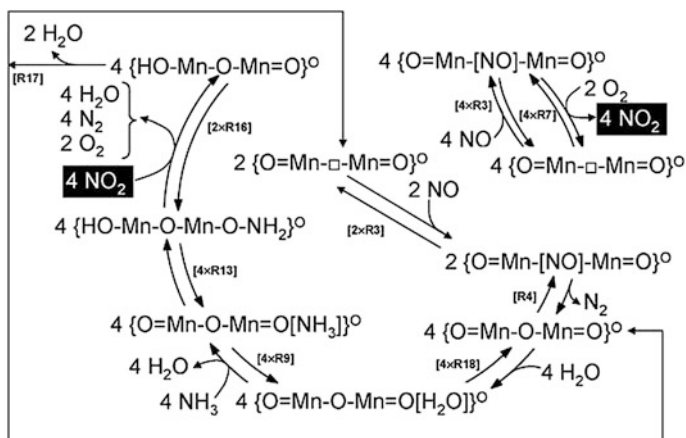


Fig. 6.11 Mechanism of the steady-state ammonia-SCR reaction in the presence of oxygen over carbon supported manganese oxide catalysts [94]

In the SCR reaction, gaseous NH_3 molecules are first adsorbed on the catalyst to form coordinated NH_3 and NH_2 . NO molecules are also adsorbed on the catalyst and then oxidized to nitrate and nitrite. The reaction of NH_2 and NO , and then formation of nitrosamine (NH_2NO) is a typical SCR mechanism reported for $\text{V}_2\text{O}_5/\text{TiO}_2$ and manganese based catalysts. The NH_2NO decomposes to give N_2 and H_2O . At high temperatures, N_2O was produced by the reaction between NH_3 and nitrate. Marban et al. [94] proposed an SCR reaction mechanism shown in Fig. 6.11, for carbon supported Mn_3O_4 catalysts, which consists of the following steps; (1) NH_3 adsorption on the oxygen atoms to form the aminoxy group, (2) NO adsorption as nitrosyls on the oxygen vacancies and then oxidized to NO_2 , (3) the reaction between aminoxy with NO_2 to form N_2 and water.

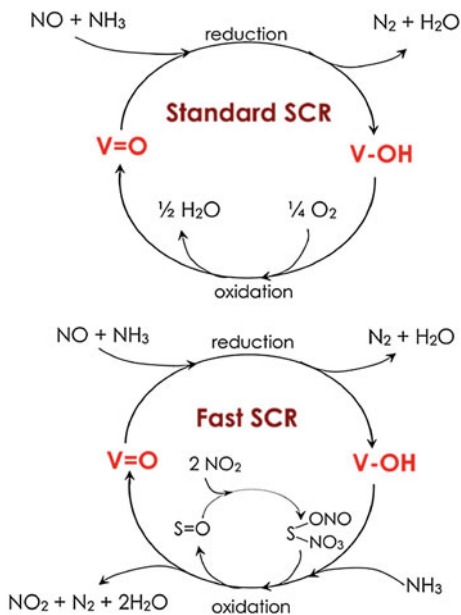
Recently, the redox mechanism of the ammonia-SCR at low temperature over a commercial $\text{V}_2\text{O}_5\text{-WO}_3/\text{TiO}_2$ catalyst was investigated by Tronconi et al. [95]. A unifying redox approach is proposed, in which vanadium sites are reduced by the reaction between NO and NH_3 and are reoxidized either by oxygen (standard SCR) or by nitrates (fast SCR), with the latter formed via NO_2 disproportionation [95] and the reaction scheme is shown in Fig. 6.12.

6.2 H_2 -SCR

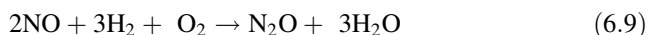
6.2.1 Introduction

It has long been known that NO is reduced by H_2 in low concentrations of O_2 , which is one of the main reactions taking place in three-way catalytic converters for gasoline engines (i.e., air/fuel ~ 14.7 , $\text{O}_2 \sim 0.5\%$) [96]. All noble metals have

Fig. 6.12 Redox cycles of the standard and fast reactions over V_2O_5 - WO_3 / TiO_2 catalysts. $V=O$ and $V-OH$ are oxidized and reduced vanadium sites, respectively. $S=O$ is a nonreducible oxidation site [95]



been investigated for the H_2 - NO reaction. Studies on H_2 -SCR of NO in excess O_2 (i.e., approximately $>2\%$ O_2) are relatively few and recent, beginning in the mid-1990s. Recently, hydrogen has been used in an effort to regenerate NO_x traps as well as for possible application in low-temperature SCR. The few studies were focused on supported Pt and Pd. The main reactions taking place in the $NO/H_2/O_2$ system are



Thus, a desirable catalyst would have high activities for Reaction (6.8) and minimized activities for the other two reactions particularly, Reaction (6.10). Excess H_2 ($H_2/NO \gg 2$) is typically needed. The mechanism of the H_2 -SCR reaction is far less understood than that for NH_3 -SCR. In this part, we will summarize the main catalysts that have been investigated for H_2 -SCR.

Table 6.2 NO conversion and selectivity of supported Pt catalysts [98]

Support	Surface area (m ² g ⁻¹)	Temperature ^a (°C)	No conversion (%)	Selectivity (%)	
				N ₂	N ₂ O
TiO ₂	58.2	90	13.6	–	–
ZrO ₂	85.5	110	71.6	57.4	42.6
SnO ₂	37.6	125	41.3	52.6	47.4
CeO ₂	64.6	150	18.5	–	–
SiO ₂	201.5	70	84.2	35.5	64.5
Al ₂ O ₃	160.5	80	91.9	40.2	59.8
TiO ₂ –ZrO ₂	207.3	90	88.8	53.2	46.8
SnO ₂ –TiO ₂	53.6	110	9.5	–	–
SnO ₂ –ZrO ₂	51.8	80	68.7	40.8	59.2
CeO ₂ –TiO ₂	73.1	130	42.2	41.1	58.9
CeO ₂ –ZrO ₂	62.2	140	35.7	50.7	40.3
ZrO ₂ –Al ₂ O ₃	208.8	90	87.2	36	64
TiO ₂ –SiO ₂	285.5	70	66.6	30.3	69.7

6.2.2 Catalysts and Mechanistic Aspects of H₂-SCR

6.2.2.1 Pt/SiO₂, Pt/Al₂O₃, and Pt on Other Metal-Oxide Supports

Pt/SiO₂ and Pt/Al₂O₃ are two of the most studied catalysts for H₂ SCR reaction. Burch and Coleman reported that 1 % Pt/Al₂O₃ and 1 % Pt/SiO₂ catalysts were active for NO reduction with H₂ in the presence of excess oxygen at low temperatures. The SiO₂ supported catalyst was found to be more active at lower temperatures than the Al₂O₃ supported catalyst. 50 and 75 % NO conversions were respectively obtained over Pt/Al₂O₃ catalyst at 140 °C and over Pt/SiO₂ catalyst at 90 °C (at 2,000 ml min⁻¹ g⁻¹ catalyst). The selectivity for N₂O was significantly increased at low temperatures and in the presence of water [97].

The good activities of Pt/SiO₂ and Pt/Al₂O₃ at low temperatures were also confirmed by Machida et al., who investigated the selective NO_x-H₂ reaction over Pt catalysts supported on various metal oxides, including TiO₂, ZrO₂, SiO₂, Al₂O₃, CeO₂, and their composites. Their results showed that Pt/SiO₂ and Pt/Al₂O₃ had much higher activities at low temperatures than other supported catalysts, i.e., 91.9 % NO conversion for Pt/Al₂O₃ at 80 °C and 84.2 % conversion for Pt/Al₂O₃ at 70 °C (Table 6.2). It is worth noting that the selectivities for N₂ and N₂O varied among different supports, indicating the selectivities were influenced by the oxide supports. The selectivities for N₂O were 64.5 % over Pt/SiO₂ and 59.8 % over Pt/Al₂O₃ [98].

6.2.2.2 Promoter (e.g., Na, Mo) Modified Pt/SiO₂ and Pt/Al₂O₃ Catalysts

To lower the selectivity to by-product N₂O on Pt/SiO₂, Yokota et al. introduced Na and Mo to Pt/SiO₂. A wider temperature window for NO_x conversion and a lower N₂O selectivity were achieved on the improved catalyst, Pt–Mo–Na/SiO₂ [99]. The promoter effects of Mo and Na were further studied by Burch and Coleman in their MoO₃- and Na₂O-modified Pt/Al₂O₃ and Pt/SiO₂ catalysts under lean conditions at temperatures representative of automotive “cold-start” conditions (<200 °C) [100]. The activity and N₂ selectivity of the modified catalysts were significantly increased. Steady-state isotopic-transient kinetic experiments showed the presence of high surface concentrations of N₂ precursors over the modified Pt/Al₂O₃ and Pt/SiO₂ catalysts. Attention should be paid to the amount of Na, however. It is found that small loadings of Na significantly increased the NO conversion, while large loadings of sodium poisoned the catalyst. Also, deactivation by SO₂ on the Na-promoted catalysts needs to be studied.

6.2.2.3 Pt/Mesoporous Silica

Besides the silica support aforementioned, another type of silica–mesoporous silica, with ordered pore structure and large surface area, was recently studied as Pt catalyst support. Wu et al. studied the H₂-SCR activities of Pt/Si-MCM-41 and Pt/Al-MCM-41 and found that the introduction of Al species to MCM-41 greatly promoted the H₂-SCR performance of Pt/MCM-41 [101]. The Pt/Al-MCM-41 with a Si/Al ratio of 10 exhibited 80 % NO_x conversion as well as 85 % N₂ selectivity at 140 °C (GHSV = 80,000 h⁻¹). In-situ DRIFT spectra showed that Brønsted acid sites on Al-MCM-41 changed the H₂-SCR reaction pathway and the NH₄⁺ species adsorbed on acid sites were the key intermediates for N₂ production.

6.2.2.4 Pt/Zeolites

Shibata et al. studied the effects of supports on the H₂-SCR activity and N₂ selectivity over Pt catalysts supported on various zeolites (MOR, MFI, BEA, Y) and nonzeolitic metal oxides (SiO₂, Al₂O₃, MgO) [102]. It was found that the acid strength of the supports was a determining factor for N₂ selectivity. High N₂ selectivity was achieved on Pt/zeolites, particularly Pt/MFI. A bifunctional mechanism was proposed: the formation of the NH₄⁺ intermediate on Pt through the NO reaction with H₂ and the highly SCR of NO by ammonia on the acid sites of the supports that produces N₂ (Fig. 6.13). The acid sites on zeolites store the ammonia intermediate for the selective reaction through NO and NH₄⁺, leading to the selective formation of N₂.

Yokota et al. studied the effects of supports on the catalytic performance of Pt catalysts in NO reduction with H₂ and CO in the presence of excess oxygen [99]. They found that activities of Pt catalysts on different supports followed the order:

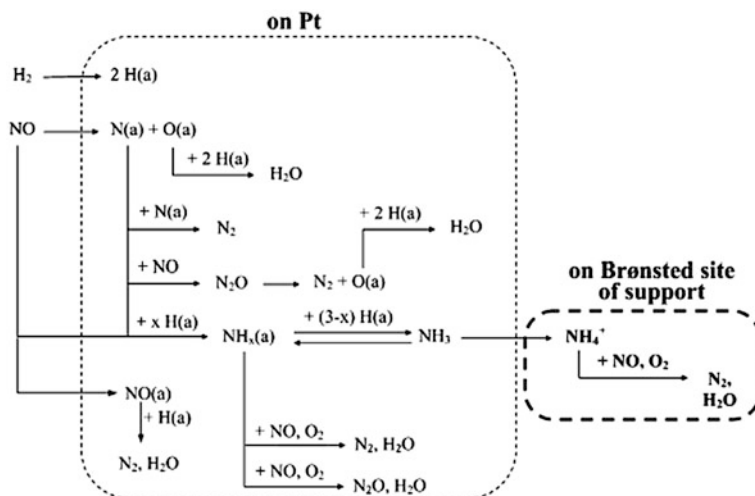


Fig. 6.13 Proposed mechanism of SCR by H_2 over Pt catalysts [102]

ZSM-5 \sim mordenite $>$ $SiO_2 > Al_2O_3$. Yokota et al. also found that the Pt/zeolite catalyst had a high activity with an N_2 selectivity of 50 %.

The promoter effect on Pt/zeolite was also investigated by Machida et al. by adding alkali or alkaline-earth metals (Na, K, Cs, Mg, Ca, Ba) to Pt/ZSM-5 [103]. The addition of Na to Pt/ZSM-5 can improve the N_2 selectivity in the low-temperature NO– H_2 reaction in excess O_2 . The adsorption of NO as NO_2^- , an intermediate to yield N_2 , was significantly increased on the Pt–Na–ZSM-5 catalyst.

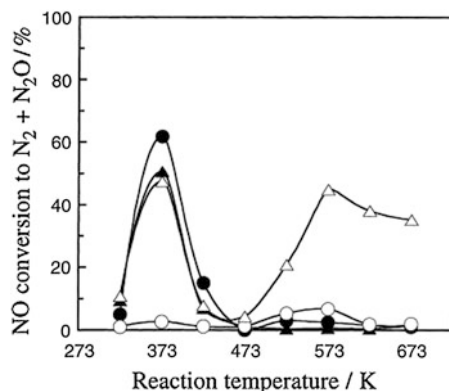
6.2.2.5 Pd/TiO₂

Ueda et al. investigated NO– H_2 reaction on Pt- and Pd-based catalysts in the presence of oxygen and moisture [104]. They were the first group to report two temperature peaks for Pd catalysts. Two conversion maxima at 373 and 573 K were observed for the supported Pd catalysts. Pd/TiO₂ demonstrated the highest conversion at 573 K among the catalysts tested (Fig. 6.14). Comparison of the rates on Pd/TiO₂ and Pt/Al₂O₃ for the competing reactions (Reactions (6.8–6.10)) disclosed a switch in the reaction pathways: direct reduction of NO by H_2 at approximately 373 K and reduction of in situ generated NO₂ by H_2 at approximately 573 K, which led to the appearance of two conversion maxima.

6.2.2.6 Pd/Ti–PILC

The catalytic reduction of NO_x with H_2 and CO in the presence of excess oxygen was studied over Pd supported on several pillared clays (PILCs) by Qi et al. [105].

Fig. 6.14 Conversion of NO into $N_2 + N_2O$ as a function of reaction temperature in the reduction of NO by H_2 over Pd and Pt catalysts. (○) Pd/ Al_2O_3 ; (△) Pd/ TiO_2 ; (●) Pt/ Al_2O_3 ; (▲) Pt/ TiO_2 . The loading amount of Pd or Pt was 1 wt.%. Reaction gas: 1,000 ppm NO, 3,000 ppm H_2 , 5 vol.% O_2 , 10 vol.% H_2O in He background at a space velocity of $20,000\text{ h}^{-1}\text{ ml g-catalyst}^{-1}$ [104]



The Pd/Ti–PILC catalyst showed high NO conversions and 90 % selectivities to N_2 at $140\text{ }^\circ\text{C}$ at $GHSV = 120,000\text{ h}^{-1}$. While the N_2 selectivity over Pd/ TiO_2 / Al_2O_3 catalyst was only 50 % under the same conditions. In contrast to the poisoning influence of CO on Pt-based catalysts, the mixed H_2 /CO feed gas significantly improved the performance of NOx reduction over Pd/Ti–PILC catalyst.

6.2.2.7 Pt/ TiO_2 – ZrO_2

Machida et al. compared a series of Pt catalysts supported on metal oxides and their binary mixtures and found that Pt supported on TiO_2 – ZrO_2 was highly active at low temperatures (Table 6.2) [98]. They studied the effect of H_2 concentration on the performance of 1 wt.% Pt/ TiO_2 – ZrO_2 catalyst in a stream of NO (0.08 vol.%)– H_2 (0.08–0.56 vol.%)– O_2 (10 vol.%) at temperatures lower than $100\text{ }^\circ\text{C}$ ($w/f = 0.24\text{ g s cm}^{-3}$). They found that the NO conversion to N_2/N_2O began at $>0.08\text{ vol.}\%$ H_2 . N_2 selectivity increased with H_2 concentration. The catalyst pretreatment is the crucial step for its performance of NO reduction; 89 % NO conversion at $90\text{ }^\circ\text{C}$ was obtained on the catalyst pre-reduced in H_2 , while a lower conversion of 50 % at $175\text{ }^\circ\text{C}$ was obtained on the catalyst treated in O_2 .

6.2.2.8 Pt/MgO– CeO_2

Costa and Efstathiou studied the activities of Pt supported on a series of metal oxides (La_2O_3 , MgO, Y_2O_3 , CaO, CeO_2 , TiO_2 , SiO_2 , and MgO– CeO_2) [106]. It was found that the 0.1 wt.% Pt/MgO– CeO_2 showed high NO conversions

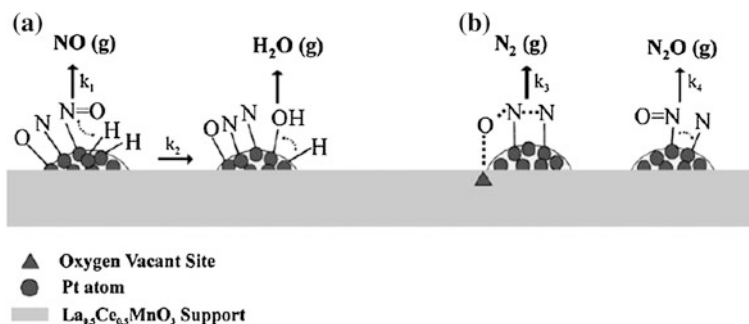


Fig. 6.15 **a** H-assisted NO desorption and dissociation mechanism and **b** N-assisted reduction mechanism of NO to N₂ and N₂O on the 0.1 wt.% Pt/La_{0.5}Ce_{0.5}MnO₃ catalyst [108]

(70–95 %) and N₂ selectivities (80–85 %) in the range of 100–200 °C with a feed stream containing 0.25 % NO, 1 % H₂, 5 % O₂, and He as balance at GHSV = 3.3×10^4 h⁻¹. In the presence of 5 % H₂O and 25–40 ppm SO₂, Pt/MgO–CeO₂ still showed >80 % N₂ selectivity. The higher N₂ selectivity observed on Pt/MgO–CeO₂ was attributed to the lower rate of H₂ combustion (1 % H₂/5 % O₂/He) on Pt/MgO–CeO₂ than that on Pt/g–Al₂O₃ and Pt/SiO₂. Hydrogen-assisted NO dissociation was considered to play an important role in the reaction [107].

6.2.2.9 Pt/La_{0.5}Ce_{0.5}MnO₃ and Pt/La_{0.7}Sr_{0.2}Ce_{0.1}FeO₃

Costa et al. also investigated 0.1 wt.% Pt supported on La_{0.5}Ce_{0.5}MnO₃ under lean-burn conditions in the range of 100–400 °C [108]. A 74 % NO conversion at 140 °C was observed on Pt/La_{0.5}Ce_{0.5}MnO₃ and a 66 % conversion at 125 °C was observed on the Pt/Al₂O₃ catalyst at a high GHSV of 80,000 h⁻¹. Pt/La_{0.5}Ce_{0.5}MnO₃ showed very high N₂ selectivities (80–90 %) in the range of 100–200 °C. As shown in Fig. 6.15, a hydrogen-assisted NO dissociation step and a nitrogen-assisted mechanism for N₂ and N₂O formation were proposed to explain the transient experiments. Similarly, a high 83 % NO conversion and a 93 % N₂ selectivity were observed on a 0.1 wt.% Pt/La_{0.7}Sr_{0.2}Ce_{0.1}FeO₃ at 150 °C [109]. In comparison, the Pt/SiO₂ catalyst only showed an 82 % NO conversion and a 65 % N₂ selectivity at 120 °C. The good performance of these catalysts was attributed to the presence of oxygen vacancies on the support surface adjacent to small platinum clusters.

6.2.2.10 Pd/TiO₂/Al₂O₃

Macleod and Lambert studied NO_x reduction with H₂ + CO under oxygen-rich conditions over Pd/TiO₂/Al₂O₃ catalyst [110]. This catalyst was found to be

Fig. 6.16 Total NO_x reduction versus temperature for 0.5 wt.% Pd/TiO₂/Al₂O₃ and 0.5 wt.% Pd/Al₂O₃. Feed contains 3,000 ppm H₂, 1,000 ppm CO, 500 ppm NO, and 5 % O₂ [110]

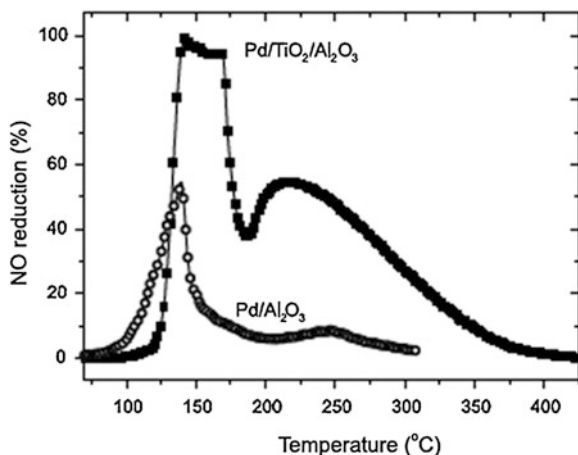
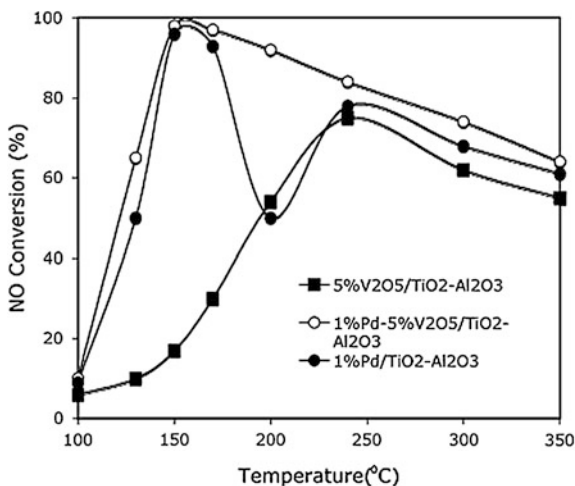


Fig. 6.17 NO conversion as a function of temperature over various catalysts. Reaction conditions: 0.1 g catalyst, total flow rate = 200 ml/min, [NO] = 500 ppm, [O₂] = 5 %, [H₂] = 4,000 ppm, He = balance [111]



capable of more than 90 % conversion of NO (at a reciprocal weight time velocity of $w/f = 0.03 \text{ g s cm}^{-3}$) at temperatures of 140–180 °C. The N₂ selectivities were higher than 70 %, while the maximum NO_x conversion was only 50 % at 140 °C over Pd/Al₂O₃ (Fig. 6.16). It is apparent that TiO₂ played a key role in the good performance of Pd/TiO₂/Al₂O₃ catalyst for NO_x reduction under oxygen-rich conditions. The oxygen vacancy generation in the TiO₂ component was proposed as one possible reason.

6.2.2.11 1 % Pd–5 % V₂O₅/TiO₂–Al₂O₃

It is noted NO_x conversion over Pd/TiO₂/Al₂O₃ catalyst was reduced to below 60 % at temperatures higher than 175 °C. However, a wider operating temperature window is required for a diesel engine exhaust stream. To meet this requirement, a 1 % Pd/5 % V₂O₅/TiO₂/Al₂O₃ catalyst was developed by Qi et al. [111]. As shown in Fig. 6.17, Qi et al. achieved a high steady-state conversion of NO (>80 %) and selectivity toward N₂ (>80 %) at reaction temperatures in the range 140–250 °C over 1 % Pd–5 % V₂O₅/TiO₂–Al₂O₃ catalyst. The addition of V₂O₅ to the initial 1 % Pd/TiO₂/Al₂O₃ catalyst effectively increased the NO conversion, especially at the temperatures around 200 °C. FTIR results further revealed that a significant amount of NH₄⁺ was formed at temperatures above 200 °C over the V₂O₅-containing catalyst, as compared to negligible NH₄⁺ observed on the V₂O₅-free catalyst. The more reactive NH₄⁺ than NH₃ explained the higher activity of the 1 % Pd–5 % V₂O₅/TiO₂–Al₂O₃ catalyst in the SCR reaction.

6.3 Challenges and Prospective

The low-temperature catalyst for SCR of NO_x from diesel engine is the key to meeting the ever-tightening emission standard, since the normal exhaust gas temperature from a diesel engine ranging from 100–250 °C for the light duty to 200–350 °C for heavy duty engines is much lower than that from a gasoline engine. Although the Cu–SSZ–13 and Cu–SAPO–34 have received extensive attention recently due to the excellent low temperature activity and high thermal durability, the demand for new catalysts with enhanced low-temperature performance is expected to remain since the diesel engine exhaust gas temperature continues to decrease when the advanced combustion technology is implemented. In addition, the sulfur poisoning still remains an issue for the Cu-based small-pore sized zeolite catalysts, even the sulfur concentration is only on the ppm level in the diesel exhaust. The weakness of the sulfur tolerance of the new Cu-based SCR catalyst is a big hurdle for its application in the developing countries, where the diesel fuel contains higher concentrations of sulfur-containing compounds. A detailed SCR reaction mechanism comparison study needs to be investigated since there is no clear interpretation to address this issue.

Up to now, the manganese-based mixed oxides have received the most attention and significant progress has been made, while the selectivity and the temperature need to further improve compared to the zeolite-based catalysts. The resistance of SO₂ on Mn-based oxides catalyst is also a big challenge for low-temperature SCR since Mn is known to be very sensitive to the sulfur. Significant efforts should be made to develop a new generation of Mn-based catalysts which can survive under the sulfur containing exhaust gas. Another approach is developing the regeneration method to recover the sulfur poisoned Mn-based catalysts. Many researchers have investigated the manganese-based mixed oxides for low-temperature

ammonia-SCR, the mechanism of the synergistic interaction between manganese and other metals still needs to be further examined.

An alternative approach for low-temperature SCR (i.e., at temperatures below 170 or 180 °C, suitable for “flue gas” applications) is H₂-SCR. Studies on H₂-SCR are relatively recent (i.e., after 1990s) and few. The few studies (<100 publications and patents) on H₂-SCR were focused on supported Pt and Pd. The H₂-SCR activities peak at around 150 °C. Needless to say, the area of H₂-SCR is in its infancy.

H₂-SCR has two significant advantages over NH₃-SCR. First, it does not have the “white powder” formation problem that plagues NH₃-SCR, particularly at low temperatures (below ~140 °C). White powder of ammonium compounds (such as bisulfate, sulfate, nitrate...) is formed in NH₃-SCR that causes equipment fouling problems. Second, H₂-SCR is devoid of the ammonia slip problem. The disadvantage of H₂-SCR is that excess H₂ (i.e., H₂/NO ratios substantially higher than the stoichiometric ratio of 2) must be used to achieve high NO conversions. Another problem with H₂-SCR is that N₂O product selectivity is generally significant. These problems, however, could be circumvented with further studies for better catalysts.

The mechanism of H₂-SCR is far less understood than that of NH₃-SCR, partly due to the competing reaction of H₂ combustion. Because of the tremendous potential for future applications of H₂-SCR, it merits more R&D efforts.

Acknowledgments We thank Drs. Sandrine Rivillon and Eric Klingenberg of Air Products and Chemicals, Inc. for helpful discussions.

References

1. Bosch H, Janssen F (1988) Catalytic reduction of nitrogen oxides: A review on the fundamentals and technology. *Catal. Today* 2: 369–532.
2. Busca G, Lietti L, Ramis G, Berti F (1998) Chemical and mechanistic aspects of the selective catalytic reduction of NO_x by ammonia over oxide catalysts: A review. *Appl. Catal. B* 18:1–36.
3. Koebel M, Elsener M, Kleemann M (2000) Urea-SCR: a promising technique to reduce NO_x emissions from automotive diesel engines. *Catal. Today* 59: 335–345.
4. Parvulescu V I, Grange P, Delmon B (1998) Catalytic removal of NO. *Catal. Today* 46: 233–316.
5. Fritz A, Pitchon V (1997) The current state of research on automotive lean NO_x catalysts. *Appl. Catal. B* 13:1–25.
6. Li J H, Chang H, Ma L, Hao J M, Yang R.T (2011) Low-temperature selective catalytic reduction of NO_x with NH₃ over metal oxide and Zeolite catalysts-A review. *Catal Today* 175: 147–156.
7. Johnson, T V (2008) Diesel emission control review. *SAE Int. J. Fuels Lubr.* 1(1): 68–81.
8. Granger P, Parvulescu V I (2011) Catalytic NO_x abatement systems for mobile sources: From three-way to lean burn after-treatment technologies. *Chem. Rev.* 111: 3155–3207.
9. Brandenberger S, Krocher O, Tissler A, Althoff R (2008) The state of the art in selective catalytic reduction of NO_x by ammonia using metal-exchanged zeolite catalyst. *Catal. Rev.* 50: 492–531.

10. Qi G, Wang Y, Yang R T (2008) Selective catalytic reduction of nitric oxide with ammonia over ZSM-5 based catalysts for diesel engine application. *Catal. Lett.* 121: 111–117.
11. Long R.Q, Yang R.T (1999) Catalytic performance of Fe-ZSM-5 catalysts for selective catalytic reduction of nitric oxide by ammonia. *J. Catal.* 188: 332–339.
12. Feng X, Hall W K (1997) FeZSM-5: A durable SCR catalyst for NO_x removal from combustion streams. *J. Catal.* 166: 368–376.
13. Chen H Y, Sachtler W M H (1998) Promoted Fe/ZSM-5 catalysts prepared by sublimation: De-NO_x activity and durability in H₂O-rich streams. *Catal. Lett.* 50: 125–130.
14. Long R Q, Yang R T (1999) SuperFe-ZSM-5 catalysts for selective catalytic reduction of nitric oxide by ammonia. *J. Am. Chem. Soc.* 121: 5595–5596.
15. Sun Q, Gao Z-X, Chen H-Y, Sachtler W M H (2001) Reduction of NO_x with ammonia over Fe/MFI: Reaction mechanism based on isotopic labeling. *J. Catal.* 20: 89–99.
16. Lobree L J, Hwang I-C, Reimer J A, Bell A T (1999) Investigations of the state of Fe in HZSM-5. *J. Catal.* 186: 242–253.
17. El-Malki E-M, van Santen R A, Sachtler W M H (2000) Active sites in Fe/MFI catalysts for NO_x reduction and oscillating N₂O decomposition. *J. Catal.* 196: 212–223.
18. Hadjiivanov K, Knözinger H, Tsyntarski B, Dimitrov L (1999) Effect of water on the reduction of NO_x with propane on Fe-ZSM-5. An FTIR mechanistic study. *Catal. Lett.* 62: 35–40.
19. Rauscher M, Kesore K, Mönning R, Schwieger W, Tißler A, Turek T (1999) Preparation of a highly active Fe-ZSM-5 catalyst through solid-state ion exchange for the catalytic decomposition of N₂O. *Appl. Catal. A* 184: 249–256.
20. Long R Q, Yang R T (2001) Fe-ZSM-5 for selective catalytic reduction of NO with NH₃: a comparative study of different preparation techniques. *Catal. Lett.* 74: 201–205.
21. Qi G, Gatt J E, Yang R T (2004) Selective catalytic oxidation (SCO) of ammonia to nitrogen over Fe-exchanged zeolites prepared by sublimation of FeCl₃. *J. Catal.* 226: 120–128.
22. Qi G, Yang R T (2005) Ultra-activity Fe/ZSM-5 catalysts for selective catalytic reduction of nitric oxide with ammonia. *Appl. Catal. B* 60: 13–22.
23. Delahay G, Valade D, Guzman-Vargas A, Coq B (2005) Selective catalytic reduction of nitric oxide with ammonia on Fe-ZSM-5 catalysts prepared by different methods. *Appl. Catal. B* 55 (2): 149–155.
24. Schwidder M, Kumar M S, Klementiev K, Pohl M M, Brückner A, Grünert W (2005) Selective reduction of NO with Fe-ZSM-5 catalysts of low Fe content I. Relations between active site structure and catalytic performance. *J. Catal.* 231: 314–330.
25. Huang H Y, Long R Q, Yang R T (2002) Kinetics of selective catalytic reduction of NO with NH₃ on Fe-ZSM-5 catalyst. *Appl. Catal. A* 235: 241–251.
26. Long R Q, Yang R T (2000) Characterization of Fe-ZSM-5 catalyst for selective catalytic reduction of nitric oxide by ammonia. *J. Catal.* 194: 80–90.
27. Long R Q, Yang R T (2001) Temperature-programmed desorption/surface reaction (TPD/TPSR) study of Fe-exchanged ZSM-5 for selective catalytic reduction of nitric oxide by ammonia. *J. Catal.* 198: 20–28.
28. Long R Q, Yang R T (2002) Reaction mechanism of selective catalytic reduction of NO with NH₃ over Fe-ZSM-5 catalyst. *J. Catal.* 207: 224–231.
29. Richter M, Eckelt R, Parlitz B, Fricke R (1998) Low-temperature conversion of NO to N₂ by zeolite-fixed ammonium ions. *Appl. Catal. B* 15: 129–146.
30. Stevenson S A, Vartuli J C, Sharma, S B (2002) The effects of steaming and sodium exchange on the selective catalytic reduction of NO and NO₂ by NH₃ over HZSM-5. *J. Catal.* 208: 106–113.
31. Hensen E J M, Zhu Q, Hendrix M, Overweg A R, Kooyman P J, Sychev M V, van Santen, R A (2004) Effect of high-temperature treatment on Fe/ZSM-5 prepared by chemical vapor deposition of FeCl₃. I. Physicochemical characterization. *J. Catal.* 221 (2): 560–574.
32. Busca G, Larrubia M A, Arrighi L, Ramis G (2005) Catalytic abatement of NO_x: Chemical and mechanistic aspects. *Catal Today* 107-108: 139–148.

33. Joyner R, Stockenhuber M (1999) Preparation, characterization, and performance of Fe-ZSM-5 catalysts. *J. Phys. Chem. B* 103 (29): 5963–5976.
34. Joyner R W, Stockenhuber M (1997) Unusual structure and stability of iron-oxygen nano-clusters in Fe-ZSM-5 catalysts. *Catal. Lett.* 45 (1–2): 15–19.
35. Heinrich F, Schmidt C, Löffler E, Menzel M, Grunert, W. (2002) Fe-ZSM-5 catalysts for the selective reduction of NO by isobutane—the problem of the active sites. *J. Catal.* 212 (2): 157–172.
36. Krishna K, Makkee M (2006) Preparation of Fe-ZSM-5 with enhanced activity and stability for SCR of NO_x. *Catal. Today* 114 (1): 23–30.
37. Hensen E J M, Zhu Q, van Santen R A (2003) Extraframework Fe-Al-O species occluded in MFI zeolite as the active species in the oxidation of benzene to phenol with nitrous oxide. *J. Catal.* 220 (2): 260–264.
38. Brandenberger S, Kröcher O, Tissler A, Althoff R (2010) The determination of the activities of different iron species in Fe-ZSM-5 for SCR of NO by NH₃. *Appl. Catal B* 95:348–357.
39. Devadas M, Krocher O, Elsener M, Wokaun A, Soger N, Pfeifer M, Demel Y, Musmann L (2006) Influence of NO₂ on the selective catalytic reduction of NO with ammonia over Fe-ZSM5. *Appl. Catal. B* 67 (3–4): 187–196.
40. Rahkamaa-Tolonen K, Maunula T, Lomma M, Huuhtanen M, Keiski R L (2005) The effect of NO₂ on the activity of fresh and aged zeolite catalysts in the NH₃-SCR reaction. *Catal. Today* 100 (3–4): 217–222.
41. Schmieg S J, Lee J H (2005) Evaluation of supplier catalyst formulations for the selective catalytic reduction of NO_x with ammonia. SAE-2005-01-3881.
42. Amiridis M D, Puglisi F, Dumesic J A, Millman W.S, Topsoe N.Y (1993) Kinetic and infrared spectroscopic studies of Fe-Y zeolites for the selective catalytic reduction of nitric-oxide by ammonia. *J. Catal.* 142 (2): 572–584.
43. Eng J, Bartholomew C H (1997) Kinetic and mechanistic study of NO_x reduction by NH₃ over H-form zeolites. 1. Kinetic and mechanistic insights into NO reduction over H-ZSM-5. *J. Catal.* 171 (1): 14–26.
44. Choi E Y, Nam I S, Kim Y G (1996) TPD Study of mordenite-type zeolites for selective catalytic reduction of NO by NH₃. *J. Catal.* 161 (2): 597–604.
45. Stevenson S A, Vartuli J C, Brooks, C F (2000) Kinetics of the selective catalytic reduction of NO over HZSM-5. *J. Catal.* 190 (2): 228–239.
46. Eng J, Bartholomew C H (1997) Kinetic and mechanistic study of NO_x reduction by NH₃ over H-form zeolites. 2. Semi-steady-state and in situ FTIR studies. *J. Catal.* 171 (1): 27–44.
47. Long R Q, Yang R T (2002) Reaction mechanism of selective catalytic reduction of NO with NH₃ over Fe-ZSM-5 catalyst. *J. Catal.* 207: 224–231.
48. Kefirov R, Penkova A, Hadjiivanov K, Dzwigaj S, Che M (2008) Stabilization of Cu⁺ ions in BEA zeolite: Study by FTIR spectroscopy of adsorbed CO and TPR. *Micro. Meso. Mater.* 116: 180–187.
49. Brandenberger S, Kröcher O, Tissler A, Althoff R (2008) The state of the art in selective catalytic reduction of NO_x by ammonia using metal-exchanged zeolite catalysts. *Catal. Rev. Sci. Eng.* 50: 492–531.
50. Bull I, Xue W M, Burk P, Boorse R S, Jaglowski W M, Koermer G S, Moini A, Patchett J A, Dettling J C, Caudle M T (2009) US Patent 7,610,662.
51. Kwak J H, Tonkyn R G, Kim D H, Szanyi J, Peden C H F (2010) Excellent activity and selectivity of Cu-SSZ-13 in the selective catalytic reduction of NO_x with NH₃. *J. Catal.* 275: 187–190.
52. Ishihara T, Kagawa M, Hadama F, Takita Y, (1997) Copper ion-exchanged SAPO-34 as a thermostable catalyst for selective reduction of NO with C₃H₆. *J. Catal.* 169:93–102.
53. Fickel D W, D'Addio E, Lauterbach J A, Lobo R F (2011) The ammonia selective catalytic reduction activity of copper-exchanged small-pore zeolites. *Appl. Catal. B* 102: 441–448.
54. Wang L, Li W, Qi G (2012) Location and Nature of Cu Species in Cu/SAPO-34 for selective catalytic reduction of NO with NH₃. *J. Catal.* 289: 21–29.

55. Kang M, Park E D, Kim J M, Yie J E (2007) Manganese oxide catalysts for NO_x reduction with NH₃ at low temperatures. *Appl. Catal. A* 327: 261–269.
56. Wu Z, Jiang B, Liu Y (2008) Effect of transition metals addition on the catalysts of manganese/titania for low temperature selective catalytic reduction of nitric oxide with ammonia. *Appl. Catal. B* 79: 347–355.
57. Stanculescu M, Caravaggio G, Dobri A, Moir J, Burich R, Charland J-P, Bulsink P (2012) Low-temperature selective catalytic reduction of NO_x with NH₃ over Mn-containing catalysts. *Appl. Catal. B* 123-124: 229–240.
58. Chen Z, Yang Q, Li H, Li X, Wang L, Tsang S C (2010) Cr-Mn mixed-oxide catalyst for selective catalytic reduction of NO_x with NH₃ at low temperature. 276: 56–65.
59. Sultana A, Sasaki M, Hamada H (2012) Influence of support on the activity of Mn supported catalysts for SCR of NO with ammonia. *Catal. Today* 185: 284–289.
60. Tang X, Hao J, Yi H, Li J (2007) Low-temperature SCR of NO with NH₃ over AC/C supported manganese-based monolithic catalysts. *Catal. Today* 126:406–411.
61. Marban G, Valdes-Solis T, Fuertes A B (2004) Mechanism of low-temperature selective catalytic reduction of NO with NH₃ over carbon-supported Mn₃O₄: Role of surface NH₃ species: SCR mechanism. *J. Catal.* 226: 138–155.
62. Qi G, Yang R T (2004) Characterization and FT-IR studies of MnO_x-CeO₂ catalyst for low temperature SCR of NO with NH₃. *J. Phys. Chem. B.* 108:15738–15747.
63. Qi G, Yang R T (2003) A superior catalyst for low-temperature NO reduction with NH₃. *Chem. Comm.* 848–849.
64. Qi G, Yang R T (2003) Performance and kinetics study for low temperature SCR of NO with NH₃ over MnO_x-CeO₂ catalyst. *J. Catal.* 217: 434–441.
65. Qi G, Yang R T (2003) Low-temperature selective catalytic reduction of NO with NH₃ over iron and manganese oxides supported on titania. *Appl. Catal. B.* 44: 217–225.
66. Qi G, Yang R T, Chang R (2005) MnO_x-CeO₂ mixed oxides prepared by co-precipitation for selective catalytic reduction of NO with NH₃ at low temperature. *Appl. Catal. B.* 51:93–106.
67. Qi G, Yang R T, Chang R (2003) Low temperature SCR of NO with NH₃ over USY-supported manganese-oxide-based catalysts. *Catal. Lett.* 87: 67–71.
68. Kapteijn F, Singoredjo L, Andreini A, Moulijn J A (1994) Activity and selectivity of pure manganese oxides in the selective catalytic reduction of nitric oxides with ammonia. *Appl. Catal. B* 3: 173–189.
69. Tang X, Li J H, Sun L, Hao J M (2010) Origination of N₂O from NO reduction by NH₃ over β-MnO₂ and α-Mn₂O₃. *Appl. Catal. B* 99: 156–162.
70. Long R Q, Yang R T (2002) Low temperature selective catalytic reduction (SCR) of NO with NH₃ over Fe-Mn based catalysts. *Chem. Commun.* 5: 452–453.
71. Machida M, Kurogi D, Kijima T (2000) MnO_x-CeO₂ binary oxides for catalytic NO_x-sorption at low temperatures. *Chem. Mater.* 12: 3165–3170.
72. Murugan B, Ramaswamy A V (2005) Nature of manganese species in Ce_{1-x}Mn_xO_{2-δ} solid solution synthesized by the solution combustion route. *Chem. Mater.* 17: 3983–3993.
73. Wu X, Lin F, Xu H, Weng D (2010) Effects of adsorbed and gaseous NO_x species on catalytic oxidation of diesel soot with MnO_x-CeO₂ mixed oxides. *Appl. Catal. B* 96: 101–109.
74. Imamura S, Shono M, Okamoto N, Hamada A, Ishida S (1996) Effect of cerium on the mobility of oxygen on manganese oxides. *Appl. Catal. A* 142: 279–288.
75. Casapu M, Krocher O, Mehring M, Nachttegaal M, Borca C, Harfouche M, Grolimund D (2010) Characterization of Nb-containing MnO_x-CeO₂ catalyst for low temperature selective catalytic reduction of NO with NH₃. *J. Phys. Chem. C* 114: 9791–9801.
76. Chen H, Sayari A, Adnot A, Larachi F (2001) Composition-activity effects of Mn-Ce-O composites on phenol catalytic wet oxidation. *Appl. Catal. B* 32: 195–204.
77. Liang Q, Wu X, Weng D, Xu H (2008) Oxygen activation on Cu/Mn-Ce mixed oxides and the role in diesel soot oxidation. *Catal. Today* 139: 113–118.

78. Kang M, Park E D, Kim J M, Yie J E (2006) Cu-Mn mixed oxides for low temperature NO reduction with NH_3 . *Catal. Today* 111: 236–241.
79. Chen Z, Yang Q, Li H, Li X, Wang L, Tsang S C (2010) Cr-MnO_x mixed-oxide catalysts for selective catalytic reduction of NO_x with NH_3 at low temperature. *J. Catal.* 276: 56–65.
80. Ding Z Y, Wade L X D, Gloyna E (1998) Supercritical water oxidation of NH_3 over a MnO₂/CeO₂ catalyst. *Ind. Eng. Chem. Res.* 37: 1707–1716.
81. Tang X, Chen J, Huang X, Xu Y, Shen W (2008) Pt/MnO_x-CeO₂ catalyst for the complete oxidation of formaldehyde at ambient temperature. *Appl. Catal. B* 81:115–121.
82. Van der Grift C J G, Woldhuis A F, Maaskant O L (1996) The shell DENO_x system for low temperature NO_x removal. *Catal. Today* 27: 23–27.
83. Wong W C, Nobe K (1986) Reduction of NO with NH_3 on Al₂O₃ and TiO₂-supported metal oxide catalysts. *Ind. Eng. Chem. Res.* 25: 179–186.
84. Kobayashi M, Kuma R, Morita A (2006) Low temperature selective catalytic reduction of NO by NH_3 over V₂O₅ supported on TiO₂-SiO₂-MoO₃. *Catal. Lett.* 112: 37–44.
85. Martin J A, Yates M, Avila P, Suarez S, Blanco J (2007) Nitrous oxide formation in low temperature selective catalytic reduction of nitrogen oxides with V₂O₅/TiO₂ catalysts. *Appl. Catal. B* 70: 330–334.
86. Singoredjjo L, Korver R, Kapteijn, Mounlijn J (1992) Alumina supported manganese oxides for the low-temperature selective catalytic reduction of nitric oxide with ammonia. *Appl. Catal. B* 1: 297–316.
87. Li J, Chen J, Ke R, Luo C, Hao J (2007) Effects of precursors on the surface Mn species and the activities for NO reduction over MnO_x/TiO₂ catalysts. *Catal. Commun.* 8: 1896–1900.
88. Wu Z, Jiang B, Liu Y (2008) Effect of transition metals addition on the catalyst of manganese/titania for low-temperature selective catalytic reduction of nitric oxide with ammonia. *Appl. Catal. B* 79: 347–355.
89. Pena D A, Uphade B S, Smirniotis P G (2004) TiO₂-supported metal oxide catalyst for low-temperature selective catalytic reduction of NO with NH_3 . I Evaluation and characterization of first row transition metals. *J. Catal.* 221: 421–431.
90. Kim Y J, Kwon H J, Heo I, Nam I-S, Cho B K, Choung J W, Cha M-S, Yeo G K (2012) Mn-Fe/ZSM-5 as a low-temperature SCR catalyst to remove NO_x from diesel engine exhaust. *Appl. Catal. B* 126: 9–21.
91. Casapu M, Krocher O, Elsener M (2009) Screening of doped MnO_x-CeO₂ catalysts for low-temperature NO-SCR. *Appl. Catal. B* 88: 413–419.
92. Yu J, Guo F, Wang Y, Zhu J, Liu Y, Su F, Gao S, Xu G (2010) Sulfur poisoning resistant mesoporous Mn-based catalyst for low-temperature SCR of NO with NH_3 . *Appl. Catal. B* 95: 160–168.
93. Kijlstra W S, Brands D S, Smit H I, Poels E K, Blik A (1997) Mechanism of the selective catalytic reduction of NO by NH_3 over MnO_x/Al₂O₃ II. Reactivity of adsorbed NH_3 and NO complexes. *J. Catal.* 171: 219–230.
94. Marban G, Valdes-Solis T, Fuertes A B (2004) Mechanism of low-temperature selective catalytic reduction of NO with NH_3 over carbon-supported Mn₃O₄: Role of surface NH_3 species: SCR mechanism. *J. Catal.* 226: 138–155.
95. Tronconi E, Nova I, Ciardelli C, Chatterjee D, Weibel M (2007) Redox features in the catalytic mechanism of the standard and fast NH_3 -SCR of NO_x over a V-based catalysts investigated by dynamix methods. *J. Catal.* 245: 1–10.
96. Taylor K C (1984) “Automotive Catalytic Converters,” Springer-Verlag, Berlin and New York.
97. Burch R, Coleman M D (1999) An investigation of the NO/H₂/O₂ reaction on noble-metal catalysts at low temperatures under lean-burn conditions. *Appl. Catal. B* 23: 115–121.
98. Machida M, Ikeda S, Kurogi D, Kijima T (2001) Low temperature catalytic NO_x-H₂ reactions over Pt/TiO₂-ZrO₂ in an excess oxygen. *Appl. Catal. B* 35: 107–116.
99. Yokota K., Fukui M, Tanaka T (1997) Catalytic removal of nitric oxide with hydrogen and carbon monoxide in the presence of excess oxygen. *Appl. Surf. Sci.* 121-122: 273–277.

100. Burch R, Coleman M D (2002) An Investigation of Promoter Effects in the Reduction of NO by H₂ under Lean-Burn Conditions. *J. Catal.* 208: 435–447.
101. Wu P, Li L, Yu Q, Wu G, Guan N (2010) Study on Pt/Al-MCM-41 for NO selective reduction by hydrogen. *Catal. Today* 158: 228–234.
102. Shibata J, Hashimoto M, Shimizu K, Yoshida H, Hattori T, Satsuma A (2004) Factors Controlling Activity and Selectivity for SCR of NO by Hydrogen over Supported Platinum Catalysts. *J. Phys. Chem. B* 108: 18327–18335.
103. Machida M, Watanabe T (2004) Effect of Na-addition on catalytic activity of Pt-ZSM-5 for low-temperature NO–H₂–O₂ reactions. *Appl. Catal. B* 52: 281–286.
104. Ueda A, Takayuki N, Masashi A, Kobayashi T (1998) Two conversion maxima at 373 and 573 K in the reduction of nitrogen monoxide with hydrogen over Pd/TiO₂ catalyst. *Catal. Today* 45: 135–138.
105. Qi G, Yang R T, Thompson L T (2004) Catalytic reduction of nitric oxide with hydrogen and carbon monoxide in the presence of excess oxygen by Pd supported on pillared clay. *Appl. Catal. A* 259: 261–267.
106. Costa C N, Efstathiou A M (2007) Low-temperature H₂-SCR of NO on a novel Pt/MgO–CeO₂ catalyst. *Appl. Catal. B* 72: 240–252.
107. Hecker W C, Bell A T (1985) Reduction of NO by H₂ over silica-supported rhodium: Infrared and kinetic studies. *J. Catal.* 92: 247–259.
108. Costa C N, Stathopoulos V N, Belessi V C, Efstathiou A M (2001) An Investigation of the NO/H₂/O₂ (Lean-deNO_x) Reaction on a Highly Active and Selective Pt/La_{0.5}Ce_{0.5}MnO₃ Catalyst. *J. Catal.* 197: 350–364.
109. Costa C N, Savva P G, Andronikou C, Lambrou P S, Polychronopoulou K, Belessi V C, Stathopoulos V N, Pomonis P J, Efstathiou A M (2002) An Investigation of the NO/H₂/O₂ (Lean De-NO_x) Reaction on a Highly Active and Selective Pt/La_{0.7}Sr_{0.2}Ce_{0.1}FeO₃ Catalyst at Low Temperatures. *J. Catal.* 209: 456–471.
110. Macleod N, Lambert R M (2002) Low-temperature NO_x reduction with H₂ + CO under oxygen-rich conditions over a Pd/TiO₂/Al₂O₃ catalyst. *Catal. Commun.* 3: 61–65.
111. Qi G, Yang R T, Rinaldi F C (2006) Selective catalytic reduction of nitric oxide with hydrogen over Pd-based catalysts. *J. Catal.* 237: 381–392.

Part III
Mechanistic Aspects

Chapter 7

Active Sites for Selective Catalytic Reduction

Wolfgang Grünert

7.1 Introduction

The “active site” is a central concept in catalyst research introduced by H. S. Taylor in 1925 [1]. It describes an ensemble of atoms in a solid surface which takes part in the rate-limiting step of a catalytic reaction mechanism. This is the stage on which the catalytic reaction spectacle plays, traditionally as thought without yet the actors. The practical importance of knowing the active site is obvious: once its structure is determined one can search for routes to prepare it in larger abundance for making better catalysts. It is important to note that solid surfaces are dynamic and respond to the properties of the reaction medium. Therefore, the actual active sites are often formed from precursor structures only under reaction conditions, and there are even cases where they disappear when these conditions are changed beyond certain limits (e.g., carbided Pd surface layers for selective hydrogenation of dienes [2]). Still, the active site concept describes only the solid-state aspect of the full picture, but the example shows that active sites can be reliably identified only under real reaction conditions.

This adds yet another aspect of complexity to a task which is challenging in itself: the search for the active sites. Catalysis occurs on metastable structures rather than on idealized stable surfaces, which usually offer low activities (=reaction rates related to surface area under specified conditions as temperature and reactant composition). We have to look for defect sites, for atomic arrangements to be found only on small particles, on interaction structures with a second component, e.g., a support or a promoter. Usually, the arrangement of atoms requested by the catalytic reaction is not the only one exposed by the catalytic element. The coexistence of the active sites with indifferent structures or even with sites catalyzing the same reaction with different activation energy and, therefore

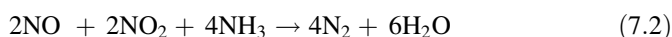
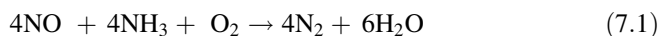
W. Grünert (✉)

Laboratory of Industrial Chemistry, Ruhr University Bochum, D-44801 Bochum, Germany
e-mail: w.gruenert@techem.rub.de

capable of dominating the catalytic behavior in a different temperature range, offers a considerable methodical challenge to any research effort.

Obviously, the search for the active sites of a reaction is a very involved task requiring the concerted application of various techniques to well-selected catalytic materials, desirably under reaction conditions. Even then progress toward reliable identification of the responsible structures may be slow due to the complexity of the catalytic surfaces. There is, however, an additional rationale for such research, because the data generated are often of considerable value for practical catalyst development. Therefore, the literature is full of opinions about active sites on catalysts for various reactions, which may be everything from well-supported proposals down to mere speculation.

The present report gives a critical overview on the state of knowledge about active sites for SCR of NO by ammonia over the most important catalysts known today. As indicated in earlier chapters, this actually involves two reactions—standard SCR (reduction of NO by NH₃ in presence of O₂, Eq. (7.1)) and fast SCR (reduction of equimolar NO/NO₂ mixtures by NH₃, in presence or absence of O₂, Eq. (7.2)). Due to recent discussions on reaction mechanisms (see Chaps. 8 and 9), the oxidation of NO to NO₂ (Eq. 7.3) will be briefly considered as well.



Initially, a short overview over the methodology used in pertinent studies will be given. The subsequent discussion will focus on the traditional V₂O₅–WO₃/TiO₂ system and on zeolites modified with transition-metal ions (“TMI”) as Fe and Cu, and only briefly touch upon new catalyst systems on the basis of Mn or Ce. The questions to be answered concern mainly the structure of the redox sites: Are they isolated TMI sharing oxygen bridges only with the support, or are they surface bound oligomers, islands, three-dimensional clusters? How does the promoter operate? Is there an influence of cation exchange positions in zeolites on activity? Is there a primary role of acidity, e.g., Brønsted sites being part of the active site, or does acidity just increase local NH₃ concentrations?

7.2 Strategies and Methods for the Identification of Active Sites

Active sites can be identified if there is a correlation between the abundance of the corresponding structural motif in a catalyst type (desirably detected under reaction conditions) and the catalytic activity. To identify such relations, one has to apply suitable methods for the structural analysis of disordered material (geometrical and

electronic structure) to either a series of catalysts which offers the whole variety of candidate species in sufficiently different concentrations, or to one catalyst on which this variety can be produced by chemical manipulations (e.g., sinter series). The resulting structural data have to be correlated to meaningful reaction rate data from all these materials. Therefore, the most popular structure characterization techniques will be reviewed in the following with respect to their potential for this kind of study. For the basics of these methods, the reader is referred to the pertinent introductory and advanced literature [3–7]. In such studies, situations may be encountered where two or more different species types are obtained in similar ratios in all preparations applied and therefore cannot be discriminated with respect to their catalytic relevance. Transient approaches suitable for such situation will be briefly outlined as well.

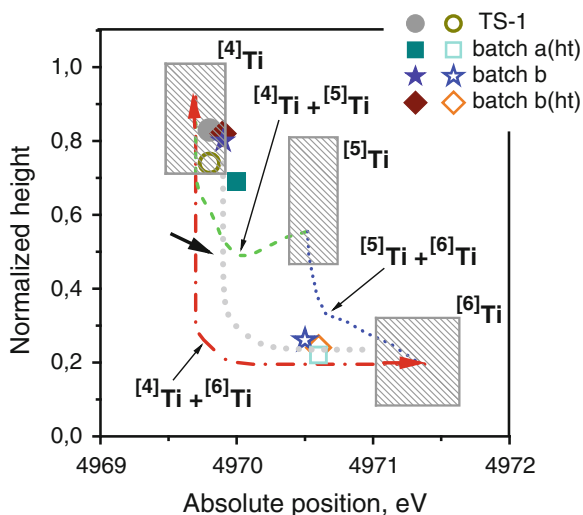
Although an ever growing choice of spectroscopic, diffraction, imaging, and sorption techniques are available to the catalytic scientist, none of them is really well adapted to the problem to be solved here. Therefore, studies on active sites generally employ a multitude of methods. Catalysis is a surface phenomenon, but hardly any technique is ideally surface sensitive—with the exception of adsorption methods, IR spectroscopy if performed on interacting probe molecules, and Ion Scattering Spectroscopy¹ (ISS). However, methods probing near surface regions or even the bulk of the material may be still of great value for the identification of active sites when the signals detected are dominated by information from the surface due to a high or even atomic dispersion of the phases under study. This tends, however, to exclude diffraction techniques, in particular XRD, because coherence lengths available from such disperse phases will fall short of those required for achieving detectable diffraction signals.

Despite impressive progress in resolution and contrast utilization, *imaging methods* like electron microscopy or scanning probe microscopy play only a supporting role in active site studies. Although atomic details of real surfaces can now be made visible, the quantification of sites for correlation with activity and the statistical significance of the small assay remain problematic. Imaging, however, can be extremely helpful for the interpretation of data from statistically more representative though more indirect techniques. Examples are the visualization of morphological changes in Cu particles interacting with ZnO at different redox potentials [8], which had been predicted on the basis of EXAFS data [9, 10], and the detection of surface amorphization of a mixed Mo–V–Te–Nb phase during selective propane oxidation [11, 12], which had been previously observed by XPS (in situ [12] and under vacuum [11, 13, 14]) just as deviations between surface and bulk compositions.

X-Ray absorption fine structure (XAFS) is a powerful technique for the study of active sites, but certain limitations have to be taken into account. It is an averaging method: information arising from all kinds of species formed by the element of

¹ Alternative designation—Low-energy Ion Scattering (LEIS).

Fig. 7.1 Analysis of Ti coordination geometry by TiK pre-edge signal position and intensity [15], applied to a mesoporous material with expected TS-1 wall structure. Ti in three batches is tetrahedrally coordinated in dehydrated state (*full symbols*), but almost completely sixfold in hydrated state (*open symbols*), except for the hydrophobic crystalline TS-1. Reproduced from [19] with permission of Elsevier



interest is superimposed. If the spectra of the candidate species are known, this superposition can in principle be used for a quantitative analysis of species concentrations. This is often done for the *Near-Edge* region (XANES) which reflects only the first coordination sphere, but it is much more complicated for the *Extended X-Ray* absorption fine structure (EXAFS) which usually probes structure to larger distances. It has been sometimes disregarded that coordination numbers extracted from EXAFS fits must not be used to construct the typical coordination sphere of an element if the latter has formed more than one species type. In such situation, which can be sometimes but not always diagnosed from the XANES, EXAFS can still provide valuable information, which is however less reliable and quantitative. The potential of the XANES to give access to the distribution of oxidation states or coordination geometries (pre-edge signals of first-row TM ions, e.g., Ti [15], V [16], Fe [17, 18]) is often used to characterize the state of an element in *in situ* or *operando* studies during catalytic reactions. Figure 7.1 shows an example dealing with ordered mesoporous materials the walls of which were claimed to consist of titania silicate TS-1 nanoslabs [19]. Position and intensity of the pre-edge peak confirmed the tetrahedral coordination of the Ti while the decay and shift of this signal upon hydration (unlike with the hydrophobic crystalline TS-1 reference) proved its accessibility.

The recent development of wavelength differentiating fluorescence detection (HERFD—high energy resolution fluorescence detection) together with the increased brilliance of synchrotron sources has initiated large progress in the differentiation of coexisting species by X-Ray absorption methods (reviewed in [20]). Detection of spectra using fluorescence lines with small lifetime broadening (K_{β}) instead of intensity in a broad energy range permits more detail to be seen in the chemical sensitive pre-edge features. If there are sufficient differences between the K_{β} fluorescence signals of species involved, EXAFS spectra predominantly

reflecting the coordination sphere of one or the other site can be acquired by appropriate setting of the detector. The measurement of fluorescence spectra tuning the excitation energy through the energy range of a XANES (RIXS—Resonant Inelastic X-Ray Scattering) creates a two-dimensional array offering rich structural information. The broader introduction of these techniques into catalyst research bears great promise for the structural analysis of real systems.

Another interesting version of XAS suitable for active site studies is soft X-Ray absorption spectroscopy. The L edges of first-row transition metals often bear a considerable diagnostic potential for the identification of oxidation states and coordinations, which at present is largely disregarded in catalysis research.

X-Ray photoelectron spectroscopy (XPS) is well known as a method for quantitative determination of surface compositions, including the differentiation of oxidation states of elements. While being primarily an elemental analysis, its potential to diagnose coordination geometries is weak although such conclusions may be sometimes indirectly drawn from the identification of surface compounds. Such analysis is often possible by combining binding energies of XPS lines with the kinetic energies of X-Ray-induced Auger lines that appear as a by-product of the photoemission process (Auger parameter). The information provided by conventional XPS may be highly relevant for active site studies although it does not characterize the external surface layer but averages over a near-surface region of a few nanometer thickness. The ultra-high vacuum requirement of the method, however, is a clear disadvantage. The advent of an in-situ version of XPS (APPES—ambient pressure photoelectron spectroscopy), where spectra can be measured under some millibar pressure at the sample, was therefore a breakthrough [21]. It has been made possible by combining differential pumping stages, which had been long known, with electron lenses [22] as indicated in Fig. 7.2.

Regarding vibrational methods, the potential of *Raman spectroscopy* to analyze surface oxide phases has been widely applied to supported oxide catalysts [23], in particular with Raman-inactive supports. Resonance Raman spectroscopy, which involves excitation of Raman spectra at wavelengths where species present exhibit an absorption maximum, offers additional opportunities for structural characterization. *IR spectroscopy* where the region of lattice vibrations used for such purpose is too complex to be productive, is highly useful for the detection of adsorbates and reaction intermediates. However, the characterization of surface structures by IR spectroscopy of probe molecules, e.g., of acidic sites by adsorbed N bases, has been a long tradition as well. Probe molecules can trace the degree of coordinative unsaturation of surface species as demonstrated, e.g., in classical studies of the Zecchina group on the characterization of supported Cr oxide species ([24] and subsequent series of publications). Their ability to discriminate between cationic adsorption sites allowed creating the experimental basis for the CoMoS model of promoter interaction in hydrodesulfurization catalysts [25]. The potential of CO to differentiate between different oxidation states of an element [26, 27] has been often applied as well. In reactions involving CO, it has been used to directly probe the exposure of different species to the reaction atmosphere, including the response of the active site distribution to changes of reaction conditions [27].

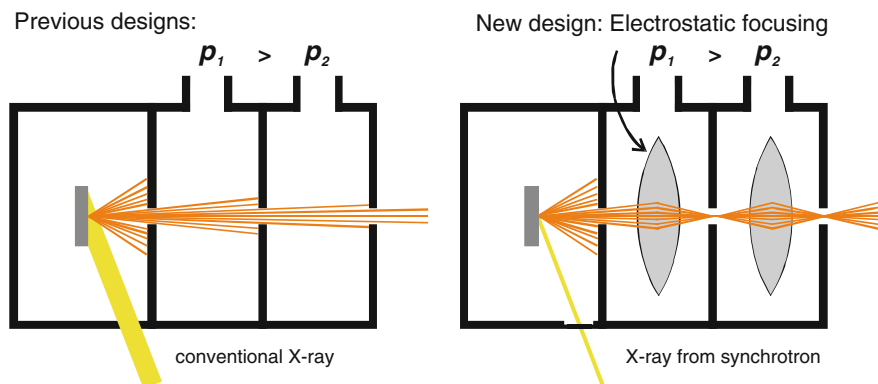


Fig. 7.2 Ambient pressure photoelectron spectroscopy: combination of differential pumping with electron optics to allow for realistic photoelectron yield from in situ cells. Reproduced from [21] with permission from Elsevier

Absolute concentrations are, however, often difficult to establish due to the lack of information on extinction coefficients and due to different adsorption probabilities under the prevailing conditions. Instructive examples for research along these lines are the observation of Cu–Zn interactions in working methanol synthesis catalysts [28] and of coexistence of metal and ionic Ru sites in alumina-supported Ru catalysts for partial oxidation of methane [29].

UV–Vis spectroscopy is another technique often used in active site studies. In the visible region, the d–d transitions are related to valence states and coordination geometries (ligand field symmetries) of cations, at shorter wavelengths ligand-to-metal charge-transfer transitions between filled orbitals with mainly ligand character and empty cation states appear, which are sensitive to the aggregation degree of the corresponding phase. While UV–Vis spectroscopy is popular as an in situ technique and yields to quantification more readily than IR spectroscopy, its limitations are related to the considerable width of the signals and to problems with line superposition and interpretation (cf. “Fe Zeolites” section).

EPR spectroscopy detects species with magnetic moments arising from electron spins, often with extraordinary sensitivity. Among them, signals from systems with an even number of unpaired spins can be obtained only at very low temperatures due to short relaxation times. EPR signals of isolated cations bear information about the symmetry of their ligand field, the identity of the cations can be judged upon by a hyperfine splitting if there is a nuclear momentum, sometimes by the signal position (g values). Disordered aggregates of paramagnetic sites cause interaction broadening of signals down to complete loss of intensity, whereas ordered arrays may lead to exchange narrowing. Collective spin coupling phenomena may be identified by measuring spectra in a wide temperature range. This is exemplified in Fig. 7.3 by comparing the temperature dependence of the EPR spectra of three Fe–ZSM–5 catalysts, where the isotropic signal at $g' = 2$ increases

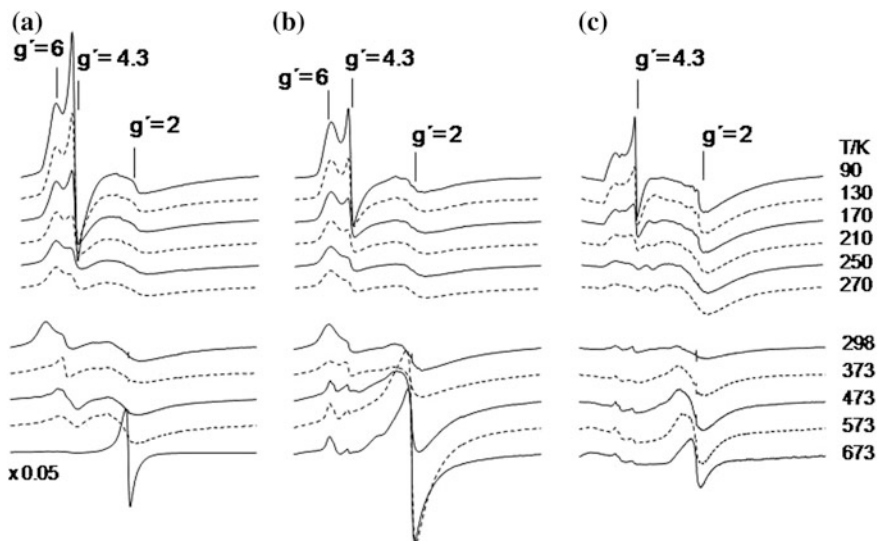


Fig. 7.3 Temperature dependence of EPR spectra of Fe-ZSM-5 catalysts prepared from H-ZSM-5 and FeCl₃ via different routes. **a** Solid-state ion exchange, **b** Chemical vapor deposition, **c** Mechanochemical treatment. The intensity variation of the signal at $g' = 2$ measured above the Neel temperature (e.g., at 673 K) indicates the clustering degree of the Fe-oxide phase. Reproduced from [30] with permission of Elsevier

to different extents at high temperatures indicating different clustering degrees of the Fe-oxide aggregates present [30].

EPR intensities are proportional to spin concentrations as long as the spins are not interacting very intensely. Quantitative analysis requires double integration of the signals and the availability of reliable spin standards. It is prone to uncertainties and therefore rarely performed. EPR is often used to characterize systems composed of d^0 ions by measuring the signals of d^1 defects which occur in the d^0 phases for entropy reasons. While this is a very useful approach, one should be cautious with quantitative conclusions because the percentage of defects is unknown and may vary among the phases present. EPR can be also performed in situ and even *operando*, provided the heating of the sample can be made without interference with the microwave field required for the measurements. The technique is described in [31].

Similar to EPR, solid-state *NMR spectroscopy* has a limited range of applications, which is defined by the magnetic moment of the corresponding elemental nuclei. While EPR may detect extremely low concentration of paramagnetic sites, NMR has sometimes sensitivity problems, in particular in the case of nuclei with low natural abundance, e.g., ¹³C or ¹⁵N. There are, however, various techniques for signal enhancement, the best known being cross-polarization where magnetization is transferred from an abundant to a dilute spin site. Information on coordination geometries, which is encoded in the g tensor in EPR, is eliminated in solid-state

NMR by the magic angle spinning technique: the NMR parameters achieved are scalars. NMR signals are greatly perturbed if there is an unpaired electron at the atom of interest.

Nevertheless, solid-state NMR can be useful for active site studies, which is nowadays predominantly employed for acid catalysis, e.g., with zeolites [32]. Chemical shifts obtained are related to the electronic state of the atom: ^1H -NMR data have been, for instance, used to determine acidity of Brønsted sites in zeolites, ^{51}V NMR can discriminate V^{5+} in various environments in supported catalysts [33]. As long as the sites are sufficiently dilute, NMR intensity is directly related to concentration. Structural information is accessible by echo techniques which allow determining distances between spin sites. By analogy with IR methodology, adsorption sites have been investigated with probe molecules also in NMR studies. While work with N bases may require isotopic enrichment of the probe, there are opportunities to detect subtle structural features by cross-polarization and double-resonance (e.g., $^{14}\text{N}/^{27}\text{Al}$) techniques [34].

The in-situ application of solid-state NMR requires heating and temperature control of the spinning sample. Techniques available for this purpose are reviewed in [35]. The method is applied preferentially for mechanistic rather than for active site studies, but the former often result in indirect conclusions on the sites involved in the detected reaction mechanisms [32].

Moessbauer spectroscopy is readily applicable only for a few elements that exhibit suitable low-energy nuclear transitions on which the method is based—to Fe, Sb, and Sn. For measurements with Ru, Ir, Pt, and Au, one faces a number of complications (low measurement temperatures, dependence on sources with short half-lives, working at synchrotrons, etc.). Co is accessible by inverse Moessbauer spectroscopy, which requires preparation of the sample with ^{57}Co , the isotope that decays into the source nucleus ^{57}Fe .

Such effort can be justified due to the high diagnostic potential of the method for structural features. The spectra indicate the electronic state of the element (including high-spin/low-spin differentiation), asymmetries in the coordination sphere, and the intensity of magnetic interactions between the atoms. In the case of iron, size determination is possible for superparamagnetic clusters. Due to the temperature dependence of the recoil-free fraction that determines the signal intensity from the corresponding structure, the spectra from samples containing iron in states of different dispersion may change with temperature, and also under the influence of an external magnetic field, which gives the chance to single out contributions from different coexisting sites.

Figure 7.4 shows an example where Moessbauer spectroscopy revealed the presence of Fe-oxide aggregates in Fe-ZSM-5 prepared by chemical vapor deposition of Fe according to [36], which was expected to contain the Fe species in nearly atomic dispersion from the EXAFS spectra [37]. This was based on the very low intensities of Fe-Fe scattering between 2 and 3 Å, uncorrected, which can be seen in Fig. 7.4a, and the lack of significant scattering intensity above 4 Å, which suggests nearly ideal dispersion of Fe. At the same time, sextets in the Moessbauer spectra in Fig. 7.4b, c clearly show the presence of large oxide aggregates. The

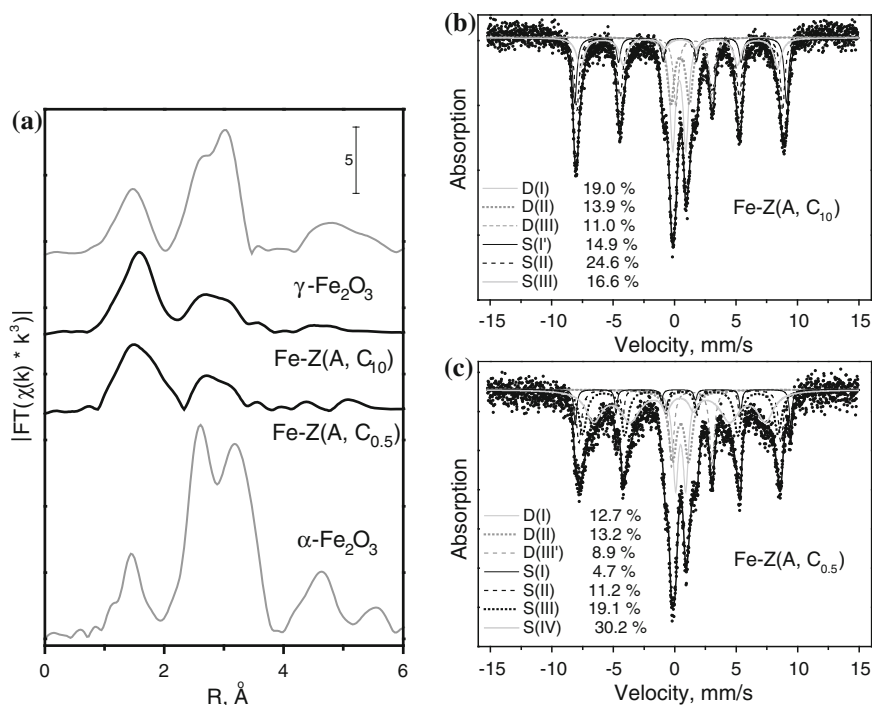


Fig. 7.4 Fe-K EXAFS (a) and Moessbauer spectra (b, c) of two Fe-ZSM-5 catalysts prepared by CVD of FeCl_3 into H-ZSM-5 and calcined with different heating protocols. The missing order at higher distances in the EXAFS spectra suggests the absence of larger aggregates, which are, however, clearly indicated by the Moessbauer spectra. Reproduced from [37] with permission of Elsevier

contradiction apparently resulted from large disorder in the particles, which may have included debris from destroyed zeolite structure. Such disorder would prevent the observation of EXAFS scattering paths and cause anomalies in the Moessbauer parameters as obtained in the fits to Fig. 7.4b, c [38].

There have been so far no in situ Moessbauer studies with catalysts, most likely due to the loss of intensity (recoil-free fraction) and of particle size differentiation with increasing temperature.

The methods discussed so far are particularly qualified for active site studies by offering the potential for in situ work—even in electron microscopy, an “environmental” version in which the sample is kept under some millibar of reactant pressure is available nowadays. Valuable insight into the structure of surfaces can be, however, also obtained by methods targeting adsorptive interactions of reactants or other probe molecules with the surface although these are usually performed in separate experiments, e.g., on catalysts previously subjected to reaction conditions.

Volumetric *chemisorption* techniques are widely used to explore the particle sizes (actually the size of the accessible surface) of dispersed metals. With oxides and sulfides, they measure the total coordinative unsaturation of the surfaces, which may be related to the catalytic properties. The energetic effects of adsorption are probed by *adsorption microcalorimetry*, which gives frequency distributions for sites with different interaction strength with the adsorbate, without of course providing information about the structural features of the detected sites. Adsorption interactions are often probed by reverting the process. For instance, desorption into a carrier gas under a (linear) temperature increase (*temperature-programmed desorption, TPD*) gives the chance to differentiate the sites according to their interaction strength with the adsorbate, though with less accuracy than calorimetry. Even nearer to catalysis is *temperature-programmed surface reaction (TPSR)*, where an adsorbate is reacted under a linear temperature profile with a reactant offered in a carrier gas. This can reveal the existence of different active sites for a reaction and give access to energetic properties of the existing sites.

Temperature-programmed reduction (TPR) and temperature-programmed oxidation (TPO) are thermal methods related to transformations of the catalyst rather than to adsorption on its surface. The former differentiates phases in the catalyst according to their reducibility, the latter, which is usually performed after having had a (redox) catalyst in a steady state with the reactant flow, probes the average reduction degree of the elements present and differentiates components according to their tendency to be reoxidized.

All thermal methods mentioned are highly productive in indicating differences between the catalysts prepared and known phases or in detecting changes by treatments, without giving any hint on the nature of species formed during preparation or further processing. Combinations of such methods with techniques of structural analysis have rarely been described in the literature. There is a special opportunity for TPD, because a version of this method (*TDS—Thermal desorption spectroscopy*) is used in surface science to investigate the adsorption properties of ideal well-characterized surfaces. Indeed, comparison of activation energies of desorption obtained by TPD of H₂ from real Cu catalysts with analogous H₂ TDS data from Cu single crystal surfaces has been used to judge upon the exposure of Cu facets in methanol synthesis catalysts [39].

The characterization techniques discussed so far are summarized in Table 7.1.

The discrimination of the active site among coexisting inactive or less active structures requires a set of samples containing the candidate species in sufficiently different abundances. A situation where such samples are not accessible by the preparation methods employed calls for *transient methods*.

Catalytic mechanisms of redox reactions most frequently involve redox cycling of (a) transition-metal ion(s) contained in the active site. Under reaction conditions, the oxidation state of the TMI in coexisting sites will adapt to the redox potential of the reaction medium in different ways depending on the redox properties of the individual structures. The different oxidation states observed under stationary reaction conditions are, however, not related to the relevance of the corresponding sites in the catalytic process because for the active site, all oxidation

Table 7.1 Characterization techniques used in heterogeneous catalysis and their potential for the identification of active sites

Technique	Potential	Limitations	In situ/ operando?
XRD	Determination of long-range order, of particle sizes	Averaging technique, on traditional level no potential for disordered structures	yes
Electron microscopy	Visualization of structures down to atomic details, usually in UHV, but environmental versions available	Site concentrations difficult to establish, analysis refers to small assay of material under study (support by averaging technique desirable)	in situ (limited)
XAFS (EXAFS/XANES)	Short-range order, also for disordered or highly disperse phases, electronic structure	On traditional level averaging technique, difficult for situations with many species of an element coexisting	yes
XPS	Atomic concentrations, oxidation states in near-surface layer, sometimes structural information, UHV technique, environmental versions available	Averaging over sampling region (depth differentiation requires synchrotron source ^a), assignment of signals may be complicated, structural information limited	in situ (limited)
LEIS (ISS)	Identification of atoms in topmost layer, concentration gradients via sputter series, vacuum technique	No information on oxidation states, averaging technique, concentration analysis possible, but with risks	no
Raman	Structural information for highly disperse phases, characterization of adsorbates	Qualitative, signal superposition for complex materials, problems with sample fluorescence	(yes)
IR	Characterization of sites (acid-base, redox) by probe molecules, of adsorbates, structural information	Concentration analysis difficult (only in transmission geometry, extinction coefficients required), structural information often limited by signal saturation	yes
UV-Vis	Analysis of oxidation states, of aggregation degree of TMI sites	Semiquantitative, broad signals may create problems with assignment, poor resolution of clustering degrees	yes

(continued)

Table 7.1 (continued)

Technique	Potential	Limitations	In situ/ operando?
EPR	Analysis of paramagnetic sites and their environment, extremely sensitive, gives information also on clustered phases	Not all oxidation states accessible, accuracy of concentration analysis limited	yes
NMR	Concentration, coordination, oxidation states of elements, sometimes information on distances between sites	Only nuclei with nonzero spin, sometimes problems with sensitivity, interference by nearby paramagnetic sites complicates application in redox catalysis	yes
Moessbauer	Oxidation states, coordination to neighbors, clustering degrees of sites	Only a few elements with suitable nuclear levels, in particular Fe, full diagnostic potential only at very low measurement temperatures	no ^b
Chemisorption	Particle sizes (metals), adsorption sites (ionic surfaces)	Particle size determination averaging; adsorption stoichiometry not always clear	no
Adsorption calorimetry	Enthalpy and entropy of adsorption (titration method) for probe molecules and reactants	Limited to simple systems (well-defined surface, one adsorptive)	no
Temperature-programmed desorption	Differentiation of adsorption sites on a surface, depending on test molecule for acid/basic or redox sites, determination of energetics of desorption	Desorption signals remain to be assigned to sites	no
Temperature-programmed reduction/oxidation	Reduction/reoxidation properties of redox phases in samples; strong in detecting interactions between phases, in simple cases determination of energetics of reduction	Nature of detected interactions remains to be elucidated	no

^a Angle-resolved XPS, which can be performed with lab sources, is a safe tool only for flat sample surfaces

^b In principle possible, but no examples known; loss of diagnostic potential at elevated temperatures seems to discourage attempts

states are possible: the actual situation is determined by the ratio between reduction and reoxidation rates, slow reoxidation resulting in low stationary oxidation states, and slow reduction in a fully oxidized site. Therefore, reduction and reoxidation rates have to be measured under typical reaction conditions, e.g., as a response to step changes of the feed composition. Sites in which any of the two rates is clearly lower than the stationary reaction rate may be rejected. More challenging but at the same time more promising is to compare how the oxidation states of the TMI in coexisting sites on one hand and the reaction rate on the other respond to step composition changes. Such step change will usually cause a change of both reaction rate and oxidation states of all coexisting sites, but only for the site causing the observed reaction will the transient response of the oxidation state coincide with that of the reaction rate.

In cases where sites can be differentiated by the IR spectra of an adsorbed reactant (see above), the step concentration change may be replaced by changing the isotopic label (e.g., $^{12}\text{CO} \rightarrow ^{13}\text{CO}$) as the adsorption of the labeled compound is easily detected by a shift in wavenumber. Such extension of the SSITKA (steady-state isotopic transient kinetic analysis), which is typically used for studies on reaction mechanisms, by integrating structural and/or surface analysis techniques is nowadays established in many laboratories. For the reactions relevant for SCR, the pertinent studies are, however, still ahead.

The information given in this chapter demonstrates the complexity of research targeting the identification of active sites in real catalysts. The report on the state of insight into active site structures in SCR catalysts which will follow in the next sections should be seen on this background. This state of knowledge comes as a mosaic with contributions of many groups which are not necessarily consistent with each other. The picture is definitely transient, in some cases the details may well change by upcoming work with more powerful methods and with broader use of transient methods.

7.3 Supported Vanadia Catalysts

Supported vanadia catalysts promoted with tungsten oxide, sometimes with molybdena, are the industrial standard in SCR applications for stationary sources but have also been applied in urea-SCR schemes (cf. Sect. 2.1). In the following, the state of knowledge about the unpromoted $\text{V}_2\text{O}_5/\text{TiO}_2$ system will be discussed first, followed by some remarks regarding the role of the WO_3 promoter.

It has been known for long that the interaction of transition-metal oxides (V_2O_5 , WO_3 , MoO_3) with high surface area supports leads to the formation of monolayer surface oxide species up to a considerable coverage degree of the support surface (see, e.g., reviews [23, 40–44]). Silica is somewhat exceptional in this respect because of its low density of sites available for interactions with the supported oxide, therefore the following discussions are not valid for SiO_2 surfaces. The question whether the support surface becomes completely covered before the supported oxide starts to grow into the third dimension was subject to some

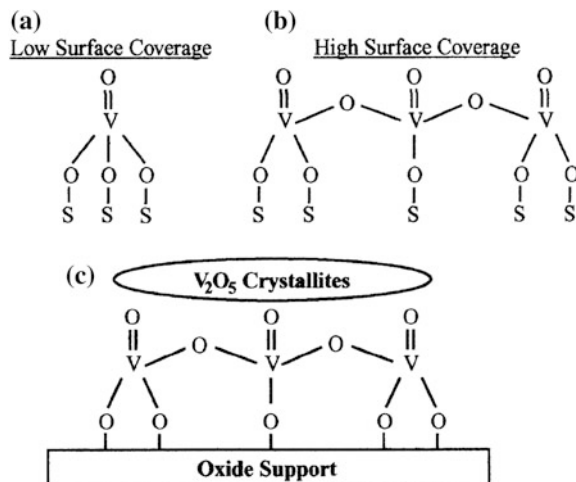


Fig. 7.5 Surface vanadium oxide species occurring on supported vanadium oxide catalysts. Reproduced from [42] with permission of Elsevier. **a** Isolated surface VO_4 species. **b** Polymeric surface VO_4 species. **c** Crystalline V_2O_5 nanoparticles above monolayer surface coverage

controversy [23, 41, 43–47]. Studies by the perfectly sensitive Ion Scattering Spectroscopy [48, 49] showed that in well-prepared catalysts the transition-metal (V or Mo) oxide species indeed cover the support completely in the dehydrated state before building second and third layers. Hydration of the fully covered surfaces results in some exposure of the support, apparently due to hydrolysis of the oxygen bridges to the latter with subsequent clustering of the supported species [43, 44]. Less optimized preparations involving ill-controlled deposition of precipitates may, of course, lead to different situations although the oxides have a tendency to spread over the support surface during heat treatments creating monolayer systems also under dry conditions. Indeed, for some systems (e.g., $\text{MoO}_3/\text{Al}_2\text{O}_3$) thermal spreading of the oxide onto the support surface is a practical alternative preparation route to aqueous techniques [50, 51].

It has been concluded from Raman spectroscopic studies that the TM oxide forms isolated surface oxide species at low coverages, which combine to two-dimensional oligomers with increasing coverage [23, 40–44]. Growth into the third dimension will result in relatively disordered clusters which can be, however, observed by Raman spectroscopy with high sensitivity, before ordered particles detectable by XRD are formed. On TiO_2 , the vanadium in isolated species is tetrahedrally coordinated by oxygen with a short $\text{V}=\text{O}$ bond and three longer bonds forming oxygen bridges to Ti atoms (Fig. 7.5). In the polyvanadates, some $\text{V}-\text{O}-\text{Ti}$ linkages are replaced by $\text{V}-\text{O}-\text{V}$ bridges, in addition, acidic $\text{V}-\text{OH}$ groups may occur.

A recent EPR spectroscopic study [52] suggests some modification of this picture (Fig. 7.6). The catalysts were made by simple impregnation of a Ti

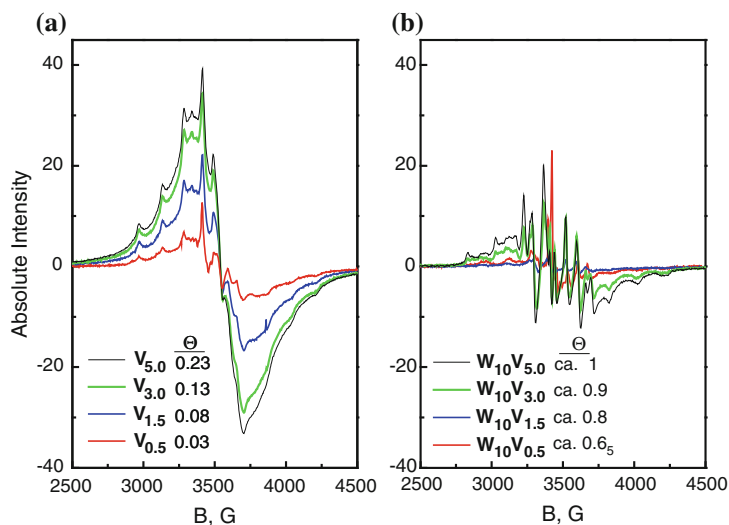
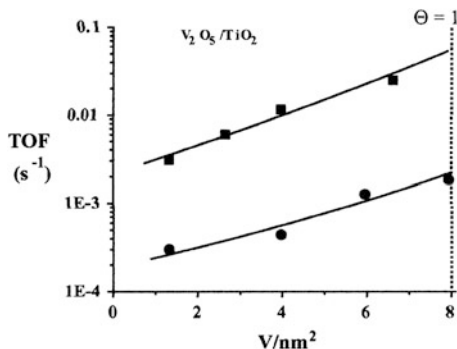


Fig. 7.6 EPR spectra of tungsten-free **a** and tungsten-containing **b** V_2O_5/TiO_2 catalysts after a reference calcination (623 K, 1 h), measured at 77 K. Spectra are normalized to the catalyst mass. Reproduced from [52] with permission of Elsevier

oxyhydrate with very high surface area resulting from the sulfate process, with subsequent calcination at a rather low temperature (623 K) with the intention just to fix the spontaneous speciation of V oxide structures on the surface. While the presence of three-dimensional clusters could be excluded by Raman spectroscopy, EPR showed a coexistence of isolated and oligomeric surface oxide species over a wide range of coverage degrees (Fig. 7.6a). The intensity ratio between the two signals present (multiplet—isolated sites, broad isotropic signal—sites in islands) confirmed the expected increased abundance of islands at larger V oxide coverages, but the clear detection of the isotropic signal at a V oxide coverage of <3 % suggests that surface vanadium oxide species have a much larger tendency to island formation on titania surfaces than so far assumed.

In the early literature, the vanadyl group ($V=O$) was thought to be the active site for the SCR reaction [53]. It was, however, soon observed that in catalyst series with varying composition the SCR rate grew stronger than linear with the vanadium content [54–57] as exemplified for V_2O_5/TiO_2 in Fig. 7.7. It was derived from the kinetic data that the polyvanadate-based sites in V_2O_5/TiO_2 would be an order of magnitude more active than the isolated sites [55]. From these observations, various proposals of binary sites with the $O=V-O-V=O$ motif emerged, as reviewed, e.g., in [58]. At the same time, the relevance of Brønsted ($V-OH$) sites was concluded from IR and isotopic labeling studies [59, 60]. The well-known reaction mechanism by Topsøe (see Chap. 8), which was supported by IR spectroscopic and TPD studies [61–63] and became the basis of a successful microkinetic model of SCR over this catalyst type [64], indeed operates on a binary site containing an vanadyl and a $V-OH$ group ($O=V-O-V-OH$).

Fig. 7.7 Relation between density of surface V atoms in V_2O_5/TiO_2 catalysts and their activity for NH_3 -SCR (●) and methanol oxidation (■). Reproduced from [42] with permission of Elsevier



On the other hand, the reality of SCR activity provided by isolated V oxide sites [55] has been supported by studies with vanadium-exchanged zeolites. A clear correlation between the intensity of the EPR signals of isolated $(VO)^{2+}$ ions and the reaction rate was found [65]. These sites obviously operate via a different, as yet unknown mechanism.

Several concepts were put forward to explain the promoting role of tungsten in $V_2O_5-WO_3/TiO_2$ catalysts. An increased surface acidity in presence of W favors the ammonia supply to the active site [66, 67]. Tungsten was observed to enhance the reducibility of the vanadia component [66, 68], which was explained by electronic interactions and was related to the observed increase of activity. An alternative approach considered the tungsten species just as competitors for the support surface, which force the surface vanadium oxide species to greater proximity and thus to the formation of the highly active binary sites [66] already at lower coverages. In this version, the surface tungsten oxide species are just spectators, the activities achieved in the promoted catalysts should be accessible without tungsten as well, but at lower BET surface areas. Tungsten is also known to favor the stability of the catalysts by delaying the sintering of the high surface area support.

The structure of surface tungsten oxide species was studied by Raman spectroscopy of monometallic WO_3/TiO_2 and of mixed $V_2O_5-WO_3/TiO_2$ catalysts [69]. Surface W oxide species are tetrahedrally coordinated ($(O)_3-W=O$) at low W content while strongly distorted octahedral sites ($(O)_5-W=O$) predominate on dehydrated surfaces at high W oxide coverage. These sites were found to coexist with tetrahedral monovanadate and polymeric surface vanadates in the mixed system. A trend to more polymeric surface V oxide species was observed with growing tungsten content, but no three-dimensional phase was seen even at total metal coverages which would significantly exceed the monolayer limit if both metals were to compete for the same surface sites [69]. No indications for bonds between surface W and V oxide species (W-O-V bridges) were reported.

In Fig. 7.6, the EPR spectra of the TiO_2 -supported monometallic and mixed oxide catalysts are compared [52]. Surprisingly, the introduction of tungsten strongly suppressed the isotropic signal from the surface V oxide islands. The effect is drastic, because the coverages in the mixed systems are very high due to

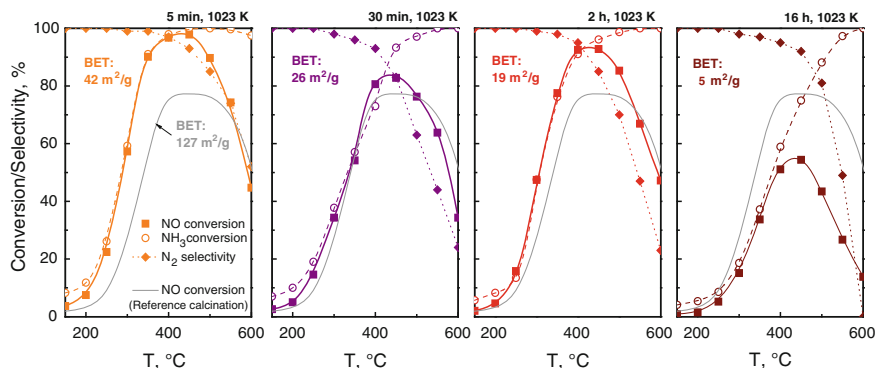


Fig. 7.8 Dependence of the SCR activity and selectivity of a V_2O_5 - WO_3 / TiO_2 catalyst (1.5 wt% V_2O_5 , 10 wt% WO_3) on the duration of a calcination in air at 1023 K. Comparison with reference calcination (1 h at 623 K). From [70]

an intermediate calcination step which caused loss of surface area. For the catalysts containing 1.5 wt% V_2O_5 , (... $V_{1.5}$), the isotropic signal almost completely vanished in presence of W although the total metal oxide coverage increased by an order of magnitude. Obviously, tungsten tends to break up island structures instead of favoring them. A complementary TPR study indeed suggested that most of the tungsten in these catalysts is in the vicinity of surface V oxide sites, not near W oxide sites [52]. Therefore, the promoting effect of tungsten is caused not by the formation but by the destruction of polyvanadate sites. Electronic interactions between W and V oxide species or a favorable influence of W on surface acidity would comply with this picture, but also a dependence of the specific activity of the active (V–O–V) sites on the size of the island in which they are contained, the smallest size offering the highest activity.

These alternatives were further differentiated by a study of the catalyst response to high temperatures [70]. Mixed oxide systems were found to activate strongly upon treatment at high temperatures in oxidizing medium (Fig. 7.8). Two activity peaks can be seen with increasing treatment duration at 1023 K (panels a and c) and concomitant decrease of the BET surface area. Under other calcination conditions, even a third activity maximum emerged. While the details of these phenomena are not yet fully understood, we found clear evidence from several methods (Raman spectroscopy, XRD, TPR) that the decrease of the support surface area causes the tungsten oxide species to segregate from the surface, not the vanadium oxide species. Therefore, the drastic activation effect seen in Fig. 7.8 is most likely related to a growth of surface V ensembles at places where the tungsten loses contact with the surface. This is incompatible with both the concept of electronic interactions between W and V oxide sites and of acidity effects determining the activity trends. Instead, it seems to indicate that the spontaneous arrangement of W and V oxide species on the titania surface leads to an excessive isolation of vanadium oxide sites. This is relaxed by segregation of W oxide

species from the surface under thermal stress, which allows for more highly active dimeric sites. Under heavy thermal stress, the surface vanadia phase remains two-dimensional while the tungsten oxide forms large WO_3 crystals. The poor performance resulting under these conditions suggests a lower activity of V–O–V dimer sites when they are part of large islands.

7.4 Zeolite-Based Catalysts

Zeolites are unique among catalyst supports in many aspects, e.g., in the availability of well-defined, energetically nonequivalent cation exchange sites. The expectation that cations exchanged into zeolites will all end up in these sites seems to be fulfilled, however, only for monovalent ions. SCR-related research has much contributed to the insight that exchange of polyvalent cations may result in complicated species distributions, probably due to the extra-lattice oxygen introduced into the system for charge neutralization.

7.4.1 Fe Zeolites

The discussion of active sites for NH_3 -SCR has been much influenced by structural data collected in earlier studies related to the SCR with hydrocarbons (HC-SCR). For the same reason, the discussion has long been focused on the ZSM-5 matrix although different zeolites, in particular zeolite Beta, meanwhile seem to be more promising for technical application. The early studies dealt with over-exchanged samples ($\text{Fe}/\text{Al} = 1$, corresponding to ≈ 5 wt% Fe at an Si/Al ratio of ≈ 15), which were first described by Feng and Hall [71] and could be reproducibly prepared by chemical vapor deposition (CVD) of FeCl_3 into H-ZSM-5 as reported by Chen and Sachtler [36]. These authors proposed that the iron which is atomically dispersed in the form of Z–O– FeCl_2 species after the CVD step, rearranges quantitatively or to a large extent into dimeric species held together by an oxygen bridge (Fe–O–Fe) after washing and calcination [36, 72]. This view was supported, e.g., by the partial reappearance after calcination of the IR band of Brønsted OH groups, which had been completely quenched by the CVD step, and by the easy (stoichiometric) oxidation of CO to CO_2 by these samples, which suggests the vicinity of two Fe atoms accommodating the two electrons transferred. The assignment of the high HC-SCR activity of these catalysts to the binuclear Fe–O–Fe sites was encouraged by analogies with the active structure in the enzyme methane monooxygenase [73] and by previous analogous assignments of activity in NO decomposition and HC-SCR to analogous Cu–O–Cu species in Cu-ZSM-5 [74].

Several groups investigated over-exchanged Fe-ZSM-5 by X-Ray absorption spectroscopy and supported unanimously the formation and catalytic relevance of the binuclear Fe–O–Fe sites [75–77]. The EXAFS spectra obtained in these studies

were successfully analyzed by models yielding coordination numbers near or equal to one for the second coordination shell (Fe–Fe). A note of caution was given by Marturano et al. [77] who found by magnetic measurements that the antiferromagnetic coupling, which is expected between the Fe atoms in binuclear sites, was not complete. Despite 30 % of the iron detected as isolated ions, the EXAFS data were still discussed in terms of predominating binuclear sites.

On the other hand, Heinrich et al. obtained Fe–Fe coordination numbers below 1 in their EXAFS analysis of over-exchanged Fe–ZSM–5 subjected to different calcination regimes [37]. Supported by the observation of a significant amount of large clusters (particles) by Moessbauer spectroscopy (cf. Fig. 7.4) they concluded that EXAFS coordination numbers can be only averaged quantities in these materials and thus identified the presence of significant amounts of isolated Fe oxo sites in their zeolites. As the SCR activities of these catalysts were comparable with those of other groups which claimed considerably less particle formation and predominant presence of binuclear Fe–O–Fe sites in their samples [36, 78], Heinrich et al. assigned the (HC-)SCR activity to sites which would be minority species in all catalysts compared, e.g., isolated sites [37]. This assignment was strongly supported by the observation of attractive SCR activity of a sample containing just 0.5 wt% Fe [79]. This catalyst, which was prepared by a different method, did not exhibit any significant Fe–Fe scattering signal in EXAFS which might have indicated binuclear Fe–O–Fe sites.

In the following, the heterogeneity of the Fe speciation in over-exchanged Fe–ZSM–5 has been confirmed by other groups as well [80] although in the mean time, >70 % of the iron had been claimed to be part of Fe–O–Fe pairs in catalysts that contained >45 % of the iron in large (2–10 nm) particles according to the Moessbauer spectra [81]. Heijboer et al. found that the EXAFS spectra of over-exchanged Fe–ZSM–5 cannot be unambiguously analyzed [80]: they presented models including next nearest Si(Al) neighbors that represent the data equally well as those published earlier [81] and resulted in much lower Fe–Fe coordination numbers (see also Pirngruber et al. [82]). Likely structures of Fe species in ZSM–5 are illustrated in Fig. 7.9, which cites molecular modeling results given in [80]. These models should be taken just as examples: EPR spectroscopy identifies, for instance, at least three different isolated sites ([30, 83], see also Fig. 7.3), which have been related to the α , β , and γ cation exchange sites meanwhile [84]. The binuclear site is nowadays rather lumped into the oligomers, which can be identified by UV–Vis signals in a particular wavelength range [30, 85]. Upon calcination, the Fe species tend to migrate toward the external surface and to aggregate still in the zeolite [37, 81], which is nicely demonstrated by TEM–EDX images from [81] and TEM images from [86] in Fig. 7.10a–c. The wavelength region related to these species in the UV–Vis spectra differs from those of the oligomers although it has remained unclear which aggregation degree would cause the wavelength shift observed [30, 85]. Finally, oxide or oxihydrate crystals segregate from the zeolite (Fig. 7.10b). The migration is favored by moisture, the intra-zeolite particles most likely destroy and include part of the zeolite structure which explains their invisibility by XRD and EXAFS (see Fig. 7.4).

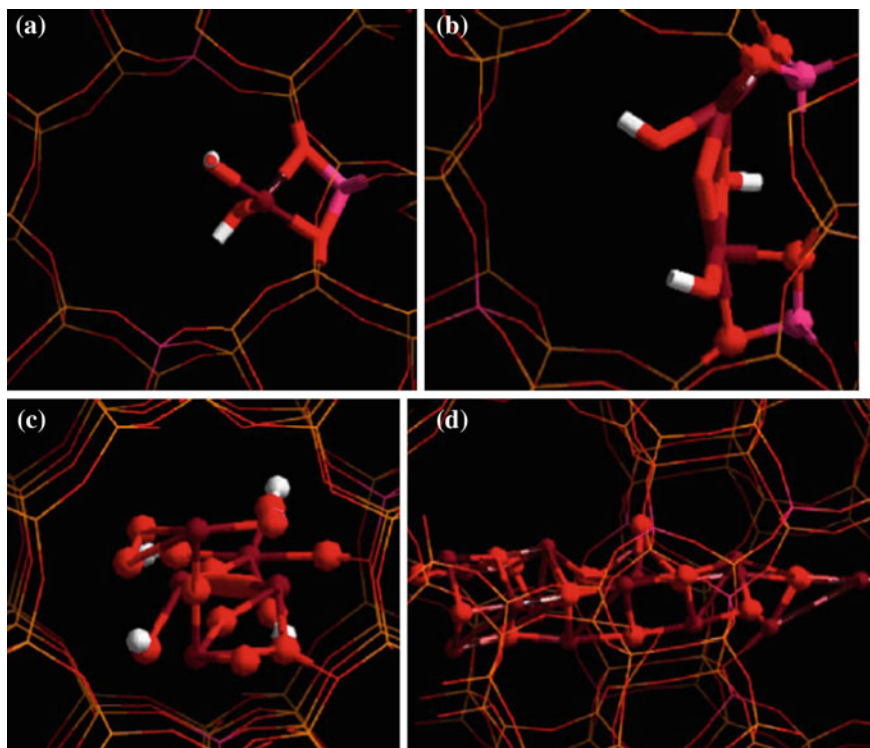


Fig. 7.9 Molecular models of Fe oxo species in zeolites. **a** mononuclear Fe oxo site, dehydrated; **b** binuclear Fe (hydr)oxo site, **c**, **d** oligomeric Fe oxo sites of different nuclearities in straight channel, seen from different sides. Framework represented by *thin lines*, atoms in extra framework species by balls: *red*—O, *pink*—Al, *dark red*—Fe, *white*—H. From [80] with permission of Elsevier

Due to the complexity of over-exchanged Fe–ZSM–5, the subsequent studies were undertaken with ZSM–5 containing small amounts of iron, and NH₃–SCR was included owing to its upcoming technological relevance. UV–Vis and EPR spectroscopy became the most important analysis techniques at the expense of EXAFS because of their potential to differentiate coexisting Fe species [30]. For a series of samples prepared by a special ion exchange technique (cf. [83]) activity in both SCR reactions was correlated with the abundance of Fe sites derived from a quantitative analysis of the UV–Vis spectra, neglecting a possible wavelength dependence of the extinction coefficient [86].

For HC–SCR, this correlation resulted in strong support for a contribution of both isolated and oligomeric Fe oxo sites to the reaction rates observed at low temperatures. At high temperatures, the oligomers catalyze the oxidation of the hydrocarbon reactant very effectively, therefore, the best catalysts for HC–SCR contain iron only in small quantities. The results for NH₃–SCR are summarized in

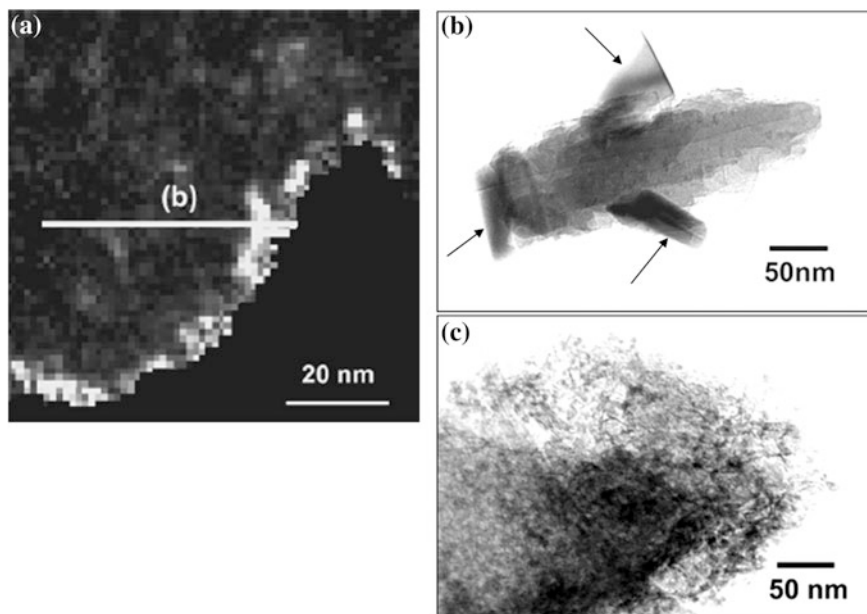
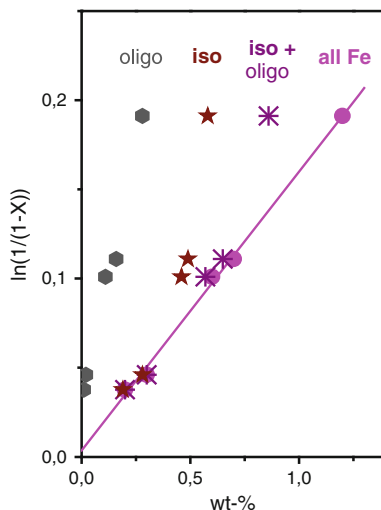


Fig. 7.10 Electron microscopy images of Fe-ZSM-5. **a** STEM/EELS micrograph (Fe/O map) of over-exchanged Fe-ZSM-5 after calcination with extremely slow temperature gradient [81], line scan along *line* (b) not shown; **b** crystallites on over-exchanged Fe-ZSM [86], **c** Fe enrichment in Fe-ZSM-5 of low Fe content (1.2 wt%)

Fig. 7.11. Surprisingly, the correlation with the total Fe content was superior even to that with the sum of oligomers and isolated sites, which was explained with the irregular structure of the intra-zeolite “particles” (cf. Fig. 7.10a, c) offering a non-negligible surface area available for catalysis. Unlike in HC-SCR, the oxidation of the reductant is much less pronounced in NH_3 -SCR over Fe-ZSM-5, therefore, the oligomers can be tolerated in the catalysts. Rather, from the course of the NO conversion curves with increasing Fe content it was proposed that the oligomers may even contribute more strongly to the total reaction rate at higher temperatures than under the conditions for which the correlation (Fig. 7.11) was made [86]. From this, the best catalysts for NH_3 -SCR would contain large amounts of iron in the highest possible dispersion.

The surprisingly good correlations between site abundance and SCR activity still leave a number of questions unanswered. As already mentioned, “isolated sites” is a quantity lumped of at least three species detectable by EPR. The redox properties of these sites in the typical feeds (NH_3 -SCR and HC-SCR) were found to be very different, octahedrally/distorted tetrahedrally coordinated isolated sites being more prone to reduction than tetrahedrally coordinated sites under conditions where oligomers withstood reduction completely [87]. As SCR most likely requires Fe to be in the +3 state in order to activate the reductant (cf. Chaps. 8 and 9),

Fig. 7.11 Correlation of the rate constant of NH_3 -SCR at 523 K with the abundance of different site types in Fe-ZSM-5 assessed from UV-Vis spectra. From data in [86]



the contribution of these sites to the observed activity should be different. The marginal influence of these differences on the quality of the correlations discussed above may arise from a low degree of variation in the concentration ratios between these sites in our series of samples. Likewise, the “oligomers” comprise a distribution of oligomerization degrees. The small NH_3 oxidation activity found with Fe-ZSM-5 arises from clustered phases, from the oligomers rather than from the particles. When we used a Fe-ZSM-5 catalyst after ≈ 2 years storage under the same reaction conditions as before, we observed the influence of ammonia oxidation on the conversion-temperature curves to be larger than in the earlier measurements (see [86, 88]) although we could not relate this to significant changes in the UV-Vis spectra. Maybe an influence of the oligomer size on ammonia oxidation activity remains to be discovered here. Finally, it has been proposed that the UV absorption of binuclear sites may fall into the wavelength region typical of isolated sites if their antiferromagnetic coupling is weak (hydroxo-bridged dimers) [82]. In our UV-Vis studies, no significant differences occurred between measurements of a calcined sample stored subsequently at ambient or in situ right after calcination, therefore, we do not consider the hydroxylated binuclear site relevant for our assignments.

The sites active for NH_3 -SCR in Fe zeolites have been addressed in a number of other, mostly more recent studies, which did not result in convergent conclusions. Based on EPR measurements, Long and Yang [83] assigned activity for NH_3 -SCR exclusively to tetrahedrally coordinated isolated sites cooperating with Brønsted sites. Exclusively isolated sites were also considered responsible for NH_3 -SCR by Krishna and Makee [89] and by Doronkin et al. (Fe-Beta [90]). Opposed to this, Klukowski et al. suggested a dual site mechanism for Fe-Beta where NH_3 and NO are activated at neighboring Fe^{3+} sites, and admitted only a minority role for a possible single-site mechanism [91]. The dual site may be part

of oligomers or consist of two nearby isolated Fe^{3+} ions. Iwasaki et al. proposed NO_2 TPD as a most useful tool for the elucidation of active sites as its high-temperature peak appears to correlate with activity in NH_3 -SCR [92]. This peak was associated with “oxo- Fe^{3+} at ion exchange sites” [92, 93] which includes, however, binuclear sites as far as both Fe ions are related to framework Al cations. In a more recent article, the binuclear sites were described as a subcategory of oligomeric sites [94], which shifts the assignment closer to that of Schwidder et al. [86]. Sobalik and coworkers have recently stressed the significance of the Al distribution in the zeolite framework for the active site structure, a motive which has been developed by scientists of the Prague Heyrovsky institute over years and has been recently reviewed in [95]. In this concept, close Al framework sites in opposite positions of a six-ring stabilize Fe^{2+} ions without extra-lattice oxygen, while single Al framework sites are coordinated with Fe^{3+} oxo species. The latter are considered responsible for the activity in NH_3 -SCR [96].

The conflicting conclusions mentioned arise at least partly from the limited potential of the available analytical methods for analysis of the complex site structure in Fe zeolites. In this situation, the group of O. Kröcher resorted to a statistical approach in which the distribution of the Fe sites was assumed to follow a (random) distribution of Al in the zeolite framework, and the formation of bi, tri, and polynuclear structures was assumed to occur when nearby Fe sites are located within certain distances [97, 98]. The site abundances obtained on this basis, which were validated by comparison with UV-Vis spectra of a samples series covering a wide range of Fe contents [98], were used to explore correlations within a large body of very accurate rate measurements at different temperatures [99]. From this, Brandenberger et al. concluded that the catalytic reaction rate results exclusively from isolated sites at low temperatures while oligomeric structures contribute at higher temperatures, which agrees to some extent with the picture proposed in [86].

The importance of acidity for NH_3 -SCR has been discussed also with respect to Fe zeolite catalysts. A favorable role of acidity is a priori plausible because this tends to increase the local concentration of the ammonia reductant near the active sites. The more fundamental question is, however, if an acidic function is part of the active sites as, for instance, in the sites driving the reaction cycle proposed by Tøpsoe [61–63] for $\text{V}_2\text{O}_5/\text{TiO}_2$ catalysts. From a comparison of SCR activities measured with Fe in nonacidic and acidic zeolite supports, Schwidder et al. concluded that acidity favors the reaction without being an essential ingredient of the active site and hence the reaction mechanism [100]. A more recent study of Brandenberger et al. arrived at similar conclusions [101], which are at variance with some earlier proposals, e.g., in [83].

The technical relevance of Fe zeolites is related to their potential to catalyze the fast SCR reaction (Eq. 7.2) rather than to their activity in standard SCR. Fast SCR is a rather facile reaction which has been proposed to proceed without any involvement of Fe sites [102, 103]. This has been confirmed in [88], but it has been shown at the same time that Fe zeolites offer sites which accelerate the reaction dramatically. Standard SCR and fast SCR are stoichiometrically related to each other: The former (Eq. 7.1) results when NO oxidation (Eq. 7.3) is added to fast SCR (Eq. 7.2).

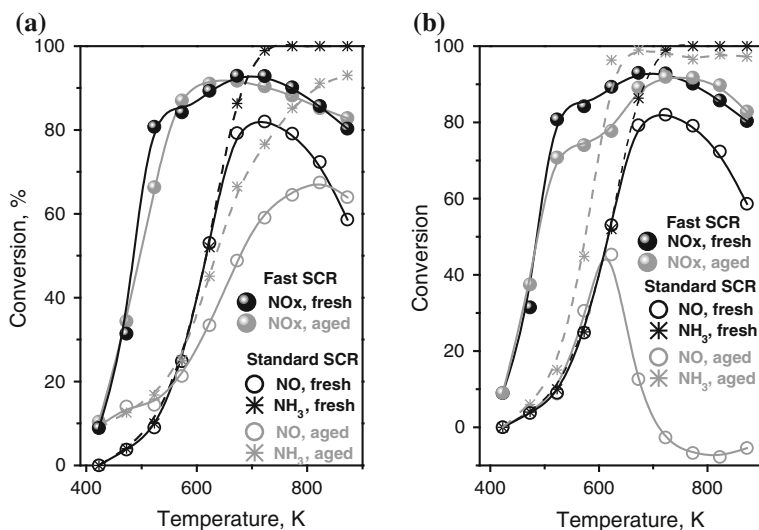


Fig. 7.12 Deactivation of an Fe-ZSM-5 catalyst in standard and fast SCR. **a** aging in moist atmosphere, 10 vol% H₂O in air, 923 K, 48 h, **b** aging in presence of water and SO₂, 5% H₂O, 200 ppm SO₂ in He at 823 K over 65 h. 1,000 ppm NO, 1,000 ppm NH₃, 2% O₂ in He, 750,000 h⁻¹, NOx being NO (standard SCR) or an equimolar NO/NO₂ mixture (fast SCR). From [88] with permission of Elsevier

It has been proposed that this relation holds also for the reaction mechanism of standard SCR, with NO oxidation as rate-determining step followed by the very fast reaction of the resulting NO/NO₂ mixture according to Eq. (7.2) (see Chap. 8, earlier work summarized in [97]). This view implies that the active sites of NO oxidation and of standard SCR are identical while those of standard and fast SCR might be different.

The latter has been indeed reported in a study by Schwidder et al. [88] where the activity for fast SCR was found to survive hydrothermal stress and impact of SO₂ much better than that for standard SCR (Fig. 7.12). From the observation that fast SCR was effectively catalyzed by a sample containing just 0.2 wt% Fe, according to UV-Vis and EPR spectroscopy almost exclusively as isolated sites and that more iron, be it as isolated, oligomeric, or particulate species, did not result in significant improvement, it was concluded that fast SCR is catalyzed by a sub-entity of the isolated sites. In recent *operando* EPR studies, Fe sites in β and γ positions remaining in the 2+ state during calcination but being oxidized to Fe³⁺ in presence of NO₂ have been identified as candidates [104].

In another recent study, it was attempted to change the fractional occupation of the ZSM-5 cation sites by the Fe species by loading the zeolite previously with different amounts of Na or Ca ions [105]. The subsequent introduction of the Fe component (ca. 0.25 wt%) was accomplished by a dry method (solid-state ion exchange) to avoid leaching of the co-cations. Figure 7.13 shows conversion

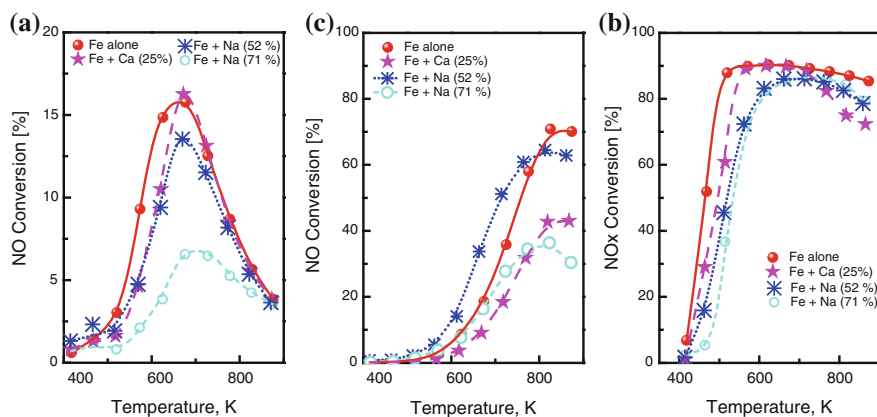


Fig. 7.13 Influence of inactive co-cations (Ca, Na, at different exchange degrees) on the catalytic properties of Fe-ZSM-5. **a** NO oxidation, **b** standard SCR, **c** fast SCR. From data in [105]

curves measured with these catalysts in the three relevant reactions (7.1) through (7.3). These curves demonstrate clearly that the active sites dominating the catalytic behavior are different for all three reactions. Thus, activity for standard SCR was improved by the presence of Na ions (ca. 50 % exchange degree) as compared to the Fe-only sample (Fig. 7.13b), while the activity for the other two reactions was deteriorated (Fig. 7.13a, c). This is another piece of evidence rejecting that standard SCR proceeds via a sequence of NO oxidation to NO_2 and fast SCR. The differences between NO oxidation and fast SCR are less striking but still pronounced (Fig. 7.13a, c): Thus Fe-ZSM-5 preoccupied with Ca or with Na (exchanged to 50 %) behave very similar in NO oxidation but clearly different in fast SCR. A further increased Na exchange degree leads to a strong deactivation in NO oxidation whereas in fast SCR, a loss in performance occurs only at low temperatures. The differences in the active site structure causing the activity changes depicted in Fig. 7.13 are subject to ongoing characterization work.

To summarize, there is no generally accepted view on the active sites responsible for the reactions relevant for NOx reduction in Fe zeolites. Several studies suggest a participation of all Fe sites accessible from the gas phase, which agrees with the observation that considerable SCR activity has also been reported for Fe oxide on open supports, e.g., tungsten-promoted FeOx/ZrO_2 [106], but correlations with exclusively isolated Fe sites have also been claimed. Research targeting the identification of the sites active for fast SCR has only just commenced. While it is clear that this reaction is catalyzed by a very stable isolated minority site, a recent *operando* EPR study supported by Moessbauer data suggests that this site may be in the Fe^{2+} state in a calcined catalyst and can be oxidized to Fe^{3+} only by NO_2 [104]. Fe ions stabilized by close Al sites in the framework as proposed by Dedecek et al. [95] might be candidates for that. Still, there is not as yet a well-established relation between the reaction mechanisms of

SCR (standard and fast) over these catalysts and the candidate sites because the mechanistic discussion was long dominated by the assumption of NO oxidation being rate determining for standard SCR, and more recent concepts still need to be related to the knowledge about the site structure in Fe zeolites.

7.4.2 Cu Zeolites

As mentioned above for Fe zeolites, the discussion on active sites in Cu zeolites has long been based on results obtained previously in research on HC-SCR, in the case of copper also on NO decomposition. The early work on all these reactions was reviewed in [107]. Actually, the activity of Cu zeolites for NH₃-SCR was discovered earlier than that for HC-SCR (NO/NH₃ reaction over Cu-Y—1975 [108, 109]; HC-SCR—1989/90 [110, 111]), but as the reaction was performed without oxygen in the feed, Cu(II) became reduced at rather low temperatures which quenched the reaction. [Cu(NH₃)₄]²⁺ complexes were considered to be the active sites [112].

Cu-ZSM-5 was the system for which the phenomenon of over-exchange was first described [110]. For NO decomposition, a steep increase of the turnover frequency around 100 % exchange degree [110, 113, 114], the conclusion that the active sites are a minority which easily interchanges between the +2 and +1 oxidation states under reaction conditions [114, 115] and the identification of such sites with binary Cu-O-Cu species [116] suggested a particular role of aggregated entities in this reaction. There was disagreement with respect to the structure of these aggregates already with the copper zeolites, where binuclear (Cu-O-Cu) sites were advocated by the majority of groups [110, 115–118] while some groups proposed the formation of small intra-zeolite oxide clusters (oligomers) [119, 120]. The latter was supported by the observation of very strong enrichment of copper in the XPS sampling region of freshly prepared Cu-ZSM-5 without any indication for the formation of massive phases [120], which would have been sensitively detected by the help of the Auger parameter [120–124]. Indeed, redox treatments decreased the copper excess in the external surface region, apparently by decomposition and redistribution of the copper oxide oligomers over the whole zeolite crystal [120].

While the beneficial role of overstoichiometric Cu is obvious for NO decomposition, there are diverging reports with respect to HC-SCR. Observations of peak activities at exchange levels slightly above 100 % [125–127] were considered to indicate a particular activity contribution of Cu-O-Cu sites or clusters, but results depended on the type of hydrocarbon reactant and on the reaction conditions. A completely different explanation given by Wichterlova et al. [128] is based on the concept of the active sites being influenced by the Al framework distribution [95]. From work with luminescence and IR spectroscopy (adsorbed NO), two different types of isolated Cu ions were differentiated: one, which predominates at low Cu content, is charge-balanced by two nearby framework Al ions, the other one, which carries extra-lattice oxygen, is formed only at higher Cu

content and was identified as the active site for NO decomposition. HC-SCR and NH₃-SCR were proposed to require the cooperation of both kinds of Cu ions. Ciambelli et al. found the normalized reaction rates (per Cu atom) of HC-SCR to increase up to full exchange, but then to decrease markedly [127], which calls into question the relevance of excess copper. In a study of propene-SCR with copper chloride species introduced into Na-ZSM-5 by dry methods (i.e., as guest species), normalized reaction rates were found to be of the same order as in usual SCR catalysts, which suggests that excess copper is just another site type for hydrocarbon-SCR, but without particular merits [121]. This is in agreement with the observation that Cu zeolites which differed strongly in NO decomposition activity exhibited less differences in HC-SCR [129].

The study with Cu chloride species hosted in Na-ZSM-5 [121] showed at the same time that HC-SCR with the reductant propene is possible without Brønsted acidity, which had been under debate as well (cf. [130–135]).

In studies with the ammonia reactant, the coexistence of isolated and binary sites was a major topic as well. In a kinetic investigation of NH₃-SCR over Cu-Y catalysts of different Cu content, Kieger et al. [136] found the turnover frequency (rate per Cu atom) to increase significantly with the copper content at low reaction temperatures while the trend was weaker above 600 K. Based on characterization by temperature-programmed reduction and reoxidation, TPD of ammonia and IR of adsorbed NH₃, the authors assigned the selective reaction observed at low temperatures to Cu–O–Cu sites which form in supercages at high copper content while analogous binary sites in the sodalite cages were considered responsible for the relatively intense N₂O formation under these conditions. Above 600 K, where the N₂O selectivity decreased markedly, all accessible copper was proposed to catalyze the selective reaction. Komatsu et al. likewise suggested a crucial role of binary Cu–O–Cu sites from kinetic studies of NH₃-SCR in Cu-ZSM-5 of varying Cu content [137]. The proposal of Wichterlová et al. according to which a cooperation between two different Cu ions is required for NH₃-SCR ([128], see above) sounds similar, but it does not invoke an oxygen bridge between them because one Cu ion is change-balanced by two framework Al ions.

The renewed interest in Cu zeolite catalysts for NH₃-SCR after the discovery of high activity, selectivity, and stability of Cu chabasite materials has led to a number of studies aimed at the elucidation of the active site in this zeolite. It has been reported that Cu ions are present in just one single crystallographic position in these catalysts. This was concluded from Rietveld refinement of XRD data, and the Cu ion was found within the cage just outside the double-six rings connecting the zeolite cages [138]. The relevance of this site for NH₃-SCR was shown in subsequent work [139, 140]. Deka et al. [141] derived similar conclusions from operando-XAFS measurements, where the detailed coordination geometry could be resolved more accurately due to the local sensitivity of EXAFS. A model of the site at different temperatures is shown in Fig. 7.14 where it can also be seen how NH₃ adsorbed onto the Cu ion at low temperatures attracts it slightly toward the center of the cage. It should be noted that this view has been challenged by Kwak et al. on the basis of TPR and IR (CO and NO probe molecules) data, according to

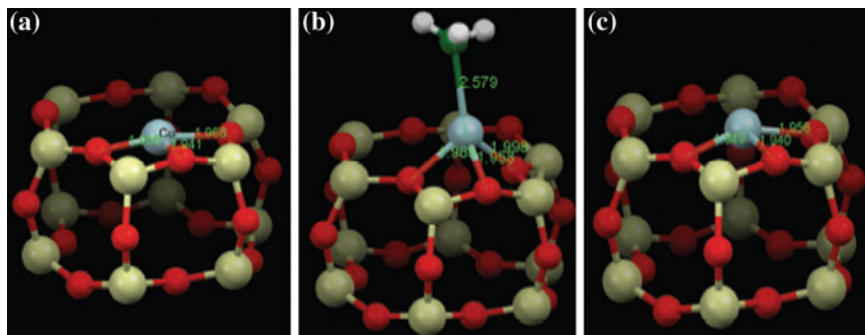


Fig. 7.14 Illustrations of the local copper environment in d6r subunit of CHA. **a** Local structure after calcination, with copper in the plane and slightly distorted from the center of the d6r subunit of CHA; **b** interaction with NH_3 at 423 K under SCR conditions resulting in a coordination geometry change; **c** under SCR conditions above 523 K. From [141] with permission from the American Chemical Society

which a second cation position is populated already at 40 % Cu exchange level [142]. The additional position, which is located more into the cage, but also coordinated to a six-ring, provides a higher redox activity to the Cu ion. Irrespective of the outcome of this controversy, it seems that the activity of Cu-SSZ-13 arises from isolated sites. This very stable activity is very much the same as the one which other Cu zeolites (e.g., Cu-ZSM-5) [143], the performance of which was described to be dominated by binary Cu-O-Cu species in earlier studies [137], can provide only in the fresh state.

7.5 Recent Catalyst Development

In recent years, much work has been devoted to the search for alternative oxide catalysts for NH_3 -SCR, and from the characterization work included in these studies, conclusions regarding the active sites have often been drawn. The most promising systems are based on the elements manganese and cerium, which are often combined with other elements or deposited on supports (see Sect. 2.4).

The extremely high activity of bulk manganese oxides, which provide very large reaction rates at temperatures below 470 K, can apparently arise from several oxidation states of Mn [144–146]. It was shown that MnO_2 is the most active phase, however, its labile oxygen favors the oxidation of ammonia to N_2O [146] while Mn_2O_3 offers significantly better selectivity for N_2 at lower reaction rates [145, 146]. The sizeable N_2O formation over these catalysts and their low thermal stability has prompted efforts to stabilize their active sites on supports or by creation of mixed oxide phases.

Carbon-supported Mn oxides show similar activities as unsupported samples. On the basis of XPS evidence, Yoshikawa et al. concluded that the Mn oxidation state on their surface is +3 [147]. At the same time, Grzybek et al. [148] were

skeptical about the potential of XPS to reliably differentiate Mn^{3+} and Mn^{4+} —at least in routine application (see below). They stated that there may be oxide crystals and two-dimensional layer structures on the carbon surface, where the crystals are more active, whereas the monolayer structures are more selective toward N_2 [149].

Observations made with MnO_x supported on other materials are somewhat different. No bulk phases can be observed on them at low Mn loadings, but the bulk oxides (e.g., Mn_2O_3) appearing at high Mn content did not improve the activity [150]. It was proposed on the basis of a multitechnique characterization study that Mn is present on TiO_2 in the form of monomeric surface oxide species at low Mn loading and as oligomeric monolayer structures upon increase of the Mn content [151]. Above the theoretical monolayer coverage, amorphous oxide layers are formed first whereas crystalline structures appear only at rather high Mn loadings. On the basis of XPS measurements, Pena et al. identified Mn^{4+} and Mn^{3+} on their Mn/TiO_2 catalysts and concluded a larger activity of the former from the catalytic behavior of the samples investigated [152]. Analogously, Mn^{4+} was considered the most active oxidation state by Zhuang et al. [153]. The latter authors observed a pronounced dependence of the activity on the Mn surface density on TiO_2 and concluded that the activity contribution of $\text{Mn}^{4+}\text{--O--Mn}^{4+}$ sites exceeds that of isolated $\text{Mn}^{4+}\text{--O--Ti}$ groups. This agrees with mechanistic proposals of Marban et al., which operate with binary Mn--O--Mn sites [154, 155]. Marban et al., however, proposed the Mn oxidation state to be +3 in these sites, and the mechanism involves a redox cycle between Mn^{3+} and Mn^{2+} in agreement with earlier concepts derived for $\text{Mn}/\text{Al}_2\text{O}_3$ catalysts [156–158]. Mn^{3+} was also advocated as the most active state by Yoshikawa et al. [147] and Li et al. [159].

The disagreement with respect to the active oxidation states is most likely related to the problem that the Mn oxidation states are not easily differentiated by XPS. Due to multiplet splitting, the 2p lines of many 3d elements are broad and asymmetric, and it is inappropriate to fit them with symmetric line profiles. The problem has been nicely illustrated by Biesinger et al. recently [160]. Moreover, binding energies of reference compounds for Mn^{3+} and Mn^{4+} ($\gamma\text{-Mn}_2\text{O}_3$, MnO_2) are within just 1 eV [148], which would be challenging even with well-behaved line profiles. Therefore, Mn 2p XPS, which is exclusively used by most of the authors, is not an appropriate tool for the discrimination between Mn oxidation states [148, 149]. Instead, the splitting of the Mn 3s signal (also by the multiplet effect) gives better evidence for the oxidation state(s) present [161], however, due to the rather weak intensity of this signal it has been rarely measured with supported catalysts.

Mixed oxides of manganese with other elements, e.g., with Fe [162] often exhibit much better thermal stability and selectivity to N_2 at only slightly diminished activity (compared with pure Mn oxides). The improved properties have been attributed to Mn--O--M ($\text{M}=\text{Cr, Fe, Ce}$) linkages [163–165], and thermally stable stoichiometric compounds ($\text{CrMn}_{1.5}\text{O}_4$ [163], $\text{Fe}_3\text{Mn}_3\text{O}_8$ [164]) have been proposed to be active in these mixed-oxide catalysts. The redox chemistry would then be distributed between two redox elements.

Cerium is another redox element successfully applied in alternative catalysts for NH_3 -SCR. It offers promising nitrogen selectivity and stability though at somewhat lower activity. To exhibit these properties, Ce has to be deposited onto supports, because the pure oxide is rather inactive unlike the Mn oxides. Apparently, the bridging bonds between Ce and different elements (Ce–O–Ti in case of TiO_2) are important for SCR catalysis. This has been the rationale to develop very interesting Ce/ TiO_x mixed oxide catalysts by homogeneous precipitation [166, 167]. In [167], the Ce–O–Ti linkages were even detected by XAFS. Likewise, Ce–O–W bridges have been considered responsible for promising properties of CeO_2 - WO_3 coprecipitated catalysts [168]. Little is known about the most favorable active oxidation state of the Ce cation. While the Lewis acidity of Ce^{4+} has stressed in [168], the same authors considered the increased Ce^{3+} surface concentration (compared to CeO_2) favorable because of a concomitant formation of Brønsted sites [169].

7.6 Concluding Remarks

Research on heterogeneous catalysts is very much driven by the desire to identify the active sites for useful reactions. The combined catalytic and characterization work required for this generates an experimental basis and useful ideas for further catalyst improvement. From such work, it appears that the SCR of NO by NH_3 can proceed on different site types over the most important catalysts known. For vanadium-based systems, there is general agreement that binary V–O–V moieties including a Brønsted site are the most active structures, and a well-accepted mechanism is available for this site. At the same time, isolated $(\text{VO})^{2+}$ ions exchanged into zeolites can catalyze the same reaction, apparently via a different mechanism. According to recent studies, the W promoter creates an optimum degree of isolation for the TiO_2 -supported binary V–O–V sites, which appear to lose their reactivity when they are incorporated into large surface oxide patches.

For Fe- and Cu-modified zeolites, there is general agreement that NH_3 -SCR can proceed on isolated cation sites, but their intrinsic activities appear to depend in an unknown way on the cation position in the zeolite. There are indications for the involvement of oligomeric oxide structures in catalysts as well although this is not generally accepted. Fast SCR over Fe zeolites uses exclusively isolated sites, probably a type stabilized as Fe^{2+} by two nearby framework Al ions.

Active site concepts for Mn- and Ce-based systems are not yet well developed, which is partly due to problems in the reliable differentiation between oxidation states in case of Mn.

Acknowledgments I would like to acknowledge a fruitful cooperation with all coauthors of own publications cited in this chapter, and for the funding by the German Science Foundation (DFG), by Interkat GmbH, Königswinter, Germany, and by Crenox (now Sachtleben Pigments, Krefeld, Germany). I am particularly grateful for the many years of inspiring exchange of ideas, materials, and results with Prof. Angelika Brückner, LIKAT Rostock, Germany. Finally, I want to thank my actual PhD students Inga Ellmers, Mariam Salazar Rodriguez, and Rosemary Fowler for support by literature work and proof reading.

References

1. Taylor HS (1925) A Theory of the Catalytic Surface. *Proc Royal Soc A* 108:105–111
2. Teschner D, Vass E, Hävecker M, Zafeirotos S, Schnörch P, Sauer H, Knop-Gericke A, Schlögl R, Chamam M, Wootsch A, Canning AS, Gamman JJ, Jackson SD, McGregor J, Gladden LF (2006) Alkyne hydrogenation over Pd catalysts: A new paradigm. *J Catal* 242 (1):26–37
3. Niemantsverdriet JW (1995) *Spectroscopy in Catalysis*. Wiley-VCH, Weinheim
4. Che M, Viedrine JC (eds) (2012) *Characterization of Solid Materials and Heterogeneous Catalysts - From Structure to Surface Reactivity*. Wiley-VCH, Weinheim
5. Weckhuysen BM, van der Voort P, Catana G (eds) (2000) *Spectroscopy of Transition Metal Ions on Surfaces*. Leuven University Press, Leuven
6. Haw JF (ed) (2002) *In-situ Spectroscopy in Heterogeneous Catalysis*. Wiley-VCH, Weinheim
7. Weckhuysen BM (ed) (2004) *In-Situ Spectroscopy of Catalysts*. Amer Scientific Pub, California
8. Hansen PL, Wagner JB, Helveg S, Rostrup-Nielsen JR, Clausen BS, Topsøe H (2002) Atom-resolved imaging of dynamic shape changes in supported copper nanocrystals. *Science* 295 (5562):2053–2055
9. Clausen BS, Schiøtz J, Gråbæk L, Ovesen CV, Jacobsen KW, Nørskov JK, Topsøe H (1994) Wetting/non-wetting phenomena during catalysis: Evidence from in situ on-line EXAFS studies of Cu-based catalysts. *Top Catal* 1 (3–4):367–376
10. Grunwaldt J-D, Molenbroek AM, Topsøe N-Y, Topsøe H, Clausen BS (2000) In Situ investigations of structural changes in Cu/ZnO catalysts. *J Catal* 194 (2):452–460
11. Wagner JB, Timpe O, Hamid FA, Trunschke A, Wild U, Su DS, Widi RK, Abd Hamid SB, Schlögl R (2006) Surface texturing of Mo–V–Te–Nb–Ox selective oxidation catalysts. *Top Catal* 38 (1–3):51–58
12. Sanfiz AC, Hansen TW, Teschner D, Schnörch P, Girgsdies F, Trunschke A, Schlögl R, Looi MH, Abd Hamid SB (2010) Dynamics of the MoVTeNb Oxide M1 Phase in Propane Oxidation. *J Phys Chem C* 114 (4):1912–1921
13. Millet JMM, Roussel H, Pigamo A, Dubois JL, Jumas JC (2002) Characterization of tellurium in MoVTeNbO catalysts for propane oxidation or ammoxidation. *Appl Catal A* 232 (1–2):77–92
14. Ueda W, Vitry D, Katou T (2004) Structural organization of catalytic functions in Mo-based oxides for propane selective oxidation. *Catal Today* 96 (4):235–240
15. Farges F, Brown GE, Rehr JJ (1997) Ti K-edge XANES studies of Ti coordination and disorder in oxide compounds: Comparison between theory and experiment. *Phys Rev B* 56 (4):1809–1819
16. Häggblad R, Hansen S, Wallenberg LR, Andersson A (2010) Stability and performance of cation vacant $\text{Fe}_{3-x}\text{V}_y\text{O}_4$ spinel phase catalysts in methanol oxidation. *J Catal* 276 (1):24–37
17. Petit P-E, Farges F, Wilke M, Solé VA (2001) Determination of the iron oxidation state in Earth materials using XANES pre-edge information. *J Synchrotron Rad* 8:952–954
18. Farges F, Lefrère Y, Rossano S, Berthereau A, Calas G, Brown Jr GE (2004) The effect of redox state on the local structural environment of iron in silicate glasses: a combined XAFS spectroscopy, molecular dynamics, and bond valence study. *J Non-Cryst Solids* 344 (3):176–188
19. Reichinger M, Schmidt W, van den Berg MWE, Aerts A, Martens JA, Kirschhock CEA, Gies H, Grünert W (2009) Alkene epoxidation with mesoporous materials assembled from TS-1 seeds – Is there a hierarchical pore system? *J Catal* 269 (2):367–375
20. Glatzel JPS, Bergmann U (2005) High resolution 1 s core hole X-ray spectroscopy in 3d transition metal complexes - electronic and structural information. *Coord Chem Rev* 249 (1–2):65–95

21. Salmeron M, Schlögl R (2008) Ambient pressure photoelectron spectroscopy: A new tool for surface science and nanotechnology. *Surf Sci Rep* 63 (4):169–199
22. Ogletree DF, Bluhm H, Lebedev G, Fadley CS, Hussain Z, Salmeron M (2002) A differentially pumped electrostatic lens system for photoemission studies in the millibar range. *Rev Sci Instr* 73 (11):3872–3877
23. Bñares MA, Wachs IE (2002) Molecular structures of supported metal oxide catalysts under different environments. *J Raman Spectrosc* 33 (5):359–380
24. Zecchina A, Garrone E, Ghiotti G, Morterra C, Borello E. (1975) Chemistry of silica supported chromium ions. I. Characterization of the samples. *J Phys Chem* 79 (10):966–972
25. Topsøe N-Y, Topsøe H (1983) Characterization of the structures and active sites in sulfided Co-Mo/Al₂O₃ and Ni-Mo/Al₂O₃ catalysts by NO chemisorption. *J Catal* 84 (2):386–401
26. Zaki MI, Vielhaber B, Knözinger H (1986) Low-temperature carbon monoxide adsorption and state of molybdena supported on alumina, titania, ceria, and zirconia. An infrared spectroscopic investigation. *J Phys Chem* 90 (14):3176–3183
27. Hadjiivanov KI, Vayssilov GN (2002) Characterization of oxide surfaces and zeolites by carbon monoxide as an IR probe molecule. *Adv Catal* 47:307–511
28. Topsøe N-Y, Topsøe H (1999) FTIR studies of dynamic surface structural changes in Cu-based methanol synthesis catalysts. *J Mol Catal A* 141 (1–3):95–105
29. Elmasides C, Kondarides DI, Grünert W, Verykios XE (1999) XPS and FTIR Study of Ru/Al₂O₃ and Ru/TiO₂ Catalysts: Reduction Characteristics and Interaction with a Methane-Oxygen Mixture. *J Phys Chem B* 103 (25):5227–5239
30. Santhosh Kumar M, Schwidder M, Grünert W, Brückner A (2004) On the nature of different iron sites and their catalytic role in Fe-ZSM-5 DeNO_x catalysts: new insights by a combined EPR and UV/VIS spectroscopic approach. *J Catal* 227 (2):384–397
31. Brückner A (2004) Electron Paramagnetic Resonance. In: Weckhuysen BM (ed) (2004) *In-situ Spectroscopy of Catalysts*. Amer Scientific Pub, California
32. Blasco T. (2010) Insights into reaction mechanisms in heterogeneous catalysis revealed by in situ NMR spectroscopy. *Chem. Soc. Rev.* 39: 4685–4702
33. Steinfeldt N, Müller D, Berndt H (2004) VO_x species on alumina at high vanadia loadings and calcination temperature and their role in the ODP reaction. *Appl Catal A* 272 (1–2):201–213
34. Holland GP, Cherry BR, Alam TM (2004) N-15 solid-state NMR characterization of ammonia adsorption environments in 3A zeolite molecular sieves. *J. Phys. Chem. B* 108:16420–16426
35. Hunger M (2008) In situ flow MAS NMR spectroscopy: State of the art and applications in heterogeneous catalysis. *Prog Nucl Magn Reson Spectrosc* 53 (3):105–127
36. Chen H-Y, Sachtler WMH (1998) Activity and durability of Fe/ZSM-5 catalysts for lean-burn NO_x reduction in the presence of water vapor. *Catal Today* 42 (1–2):73–83
37. Heinrich F, Schmidt C, Löffler E, Menzel M, Grünert W (2002) Fe-ZSM-5 catalysts for the selective reduction of NO by isobutane - The problem of the active sites. *J Catal* 212 (2):157–172
38. Heinrich F (2002) Selektive katalytische Reduktion von NO mit Kohlenwasserstoffen an eisenmodifizierten Zeolithen. PhD thesis, Ruhr University, Bochum
39. Wilmer H, Genger T, Hinrichsen O (2003) The interaction of hydrogen with alumina-supported copper catalysts: a temperature-programmed adsorption/temperature-programmed desorption/isotopic exchange reaction study. *J Catal* 215 (2):188–198
40. Bond GC, Tahir SF (1991) Vanadium oxide monolayer catalysts - Preparation, characterization and catalytic activity. *Appl Catal* 71 (1):1–31
41. Centi G (1996) Nature of active layer in vanadium oxide supported on titanium oxide and control of its reactivity in the selective oxidation and ammoxidation of alkylaromatics. *Appl Catal A* 147 (2):267–298
42. Wachs IE (2005) Recent conceptual advances in the catalysis science of mixed metal oxide catalytic materials. *Catal Today* 100 (1–2):79–94

43. Wachs IE (1996) Raman and IR studies of surface metal oxide species on oxide supports: Supported metal oxide catalysts. *Catal Today* 27 (3–4):437–455
44. Deo G, Wachs IE, Haber J (1994) Supported vanadium-oxide catalysts - molecular structural characterization and reactivity properties. *Crit Rev Surf Chem* 4 (3–4):141–187
45. Eberhardt MA, Houalla M, Hercules DM (1993) Ion scattering and electron spectroscopic study of the surface coverage of V/Al₂O₃ catalysts. *Surf Interface Anal* 20 (9):766–770
46. Vaidyanathan N, Houalla M, Hercules DM (1997) Determination of the surface coverage of WO₃/TiO₂ catalysts by CO₂ chemisorption. *Catal Lett* 43 (3–4):209–212
47. Zingg DS, Makovsky LE, Tischer RE, Brown FR, Hercules DM (1980) A surface spectroscopic study of molybdenum-alumina catalysts using x-ray photoelectron, ion scattering, and Raman spectroscopies. *J Phys Chem* 84 (22):2898–2906
48. Briand LE, Tkachenko OP, Guraya M, Gao X, Wachs IE, Grünert W (2004) Surface-analytical Studies of Supported Vanadium Oxide Monolayer Catalysts. *J Phys Chem B* 108 (15):4823–4830
49. Briand LE, Tkachenko OP, Guraya M, Wachs IE, Grünert W (2004) Methodical aspects in the surface analysis of supported molybdena catalysts. *Surf Interface Anal* 36 (3):238–245
50. Leyrer J, Zaki MI, Knözinger H (1990) Solid/solid interactions - Monolayer formation in MoO₃/Al₂O₃ physical mixtures. *J Phys Chem* 90 (20):4775–4780
51. Xie Y, Gui L, Liu Y, Zhao B, Yang N, Zhang Y, Guo Q, Duan L, Huang H, Cai X, Tang Y (1984) In: *Proceedings of the 8th International Congress on Catalysis*. Berlin, 5:147
52. Kompio PGWA, Brückner A, Hipler F, Auer G, Löffler E, Grünert W (2012) A new view on the relations between tungsten and vanadium in V₂O₅-WO₃/TiO₂ catalysts for the selective reduction of NO with NH₃. *J Catal* 286:237–247
53. Inomata M, Miyamoto A, Murakami Y (1980) Mechanism of the reaction of NO and NH₃ on vanadium oxide catalyst in the presence of oxygen under the dilute gas condition. *J Catal* 62 (1):140–148
54. Baiker A, Dollenmeier P, Glinski M, Reller A (1987) Selective catalytic reduction of nitric oxide with ammonia: I. Monolayer and Multilayers of Vanadia Supported on Titania. *Appl Catal* 35 (2):351–364
55. Went GT, Leu LJ, Rosin RR, Bell AT (1992) The effects of structure on the catalytic activity and selectivity of V₂O₅/TiO₂ for the reduction of NO by NH₃. *J Catal* 134 (2):492–505
56. Lietti L, Forzatti P (1994) Temperature Programmed Desorption/Reaction of Ammonia over V₂O₅/TiO₂ De-NO_xing Catalysts. *J Catal* 147 (1):241–249
57. Szakacs S, Altena GJ, Fransen T, Van Ommen JG, Ross JRH (1993) The Selective Reduction of NO_x with NH₃ over Zirconia-Supported Vanadia Catalysts. *Catal Today* 16 (2):237–245
58. Bosch H, Janssen FJJG (1988) *Catal Today* 2 (4):369–531
59. Ozkan US, Cai YP, Kumthekar MW (1994) Investigation of the Reaction Pathways in Selective Catalytic Reduction of NO with NH₃ over V₂O₅ Catalysts: Isotopic Labeling Studies Using ¹⁸O₂, ¹⁵NH₃, ¹⁵NO, and ¹⁵N¹⁸O. *J Catal* 149 (2):390–403
60. Gasior M, Haber J, Machej T, Czeppe T (1988) Mechanism of the reaction NO + NH₃ on V₂O₅ catalysts. *J Mol Catal* 43 (3):359–369
61. Topsøe N-Y (1994) Mechanism of the Selective Catalytic Reduction of Nitric Oxide by Ammonia Elucidated by in Situ On-Line Fourier Transform Infrared Spectroscopy. *Science* 265 (5176):1217–1219
62. Topsøe N-Y, Dumesic JA, Topsøe H (1995) Vanadia-Titania Catalysts for Selective Catalytic Reduction of Nitric-Oxide by Ammonia .2. Studies of Active-Sites and Formulation of Catalytic Cycles. *J Catal* 151 (1):241–252
63. Topsøe N-Y, Topsøe H, Dumesic JA (1995) Vanadia-Titania Catalysts for Selective Catalytic Reduction (SCR) of Nitric-Oxide by Ammonia .1. Combined Temperature-Programmed in-Situ FTIR and Online Mass-Spectroscopy Studies. *J Catal* 151 (1):226–240

64. Dumesic JA, Topsøe N-Y, Topsøe H, Chen Y, Slabiak T (1996) Kinetics of Selective Catalytic Reduction of Nitric Oxide by Ammonia over Vanadia/Titania. *J Catal* 163 (2):409–417
65. Wark M, Brückner A, Liese T, Grünert W (1998) Selective Catalytic Reduction of NO by NH₃ over Vanadium-Containing Zeolites. *J Catal* 175(1):48–61
66. Alemany LJ, Lietti L, Ferlazzo N, Forzatti P, Busca G, Giamello E, Bregani F (1995) Reactivity and Physicochemical Characterization of V₂O₅-WO₃/TiO₂ De-NO_x Catalysts. *J Catal* 155 (1):117–130
67. Broclawik E, Góra A, Najbar M (2001) The role of tungsten in formation of active sites for no SCR on the V-W-O catalyst surface - quantum chemical modeling (DFT). *J Mol Catal A* 166 (1):31–38
68. Lietti L, Alemany JL, Forzatti P, Busca G, Ramis G, Giamello E, Bregani F (1996) Reactivity of V₂O₅-WO₃/TiO₂ catalysts in the selective catalytic reduction of nitric oxide by ammonia. *Catal Today* 29 (1–4):143–148
69. Vuurman MA, Wachs IE, Hirt AM (1991) Structural determination of supported vanadium pentoxide-tungsten trioxide-titania catalysts by in situ Raman spectroscopy and x-ray photoelectron spectroscopy. *J Phys Chem* 95 (24):9928–9937
70. Kompio PGWA (2010) Der Einfluss von Hochtemperaturbehandlungen auf V₂O₅-WO₃/TiO₂-Katalysatoren für die selektive katalytische Reduktion von Stickoxiden mit Ammoniak. PhD thesis, Ruhr University; Bochum
71. Feng X, Hall WK (1996) On the unusual stability of overexchanged FeZSM-5. *Catal Lett* 41 (1–2):45–46
72. Voskoboinikov TV, Chen H-Y, Sachtler WMH (1998) On the nature of active sites in Fe/ZSM-5 catalysts for NO_x abatement. *Appl Catal B* 19 (3–4):279–287
73. Chen H-Y, El-Malki E-M, Wang X, Van Santen RA, Sachtler WMH (2000) Identification of active sites and adsorption complexes in Fe/MFI catalysts for NO_x reduction. *J Mol Catal A* 162 (1–2):159–174
74. Iwamoto M, Yahiro H, Tanda K, Mizuno N, Mine Y, Kagawa S (1991) Removal of Nitrogen Monoxide through a Novel Catalytic Process. 1. Decomposition on Excessively Copper Ion Exchanged ZSM-5 Zeolites. *J Phys Chem* 95 (9):3727–3730
75. Battiston AA, Bitter JH, Koningsberger DC (2000) XAFS characterization of the binuclear iron complex in overexchanged Fe/ZSM5 - structure and reactivity. *Catal Lett* 66 (1–2):75–79
76. Marturano P, Drozdová L, Kogelbauer A, Prins R (2000) Fe/ZSM-5 Prepared by Sublimation of FeCl₃: The Structure of the Fe Species as Determined by IR, ²⁷Al MAS NMR, and EXAFS Spectroscopy. *J Catal* 192 (1):236–247
77. Marturano P, Drozdová L, Pirngruber GD, Kogelbauer A, Prins R (2001) The mechanism of formation of the Fe species in Fe/ZSM-5 prepared by CVD. *PCCP* 3:5585–5595
78. Battiston AA, Bitter JH, Koningsberger DC (2003) Reactivity of binuclear Fe complexes in over-exchanged Fe/ZSM5, studied by in situ XAFS spectroscopy – 2. Selective catalytic reduction of NO with isobutane. *J Catal* 218 (1):163–177
79. Heinrich F, Schmidt C, Löffler E, Grünert W (2001) A highly active intra-zeolite iron site for the selective catalytic reduction of NO by isobutane. *Catal Comm* 2 (10):317–321
80. Heijboer WM, Koningsberger DC, Weckhuysen BM, de Groot FMF (2005) New frontiers in X-ray spectroscopy in heterogeneous catalysis: Using Fe/ZSM-5 as test-system. *Catal Today* 110 (3–4):228–238
81. Battiston AA, Bitter JH, de Groot FMF, Overweg AR, Stephan O, van Bokhoven JA, Kooyman PJ, van der Spek D, Vankó G, Koningsberger DC (2003) Evolution of Fe species during the synthesis of over-exchanged Fe/ZSM5 obtained by chemical vapor deposition of FeCl₃. *J Catal* 213 (2):251–271
82. Pirngruber GD, Roy PK, Prins R (2006) On determining the nuclearity of iron sites in Fe-ZSM-5 - a critical evaluation. *Phys Chem Chem Phys* 8 (34):3939–3950
83. Long RQ, Yang RT (2001) Fe-ZSM-5 for selective catalytic reduction of NO with NH₃: a comparative study of different preparation techniques. *Catal Lett* 74 (3–4):201–205

84. Berrier E, Ovsitser O, Kondratenko EV, Schwidder M, Grünert W, Brückner A (2007) Temperature-dependent N_2O decomposition over Fe-ZSM-5: Identification of sites with different activity. *J Catal* 249 (1):67–78
85. Bordiga S, Buzzoni R, Geobaldo F, Lamberti C, Giamello E, Zecchina A, Leofanti G, Petrini G, Tozzola G, Vlaic G (1996) Structure and reactivity of framework and extraframework iron in Fe-silicate as investigated by spectroscopic and physicochemical methods. *J Catal* 158 (2):486–501
86. Schwidder M, Santhosh Kumar M, Klementiev KV, Pohl MM, Brückner A, Grünert W (2005) Selective Reduction of NO with Fe-ZSM-5 Catalysts of Low Fe content I. Relations between Active Site Structure and Catalytic Performance. *J Catal* 231 (2):314–330
87. Santhosh Kumar M, Schwidder M, Grünert W, Bentrup U, Brückner A (2006) Selective reduction of NO with Fe-ZSM-5 catalysts of low Fe content. II. Assigning the function of different Fe sites by spectroscopic in situ studies. *J Catal* 239 (1):173–186
88. Schwidder M, Heikens S, De Toni A, Geisler S, Berndt M, Brückner A, Grünert W (2008) The role of NO_2 in the Selective Catalytic Reduction of Nitrogen Oxides over Fe-ZSM-5 Catalysts – Active Sites for the Conversion of NO and of NO/ NO_2 mixtures. *J Catal* 259 (1):96–103
89. Krishna K, Makkee M (2006) Preparation of Fe-ZSM-5 with enhanced activity and stability for SCR of NO_x . *Catal Today* 114 (1):23–30
90. Doronkin DE, Stakheev AY, Kucherov AV, Tolkachev NN, Kustova M, Høj M, Baeva GN, Bragina GO, Gabrielsson P, Gekas I, Dahl S (2009) Nature of Active Sites of Fe-Beta Catalyst for NO_x -SCR by NH_3 . *Top Catal* 52 (13–20):1728–1733
91. Klukowski D, Balle P, Geiger B, Waglöhner S, Kureti S, Kimmeler B, Baiker A, Grunwaldt J-D (2009) On the mechanism of the SCR reaction on Fe/HBEA zeolite. *Appl Catal B* 93 (1–2):185–193
92. Iwasaki M, Yamazaki K, Banno K, Shinjoh H (2008) Characterization of Fe/ZSM-5 $DeNO_x$ catalysts prepared by different methods: Relationships between active Fe sites and NH_3 -SCR performance. *J Catal* 260 (2):205–216
93. Iwasaki M, Shinjoh H (2010) Analysis of the adsorption state and desorption kinetics of NO_2 over Fe-zeolite catalysts by FTIR and temperature programmed desorption. *Phys Chem Chem Phys* 12 (10):2365–2372
94. Iwasaki M, Shinjoh H (2010) NO evolution reaction with NO_2 adsorption over Fe/ZSM-5: In situ FT-IR observation and relationships with Fe sites. *J Catal* 273 (1):29–38
95. Dědeček J, Sobalik Z, Wichterlová B (2012) Siting and Distribution of Framework Aluminium Atoms in Silicon-Rich Zeolites and Impact on Catalysis. *Catal Rev Sci Eng* 54:135–223
96. Sobalik Z, Sazama P, Dědeček J, Wichterlová B Critical evaluation of the role of the distribution of Al atoms in the framework for the activity of metallo-zeolites in redox N_2O / NO_x reactions *Appl Catal A* 2014: in press doi: [10.1016/j.apcata.2013.07.033](https://doi.org/10.1016/j.apcata.2013.07.033)
97. Brandenberger S, Kröcher O, Tissler A, Althoff R (2008) The state of the art in selective catalytic reduction of NO_x by ammonia using metal-exchanged zeolite catalysts. *Catal Rev - Sci Eng* 50 (4):492–531
98. Brandenberger S, Kröcher O (2010) Estimation of the fractions of different nuclear iron species in uniformly metal-exchanged Fe-ZSM-5 samples based on a Poisson distribution. *Appl Catal B* 373 (1–2):168–175
99. Brandenberger S, Kröcher O, Tissler A, Althoff R (2010) The determination of the activities of different iron species in Fe-ZSM-5 for SCR of NO by NH_3 . *Appl Catal B* 95 (3–4):348–357
100. Schwidder M, Santhosh Kumar M, Bentrup U, Pérez-Ramírez J, Brückner A, Grünert W (2008) The role of Brønsted Acidity in the SCR of NO over Fe-MFI Catalysts. *Microporous Mesoporous Mater* 111 (1–3):124–133
101. Brandenberger S, Kröcher O, Wokaun A, Tissler A, Althoff R (2010) The role of Brønsted acidity in the selective catalytic reduction of NO with ammonia over Fe-ZSM-5. *J Catal* 268 (2):297–306

102. Yeom YH, Heno J, Li MJ, Sachtler WMH, Weitz E (2005) The role of NO in the mechanism of NO_x reduction with ammonia over a BaNa-Y catalyst. *J Catal* 231 (1):181–193
103. Li MJ, Yeom Y, Weitz E, Sachtler WMH (2006) An acid catalyzed step in the catalytic reduction of NO_x to N₂. *Catal Lett* 112 (3–4):129–132
104. Pérez Vélez R, Ellmers I, Huang H, et al. Identifying active sites for fast NH₃-SCR of NO/NO₂ mixtures over Fe-ZSM-5 by operando EPR and UV-vis spectroscopy. *J Catal* 2014:submitted
105. Ellmers I, Velez RP, Bentrup U, Brückner A, Grünert W (2014) Oxidation and Selective Reduction of NO over Fe-ZSM-5 – How related are these reactions? *J. Catal* 311:199–211 in press.
106. Apostolescu N, Geiger B, Hizbullah K, Jan MT, Kureti S, Reicher D, Schott F, Weisweiler W (2006) Selective catalytic reduction of nitrogen oxides by ammonia on iron oxide catalysts. *Appl Catal B* 62 (1–2):104–114
107. Centi G, Perathoner S (1995) Nature of active species in copper-based catalysts and their chemistry of transformation of nitrogen oxides. *Appl Catal A* 132 (2):179–259
108. Seiyama T, Arakawa T, Matsuda T, Yamazoe N, Takita Y (1975) Catalytic Reduction of Nitric-oxide with Ammonia over Transition-metal Ion-exchanged Y-zeolites. *Chem Lett* 4 (7):781–784
109. Seiyama T, Arakawa T, Matsuda T, Takita Y, Yamazoe N (1977) Catalytic activity of transition metal ion exchanged Y zeolites in the reduction of nitric oxide with ammonia. *J Catal* 48 (1–3):1–7
110. Iwamoto M, Yahiro H, Mine Y, Kagawa S (1989) Excessively Copper ion-exchanged ZSM-5 zeolites as highly active catalyst for direct decomposition of nitrogen monoxide. *Chem Lett* 18 (2):213
111. Held W, König A, Richter T, Puppe L (1990) Catalytic NO_x reduction in net oxidizing exhaust gas. SAE-Technical Paper: 900496 doi: [10.4271/900496](https://doi.org/10.4271/900496)
112. Williamson WB, Lunsford JH (1976) Nitric oxide reduction with ammonia over copper(II) Y zeolites. *J Phys Chem* 80 (24):2664–2671
113. Campa MC, Indovina V, Minelli G, Moretti G, Pettiti I, Porta A, Riccio A (1994) The catalytic activity of Cu-ZSM-5 and Cu-Y zeolites in NO decomposition: dependence on copper concentration. *Catal Lett* 23 (1–2):141–149
114. Valyon J, Keith Hall W (1993) On the preparation and properties of Cu-ZSM-5 catalysts for NO decomposition. *Catal Lett* 19 (2–3):109–119
115. Moretti G (1994) Turnover frequency for NO decomposition over Cu-ZSM-5 catalysts: insight into the reaction mechanism. *Catal Lett* 28 (2–4):143–152
116. Lei GD, Adelman BJ, Sárkányi J, Sachtler WMH (1995) Identification of copper(II) and copper(I) and their interconversion in Cu/ZSM-5 De-NO_x catalysts. *Appl Catal B* 5 (3):245–256
117. Moretti G, Ferraris G, Fierro G, Lo Jacono M, Morpurgo S, Faticanti M (2005) Dimeric Cu(I) species in Cu-ZSM-5 catalysts: the active sites for the NO decomposition. *J Catal* 232 (2):476–487
118. Sárkányi J, d'Itri JL, Sachtler WMH (1992) Redox chemistry in excessively ion-exchanged Cu/Na-ZSM-5. *Catal Lett* 16 (3):241–249
119. Wichterlová B, Dedeczek J, Tvarůžková Z (1994) Cu coordination in zeolite matrix. Relationship to nitric oxide binding and decomposition. *Stud Surf Sci Catal* 84 :1555–1562
120. Grünert W, Hayes NW, Joyner RW, Shpiro ES, Siddiqui MRH, Baeva GN (1994) Structure, Chemistry, and Activity of Cu-ZSM-5 Catalysts for the Selective Reduction of NO_x in the Presence of Oxygen. *J Phys Chem* 98 (42):10832–10846
121. Liese T, Grünert W (1997) Cu-Na-ZSM-5 Catalysts Prepared by Chemical Transport: Investigations on the Role of Brønsted Acidity and of Excess Copper in the Selective Catalytic Reduction of NO by Propene. *J Catal* 172 (1):34–45
122. Jirka I, Wichterlová B, Maryská M (1991) ESCA study of incorporation of copper into Y zeolite. *Stud Surf Sci Catal* 69 (1):269–276

123. Sexton BA, Smith TD, Sanders JV (1985) Characterization of copper-exchanged Na-A, X and Y zeolites with X-ray photoelectron spectroscopy and transmission electron microscopy. *J Electron Spectrosc Relat Phenom* 35 (1):27–43
124. Morales J, Espinos JP, Caballero A, Gonzalez-Elipse AR, Mejias JA (2005) XPS study of interface and ligand effects in supported Cu₂O and CuO nanometric particles. *J Phys Chem B* 109 (16):7758–7765
125. Sato S, Yu-u Y, Yahiro H, Mizuno N, Iwamoto M (1991) Cu-ZSM-5 zeolite as highly active catalyst for removal of nitrogen monoxide from emission of diesel engines. *Appl Catal* 70 (1):L1–L5
126. Kharas KCC (1993) Performance, selectivity, and mechanism in Cu-ZSM-5 lean-burn catalysts. *Appl Catal B* 2 (2–3):207–224
127. Ciambelli P, Corbo P, Gambino M, Minelli G, Moretti G, Porta P (1995) Lean NO_x reduction CuZSM5 catalysts: Evaluation of performance at the spark ignition engine exhaust. *Catal Today* 26 (1):33–39
128. Wichterlová B, Sobalik Z, Vondrová A (1996) Differences in the structure of copper active sites for decomposition and selective reduction of nitric oxide with hydrocarbons and ammonia. *Catal Today* 29 (1–4):149–153
129. Centi G, Nigro C, Perathoner S, Stella G (1994) Reactivity of Cu-Based Zeolites and Oxides in the Conversion of NO in the Presence or Absence of O₂. *Environmental Catalysis: ACS Symposium Ser.* 552 (3):22–38
130. Shelef M (1995) Selective catalytic reduction of NO_x with N-free reductants. *Chem Rev* 95 (1):209–225
131. Hamada H, Kintaichi Y, Sasaki M, Ito T, Tabata M (1990) Highly selective reduction of nitrogen oxides with hydrocarbons over H-form zeolite catalysts in oxygen-rich atmosphere. *Appl Catal* 64 (1–2):L1–L4
132. Loughran CE, Resasco DE (1995) Bifunctionality of palladium-based catalysts in the reduction of nitric oxide by methane in the presence of oxygen. *Appl Catal B* 7 (1–2):113–126
133. Kikuchi E, Yogo K (1994) Selective catalytic reduction of nitrogen monoxide by methane on zeolite catalysts in an oxygen-rich atmosphere. *Catal Today* 22 (1):73–86
134. Centi G, Perathoner S, Dall’Olio L (1994) High activity of copper-borallite in the reduction of nitric oxide with propane/oxygen. *Appl Catal B* 4 (4):L275–L281
135. Jen H-W, McCabe RW, Gorte RJ, Parillo DJ (1994) Reduction of NO Under Lean Conditions Over ZSM-5-Based Catalysts: Effect of Cu Loading and Zeolite Type. *Am Chem Soc, Div Petr Chem* 39:104–109
136. Kieger S, Delahay G, Coq B, Neveu B (1999) Selective Catalytic Reduction of Nitric Oxide by Ammonia over Cu-FAU Catalysts in Oxygen-Rich Atmosphere. *J Catal* 183 (2):267–280
137. Komatsu T, Nunokawa M, Moon IS, Takahara T, Namba S, Yashima T (1994) Kinetic Studies of Reduction of Nitric Oxide with Ammonia on Cu²⁺-Exchanged Zeolites. *J Catal* 148 (2):427–437
138. Fickel DW, Lobo RF (2010) Copper Coordination in Cu-SSZ-13 and Cu-SSZ-16 Investigated by Variable-Temperature XRD. *J Phys Chem C* 114 (3):1633–1640
139. Korhonen ST, Fickel DW, Lobo RF, Weckhuysen BM, Beale AM (2011) Isolated Cu²⁺ ions: active sites for selective catalytic reduction of NO. *Chem Commun* 47 (47):800–802
140. Fickel DW, D’Addio E, Lauterbach JA, Lobo RF (2011) The ammonia selective catalytic reduction activity of copper-exchanged small-pore zeolites. *Appl Catal B* 102 (3–4):441–448
141. Deka U, Juhin A, Eilertsen EA, Emerich H, Green MA, Korhonen ST, Weckhuysen BM, Beale AM (2012) Confirmation of Isolated Cu²⁺ Ions in SSZ-13 Zeolite as Active Sites in NH₃-Selective Catalytic Reduction. *J Phys Chem C* 116 (7):4809–4818
142. Kwak JH, Zhu H, Lee JH, Peden CHF, Szanyi J (2012) Two different cationic positions in Cu-SSZ-13? *Chem Commun* 48 (39):4758–4760
143. Kwak JH, Tran D, Burton SD, Szanyi J, Jolee JH, Peden CHF (2012) Effects of hydrothermal aging on NH₃-SCR reaction over Cu/zeolites. *J Catal* 287 (1):203–209

144. Li J, Chang H, Ma L, Hao J, Yang RT (2011) Low-temperature selective catalytic reduction of NO_x with NH₃ over metal oxide and zeolite catalysts-A review. *Catal Today* 175 (1):147–156
145. Kapteijn F, Singoredjo L, Andreini A, Moulijn JA (1994) Activity and selectivity of pure manganese oxides in the selective catalytic reduction of nitric oxide with ammonia. *Appl Catal B* 3 (2–3):173–189
146. Tang X, Li J, Sun L, Hao J (2010) Origination of N₂O from NO reduction by NH₃ over Beta-MnO₂ and alpha-Mn₂O₃. *Appl Catal B* 99 (1–2):156–162
147. Yoshikawa M, Yasutake A, Mochida I (1998) Low-Temperature selective catalytic reduction of NO_x by metal oxides supported on active carbon fibers. *Appl Catal A* 173 (2):239–245
148. Grzybek T, Klinik J, Rogoz M, Papp H (1998) Manganese supported catalysts for selective catalytic reduction of nitrogen oxides with ammonia - Part 1 - Characterization. *J Chem Soc-Faraday Trans* 94 (18):2843–2850
149. Grzybek T, Pasel J, Papp H (1999) Supported manganese catalysts for the selective catalytic reduction of nitrogen oxides with ammonia II. Catalytic experiments. *Phys Chem Chem Phys* 1 (2):341–348
150. Qi G, Yang RT (2003) Low-temperature selective catalytic reduction of NO with NH₃ over iron and manganese oxides supported on titania. *Appl Catal B* 44 (3):217–225
151. Ettireddy PR, Ettireddy N, Mamedov S, Boolchand P, Smirniotis PG (2007) Surface characterization studies of TiO₂ supported manganese oxide catalysts for low temperature SCR of NO with NH₃. *Appl Catal B* 76 (1–2):123–134
152. Pena DA, Uphade BS, Smirniotis PG (2004) TiO₂-supported metal oxide catalysts for low-temperature selective catalytic reduction of NO with NH₃: I. Evaluation and characterization of first row transition metals. *J Catal* 221 (2):421–431
153. Zhuang K, Qiu J, Tang F, Xu B, Fan Y (2011) The structure and catalytic activity of anatase and rutile titania supported manganese oxide catalysts for selective catalytic reduction of NO by NH₃. *Phys Chem Chem Phys* 13 (10):4463–4469
154. Marbán G, Valdés-Solís T, Fuertes A (2004) Mechanism of low-temperature SCR of NO with NH₃ over carbon-supported Mn₃O₄. *Phys Chem Chem Phys* 6 (2):453–464
155. Marbán G, Valdés-Solís T, Fuertes AB (2004) Mechanism of low-temperature selective catalytic reduction of NO with NH₃ over carbon-supported Mn₃O₄: Role of surface NH₃ species: SCR mechanism. *J Catal* 226 (1):138–155
156. Kapteijn F, Singoredjo L, Vandriel M, Andreini A, Moulijn JA, Ramis G, Busca G (1994) Alumina-Supported Manganese Oxide Catalysts .2. Surface Characterization and Adsorption of Ammonia and Nitric-Oxide. *J Catal* 150 (1):105–116
157. Kijlstra WS, Brands DS, Poels EK, Bliet A (1997) Mechanism of the Selective Catalytic Reduction of NO by NH₃ over MnO_x/Al₂O₃. *J Catal* 171 (1):208–218
158. Kijlstra WS, Brands DS, Smit HI, Poels EK, Bliet A (1997) Mechanism of the Selective Catalytic Reduction of NO with NH₃ over MnO_x/Al₂O₃. *J Catal* 171 (1):219–230
159. Li J, Chen J, Ke R, Luo C, Hao J. Effects of precursors on the surface Mn species and the activities for NO reduction over MnO_x/TiO₂ catalysts (2007) *Catal Commun* 8 (12):1896–1900
160. Biesinger MC, Payne BP, Grosvenor AP, Lau LW M, Gerson AR, Smart RSC (2011) Resolving surface chemical states in XPS analysis of first row transition metals, oxides and hydroxides: Cr, Mn, Fe, Co and Ni. *Appl Surf Sci* 257 (7):2717–2730
161. Murray JW, Dillard JG, Giovanoli R, Moers H, Stumm W (1985) Oxidation of Mn(II): Initial mineralogy, oxidation state and ageing. *Geochimica et Cosmochimica Acta* 49 (2):463–470
162. Long RQ, Yang RT, Chang R (2002) Low temperature selective catalytic reduction (SCR) of NO with NH₃ over Fe-Mn based catalysts. *Chem Comm* (5):452–453
163. Chen Z, Yang Q, Li H, Li X, Wang L, Tsang SC (2010) Cr-MnO_x mixed-oxide catalysts for selective catalytic reduction of NO_x with NH₃ at low temperature. *J Catal* 276 (1):56–65

164. Chen ZH, Wang FR, Li H, Wang L, Yang Q, Li X (2011) Low-Temperature Selective Catalytic Reduction of NO_x with NH₃ over Fe-Mn Mixed-Oxide Catalysts Containing Fe₃Mn₃O₈ Phase. *Ind Eng Chem Research* 51 (1):202–212
165. Qi G, Yang RT, Chang R (2004) MnO_x-CeO₂ mixed oxides prepared by co-precipitation for selective catalytic reduction of NO with NH₃ at low temperatures. *Appl Catal B: Environ* 51 (2):93–106
166. Shan W, Liu F, He H, Shi X, Zhang C (2011) The Remarkable Improvement of a Ce-Ti based Catalyst for NO_x Abatement, Prepared by a Homogeneous Precipitation Method. *Chem Cat Chem* 3: (8)1286–1289
167. Li P, Xin Y, Li Q, Wang Z, Zhang Z, Zheng L (2012) Ce-Ti Amorphous Oxides for Selective Catalytic Reduction of NO with NH₃: Confirmation of Ce-O-Ti Active Sites. *Environ Sci Tech* 46 (17):9600–9605
168. Chen L, Li J, Ablikim W, Wang J, Chang H, Ma L, Xu J, Ge M, Arandiyani H (2011) CeO₂-WO₃ Mixed Oxides for the Selective Catalytic Reduction of NO_x by NH₃ Over a Wide Temperature Range. *Catal Lett* 141 (12):1859–1864
169. Chen L, Li J, Ge M (2010) DRIFT Study on Cerium-Tungsten/Titanium Catalyst for Selective Catalytic Reduction of NO_x with NH₃. *Environ Sci Tech* 44 (24):9590–9596

Chapter 8

Mechanistic Aspect of NO–NH₃–O₂ Reacting System

Masaoki Iwasaki

8.1 Introduction

This chapter delineates the mechanistic aspects of the NO–NH₃–O₂ reacting system, also known as the *standard SCR* reaction. The standard SCR technology was first developed in the 1970s, and thus has a long history in the research area of catalyst development as well as the associated reaction mechanisms. Nevertheless, the reaction mechanisms do not always coincide even among the most popular systems such as the Cu or Fe ion-exchanged zeolites and vanadium-based catalysts. However, such extensive research activities conducted might be reaching a substantial agreement on several mechanistic details.

In this chapter, the reaction mechanisms of the standard SCR reaction are discussed from various perspectives including steady-state kinetics, the relations with NH₃/NO oxidation ability and acid site amount, the effect of coexisting gases, and transient reaction behavior. Through these comprehensive analyses, some similarities and differences of the reaction mechanism among the conventional SCR catalysts could be extracted. Also, new perspectives on standard SCR mechanism could be suggested.

8.2 Steady-State Reaction Analysis

8.2.1 NH₃/NO/O₂, NH₃/O₂, and NO/O₂ Reactions

To have a grasp of basic reaction behaviors, standard SCR as well as NH₃/NO oxidation reactions were investigated under steady-state condition. For the samples, three conventional SCR catalysts, V–W/TiO₂, Fe/ZSM-5, and Cu/ZSM-5,

M. Iwasaki (✉)

Toyota Central R&D Laboratories, Inc., 41-1 Yokomichi, Nagakute, Aichi 480-1192, Japan
e-mail: iwasaki@mosk.tytlabs.co.jp

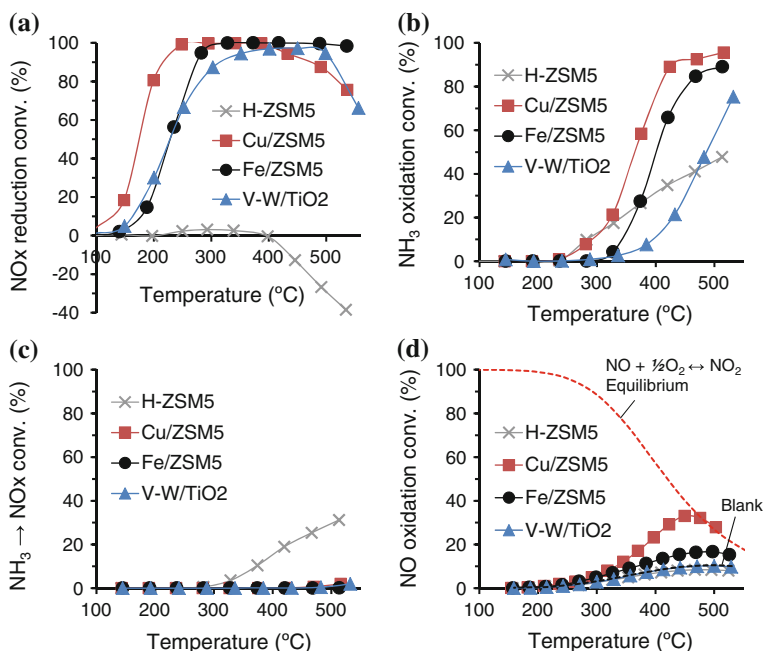


Fig. 8.1 **a** NO_x conversion under standard SCR reaction, **b** total NH₃ conversion and **c** NH₃ → NO_x conversion under NH₃ oxidation reaction, **d** NO → NO₂ conversion under NO oxidation reaction. **a**: 0.05 % NO, 0.06 % NH₃, 8 % O₂, 10 % CO₂, 8 % H₂O with N₂, **b**, **c**: 0.1 % NH₃, 8 % O₂, 10 % CO₂, 8 % H₂O with N₂, **d**: 0.1 % NO, 8 % O₂, 10 % CO₂, 8 % H₂O with N₂

were tested. Additionally, H-ZSM-5 was also tested as a reference. Figure 8.1a–d shows the catalytic activity of standard SCR, NH₃ oxidation, and NO oxidation reactions. The compositions of the feed gas were as follows: 0.05 % NO, 0.06 % NH₃, 8 % O₂, 10 % CO₂, 8 % H₂O with N₂ for standard SCR; 0.1 % NH₃, 8 % O₂, 10 % CO₂, 8 % H₂O with N₂ for NH₃ oxidation; 0.1 % NO, 8 % O₂, 10 % CO₂, 8 % H₂O with N₂ for NO oxidation.

For standard SCR reaction (NH₃/NO/O₂ system) in Fig. 8.1a, Cu/ZSM-5 showed the highest activity in low temperature region (<300 °C), while Fe/ZSM-5 was the highest above 400 °C. On the other hand, H-ZSM-5 has little activity, and also negative conversions were seen over 400 °C due to NH₃ oxidation to NO_x. The conversion of V-W/TiO₂ was nearly equal to that of Fe/ZSM-5 around 250 °C, though their temperature profiles differed slightly; V-W/TiO₂ was more active in the lower temperature (<200 °C), while the situation was the opposite in the higher temperature (>300 °C), which is also verified by Arrhenius plots in the Sect. 8.2.2. Since N₂O was not detected for all the conditions, only the standard SCR reaction ($2\text{NO} + \frac{1}{2}\text{O}_2 + 2\text{NH}_3 \rightarrow 2\text{N}_2 + 3\text{H}_2\text{O}$) progresses except for unselective NH₃ oxidation which was initiated at the higher temperature region (>400 °C).

From Fig. 8.1b, NH₃ oxidation without inlet NO started above 300 °C for all the catalysts, which is much higher onset temperature than the SCR reaction. As by-products, N₂O was not detected for all the catalysts, and NO_x was produced only for H–ZSM-5 above 300 °C (Fig. 8.1c). It indicates that NH₃ oxidation reaction to N₂ ($2\text{NH}_3 + \frac{3}{2}\text{O}_2 \rightarrow \text{N}_2 + 3\text{H}_2\text{O}$) mainly proceeds for the three SCR catalysts. As for H–ZSM-5, on the other hand, a large amount of NO_x was produced from NH₃, probably because the rate of NH₃ oxidation to NO_x should be much faster than that of SCR reaction between produced NO_x and residual NH₃.

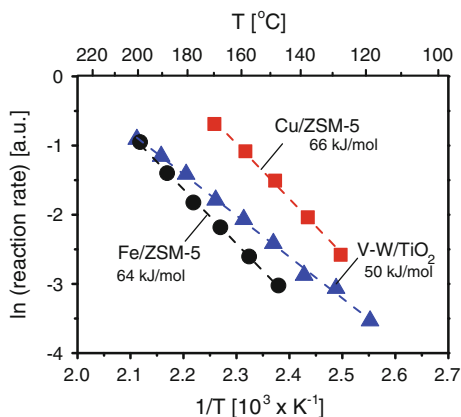
Figure 8.1d shows the NO oxidation conversion to NO₂ under the NH₃ absent condition. For all the samples, the NO oxidation conversion was much lower than SCR and NH₃ oxidation conversions, suggesting that NO is hard to be oxidized. Also, the NO oxidation ability (Cu–ZSM-5 > Fe–ZSM-5 > V–W/TiO₂ ≈ H–ZSM-5 ≈ Blank) does not necessarily coincide with the trend of SCR conversion (Cu–ZSM-5 > Fe–ZSM-5 ≈ V–W/TiO₂ ≫ H–ZSM-5). However, NO oxidation is believed to be a very important step in the SCR process, and thus it is discussed in more detail in another section.

8.2.2 Apparent Activation Energy

The apparent activation energies of the Fe/ZSM-5, Cu/ZSM-5, and V–W/TiO₂ catalysts were determined from the Arrhenius plots of the logarithm of the apparent rate versus 1/T as shown in Fig. 8.2. The reaction rates were measured with maintaining pseudo-differential condition. The composition of the gas was kept as 0.05 % NO, 0.05 % NH₃, 8 % O₂, 8 % CO₂, 10 % H₂O with the remainder N₂. The temperature range was varied from 120 to 200 °C because in the higher temperature region, other contributions such as diffusion limitation and/or NH₃ oxidation might be affected [1, 2]. The apparent activation energies of the Fe/ZSM-5 and Cu/ZSM-5 catalysts were estimated to be 64 and 66 kJ/mol which is roughly equivalent. On the other hand, the V–W/TiO₂ catalyst showed a more gradual slope than the zeolites and the activation energy was estimated to be 50 kJ/mol. This difference would be a main reason for the different temperature profiles between Fe/ZSM-5 and V–W/TiO₂ in Fig. 8.1a.

Efstathiou and Fliatoura [3] investigated the apparent activation energy of a V/TiO₂ catalyst while varying the NO and NH₃ concentration (0.05–0.2 %) at 150–190 °C. They reported that the change of the activation energy with the NO and NH₃ concentration was small and obtained a value of 48.5 kJ/mol (11.6 kcal/mol) under 0.1 % NO and 0.05 % NH₃ [3], which agrees well with the values estimated from Fig. 8.2.

Fig. 8.2 Arrhenius plots of the logarithm of apparent SCR rate versus the inverse of temperature. Apparent activation energies are compared. Gas composition = 0.05 % NO, 0.05 % NH₃, 8 % O₂, 8 % CO₂, 10 % H₂O with the remainder N₂



8.2.3 Apparent Reaction Orders

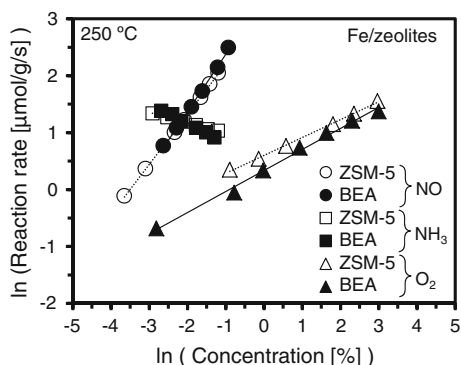
Reaction orders contain important information for predicting the rate-determining step as well as the reaction mechanism. Apparent reaction orders can be estimated by measuring the reaction rates with varying gas concentration (partial pressure) under pseudo-differential condition. Figure 8.3 shows the dependence of the standard SCR rate on the NO, O₂, and NH₃ concentrations over Fe/ZSM-5 and Fe/BEA. Although the balance gas compositions were different for the two samples, i.e., 10 % CO₂, 5 % H₂O, and N₂ for Fe/ZSM-5 versus only N₂ for Fe/BEA, both showed identical dependence. The SCR rates increased with NO and O₂ concentrations but slightly decreased with NH₃ concentration. This indicates that the standard SCR reaction is promoted by NO and O₂ but is inhibited by NH₃. Since all the data gave linear relationships under the log–log plots, the reaction rate can be simply expressed using the power law

$$r_s = k_{\text{app}}[\text{NO}]^\alpha[\text{O}_2]^\beta[\text{NH}_3]^\gamma$$

where r_s is the standard SCR rate, k_{app} is the apparent rate constant, and α , β , and γ are the apparent reaction orders for NO, O₂, and NH₃, respectively. Thus, the apparent reaction orders can be estimated from the slopes in Fig. 8.3, and are summarized in Table 8.1 along with the reported literature data [4–10]. As seen from Table 8.1, the reaction orders obtained here are comparable for the reported values for Fe/zeolites [6–8]; the NO orders are slightly lower than first order, the O₂ orders are slightly lower than half, while the NH₃ orders are negative.

Meanwhile, H-ZSM-5 shows approximately first order for O₂ [9, 10]. The reason for the difference in the O₂ orders between H-type zeolites and Fe/Cu zeolites could be due to the contribution of different forms of O₂ toward the rate-determining step; for instance, undissociated molecular O₂ or dissociated atomic O might participate in the elementary reaction.

Fig. 8.3 Log–log plots of apparent SCR rate versus NO, O₂, and NH₃ concentrations for Fe/ZSM-5 and Fe/BEA. Balance gas is 10 % CO₂, 5 % H₂O, and N₂ for Fe/ZSM-5, and only N₂ for Fe/BEA. Apparent activation orders are listed in Table 8.1



If one assumes that the rate-determining step in the standard SCR is the oxidation of NO, the reaction order for the NO oxidation should have a similar value with that for the SCR reaction. To confirm this presumption, the dependence of the NO oxidation rate on the NO and O₂ concentrations were investigated by using Fe/ZSM-5 and Fe/BEA. The estimated apparent orders are listed in Table 8.1 along with the relevant literature data [11]. The apparent reaction orders for the two Fe/zeolites showed similar values despite different structure and coexisting gases. Also, the reaction orders are nearly in accordance with the literature data reported by Metkar et al. [11]. They measured the NO and O₂ orders in the presence of NO₂ feed as an inlet gas, and found that the reaction orders for NO and O₂ did not change when the inlet NO₂ concentration was changed. By comparing the NO and O₂ orders between the NO oxidation and the SCR reaction (Table 8.1), one can find a similarity which is nearly first order for NO and nearly half order for O₂. Thus, the rate-determining step in the standard SCR might be the NO oxidation step. The same holds true when the activation energies are compared; Metkar et al. [11] reported that the activation energy for the NO oxidation (39 kJ/mol) is nearly equal to the activation energy for the standard SCR reaction (42 kJ/mol) over Fe/ZSM-5.

However, there is a crucial difference between the two reactions, which is NO₂ order for the two reactions; the order is positive for the SCR reaction [4], whereas it is negative for the NO oxidation [11]. In fact, Iwasaki et al. [4] investigated the NO₂ order during NO/NO₂/NH₃ reaction system (the so-called fast SCR condition) and found that the NO₂ order is positive for Fe/ZSM-5. Also, Metkar et al. [11] investigated the NO₂ order during the NO oxidation and estimated to be -0.42 to -0.49 for Fe/ZSM-5 and -0.89 to -1.00 for Cu/CHA. These differences would result from the different behavior of NO₂ on the surface; the NO₂ produced is consumed immediately by NH₃ during the SCR reaction, whereas the NO₂ and nitrate products are strongly adsorbed on the surface during the NO oxidation reaction, which is verified by in situ FT-IR in other chapter.

Table 8.1 Apparent reaction orders of standard SCR and NO oxidation reactions using zeolite catalysts

Reaction	Catalyst	NO order	O ₂ order	NH ₃ order	Temperature (°C)	Coexisting gas	Ref
Standard SCR	Fe/BEA	1.00	0.37	-0.34	250	N ₂	U.D. ^a
Standard SCR	Fe/ZSM-5	0.81-0.90	0.29-0.34	-0.11 to -0.21	200-300	10 % CO ₂ , 5 % H ₂ O, N ₂	[4]
Standard SCR	Fe/ZSM-5	0.55-0.94	0.36-0.41	-0.11 to -0.15	260-300	He	[6]
Standard SCR	Fe/ZSM-5	0.90-1.02	0.33-0.39	-0.28 to -0.49	210-350	5 % H ₂ O, N ₂	[7]
Standard SCR	Fe/ZSM-5	0.97-1.09	0.52-0.59	-0.27 to -0.32	200-300	Ar	[8]
Standard SCR	Cu/ZSM-5	1	0.60	0	300	He	[5]
Standard SCR	H-ZSM-5	1.00	0.77	-0.45	500	He	[9]
Standard SCR	H-ZSM-5	0.73	1.06	-0.61	340-440	0-20 % H ₂ O, N ₂	[10]
NO oxidation	Fe/BEA	0.81	0.56	-	250	N ₂	U.D. ^a
NO oxidation	Fe/ZSM-5	0.90	0.67	-	280	10 % CO ₂ , 5 % H ₂ O, N ₂	U.D. ^a
NO oxidation	Fe/ZSM-5	0.9-1.0	0.55-0.59	-0.42 to -0.49 ^b	200-290	330 ppm NO ₂ + Ar	[11]
NO oxidation	Cu/CHA	0.85-1.0	0.47-0.51	-0.89 to -1.00 ^b	200-290	330 ppm NO ₂ + Ar	[11]

^a U.D.: Unpublished data^b NO₂ order

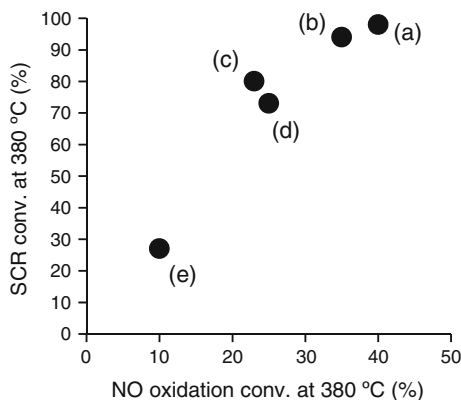


Fig. 8.4 SCR conversion versus NO oxidation conversion for Fe/zeolites prepared by different Fe loading methods and amounts of Fe. The data is used from Ref [13]. Gas composition = 0.2 % NO, 0 or 0.2 % NH₃, and 2 % O₂ with remainder He. The specification of the samples is described by “preparation method_Fe/Al ratio”: **a** sublimation with FeCl₃_0.83, **b** sublimation with FeCl₃_0.49, **c** ion-exchange with Fe(acac)₃ followed by evaporation_0.96, **d** ion-exchange by Fe(acac)₃ followed by washing_0.21, **e** ion-exchange by Fe(NO₃)₃ followed by precipitation_0.35

8.2.4 Relationship with NO Oxidation Activity

As mentioned in Sect. 8.2.3, the oxidation of NO would be a crucial step in the standard SCR reaction. In fact, there are many reports in the literature which suggest that the SCR activity is correlated with the NO oxidation conversion when the same type of active metal is compared [12–17]. On the other hand, some literature indicates that there is no correlation between them especially when comparing different active species, such as Fe and Cu [11, 18–20]. In this section, the reason for this inconsistency has been discussed.

Figure 8.4 shows the relationship between the standard SCR conversion and NO oxidation reaction conversion using Fe/zeolites prepared by different Fe loading methods and Fe loading amounts. The data which is used from Ref. [13] by Delahay et al. demonstrates a positive correlation between them, implying that the active sites for NO reduction are identical with the NO oxidation sites. Figure 8.5 shows the relationship between standard SCR conversion and NO oxidation reaction conversion when several Fe/zeolites with different pore structures and Si/Al₂ ratios were used [16]. As can be seen from the figure, the SCR conversion in this case correlates well with the NO oxidation conversion. Thus, the activity relationship is preserved even when different types of zeolites are used.

However, when the comparison is made between different kinds of active metals, the SCR conversion does not always correlate with the extent of NO oxidation. For instance, Metkar et al. [11, 19]. have reported that Fe/ZSM-5 showed a higher NO oxidation conversion than Cu/CHA, while Cu/CHA

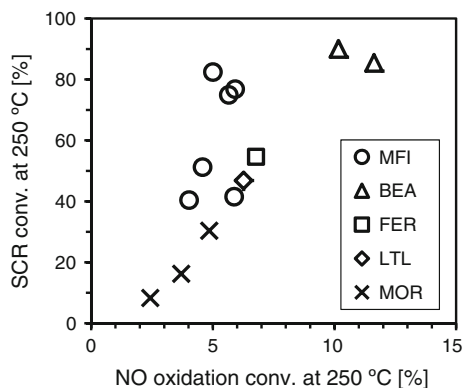


Fig. 8.5 SCR conversion versus NO oxidation conversion of Fe/zeolites with different structure and Si/Al₂ ratio [16]. Gas composition = 0.1 % NO, 0 or 0.12 % NH₃, 8 % O₂, 10 % CO₂, and 8 % H₂O with remainder N₂

possessed a greater SCR activity than Fe/ZSM-5. Thus, it seems that the SCR activity is not dependent on the NO oxidation under the comparison between Fe and Cu. The key to solve this discrepancy is that the determining factors for the two reactions would be different. Delahay et al. [13] discussed that the difference in activity between SCR and NO oxidation can only be explained if the NO oxidation reaction is controlled by the desorption of NO₂. In fact, the desorption energy of NO₂ from Fe/ZSM-5 is very high (138 kJ/mol) [21], and the same goes for Cu/zeolites. Furthermore, the adsorption strength of NO₂ is dependent on the metal species; for example, Fig. 8.6 shows the NO₂-TPD experiment reported by Metkar et al. [11]. The NO₂-TPD spectra indicate that NO₂ is more strongly bound to Cu/zeolite compared to Fe/zeolite [11]. The same result has been obtained by Tronconi et al. [22]. These NO₂-TPD results are in line with the reaction order results that Cu/zeolite has larger negative NO₂ order than Fe/zeolite as is stated in the Sect. 8.2.3 and Table 8.1 [11].

Taking the above results into consideration, we can conclude that the oxidation of NO in the absence of NH₃ is strongly affected by the NO₂ adsorption strength which depends on the type of active metal used. In other words, the rate-determining step of the NO oxidation under NH₃ absent condition would be the NO₂ desorption process. Figure 8.7 shows NO oxidation scheme over metal ion-exchanged zeolite by assuming that NO oxidation proceeds with the redox cycle of the metal ions. As the states of the metal ions, both mononuclear and binuclear states were considered. In this figure, the desorption step of the adsorbed NO₂, that is the reduction step of the metal ions from Mⁿ⁺ to M⁽ⁿ⁻¹⁾⁺, would probably be the slowest process, which should be determined by the type of metal.

Regarding standard SCR reaction, on the other hand, the NO₂ desorption does not seem to be the rate-determining step because produced NO₂ should react with NH₃ immediately, which is elucidated and discussed in more detail in the other sections. Therefore, it is difficult to make a correlation between SCR activity and

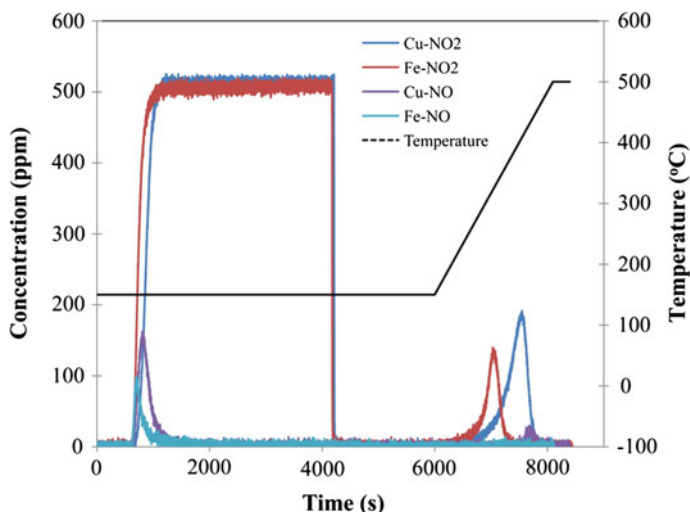
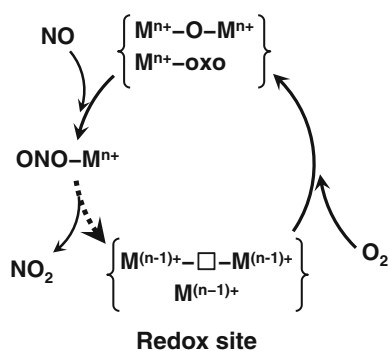


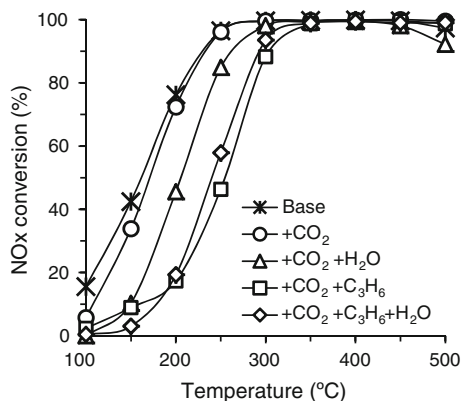
Fig. 8.6 NO₂-TPD experiments carried out on Fe- and Cu-zeolite catalysts. NO₂ adsorption = 150 °C; temperature ramp = 10 °C/min. Reprinted with permission from [11]

Fig. 8.7 Schematic representation of catalytic cycle for NO oxidation reaction over metal-exchanged zeolite catalysts. Redox sites are associated with oxo-metal (isolated or binuclear) ion-exchanged sites



NO oxidation when different active metals are compared. Nevertheless, the author believes that the SCR activity is correlated with NO oxidation ability “in the presence of NH₃”, simply because the fast SCR (NO/NO₂/NH₃ system) rate is extremely faster than the standard SCR rate. The point is that NO oxidation conversion (NO₂ formation rate) under “NH₃ absent condition” does not necessarily correspond to NO oxidation ability under “NH₃ present condition,” i.e., standard SCR condition. Thus, the author presumes that although NO₂ is hard to be desorbed from Cu sites, Cu would have a greater potential to oxidize NO to NO₂ under NH₃ present condition. However, quantifying this ability is very difficult because the production rate of NO₂ adspecies can hardly be measured in the presence of NH₃. Thus, an advanced technique which makes it possible to verify the assumption is desired.

Fig. 8.8 SCR conversion of Fe/BEA in the presence of 10 % CO₂, 8 % H₂O, and/or 333 ppm C₃H₆. Base gas composition: 0.1 % NO, 0.12 % NH₃, and 8 % O₂ with the remainder N₂



8.2.5 Effect of Coexisting Gases and Poisoning

Considering the practical use of SCR catalysts for diesel engines, we have to take into account the possible effects due to the presence of other compounds such as CO, CO₂, H₂O, HC, and the poisoning effect from SO₂ which are all present during the combustion of fuel. Figure 8.8 shows the standard SCR conversion of Fe/BEA in the presence of CO₂, H₂O, and C₃H₆. The base gas was 0.1 % NO, 0.12 % NH₃, and 8 % O₂ with the remainder N₂. When 10 % CO₂ was added to the base gas, the NO_x conversion slightly declined, which indicates that CO₂ has a little inhibitory effect on the SCR reaction. Next, the addition of 8 % H₂O and/or 333 ppm C₃H₆ to the base + CO₂ feed further lowered the NO_x conversion. Here, the addition of 333 ppm C₃H₆ decreased the activity much more than 8 % H₂O did, despite the low HC concentration. Additionally, the NO_x conversion under the presence of both 333 ppm C₃H₆ and 8 % H₂O was higher than that in presence of 333 ppm C₃H₆ only, suggesting that H₂O suppresses the strong inhibition by C₃H₆. Thus, the degree of inhibitory effect on the SCR reaction follows the order: C₃H₆ > H₂O > CO₂.

Li et al. [23] and He et al. [24] have investigated the effect of the regeneration temperature on the Fe/ZSM-5 and Fe/BEA catalysts, respectively, after C₃H₆ poisoning. Figure 8.9a shows the change in the NO_x conversions in response to the presence (on) and absence (off) of C₃H₆ at several temperatures over Fe/ZSM-5 [23]. When 0.1 % C₃H₆ was added to the feed (10 min), all the conversions decreased, but the extent of decrease differed with the temperature. Then, after the removal of C₃H₆ from the feed (40 min), all the conversions except at 200 °C recovered. However, the extent of recovery depended on the temperature; with no improvement observed at 200 °C, while the conversions recovered to some extent at 300 and 400 °C. At 500 °C, the NO_x conversion completely recovered to the initial conversion level before the addition of C₃H₆. Figure 8.8b shows the comparison of SCR activities of fresh, poisoned, and regenerated samples [23]. The term “poisoned” means that the catalyst was pretreated with C₃H₆ containing gas

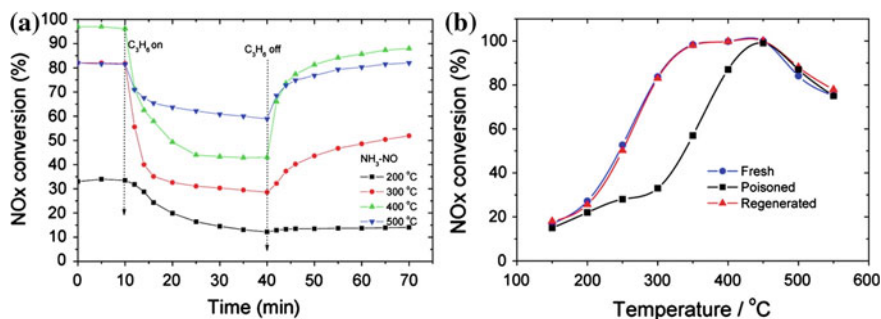


Fig. 8.9 **a** The change in NO_x conversions with response to the C₃H₆ on and off at 200–500 °C for Fe/ZSM-5. **b** NO_x conversions of fresh, C₃H₆ poisoned (at 200 °C), and regenerated (in 10 % O₂ at 550 °C for 30 min) samples. Gas composition = 0.1 % NO, 0.1 % NH₃, 0.1 % C₃H₆ (when used), 5 % O₂, and 2 % H₂O with remainder He. Reprinted with permission from [23]

at 200 °C, while “regenerated” means that the poisoned catalyst was treated at 550 °C in presence of 10 % O₂. It can be seen that the NO_x conversion of the poisoned sample clearly decreased at 200–400 °C. However, the regenerated sample showed almost similar activity to the fresh one, indicating that the catalyst can be completely regenerated by the 550 °C treatment. In addition, an FT-IR study suggested that the hydrocarbon oxygenates such as formate-, acetate-, and nitrogen-containing organic compounds were created on the surface [23]. Thus, they concluded that the major cause for the deactivation was the carbonaceous deposition onto Fe³⁺ sites which are responsible for the oxidation of NO to NO₂. In fact, they have also confirmed that the NO oxidation activity was significantly inhibited by the C₃H₆ poisoning [23].

Malpartida et al. [25] have reported the effect of HC types on the SCR reactivity using Fe/ZSM-5. Figure 8.10 shows NO conversion when different types of HCs (C₃H₆, C₇H₈, C₁₀H₂₂) coexisted [25]. The addition of any type of HC led to a decrease in the NO conversion, but its effect was different for different HCs; the rate of decline was limited in the case of C₃H₆ but was more significant in the presence of toluene (C₇H₈) and decane (C₁₀H₂₂). In situ FT-IR observed the deposition of C-species, and its quantity was dependent on the HCs; C₁₀H₂₂ > C₇H₈ > C₃H₆, which is in the reverse order with respect to the NO conversion [25]. Thus, they concluded that the most important effect from HC poisoning at low temperature is the competitive adsorption between the hydrocarbon molecules and NH₃ onto the active Fe sites [25].

Next, the effect of SO₂ poisoning and regeneration is presented. Figure 8.11 shows the influence of H₂O and SO₂ on the SCR conversion over Fe/ZSM-5 [26]. It is evident that SO₂ exerts a poisoning influence at low temperature both in case of dry as well as moist feed. Remarkably, this effect is reversed at a high temperature, i.e., above 450 °C (723 K), the NO conversion is the highest even in the presence of SO₂.

Fig. 8.10 SCR conversion of Fe/ZSM-5 as a function of the temperature for different HC composition: without HC, 85 ppm C_3H_6 , 85 ppm C_7H_8 , 85 ppm $C_{10}H_{22}$, and 85 ppm mixed HCs (17 ppm C_3H_6 , 25 ppm C_7H_8 and 43 ppm $C_{10}H_{22}$). Base gas composition: 150 ppm NO, 150 ppm NH_3 , 300 ppm CO, 14 % O_2 , 4 % CO_2 , and 1 % H_2O with remainder Ar. Reprinted with permission from [25]

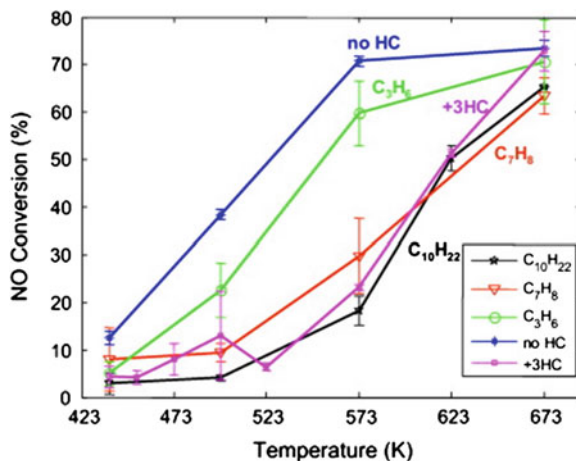
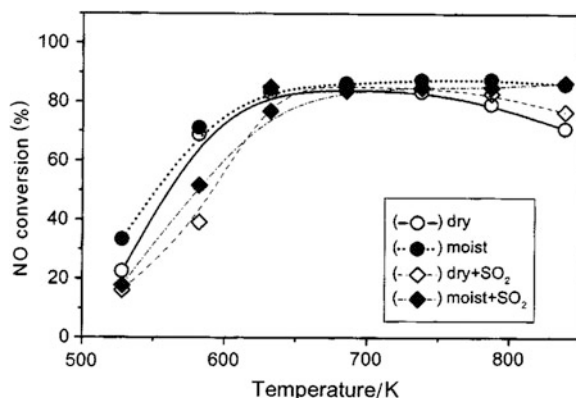


Fig. 8.11 Influence of H_2O and SO_2 on the NO conversion over Fe/ZSM-5. Dry condition: 0.1 % NO, 0.1 % NH_3 , and 2 % O_2 with the remainder He. Moist condition: as dry, with 2.5 % H_2O added, '+ SO_2 ', with 200 ppm SO_2 added. Reprinted with permission from [26]



Finally, the effect of regeneration on the SO_2 -poisoned catalysts is presented [27]. First, hydrothermally aged samples (700 °C for 5 h) were poisoned by a feed containing 30 ppm SO_2 until the adsorption saturated at 300 °C, and was then regenerated under standard SCR condition by maintaining at 550 °C for 10 min. Figure 8.12 shows the NO_x conversions before the SO_2 poisoning and after the SO_2 regeneration for Fe/zeolites, Cu/ZSM-5, and V-W/TiO₂. Obviously, all the regenerated Fe/zeolites maintained equivalent activity with those free from SO_2 . Meanwhile, the Cu/ZSM-5 catalyst greatly deteriorated even after the regeneration. This suggests that the major cause of the deterioration is not the zeolite structure but the type of ion-exchanged metal. Therefore, Fe/zeolites possess a higher endurance for SO_2 poisoning than Cu/zeolites in this case. In addition,

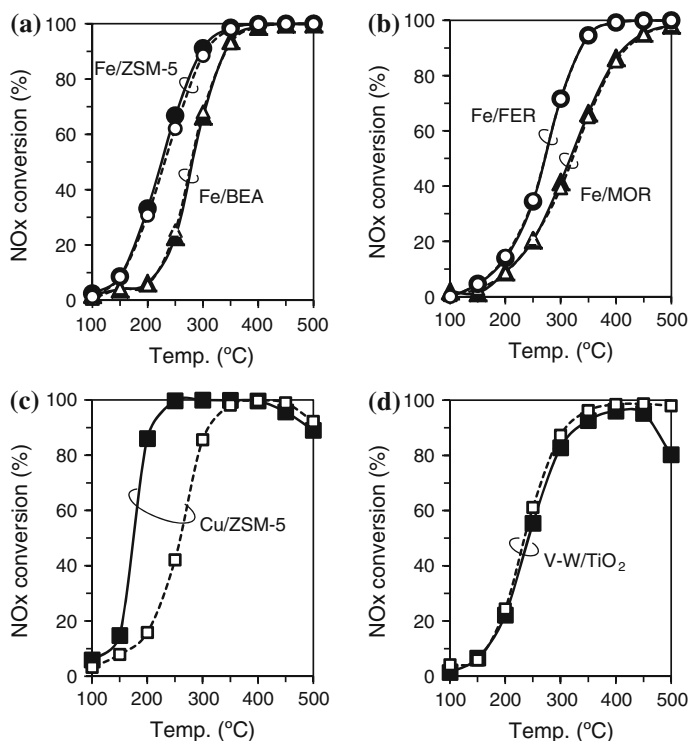


Fig. 8.12 NO_x conversions of hydrothermally aged (700 °C for 5 h) Fe/zeolites with different structures (a, b), Cu/ZSM-5 (c), and V–W/TiO₂ (d) before SO₂ poisoning (filled symbols) and after SO₂ poisoning and regeneration (open symbols). SCR feed: 0.1 % NO, 0.12 % NH₃, 8 % O₂, 10 % CO₂, and 8 % H₂O with remainder N₂. SO₂ poisoning and regeneration: poisoning under 30 ppm SO₂ + SCR feed at 300 °C for 20 min, followed by regenerating under SCR feed at 550 °C for 10 min

V–W/TiO₂ shows also high endurance for SO₂. Interestingly, regenerated V–W/TiO₂ has greater activity than SO₂ free one at 500 °C. This is probably because the SO₂ poisoning inactivates aggregated V species which provoke NH₃ unselective oxidation at high temperature.

8.3 Transient Reaction Analysis

8.3.1 Periodic NH₃ Supply

As the composition and the concentration of diesel exhaust gases vary significantly depending on the engine operation, it is quite important to understand the transient behavior of NO_x reduction following NH₃ supply and shutoff. In this section, the effect of the periodical supply of NH₃ on the NO_x reduction behavior is presented.

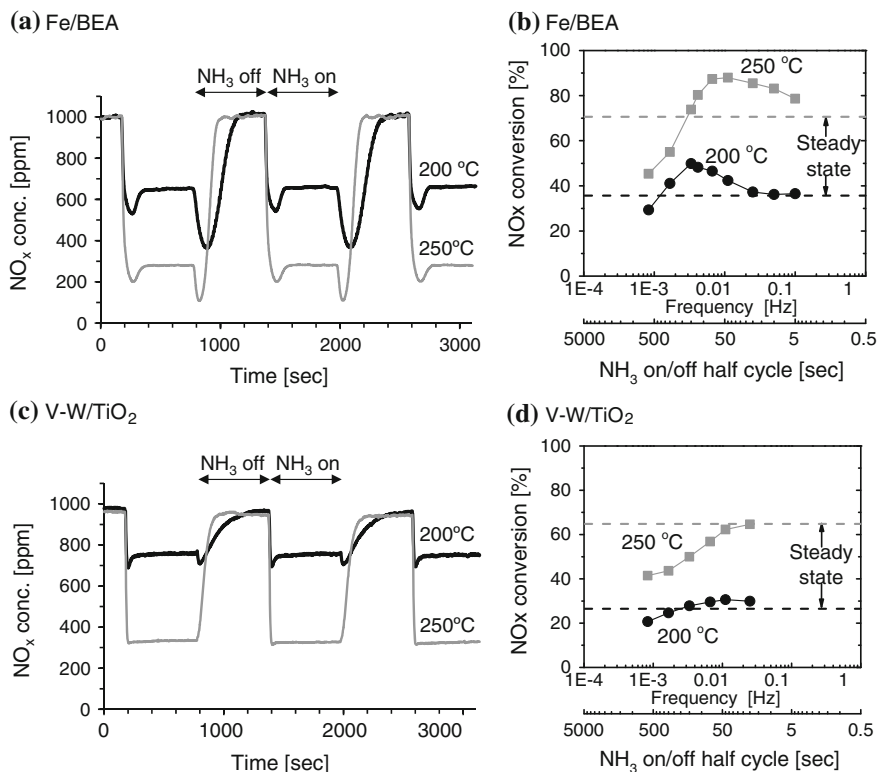


Fig. 8.13 NO_x concentration (a, c) and average NO_x conversion (b, d) under periodic supply of NH₃ with Fe/BEA (a, b) and V-W/TiO₂ (c, d) catalysts. Gas composition = 0.1 % NO, 0.2 % NH₃, 8 % O₂, 10 % CO₂, and 8 % H₂O with the remainder N₂; catalyst weight = 1 g; flow rate = 3.5 l/min

As a first test, symmetrical NH₃ on/off cycles were conducted by changing the switching time from 5/5 to 600/600 s/s at 200 and 250 °C. Figure 8.13a shows the outlet NO_x concentration with the Fe/BEA zeolite catalyst under 600/600 s switching condition. The feed gas was a mixture having the composition: 0.1 % NO, 8 % O₂, 10 % CO₂, 8 % H₂O, and the remainder N₂ with a periodical supply of 0.2 % NH₃. When NH₃ was added to the feed, the NO_x concentration quickly decreased due to the SCR reaction, went through a minimum, and then slowly approached a steady-state level. When NH₃ was removed from the feed, the NO_x concentration was reduced to a greater degree than the steady-state level, went through a minimum and then reached the inlet NO_x value. Similar results have been reported by many researchers [4, 5, 18, 28–30]. This indicates that the SCR reaction using adsorbed NH₃ continues even after the NH₃ feed is shutoff, and furthermore, the reaction is accelerated in the absence of gaseous NH₃. In other words, SCR is inhibited by the presence of gaseous NH₃ and/or by a high coverage of adsorbed NH₃. In Fig. 8.13a, one can see that the degree of transient NO_x

reduction is pronounced at a lower temperature. This can be due to the following two factors: First, the amount of adsorbed NH₃ available for the SCR reaction increases with decrease in the temperature [4, 28, 30, 31] and second, the inhibiting effect of gaseous NH₃ and/or high NH₃ coverage is intensified at a lower temperature [4].

Figure 8.13b shows the average NO_x conversion with change in the NH₃ on/off cycle time. Interestingly, under certain conditions the average NO_x conversion exceeded the steady-state conversion. It suggests that an intermittent supply of NH₃ is more effective than a continuous supply. Additionally, because of the difference in the NH₃ adsorption capacity, the maximum conversion at 200 °C is shifted to longer cycle time (smaller frequency) as compared to that at 250 °C. Thus, depending on the temperature there is an optimum NH₃ on/off condition. The optimum condition would be varied with several factors such as NH₃ storage capacity and W/F. Recently, the contributions of these parameters have also been elucidated by fitting procedure of simulation studies [30, 32, 33].

Figure 8.13c shows the NO_x profile with a commercial V–W/TiO₂ catalyst. In this case, the NO_x concentration monotonically decreased and increased in response to the NH₃ on/off switching. The transient NO_x removal behavior was hardly observed in this case. This is probably due to the low NH₃ adsorption capacity of the V-based catalyst, which has been verified later. Figure 8.13d shows the average NO_x conversions with the V–W/TiO₂ catalyst versus the NH₃ on/off cycle time. The average conversions were mostly less than the steady-state level.

Next, asymmetric NH₃ on/off switching (on/off = 60/120 s) with variation of the temperature (150–400 °C) were conducted. Figure 8.14a–c shows the average NO_x conversions for the Fe/ZSM-5, Cu/ZSM-5, and V–W/TiO₂ catalysts. In case of the Fe/ZSM-5 catalyst (Fig. 8.14a), the NO_x conversions under the periodic condition were higher than those under the steady-state condition below 300 °C, which is in conformity with the result depicted in Fig. 8.13b. Similar enhancement in the NO_x reduction in the low temperature region was observed over H–ZSM-5 by Wallin et al. [28]. They have reported that NO_x reduction was enhanced by up to five times as compared to a continuous supply of NH₃ by changing the NH₃ pulse condition at 200–300 °C [28].

The same observation holds true for the Cu/ZSM-5 catalyst (Fig. 8.14b) below 250 °C. However, at 400 °C the periodic conversion is less than the steady-state one. The reason for this lower activity for the periodic condition is probably due to the decrease of the reaction selectivity between NO and NH₃ [34, 35]. As shown in Fig. 8.1b, Cu/ZSM-5 exhibits higher activity for NH₃ oxidation than Fe/ZSM-5 and V–W/TiO₂. Thus, it can be assumed that a part of the adsorbed NH₃ is consumed by O₂ under NH₃ off condition, leading to the lower activity for the periodic measurement.

Meanwhile, the periodic conversions with V–W/TiO₂ were roughly in accordance with the steady-state conversions at the low temperatures (≤ 250 °C). However, in the high temperature region (≥ 300 °C), the periodic conversions greatly decreased despite the fact that the steady-state conversions monotonically increased with the temperature. This is because the NH₃ adsorption capacity

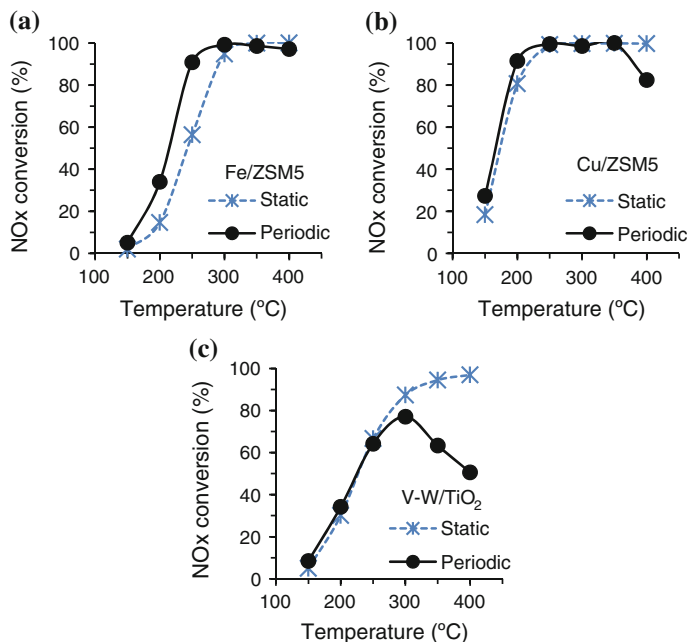
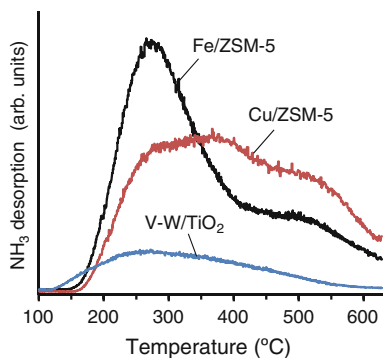


Fig. 8.14 Average NO_x conversion for **a** Fe/ZSM-5, **b** Cu/ZSM-5, and **c** V-W/TiO₂ under periodic and static supply of NH₃. Catalyst weight = 1 g; flow rate = 3.5 l/min. Periodic: NH₃ on/off = 60/120 s/s; 0.02 % NO, 0.073 % NH₃, 8 % O₂, 10 % CO₂, and 8 % H₂O with the remainder N₂. Static: 0.05 % NO, 0.06 % NH₃, 8 % O₂, 10 % CO₂, and 8 % H₂O with the remainder N₂

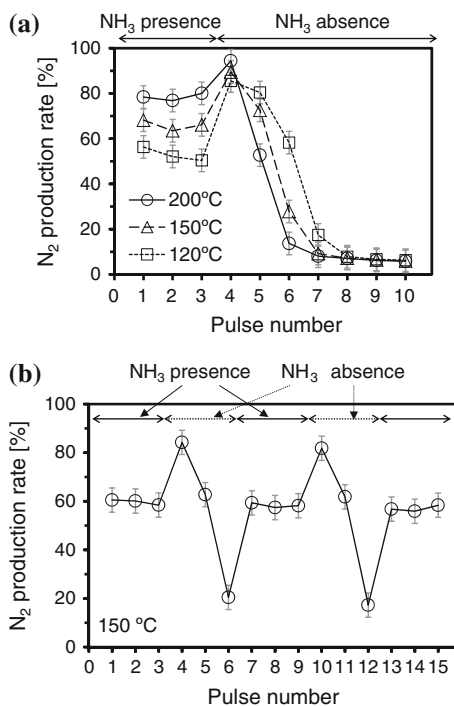
Fig. 8.15 NH₃-TPD spectra for Fe/ZSM-5, Cu/ZSM-5 and V-W/TiO₂ catalysts. NH₃ adsorption = 150 °C; temperature ramp = 20 °C/min; W/F = 3.3 g min/l



available for the transient SCR reaction in case of the V-W/TiO₂ catalyst is low, especially at the high temperature. To confirm this, NH₃-TPD spectra are presented in Fig. 8.15. In fact, the amount of desorbed NH₃ from the V-W/TiO₂ catalyst is very little compared to the zeolite-based catalysts.

Fig. 8.16 N₂ production rate by NO pulse reaction in the presence and absence of NH₃ feed over Fe/ZSM-5.

Continuous gas flow = 0.1 l/min, either 0 or 0.04 % NH₃, and 10 % O₂ with remainder He; NO pulse = 0.34 ml; catalyst weight = 0.25 g. Reprinted with permission from [4]

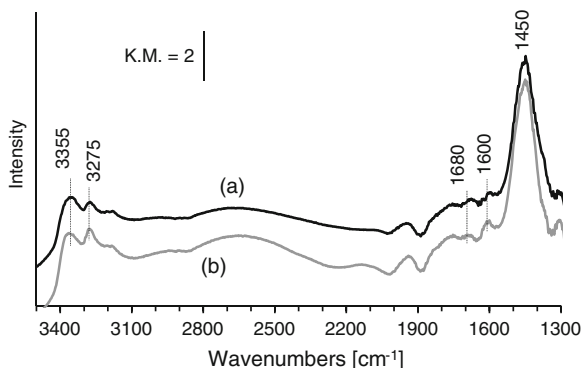


8.3.2 NO Pulse Reaction

To investigate the catalytic effect of Fe/ZSM-5 on the transient NO_x reduction in more detail, the NO pulse reaction test was conducted with monitoring of the N₂ production [4]; NO pulses were introduced to a continuous gas flow consisting of either 0 or 400 ppm NH₃, 10 % O₂, with the remainder He. Figure 8.16a shows the N₂ production rates in the presence and absence of the NH₃ feed. In the presence of NH₃ (pulses 1–3), the N₂ production rates were almost constant and increased with increasing temperature. When NH₃ was removed from the feed, the amount of N₂ increased (pulse 4) and then decreased (pulses 5–10), suggesting that the SCR reaction between the adsorbed NH₃ and pulsed NO is promoted in the absence of NH₃. The total amount of N₂ produced in the absence of NH₃ (pulses 4–10) which corresponds to the amount of NH₃ adsorbed is larger at lower temperatures [4, 31].

Figure 8.16b shows the N₂ production rates when the presence and absence of NH₃ is repeated at the interval of three pulses. The N₂ production rates in the first NH₃ absent region (pulses 4 and 10) were higher than those in the NH₃ present regions; this suggests that the promotional effect of the absence of NH₃ is repeatable. This is in conformity with the behavior observed during the periodical NH₃ supply test as shown in Fig. 8.13a.

Fig. 8.17 Difference FT-IR spectra over Fe/BEA in presence of 730 ppm NH₃ flowing at 150 °C (a), and after the purge with 10 % O₂ at 150 °C (b)



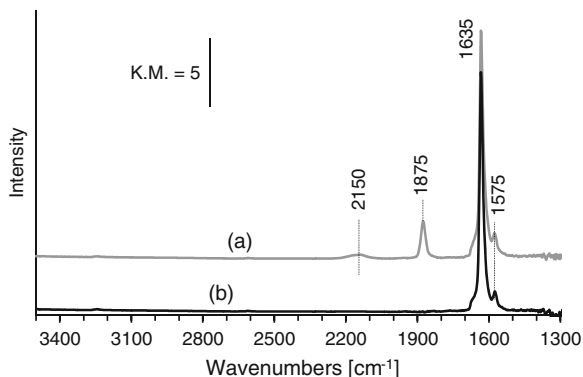
8.3.3 *In Situ FT-IR Analysis*

To trace the surface-adsorbed species during the transient NO_x reduction, in situ FT-IR analysis was applied. Analyzing the transient change of these adsorbates would help in understanding the SCR mechanism and identifying the rate-determining step.

Before the transient reaction analysis, the steady-state adsorption species formed when NH₃/N₂ or NO + O₂/N₂ was passed over the Fe/BEA catalyst have been presented. Figure 8.17a shows the difference spectra before and after 730 ppm NH₃ flow at 150 °C. Prior to the NH₃ adsorption, the sample was pre-treated with 10 % O₂ for 30 min at 550 °C followed by cooling it down to 150 °C. A strong band at 1,450 cm⁻¹ and a weak band at 1,680 cm⁻¹ can be assigned to the symmetric and asymmetric bending vibrations respectively, of chemisorbed NH₄⁺ on the Brønsted acidic sites [12, 36, 37]. Meanwhile, weaker bands at 1,300 and 1,600 cm⁻¹ can be assigned to the symmetric and asymmetric bending vibrations respectively, of coordinately linked NH₃ to Lewis acidic sites [12, 36, 37]. The bands at 3,275 and 3,355 cm⁻¹ can be assigned to the N–H stretching vibration of NH₄⁺ ions with the three hydrogen atoms bonded to the three oxygen ions of the AlO₄ tetrahedra (3H structure) [12, 36, 38]. The broad band between 2,600 and 2,900 cm⁻¹ can be attributed to the N–H stretching vibration of physisorbed NH₃ [12, 36, 37]. Figure 8.17b shows the NH₃-adsorbed spectra after purging with 10 % O₂/N₂ at 150 °C. There is no change after the O₂ purge, suggesting that neither oxidation nor desorption of adsorbed NH₃ occurred at this temperature.

Figure 8.18a shows the difference spectra before and after NO + O₂ flow. After pretreatment with 10 % O₂ at 550 °C, the sample was treated with a flow of 1,000 ppm NO, 10 % O₂ at 150 °C. A strong sharp band was observed at 1,635 cm⁻¹ which can be assigned to nitro (NO₂) group on the ion-exchanged Fe sites [36, 39–41]. Thus, NO was oxidized to NO₂ over the Fe sites and adsorbed

Fig. 8.18 Difference FT-IR spectra over Fe/BEA in presence of 1,000 ppm NO and 10 % O₂ flowing at 150 °C (a), and after the purge with 10 % O₂ at 150 °C (b)

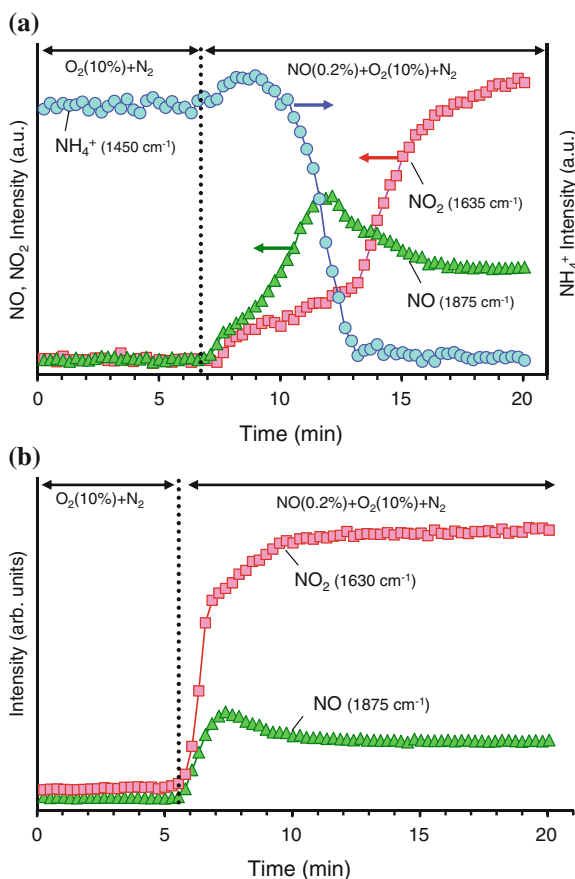


there. Small bands at 1,575 and 1,875 cm^{-1} can be assigned to nitrate and NO species, respectively, on the Fe sites [36, 39–41]. Additionally, a very weak broad band at 2,150 cm^{-1} could be assigned to NO⁺ species adsorbed on the Brønsted acidic sites [36, 39–41]. Figure 8.18b shows the NO_x-adsorbed spectra after purging with 10 % O₂ at 150 °C. The bands at 2,150 and 1,875 cm^{-1} disappeared, and only the NO₂ and nitrate bands remained.

Next, a transient reaction test was carried out by introducing NO + O₂ onto NH₃ preadsorbed on the Fe/BEA catalyst at 150 °C. Figure 8.19a shows the peak intensity profiles of the three main bands; 1,450 cm^{-1} (NH₄⁺), 1,635 cm^{-1} (NO₂), and 1,875 cm^{-1} (NO). When 0.2 % NO was added to 10 % O₂ + N₂ feed (7 min), the NH₄⁺ band slightly increased and then decreased with increase in the NO and NO₂ bands. After the disappearance of the NH₄⁺ band (13 min), the NO and NO₂ bands reached a steady-state level (20 min). Interestingly, the NO band went through a maximum at around 12 min, whereas the NO₂ band increased sharply after the NH₄⁺ band vanished (≥ 13 min). Thus, the NO₂ band was lower than the NO band in the presence of the NH₄⁺ band, but it exceeded after the disappearance of the NH₄⁺ band. In other words, the band intensities between NO and NO₂ reversed before and after the disappearance of the NH₄⁺ band.

Figure 8.19b shows the intensity profiles of the NO and NO₂ bands in the absence of preadsorbed NH₃. In this case, the NO₂ band intensity remained constantly higher than the NO band, which is consistent with the steady-state result observed in Fig. 8.18a. Comparing Fig. 8.19a and b we can make the following hypotheses: While the SCR reaction with using adsorbed NH₃ was occurring, (a) NO₂ formation from the oxidation of NO is inhibited by adsorbed NH₄⁺, and/or (b) the NO₂ produced is immediately consumed via the reaction with the adsorbed NH₄⁺. In any case, it could be said from this result that the rate-determining step of the surface SCR reaction would be the formation of NO₂ adspecies by NO oxidation over the active Fe sites.

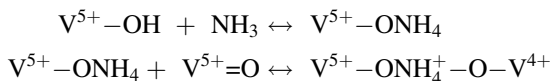
Fig. 8.19 IR peak intensity profiles of NO, NO₂, and NH₄⁺ bands at 150 °C. 0.2 % NO was added to 10 % O₂ feed in the presence of preadsorbed NH₃ (a), or in the absence of preadsorbed NH₃ (b)



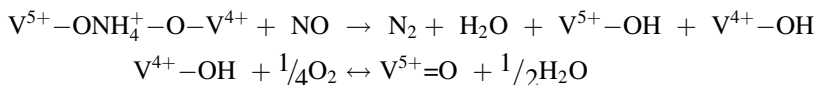
8.4 Reaction Mechanisms

8.4.1 Vanadium-Based Catalysts

In this section, some mechanistic implications of the SCR reaction over vanadium catalysts have been discussed based on the previous literature. The standard SCR reaction over V-based catalysts is generally considered to occur between the strongly adsorbed NH₃ and gaseous or weakly adsorbed NO [42–49]. The proposed reaction mechanisms often involve two adjacent vanadium species, namely the terminal oxygen species, i.e., V = O (redox sites), and the hydroxyl group, i.e., V–OH (Brønsted acidic sites). Topsøe et al. [44–46] suggested that the reaction scheme involves the adsorption of NH₃ on the Brønsted acidic sites (V⁵⁺–OH) followed by activation of adsorbed NH₃ via reaction at the redox sites (V⁵⁺ = O):



This activated form of NH₃ reacts with gaseous or weakly adsorbed NO, producing N₂ and H₂O, and leading to partially reduced state (V⁴⁺–OH). This reduced species could be reoxidized by oxygen to the V⁵⁺=O species.

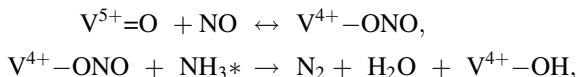


Topsøe et al. [44–46] reported that under high O₂ concentration condition (>1 %), the NH₃ activation step is fast and equilibrated, and thus the rate-limiting step is the reaction of NO with activated NH₄⁺.

Kamata et al. [48] estimated the ratio of the redox sites (V⁵⁺=O) to the Brønsted acidic sites (V⁵⁺–OH) by steady-state kinetic analysis. The relative amount of V⁵⁺=O sites varied from ~0.1 to ~0.4 with the partial pressure of O₂, indicating that the number of V⁵⁺=O sites are less than the number of V⁵⁺–OH sites.

Roduit et al. [1] proposed a global kinetic model for the standard SCR reaction based on V-based catalysts. The kinetic model accounts for three different reactions and intraparticle diffusion. The three reactions are Langmuir–Hinshelwood; LH-type SCR, Eley–Rideal; ER-type SCR, and direct NH₃ oxidation. The main SCR pathway proceeds via the ER-type mechanism, but in the low temperature region ($T \leq 200$ °C), LH-type reaction occurs. Furthermore, at high temperatures ($T \geq 300$ °C), NH₃ oxidation and intraparticle mass transfer also takes place [1].

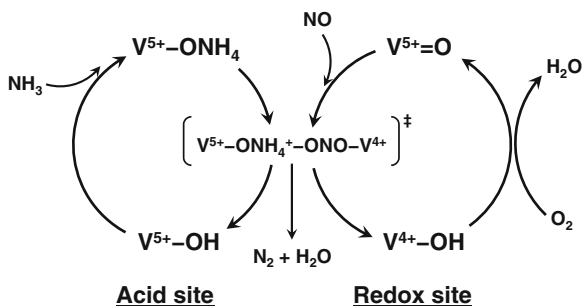
Tronconi et al. [50, 51] observed a transient improvement of SCR activity just after NH₃ shut off at low temperature. From this result, they pointed that the inhibitory effect of NH₃ cannot be accommodated by a simple ER kinetics assuming the reaction between adsorbed NH₃ and gaseous NO. They, then proposed that NO is oxidized by the V catalyst to a nitrite species, but the equilibrium is highly unfavorable and shifts to the right only in the presence of NH₃ [52]. The NH₃ which adsorbs on nearby acidic sites react with the nitrites to give N₂ and H₂O via decomposition of unstable ammonium nitrite intermediates, for example, according to



where NH₃^{*} represents adsorbed ammonia on the acidic sites. In this case, the inhibitory effect of NH₃ could be more easily explained by either a competitive adsorption of NH₃ onto the V sites involved in NO activation or an adverse electronic interaction of the adsorbed NH₃ with the vanadium oxidizing centers [52].

Taking into account the above contributions, the SCR schemes at low temperature condition can be generalized as in Fig. 8.20. The catalytic cycle could be divided into two parts which takes place on; (a) acidic sites meant for NH₃

Fig. 8.20 Schematic representation of catalytic cycle for standard SCR reaction over vanadium-based catalyst. Acidic site and redox site are associated with $V^{5+}-OH$ and $V^{5+}=O$, respectively



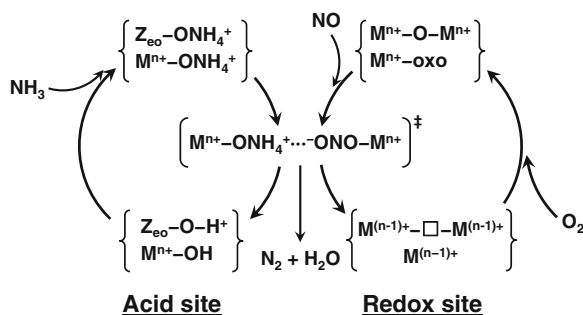
adsorption/activation and (b) redox sites meant for adsorbed NH_3 activation and NO adsorption/activation. This reaction mechanism suggests the requirement of two types of surface vanadium atoms. Many papers have suggested that the NO_x conversion is correlated with the amount of $V=O$ sites, and concluded that the redox site is indispensable to induce the SCR reaction [42, 44, 48, 49]. However, assuming the usage of transient SCR with preadsorbed NH_3 , the amount of acidic sites would also play a key role, because very little NH_3 can be adsorbed and available for the transient SCR reaction.

8.4.2 Fe- or Cu-Exchanged Zeolite Catalysts

Numerous studies have been conducted to reveal the SCR reaction mechanism [4, 8, 18, 30, 35–37, 53–57] as well as active species [7, 58–66] for metal-exchanged zeolites. Recently, spectroscopic studies including EXAFS analysis revealed that a binuclear structure ($M-O-M$) is created on the ion-exchanged sites [60–63]. Also, it has been commonly accepted that such binuclear species play an important role as active sites for several reactions such as N_2O/NO decomposition [67–70] and C_6H_6/CH_4 oxidation by N_2O [71–74]. Komatsu et al. [5] hypothesized that paired Cu^{2+} is the active copper species in view of the relationship between the SCR activity and the copper concentration. Similarly, Chen and Sachtler [58], and Mauvezin et al. [59] assumed that an oxygen-bridged binuclear iron complex acts as the active site for the SCR reaction because CO consumption in CO -TPR was nearly half of the amount of Fe . Schwidder et al. [29, 64] and Brandenberger et al. [7, 65] suggested that not only mononuclear Fe but also the binuclear species contribute to the SCR reaction.

For the SCR mechanism, Delahay et al. [13, 75] proposed a Fe^{2+}/Fe^{3+} (or Cu^+/Cu^{2+}) redox cycle as a part of the SCR scheme; the extra-framework oxygen on Fe^{3+} (Cu^{2+}) oxo/hydroxo species reacts with NO to form a surface nitrogen oxide intermediate ($Fe^{3+}-N_xO_y$ or $Cu^{2+}-N_xO_y$). Then, this species reacts with NH_3 to form N_2 and H_2O with concomitant reduction of Fe^{3+} (Cu^{2+}) to Fe^{2+} (Cu^+) species. The Fe^{2+} (Cu^+) species is reoxidized back to Fe^{3+} (Cu^{2+}) oxo/hydroxo species by O_2 [13, 75].

Fig. 8.21 Schematic representation of catalytic cycle for standard SCR reaction over metal-exchanged zeolite catalysts. Acid sites are associated with Lewis or Brønsted sites at ion-exchanged metal or free proton sites. Redox sites are associated with oxo-metal (isolated or binuclear) ion-exchanged sites



Considering these previous reports, one can assume the following general SCR mechanism (Fig. 8.21): First, the reaction sites would be composed of acidic sites and redox sites similar to the V catalyst. However, in some cases, there is a possibility that one site can possess both the properties. For the acidic sites, the ion-exchanged metal sites (Brønsted or Lewis type) or residual free proton sites (Brønsted type) can be expected. Strong NH_3 adsorption on such acidic sites during the SCR reaction has been reported in the literature [36, 37, 54]. Regarding the redox sites, the ion-exchanged metal cations (mononuclear and/or binuclear oxo species) can be expected. From TPR study, these sites are known to be easily reduced compared to extra-framework bulk metal oxides [63, 73, 76–78]. Also, Nobukawa et al. [73, 74] reported that very reactive oxygen atoms can be created over the binuclear Fe sites after N_2O treatment, and that it can desorb easily during a TPD run. This reactive oxygen atom in the nascent state is able to oxidize CH_4 to CO/CO_2 which is one of the difficult reactions to occur [73, 74].

By comparing the SCR scheme (Fig. 8.21) with NO oxidation scheme (Fig. 8.7), one can find similarities and differences. First of all, both reactions seem to progress via similar redox cycles of the active metal. However, judging from the reaction kinetic analysis discussed in Sects. 8.2.3 and 8.2.4, the rate-determining step of NO oxidation would be NO_2 desorption process. As for the SCR reaction, on the other hand, the process prior to the formation of NO_2 related adspecies (e.g., nitrite or nitrate intermediate) would be the rate-determining step, as is discussed in Sect. 8.3.3. Therefore, the slowest step in the redox cycles would be different in the two reactions.

For the SCR reaction, NO activation to form NO_2 species would be the key step. For a deeper understanding of the SCR mechanism, further reaction kinetic analysis combined with tracing the reversible valence change of active metal is necessary. However, it can be said from the result of Sects. 8.3.1 and 8.3.2 that gaseous and/or high coverage NH_3 inhibits the rate-determining step, and thus reaction rate can be

promoted by improving the reaction conditions such as adapting the periodic operation. Additionally, the acid site amount is also an important factor affecting the SCR activity especially for the periodic operation condition.

8.5 Conclusions

In this chapter, the mechanistic aspects of the $\text{NO-NH}_3\text{-O}_2$ reacting system were addressed by using three conventional SCR catalysts, Cu or Fe ion-exchanged zeolites and V-W/TiO_2 . There had been several differences among the catalysts. For instance, the temperature profiles of SCR activity were different between the zeolite-based catalysts and V-W/TiO_2 . Regarding the tolerance for SO_2 poisoning, Fe/zeolite and V-W/TiO_2 showed high durability, while Cu/zeolite greatly deteriorated in the low temperature activity due to the different affinity between the active metals and sulfur.

Also, the periodic operation (NH_3 on/off cycling) had positive effect on the low temperature activity for Fe- and Cu-exchanged zeolites, because of strong inhibition by gaseous NH_3 and/or high NH_3 coverage. For V-W/TiO_2 , on the other hand, the periodic operation had not positive effect but negative especially under high temperature condition due to its lower NH_3 storage capacity.

However, the reaction mechanism could be depicted as common schemes which would be composed of (a) acidic sites meant for NH_3 adsorption/desorption, and (b) redox sites meant for NO oxidation and forming $\text{NO}_x\text{-NH}_y$ intermediate species. Although the SCR activities of the three catalysts were not always correlated with NH_3/NO oxidation abilities as well as acid site amount, each property plays an important role for explaining the reaction behaviors under high temperature and/or periodic conditions, as well as determining the reaction mechanisms. In situ FT-IR analysis of the SCR reaction between $\text{NO} + \text{O}_2$ and preadsorbed NH_3 over Fe/zeolite suggested that the rate-determining step of the surface SCR would be the formation of NO_2 adspecies by NO oxidation over Fe sites, which is an important insight to clarify the detailed SCR mechanism.

References

1. Roduit B, Wokaun A, Baiker A (1998) *Ind Eng Chem Res* 37:4577–4590.
2. Metkar PS, Balakotaiah V, Harold MP (2011) *Chem Eng Sci* 66:5192–5203.
3. Efstathiou AM, Fliatoura K (1995) *Appl Catal B: Environ* 6:35–59.
4. Iwasaki M, Yamazaki K, Shinjoh H (2009) *Appl Catal A: Gen* 366:84–92.
5. Komatsu T, Nunokawa M, Moon IS, Takahara T, Namba S, Yashima T (1994) *J Catal* 148:427–437.
6. Huang HY, Long RQ, Yang RT (2002) *Appl Catal A: Gen* 235:241–251.
7. Brandenberger S, Kröcher O, Tissler A, Althoff R (2010) *Appl Catal B: Environ* 95:348–357.

8. Metkar PS, Salazar N, Muncrief R, Balakotaiah V, Harold MP (2011) *Appl Catal B: Environ* 104:110–126.
9. Moon IS, Namba S, Yashima T (1993) *J Jpn Petrol Inst* 36:339–342.
10. Eng J, Bartholomew CH (1997) *J Catal* 171:14–26.
11. Metkar PS, Balakotaiah V, Harold MP (2012) *Catal Today* 184:115–128.
12. Long RQ, Yang RT (2002) *J Catal* 207:274–285.
13. Delahay G, Valade D, Guzman-Vargas A, Coq B (2005) *Appl Catal B: Environ* 55:149–155.
14. Devadas M, Kröcher O, Elsener M, Wokaun A, Mitrikas G, Söger N, Pfeifer M, Demel Y, Mussmann L (2007) *Catal Today* 119:137–144.
15. Balle P, Geiger B, Kureti S (2009) *Appl Catal B: Environ* 85:109–119.
16. Iwasaki M, Yamazaki K, Shinjoh H (2011) *Appl Catal B: Environ* 102:302–309.
17. Wilken N, Wijayanti K, Kamasamudram K, Currier NW, Vedaiyan R, Yezerets A, Olsson L (2012) *Appl Catal B: Environ* 111–112:58–66.
18. Grossale A, Nova I, Tronconi E (2008) *Catal Today* 136:18–27.
19. Metkar PS, Harold MP, Balakotaiah V (2012) *Appl Catal B: Environ* 111–112:67–80.
20. Colombo M, Nova I, Tronconi E (2010) *Catal Today* 151:223–230.
21. Iwasaki M, Shinjoh H (2010) *Phys Chem Chem Phys* 12:2365–2372.
22. Tronconi E, Nova I, Colombo M (2010) *Ind Eng Chem Res* 49:10374–10385.
23. Li JH, Zhu RH, Cheng YS, Lambert CK, Yang RT (2010) *Environ Sci Technol* 44:1799–1805.
24. He CH, Wang YH, Cheng YS, Lambert CK, Yang RT (2009) *Appl Catal A: Gen* 368:121–126.
25. Malpartida I, Marie O, Bazin P, Daturi M, Jeandel X (2011) *Appl Catal B: Environ* 102:190–200.
26. Ma AZ, Grunert W (1999) *Chem Commun*:71–72.
27. Iwasaki M (2011) R&D Review of Toyota CRDL 42:21–32 <http://www.tytlabs.co.jp/review/>
28. Wallin M, Karlsson C-J, Skoglundh M, Palmqvist A (2003) *J Catal* 218:354–364.
29. Schwidder M, Heikens S, De Toni A, Geisler S, Berndt M, Bruckner A, Grunert W (2008) *J Catal* 259:96–103.
30. Sjövall H, Blint RJ, Gopinath A, Olsson L (2009) *Ind Eng Chem Res* 49:39–52.
31. Kröcher O, Devadas M, Elsener M, Wokaun A, Söger N, Pfeifer M, Demel Y, Mussmann L (2006) *Appl Catal B: Environ* 66:208–216.
32. Auvray X, Partridge WP, Choi J-S, Pihl JA, Yezerets A, Kamasamudram K, Currier NW, Olsson L (2012) *Appl Catal B: Environ* 126:144–152.
33. Colombo M, Nova I, Tronconi E, Schmeißer V, Bandl-Konrad B, Zimmermann L (2012) *Appl Catal B: Environ* 111–112:106–118.
34. Sjövall H, Olsson L, Fridell E, Blint RJ (2006) *Appl Catal B: Environ* 64:180–188.
35. Olsson L, Sjövall H, Blint RJ (2008) *Appl Catal B: Environ* 81:203–217.
36. Long RQ, Yang RT (2000) *J Catal* 194:80–90.
37. Sun Q, Gao ZX, Wen B, Sachtler WMH (2002) *Catal Lett* 78:1–5.
38. Eng J, Bartholomew CH (1997) *J Catal* 171:27–44.
39. Gao ZX, Qi S, Sachtler WMH (2001) *Appl Catal B: Environ* 33:9–23.
40. Iwasaki M, Yamazaki K, Banno K, Shinjoh H (2008) *J Catal* 260:205–216.
41. Iwasaki M, Shinjoh H (2010) *J Catal* 273:29–38.
42. Inomata M, Miyamoto A, Murakami Y (1980) *J Catal* 62:140–148.
43. Marshneva VI, Slavinskaya EM, Kalinkina OV, Odegova GV, Moroz EM, Lavrova GV, Salanov AN (1995) *J Catal* 155:171–183.
44. Topsøe NY, Dumesic JA, Topsøe H (1995) *J Catal* 151:241–252.
45. Topsøe NY, Topsøe H, Dumesic JA (1995) *J Catal* 151:226–240.
46. Dumesic JA, Topsøe NY, Topsøe H, Chen Y, Slabiak T (1996) *J Catal* 163:409–417.
47. Lietti L, Nova I, Tronconi E, Forzatti P (1998) *Catal Today* 45:85–92.
48. Kamata H, Takahashi K, Ingemar Odenbrand CU (1999) *J Catal* 185:106–113.
49. Centeno M, Carrizosa I, Odriozola J (1999) *Phys Chem Chem Phys* 1:349–354.

50. Tronconi E, Nova I, Ciardelli C, Chatterjee D, Bandl-Konrad B, Burkhardt T (2005) *Catal Today* 105:529–536.
51. Ciardelli C, Nova I, Tronconi E, Konrad B, Chatterjee D, Ecke K, Weibel M (2004) *Chem Eng Sci* 59:5301–5309.
52. Tronconi E, Nova I, Ciardelli C, Chatterjee D, Weibel M (2007) *J Catal* 245:1–10.
53. Long RQ, Yang RT (2001) *J Catal* 198:20–28.
54. Long RQ, Yang RT (2002) *J Catal* 207:224–231.
55. Sun Q, Gao ZX, Chen HY, Sachtler WMH (2001) *J Catal* 201:89–99.
56. Grossale A, Nova I, Tronconi E, Chatterjee D, Weibel M (2008) *J Catal* 256:312–322.
57. Iwasaki M, Shinjoh H (2010) *Appl Catal A: Gen* 390:71–77.
58. Chen HY, Sachtler WMH (1998) *Catal Today* 42:73–83.
59. Mauvezin M, Delahay G, Coq B, Kieger S, Jumas JC, Olivier-Fourcade J (2001) *J Phys Chem B* 105:928–935.
60. Marturano P, Drozdova L, Kogelbauer A, Prins R (2000) *J Catal* 192:236–247.
61. Marturano P, Drozdova L, Pirngruber GD, Kogelbauer A, Prins R (2001) *Phys Chem Chem Phys* 3:5585–5595.
62. Battiston AA, Bitter JH, de Groot FMF, Overweg AR, Stephan O, van Bokhoven JA, Kooyman PJ, van der Spek C, Vanko G, Koningsberger DC (2003) *J Catal* 213:251–271.
63. Battiston AA, Bitter JH, Heijboer WM, de Groot FMF, Koningsberger DC (2003) *J Catal* 215:279–293.
64. Schwidder M, Kumar MS, Klementiev K, Pohl MM, Bruckner A, Grunert W (2005) *J Catal* 231:314–330.
65. Brandenberger S, Kröcher O, Tissler A, Althoff R (2010) *Appl Catal A: Gen* 373:168–175.
66. Iwasaki M, Shinjoh H (2011) *Chem Commun* 47:3966–3968.
67. Moretti G, Ferraris G, Fierro G, Jacono ML, Morpurgo S, Faticanti M (2005) *J Catal* 232:476–487.
68. Hansen N, Heyden A, Bell AT, Keil FJ (2007) *J Catal* 248:213–225.
69. Guesmi H, Berthomieu D, Kiwi-Minsker L (2008) *J Phys Chem C* 112:20319–20328.
70. Pirngruber GD, Roy PK, Weiher N (2004) *J Phys Chem B* 108:13746–13754.
71. Li G, Pidko EA, van Santen RA, Feng Z, Li C, Hensen EJM (2011) *J Catal* 284:194–206.
72. Xia H, Sun K, Sun K, Feng Z, Li WX, Li C (2008) *J Phys Chem C* 112:9001–9005.
73. Nobukawa T, Yoshida M, Okumura K, Tomishige K, Kunimori K (2005) *J Catal* 229:374–388.
74. Nobukawa T, Sugawara K, Okumura K, Tomishige K, Kunimori K (2007) *Appl Catal B: Environ* 70:342–352.
75. Delahay G, Kieger S, Tanchoux N, Trens P, Coq B (2004) *Appl Catal B: Environ* 52:251–257.
76. Yoshida M, Nobukawa T, Ito SI, Tomishige K, Kunimori K (2004) *J Catal* 223:454–464.
77. Pérez-Ramírez J, Mul G, Kapteijn F, Moulijn JA, Overweg AR, Doménech A, Ribera A, Arends IWCE (2002) *J Catal* 207:113–126.
78. Lobree LJ, Hwang IC, Reimer JA, Bell AT (1999) *J Catal* 186:242–253.

Chapter 9

The Role of NO₂ in the NH₃–SCR Catalytic Chemistry

Enrico Tronconi and Isabella Nova

9.1 Introduction

As discussed in other chapters of this book, ammonia SCR was first introduced over three decades ago to control NO_x emissions from power stations and other stationary sources. It is nowadays an extensively investigated and very well-known process, being still the best available commercial DeNO_x technology for efficiency, selectivity, and economics.

It relies primarily on the so-called Standard SCR reaction, wherein NH₃ reduces NO in the presence of oxygen to harmless N₂ and H₂O. Classical catalysts are ternary mixed oxide systems based on V₂O₅–WO₃/TiO₂, and the operating temperature window is rather narrow, namely 300–400 °C.

At the beginning of the new century, the automotive industry started to develop NH₃—or urea SCR systems to reduce NO_x contained in the exhaust gases of internal combustion engines operated with excess air, such as, for example, Diesel engines. To transfer the SCR technology from stationary sources to vehicles, however, the OEMs had to face a number of engineering challenges. Many such challenges have to do with the more complex chemistry resulting from the presence of NO₂ in the SCR reacting system in addition to NO. In most EGA configurations, in fact the exhaust gases from the engine, containing mostly NO, are passed over an oxidation catalyst (DOC) before reaching the SCR converter downstream. Over the DOC, HCs and CO are completely oxidized, and NO is partially oxidized to NO₂. But NO₂ originates additional reactions over the SCR catalyst, including the very important Fast SCR reaction, which boosts the DeNO_x activity at low temperature, especially over V-based and Fe-zeolite catalysts.

Indeed, at the start of the mobile SCR applications the catalytic mechanism and the kinetics of the full NO–NO₂–NH₃ reacting system were still largely debated,

E. Tronconi (✉) · I. Nova

Dipartimento di Energia, Laboratorio di Catalisi e Processi Catalitici, Politecnico di Milano,
Piazza Leonardo da Vinci 32, 20133 Milan, Italy
e-mail: enrico.tronconi@polimi.it

preventing an effective quantitative description. The aim of this contribution is to review the catalytic chemistry associated with the urea SCR technology, focusing specifically on the steps involving NO_2 : for this purpose we will use data and results from the investigation of several SCR catalysts performed in our labs during the last decade.

In the following we will address first the adsorption—desorption of NO_x on SCR catalysts to show that not only the storage of ammonia, as universally recognized, but also the storage of nitrates on the catalyst surface may be quite relevant to the dynamic behavior of SCR systems. We will then proceed to prove that such surface nitrates are not just spectators, but actually play a crucial role in the SCR catalytic chemistry. This will set the stage for demonstrating the individual mechanistic steps associated with the important Fast SCR reaction, using transient reaction analysis. The mechanisms of ammonium nitrate formation and of the NO_2 –SCR reaction will be also discussed. Potential implications of the resulting overall mechanistic picture will be illustrated in the last section of the chapter: here, we will introduce the Enhanced SCR reaction, wherein nitrates, rather than being formed and converted as intermediates, are intentionally cofed (in the form of an aqueous solution of ammonium nitrate) along with NO and NH_3 to the SCR catalyst in order to boost the low-temperature DeNO_x activity to the same levels of the Fast SCR reaction, without the need of including NO_2 in the NO_x feed mixture.

9.2 Experimental

Catalytic activity data herein reported were collected over state-of-the-art commercial vanadium-based, Fe- and Cu-promoted zeolite SCR catalysts. The original monolith samples were crushed to powder, sieved, and loaded in a quartz microflow reactor (60–80 mg) consisting of a quartz tube (6 mm i.d.) placed in an electric oven. This experimental setup affords isothermal operation of fast transients in a chemical regime, free of any diffusional intrusions. He as carrier gas enables evaluation of N-balances.

The reactor outlet was directly connected to a quadrupole mass spectrometer (Balzers QMS 200) and to a UV-analyzer (ABB LIMAS 11HW) in parallel. NH_3 , NO , NO_2 , N_2O , O_2 , and He were dosed from bottled calibrated gas mixtures by mass flow controllers, while water vapor was added by means of a saturator. The catalyst temperature was measured by a K-type thermocouple directly immersed in the catalytic bed.

The catalysts were typically conditioned in a T-ramp at $5\text{ }^\circ\text{C}/\text{min}$ up to $600\text{ }^\circ\text{C}$ in $8\text{ }\%$ O_2 v/v, and $8\text{ }\%$ H_2O v/v followed by hold at $600\text{ }^\circ\text{C}$ for 5 h. Kinetic runs included transient and steady-state isothermal experiments in the 150 – $550\text{ }^\circ\text{C}$ temperature range. Typical feed concentrations of NO_x and NH_3 ranged between 0 and 1,000 ppm, always in the presence of O_2 ($8\text{ }\%$ v/v), H_2O ($8\text{ }\%$ v/v) unless otherwise specified, with balance He. A detailed description of the experimental equipment and procedures can be found elsewhere [1–3].

9.3 Surface Storage of NO_x

9.3.1 NO₂ Adsorption/Desorption

It has been well known for many years that NH₃ gets strongly adsorbed onto the acidic SCR catalysts and reacts with NO_x from the adsorbed state. Indeed, the dynamic behavior of SCR converters is largely dominated by the balance between the rates of NH₃ adsorption, desorption, and surface reaction [4] with NO_x. On the other hand, NO is known to adsorb in negligible amounts onto SCR catalysts; however, this is not the case for NO₂. Figure 9.1 compares NO₂ concentration step feed experiments over a Cu- and a Fe-zeolite SCR catalyst. It is clearly apparent that NO₂ is stored in significant amounts onto both catalysts until saturation: at the same time, NO evolution is observed.

Several literature reports confirm, in fact, that zeolite catalysts are able to adsorb NO₂ in the form of nitrates. NO₂ chemisorption can be described by the following two-step mechanism, schematically representing disproportionation and heterolytic chemisorption of NO₂ to form surface nitrites and nitrates, step (9.1), followed by NO₂ oxidizing the nitrites to nitrates, step (9.2):



The combination of (9.1) and (9.2) results in the following global stoichiometry,



where one mole of gaseous NO is produced for every three moles of adsorbed NO₂. Figure 9.1 confirms that such a proportion was approximately respected in our experiments: e.g., a NO/ΔNO₂ ratio of about 0.35 was indeed observed over the Cu- and the Fe-zeolite systems, in agreement with (9.3).

The nitrates storage capacity of the two zeolite systems at 50 °C was determined from Fig. 9.1 taking into account the stoichiometry of reaction (9.3), resulting in about 0.87 and 0.50 mmol/g_{active phase} for the Cu- and the Fe-zeolite, respectively. Expectedly, the storage capacity was found to decrease with increasing adsorption temperature.

In a first attempt to confirm the presence of nitrates onto the catalyst surface, and in order to study their thermal stability, TPD runs were performed after saturation of the catalyst samples with NO₂. During the temperature ramps evolution of NO₂, NO and oxygen were indeed recorded, in line with what was already observed over other zeolite systems [5, 6] and over V₂O₅-WO₃/TiO₂ catalysts [7].

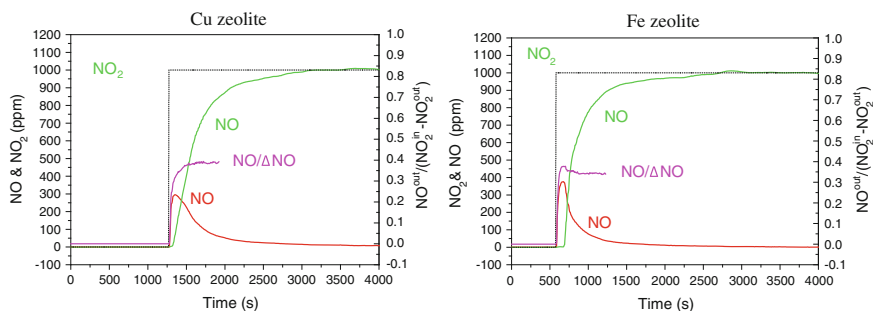


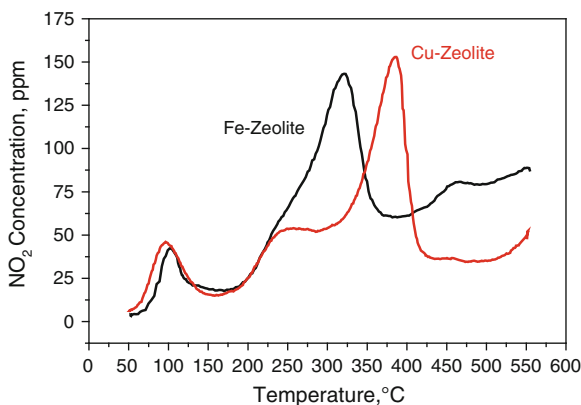
Fig. 9.1 Temporal evolution of NO_2 , NO outlet concentrations and of $\text{NO}/\Delta\text{NO}_2$ during NO_2 step feed experiments over commercial Cu- and Fe-zeolite catalysts. $T = 50^\circ\text{C}$. Feed composition: $\text{NO}_2 = 1000$ ppm, $\text{H}_2\text{O} = 1\%$ v/v, $\text{O}_2 = 0\%$ v/v. Adapted from [8]

Figure 9.2 compares the NO_2 traces from TPD runs after NO_2 adsorption at 50°C over the Fe- and the Cu-zeolite catalysts. In addition to the low-T peak associated with physisorbed species, an important NO_2 peak from nitrates decomposition was observed above 200°C over both systems: it appears however that nitrates formed by NO_2 disproportionation were more stable on the Cu catalyst. This aspect is possibly correlated with the different activity performances exhibited by the two catalysts in the Fast SCR and in the NO_2 -SCR reactions [8, 9].

9.3.2 FTIR in Situ Study of NO_2 Adsorption

FT-IR in situ transient reaction analysis was also applied to investigate in more depth NO_2 storage on a commercial Fe-ZSM-5 (Zeolyst) sample [10]. The FT-IR data were collected in the transmission mode in a flow cell adapted to ensure full mixing and a fast response to isothermal concentration step changes of the feed concentration. The study clearly identified the formation of various ferric nitrates as the prevailing and stable terminal products of NO_2 storage on Fe-ZSM-5. Other detected surface intermediates included nitrosonium ions (NO^+) in cationic position, likely exchanging the proton of the Si-OH-Al bridge in the zeolites, originated by disproportionation/heterolytic chemisorption of NO_2 [6], and Fe(II) NO nitrosyls from NO adsorption onto reduced Fe sites. The formation of nitrite (NO_2^-) intermediates was not detected, which is explained by their high reactivity and/or by the superposition of their IR features on the reflexes of the zeolites: their participation in the surface chemistry is however quite likely, in view of the detection of NO^+ adspecies, which share the same N oxidation state (+3) and are closely related to the nitrites by equilibria such as $\text{NO}^+ + \text{O}^{2-} \leftarrow \rightarrow \text{NO}_2^-$. Such conclusions are well in line with several recent publications from the IR spectroscopy literature addressing the adsorption of NO_2 on metal-exchanged zeolites [11–13].

Fig. 9.2 NO₂ concentration profiles during TPD (T = 50–550 °C at 20 K/min, GHSV = 193,000 Ncc/h/g_{ap} (Fe), 266,000 Ncc/h/g_{ap} (Cu)) after NO₂ adsorption (Feed: 1,000 ppm NO₂, T = 50 °C, 3 % H₂O, 0 % O₂, balance He). Adapted from [9]



9.3.3 Effect of the Catalyst Redox State on NO₂ Adsorption

The effect of the catalyst red-ox state on the adsorption of NO₂ on Fe- and Cu-promoted zeolite SCR catalysts has been found to be also quite significant [14]. In this study, the catalysts were either preoxidized or prereduced prior to NO₂ adsorption by exposing them to O₂ or to NH₃, respectively, at high temperature. For both catalytic systems, results from the analysis of the gas phase during NO₂ step feed changes in the absence of gaseous water emphasize an important role of the catalyst red-ox state in the dynamics of NO₂ adsorption: the molar ratio of released NO to converted NO₂ was close to 1/3 in the case of oxidized catalysts, in line with the two-steps mechanism leading to the formation of surface nitrates, reactions (9.1)–(9.3), but was significantly greater when the catalyst was prereduced. This is shown for example for the Fe-zeolite in Fig. 9.3a, b. The extra NO evolution is explained considering that, before being stored in the form of nitrates, NO₂ effectively oxidizes the reduced catalyst, while being reduced to NO.

It was also found that the initial catalyst red-ox state influences the amount of nitrates adsorbed on the catalyst surface, the prereduced sample exhibiting a greater storage capacity (see Fig. 9.3c, d). In line with the literature reports [13], the greater amount of stored nitrates observed on the prereduced samples of both catalysts can be justified invoking the redispersion of Fe and Cu ions during the reduction phase, which thus provides additional sites for nitrates storage.

Another interesting finding from this study was that, in the case of the Fe-zeolite, the NO₂ adsorption/desorption dynamics over the preoxidized catalyst were essentially unaffected by the presence of gaseous oxygen (see Fig. 9.3a–d).

A different situation was noted in the case of the Cu-zeolite catalyst, for which a significant effect of the oxygen on the NO₂ adsorption dynamics was apparent. Indeed, when oxygen was present in the feed stream together with NO₂, a lower amount of NO was produced upon NO₂ step feed with respect to what observed

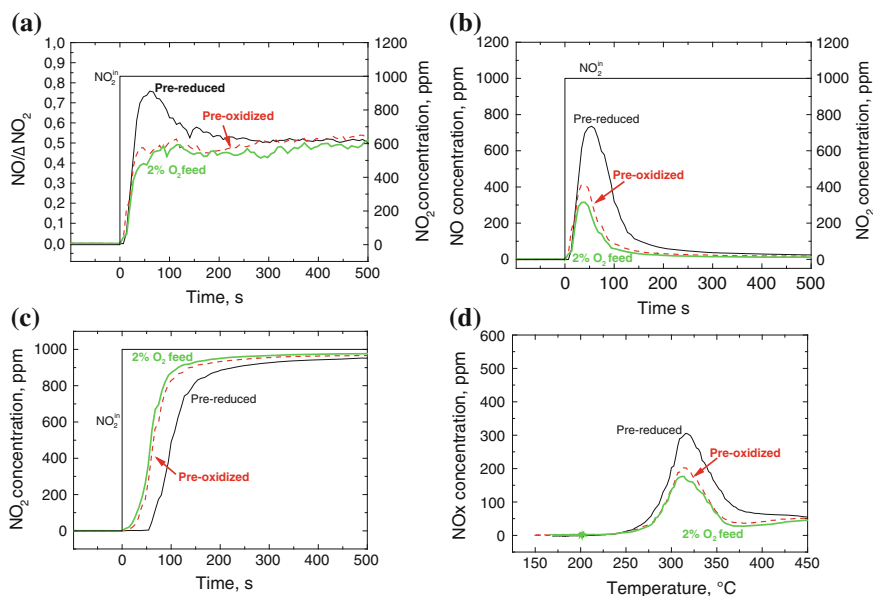


Fig. 9.3 NO₂ adsorption and TPD over Fe-zeolite. Adsorption phase: T = 200 °C, Q = 71 cm³/min (STP), NO₂ = 1,000 ppm, O₂ = 2 % v/v (only for green lines), carrier gas = He; TPD: T-ramp = 20 °C/min, Q = 71 cm³/min (STP), He flow. **a** NO/(NO₂ⁱⁿ - NO₂^{out}) as a function of time during the first 500 s of NO₂ feed. **b** NO concentration as a function of time during the first 500 s of NO₂ feed. **c** NO₂ concentration as a function of time during the first 500 s of NO₂ feed. **d** NO_x concentration as a function of catalysts temperature during TPD phase. *Black lines* = prerduced sample. *Red lines* = preoxidized sample. *Green lines* = preoxidized sample in the presence of oxygen during adsorption phase. Adapted from [14]

over both the preoxidized and the prerduced samples, with NO/ΔNO₂ ratio of about 0.35–0.38 in line with those expected from an oxidized catalyst. Accordingly, we can speculate that the preoxidizing procedure was not completely effective over the tested Cu-zeolite sample. Indeed the catalyst, prior to NO₂ adsorption, was flushed with helium at 200 °C. We can thus assume that, in the case of the tested Cu-zeolite a partial reduction of the catalytic surface occurred at 200 °C during the catalyst exposure to an inert atmosphere [15]. This was not observed in the case of the Fe-zeolite, which suggests a greater reducibility of the Cu catalyst.

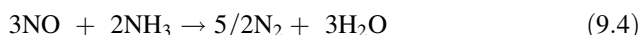
Thus, it seems now well established that the presence of NO₂ in the NH₃-SCR reacting system involves the formation of nitrates adspecies in significant amounts over both Fe- and Cu-promoted zeolites catalysts. The similarity with the chemistry of NO_x storage onto Pt-Ba/Al₂O₃ Lean NO_x Traps (LNT) has been noted in this respect [16]. At this point, the question is whether such species are just spectators or rather participate actively in the NH₃-SCR mechanism. We address this important issue in the next paragraph.

9.4 The Role of Surface Nitrates in the Fast SCR Mechanism

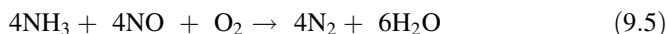
9.4.1 NH₃ + NO_x Temperature Programmed Reaction (TPR) Runs

Information concerning the involvement of surface nitrates in the NO/NO₂-NH₃ SCR reactivity is provided by Fig. 9.4, wherein we compare the T-dependences of NO conversion over a Fe-zeolite catalyst measured during four different NO + NH₃ Temperature Programmed Reaction (TPR) experiments with equal space velocities and heating rates (20 K/min), but with different feed gas compositions [1].

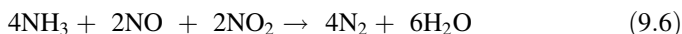
In the experiment associated with curve A the feed included NO + NH₃ (1,000 ppm each) + H₂O (1 % v/v), but no oxygen: the observed temporal evolution of the outlet concentrations, indicating the onset of a DeNO_x activity only above 300 °C, was found expectedly in agreement with the so-called “Slow” SCR reaction, i.e., the poorly active DeNO_x reaction between NO and NH₃ which proceeds in the absence of oxygen,



When the same Temperature Programmed Reaction (TPR) experiment was replicated with 2 % O₂ v/v in the feed (curve B), a greater DeNO_x activity was observed as a result of the occurrence of the Standard SCR reaction (9.5) instead of the slower reaction (9.4).



Curve C shows the even much higher DeNO_x activity resulting from running the same T-ramp with a feed containing 1,000 ppm of NH₃ and 500 ppm each of NO and NO₂: curve C is of course representative of the NO (and NO_x) conversion in the Fast SCR reaction (9.6):



Whose rate is known to largely exceed the rate of Standard SCR (9.5) at low temperatures.

During the fourth and final Temperature Programmed Surface Reaction (TPSR) experiment, associated with curve D, a feed containing NO + NH₃ (1,000 ppm each) + H₂O (1 % v/v), but no oxygen and no NO₂, was passed over a catalyst sample preexposed to 1,000 ppm of NO₂ + 1 % H₂O at 60 °C. Figure 9.4 shows that during the initial part of this T-ramp, up to about 200 °C, the evolution of the NO conversion matched closely that observed in the case of the Fast SCR TPR run, curve C. In the following part of the experiment the NO conversion dropped sharply close to zero, before eventually approaching the behavior observed for the Slow SCR reaction, i.e., curve A.

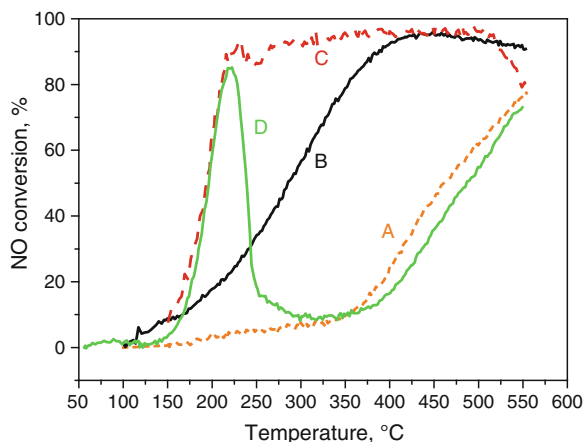


Fig. 9.4 Temperature programmed reaction experiments over Fe-ZSM-5. $W_{\text{cat}} = 0.080$ mg, Flow rate = $72 \text{ cm}^3/\text{min}$ (STP). *Curve A* (Slow SCR): Feed = 1 % H_2O , 0 % O_2 , $\text{NH}_3 = 1,000$ ppm, $\text{NO} = 1,000$ ppm + He. *Curve B* (Standard SCR): Feed = 1 % H_2O , 2 % O_2 , $\text{NH}_3 = 1,000$ ppm, $\text{NO} = 1,000$ ppm + He. *Curve C* (Fast SCR): Feed = 1 % H_2O , 0 % O_2 , $\text{NH}_3 = 1,000$ ppm, $\text{NO} = 500$ ppm, $\text{NO}_2 = 500$ ppm + He. *Curve D*: Feed = 1 % H_2O , 0 % O_2 , $\text{NH}_3 = 1,000$ ppm, $\text{NO} = 1,000$ ppm + He over catalyst pretreated with NO_2 (1,000 ppm) + H_2O (1 %) at 60°C . Adapted from [1]

A plausible rationalization of the similarity between the initial parts of curves C (Fast SCR) and D ($\text{NO} + \text{NH}_3$ over catalyst pretreated with NO_2) in Fig. 9.4 is that in both cases NO and ammonia in the feed were reacting with surface nitrates, either directly and simultaneously formed via NO_2 disproportionation (curve C), or previously formed and stored on the catalyst during its pretreatment with NO_2 (curve D). It is worth emphasizing that in this experiment the DeNO_x activity in the presence of surface nitrates (but in the absence of gaseous NO_2) was found virtually identical to that associated with the Fast SCR reaction in the low temperature region up to about 200°C . This is quite consistent with other transient experiments showing that both over Fe-zeolite [1] and over $\text{V}_2\text{O}_5/\text{WO}_3/\text{TiO}_2$ [17] the rate of reduction of ammonium nitrate at the catalyst surface by NO at low temperature (around 170°C) was essentially identical to that of the Fast SCR reaction.

The drop of NO conversion exhibited by curve D at $T > 200^\circ\text{C}$ in Fig. 9.4 is explained by depletion of surface nitrates; in fact, in another similar experiment (not reported), wherein the catalyst had been pretreated with NO_2 at 150°C rather than at 60°C , an earlier drop in the NO conversion was observed due to the reduced amount of nitrates stored at the higher temperature. Eventually, the match between curves D and A at $T > 300^\circ\text{C}$ confirms the absence of any residual oxidizing agent (but NO) in the final part of the T-ramp experiment over the NO_2 pretreated sample.

Similar TPR experiments performed over a Cu-zeolite catalyst provided similar results.

9.4.2 Role of Nitrates in the NO/NO₂-NH₃ SCR Mechanism

The TPR data in Fig. 9.4 clearly prove that the DeNO_x activity grows with increasing oxidizing potential of the SCR reaction environment. Essentially, they provide a ranking of the oxidizers involved in the NH₃-SCR reactions, with NO being a poorer oxidizer than O₂, which is in turn a much less powerful oxidizer than NO₂/nitrates. This is in line with a red-ox interpretation of the NH₃-SCR chemistry wherein catalyst reoxidation is the slow, rate controlling step of the red-ox cycle at low temperature [7, 18]. In addition, the comparative analysis of curves C and D in Fig. 9.4 further demonstrates that the oxidizing power of NO₂ is actually not different from that of surface nitrates. While this result does not rule out a direct participation of NO₂ in the SCR chemistry, it suggests however that surface nitrates, rather than gaseous NO₂, may be responsible for the rapid catalyst reoxidation in the case of the Fast SCR reaction over Fe-zeolites, as proposed in the past for V-based catalysts [7].

So far we have proven that not only nitrates are stored onto Fe- (and Cu-) zeolite catalysts in the presence of NO₂, but also that they do participate effectively in the NH₃-SCR catalytic chemistry, being indeed responsible for the very high DeNO_x activity associated with the Fast SCR reaction. In the next paragraph we make use of transient reaction analysis to elucidate in more detail the reactivity of surface nitrates with NO and NH₃, i.e., the SCR reactants: in so doing, we will also explore the individual steps of the Fast SCR mechanism.

9.5 Mechanistic Studies by Transient Response Methods

We summarize in this Section a kinetic investigation of the NO₂-related SCR reactions performed by running transient response experiments over a Cu-zeolite catalyst [2]. Its goal was to challenge our mechanistic understanding of the SCR catalytic chemistry on a quantitative basis, describing the kinetics of the important NO/NO₂-NH₃ SCR reactions by a set of pseudoelementary steps, rather than adopting empirical global rate equations. The transient kinetic runs consisted of isothermal concentration step changes, temperature programmed desorption (TPD), and temperature programmed surface reaction (TPSR) experiments. All the runs were performed in the absence of oxygen in order to prevent any contributions from the Standard SCR and NH₃ oxidation reactions, since the study was intentionally focused on the mechanistic role of NO₂. On the opposite, water was always included in the feed stream, in line with real engine exhausts composition. The experimental results were used to estimate intrinsic rate parameters of all the reaction steps in a detailed kinetic mechanism [2]. For the purpose of the present contribution, however, we will discuss the mechanistic information only on a qualitative basis.

9.5.1 Reactivity of Surface Nitrates with NO and with NH₃

Assuming that nitrates have been formed by NO₂ interaction with the catalyst, as shown in the previous paragraph, we proceed here to examine their reactivity with either one of the other two Fast SCR reactants, namely NO and NH₃.

The reactivity of surface nitrates with NO is demonstrated by a transient experiment where we first adsorbed NO₂ (1,000 ppm, concentration step change, in a stream of water (3 % v/v) and Helium) on the Cu-zeolite at 200 °C, then we added 1,000 ppm of NO to the water/Helium feed stream, and eventually performed a T-ramp where the catalyst temperature was linearly increased from 200 to 550 °C at 20 °C/min.

The results of the full experiment are displayed in Fig. 9.5. In the first stage, saturation of the catalyst by NO₂ is apparent, with the associated NO evolution indicating formation of surface nitrates according to (9.1)–(9.3).

Upon NO feed an immediate evolution of NO₂ was detected, then the latter species rapidly dropped to zero while NO approached its feed value. A similar behavior had been observed also over V-based [19] and Fe-zeolite SCR catalysts [20]. In analogy, also over the herein tested Cu-zeolite the formation of NO₂ was likely associated with the prompt reduction of nitrates to nitrites by NO and the subsequent reaction of nitrites and nitrates to give NO₂, according to the reverse of reactions (9.2) and (9.1), respectively. During the subsequent T-ramp (TPSR phase), only a limited additional oxidation of NO with corresponding production of NO₂ was detected, again likely related to the reduction of adsorbed nitrates. The presence of residual surface nitrates during the TPSR phase was also confirmed by additional dedicated TPSR runs with NH₃, not reported for brevity, which showed some N₂ evolution. An analogous test was also performed at 50 °C (not shown), which confirmed the same qualitative behavior, thus emphasizing the reducibility of surface nitrates by NO at temperatures as low as 50 °C, as also observed over Fe-zeolites [1].

Figure 9.6 shows that, on the contrary, when the same TPSR experiment was replicated with a step feed of NH₃ instead of NO, no reaction was detected: ammonia is thus unable to reduce the surface nitrates at 200 °C (as well as at lower temperatures, results not shown), which is apparently paradoxical, since NH₃ is in principle a much better reducing agent than NO. Indeed, subsequent T-ramp experiments evidenced the reduction of surface nitrates by NH₃, but only starting from T > 220 °C [21].

Thus, a preliminary conclusion here is that surface nitrates formed via NO₂ disproportionation, though thermally stable, are readily reduced at very low temperature by NO, if available, forming NO₂, while their direct reduction by NH₃ proceeds only at higher temperatures.

Next, we discuss how such a reduction step contributes to the overall SCR pathways leading from NO_x + NH₃ to N₂.

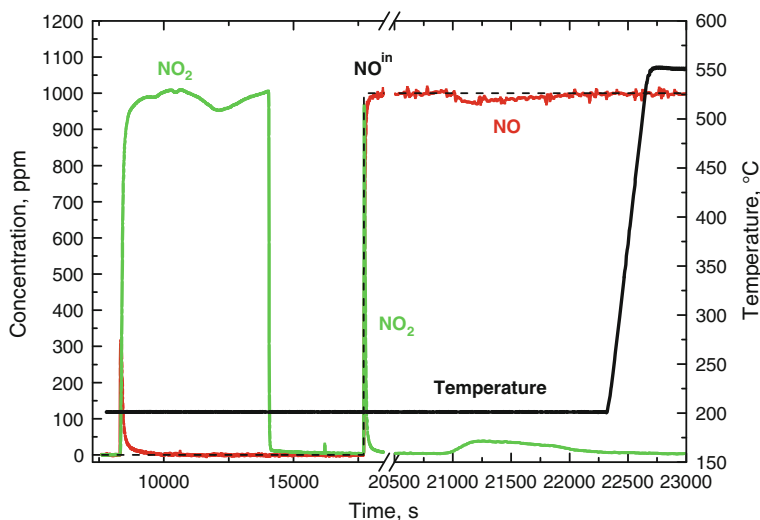
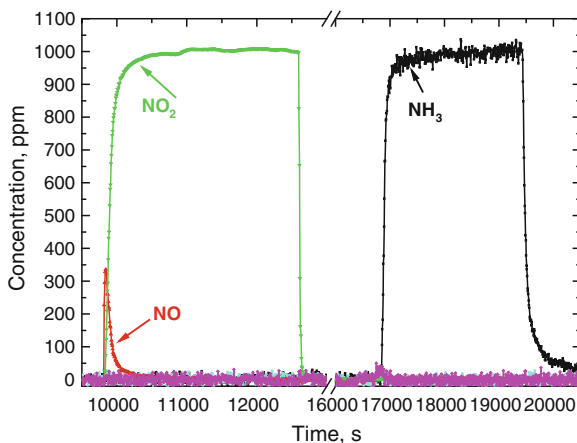


Fig. 9.5 NO TPSR with preadsorbed nitrates. Nitrates adsorption phase (not shown)— $T = 200\text{ }^\circ\text{C}$, Feed: $\text{NO}_2 = 0\text{--}1,000\text{ ppm}$, $\text{H}_2\text{O} = 3\text{ }\%$ v/v, $\text{O}_2 = 0\text{ }\%$. NO TPSR—Feed: $\text{NO} = 0\text{--}1,000\text{ ppm}$, $\text{H}_2\text{O} = 3\text{ }\%$ v/v, $\text{O}_2 = 0\text{ }\%$. Isothermal phase temperature = $200\text{ }^\circ\text{C}$, T-ramp = $20\text{ }^\circ\text{C}/\text{min}$. Adapted from [2]

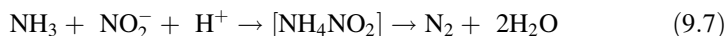
Fig. 9.6 NH_3 TPSR with preadsorbed nitrates. Nitrates adsorption phase— $T = 200\text{ }^\circ\text{C}$, Feed: $\text{NO}_2 = 0\text{--}1,000\text{ ppm}$, $\text{H}_2\text{O} = 3\text{ }\%$ v/v, $\text{O}_2 = 0\text{ }\%$. NH_3 TPSR—Feed: $\text{NH}_3 = 0\text{--}1,000\text{ ppm}$, $\text{H}_2\text{O} = 3\text{ }\%$ v/v, $\text{O}_2 = 0\text{ }\%$. Isothermal phase temperature = $200\text{ }^\circ\text{C}$. Adapted from [2]



9.5.2 The Role of Nitrites

Mechanistic studies over Fe-zeolite catalysts [1, 20, 21] suggest that at temperatures as low as $150\text{--}200\text{ }^\circ\text{C}$ and in the presence of NH_3 , the nitrites intermediate (NO_2^-) produced by NO_2 disproportionation, reaction (9.1), preferentially reacts

with ammonia, if present, forming unstable ammonium nitrite which readily decomposes to N_2 and H_2O according to (9.7) [22, 23]:



Decreasing the catalyst temperature results instead in favoring the oxidation of nitrites by NO_2 , i.e., reaction (9.2), with consequent NO formation and corresponding decrease of the N_2 evolution. The same qualitative trend was observed over a Cu-zeolite system, as shown by a set of dedicated experimental runs discussed in the following. The tests consisted first in the isothermal adsorption of NH_3 , obtained feeding 1,000 ppm of NH_3 (concentration step change), 3 % v/v H_2O , and balance He at a constant temperature (200 °C). Then, after removing NH_3 from the feed and flushing the catalyst with H_2O and Helium, still at the same temperature, the catalyst was exposed to a 1,000 ppm NO_2 step feed. Finally the temperature was linearly increased at a constant rate of 20 °C/min up to 550 °C in order to clean the catalyst surface. The same test was repeated decreasing the temperature of the isothermal phase to 150 °C and to 120 °C. Figure 9.7 compares the results collected during the NO_2 feed transient at 200 °C (Fig. 9.7a) and 120 °C (Fig. 9.7b).

In both tests, the NO_2 outlet trace exhibited first a dead time, then it slowly grew and eventually approached the feed concentration level. Also, immediate evolution of N_2 and NO was recorded at both temperatures upon NO_2 feed, then the signals of the same species slowly decreased with time, eventually approaching zero. Figures 9.7a, b clearly point out however that the increase of catalyst temperature from 120 to 200 °C over the Cu-zeolite resulted in an incremented NO formation and a corresponding decreased N_2 evolution: a higher temperature thus favors the reduction of nitrites by ammonia, reaction (9.7), against the oxidation of nitrites to nitrates, reaction (9.2), in line with what reported for Fe-zeolites.

These data thus prove that the reactivity of surface nitrites with ammonia. Reaction (9.7) provides the crucial (but facile) selective pathway to dinitrogen in the NO/NO_2-NH_3 SCR catalytic chemistry.

9.5.3 Overall Mechanistic Scheme

Based on the data presented and discussed so far, the reactivity of $NO/NO_2 + NH_3$ over Fe- and Cu-promoted zeolites at low temperatures appears consistent with what previously reported over vanadium-based catalysts [7, 17, 19, 24] as well as with the mechanistic proposals for the Fast SCR chemistry over BaNa-Y [22, 23].

In such a chemistry, the reactivity demonstrated in the previous paragraphs attributes the following roles to the three main SCR reactants: (1) NO_2 forms surface nitrates and nitrites via a disproportionation route; (2) NO reduces the nitrates to nitrites; (3) NH_3 decomposes/reduces the nitrites to N_2 . The related basic reaction steps, originally identified by transient reaction analysis and recently confirmed also by in situ FT-IR [10] over Fe-ZSM-5, are summarized in Table 9.1.

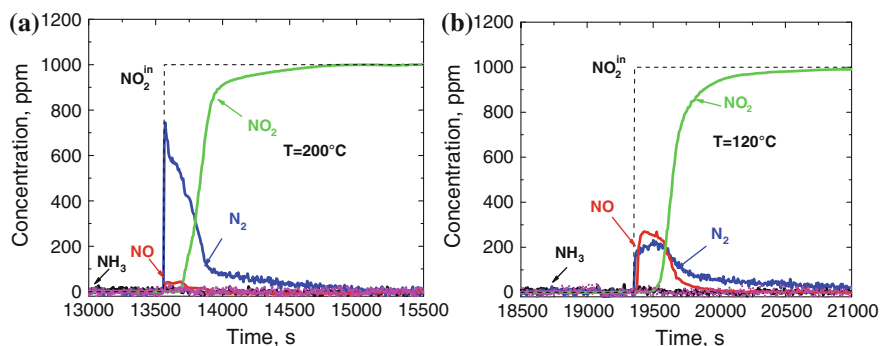


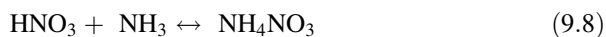
Fig. 9.7 Reactivity of NO₂ with preadsorbed NH₃. NH₃ adsorption phase (not shown)—Feed: NH₃ = 0–1,000 ppm, H₂O = 3 % v/v, O₂ = 0 %. NO₂ feed phase—Feed: NO₂ = 0–1,000 ppm, H₂O = 3 % v/v, O₂ = 0 %. **a** T = 200 °C. **b** T = 120 °C. Adapted from [2]

This chemistry explains the optimal 1:1 molar ratio of NO and NO₂ in the Fast SCR reaction. It also explains the full range of selectivities observed upon varying the NO₂/NO_x feed ratio [25–28]. In the presence of NO₂ excess (NO₂/NO_x > 1/2), in fact, incomplete reduction of nitrates by NO, the critical step R7 in Table 9.1, is responsible for the undesired formation of NH₄NO₃ at very low temperatures (step R6 in Table 9.1), and of N₂O at intermediate temperatures (step R8 in Table 9.1).

9.5.4 Ammonia Blocking of Nitrates Reduction

We have shown in Sect. 9.5.2 that the reduction of surface nitrates by NO, the key step in the Fast SCR mechanism over Me-exchanged zeolites and V-based catalysts, is active already at 50 °C. A dedicated study over an Fe-BEA catalyst [20] pointed out, however, that in the presence of ammonia the reaction between NO and nitrates is stopped and proceeds only on raising the temperature up to 140–160 °C, which thus represents an intrinsic lower bound to the Fast SCR activity. Similar results were reported for a BaNa-Y zeolite [5].

The NH₃ blocking effect is possibly associated with a strong interaction between ammonia and nitrate species when both are present on the catalyst surface. More specifically, at low temperature NH₃ could react with nitrates to form ammonium nitrate precursors (or strongly interacting ammonia-nitrate adspecies), e.g.,



thus blocking the critical reactivity of nitrates with NO. Only upon increasing the temperature or reducing the NH₃ concentration, nitrates are released due to dissociation of the ammonia-nitrate complex, as the (9.8) equilibrium is shifted to the left [5, 20].

Table 9.1 The Fast SCR chemistry

Basic reaction steps in NO/NO₂-NH₃ SCR chemistry over V-based and metal-promoted zeolite catalysts

<i>Involving NO₂ only</i>	
$2\text{NO}_2 \rightleftharpoons \text{N}_2\text{O}_4$	R1 NO ₂ dimerization
$\text{N}_2\text{O}_4 + \text{O}^{2-} \rightleftharpoons \text{NO}_2^- + \text{NO}_3^-$	R2 disproportionation
$\text{NO}_2 + \text{NO}_2^- \rightleftharpoons \text{NO} + \text{NO}_3^-$	R3 nitrites oxidation by NO ₂
<i>In the presence of NH₃</i>	
$2\text{NH}_3 + \text{H}_2\text{O} \rightleftharpoons 2\text{NH}_4^+ + \text{O}^{2-}$	R4 NH ₃ adsorption
$\text{NH}_4^+ + \text{NO}_2^- \rightleftharpoons [\text{NH}_4\text{NO}_2] \rightarrow \text{N}_2 + 2\text{H}_2\text{O}$	R5 nitrites reduction by NH ₃ , see (9.7)
$\text{NH}_4^+ + \text{NO}_3^- \rightleftharpoons \text{NH}_4\text{NO}_3$	R6 formation/dissociation of AN
$\text{NH}_4\text{NO}_3 \rightarrow \text{N}_2\text{O} + 2\text{H}_2\text{O}$	R8 formation of N ₂ O
<i>In the presence of NO</i>	
$\text{NO} + \text{NO}_3^- \rightleftharpoons \text{NO}_2 + \text{NO}_2^-$	R7 reduction of nitrates by NO = R3 reverse
<i>Fast SCR</i>	
$2\text{NH}_3 + \text{NO} + \text{NO}_2 \rightarrow 2\text{N}_2 + 3\text{H}_2\text{O}$	(6) = R4 + R1 + R2 + R7 + 2 * R5

Notably, the inhibiting effect of NH₃ on the Fast SCR activity at low temperature is not due to the ammonia competitive chemisorption on the catalytic sites, but occurs because ammonia captures a key intermediate in an unreactive form. In this respect, one way to partially prevent this undesired effect is to modify the equilibrium of ammonium nitrate dissociation, e.g., by increasing the temperature or by decreasing the gas-phase ammonia concentration. Since the blocking effect is related to the acid properties of the formed nitrates, another possibility to moderate its negative impact on the Fast SCR reactivity at low T would be to modify the catalyst acid/base properties in order to favor the interaction of ammonia with the catalyst sites rather than with the nitrates [5].

9.5.5 Considerations on the Red-ox Nature of the NH₃-SCR Mechanisms

It is worth noticing that the steps discussed above for the Fast SCR chemistry, reaction (9.6) does not involve changes in the formal oxidation state of the catalytic sites. In fact, formation of nitrates and nitrites occurs via disproportionation of NO₂ (steps R1 + R2 in Table 9.1), reduction of nitrates to nitrites is compensated by the simultaneous oxidation of NO to NO₂ (step R3), and decomposition of nitrites to N₂ by NH₃ (step R5) is also red-ox neutral. Accordingly, we can expect that in the presence of NO₂, a strong oxidizer, the SCR catalyst sites remain at their highest oxidations states. This is a substantial difference from the case of the Standard SCR reaction (9.5), wherein reduction of NO by NH₃ to N₂ does involve catalyst reduction, and therefore closure of the catalytic cycle

requires catalyst reoxidation by O₂ (likely a rate limiting step at low temperature). Recent published work based on in situ FTIR studies over Fe-ZSM-5 [10] and on X-Ray Absorption Spectroscopy investigations of Cu-CHA [29] confirms that only fully oxidized metal sites (Fe(III) and Cu(II), respectively) are present at the catalyst surface under Fast SCR conditions, so with NO₂, whereas a mixed situation, including both oxidized and reduced sites, prevails under Standard SCR conditions, i.e., in the absence of NO₂.

It is worth emphasizing, however, that these results do not rule out a Mars-Van Krevelen mechanism for the Fast SCR chemistry, as they simply show that the balance between oxidized and reduced catalytic sites is shifted toward the former ones in the presence of NO₂. Indeed, it has been shown that over a V-based catalyst the global reaction (9.6), and specifically its key step R7 in Table 9.1, is actually associated with a red-ox cycle involving the very effective reoxidation of reduced sites by surface nitrates [7]. In fact, step R7 did not proceed over a V-free WO₃/TiO₂ sample, due to the lack of the red-ox catalytic sites associated with the V component [7]. In the framework of a general red-ox interpretation of the SCR mechanisms, this explains the higher rate of the Fast SCR reaction as compared to the Standard SCR chemistry, wherein the less active gaseous oxygen is responsible for the slower, rate limiting catalyst reoxidation step [30]. Notably, the result of the NO/NO₂-NH₃ transient experiments in the previous Sections, where O₂ was not included in the feed mixture, point out that gaseous oxygen is not needed for NO_x conversion, being replaced by nitrates as the oxidizing species in the red-ox cycle.

Thus, not only nitrates adspecies, formed upon inclusion of NO₂ in the SCR reacting system, participate in the NO/NO₂-NH₃ catalytic chemistry: their role as strong oxidizers is indeed critical for the very important Fast SCR activity.

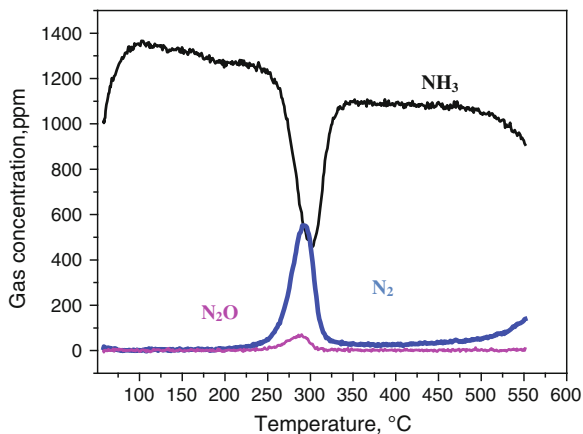
9.5.6 Higher Temperatures: The NO₂-SCR Reaction

Contrary to NO (Fig. 9.5), ammonia was unable to reduce directly nitrates up to 200 °C over V-based and metal-promoted zeolites catalysts (Fig. 9.6): but what happens at higher temperatures?

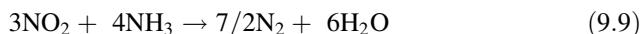
Figure 9.8 shows a transient experiment over Cu-zeolite in which the catalyst was first saturated with nitrates, feeding NO₂ at 50 °C. Then the NO₂ feed was shut off, the ammonia feed was started, and the temperature was linearly increased up to 550 °C. Clearly, ammonia did not react with surface nitrates at low temperature, but starting from about 230 °C ammonia consumption was observed, with formation of nitrogen mainly (the minor formation of N₂O is discussed in the next paragraph). This reaction stopped when all the surface nitrates were depleted. So ammonia is able to reduce nitrates as well, but only at higher temperature if compared to NO.

The run in Fig. 9.8, showing the reactivity of nitrates with ammonia, has been compared with a Temperature Programmed Reaction run over the same catalyst, where the feed included gaseous ammonia and NO₂, and during which we also observed consumption of ammonia, and production of N₂ and of N₂O. Most

Fig. 9.8 NH₃ TPSR with preadsorbed nitrates over Cu-zeolite. Nitrates adsorption phase—T = 50 °C, Feed: NO₂ = 0–1,000 ppm, H₂O = 3 % v/v, O₂ = 0 %, balance He. NH₃ TPSR—Feed: NH₃ = 0–1,000 ppm, H₂O = 3 % v/v, O₂ = 0 %, balance He. Isothermal phase temperature = 50 °C, T-ramp = 20 °C/min. [2]



interestingly, the N₂ temporal evolution observed in this case matched closely the one in Fig. 9.8. This strongly suggests that the reactivity of surface nitrates with ammonia is the same as that of NO₂ with ammonia, that is, the NO₂ SCR reaction:



whose mechanism is therefore likely associated with the direct oxidation of ammonia by surface nitrates. Again, similar data and conclusions apply also to other SCR catalysts [2, 21].

9.5.7 Selectivity Issues: The Formation of NH₄NO₃, N₂O

The reactivity of nitrates has to do not only with the selective (to N₂) and desired Fast and NO₂ SCR reactions, but also with the unselective reactions responsible for the formation of undesired by-products.

At low temperatures, below 200 °C, ammonia is not able to reduce nitrates, but it can however react with them to form ammonium nitrate [18, 24],



In our early study over a V-based catalyst [24], reaction (9.10) was identified by the stoichiometry of NO₂ + NH₃ conversion, and of N₂ formation. Ammonium nitrate, formed and deposited onto the catalyst, could not of course be directly detected, but its formation was confirmed both by the lack in the N-balance, by dedicated IR analyses performed on the catalyst downloaded from the reactor after the experiment, and by subsequent TPD runs which showed formation of N₂O (see Fig. 9.9), in line with the well-known thermal decomposition of ammonium nitrate,

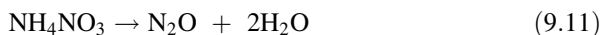
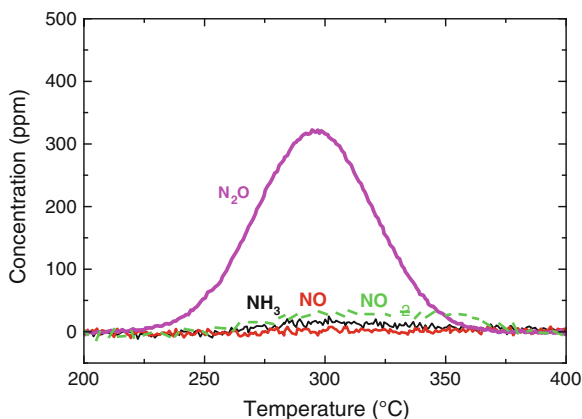


Fig. 9.9 TPD of preadsorbed NH₄NO₃ over WO₃/TiO₂. Carrier gas = He. T-ramp = 20 °C/min. Reprinted from [7]



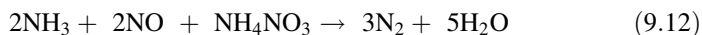
Again, similar findings apply also to the new generation of metal-promoted zeolites [1, 2].

Hence, in the presence of NO₂ not only the activity of SCR catalysts, but also their selectivity appears to be governed by the reactivity of nitrates. When NO is available in addition to NH₃, and the temperature exceeds a threshold related to the dissociation of ammonium nitrate, the desired reduction of the surface nitrates by NO can proceed effectively, resulting in the most efficient selective DeNO_x pathway, i.e., the Fast SCR reaction. On the other hand, if an excess of NO₂ prevails in comparison to NO, the unselective pathways (9.10) and (9.11) will prevail at lower and higher temperatures, respectively.

9.6 Feeding Nitrates: The Enhanced SCR Reaction

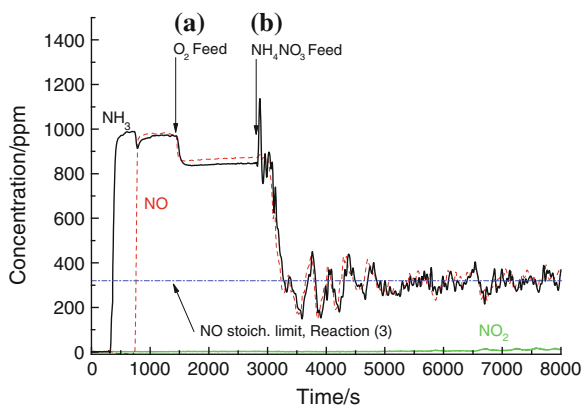
9.6.1 The Boosting Action of Ammonium Nitrate

The role of nitrates as key intermediates in the Fast SCR mechanism has been fully confirmed in recent years by the discovery of the so-called “Enhanced SCR” reaction [3, 31],



Reaction (9.12) involves the selective catalytic reduction of NO by its reaction with ammonia and with nitrate species, supplied, e.g., in the form of aqueous solution of ammonium nitrate sprayed into the gaseous feed stream to the SCR catalyst. Reaction (9.12) results in very high DeNO_x efficiencies at low temperatures, similar to those of Fast SCR, even though no NO₂ is fed to the SCR catalyst. Accordingly, it can in principle replace reaction (9.6) in boosting the DeNO_x

Fig. 9.10 Transient experiment over the Fe-ZSM-5 catalyst at $T = 205\text{ }^{\circ}\text{C}$, $\text{GHSV} = 33,000\text{ h}^{-1}$. Temporal evolution of NO, NH_3 , and NO_2 outlet concentrations upon addition of a 2 vol % O_2 to 1,000 ppm NO, 1,000 ppm NH_3 in N_2 (at $t = 1450\text{ s}$); **b** 340 ppm $\text{NH}_4\text{NO}_3 + 1\text{ vol } \% \text{H}_2\text{O}$ to 1,000 ppm NO, 1,000 ppm NH_3 , 2 % O_2 in N_2 (at $t = 2800\text{ s}$). Adapted from [31]



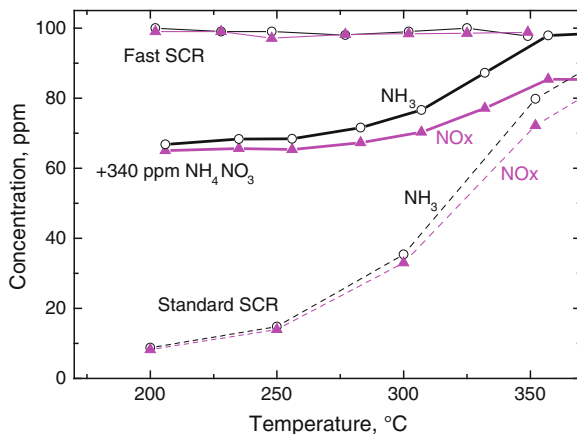
activity without, however, any need of preoxidizing NO to NO_2 upstream of the SCR converter.

The enhancement of the SCR activity is best illustrated by Fig. 9.10, which shows the temporal evolution of the NO, NH_3 and NO_2 outlet concentrations during a transient run at $205\text{ }^{\circ}\text{C}$ over an Fe-ZSM-5 washcoated monolith catalyst. Initially, only equimolar amounts of NH_3 and NO (1,000 ppm each) were fed to the catalyst in a nitrogen stream, with negligible conversion. At $t = 1450\text{ s}$, O_2 (2 % v/v) was added to the reactor feed, resulting in the onset of only a limited conversion of NO and NH_3 (about 15 %) associated with the Standard SCR reaction (9.5). At $t = 2800\text{ s}$, a pump started to inject an aqueous solution of ammonium nitrate in the test reactor feed stream, resulting in feed concentrations of 340 ppm NH_4NO_3 and 1 % H_2O v/v. As a consequence, the outlet NO and NH_3 concentrations dropped rapidly, eventually approaching after a few oscillations the conversion (68 %) predicted by reaction (9.12) in case of complete depletion of the limiting reactant NH_4NO_3 . NO_2 evolution was negligible (<10 ppm) during the whole transient.

It is clearly apparent from Fig. 9.10 that addition of ammonium nitrate to NO- NH_3 - O_2 dramatically increased the low temperature NO reduction activity over Fe-ZSM-5. Furthermore, the added NH_4NO_3 itself was totally and selectively converted according to reaction (9.12). The substantial enhancement of the NO_x removal efficiency due to NH_4NO_3 addition as compared to the Standard SCR was confirmed also at higher temperatures, though it progressively decreased with growing temperature.

The “Enhanced SCR” chemistry was further examined in a similar transient experiment at $205\text{ }^{\circ}\text{C}$ ($\text{GHSV} = 36,000\text{ h}^{-1}$), wherein the Fe-ZSM-5 catalyst was first exposed to a feed containing 500 ppm NO, 750 ppm NH_3 , 0 % O_2 in N_2 , to which an aqueous solution of nitric acid, corresponding to feeding 250 ppm HNO_3 and 1 % H_2O , was added in a second stage. In this case a steady-state conversion of both NO and NH_3 close to 90 % was observed, consistent with the stoichiometry of

Fig. 9.11 Effect of the addition of 340 ppm of NH₄NO₃ to the feed stream on the steady-state NO_x and ammonia conversions over the Fe-ZSM-5 catalyst as a function of temperature in comparison to Standard and Fast SCR. GHSV = 33,000 h⁻¹. Feed = 1,000 ppm NO, 1,000 ppm NH₃, 1 % H₂O, 2 % O₂ in N₂. Standard SCR runs: NO₂/NO_x = 0; Fast SCR runs: NO₂/NO_x = 1/2. Adapted from [3]



which is of course equivalent to reaction (9.12) upon considering dissociation of NH₄NO₃ into ammonia and nitric acid. Thus, the observed activity enhancement is likely due to the participation of nitrate species in the reaction. The result of this particular experiment points out as well that oxygen is unnecessary for NO conversion, again in agreement with (9.12) or (9.13).

Figure 9.11 compares steady-state NO_x and ammonia conversions in Standard (feed: 1,000 ppm NO, 1,000 ppm NH₃, 2 % O₂, 1 % H₂O in N₂) and Fast SCR (feed: 500 ppm NO, 500 ppm NO₂, 1,000 ppm NH₃, 2 % O₂, 1 % H₂O in N₂) runs over the Fe-zeolite catalyst with those measured when feeding 1,000 ppm NO, 1,000 ppm NH₃, 2 % O₂ in N₂ along with 340 ppm of NH₄NO₃ + 1 % H₂O.

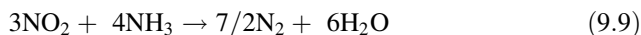
When only NO and ammonia were fed to the system with oxygen and water, the activity was poor, conversion being still far from complete even at 350 °C. The outlet concentration levels of NO and ammonia were in line with the occurrence of the Standard SCR reaction (9.1); however, at temperatures above 300 °C a growing negative deviation from the expected 1/1 NO/NH₃ molar consumption ratio was observed, possibly related to the onset of the ammonia oxidation, which is known to proceed on Fe-zeolites in this temperature range [1, 20, 21, 27]. When an equimolar mixture of NO and NO₂ (500 ppm each) was fed to the Fe-zeolite catalyst along with ammonia, though, 100 % conversions were observed already at 200 °C, in line with the strong sensitivity of Fe-zeolite catalysts to the NO₂ feed content and with the corresponding high activity of the Fast SCR reaction (9.6) [1, 27, 32, 33].

In the case of the runs with NH₄NO₃ feed, the steady-state NO and ammonia conversions were as high as 68 % (i.e., limited by the feed concentration of ammonium nitrate) already at 200 °C, and they remained more or less stable up to 250 °C, when they began to grow slowly with temperature. The outlet

concentrations measured in the range 200–250 °C are consistent with the stoichiometry of reaction (9.12): actually they correspond to the stoichiometric limit imposed by the feed concentration of ammonium nitrate and further originate from the poor activity of the Standard SCR reaction over this catalytic system.

At temperatures in excess of 250 °C the situation was modified: both the NO and the ammonia conversion increased, eventually approaching 100 % at the highest temperatures. Notably, NO₂ was not detected in significant amounts at any investigated temperature.

The incremented activity is due to the increasing contributions of the Standard SCR reaction and of the ammonia oxidation with growing temperature. At these temperatures also the “NO₂–SCR” reaction should be taken into account,



whose mechanism is likely associated with the oxidation of ammonia by surface nitrates [21], as discussed in Sect. 9.5.6 above: ammonia oxidation, either by oxygen or by nitrates, is responsible eventually for the reduced NO_x/NH₃ conversion ratio.

Thus, Figs. 9.10 and 9.11 confirm that over Fe–ZSM–5 addition of ammonium nitrate to the feed stream resulted in promoting the DeNO_x activity with respect to the Standard SCR reaction. Due to the substoichiometric feed contents of NH₄NO₃ in these runs, the NO_x conversion of the Fast SCR reaction was not reached. N₂O formation was found to be very limited, and comparable to what observed under Fast SCR conditions. Similar results were obtained in the case of V₂O₅–WO₃/TiO₂ SCR catalysts [3].

In a subsequent study, the effects of different operating variables, namely space velocity (between 18 and 75 kh⁻¹), temperature (between 180 and 250 °C), and ammonium nitrate feed content (between 20 and 100 % of the stoichiometric feed concentration), were systematically investigated over a commercial V-based Haldor Topsøe catalyst in order to identify the best process conditions [34]. Data from this study confirmed the occurrence of the very active Enhanced SCR reaction over the V-based catalyst, and pointed out that the added NH₄NO₃ itself was totally and selectively converted. As shown for example in Fig. 9.12, the addition of AN to the feed stream at 200 °C leads to a significant increase in the NO_x conversion compared to the Standard SCR reaction at all the investigated space velocities. The upper Fast SCR bound was approached, but the substoichiometric AN feed contents (100 and 200 ppm) limited the NO conversions associated with the E-SCR reaction. Notably, the NO_x conversions were identical within experimental error when feeding either ammonium nitrate (AN) or NO₂ in the same proportions (i.e., same AN to NO or NO₂ to NO_x feed ratio).

Experiments were also performed feeding the stoichiometric amount of ammonium nitrate (250 ppm). In these cases, however, the measured NO_x conversions did not reach those of Fast SCR: this was ascribed to an incomplete conversion of the stoichiometric AN feed content due to competition with the Standard SCR activity, causing buildup of AN on the catalyst and thus inhibiting

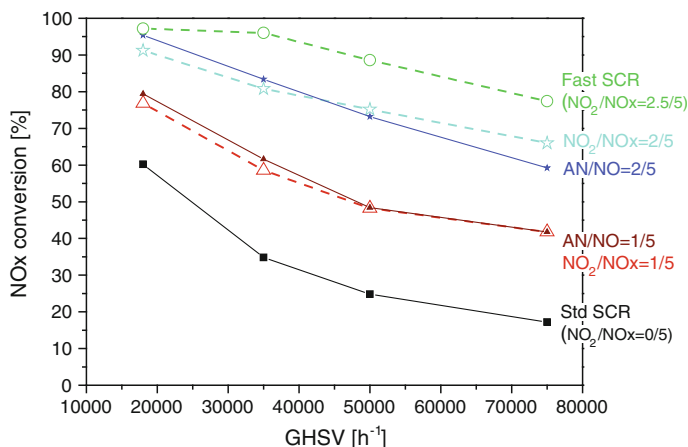


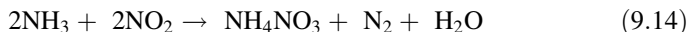
Fig. 9.12 NO_x steady-state conversions versus GHSV over V₂O₅-WO₃/TiO₂ in NO-NH₃-O₂ runs (Standard SCR), NO/NO₂-NH₃-O₂ runs (Fast SCR) and NO-NH₃-O₂-AN or NO-NH₃-O₂-NO₂ runs with different AN/NO or NO₂/NO_x feed contents (1/5, 2/5) at 200 °C. Feed: 500 ppm NO_x, 100–200 ppm AN, 500 ppm NH₃, 10 % O₂, 10 % H₂O + N₂. Reprinted from [34]

the DeNO_x activity. N₂O formation was found negligible at all the reaction conditions which granted a complete conversion of the AN injected in the feed stream.

In terms of DeNO_x efficiency, the best result of this study was collected at 180 °C with a space velocity of 18 kh⁻¹: at these conditions the NO_x conversion increased from 40 % in the absence of AN feed up to 86–93 % with the feed containing 200 or 250 ppm of AN. Furthermore, on decreasing the NH₃/NO feed ratio from 1 down to 0.85, the ammonia slip was reduced below 10 ppm while maintaining the NO_x conversion at its stoichiometric limit.

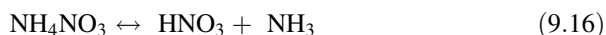
9.6.2 Analysis of the Enhanced SCR Chemistry

It is worth noticing that both the Fast SCR and the Enhanced SCR chemistries can be formally represented according to a simple sequential scheme, that we originally proposed for the Fast SCR mechanism only. We showed by transient kinetic experiments [17] that at temperatures as low as 150–170 °C the Fast SCR reaction proceeds via a two-step sequence in which ammonium nitrate is first formed from NO₂ and NH₃, reaction (9.14), and then reacts with NO, reaction (9.15):



The sum of (9.14) and (9.15) yields in fact the Fast SCR, reaction (9.6), wherein NO_2 is a reactant and NH_4NO_3 acts as an intermediate. The same sequence, however, also describes the Enhanced SCR chemistry, wherein however NH_4NO_3 is now a reactant and NO_2 becomes an intermediate: the stoichiometry of reaction (9.12) is obtained in this case adding (9.15), multiplied by two, to (9.11).

Clearly, the analogy between the Fast SCR and the Enhanced SCR chemistries has deeper roots than just a combination of stoichiometries. It actually originates from the key mechanistic role played by nitrates adspecies in both reactions. Such nitrates are either formed via NO_2 dimerization, disproportionation, and heterolytic chemisorption in the Fast SCR chemistry (see Sect. 9.5.3 and Table 9.1), or are formed directly by nitric acid adsorption when feeding aqueous solutions of NH_4NO_3 or nitric acid in the case of Enhanced SCR. It is well known that ammonium nitrate participates in the dissociation equilibrium (9.16) with nitric acid and ammonia,



Once formed, the nitrates adspecies can then participate in the same catalytic steps involved in the Fast SCR mechanism, namely their rate controlling reduction by NO to nitrites, followed by the rapid reaction of nitrites with NH_3 to give dinitrogen, along the same pathways already outlined in Sect. 9.5.3 above [3]. This is in fact consistent with the observation that feeding nitrate species in aqueous solution rather than gaseous NO_2 results in a DeNO_x activity similar to that of the Fast SCR reaction. In both cases the strong promotion of NO_x reduction at low temperature results from the extreme oxidizing properties of the nitrates, which can speed up the rate limiting step of catalyst reoxidation in the SCR red-ox cycle [4, 7, 35, 36].

From a conceptual standpoint, injecting nitrates in order to reduce NO_x may seem quite paradoxical. Nevertheless, data prove that this is indeed effective for promoting the DeNO_x activity at low temperature.

9.7 Summary and Conclusions

Our understanding of the NH_3 -SCR catalytic chemistry in the presence of NO_2 has greatly improved in the last few years. The key has been the identification of the crucial role of surface nitrates, which do not act as terminal reaction products, as originally suspected, but are directly responsible for the very high Fast SCR activity. It is also found that the reactivity of nitrates is quite general, being similar over the classical ternary V-W-Ti SCR catalysts as well as over the new generation of Fe- and Cu-promoted zeolite catalysts. These results open the way to chemically consistent, accurate, reliable, and comprehensive simulation models of SCR-based EGA systems, as required by the automotive industry in order to fulfil the upcoming emissions regulations.

Acknowledgments The financial support of Daimler AG (Germany) to our investigation of NH₃-SCR during many years is gratefully acknowledged. The authors are indebted to Dr. Bernd Krutzsch, Dr. Michel Weibel, and Dr. Volker Schmeisser (Daimler) for many useful suggestions and discussions.

The work on the Enhanced SCR concept has been financially supported by Haldor Topsoe A/S (DK) and more recently by the European Integrated Project “CO₂ Reduction for long distance transport” (CORE), EU Grant Agreement no. 284909.

References

1. Grossale A., Nova I., Tronconi E., Chatterjee, D., Weibel, M., *J.Catal.* (2008) 256:312–322
2. Colombo M, Nova, I, Tronconi E., *Catalysis Today* (2012) 197: 243– 255.
3. Forzatti, P, Nova, I, Tronconi, E, *Ind. Eng. Chem. Res.* (2010) 49: 0386–10391
4. Nova, I, Beretta, A, Groppi, G, Lietti, L, Tronconi, E, Forzatti P, “Monolithic catalysts for NO_x removal from stationary sources”, in “Structured catalysts and reactors”, 2nd Edition, Edt.s A. Cybulski and J.A. Moulijn, Taylor and Francis 2006, p. 171–214
5. Savara, A, Danon, A, Sachtler, WMH, Weitz, E. *Physical Chemistry Chemical Physics* (2009) 11:1180–1188.
6. Yeom, Y, Li, M, Savara, A, Sachtler, WMH, Weitz, E., *Catalysis Today* (2008) 136: 55–63.
7. Tronconi E, Nova I, Ciardelli C, Chatterjee D, Weibel M., *Journal of Catalysis* (2007) 245(1):1–10
8. Colombo, M, Nova I, Tronconi E, *Applied Catalysis B: Environmental* (2012) 111–112:433–444
9. Grossale, A Nova I, Tronconi E, Chatterjee, D, Weibel, M, *Topics in Catalysis*, (2009) 52:1837–1841
10. Ruggeri, MP, Grossale, A, Nova I, Tronconi E, Jirglova, H, Sobalik, Z, *Catalysis Today* (2012) 184: 107–114
11. Rivallan, M, Ricchiardi, G, Bordiga, S, Zecchina A, *J. Catal* (2009) 264: 104
12. Iwasaki, M, Shinjoh, H, *J. Catal*, (2010) 273: 29
13. Ahrens, M, Marie, O, Bazin, P, Daturi, M, *J. Catal* (2010) 271: 1
14. Colombo, M, Nova I, Tronconi E, *Applied Catalysis B: Environmental*, (2012) 111–112: 434–444
15. Szanyii, J, Kwak, JH, Zhu, H, Peden, CHF, *Physical Chemistry Chemical Physics* (2013) 15: 2368–2380
16. Forzatti, P, Lietti, L, Nova I, Tronconi E, *Catalysis Today* (2010) 151: 202–211.
17. Ciardelli C, Nova I, Tronconi E, Chatterjee D, Bandl-Konrad B, *Chemical Communications* (2004) 23:2718–271.
18. Koebel, M, Madia, G, Raimondi, F, Wokaun, A, *J. Catal.* (2002) 209 159
19. Nova I, Ciardelli C, Tronconi E, Chatterjee D, Bandl-Konrad B, *Catalysis Today* (2006) 114(1):3–12
20. Grossale A., Nova I., Tronconi E., *Journal of Catalysis*, (2009) 265: 141–147.
21. A. Grossale, I. Nova, E. Tronconi, *Catalysis Letters*, 130 (2009) 525–531.
22. Chen, HY, Sun, Q, Wen, B, Yeom, YH, Weitz, E, Sachtler, WMH, *Catalysis Today*, (2004) 96 1–10.
23. Li, M, Yeom, YH, Weitz, E, Sachtler, WMH, *Journal of Catalysis*, 235 (2005) 201–208.
24. Ciardelli C, Nova I, Tronconi E, Bandl-Konrad B, Chatterjee D, Weibel M, Krutzsch B, *Applied Catalysis B: Environmental* (2007) 70(1–4):80–90
25. Kröcher, O, Devadas, M, Elsener, M, Wokaun, A, Söger, N, Pfeifer, M, Demel, Y, Musmann, L, *App. Catal. B: Environ.* (2006) 66: 208

26. Devadas, M, Kröcher, O, Elsener, M, Wokaun, A, Mitrikas, G, Söger, N, Pfeifer, M, Demel, Y, Mussmann, L, *Catal. Today* (2007) 119: 137
27. Grossale A., Nova I., Tronconi E., *Catal. Today*, (2008) 136:18.
28. Colombo M, Nova I, Tronconi E *Catal Today* (2010) 151 (3–4):223–230
29. McEwen, JS, Anggara, T, Schneider, WF, Kispersky, VF, Miller, JT, Delgass, WT, Ribeiro, FH, *Catalysis Today* (2012) 184: 129–144.
30. Hoj, M, Beier, MJ, Grunwaldt, JD, Dahl, S, *Applied Catalysis B: Environmental* (2009) 93:166–176
31. Forzatti P, Nova I., Tronconi E., *Angewandte Chemie International Edition*, (2009) 48(44):8366–8368
32. Brandenberger, S.; Kroecher, O.; Tissler, A.; Althoff, R. The State of the Art in Selective Catalytic Reduction of NO_x by Ammonia Using Metal-Exchanged Zeolite Catalysts. *Catal. Rev.: Sci. Eng.* **2008**, 50 (4), 492–531.
33. Sjovall, H.; Blint, R. J.; Gopinath, A.; Olsson, L. A Kinetic Model for the Selective Catalytic Reduction of NO_x with NH₃ over an Fe-zeolite Catalyst. *Ind. Eng. Chem. Res.* **2010**, 49 (1), 39–52
34. Forzatti P, Nova I., Tronconi E., Kustov, A, Thøgersen, JR, *Catalysis Today* (2012) 184: 153–159
35. Busca G, Lietti L, Ramis G, Berti F, *Appl. Catal. B: Environmental* (1998) 18:1.
36. Nova I, Ciardelli C, Tronconi E, Chatterjee D, Weibel M, *AIChE Journal* (2009) 55(6) 1514–1529

Part IV
Reaction Kinetics

Chapter 10

Kinetics of NH₃-SCR Reactions Over V₂O₅-WO₃/TiO₂ Catalyst

Isabella Nova and Enrico Tronconi

10.1 Introduction

The SCR technology for the control of NO_x emissions from Diesel vehicles was first brought to the market in 2005 for heavy-duty vehicle applications by Daimler under the trade mark BLUETEC[®], based on the use of extruded honeycomb monolith catalysts consisting of V₂O₅-WO₃/TiO₂. The application of such a new technology was optimized by using an unsteady kinetic model of the SCR process specifically developed for mobile applications: indeed, simulation tools able to describe the performance of catalytic converters as a function of the several operating parameters have been proved to be very useful in the development and design of new technologies. Nevertheless, their capability in predicting accurately NO_x and ammonia emissions mainly relies on the close adherence of kinetic schemes to the real catalytic process.

In this chapter, the development of an unsteady kinetic model of the NH₃-SCR process for vanadium-based catalysts is presented. The model was based on the results from an extensive investigation of reactivity, chemistry, catalytic mechanism, and kinetics of the full NH₃-NO/NO₂ SCR reacting system over a commercial V₂O₅-WO₃/TiO₂ catalyst performed in our laboratories [1–10].

I. Nova (✉) · E. Tronconi
Dipartimento di Energia, Laboratorio di Catalisi e Processi Catalitici, Politecnico di Milano,
Piazza L. da Vinci 32, 20133 Milan, Italy
e-mail: isabella.nova@polimi.it

10.2 Methods

10.2.1 Experimental Rig and Procedures

The experimental rig used for all the kinetic runs over the powdered catalyst has three main sections dedicated to feed of the reacting mixture, reaction, and analysis of the outlet gas, respectively.

The feed mixture was prepared by combining the pure synthetic reacting gases from calibrated cylinders, namely ammonia, NO, NO₂, and oxygen. Contrary to the usual approach in the literature, helium instead of nitrogen was used as inert carrier gas, so that N₂, which is the main product of the SCR reaction, could be measured by the analytical system. The cylinders of NH₃, NO, and NO₂ also contained some Argon that was used as a tracer and internal standard for the analysis. The flow of each component was controlled by means of seven mass-flow meters (Brooks Inst. 5850S) connected to switchboards. Water vapor was fed by means of a saturator by controlling its temperature. All the lines downstream of the saturator were heated to 100 °C in order to prevent water condensation. 4-way valves were also present in the rig, to allow a rapid cross change between the inlets and the outlets, so that the reactant could be instantaneously fed or released from the reactor.

The microreactor consisted of a quartz tube (i.d. 6 mm) inserted in a furnace: water, oxygen, and balance helium came from steel pipelines and entered the reactor after being premixed, while ammonia and NO_x flew separately through two pulse valves and two capillaries so that they could be stepwise fed directly to the top of the reactor. The reaction temperature was measured and controlled (by acting on the furnace heating power) by a thermocouple immersed in the catalyst bed. The outlet gas was then sent to the analysis system. The entire line downstream of the reactor was heated to 200 °C in order to prevent formation of ammonium nitrate, which is a possible product of the reaction between NO₂ and NH₃ [2–10].

A Mass Spectrometer (MS) (Balzers QMS200) was used for species analysis. This instrument can provide the qualitative and quantitative temporal evolution of the composition of the outlet gas mixture. The following m/e ratios were monitored in order to follow the transient behavior of the most relevant species: 15 (NH₃), 18 (H₂O), 28 (N₂), 30 (NO), 32 (O₂), 40 (Ar), 44 (N₂O), and 46 (NO₂). The MS data were elaborated taking into account the species cross-sensitivities and the response factors periodically estimated by means of specific calibration runs in a blank reactor, thus obtaining the outlet concentrations of reactants and products. A UV analyzer (ABB Limas 11HW), which provided accurate continuous simultaneous measurements of ammonia, NO, and NO₂, was also coupled in parallel to the MS [10].

Different kinds of transient experiment aimed either at the elucidation of reaction mechanistic features or at the estimation of kinetic parameters were performed over the powdered catalyst. Operating conditions as similar as possible

to those of real aftertreatment systems were chosen for the experiments: 50–550 °C temperature range, 0–1,000 ppm NO_x and NH₃ feed concentration, presence of water and oxygen. Unfortunately, while real exhausts contain about 10 % v/v of water and of oxygen, it was not possible to feed systematically such concentrations in our microreactor runs because of limitations related to the use of the mass spectrometer: high concentrations of water vapor strongly influenced the other signals, thus making the analysis very imprecise; high oxygen contents caused the consumption of the tungsten filament responsible for the ionization of the molecules. The effect of water and oxygen on the SCR reactivity was in any case addressed and a good compromise was found using feed contents of 1 % H₂O and 2 % O₂ v/v: such conditions well represent the SCR reactivity under real conditions and at the same time allow the use of a MS analyzer. Analogously, hydrocarbons and CO₂ were not fed to the microreactor, but their effect on the SCR reactivity is known to be negligible.

Transient response method (TRM) runs [11] consisted of stepwise changes of concentration of one species in the feed mixture, realized by using the pulse valves previously described, which assured constant conditions of pressure and global flow. The temperature was normally kept constant during the whole experiment. In particular, the effect of NO/NO₂ ratio on the SCR activity was investigated. Space velocities between 90,000 and 210,000 h⁻¹ were used in these experiments.

Ammonia adsorption–desorption + Temperature Programmed Desorption (TPD) runs [11] were performed in order to study the adsorption–desorption of NH₃ onto the catalyst. Experiments were typically performed at a GHSV of 92,000 h⁻¹ by feeding 1,000 ppm of ammonia in the presence of 2 % O₂ and 1 % H₂O at constant adsorption temperature (between 200 and 400 °C); when the catalyst adsorption capacity was saturated, NH₃ and O₂ were shut off and a temperature ramp from 50 to 550 °C at 15 °C/min was started. Temperature Programmed Reaction (TPR) runs [11] were performed to study the gas-phase reactivity on increasing temperature: the reactants were fed at constant temperature, then a temperature ramp at 2, 10, or 20 °C/min was run. TPR experiments were typically carried out in the presence of oxygen (2 %) and water vapor (1 %) with GHSV between 90,000 and 230,000 h⁻¹; the reactant feed concentration varied between 250 and 1,000 ppm.

10.2.2 Mathematical Model of the Microreactor for Kinetic Tests

Once defined the reaction network that describes the different investigated reacting systems and understood the main features of the reaction mechanisms, consistent kinetic schemes and rate expressions were derived, as extensively described in the following. In order to estimate the rate parameters in such expressions, transient experimental data collected over the powdered SCR catalyst were analyzed

according to a heterogeneous one-dimensional plug-flow dynamic model of the test microreactor, assuming the catalytic bed to be isothermal and isobaric [12]. The reactor dynamic model adopted for the kinetic analysis of the experimental runs was based upon the following unsteady differential material balance equations for gaseous (i) and adsorbed (j) species:

adsorbed phase:

$$\Omega_j \frac{\partial \theta_j}{\partial t} = -R_j \quad (10.1)$$

gaseous phase:

$$\varepsilon \frac{\partial C_i}{\partial t} = -v \frac{\partial C_i}{\partial z} - (1 - \varepsilon)R_i \quad (10.2)$$

where C_i is the gas-phase concentration of species i , θ_j is the surface coverage of adsorbed species j , ε is the void fraction of catalyst bed, v is the gas linear velocity (m/s), and Ω is the maximum catalyst adsorption capacity (mol/m³cat). R is the intrinsic rate of formation of the species i or j , and was calculated according to the following general expression:

$$R_i = \sum_{k=1}^{NR} r_k \cdot v_{i,k} \quad (10.3)$$

where i is the index of the species considered, r_k is the intrinsic rate of reaction k , and $v_{i,k}$ is the stoichiometric coefficient of species i in reaction k .

The system of partial differential equations (PDE) formed by the unsteady mass balances of the relevant species was numerically integrated according to the method of lines, after developing a suitable FORTRAN code written. The discretization of the variables along the axial coordinate z was based on the finite differences method [13], using typically a grid with 31 equispaced points. In order to integrate the resulting ordinary differential equations system in time the LSODI library routine, based on Gear's method [14], was used. The kinetic parameters were estimated by global multiresponse nonlinear regressions based on the least squares method. For this purpose the BURENL routine developed by Prof. Guido Buzzi-Ferraris [15] was used.

10.3 NH₃/O₂ Reacting System

The experimental investigation started from the study of the simplest reacting system, i.e., including only ammonia and oxygen as reactants. Basically, two main processes are expected to occur in this case, namely the adsorption–desorption of

NH₃, and, at higher temperature, its oxidation by gaseous oxygen. The two processes were addressed sequentially, as discussed in the following.

The capability to adsorb ammonia is an important characteristic of SCR catalysts. Indeed all authors who had previously studied the SCR process for stationary applications agreed that in the SCR reactions ammonia reacts from a strongly adsorbed state [16–21]. Moreover, the affinity of such a reactant for the catalyst surface decreases the so-called ammonia slip that is the undesired release of unreacted ammonia from the reactor. Accordingly, a good understanding of the ammonia adsorption–desorption process is strictly required for a correct description of the SCR process.

The effect of water concentration on ammonia adsorption was first studied by performing different runs in the presence of 1 % and of 10 % of water. It was found that the ammonia storage capacity hardly changed (305 vs. 300 mol_{NH₃}/m_{cat}³ at 150 °C) if 1 or 10 % v/v of water was added to the feed. Analogous experiments were then performed in order to study the effect of oxygen feed concentration on the ammonia storage capacity, feeding 2 and 10 % O₂ v/v. It was found that the oxygen feed concentration had no effect on the ammonia adsorption process, too.

In order to obtain quantitative information about NH₃ adsorption-desorption as a function of temperature over the commercial V-based SCR catalyst used in our research, specific transient runs were performed. The experiments consisted in stepwise feeding 1,000 ppm of NH₃ while flowing oxygen (2 %), water (1 %), and balance helium at constant temperature, namely 50, 100, 150, and 200 °C. Depending on temperature, different amounts of ammonia were adsorbed onto the catalyst at this stage. When the signal of outlet ammonia approached the feed level, indicating saturation, NH₃ was shutoff and desorption of weakly adsorbed ammonia occurred. Then, after interrupting the oxygen feed in order to prevent ammonia oxidation, a temperature ramp at 15 °C/min from 50 to 550 °C was run so to provoke complete thermal desorption of ammonia [22–24].

Figure 10.1a shows the results of the run performed at the adsorption temperature of 50 °C: NH₃ inlet concentration (black dotted line), NH₃ outlet concentration (symbols), and catalyst temperature (blue solid line—right axis) are plotted as a function of time on stream. Upon NH₃ step addition (at $t = 0$ s) its outlet concentration exhibited a dead time, during which the fed NH₃ was completely adsorbed onto the catalyst surface, and then it increased with time, approaching the inlet value of 1,000 ppm after about 3,500 s. Upon NH₃ shutoff ($t = 4,000$ s) the outlet NH₃ concentration started decreasing with time as desorption of previously adsorbed NH₃ occurred. However, complete desorption of NH₃ was achieved only by performing an additional TPD run. Indeed, as soon as the catalyst was heated, the NH₃ signal increased again, reaching a peak value at about 250 °C, then it dropped back to zero for temperatures above 450 °C.

Figure 10.1b, c, and d illustrate the results of similar runs performed by adsorbing ammonia, respectively at 100 (b), 150 (c), and 200 °C (d). As temperature increased, a lower ammonia adsorption capacity of the system could be

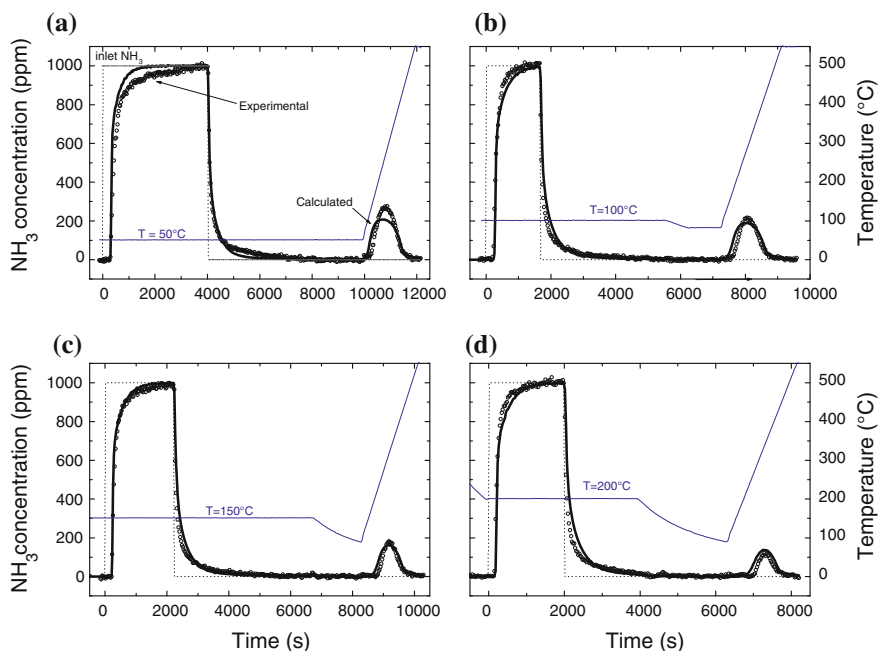


Fig. 10.1 Adsorption–desorption + TPD runs: GHSV = 92,000 h⁻¹; NH₃ = 1,000 ppm, H₂O = 1 %, O₂ = 2 %. **a** T = 50 °C; **b** T = 100 °C; **c** T = 150 °C; **d** T = 200 °C. Symbols: experimental; solid lines: model fit. Adapted from Ref. [1]

noticed, associated with shorter dead times and smaller TPD areas. This is in line with the thermodynamics of the exothermic NH₃ adsorption process [17, 18].

Much research has been devoted in the past few decades to the SCR process on V-based catalysts for stationary applications, thus resulting in a large amount of literature. In particular, the adsorption–desorption characteristics of ammonia on V-based catalysts have been investigated by means of TPD and FTIR techniques and by means of TRMs [18]. It is generally agreed that ammonia adsorbs as two different strongly held species: (i) molecularly adsorbed ammonia, through a Lewis-type interaction with coordinatively unsaturated cations and (ii) ammonia adsorbed as ammonium ions, onto Brønsted acidic -OH surface hydroxyl groups. Authors, however, have different opinions about which sites are responsible for the different adsorbed species. FTIR studies of Topsøe and co-workers [21, 25] for instance revealed that ammonia adsorbs on the titania surface mainly as coordinated NH₃, reflecting that predominating Lewis acid sites are present on pure titania, whereas the V–OH surface species are the Brønsted acid sites where adsorption of ammonium ions occurs. On the other hand, Ramis and coworkers proposed that both Lewis acidity and Brønsted acidity occur over vanadium sites [26]. The FTIR investigation over V₂O₅-WO₃/TiO₂ catalysts carried out by Lietti and coworkers [27] indicated that both tungstenyls and vanadyls centers act as

Lewis sites for molecularly adsorbed ammonia, and only a minor adsorption of protonated ammonia with low thermal stability was pointed out. On contrary, Amiridis et al. [28] suggested that the V₂O₅-WO₃ interaction generates Brønsted sites.

A considerable amount of the literature is also available about the research of a suitable rate expression for the NH₃ adsorption–desorption process [12, 22–24, 29, 30]. Some authors described this process according to a Langmuir isotherm [31]. Nevertheless, specific works on this topic suggest different approaches. For instance, Lietti et al. [12] proposed that NH₃ adsorption occurs via a nonactivated process ($E_a = 0$), in line with the spontaneity of adsorption of a basic molecule, like ammonia, onto the acidic catalyst surface. Moreover, in such a work, five different rate expressions were used for NH₃ desorption, including a simple Langmuir approach and more complicated expressions that take into account the catalyst surface heterogeneity, in agreement with the physicochemical characterization of the catalysts. These included Temkin-type, modified Temkin-type, and Freundlich coverage dependences of the desorption energies, along with an empirical coverage dependence that is representative of the existence of two adsorption sites on the catalyst surface having different acid strengths. It was found that Langmuir kinetics fail in describing accurately the experimental data, while a satisfactory data fit was achieved by using Temkin-type desorption kinetics. Modest improvements were obtained by using more complicated coverage dependences of the desorption energies (e.g., modified Temkin-type or the empirical “dual sites”).

Temkin-type rate expressions will be applied in the following to fit the NH₃ adsorption–desorption data presented above. The experimental data of Fig. 10.1 were analyzed according to the transient one-dimensional isothermal heterogeneous plug-flow model of the test microreactor and fitted by nonlinear regression to provide estimates of the relevant kinetic parameters, and thus extract the intrinsic kinetics of the ammonia adsorption–desorption. The model of the test microreactor was based on the following equations, that represent the adaptation of the general equations (10.1) and (10.2) to the considered reacting system.

NH₃ mass balance (adsorbed phase):

$$\Omega \frac{\partial \theta}{\partial t} = r_{\text{ads}} - r_{\text{des}} \quad (10.4)$$

NH₃ mass balance (gas phase):

$$\varepsilon \frac{\partial C_{\text{NH}_3}}{\partial t} = -v \frac{\partial C_{\text{NH}_3}}{\partial z} - (1 - \varepsilon)(r_{\text{ads}} - r_{\text{des}}) \quad (10.5)$$

Based on the literature indications above-mentioned, and supported by preliminary fits of the experimental data, a nonactivated NH₃ adsorption process and Temkin-type NH₃ adsorption/desorption kinetics have been assumed, i.e.,:

$$r_{\text{ads}} = k_{\text{ads}} C_{\text{NH}_3} \theta_{\text{free}} \quad (10.6)$$

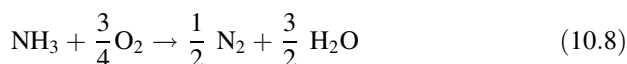
$$r_{\text{des}} = k_{\text{des}}^o \exp\left[-\frac{E_{\text{des}}^o}{RT}(1 - \alpha\theta_{\text{NH}_3})\right]\theta_{\text{NH}_3} \quad (10.7)$$

where $\theta_{\text{free}} = 1 - \theta_{\text{NH}_3}$.

Figure 10.1 illustrates the comparison between experimental data (symbols) and model fit (solid lines) after global nonlinear regression on the four runs: a good agreement is evident in all cases. Particularly, the model well reproduced the dead time of the outlet NH_3 concentration, which is representative of the NH_3 storage capacity. In addition, TPD runs were fairly well fitted in a large range of temperatures. The parameter estimates associated with the fit in Fig. 10.1 well compared with the corresponding estimates obtained in previous works performed over both model and commercial V-based SCR catalysts for stationary applications [12, 23, 24].

The reaction of ammonia with oxygen over V-based catalysts produces, depending on the operating temperature, nitrogen, NO, or N_2O .

In analogy with the method followed for the NH_3 adsorption-desorption process, first we studied the effect of water and oxygen on the ammonia oxidation reaction, then we proceeded to specific kinetic runs for the estimation of the rate parameters. Some authors found indeed an inhibiting effect of water on ammonia oxidation over V-based catalysts [22, 31]. In order to verify if such a behavior was characteristic of the catalyst herein investigated, the effect of water concentration on ammonia oxidation was studied by running TPR experiments in the presence of 1 or 10 % water, with 500 ppm ammonia, 2 % oxygen, and balance He, with a GHSV of $92,000 \text{ h}^{-1}$: the comparison of the results of the runs ruled out any significant effect of water concentration in the range 1–10 % v/v on the NH_3 oxidation reaction



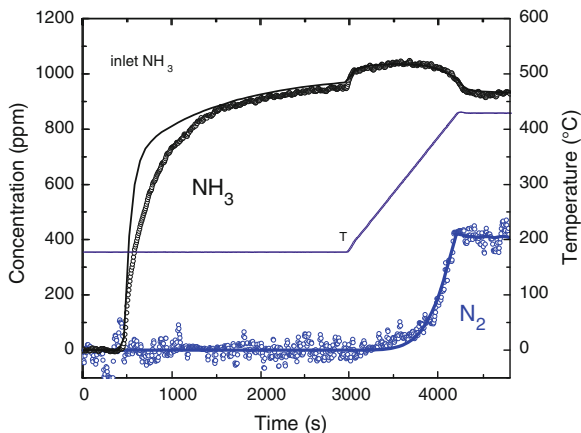
The influence of oxygen content was then studied by means of TPR experiments run with 2 or 10 % O_2 in the presence of 500 ppm ammonia, and balance He with a GHSV of $92,000 \text{ h}^{-1}$. In this case, a minor promoting effect of oxygen concentration was seen.

Specific runs were carried out in order to extract the intrinsic kinetics of ammonia oxidation and at the same time to validate the kinetics of the ammonia adsorption–desorption process, previously fitted.

In the experiment of Fig. 10.2, at time = 3,000 s a temperature ramp at $12 \text{ }^\circ\text{C}/\text{min}$ was started while flowing 1000 ppm ammonia, 2 % oxygen, and balance He. Adsorption of ammonia occurred as soon as NH_3 was admitted to the reactor at $t = 500 \text{ s}$, while its desorption was evident during the temperature ramp. Moreover, ammonia oxidation started to occur when the catalyst temperature exceeded $350 \text{ }^\circ\text{C}$, as apparent from the consumption of ammonia and the production of nitrogen, in line with reaction (10.8).

The experiment in Fig. 10.2 was analyzed according to the usual plug-flow model of the test microreactor, Eqs. (10.1) and (10.2). The ammonia mass balance equations were modified in order to include the oxidation reaction, which was

Fig. 10.2 NH₃ oxidation
 TPR: GHSV = 230,000 h⁻¹;
 NH₃ = 1,000 ppm,
 H₂O = 1 %, O₂ = 2 %. T
 ramp 175–425 °C at 12 °C/
 min. Symbols: experimental;
 solid lines: model fit



considered to proceed via adsorbed ammonia. Moreover, the gaseous nitrogen mass balance was introduced:

NH₃ mass balance (adsorbed phase):

$$\Omega \frac{\partial \theta}{\partial t} = r_{\text{ads}} - r_{\text{des}} - r_{\text{ox}} \quad (10.9)$$

NH₃ and N₂ mass balances (gas phase):

$$\varepsilon \frac{\partial C_{\text{NH}_3}}{\partial t} = -v \frac{\partial C_{\text{NH}_3}}{\partial z} - (1 - \varepsilon)(r_{\text{ads}} - r_{\text{des}}) \quad (10.10)$$

$$\varepsilon \frac{\partial C_{\text{N}_2}}{\partial t} = -v \frac{\partial C_{\text{N}_2}}{\partial z} + (1 - \varepsilon) \cdot \frac{1}{2} r_{\text{ox}} \quad (10.11)$$

For the rate of ammonia oxidation, an empiric expression has been assumed [22–24], i.e.,:

$$r_{\text{ox}} = k_{\text{ox}} \theta_{\text{NH}_3} (p_{\text{O}_2}/0.02)^\beta \quad (10.12)$$

that incorporates the experimentally observed effect of oxygen.

The kinetic parameters of ammonia oxidation were fitted by multiresponse nonlinear regression, while the parameter estimates for the ammonia adsorption–desorption kinetics were kept unchanged with respect to those obtained from the fit previously performed. Notably, in this case both the NH₃ and the N₂ outlet concentrations were regarded as regression responses.

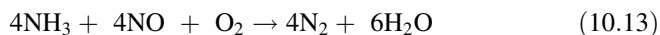
Figure 10.2 shows the result of the fit in terms of experimental (symbols) and calculated (solid lines) outlet concentrations of NH₃ and nitrogen as a function of time: the agreement is satisfactory.

It is worthy of note that the kinetic model was capable to capture both the light-off temperature of ammonia oxidation and the slope with which it proceeds upon increasing the temperature. Moreover, the ammonia adsorption–desorption

dynamics, which are very demanding especially during the T-ramp, were very well predicted, thus validating the fit performed for the ammonia adsorption/desorption process at different operating conditions of GHSV and heating rate.

10.4 NH₃-NO/O₂ Reacting System

After studying the adsorption, desorption and oxidation of ammonia, the research work was focused on the NH₃-NO/O₂ reacting system. With such a feed mixture, the main reaction occurring over V-based catalysts is the so-called “standard” SCR: in the presence of oxygen, NO reacts with ammonia according to



In order to develop a kinetic model that is able to describe the reactivity of the NH₃-NO/O₂ reacting system, transient experiments in a wide range of temperatures (50–550 °C) were performed. The effect of the operating conditions on the NO conversion and on the selectivity to N₂ was also investigated. NO + NH₃/O₂ TPR runs were first carried out with different oxygen feed contents (Fig. 10.3, symbols): 1,000 ppm of ammonia and 1,000 ppm of NO were fed @50 °C to the test microreactor in a stream containing 1 % water, 2 or 6 % oxygen, balance helium with GHSV of 92,000 h⁻¹, and then a temperature ramp was started at 2 °C/min.

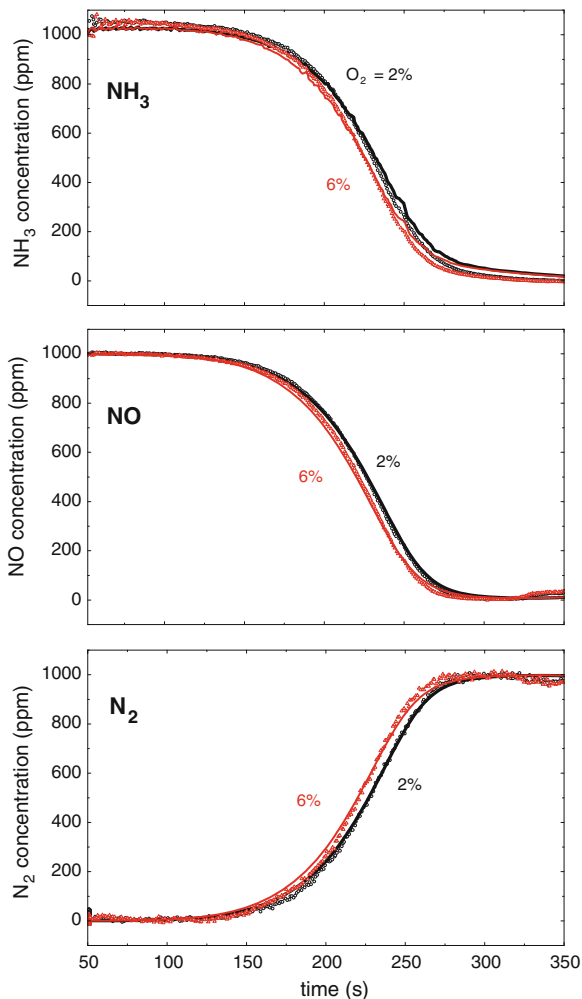
As the temperature reached 150 °C, consumption of NO and NH₃, and production of nitrogen occurred in line with the stoichiometry of reaction (10.13). When the catalyst temperature reached 350 °C, total conversion of NO, with 100 % selectivity to nitrogen, was observed. The ammonia signal was slower than NO in reaching full conversion because of the desorption dynamics present during the T-ramp and of the instrumental delay of the ammonia signal. No formation of either NO₂ or N₂O was observed, while a moderate promoting effect of oxygen on the SCR activity was clearly apparent over the whole investigated T-range.

Additional TPR experiments were performed to investigate the influence of space velocity (92,000–230,000 h⁻¹) and of the water feed content (1–10 %) on the SCR reactivity. It was found that NO and NH₃ conversions decreased on increasing the space velocity and that there was no significant influence of the water feed content on the SCR reaction (10.13).

Transient response method (TRM) experiments were then performed with the aim of investigating the dynamic response of the system to step changes of the reacting mixture composition. Figure 10.4 (a, b, and c symbols) show some TRM runs carried out at different T.

Looking at the run performed at 200 °C, it appeared that as, at $t = 0$ s, 1,000 ppm of ammonia were instantaneously added to the feed, the NO outlet concentration quickly decreased from the feed value to about 750 ppm. At the same time, the N₂ trace increased as a mirror image from 0 up to about 250 ppm,

Fig. 10.3 $\text{NO} + \text{NH}_3$ TPR runs: $\text{GHSV} = 92,000 \text{ h}^{-1}$; $\text{NH}_3 = \text{NO} = 1,000 \text{ ppm}$, $\text{H}_2\text{O} = 1 \%$, $\text{O}_2 = 2$ or 6% . T ramp: $2 \text{ }^\circ\text{C}/\text{min}$. Symbols: experimental; solid lines: model fit using the MR rate law, Eqs. (10.31) + (10.32). Adapted from Ref. [5]



while the NH_3 outlet concentration trace exhibited a dead time before growing up to 750 ppm. This behavior is due to the fact that NH_3 was involved both in an adsorption process upon the catalyst surface and in the SCR reaction. The steady-state values of NH_3 , NO , and N_2 were consistent with the stoichiometry of the SCR reaction (10.13), with a conversion of roughly 25%. At a time of about 2,600 s the NH_3 feed was shut down and the NH_3 outlet concentration trace dropped quickly.

During both the NH_3 start-up phase and the NH_3 shutoff period N_2 and NO exhibited peculiar dynamics. A major effect was observed when the NH_3 feed concentration was restored to 0 ppm: the NO outlet concentration first decreased, passed through a minimum and then began to increase due to the depletion of adsorbed ammonia. A symmetrical evolution was observed for N_2 , thus proving

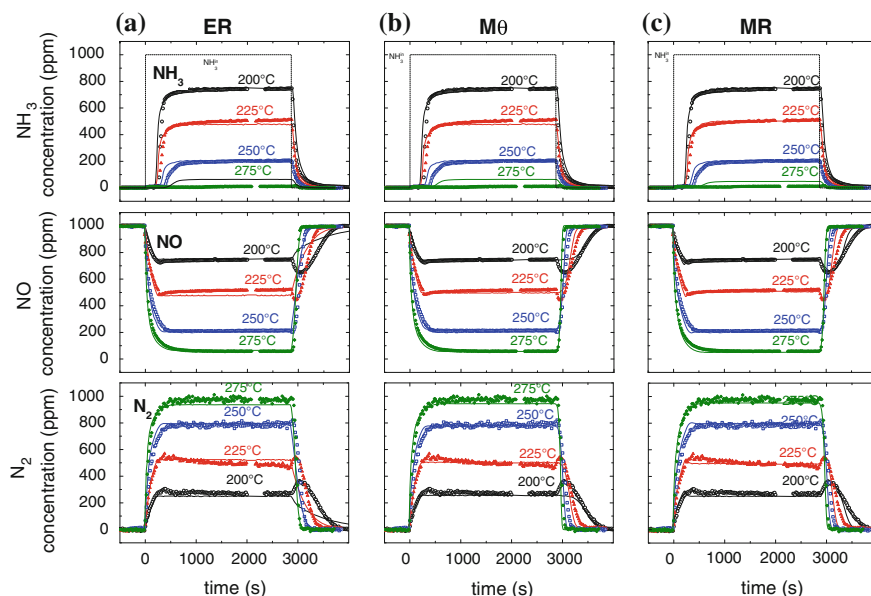


Fig. 10.4 Transient SCR experiments at different temperatures: $GHSV = 92,000 \text{ h}^{-1}$; $\text{NH}_3 = 0\text{-}1,000\text{-}0 \text{ ppm}$, $\text{NO} = 1,000 \text{ ppm}$, $\text{H}_2\text{O} = 1 \%$, $\text{O}_2 = 2 \%$. Symbols: experimental; solid lines: model fit using **a** the ER rate model Eq. (10.18), **b** the $M\theta$ rate law Eq. (10.19), **c** the MR rate law Eqs. (10.31) + (10.32). Adapted from Ref. [5]

that during the transient phase of ammonia shutdown, when only adsorbed NH_3 was reacting with NO continuously fed to the reactor, the deNO_x activity of the system was temporarily enhanced until complete consumption of the residual NH_3 on the catalyst surface. This confirmed that excess ammonia inhibits the SCR reaction (10.13), as already pointed out by several authors [24, 32–35] over vanadium-based catalysts, but also over Fe-zeolite systems [36–38].

A minor transient feature was also manifested when ammonia was admitted to the reactor ($t = 0 \text{ s}$): the NO outlet concentration immediately decreased, went through a weak minimum near 250 s, and finally slightly increased, reaching steady state in correspondence at the end of the ammonia feed phase. Again, the nitrogen evolution was symmetrical to that of NO. The same ammonia inhibition effect invoked to explain the enhancement in the deNO_x conversion at ammonia shutdown could explain this transient behavior, too. In fact both features suggested the existence of an optimal ammonia surface concentration, which was lower than the coverage established at steady state.

Experiments similar to the one just described were performed at higher temperatures (225–350 °C). On increasing the reaction temperature the steady-state concentrations of NH_3 and NO were lowered while nitrogen concentration increased, in agreement with the increase of the SCR activity with temperature. The stoichiometry of reaction (10.13) was always respected and the deNO_x

reaction was fully selective to nitrogen in the whole T-range investigated. For temperatures higher than 275 °C total conversion was achieved.

With regard to dynamics, faster transients were observed on increasing the reaction temperature, as a shorter time was needed for the signals to reach steady state. Moreover, the transient features of the NO and N₂ traces at the ammonia shutoff, associated with the optimal ammonia surface concentration previously mentioned, gradually vanished as the temperature increased. This is in line with the decrease of adsorbed NH₃ on increasing temperature previously observed.

Analogous TRM runs were carried out at 200, 225, 250, and 275 °C in the same conditions of the experiments just shown (1,000 ppm NH₃, 1,000 ppm NO, 1 % H₂O, GHSV = 92,000 h⁻¹), but with 6 % of oxygen in the feed. Figure 10.5 (symbols) illustrates the results of such runs.

With 6 % of oxygen feed the steady-state conversions resulted slightly higher than the conversions with 2 % oxygen at the corresponding temperature, in line with the results of the TPR experiments (Fig. 10.3).

The kinetic analysis of the whole set of transient data collected over the powdered SCR catalyst was addressed using the dynamic one-dimensional isothermal heterogeneous plug-flow model of the test microreactor described above.

Reactions R.1–R.4 of Table 10.1 were included in the kinetic model and the ammonia and nitrogen mass balance equations were modified in order to include account of the standard SCR reaction (10.13). Moreover, the mass balance of gaseous NO was introduced:

(a) adsorbed phase

NH₃*

$$\Omega \frac{\partial \theta_{\text{NH}_3}}{\partial t} = r_{\text{ads}} - r_{\text{des}} - r_{\text{ox}} - r_{\text{NO}} \quad (10.14)$$

(b) gas phase

NH₃

$$\varepsilon \frac{\partial C_{\text{NH}_3}}{\partial t} = -v \frac{\partial C_{\text{NH}_3}}{\partial z} - (1 - \varepsilon)(r_{\text{ads}} - r_{\text{des}}) \quad (10.15)$$

N₂

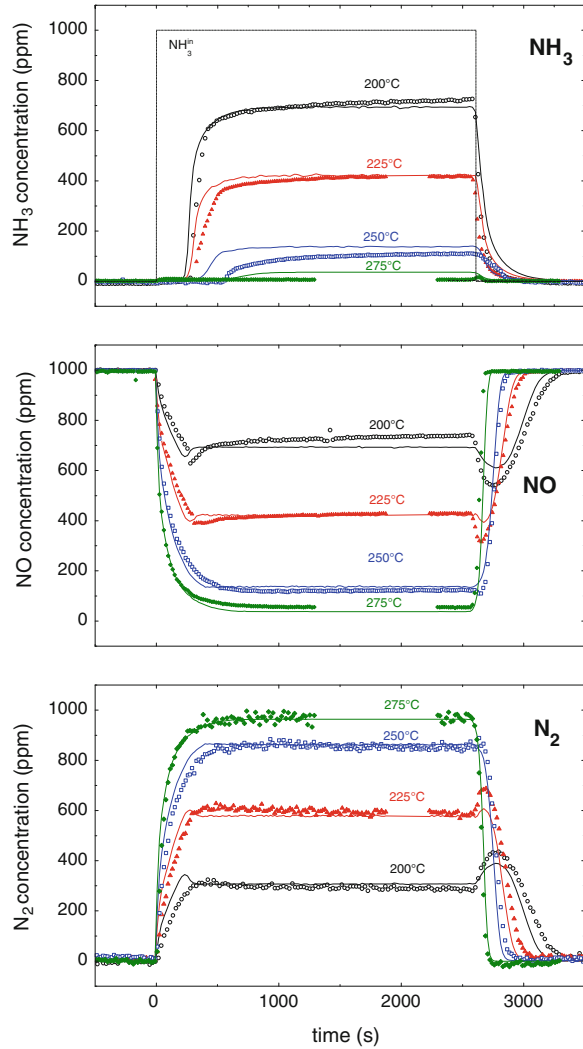
$$\varepsilon \frac{\partial C_{\text{N}_2}}{\partial t} = -v \frac{\partial C_{\text{N}_2}}{\partial z} + (1 - \varepsilon)(r_{\text{NO}} + \frac{1}{2}r_{\text{ox}}) \quad (10.16)$$

NO

$$\varepsilon \frac{\partial C_{\text{NO}}}{\partial t} = -v \frac{\partial C_{\text{NO}}}{\partial z} - (1 - \varepsilon) \cdot r_{\text{NO}} \quad (10.17)$$

In order to challenge different mechanistic proposals for the SCR catalytic kinetics on a quantitative basis, three rate expressions for the SCR reaction (r_{NO}) were examined: they will be herein discussed in relation to their ability to reproduce the dynamic features of our experiments. In all cases, together with the

Fig. 10.5 Transient SCR experiments at different temperatures: GHSV = 92,000 h⁻¹; NH₃ = 0-1,000-0 ppm, NO = 1,000 ppm, H₂O = 1 %, O₂ = 6 %. Symbols: experimental; solid lines: model fit using the MR rate law Eqs. (10.42) + (10.43). Adapted from Ref. [5]



standard SCR reaction (10.13), the reactions of adsorption–desorption of NH₃, and ammonia oxidation to N₂ (10.8) were considered and the kinetic expressions discussed in the previous sections were used jointly with each one of the SCR rate expressions introduced in the following.

Eley–Rideal Kinetics (ER)—In line with several literature indications [18, 19], we started from an Eley–Rideal (ER) rate law [1, 3, 5, 12, 19, 22] assuming that the SCR reaction occurs between adsorbed ammonia and gaseous (or weakly adsorbed) NO:

$$r_{\text{NO}} = k_{\text{NO}}^{\text{O}} \cdot e^{-\frac{E_{\text{NO}}}{RT}} \cdot C_{\text{NO}} \cdot \theta_{\text{NH}_3} \quad (10.18)$$

Table 10.1 List of reactions and corresponding rate expressions included in the SCR kinetic model

R.1	$S_2 + NH_3 \rightarrow S_2[NH_3]$	NH ₃ adsorption	$r_{ads} = k_{ads} C_{NH_3} (1 - \theta_{NH_3} - \theta_{HNO_3})$	Eq. (10.6)
R.2	$S_2[NH_3] \rightarrow S_2 + NH_3$	NH ₃ desorption	$r_{des} = k_{des}^0 \exp\left[-\frac{E_{des}^0}{RT} (1 - \theta_{NH_3})\right] \theta_{NH_3}$	Eq. (10.7)
R.3	$S_2[NH_3] + \frac{3}{4} O_2 \rightarrow \frac{1}{2} N_2 + \frac{3}{2} H_2O$	NH ₃ oxidation	$r_{ox} = k_{ox} \theta_{NH_3} (p_{O_2}/0.02)^\beta$	Eq. (10.12)
R.4	$NO + S_2[NH_3] + \frac{1}{4} O_2 \rightarrow N_2 + \frac{3}{2} H_2O + S_2$	Standard SCR		
R.5	$NO + S_2[HNO_3] + S_2[NH_3] \rightarrow N_2 + 2 H_2O + NO_2 + 2 S_2$	Fast SCR	$r_{DeNOx} = \frac{k_{NO} C_{NO} \theta_{NH_3}}{\left(1 + K_{NH_3} \frac{\theta_{NH_3}}{1 - \theta_{NH_3} - \theta_{HNO_3}}\right) \left(1 + \frac{k_{NO} C_{NO} \theta_{NH_3}}{k_{NO_2} p_{O_2}^{1/4} + k_{NO_2} \theta_{HNO_3}}\right)}$	Eq. (10.57)
R.6	$2 NO_2 + S_2[NH_3] \rightarrow N_2 + H_2O + S_2[HNO_3]$	Nitrates formation	$r_{amm} = \frac{k_{amm} C_{NO_2} \theta_{NH_3} (1 - \theta_{NH_3} - \theta_{HNO_3})}{\theta_{HNO_3}}$	Eq. (10.64)
R.7	$HNO_3 + S_2 \rightarrow S_2[HNO_3]$	Nitrates adsorption	$r_{admit} = k_{admit} C_{HNO_3} (1 - \theta_{NH_3} - \theta_{HNO_3})$	Eq. (10.65)
R.8	$S_2[HNO_3] \rightarrow HNO_3 + S_2$	Nitrates desorption	$r_{desnit} = k_{desnit} \theta_{HNO_3}$	Eq. (10.66)
R.9	$S_2[NH_3] + \frac{3}{4} NO_2 \rightarrow \frac{7}{8} N_2 + \frac{3}{2} H_2O$	NO ₂ SCR	$r_{NO_2S} = k_{NO_2S}^0 \exp\left(-\frac{E_{NO_2S}}{RT}\right) C_{NO_2} \theta_{NH_3}$	Eq. (10.67)
R.10	$S_2[NH_3] + S_2[HNO_3] \rightarrow N_2O + 2 H_2O + S_2$	N ₂ O formation	$r_{N_2O} = k_{N_2O}^0 \exp\left(-\frac{E_{N_2O}}{RT}\right) \theta_{HNO_3} \theta_{NH_3}$	Eq. (10.68)

A global multiresponse nonlinear regression of the five TRM and TPR runs performed with 2 % v/v O₂ (see Figs. 10.3 and 10.4) provided the estimates of the two rate parameters in Eq. (10.18) (k_{NO}° , E_{NO}).

The data fits obtained using Eley–Rideal kinetics, Eq. (10.18), are compared in Fig. 10.4a (solid lines) with the TRM data at 2 % oxygen. In all cases, a satisfactory agreement was achieved between experimental and calculated data, but for the NH₃ startup and shutdown transients at the lowest investigated temperatures: in these cases, the minima in the NO concentration trace and the corresponding maxima in the N₂ trace were not reproduced by the model. This is not surprising, since Eq. (4.16) does not take into account the inhibiting effect of NH₃ on the SCR reaction to which such a nonmonotonic behavior is ascribed [3–5].

Modified θ_{NH_3} Kinetics (M θ)—A modified Eley–Rideal rate expression (Modified θ_{NH_3} , M θ) was also proposed in the literature [12, 22–24] in order to describe transient data collected at low temperatures indicating that a “reservoir” of NH₃ species, possibly adsorbed on poorly reactive but abundant W and Ti acidic sites, is present and available for the SCR reaction upon ammonia desorption followed by re-adsorption at the active V sites:

$$r_{\text{NO}} = k_{\text{NO}}^{\circ} \cdot e^{-E_{\text{NO}}/RT} \cdot C_{\text{NO}} \cdot \theta_{\text{NH}_3}^* \cdot (1 - e^{-\theta_{\text{NH}_3}/\theta_{\text{NH}_3}^*}) \quad (10.19)$$

Equation (10.19) implies that r_{NO} becomes essentially independent of the ammonia surface coverage above a critical NH₃ coverage identified by $\theta_{\text{NH}_3}^*$.

Like for the ER rate expression, a global multiresponse nonlinear regression of all the TRM and TPR runs performed with 2 % O₂ provided the estimates of the three rate parameters in Eq. (10.19) (k_{NO}° , E_{NO} , $\theta_{\text{NH}_3}^*$).

Figure 10.4b (solid lines) shows the fit obtained using Eq. (10.19) for the TRM data with 2 % oxygen. It clearly appears that this kinetic expression afforded a good agreement between experimental and calculated data, again with the exception of the outlet concentrations of nitric oxide and nitrogen during the NH₃ startup and shutdown transients at the lower temperatures, where it predicted a prolonged duration of the NO conversion associated with depletion of the NH₃ surface “reservoir”, but failed to account for the maximum in the deNO_x rate at decreasing ammonia coverage. In fact, like in the case of ER kinetics, the derivation of the Modified θ_{NH_3} rate expression did not consider the ammonia inhibition effect.

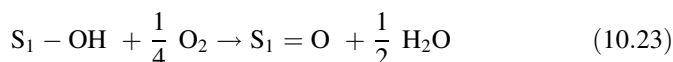
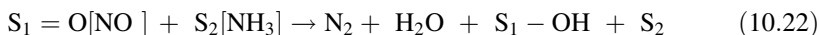
Modified Redox Kinetics (MR)—In order to take into account the redox nature of the Standard SCR reaction and the observed transient features indicating an ammonia inhibition effect, a new kinetic model was derived.

It assumed that two different types of sites are available on the surface of the V₂O₅-WO₃/TiO₂ catalyst: one Redox site for O₂ and NO adsorption/reaction (S₁) and one acidic site for NH₃ adsorption (S₂). Kapteijn et al. [34] and Valdés-Solis et al. [39, 40] also reported similar assumptions to derive SCR rate expressions for Mn₂O₃-WO₃/Al₂O₃ catalysts and for carbon-supported V₂O₅ catalysts, respectively.

Even if not strictly relevant for kinetic purposes, in agreement with spectroscopic and mechanistic evidence [21, 25, 41], it was proposed that S₁-sites are

associated with vanadyl species, whereas S₂-sites were associated with other nonreducible, strongly acidic surface sites, such as Vanadium-related Brønsted or Lewis sites, or also with sites related to the other oxide catalyst components: it is well known in fact that NH₃ adsorption occurs also onto V-free WO₃/TiO₂ catalysts [27] and that these NH₃ adspecies can act as a “reservoir” for NH₃ storage/reaction, as implied also in the Mθ rate law [12] previously discussed.

Starting from oxidized S₁ sites, we proposed the following Modified Redox (MR) kinetic scheme:



where step (10.20) accounts for a weak NO adsorption, step (10.21) is the strong ammonia adsorption, the DeNO_x step (10.22) involves reduction of the S₁ sites, and reoxidation of reduced S₁ sites is represented by step (10.23).

In addition to steps (10.20)–(10.23), we further assume the following reversible “NH₃ spillover” step involving adjacent S₁- and S₂-sites:



When proceeding to the right, step (10.24) results in NH₃ blocking sites S₁, which are thus subtracted from the redox cycle. Accordingly, step (10.24) can in principle account for the observed ammonia inhibition.

The overall balances of S₁- and S₂-sites yield:

$$1 = \sigma_{=O} + \sigma_{NO} + \sigma_{NH_3} + \sigma_{OH} \quad (10.25)$$

$$1 = \theta_{free} + \theta_{NH_3} \quad (10.26)$$

where the terms in the RHS of Eq. (10.25) represent the fractional coverages of S₁ = O, S₁ = O[NO], S₁ = [NH₃] and S₁-OH, respectively, while θ_{NH₃} in Eq. (10.26) indicates the fractional coverage of S₂[NH₃].

We then expressed the rates of step (10.22), i.e., the surface reaction between activated NO and adsorbed NH₃, involving reduction of S₁-sites, and of step (10.23), involving reoxidation of S₁-sites, as, respectively,

$$r_{red} = r_{NO} = k_{NO}K_{NO}C_{NO}\theta_{NH_3}\sigma_{=O} \quad (10.27)$$

$$r_{reox} = k_{reox}p_{O_2}^{1/4}\sigma_{OH} \quad (10.28)$$

Equation (10.27) implies assuming quasi-equilibrium for step (10.20).

On imposing that r_{NO} = r_{reox}, we obtained a relationship between the surface concentrations of reduced and oxidized S₁ sites,

$$\sigma_{\text{OH}} = \frac{k_{\text{NO}}K_{\text{NO}}C_{\text{NO}}\theta_{\text{NH}_3}}{k_{\text{reox}}\rho_{\text{O}_2}^{1/4}}\sigma_{=o} \quad (10.29)$$

Thus, from Eq. (10.25), on further assuming negligible surface concentration of NO due to its weak adsorption,

$$\sigma_{=o} = \frac{1 - \sigma_{\text{NH}_3}}{1 + \frac{k_{\text{NO}}K_{\text{NO}}C_{\text{NO}}\theta_{\text{NH}_3}}{k_{\text{reox}}\rho_{\text{O}_2}^{1/4}}} \quad (10.30)$$

and, from Eq. (10.27),

$$r_{\text{NO}} = \frac{k_{\text{NO}}^o \cdot e^{-E_{\text{NO}}/RT} C_{\text{NO}}\theta_{\text{NH}_3}}{1 + k_{\text{O}_2} \frac{C_{\text{NO}}\theta_{\text{NH}_3}}{\rho_{\text{O}_2}^{1/4}}} (1 - \sigma_{\text{NH}_3}) \quad (10.31)$$

where $k_{\text{NO}}^o \cdot e^{-E_{\text{NO}}/RT} = k_{\text{NO}}K_{\text{NO}}$, and $k_{\text{O}_2} = \frac{k_{\text{NO}}K_{\text{NO}}}{k_{\text{reox}}}$.

In order to arrive at a closed form for the deNO_x rate equation, σ_{NH_3} had to be evaluated. Assuming the rate of NH_3 spillover, step (7), to be of the same order of magnitude as the rate of NH_3 buildup—depletion on S_2 -sites, which determines the characteristic time for the SCR transients, a kinetic approach was taken, resulting in the following balance for the S_1 - NH_3 sites:

$$\frac{d\sigma_{\text{NH}_3}}{dt} = k_{\text{sp}} \left[\theta_{\text{NH}_3}(1 - \sigma_{\text{NH}_3}) - \frac{\sigma_{\text{NH}_3}(1 - \theta_{\text{NH}_3})}{K_{\text{NH}_3}} \right] \quad (10.32)$$

The evaluation of the SCR rate r_{NO} according to Eq. (10.31) then required time integration of Eq. (10.32).

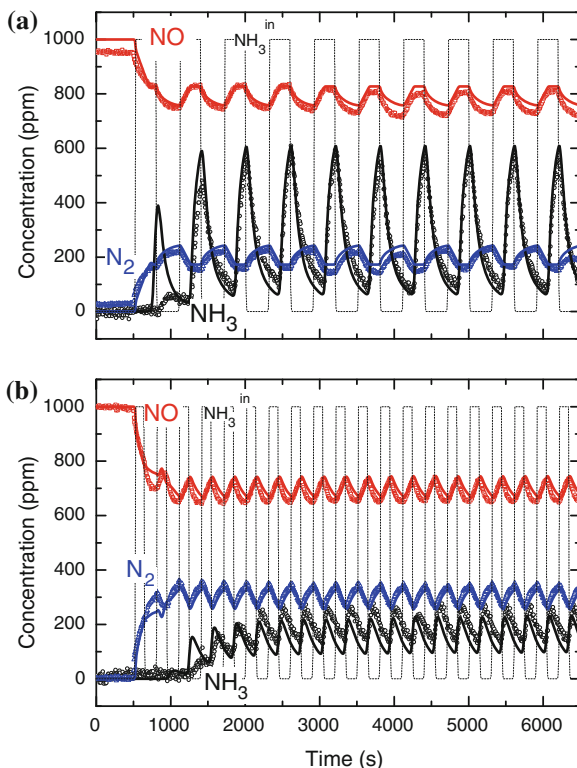
A global multiresponse nonlinear regression was performed to fit Eqs. (10.31) and (10.32) to all the performed TRM and TPR runs. Notably, since Eq. (10.31) included an explicit kinetic dependence on oxygen, data at both 2 and 6 % v/v O_2 feed content were included in the regression in this case for a total of 10 transient runs. The temperature dependence of k_{O_2} , K_{NH_3} , and k_{sp} was neglected in the regression to minimize the number of parameters, and a reparameterized form of Eq. (10.31) was used in order to reduce correlations among the parameter estimates.

Figure 10.4c (solid lines) illustrates the adequacy of the global fit of the TRM runs with 2 % O_2 : the MR rate law could evidently capture the complex maxima–minima features of the experimental NO and N_2 traces (symbols) at low T at both NH_3 startup and shutdown much better than Eq. (10.18) (Fig. 10.4a—solid lines) and Eq. (10.19) (Fig. 10.4b—solid lines).

Since the MR rate model, Eqs. (10.31) + (10.32) relies on the assumption that the SCR reaction is governed by a redox mechanism and therefore predicts a kinetic dependence on oxygen, it was further validated against the experimental data collected at the higher oxygen content. Figures 10.4 and 10.5 compare model predictions (solid lines) obtained using the MR rate law with the corresponding experimental results (symbols) obtained performing TRM runs at different

Fig. 10.6 Transient SCR experiments at different temperatures with high frequency NH_3 feed pulses at 200 °C:

GHSV = 92,000 h^{-1} ;
 NH_3 = 0-1,000-0 ppm,
 NO = 1,000 ppm,
 H_2O = 1 %, O_2 = 2 %.
a pulse frequency: 5 min on/
 5 min off; **b** pulse frequency:
 2, 5 min on/2, 5 min off.
 Symbols: experimental; solid
 lines: model fit using the MR
 rate law Eqs.
 (10.31) + (10.32). Adapted
 from Refs. [3, 5]

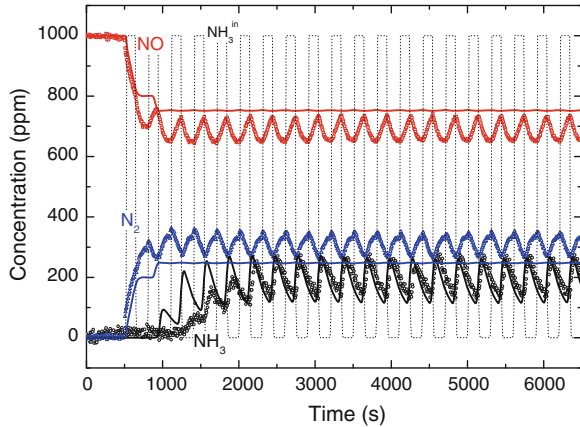


temperatures in the presence of 6 % v/v of oxygen and TPR runs with either 2 or 6 % v/v oxygen in the feed stream, respectively. Inspection of Figs. 10.4 and 10.5 confirms that changing the DeNO_x rate law from the ER-based Eqs. (10.18) or (10.19) to the new MR kinetic model, Eqs. (10.31) + (10.32) allowed about a remarkable improvement in the description of fast SCR transients and brought a good description of the experimental oxygen effect: this supports the redox mechanism for the SCR reaction.

The parameter estimates provided by the fit based on MR kinetics were also used to simulate the experiments of Fig. 10.6: pulsed ammonia steps (1,000 ppm) were fed at 200 °C while feeding 1,000 ppm of NO, 2 % O_2 , 1 % H_2O in He with a GHSV of 92,000 h^{-1} . Two runs were performed with different pulse frequency. Notably, these were particularly demanding conditions with respect to the ammonia inhibition effect. The simulation results are also displayed in Fig. 10.6 (solid lines): it clearly appears that, on a purely predictive basis, the MR rate expression was able to follow the fast transients of these experiments.

On the other hand, neither the simple Eley–Rideal kinetics Eq. (10.18) nor the Modified θ_{NH_3} Kinetics Eq. (10.19) were able to simulate successfully the same experimental transients. Figure 10.7 shows for example the simulation obtained with the Modified θ_{NH_3} Kinetics Eq. (10.19) for the same run shown in Fig. 10.6b:

Fig. 10.7 Transient SCR experiments at different temperatures with high frequency NH_3 feed pulses: data as in Fig. 10.6b. Symbols: experimental; solid lines: model fit using the $M\theta$ rate law Eq. (10.19). Adapted from Ref. [5]



the complex maxima-minima transient behavior was not reproduced by such kinetic expression.

It is worth mentioning that a simplified expression of Eq. (10.31) could be readily obtained under the limiting assumption of fast NH_3 spillover: in line with this hypothesis, in fact, quasi-equilibrium for step (10.24) could be assumed to derive

$$1 - \sigma_{\text{NH}_3} = \frac{1}{1 + K_{\text{NH}_3} \frac{\theta_{\text{NH}_3}}{1 - \theta_{\text{NH}_3}}} \quad (10.33)$$

On substituting Eq. (10.33) into (10.31), the following explicit form of the redox SCR rate equation was achieved:

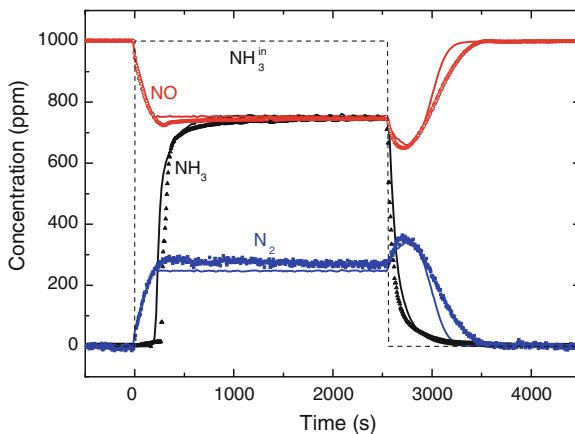
$$r_{\text{NO}} = \frac{k_{\text{NO}}^o \cdot e^{-E_{\text{NO}}^o/RT} C_{\text{NO}} \theta_{\text{NH}_3}}{\left(1 + K_{\text{NH}_3} \frac{\theta_{\text{NH}_3}}{1 - \theta_{\text{NH}_3}}\right) \left(1 + k_{\text{O}_2} \frac{C_{\text{NO}} \theta_{\text{NH}_3}}{P_{\text{O}_2}^{1/4}}\right)} \quad (10.34)$$

Equation (10.34) involves one adjustable parameter less than the general form, Eq. (10.31) + (10.32). It was fitted to the transient TRM and TPR runs at 2 and 6 % O_2 , too. The fit results were essentially identical to those reported in Figs. 10.3, 10.4, and 10.5, but for the small transient features observed during ammonia step feed to the reactor in the low-T TRM runs, which were not reproduced by Eq. (10.34).

As an example, the comparison between the model fit based on Eq. (10.34) and the experimental data for the TRM run with 2 % oxygen at 200 °C is illustrated in Fig. 10.8.

Equations (10.31) + (10.32), or their simplified form Eq. (10.34), have specific implications with respect to important SCR kinetic and mechanistic issues. Herein, we discuss such implications in relation to Eq. (10.34) for the sake of simplicity, but the following considerations apply as well to the more general form, Eqs. (10.31) + (10.32).

Fig. 10.8 Transient SCR experiment at 200 °C: GHSV = 92,000 h⁻¹; NH_3 = 0-1,000-0 ppm, NO = 1,000 ppm, H_2O = 1 %, O_2 = 2 %. Symbols: experimental; solid lines: model fit using Eq. (10.34). Adapted from Ref. [5]



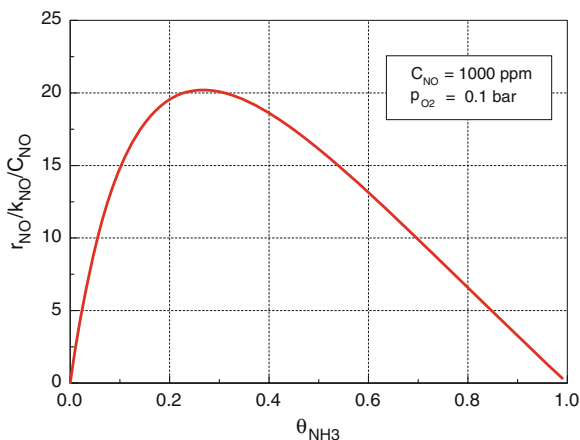
The MR rate expression Eq. (10.34) differs from the Eley-Rideal rate Eq. (10.18) only in its denominator, which accounts both for the adverse kinetic effect of NH_3 and for the favorable O_2 dependence: at low ammonia coverage (as, e.g., at high temperature), the denominator tends to unity and Eq. (10.34) formally reduces to Eq. (10.18). Indeed, this is consistent with the experimental indications discussed above: the ammonia inhibiting effect is particularly evident at low temperatures, but tends to disappear in the runs performed at temperatures of 250 °C and above, where ammonia coverage becomes lower. Likewise, the oxygen dependence is reportedly most manifest at low temperatures.

The improved transient kinetic fit associated with MR kinetics originates from the capability of Eq. (10.34) to accommodate the NH_3 inhibition effects, which pointed out the existence of optimal ammonia surface concentrations. This can be better focused by analyzing the dependence of Eq. (10.34) on the ammonia coverage θ_{NH_3} . In Fig. 10.9, $r_{\text{NO}}/k_{\text{NO}}/C_{\text{NO}}$ is plotted as a function of θ_{NH_3} for a given set of conditions ($p_{\text{O}_2} = 0.1$ bar and $C_{\text{NO}} = 1,000$ ppm): a maximum in the SCR reaction rate is clearly apparent at approximately $\theta_{\text{NH}_3} = 0.28$, the optimal value depending on reaction conditions. Thus, the DeNO_x efficiency is enhanced if the mean ammonia coverage is brought close to its optimal value, which could be predicted by Eq. (10.34): this observation has of course important consequences for the rational selection of the urea injection strategy in SCR systems for vehicles.

In connection to NH_3 inhibition, it is important to stress that the transient effects observed at low temperature during the NH_3 shutdown phase exhibited characteristic times of a few minutes (see Fig. 10.8), i.e., they are of the same order of magnitude as the characteristic times for buildup/depletion of ammonia adsorbed onto the SCR catalyst. This is consistent with step (10.24) in the derivation of the MR kinetic model, which attributes the blocking of the active sites S_1 to spillover of ammonia adsorbed on S_2 sites.

The derivation of the simplified MR rate law Eq. (10.34) assumed quasi-equilibrium for step (10.24), that is the NH_3 spillover step, thus meaning that as soon as ammonia is adsorbed onto S_2 - sites it can spill to adjacent S_1 - redox sites.

Fig. 10.9 θ_{NH_3} dependence of MR rate law, Eq. (4.27). $p_{\text{O}_2} = 0.1$ bar and $C_{\text{NO}} = 1,000$ ppm. Adapted from Ref. [5]



This would imply that S_1 - and S_2 -sites are characterized by a similar NH_3 adsorption capability. Indeed, it is reported [27] that ammonia can adsorb onto all the different types of sites (vanadia, tungsta and titania), which are, however, characterized by different acidity; more specifically, the most acidic sites are known to be tungsta and titania, while vanadia, also due to the fact that is present in smaller amount, contributes to a less extent to determine the overall ammonia adsorption capacity of these catalysts. Considering also that S_1 -sites may be associated with vanadyl species, whereas the S_2 -sites are likely associated with the other acidic surface sites, it appeared that the quasi-equilibrium assumption for step (10.24) may be not totally consistent with the physicochemical properties of V/W/Ti catalysts. According to a more plausible picture, as soon as it is admitted to the reactor ammonia starts adsorbing onto the more acidic and more abundant S_2 -sites: when the catalyst is close to saturation, ammonia is partially transferred to the less acidic and less abundant S_1 - sites and blocks them, thus inhibiting the SCR reaction. Then, the spillover step (10.24) is likely a slow, activated, kinetically controlled process, in line with the better description of the low-T transients at ammonia step feed provided by Eq. (10.31). Nevertheless, at least for the conditions herein investigated, the quasi-equilibrium assumption for step (10.24) in Eq. (10.34) seems to grant an excellent approximation for practical and engineering purposes, as apparent, e.g., from Fig. 10.8.

10.5 NH_3 -NO/ NO_2 Reacting System

A systematic kinetic investigation of the NH_3 -NO/ NO_2 SCR system was carried out over the full range of NO/ NO_x feed ratios (from zero to unity) and over a representative range of temperatures (160–425 °C). In total, 31 such TRM runs were performed.

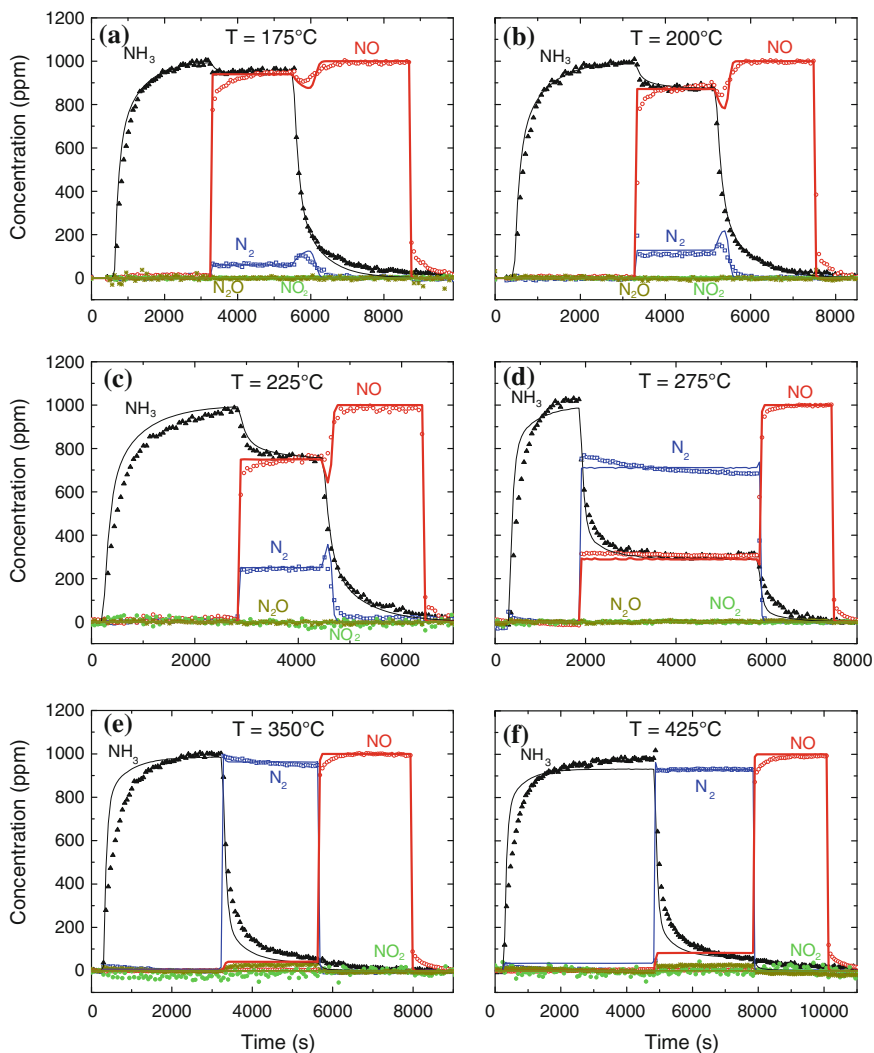


Fig. 10.10 Transient SCR experiments at different temperatures: $\text{GHSV} = 21,000 \text{ h}^{-1}$; $\text{NH}_3 = 0\text{--}1,000\text{--}0 \text{ ppm}$, $\text{NO} = 0\text{--}1,000\text{--}0 \text{ ppm}$, $\text{H}_2\text{O} = 1 \%$, $\text{O}_2 = 2 \%$, $\text{NO}/\text{NO}_x = 1$. **a** $T = 175 \text{ }^\circ\text{C}$, **b** $T = 200 \text{ }^\circ\text{C}$, **c** $T = 225 \text{ }^\circ\text{C}$, **d** $T = 275 \text{ }^\circ\text{C}$, **e** $T = 350 \text{ }^\circ\text{C}$, **f** $T = 425 \text{ }^\circ\text{C}$. Symbols: experimental; solid lines: model fit. Adapted from Ref. [8]

Figure 10.10 illustrates the results obtained at different temperatures in transient reaction experiments with a $\text{NO}/\text{NO}_x = 1$ feed ratio, corresponding to a feed mixture of 1,000 ppm of NH_3 , 1,000 ppm of NO , 2 % O_2 and 1 % H_2O v/v, with balance He. These experiments were very similar to those shown in Fig. 10.4 involving only the standard SCR reaction and are reported here for completeness.

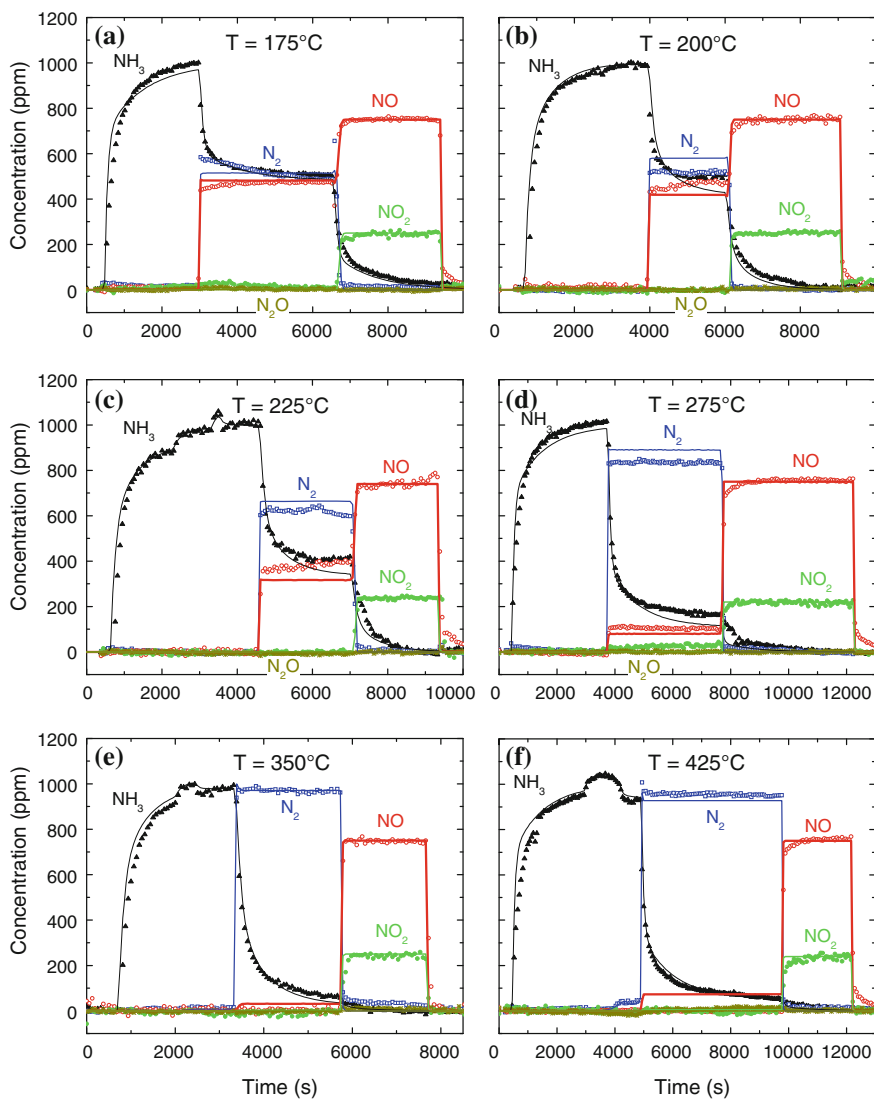
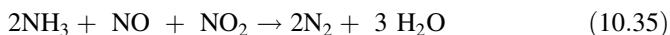


Fig. 10.11 Transient SCR experiments at different temperatures: $GHSV = 21,000 \text{ h}^{-1}$; $\text{NH}_3 = 0\text{-}1,000\text{-}0 \text{ ppm}$, $\text{NO} = 0\text{-}750\text{-}0 \text{ ppm}$, $\text{NO}_2 = 0\text{-}250\text{-}0 \text{ ppm}$, $\text{H}_2\text{O} = 1 \%$, $\text{O}_2 = 2 \%$. $\text{NO}/\text{NO}_x = 0.75$. **a** $T = 175 \text{ }^\circ\text{C}$, **b** $T = 200 \text{ }^\circ\text{C}$, **c** $T = 225 \text{ }^\circ\text{C}$, **d** $T = 275 \text{ }^\circ\text{C}$, **e** $T = 350 \text{ }^\circ\text{C}$, **f** $T = 425 \text{ }^\circ\text{C}$. Symbols: experimental; solid lines: model fit. Adapted from Ref. [8]

Figure 10.11 shows data collected when a stream consisting of 1,000 ppm of NH_3 , 750 ppm of NO , 250 ppm of NO_2 , 2 % O_2 , and 1 % H_2O , with balance He was fed to the reactor at different temperatures ($R = \text{NO}/\text{NO}_x = 0.75$).

In the case of the experiment performed at $175 \text{ }^\circ\text{C}$ (Fig. 10.11a), at $t = 3,000 \text{ s}$ the NO_x mixture was added to the ammonia feed, and the reaction took place.

At steady-state production of 500 ppm of nitrogen was observed, associated with total consumption of NO₂ and with consumptions of 250 ppm of NO and 500 ppm of NH₃. These values reflect exactly the stoichiometry of the Fast SCR, reaction (10.35),



which was undoubtedly responsible for such an enhanced activity at low T as compared to Fig. 10.10. Indeed, the addition of NO₂ to the reacting system resulted in a marked increase of the NO_x conversion, which went from 5 % measured in the case of the Standard SCR reaction (Fig. 10.10a), up to roughly 50 %. It should be also noticed that in this run the overall deNO_x efficiency was limited by the NO₂ feed concentration. In fact, analyzing the run performed at 200 °C (Fig. 10.11b), it appears that the NO_x conversion did not grow further: this was related to the fact that the limiting reactant NO₂ was totally converted already at 175 °C.

At $T > 200$ °C (Fig. 10.11c–f) as expected, the standard SCR also became significantly active, as demonstrated by the increased NH₃ and NO conversions and N₂ production. Again, the limited amount of 25 % of NO₂ in the feed stream remarkably promoted the low temperature deNO_x efficiency with respect to the case in which only NO was present: in fact, at 275 °C the gain in NO_x conversion was still significant (from 70 to nearly 90 %).

Experiments were then performed feeding 1,000 ppm of ammonia and NO and NO₂ in equimolar amounts (500 ppm each, $R = \text{NO}/\text{NO}_x = 0.5$) in the presence of 2 % O₂ and 1 % H₂O, with balance He. The results in the T-range 160–350 °C are reported in Fig. 10.12a–f.

At 200 °C (Fig. 10.12c), after achieving steady state, a production of 700 ppm of nitrogen was observed, together with a consumption of 350 ppm of NO, 350 ppm of NO₂ and 700 ppm of NH₃. Such values reflect exactly the stoichiometry of the Fast SCR, reaction (10.35), with a 70 % conversion of NO_x.

The Fast SCR was the prevailing reaction in the whole analyzed T-range, between 175 and 425 °C, and indeed, the conversions of NO and NO₂ resulted very similar while the trends of ammonia and nitrogen were mirror-like, in agreement with (10.35).

Conversely, the run performed at 225 °C showed a higher NO conversion with respect to NO₂: the result was explained considering the simultaneous occurrence of the standard SCR reaction (10.13), which indeed was active at such T (see Fig. 10.10). As shown in the following (see Fig. 10.14), at higher temperatures the NO₂ SCR reaction (10.36)



also became active on V-based systems [7] so that the excess NO₂ detected at 225 °C was consumed and total conversion of both NO and NO₂ was achieved.

A peculiar behavior was noted in the run at 160 °C: a significant deviation between NO and NO₂ conversions was evident associated with a lack in the N-

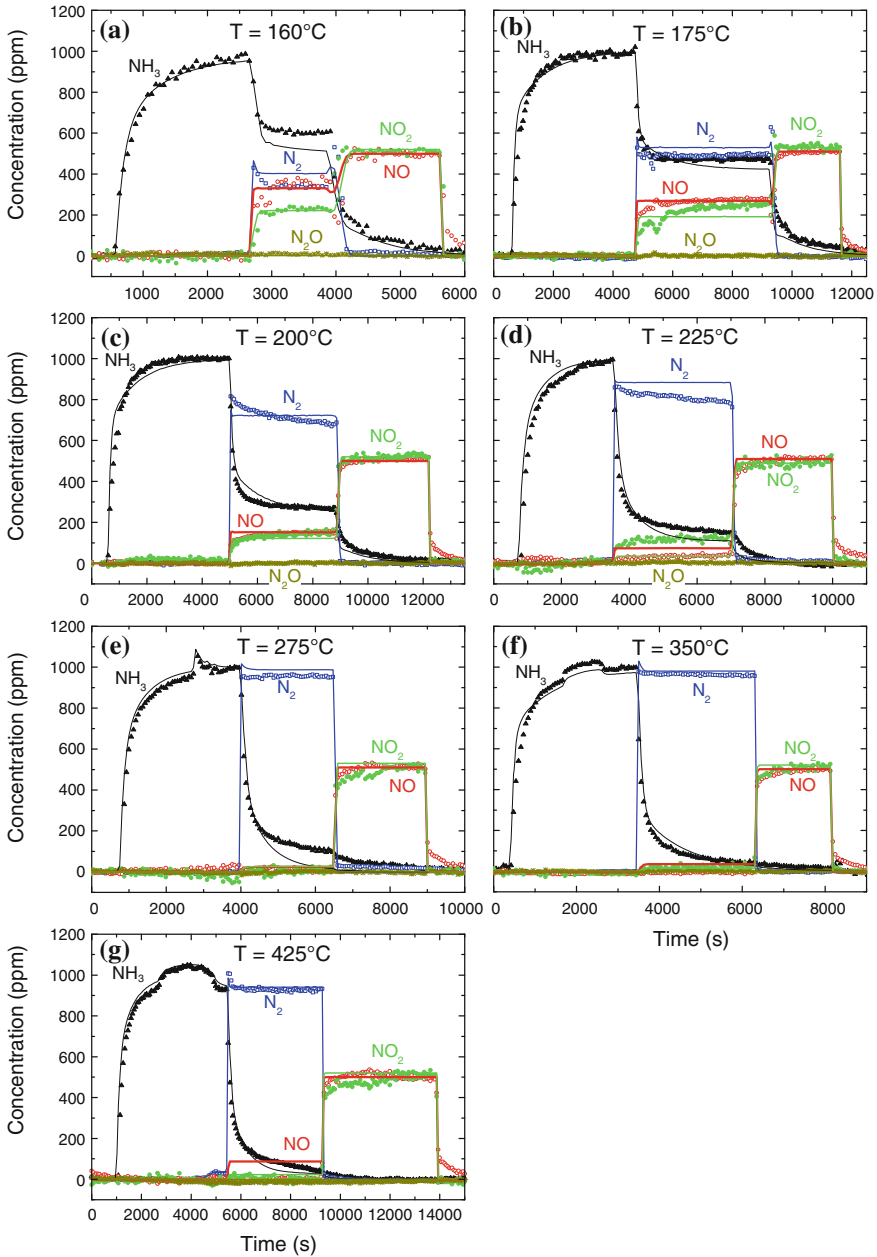


Fig. 10.12 Transient SCR experiments at different temperatures: GHSV = 21,000 h⁻¹; NH₃ = 0-1,000-0 ppm, NO = 0-500-0 ppm, NO₂ = 0-500-0 ppm, H₂O = 1 %, O₂ = 2 %. NO/NO_x = 0.5. **a** $T = 160^\circ\text{C}$, **b** $T = 175^\circ\text{C}$, **c** $T = 200^\circ\text{C}$, **d** $T = 225^\circ\text{C}$, **e** $T = 275^\circ\text{C}$, **f** $T = 350^\circ\text{C}$, **g** $T = 425^\circ\text{C}$. Symbols: experimental; solid lines: model fit. Adapted from Ref. [8]

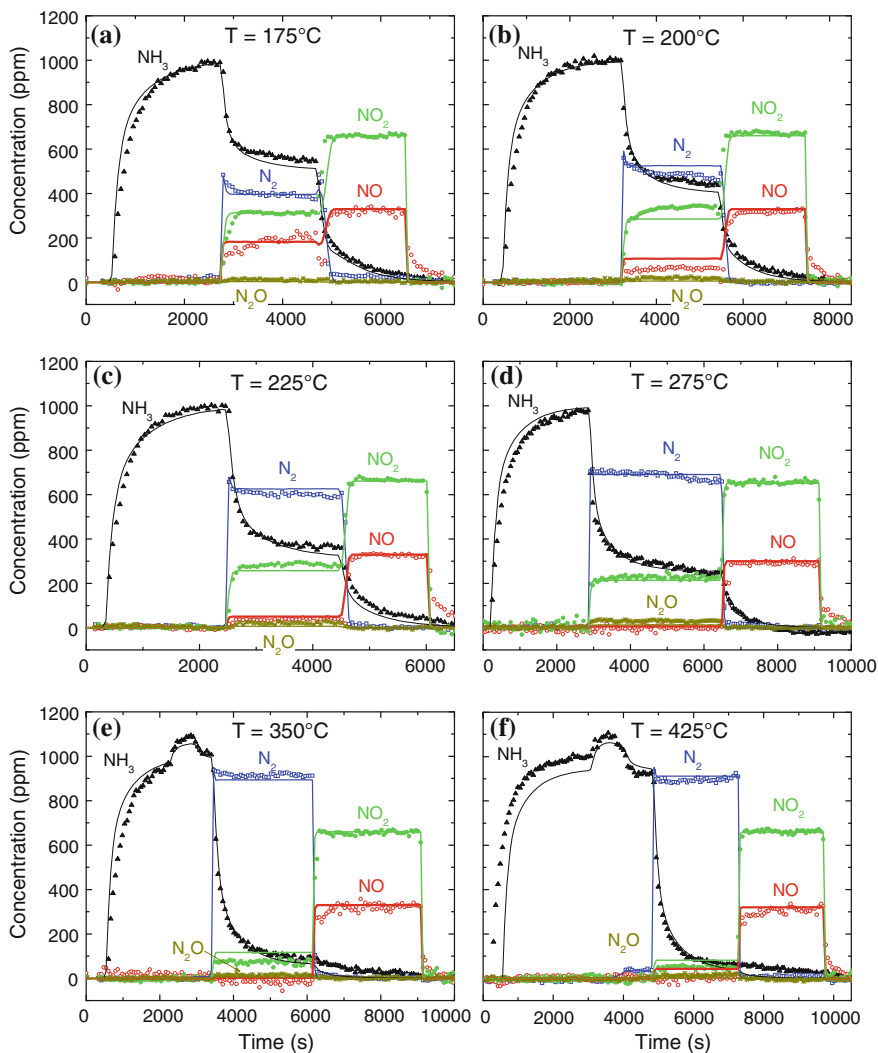


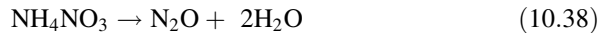
Fig. 10.13 Transient SCR experiments at different temperatures: GHSV = 21,000 h⁻¹; NH₃ = 0-1,000-0 ppm, NO = 0-330-0 ppm, NO₂ = 0-670-0 ppm, H₂O = 1 %, O₂ = 2 %. NO/NO_x = 0.33. **a** $T = 175^\circ\text{C}$, **b** $T = 200^\circ\text{C}$, **c** $T = 225^\circ\text{C}$, **d** $T = 275^\circ\text{C}$, **e** $T = 350^\circ\text{C}$, **f** $T = 425^\circ\text{C}$. Symbols: experimental; solid lines: model fit. Adapted from Ref. [8]

balance: as discussed below, at such a low temperature NO₂ can be consumed in fact not only by the Fast SCR, but also by the ammonium nitrate formation reaction (10.37) [1, 7],



Figure 10.13a–f shows the results of six TRM runs performed feeding 1,000 ppm of NH_3 , 670 ppm of NO_2 , 330 ppm of NO , 2 % O_2 and 1 % H_2O , with balance He ($R = \text{NO}/\text{NO}_x = 0.33$), thus in excess of NO_2 in the NO_x feed mixture.

Inspection of Fig. 10.13a–d, data obtained at $T \leq 275$ °C, indicated that all the NO in the feed was consumed according to the Fast SCR stoichiometry, reaction (10.35), while the steady-state concentrations of the other species pointed out also the formation of ammonium nitrate (10.37) and of N_2O



At higher temperatures (Fig. 10.13e and f), an enhanced consumption of reactants was observed, accompanied by production of nitrogen. This feature was ascribed to the onset of the NO_2 -SCR reaction (10.36).

In order to investigate the reactivity of the SCR system in the presence of $\text{NH}_3 + \text{NO}_2$ only, TRM runs were performed in the 175–425 °C range using a feed mixture containing 1,000 ppm of NH_3 , 1,000 ppm of NO_2 , 2 % O_2 , and 1 % H_2O , with balance He ($R = \text{NO}/\text{NO}_x = 0$): the results are reported in Fig. 10.14a–f.

At $T = 175$ °C (Fig. 10.14a), as soon as NO_2 was fed to the reactor an equimolar consumption of the two reactants NO_2 and NH_3 with a simultaneous production of nitrogen was observed. This was well explained by the occurrence of reaction (10.37), with a conversion of about 50 % [1, 7]: this reaction involves in fact formation of solid ammonium nitrate, a salt that is in equilibrium with gaseous HNO_3 and NH_3 below about 170 °C. Indeed, in this experiment a lack of 25 % in the N-balance at steady state was apparent, which was ascribed to the precipitation of a corresponding amount of NH_4NO_3 and was consistent with the concentrations of ammonia, NO_2 , nitrogen, and NH_4NO_3 according to the stoichiometry of reaction (10.37).

By increasing the temperature of the experiments (Fig. 10.14b–f), N_2O appeared among the reaction products, possibly due to a partial decomposition of ammonium nitrate species (reaction 10.38) and its concentration increased up to 275 °C. In the high-temperature region (Fig. 10.14d–f), a sudden increase in the conversion of the reactants NO_2 and NH_3 and in the production of nitrogen was observed. This was due to the onset of the NO_2 SCR, reaction (10.36), which involves conversion of NH_3 and NO_2 in nonequimolar amounts.

The influence of the reactants feed concentrations on the activity of the Fast SCR reaction (10.35) was investigated by means of 11 additional TRM runs, where a feed containing NO_x with constant $R = \text{NO}/\text{NO}_2 = 1$ was stepwise added to a feed stream of NH_3 , O_2 (2 %), H_2O (1 %), and balance helium at 200 °C. The runs included different ammonia (1,000, 700, and 550 ppm) and NO_x (1,000, 700, 550, and 300 ppm) feed contents [8].

The data collected varying the NO_x feed concentrations for constant ammonia feed showed that the steady-state levels of reactants and products agreed as expected with the stoichiometry of the Fast SCR reaction (10.35), with an overall

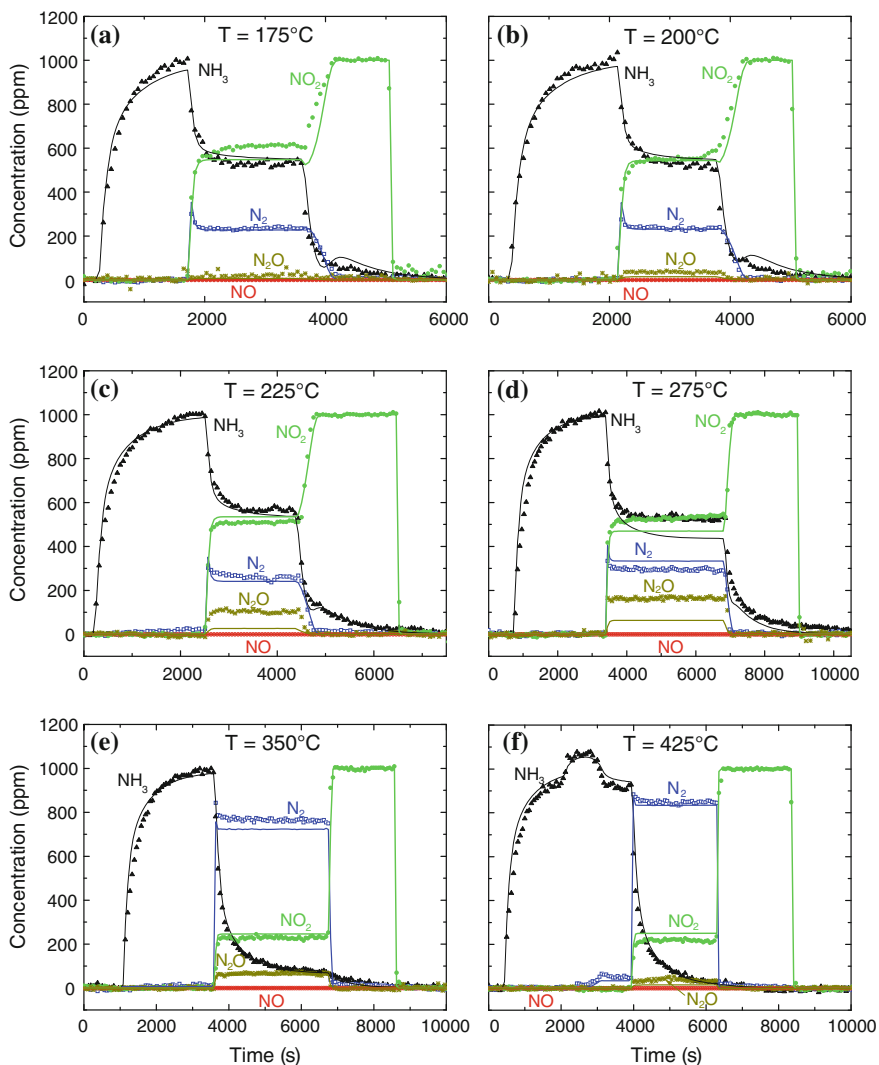


Fig. 10.14 Transient SCR experiments at different temperatures: $\text{GHSV} = 21,000 \text{ h}^{-1}$; $\text{NH}_3 = 0\text{-}1,000\text{-}0 \text{ ppm}$, $\text{NO}_2 = 0\text{-}1,000\text{-}0 \text{ ppm}$, $\text{H}_2\text{O} = 1 \%$, $\text{O}_2 = 2 \%$. $\text{NO}/\text{NO}_x = 0$. **a** $T = 175 \text{ }^\circ\text{C}$, **b** $T = 200 \text{ }^\circ\text{C}$, **c** $T = 225 \text{ }^\circ\text{C}$, **d** $T = 275 \text{ }^\circ\text{C}$, **e** $T = 350 \text{ }^\circ\text{C}$, **f** $T = 425 \text{ }^\circ\text{C}$. Symbols: experimental; solid lines: model fit. Adapted from Ref. [8]

conversion which was only slightly affected by the variation of the reactant concentrations.

Minor differences were found only in the dynamics of reactants admission or removal from the reactor: indeed, by increasing the NO_x concentration or on decreasing that of ammonia, an enhancement of the transient features associated

with NO_x admission was evident; conversely, the transient behaviors at NH_3 shutoff seemed more marked when decreasing NO_x concentration or increasing ammonia content. This effect could still be related to the ammonia inhibition effect already discussed.

The kinetic analysis of the large set of transient data collected varying in the NO_2/NO_x feed ratio was addressed according to a dynamic one-dimensional isothermal heterogeneous plug-flow model of the test microreactor coupled with a nonlinear regression code as already described in the previous paragraphs.

The test reactor model comprised the following transient mass balance equations of adsorbed ammonia and nitrates, and of gaseous NH_3 , N_2 , NO , NO_2 , N_2O , HNO_3 as reported in the following:

adsorbed phase: NH_3 and HNO_3

$$\Omega \frac{\partial \theta_{\text{NH}_3}}{\partial t} = r_{\text{ads}} - r_{\text{des}} - r_{\text{ox}} - r_{\text{DeNO}_x} - r_{\text{amm}} - r_{\text{NO}_2} - r_{\text{N}_2\text{O}} \quad (10.39)$$

$$\Omega \frac{\partial \theta_{\text{HNO}_3}}{\partial t} = r_{\text{amm}} + r_{\text{adnit}} - r_{\text{desnit}} - r_{\text{fst}} - r_{\text{N}_2\text{O}} \quad (10.40)$$

gas phase: NH_3 , N_2 , NO , NO_2 , N_2O , HNO_3

$$\varepsilon \frac{\partial C_{\text{NH}_3}}{\partial t} = -v \frac{\partial C_{\text{NH}_3}}{\partial z} + (1 - \varepsilon)(-r_{\text{ads}} + r_{\text{des}}) \quad (10.41)$$

$$\varepsilon \frac{\partial C_{\text{N}_2}}{\partial t} = -v \frac{\partial C_{\text{N}_2}}{\partial z} + (1 - \varepsilon)(1/2r_{\text{ox}} + r_{\text{DeNO}_x} + r_{\text{amm}} + 7/8r_{\text{NO}_2}) \quad (10.42)$$

$$\varepsilon \frac{\partial C_{\text{NO}}}{\partial t} = -v \frac{\partial C_{\text{NO}}}{\partial z} + (1 - \varepsilon)(-r_{\text{DeNO}_x}) \quad (10.43)$$

$$\varepsilon \frac{\partial C_{\text{NO}_2}}{\partial t} = -v \frac{\partial C_{\text{NO}_2}}{\partial z} + (1 - \varepsilon)(r_{\text{fst}} - 2r_{\text{amm}} - 3/4r_{\text{NO}_2}) \quad (10.44)$$

$$\varepsilon \frac{\partial C_{\text{N}_2\text{O}}}{\partial t} = -v \frac{\partial C_{\text{N}_2\text{O}}}{\partial z} + (1 - \varepsilon)r_{\text{N}_2\text{O}} \quad (10.45)$$

$$\varepsilon \frac{\partial C_{\text{HNO}_3}}{\partial t} = -v \frac{\partial C_{\text{HNO}_3}}{\partial z} + (1 - \varepsilon)(-r_{\text{adnit}} + r_{\text{desnit}}) \quad (10.46)$$

In line with previous findings [1, 7], we further assumed that any gaseous HNO_3 leaving the test reactor reacted with NH_3 to form NH_4NO_3 reaction (10.37), that therefore went undetected and built-up somewhere downstream from the reactor, thus giving rise to a lack in the overall N-balance.

The set of PDEs (10.39)–(10.46), with obvious initial and boundary conditions was solved numerically according to the method of lines, based on axial discretization with backward finite differences and on time integration by Gear's algorithm.

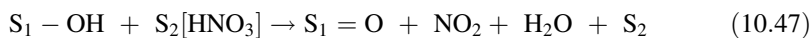
The same estimates of kinetic parameters for ammonia adsorption/desorption and oxidation as previously obtained were retained with no further adjustment.

The nitrates adsorption capacity was set to the same value of the ammonia storage capacity Ω , based on adsorption runs of NO₂ showing a comparable storage of ammonia and NO₂ and in line with the assumption that ammonia and nitrates are adsorbed on the same S₂ sites.

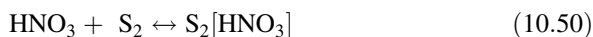
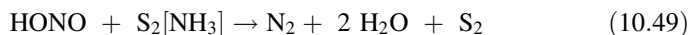
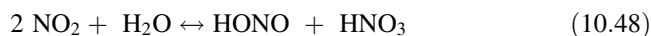
Concerning the rate parameters in the remaining rate expressions for the SCR reactions, the temporal evolutions of the outlet NH₃, NO, N₂, NO₂, N₂O concentrations were used as fitted responses in a global multiresponse nonlinear regression of 42 different TRM experiments performed with feeds including water and oxygen, using a robust multimethod regression routine. With respect to the large number of fitting parameters required to account for the comprehensive reaction scheme, and in order to minimize correlations, a sequential fitting strategy was followed. Thus, first the rate parameters associated with formation, adsorption–desorption of nitrates, (r_{amm} , r_{nit}), were estimated by regressions of results from runs with feeds containing NO₂ + NH₃ only. In a subsequent stage, the estimates of the rate parameters of the fast SCR rate expression (r_{fst}) were secured by regression on runs involving NO + NO₂ + NH₃ at temperatures below 250 °C, where the NO₂ SCR reaction was not active. Finally, the rate parameters for the NO₂ SCR and the formation of N₂O were estimated from the high-temperature TRM runs.

Concerning the rate expressions, extending the dual-site Redox kinetics already presented for the NH₃–NO/O₂ reacting subsystem, a new global kinetic model for the full NH₃–NO/NO₂ SCR reacting system was derived.

The catalyst reduction steps are steps (10.20)–(10.22), already written for the NH₃–NO reacting system, were still assumed for the Fast SCR reaction, while for the reoxidation steps, a new step (10.47) was added to step (10.23), which considered the catalyst reoxidation by oxygen, to include the possibility for nitrates to reoxidize the catalytic sites:



In addition, we considered two different non-redox reaction steps: ammonia spillover, step (10.24), and nitrates formation, steps (10.48)–(10.50):

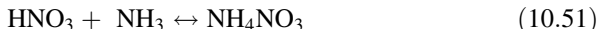


Steps (10.48)–(10.50) describe the formation of surface nitrates S₂[HNO₃] onto the catalyst via disproportion of NO₂, in line with literature indications for V-based and zeolite SCR catalysts [44–46]. It was postulated that surface nitrates are formed onto non-redox S₂ sites. A basis for this assumption was the observation that NO₂ disproportion with nitrates storage, as well as the related formation of

ammonium nitrate in the presence of ammonia, occurred also over a V-free WO_3/TiO_2 catalyst [6] and over other non-redox materials [42–44].

Notice that, in the absence of NO_2 , and thus of surface nitrates, steps (10.20)–(10.23) only were left, which sum up to the stoichiometry of the standard SCR reaction (10.13), whereas the combination of steps (10.20)–(10.22), (10.47), (10.48)–(10.50) resulted in the Fast SCR reaction (10.35).

Finally, step (10.50) accounted for the reversible desorption of nitrates. It is worth mentioning that nitric acid could react with ammonia to form ammonium nitrate salt,



Notice that NO_2 played no direct role in the redox cycle. Indeed, we have shown in [6] that in T-ramp experiments the rate of NO conversion at low T was essentially identical either when feeding $\text{NO} + \text{NH}_3 + \text{NO}_2$ to a clean V-catalyst, or when feeding $\text{NO} + \text{NH}_3$ only to the V-catalyst presaturated with nitrates.

The overall balances of S_1 - is still Eq. (10.25), that was considered for the standard SCR reaction, while in that of S_2 -sites θ_{HNO_3} was also taken into account:

$$S_2 - \text{sites} : 1 = \theta_{\text{free}} + \theta_{\text{NH}_3} + \theta_{\text{HNO}_3} \quad (10.52)$$

Considering the rate of step (10.22), i.e., the reduction step, Eq. (10.27) is still valid, while for the reoxidation of S_1 -sites we have Eq. (10.53) that includes the reoxidation by both oxygen and surface nitrates:

$$r_{\text{reox}} = r_{\text{reoxO}_2} + r_{\text{reoxHNO}_3} = (k_{\text{ox1}}p_{\text{O}_2}^{1/4} + k_{\text{ox2}}\theta_{\text{HNO}_3})\sigma_{\text{OH}} \quad (10.53)$$

Following a Mars-van Krevelen approach, the rate of reduction r_{red} was set equal to r_{reox} , the overall rate of oxidation, and thus, the following relationship between the surface concentrations of reduced S_1 sites (σ_{OH}) and of oxidized S_1 sites ($\sigma = \sigma_{\text{O}}$) was obtained:

$$\sigma_{\text{OH}} = \frac{k_{\text{NO}}K_{\text{NO}}C_{\text{NO}}\theta_{\text{NH}_3}}{k_{\text{ox1}}p_{\text{O}_2}^{1/4} + k_{\text{ox2}}\theta_{\text{HNO}_3}}\sigma_{\text{O}} \quad (10.54)$$

On further neglecting the surface concentration of NO due to its weak adsorption, from Eq. (10.25)

$$1 - \sigma_{\text{NH}_3} = \left(1 + \frac{k_{\text{NO}}K_{\text{NO}}C_{\text{NO}}\theta_{\text{NH}_3}}{k_{\text{ox1}}p_{\text{O}_2}^{1/4} + k_{\text{ox2}}\theta_{\text{HNO}_3}} \right) \sigma_{\text{O}} \quad (10.55)$$

Under the limiting assumption of fast NH_3 spillover, quasi-equilibrium for step (10.24) was invoked, leading to

$$1 - \sigma_{\text{NH}_3} = \frac{1}{1 + K_{\text{NH}_3} \frac{\theta_{\text{NH}_3}}{1 - \theta_{\text{NH}_3} - \theta_{\text{Nit}}}} \quad (10.56)$$

Thus, on combining Eqs. (10.55) and (10.56) with Eq. (10.27)

$$r_{\text{DeNO}_x} = r_{\text{red}} = r_{\text{reox}} = \frac{k_{\text{NO}}^o \cdot e^{-E_{\text{NO}}^o/RT} C_{\text{NO}} \theta_{\text{NH}_3}}{\left(1 + K_{\text{NH}_3} \frac{\theta_{\text{NH}_3}}{1 - \theta_{\text{NH}_3} - \theta_{\text{HNO}_3}}\right) \times \left(1 + \frac{k_{\text{NO}} C_{\text{NO}} \theta_{\text{NH}_3}}{k_{\text{ox1}} p_{\text{O}_2}^{1/4} + k_{\text{ox2}} \theta_{\text{HNO}_3}}\right)} \quad (10.57)$$

Notably, Eq. (10.57) expresses the overall reduction rate of NO, associated with both the Standard SCR reaction r_{std} (reaction 10.13), and the Fast SCR reaction r_{fst} (reaction (10.35)): thus $r_{\text{DeNO}_x} = r_{\text{std}} + r_{\text{fst}}$.

It is interesting to examine the asymptotic behavior of the rate law Eq. (10.57) under different conditions. In the absence of NO₂, $\theta_{\text{HNO}_3} \rightarrow 0$ and Eq. (10.57) reduced to the dual-site Modified Redox (MR) rate law derived for the Standard SCR reaction in Eq. (10.34).

In order to decouple the contributions of r_{std} and r_{fst} in the overall NO reduction rate r_{deNO_x} , we consider that

$$r_{\text{DeNO}_x} = r_{\text{std}} + r_{\text{fst}} = r_{\text{reoxO}_2} + r_{\text{reoxHNO}_3} \quad (10.58)$$

and that

$$\frac{r_{\text{reoxHNO}_3}}{r_{\text{reoxO}_2}} = D \frac{\theta_{\text{HNO}_3}}{p_{\text{O}_2}^{1/4}} \quad (10.59)$$

with $D = k_{\text{ox2}}/k_{\text{ox1}}$ representing the ratio of the rate constants for the two reoxidation mechanisms. Accordingly,

$$r_{\text{std}} = r_{\text{DeNO}_x} \frac{1}{1 + D \frac{\theta_{\text{HNO}_3}}{p_{\text{O}_2}^{1/4}}} \quad (10.60)$$

and r_{fst} can be obtained from $r_{\text{DeNO}_x} - r_{\text{std}}$.

Finally, it was worth noticing that according to Eq. (10.57) the Fast SCR should be active even in the absence of oxygen, the reoxidation of the V-sites being carried out by nitrates only: in such a case, the deNO_x rate expression Eq. (10.57) reduced in fact to

$$r_{\text{NO}} = \frac{k_{\text{NO}} C_{\text{NO}} \theta_{\text{NH}_3}}{\left(1 + K_{\text{NH}_3} \frac{\theta_{\text{NH}_3}}{1 - \theta_{\text{NH}_3} - \theta_{\text{HNO}_3}}\right) \left(k_{\text{nit}} \frac{C_{\text{NO}} \theta_{\text{NH}_3}}{\theta_{\text{HNO}_3}}\right)} \quad (10.61)$$

where $k_{\text{nit}} = k_{\text{NO}}/k_{\text{ox2}}$.

The occurrence of the Fast SCR reaction when feeding NO, NO₂ and NH₃ in the absence of gaseous oxygen was indeed observed [6].

To close the model, an expression for the rate of nitrates formation r_{amm} must be provided. This is done assuming that step (10.48) is a fast unfavorable equilibrated disproportionation of NO₂, followed by the rate determining reaction of nitrous acid with adsorbed ammonia to form unstable ammonium nitrite, which readily decomposes to nitrogen (step (10.49)). Accordingly,

$$r_{\text{amm}} = k_2[\text{HONO}]\theta_{\text{NH}_3} \quad (10.62)$$

Assuming equilibrium for steps (10.48) and (10.50), and taking into account the balance of S_2 -sites, (Eq. 10.52),

$$[\text{HONO}] \cong K_1 \frac{C_{\text{NO}_2}^2(1 - \theta_{\text{NH}_3} - \theta_{\text{HNO}_3})}{\theta_{\text{HNO}_3}} \quad (10.63)$$

In deriving Eq. (10.63), the H_2O dependence was incorporated into K_1 , and a small surface concentration of adsorbed nitrite species in view of their rapid reaction with ammonia was assumed.

Finally, on combining Eqs. (10.62) with (10.63), and setting $k_{\text{amm}} = (K_1 k_2)$, we got

$$r_{\text{amm}} = \frac{k_{\text{amm}} C_{\text{NO}_2}^2 \theta_{\text{NH}_3} (1 - \theta_{\text{NH}_3} - \theta_{\text{HNO}_3})}{\theta_{\text{HNO}_3}} \quad (10.64)$$

Notice that the derivation of Eq. (10.64) did not involve the redox sites S_1 : as already discussed, this is indeed consistent with experimental evidence showing that formation of nitrates occurs on V-free catalysts as well on V-based systems, and with other literature indications that show nitrates formation over zeolites [42–44] and alumina-based catalysts [45] in the absence of redox components.

In line with the facile formation of nitrates already at low temperatures [44], and with the modest T-dependence of NH_4NO_3 formation experimentally observed [4, 7, 46], no activation energy was assigned to k_{amm} .

To describe the full $\text{NH}_3\text{--NO/NO}_2\text{--O}_2$ reacting system in the whole range of temperatures and NO_2/NO_x feed ratios, other reactions apart from those that describe the redox cycles, resulting in the Standard and Fast SCR reactions, had to be incorporated in the kinetic model. Such additional reaction steps included ammonia adsorption/desorption and oxidation, nitrates adsorption and desorption, NO_2 SCR, and N_2O formation (see Table 10.1).

The rates of adsorption–desorption of nitrates (R.7 and R.8 in Table 10.1) were given the following expressions:

$$r_{\text{adsnit}} = k_{\text{adsnit}} C_{\text{HNO}_3} (1 - \theta_{\text{NH}_3} - \theta_{\text{HNO}_3}) \quad (10.65)$$

$$r_{\text{desnit}} = k_{\text{desnit}} \theta_{\text{HNO}_3} \quad (10.66)$$

The T-dependence of k_{adsnit} and k_{desnit} , which played a minor role under typical reaction conditions, was neglected in order to minimize the number of fitting parameters.

Finally, for the rate of the NO_2 SCR reaction (10.36) and of N_2O formation (10.38) we adopted, respectively,

$$r_{\text{NO}_2\text{S}} = k_{\text{NO}_2\text{S}}^0 \exp\left(-E_{\text{NO}_2\text{S}}/RT\right) C_{\text{NO}_2} \theta_{\text{NH}_3} \quad (10.67)$$

$$r_{\text{N}_2\text{O}} = k_{\text{N}_2\text{O}}^0 \exp\left(-E_{\text{N}_2\text{O}}/RT\right) \theta_{\text{HNO}_3} \theta_{\text{NH}_3} \quad (10.68)$$

Figure 10.10 shows the results of the model fit of the six TRM runs with NO/NO_x feed ratio = 1. The good agreement between experimental (symbols) and calculated (solid lines) traces both at steady state and during concentration step changes, confirmed the goodness of the model in predicting the reactivity of the NH₃ + NO reaction also at different space velocities with respect to those adopted in the kinetic investigation of the Standard SCR reaction alone, shown, e.g., in Fig. 10.6.

The results of the model fit of the TRM runs with NO/NO_x feed ratio = 0 are shown in Fig. 10.14. The fine prediction of the steady state levels of NH₃, NO₂, and N₂ at all temperatures means that the kinetics of all the involved reactions was correctly estimated. Only N₂O was underestimated to some extent in the intermediate temperatures.

It is worth emphasizing how successful the model was in catching the complex transient behavior observed in the low temperature runs at the reactants step changes: when NO₂ was admitted to the reactor the nitrogen experimental signal clearly showed a peak, then decreased with time, eventually approaching its steady state after about 200 s. Such an effect was due to the storage of nitrates, which deactivated the catalyst once produced by the disproportion of NO₂. A second characteristic transient feature was observed at NH₃ shutoff, still at low temperatures: nitrogen production did not drop immediately to zero, but showed a slow decrease. Analogously, the NO₂ signal did not instantly recover its 1,000 ppm inlet concentration level. This effect was caused by the presence of adsorbed ammonia that reacted with NO₂ after the interruption of NH₃ feed. Both these transient phenomena were well predicted by the model, which accounts for adsorption-desorption of both ammonia and nitrates, i.e., the processes dominating the system transient behavior. The ability of reproducing the dynamic behavior of the catalytic system is not only a valuable practical point in view of nonstationary SCR applications, but also represents an important verification of the mechanistic assumptions on which the model is grounded.

The fit of the TRM runs with NO/NO_x feed ratio = 0.5 is shown in Fig. 10.12. For these conditions dominated by the fast SCR reaction (10.35), a satisfactory match between experimental and calculated data was generally observed in the whole temperature range.

Figures 10.11 and 10.13 show the model fit over the six TRM runs with NO/NO_x feed ratio = 0.75 and over the six TRM runs with NO/NO_x feed ratio = 0.33, respectively. The model did a good job in this case, too: the steady state levels were correctly predicted, thus revealing a good estimation of the relative rates of the standard and the fast SCR upon varying the relative feed contents of NO and NO₂.

10.6 Conclusions

This chapter shows the development of an unsteady NH_3 -SCR kinetic model of over a Vanadium-based catalyst. The model was based on the results from an extensive investigation of reactivity, chemistry, catalytic mechanism, and kinetics of the full NH_3 -NO/ NO_2 SCR reacting system over a commercial V_2O_5 - WO_3 / TiO_2 catalyst performed in our laboratories [1–10].

Briefly, it was found that the Fast SCR reaction proceeds via a sequential scheme, which implies NO_2 dimerization, its disproportionation to surface nitrites and nitrates and their successive reactions with NH_3 , with formation of ammonium nitrites and nitrates. Ammonium nitrite then rapidly decomposes to nitrogen, while ammonium nitrate is reduced by NO to nitrites, forming NO_2 [2, 3, 7]. It was further experimentally shown that such a crucial step proceeds via a redox cycle involving the very effective reoxidation of the reduced V-sites by surface nitrates [6, 9]. This explains the higher rate of the Fast SCR reaction as compared to the Standard SCR chemistry, in which the rate limiting catalyst reoxidation is carried out less rapidly by gaseous oxygen [6].

Consistently, the kinetic model herein presented unifies Standard and Fast NH_3 -SCR kinetics according to a single redox scheme. In such a scheme, just one catalyst reduction step is considered, which involves the co-participation of ammonia and NO. As opposite, the rate controlling reoxidation of the V catalyst sites is performed by gaseous oxygen, when NO_x include nitric oxide only, whereas in the presence of NO_2 a much higher reoxidation rate is obtained at low T at the expense of nitrates adspecies formed by NO_2 adsorption onto the catalyst surface. Notably, the mechanistic redox kinetic model based on such assumptions was able to reproduce successfully both the steady-state and transient behavior of the complete NH_3 -NO/ NO_2 SCR reacting system over the full range of NO/ NO_x feed ratios, going from zero (formation of ammonium nitrate from $\text{NH}_3 + \text{NO}_2$) to one ($\text{NH}_3 + \text{NO}$ standard SCR), and including of course the most important NO/ NO_2 equimolar case corresponding to the $\text{NH}_3 + \text{NO} + \text{NO}_2$ Fast SCR reaction.

Acknowledgments Daimler AG is gratefully acknowledged for financial support.

References

1. Ciardelli C, Nova I, Tronconi E, Konrad B, Chatterjee D, Ecke K, Weibel M, *Chemical Engineering Science* (2004) 59:5301–5309
2. Ciardelli C, Nova I, Tronconi E, Chatterjee D, Bandl-Konrad B, *Chemical Communications* (2004) 23:2718–271
3. Tronconi E, Nova I, Ciardelli C, Chatterjee D, Bandl-Konrad B, Burkhardt T, *Catalysis Today* (2005) 105(3-4):529–536
4. Nova I, Ciardelli C, Tronconi E, Chatterjee D, Bandl-Konrad B, *Catalysis Today* (2006) 114(1):3–12

5. Nova I, Ciardelli C, Tronconi E, Chatterjee D, Bandl-Konrad B, *AIChE Journal* (2006) 52(9):3222–3233
6. Tronconi E, Nova I, Ciardelli C, Chatterjee D, Weibel M., *Journal of Catalysis* (2007) 245(1):1–10
7. Ciardelli C, Nova I, Tronconi E, Bandl-Konrad B, Chatterjee D, Weibel M, Krutzsch B, *Applied Catalysis B: Environmental* (2007) 70(1-4):80–90
8. Nova I, Ciardelli C, Tronconi E, Chatterjee D, Weibel M, *AIChE Journal* (2009) 55(6) 1514–1529
9. Nova I, Ciardelli C, Tronconi E, Chatterjee D, Weibel M, *Topics in Catalysis* (2007) 42-43(1-4):43–46
10. Ciardelli C, Nova I, Tronconi E, Ascherfeld M, Fabinski W, *Topics in Catalysis*, (2007) 42-43(1-4):161–164
11. Tronconi E, Nova I, Colombo M, *Ind. Eng. Chem. Res.* (2010) 49(21):10374–10385
12. Lietti L, Nova I, Camurri S, Tronconi E, Forzatti P, *AIChE J.* (1997) 43:2559
13. Finlayson B, *Non Linear Analysis in Chemical Engineering*, (1980) McGraw-Hill, New York
14. Hindmarsh AC, *ACM-Signum Newsletter* (1980) 15:10
15. Donati G, Buzzi-Ferraris G, *Chem. Eng. Sci.*, (1974) 29:1504
16. Madia G, Elsener M, Koebel M, Raimondi F, Wokaun A, *Appl. Catal. B: Environmental* (2002) 39:181
17. Amiridis MD, Wachs IE, Deo G, Jehng J, Kimy DS, *J. Catal.* (1996) 161: 247
18. Busca G, Lietti L, Ramis G, Berti F, *Appl. Catal. B: Environmental* (1998) 18:1
19. Forzatti P, Lietti L, Tronconi E, Nitrogen oxides removal in Industrial. *Encyclopedia of Catalysis*, 2nd Ed., (2010) I.T Horvath (Ed.), John Wiley & Sons, New York
20. Bosch H, Janssen F, *Catal. Today*(1988) 2:369
21. Topsøe NY, Topsøe H, Dumesic JA, *J. Catal.* (1995) 151:226
22. Nova I, Lietti L, Tronconi E, Forzatti P, *Chem. Eng. Sci.* (2001) 56:1229
23. Lietti L, Nova I, Tronconi E, Forzatti P in *Reaction Engineering for Pollution Prevention* M.A. Abraham, R.P. Hesketh (Eds.), Elsevier Science (2000) 85–112
24. Nova I, Lietti L, Tronconi E, Forzatti P, *Catalysis Today*, (2000) 60:73–82
25. Topsøe NY, Dumesic JA, Topsøe H, *J. Catal.* (1995) 151:241
26. Ramis G, Yi L, Busca G, *Catal. Today* (1996) 28:373
27. Lietti L, Alemany JL, Forzatti P, Busca G, Ramis G, Giamello E, Bregani F, *Catal. Today* (1996) 29:143
28. Amiridis MD, Duevel RV, Wachs IE, *Appl. Catal. B* (1999) 20:111
29. Srnak TZ, Dumesic JA, Clausen BS, Tornquist E, Topsøe NY, *J. Catal.* (1991) 135:246
30. Roduit B, Wokaun A, Baiker A, *Ind. Eng. Chem. Res* (1998) 37:4577
31. Lietti L, Nova I, Forzatti P, *Topics in Catalysis*, (2000) 11/12:111–122
32. Willey RJ, Elridge JW, Kittrell JR, *Ind. Eng. Chem. Prod. Res. Dev* (1985) 24: 226
33. Willey RJ, Lai H, Peri JB, *J. Catal.* (1991) 130:319
34. Kapteijn F, Singoredjo L, Dekker NJJ, Moulijn JA, *Ind. Eng. Chem. Res.* (1993) 32:445
35. Koebel M, Elsener M, *Chem. Eng. Sci.* (1998) 53: 657
36. Iwasaki IM, Yamazaki K, Shinjoh H, *Applied Catalysis A: General* (2009) 366:84–92
37. Sjövall H, Blint RJ, Gopinath A, Olsson L, *Industrial & Engineering Chemistry Research* (2010) 49:39–52
38. Malmberg S, Votsmeier M, Gieshoff J, Soger N, Mussmann L, Schuler A, Drochner A, *Topics in Catalysis* (2007) 42–43:33–36
39. Valdes-Solis T, Marban G, Fuertes AB, *Appl. Catal. B.* (2003) 46:261
40. Valdes-Solis T, Marban G, Fuertes AB, *Ind. Eng. Chem. Res.* (2004) 43:2349
41. Wachs IE, Deo G, Weckhuysen BM, Andreini A, Vuurman MA, de Boer M, Amiridis MD, *J. Catal.* (1996) 161:211

42. Grossale A., Nova I., Tronconi E., Chatterjee, D., Weibel, M., *J.Catal.* (2008) 256:312-322
43. Yeom Y, Henao J, Li MJ, Sachtler WMH, Weitz E, *J. Catal.* (2005) 231:181–193
44. Despres J, Koebel M, Kröcker O, Elsener M, Wokaun A, *Appl. Cat. B: Environmental.* (2003) 43:389–395
45. Apostolescu N, Schroder T, Kureti S, *App.Cat. B: Environmental* (2004) 51:43–50
46. Grossale A, Nova I, Tronconi E, *Cat. Today* (2007) 136:18–27

Chapter 11

Lean NO_x Reduction by NH₃ on Fe-Exchanged Zeolite and Layered Fe/Cu Zeolite Catalysts: Mechanisms, Kinetics, and Transport Effects

Michael P. Harold and Pranit Metkar

11.1 Introduction

Rising transportation fuel costs have increased the use of diesel-powered vehicles, which are more fuel efficient than their gasoline counterparts. But the lean diesel exhaust contains NO_x (NO + NO₂) which is notoriously difficult to reduce in the presence of excess O₂. Selective catalytic reduction (SCR) of NO_x with NH₃ generated from onboard hydrolysis of urea has emerged as the catalytic process of choice for reduction of NO_x from the exhaust of medium- and heavy-duty vehicles and engines. Various catalysts have been studied and researched for ammonia-based SCR. The earlier success of Vanadia-based catalysts, such as V₂O₅/WO₃/TiO₂ for stationary source applications, has led to their study for mobile applications [1–8]. However, while the V-based catalyst has very good selectivity to N₂ at temperatures below 500 °C, the catalyst suffers from significant deactivation at higher temperatures that may be encountered during driving conditions. Moreover, the catalyst is volatile at higher temperatures which could lead to the undesirable release of V species. For these reasons, recent research has focused on Fe- and Cu-based zeolite catalysts which are found to have high NO_x activity and selectivity over a wide range of temperatures [9–12]. The performance of Cu- and Fe-zeolite catalysts has been reported in [13–27], respectively. In general, Cu-based catalysts have higher activity at lower temperatures (<300 °C) whereas Fe-based catalysts are more active at higher temperatures (>350 °C). BASF has commercialized the eight-membered ring, small pore Cu-exchanged chabazite zeolite, originally

M. P. Harold (✉) · P. Metkar
Department of Chemical and Biomolecular Engineering, University of Houston, 4800
Calhoun Road, Houston, TX 77204, USA
e-mail: mharold@uh.edu

P. Metkar
DuPont Company, Central Research and Development, Wilmington, DE 19880, USA

discovered by Zones [28]. This catalyst has excellent thermal durability and hydrocarbon tolerance [29, 30]. A related catalyst, Cu-modified SAPO-34, was commercialized during the same period by Johnson-Matthey [31].

The NH_3 -based SCR reaction system involves several overall reactions which we identify in the next section. In order to design new catalysts, it is advantageous to understand the workings of existing Fe-based catalysts. This includes the mechanism and kinetics of the main reactions, potential differences in the composition and structure of catalysts, the influence of transport processes, monolith reactor features and performance, among other factors. To this end, our objective for this chapter is to provide an overview of Fe-exchanged zeolite SCR which spans catalyst, kinetics, and reactor features. We do not delve into detail about the catalyst structure and related matters; these were amply covered in a review by Brandenberger et al. [32] a few years ago. Nor do we get into the detail of SCR reactor modeling; this subject was well covered by a review in the same year by Guthenke et al. [33]. Instead, we present representative kinetics and reactor performance data for the SCR reaction system on Fe-exchanged zeolites. Some of the data are either previously unpublished or are taken from the recent literature. Based on these data, the latest views of the SCR mechanism are discussed and corresponding mechanistic-based kinetic models are compared and contrasted. Recent studies investigating the effect of transport processes on the apparent reaction kinetics and reactor behavior are highlighted as well as recently developed catalysts that combine Fe with another metal such as Cu. Finally, we describe the features and predictive capabilities of SCR monolith reactor models that contain kinetic descriptions of varying complexity together with the applicable transport processes.

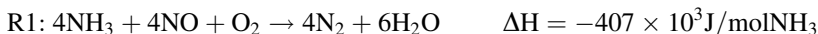
11.2 Reaction System Performance Features

Bench-scale flow reactor experiments are an effective way of examining the main performance features of the SCR reaction system on various catalysts. In this section, we review these features for Fe-based catalysts as a backdrop to considering more fundamental kinetics and mechanistic studies in Sect. 11.3 and transport effects in Sect. 11.4. The selective catalytic reduction of NO_x by ammonia on Fe-ZSM-5 catalyst has been studied in detail by various research groups [19–22, 26, 27, 34–42]. The results from earlier studies of vanadia-based catalysts have underpinned the more recent studies of zeolite-based catalysts. For example, Koebel et al. [3, 6, 43] carried out a detailed study of the SCR chemistry on V-based catalysts. Nova et al. [5, 8, 44, 45] studied the chemistry of SCR over V-based catalyst and proposed a mechanism for the fast SCR reaction. To this end, the data here are by no means unique but are intended to highlight the important trends.

The selective catalytic reduction of gas mixtures containing NO and NO_2 is a complex system involving multiple simultaneous reactions. In order to develop new catalysts and more efficient SCR converters, knowledge of the main reaction

system features and underlying kinetics is essential. Representative performance data presented later in this section are interpreted with the main global reactions in mind. To this end, the selective catalytic reduction of NO/NO₂ by NH₃ involves following three main reactions that lead to the desired N₂ product:

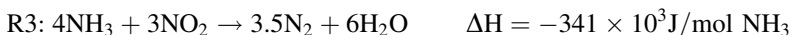
- *Standard SCR Reaction:* This reaction involves NO and NH₃ reacting in presence of O₂: (The heat of the reaction is estimated using standard heats of formation of the reacting and product species with H₂O in gaseous form.)



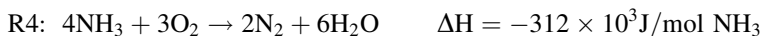
- *Fast SCR Reaction:* When both NO and NO₂ in the feed react simultaneously to produce N₂ and H₂O; it is called as “fast SCR” reaction (2) because it is much faster than the standard SCR reaction (1):



- *NO₂ SCR Reaction:* This involves the reaction between NO₂ and NH₃ and unlike the standard and fast SCR reactions it has a 4:3 NH₃:NO₂ stoichiometry:



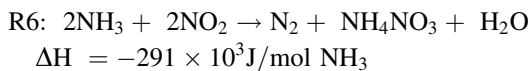
Along with the three desired N₂-selective reactions, a number of side reactions occur which result in the undesired consumption of NH₃ or generation of by-products other than N₂, principally N₂O, NH₄NO₃, and HNO₃. NH₃ oxidation is an important side reaction occurring at temperature exceeding 350 °C on Fe-based catalysts. This reaction is undesired since it competes with the selective SCR reactions for the reductant ammonia. On the Fe-zeolite catalysts, NH₃ is selectively oxidized to N₂ by:



On the other hand, the oxidation of NO to NO₂ occurs in the temperature range of interest ($T > 150$ °C):



This reaction is desirable because NO₂ is more effectively reduced by NH₃ than is NO. The existence of NO₂ complicates the reaction system. In particular, the net formation of ammonium nitrate occurs at lower temperatures (ca. 275 °C) as described in detail later:



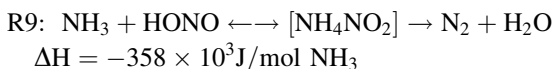
Mechanisms involving ammonium nitrate are described in several papers [3, 4, 8, 19, 27, 46, 47]. Koebel and coworkers [1, 3, 4] showed that the first step in this chemistry is NO₂ dimerization



The N₂O₄ thus formed reacts with water to form nitrous and nitric acids



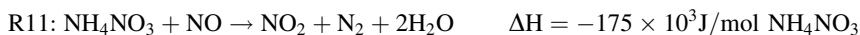
HONO and NH₃ further react to form ammonium nitrite which is unstable above 100 °C, decomposing to N₂ and H₂O



The formation of NH₄NO₃ can also occur by the reaction between NH₃ and HNO₃



The reduction of nitrates by NO has been proposed to be a rate-determining step in the fast SCR chemistry for V-based catalysts [5, 48]:

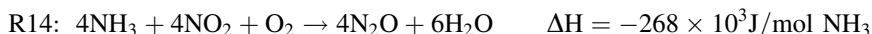


This was later confirmed for Fe-based zeolite catalysts by Grossale et al. [27] and Iwasaki et al. [26]. The importance of nitrate reduction was independently revealed by Yeom et al. [49].

Ammonium nitrate decomposes to N₂O at higher temperatures (≥200 °C):



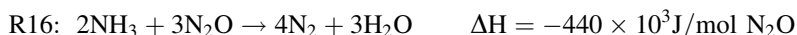
N₂O is a greenhouse gas and therefore is an undesired by-product and is expected to be controlled in the coming years. N₂O formation also occurs by the overall reaction



The N₂O decomposes to N₂ and O₂ at higher temperatures:



Finally, Devadas et al. [34] studied the fate of N₂O on Fe-ZSM-5. They observed that ammonia may react with N₂O according to

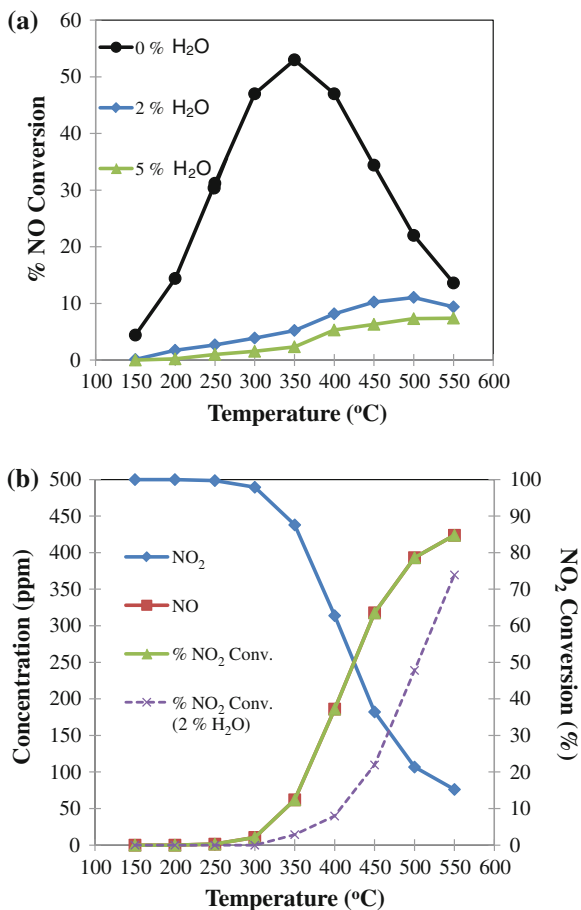


11.2.1 NO Oxidation and NO₂ Decomposition

The NO oxidation reaction has been studied by a number of groups, earlier for V-based catalysts by Suárez et al. [50] and more recently for Fe- and Cu-based catalysts. As mentioned above, the formation of NO₂, when the feed is devoid of NO₂, has been considered an important overall reaction in the SCR system. Earlier studies argued that NO oxidation to NO₂ is an important if not rate-determining step for standard SCR [20, 51, 52]. Metkar et al. [42] suggested, consistent with similar proposals from others for Fe [26] and Cu [53], that the formation of adsorbed NO₂ is the rate-determining step. More recently, Tronconi et al. [54] proposed that NO oxidation to gaseous NO₂ is not the rate-determining step based on a comparison of its rate to that of standard SCR in the absence and presence of H₂O over Fe- and Cu-based zeolites. Schwidder et al. [21] also argued that the formation of gas phase NO₂ cannot be the rate-determining step for standard SCR over Fe-zeolites. This debate about the mechanism encourages a detailed evaluation of the reaction and differences in the activities of various SCR catalysts over a range of conditions. Here we highlight the main features on a commercial Fe-zeolite and synthesized (at UH) Fe-ZSM-5 monolithic catalyst.

NO oxidation displays a distinct maximum in conversion as a function of temperature (Fig. 11.1a). The reaction is kinetically limited up to about 300 °C, beyond which it becomes equilibrium limited due to NO₂ decomposition, a trend that is well-known in the Pt-catalyzed system [55]. The reaction is significantly inhibited by the large excess of H₂O found in exhaust streams. Specifically, when water is added to the mixture of NO and O₂ the rate of NO₂ production drops precipitously. Figure 11.1a shows up to a 90 % drop in the NO conversion over a range of temperatures. The importance of the reverse reaction is seen in Fig. 11.1b, which shows the conversion of NO₂ by decomposition as a function of temperature. These data reveal that the decomposition commences at about 300 °C and becomes more pronounced at higher temperatures, with about 85 % of the NO₂ decomposed by a temperature of 550 °C. The decomposition, like the forward reaction, is significantly inhibited by H₂O. Experiments with a feed mixture of NO, NO₂, and O₂ show the decomposition commencing at a somewhat higher temperature (350 °C in the data shown in Fig. 11.2a reported by Metkar et al. [56]). A focused experiment was carried out to examine more closely the effect of the product NO₂ on the NO oxidation conversion through the incremental addition of NO₂ to a NO + O₂ feed mixture. Figure 11.2b shows a decrease in the conversion with added NO₂ at temperatures in which the rate of NO₂ decomposition was negligible. The dependence reveals that the conversion is a decreasing function of supplemental NO₂, showing that NO₂ inhibits the NO oxidation. We return to this point later.

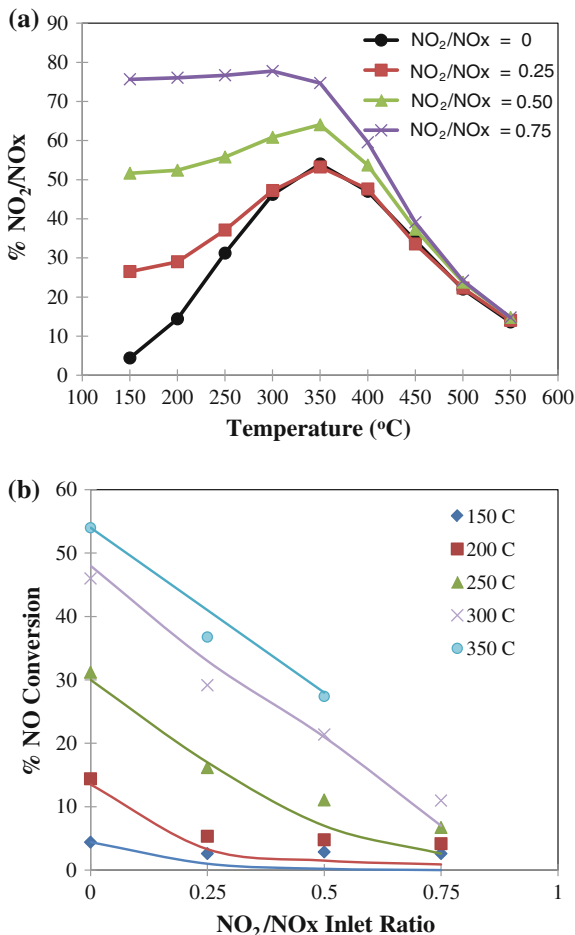
Fig. 11.1 a Steady-state conversion of NO versus catalyst temperature during the NO oxidation for different H₂O feed concentrations. Inlet feed: 500 ppm NO, 5 % O₂, 0 or 2 or 5 % H₂O. Total flow: 1,000 sccm, Balance gas: Ar. **b** Steady-state conversion of NO₂ versus catalyst temperature during its decomposition. Feed: 500 ppm NO₂, 0–2 % H₂O. Total flow: 1,000 sccm. Space velocity: 57,000 h⁻¹. Balance gas: Ar. (Adapted from Metkar et al. [42] and used with permission.)



11.2.2 NH₃ Oxidation

The oxidation of NH₃ occurs on Fe-exchanged catalysts and contributes to less than 100 % conversion of NO_x at high temperature due to the consumption of the reductant. Figure 11.3 compares a commercial Fe-zeolite catalyst with an as-synthesized Fe-ZSM-5 catalyst (18 wt.% washcoat loading) in the absence of water in the feed. The two catalysts give nearly identical results. The addition of 2 % H₂O in the feed leads to a modest decrease in the NO conversion for the commercial catalyst. As we show later, this modest Fe activity can be exploited in dual component SCR catalyst formulations in which the other metal (Cu) is a much more active ammonia oxidation catalyst.

Fig. 11.2 a Steady-state outlet NO₂/NOx concentration ratio versus temperature during the NO oxidation reaction with several different feed compositions Inlet feed: 500 ppm NOx (NO + NO₂), 5 % O₂. Total flow: 1,000 sccm. Balance gas: Ar. **b** Steady-state NO conversion during NO oxidation versus NO₂/NOx feed ratio for several temperatures. (Adapted from Metkar et al. [56] and used with permission.)

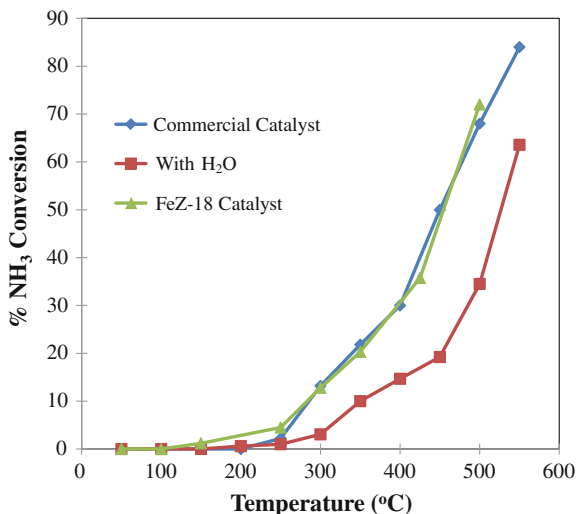


11.2.3 Selective Catalytic Reduction of NOx

The selective catalytic reduction of NOx by ammonia on Fe-zeolite catalysts displays interesting performance trends over a range of temperatures and NO/NO₂ feed ratios. Feeds containing various NO₂/NOx inlet ratios (0–1) provide insight into the effect of NO₂ which can be appreciable on Fe-exchanged catalysts.

The features of the standard SCR reaction (R1) system (feed devoid of NO₂) are first highlighted. A typical temperature sweep experiment (Fig. 11.4a) shows the changes in the effluent concentrations as a function of temperature when a dry feed containing equal concentrations of NO and NH₃ (NO = NH₃ = 500 ppm) in excess O₂ was passed over an Fe-ZSM-5 catalyst. Negligible NO conversions (<20 %) were observed up to 250 °C. At a temperature of about 300 °C there is a nonlinear increase in NO conversion, which approaches 91 % at 450 °C. The NH₃

Fig. 11.3 Comparison of the steady-state ammonia converted during the ammonia oxidation on commercial and FeZ-18 catalysts. Effect of water on ammonia oxidation reaction is studied on the commercial catalyst. Feed: 500 ppm NH₃, 5 % O₂, and 0 or 2 % water. Total flow rate: 1,000 sccm. Balance gas: Ar. (Adapted from Metkar et al. [42] and used with permission.)

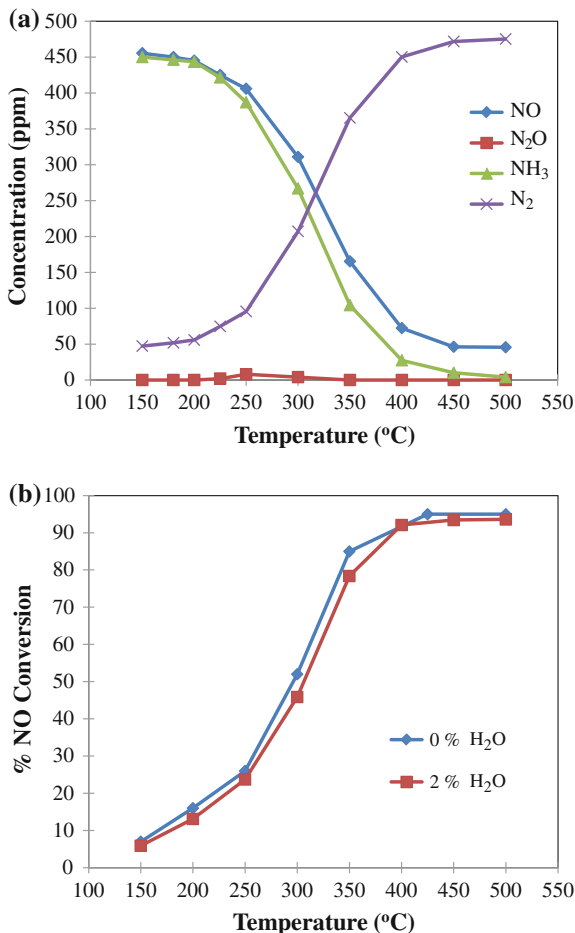


conversion always exceeds the NO conversion (for $T \geq 300$ °C) because of the aforementioned NH₃ oxidation side reaction. A negligible N₂O yield (<10 ppm) was observed in the temperature range of 250–300 °C. When H₂O was added (2 %) there was only a negligible decrease in the NO conversion (Fig. 11.4b), unlike the much larger effect of H₂O for the oxidations of both NO and NH₃ on the same catalyst. We return to this difference later as it provides clues about the SCR mechanism.

The addition of NO₂ to the feed leads to significant changes in the reactant conversions and product distribution. Figure 11.5a shows the results obtained when a NO₂/NO_x feed ratio of 0.25 (total NO_x concentration and NH₃ both at 500 ppm) in the presence of 5 % O₂ and no H₂O is contacted on the FeZSM-5 catalyst. It is interesting to note that the apparent NO₂ conversion is essentially complete for the entire temperature range. A substantial increase in the NO_x conversion is encountered at lower temperatures compared to that of the standard SCR reaction, and N₂ is the only N-containing product under these conditions. The N-balance is satisfied over the entire temperature range which rules out the formation of any undetected by-products like ammonium nitrate. (We return to this issue later.). A stoichiometric consumption (1:1) of NO_x and NH₃ is observed up to 250 °C; beyond this point the ammonia consumption exceeds the NO_x conversion due to the ammonia oxidation side reaction, although the difference does not exceed 20 ppm. This parasitic NH₃ oxidation has been observed in other studies and is thought to be a result of an enhancing effect of NO_x on the ammonia oxidation that would otherwise not be encountered. In contrast to the standard SCR results, these data indicate that the ammonia oxidation side reaction is less detrimental to the overall NO_x conversion in the presence of NO₂. A negligible production of N₂O and complete conversion of NO₂ occurred at all temperatures. The amount of NO consumed is comparable to the amount of NO₂ consumed up to

Fig. 11.4 a Steady-state product distribution versus temperature for standard SCR on commercial Fe-zeolite catalyst. Space velocity 57,000 h⁻¹. Total Flow rate = 1,000 sccm. Balance gas: Ar. Feed: 500 ppm NO, 500 ppm NH₃, 5 % O₂.

b Effect of water on standard SCR reaction carried out on the commercial Fe-zeolite catalyst. Inlet feed: 500 ppm NH₃, 500 ppm NO, 5 % O₂, and 0 or 2 % H₂O. Total flow: 1,000 sccm. Balance gas: Ar. (Used with permission [42].)



225 °C. The consumption of equimolar amounts of NO and NO₂ suggests that the fast SCR reaction is the main reaction taking place at these low temperatures and is therefore much faster than the standard SCR reaction. At temperatures above 250 °C, an additional quantity of NO is consumed due to the increase in the standard SCR reaction rate. Finally, although not shown here, when water was added to the feed (2 %), it was found to have only a negligible effect on NO_x conversions at most of the temperatures.

When the feed contains equal amounts of NO and NO₂, this corresponds to the stoichiometry of the fast SCR reaction (R2). Typical results obtained for Fe-ZSM-5 catalyst are shown in Fig. 11.5b using a feed devoid of H₂O. The chemistry proceeds much faster than the standard SCR reaction. Very high NO_x conversion is obtained at temperatures as low as 180 °C; e.g., a NO_x conversion of 74 % was obtained at 180 °C. N₂ is the main product of this reaction with a negligible

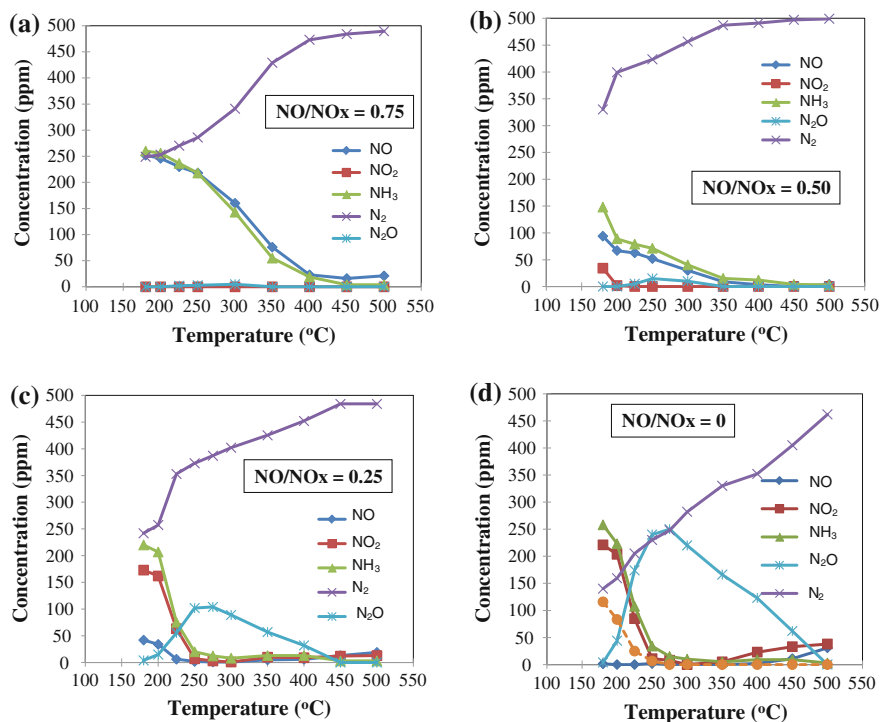


Fig. 11.5 Steady-state product distribution obtained for SCR of NO_x with NH₃ as a function of temperature. Space velocity 57,000 h⁻¹. Total Flow rate = 1,000 sccm. Balance gas: Ar. Feed: 500 ppm NH₃, 5 % O₂. **a** 375 ppm NO, 125 ppm NO₂; **b** 250 ppm NO, 250 ppm NO₂; **c** 125 ppm NO, 375 ppm NO₂; **d** 0 ppm NO, 500 ppm NO₂

amount of N₂O (<20 ppm) obtained in the 250–300 °C range. Ammonia is consumed in nearly equimolar amounts as that of NO_x. This suggests that the oxidation of ammonia by O₂ is not as important as it is for standard SCR. Similar trends for the fast SCR reaction were reported in the literature on Fe-zeolite and other catalysts [1, 3, 5, 6, 14, 25, 34, 36]. There are two notable trends. First, the amount of NO₂ consumed exceeds the amount of NO consumed up to about 300 °C. Since the stoichiometry of the fast SCR reaction (R2) involves an equimolar consumption of NO and NO₂, this means that NO₂ is consumed by another reaction. Second, there is a lack of closure of the overall N-balance; i.e., not all of the N atoms fed are accounted for in the product. These trends are related. The likely culprit is the ammonium nitrate (AN) formation by reaction (R6). AN deposits as a solid onto the surface and cannot be detected in the gas phase by FTIR but can be detected by the FTIR postmortem [5], obviously not as straightforward as in situ gas phase FTIR [3, 5, 6, 27, 34, 36]. For the NO/NO_x = 0.5 feed there was ca. 64 and 42 ppm of N missing at the temperatures of 180 and 200 °C, respectively. This implies the formation of 32 and 21 ppm

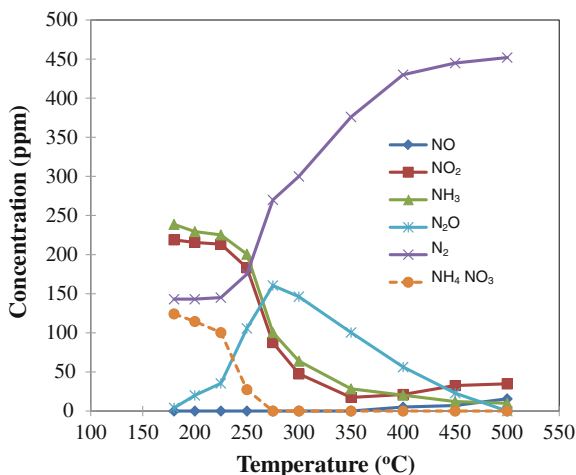
NH₄NO₃, respectively. The N-balance approached closure with increasing temperature such that by 250 °C there was no net ammonium nitrate formation. Finally, the effect of H₂O was examined for this fast SCR reaction system. Similar to the standard SCR reaction, water was found to have a negligible effect.

At still higher NO₂ feed fractions (NO/NO_x = 0.25), the NO_x reduction activity of Fe/ZSM-5 remains high but shows signs of declining from its peak level (Fig. 11.5c). About 55 % of the NO₂ is converted in the temperature range of 180–200 °C. By 250 °C, the NO₂ conversion increases sharply to >98 %. However, above 350 °C the NO₂ conversion decreases; by 500 °C the NO_x conversion is 93 % and the effluent NO concentration increases to 20 ppm. As before, at higher temperatures the NH₃ consumption exceeds the NO_x consumption due to NH₃ oxidation (reaction R4). An added feature is the more pronounced production of N₂O at lower temperatures. As in the fast SCR case, the N-balance did not close at lower temperatures (<250 °C), which as described earlier infers the formation of ammonium nitrate. The imbalance of N accounted for an estimated 56 ppm of NH₄NO₃ formed at 180 °C. By 250 °C, the inferred concentration decreased to 9 ppm. At higher temperatures the N-balance closed, suggesting the complete decomposition of ammonium nitrate. The maximum N₂O concentration occurred at 275 °C for this NO₂/NO_x = 0.75 feed. The decrease in N₂O at higher temperatures is attributed to either its decomposition to N₂ (R15), to its reaction with NH₃ (R16), or to an increase in the rate of NO₂ SCR (R3). Most likely, a combination of these factors contributes to these trends. By 450–500 °C, N₂ was the only N-containing product.

A pure NO₂ feed (NO₂/NO_x = 1) is a special case in which the standard and fast SCR chemistries are essentially turned off, at least at temperatures below the decomposition of NO₂ (<400 °C). The so-called “NO₂ SCR” reaction (R3) is dominant under these conditions. This reaction to desired product N₂ has NH₃:NO₂ ratio of 1.33, unlike the NH₃:NO_x = 1 ratio for the standard and fast SCR reactions. The by-products N₂O and NH₄NO₃ are more prevalent compared to their yields at lower NO₂:NH₃ ratios. The integral product distribution data for a dry NO₂ + NH₃ feed is shown in Fig. 11.5d. About 60 % NO₂ conversion is achieved at temperatures as low as 180–200 °C. The N-balance did not close under these conditions (ca. 230 ppm was missing in the N-balance at 180 °C), once again indicating the formation of undetected ammonium nitrate. The N-balance inferred that about 115 and 83 ppm of NH₄NO₃ was formed at 180 and 200 °C, respectively. The yields of N₂ and NH₄NO₃ suggest that reaction R6 is the main global reaction occurring under these conditions. A significant amount of N₂O was detected in the temperature range of 225–450 °C. There was a sudden increase in the N₂O concentration from 200 to 250 °C. The maximum amount of N₂O (ca. 250 ppm) occurred at 275 °C. The fate of N₂O at higher temperatures is discussed in more detail later.

The data reveal a significant decrease in the NO₂ concentration between 200 and 250 °C at which point nearly 97 % conversion is achieved. This trend is attributed to an enhanced NO₂ SCR reaction rate. Indeed, the presence of effluent NO clearly indicates the decomposition of NO₂ (reaction R5) while incompletely converted

Fig. 11.6 Steady-state product distribution obtained during NO_2 SCR as a function of temperature. Space velocity $57,000 \text{ h}^{-1}$. Total Flow rate = 1,000 sccm. Balance gas: Ar. Feed: 500 ppm NO_2 , 500 ppm NH_3 , 5 % O_2 , and 2 % H_2O



NO_2 suggests depletion of NH_3 . Very high NO_2 conversions ($\sim 95\%$) are obtained in the temperature range of 250–350 °C but the NO_2 conversion dropped below 90 % at higher temperatures ($T > 400$ °C). Again, this is attributed to the NO_2 decomposition. At still higher temperatures (> 350 °C), NH_3 is consumed in somewhat larger amounts compared to NO_2 , the signature of ammonia oxidation. Essentially, O_2 competes with NO_2 as an oxidant of NH_3 . In contrast, under the fast SCR conditions (equimolar feed NO and NO_2) complete conversion of NO_x is obtained at temperatures of 350 °C and higher. The difference in NO_2 and NH_3 consumption also points to the 4:3 NH_3 : NO_2 stoichiometry of reaction R3.

The NO_2 SCR reaction system was also carried out in the presence of 2 % H_2O on the Fe-ZSM-5 catalyst. The product distribution (Fig. 11.6) indicates some inhibition of the NO_2 SCR reaction by water. The inhibition is more pronounced in the temperature range of 200–300 °C. A possible reason for this result is that water blocks active sites required for NO_2 SCR. It is also noted that the amount of N_2O , probably generated by the decomposition of NH_4NO_3 , decreases in the presence of water. This may suggest that NH_4NO_3 decomposes to NH_3 and HNO_3 (reverse reaction or R10 instead of (R13)) in the presence of H_2O [34].

The experiments with feeds containing NO_2 lead to the generation of N_2O as an important by-product, especially when the feed contains more NO_2 than NO . A negligible amount (< 20 ppm) of N_2O is obtained up to $\text{NO}_2/\text{NO}_x = 0.5$; i.e., standard and fast SCR. For higher NO_2/NO_x feed ratios (> 0.5), the N_2O yield is prominent for a narrow range of temperatures, as shown in Figs. 11.5d and 11.6 for the NO_2 -only feed without and with H_2O , respectively. The increase in N_2O with temperature parallels a decrease in the unaccounted-for N, suggesting that N_2O is formed via NH_4NO_3 decomposition (reaction R3). The formation of N_2O is balanced by its consumption, leading to a maximum in the N_2O yield. For example, for NO_2/NO_x feed ratios exceeding 0.75, a maximum N_2O is obtained at

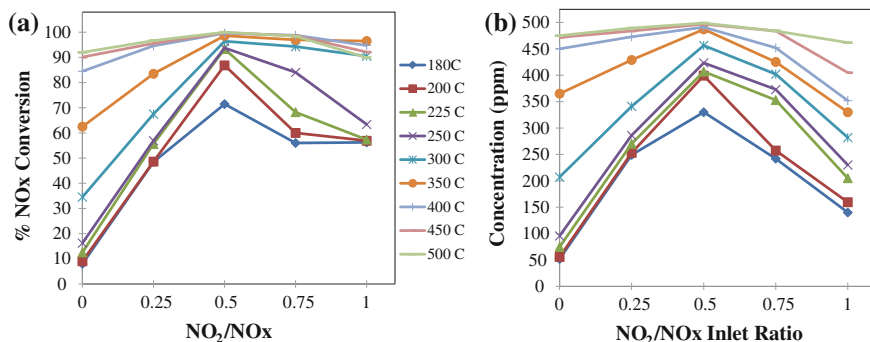


Fig. 11.7 **a** Effect of NO₂/NO_x feed ratios and catalyst temperature on the NO_x conversion on FeZ-18 catalyst. Space velocity 57,000 h⁻¹. Total Flow rate = 1,000 sccm. Balance gas: Ar. Feed: 500 ppm total NO_x, 500 ppm NH₃, 5 % O₂, and 2 % H₂O. **b** Effect of NO₂/NO_x feed ratio on N₂ selectivity

about 275 °C. The sharp decrease in N₂O yield with temperature is attributed to two factors:

- The rates of the N₂ selective reactions, i.e., NO₂ SCR, fast SCR, and standard SCR, increase with temperature, and as a result the side reactions responsible for N₂O production decrease.
- The N₂O itself decomposes to N₂ by reaction R15 and hence its effluent concentration decreases at higher temperatures.

The second reason appears more likely. Devadas et al. [34] observed that N₂O decomposes to N₂ and O₂ starting at 350 °C. Our results show that there was no N₂O in the outlet at temperatures above 450 °C. Another possibility for N₂O consumption is reaction with NH₃ (reaction R16). Devadas et al. found that the presence of NH₃ increased the rate of N₂O decomposition. More recently, Colombo et al. [57] reported on data and kinetic modeling for N₂O decomposition and N₂O reduction by NH₃ on Fe-zeolites. In our experiments, we obtained very high NO_x conversions (>90 %) for dry feeds and temperatures ≥250 °C. NH₃ consumption was nearly 100 % for these temperatures and hence it was difficult to determine how much NH₃ was involved in the reduction of N₂O (R16) and how much NH₃ was oxidized to N₂ (reaction R4). Similar trends for N₂O production on Fe-zeolite and other catalysts were reported in the literature [2, 25, 34, 36].

It is clear that the NO₂/NO_x ratio is a critical parameter affecting SCR catalyst performance. The ratio has important effects on both the overall NO_x conversion and the product distribution. The effects of NO₂/NO_x ratio and temperature on the overall NO_x conversion and N₂ yield (concentration) are shown in Fig. 11.7a and b respectively, for a wet feed (2 % H₂O). The conversion data (Fig. 11.7a) show a significant enhancement effect of NO₂ on the deNO_x efficiency of the Fe-ZSM-5 catalyst at lower temperatures. At low temperature (180 °C), negligible NO_x reduction (<15 %) occurs for the standard SCR reaction. Introduction of 125 ppm

NO_2 increased this value to 50 % while for an equimolar feed the conversion increased to 74 %. This enhancement is attributed to the fast SCR chemistry for which NO_2 is the limiting reactant. As we discuss below, the standard SCR reaction may require the formation of NO_2 to produce N_2 . Thus, feeding NO_2 removes this limitation. However, a further increase in NO_2 ($\text{NO}_2/\text{NO} > 1$) leads to a decrease in the NO_x conversion to about 55 % for the pure NO_2 feed. Similar trends were observed for 200 °C. As mentioned earlier, water has a negligible effect on NO_x reduction up to the NO_2/NO_x feed ratio of 0.5. But for NO_2/NO_x feed ratios exceeding 0.5, some inhibition on the NO_x reduction was observed in the temperature range of 200–300 °C. The optimum NO_2/NO_x ratio for maximum NO_x conversion is 0.5 (fast SCR reaction) for the wet feeds, in line with previous literature studies [34, 36].

Along with de NO_x efficiency, it is important to achieve a maximum yield and/or selectivity of desired product N_2 . The effluent N_2 concentrations indicate that the equimolar feed ($\text{NO}_2/\text{NO}_x = 0.5$) is optimal in terms of N_2 selectivity over the entire temperature range for both the dry and wet feeds (e.g. Figs. 11.5, 11.7b). Unlike the NO_x conversion, the N_2 production is a monotonic function of temperature for a fixed NO_2/NO_x ratio. This feature suggests the by-product pathways emerge for nonequimolar feeds. Taken together, Fig. 11.7a (NO_x conversion) and b (N_2 yield) show that the equimolar NO/NO_2 feed achieves both a high conversion and N_2 selectivity. As NO_2/NO_x is decreased below 0.5, the conversion decreases because less NO_2 is available to react with NH_3 and NO via the fast chemistry. As a result, the slower standard SCR chemistry takes over and the conversion declines. For $\text{NO}_2/\text{NO}_x > 0.5$, the emergence of both ammonium nitrate and NO_2 decomposition impact the overall NO_x conversion. For temperatures less than 250 °C, the ammonium nitrate is not completely decomposed and inhibits the NO_x reduction. For higher temperatures (≥ 350 °C) some NO_2 decomposition occurs along with 3:4 $\text{NO}_2:\text{NH}_3$ stoichiometry of NO_2 SCR, leading to a reduction in the NO_x conversion. Ammonia oxidation also emerges at these temperatures. Thus, for temperatures of 350 °C and higher, the highest de NO_x conversion was observed for the feed ratio of NO_2/NO_x of 0.5; i.e., fast SCR reaction. The fast and standard SCR reactions are clearly beneficial for N_2 formation whereas the pathways to and through ammonium nitrate leads to non-negligible amounts of N_2O . Considering all these factors, a NO_2/NO_x ratio of 0.5 proves to be the ideal ratio that achieves maximum NO_x removal efficiency and highest product selectivity toward N_2 . Similar steady-state results were reported in the literature [12, 34, 36, 58].

11.3 Kinetics and Mechanistic Considerations

The catalytic reaction system containing NO , NO_2 , NH_3 , O_2 , and H_2O on Fe-exchanged zeolites is quite complex as it involves multiple reaction pathways to several products (N_2 , N_2O , NH_4NO_3), on catalysts with multiple adsorption sites (Bronsted acid sites, metal-exchanged sites), complicated by rate inhibition

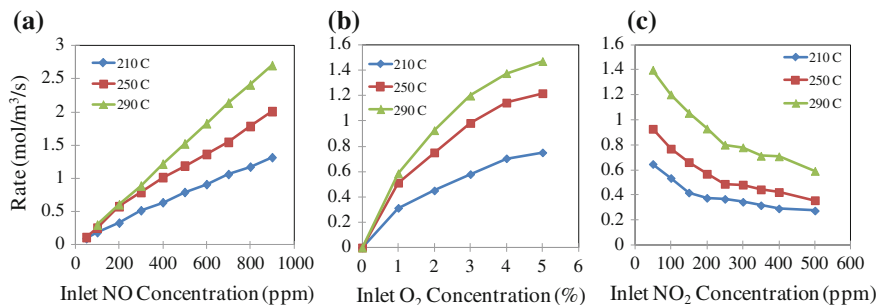


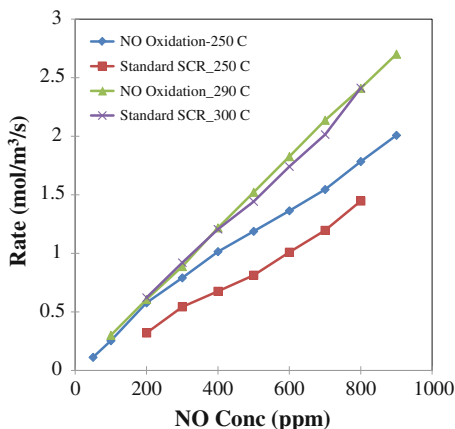
Fig. 11.8 Dependence of differential rate on NO, O₂, and NO₂ during NO oxidation on Fe-ZSM-5. (Adapted from Metkar et al. [56] and used with permission.)

(by NH₃ and NH₄NO₃) and solid deposits (NH₄NO₃) at low temperature, and diffusion limitations (intracrystalline, washcoat) at higher temperatures. In this section we present some of the key kinetics findings, and highlight the current understanding about mechanistic-based kinetics. We will first consider the standard SCR reaction and then proceed to systems containing NO₂ in the feed.

11.3.1 NO Oxidation

Several studies have argued that the oxidation of NO to NO₂, either as a product species in the gas phase or an intermediate adsorbed on the surface, are plausible rate-determining steps for the standard SCR reaction on Fe-exchanged zeolites. If this is the case, then an important first step toward developing a mechanistic-based kinetic model for standard SCR is to establish one for NO oxidation. Metkar et al. [59]. measured the activation energy and reaction orders for NO oxidation on Fe-ZSM-5 (Fig. 11.8). The rate data, which were obtained under differential conditions (fractional conversion, $X_{\text{NO}} < 0.15$) at three different temperatures and in the absence of H₂O, revealed apparent reaction orders of 1, 0.5, and -0.3 with respect to NO, O₂, and NO₂, respectively. The inhibition by NO₂ of the forward NO oxidation is not a result of the reversible NO₂ decomposition because that reaction was shown to be negligible at these temperatures. The activation energy was determined to be 39 kJ/mole for the kinetics measurements below 300 °C. The investigators ruled out the existence of washcoat or external transport limitations in this temperature range. In another study, Metkar et al. [42]. showed that the rate of NO oxidation in the absence of H₂O is very close to that of the standard SCR reaction. Figure 11.9 shows the near overlap of the differential rates of NO oxidation and standard SCR at 290–300 °C. The divergence of the two rates at lower temperature is explained by NH₃ inhibition of the SCR reaction, as we elaborate on later. The same study reported that apparent activation energies for the two reactions are quite similar; 39 kJ/mole for NO oxidation and 42 kJ/mole

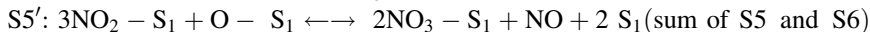
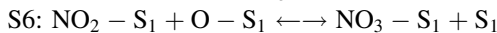
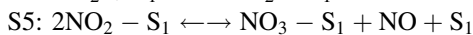
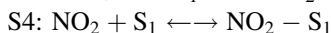
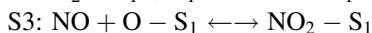
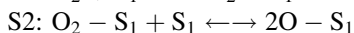
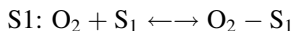
Fig. 11.9 Comparison of differential rates of NO oxidation and standard SCR reaction at two different temperatures. (Used with permission [42] and used with permission.)



for standard SCR. The investigators concluded that the experimental evidence was sufficiently compelling that at the very least the formation of surface-bound NO_2 or related species is the rate-limiting step for standard SCR reaction chemistry.

To this end, it is instructive to compare and contrast two models that have been communicated recently for NO oxidation. The first model is one developed by Harold, Balakotaiah and coworkers and is based on a Langmuir–Hinshelwood framework; it is referred to as the “LH” model. The second model, developed by Tronconi, Nova and coworkers, is based on a redox framework and is referred to as the “Redox” model.

The LH Model comprises the following steps for NO oxidation on Fe-ZSM-5:



where S_1 denotes an Fe exchange site on the zeolite (Fe-), and therefore $\text{O}-\text{S}_1$, NO_2-S_1 , and NO_3-S_1 denote an oxygen adatom, adsorbed NO_2 (or nitrite precursor), and nitrate, respectively. The existence of these species is supported by IR measurements and other data, although the situation is potentially more complicated than the listed steps. For example, in an earlier study on protonated pentasil zeolites, Eng and Bartholomew [60] showed in situ IR data confirming the presence of a NO_2 -type intermediate on the surface. Rivallan et al. [61] provided “indirect and convincing evidence” for the presence of adsorbed oxygen. Fedeyko et al. [62] provided IR spectroscopic evidence for nitrite/nitrate and nitro groups on Fe-exchanged zeolites and showed that the nitro group is the more reactive of the two. Iwasaki and Shinjoh [63] described a mechanism for nitrate formation that

involves a bi-nuclear site in which NO₂ couples with O positioned between adjacent Fe atoms. Their model considers NO₂ an important surface species. Sachtler et al. [64] proposed that the dimer species N₂O₄, produced via reaction R7, disproportionates on the catalyst surface, yielding NO⁺ and NO₃⁻. A variant on this mechanism is the production of N₂O₃ through the equilibrium reaction of NO and NO₂ [65]. Subsequently, N₂O₃ disproportionates into NO⁺ and NO₂⁻, both of which are thought to be reactive NO_x surface species upon the addition of NH₃. Given these observations, additional steps and surface species may be warranted in the above six-step LH model.

Now, assuming the reaction between gas phase NO and adsorbed oxygen forming surface-bound NO₂ (S3) is the rate-determining step and all other steps are at equilibrium (including step S5', the sum of S5 and S6), the following rate expression is derived:

$$R_{\text{NO}_{\text{oxi}}} = k_{f3} \sqrt{K_1 K_2} \left(X_{\text{NO},s} \sqrt{X_{\text{O}_2,s}} - \frac{X_{\text{NO}_2,s}}{K_{\text{eq}}} \right) \theta_v \quad (11.1)$$

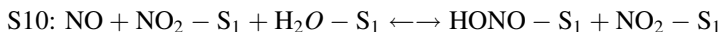
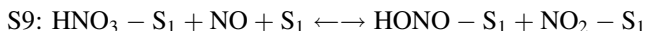
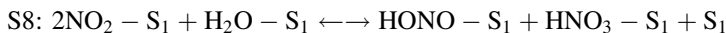
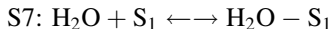
which, upon solving for θ_v , gives the following rate expression:

$$R_{\text{NO}_{\text{oxi}}} = \frac{k_{f3} \sqrt{K_1 K_2} \left(X_{\text{NO},s} \sqrt{X_{\text{O}_2,s}} - \frac{X_{\text{NO}_2,s}}{K_{\text{eq}}} \right)}{1 + K_1 X_{\text{O}_2,s} + \sqrt{K_1 K_2 X_{\text{O}_2,s}} + K_4 X_{\text{NO}_2,s} + \sqrt{\frac{K_5 K_4^2 X_{\text{NO}_2,s}^2 \sqrt{K_1 K_2 X_{\text{O}_2,s}}}{X_{\text{NO},s}}}} \quad (11.2)$$

This complex expression predicts the correct reaction orders and trends in NO oxidation data over a wide range of conditions, such as inhibition by adsorbed NO₂. It is interesting to note that the tuned model predicts that the coverage of the nitrates (NO₃-S₁) is only important at lower temperature and that the four-step model is adequate for predicting steady-state kinetics. Indeed, Yeom et al. [49] argued that nitrites are more reactive than nitrates during SCR to the extent that ammonium nitrate effectively “traps” a NO_x molecule as a less reactive species. These points lead to the following simplified rate expression, stressing again that this result is valid when H₂O is absent:

$$R_{\text{NO}_{\text{oxi}}} = \frac{k_{f3} \sqrt{K_1 K_2}}{1 + K_1 X_{\text{O}_2,s} + \sqrt{K_1 K_2 X_{\text{O}_2,s}} + K_4 X_{\text{NO}_2,s}} \left(X_{\text{NO},s} \sqrt{X_{\text{O}_2,s}} - \frac{X_{\text{NO}_2,s}}{K_{\text{eq}}} \right) \quad (11.3)$$

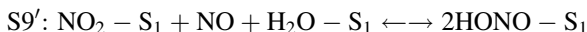
The situation is more realistic but more complex in the presence of H₂O. Ahrens et al. [66], pointed out that the formation of nitrates is suppressed through the generation of nitric and nitrous acids. They reported that gas phase NO₂ is effectively removed due to the presence of the acids on the surface at near-ambient conditions. They and others have referred to the well-known chemistry when NO₂ is contacted with H₂O and leads to a mixture of nitrous and nitric acids, which occurs in the upper atmosphere [66, 67]. Some of the more important steps are as follows:



Note that these steps have been written as surface-catalyzed reactions; Ahrens et al. [66] pointed out these steps may also occur in the gas phase. Ross and DeVore [68] showed that HNO_3 desorbs from boehmite at temperatures up to ca. 180 °C. In essence, the additional steps involving water direct the pathways toward a mixture of acids and away from surface nitrites/nitrates. Keeping with the same RDS assumption (step S3), the following rate expression is obtained for θ_v :

$$\theta_v = \frac{1}{1 + K_1 X_{\text{O}_2,s} + \sqrt{K_1 K_2 X_{\text{O}_2,s}} + K_4 X_{\text{NO}_2,s} + K_7 X_{\text{H}_2\text{O},s} + \sqrt{K_4 K_{10} K_7 X_{\text{NO}_2,s} X_{\text{NO}_2,s} X_{\text{H}_2\text{O},s}} + \frac{K_4^2 K_7 K_8 X_{\text{NO}_2,s} \sqrt{X_{\text{H}_2\text{O},s}}}{\sqrt{K_4 K_7 K_{10} X_{\text{NO}_2,s} X_{\text{NO}_2,s}}}} \quad (11.4)$$

Upon the substitution of Eq. (11.4) into (11.1), the resulting rate expression shows the contributions of three new species, $\text{H}_2\text{O}(\text{ad})$, $\text{HONO}(\text{ad})$, and $\text{HNO}_3(\text{ad})$, in the denominator. A simplification of the rate expression is possible if it is assumed that the reduction of nitric acid by NO (S9) is fast; this gives:

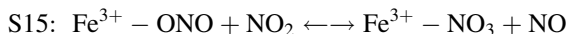
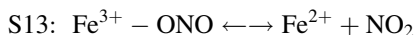


This combined step shows that adsorbed NO_2 , a surface nitrite precursor, reacts to give nitrous acid, a key reactive surface species. As we will show later, nitrous acid is an important surface species linking the NO oxidation to standard SCR. Finally, the above rate expression can be further simplified if $\text{O}-\text{S}_1$, NO_2-S_1 , and $\text{H}_2\text{O}-\text{S}_1$ are considered the dominant adsorbed species:

$$\theta_v = \frac{1}{1 + \sqrt{K_2 P_{\text{O}_2}} + K_3 P_{\text{NO}_2} + K_w P_{\text{H}_2\text{O}}} \quad (11.5)$$

The resulting rate expression predicts the correct trends for NO oxidation in the presence of water such as reaction orders, inhibition, etc.

Recent work by Tronconi and coworkers [54] advocates the Redox model for Fe-based zeolites during NO oxidation in the presence of H_2O . This model builds on mechanism proposals by Kefirov et al. [69], Panov et al. [70], Sun et al. [71], Delahay et al. [41], and Daturi et al. [66]. The mechanistic sequence involves the following steps:



The sum of S11–S14 yields the overall NO oxidation reaction (R5). The proposed mechanism involves the oxidation of NO by ferric hydroxide (Fe³⁺–OH), producing HONO. The production of the Fe nitrite surface species (Fe³⁺–ONO) subsequently occurs by the reaction of nitrous acid with additional Fe³⁺–OH. The latter species has been shown to be thermally stable under UHV conditions at temperatures up to ca. 400 °C [70]. Decomposition of the nitrite results in reduction to Fe²⁺ and yields NO₂. Reoxidation of Fe²⁺ occurs with molecular oxygen in S14. The proposed mechanism considers that the decomposition step S13 is the rate-determining step, so steps S11, S12, and S14 are equilibrated and the concentration of nitrous acid and other species is determined by the equilibrium of steps S11 and S12. In essence, the Redox model requires the formation of nitrite for NO₂ to be generated.

The Redox model helps to explain the inhibiting effect of H₂O during NO oxidation. Specifically, an increase in the H₂O concentration decreases the net formation of nitrites and nitrates because of an unfavorable equilibrium of step S12. This supports the observation by Tronconi et al. of negligible DRIFTS evidence for nitrite and nitrate species on Fe-zeolites during NO oxidation in the presence of H₂O [54]. Kamasamudram et al. [11], compared the low temperature (200 °C) NO_x storage during NO oxidation under dry and wet conditions. Appreciable NO₂ evolved from the dry catalyst while the amount evolved from the wet catalyst was negligible. These observations may suggest that the water inhibits the formation of Fe nitrites and nitrates, consistent with the Redox mechanism. The Redox model predicts NO₂ inhibition through the generation of nitrates via reaction step S15. Moreover, the reversible nature of the RDS means that the net rate of NO oxidation is lessened at higher NO₂ concentrations. In addition, NO oxidation is inhibited by NO₂ which suggests that NO_x storage is not necessary for site blockage.

A rate expression can be derived if one assumes that HONO, H₂O, and NO₂ as gas phase species, if step S13 is assumed the RDS, and the rest of the steps are therefore at equilibrium. A rate expression comprising steps S11–S15 gives

$$R_{\text{oxi}} = \frac{k_{12} C_s [K_{10}K_{11}K_{13}p_{\text{NO}}p_{\text{O}_2}^{1/2} - \frac{p_{\text{NO}_2}}{K_{12}}]}{1 + \left(K_{13}p_{\text{H}_2\text{O}}p_{\text{O}_2}^{1/2}\right)^{1/2} + K_{10}K_{11}K_{13}p_{\text{O}_2}^{1/2} (p_{\text{NO}} + K_{14}p_{\text{NO}_2})} \quad (11.6)$$

where C_s is the total site concentration. The expression predicts that the rate dependence on NO is between 0 and 1, on O₂ is between 0 and 0.5, and on NO₂ is between 0 and –1. The expression also predicts inhibition by water.

Several discriminating “Effects” should be considered in assessing the viability of the two competing mechanistic models. These effects include

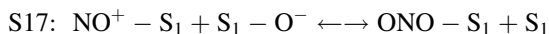
- (I) inhibition of the overall rate of oxidation by water;
- (II) removal of Fe nitrites/nitrates by water; and
- (III) inhibiting effect of the product NO₂ on the overall rate.

Both models capture Effect (I), the Redox model appears more consistent with Effect (II), while both models predict the NO₂ inhibition Effect (III), albeit in

different ways. Some elaboration on these points is instructive. Both models capture the inhibiting effect of water but the Redox model does so via reaction equilibrium-limited nitrite and NO_2 generation; i.e., nitrite formation is required for NO_2 production. In contrast, the LH model predicts the inhibition through the competitive adsorption of water and of acids generated from the reaction between water and NO_2 . Regarding Effect (III), the Redox model considers that NO_2 inhibition is a result of the reversibility of the nitrite decomposition and the generation of surface nitrates. These differences in the models bring to the forefront the question as to whether NO_2 , HONO, HNO_3 , and even H_2O are, in fact, surface species. That is, disproportionation of NO_2 by water given by S8 is a well-known acid-catalyzed reaction [72]. Whether the acid products HONO and HNO_3 reside on the surface as physisorbed or chemisorbed species is an open question. That said, as described earlier, there is experimental evidence for the existence of adsorbed NO_2 or related species. Such species would be likely to inhibit the oxidation. A variant on the LH model may lead to HONO formation through reaction between NO and surface hydroxyl groups, as in step S11 in the Redox model. Sachtler et al. [49] suggested the formation of a NO^+ active species through the disproportionation of N_2O_3 :



N_2O_3 is present in an equilibrium mixture of NO, O_2 , and NO_2 [65]. However, this pathway requires formation of gas phase NO_2 to account for the existence of N_2O_3 . Once formed, the NO^+ and surface hydroxyl may react to give surface nitrite, the precursor of nitrous acid



On the other hand, the direct reaction of gas phase NO with $\text{S}_1\text{-OH}$, i.e.,



has the appeal of not requiring the formation of NO_2 , as would the N_2O_3 decomposition route (S16 and S17) require. Such an Eley-Rideal type step is consistent with the fact that NO negligibly adsorbs. The Redox model as well does not require NO adsorption (S11 and S12).

Final mention should be made of a third mechanism that may be operative that borrows from a known process during Pt-catalyzed NO oxidation: NO_2 generated during NO oxidation leads to the formation of an inactive metal oxide unaffected by water but removed through reaction with NH_3 [55, 73]. During exposure of NO_2 , Pt slowly loses its activity over the course of several hours. The activity can be restored upon exposure to a reductant. Were a process similar to this to occur on Fe, then the inhibition could be explained. But Pt is less prone to oxidation while Fe readily forms oxides that are easily reduced for sufficiently high Fe loadings. Clearly, additional work is needed to shed light on the working mechanism that is consistent with steady-state and transient kinetics details and in situ surface species measurements.

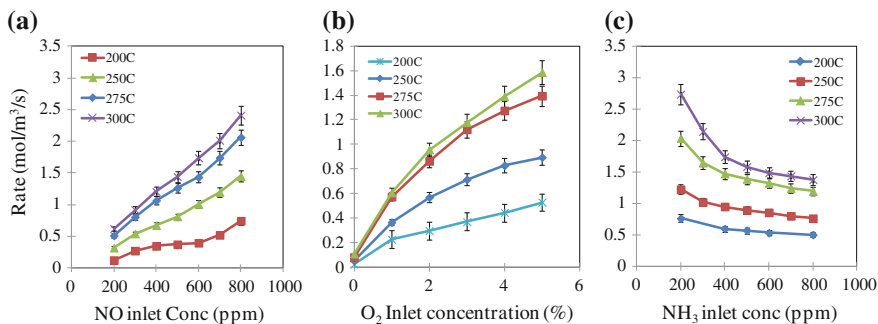


Fig. 11.10 Dependence of differential rate on NO, O₂, and NH₃ during standard SCR on Fe-ZSM-5. (Adapted from Metkar et al. [42] and used with permission.)

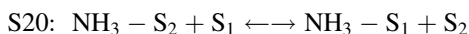
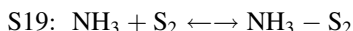
11.3.2 Standard SCR Reaction

The addition of NH₃ to the NO + O₂ + H₂O mixture comprises the standard SCR reaction (reaction R1). In this section we discuss possible mechanisms and associated kinetics of this reaction, building on the LH and Redox models for NO oxidation. The activation energy and reaction orders were reported by Metkar et al. [42] for the same catalyst that was studied for NO oxidation. Figure 11.10 shows data indicating orders of 1, 0.5, and -0.3 for NO, O₂, and NH₃, respectively. The corresponding activation energy was determined to be 42 kJ/mole. These data were collected under conditions in which the conversion was less than 15 % and the mass transport limitations were not important. Similar reaction order values were reported by Brandenberger et al. [74] in their detailed kinetics study. Devadas et al. [34] also reported a similar activation energy of 39 kJ/mole. The 39–42 kJ/mole activation energy values compare favorably with the value of 36 kJ/mole reported by Brandenberger et al. [74] who suggested that monomeric Fe species are responsible for a large fraction of the standard SCR at temperatures below 300 °C. They showed that at higher temperatures the reaction occurs on Fe dimers and clusters having a much higher activation energy of 77 kJ/mole. These findings are consistent with the earlier study of Schwidder et al. [21] who proposed that standard (and fast) SCR reactions occur on isolated and oligomeric Fe sites.

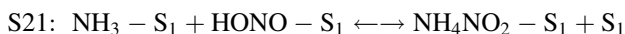
A viable rate model derived from a mechanism should be able to predict these measured kinetic parameter values. Unlike NO oxidation, the standard SCR on Fe-exchanged zeolites is not appreciably inhibited by water. Metkar et al. [42] proposed that the inhibition of the NO oxidation is mitigated by the reactive removal of the responsible inhibiting species. This mechanistic picture is supported by earlier work on Fe-zeolites. A fundamental study was carried out by Sun et al. [22] for SCR on Fe/MFI catalyst using isotopically labeled nitric oxide, ¹⁵NO. Their data showed that the preferred route to molecular nitrogen involve N atoms from NH₃ and ¹⁵NO, giving the mixed product (¹⁵NN). On the other hand, undesired oxidation of NH₃ led to the unlabeled product (N₂). From these data,

Sachtler and coworkers suggested that NH_3 "...intercepts this oxidation state of N^{3+} and reduces it to N_2 ." They argued that an adsorbed intermediate species with oxidation state less than that of NO_2 (N^{4+}) or NO_3^- (N^{5+}) reacted with adsorbed NH_3 , forming NH_4NO_2 , which then rapidly decomposed to N_2 . This may indeed suggest that the above-mentioned step S16, involving N_2O_3 disproportionation to NO^+ and NO_2^- , may supply these species, which then react selectively with NH_3 .

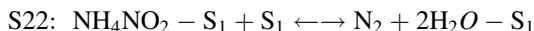
The resulting LH type model builds on this concept by considering that adsorbed NH_3 reacts with surface NOx species. It is noted that NH_3 adsorption on Fe-zeolite systems is not inhibited by the co-adsorption of water. A simple interpretation of this key observation is that the adsorption of NH_3 and H_2O occur on different sites. NH_3 adsorption on protonated zeolites is known to occur on the Bronsted acid sites, and that has led Tronconi, Nova, and coworkers among others to propose for vanadia-based catalysts the exchange of NH_3 between two types of sites. Applying this concept for Fe-zeolite catalysts gives:



The selective reduction of NO then proceeds though reaction between the adsorbed NH_3 and HONO:



NH_4NO_2 is known to be unstable above 100 °C [75]:



As mentioned above, Sun et al. [22] showed that formation and decomposition of ammonium nitrite is a major route to N_2 with one of the N atoms originating from NH_3 and the other from NO. Thus, the formation (S21) and rapid decomposition (S22) of ammonium nitrite serves to drive the reversible steps S8–S10 to the right, removing the HONO and related surface species responsible for inhibition of NO oxidation in the presence of H_2O . This may help to explain why the NO oxidation rate in the presence of water (and absence of NH_3) is considerably slower than the standard SCR rate. Only when the reductant NH_3 is added, is the inhibiting surface species removed, which effectively increases the rate of NO oxidation to surface-bound NO_2 .

A kinetic rate model based on the LH mechanism leads to the following result:

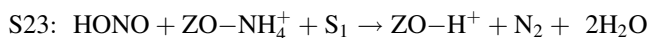
$$R_{\text{SCR}} = k'_1 P_{\text{NO}} \sqrt{K_2 P_{\text{O}_2}} \theta'_v \quad (11.7)$$

where we have simplified the expression for θ_v based on the assumption that the rapid removal of HONO and NO_2 surface through reaction with NH_3 ; i.e.,

$$\theta'_v = \frac{1}{1 + \sqrt{K_2 P_{\text{O}_2}} + K_4 K_5 P_{\text{NH}_3}} \quad (11.8)$$

The resulting expression has an inhibition term (denominator) that contains only terms associated with O₂ and NH₃. The functional form of the expression predicts the main trends in the kinetic data for the standard SCR reaction system, such as first order w/r NO, half-order w/r O₂ (when neglecting the term containing P_{O₂} in the denominator), and negative order w/r NH₃. One cautionary point to note is that in assuming the rate is limited by the production of surface-bound NO₂ (or HONO) with subsequent rapid reaction with adsorbed NH₃, the rate is zero order w/r NH₃ in the limit of P_{NH₃} → 0. In this limit step S21 would become rate limiting and the rate would revert to a positive order dependence w/r NH₃.

The corresponding standard SCR model based on the Redox mechanism for NO oxidation is similar in the sense that adsorbed NH₃ reacts with an intermediate such as HONO



where ZO-NH₄⁺ is NH₃ adsorbed on a Bronsted acid site. Step S23 is similar to the combination of S21 and S22 of the LH model. One difference is that reoxidation of the iron via step S14 is the proposed rate-determining step of the Redox model for standard SCR, as opposed to the formation of NO₂ in the LH model. Thus, the proposal of Ruggeri et al. [54], is that NH₃ “intercepts” the HONO intermediate. In fact, this proposal borrows from the study of Sun et al. [22], who, as discussed earlier, suggested a mechanistic picture in which an adsorbed NH₃ reacts with a surface NO_x species whose oxidation state is less than that of NO₂. In the absence of NH₃, Ruggeri et al. [54], suggest that HONO reacts via step S12, forming Fe nitrite, which decomposes to NO₂.

11.3.3 Ammonia Inhibition

A complicating yet interesting feature of SCR on Fe-based catalysts is inhibition by NH₃. The rate described by Eq. (11.8) is based on the assumption that NH₃ adsorbs onto acid sites and then exchanges with metal sites. Differential kinetics data presented earlier (Fig. 11.10) together with other data from the literature show that the rate declines with increasing concentration of NH₃ [42, 62, 74]. Metkar et al. [42] carried out an experiment in which NH₃ was gradually added to a feed containing NO and O₂ without and with water (Fig. 11.11). The addition of NH₃ led to a decrease in the generated NO₂ in both experiments. A simple interpretation of the decreasing NO₂ trend is that NH₃ reacts with NO and O₂ via the standard SCR reaction. This removes an equivalent amount of NO—because of the 1:1 stoichiometry of standard SCR—that would otherwise be oxidized to NO₂. Since the decrease in NO₂ is disproportionately larger, this indicates that the added NH₃ inhibits the surface oxidation of NO to NO₂, considered the rate-determining step for standard SCR in the LH model. It would therefore appear necessary to account for site blocking in the standard SCR kinetic model.

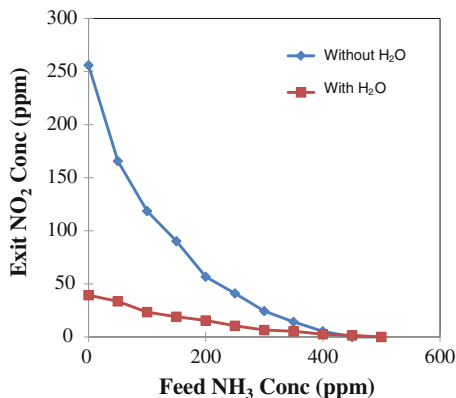


Fig. 11.11 Effluent NO₂ concentration as a function of the concentration of NH₃ fed containing NO and O₂ in the presence (1.5 %) and absence of water. Feed: 500 ppm NO, 5 % O₂, 0 or 1.5 % H₂O. Total flow: 1,000 sccm. Balance gas: Ar. Catalyst Temperature: 350 °C. (Adapted from Metkar et al. [42] and used with permission.)

The standard SCR LH model predicts the inhibition by NH₃ as mentioned earlier in relation to Eq. (11.8). The standard SCR Redox model can also predict NH₃ inhibition through the addition of another step that accounts for NH₃ adsorption on Fe sites. This follows from recent work from the Milano group in which ammonia adsorption can result in hysteresis associated with NH₃ feed transients, among other features.

11.3.4 Selective Catalytic Reaction with NO and NO₂

The chemistry changes dramatically when NO₂ is present in the feed. As presented earlier (cf. Figs. 11.5, 11.7), when NO₂/NO < 1 a large enhancement in the NO_x conversion is observed with increasing NO₂. On the other hand, NO_x reduction inhibition is encountered as NO₂ increases for NO₂/NO > 1. The species responsible for the inhibition may be NH₃ and/or NH₄NO₃. As will be shown, the results are much more complex because of the existence of multiple reaction pathways.

We have presented earlier differential kinetics data for the NO oxidation and standard SCR reactions. Here we report on a similar set of experiments involving a feed with different amounts of NO, NO₂, and NH₃. Metkar et al. [42] showed for standard SCR that a space velocity of 285,000 h⁻¹ was needed to keep the NO conversion below 15 % in the temperature range of 200–300 °C. In contrast, when the SCR reaction was carried out with an equimolar NO/NO₂ feed, a space velocity of 2 × 10⁶ h⁻¹ was needed to ensure differential conversion for temperatures below 245 °C. This high space velocity was achieved by reducing the

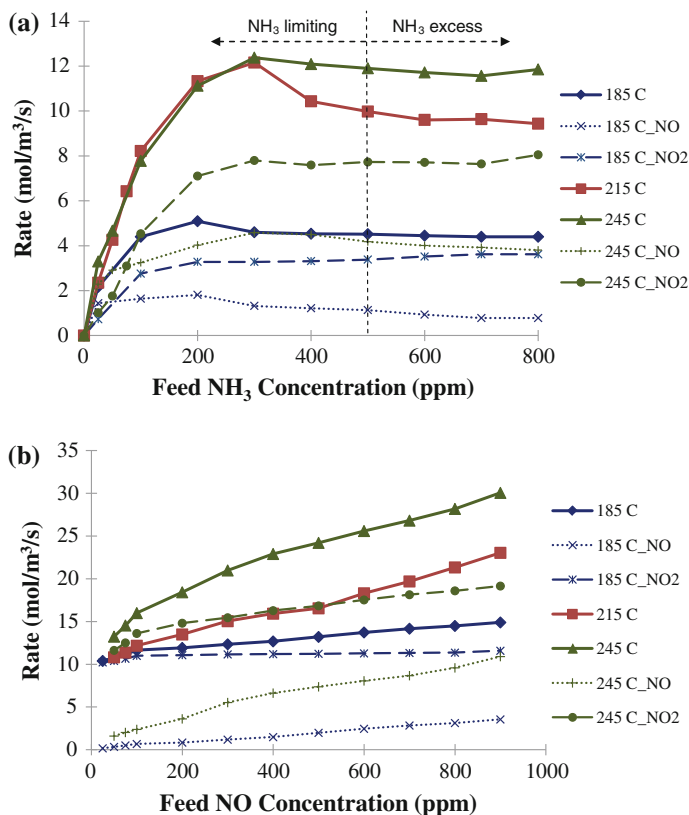


Fig. 11.12 **a** Dependence of differential rate of NO and NO₂ consumption on the feed concentration of NH₃. Space velocity $2 \times 10^6 \text{ h}^{-1}$. Total Flow rate = 1,000 sccm. Balance gas: Ar. Feed: 250 ppm NO, 250 ppm NO₂, 5 % O₂. **b** Dependence of differential rate of NO and NO₂ consumption on the feed concentration of NO. Space velocity $2 \times 10^6 \text{ h}^{-1}$. Total Flow rate = 1,000 sccm. Balance gas: Ar. Feed: 500 ppm NO₂, 1,000 ppm NH₃. **c** Dependence of differential rate of NO and NO₂ consumption on the feed concentration of NO₂. Space velocity $2 \times 10^6 \text{ h}^{-1}$. **d** Dependence of differential rate of NO and NO₂ consumption on the feed concentration of NO_x (NO = NO₂). Total Flow rate = 1,000 sccm. Balance gas: Ar. Feed: 500 ppm NO, 1,000 ppm NH₃

size of the catalyst to 4 channels and 5 mm length with the total flow rate maintained at 1,000 sccm. Since the temperature was below 300 °C, the decomposition of NO₂ was negligible. The effluent NO and NO₂ concentrations were used to calculate an average rate normalized by the washcoat volume using 50 μm as the estimated thickness. We refer to the overall NO_x consumption rate as R_{NO_x} , the NO₂ rate as R_{NO_2} , and the NO rate as R_{NO} . The results from three experiments shown in Fig. 11.12a–d, respectively, report these rates as a function of NO, NO₂, and NH₃ over the 185–245 °C temperature range. Higher temperatures were not considered because differential conversion could not be achieved.

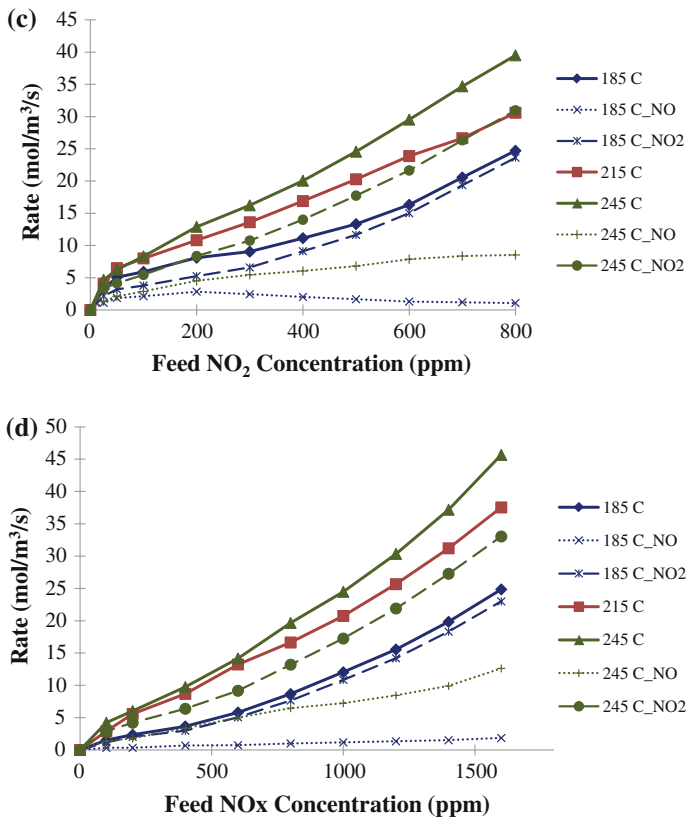


Fig. 11.12 continued

It should be mentioned that washcoat diffusion limitations become more important for the fast SCR reaction. As discussed in more detail later, diffusional limitations emerge at a rather low temperature for fast SCR; ca. 225 °C for an Fe-ZSM5 catalyst having a ca. 24 % mass loading (Metkar et al. [76]). For this reason, diffusional limitations cannot be ruled out for the 245 °C differential rate data.

The data reported in Fig. 11.12a show the dependence on NH₃ concentration with the NO and NO₂ concentrations each fixed at 250 ppm, O₂ fixed at 5 %, and no H₂O in the feed. The total NO_x reduction rate for three temperatures and the individual NO and NO₂ consumption rates are shown for the bounding temperatures. The figure reports the individual rates of NO and NO₂ consumption; their sums equal the overall rate, R_{NO_x}. Indicated in the figure is the NH₃ concentration at which the fast SCR feed is achieved. To the left of that point the reaction system is deficient in NH₃, while to the right the NH₃ is in excess with respect to the stoichiometry ratio NO:NO₂:NH₃ = 1:1:2. For each of the three temperatures R_{NO_x} exhibits a slight maximum, with the maximum shifting to higher NH₃ concentration with increasing temperature. To the right of the maximum the total

rate slightly decreases with increasing NH₃ concentration, although the data indicate that the decrease is somewhat more pronounced at the higher temperatures. To the left of the rate maximum, an interesting feature is the coincidence of the 215 and 245 °C R_{NO_x} data. At each temperature, the NO₂ consumption rate (R_{NO₂}) exceeded the rate of NO consumption (R_{NO}) except when NH₃ was less than 100 ppm. Below that concentration R_{NO₂} < R_{NO}

The trends in the rate data as a function of NH₃ in Fig. 11.12a reveal two notable features. First, the existence of the rate maximum is evidence for inhibition by NH₃, encountered during standard SCR (Fig. 11.10). At higher NH₃ concentration the NH₃ blocks sites for adsorption and reaction. In the case of standard SCR, ammonia blocks the adsorption of oxygen and hence the conversion of NO into NO₂. In the case of fast SCR, ammonia similarly blocks the adsorption of NO₂, a necessary step for the subsequent formation of nitrites/HONO that reacts with NH₃ to form N₂. Second, the inequality of the NO and NO₂ consumption rates suggests that multiple paths to N₂ occur simultaneously. The fast SCR stoichiometry (reaction R2) implies the rates should be equal. But the equimolar NO/NO₂ feed containing 500 ppm NH₃ shows that the NO₂ consumption rate is nearly twice that of NO consumption. This suggests that NO₂ is consumed by an additional route such as reaction R3 (“NO₂ SCR”) and/or R6 (AN formation). This trend is consistent with the integral consumption of NO and NO₂; i.e., the fast SCR feed case shown in Fig. 11.5b indicates that NO₂ is consumed more rapidly than NO as a function of temperature. It is interesting to note in Fig. 11.12a that the NH₃ appears to inhibit the rate of NO but not of NO₂ consumption. This subtle feature needs further investigation because it may mean that the adsorption of NO₂ is not inhibited to the same degree as the adsorption of oxygen. When NH₃ is below 100 ppm, the NO consumption rate overtakes that of NO₂. This feature also deserves further consideration.

A similar experiment was carried out for NO and the results are reported in Fig. 11.12b. In this experiment, the dry feed NH₃ and NO₂ concentrations were kept constant at 1,000 and 500 ppm, respectively, while the NO feed concentration was varied from 0 to 900 ppm. O₂ was not fed in order to avoid the occurrence of the standard SCR and NH₃ oxidation by O₂ reactions. The total NO_x consumption rate is an increasing function of the NO concentration at all temperatures but steeper at lower concentrations, indicating an apparent NO order less than unity. This is in contrast to an order of unity for the standard SCR reaction (Fig. 11.10). Like the results with NH₃ in Fig. 11.12a, the NO₂ consumption rate exceeds the NO consumption rate. In contrast with the NH₃ experiment, however, at a NO concentration of zero the NO₂ consumption rate is nonzero due to the direct reaction between NO₂ and NH₃ that does not require NO. On the other hand, the NO consumption rate passes through the origin. That the NO consumption rate is nonzero in the absence of O₂ points to reaction of NO with surface nitrates, forming NO₂; i.e., reverse of reaction S5.

Similar studies were repeated by varying the feed NO₂ concentration in the same temperature range (Fig. 11.12c). NO and NH₃ feed concentrations were kept constant at 500 and 1,000 ppm, respectively. Again, no O₂ was present in the feed.

In this experiment all of the rate curves pass through the origin. This shows that NO reaction with NH_3 is negligible in the absence of NO_2 or O_2 . The data also show that the apparent reaction order with respect to NO_2 is positive. In fact the shapes of the NO_2 consumption rate curves are sigmoidal, while the NO rate curves exhibit a shallow maximum. These are features should be predicted by any viable kinetic model.

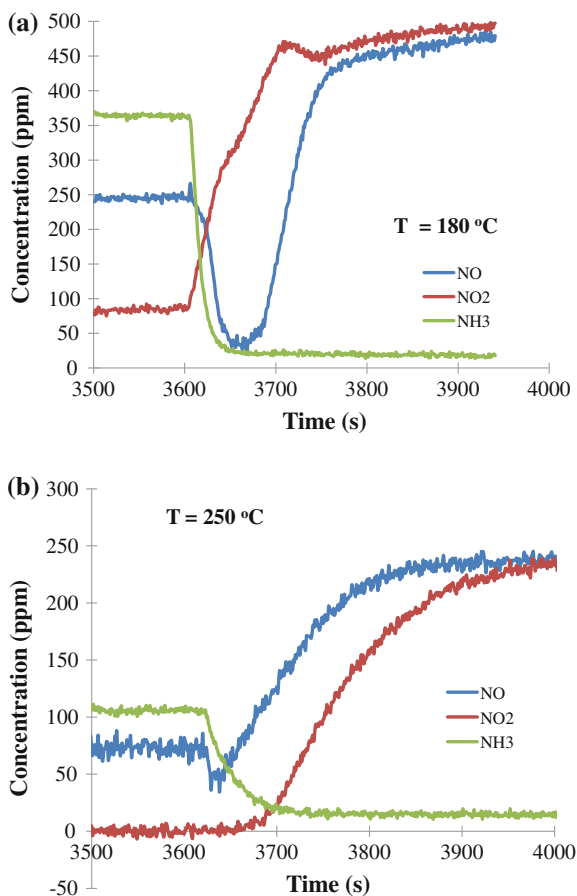
In addition to the experiments shown in Fig. 11.12a–c, we simultaneously increased NO and NO_2 concentrations in the feed while holding the NH_3 concentration fixed. NO and NO_2 were fed in equimolar ratio while keeping the NH_3 constant at 1,000 ppm and the feed gas devoid of O_2 . The data in Fig. 11.12d shows that the NO_x consumption rate is an increasing function of the equimolar NO_x feed. Moreover, a sigmoidal character to the data is apparent. As in the above-described experiments, the NO_2 consumption rate exceeded that of NO. This trend is consistent with earlier results obtained for integral NO_x conversion experiments.

Similar experiments were carried out to determine the effect of oxygen concentration on the fast SCR reaction. For these experiments, 500 ppm NO, 500 ppm NO_2 , and 1,000 ppm NH_3 were kept constant in the inlet feed and Ar was used as a balance gas with 1,000 scfm as the total flow rate. The inlet O_2 concentration was varied in the range of 0–5 % for temperatures of 185, 220, and 245 °C. The O_2 was found to have no effect on the fast SCR reaction. Hence the apparent reaction order with respect to O_2 can be considered to be zero.

From these rate data the following observations can be made. The NO_x consumption rate for the fast SCR reaction has apparent positive orders with respect to both NO and NO_2 . However, the complex dependence on NO_2 in particular indicates multiple reaction pathways in the presence of NO. The apparent order for ammonia varies between positive and negative while the apparent reaction order for O_2 is nearly zero. From Fig. 11.12a it is clear that the increasing NH_3 reduces the R_{NO} slightly while having a negligible effect on R_{NO_2} . Grossale et al. [40] described the role of NH_3 inhibition on the fast SCR chemistry at lower temperatures. They concluded that the NH_3 blocking effect is due to the strong interactions between NH_3 and nitrates. That is, fast SCR is inhibited by AN formed through the reaction of NH_3 and surface nitrates. To this end, NO reduction of AN is a plausible rate-determining step. Below we describe an experiment that provides additional evidence for this. Finally, the apparent activation energy for the fast SCR reaction with respect to the rate of NO_x conversion at different temperatures was found to be 18 kJ/mol, which is somewhat less than that of standard SCR reaction (ca. 40 kJ/mole). Devadas et al. [34]. reported a value of about 7 kJ/mol for the fast SCR and temperatures up to 350 °C. At this temperature, diffusion limitations cannot be ruled out and thus the value they have obtained may not be valid for the intrinsic kinetic regime. An examination of mass transfer is presented in the next section.

Transient experiments provide additional probes of mechanistic issues not obtainable from steady-state experiments. Studies by Tronconi and coworkers

Fig. 11.13 Dependence of species concentrations on time for experiment in which NH₃ was shut off at $t = 3,600$ s mark; in **a** the temperature was 180 °C whereas in **b** the temperature was 250 °C



have illustrated this for V-based catalysts [48] and Fe-based catalysts [27]. Here we describe similar experiments carried out at UH. In order to study the ammonia inhibition effect in more detail, we carried out transient experiments in which a mixture containing 500 ppm each of NO and NO₂, and 1,000 ppm NH₃ was fed to the reactor for 1 h and then NH₃ was suddenly switched off. The transient response of the NO and NO₂ concentrations was monitored during this procedure. Figure 11.13a, b shows the results obtained at 180 and 250 °C, respectively. The premise of the experiment was to examine if any ammonia nitrate was present on the catalyst. At 180 °C, immediately after the NH₃ stoppage it was observed that the NO concentration dropped for a while, went through a minimum and then increased; in contrast, the NO₂ and N₂ both increased with the stoppage of NH₃. Thus, NO was apparently being consumed at 180 °C. At 250 °C, the dip in NO concentration was small, while at 300 °C, no dip in the NO concentration was observed. These observations indicated that the dip in NO concentration is due to the reaction of NO with NH₄NO₃ present on the catalyst (reaction R11).

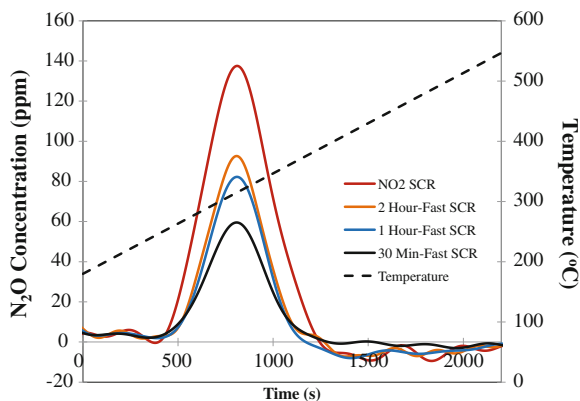


Fig. 11.14 Comparison of N_2O evolved obtained during the temperature programmed desorption (TPD) after catalyst was exposed to four different reaction conditions at 180°C . A temperature ramp of $10^\circ\text{C}/\text{min}$ was applied evolve the N_2O from the catalyst. The Fast SCR experiments involved a feed mixture containing 500 ppm NO, 500 ppm NO_2 , 1,000 ppm NH_3 , 5 % O_2 fed to the reactor for durations of 30 min, 1, and 2 h. The NO_2 CR experiments involved a feed mixture of 1,000 ppm NO_2 , 1,000 ppm NH_3 , and 5 % O_2 for a duration of 2 h

As observed in the steady-state experiments above, the NH_4NO_3 present on the catalyst decreased with time and at 300°C , there was essentially no NH_4NO_3 present for the fast SCR case.

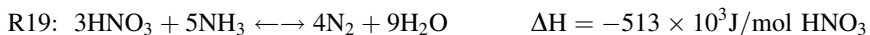
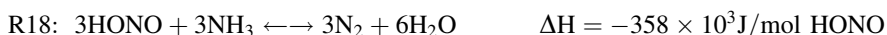
To examine the effect of NH_4NO_3 formation on the overall conversion, we carried out some TPD experiments after the catalyst was exposed to a feed containing 1,000 ppm of both NH_3 and NO_x ($\text{NO} + \text{NO}_2$) in the presence of 5 % O_2 for different durations (between 0.5 and 2 h); see Fig. 11.14. The catalyst temperature was maintained constant at 180°C during this exposure. After the prescribed time had lapsed, all the gases except Ar were switched off for 30 min to remove any physisorbed species, and then a temperature ramp of $10^\circ\text{C}/\text{min}$ was applied. During the temperature ramp, N_2O was evolved, reaching a peak value in the temperature range of $250\text{--}300^\circ\text{C}$. The amount of N_2O generated, which was calculated by integrating the N_2O peak, provided an estimate of the amount of NH_4NO_3 present on the catalyst; i.e., the AN decomposition product is N_2O . The amount of N_2O evolved was different for each of the feeds. The largest amount evolved was obtained for the 2 h experiment with 1,000 ppm NO_2 . This amount exceeded by more than 50 % the amount obtained during the 2 h experiment with the equimolar mixture of NO_2 and NO (0.43 mol). The 1 h long equimolar feed resulted in only slightly less N_2O evolved (0.37 mol), indicating that the catalyst had reached a constant level of AN by 2 h even though the catalyst had capacity for additional NH_4NO_3 accumulation at this temperature (based on the $\text{NO}_2 + \text{NH}_3$ exposure). At the very least, these experiments demonstrate that NH_4NO_3 is present on the catalyst surface and that it is the probable inhibiting species in this temperature range. The lesser amount accumulated with the $\text{NO}=\text{NO}_2$ feed compared to the NO_2 feed indicated a mitigating role of the NO.

The likely explanation is that NO served to react with (reduce) the NH₄NO₃, freeing up sites and increasing the conversion. Furthermore, the rather slow approach to steady state in these experiments indicated that the reduction of NH₄NO₃ by NO is a likely rate determining under these conditions.

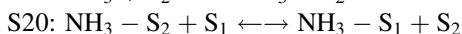
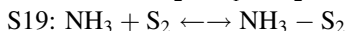
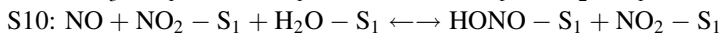
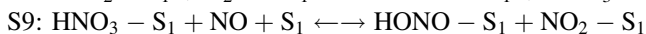
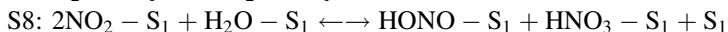
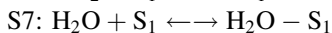
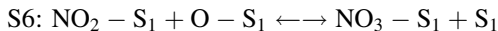
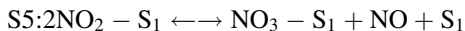
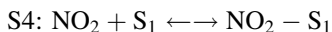
Various mechanistic-based kinetic models that describe the effect of NO₂ have appeared in the literature. Here we attempt to summarize the current understanding of the mechanism and associated kinetics. As before, we consider both the LH and Redox approaches.

Tronconi and coworkers have proposed a fast SCR kinetic mechanistic model that is based on a Redox mechanism [27, 57, 58]. Like the LH SCR model, the Redox SCR model has adsorbed NH₃ reacting with gas phase HONO or surface nitrites, forming NH₄NO₂, which decomposes to N₂ (cf. S22). The nitrites are formed through the reduction of nitrates by NO (step S9). Additional steps would include the formation of NH₄NO₃ and its decomposition to N₂O, among others.

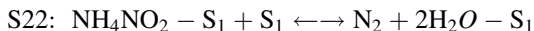
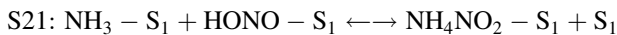
The role of NO₂ during SCR was considered by Grossale et al. [19, 77] in the context of a redox process. For example, they proposed a series of global reactions that would explain the 3:4 NO₂:NH₃ stoichiometry of the NO₂ SCR reaction R3 in the presence of H₂O.



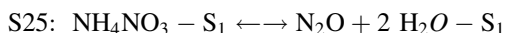
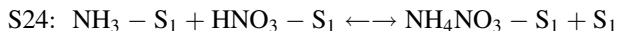
The investigators coined the term “fast ammonia oxidation” reaction system. The global reactions are similar to the surface reactions contained in the context of the LH fast SCR model. One difference is that in the absence of NO the reduction of surface nitrate does not occur. In related work, the Milano group showed among other things that surface nitrates are preferentially reduced by NO, if available; i.e., fast SCR. In the absence of NO the nitrates are less effectively reduced by NH₃; i.e., NO₂ SCR [27]. The alternative LH model considers that for a feed consisting of NO, NO₂, and NH₃ (in excess O₂ and H₂O) the co-adsorption of NO₂ and NH₃ is followed by a series of steps that lead to the acidic species HONO and HNO₃:



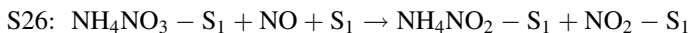
The LH model, like the Redox model, considers that the reaction of the acids with surface NH_3 leads ultimately to NH_4NO_2 and NH_4NO_3 . The nitrite pathway is the selective one to N_2



The nitrate pathway can lead to N_2 but also involves a nonselective decomposition pathway to by-product N_2O



In addition, the NO reduction of AN, analogous to HNO_3 reduction, is plausible, following the above-described experiments which quantified the net production of AN; i.e.,



Finally, the “ NO_2 SCR” reaction R3 involves a selective pathway to N_2 .

The LH model comprising this set of steps can be used to derive a governing rate expression if a single rate-determining step is identified. Which step is the limiting one will depend on the relative quantities of NO and NO_2 . In the limit of the feed $\text{NO}_2 \rightarrow 0$, the mechanism should resort to the standard SCR reaction which would have to include NO oxidation steps S1, S2, and S3. With increasing NO_2 in the feed, the conversion data clearly shows an enhancing effect of NO_2 . The overall chemistry is de-bottlenecked following the argument that the formation of adsorbed NO_2 is the rate-limiting process in the $\text{NO}_2 \rightarrow 0$ limit. Then the formation of the two key intermediates, NH_4NO_2 and NH_4NO_3 , are the primary, potentially limiting pathways affecting the conversion and product distribution. The rates of interconversion of their precursors, nitrous and nitric acids and/or Fe nitrites and nitrates, are critical. For example, when NO is added systematically to a feed containing NO_2 and NH_3 , an increase in the N_2 yield and decrease in the NH_4NO_3 yield results (Fig. 11.15). It has been shown that the addition of NO causes the reduction of nitrates to nitrites [36, 77]. The aforementioned transient tests (Fig. 11.14) underscore this point. Indeed, the fact that the highest rates are obtained with an equimolar mixture is explained by the sum of steps S8 and S9



That is, the role of NO is to convert nitrates to nitrites, which are rapidly converted to N_2 in the presence of NH_3 . This follows from earlier works advocating the Redox model, such as Grossale et al. [27]. The analog of step S9' indeed represents a redox step involving the change in the formal oxidation state of N from +5 (nitrates) to +3 (nitrites). Earlier we showed transient kinetic evidence that the NO reduction of NH_4NO_3 (step S25) may be rate determining at lower temperature. A similar reaction is the NO reduction of nitric acid (S9) or nitrates.

These steps increase the coverage of surface nitrites which rapidly convert to N₂. The differential rate data for temperatures below 250 °C presented earlier show clear evidence for multiple reaction pathways: The differential rate of NO₂ consumption exceeds that of NO at lower temperatures. This points to the formation of NH₄NO₃ and its inhibition of N₂ formation, but also the mitigation of the inhibition by and AN reduction by NO. It can be shown that an overall rate based on the reduction of HNO₃ and/or NH₄NO₃ as the RDS has the functional features to predict the main trends in the experimental data. Further analysis of microkinetic models that include these steps S1–S10 and S19–S26 is needed. Later we describe global kinetic models that predict these data as a first step toward this goal.

In the limit of the feed NO₂/NO_x → 1, the LH mechanism should predict the NO₂ SCR reaction behavior. That the overall stoichiometry to N₂ product is 4:3 NH₃:NO₂ and not 1:1 points to the different chemical pathways. In the absence of gas phase NO, the reduction of HNO₃ or NO₃⁻ will not occur. This helps to explain why NH₄NO₃ and its decomposition product N₂O are important by-products at low to moderate temperatures. On the other hand, at high temperatures (>400 °C) NO₂ decomposition will occur, yielding adsorbed NO and O. Moreover, adsorbed NH₃ may react with O adatoms forming N₂ and NO as products. In turn, the NO can then serve in the role of reductant, generating HONO/NO₂ through reaction with HNO₃/NO₃⁻. Detailed kinetics data are needed to build such a mechanistic-based model.

11.4 Reaction and Transport Interactions

An important aspect of catalytic reactor design is understanding, quantifying, and managing mass and heat transport limitations. While heat transport limitations are negligible in NH₃-based SCR due to the low reactant concentrations, mass transport limitations cannot be similarly ruled out. This includes mass transport at three levels: external mass transport from the bulk gas to the catalyst surface, washcoat diffusion within the mesoporous layer containing zeolite crystallites supported by a high surface area binder material such as alumina, and crystallite-scale diffusion within the pores of the zeolite crystallites. In practice, zeolite diffusion is lumped with the intrinsic catalytic processes due in part to the difficulty of separating the two processes. Here we highlight our understanding of the impact of the first two processes on the SCR catalyst performance in a monolith containing a washcoat of Fe-exchanged zeolitic crystallites (Fig. 11.15).

In a recent study, Metkar et al. [78] presented a systematic analysis in which the washcoat loading and monolith length were varied to quantify the extent of diffusion limitations during SCR on a Fe-exchanged monolith catalyst. Figure 11.16 compares the conversions obtained with two Fe-ZSM-5 catalysts having the same total washcoat loadings but different washcoat aspect ratios (thickness, length). Each catalyst was subjected to the same conditions; since this included total flow rate the ratio of the catalyst mass and total flow rate (W/F value) was fixed. This

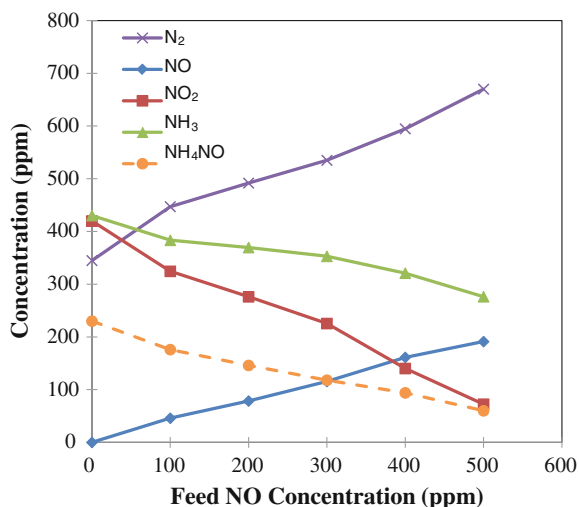


Fig. 11.15 Effect of feed NO concentration on the product distribution during SCR on FeZ-18 catalyst at 185 °C. Space velocity 57,000 h⁻¹. Total Flow rate = 1,000 sccm. Balance gas: Ar. Feed: 1,000 ppm NO_x (NO + NO₂), 1,000 ppm NH₃, 5 % O₂, and 2 % H₂O

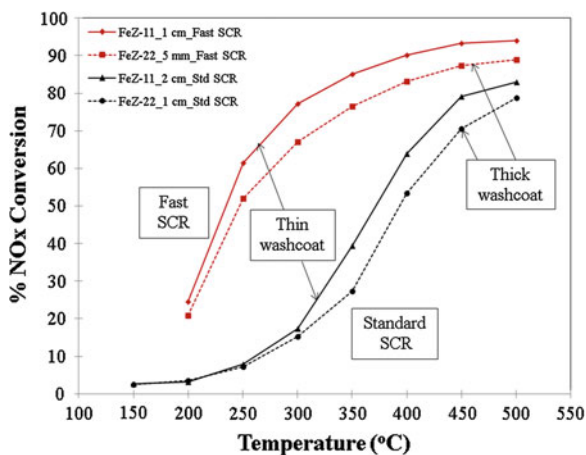


Fig. 11.16 Dependence of steady-state NO_x conversion versus temperature for fast and standard SCR on two different catalysts. FeZ-22: 5 mm (fast SCR) and 1 cm (standard SCR); Fe-11: 1 cm (fast SCR) and 2 cm (standard SCR). Feed conditions: 500 ppm NO_x, 500 ppm NH₃, 5 % O₂, balance Ar; 1,000 sccm (GHSV = 57 K h⁻¹). (Used with permission [78] and used with permission.)

method identifies the emergence of washcoat diffusion limitations as the temperature is increased. In the purely kinetic regime no difference would be encountered because the catalyst is fully utilized. In the case of a very fast reaction external

mass transport limitations emerge at high temperatures. In this latter case only a small fraction of the washcoat would be utilized. The fixed W/F test could be augmented by an experiment in which the residence time is maintained constant to provide additional insight about external mass transfer.

The analysis of Metkar et al. shows that for standard and fast SCR on Fe-exchanged zeolites, the extent of mass transport limitations varies but appears to be important for most practical operating conditions and typical washcoat loadings. The results obtained on different Fe-exchanged zeolite samples clearly show the onset of mass transport limitations above a threshold temperature. That temperature value depends on the SCR feed composition (standard, fast, NO₂ types). A threshold temperature of about 300 °C for standard SCR and 250 °C for fast SCR was estimated. An estimate of the apparent activation energy that was about half the value determined when mass transport limitations were negligible provided further evidence. Metkar et al. [42] reported an apparent activation energy of 24 kJ/mole during differentially operated standard SCR on the same washcoated Fe-ZSM-5 in the temperature range of 350–500 °C. A smaller sample enabled a high space velocity ($2 \times 10^6 \text{ h}^{-1}$) to achieve the differential conditions. The 24 kJ/mole was slightly over one-half the value obtained at lower temperatures (42 kJ/mole). The one-half value of the apparent activation energy is a signature of diffusion limitations. Metkar et al. showed how the analysis can also be used to estimate the effective diffusivity through the use of the Weisz-Prater modulus and confirmed by simulations using a $1 + 1 \text{ D}$ monolith reactor model. An activation energy as low as 7 kJ/mole was reported by Devadas et al. [23] for fast SCR and may indicate the presence of external mass transport limitations. A study by Nova et al. [79] indicated the presence of transport limitations for Cu-zeolite catalysts. Monoliths having three different cell densities (200, 400 and 600 CPSI) were compared for the same mass loading of washcoat. The study concluded that diffusional limitations were present for the 200 CPSI monolith catalysts and possibly the 400 CPSI sample. On the other hand, a more recent study by Colombo et al. [57] indicated that diffusion limitations are negligible to modest based on a comparison of monolith and crushed monolith powder catalysts. The authors cautioned about the generalization of these findings. Differences in the extent of transport limitations can be attributed to differences in the intrinsic activities of the catalysts, for example. In summary, it is clear that the issue of diffusion limitations is a nontrivial one but deserves attention in the design of SCR reactors.

Indisputable experimental evidence for the existence of diffusional limitations is the data from a study of dual-layer Fe–Cu zeolite catalysts carried out by Metkar et al. [80]. In that study, monoliths were sequentially coated with layers of Cu- and Fe-exchanged zeolite catalyst. The results showed that a monolith comprising a top layer of Fe-ZSM-5 and a bottom layer of Cu-ZSM-5 resulted in an expanded, high NO_x conversion temperature window. At sufficiently high temperature the dual layer catalyst conversion approached that of the single layer, Fe-only catalyst, suggesting that only the top Fe layer of the dual component was utilized. That is, washcoat diffusion limitations of the limiting reactant, in this case NH₃, prevented the utilization of the underlying Cu layer. With feeds spanning standard, fast, and

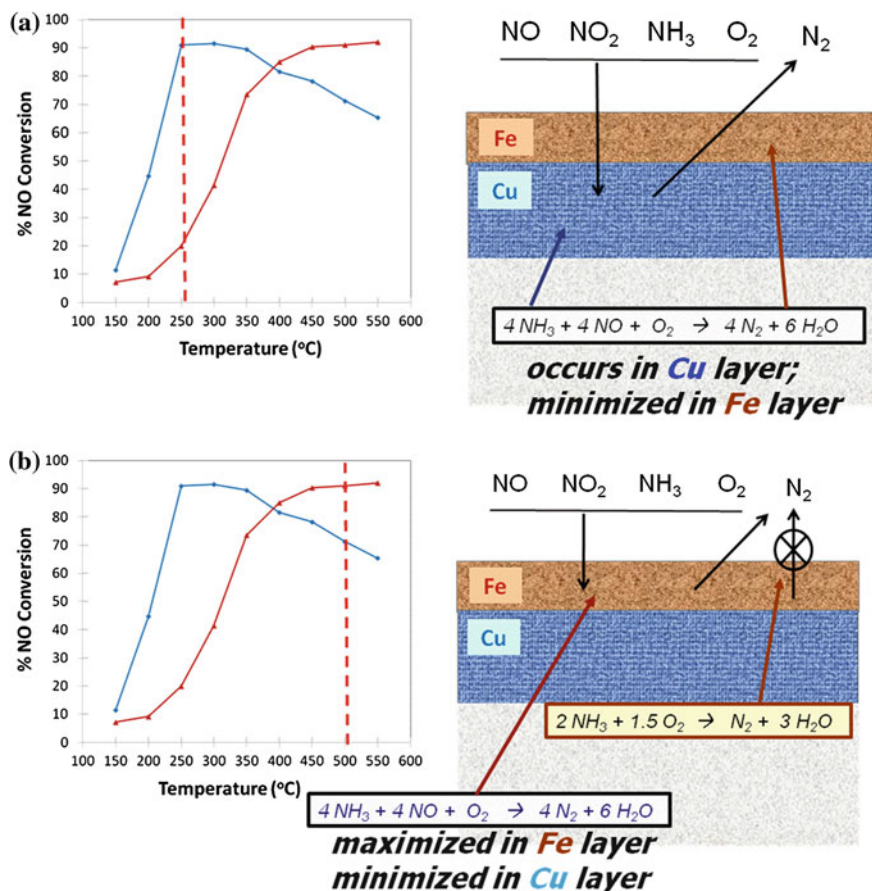


Fig. 11.17 Schematic representation of dual layer Fe/Cu monolith catalyst. (Used with permission [80].)

NO₂ SCR compositions, superior NO_x conversion performance was achieved with the layered architecture. The schematic shown in Fig. 11.17 explains the concept while Fig. 11.18 provides typical data for several monolith samples. The catalyst design and operating strategy was to exploit differences in the intrinsic activity and selectivity of the two catalysts through coupled reaction and diffusion. At low temperature the top layer should behave in the limit as simply as a diffusion barrier, whereas at high temperature the top layer should be sufficiently active so as to confine most of the conversion in that layer. This was of definite benefit because at low temperature, the Fe layer was much less active than the underlying Cu layer which was selective for N₂, while at high temperature reaction occurred in the more selective Fe top layer.

To illustrate, the data in Fig. 11.18 shows that a washcoat catalysts containing different fractions of Fe and Cu but a fixed total loading result in quite different

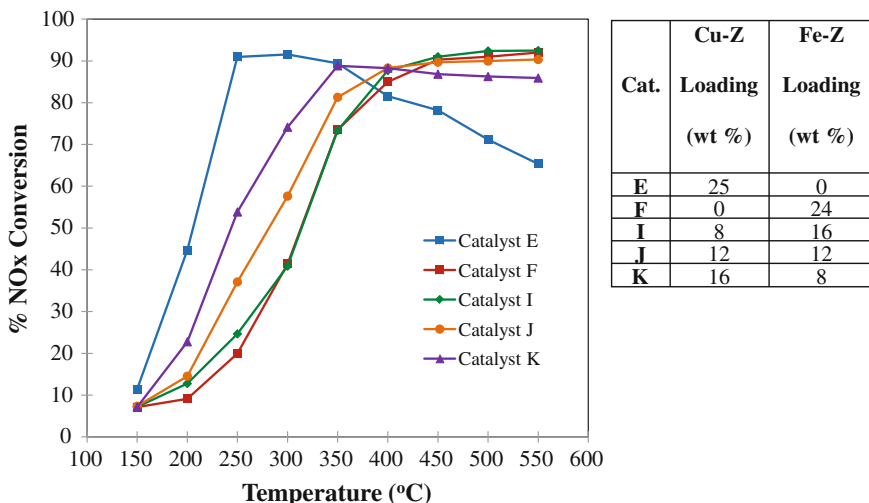


Fig. 11.18 Dependence of steady-state NOx conversion versus temperature for several monolith catalysts with compositions shown in table. (Adapted from Metkar et al. [80] and used with permission.)

NOx conversions. The 50:50 Fe:Cu-layered catalyst achieved a NOx conversion that was essentially the arithmetic average of the individual Fe- and Cu-exchanged catalysts. In contrast, the dual layer catalyst with a thin Fe-zeolite (33 % of the total washcoat loading) layer on top of a thicker Cu-zeolite layer (67 %) resulted in a high NOx conversion over a wide temperature range and NO₂/NOx feed ratio values. In the lower temperature range, the conversion approached that of the Cu-zeolite, whereas at higher temperatures the conversion approaches that of the Fe-zeolite.

These dual layer results provide clear evidence of the existence of mass transport limitations. That the conversion for the dual-layer Fe/Cu catalyst (I, J, K) approached that for the Fe (top) layer at sufficiently high temperature indicates that significant transport limitations were present. In fact, the experiment helps to pinpoint the temperature at which the onset of diffusion limitations occurs for an Fe top layer of a prescribed loading (thickness). As the Fe top layer thickness decreases, the temperature at which the dual layer catalyst conversion is within a few percent of the single layer Fe catalyst (sample F) conversion increases. For example, the conversion for the thickest Fe top layer catalyst (sample I) approaches that of the single layer Fe catalyst at about 300 °C. For next thinner top layers (samples J), the temperature increases to 400 °C. Were diffusion limitations not present, the conversion would approach the arithmetic average of the Fe and Cu catalysts, not unlike a mixed layer catalyst.

In conclusion, mass transport limitations cannot be ignored during SCR for moderate to high temperatures and realistic washcoat loadings. This is particularly true for more active catalysts and/or fast SCR conditions. This opens the need for

increasing the gas–solid interfacial area and decreasing the effective washcoat thickness. This may be accomplished through higher density monoliths, for example.

11.5 Reactor Modeling Developments

Progress has been made towards the development of monolith reactor models that predict SCR performance under both steady state and transient operation. Guthenke et al. [33], provided a thorough review of SCR reactors. Most of the earlier work in this area was done for the more established Vanadia-based catalysts and involved the use of global kinetic models [81–83]. More recent works by Nova et al. provided detailed transient model for the SCR reaction system on Vanadia-based catalyst [8, 45]. Olsson and coworkers developed both global and detailed kinetic models for NH_3 -SCR reactions on Cu-ZSM-5 catalysts [14, 15, 49]. More recent works have communicated models for NH_3 -SCR reactions on Fe-zeolite catalysts [25, 57, 76, 84].

We highlight in this section some of these more recent developments of reactor models for Fe-based catalysts based on global kinetic descriptions. Our intent is to describe the state of the art, pointing out the main features and limitations of the two recent models. There remains a need to build on the emerging understanding of the mechanistic features of SCR through the use of reactors based on microkinetic models. That will undoubtedly be an area of activity in the coming years [15].

A transient global kinetic model was developed for Fe-exchanged zeolite monolith catalysts by Sjovald et al. [25]. The model incorporates several global reactions involving measured stable species, external mass transfer, and accumulation of adsorbed NH_3 . The model treats all reacting and product species as gas phase species except for NH_3 and NH_4NO_3 . The model accounts for the known nonideal adsorption and accumulation of NH_3 and assumes that NH_4NO_3 formation and accumulation occurs on a second type of site. In addition to the NH_4NO_3 formation reaction from NO_2 and adsorbed NH_3 , the model includes NO oxidation by O_2 , standard SCR, fast SCR, and NO_2 SCR. The model does not account for N_2O formation which is known to be a product of NH_4NO_3 decomposition. Instead the NH_4NO_3 is assumed to decompose to NO_2 , O_2 , and H_2O . The authors modify the stoichiometry of the standard SCR reaction to account for documented “overconsumption” of NH_3 in the presence of NO. In accounting for the coverage of NH_3 , the model considers that rate of the standard SCR reaction is proportional to the fraction of vacant sites, so as a result the model predicts the known rate inhibition NH_3 . The model does not account for a similar inhibitory effect of NH_3 on the fast SCR chemistry as we have described earlier, however. Finally, the model does not consider the existence of washcoat diffusion limitations which are undoubtedly present above 250 °C when NO_2 is in the feed, or 300 °C during standard SCR. Thus, application of the model to other catalysts would require modification of the kinetic parameters.

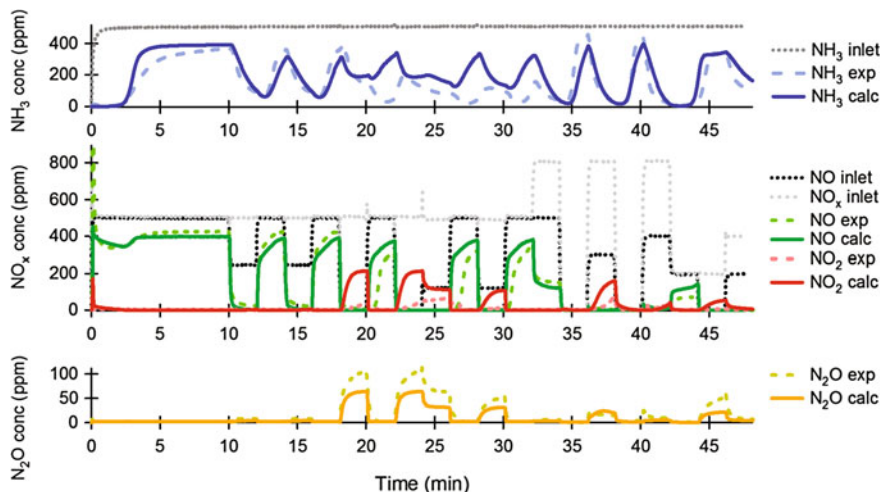


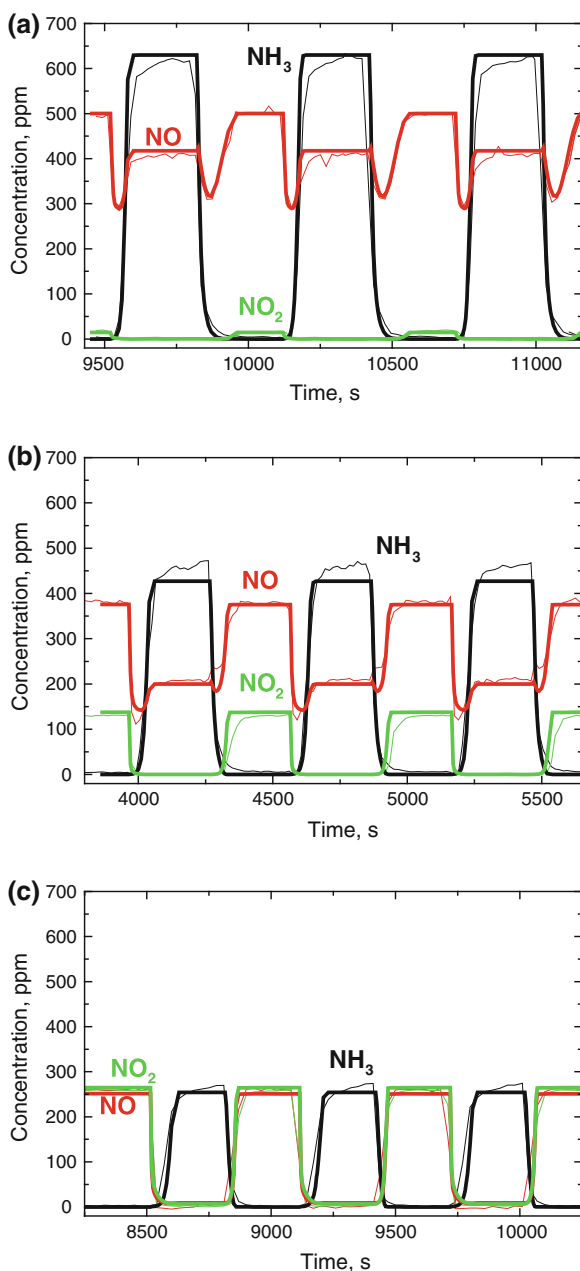
Fig. 11.19 Experimental and model-predicted effluent species concentrations during transient SCR (Used with permission [25].)

The Sjøvall et al. [25]. global model was tuned (i.e., parameters estimated) for a systematic and sequential set of experiments spanning NH₃ TPD, NO and NH₃ oxidation, standard SCR, fast SCR, and NO₂ SCR. The model was then validated by its ability to predict SCR for NO₂/NO_x feed ratios other than the ones used to tune the model ($\sim 0, 0.5, 0.75$). The results of the simulations, which considered both steady-state and transient experiments, reveal good agreement (Fig. 11.19). The transient predictions are especially noteworthy, showing how the catalyst responds to time-varying feeds containing different ratios of NO and NO₂.

Another recent model by Colombo et al. [57]. considered standard, fast, and NO₂ SCR on Fe-exchanged zeolites. This model builds off earlier models for vanadia and Fe catalysts, the new feature being inclusion of NO₂/NO_x \rightarrow 1 SCR chemistry. The model includes nonideal isotherm treatment of NH₃ adsorption to predict the ammonia coverage, rate expressions for NO oxidation, NH₃ oxidation, standard SCR (low and low temperature), ammonium nitrate formation and sublimation, N₂O formation, fast SCR, and N₂O formation and consumption. Some specific features are incorporated into rate expressions to account for certain effects. A Mars–Van Krevelen rate expression that includes NH₃ site blocking is used. The model predicts many of the trends in data obtained for commercial Fe-exchanged monolith catalyst (Fig. 11.20). Validation was demonstrated through simulations of NO₂/NO_x = 0.25 and 0.75 feeds. Very good agreement was demonstrated between model and experiment. This was described in the study by Guthenke et al. [33] in which the intrinsic kinetics were incorporated into a 1 + 1 D monolith model.

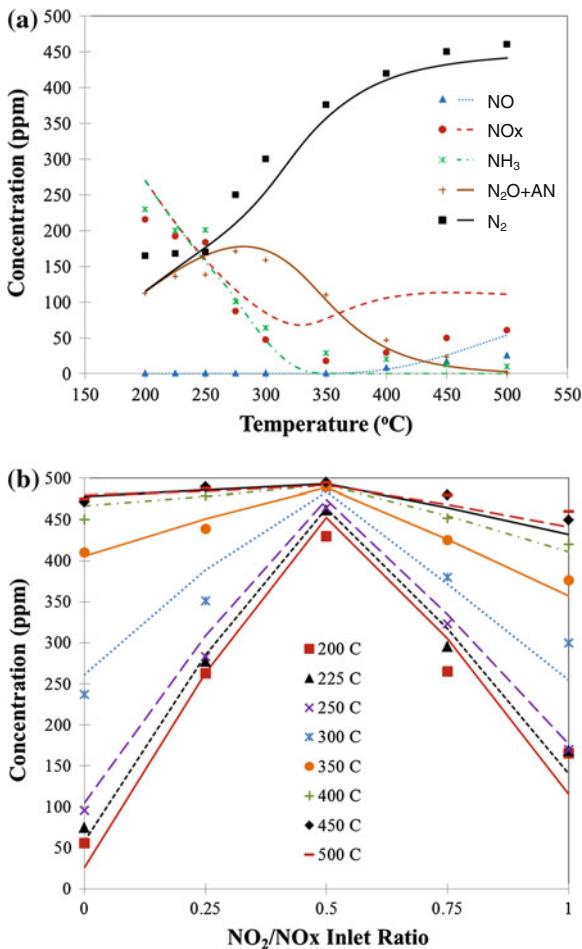
The recently developed SCR reactor model reported by Metkar et al. [76] also utilized a global kinetic description. The reactor and kinetic models have similar features to the Sjøvall et al. model but with some added features. Similarities included the incorporation of the key overall reactions and NH₃ adsorption.

Fig. 11.20 Experimental and model-predicted effluent species concentrations during transient SCR with three different feed concentrations. **a** NO = 500 ppm; **b** NO = 375 ppm, NO₂ = 125 ppm; **c** NO = NO₂ = 250 ppm (Used with permission [57].)



In contrast to the Sjøvall et al. model, the Metkar et al. model considered only steady-state data, but accounted for N₂O formation and consumption as well as washcoat diffusion. Specifically, the model accounted for NH₃ adsorption, NH₃

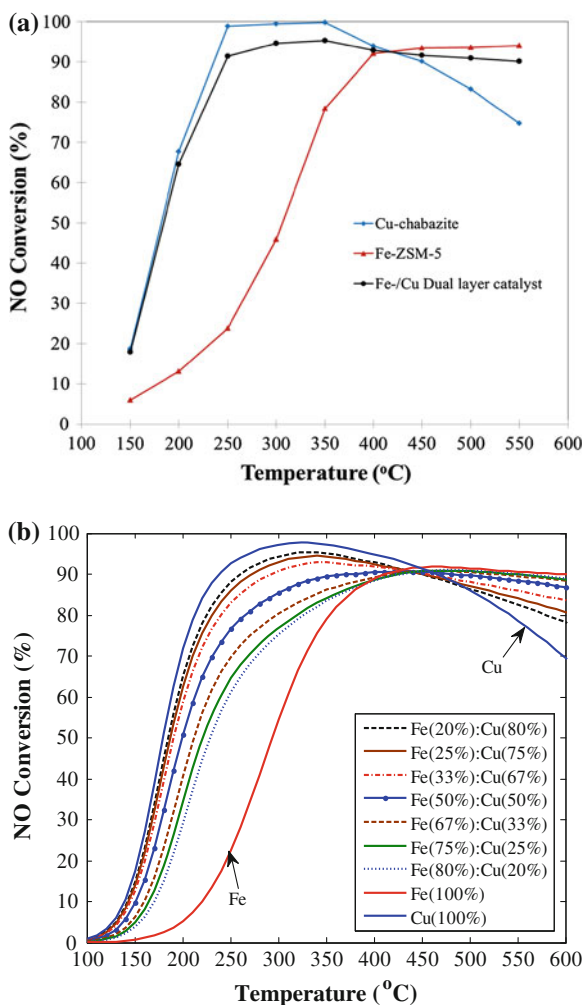
Fig. 11.21 Comparison of experimental (*symbols*) and model-predicted (*lines*) steady-state concentrations of various species obtained during the NO₂ SCR reaction studies carried out on Fe-ZSM-5. Feed: 500 ppm NO₂, 500 ppm NH₃, 5 % O₂, 2 % H₂O. (Adapted from Metkar et al. [76] and used with permission.)



oxidation, NO oxidation, standard SCR, fast SCR, NO₂ SCR, ammonium nitrate formation and its decomposition to N₂O, N₂O decomposition, and N₂O reduction by NH₃. The study also included a global kinetic model for the commercial Cu/chabazite zeolite catalyst commercialized by BASF Inc. This enabled the investigators to simulate combined Fe–Cu catalyst in the sequential brick and dual layer architectures.

The Metkar et al. [76] study followed a similar approach to that of Sjoval et al. [25], utilizing a systematic set of experiments with increasingly complex feeds to estimate parameters. The model was validated by simulating monoliths of different lengths and feeds with different compositions. The model captured very well the NO_x and NH₃ conversions and reasonably well the selectivity to the N₂O by-product. An example comparison of model and experiment is shown in Fig. 11.21a. It is interesting to note that the model predicted the onset of washcoat

Fig. 11.22 Steady-state NO conversions obtained during the standard SCR reaction on combined Cu- and Fe-exchanged zeolites. The dual layer catalysts for the experiments **a** comprised Fe-ZSM-5 (10–12 wt.%) on the underlying Cu-CHA commercial catalyst. The modeling **b** considered Fe-ZSM-5 as the top layer and Cu-CHA as the bottom layer. (Adapted from Metkar et al. [76] and used with permission.)



diffusion limitations reported in an earlier study. The capability of the model to predict trends over a wide range of temperature and feed compositions is shown in Fig. 11.21b. The model captures most of the overall and specific trends, such as the strong sensitivity to NO_2 at lower temperatures and the existence of the maximum N_2 yield at a $\text{NO}:\text{NO}_2$ feed ratio of unity, among other features.

The Metkar et al. [76] model was also used to predict the performance of combined Fe- and Cu-zeolite monolithic catalysts in the form of either sequential bricks or dual layers. Without any adjustment of the kinetic parameters from the tuning of the single component catalysts, the model predicted all of the main trends in the combined system data. An example result is shown in Fig. 11.22. The model predicts the wide expansion in the temperature window giving a high conversion

when the Fe-zeolite monolith was positioned upstream of the Cu-zeolite monolith, or was the top layer of a dual layer monolith. It is important to note that the simulation of the dual layer catalysts would not have been possible without accounting for the internal diffusion of reacting species in the washcoat layer(s). The model confirmed that there exists an optimal loading of Fe-zeolite in the form of a separate monolith brick or top layer. Current work in our group reveals an interesting interplay of reaction and diffusion, enabling the determination of which architecture is best in terms of NO_x conversion over a range of temperatures.

11.6 Concluding Remarks

The development of metal-exchange zeolites for lean NO_x reduction is one of the more significant developments in catalysis in recent years. In this chapter, we have attempted to capture the latest understanding of Fe-zeolite catalysts in terms of catalyst performance, mechanism, kinetics, reaction-transport interactions, and their combination with Cu-exchanged zeolites in multi-component Fe/Cu monolith catalysts.

The role of kinetic and reactor modeling is crucial in the continued advancement of these catalysts as they are optimized for specific applications. We have described different mechanisms for SCR for feed compositions spanning the standard to fast to NO₂ types. Convergence to the correct mechanisms is essential if predictive mechanistic-based kinetic models are to be developed. To date the kinetic models have been of the global variety. While these are useful for reactor optimization, microkinetic models are needed to guide rational catalyst design and the discovery of new catalyst formulations.

Finally, certain aspects that have not been covered in this chapter include coupled NH₃ and hydrocarbon SCR and SCR catalyst poisoning and aging/deactivation. Understanding and hopefully predicting the useful life of these catalysts is paramount. A molecular-level understanding of the mechanisms of hydrocarbon and sulfur poisoning and thermal degradation relies on mechanistic-based kinetic models.

Acknowledgments The authors wish to thank the U.S. Department of Energy Office of Vehicle Technologies for their support of our research in diesel emissions reduction using SCR. We also acknowledge the fruitful collaborations over the course of several years with Vemuri Balakotaiah (UH) and the helpful discussions with Bill Epling (UH), Krishna Kamasamudram (Cummins Inc.), and Enrico Tronconi (Politecnico di Milano).

References

1. G. Madia, M. Elsener, M. Koebel, F. Raimondi, a Wokaun, *Applied Catalysis B: Environmental* 39 (2002) 181.
2. C. Ciardelli, I. Nova, E. Tronconi, D. Chatterjee, B. Bandl-Konrad, M. Weibel, B. Krutzsch, *Applied Catalysis B: Environmental* 70 (2007) 80.
3. M. Koebel, M. Elsener, G. Madia, *Industrial & Engineering Chemistry Research* 40 (2001) 52.
4. G. Madia, M. Koebel, M. Elsener, A. Wokaun, *Industrial & Engineering Chemistry Research* 41 (2002) 4008.
5. I. Nova, C. Ciardelli, E. Tronconi, D. Chatterjee, B. Bandl-Konrad, *Catalysis Today* 114 (2006) 3.
6. M. Koebel, G. Madia, M. Elsener, *Catalysis Today* 73 (2002) 239.
7. E. Tronconi, I. Nova, C. Ciardelli, D. Chatterjee, B. Bandl-Konrad, T. Burkhardt, *Catalysis Today* 105 (2005) 529.
8. I. Nova, C. Ciardelli, E. Tronconi, D. Chimica, I. Chimica, P. Milano, I.- Milan, D. Chatterjee, B. Bandl-konrad, D. Ag, A. Rbp, D.- Stuttgart, *AIChE Journal* 52 (2006).
9. D. Chatterjee, P. Kočí, V. Schmeißer, M. Marek, M. Weibel, B. Krutzsch, *Catalysis Today* 151 (2010) 395.
10. K. Kamasamudram, N.W. Currier, X. Chen, A. Yezerets, *Catalysis Today* 151 (2010) 212.
11. K. Kamasamudram, N.W. Currier, T. Szailer, A. Yezerets, *SAE International* (2010).
12. M. Colombo, I. Nova, E. Tronconi, *Catalysis Today* 151 (2010) 223.
13. H. Sjövall, L. Olsson, E. Fridell, R.J. Blint, *Applied Catalysis B: Environmental* 64 (2006) 180.
14. L. Olsson, H. Sjövall, R.J. Blint, *Applied Catalysis B: Environmental* 81 (2008) 203.
15. H. Sjövall, R.J. Blint, L. Olsson, *Applied Catalysis B: Environmental* 92 (2009) 138.
16. G. Delahay, B. Coq, L. Broussous, *Applied Catalysis B: Environmental* 12 (1997) 49.
17. G. Delahay, S. Kieger, N. Tanchoux, P. Trens, B. Coq, *Applied Catalysis B: Environmental* 52 (2004) 251.
18. J.H. Baik, S.D. Yim, I.-S. Nam, Y.S. Mok, J.-H. Lee, B.K. Cho, S.H. Oh, *Industrial & Engineering Chemistry Research* 45 (2006) 5258.
19. A. Grossale, I. Nova, E. Tronconi, *Catalysis Letters* 130 (2009) 525.
20. R. Long, *Journal of Catalysis* 207 (2002) 224.
21. M. Schwidder, S. Heikens, a Detoni, S. Geisler, M. Berndt, a Bruckner, W. Grunert, *Journal of Catalysis* 259 (2008) 96.
22. Q. Sun, Z. Gao, H. Chen, W. Sachtler, *Journal of Catalysis* 201 (2001) 88.
23. M. Devadas, O. Krocher, M. Elsener, a Wokaun, N. Soger, M. Pfeifer, Y. Demel, L. Mussmann, *Applied Catalysis B: Environmental* 67 (2006) 187.
24. O. Kröcher, M. Devadas, M. Elsener, A. Wokaun, N. Söger, M. Pfeifer, Y. Demel, L. Mussmann, *Applied Catalysis B: Environmental* 66 (2006) 208.
25. H. Sjoval, R.J. Blint, A. Gopinath, L. Olsson, *Industrial & Engineering Chemistry Research* 49 (2010) 39.
26. M. Iwasaki, K. Yamazaki, H. Shinjoh, *Applied Catalysis A: General* 366 (2009) 84.
27. A. Grossale, I. Nova, E. Tronconi, D. Chatterjee, M. Weibel, *Journal of Catalysis* 256 (2008) 312.
28. S. Zones, Zeolite SSZ-13 and Its Method of Preparation, U.S. Patent US4544538, 1985.
29. I. Bull, W.-M. Xue, P. Burk, R.S. Boorse, W.M. Jaglowski, G.S. Koermer, A. Moini, J.A. Patchett, J.C. Dettling, M.T. Caudle, Copper CHA Zeolite Catalysts, U.S. Patent US7601662, 2009.
30. S.J. Schmiege, S.H. Oh, C.H. Kim, D.B. Brown, J.H. Lee, C.H.F. Peden, D.H. Kim, *Catalysis Today* 184 (2012) 252.
31. H.-X. Li, W.E. Cormier, B. Moden, Novel Microporous Crystalline Material Comprising a Molecular Sieve, U.S. Patent US 2008/0241060 A1, 2010.
32. S. Brandenberger, O. Kröcher, A. Tissler, R. Althoff, *Catalysis Reviews* 50 (2008) 492.

33. A. Guthenke, D. Chatterjee, M. Weibel, B. Krutzsch, P. Koci, I. Nova, E. Tronconi, *Advances in Chemical Engineering* 33 (2008) 103.
34. M. Devadas, O. Krocher, M. Elsener, a Wokaun, N. Soger, M. Pfeifer, Y. Demel, L. Mussmann, *Applied Catalysis B: Environmental* 67 (2006) 187.
35. H.Y. Huang, R.Q. Long, R.T. Yang, *Applied Catalysis A: General* 235 (2002) 241.
36. A. Grossale, I. Nova, E. Tronconi, *Catalysis Today* 136 (2008) 18.
37. H.-Y. Chen, T. Voskoboinikov, W.M.H. Sachtler, *Journal of Catalysis* 186 (1999) 91.
38. M. Iwasaki, K. Yamazaki, K. Banno, H. Shinjoh, *Journal of Catalysis* 260 (2008) 205.
39. M. Devadas, O. Krocher, a Wokaun, *Reaction Kinetics and Catalysis Letters* 86 (2005) 347.
40. A. Grossale, I. Nova, E. Tronconi, *Journal of Catalysis* 265 (2009) 141.
41. G. Delahay, D. Valade, a Guzmanvargas, B. Coq, *Applied Catalysis B: Environmental* 55 (2005) 149.
42. P.S. Metkar, N. Salazar, R. Muncrief, V. Balakotaiah, M.P. Harold, *Applied Catalysis B: Environmental* 104 (2011) 110.
43. M. Koebel, *Journal of Catalysis* 209 (2002) 159.
44. I. Nova, C. Ciardelli, E. Tronconi, D. Chatterjee, M. Weibel, *Topics in Catalysis* 42-43 (2007) 43.
45. I. Nova, C. Ciardelli, E. Tronconi, D. Chatterjee, M. Weibel, *AIChE Journal* 55 (2009) 1514.
46. Y.H. Yeom, B. Wen, W.M.H. Sachtler, E. Weitz, *Journal of Physical Chemistry B* 108 (2004) 5386.
47. Y. Yeom, M. Li, A. Savara, W. Sachtler, E. Weitz, *Catalysis Today* 136 (2008) 55.
48. C. Ciardelli, I. Nova, E. Tronconi, B. Bandl-konrad, *Chem. Communications* 3264 (2004) 2718.
49. Y. Yeom, J. Henaio, M. Li, W. Sachtler, E. Weitz, *Journal of Catalysis* 231 (2005) 181.
50. S. Suárez, S. Moon, P. Avila, P. Grange, J. Blanco, *75* (2002) 331.
51. J.R. Klovsky, P. Koradla, C.T. Lim, *Industrial & Engineering Chemistry Product Research and Development* 19 (1980) 218.
52. M. Richter, R. Eckelt, B. Parltitz, R. Fricke, *Applied Catalysis B: Environmental* 15 (1998) 129.
53. L. Olsson, H. Sjövall, R.J. Blint, *Applied Catalysis B: Environmental* 87 (2009) 200.
54. M.P. Ruggeri, I. Nova, E. Tronconi, in: CAPoC9, Brussels, 2012.
55. D. Bhatia, R.W. McCabe, M.P. Harold, V. Balakotaiah, *Journal of Catalysis* 266 (2009) 106.
56. P.S. Metkar, V. Balakotaiah, M.P. Harold, *Catalysis Today* 184 (2012) 115.
57. M. Colombo, I. Nova, E. Tronconi, V. Schmeißer, B. Bandl-Konrad, L. Zimmermann, *Applied Catalysis B: Environmental* 111-112 (2012) 106.
58. A. Grossale, I. Nova, E. Tronconi, D. Chatterjee, M. Weibel, *Topics in Catalysis* 52 (2009) 1837.
59. P.S. Metkar, V. Balakotaiah, M.P. Harold, *Catalysis Today* 184 (2012) 115.
60. J. Eng, C.H. Bartholomew, *Journal of Catalysis* 171 (1997) 27.
61. M. Rivallan, G. Ricchiardi, S. Bordiga, A. Zecchina, *Journal of Catalysis* 264 (2009) 104.
62. J.M. Fedeyko, B. Chen, H.-Y. Chen, *Catalysis Today* 151 (2010) 231.
63. M. Iwasaki, H. Shinjoh, *Journal of Catalysis* 273 (2010) 29.
64. M. Li, Y. Yeom, E. Weitz, W. Sachtler, *Journal of Catalysis* 235 (2005) 201.
65. C.H. Bibart, G.E. Ewing, *The Journal of Chemical Physics* 61 (1974) 1293.
66. M. Ahrens, O. Marie, P. Bazin, M. Daturi, *Journal of Catalysis* 271 (2010) 1.
67. M.E. Jenkin, O.X. Ora, *Atmospheric Environment* 22 (1987) 487.
68. M.W. Ross, T.C. DeVore, *The Journal of Physical Chemistry. A* 112 (2008) 6609.
69. R. Kefirov, E. Ivanova, K. Hadjiivanov, S. Dzwigaj, M. Che, *Catalysis Letters* 125 (2008) 209.
70. G. Panov, E. Starokon, L. Pirutko, E. Paukshtis, V. Parmon, *Journal of Catalysis* 254 (2008) 110.
71. Q. Sun, Z. Gao, B. Wen, W.M.H. Sachtler, *Catalysis Letters* 78 (2002) 3.
72. Y. Kameoka, R.L. Pigford, *Industrial & Engineering Chemistry Research* 16 (1977) 163.

73. B.R. Kromer, L. Cao, L. Cumarantunge, S.S. Mulla, J.L. Ratts, A. Yezerets, N.W. Currier, F.H. Ribeiro, W.N. Delgass, J.M. Caruthers, *Catalysis Today* 136 (2008) 93.
74. S. Brandenberger, O. Kröcher, A. Tissler, R. Althoff, *Applied Catalysis B: Environmental* 95 (2010) 348.
75. M. Li, J. Henao, Y. Yeom, E. Weitz, W.M.H. Sachtler, *Catalysis Letters* 98 (2004) 5.
76. P.S. Metkar, M.P. Harold, V. Balakotaiah, *Chemical Engineering Science* 87 (2013) 51.
77. M.P. Ruggeri, A. Grossale, I. Nova, E. Tronconi, H. Jirglova, Z. Sobalik, *Catalysis Today* 184 (2012) 107.
78. P.S. Metkar, V. Balakotaiah, M.P. Harold, *Chemical Engineering Science* 66 (2011) 5192.
79. I. Nova, D. Bounechada, R. Maestri, E. Tronconi, A.K. Heibel, T.A. Collins, T. Boger, *Industrial & Engineering Chemistry Research* 50 (2011) 299.
80. P.S. Metkar, M.P. Harold, V. Balakotaiah, *Applied Catalysis B: Environmental* 111-112 (2012) 67.
81. J.A. Dumesic, N. Topsøe, H. Topsøe, Y. Chen, T. Slabiak, 417 (1996) 409.
82. B. Roduit, A. Wokaun, A. Baiker, *Industrial & Engineering Chemistry Research* 37 (2000) 4577.
83. R. Willi, B. Roduit, R.A. Koepfel, A. Wokaun, I. Chemistry, *Chemical Engineering Science* 51 (2000) 2897.
84. S. Malmberg, M. Votsmeier, J. Gieshoff, N. Söger, L. Mußmann, a. Schuler, a. Drochner, *Topics in Catalysis* 42-43 (2007) 33.

Chapter 12

Kinetic Modeling of Ammonia SCR for Cu-Zeolite Catalysts

Louise Olsson

In this chapter, kinetic models for ammonia SCR over Cu-zeolites are described. Both global and detailed models are presented and both commercial materials as well as model samples are used. In the SCR system, several reactions are important in order to describe the mechanism and these reactions are discussed below. Ammonia storage and desorption on the catalyst surface is crucial in order to capture the transient behavior of the catalytic system. These steps are examined using both temperature programmed desorption experiments, as well as with the help of microcalorimetry techniques. In more detailed kinetic models, adsorption of other species like water and NO_x are also considered. Depending on the NO_2 to NO_x ratio, different SCR reactions will occur; standard SCR, rapid SCR, and slow NO_2 SCR. These reactions are added to kinetic models, either in global format or more detailed reaction steps. In addition, there are several other reactions occurring during the SCR process, such as, for example, NO oxidation to produce NO_2 . Unfortunately, there are also several unwanted side reactions taking place, like ammonia oxidation and N_2O formation. These steps are crucial to add to kinetic models and are described in this chapter.

12.1 Introduction

An important group of catalysts for NO_x reduction through ammonia SCR is represented by copper exchanged zeolites [1–9]. Many different zeolites have been investigated, for example, Cu-ZSM-5 [10–13], Cu-faujasite [14], Cu-Beta [15, 16], and Cu-Y [17]. Recently, copper zeolites with chabazite (CHA) structure have received great attention due to their high thermal stability and hydro carbon resistance [18]. Both Cu-SAPO-34 [19] and Cu-SSZ-13 [18] have a CHA structure

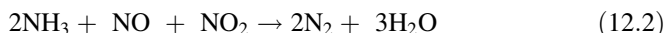
L. Olsson (✉)

Competence Centre for Catalysis, Chemical Engineering, Chalmers University
of Technology, SE-412 96 Gothenburg, Sweden
e-mail: louise.olsson@chalmers.se

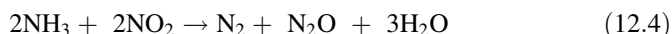
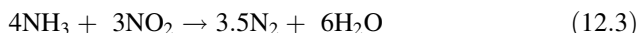
and have been investigated for NH_3 SCR. The NO_x conversion depends on the NO_2 ratio in the feed. When only NO is present, the standard SCR reaction occurs as follows:



while if equimolar amounts of NO and NO_2 are present, the fast SCR reaction dominates at a much higher rate:



However, if the NO_2 to NO_x ratio is high, the slow NO_2 SCR reaction occurs while the amount of N_2O produced is also increased:



Kinetic models for ammonia SCR have been developed for vanadia on titania [20–24], Cu-ZSM-5 [10–13], Cu-faujasite [14], HZSM-5 [25], and Fe zeolites [26–28]. In this chapter, the focus is on kinetic models for ammonia SCR over copper zeolites. Both global and detailed kinetic models will be described and many subreactions in the mechanism, such as ammonia storage, ammonia oxidation, NO oxidation etc., will be discussed in detail.

12.2 Kinetic Models for Ammonia and Water Storage Over Cu-Zeolites

The copper zeolites store large amounts of ammonia. This is an important feature of these catalysts, since ammonia stored at the surface at medium temperatures can be used at low temperatures, where it is not possible to dose urea due to by-product formation. It is, therefore, crucial to describe ammonia storage and desorption in a kinetic model accurately to be able to predict transient variations.

The most common way to describe ammonia adsorption and desorption in SCR catalysts, in general, is to use the Temkin type isotherm [10, 13, 24, 27, 29]. The Temkin adsorption isotherm considers the adsorbate-adsorbate interactions, and in the models therefore coverage dependent heat of adsorption is used. This also results in that the activation energy for desorption of NH_3 is coverage dependent:

$$E_{\text{des}} = E_{\text{des}}(0)(1 - \alpha\theta_{\text{NH}_3}) \quad (12.5)$$

where $E_{\text{des}}(0)$ is the activation energy for desorption for zero coverage, α is a constant, and θ_{NH_3} is the coverage of ammonia on the surface. The heat of adsorption can be determined by fitting parameters to TPD experiments, which is the most common method. However, calorimetry is a powerful technique for measuring the heat of adsorption directly [16]. The advantage of this method is

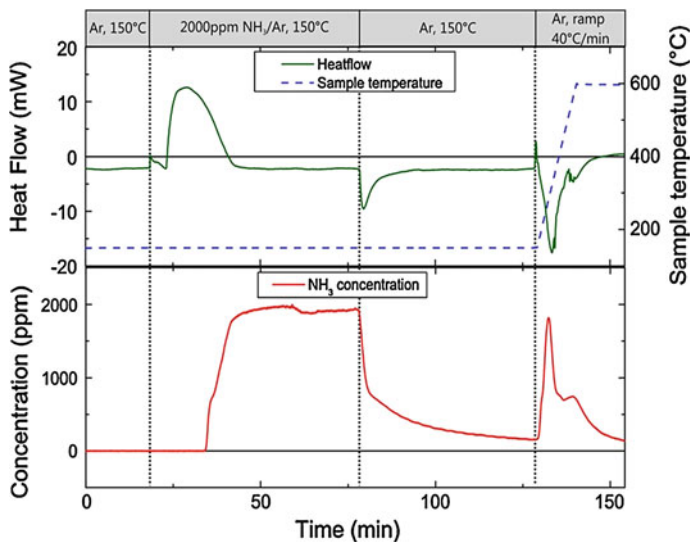


Fig. 12.1 Ammonia TPD experiment on Cu-Beta. The top panel shows the heat flow and the lower panel the ammonia concentration [16]. Reprinted with permission from Wilken et al. [16]. Copyright (2010) Elsevier

that it measures ΔH , thereby avoiding correlations between some of the parameters (for example, between the pre-exponential factor and activation barrier for desorption). Heat of adsorption of ammonia on zeolites has been measured previously, resulting in ΔH for zero coverage of -130 kJ/mol for H-ZSM-5 ($\text{SiO}_2/\text{Al}_2\text{O}_3$ ratio of 30) [30], -130 kJ/mol for H-Beta ($\text{SiO}_2/\text{Al}_2\text{O}_3$ ratio of 19.6) [30] and -120 – 130 kJ/mol for H-ZSM-5 ($\text{SiO}_2/\text{Al}_2\text{O}_3$ ratio of 110) [31]. Average ΔH is also reported, resulting in -114 kJ/mol for H-ZSM-5 ($\text{SiO}_2/\text{Al}_2\text{O}_3$ ratio of 110) [31] and -104.8 kJ/mol for Cu-ZSM-5 ($\text{SiO}_2/\text{Al}_2\text{O}_3$ ratio of 30) [32].

Wilken et al. [16] conducted an ammonia TPD experiment in the calorimeter, while simultaneously measuring the heat produced/used, the results of which are shown in Fig. 12.1. In this experiment, the Cu-BEA catalyst is exposed to 2,000 ppm NH_3 , which results in an exotherm and simultaneously there is a total uptake of all ammonia. When the catalyst is saturated with ammonia, ammonia breaks through and no heat is released. After the ammonia step, the catalyst is flushed with Ar only and weakly bound ammonia is released. This reaction is endotherm and heat is consumed (see top panel Fig. 12.1). In the last step, the temperature is increased and ammonia is desorbing. This experiment resulted in an average heat of adsorption of about -100 kJ/mol [16]. However, as mentioned above, the heat of adsorption of ammonia is coverage dependent. Wilken et al. [16] developed a method for determining the coverage dependent heat of adsorption at atmospheric pressure. Initially, the catalyst was exposed to ammonia at 500 °C (see Fig. 12.2). Only the most strongly bound ammonia is adsorbed at this high temperature, which results in a low ammonia coverage with high ΔH . The catalyst

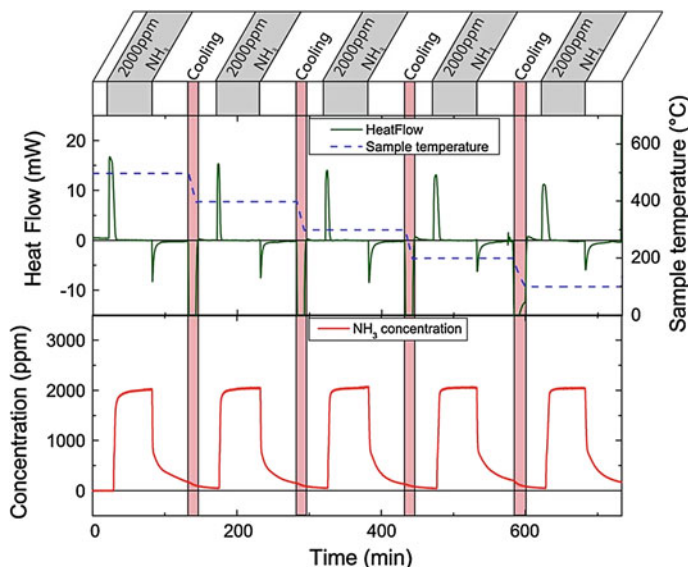
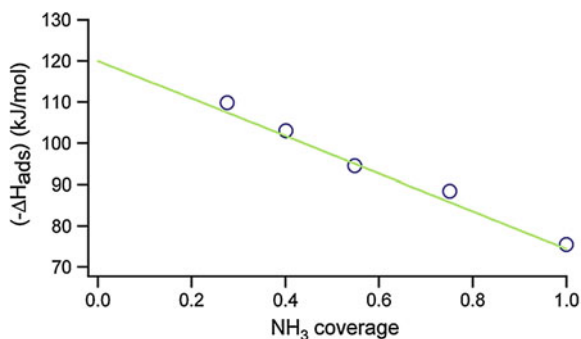


Fig. 12.2 Stepwise ammonia adsorption experiment over Cu-Beta [16]. Reprinted with permission from Wilken et al. [16]. Copyright (2010) Elsevier

Fig. 12.3 Heat of adsorption versus ammonia coverage, where the circles represent experimental values and the line is a linear fit [16]. Reprinted with permission from Wilken et al. [16]. Copyright (2010) Elsevier



is, thereafter, exposed to Ar only and the temperature decreases to 400 °C. At this temperature, another ammonia step is performed which results in a lower heat of adsorption. This procedure is repeated at 300, 200, and 100 °C (see Fig. 12.2), which results in lowering the heat released for each step. The results of this stepwise ammonia adsorption experiment are used to calculate the heat of adsorption and the corresponding ammonia coverage on the surface, which is described in more detail in Ref. [16]. These results are shown in Fig. 12.3.

The results clearly show a linear dependence of the heat of adsorption as a function of ammonia coverage. A linear fit of the experimental points results in:

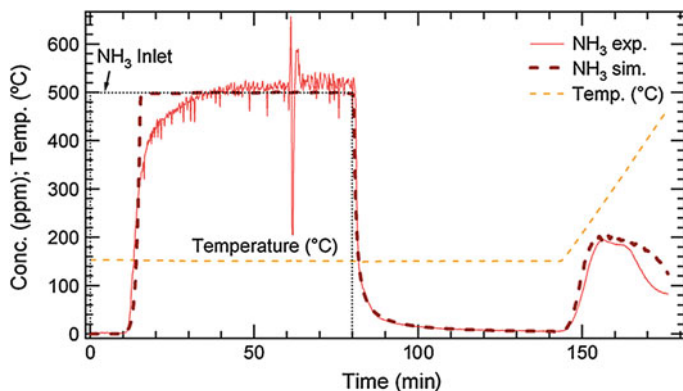


Fig. 12.4 Experiment (*solid line*) and simulation (*dashed line*) from an NH_3 TPD experiment over Cu-ZSM-5 catalyst [10]. Reprinted with permission from Olsson et al. [10]. Copyright (2008) Elsevier

$$E_{\text{desorption, NH}_3} = 120.0 \cdot (1 - 0.38 \cdot \theta_{\text{NH}_3}) \quad (12.6)$$

The microcalorimetry data have been successfully used in kinetic models (not shown here).

12.2.1 Global Kinetic Model for Ammonia Storage and Desorption

In an earlier study, Olsson et al. [10] fitted the parameters for ammonia adsorption and desorption to an ammonia TPD experiment conducted over Cu-ZSM-5, using coverage dependent activation energy for ammonia desorption, occurring on one storage site S1 according to:



The results of the experiment and model are shown in Fig. 12.4. Initially, there is a total uptake of all ammonia for about 10 min. This is followed by a breakthrough of ammonia until saturation is reached. After about 80 min, the ammonia is shut off and some weakly bound ammonia is released. Finally, the temperature is increased and a large ammonia desorption follows. The desorption peak is broad and contains a shoulder. Thus, there are different types of ammonia storage sites available in the catalyst. The model (see Fig. 12.4) describes this broad feature well by a coverage dependent heat of adsorption. It should be mentioned that S1, which is used in the global kinetic model is the total amount of sites that can adsorb ammonia, thus likely covering both Brønsted acid sites as well as different copper sites.

12.2.2 Detailed Kinetic Model for Ammonia and Water Storage

In addition, detailed kinetic models for ammonia adsorption and desorption [13], NO oxidation [11], and SCR [12] over Cu-ZSM-5 was developed. The active sites for all reactions are, in this model, the copper sites, which are denoted S1a and the amount determined from ICP-AES. In addition, on this site, all the molecules can adsorb (NH_3 , O_2 , NO_2 , H_2O). However, according to electron paramagnetic resonance studies (EPR) [33, 34] and density functional theory calculations [17], it has been previously suggested in the literature that copper is capable of coordinating up to four ammonia molecules. This is in accordance with the mechanism for SCR by Komatsu et al. [35], where four ammonia molecules are attached to copper. We, therefore, used up to four ammonia molecules, bound to each copper site [13] and practically this is done by introducing S1b, where ammonia can adsorb. S1b is three times larger than the amount of copper sites, resulting in that S1a + S1b is four times larger than the Cu-sites. Further, water was also found to adsorb in large quantities and therefore, water is adsorbed on S1b. In the surface description also, acid sites, denoted S2, and physisorbed sites, denoted S3 are included. In this section, the ammonia storage and desorption is described and in the following sections details are given for the other adsorbates as well as the reactions. The results of the detailed ammonia storage kinetic model together with an ammonia TPD experiment conducted at room temperature, are shown in Fig. 12.5a and the calculated mean coverages in Fig. 12.5b. The calculated coverages suggest that ammonia on the Brönstedt acid sites (S2) and ammonia on S1b (copper site, where ammonia and water adsorb) is the most strongly bound ammonia. The strength of ammonia on the copper site responsible for the reactions (S1a), was critical in order not to block the adsorption of oxygen and NO_x species, and thereby the activity for the different reactions. Both the global (see Fig. 12.4) and detailed (see Fig. 12.5) kinetic models describe the experimental features well, except for the slow storage of ammonia when the catalyst is close to saturation. It is possible that there is a mass-transport limitation or sterical hindrance when reaching saturation that causes this behavior. However, when examining the total amount of ammonia stored, this discrepancy is only a small fraction. In addition, in a real application, the catalyst will never be completely saturated since a very large ammonia slip would then occur.

Further, a detailed model of water adsorption and desorption was developed; the results of a water TPD experiment are shown in Fig. 12.6 [13]. Water is released with a distinct peak at lower temperature; however, water continues to be released up to very high temperatures. These results clearly demonstrate the complex interactions between water and zeolite.

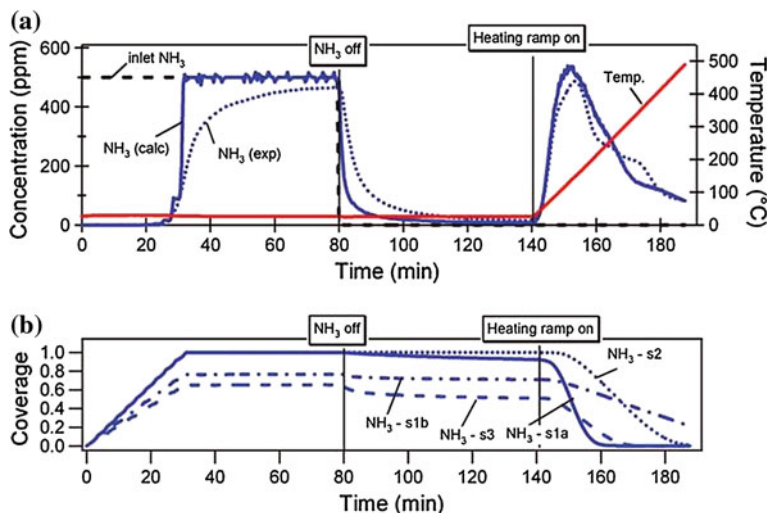
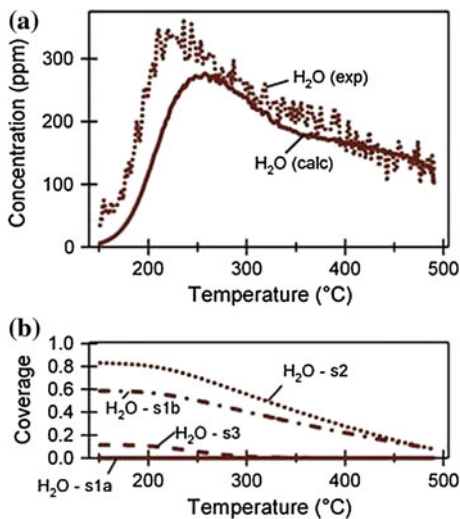


Fig. 12.5 Ammonia TPD experiment at room temperature over Cu-ZSM-5. **a** The concentrations of ammonia from the experiment and model. **b** The calculated mean coverages [13]. Reprinted with permission from Sjövall et al. [13]. Copyright (2009) American Chemical Society

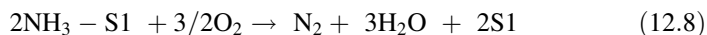
Fig. 12.6 Water TPD experiment over Cu-ZSM-5. **a** The concentrations of water from the experiment and model. **b** The calculated mean coverages [13]. Reprinted with permission from Sjövall et al. [13]. Copyright (2009) American Chemical Society



12.3 Kinetic Models for Ammonia Oxidation Over Cu-Zeolites

12.3.1 Global Kinetic Model for Ammonia Oxidation

At high temperature, ammonia is oxidized by oxygen, which decreases the selectivity of the standard SCR reaction. In a kinetic model that should describe a broad temperature interval, it is therefore crucial to have a good description of the ammonia oxidation. Accordingly, we investigated ammonia oxidation separately in order to decrease the correlation between the parameters. In the global kinetic model, the following reaction was added in which ammonia stored on the surface is oxidized to produce N_2 and H_2O :



Since no by-products like NO or N_2O were observed during ammonia oxidation, these reactions were excluded from the model. The results from the model and experiment are shown in Fig. 12.7 [10]. Prior to this experiment, the catalyst was pretreated with oxygen at high temperature in order to clean the surface from ammonia. When introducing the gas mixture consisting of ammonia, oxygen, and water, there was a long total uptake of ammonia attributable to the large storage [10]. At low temperature, no ammonia oxidation is observed and ammonia desorption is only visible when the temperature increases. However, significant ammonia oxidation is observed from 300 °C and increases with increasing temperature.

12.3.2 Detailed Kinetic Model for Ammonia Oxidation

Ammonia oxidation was included in the detailed model [12] (results not included). In this model, two reaction steps were added, where ammonia on the surface was oxidized either with oxygen alone or in a second step in a combination with hydroxyl groups. The hydroxyls are produced according to:



It was essential to add the reaction step, where ammonia reacts with hydroxyl groups in the detailed model, since the coverage of hydroxyl groups was large on the surface, but the simultaneous ammonia conversion only slightly decreased. Without this reaction step, the ammonia oxidation rate was significantly too low in the presence of water. For the global model described in Ref. [10], the effect of water was not included since all experiments contained high levels of water, and the model was therefore tuned in the presence of water.

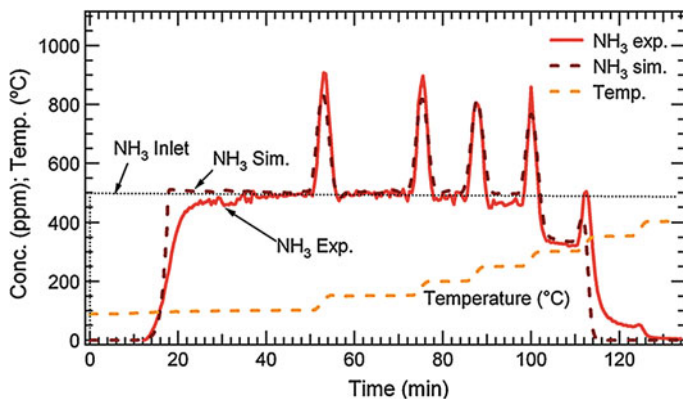
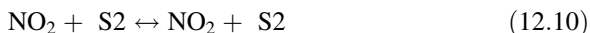


Fig. 12.7 Ammonia oxidation over Cu-ZSM-5 using 8 % O₂, 5 % H₂O, and 500 ppm NH₃ [10]. Reprinted with permission from Olsson et al. [10]. Copyright (2008) Elsevier

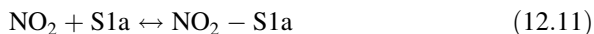
12.4 Kinetic Models for NO_x Storage and NO Oxidation Over Cu-Zeolites

12.4.1 Detailed Kinetic Model for NO Oxidation

NO_x storage is observed over copper zeolites [11, 36]. Colombo et al. [36] examined the NO₂ storage over pre-oxidized and pre-reduced Cu-CHA, with the results shown in Fig. 12.8. Slightly more NO is observed during the storage process for the pre-reduced sample, but this effect will not be discussed in this chapter. Instead, we will focus on the storage of the pre-oxidized catalyst. When the catalyst is exposed to NO₂ only, significant storage is observed (see Fig. 12.8c) and NO is simultaneously produced (Fig. 12.8b) due to the formation of nitrates. The nitrates formed are stable and decompose with a maximum NO_x desorption of about 400 °C (see Fig. 12.8d). We observed that NO₂ is also adsorbed on the pure zeolite (H-ZSM-5) [11]. In the detailed kinetic model, this feature was modeled separately using a reaction step:



where S2 is an acidic site in the zeolite. The parameters for this storage were later used when modeling the NO₂ storage over Cu-ZSM-5 [11] (see Eq. 12.11). In addition, the following reaction steps were added to describe the NO oxidation:



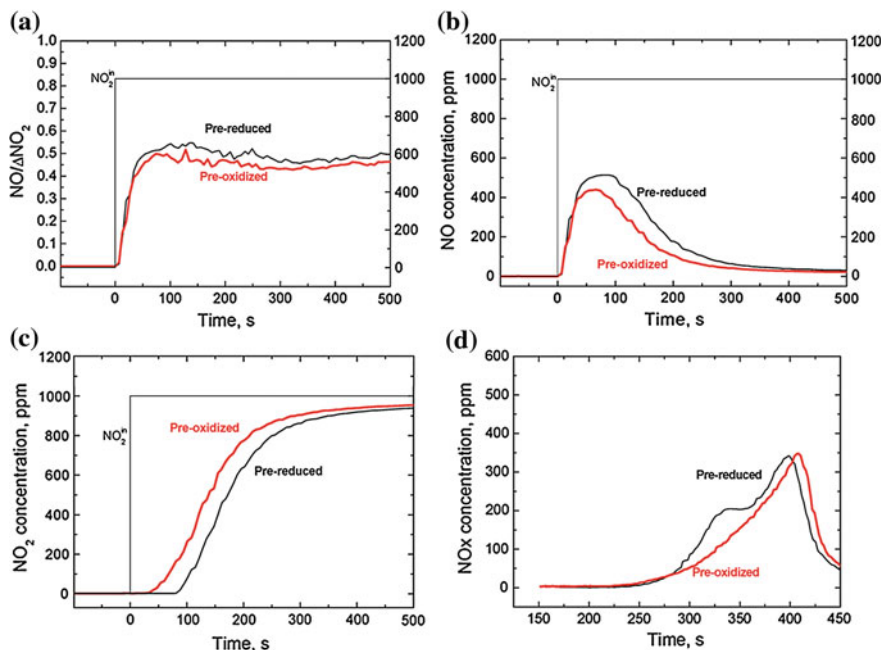
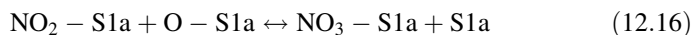


Fig. 12.8 NO_2 TPD experiment at 200 °C over Cu-CHA. **a** The ratio of NO produced divided by NO_2 consumed. **b** NO concentration in the initial part of the adsorption. **c** NO_2 concentration in the initial part of the adsorption and **d** NO_x concentration during TPD [36]. Reprinted with permission from Colombo et al. [36]. Copyright (2012) Elsevier

where S1a is the active copper site. In order to simplify the detailed kinetic model [11], an Eley-Rideal mechanism was used for NO oxidation (see Eq. 12.14). Only minor amounts of NO were observed to adsorb on this catalyst, which is why NO storage was not critical to the model. However, it is still possible that the actual mechanism occurs through a Langmuir-Hinshelwood mechanism, but it is not necessary to include this step in the model in order to describe the experimental features.

NO was observed when exposing the catalyst to NO_2 ; thus, it is important to add a reaction step whereby nitrites are oxidized by NO_2 , to simultaneously produce nitrates and NO (see Eq. 12.15). Experimentally, we observe that when increasing the temperature and exposing the catalyst to Ar only, nitrates are decomposing. However, the reverse reaction in Eq. (12.15) requires NO in the gas phase and will not take place in pure Ar. Since this is not the case experimentally, an additional step was added in which nitrates decompose directly. In order to make the model thermodynamically consistent, this reaction was also reversible [11].



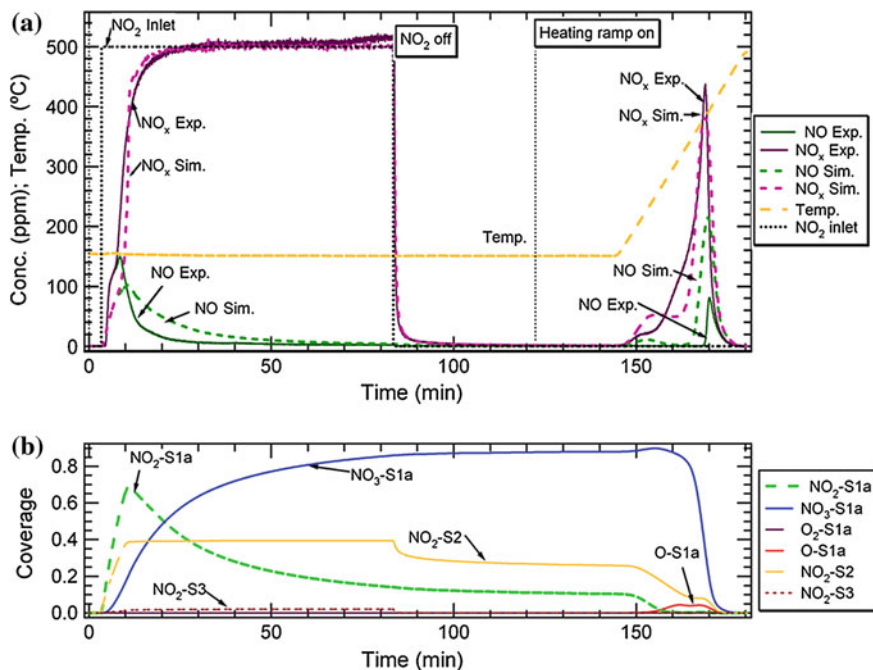


Fig. 12.9 NO₂ TPD at 150 °C over Cu-ZSM-5 [11]. **a** Solid lines Experiment and dashed lines kinetic model. **b** Calculated mean coverages on the surface. Reprinted with permission from Olsson et al. [11]. Copyright (2009) Elsevier

The results of the experiment (solid line) and the kinetic model (dashed line) for the NO₂ TPD at 150 °C over Cu-ZSM-5 are shown in Fig. 12.9 [11]. The model describes the experimental features adequately. In the lower panel of Fig. 12.9, the coverage on the surface is shown. Based on these results, it becomes evident that nitrites are initially formed on the copper sites and are later converted to nitrates.

An interesting feature was observed involving NO oxidation at low temperature under dry conditions over Cu-ZSM-5. This was observed in an experiment where the catalyst was exposed to NO and oxygen only and the temperature increased in a number of successive steps (30, 50, 100, 30, 50 and 100 °C), see Fig. 12.10 [11]. At 30 °C, substantial NO oxidation to NO₂ is observed. Surprisingly, when increasing the temperature to 50 °C, the NO₂ is decreasing and when further increasing it to 100 °C, the NO oxidation almost vanishes. The behavior is reproducible as seen by increased NO₂ production when the temperature is once again lowered to 30 °C. We suggest that the reason is that at very low temperatures, there are physisorbed species on the surface that account for the low temperature activity. When the temperature increases, the coverage of these species is decreasing, which is also the case with NO oxidation. At higher temperature, the regular NO oxidation takes place, which in the model is occurring on the copper sites. In the detailed kinetic

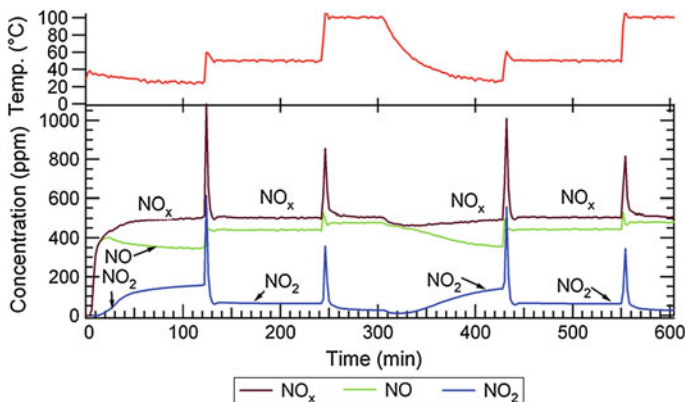
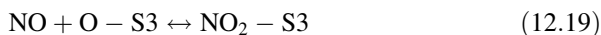


Fig. 12.10 NO oxidation experiment over Cu-ZSM-5 using 500 ppm NO and 8 % O₂ and changing the temperature stepwise (30, 50, 100, 30, 50 and 100 °C) [11]. Reprinted with permission from Olsson et al. [11]. Copyright (2009) Elsevier

model, three reversible reactions were added in order to describe the low temperature NO oxidation:



where S3 denotes a site for physisorbed species.

The combination of reactions (12.10–12.19) was used in the kinetic model for NO_x storage and NO oxidation under dry conditions over a large temperature interval, with the results shown in Fig. 12.11. The model accurately describes the NO oxidation, both at low and high temperature [11]. At high temperatures, the NO oxidation activity drops because of thermodynamic restrictions. The lower panel in Fig. 12.11 shows the mean coverages on the surface; it becomes clear that the S3 site is only active at low temperature because at higher temperatures, the coverage on this site is very low. In addition, due to the decomposition of nitrates, NO_x is desorbing from the surface when the temperature between steps increases.

NO oxidation in the presence of water is simulated using a detailed kinetic model [12], where NO oxidation on Cu-ZSM-5 [11], the above described water adsorption [13] and OH formation [12] are used together (Fig. 12.12). The model describes the significantly lower NO oxidation observed in the experiment due to the blocking of OH groups on the active copper site (S1a) seen in the coverages in the lower panel of Fig. 12.12 [12]. In addition, water blocks the NO₂ storage and, therefore, only very small amounts of NO_x are desorbing when the temperature between steps increases. It should be mentioned that during NO oxidation, both NO and NO₂ are simultaneously present. The NO will destabilize the nitrates and thereby, less NO_x is stored.

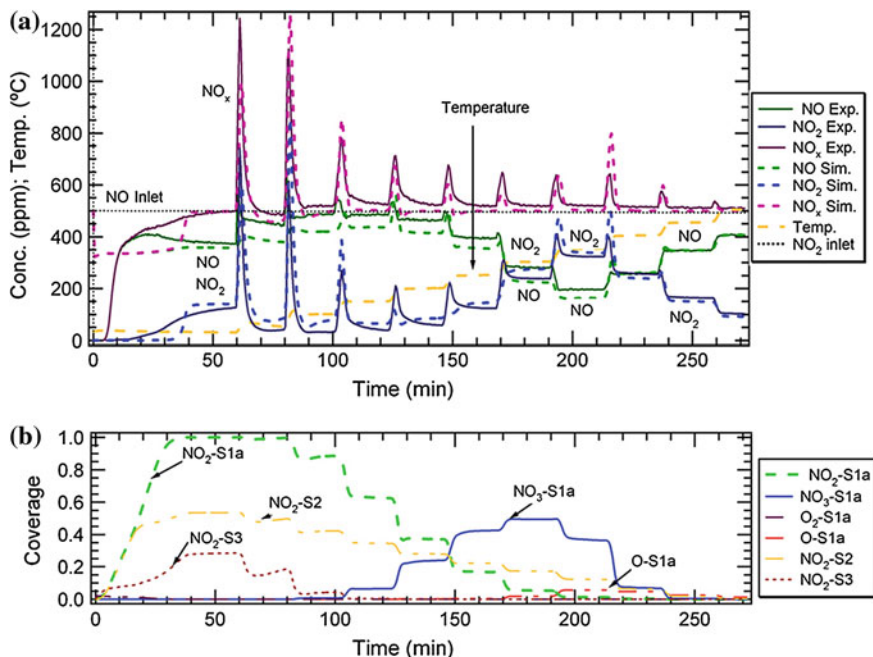


Fig. 12.11 NO oxidation experiment (500 ppm NO and 8 % O₂) and increasing the temperature stepwise over Cu-ZSM-5 [11]. **a** Solid lines Experiment and dashed lines kinetic model. **b** Calculated mean coverages on the surface. Reprinted with permission from Olsson et al. [11]. Copyright (2009) Elsevier

12.4.2 Global Kinetic Model for NO Oxidation

Metkar et al. [9] developed a global kinetic model from a derivation of detailed reaction steps. They used reactions described in (12.11–12.14 [11]) and combined two reactions (see Eqs. 12.15–12.16 [11]). They received the best results when assuming the Eley-Rideal step, during the NO oxidation (Eq. 12.14) as rate determining. The resulting rate expression was:

$$R_{NO_{oxi}} = \frac{k_{f3}\sqrt{k_1k_2}}{1 + K_1X_{O_2,s} + \sqrt{K_1K_2X_{O_2,s}} + K_4X_{NO_2,s} + \sqrt{\frac{K_5'K_4^3X_{NO_2,s}^3\sqrt{K_1K_2X_{O_2,s}}}{X_{NO,S}}}} \left(X_{NO,S}\sqrt{X_{O_2,s}} - \frac{X_{NO_2,S}}{K_{eq}} \right) \quad (12.20)$$

The results from this global NO oxidation model is shown in Fig. 12.13 [9]. In this figure, results from both Fe-ZSM-5 (solid lines) and Cu-CHA are shown (dashed lines). The markers show the experimental points. The model accurately

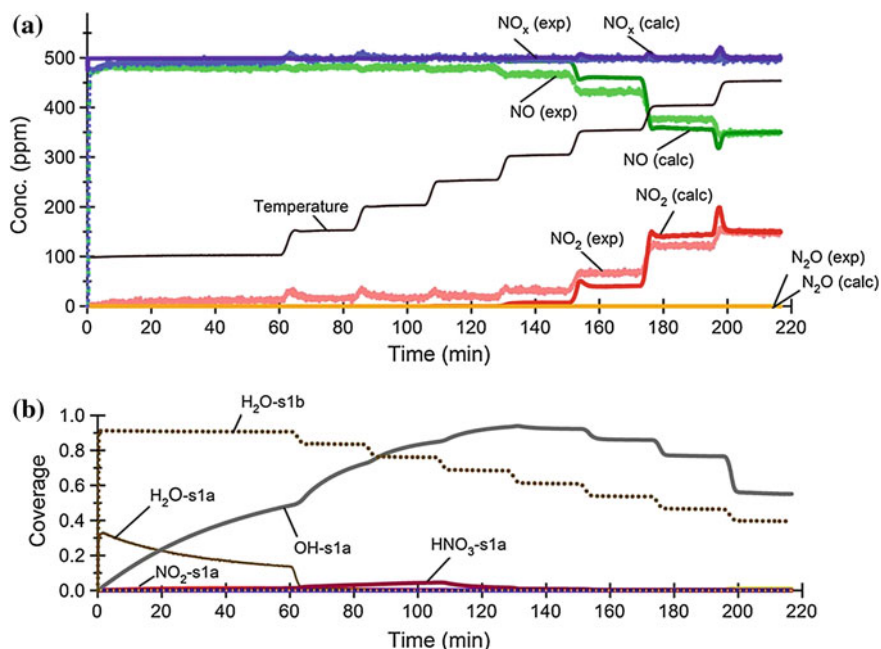
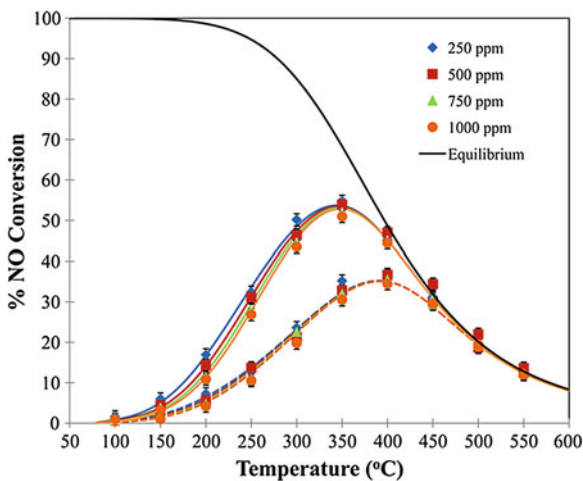


Fig. 12.12 NO oxidation experiment in the presence of water (500 ppm NO, 8 % O₂ and 5 % H₂O) and increasing the temperature stepwise over Cu-ZSM-5 [12]. **a** Solid lines Experiment and dashed lines kinetic model. **b** Calculated mean coverages on the surface. Reprinted with permission from Sjövall et al. [12]. Copyright (2009) Elsevier

Fig. 12.13 NO oxidation in dry conditions (250–1000 ppm NO and 5 % O₂) over Fe-ZSM-5 (solid lines) and Cu-CHA (dashed lines). Symbols Experimental data, continuous lines model [9]. Reprinted with permission from Metkar et al. [9]. Copyright (2012) Elsevier

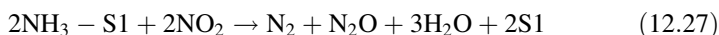
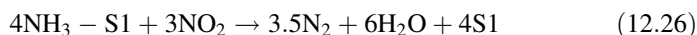
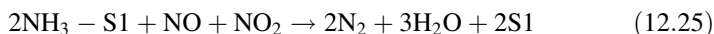
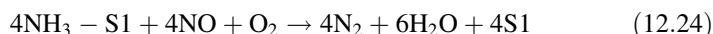
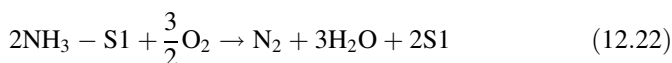


describes the experimental observations for various NO concentrations over the whole temperature interval. In the work by Olsson et al. [10] a kinetic model for NO oxidation is also included.

12.5 Kinetic Models for SCR Reactions Over Cu-Zeolites

12.5.1 Global Kinetic Models for SCR Over Cu-Zeolites

We developed a global kinetic model for ammonia SCR over Cu-ZSM-5 [10], consisting of seven reaction steps:



The first step is ammonia adsorption/desorption and this step was tuned to an ammonia TPD experiment described in an earlier section (Eq. 12.21, see Fig. 12.4). The second step is ammonia oxidation (Eq. 12.22) and the third step NO oxidation (Eq. 12.23). The parameters for these three steps were determined by separate experiments. In Eq. (12.24), the reaction for standard SCR is described and in Eq. (12.25), the rapid SCR with equimolar amounts of NO and NO₂ is covered. NH₃ also reacts with NO₂ alone, which is described in Eq. (12.26). The final step (see Eq. 12.27) is N₂O production from a reaction between adsorbed ammonia and NO₂. The results from exposing the Cu-ZSM-5 catalyst to 500 ppm NO, 500 ppm NH₃, 8 % O₂ and 5 % H₂O, while increasing the temperature stepwise are shown in Fig. 12.14 [10]. Initially, there is a total uptake of ammonia for an extended time period, but due to minor NO storage, NO breaks through immediately. The temperature is then increased to about 150 °C, while loosely bound ammonia is released. At this temperature, the standard SCR reaction is active and equimolar consumption of NO and NH₃ is seen. At 200 °C, the conversion of NO_x is close to 100 %. At high temperature, the NO_x conversion again decreases due to the ammonia oxidation. Also, some NO₂ is produced, since the back part of the catalyst is not exposed to ammonia, NO oxidation may occur. The global model described

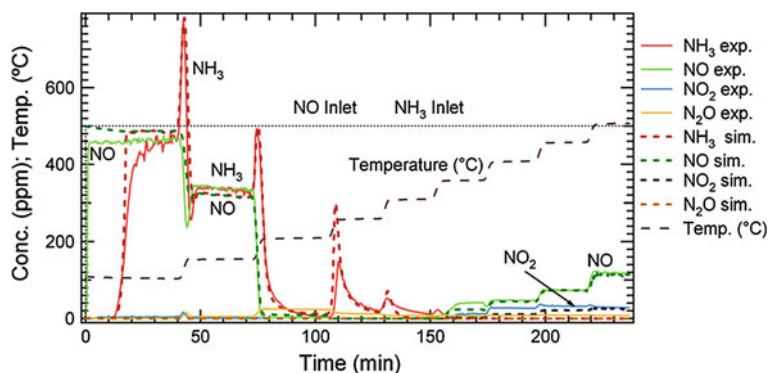


Fig. 12.14 NO, NO₂, NH₃ and N₂O concentration from experiment (solid line) and model (dashed line) after exposing the Cu-ZSM-5 catalyst to 500 ppm NO, 500 ppm NH₃, 8 % O₂ and 5 % H₂O and stepwise increasing the temperature [10]. Reprinted with permission from Olsson et al. [10]. Copyright (2008) Elsevier

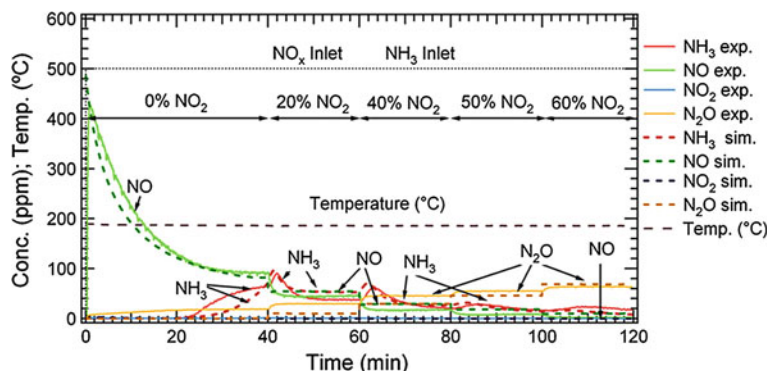


Fig. 12.15 NO, NO₂, NH₃ and N₂O concentration from experiment (solid line) and model (dashed line) after exposing the Cu-ZSM-5 catalyst to 500 ppm NO_x, 500 ppm NH₃, 8 % O₂ and 5 % H₂O and stepwise increasing the NO₂ content [10]. Reprinted with permission from Olsson et al. [10]. Copyright (2008) Elsevier

was developed based on a series of experiments with a variety of gas compositions and over a broad temperature range [10]. In Fig. 12.15, results from an experiment and corresponding model are illustrated while changing the NO₂ to NO_x ratio from 0 % up to 60 %, with an inlet gas temperature of 175 °C. Prior to this experiment, the catalyst was pretreated with oxygen at high temperature in order to clean the surface from ammonia. The Cu-ZSM-5 catalyst is exposed to the gas mixture (500 ppm NO, 500 ppm NH₃, 500 ppm O₂, and 5 % H₂O) from the inception of the experiment. During the first 20 min, no ammonia is detected because the storage of substantial amounts of ammonia on the surface, in combination with that ammonia is consumed in the SCR reaction. The NO concentration is decreasing from over

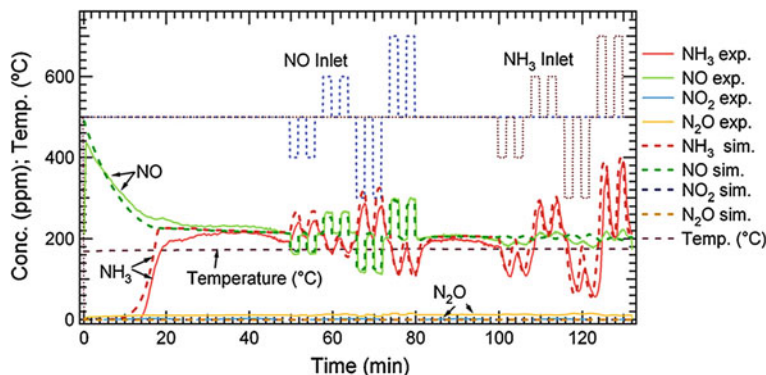


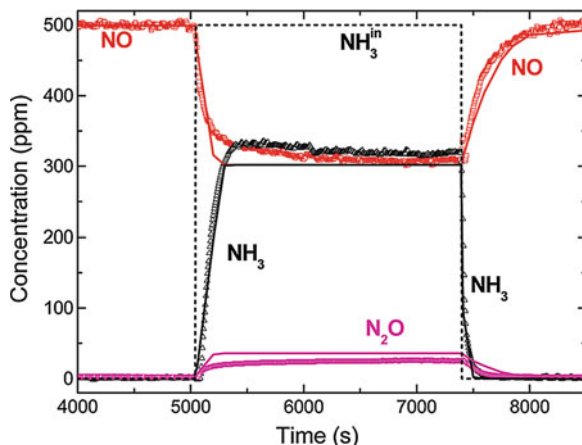
Fig. 12.16 NO, NO₂, NH₃, and N₂O concentration from a validation experiment (*solid line*) and model (*dashed line*) after exposing the Cu-ZSM-5 catalyst to 500 ppm NO_x, 500 ppm NH₃, 8 % O₂, and 5 % H₂O and thereafter changing NO and NH₃ concentrations in short steps [10]. Reprinted with permission from Olsson et al. [10]. Copyright (2008) Elsevier

400 ppm down to approx. 100 ppm. The reason for this decrease, which is also accurately described in the model, is that the SCR rate depends on the coverage of ammonia on the surface. The ammonia coverage is increasing over time, which results in an increased SCR reaction rate and, thereby, higher NO conversion. Further, when increasing the NO₂ content, the activity for NO_x reduction increases and reaches a maximum at 50–60 % of the NO₂ to NO_x ratio. At higher NO₂ levels, the activity over Cu-zeolites [8] again decreases. In addition, the N₂O concentration is increasing with increasing NO₂ fraction, which is explained by the last reaction (Eq. 12.27).

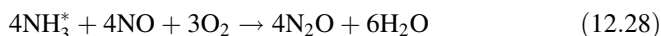
In kinetic model development, it is crucial to validate the model with experiments not included during the development of the model. The results in Fig. 12.16 illustrate a validation experiment [10]. In this experiment, the catalyst is initially exposed to 500 ppm NO, 500 ppm NH₃, 8 % O₂, and 5 % H₂O and when a steady state is reached, the concentration of NO and thereafter ammonia is altered in short steps. Interestingly, when the NO concentration changes, the NO outlet also rapidly changes, but when performing the corresponding change in ammonia concentration, the NO level remains practically constant due to the large buffering of ammonia on the surface. The ammonia coverage is similar during the 2 min time, when the ammonia level is changed because the ammonia storage on the catalyst is excessive. Since the SCR rate depends on the coverage of ammonia on the surface as opposed to the gas phase, this results in the same SCR rate, which is why the NO conversion is practically the same.

Nova et al. [37] presented a global kinetic model for ammonia SCR over a Cu-zeolite catalyst. They used the same seven reactions as presented above (Eqs. 12.21–12.27). In addition, they added two more reactions. In the first reaction (Eq. 12.28), N₂O is formed from a reaction between ammonia on the surface (denoted NH₃^{*}) and NO and in the second reaction, ammonium nitrate is formed

Fig. 12.17 Transient SCR experiment at 200 °C over Cu zeolite. In this experiment, the catalyst is exposed to (1) 500 ppm NO, 8 % O₂, 5 % H₂O (2) 500 ppm NO, 500 ppm NH₃, 8 % O₂, 5 % H₂O, and (3) 500 ppm NO, 8 % O₂, 5 % H₂O [37]. Reprinted with permission from Nova et al. [37]. Copyright (2011) American Chemical Society

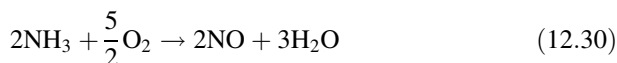


during a reaction with ammonia on the surface and NO₂ in the gas phase (Eq. 12.29).



The results from this model are shown in Fig. 12.17, where a transient experiment is conducted at 200 °C. The ammonia concentration drops fast, while the NO concentration slowly increases, when turning off ammonia during step three. The reason is that there are large amounts of ammonia adsorbed on the surface, which is why the SCR reaction can continue for a substantial amount of time until the ammonia coverage is zero. The model can describe the experimental findings well [37]. The model presented by Nova et al. [37] was also used to simulate experiments during which the NO₂ to NO_x ratio varied. The results from these experiments and the corresponding model are shown in Fig. 12.18 [37], where Fig. 12.18a shows the NO_x conversion, Fig. 12.18b the NH₃ conversion, and Fig. 12.18c the N₂O formation. The NO_x conversion is at a maximum for the NO₂ to NO_x ratio of 66 % and decreases when the NO₂ level further increases because the slower NO₂ SCR reaction dominates. The N₂O production shows a maximum at lower temperatures, likely due to that ammonium nitrate is an intermediate for N₂O production and ammonium nitrates decompose at high temperatures.

Pant and Schmiege [7] used the model developed by Olsson et al. [10] (see Eqs. 12.21–12.27) with one exception. Instead of ammonia oxidation to N₂, as described in Eq. (12.22), ammonia oxidation to NO was used:



One of the reasons was that they observed NO formation over their catalyst at high temperatures. Pant and Schmiege [7] investigated the influence of changing the

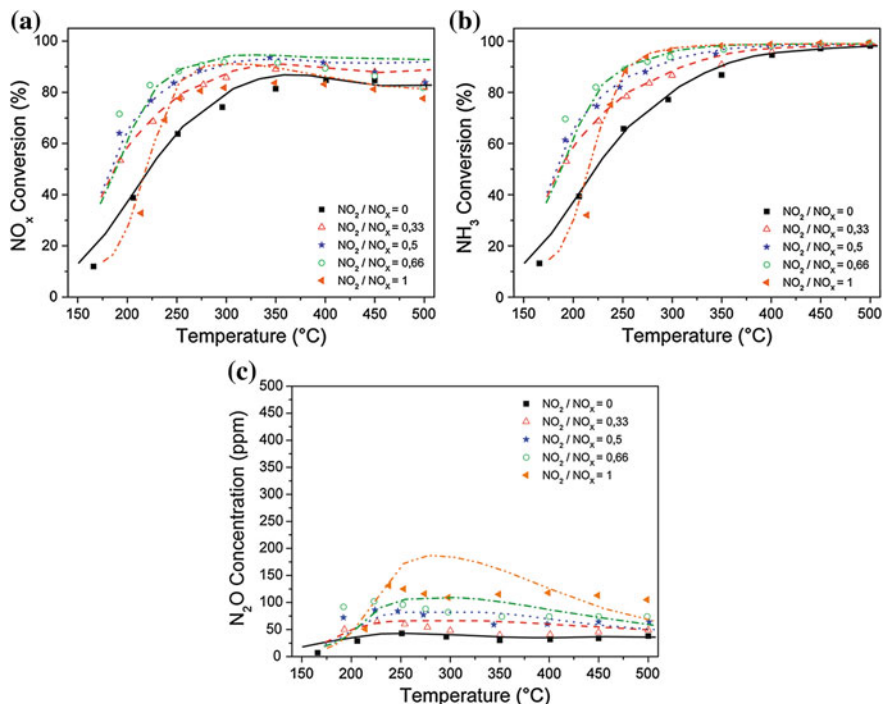


Fig. 12.18 Experiment (markers) and kinetic model (solid lines), when exposing a Cu-zeolite to 500 ppm NO_x, 500 ppm NH₃, 8 % O₂ and 5 % H₂O and varying the NO₂ content [37]. Reprinted with permission from Nova et al. [37]. Copyright (2011) American Chemical Society

space velocity (the gas composition was also varied), with the results presented in Fig. 12.19. In these experiments, real diesel exhaust and urea injection have been used.

Baik et al. [38] simulated urea SCR and included the following equations for the concentration of urea, HNCO, NO, and NH₃:

$$\frac{dC_{\text{Urea}}}{d\tau} = -k_3 C_{\text{Urea}} \tag{12.31}$$

$$\frac{dC_{\text{HNCO}}}{d\tau} = k_3 C_{\text{Urea}} - k_4 C_{\text{HNCO}} C_{\text{H}_2\text{O}} \tag{12.32}$$

$$-\frac{dC_{\text{NO}}}{d\tau} = \frac{K_1 C_{\text{NO}} C_{\text{NH}_3}}{(1 + K_{\text{NO}} C_{\text{NO}})(1 + K_{\text{NH}_3} C_{\text{NH}_3})} \tag{12.33}$$

$$-\frac{dC_{\text{NH}_3}}{d\tau} = \frac{K_1 C_{\text{NO}} C_{\text{NH}_3}}{(1 + K_{\text{NO}} C_{\text{NO}})(1 + K_{\text{NH}_3} C_{\text{NH}_3})} + \frac{k_2 C_{\text{NH}_3}}{(1 + K_{\text{NH}_3} C_{\text{NH}_3})} \tag{12.34}$$

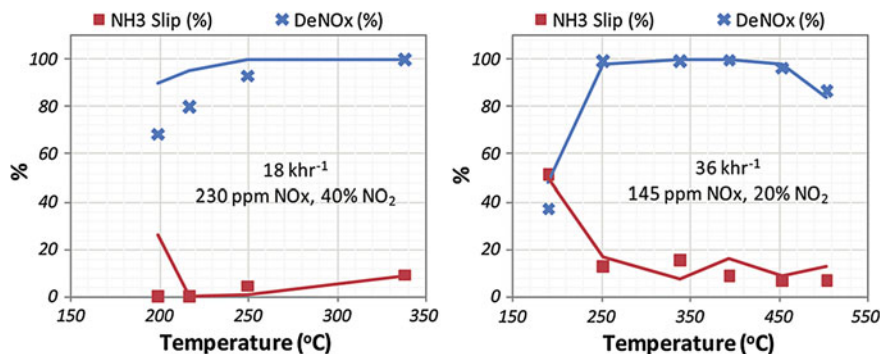
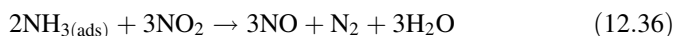
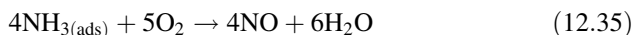


Fig. 12.19 Ammonia slip and deNO_x activity versus exhaust temperature for a Cu-zeolite. The NH₃/NO_x ratio was 1.3. The NO_x concentration and space velocity is shown in the panels [7]. The symbols represent the experimental points and the solid lines the model. Reprinted with permission from Pant and Schmiege [7]. Copyright (2011) American Chemical Society

The results from this model, when varying the space velocity, are shown in Fig. 12.20 [38]. In these experiments, urea was used as an ammonia source and the thermal decomposition of urea was conducted at 350 °C in order to completely decompose urea into ammonia and HNCO [39].

Watling et al. [40] used a kinetic model for simulating the New European Drive Cycle (NEDC) test over a Cu-zeolite coated filter. The reactions used to describe the SCR system are shown in Eqs. (12.21–12.27) in addition to the following two reactions:



In the first reaction (Eq. 12.35), ammonia is oxidized to NO, a step that was also used by Pant and Schmiege [7]. In the second reaction, NO₂ is reduced to NO by reacting with ammonia. The model is used to describe the cumulative NO_x during an NEDC test and the results from the test and model are shown in Fig. 12.21. The model accurately describes the cumulative NO_x.

12.5.2 Detailed Kinetic Models for SCR Over Cu-Zeolites

A detailed kinetic model was developed [11–13] and constructed out of several submodels previously described in this chapter. The different sites used in the model is discussed in Sect. 12.2.2. The submodels include: (i) ammonia adsorption/desorption, (ii) water adsorption/desorption, (iii) ammonia oxidation, (iv) NO₂ storage, and (v) NO oxidation. The results of these studies were used in developing

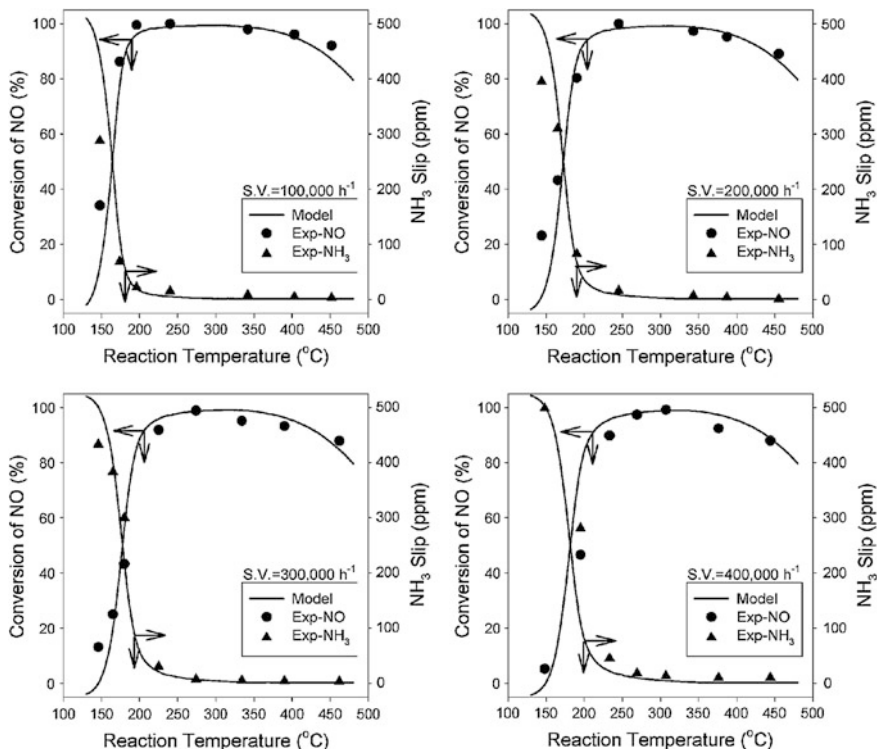
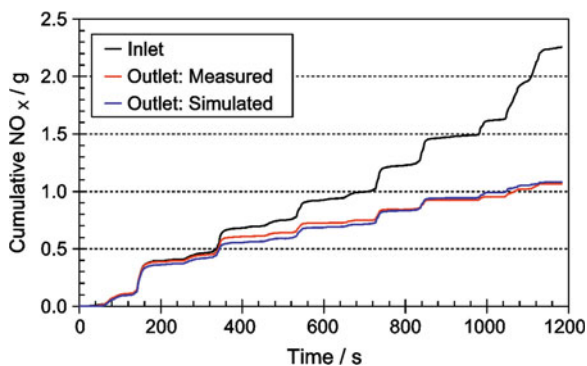
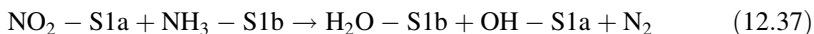


Fig. 12.20 Urea SCR over Cu-ZSM-5, when varying space velocity [38]. Reprinted with permission from Baik et al. [38]. Copyright (2006) American Chemical Society

Fig. 12.21 Measured and simulated cumulative NO_x using a Cu-zeolite coated DPF (denoted Cu-SCR[®]) in an NEDC test [40]. Reprinted with permission from Watling et al. [40]. Copyright (2012) Elsevier



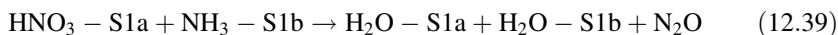
the SCR steps. In the first SCR reaction, formed nitrites react with adsorbed ammonia according to:



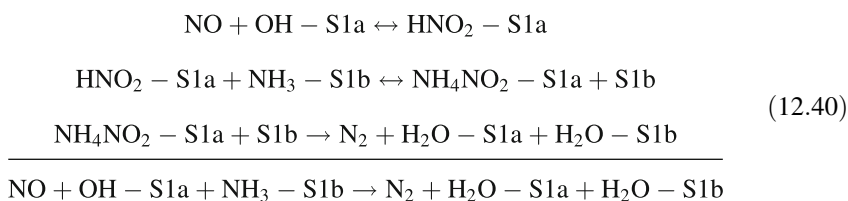
In the presence of water, it is likely that HNO_3 is formed on the surface, which have been suggested for SCR over vanadia catalysts [41]. We have, therefore, added a reaction step to form HNO_3 (Eq. 12.38).



HNO_3 can then react with ammonia on the surface to produce ammonium nitrate, which can decompose to produce N_2O . In order to simplify the model, these two steps in the model are described as one step:

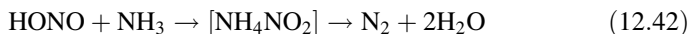


Further, it is suggested that HNO_2 is formed over vanadia, and then produces ammonium nitrite, which rapidly decomposes to produce water and N_2 [41]. This mechanism was also used to derive the last step in the detailed model (Eq. 12.40) [12]:



The model was developed through a large set of experiments, during which gas composition and temperature varied [12], and below are two illustrated examples. In the first experiment, the Cu-ZSM-5 catalyst was exposed to 500 ppm NO, 8 % O_2 , and the ammonia concentration varied from 200 to 800 ppm in steps to 175 °C. The results of the experiment and model are shown in Fig. 12.22, in which the top panel shows the concentrations and the lower panel shows the calculated mean coverage on the surface. The results of the coverages from the model show that on the S1a (active copper site), the dominant species at lower ammonia concentrations is nitrites ($\text{NO}_2\text{-S1a}$), but some nitrates are also present. At higher ammonia concentrations, the nitrite coverage decreases simultaneously as the ammonia coverage increases. This experiment was repeated with 5 % water present and a 50 % NO_2 to NO_x ratio. The results are shown in Fig. 12.23. The NO_2 content, in combination with high water levels, results in larger HNO_3 coverage on the active copper sites (see reaction in Eq. 12.38), which gives a higher rate of N_2O production (see Eq. 12.39), and is visible by the higher N_2O concentration in the experiment, as well as in the model.

Grossale et al. [8] present a detailed kinetic model for ammonia SCR over Fe and Cu-zeolites, where the NO_2 reactions are described by the following steps:



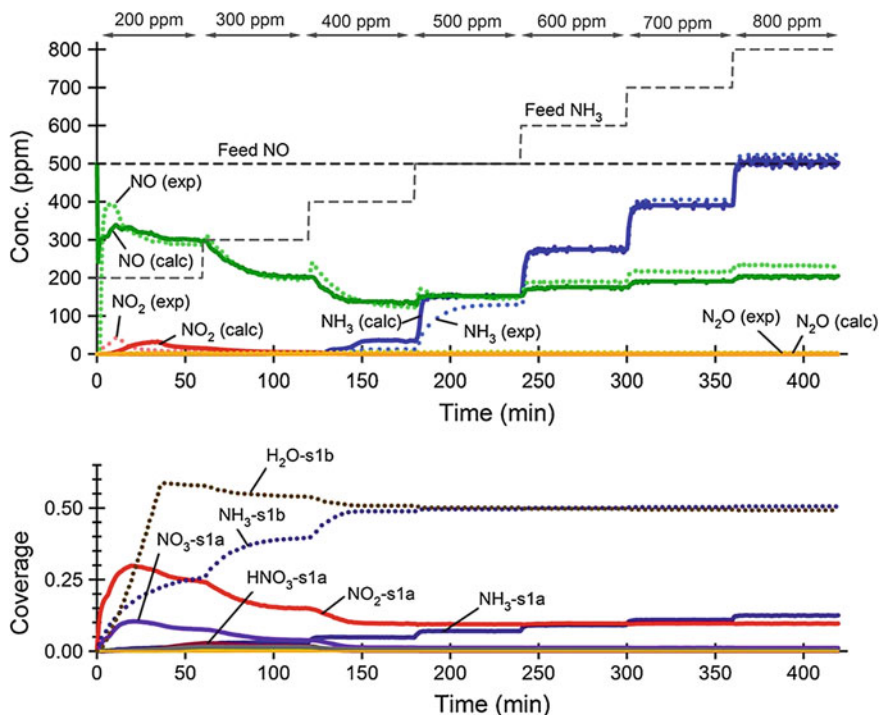
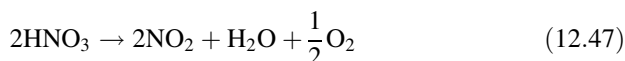
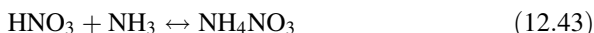


Fig. 12.22 Experiment (*dotted lines*) and model (*solid lines*), from a test where a Cu-ZSM-5 catalyst was exposed to 500 ppm NO, 8 % O₂, and varying the ammonia concentration from 200 to 800 ppm in steps at 175 °C. The lower panel shows the mean calculated coverages on the surface [12]. Reprinted with permission from Sjövall et al. [12]. Copyright (2009) Elsevier



These reactions are used together with reactions, e.g., for standard SCR, ammonia spillover [8] and the results from the model to describe NO₂/NO_x variations for Cu-zeolite, as shown in Fig. 12.24. The model accurately describes the NO₂/NO_x dependence across a broad temperature interval.

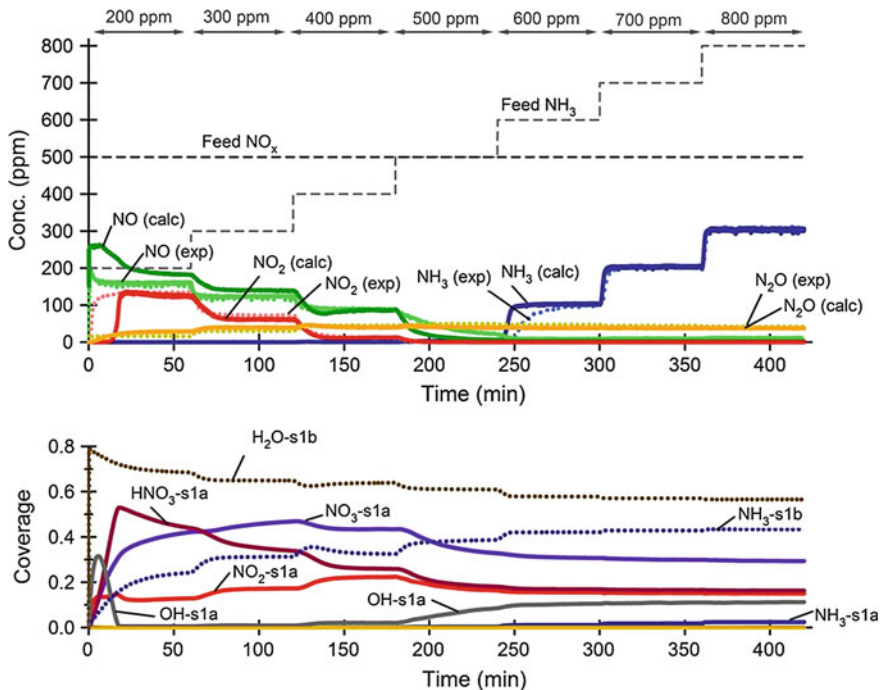
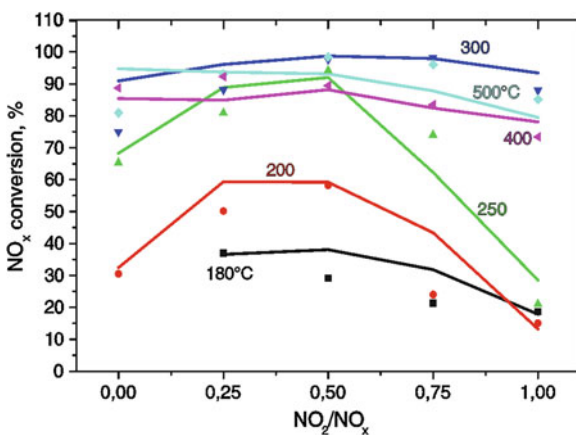


Fig. 12.23 Experiment (dotted lines) and model (solid lines), from a test where a Cu-ZSM-5 catalyst was exposed to 250 ppm NO, 250 ppm NO₂, 8 % O₂, 5 % H₂O and varying the ammonia concentration from 200 to 800 ppm in steps at 175 °C. The lower panel shows the calculated mean coverages on the surface [12]. Reprinted with permission from Sjövall et al. [12]. Copyright (2009) Elsevier

Fig. 12.24 SCR experiments when varying NO₂ to NO_x ratio over a Cu-zeolite at different temperatures. The inlet feed gas consists of 500 ppm NO_x, 500 ppm NH₃, 3 % H₂O and 2 % O₂. Solid lines (kinetic model) and symbols (experiment) [8]. Reprinted with permission from Grossale et al. [8]. Copyright (2009) Springer



12.6 Conclusions

This chapter is a review of the state of the art in kinetic modeling of ammonia/urea SCR over copper containing zeolites. Both fundamental detailed kinetic models as well as more globalized models are discussed. Several submodels are studied for the SCR system: (i) ammonia adsorption and desorption, (ii) NO₂ adsorption and desorption, (iii) water adsorption and desorption, (iv) ammonia oxidation, (v) NO oxidation, (vi) standard SCR, (vii) rapid SCR, (viii) slow NO₂ SCR, (ix) N₂O formation, and (x) urea decomposition and hydrolysis to produce ammonia. As can be seen from this large number of steps, this is a complex system.

A good description of the ammonia storage and desorption is critical in order to describe transient features of the SCR system, and usually a Temkin type of kinetics is used that considers the adsorbate–adsorbate interactions. The parameters for these reactions are usually fitted to TPD experiments, but also microcalorimetry studies are presented. The most common approach is to consider one ammonia adsorption site, but more detailed kinetic models use several adsorption sites. Ammonia oxidation is a reaction occurring at high temperatures, which unfortunately decreases the selectivity of the NO_x reduction in SCR. It is therefore crucial to include this reaction in kinetic models for this system.

Different SCR reaction occurs depending on the NO₂ to NO_x ratio, where standard SCR occurs with NO only, rapid SCR with equimolar amount of NO and NO₂, and slow NO₂ SCR with NO₂ only. In several global kinetic models, these three reactions are added. In more detailed models, more surface species are considered, for example, nitrites, nitrates, HNO₃, oxygen, and hydroxyls. N₂O is an unwanted by-product during the SCR process over copper zeolites that are increasing with the NO₂ content. The mechanism for the N₂O production is suggested to be from decomposition of ammonium nitrate. In addition, there are models available that incorporate the urea decomposition and hydrolysis, in addition to the SCR reactions.

References

1. H. Sjövall, L. Olsson, E. Fridell, and R. J. Blint, *Applied Catalysis B* 64 (2006) 180.
2. H. Sjövall, E. Fridell, R. J. Blint, and L. Olsson, *Topics in Catalysis* 42–43 (2007) 113.
3. J.-H. Park, H. J. Park, J. H. Baik, I.-S. Nam, C.-H. Shin, J.-H. Lee, B. K. Cho, and S. H. Oh, *Journal of Catalysis* 240 (2006) 47.
4. S. Kieger, G. Delahay, B. Coq, and B. Neveu, *Journal of Catalysis* 183 (1999) 267.
5. J. A. Sullivan, J. Cunningham, M. A. Morris, and K. Keneavey, *Applied Catalysis B: Environmental* 7 (1995) 137.
6. K. Rahkamaa-Tolonen, T. Maunula, M. Lomma, M. Huuhtanen, and R. L. Keiski, *Catalysis Today* 100 (2005) 217.
7. A. Pant and S. J. Schmiege, *Industrial & Engineering Chemistry Research* 50 (2011) 5490.
8. A. Grossale, I. Nova, E. Tronconi, D. Chatterjee, and M. Weibel, *Topics in Catalysis* 52 (2009) 1837.

9. P. S. Metkar, V. Balakotaiah, and M. P. Harold, *Catalysis Today* 184 (2012) 115.
10. L. Olsson, H. Sjövall, and R. J. Blint, *Applied Catalysis B-Environmental* 81 (2008) 203.
11. L. Olsson, H. Sjövall, and R. J. Blint, *Appl. Catal. B: Environmental*. 87 (2009) 200.
12. H. Sjövall, R. J. Blint, and L. Olsson, *Appl. Catal. B* 92 (2009) 138.
13. H. Sjövall, L. Olsson, and R. J. Blint, *J. Phys Chem. C* 113 (2009) 1393.
14. G. Delahay, S. Kieger, N. Tanchoux, P. Trems, and B. Coq, *Applied Catalysis B: Environmental* 52 (2004) 251.
15. N. Wilken, K. Wijayanti, K. Kamasamudram, N. W. Currier, R. Vedaiyan, A. Yezerets, and L. Olsson, *Appl. Catal. B* 111 (2012) 58.
16. N. Wilken, K. Kamasamudram, N. W. Currier, J. Li, A. Yezerets, and L. Olsson, *Catalysis Today* 151 (2010) 237.
17. A. Delabie, K. Pierloot, M. H. Groothaert, B. M. Weckhuysen, and A. Schoonheydt, *Microporous and mesoporous materials* 27 (2000) 209.
18. J. H. Kwak, D. Tran, S. D. Burton, J. Szanyi, J. H. Lee, and C. H. F. Peden, *Journal of Catalysis* 289 (2012) 272.
19. L. Wang, W. Li, G. S. Qi, and D. Weng, *Journal of Catalysis* 289 (2012) 21.
20. I. Nova, L. Lietti, E. Tronconi, and P. Forzatti, *Chemical Engineering Science* 56 (2001) 1229.
21. B. Roduit, A. Wokaun, and A. Baiker, *Industrial & Engineering Chemistry Research* 37 (1998) 4577.
22. J. A. Dumesic, N.-Y. Topsoe, H. Topsoe, Y. Chen, and T. Slabiak, *Journal of Catalysis* 163 (1996) 409.
23. L. Lietti, I. Nova, E. Tronconi, and P. Forzatti, *Catal. Today* 45 (1998).
24. D. Chatterjee, T. Burkhardt, M. Weibel, E. Tronconi, I. Nova, and C. Ciardelli, *SAE 2006-01-0468* (2006).
25. S. A. Stevenson, J. C. Vartuli, and C. F. Brooks, *Journal of Catalysis* 190 (2000) 228.
26. S. Malmberg, M. Votsmeier, J. Gieshoff, N. Söger, L. Mußmann, A. Schuler, and A. Drochner, *Topics in Catalysis* 42–43 (2007) 33.
27. D. Chatterjee, T. Burkhardt, M. Weibel, I. Nova, A. Grossale, and E. Tronconi, *SAE 2007-01-1136* (2007).
28. H. Sjövall, R. J. Blint, A. Gopinath, and L. Olsson, *Industrial & Engineering Chemistry Research* 49 (2010) 39.
29. E. Tronconi, I. Nova, C. Ciardelli, D. Chatterjee, B. Bandl-Konrad, and T. Burkhardt, *Catalysis Today* 105 (2005) 529.
30. C. Busco, A. Barbaglia, M. Broyer, V. Bolis, G. M. Foddanu, and P. Ugliengo, in *Thermochimica Acta* Vol. 418 (1–2), 2004, p. 3.
31. P. Felix, C. Savill-Jowitt, and D. R. Brown, *Thermochimica Acta* 433 (2005) 59.
32. G. Boskovic, T. Vulic, E. Kis, and P. Putanov, *Chemical Engineering & Technology* 24 (2001) 269.
33. W. B. Williamson, D. R. Flentge, and J. H. Lunsford, *J. of Catal.* 37 (1975) 258.
34. W. B. Williamson and J. H. Lunsford, *J. of Phys. Chem.* 80 (1976) 2664.
35. T. Komatsu, M. Nunokawa, I. S. Moon, T. Takahara, S. Namba, and T. Yashima, *Journal of Catalysis* 148 (1994) 427.
36. M. Colombo, I. Nova, and E. Tronconi, *Applied Catalysis B-Environmental* 111 (2012) 433.
37. I. Nova, D. Bounechada, R. Maestri, E. Tronconi, A. K. Heibel, T. A. Collins, and T. Boger, *Industrial & Engineering Chemistry Research* 50 (2011) 299.
38. J. H. Baik, S. D. Yim, I. S. Nam, Y. S. Mok, J. H. Lee, B. K. Cho, and S. H. Oh, *Industrial & Engineering Chemistry Research* 45 (2006) 5258.
39. S. D. Yim, S. J. Kim, J. H. Baik, I.-S. Nam, Y. S. Mok, J.-H. Lee, B. K. Cho, and S. H. Oh, *Ind. Eng. Chem. Res.* 43 (2004) 4856.
40. T. C. Watling, M. R. Ravenscroft, and G. Avery, *Catalysis Today* 188 (2012) 32.
41. C. Ciardelli, I. Nova, E. Tronconi, D. Chatterjee, T. Burkhardt, and M. Weibel, *Chemical Engineering Science* 62 (2007) 5001.

Part V
Modeling and Control

Chapter 13

SCR Reactor Models for Flow-Through and Wall-Flow Converters

Dimitrios Karamitros and Grigorios Koltsakis

13.1 Introduction

The stringent emissions legislation along with the multiplicity of aftertreatment options and designs has increased the interest to develop and apply mathematical models of catalytic devices in order to optimize their efficiency and control. Over the last years, the use of simulation tools in the development process has been recognized as a cost- and time-efficient strategy.

SCR devices are basically “flow through” reactor devices, consisting of a multitude of parallel channels, sometimes referred to as honeycomb structures. Most of the content of this chapter will deal with such type of reactor design. Recently, there is an increasing interest to combine the SCR coating with a wall-flow particulate filter. Such systems may become commercial soon and present a high scientific and technological importance. Therefore, part of this work will be dedicated to wall-flow reactors with SCR coating.

These devices are inherently three-dimensional, since the catalyst channels may have different inlet conditions, wall temperature, and conversion rates. Ideally, a 3D simulation involving the flow entering the monolith would be necessary with the proper upstream exhaust configuration and ambient heat transfer characteristics. This requires a significant amount of computational effort in order to model the complete system, therefore, simplified single-channel approaches have been proposed as more practical alternatives.

As with all types of reactor models, the main difficulty lies in the availability of detailed and accurate kinetic mechanisms. The chemical reactions within an aftertreatment device are a function of the catalyst formulation, washcoat material and its aging status, resulting in a large number of kinetic parameters. As a result,

D. Karamitros · G. Koltsakis (✉)
Laboratory of Applied Thermodynamics, Aristotle University Thessaloniki, Thessaloniki,
Greece
e-mail: Grigoris@auth.gr

global, rather than elementary kinetic mechanisms are used which are approximate in nature and require moderate calibration efforts [1].

One-dimensional catalyst modeling for exhaust aftertreatment has been proposed since the late 1960s with Vardi's and Biller's work [2]. Their work was very similar to pipe wall models examining only the effects of heat transfer on the warm-up of a catalyst. A few years later, Kuo et al. [3] simulated a catalytic converter using a series of completely mixed reactors. In this work, they expanded the model to include exothermic/endothermic reactions on the surface as well as the propagation of chemical species throughout the device. At these times, the interest was basically in gasoline aftertreatment using oxidation and three-way catalysis. Harned [4] later revised the reactor model to better represent the flow-through a monolithic device while also adding a "film" model representing species on the surface of the catalyst. Oh and Cavendish [5] examined the kinetic expressions in more detail. These classical models have been in widespread use and proven their effectiveness in designing catalyst systems for lower emission levels, even though they employ simplified formulations for the fluid flow through the device. Later works have mainly addressed improved reaction schemes to address transient phenomena [6], extensions for diesel oxidation catalysts and SCR applications [7–11] as well as multidimensional extensions [12, 13].

In this work, we will initially present the fundamentals of flow-through catalyst modeling focusing on the commonly used expressions for heat, mass transfer, and heterogeneous reaction modeling in the channels of monolithic reactors. An extensive review of the different reaction models applicable to the known SCR technologies are outside the scope of this work; therefore, we confine our scope to an indicative set of a global reaction scheme. The importance of washcoat (internal) diffusion modeling is discussed in a separate section, since this specific topic is still one of the most debatable issues in SCR modeling. Next, we discuss the issue of model parameter calibration and how SCR kinetic models developed in small-scale reactors are applicable in real-world full-scale applications. A separate section is devoted to modeling of SCR coated wall-flow filters, which are considered as promising design alternatives and present interesting interactions with soot filtration and oxidation processes. Since modern exhaust systems are frequently based on more than one aftertreatment devices, modeling of the complete exhaust system is of particular interest. Therefore, we devote a section on the modeling of combined SCR with other catalytic functionalities, including in-series positioning and multilayered catalyst technologies.

13.2 Fundamentals of Flow-Through Catalyst Modeling

Most literature models apply similar simplifying assumptions to model the flow, thermophysical, and chemical phenomena in the catalyst channels:

Fig. 13.1 Schematic of a 1D channel



- Uniform flow, temperature, and concentrations distribution at the entrance of all channels.
- Negligible heat losses to ambient.

The above two assumptions justify the use of the single-channel (1D) approach (Fig. 13.1).

The mathematical model should consider the five main steps involved in the conversion of species in a catalytic converter, namely [14]:

1. External mass transfer of the reactants from the channel flow to the channel surface.
2. Internal mass transfer of the reactants through the washcoat.
3. Conversion of reactants to products on the catalytic sites.
4. Internal mass transfer of the products through the washcoat.
5. External mass transfer of the products from the channel surface to the channel flow.

To simplify the problem, the following assumptions are commonly used:

- Quasi-steady-state approach: The transient terms in the gas phase are considered to be negligible compared to the convective terms.
- The flow in the channels is considered laminar with $Ma < 0.3$. This is true for the full practical range of real-world operating conditions.
- Ideal gas behavior and constant pressure (negligible pressure drop).
- Dilute mixture (low concentration of key reactants) in order to approximate diffusion processes by Fick's law.
- Negligible axial diffusion of energy and species for the gas phase.

In the following sections, the basic governing equations of the catalyst model will be outlined.

13.2.1 Balance Equations

The calculation of the temperature and species concentrations in the channel is based on the solution of the quasi-steady equations for the gas phase heat and mass transfer. In order to avoid the solution of the complete boundary layer, the so-called film-approach is used which is based on the use of local heat transfer coefficients.

$$\rho_g C_{p,g} v_g \frac{\partial T_g}{\partial z} = -h \cdot \left(\frac{S_F}{\varepsilon} \right) \cdot (T_g - T_s) \quad (13.1)$$

where ρ is the density [kg/m³], C_p the specific heat capacity [J/kgK], v the velocity [m/s], T the temperature [K], h the heat transfer coefficient [W/m²K], S_F the monolith specific surface area [m²/m³], and ε the macroscopic void fraction [–]. Subscripts g and s denote the exhaust gas and the solid substrate, respectively.

Similarly to the heat transfer equation, a “film” approach is also used to account for the gas phase mass transfer resistance.

$$\frac{\partial(v_g y_{g,j})}{\partial z} = -k_j \cdot \left(\frac{S_F}{\varepsilon} \right) \cdot (y_{g,j} - y_{s,j}) \quad (13.2)$$

where y_j is the molar fraction of species j [–] and k_j the mass transfer coefficient of species j [m/s].

The heat and mass transfer coefficients are calculated based on the following definitions:

$$h = \frac{Nu \cdot \lambda_g}{d_h}, k_j = \frac{Sh \cdot D_{mol,j}}{d_h} \quad (13.3)$$

where λ_g the thermal conductivity [W/(m · K)], $D_{mol,j}$ the molecular diffusion [m²/s], and d_h the hydraulic diameter [m].

The semi-empirical global transport correlation proposed by Hawthorn [15] is the most commonly used for the definition of local Nusselt and Sherwood numbers, applicable to laminar flows in square ducts:

$$Nu = 2.976 \left(1 + 0.095 \cdot \frac{Re \cdot Pr \cdot d_h}{z} \right)^{0.45} \quad (13.4)$$

$$Sh = 2.976 \left(1 + 0.095 \cdot \frac{Re \cdot Sc \cdot d_h}{z} \right)^{0.45} \quad (13.5)$$

where Pr is the local Prandtl number and Sc is the local Schmidt number. A more detailed review of various empirical and theoretical correlations for various channel shapes is given by West et al. [16] and Ramanathan et al. [17].

In many cases, the influence of internal diffusion is considered negligible and the modeling steps 2 and 4 are lumped into the reaction rate of step 3. The surface reaction model approximates the washcoat with a solid–gas interface where it is assumed that all reactions take place. In this case, there is no concentration gradient in the washcoat and therefore only one surface species concentration is defined.

The total reaction rate on the surface for each species (including storage reactions) is equal to the local external species mass transfer to/from the exhaust gas:

$$\frac{\rho_g}{M_g} k_j \left(\frac{S_F}{\varepsilon} \right) (y_{g,j} - y_{s,j}) = R_j \quad (13.6)$$

M_g is the gas molecular weight [kg/mol]. The surface reaction rates for each species R_j [mol/m³s] are calculated based on the specific reaction scheme and are functions of local surface concentrations, coverages, and temperature. The major reactions that describe the NO_x-NH₃ reacting system and their respective rate expressions will be given in Sect. 13.3.2.

The 1D transient energy balance of the solid phase is described by the heat conduction equation:

$$\rho_s C_{p,s} \frac{\partial T_s}{\partial t} = \lambda_s \frac{\partial^2 T_s}{\partial z^2} + S \quad (13.7)$$

The source term S includes the contribution of convective heat transfer H_{conv} of the gas flow in channels and of the heat released or adsorbed H_{react} by chemical reactions and adsorption.

$$S = H_{\text{conv}} + H_{\text{react}} \quad (13.8)$$

Convection of heat due to flow in channel

$$H_{\text{conv}} = h \left(\frac{S_F}{1 - \varepsilon} \right) (T_g - T_s) \quad (13.9)$$

Reaction heat release

$$H_{\text{react}} = \frac{1}{1 - \varepsilon} \sum_{k=1}^{n_k} \Delta H_k R_k \quad (13.10)$$

where ΔH is the reaction heat [J/mol] and R_k the reaction rate [mol/m³s]. Subscript k denotes the reaction index.

The above equations describe the basic 1D catalyst model. The extension of this model to 1D + 1D with diffusion in the catalytic layer is discussed in the following section.

13.2.2 Washcoat Internal Diffusion Modeling

In many SCR applications, the thickness and effective diffusivity of the active layer may not allow the simplifying assumption of negligible internal diffusion resistance. In these cases, a more detailed approach which models mass transfer both in the gas phase and in the washcoat/active volume pores is needed.

The schematic and the basic geometric properties of the monolith channel cross-section are presented in Fig. 13.2 for the cases of a coated and of an extruded monolith.

The convective mass transfer from the bulk gas to the washcoat/wall surface is now written as:

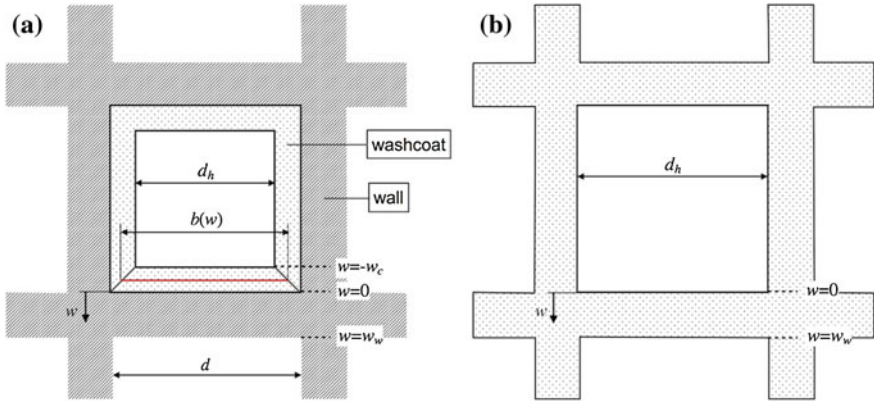


Fig. 13.2 Basic geometric properties of the monolith channel (a) coated (b) extruded catalyst

$$\frac{\partial(v_g y_{g,j})}{\partial z} = k_j \left(\frac{S_F}{\varepsilon} \right) (y_{s,j}|_{w=-w_c} - y_{g,j}) \quad (13.11)$$

where w_c is the washcoat layer thickness [m].

Following the quasi-steady assumption, the transient accumulation terms are neglected and the species balance inside the catalytic layer is formulated as:

$$-D_{w,j} \frac{\partial^2 y_{s,j}}{\partial w^2} = \sum_k n_{j,k} R_k \quad (13.12)$$

where $D_{w,j}$ is the effective diffusivity of species j in the washcoat pores [m^2/s] and $n_{j,k}$ the stoichiometric coefficient of species j in the reaction k .

In the catalytic washcoat layer, $w = 0$ corresponds to the wall boundary while $w = -w_c$ to the external surface of the washcoat. The boundary conditions for the washcoat layer are:

$$D_{w,j} \frac{\partial y_{s,j}}{\partial w} \Big|_{w=-w_c} = k_j (y_{g,j} - y_{s,j}|_{w=-w_c}) \quad (13.13)$$

$$\frac{\partial y_{s,j}}{\partial w} \Big|_{w=0} = 0 \quad (13.14)$$

Different theoretical models have been proposed to estimate the effective diffusivity $D_{w,j}$. The most commonly used approximations are the mean transport pore model [18] and the random pore model [19].

The mean transport pore model uses the expression:

$$\frac{1}{D_{w,j}} = \frac{\tau}{\varepsilon_{\text{pore}}} \left(\frac{1}{D_{\text{mol},j}} + \frac{1}{D_{\text{knud},j}} \right) \quad (13.15)$$

with the Knudsen diffusivity:

$$D_{\text{knud},j} = \frac{d_{\text{pore}}}{3} \sqrt{\frac{8RT}{\pi M_j}} \quad (13.16)$$

where $D_{\text{mol},j}$ and M_j are the molecular diffusivity [m^2/s] and the molecular mass [kg/mol] of species j , respectively. The values of the porosity $\varepsilon_{\text{pore}}[-]$ and mean pore size $d_{\text{pore}}[\text{m}]$ are based on the microstructural properties of the washcoat while tortuosity $\tau[-]$ is an empirical parameter.

It should be mentioned that the mean transport pore model is probably not the best option for SCR catalyst layers, as it assumes a uniform pore size distribution. The actual pore size distribution of the SCR layers is highly bimodal with two distinct maxima: micropores and mesopores. The random pore model considers a bi-dispersive washcoat material with two characteristic pore sizes with their respective mean pore sizes and void fractions. The total diffusivity is calculated as a combination of the respective Knudsen diffusivities:

$$D_{\text{w},j} = \varepsilon_{\text{meso}}^2 D_{\text{knud},j}^{\text{meso}} + \varepsilon_{\text{micro}}^2 D_{\text{knud},j}^{\text{micro}} + \frac{4(\varepsilon_{\text{micro}} - \varepsilon_{\text{meso}}^2)}{\frac{1}{D_{\text{knud},j}^{\text{meso}}} + \frac{((1-\varepsilon_{\text{meso}})/\varepsilon_{\text{micro}})^2}{D_{\text{Knud},j}^{\text{micro}}}} \quad (13.17)$$

A novel method for the study of diffusion through catalytic layers has been recently proposed by Novak et al. [20]. The authors predicted the effective diffusivity by employing a detailed pore scale model. This model is based on the digital reconstruction of the porous layers as 3D matrices using the information from cross-section electron microscopy and particle size analysis.

13.2.3 Multidimensional Model Extension

If the nonuniformities in the temperature and species concentrations among the catalyst channels need to be considered, a 2D or 3D modeling approach is required. In this case, the transient energy balance equation of the monolith should be extended to two or three dimensions. The heat conduction equation of the solid phase is formulated in polar coordinates for 2D simulations (13.18) and in Cartesian coordinates for 3D simulations (13.19).

$$\rho_s C_{p,s} \frac{\partial T_s}{\partial t} = \lambda_{s,z} \frac{\partial^2 T_s}{\partial z^2} + \lambda_{s,z} \frac{1}{r} \frac{\partial}{\partial r} \left(r \frac{\partial T_s}{\partial r} \right) + S \quad (13.18)$$

$$\rho_s C_{p,s} \frac{\partial T_s}{\partial t} = \lambda_{s,x} \frac{\partial^2 T_s}{\partial x^2} + \lambda_{s,y} \frac{\partial^2 T_s}{\partial y^2} + \lambda_{s,z} \frac{\partial^2 T_s}{\partial z^2} + S \quad (13.19)$$

The other catalyst equations are the same, as described above for the 1D model.

13.3 Reaction Modeling

13.3.1 Adsorption Model

The adsorption and desorption of NH_3 from the catalyst surface is one of the major processes involved in the SCR chemistry [21, 22]. The accurate description of this process over a wide temperature range is the basis for the successful modeling of the SCR catalytic behavior, especially during transient operation [23].



13.3.1.1 The Single-Site Approach

A simple approach to capture the ammonia adsorption/desorption kinetics is the single-site approach, where NH_3 is assumed to adsorb on a global single-surface site. A nonactivated ammonia adsorption process is considered while a Temkin-type coverage dependence of the activation energy is assumed for the desorption process [24]. The reaction rate expression of adsorption is given in Eq. (3.21):

$$R_{\text{ads}} = k_{\text{ads}} c_{\text{NH}_3} (1 - \theta_{\text{NH}_3}) \quad (13.21)$$

where c_{NH_3} is the gas concentration of NH_3 [mol/m^3], θ_{NH_3} is the NH_3 coverage, and k_{ads} is the adsorption rate constant [$1/\text{s}$].

The reaction rate and the Temkin-type rate constant for the desorption process are given in Eqs. (13.22) and (13.23), respectively:

$$R_{\text{des}} = k_{\text{des}} \theta_{\text{NH}_3} \quad (13.22)$$

$$k_{\text{des}} = k_{\text{des}}^0 \cdot e^{\left(-\frac{E_{\text{des}}(1-\gamma\theta)}{RT}\right)} \quad (13.23)$$

where γ describes the dependence from the surface coverage of the activation energy E_{des} .

13.3.1.2 The Dual-Site Approach

At least two families of acid sites for ammonia adsorption are present on zeolites surfaces, namely: (i) Brønsted acid sites, where ammonia is strongly bonded, and (ii) Lewis acid sites, where ammonia is weakly adsorbed, especially in the presence of water [25, 26]. Furthermore, the presence of physisorbed ammonia cannot be ruled out, especially at low temperatures.

A dual-site model for the storage and the release of NH_3 over a Fe-zeolite catalyst has been proposed by Colombo et al. [23]. The acid sites where ammonia is either weakly adsorbed or physisorbed are denoted as “Site-1” while the strong adsorption sites are denoted as “Site-2.” The following rate expressions describe the rates of ammonia adsorption/desorption for each site:

$$R_{\text{ads-Site-1}} = k_{\text{ads-Site-1}} c_{\text{NH}_3} (1 - \theta_{\text{NH}_3\text{-Site-1}}) \quad (13.24)$$

$$R_{\text{des-Site-1}} = k_{\text{des-Site-1}}^0 \cdot e \left[-\frac{E_{\text{des-Site-1}}^0}{RT} (1 - \gamma_{\text{Site-1}} \cdot \theta_{\text{NH}_3\text{-Site-1}}) \right] \cdot \theta_{\text{NH}_3\text{-Site-1}} \quad (13.25)$$

$$R_{\text{ads-Site-2}} = k_{\text{ads-Site-2}} c_{\text{NH}_3} (1 - \theta_{\text{NH}_3\text{-Site-2}}) \quad (13.26)$$

$$R_{\text{des-Site-2}} = k_{\text{des-Site-2}}^0 \cdot e \left(-\frac{E_{\text{des-Site-2}}}{RT} \right) \cdot \theta_{\text{NH}_3\text{-Site-2}} \quad (13.27)$$

Nonactivated ammonia adsorption is assumed on both sites ($R_{\text{ads-Site-1}}$ and $R_{\text{ads-Site-2}}$) while different rate expressions are used to describe NH_3 desorption. Since “Site-1” includes different types of Lewis acid sites and also ammonia physisorbed on the catalyst surface, Temkin-type coverage dependent adsorption is adopted in order to take such a site heterogeneity ($R_{\text{des-Site-1}}$) into account. On the contrary, the nature of Brønsted acid sites is well defined for zeolites, being indeed associated with the so-called “bridging hydroxyls,” thus it is reasonable to assume that these sites are homogeneous in terms of ammonia adsorption strength. Based on this assumption, simple Arrhenius kinetics are adopted for the NH_3 desorption process from “Site-2.”

13.3.1.3 Multisite Approach

The multisite approach was previously described by Sjövall et al. [27] and investigated by Skarlis et al. [22]. The proposed model describes the storage of NH_3 on a Cu-zeolite by including four different surface sites: (i) a metal site where a single molecule of NH_3 can be stored, (ii) a second metal site where up to three molecules of NH_3 can be adsorbed, (iii) an acid site, and (iv) a site for physisorption. The mathematical expressions for the adsorption/desorption reaction rates of each site is the same as the single-site approach which was previously discussed (Eqs. 13.21–13.23). The parameters of the above-mentioned set of equations need to be estimated for each of the four surface sites.

13.3.1.4 Alternative Approaches

In this approach, the mass of each species which can be adsorbed in equilibrium conditions, as a function of temperature, is described by the Dubinin–Radushkevich adsorption theory [28]. According to this approach, the adsorbate in intimate

contact with the solid is assumed to be in liquid form. The equation of the D-R isotherm gives the adsorbed mass at equilibrium x_{eq} as function of temperature and partial pressure:

$$\ln(x_{\text{eq},j}) = \ln(W_0 \cdot \rho_j) - D_j \left[\ln\left(\frac{p_j}{p_{\text{sat},j}}\right) \right]^2 \quad (13.28)$$

$$D_j = A_{\text{ze}} \left(\frac{RT}{\beta_j} \right)^2$$

where W_0 is the total volume of all micropores and A_{ze} is a constant characteristic of the pore size distribution (both depend on the properties of the solid). β_j is the affinity coefficient which depends on the adsorbate, ρ_j is the liquid phase density, $p_{\text{sat},j}$ is the saturation pressure, and p_j is the partial pressure of the adsorbate at the gas–solid interface. The above equations imply that the mass of ammonia that can be adsorbed at equilibrium conditions is a function of the local gas concentration, the local temperature, and the saturation pressure, which is also a function of temperature. To predict the adsorption–desorption rates toward equilibrium, a linear driving force is employed:

$$R = \frac{\partial x}{\partial t} = k(x_{\text{eq}} - x) \quad (13.29)$$

where k is a temperature-dependent rate parameter. Adsorption occurs when the mass of adsorbed ammonia is smaller than the equilibrium mass, for the conditions examined, and desorption occurs when the mass of adsorbed ammonia is higher than the respective equilibrium mass. The rate parameter is constant in the case of adsorption, since adsorption is assumed to be a non-activated process, and exhibits an exponential dependence from temperature in the case of desorption:

$$k = k_{\text{ads}} = \text{const, if } x < x_{\text{eq}}$$

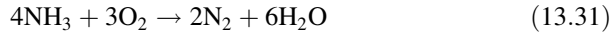
$$k = k_{\text{des}} = k_{\text{des}}^0 - \frac{E_{\text{des}}}{\mathfrak{R}T}, \text{ if } x > x_{\text{eq}} \quad (13.30)$$

13.3.2 *de-NO_x Reactions*

Several kinetic models regarding the reduction of NO_x with NH₃ have been reported in the literature for various catalyst technologies: Tronconi et al. [29] and Chatterjee et al. [30] for Vanadia-based catalysts, Malmberg et al. [21] and Schuler et al. [31] for Fe–zeolite catalysts and Olsson et al. [32] for Cu–zeolite catalysts. Neglecting detailed kinetic mechanisms and reaction intermediates, which are beyond the scope of this chapter, a similar global modeling approach can be used for the common SCR catalytic materials. The major reactions, considered in this model, are given below.

13.3.2.1 Ammonia Oxidation

The ammonia oxidation is an undesired reaction which occurs at high temperatures, typically above 400 °C [27, 33].



According to Schuler et al. [31], who investigated the NH_3 oxidation on iron-exchanged zeolites, reaction (13.31) can be described according to the following rate expression:

$$R_{\text{NH}_3-\text{ox}} = k_{\text{NH}_3-\text{ox}}^0 \cdot e^{\left(-\frac{E_{\text{NH}_3-\text{ox}}}{RT}\right)} \cdot \left(\frac{y_{\text{O}_2}}{y_{\text{O}_2}^{\text{ref}}}\right)^\beta \quad (13.32)$$

where y_{O_2} is the molar fraction of O_2 , $y_{\text{O}_2}^{\text{ref}}$ is a reference molar fraction of O_2 , and β the reaction order with regard to O_2 .

13.3.2.2 NO Oxidation

In zeolite-based catalysts, the NO_2/NO_x ratio is known to have a significant effect on the de- NO_x performance [34, 35]. The ability of the catalyst to modify the NO_2/NO_x ratio in situ has to be considered by the $\text{NO} \leftrightarrow \text{NO}_2$ oxidation/decomposition reaction:

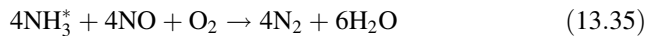


The respective reaction rate expression, which is based on experimental results, is proposed by Schuler et al. [31]:

$$R_{\text{NO}-\text{ox}} = k_{\text{NO}-\text{ox}}^0 \cdot e^{\left(-\frac{E_{\text{NO}-\text{ox}}}{RT}\right)} \cdot \left(c_{\text{NO}} \cdot y_{\text{O}_2}^{0.5} - \frac{c_{\text{NO}_2}}{K_{\text{eq}}}\right) \quad (13.34)$$

13.3.2.3 Standard SCR Reaction

According to the “standard” SCR reaction equal molar amounts of NH_3 and NO react with oxygen in order to form nitrogen and water:



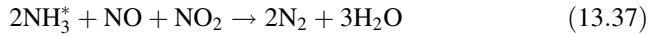
The inhibition of NH_3 on the standard SCR reaction, which was observed on vanadium-based catalysts, can be described by a two-site Langmuir–Hinshelwood rate expression as proposed by Chatterjee et al. [11]:

$$R_{\text{Standard-SCR}} = k_{\text{Standard-SCR}}^0 \cdot e^{\left(-\frac{E_{\text{Standard-SCR}}}{RT}\right)} \frac{c_{\text{NO}} \cdot \theta_{\text{NH}_3}}{1 + k_{\text{LH}} \frac{\theta_{\text{NH}_3}}{1 - \theta_{\text{NH}_3}}} \left(\frac{y_{\text{O}_2}}{y_{\text{O}_2}^{\text{ref}}}\right)^\beta \quad (13.36)$$

where k_{LH} is a rate parameter which describes the inhibition by NH_3 . The similar effect occurs on Fe-exchanged zeolites, where Eq. (13.36) was found to be valid [21].

13.3.2.4 Fast SCR Reaction

The fast SCR reaction describes the reaction taking place when both NO and NO_2 are present in the exhaust gas:

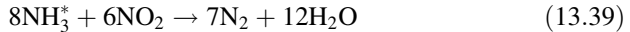


In a global modeling approach, it is assumed that NO and NO_2 react with the adsorbed ammonia directly from the gas phase and consequently an Eley–Rideal mechanism-based expression is commonly used to describe the reaction rate:

$$R_{\text{Fast-SCR}} = k_{\text{Fast-SCR}}^0 e^{\left(-\frac{E_{\text{Fast-SCR}}}{RT}\right)} \cdot c_{\text{NO}} \cdot c_{\text{NO}_2} \cdot \theta_{\text{NH}_3} \quad (13.38)$$

13.3.2.5 NO_2 SCR Reaction

The NO_2 SCR reaction provides a pathway for the direct conversion of NO_2 , in the absence of NO [36], and has been found useful to predict the effect of NO/ NO_2 ratio on SCR performance.

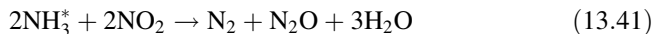


In analogy to the fast SCR reaction, an Eley-Rideal expression is assumed for the reaction rate, as the gaseous NO_2 reacts with the stored ammonia.

$$R_{\text{NO}_2\text{-SCR}} = k_{\text{NO}_2\text{-SCR}}^0 e^{\left(-\frac{E_{\text{NO}_2\text{-SCR}}}{RT}\right)} \cdot c_{\text{NO}_2} \cdot \theta_{\text{NH}_3} \quad (13.40)$$

13.3.2.6 N_2O Formation

It has been experimentally observed that the N_2O production (13.41) is favored by increased NO_2/NO_x ratios and also by lower temperatures (200–350 °C) [34].



The rate expression for the above reaction:

$$R_{\text{N}_2\text{O}} = k_{\text{N}_2\text{O-SCR}}^0 e^{\left(-\frac{E_{\text{N}_2\text{O}}}{RT}\right)} \cdot c_{\text{NO}_2} \cdot \theta_{\text{NH}_3} \quad (13.42)$$

13.3.2.7 Ammonium Nitrate Formation/Decomposition

At low temperatures ($T < 200$ °C), a mechanism for the formation of ammonium nitrate has to be considered [37]. This reaction requires NO_2 as the oxidizing reactant and has been reported on various vanadia- and zeolite-based catalysts [33, 38].



Ammonium nitrate is decomposed to N_2O at higher temperatures ($T > 200$ °C) according to the reaction:



13.3.3 Parameter Calibration

The parameters of the reaction rates, consisting of pre-exponential factors and activation energies have to be calibrated in order to attain an optimal fit between simulated and experimental data. A step-by-step procedure is followed based on experiments which are specifically designed to minimize the number of parameters that have to be calibrated simultaneously. The sequence can be organized as follows: First, parameters related to ammonia adsorption and desorption processes are identified, in the absence of SCR reactions. Second, NO oxidation parameters are calibrated without ammonia in the feed stream. Finally, the calibration of the remaining parameters is performed all together [39]. Different experimental methods and procedures involved in the derivation of global SCR reaction kinetics will be presented in Sect. 13.5.

13.4 Importance of Washcoat Diffusion Modeling

The scope of this paragraph is to analyze the impact of internal washcoat diffusion on the performance of zeolite-based catalysts both by experimental and simulation results. In the first part, an experimental study of mass transfer limitations in Fe- and Cu-zeolite catalysts performed by Metkar et al. [40] is presented. The authors investigated catalysts with different washcoat loadings, washcoat thicknesses, and lengths under various SCR reactions in order to identify the presence of diffusion limitations throughout an extended temperature range. In the second part, the flow-through catalyst model, presented in Sect. 13.2, was employed to reproduce the test conditions of the fore-mentioned experiments.

13.4.1 Experimental Results

In order to study the internal mass transfer limitations in various representative SCR reactions, Metkar et al. used Fe- and Cu-zeolite monolith samples named as FeZ-XX-Ycm and CuZ-XX-Ycm where XX denotes the washcoat loading (% weight) and Y the length of the catalyst (cm). For each catalyst technology two samples were tested, the second one having half the washcoat loading and double the length so as to keep the same washcoat mass. Experiments were carried out in the 150–550 °C temperature range while a constant flow rate was used so as to keep constant space velocity per unit of catalyst mass. Detailed description of the experimental protocols can be found in [40].

13.4.1.1 NO–NH₃ Reacting System

Experimental results for the standard SCR reaction study are presented in Fig. 13.3. A substantial performance degradation is observed for the low length—high washcoat loading samples. The difference in NO_x conversions is observed above 250 °C for Cu-zeolites and 350 °C for Fe-zeolites, indicating that diffusion limitations are present.

13.4.1.2 NO–NO₂–NH₃ Reacting System

Similar experimental procedure was carried out for the NO–NO₂–NH₃ reacting system. The presence of NO₂/NO_x ratio of 50 % in the feed stream greatly enhances the NO_x conversion efficiency as the fast SCR is the governing reaction in the system. Higher space velocities were necessary to achieve lower conversions and to make the observation of mass transfer limitations possible. The experimental results obtained for the Fe-zeolite catalysts are shown in Fig. 13.4. Washcoat diffusion limitations are present throughout the whole temperature range with the short monolith sample constantly achieving lower NO_x conversions.

13.4.2 Simulation Study and Effective Diffusivity Investigation

The kinetic parameters of the 1D + 1D model were calibrated to fit the experimental results produced by Metkar et al. [40]. Thermophysical properties and microstructural data for the zeolite washcoat and the substrate were obtained from the literature. In Fig. 13.5a simulated and experimental results are presented for the pair of FeZ–XX catalysts. An overall good agreement is observed, with the

Fig. 13.3 Experimental steady-state NO_x conversions obtained during the standard SCR reaction over FeZ-XX and CuZ-XX catalysts. Reprinted from Metkar et al. [40], with permission from Elsevier

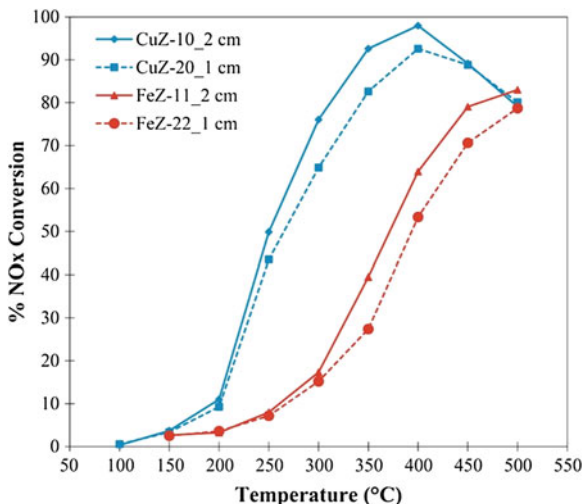
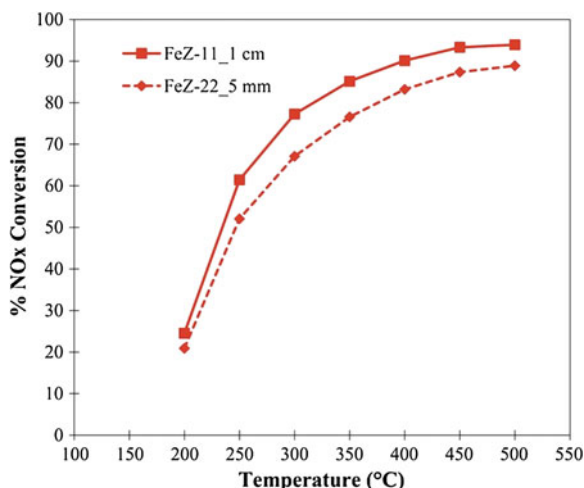


Fig. 13.4 Experimental steady-state NO_x conversions obtained during the fast SCR reaction over FeZ-XX catalysts. Reprinted from Metkar et al. [40], with permission from Elsevier



model being able to predict the decrease in NO_x conversion due to diffusion limitations for the case of short catalyst with thick coating.

Washcoat tortuosity $\tau[-]$ is an important empirical parameter in the computation of the effective diffusivity of species inside the washcoat pores (13.15). A parametric analysis of washcoat tortuosity, shown in Fig. 13.5b, resulted in a value of $\tau = 2.0$ as the best value to reflect the extent of the internal diffusion impact on de-NO_x activity.

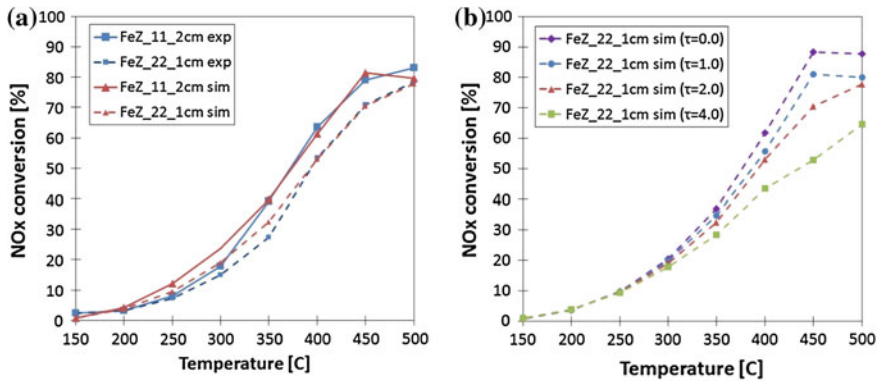


Fig. 13.5 Comparison of experimental and simulation results (a) and parametric analysis of washcoat tortuosity factor (b) in terms of NO_x conversion efficiency. (Dashed lines represent results for the high washcoat-short length catalyst.) Source of experimental data Metkar et al. [40]

13.5 From Lab Reactor Tests to Real-World System Modeling

The aim of this section is to present the different procedures involved in the derivation of the SCR global reaction kinetics and their incorporation into the previously described (1D + 1D) mathematical model in order to predict the dynamic behavior of full-scale converters under real-world conditions.

13.5.1 Overview of Model Parameterization Approaches

The development of global reaction kinetics is a stage wise scale-up approach. The various stages of this multiscale approach are summarized in Fig. 13.6 and include: (a) microreactor experiments over powdered catalyst for the determination of the intrinsic reaction kinetics, (b) synthetic gas bench experiments over small monolith samples to account for intraporous diffusion of species, and (c) validation on steady-state and transient engine tests.

13.5.2 Microreactor and Monolith Reactor Tests

The first stage of the investigation includes steady and transient microreactor experiments for the determination of the intrinsic kinetics of the various NH₃-NO_x reactions. According to this approach, a part of the initial extruded or washcoated catalyst is crushed into a fine powder form and placed inside a microreactor.

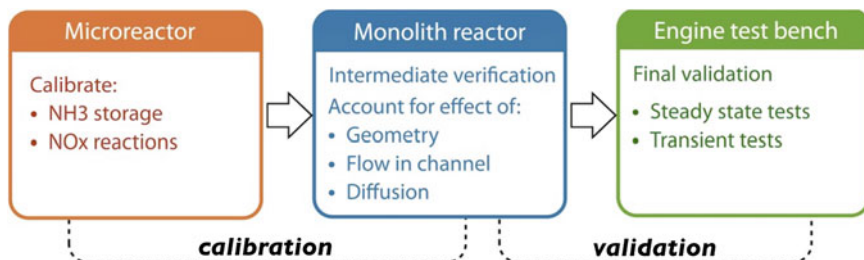
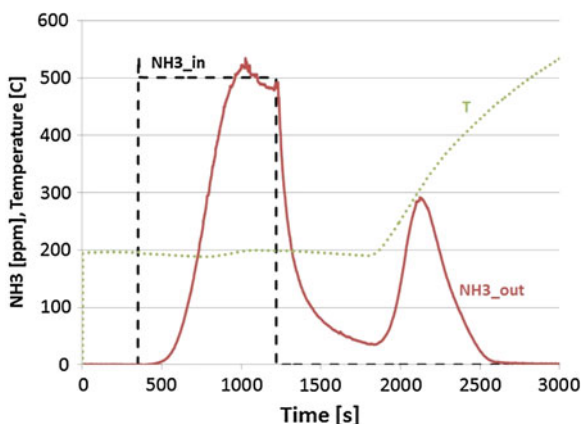


Fig. 13.6 Stages for the derivation of global reaction kinetics

Fig. 13.7 NH_3 adsorption–desorption experiment



The latter consists of a tubular fixed bed reactor encased in a furnace through which the reacting feed flows. This experimental setup guarantees negligible transport limitations, measurement of fast transients, and controlled isothermal conditions.

A typical experiment for the investigation of the NH_3 adsorption–desorption reaction is shown in Fig. 13.7. The figure shows the evolution of the outlet NH_3 concentration during a step of NH_3 inlet feed followed by a temperature programmed desorption.

The second stage of the scale-up approach involves monolith reactor experiments over small catalyst samples with a volume of a few cubic centimeters. The data obtained from this intermediate stage serve either as a primary validation of the intrinsic reaction kinetics or for kinetic parameter estimation in case microreactor experiments have been omitted. Monolith reactor experiments are able to reproduce more accurately the phenomena prevailing in real full-scale converters taking into account the catalyst's geometry, the flow dynamics along the channel, and the intraporous diffusion over the washcoat. At the same time, the experiments are performed under controlled laboratory conditions, involving isothermal operation and the use of synthetic gas mixtures.

Figure 13.8 illustrates the results of steady-state experiments at various temperatures over a small monolith sample with the feed stream consisting primarily

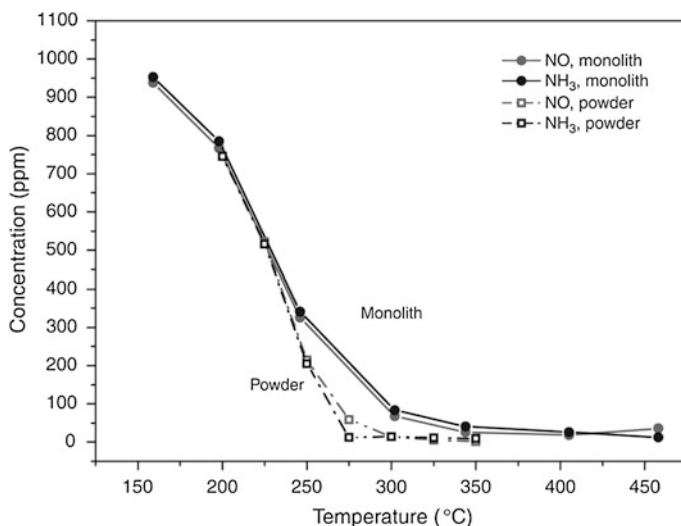


Fig. 13.8 Steady-state NO and NH₃ concentrations versus temperatures in runs over a small monolith catalyst and over the same catalyst crushed to powder. Reprinted from Güthenke et al. [41], with permission from Elsevier

of NO and NH₃. For comparison purposes, the figure shows also the outlet concentrations measured during identical experiments over the catalyst in powder form. In the latter case, the flow rate was adjusted in order to keep the same flow rate per active catalyst mass. In the low temperature region, the concentrations measured over the monolith and over the powder catalyst coincide. On the contrary, for temperatures above 225 °C deviations are observed, corresponding to lower conversions for the monolith which are attributed to diffusion limitations.

13.5.3 Real-World Full-Scale Applications

In the third and final stage, the reaction kinetics are validated under real application conditions by performing engine test bench experiments. The up-scaling from small monolith samples to full-scale monolithic converters does not involve changes in the catalyst morphology or the flow dynamics. The major difference, apart from the increased catalyst size, is the use of real engine exhaust as feed gas which enables the observation of possibly neglected composition effects on the reaction kinetics.

One of the main challenges in this type of model applications is the correct estimation of NH₃ concentration at the entrance of the catalyst, which is used as an inlet parameter to the model. The problem arises from the fact that NH₃ is sometimes not directly measured at catalyst entrance but rather estimated based on the instantaneous injection of urea–water solution in the exhaust stream.

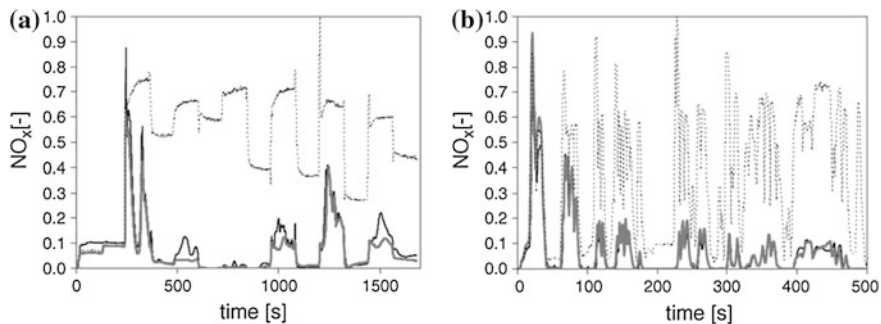


Fig. 13.9 Normalized NO_x concentration at SCR catalyst inlet and outlet of an ESC (a) and an ETC (b) test cycle. *Dotted black lines*-inlet values, *solid black lines*-outlet measurement, *gray lines*-outlet simulation. Reprinted from Tronconi et al. [29], with permission from Elsevier

In addition, the uniformity of NH_3 concentration at catalyst entrance is not always perfect which obviously challenges the use of single-channel approaches.

An example of model validation on standard European test cycles (ESC and ETC), performed by Tronconi et al. [29], is shown in Fig. 13.9. An excellent correlation between the NO_x concentrations downstream of the catalyst is observed with an error of 3–4 % for the total NO_x conversion in both cycles.

13.6 Fundamentals of SCR on DPF Modeling

In addition to selective catalytic reduction (SCR) systems, the Diesel particulate filter (DPF) technology is also adopted in many current and future low-emission diesel exhaust configurations both in light-duty and heavy-duty applications. Usually, the systems are implemented as separate devices. A combined DPF + SCR system, referred to as SCR[®] (also referenced as WSCR, SDPF, or SCR_oF) in which the porous walls of the DPF are impregnated with SCR active material promises big improvements in terms of packaging volume and costs, but requests high detail in modeling. In this section, a simulation study on the phenomena that are expected to play a key role in SCR[®] systems is presented. A detailed mathematical description of the wall-flow filter model and the associated soot oxidation reactions are given in the first part. The second part addresses the effect of mass transfer limitations by comparing flow-through and wall-flow SCR monoliths while the last part is dedicated to the interactions between soot and de- NO_x activity.

13.6.1 Wall-Flow Filter Model

A pioneering 1D model for the wall-flow DPF was originally presented in 1984 by Bissett [42]. A few years later, Konstandopoulos and Johnson developed a pressure

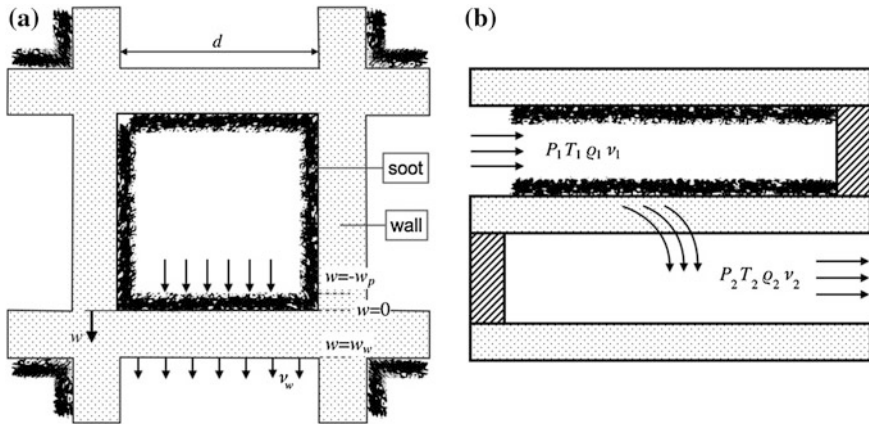


Fig. 13.10 Schematic of channel model. **a** Front view, **b** side view

drop model for an unloaded filter [43]. By assuming uniform soot layer distribution over the channel, the above model was extended to loaded filter, taking into account the reduction of channel cross-section due to the growth of soot layer [44]. Bissett’s work has been extended by Koltsakis et al. [45] to describe the soot regeneration in terms of thermal and catalytic reactions.

A schematic of the side and front view of a filter channel is given in Fig. 13.10. The governing equations for the conservation of mass, momentum, energy, and species are given in the following subsections.

13.6.1.1 Mass-Momentum Balance

Conservation of mass of channel gas

The mass balance equation for the gas flowing in the inlet and outlet channels is written as:

$$\frac{\partial}{\partial z} (d_i^2 \rho_i v_i) = (-1)^i \cdot 4d \rho_w v_w \tag{13.45}$$

where subscript i identifies regions 1 (inlet channel) and 2 (outlet channel), subscript w denotes the substrate wall, d is the hydraulic diameter of a clean channel [m], ρ_w and v_w are, respectively, the density [kg/m³] and velocity [m/s] of gas passing through the soot cake and wall.

Conservation of axial momentum of channel gas

Taking into account the mass loss/gain through the porous wall and the friction in the axial direction z , the momentum balance of exhaust gas can be formulated:

$$\frac{\partial p_i}{\partial z} + \frac{\partial}{\partial z} (\rho_i v_i^2) = -\alpha_1 \mu v_i / d_i^2 \tag{13.46}$$

where p is the gas pressure [Pa], α_1 is a constant in channel pressure drop correlation [-], and μ is the dynamic viscosity [Pa · s].

13.6.1.2 Energy Balance

Energy balance of the gas phase

Inlet channel:

$$C_{p,g}\rho_1v_1\Big|_z\frac{\partial T_1}{\partial z} = h_1\frac{4}{d_1}(T_s - T_1) \quad (13.47)$$

where subscript s denotes the solid.

Outlet channel:

$$C_{p,g}\rho_2v_2\Big|_z\frac{\partial T_2}{\partial z} = (h_2 + C_{p,g}\rho_wv_w)\frac{4}{d}(T_s - T_2) \quad (13.48)$$

Energy balance of the solid phase

The temperature field in the filter is described by the equation of transient heat conduction with heat sources in axisymmetric coordinates:

$$\rho_s \cdot C_{p,s}\frac{\partial T_s}{\partial t} = \lambda_{s,z}\frac{\partial^2 T_s}{\partial z^2} + S \quad (13.49)$$

For the case of 2D and 3D modeling, Eqs. (13.18) and (13.19) can be used, respectively. The source term S includes the contribution of the convective heat transfer of the gas flow in the channels and through the wall as well as the exothermic heat release:

$$S = H_{\text{conv}} + H_{\text{wall}} + H_{\text{react}} \quad (13.50)$$

Convection of heat due to flow along channels

$$H_{\text{conv}} = h_1 \cdot S_F \cdot (T_1 - T_s) + h_2 \cdot S_F \cdot (T_2 - T_s) \quad (13.51)$$

Convection of heat due to flow through wall

$$H_{\text{wall}} = \rho_w \cdot v_w \cdot S_F \cdot C_{p,g} \cdot (T_1 - T_s) \quad (13.52)$$

Reaction heat release

$$H_{\text{react}} = S_F \sum_k \left(\int_{-w_p}^{w_w} f_w R_k dw \right) \cdot \Delta H_k \quad (13.53)$$

where w_p is the soot layer thickness [m] and w_w the substrate wall thickness [m]. The geometrical parameter f_w is defined as:

$$f_w = \frac{b(w)}{d} \quad (13.54)$$

The width available to flow $b(w)$ varies in the particulate layer and remains constant in the wall:

$$b(w) = \begin{cases} d + 2w, & w < 0 \\ d, & w \geq 0 \end{cases} \quad (13.55)$$

13.6.1.3 Species Balance

The governing equation for the mass conservation of any species in the soot layer and wall is:

$$v_w \frac{\partial y_j}{\partial w} - D_{w,j} \frac{\partial}{\partial w} \left(f_w \frac{\partial y_j}{\partial w} \right) = \frac{f_w}{c_m} \sum_k n_{j,k} R_k \quad (13.56)$$

where c_m is the molar concentration of the gas [mol/m^3] and $c_{j,k}$ the stoichiometric coefficient of species j in a reaction k . The calculation of the effective diffusivity $D_{w,j}$ is based on the previously described parallel pore model given by Eqs. (13.15) and (13.16).

The boundary conditions couple the phenomena in the wall with the gas concentrations in the channels. The convective mass transfer from the bulk gas to the wall surface is computed according to the “film” approach with mass transfer coefficients $k_{i,j}$ corresponding to laminar flow for both inlet and outlet channels:

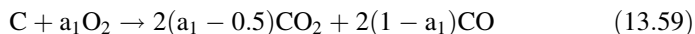
$$\frac{\partial(v_1 y_{1,j})}{\partial z} = -\frac{4}{d \cdot f_w^2} v_w y_{1,j} + \frac{4}{d \cdot f_w} k_{1,j} (y_{1s,j} - y_{1,j}) \quad (13.57)$$

$$\frac{\partial(v_2 y_{2,j})}{\partial z} = \frac{4}{d \cdot f_w^2} v_w y_{2s,j} + \frac{4}{d \cdot f_w} k_{2,j} (y_{2s,j} - y_{2,j}) \quad (13.58)$$

13.6.2 SCR Kinetic Model and Soot Oxidation Kinetics

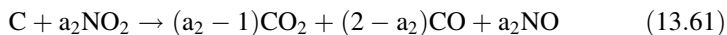
For the purposes of this study, a superimposition of the SCR chemistry and the soot reactivity is assumed. To account for NH_3 -SCR reactions in the wall-flow filter the same kinetic model presented in Sect. 13.2 is used. Soot oxidation is modeled by two parallel reactions with O_2 and NO_2 [46, 47]. The respective rate expressions are also given below.

Soot oxidation with O₂



$$R = A \cdot e^{-\frac{E}{RT}} \cdot p_{\text{O}_2}^n \quad (13.60)$$

Soot oxidation with NO₂



$$R = A \cdot e^{-\frac{E}{RT}} \cdot p_{\text{NO}_2} \quad (13.62)$$

where a_1 and a_2 are indexes of the completeness of the reactions, characterizing the selectivity toward CO or CO₂ production.

13.6.3 Wall-Flow Versus Flow-Through Monoliths

In this section, we present a simulation study to compare the steady-state de-NO_x performance of catalytically coated DPF filters with integrated SCR capability with the respective flow-through SCR catalysts. The comparison is based on a theoretical basis, using the mathematical models presented in previous sections. Aim of the study is to quantify the effect of the mass transfer limitations in the case of the flow-through SCR catalyst, which are much less present in the case of the wall-flow SCR[®] filter.

Both SCR and SCR[®] systems are assumed to have equal external dimensions and to contain exactly the same amount of active catalytic material. On the contrary, different cell density and wall thickness have been chosen so that they are closer to real-world applications. The geometric properties of the two systems are given in Table 13.1.

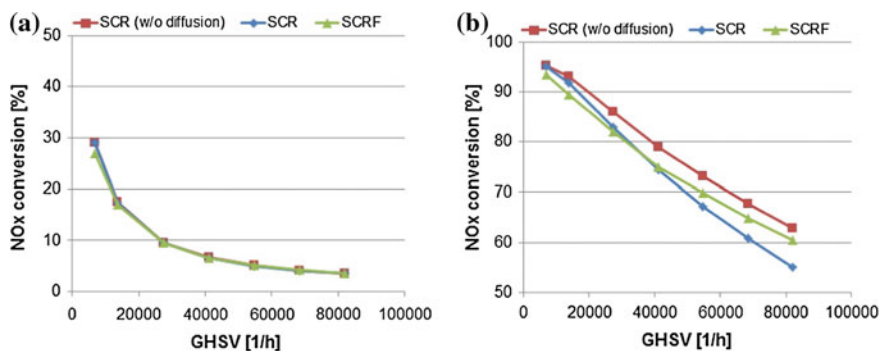
The reaction scheme and kinetic rate data used in the study are based on reference values. However, the results expected from this specific study are not subject to the accuracy of the kinetic data, as we are mainly interested in the global comparison between the two different reactor types.

Simulations were performed for both the SCR and the SCR[®] at various flow rates and temperatures (200 °C and 350 °C). In the case of the flow-through SCR, simulations were performed with and without considering the internal diffusion limitations. In every case the inlet feed stream contained equal amounts of NO and NH₃ (500 ppm) together with 8 % O₂, 6 % H₂O, and balance N₂.

Figure 13.11a shows NO_x conversion efficiency with respect to space velocity at 200 °C where it is evident that diffusion limitations are absent. SCR de-NO_x efficiency, computed either with the surface reaction or the internal diffusion model, is in complete agreement with the one calculated for the SCR[®]. On the contrary, washcoat diffusion becomes significant at the temperature of 350 °C (Fig. 13.11b). Examining the SCR curves only, the trends of NO_x conversions

Table 13.1 Geometric and thermophysical properties of the SCR (a) and SCR^F® (b)

Substrate	Cordierite
<i>(a) SCR</i>	
Catalytic material	Vanadia/Titania
Catalyst diameter	0.144 m
Catalyst length	0.254 m
Cell density	400 cpsi
Wall thickness	6 mils
Substrate density	1,250 kg/m ³
Washcoat load	150 g/l
<i>(b) SCR^F®</i>	
Catalytic material	Vanadia/Titania
Filter diameter	0.144 m
Filter length	0.254 m
Cell density	300 cpsi
Wall thickness	12 mils
Substrate density	1,250 kg/m ³
Washcoat load	150 g/l

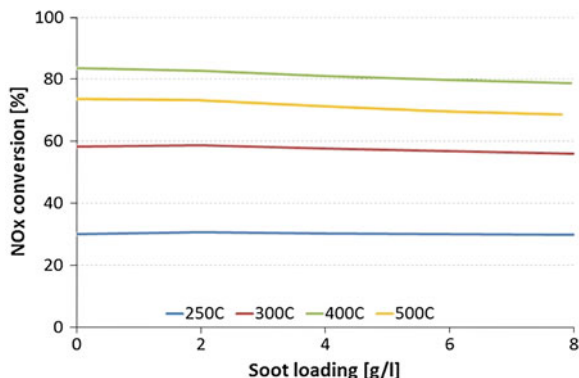
**Fig. 13.11** Simulation results of NO_x conversion versus space velocity for SCR (with and without diffusion limitations) and SCR^F® systems at 200 °C (a) and 350 °C (b)

remain the same until 20,000 h⁻¹ but for higher space velocities a significant difference can be observed denoting strong diffusional limitations. The SCR^F shows initially slightly lower NO_x conversions but for space velocities above 40,000 h⁻¹ it is about 5 % more efficient than the diffusion-limited SCR.

13.6.4 Interactions Between Soot and de-NO_x Activity

SCR^F® systems may appear as an attractive solution due to their higher de-NO_x performance at clean state compared to the SCR catalysts, as presented in

Fig. 13.12 Simulated NO_x conversion as a function of soot load. Temperatures: 250–300–400–500 °C. Adapted from Colombo et al. [48]



Sect. 13.6.3. However, the general case of soot-loaded SCRF[®] has to be considered in order to account for the competitive interactions between SCR activity and soot oxidation which will be discussed in this section.

13.6.4.1 Effect of Soot on de- NO_x Performance

Colombo et al. [48] studied the impact of soot on de- NO_x efficiency by performing steady-state SCRF[®] simulations for different initial soot loadings at various temperatures. Figure 13.12 summarizes simulation results obtained in the case that the inlet feed consists primarily of NO and NH_3 . A NO_x conversion decrease due to soot accumulation can be observed at high temperatures but it is only limited to a maximum 5 %, at least for the simulated conditions. The negative effect of soot load on de- NO_x activity for the NO – NH_3 reacting system was attributed by the authors to the increasing diffusion limitations of the species across the soot layer.

The same authors performed simulations for the NH_3 – NO_2 reacting system. Figure 13.13 shows the respective results obtained at 400 and 500 °C in terms of NO_x conversion as a function of soot load. Analyzing simulation results at 400 °C (Fig. 13.13a), a promoting effect of soot was observed focusing on NO_x conversion. On the contrary, increasing the temperature to 500 °C resulted in a different picture for NO_x conversion, as shown in Fig. 13.13b. A peculiar behavior was predicted by simulations as an optimum value of NO_x conversion is apparent at this temperature for a soot loading of about 3.5 g/l. Detailed analysis of simulation results revealed that the discussed behaviors were related to the interaction between passive regeneration of soot and SCR reactivity. The former process consumes NO_2 and soot producing CO_x and NO . In this way, the local NO_2/NO_x ratio is different from that of the feed stream, thus altering the de- NO_x performance. Indeed, from both literature indications [27, 33, 49] and analysis of utilized kinetic parameters, the NO_x conversion rate was found to be maximum for $\text{NO}_2/\text{NO}_x = 0.5$, while lower rates were calculated in excess of either NO_2 or NO , with the latter case resulting in the slowest de- NO_x process, at least in the 250–500 °C temperature window.

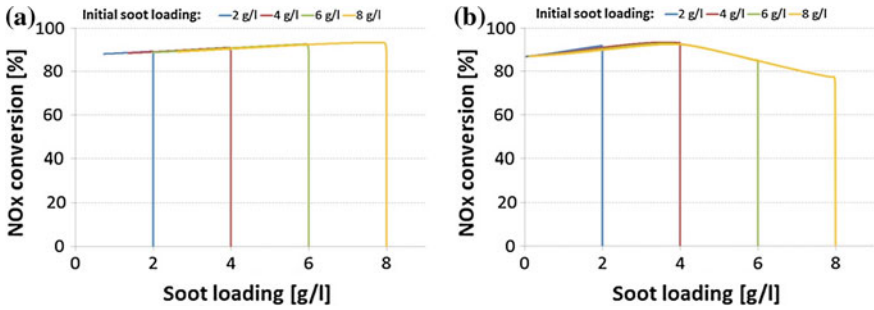


Fig. 13.13 Simulated NO_x conversion as a function of soot load at (a) 400 °C and (b) 500 °C. Adapted from Colombo et al. [48]

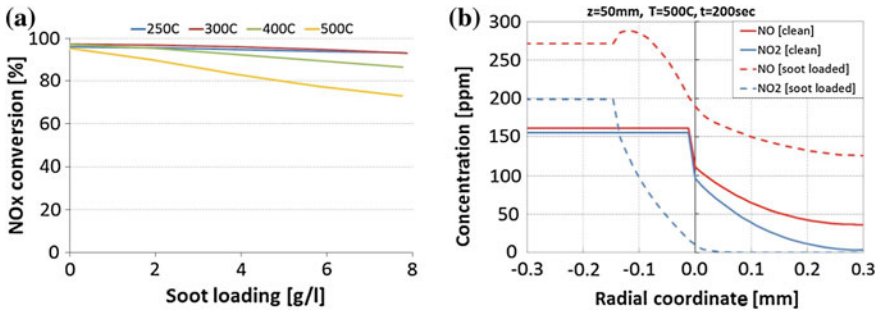


Fig. 13.14 NO_x conversion as a function of soot loading (a) and radial concentration profiles for NO and NO₂ at 500 °C (b). Adapted from Colombo et al. [48]

The last investigated reacting system involved the simultaneous presence of both NO and NO₂ in the feed stream, this situation being the most common under real operating conditions. Simulation results are summarized in Fig. 13.14a, where steady-state NO_x conversion is plotted as a function of total soot load for different temperatures. NO_x conversions close to 100 % were computed in the whole investigated temperature range at clean filter conditions. Increasing the soot load resulted just in a slight decrease of NO_x conversion for temperatures lower than 300 °C. At higher temperatures the effect of soot presence became much more pronounced, leading to a significant decrease of NO_x conversion for the highest temperature and load conditions.

To explain the computed behaviors, the authors analyzed the radial profiles of NO and NO₂ both in the presence and absence of soot. Figure 13.14b shows computed profiles obtained at 500 °C at a fixed axial location. In the case of soot free SCR[®] (continuous lines), local NO₂/NO_x ratios close to 0.5 were observed which lead to high de-NO_x rates. On the opposite, in the case of the soot-loaded SCR[®] (dashed lines), NO₂ was almost completely consumed in the soot layer, thus resulting in a strong excess of NO in the catalyzed wall. Under these

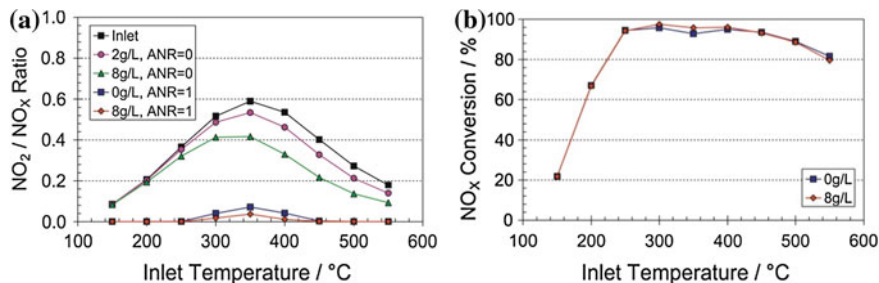


Fig. 13.15 SCRf[®] NO_2/NO_x ratio (a) and predicted effect of soot loading on NO_x conversion as a function of temperature for a Cu-SCRf[®] (b). Reprinted from Watling et al. [50], with permission from Elsevier

conditions lower de- NO_x rates were achieved, being the Standard SCR the main reaction occurring in the system.

Watling et al. [50] also investigated the effect of the presence of soot on NO_x conversion by performing a series of simulations for a Cu-SCRf[®] at various soot loadings and temperatures between 150–550 °C. The gas feed to the SCRf[®] contained 500 ppm NO_x and 15 % O_2 with a space velocity of 55,000 h^{-1} . A realistic NO_2/NO_x ratio was used at the inlet, as presented in Fig. 13.15a.

The results, presented in Fig. 13.15b, show no significant effect of soot on NO_x conversion. At low temperatures, the NO_2 consumption by soot is slow and has little impact on the NO_2/NO_x ratio. At mid temperatures, the presence of soot actually enhances the de- NO_x performance. As mentioned before, optimum SCR activity is achieved when inlet $\text{NO}_2/\text{NO}_x = 0.5$ due to the fast SCR reaction. NO_2/NO_x ratio is higher than 0.5 between 300 °C and 400 °C. Soot oxidation with NO_2 results in a decrease in NO_2/NO_x to a value closer to 0.5 and thus enhancing the NO_x conversion.

13.6.4.2 Effect of de- NO_x Activity on Filter Regeneration

Colombo et al. [48] performed a simulation study of the de- NO_x activity effect on soot regeneration. Simulations were carried out at a fixed temperature of 500 °C and with a feed mixture containing equal amounts of ammonia and NO_x . The initial soot load was set to 8 g/l and simulations were repeated with two different NO_2/NO_x ratios, namely 0 and 1. For both reacting systems, simulations were first performed considering the SCR reactivity and then repeated by deactivating the de- NO_x reactions. The computed evolution of the total soot mass and of wall soot was followed as a function of time, as shown in Fig. 13.16.

In the case of the NH_3 - NO reacting system (Fig. 13.16a), the presence of de- NO_x activity slightly favored soot consumption. Analysis of simulation data proved that the promoting effect was related to the slight exothermicity of de- NO_x reactions. For the NH_3 - NO_2 reacting system a different picture came out from simulations, with soot consumption resulting faster in the absence of any de- NO_x

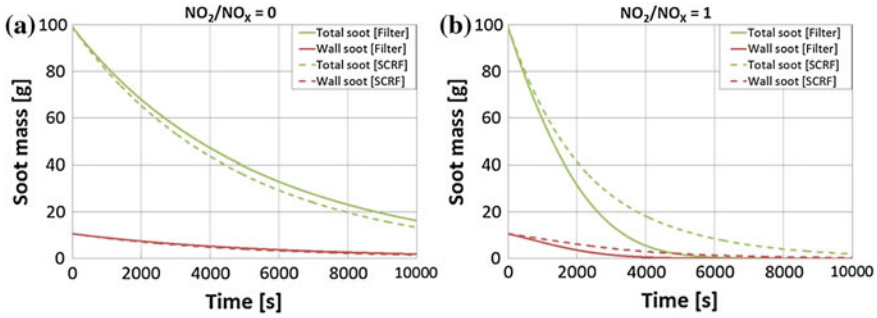
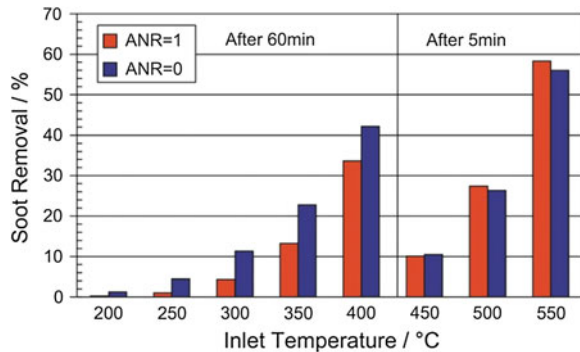


Fig. 13.16 Total soot mass and wall soot mass as a function of time for $NO_2/NO_x = 0$ (a) and $NO_2/NO_x = 1$ (b). Adapted from Colombo et al. [48]

Fig. 13.17 Predicted soot removal in a 60 (200–400 °C) min period or a 5 (450–550 °C) min period with (ANR = 1) and without (ANR = 0) SCR activity (Feed: 500 ppm NO_x , 15 % O_2 , 55,000 h^{-1} space velocity, inlet NO_2/NO_x as in Fig. 13.15a.) Reprinted from Watling et al. [50], with permission from Elsevier



activity (Fig. 13.16b). Again, analysis of simulation data pointed out that, in presence of de- NO_x activity, NO_2 is competitively consumed in both soot passive regeneration and SCR reactions, thus resulting in lowering soot consumption rate.

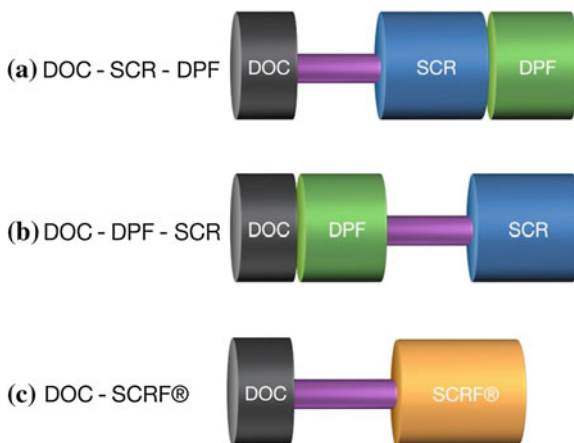
Equivalent simulation results have been produced by Watling et al. [50], who examined the rate of soot oxidation both in the presence and absence of NH_3 for a Cu-SCR[®] (see Fig. 13.17).

For temperatures up to 400 °C the rate of soot removal is significantly reduced as SCR activity greatly reduces the available NO_2 for soot oxidation. At higher temperatures, the NO_x conversion is predicted to no longer have a negative impact on soot oxidation. At 500–550 °C, soot regeneration is actually enhanced, fact that is attributed to the 5 °C exotherm generated by the SCR reactions.

13.7 Integrated Exhaust System Modeling

Due to the increasing pressure to develop small size and low-cost aftertreatment systems meeting the legislative demands, it is desirable to integrate multiple functionalities and exploit any possible synergies between devices. Typical

Fig. 13.18 Schematic of the 3 different design layouts for integration of DPF + SCR system



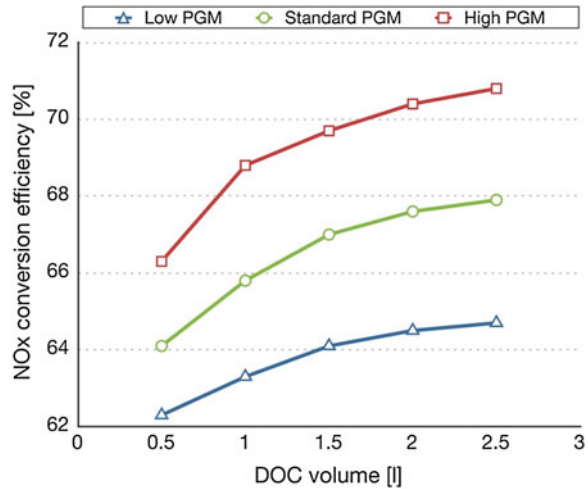
examples include DPF's catalyzed with de- NO_x catalysts, as well as LNT-SCR and SCR-ASC combinations using layered coating technology. The design of such advanced exhaust line configurations requires a multidimensional optimization process.

13.7.1 Model-Based DPF + SCR System Optimization

The design optimization problem associated with the relative position of the SCR in a DOC + SCR + DPF exhaust line is addressed in this section [51]. The study refers to a medium size passenger car exhaust system. Placing the SCR catalyst upstream of the DPF reduces its warm-up time, thus enabling the reduction of cold start NO_x emissions. At the same time, however, the exhaust gas reaching the DPF will be poor in NO_2 , thus minimizing the passive regeneration potential and increasing the regeneration frequency. Instead, a DPF placement in front of the SCR catalyst would be ideal for its regeneration management, but would pose big problems for the SCR cold-start efficiency due to the large DPF thermal mass.

Three basic concepts for positioning a DPF and an SCR system were compared in [51], as shown in Fig. 13.18. Concept (a) assumes a close-coupled DOC followed by a connecting pipe where the urea dosage and mixing takes place. The SCR catalyst is then placed upstream of the DPF. In concept (b) the DPF is placed immediately after the close-coupled DOC. The urea dosage/mixing is done in the connecting pipe before the SCR. Concept (c) assumes a combined DPF/SCR system which is placed downstream the close-coupled DOC with an intermediate connecting pipe.

Fig. 13.19 NEDC de-NO_x efficiency for different DOC sizes and PGM loadings



Concept (a): DOC-Pipe-SCR-DPF

Effect of DOC size and PGM activity: The presence of a DOC has two main implications on the SCR system efficiency. The DOC thermal inertia affects the SCR inlet temperature while the production of NO₂ over the DOC alters the NO₂/NO_x ratio upstream of the SCR. The latter case is of greater interest since the thermal mass of the DOC is relatively low and it only affects the de-NO_x performance during the light-off phase. Chatterjee et al. [52] stated that SCR efficiency is mainly influenced by the DOC generated NO₂/NO_x ratio, with the DOC noble metal loading and volume being the two parameters that can be modified independently to optimize the system performance. A computational study performed by Koltsakis et al. [53] relates the NO_x conversion efficiency with the DOC PGM loading and volume (Fig. 13.19).

It is apparent that higher PGM loading leads to an increase of the de-NO_x efficiency due to a more favorable NO₂/NO_x ratio, closer to 50%. An increase of the DOC volume with a constant specific noble metal loading has also a positive effect on the NO_x conversion. This is due to the higher PGM amount of the DOC which increases the NO oxidation rate.

Concept (b): DOC-DPF-Pipe-SCR

Effect of DPF thermal inertia: The effect of the thermal inertia of the components upstream of the SCR is expected to be more pronounced in the case where the SCR is located after the DPF. In this case, it is not only the thermal inertia of the DOC which delays the SCR warm-up but also the thermal mass of the DPF. To examine this effect, four different DPF formulations, with alternating substrate material and volume, were considered along the baseline DOC. The simulated DPF's were: the baseline (SiC, 2.5 l), a (Cordierite, 2.5 l), a (SiC, 3.75 l), and a (Cordierite, 3.75 l). The effect of the thermal response on the average NO_x conversion efficiency is illustrated in Fig. 13.20. For the baseline DPF volume of 2.5 l, the substrate material of the DPF appears to have an impact of up to 5% in the

Fig. 13.20 Effect of the upstream DPF thermal inertia on the average simulated NO_x conversion efficiency of the SCR system

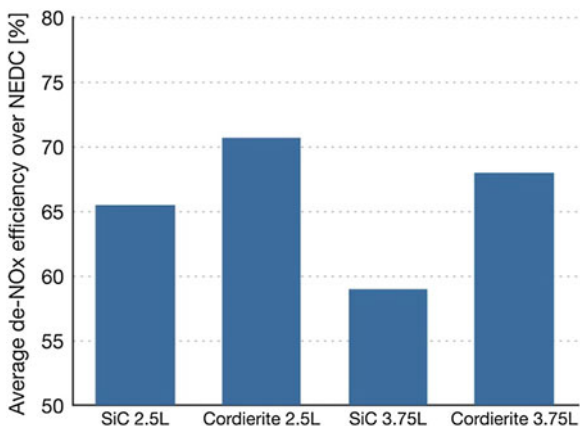
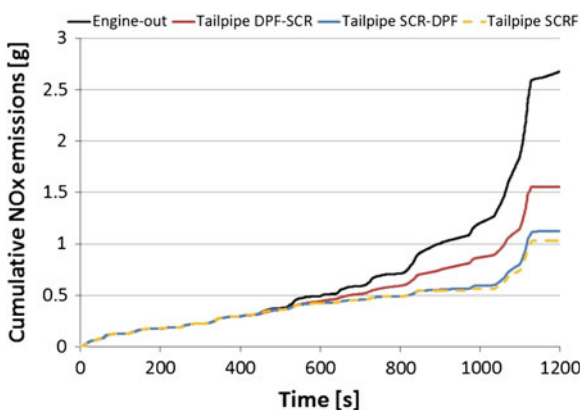


Fig. 13.21 Comparison of the cumulative NO_x emissions over the NEDC for the three configurations simulated



average NO_x conversion efficiency, due to the delayed warm-up of the SCR catalyst. This impact is even more pronounced in the case of the larger substrate volume (9 %), while the impact of the volume itself ranges from 4–7 %.

Concept (c): DOC-Pipe-SCRf[®]

The third concept evaluated is a catalytically coated DPF filter with integrated SCR capability. To achieve equivalent NO_x conversion, the same volume as the SCR catalyst in the previous configuration is used. With the same reaction kinetics used for the SCR catalyst, the de-NO_x performance of all three configurations is simulated and the results are presented in Fig. 13.21. The combined system, presents similar warm-up behavior with respect to NO_x conversion with the DOC-SCR-DPF system, and faster compared to the DPF-SCR configuration. In the warmed-up part of the driving cycle, the DOC-SCRf[®] system presents practically the same conversion efficiency with the DOC-SCR-DPF system. During the extra urban part of the driving cycle, the SCRf[®] system appears to have slightly better conversion efficiency, compared to the SCR system. This can be attributed to the

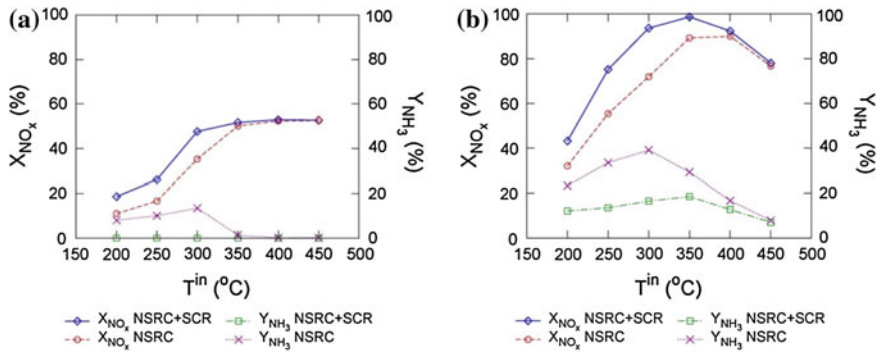


Fig. 13.22 NO_x conversion and NH_3 yields as a function of temperature in the NSRC + SCR system during lean/rich cycling with $t_{lean} = 180$ s and $t_{rich} = 3$ s (a) and $t_{rich} = 10$ s (b). Reprinted from Chatterjee et al. [54], with permission from Elsevier

mass transfer limitations in the case of the flow-through SCR monolith, which are not present in the case of the wall-flow SCR[®] monolith.

13.7.2 Combined LNT-SCR Concepts

The combination of lean NO_x trap (LNT), also referred to as NO_x storage and reduction catalyst (NSRC), and selective catalytic reduction (SCR) systems provides the potential to increase the efficiency of single LNT systems. During the lean-phase operation, NO_x emissions are being adsorbed in the LNT while the stored NO_x are reduced during the short rich phase operation. In the latter phase, NH_3 is produced as a secondary product of the NO_x reduction and then adsorbed in the SCR where it is utilized to further reduce the NO_x emissions. The NH_3 -SCR reactor can be either located downstream of the LNT (double-bed LNT-SCR) or merged within the same substrate with the LNT (dual-layer LNT-SCR).

A simulation study of a dual-bed LNT-SCR system (noted by the authors as NSRC + SCR) has been performed by Chatterjee et al. [54]. The performance of the system was evaluated, in terms of NO_x conversion and NH_3 release, in defined periodic lean/rich operation for various temperatures and at different rich phase durations (Fig. 13.22).

At the short regeneration phase of 3 s (Fig. 13.22a) the de- NO_x efficiency is low and NH_3 is generated over the NSRC only below 350 °C. All NH_3 is consumed in the SCR leading to improvement of NO_x conversion at low temperatures. At the longer rich phase of 10 s, higher NO_x conversions are obtained and more NH_3 is generated. Above 350 °C the NO_x reduction in the NSRC alone is so high that the NO_x concentration in the SCR inlet is very low. Consequently, NH_3 is in excess and part of it remains unused.

A similar modeling study was presented by Koltsakis et al. [55]. In the latter case, three different configurations have been simulated including a dual-layer

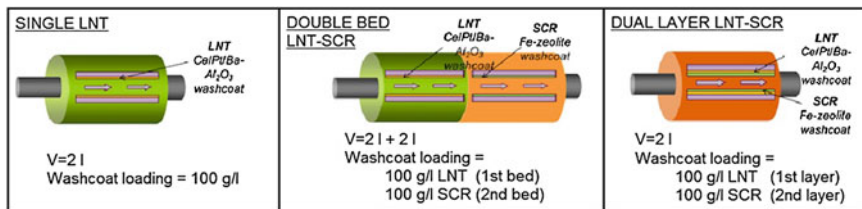
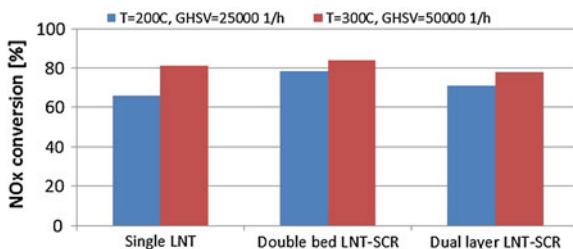


Fig. 13.23 Catalyst characteristic and geometrical data

Fig. 13.24 Simulated cumulative NO_x emissions for the 3 different configurations at 200 °C (a) and 300 °C (b)



LNT/SCR concept. Catalyst formulations and characteristics are presented in Fig. 13.23.

All three catalyst configurations have been tested in a scenario comprising of consecutive lean-rich cycles at different temperatures and space velocities in the range of practical interest for diesel engine applications. Comparative results for the three systems, in terms of NO_x conversion efficiency, are presented in Fig. 13.24.

The single-bed LNT simulation results showed significant amounts of NH₃ production at 200 °C, whereas at 300 °C the ammonia production during rich mode was less. Consequently, NH₃ content is available to be utilized by the combined systems for the further increase of the overall de-NO_x performance.

The additional SCR catalyst, positioned behind the LNT, is able to store the NH₃ emitted during rich mode and subsequently use it to reduce the incoming NO_x during the lean mode. An overall 78 % de-NO_x efficiency is observed at 200 °C for the double-bed LNT-SCR system, whereas the single LNT catalyst shows a performance of around 66 %. Qualitatively the same results are observed at 300 °C, where the combined system achieves an 84 % de-NO_x efficiency compared to the 81 % of the single-bed LNT.

The concept of the dual-layer LNT-SCR system is qualitatively similar to the dual-bed LNT-SCR system. In this case, NH₃ is produced in the bottom layer and before diffusing back to the gas phase, it is being stored in the top SCR layer. The stored NH₃ is subsequently used to reduce NO_x during lean mode. The dual-layer catalyst simulation predicts lower conversion efficiencies compared to the dual-bed suggesting that the SCR functionality of the top layer is not as efficient as in the case of the separate downstream brick.

A close comparison of the simulation results of Fig. 13.24 clearly shows that the dual-bed LNT-SCR configuration is superior in terms of de-NO_x efficiency compared to single-bed systems. This means that the cost and volume advantages of a single-bed system cannot be exploited without some drawbacks in the performance. At the low temperature/low GHSV regime, the addition of the SCR catalyst both in the form of an additional catalyst bed or overlying washcoat layer can significantly increase the overall de-NO_x performance. However, the simulation at 300 °C and at a GHSV of 50,000 h⁻¹ shows that dual-layer system does not increase the overall de-NO_x efficiency—in fact the overall performance is slightly worse by about 3 % compared to the single-bed LNT catalyst. This suggests that the benefit of the SCR layer is counterbalanced by the additional diffusion resistance due to the thicker washcoat layer.

13.7.3 Combined SCR-ASC Concept

The challenge for the NH₃-SCR systems is to maximize the NO_x conversion efficiency by keeping at the same time the NH₃ release to a minimum. However, under certain conditions an increase of the de-NO_x performance can only be achieved by increasing the reductant quantity and consequently allowing higher NH₃ slip. In order to minimize the released NH₃, the addition of an ammonia slip catalyst ASC (also referenced as ammonia oxidation catalyst AOC) downstream the SCR is considered as an efficient and reliable solution.

Colombo et al. [56] analyzed the performance of three different NH₃ slip catalyst configurations in terms of NH₃ conversion and products selectivity. The studied systems include a single-layered PGM monolith, a single-layered SCR + PGM (noted by the authors as “mechanical mixture”) and a dual-layered SCR + PGM system (SCR layer on top). Simulation results in terms of NH₃ concentration during a steady temperature increase are shown in Fig. 13.25. The dual-layered SCR + PGM system involves the addition of NH₃ oxidation functionality to the rear part of the SCR by combining a platinum-based lower layer and an SCR layer placed on top. The PGM catalysts are extremely active in the NH₃ oxidation even at low temperatures, with NH₃ oxidation products including NO_x and N₂O besides N₂. With the introduction of an SCR layer on top of the PGM one, the unselective NO_x products diffuse back in the SCR layer to react with NH₃ and to give N₂. The combination of PGM and SCR chemistries greatly enhances the selectivity toward N₂. While the upper placed SCR layer improves the selectivity, it also acts as a diffusive barrier decreasing the NH₃ conversion efficiency. This is depicted by the higher simulated NH₃ concentration for the dual-layered SCR + PGM system compared to the single-layered PGM monolith. On the contrary, the single-layered SCR + PGM catalyst, while still taking advantage of the positive interaction between PGM and SCR chemistries, achieves equivalent NH₃ conversion efficiencies as the single PGM catalyst.

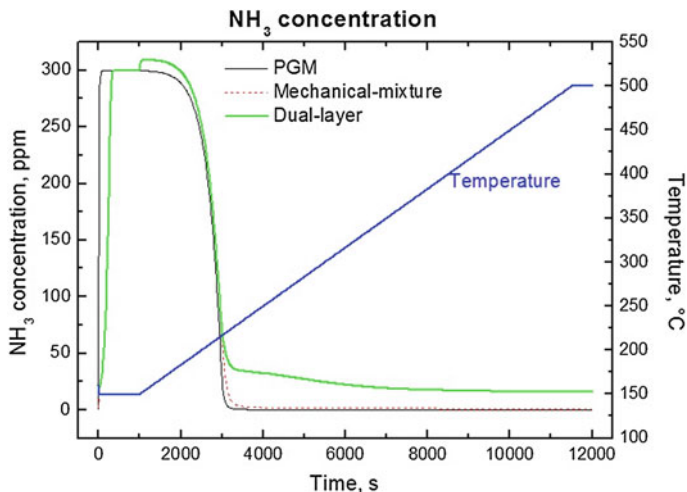


Fig. 13.25 NH_3 concentration during a simulated T-ramp at 2 K/min over different monolith catalysts. Inlet conditions: $\text{NH}_3 = 300$ ppm, $\text{H}_2\text{O} = 5\%$ v/v; $\text{O}_2 = 6\%$ v/v; GHSV = 100,000 h^{-1}

13.8 Conclusion: Perspectives

Given the high NO_x conversion efficiency requirements and the cost issues associated with advanced exhaust aftertreatment development, the need for computer-aided approaches is nowadays established. The modeling of SCR converters has been based on earlier developments in the area of gasoline and diesel exhaust aftertreatment based on flow-through and wall-flow monolithic devices.

In this work, we discussed the fundamental equations describing the transient heat and mass transfer phenomena at the device scale. These equations have been established on reasonable approximations that have proven their validity in real-world applications. As with other aftertreatment applications, the main modeling challenges lie in the formulation of reaction schemes and respective rate expressions that realistically describe the heterogeneous processes on the active catalyst sites. Given the multiplicity of available catalyst technologies and the need for modeling at various catalyst aging states, the reaction models should be simple enough to be parameterized with reasonable efforts.

Current research efforts are indeed focusing on deeper understanding of the surface processes involved in SCR chemistry, especially in the environment of real diesel exhaust containing a multitude of species that could potentially interact in the main reaction paths. As the SCR technology is expanding from heavy-duty to the light-duty sector, cold-start issues and modeling of phenomena at temperatures below 200 °C are becoming of major interest. This includes more advanced models of NH_3 adsorption and desorption, interactions with water as well as nitrate formation mechanisms.

The effect of internal diffusion within the active material is expected to receive further attention from the modeling community, as the pressure to find best compromises among flow resistance, active material, and reactor volume will keep increasing. In this respect, extruded catalyst technologies compete with traditional coated substrates or even with high porosity impregnated substrates. Accurate modeling of the diffusional processes in the above technologies shall rely on deep understanding and characterization of effective diffusivities and proper level of modeling detail.

The combined SCR-DPF technology will definitely be a technological and modeling challenge. The commercial success of the technology could be supported by simulation-driven optimization approaches. The combination of SCR and ammonia slip catalysts, especially in the case of multilayered technologies is another example of advanced engineering solutions where modeling is expected to play a key role.

Last but not least, the reactor-level modeling is expected to further interact with 3D flow modeling in the exhaust system, especially with respect to flow homogeneity. State-of-the-art 3D CFD exhaust system models are able to provide useful conclusions on the flow and NH_3 uniformity at steady-state operating modes. However, the computational effort required for transient cycle calculations remains formidable even with supercomputers. Coupling of 3D flow calculations with transient reactor models remains one of the main challenges for exhaust system modelers in the coming years.

List of symbols

A. Latin letters

a_1	Constant in channel pressure drop correlation	–
A_{ze}	Pore size distribution constant	$(\text{mol/J})^2$
c	Concentration	mol/m^3
C_p	Specific heat capacity	$\text{J}/(\text{kg} \cdot \text{K})$
d_h	Hydraulic diameter of a channel	m
D_{knud}	Knudsen diffusivity	m^2/s
D_{mol}	Molecular diffusivity	m^2/s
d_{pore}	Mean pore size	m
D_w	Effective diffusivity	m^2/s
E	Activation energy of reaction	J/mol
f_w	Geometric parameter	–
h	Heat transfer coefficient	$\text{W}/\text{m}^2 \cdot \text{K}$
H	Heat source component	W/m^3
k	Kinetic constant of reaction	units depend on reaction
k_j	Mass transfer coefficient	m/s
M	Molecular weight	kg/mol
n	Stoichiometric coefficient	–

(continued)

(continued)

p_j	Partial pressure	Pa
$p_{\text{sat},j}$	Saturation pressure	Pa
R	Universal gas constant	J/(mol · K)
r	Radial coordinate	–
R_j	Reaction rate	mol/(m ³ · s)
S	Heat source term	W/m ³
S_F	Monolith specific surface area	m ² /m ³
T	Temperature	K
t	Time	s
v	Velocity	m/s
w	Dimension perpendicular to wall surface	–
W_0	Total volume of micropores per reactor volume	m ³ /m ³
w_c	Washcoat layer thickness	m
w_p	Soot layer thickness	m
w_w	Wall thickness	m
x_{eq}	Adsorbed mass at equilibrium	kg
y_j	Molar fraction	–
z	Axial coordinate along monolith	m
<i>B. Greek letters</i>		
β	Reaction order with regard to O ₂	–
β_j	Affinity coefficient	–
γ	Surface coverage dependence factor	–
ΔH	Reaction heat	J/mol
ε	Macroscopic void fraction	–
$\varepsilon_{\text{pore}}$	Porosity of the washcoat	–
θ_{NH_3}	Surface coverage of NH ₃	–
λ	Thermal conductivity	W/m · K
μ	Dynamic viscosity	Pa · s
ρ	Density	kg/m ³
τ	Tortuosity	–
<i>C. Subscripts and Superscripts</i>		
g	Exhaust gas	
j	Species index	
k	Reaction index	
s	Solid	
w	Substrate wall	
<i>D. Abbreviations</i>		
ads	Adsorption	
ANR	Ammonia to NO _x ratio	
AOC	Ammonia oxidation catalyst	
ASC	Ammonia slip catalyst	
de-NO _x	Abatement of nitrogen oxides	
des	Desorption	
DOC	Diesel oxidation catalyst	

(continued)

(continued)

DPF	Diesel particulate filter
LNT	Lean NO _x trap
NO _x	Nitrogen oxides, NO and NO ₂ only
NSRC	NO _x storage and reduction catalyst
PGM	Platinum group metals
SCR	Selective catalytic reduction of NO _x
SCRF [®]	DPF with integrated SCR capability (equivalent to WSCR, SCRof, and SDPF)

References

1. Koltsakis GC, Stamatelos AM (1997) Catalytic Automotive Exhaust Aftertreatment. *Progress in Energy and Combustion Science* 23:1–39
2. Vardi J, Biller WF (1968) Thermal Behavior of Exhaust Gas Catalytic Converter. *Industrial & Engineering Chemistry Process Design and Development* 7:83–90
3. Kuo JC, Morgan CR, Lassen HG (1971) Mathematical Modeling of CO and HC Catalytic Converter Systems. SAE paper 710289
4. Harned JL (1972) Analytical Evaluation of a Catalytic Converter System. SAE paper 720520
5. Oh SH, Cavendish JC (1982) Transients of monolithic catalytic converters: response to step changes in feedstream temperature as related to controlling automobile emissions. *Industrial & Engineering Chemistry Research* 37:21–29
6. Pattas KN, Stamatelos AM, Pistikopoulos PK, Koltsakis GC, Konstantinidis PA, Volpi E, Leveroni E (1994) Transient Modeling of 3-Way Catalytic Converters. *Journal of Fuels and Lubricants* 103:565–578
7. Stamatelos AM, Koltsakis GC, Kandyilas IP, Pontikakis GN (1999) Computer aided engineering in diesel exhaust aftertreatment systems design. *Proceedings of the Institution of Mechanical Engineers, Journal of Automobile Engineering* 213:545–560
8. Pontikakis GN, Koltsakis GC, Stamatelos AM, Noirot R, Agliany Y, Colas H, Versaevl P, Bourgeois C (2001) Experimental and modeling study on zeolite catalysts for diesel engines. *Topics in Catalysis* 16/17:329–335
9. Sampara CS, Bissett EJ, Chmielewski M, Assanis D (2007) Global Kinetics for Platinum Diesel Oxidation Catalysts. *Industrial & Engineering Chemistry Research* 46:7993–8003
10. Lafossas F, Matsuda Y, Mohammadi A, Morishima A, Inoue M, Kalogirou M, Koltsakis G, Samaras Z (2011) Calibration and Validation of a Diesel Oxidation Catalyst Model: from Synthetic Gas Testing to Driving Cycle Applications. SAE paper 2011-01-1244
11. Chatterjee D, Burkhardt T, Bandl-Konrad B, Tillmann B, Tronconi E, Nova I, Ciardelli C (2005) Numerical Simulation of Ammonia SCR-Catalytic Converters: Model Development and Application.
12. Koltsakis GC, Konstantinidis PA, Stamatelos AM (1997) Development and application range of mathematical models for 3-way catalytic converters. *Applied Catalysis B: Environmental* 12:161–191
13. Chen D, Bissett E, Oh S, Van Ostrom D (1988) A Three-Dimensional Model for the Analysis of Transient Thermal and Conversion Characteristics of Monolithic Catalytic Converters. SAE paper 880282
14. Santos H, Costa M (2008) The relative importance of external and internal transport phenomena in three way catalysts. *International Journal of Heat and Mass Transfer* 51:1409–1422
15. Hawthorn RD (1974) Afterburner catalysts: effects of heat and mass transfer between gas and catalyst surface. *AIChE Symposium Series* 70:428–438

16. West DH, Balakotaiah V, Jovanovic Z (2003) Experimental and theoretical investigation of the mass transfer controlled regime in catalytic monoliths. *Catalysis Today* 88:3–16
17. Ramanathan K, Balakotaiah V, West DH (2003) Light-off criterion and transient analysis of catalytic monoliths. *Chemical Engineering Science* 58:1381–1405
18. Wheeler A (1955). *Catalysis*, p 105
19. Wakao N, Smith JM (1962) Diffusion in catalyst pellets. *Chemical Engineering Science* 17:825
20. Novák V, Kočí P, Marek M, Stepánek F, Blanco-García P, Jones G (2012) Multi-scale modelling and measurements of diffusion through porous catalytic coatings: An application to exhaust gas oxidation. *Catalysis Today* 188:62–69
21. Malmberg S, Votsmeier M, Gieshoff J, Söger N, Mußmann L, Schuler A, Drochner A (2007) Dynamic phenomena of SCR-catalysts containing Fe-exchanged zeolites - experiments and computer simulations. *Topics in Catalysis* (42-43):33–36
22. Skarlis S, Berthout D, Nicolle A, Dujardin C, Granger P (2012) Modeling NH₃ storage over Fe- and Cu-zeolite based, Urea-SCR catalysts for mobile diesel engines. *Social and Behavioral Sciences* 48:1672–1682
23. Colombo M, Koltsakis G, Nova I, Tronconi E (2011) Modelling the ammonia adsorption-desorption process over an Fe-zeolite catalyst for SCR automotive applications. *Catalysis Today*. doi:10.1016/j.cattod.2011.09.002
24. Lietti L, Nova I, Camurri S, Tronconi E, Forzatti P (1997) Dynamics of the SCR-DeNO_x Reaction by the Transient-Response Method. *AIChE Journal* 43
25. Borade RB, Adnot A, Kaliaguine S (1991) Acid sites in Al-ZSM-22 and Fe-ZSM-22. *Zeolites* 11:710–719
26. Rodríguez-González L, Hermes F, Bertmer M, Rodríguez-Castellón E, Jiménez-López A, Simon U (2007) The acid properties of H-ZSM-5 as studied by NH₃-TPD and ²⁷Al-MAS-NMR spectroscopy. *Applied Catalysis A: General* 328:174–182
27. Sjövall H, Blint RJ, Gopinath A, Olsson L (2010) A Kinetic Model for the Selective Catalytic Reduction of NO_x with NH₃ over an Fe-zeolite Catalyst. *Industrial & Engineering Chemistry Research* 49:39–52
28. Thomas JM, Thomas WJ (1997) *Principles and Practices of Heterogeneous Catalysis*. VCH editions,
29. Tronconi E, Nova I, Ciardelli C, Chatterjee D, Bendl-Konrad B, Burkhardt T (2005) Modelling of an SCR catalytic converter for diesel exhaust after treatment: dynamic effects at low temperature. *Catalysis Today* 105:529–536
30. Chatterjee D, Burkhardt T, Weibel M, Nova I, Grossale A, Tronconi E (2007) Numerical Simulation of Zeolite- and V-Based SCR Catalytic Converters. SAE paper 2007-01-1136
31. Schuler A, Votsmeier M, Kiwic P, Gieshoff J, Hauptmann W, Drochner A, Vogel H (2009) NH₃-SCR on Fe zeolite catalysts - From model setup to NH₃ dosing. *Chemical Engineering Journal* 154:333–340
32. Olsson L, Sjövall H, Blint RJ (2008) A kinetic model for ammonia selective catalytic reduction over Cu-ZSM-5. *Applied Catalysis B: Environmental* 81:203–217
33. Grossale A, Nova I, Tronconi E (2008) Study of a Fe-zeolite-based system as NH₃-SCR catalyst for diesel exhaust aftertreatment. *Catalysis Today* 136:18–27
34. Kamasamudram K, Currier NW, Chen X, Yezerets A (2010) Overview of the practically important behaviors of zeolite-based urea-SCR catalysts, using compact experimental protocol. *Catalysis Today* 151:212–222
35. Watling TC, Tutuianu M, Desai MR, Dai J, Markatou P, Johansson A (2011) Development and Validation of a Cu-Zeolite SCR Catalyst Model. SAE paper 2011-01-1299
36. Ciardelli C, Nova I, Tronconi E, Chatterjee D, Bendl-Konrad B, Weibel M, Krutzsch B (2007) Reactivity of NO/NO₂-NH₃ SCR system for diesel exhaust aftertreatment: Identification of the reaction network as a function of temperature and NO₂ feed content. *Applied Catalysis B: Environmental* 70 (1–4):80–90

37. Koebel M, Elsener M, Madia G (2001) Reaction Pathways in the Selective Catalytic Reduction Process with NO and NO₂ at Low Temperatures. *Industrial & Engineering Chemistry Research* 40:52–59
38. Madia G, Koebel M, Elsener M, Wokaun A (2002) Side Reactions in the Selective Catalytic Reduction of NO_x with Various NO₂ Fractions. *Industrial & Engineering Chemistry Research* 41:4008–4015
39. Sharifian L, Wright YM, Boulouchos K, Elsener M, Kröcher O (2010) Simulation of NO_x Reduction in an Ammonia-SCR System with an Fe-Zeolite Catalyst and Calibration of Related Parameters. ASME Conference Publications
40. Metkar P, Balakotaiah V, Harold M (2011) Experimental study of mass transfer limitations in Fe- and Cu-zeolite-based NH₃-SCR monolithic catalysts. *Chemical Engineering Science* 66:5192–5203
41. Güthenke A, Chatterjee D, Weibel M, Krutzsch B, Kočí P, Marek M, Nova I, Tronconi E (2008) Current status of modeling lean exhaust gas aftertreatment catalysts. *Advances in Chemical Engineering* 33:103–211
42. Bissett EJ (1984) Mathematical Model of the Thermal Regeneration of a Wall-Flow Monolith Diesel Particulate Filter. *Chemical Engineering Science* 39:1233–1244
43. Konstandopoulos AG, Johnson JH (1989) Wall-flow Diesel Particulate Filters - Their Pressure Drop and Collection Efficiency. SAE paper 890405
44. Konstandopoulos AG, Skaperdas E, Papaioannou E, Zarvalis D, Kladopoulou E (2000) Fundamental Studies of Diesel Particulate Filters: Transient Loading, Regeneration and Aging. SAE paper 2000-01-1016
45. Koltsakis GC, Stamatelos AM (1997) Modes of catalytic regeneration in diesel particulate filters. *Industrial and Engineering Chemistry Research* 36:4155-4165
46. Kalogirou M, Katsaounis D, Koltsakis G, Samaras Z (2007) Measurements of diesel soot oxidation kinetics in an isothermal flow reactor-catalytic effects using Pt based coatings. *Topics in Catalysis* 42-43:247–251
47. Kandylas I, Haralampous O, Koltsakis G (2002) Diesel Soot Oxidation with NO₂: Engine Experiments and Simulations. *Industrial & Engineering Chemistry Research* 41:5372–5384
48. Colombo M, Koltsakis G, Koutoufaris I (2011) A modeling study of soot and de-NO_x reaction phenomena in SCR systems. SAE paper 2011-37-0031
49. Iwasaki M, Shinjoh H (2010) A comparative study of “standard”, “fast” and “NO₂” SCR reactions over Fe/zeolite catalyst. *Applied Catalysis A: General* 390:71–77
50. Watling TC, Ravenscroft MR, Avery G (2012) Development, validation and application of a model for an SCR catalyst coated diesel particulate filter. *Catalysis Today* 188:32–41
51. Tsinoglou DN, Haralampous OA, Koltsakis GC, Samaras ZC (2007) Model-based optimization methods of combined DPF + SCR systems. SAE paper 2007-24-0098
52. Chatterjee D, Burkhardt T, Rappe T, Güthenke A, Weibel M (2008) Numerical Simulation of DOC + DPF + SCR Systems: DOC Influence on SCR Performance. SAE paper 2008-01-0867
53. Koltsakis G, Koutoufaris I, Haralampous O, Tournalias P, Krämer L (2007) Model-based design of combined DPF-SCR systems for passenger cars. Paper presented at the FAD conference 2007
54. Chatterjee D, Kočí P, Schmeißer V, Marek M, Weibel M, Krutzsch B (2010) Modelling of a combined NO_x storage and NH₃-SCR catalytic system for Diesel exhaust gas aftertreatment. *Catalysis Today* 151:395-409
55. Koltsakis GC, Haralampous OA, Koutoufaris IZ (2010) Applications of Multi-layer Catalyst Modeling in deNO_x and DPF Systems. SAE paper 2010-01-0893
56. Colombo M, Nova I, Tronconi E, Koltsakis G (2012) A Modeling Study of NH₃ Slip Catalysts: Analysis of the SCR/PGM Interactions. *Topics in Catalysis*. doi:10.1007/s11244-013-9948-x

Chapter 14

Diesel Engine SCR Systems: Modeling, Measurements, and Control

Ming-Feng Hsieh and Junmin Wang

14.1 Introduction

Selective catalytic reduction (SCR) systems have been successfully employed in industries for many decades. In recent years, its application scope on mobile vehicles has been significantly expanded due to the increasingly stringent emission regulations on Diesel engine powered vehicles worldwide. Comparing to the stationary applications (e.g., NO_x reduction for power generation systems), mobile vehicle SCR systems present significant control challenges primarily due to the highly transient vehicle engine operations and thus the unpredictable engine-out emissions. Estimation and control of mobile vehicle SCR systems are the foci of this chapter.

Practical challenges on vehicle SCR system control mainly arise from the following aspects. First of all, the dynamics of many chemical reactions occurring within a urea-SCR together with the engine-out emissions and environmental variations create a nonlinear and complex plant for SCR urea dosing controller designs. In addition, many of the critical states within the SCR catalysts are hard to be directly measured on mobile vehicles due to the accessibility and cost constraints. For example, the amount of ammonia adsorbed by a catalyst, i.e., the NO_x reduction reductant, is difficult to be directly measured. Moreover, current vehicle NO_x sensors are cross-sensitive to ammonia, which causes issues on the tailpipe NO_x measurement. The inaccurate NO_x measurement not only affects the urea injection control but also the onboard diagnostics (OBD) which has been required by governmental regulations. Ammonia sensors are possible to be utilized as alternatives for providing feedback signals. But OBD systems need to correct the

M.-F. Hsieh
Cummins Inc., Columbus, IN 47201, USA

J. Wang (✉)
Department of Mechanical and Aerospace Engineering, The Ohio State University,
Columbus, OH 43210, USA
e-mail: wang.1381@osu.edu

tailpipe NO_x concentration measurement to ensure the performance and emission reduction of the aftertreatment systems. Due to these aforementioned practical issues, systematic model-based SCR urea dosing control has been a great challenge. In this chapter, SCR control-oriented modeling is introduced in the first section to explain the basic system dynamics and characteristics. After that, some sensing and estimating systems for SCR catalysts are presented. Difficulties of current sensing systems and possible solutions are explained. At the end, SCR catalyst control systems and methods are discussed. An SCR ammonia storage distribution control method that can effectively reduce the SCR-outlet NO_x and NH_3 emissions is introduced.

14.2 SCR Control-Oriented Modeling

14.2.1 Introduction

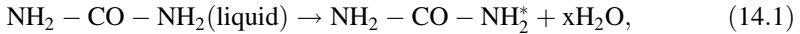
While the dynamics of chemical reactions occurring within an SCR catalyst are quite complex, lumped-parameter 0-D mathematic models that can describe the essential SCR dynamics are preferred and often necessary for systematic real-time estimation and control system design purposes. The main challenge associated with the SCR catalyst control-oriented model development is to describe the SCR dynamics in a mathematically tractable way grounded in the in-depth understanding of the chemical reactions. Several studies that focused on the discoveries of fundamental SCR reactions using laboratory setups have been reported [1–9]. These studies offer insightful understandings to the chemical reaction mechanisms and the spatiotemporal distributions of species concentrations and temperature within the SCR catalysts. Accurately modeling the chemical reactions and fluid dynamics inside a catalyst requires the use of partial differential equations, which are computationally expensive and hard to be employed for real-time controller designs. Model reduction and valid assumptions need to be made in order to develop control-oriented SCR models. Several SCR models for the purposes of controller designs have been proposed recently, e.g., [10–13]. The following subsection introduces the basic approaches of developing SCR control-oriented models and the main assumptions made for such control-oriented models.

14.2.2 Main SCR Reactions

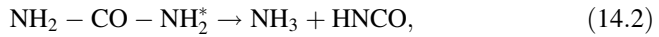
The SCR NO_x reduction process can be summarized by three major steps. In the first step, urea solution (AdBlue), as the source of the reductant (NH_3), is injected at the upstream of the catalyst and then is converted to NH_3 . In the second step, the NH_3 inside the catalyst is adsorbed on the catalyst substrate. The adsorbed NH_3

can then catalytically react with NO_x and convert them to nitrogen molecules and water, which is the third step. The key reactions of these processes are explained by the equations below:

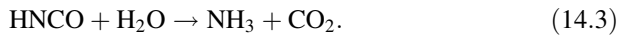
AdBlue (32.5 % aqueous urea solution (AdBlue)) evaporation:



Urea decomposition:



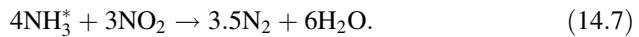
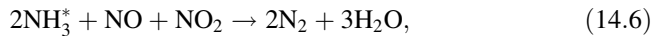
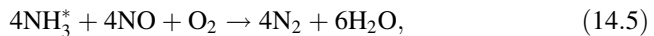
Isocyanic acid (HNCO) hydrolyzation:



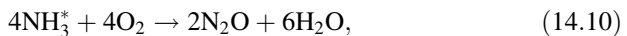
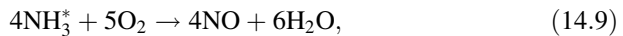
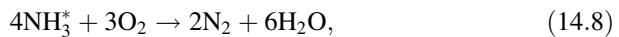
NH_3 Adsorption/Desorption:



NO_x Conversion:



Ammonia Oxidation and NO Oxidation:

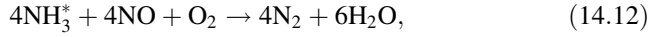


14.2.3 Control-Oriented SCR Model

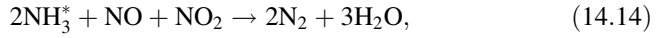
The main reactions to be considered in the SCR control-oriented model are reactions of Eqs. (14.4), (14.5), (14.6), (14.8), and (14.11). Reactions which are ignored are the “slow SCR” in Eq. (14.7), ammonia oxidation to NO in Eq. (14.9), ammonia oxidation to N_2O in Eq. (14.10), and the AdBlue to ammonia reactions of Eqs. (14.1), (14.2), and (14.3). Because the “fast SCR” is comparably much faster and most NO_2 can be converted by this process, the NO_x after the upstream SCR catalyst is mostly NO. Consequently, the “slow SCR” in Eq. (14.7) is assumed to be a minor reaction. For ammonia oxidation, it has been reported that most of the SCR catalysts used on vehicles are 100 % selective toward N_2 [14],

and the oxidation reactions toward other species are all ignored. Besides, from the observations of ammonia measurements before the upstream SCR catalyst in [11]; it is believed that AdBlue can be completely converted to ammonia at the very upstream part of the SCR if the catalyst is well designed as well as the temperature and gas space velocity are sufficiently high. The AdBlue to ammonia conversion is thus assumed to be 100 % before entering the SCR catalyst.

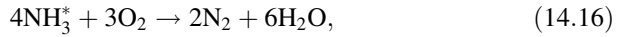
The reaction rates of the processes being considered are modeled by Arrhenius equations. The reaction rate models are presented below:



$$R_1 = K_1 e^{-\frac{E_1}{RT}} C_{\text{NO}} C_{\text{O}_2} \theta \Theta V^2, \quad (14.13)$$



$$R_2 = K_2 e^{-\frac{E_2}{RT}} C_{\text{NO}} C_{\text{NO}_2} \theta \Theta V^2, \quad (14.15)$$



$$R_3 = K_3 e^{-\frac{E_3}{RT}} C_{\text{O}_2} \theta \Theta V, \quad (14.17)$$



$$\text{forward: } R_{4F} = K_{4F} e^{-\frac{E_{4F}}{RT}} C_{\text{NH}_3} (1 - \theta) \Theta V, \quad (14.19)$$

$$\text{reverse: } R_{4R} = K_{4R} e^{-\frac{E_{4R}}{RT}} \theta \Theta, \quad (14.20)$$



$$R_5 = K_5 e^{-\frac{E_5}{RT}} C_{\text{NO}} C_{\text{O}_2} V^2, \quad (14.22)$$

where R_i are the reaction rates (mole/sec/m³), T is temperature, C_x represents mole concentration of species x (mole/m³), E_i (joule) and K_i (unit depends on the elements in the reaction rate Arrhenius model) are the activation energy and rate constant of Arrhenius reaction model, V is the catalyst volume (m³), δ is the ammonia desorption efficiency, and θ is the ammonia coverage ratio defined as $\theta = M_{\text{NH}_3^*} / \Theta$. $M_{\text{NH}_3^*}$ represents the mole number of ammonia adsorbed by the SCR catalyst and Θ is the ammonia storage capacity of the catalyst (mole), which varies with temperature [3, 15, 16] and is modeled by the following equation:

$$\Theta = S_1 e^{-S_2 T}, \quad (14.23)$$

where S_1 and S_2 , are positive constants. Note that the ammonia storage capacity can be significantly changed in an aged SCR system. The storage parameters (S_1 and S_2) need to be updated to capture the effect of catalyst aging. Another approach is to use an estimator to estimate the ammonia storage capacity variation

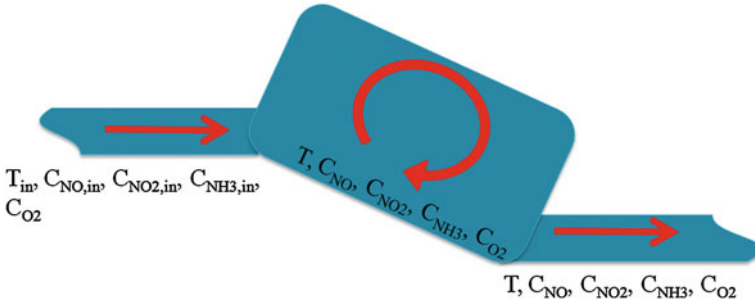


Fig. 14.1 CSTR model of SCR catalyst [54]

and update the model intermittently. An ammonia storage variation estimation approach based on Extended Kalman Filter (EKF) is available in [17].

To avoid partial differential equations in the control-oriented model, the SCR catalyst is assumed to be a continuous stirred tank reactor (CSTR), as shown in Fig. 14.1, for developing a 0-D model [12]. Under this CSTR assumption, the states are considered homogenous within the catalyst. Based on the CSTR assumption and the mass conservation law, the dynamic equations of the considered states in a single SCR catalyst can be expressed below.

$$V\dot{C}_{\text{NO}} = FC_{\text{NO},\text{in}} - R_1 - 0.5R_2 - R_5 - FC_{\text{NO}}, \quad (14.24)$$

$$V\dot{C}_{\text{NO}_2} = FC_{\text{NO}_2,\text{in}} - 0.5R_2 - R_5 - FC_{\text{NO}_2}, \quad (14.25)$$

$$V\dot{C}_{\text{NH}_3} = FC_{\text{NH}_3,\text{in}} - R_{4F} + R_{4R} - FC_{\text{NH}_3}, \quad (14.26)$$

$$\dot{M}_{\text{NH}_3} = R_{4F} - R_{4R} - R_1 - R_2 - R_3, \quad (14.27)$$

where F is the exhaust flow rate into the catalyst, and it is assumed equal to the catalyst outlet flow rate, and $C_{x,\text{in}}$ represent the species concentrations at the upstream of the catalyst. Practically, $C_{\text{NO},\text{in}}$ and $C_{\text{NO}_2,\text{in}}$ cannot be directly measured because the current onboard NO_x sensors cannot differentiate NO and NO_2 from NO_x . To address this problem, an observer needs to be designed to estimate $C_{\text{NO},\text{in}}$ and $C_{\text{NO}_2,\text{in}}$. An example on how to design such an observer can be found in [18]. $C_{\text{NH}_3,\text{in}}$, on the other hand, can be predicted by the AdBlue injection rate and is modeled by the following equation:

$$\dot{C}_{\text{NH}_3,\text{in}} = -\alpha C_{\text{NH}_3,\text{in}} + 2\alpha \frac{\tau u_{\text{AdBlue}}}{N_{\text{urea}} F}, \quad (14.28)$$

where α is a time-constant, τ is the mass fraction of urea in the AdBlue solution, N_{urea} is the atomic number of urea, and u_{AdBlue} is the mass injection rate of AdBlue upstream of the SCR system. The above SCR dynamic equations can then be rearranged into a state-space form as shown in Eq. (14.29).

$$\begin{bmatrix} \dot{C}_{\text{NO}} \\ \dot{C}_{\text{NO}_2} \\ \dot{C}_{\text{NH}_3} \\ \dot{\theta}_{\text{NH}_3} \\ \dot{C}_{\text{NH}_3,\text{in}} \end{bmatrix} = \begin{bmatrix} -r_1 C_{\text{NO}} C_{\text{O}_2} \theta_{\text{NH}_3} \Theta V - \frac{1}{2} r_2 C_{\text{NO}} C_{\text{NO}_2} \theta_{\text{NH}_3} \Theta V - r_5 C_{\text{NO}} C_{\text{O}_2} V - \frac{F}{V} C_{\text{NO}} + \frac{F}{V} C_{\text{NO},\text{in}} \\ -\frac{1}{2} r_2 C_{\text{NO}} C_{\text{NO}_2} \theta_{\text{NH}_3} \Theta V + r_5 C_{\text{NO}} C_{\text{O}_2} V - \frac{F}{V} C_{\text{NO}_2} + \frac{F}{V} C_{\text{NO}_2,\text{in}} \\ -C_{\text{NH}_3} \left[\Theta r_{4F} (1 - \theta_{\text{NH}_3}) + \frac{F}{V} \right] + \frac{1}{V} r_{4R} \Theta \theta_{\text{NH}_3} + \frac{F}{V} C_{\text{NH}_3,\text{in}} \\ -\theta_{\text{NH}_3} (r_{4F} C_{\text{NH}_3} V + r_3 C_{\text{O}_2} V + r_{4R} + r_1 C_{\text{NO}} C_{\text{O}_2} V^2 + r_2 C_{\text{NO}} C_{\text{NO}_2} V^2) + r_{4F} C_{\text{NH}_3} V \\ -\alpha C_{\text{NH}_3,\text{in}} + 2\alpha C_{\text{AdBlue},\text{inj}} \end{bmatrix}, \quad (14.29)$$

$$r_i = K_i e^{-\frac{E_i}{RT}}, i = 1, 2, 3, 4F, 4R, 5. \quad (14.30)$$

Parameters of the model are strenuous to be calibrated due to the high number of parameters and the complexity of the chemical reactions. One way to calibrate the model effectively is to use the Genetic Algorithm (GA) to optimize the model parameters such that the model predictions best match with the calibration measurement data. GA has been known of optimizing complex and nonconvex equations. This feature makes it a good candidate to calibrate the SCR model. Detailed explanation of how to use GA to calibration the model and a calibration example is available in [11].

Notice that the model in Eq. (14.29) is to capture the main dynamics of a nominal SCR system. This dynamics can change as catalyst ages, but the main structure of the model should remain the same. Parameters of the chemical reaction rates and catalyst ammonia storage in the model should be updated if an aged system is to be considered. Because different catalyst formulations can have very different aging behaviors, it is not easy to have a general model to simulate the catalyst aging effects. A straightforward approach of capturing the catalyst aging behaviors would be to recalibrate the model for an aged catalyst, and then interpolate the characteristics between a fresh and an aged system to describe the aging process.

14.3 SCR Sensing and Estimation Systems

According to the SCR control-oriented model shown in Eq. (14.29), the key states of an SCR catalyst are: SCR inlet $\text{NO}_{(x)}$ concentration, SCR inlet NH_3 concentration, exhaust flow rate, SCR catalyst temperature, SCR-outlet NO_x concentration, SCR-outlet NH_3 concentration, and SCR catalyst ammonia coverage ratio. Current vehicle onboard sensors are capable of measuring gas flow rate, temperature, NO_x concentration, and NH_3 concentration. However, the current production NO_x sensors are cross-sensitive to NH_3 , which make the accurate measurement of SCR-outlet NO_x concentration difficult. Without the information of SCR-outlet NO_x concentration, closed-loop SCR control is difficult, and so is the diagnostics of SCR NO_x reduction capability. Moreover, the catalyst ammonia coverage ratio (θ_{NH_3}) is also hard to be directly measured. Ammonia coverage ratio is an inherent state in the SCR catalyst which directly affects the catalytic reactions. This state is

important for SCR urea real-time dosing control applications since it couples the tailpipe NO_x and NH_3 dynamics.

NO_x sensor ammonia cross-sensitivity and SCR catalyst ammonia coverage ratio have been the main challenges of the SCR sensing systems. The rest of this subsection provides some insight into these two problems and introduces some current solutions.

14.3.1 NO_x Sensor NH_3 Cross-Sensitivity

Figures 14.2, 14.3, and 14.4 show the test results of the NO_x sensor ammonia cross-sensitivity based on the SCR system depicted in Figs. 14.16 and 14.17. The measurements of the NO_x sensor between the two SCR catalysts together with the readings of a Horiba gas analyzer, the ammonia sensor, and the thermocouple are located at the same region. Different engine operating conditions and AdBlue injection rates were examined. In Fig. 14.2, the engine speed and accelerator pedal position were maintained at 1700 RPM and 27 %, and AdBlue injection started at the twentieth second with 0.15 g/s injecting rate in constant until the eight hundredth second. In the test of Fig. 14.3, these values were set to 1000 RPM, 18 %, and 0.1 g/s, respectively. The test presented in Fig. 14.4 consists of transient speed and accelerator pedal position profiles as shown in Fig. 14.5, and the AdBlue injection rate was kept at 0.1 g/s.

Assuming the NO_x sensor is only cross-sensitive to ammonia and the Horiba gas analyzer readings are the actual exhaust gas NO_x concentrations, based on these data and the NO_x sensor ammonia cross-sensitivity model in Eq. (14.31), it can be clearly observed that the cross-sensitivity K_{cs} is different in these tests and also changes with time. By the preliminary examinations of the data, it can be seen that the cross-sensitivity in the test of Fig. 14.2 was about 2, and was decreased to 0.5 in the test of Fig. 14.3. Furthermore, the value in the test of Fig. 14.4 was changing with time. In the light of these observations, it can be concluded that the NO_x sensor ammonia cross-sensitivity is dynamic and cannot be simply treated as a constant for estimating the actual NO_x concentration in exhaust gas.

$$C_{\text{NO}_x, \text{sen}} = C_{\text{NO}_x}^* + K_{cs} C_{\text{NH}_3}, \quad (14.31)$$

14.3.1.1 EKF Approach for NO_x Sensor Reading Correction

The challenge of estimating the NO_x sensor ammonia cross-sensitivity factor lies in the fact that a dynamic model is hard to be developed. For the SCR-out NO_x concentration estimation, it is possible to employ an accurate SCR model with a NO_x sensor upstream of the SCR catalyst and the amount of AdBlue injection. However, such prediction requires a high-accuracy SCR model, which is

Fig. 14.2 Engine speed 1700 RPM, accelerator pedal 27 %, AdBlue injection 0.15 g/s between 20 and 800 s [26]

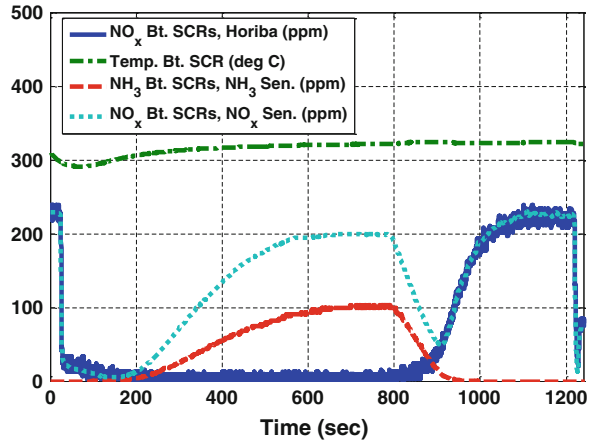


Fig. 14.3 Engine speed 1000 RPM, gas pedal 18 %, AdBlue injection 0.1 g/s between 20 and 2400 s [26]

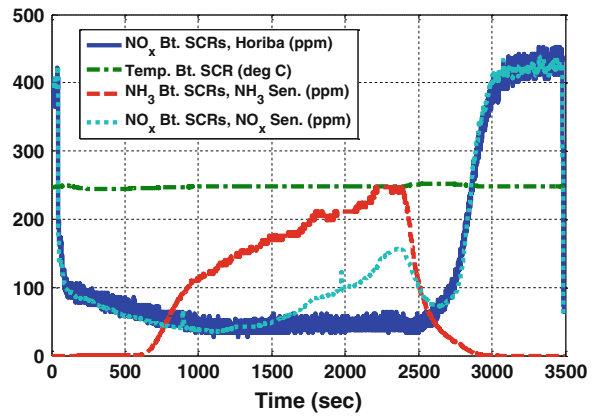


Fig. 14.4 Transient test, AdBlue injection 0.15 g/s [26]

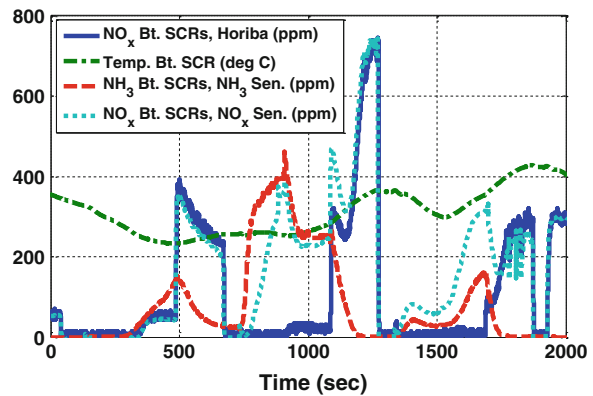
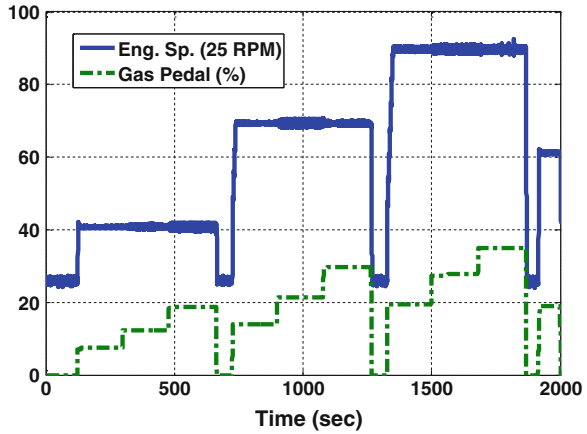


Fig. 14.5 Engine speed and accelerator pedal profiles of the test in Fig. 4 [26]



challenging to be implemented on a mobile vehicle onboard controller because of the limited computational capability. To address the above problems, a possible solution is to use an extended Kalman filter (EKF) to estimate the NO_x sensor ammonia cross-sensitivity factor and the actual NO_x concentration at the same time [19].

Kalman filter is well known as an efficient recursive filter that can optimally estimate the states of linear dynamic systems from a series of noisy measurements [20]. For nonlinear systems, extended Kalman filters [21, 22] have been developed and validated by many studies to be effective in real applications [17, 23–25]. Unlike model-based estimators which heavily rely upon the plant models, a specific feature of a Kalman filter is that it finds the stochastic relations between model predictions and sensor measurements, and then estimates system states in an optimal approach. By utilizing this feature of the Kalman filter, a slowly time-varying state can be treated as a constant and its variation can be estimated by comparing the model predictions and measurements in a stochastic manner.

14.3.1.2 EKF for Cross-Sensitivity Factor and NO_x Concentration Estimations

According to the studies in [11] and [26], the cross-sensitivity factor K_{cs} variation is mainly caused by temperature change. Because engine exhaust temperature dynamics after the SCR catalyst is generally slow, the cross-sensitivity factor K_{cs} in Eq. (14.31) is assumed to be a slowly time-varying variable, and it can be modeled by the following equation:

$$\dot{K}_{cs} = 0. \quad (14.32)$$

Based on the SCR model in Eq. (14.29), the NO_x concentration is modeled by the following equation:

$$\begin{aligned} \dot{\hat{C}}_{\text{NO}}^* &= -r_1 C_{\text{NO}}^* C_{\text{O}_2} \theta_{\text{NH}_3} \Theta V - \frac{1}{2} r_2 C_{\text{NO}}^* C_{\text{NO}_2}^* \theta_{\text{NH}_3} \Theta V - r_5 C_{\text{NO}}^* C_{\text{O}_2} V - \frac{F}{V} C_{\text{NO}}^* \\ &\quad + \frac{F}{V} C_{\text{NO},\text{in}}, \end{aligned} \quad (14.33)$$

$$\dot{\hat{C}}_{\text{NO}_2}^* = -\frac{1}{2} r_2 C_{\text{NO}}^* C_{\text{NO}_2}^* \theta_{\text{NH}_3} \Theta V + r_5 C_{\text{NO}}^* C_{\text{O}_2} V - \frac{F}{V} C_{\text{NO}_2}^* + \frac{F}{V} C_{\text{NO}_2,\text{in}}, \quad (14.34)$$

$$C_{\text{NO}_x}^* = C_{\text{NO}}^* + C_{\text{NO}_2}^*, \quad (14.35)$$

where $C_{\text{NO},\text{in}}$ and $C_{\text{NO}_2,\text{in}}$ are estimated by an observer using the NO_x sensor upstream of the SCR catalyst as described in [18, 27–29]. Since the NO_x sensor used for $C_{\text{NO},\text{in}}$ and $C_{\text{NO}_2,\text{in}}$ estimations is located upstream of the AdBlue injector, it is not affected by the ammonia cross-sensitivity and it can be assumed that $C_{\text{NO},\text{in}} = C_{\text{NO},\text{in}}^*$ and $C_{\text{NO}_2,\text{in}} = C_{\text{NO}_2,\text{in}}^*$. Here θ_{NH_3} is the SCR ammonia surface coverage ratio which can be estimated by the observer presented in the next section.

By the above models, the prediction equation in a discrete form is obtained as

$$x(k|k-1) = \begin{bmatrix} \hat{K}_{\text{cs}}(k|k-1) \\ \hat{C}_{\text{NO}}^*(k|k-1) \\ \hat{C}_{\text{NO}_2}^*(k|k-1) \end{bmatrix} = \begin{bmatrix} \hat{K}_{\text{cs}}(k-1|k-1) \\ \hat{C}_{\text{NO}}^*(k-1|k-1) + \Delta t \dot{\hat{C}}_{\text{NO}}^*(k-1|k-1) \\ \hat{C}_{\text{NO}_2}^*(k-1|k-1) + \Delta t \dot{\hat{C}}_{\text{NO}_2}^*(k-1|k-1) \end{bmatrix}, \quad (14.36)$$

where Δt is the EKF updating period. The EKF measurement is the NO_x sensor reading between the two SCR catalysts, which can be described as:

$$z(k) = C_{\text{NO}_x,\text{sen}}(k) = \hat{C}_{\text{NO}}^*(k|k-1) + \hat{C}_{\text{NO}_2}^*(k|k-1) + \hat{K}_{\text{cs}}(k|k-1) C_{\text{NH}_3}(k), \quad (14.37)$$

where C_{NH_3} is the ammonia concentration measured by the ammonia sensor between the two SCR catalysts and the reading is assumed to be accurate enough.

Based on the prediction and measurement equations of Eqs. (14.36) and (14.37), the extended Kalman filter for the estimations of NO and NO_2 (NO_x) concentrations and the sensor ammonia cross-sensitivity factor can be constructed.

14.3.1.3 Experimental Validations of the EKF

Figures 14.6, 14.7, 14.8, and 14.9 show the experimental results of the EKF estimations together with the NO_x concentrations predicted by the SCR model in Eq. (14.29) and measured by a NO_x sensor and a Horiba gas analyzer. Because the NO_2 concentrations measured after the SCR catalyst are always very low due to

Fig. 14.6 Comparison NO_x concentration estimated by EKF, predicted by SCR model, measured by NO_x sensor, and measured by Horiba gas analyzer in the test same as Fig. 2 [26]

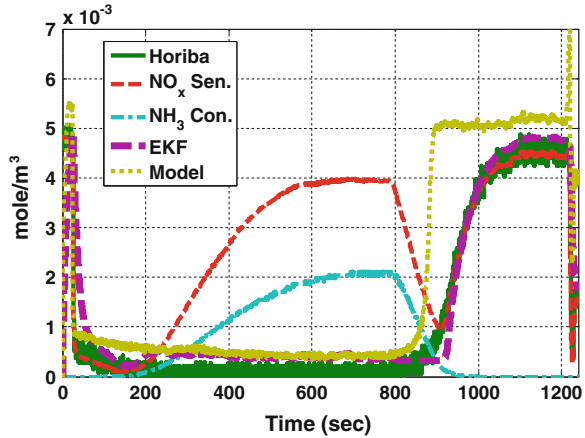
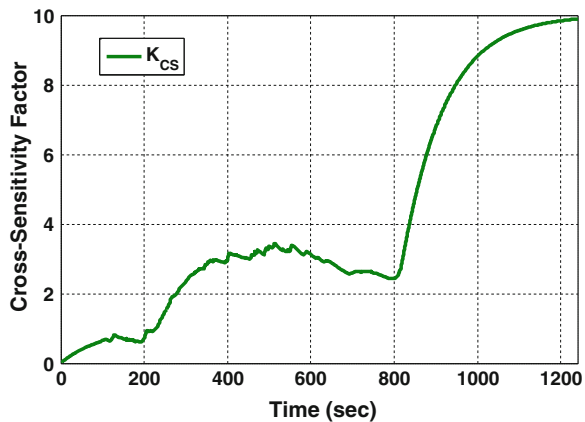


Fig. 14.7 EKF estimated ammonia cross-sensitivity of the NO_x sensor in the test of Fig. 6 [26]



the high reaction rate of the “fast SCR reaction” in Eq. (14.6), separate NO and NO_2 estimations are not addressed in this section, instead, the lumped NO_x concentration is used.

From Figs. 14.6 and 14.8, it can be observed that by using the SCR model in Eq. (14.29) to predict the NO_x concentration, i.e., without using the NO_x sensor after SCR, the predicted value can be insensitive to the presence of ammonia. However, due to the uncertainties between the real plant and the simplified model, noticeable differences can be seen especially during transient periods. On the other hand, when the EKF was used to estimate the NO_x concentration, the NO_x EKF estimation results were considerably improved and they are very close to the Horiba gas analyzer measured NO_x concentrations, which are assumed to be the actual values.

Figures 14.7 and 14.9 show the estimated NO_x sensor ammonia cross-sensitivity of the tests been examined. It can be seen that, when ammonia slip was present to the NO_x sensor, cross-sensitivity variations in each test can be correctly captured.

Fig. 14.8 Comparison NO_x concentration estimated by EKF, predicted by SCR model, measured by NO_x sensor, and measured by Horiba gas analyzer in the test same as Fig. 3 [26]

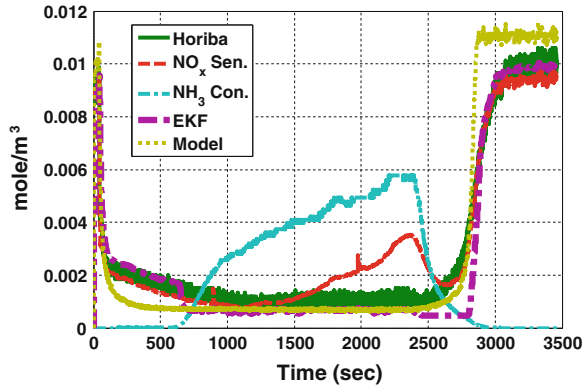
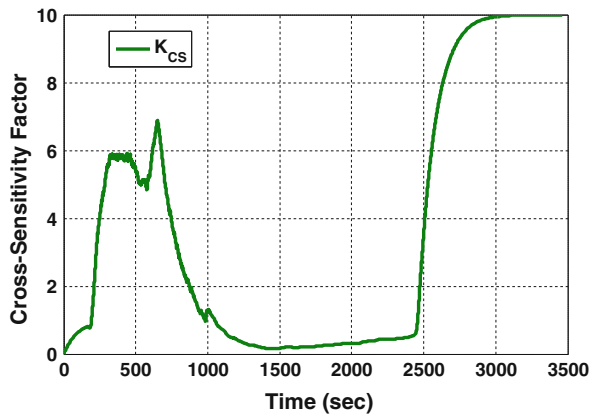


Fig. 14.9 EKF estimated ammonia cross-sensitivity of the NO_x sensor in the test of Fig. 14.8 [26]



During some time periods the ammonia cross-sensitivity estimations were raised to higher ranges, e.g., at the end of each test and between the 200–1,000 s in Fig. 14.9. These are because the ammonia slip was close to zero (lack of persistence of excitation) such that a higher cross-sensitivity was required to explain the difference between the NO_x concentrations predicted by the model and sensor measurements. When ammonia is presented, the estimated cross-sensitivity converged back to the reasonable value as can be seen at around the thousandth second in Fig. 14.9. This cross-sensitivity error would not have a significant effect to the NO_x concentration estimation since the ammonia emissions in these ranges were very low and the influence of cross-sensitivity was very limited. By setting a saturation to constrain the estimated cross-sensitivity value in a reasonable range (0–10 in the tests), undesired divergence can be avoided and the settling time to the actual cross-sensitivity, when ammonia slip is presented, can be reduced. On the other hand, even though the cross-sensitivity value is not directly useful for control applications, it has the potential to be used to diagnose the malfunction or aging effects of NO_x and NH_3 sensors by checking the estimated value to be within a reasonable range which can change with temperature variations.

It is also important to note that the EKF estimation can lump model uncertainties into the slow variation term K_{cs} . So the variation term can contain more uncertainties if the EKF model is not accurate. This should be kept in mind if K_{cs} is further to be used for diagnostics purpose.

14.3.2 SCR Catalyst Ammonia Coverage Ratio Estimation

SCR catalyst ammonia coverage ratio is a critical state that affects the SCR system dynamics as well as the NO_x conversion and tailpipe ammonia slip [30–33]. However, it is generally difficult to measure this signal onboard, even though some lab-based measurement methods have been proposed [34]. To perform appropriate real-time urea dosing control, it is thus beneficial to design an observer to estimate the SCR ammonia coverage ratio in real-time. In this subsection, two different nonlinear observers are designed based on the developed nonlinear SCR model (Eq. 14.29). The first observer is designed based on the ammonia coverage ratio dynamics. The sensitivity analysis of the observer shows that the observer is sustainable of small NO_x and ammonia measurement errors, but is very sensitive to temperature measurement uncertainty. Besides, since the NO_x sensor cross-sensitivity might not be completely compensated by the EKF correction approach at some points, e.g., before cross-sensitivity factor converges, the second observer is designed to be robust with respect to the temperature measurement errors and the NO_x sensor uncertainty. In this observer, in addition to the ammonia coverage ratio dynamics, the ammonia concentration dynamics is also considered in the observer design, and a sliding mode approach was employed to increase the observer robustness with respect to the specific measurement errors and uncertainties. The sensitivity analyses of the observers are conducted and the effectiveness of the observers is verified by simulations with a vehicle model through the FTP75 test cycle.

14.3.2.1 Observer 1: Design Based on Coverage Ratio Dynamics

The first observer design is based on the NH_3 coverage ratio dynamics as shown in the SCR model of Eq. (14.29):

$$\begin{aligned} \dot{\theta}_{\text{NH}_3} = & -\theta_{\text{NH}_3} (r_{4F} C_{\text{NH}_3} V + r_3 C_{\text{O}_2} V + r_{4R} + r_1 C_{\text{NO}} C_{\text{O}_2} V^2 + r_2 C_{\text{NO}} C_{\text{NO}_2} V^2) \\ & + r_{4F} C_{\text{NH}_3} V. \end{aligned} \quad (14.38)$$

From the SCR model, it can be seen that all the states and parameters but the ammonia coverage ratio θ_{NH_3} are available. Besides, since the NO_2 concentration after the SCR catalyst (C_{NO_2}) is always low, it can be assumed that $C_{\text{NO}_2} = 0$. Under this assumption, an observer can be designed in a straightforward manner.

With the above assumptions, the following observer can ensure the convergence of the estimation error.

$$\begin{aligned}\dot{\hat{\theta}}_{\text{NH}_3} &= -(r_{4F}C_{\text{NH}_3}V + r_3C_{\text{O}_2}V + r_{4R} + r_1C_{\text{NO}}C_{\text{O}_2}V^2)\hat{\theta}_{\text{NH}_3} + r_{4F}C_{\text{NH}_3}V \\ &= -M_1\hat{\theta}_{\text{NH}_3} + M_2, \hat{\theta}_{\text{NH}_3} \leq 1,\end{aligned}\quad (14.39)$$

where M_1 and M_2 are positive. The stability of this observer can be proved based on the Lyapunov theory, details of the stability proof can be found in [35, 36].

14.3.2.2 Observer 2: Design Based on Coverage Ratio and NH_3 Dynamics

To reduce the estimation error caused by the temperature measurement and parametric uncertainties, a robust observer using the sliding mode technique by considering the NH_3 dynamics is designed. As the ammonia sensor is not cross-sensitive against NO_x , such a feature can be beneficial for the observer design. Also, based on the sensitivity analysis of the observer, the observer is robust to NO_x sensor uncertainty, which is preferable especially when the NO_x sensor cross-sensitivity is not completely compensated by the EKF correction approach.

Sliding mode observer is known for its robustness with respect to bounded uncertainties [37–41]. The observer considering the dynamics of ammonia coverage ratio and ammonia reaction is proposed as follows: The estimation error $\tilde{\theta}_{\text{NH}_3}$ of the following observer will converge to zero in a finite period of time.

$$\dot{\tilde{\theta}}_{\text{NH}_3} = -\hat{\theta}_{\text{NH}_3}(r'_{4F}C_{\text{NH}_3}V + r'_3C_{\text{O}_2}V + r'_{4R}) + r'_{4F}C_{\text{NH}_3}V + K_\theta \text{sign}(C_{\text{NH}_3} - \hat{C}_{\text{NH}_3}), \quad (14.40)$$

where

$$\begin{aligned}\dot{\hat{C}}_{\text{NH}_3} &= -C_{\text{NH}_3} \left[\Theta r'_{4F} \left(1 - \hat{\theta}_{\text{NH}_3,2} \right) + \frac{F}{V} \right] + \frac{1}{V} r'_{4R} \Theta \hat{\theta}_{\text{NH}_3} + \frac{F}{V} C_{\text{NH}_3, \text{in}} \\ &\quad + K_{\text{NH}_3} \text{sign}(C_{\text{NH}_3} - \hat{C}_{\text{NH}_3}).\end{aligned}\quad (14.41)$$

The stability of this observer can also be proved based on the Lyapunov theory as detailed in [35, 36].

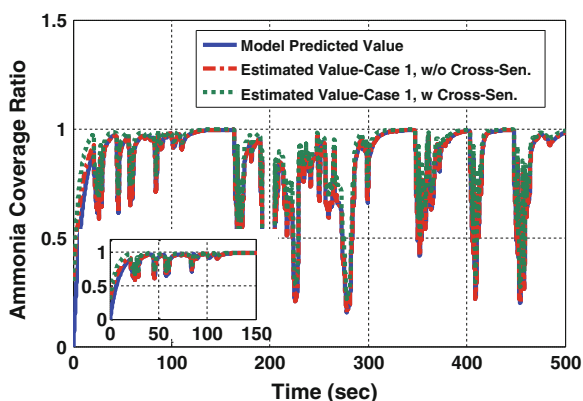
14.3.2.3 Simulation Validations and Analyses

Simulated sensor errors were applied to the system to evaluate the observer sensitivities with respect to the measurement uncertainties. In this section, NO_x sensor ammonia cross-sensitivity factor is modeled as a slow time-varying signal. If not specified, NO_x sensor is subjected to a cross-sensitivity to ammonia as modeled in

Table 14.1 Simulation cases with corresponding observers and sensor measurement variances

Case	Observers	NH ₃ Measurement variances	NO _x Measurement Variances	T Measurement Variances	K _x Variances	NH ₃ Storage capacity variation
1	1	1	1	1	1	1
2	1	1.5	1	1	1	1
3	1	1	1.8	1	1	1
4	1	1	1	1.1	1	1
5	2	1	1.8	1	1	1
6	2	1	1	1.1	1	1
7	2	1	0	1	1	1
8	2	1	1	1	1.5	1
9	2	1	1	1	1	1.5

Fig. 14.10 Performance of the observer 1 based on ammonia coverage ratio dynamics [35]



Eq. (14.31) and the cross-sensitivity is eliminated by the EKF. Nine cases were compared as listed in Table 14.1. The variances represent the sensor errors (i.e., 1 means there is no sensor error, 1.1 means the measured value is 1.1 times the actual value, and 0 means there is no measurement available and the measurement is 0). The K_x is the pre-exponential factors of the considered SCR reactions. Also the ammonia storage capacity uncertainties are considered in observer 2. The initial NH₃ coverage ratio was set to 0.3 in the observers while the real value starts from 0.

Three signals compared in Fig. 14.10 are the actual ammonia coverage ratio predicted by the model, coverage ratio estimated by observer 1 in Eq. (14.39) subjected to a NO_x sensor without cross-sensitivity, and coverage ratio estimated by observer 1 subjected to a NO_x sensor with cross-sensitivity and the EKF correction. As can be seen in both cases, the estimated signals converged to and tracked the actual values fairly well. Comparing the cases where the NO_x sensor

Fig. 14.11 Observer 1 based on ammonia coverage ratio dynamics with sensor error [35]

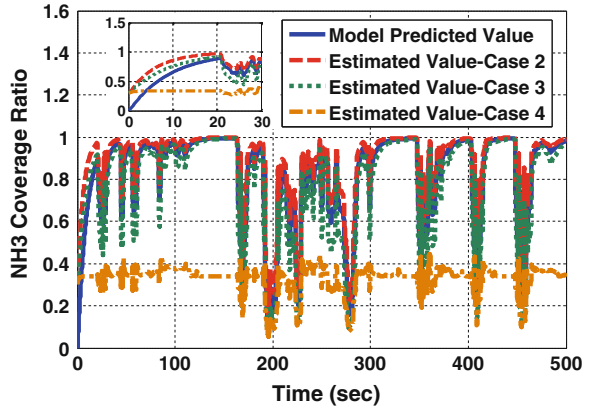
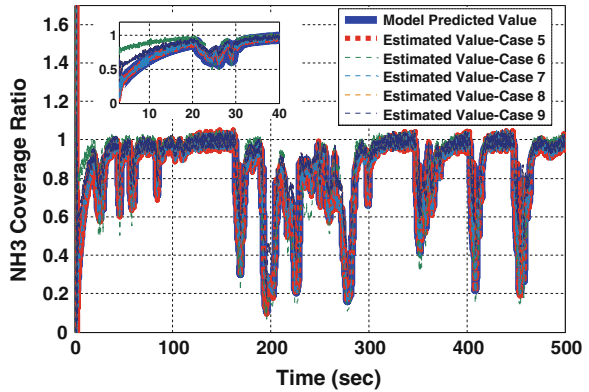


Fig. 14.12 Observer 2 based on ammonia coverage ratio dynamics and ammonia dynamics [35]



does not have a cross-sensitivity and the one with a cross-sensitivity but subjected to the EKF correction, it can be observed that the difference between them can be hardly identified. This also verifies the applicability of the EKF for NO_x sensor cross-sensitivity elimination.

Figure 14.11 shows the results when sensor errors were introduced to the observer. It can be seen that the NO and NH_3 sensor errors did not introduce significant influences to the estimations. However, a small offset of the temperature measurement caused an obvious difference between the real value and the estimated one. The same result (high sensitivity to temperature error) can also be obtained from the analysis of the observer sensitivities as conducted in [36].

Figure 14.12 shows the simulation results using the second observer described by Eq. (14.40). The observer depends on the measurement of NH_3 concentration. As expected, the observer is now robust to the temperature and NO_x measurement errors and also to the chemical reaction rate errors. Since the observer can be robust to the NO_x sensor measurement error, the NO_x sensor cross-sensitivity issue

will not cause a significant estimation error to the observer. It can be seen that the estimated value contains noticeable noise, which is due to the chattering effect at the sliding mode. As can be seen in Case 7, the observer can still estimate the signal very accurately even without the NO_x measurement. In Case 8, parametric uncertainties of the chemical reaction rates were imposed in a fashion such that the reduction rate constants of all considered chemical reactions were 1.5 times higher than the corresponding values in the model. Since the observer was designed to be robust to the reaction rates, the estimated ammonia coverage ratio still converged to the model value very well. Case 9 shows the situation when the SCR catalyst ammonia storage capacity is 1.5 times of the modeled value. As expected, the observer is also robust to this uncertainty.

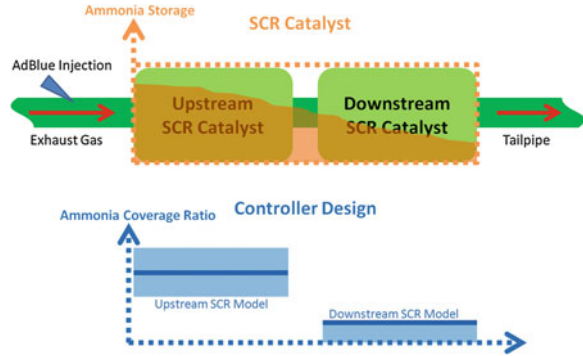
14.4 SCR Control

Several SCR control designs for automotive and commercial vehicle applications have been proposed in recent years [10, 15, 30, 42–51]. Most of them focused on feed-forward controller designs or utilized linearized SCR models for feedback controller designs [10, 30, 45, 46, 48]. The study in [15] pointed out that open-loop feed-forward control cannot well handle the engine transient exhaust gas conditions and feedback control is necessary to compensate for the uncertainties during real-world driving as well as test cycles. To meet the recent stringent emission standards, some feedback controllers which utilize NO_x sensors have been proposed [10, 30, 42, 45–47]. However, due to the NO_x sensor ammonia cross-sensitivity and ammonia slip concerns, NO_x -based feedback control alone may be difficult to meet the SCR control objectives [15, 46, 47, 52]. Of late, with the availability of the automotive ammonia sensor from some suppliers such as Delphi, several NH_3 -based feedback controls have been studied [49–51]. Such ammonia sensors may not be cross-sensitive to NO_x or other major exhaust gas species, and is being considered by the industry as an alternative feedback sensor for urea-SCR system control. But because the sensor has not been in production yet, practical applications of ammonia sensor-based SCR control are rarely seen.

The objective of urea-SCR control is to simultaneously minimize the tailpipe NO_x and ammonia emissions. Due to the nature of SCR dynamics, intuitively, increasing AdBlue injection rate can generally decrease SCR-out NO_x emissions but also result in ammonia slip increases, and vice versa. To achieve low NO_x and ammonia emissions simultaneously, specific control approaches need to be designed to handle the SCR nonlinear dynamics.

With an adequate amount of ammonia being adsorbed on the SCR substrate, high NO_x reduction rate can be realized. It is thus believed that consistent SCR NO_x reduction can be ensured by ammonia storage control. However, besides the NO_x reduction, tailpipe ammonia slip constraint is another objective needs to be taken into account. From the SCR model in Eq. (14.29) and the ammonia adsorption/desorption reactions in Eq. (14.4), it can be seen that high ammonia

Fig. 14.13 Schematic presentation of ammonia storage distribution control strategy [53]



coverage ratio/storage can directly lead to high SCR-out ammonia slip. Therefore, for low tailpipe ammonia slip, low ammonia coverage ratio/storage is desired, which contradicts to the intention of SCR NO_x reduction (requires high ammonia coverage ratio).

To address the aforementioned contradiction, an ammonia storage distribution control (ASDC) approach is proposed. A schematic presentation of the ASDC concept is shown in Fig. 14.13. The control approach is to simultaneously achieve NO_x and ammonia slip reductions by regulating the ammonia storage distribution along the axial direction of the SCR catalyst. The urea injection control objectives are: (1) to have rich ammonia storage at the upstream part of the SCR catalyst for accomplishing sufficient and efficient NO_x reduction; and (2) to have lean ammonia storage at the downstream part such that the ammonia slip from the ammonia rich region (upstream) can be adsorbed and the tailpipe ammonia slip due to ammonia desorption from the downstream catalyst is limited. By this control approach, the SCR catalyst can be fully utilized such that the SCR NO_x reduction and AdBlue utilization efficiencies can be enhanced while restricting the tailpipe ammonia slip.

To verify this ammonia storage distribution control approach in practice, a two-catalyst SCR system is developed. A controller is designed to control the AdBlue injection such that the ammonia coverage ratio of the upstream catalyst is kept at a higher value and the ammonia coverage ratio of the downstream catalyst is limited under a lower level as presented in Fig. 14.13.

14.4.1 Control-Oriented SCR Model

The control-oriented SCR model proposed in Eq. (14.29) is extended to a two-cell model for the ASDC application as shown in Eq. (14.42), and a schematic presentation is shown in Fig. 14.14.

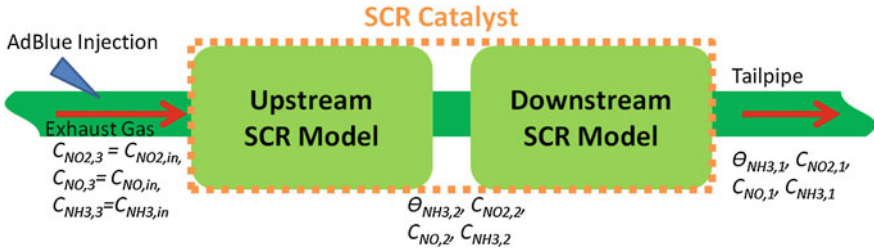


Fig. 14.14 Schematic presentation of a two-cell SCR model [53]

$$\begin{bmatrix} \dot{C}_{NO,i} \\ \dot{C}_{NO_2,i} \\ \dot{C}_{NH_3,i} \\ \dot{\theta}_{NH_3,i} \end{bmatrix} = \begin{bmatrix} -r_{1,i} C_{NO,i} C_{O_2,i} \theta_{NH_3,i} \Theta_i V_i - \frac{1}{2} r_{2,i} C_{NO,i} C_{NO_2,i} \theta_{NH_3,i} \Theta_i V_i - r_{5,i} C_{NO,i} C_{O_2,i} V_i - \frac{F_i}{V_i} C_{NO,i} + \frac{F_i}{V_i} C_{NO,i+1} \\ -\frac{1}{2} r_{2,i} C_{NO,i} C_{NO_2,i} \theta_{NH_3,i} \Theta_i V_i - r_{5,i} C_{NO,i} C_{O_2,i} V_i - \frac{F_i}{V_i} C_{NO,i} + \frac{F_i}{V_i} C_{NO,i+1} \\ -C_{NH_3,i} \left[\Theta_i r_{4F,i} (1 - \theta_{NH_3,i}) + \frac{F_i}{V_i} \right] + \frac{1}{V_i} r_{4R,i} \Theta_i \theta_{NH_3,i} + \frac{F_i}{V_i} C_{NH_3,i+1} \\ -\theta_{NH_3,i} (r_{4F,i} C_{NH_3,i} V_i + r_{3,i} C_{O_2,i} V_i + r_{4R,i} + r_{1,i} C_{NO,i} C_{O_2,i} V_i^2 + r_{2,i} C_{NO,i} C_{NO_2,i} V_i^2) + r_{4F,i} C_{NH_3,i} V_i \end{bmatrix}$$

$i = 1, 2.$

(14.42)

Notice that because the catalyst volume of the above model is $\frac{1}{2}$ of the complete SCR catalyst volume, the two-cell model not only can capture the state variations from upstream to downstream, but also has a better approximation to the CSTR assumption comparing to a single-cell model where the catalyst volume is twice larger. Besides, by the ammonia coverage ratio observers proposed in the last section and by assuming temperature, NO_x concentration and ammonia concentration measurements are available at the downstream of the SCR catalysts and between the two catalysts; the model in Eq. (14.42) is full-state available.

14.4.2 Controller Design and Architecture

In order to handle the complicated dynamics caused by the cascade connection of two SCR models, the backstepping control approach is used to design the controller. Also because the catalyst ammonia storage capacity has the highest uncertainty among other model variables [11], the controller is designed to be adaptive to the ammonia storage capacity. To regulate the ammonia coverage ratio of the upstream catalyst $\theta_{NH_3,2}$ to a desired value $\theta_{NH_3,2}^*$ while constraining the ammonia coverage ratio of the downstream catalyst $\theta_{NH_3,1}$ under an upper limit of $\theta_{NH_3,1}^*$, based on the control plant model, the urea dosing control law is proposed below:

$$C_{\text{NH}_3,\text{in}} = -\frac{V_2}{F_2} \left\{ G(\tilde{\theta}_{\text{NH}_3,1}) \left[\tilde{\theta}_{\text{NH}_3,2} r_{4F,2} V_2 (1 - \theta_{\text{NH}_3,2}) - \dot{\tilde{C}}_{\text{NH}_3,2} - \frac{F_2}{V_2} C_{\text{NH}_3,2} - C_{\text{NH}_3,2} r_{4F,2} (1 - \theta_{\text{NH}_3,2}) \right] + \frac{1}{V_2} r_{4R,2} \theta_{\text{NH}_3,2} \dot{\Theta}_2 + K_2 \tilde{C}_{\text{NH}_3,2} |\tilde{\theta}_{\text{NH}_3,2}| \right\}, \quad (14.43)$$

where,

$$\tilde{\theta}_{\text{NH}_3,1} = \theta_{\text{NH}_3,1} - \theta_{\text{NH}_3,1}^*, \quad (14.44)$$

$$\tilde{\theta}_{\text{NH}_3,2} = \theta_{\text{NH}_3,2} - \theta_{\text{NH}_3,2}^*, \quad (14.45)$$

$$\tilde{C}_{\text{NH}_3,2} = C_{\text{NH}_3,2} - \bar{C}_{\text{NH}_3,2}, \quad (14.46)$$

$$\dot{\Theta}_2 = \tilde{C}_{\text{NH}_3,2} \left[C_{\text{NH}_3,2} r_{4F,2} (1 - \theta_{\text{NH}_3,2}) - \frac{1}{V_2} r_{4R,2} \theta_{\text{NH}_3,2} \right], \quad (14.47)$$

$$\bar{C}_{\text{NH}_3,2} = \frac{1}{r_{4F,2} V_2 (1 - \theta_{\text{NH}_3,2})} \left[\theta_{\text{NH}_3,2} (r_{3,2} C_{\text{O}_2,2} V_2 + r_{4R,2} + r_{1,2} C_{\text{NO},2} C_{\text{O}_2,2} V_2^2) G(\tilde{\theta}_{\text{NH}_3,1}) - K_1 \tilde{\theta}_{\text{NH}_3,2} \right], \quad (14.48)$$

$$G(x) = \frac{1}{2} \text{sign}(-x) + \frac{1}{2}, \text{sign}(0) \equiv 0, \quad (14.49)$$

$K_1, K_2, K_3 > 0$.

The stability of the control law can be proved based on a backstepping analysis approach. Details of the stability proof process can be found in [53].

The complete SCR control architecture for practical applications is summarized in Fig. 14.15, which includes the SCR ammonia coverage ratio observer proposed in Eq. (14.40) (observer 2) and the EKF NO_x sensor correction approach discussed previously.

14.4.3 Experimental Setup

A schematic presentation and a picture of the experimental setup are shown in Figs. 14.16 and 14.17, respectively, which include: a medium-duty Diesel engine, Diesel oxidation catalyst (DOC)/Diesel particulate filter (DPF), and two SCR catalysts in series at downstream of the DOC/DPF. For the emission measurement system, a Horiba MEXA 7500 gas analyzer was used to measure the tailpipe NO_x emissions. Three Siemens VDO (NGK) NO_x sensors and two Delphi ammonia sensors were used to provide feedback information to the SCR controller and to monitor the emission levels at different locations as shown in Figs. 14.16 and 14.17.

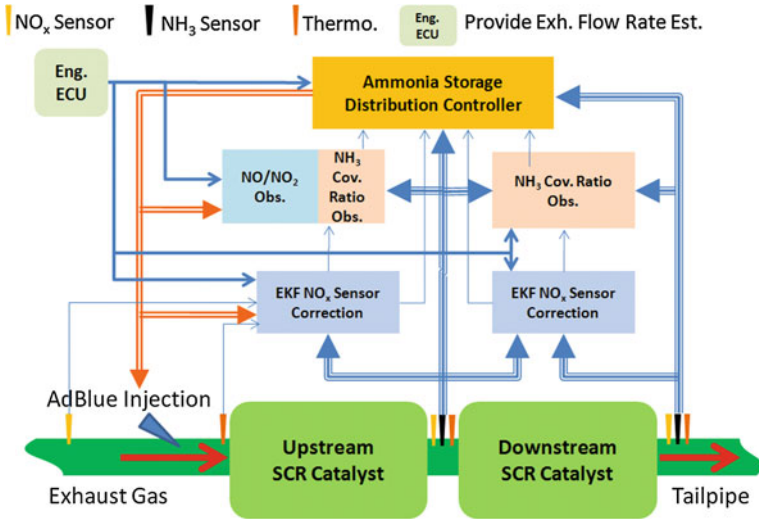


Fig. 14.15 Schematic presentation of the controller architecture [53]

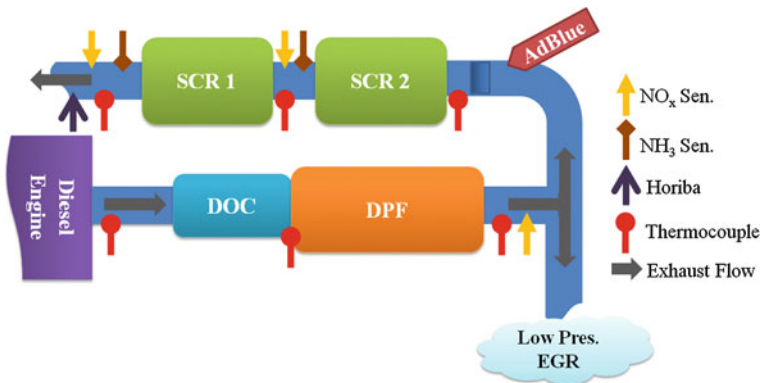


Fig. 14.16 Schematic presentation of the experiment setup [53]

The NO_x sensors were calibrated with a Horiba gas analyzer up to 1500 PPM and the ammonia sensors were calibrated with a FTIR up to 500 PPM. Notice that this experimental setup is to validate the concept of controlling ammonia storage distribution, and multiple NO_x and NH₃ sensors are used. The number of sensors used for SCR control can be limited in real applications due to cost consideration.

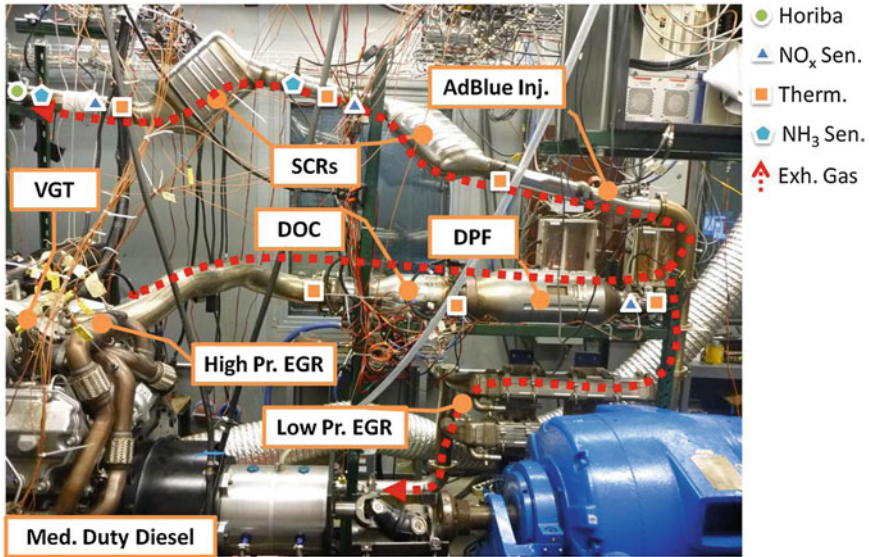


Fig. 14.17 Diesel engine and aftertreatment system test bench [53]

14.4.4 Experimental Results of US06 Test Cycle

Figure 14.18 shows the engine speed, torque, and SCR temperatures during the US06 test cycle conducted on a diesel engine motoring dynamometer setup. The ammonia coverage ratios of the two catalysts are shown in Fig. 14.19. The desired values of $\theta_{\text{NH}_3,1}^*$ and $\theta_{\text{NH}_3,2}^*$ were set to 0.3 and 0.6, respectively.

At the time around the four hundredth second, the downstream ammonia coverage ratio was increased and approached the upper limit (0.3). This increase was due to the temperature rise which induced an SCR ammonia storage capacity decrease. In this situation, as can be seen in Fig. 14.20, the controller reduced the AdBlue injection rate such that the downstream ammonia coverage ratio was restricted under the limit. In addition, as can be seen in Fig. 14.19, to satisfy the downstream catalyst ammonia coverage ratio constraint, lower upstream ammonia coverage ratio was inevitably accompanied. However, by comparing the ammonia coverage ratios of the two catalysts, the value of the upstream catalyst was always higher than that of the downstream catalyst, and the constraint of the ammonia coverage ratio for the downstream catalyst value was also satisfied. Thus, the main objectives of the ASDC were achieved.

Figure 14.20 illustrates the measured NO_x and ammonia concentrations before, between, and after the SCR catalysts during the US06 test cycle. As can be observed, with the rich ammonia storage at the upstream catalyst, the engine exhaust NO_x emissions were consistently reduced to low levels even if the engine-out NO_x concentrations varied in a high frequency fashion. A zoom-in figure of the

Fig. 14.18 Engine operating condition and SCR catalyst temperatures in the US06 cycle test [53]

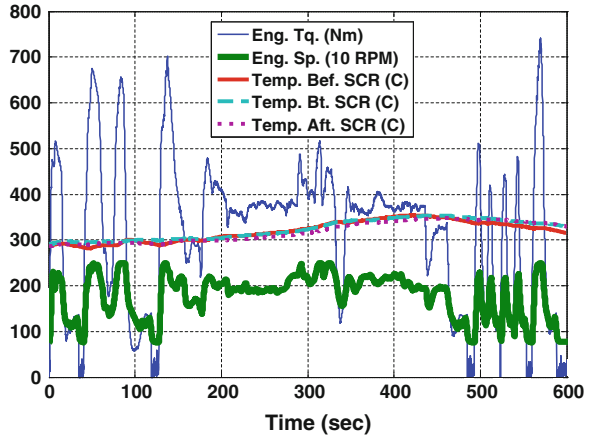


Fig. 14.19 Ammonia coverage ratios of the two SCR catalysts in the US06 cycle test [53]

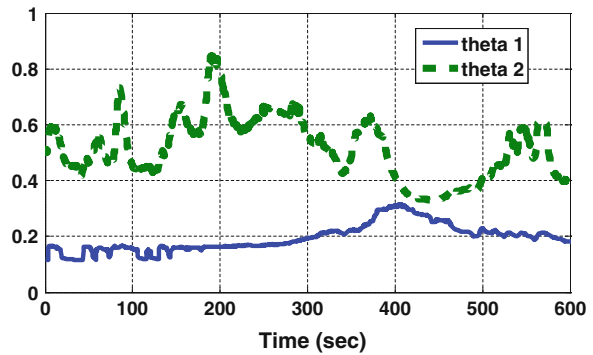


Fig. 14.20 Measured NO_x and NH_3 concentrations before, between, and after the SCR catalysts in the US06 cycle test [53]

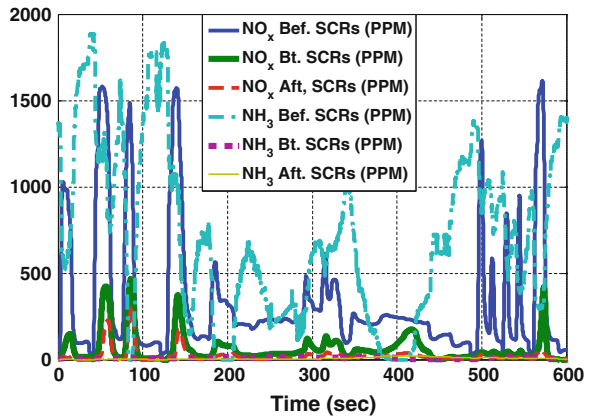
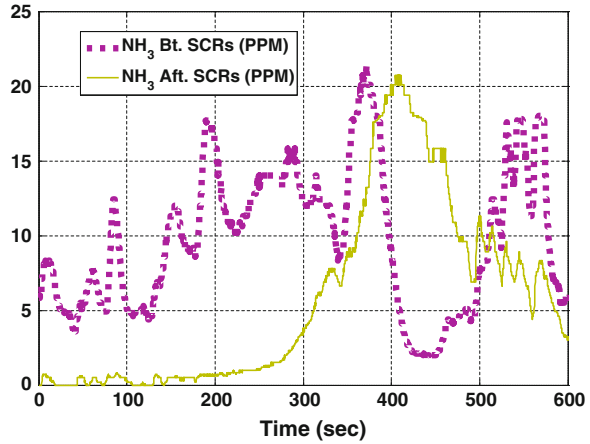


Fig. 14.21 Measured ammonia slips between the two SCR catalysts and downstream of the SCR catalysts (tailpipe) in the US06 cycle test [53]



ammonia concentrations between and after the SCR catalyst is presented in Fig. 14.21. As it indicates, the higher ammonia slip from the upstream catalyst can be reduced by the downstream catalyst. At the time period between 400–500 s, higher ammonia slip was observed after the downstream SCR catalyst (i.e., at the tailpipe). This was primarily due to the ammonia storage capacity reduction caused by the increased catalyst temperature as mentioned before. The SCR ammonia storage capacity decrease induced a higher ammonia coverage ratio, which caused faster ammonia desorption rates and higher ammonia slip out of the downstream catalyst. As can be clearly observed from the ammonia concentration upstream of the SCR catalysts, the controller was able to reduce the AdBlue injection in this situation to avoid high ammonia slip from the catalysts. From the measurements, it can be seen that the tailpipe ammonia slip was reduced after it reached the maximum value of 20 ppm. The ammonia coverage ratios together with the tailpipe NO_x and ammonia emissions resumed into the regular ranges after this transient temperature variation. More details about the experimental validations of the SCR ammonia storage distribution controller can be found in [53].

14.5 Conclusions

SCR control for mobile vehicle applications has been a great challenge in the aspects of estimation and controller designs. Some of the major issues, e.g., NO_x sensor ammonia cross-sensitivity, SCR ammonia storage estimation, and SCR controller design, have been introduced in this chapter, and possible solutions are addressed. Most of the present solutions have been experimentally validated (except the observer for ammonia coverage ratio which currently cannot be directly measured). However, there are still some concerns which make robust and high NO_x conversion efficiency SCR control challenging to be realized in

real-world vehicle driving. For example, costs of the emissions sensors (i.e., NO_x and NH₃ sensors) and uncertainties from urea injection quantity, SCR formulation, and other measurements. Open problems on sensor reduction and development, as well as robustness of the control systems still need further research.

References

1. Grossale A et al (2008) The chemistry of the NO/NO₂-NH₃ “fast” SCR reaction over Fe-ZSM₅ investigated by transient reaction analysis, *Journal of Catalysis*, 256:312–322
2. Nova I et al (2007) NH₃-NO/NO₂ SCR for Diesel exhausts aftertreatment: mechanism and modeling of a catalytic converter, *Topics in Catalysis*, 42:43–46
3. Ciardelli C et al (2004) SCR-DeNO_x for diesel engine exhaust aftertreatment: unsteady-state kinetic study and monolith reactor modeling, *Chemical Engineering Science*, 59:5301–5309
4. Tronconi E et al (2005) Modeling of an SCR catalyst converter for diesel exhaust after treatment: dynamic effects at low temperature, *Catalysis Today*, 105:529–536
5. York A et al (2004) Modeling an ammonia SCR DeNO_x catalyst: model development and validation, *Proceedings of the SAE 2004 World Congress*, SAE paper 2004-01-0155
6. Chatterjee D et al (2005) Numerical simulation of ammonia SCR-Catalytic converters: model development and application, *SAE 2005 World Congress*, SAE paper 2005-01-0965
7. Piazzesi G et al (2006) Isocyanic acid hydrolysis over Fe-ZAM₅ in urea SCR”, *Catalysis Communications*, 7:600–602
8. Sluder CS et al (2004) Low temperature urea decomposition and SCR performance”, *SAE 2004 World Congress*, SAE paper 05FL-55
9. Birkhold F et al (2007) Modeling and simulation of the injection of urea-water-solution for automotive SCR DeNO_x-systems, *Applied Catalysis B: Environmental*, 70:119–127
10. Schar CM et al (2004) Control-oriented model of an SCR catalytic converter system, *2004 SAE World Congress*, SAE paper 2004-01-0153
11. Hsieh M-F, Wang J (2011) Development and experimental studies of a control-oriented SCR model for a two-catalyst SCR system, *Control Engineering Practice*, 19(4):409–422
12. Upadhyay D, Van Nieuwstadt M (2002) Modeling of a urea SCR catalyst with automotive application, *Proceedings of the ASME International Mechanical Engineering Congress & Exposition*
13. Devarakonda M et al (2008) Adequacy of reduced order models for model-based control in a urea-SCR aftertreatment system, *SAE 2008 World Congress*, SAE paper 2008-01-0617
14. Devadas M, Krocher O, Wokaun A (2005) Catalytic investigation of FeZSM₅ in the selective catalytic reduction of NO_x with NH₃, *Reaction Kinetics and Catalysis Letters*, 86:347–354
15. Willems F et al (2007) Is closed-loop SCR control required to meet future emission targets?, *SAE 2007 World Congress*, SAE paper 2007-01-1574
16. Joo K et al (2008) The study of NO_x reduction using urea-SCR system with CPF and DOC for light Duty vehicle: the Diesel NO_x reduction system, *2008 SAE World Congress*, SAE paper 2008-02-1183
17. Hsieh M-F, Wang J (2010) An extended Kalman filter for ammonia coverage ratio and capacity estimations in the application of Diesel engine SCR control and onboard diagnostics, *Proceedings of the 2010 American Control Conference*, 5875–5879
18. Hsieh M-F, Wang J (2011) NO and NO₂ Concentration Modeling and Observer-Based Estimation across a Diesel Engine Aftertreatment System, *ASME Transactions Journal of Dynamic Systems, Measurement, and Control*, 133(4):041005
19. Hsieh M-F, Wang J (2010) An extended Kalman filter for NO_x sensor cross-sensitivity error elimination in Diesel engine selective catalytic application, *Proceedings of the 2010 American Control Conference*, 3033–3038

20. Kalman R (1960) A new approach to linear filtering and prediction problems, *ASME Journal of Basic Engineering*, 82(D):35–45
21. Julier SJ, Uhlmann JK (1997) A new extension of the Kalman filter to nonlinear system, *Proceedings of the Int. Symp. Aerospace/Defense Sensing, Simulation, and Control*
22. Wan EA, Van Der Merwe R (2000) The unscented Kalman filter for nonlinear estimation, *Proceedings of the IEEE 2000 Adaptive Systems for Signal Processing: Communication, and Control Symposium*, 153–158
23. Baumgartner ET, Skaar SB (1994) An autonomous vision-based mobile robot, *Proceedings of the IEEE Transaction on Automatic Control*, 39(3):493–502
24. Carlson HA et al (2006) A regulator and filter for tracking aerodynamic force”, *Proceedings of the IEEE Conference on Decision and Control*, 4591–4596
25. Redmill K et al (2001) DGPS/INS integrated positioning for control of automated vehicle, *Proceedings of the 2001 IEEE Intelligence Transportation Systems Conference*
26. Hsieh M-F, Wang J (2011) Design and experimental validation of an extended Kalman filter-based NO_x concentration estimator in selective catalytic reduction system applications, *Control Engineering Practice*, 19(4): 346–353.
27. Hsieh M-F, Wang J (2010) A physically-based, control-oriented diesel oxidation catalyst (DOC) model for the applications of NO/NO₂ ratio estimation using a NO_x Sensor, *Proceedings of the ASME Dynamic Systems and Control Conference*
28. Hsieh M-F, Wang J (2010) A physically-based, control-oriented Diesel particulate filter (DPF) model for the applications of NO/NO₂ ratio estimation using a NO_x sensor, *Proceedings of the ASME Dynamic Systems and Control Conference*
29. M. Hsieh and J. Wang, “Observer-based estimation of Diesel engine aftertreatment system NO and NO₂ concentrations”, *Proceedings of the ASME Dynamic Systems and Control Conference*, (Invited Paper), 2010.
30. Upadhyay D, Van Nieuwstadt M (2006) Model based analysis and control design of a urea-SCR deNO_x aftertreatment system, *ASME, Journal of Dynamic Systems, Measurement, and Control*, 128:737–741
31. Hsieh M-F, Wang J (2009) Backstepping based nonlinear ammonia surface coverage ratios control for diesel engine selective catalytic reduction systems, *Proceedings of the ASME Dynamic Systems and Control Conference*
32. Hsieh M-F, Wang J (2009) Diesel engine selective catalytic reduction ammonia surface coverage control using a computationally-efficient model predictive control assisted method, *Proceedings of the ASME Dynamic Systems and Control Conference*
33. Hsieh M-F, Wang J (2011) A two-cell backstepping based control strategy for Diesel engine selective catalytic reduction systems, *IEEE Transactions on Control Systems Technology*, 19(6):1504–1515
34. Kubinski DJ, Visser JH (2008), Sensor and method for determining the ammonia loading of a zeolite SCR catalyst, *Sensor and Actuator*, 130:425–429
35. Hsieh M-F, Wang J (2010) Observer-based estimation of selective catalytic reduction (SCR) catalyst ammonia storage *Journal of Automobile Engineering, Proceedings of the Institution of Mechanical Engineers Part D*, 224(9):1199–1211
36. Hsieh M-F, Wang J (2009) Nonlinear observer designs for Diesel engine selective catalytic reduction (SCR) ammonia coverage ratio estimation, *Proceedings of the 48th IEEE Conference on Decision and Control*, 6596–6601.
37. Drakunov SV (1992) Sliding-mode observers based on equivalent control method, *Proceedings of the 31th Conference on Decision and Control*, 2:2368–2369
38. Drakunov SV, Utkin V (1995) Sliding mode observers tutorial”, *Proceedings of the 34th Conference on Decision and Control*, 4:3376–3378
39. Xiong Y, Saif M (2001) Sliding mode observer for nonlinear uncertain systems, *IEEE Transactions on Automatic Control*, 46(12):2012–2017
40. Utkin V et al (1999) Sliding mode control in electromechanical systems, *Taylor and Francis*
41. Slotine JJ et al (1987) On sliding observers for nonlinear systems,” *ASME Journal of Dynamic Systems, Measurement, and Control*, 109:245–252

42. Song Q, Zhu G. (2002) Model-based closed-loop control of urea SCR exhaust aftertreatment system for Diesel engine, SAE 2002 World Congress, 2002-01-028
43. Johnson TV (2009) Review of diesel emissions and control, *International Journal of Engine Research*, 10(5):275–285
44. Johnson TV (2010) Review of Diesel emissions and control, *SAE 2010 World Congress*, 2010-01-0301
45. Chi JN, DaCosta HFM (2005) Modeling and control of a Urea-SCR aftertreatment system, *2005 SAE World Congress* SAE 2005-01-0966
46. Schar CM et al (2006) Control of an SCR catalyst converter system for a mobile heavy-duty application, *IEEE Transactions on Control System Technology*, 14(4):641–652
47. Devarakonda M et al (2009) Model-based estimation and control system development in a Urea-SCR aftertreatment system, *SAE International Journal of Fuels and Lubricants*, 1(1):646–661
48. Seher DHE et al (2003) Control strategy for NO_x - emission reduction with SCR, *Proceedings of the International Truck & Bus Meeting & Exhibition*
49. Devarkonda M et al (2009) Model-based control system design in a urea-SCR aftertreatment system based on NH₃ sensor feedback, *International Journal of Automotive Technology*, 10(6):653–662
50. Herman A et al (2009) Model based control of SCR dosing and OBD strategies with feedback from NH₃ sensors, *SAE 2009 World Congress*, SAE paper 2009-01-0911
51. Wang DY et al (2009) Ammonia sensor for close-loop SCR control, SAE 2008 World Congress, *SAE International Journal of Passenger Cars- Electronic and Electrical Systems*, 1(1):323–333
52. Hsieh M-F, Wang J (2010) An extended Kalman filter for NO_x sensor ammonia cross-sensitivity elimination in selective catalytic reduction applications, *Proceedings of the 2010 American Control Conference*.
53. Hsieh M-F, Wang J (2012) Adaptive and efficient ammonia storage distribution control for a two-catalyst SCR system, *ASME Journal of Dynamic Systems, Measurement and Control*, 134(1): 011012.
54. Hsieh M-F (2010) Control of Diesel Engine Urea Selective Catalytic Reduction Systems, Ph.D. Dissertation, The Ohio State University.

Part VI
Ammonia Supply

Chapter 15

DEF Systems and Aftertreatment Architecture Considerations

Ryan Floyd, Levin Michael and Zafar Shaikh

As emissions regulations become more stringent, new aftertreatment technologies are necessary. To assist in the reduction of NO_x emissions, liquid-based SCR technologies have been adopted globally. The most common technique used to introduce ammonia (NH_3) into the exhaust stream is via a dosing system metering diesel exhaust fluid (DEF). SCR system efficiency relies heavily on how uniformly the NH_3 is distributed across the catalyst face. The challenge of preparing uniform NH_3 mixture includes the following (see Fig. 15.1):

- Spraying atomized urea/water solution (DEF) into a mixing section.
- Interaction between liquid drops and exhaust gas, as influenced by varying gas velocity and temperature, dosed urea quantity, droplet size, and quantity control method (pulse width or pulse frequency).
- Decomposition of urea and formation of NH_3 and HNCO gaseous compounds.
- Evaporation of water from droplet surfaces and corresponding increase in urea concentration inside the droplets.
- Uniform mixing of NH_3 , HNCO , and the remainder of nondecomposed high-concentration urea particles.

Complete decomposition of urea into NH_3 is not possible given insufficient residence time inside typical mixing spaces found in automotive applications. But as long as a uniform mix is available at the SCR entry, urea decomposition will continue in uniform manner inside the SCR. Thus, most attention in developing the mixing section is devoted to achieving a uniform concentration of gases at the SCR entry.

R. Floyd (✉)

XNO_x Systems Development, SCR Integration and Test Fleet at Tenneco, Jackson,
MI 49201, USA
e-mail: RFloyd1@Tenneco.com

L. Michael · Z. Shaikh

Ford Motor Co, Dearborn, MI, USA

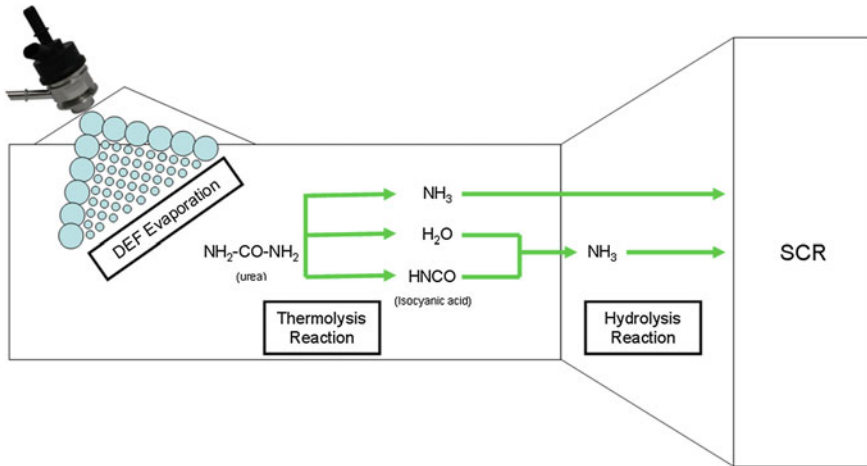


Fig. 15.1 High-level overview of DEF decomposition mechanism

The mixing uniformity challenge has to be met throughout the wide and continuously varying range of exhaust flow and temperature, which produces variability of spray dispersion and deflection from its injection angle, resulting in variability of spray interaction with mixing elements. These phenomena are influenced by injector performance characteristics that include droplet size, spray cone-type (filled, hollow, or individual jets), injection angle, as well as injector tip recess relative to the pipe ID, and gas flow pattern near the spray entry.

The complexity associated with implementing a liquid-based SCR system increases with more stringent NO_x reduction targets. In general, the more stringent the emissions, the more efficient the SCR system must be. To achieve an efficient system, aftertreatment geometry, injector technology, dosing rates, and engine calibration all need to be considered and optimized as a system. Due to their interactive dependencies, taking a component-level approach to integration will prove difficult to meet EPA 2010, Euro VI, and Tier IV Final emission regulations. Because the NO_x reduction targets for these regulations are so aggressive (0.27, 0.4 and 0.4 g/kWh respectively), the implementation of SCR technology should be understood at a system level for maximum efficiency. Having a system level understanding means that all of the necessary inputs and their interactions have been considered and will be implemented in a way where they work together to achieve the NO_x reduction goals of the system. Figure 15.2 provides a pictorial description of the points mentioned above. Understanding the role that each of the inputs plays with respect to achieving NO_x reduction leads to the creation of an optimized system.

After each input has been identified, the engineering process of creating the system begins. The best way to optimize the NO_x abatement system is to follow a defined development process. Figure 15.3 outlines a typical systematic NO_x abatement development process. This process requires an in-depth understanding

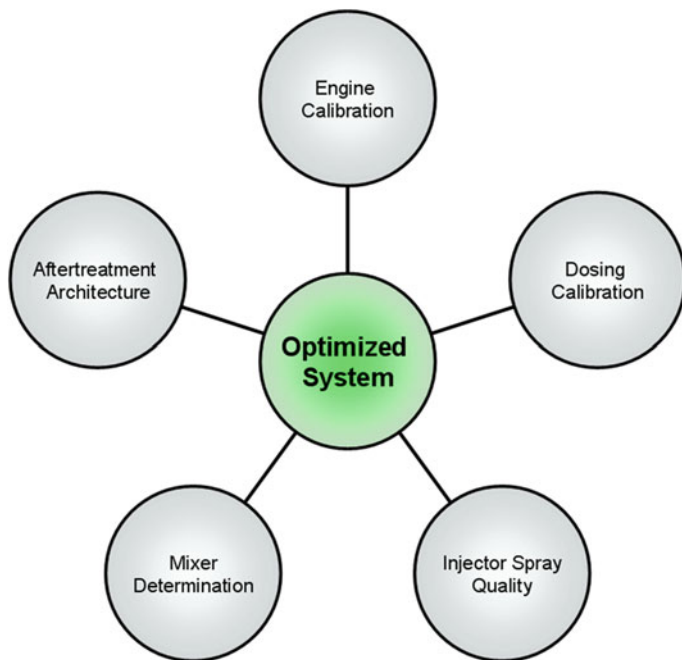
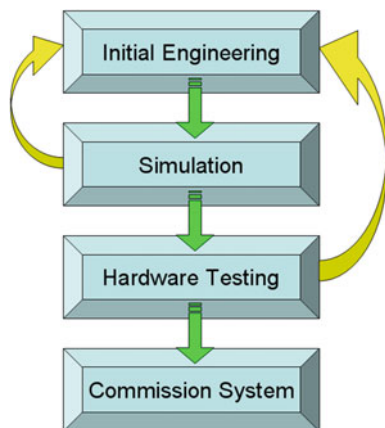


Fig. 15.2 Requirements for an optimized NO_x abatement system

Fig. 15.3 NO_x abatement system development process flow



of the application being targeted for the NO_x abatement system. From this information, simulation and hardware testing can occur. Both 1D and 3D simulations can provide valuable information relative to creating and optimizing a NO_x abatement system. Although significant benefit can come from simulation work, if the input values are not accurate and the simulation work is not correlated with hardware testing, it can lead to wasted time and effort. Once proper correlation has

occurred between hardware and simulation, the simulation tools can be used in an iterative process to improve a design before hardware is built. This correlation may be necessary for each targeted application. It is not guaranteed that once the simulation tool correlates to an aftertreatment hardware set, that it will always correlate to all applications. Simulation programs provide an opportunity to quickly evaluate designs without the additional costs associated with building hardware and running engine dynamometer test cells. After the NO_x abatement system has been thoroughly analyzed in simulation, hardware needs to be created and tested. Hardware testing should be performed in a way that evaluates the NO_x reduction efficiency, deposit formation concerns, and overall system robustness. If during this process it is shown that the system will not achieve the intended performance, iterations of the overall design of the system must occur. The subsequent design iterations should begin in the simulation step, with the actual hardware results being fed back into the models for more accurate simulation results in the future.

The most critical piece of the development process flow is the initial engineering step. Figure 15.4 outlines the steps associated with the initial engineering step. Without proper effort during this stage, the project can start down the wrong path, which can ultimately lead to on-application performance issues. The two most common performance issues are NO_x reduction efficiency and urea deposit concerns. The three primary steps to initial engineering are defining system goals, quantifying inputs, and designing the system. The first step related to defining system goals relates to determining what emission regulation the application needs to adhere to, what type of DEF delivery system will be targeted, what the NO_x reduction and backpressure targets will be, and others that define the boundary conditions of the project. The second step, quantifying inputs, relates to retrieving information specific to the application including but not limited to engine emission data, allowable packaging space claim for the NO_x abatement system and typical duty cycle usage. The final step related to initial engineering is the creation of the initial design. The initial design will incorporate the information gained while defining goals for the system and quantifying the inputs. Incorporating this information into the design will provide a good starting point for the design prior to beginning the simulation phase. The more accurate the information feeding the design, the more robust and representative the design will be.

Following a defined development process will help reduce the amount of time necessary to complete a full NO_x abatement system design and system implementation. Successfully completing each step will also reduce the risk associated with in-field failures or issues related to meeting emission certification. Not following a defined process can lead to wasted resources (time, effort, and money) pursuing designs that will not be able to achieve the desired performance requirements. The remainder of this chapter will be focused on describing the primary inputs to an SCR aftertreatment system outlined in Fig. 15.2.

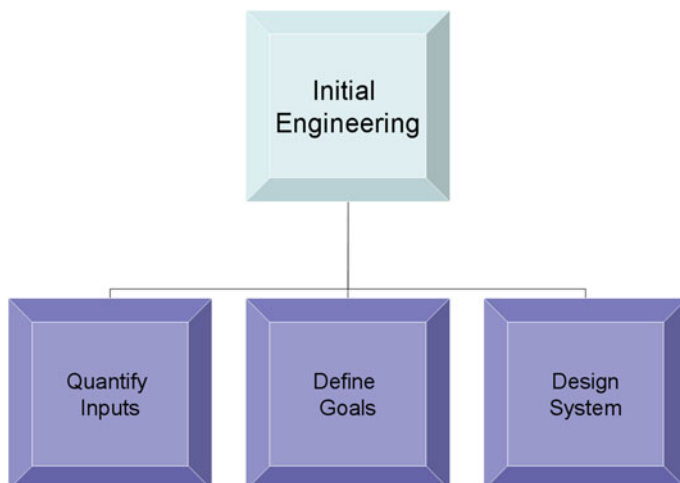


Fig. 15.4 Overview of the initial engineering step

15.1 Role of Engine and Dosing Calibration

As mentioned previously, DEF is metered into the aftertreatment system to reduce tailpipe NO_x emissions. The amount of DEF that needs to be metered into the aftertreatment system is part of the dosing calibration. This dosing calibration is directly linked to the engine calibration. The amount of NO_x created during the combustion process is driven by the engine calibration. Through proper tuning, the dosing calibration is created in a way to meter the proper amount of DEF into the system to reduce the tailpipe NO_x to meet the targeted NO_x level. Figure 15.5 shows how engine calibration and dosing calibration are related to the systemic approach to designing a robust SCR system.

Determining steady-state dosing quantity is a straightforward process. Although this process is straightforward, it does not necessarily reflect the dosing quantity that will be used in the application's final dosing calibration. The reason for the difference is that the final dosing calibration will also consider the SCR catalyst storage characteristics, exhaust gas temperature and targeted reduction to meet the emission regulation. For the purposes of this section, only the chemistry will be considered. Equation 15.1 outlines the equation used to determine the ammonia (NH_3) concentration from a given amount of injected DEF. This equation can also be used to determine the necessary amount of DEF that needs to be injected to create a certain amount of NH_3 . Within the equation, $M_{\text{H}_4\text{N}_2\text{CO}}$ is the molecular mass of urea, which is equal to 60.0 g/mol. The average exhaust molecular mass is assumed to be 28.8 g/mol and is denoted as M_{exh} . Lastly, \dot{m}_{exh} represents that mass flow rate of the exhaust in kg/h.

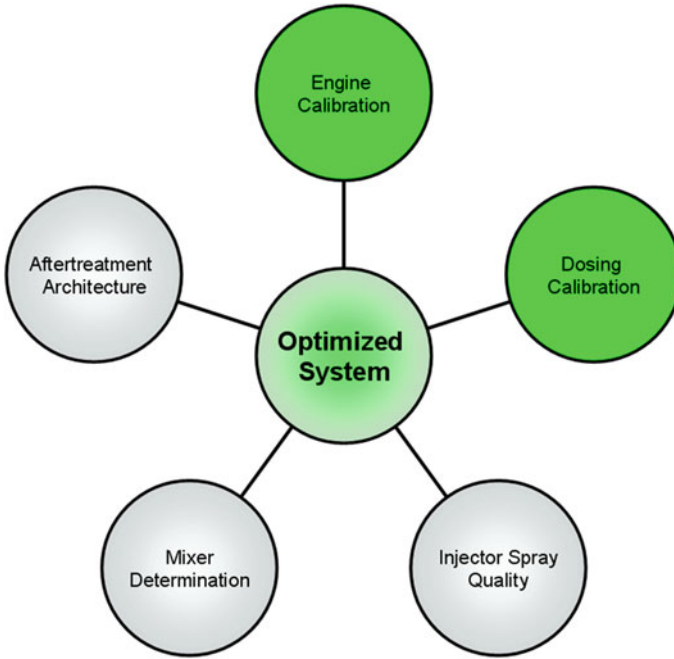


Fig. 15.5 Role of engine and dosing calibration in SCR system optimization

$$\text{NH}_3 [\text{ppm}] = \frac{\text{DEF}[\text{g/h}] * 0.325 * 2}{\frac{M_{\text{H}_4\text{N}_2\text{CO}}}{\dot{m}_{\text{exh}} * 1000} * M_{\text{exh}}} * 10^6 \quad (15.1)$$

The amount of NH_3 that needs to be injected under a given condition relates to the targeted ammonia to NO_x ratio (ANR). If the ANR is equal to one, then the amount of NH_3 (ppm) should be equal to the NO_x concentration (ppm) measured during the targeted steady-state condition. As mentioned previously, the ANR term will vary based on engine condition and the chosen catalyst washcoat technology. Figure 15.6 shows an example of an ANR sweep. An ANR sweep is a steady-state test where the amount of DEF injected is increased and the NO_x reduction and ammonia slip is measured at the outlet of the SCR. Ammonia slip represents the ammonia concentration measured that passed through the catalyst without reacting with the NO_x . An ANR sweep is a good tool that can be used to evaluate the steady-state performance of the system. As shown in Fig. 15.6, as the ANR ratio is increased, more NO_x is reduced while ammonia slip increases.

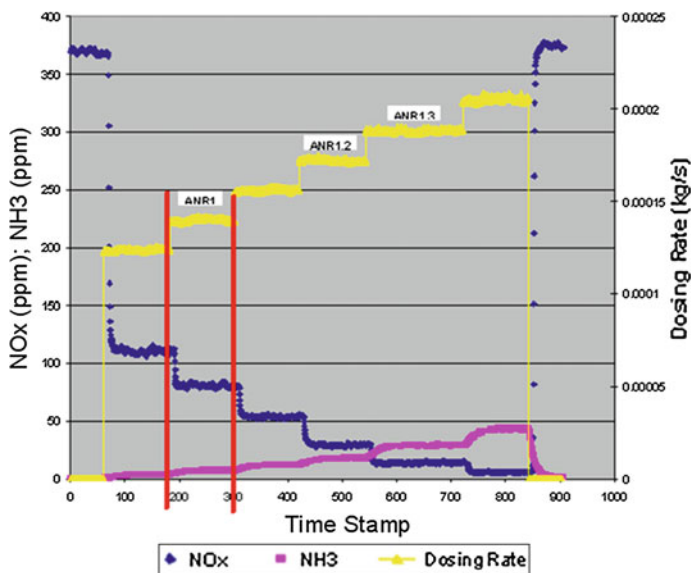


Fig. 15.6 ANR sweep example

15.2 Overview of Injection Technology and Spray Quality

For systems that utilize DEF injection, there are two primary technologies utilized. One type of doser mixes air with the liquid DEF to create the spray that is introduced into the aftertreatment system. This type of system is called an air-assisted system and it utilizes a metering pump and a dumb nozzle. The second type of system is called an airless system, which utilizes an injector to meter liquid DEF directly into the exhaust. The focus of this section will be on airless technology, specifically, two different styles of metering injectors, pressure swirl and liquid jet. Regardless of the injection technology, two main inputs need to be understood when implementing it into the system. The two inputs are dosing quantity and spray quality. Dosing quantity relates to the amount of DEF that needs to be introduced into the exhaust to reduce the targeted amount of NO_x for a given condition and was covered in Sect. 15.1. Spray quality is associated with the evaporation and decomposition of the DEF spray droplet as well as how the spray interacts with the exhaust flow. Figure 15.7 highlights the role of injector spray quality in an optimized SCR system design.

While spray quantity is important to achieving NO_x reduction performance, it is independent of the type of injector technology chosen. Instead, spray quality is a primary metric used in determining the injector and mixing technology that is used. Spray quality is a measure of the size, speed, and pattern of the DEF droplets that enter the exhaust stream. Two types of test equipment used to quantify spray quality are shown in Fig. 15.8. The piece of equipment shown on the left of the

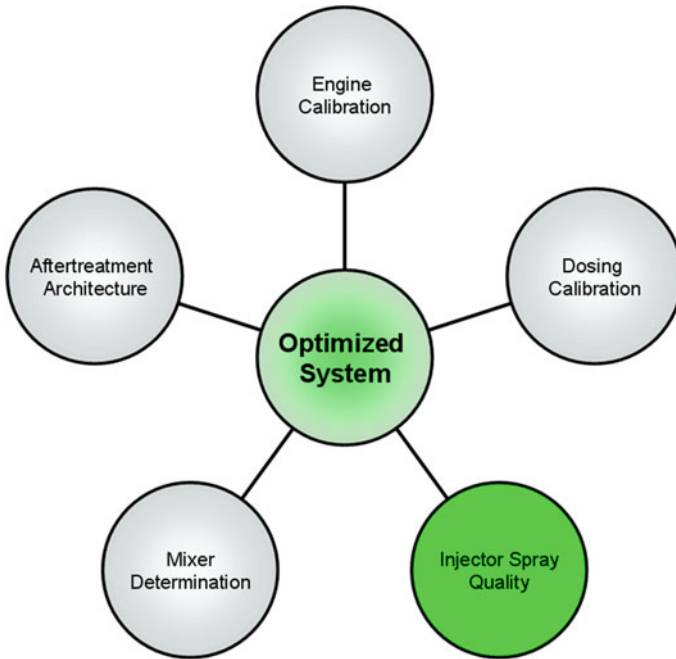


Fig. 15.7 Role of injector spray quality in SCR system optimization



Fig. 15.8 Spray quality measurements equipment. *Left* PDPA. *Right* Patternator

picture is a Phase Doppler Particle Analyzer (PDPA) and the piece of equipment on the right is called a patternator. The PDPA is able to provide droplet size, spray angle, particle concentration, droplet distribution, droplet measurement count, and velocity values. These values are measured using light refraction of the droplets that pass through an intersecting laser probe volume during a set period of time. A patternator is used to identify the spray pattern created by an injector as well as

<ul style="list-style-type: none"> • SMD (D32) <ul style="list-style-type: none"> – Sauter mean diameter – Considered industry standard average diameter measurement for spray 	$\frac{\sum n_i D_i^3}{\sum n_i D_i^2}$
<ul style="list-style-type: none"> • D10 <ul style="list-style-type: none"> – Arithmetic mean 	$\left(\frac{\sum n_i D_i}{\sum n_i} \right)$
<ul style="list-style-type: none"> • D31 <ul style="list-style-type: none"> – Evaporative mean 	$\left(\frac{\sum n_i D_i^3}{\sum n_i D_i} \right)^{1/2}$

Fig. 15.9 Spray quality calculations—SMD, D10 and D31

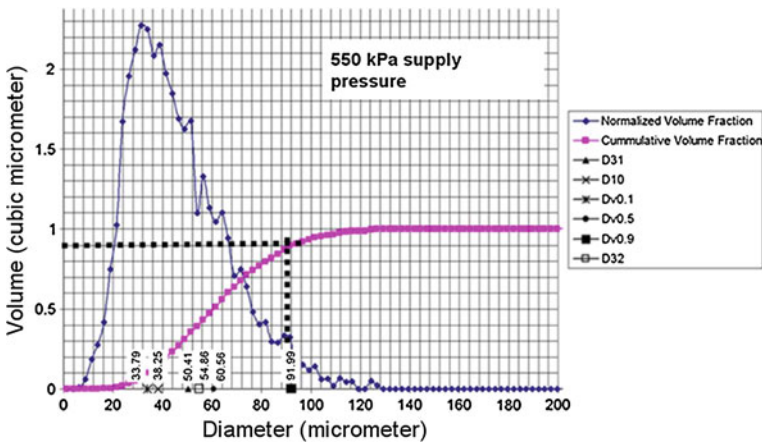


Fig. 15.10 Spray quality calculations—droplet distribution curve and Dv0.9

identifying the spray angle, roundness of the spray pattern, and skewness associated with the spray. Each piece of equipment provides valuable information needed to describe the spray quality of a given injector.

Not only are these tools important for injector development, they also provide critical information used as inputs for computational fluid dynamics (CFD) analysis. As mentioned previously, simulation plays a critical role in SCR system development. The more accurate the measurements are while quantifying an injector’s spray quality, the more accurate the simulated spray quality will be which will in turn give better correlation between simulation and hardware testing.

There are multiple spray measurements used to quantify an injectors spray quality. Some of these measurements include D10 (arithmetic mean), D32 (Sauter mean diameter), D31 (evaporative mean diameter), Dv0.9, and droplet distribution curve. Figure 15.9 provides a description and equation used to calculate SMD, D10, and D31. Figure 15.10 shows a typical droplet distribution curve with an overlay to show the Dv0.9 calculation. The Dv0.9 value represents the point where

Table 15.1 Sample spray quality measurement

Diameter measured (μm)	Count
25	12
45	50
65	150
85	32
105	40

90 % of the measured spray has less than the measurement reported for the $Dv_{0.9}$ value. This description also applies to $Dv_{0.1}$ (10 %) and $Dv_{0.5}$ (50 %) measurements.

To provide clarity when calculating Sauter mean diameter (D_{32}), an example has been provided below. The SMD measurement represents a one number descriptor used to compare different sprays and is considered industry standard for comparing spray quality. Table 15.1 provides a truncated sampling of a hypothetical spray. For this example, whole numbers are used to signify the number of droplets counted for a given diameter measurement. This data can be used to calculate the SMD for the example outlined below. Equations 15.2–15.4 show an example of how to calculate SMD based on the data provided in Table 15.1.

$$\frac{\sum n_i D_i^3}{\sum n_i D_i^2} \quad (15.2)$$

$$\frac{[12 * 25^3] + [50 * 45^3] + [150 * 65^3] + [32 * 85^3] + [40 * 105^3]}{[12 * 25^2] + [50 * 45^2] + [150 * 65^2] + [32 * 85^2] + [40 * 105^2]} \quad (15.3)$$

$$\text{SMD} = 79 \mu\text{m} \quad (15.4)$$

The information provided during the spray characterization process can be used to evaluate different injector technologies. The following examples are a comparison between a commercially available liquid jet style injector and to a pressure swirl style injector. Both injectors fall into the category of an airless injector. The liquid jet injector has three holes that the DEF is injected through whereas the pressure swirl injector only has one hole that the spray flows through. Figure 15.11 shows a side-by-side comparison of the patternator measurements collected. These measurements were made 49 mm from the exit of the injector. The plot for the pressure swirl injector shows that the spray created is a uniform circle with the highest concentration of droplets measured at the center of the spray. The liquid jet injector shows that the highest concentrations of the droplets are measured within the three jets.

Along with the patternator data, the PDPA was used to measure the droplet sizes and velocities. Like the patternator measurements, PDPA measurements were made 49 mm from the outlet of the injector. Figure 15.12 shows the velocity measurement as the measurement probe volume of the PDPA traversed axially through the spray cone. This means that the left side of plot represents the left side

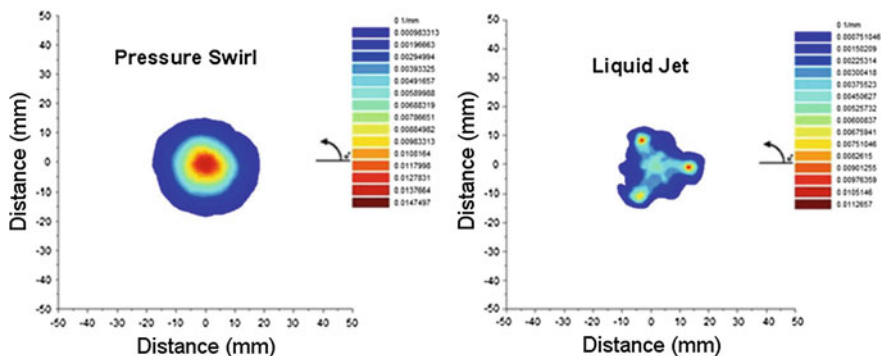


Fig. 15.11 Spray quality comparison—Patternator

of the spray and the right edge of the plot represents the right edge of the spray. For the pressure swirl style injector, the average velocity measured 49 mm from the injector exit is relatively consistent across the entire spray cone. For the liquid jet injector, the measurement probe volume was intentionally traversed through two of the three jet streams. For this injector, it was found that the individual jet streams had the highest concentration of drops (Fig. 15.11) and that these drops have a higher velocity than the other drops in the spray. The penetration of the droplets into the exhaust stream is based on the relationship between the droplet velocity and the exhaust gas velocity. This relationship quantifies whether or not the spray will impact the exhaust pipe walls (or the mixing element) and will be addressed further in the mixer determination section below.

Lastly, droplet distribution curves and droplet size characteristic measurements were made for each of the sprays. Figure 15.13 shows the droplet size characteristics for the pressure swirl injector and Fig. 15.14 shows the droplet size characteristics for the liquid jet injector. The droplet size distribution is shown in both a cumulative and normalized sense. The cumulative volume fraction is used to determine $Dv0.1$, $Dv0.5$, and $Dv0.9$ measurements. The calculated values for $D10$, $D31$, and SMD are also shown on each plot. In general, the pressure swirl injector analyzed had a tighter distribution of injected droplets. The tighter distribution means that there are fewer larger droplets measured, which create smaller values for all of the key droplet characteristics, measured ($D31$, $D10$, $Dv0.1$, $Dv0.5$, $Dv0.9$, and $D32$).

Spray quality plays a critical role in system level performance. Regardless of the doser technology chosen, a thorough understanding of the developed spray characteristics is required to begin to model system level interactions. The spray interaction with the exhaust gas flow is the first portion of the DEF system performance described earlier in Fig. 15.1. Integrating good spray quality into an optimized SCR system design reduces the risk that the overall system will have issues related to droplet impingement, incomplete decomposition, or deposit formation.

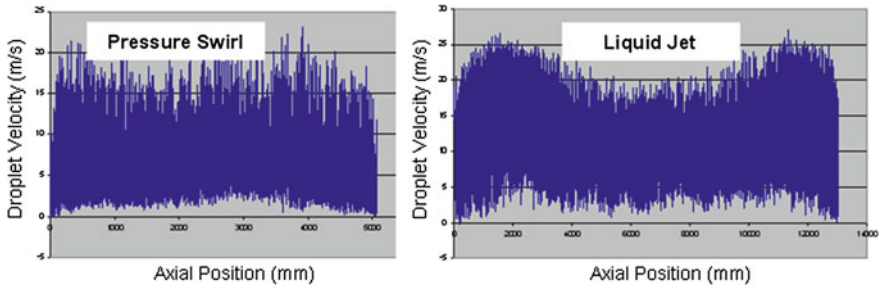


Fig. 15.12 Spray quality comparison—droplet velocity

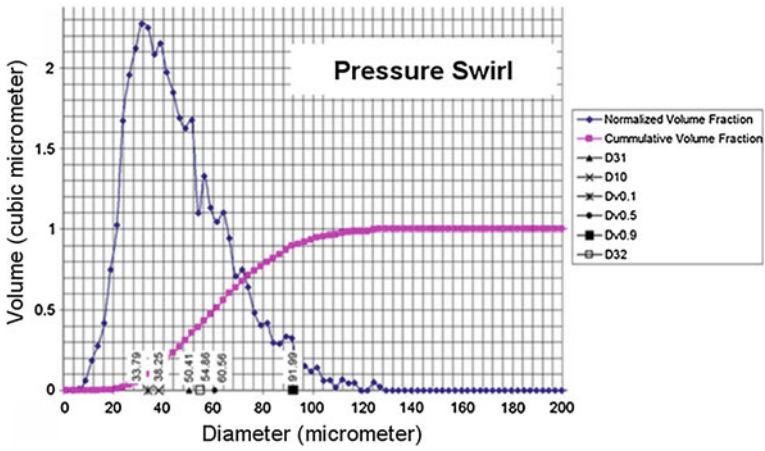


Fig. 15.13 Spray quality comparison—droplet size (pressure swirl injector)

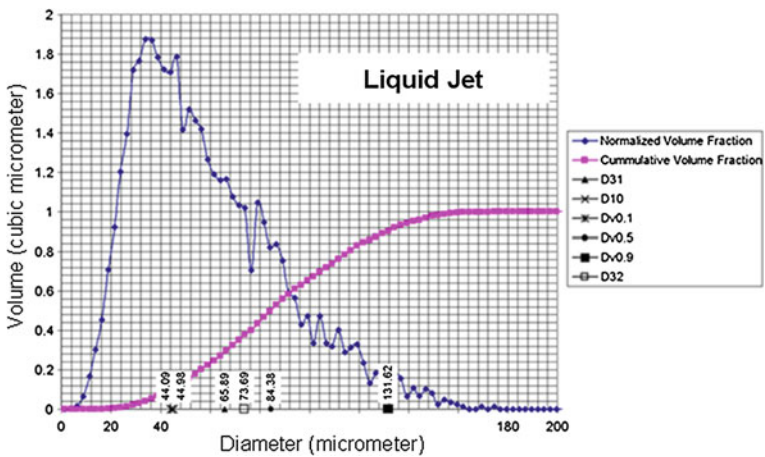


Fig. 15.14 Spray quality comparison—droplet size (liquid jet injector)

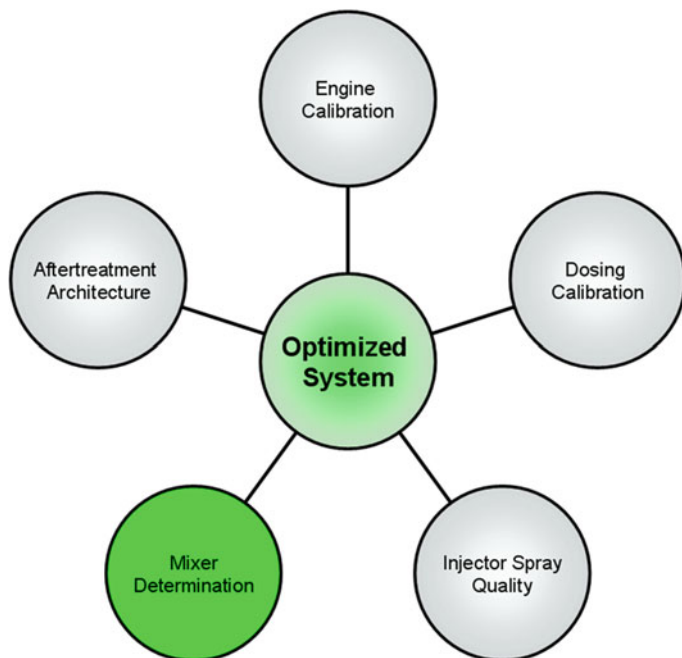


Fig. 15.15 Role of mixer determination in SCR system optimization

15.3 Overview of SCR System Mixing Devices

Mixing devices are used in SCR aftertreatment systems to improve system performance. Figure 15.15 shows the role of mixer determination in the SCR system design process. The type of mixer chosen, and how it is integrated into the aftertreatment system, can help improve system performance by improving SCR uniformity and reducing the risk of deposit formation due to incomplete DEF decomposition. Improper integration of a mixing element can hinder system performance and introduce deposit formation concerns.

There are multiple types of mixing devices used in current production SCR systems globally. For the purposes of this section, the focus will be spent on three different types of mixers; a 2-stage mixer, an in-pipe style mixer, and a swirl style mixer (Fig. 15.16). Each of these styles performs well under certain applications and operational duty cycles, and not so well in others. Along with mixer type, injector placement and injector mount geometry also needs to be considered when designing the mixing portion of the decomposition tube. The decomposition tube is considered as the portion of the aftertreatment system from the injector to the mixer outlet. Although decomposition continues to occur after the mixing unit, the section immediately following the mixing unit will be called the mixing tube.

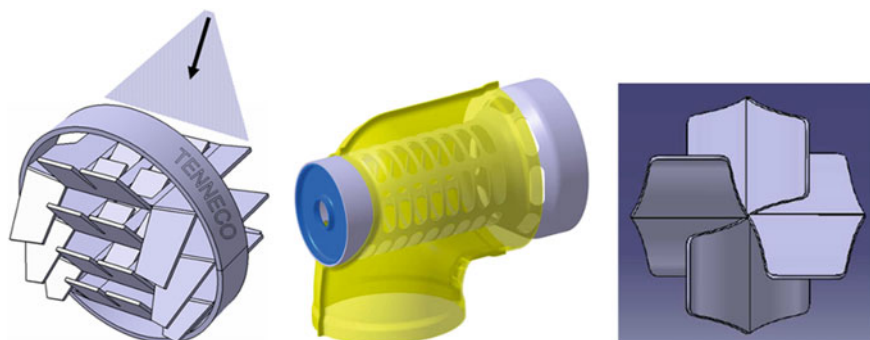


Fig. 15.16 Mixer designs, 2-stage (*left*), in-pipe (*center*) and swirl style (*right*)

Attributes of a well-designed mixing/decomp tube include shortening allowable decomposition/mixing length, reducing DEF consumption and managing lower temperature applications. Figure 15.17 shows an example of how the proper use of a mixing device can help reduce DEF consumption and improve NO_x reduction efficiency. The original system had a nonoptimized mixing solution present. Following the defined process outlined in Fig. 15.3, the system now required a lower dosing rate (under the steady state test point tested) to achieve the same amount of NO_x reduction. It is important to understand that from a chemical perspective, the mixing device chosen will not help create additional ammonia. Instead, this example is highlighting the fact that optimizing the mixer selection and location will improve the velocity and species uniformity on the inlet of the catalyst, thereby increasing the amount of catalyst used.

The primary goal of system optimization is to achieve high velocity and species uniformity at the inlet of the SCR. Having high velocity uniformity means that the gas flowing through the SCR catalyst is well distributed. A high species uniformity means that the concentration of the species (ammonia and isocyanic acid) are evenly distributed across the SCR inlet. Equation 15.5 provides how to calculate uniformity where X is the variable being measured, A is the total area of the catalyst sampled and A_i is the area of each individual node measured within the overall area.

$$\gamma = 1 - \frac{1}{2} \sum_{i=1}^n \frac{|X_i - X_{\text{mean}}| A_i}{A X_{\text{mean}}} \quad (15.5)$$

Without good distribution, the SCR system will be prone to increased DEF consumption, decreased NO_x reduction, and increased NH_3 slip (Fig. 15.18). Although Fig. 15.18 shows a comparison between a no mixer scenario and to an SCR system with a mixer, the trend will remain true for a system with an optimized mixing solution compared to one without an optimized mixing solution. Therefore, it is important that care is taken when determining a mixer for an application as well as how the mixer is implemented.

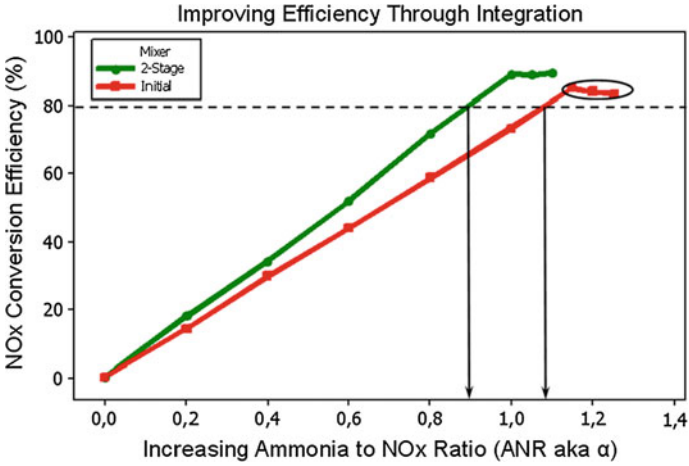


Fig. 15.17 System optimization through mixer integration

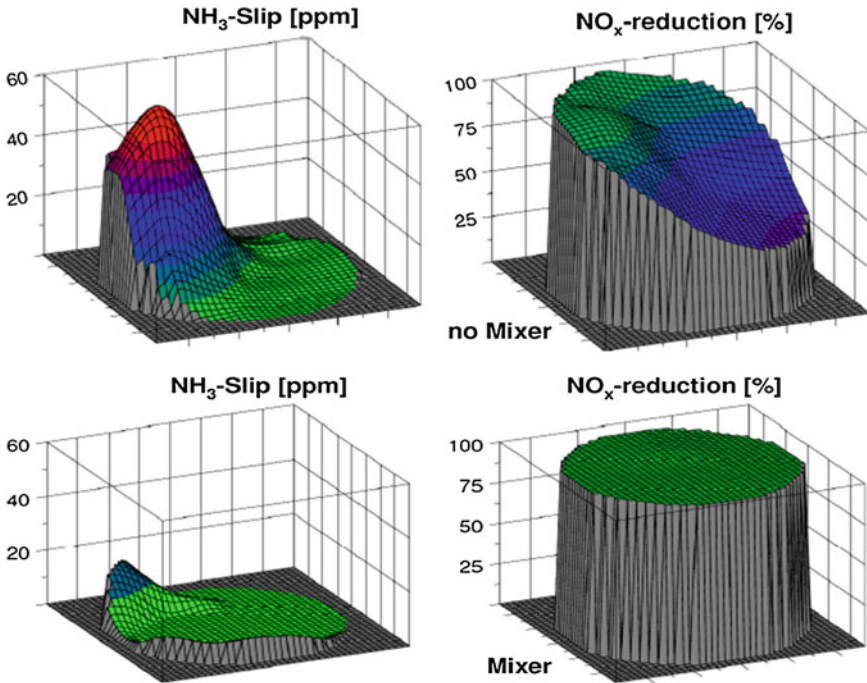
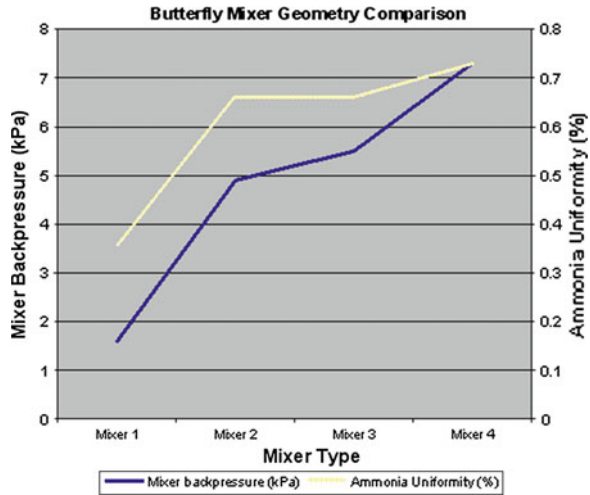


Fig. 15.18 The role of efficient mixing in SCR systems

A primary concern with mixing devices is the increase in backpressure associated with implementing a mixing device. The trade-off between mixing efficiency and backpressure are key factors in designing the decomposition tube.

Fig. 15.19 Backpressure versus mixing performance trade-off curve—butterfly mixer



In general, higher mixing efficiency (turbulence after the mixer) produces higher backpressure. Figure 15.19 provides a backpressure versus mixing performance (NO_x reduction efficiency uniformity) for the butterfly mixer shown in Fig. 15.16. The aggressiveness of the angles of the blades has been adjusted to improve species uniformity at the SCR inlet. As shown in Fig. 15.19, the steeper the angle of the blades, the greater the backpressure as well as the greater the mixing efficiency.

After the type of mixer has been determined and the applications backpressure requirements are understood, the mixer placement needs to be determined. For this step, a CFD program can be used to determine the ideal position for the mixer. Using a CFD program will require having accurate information related to the duty cycle of the application as well as the injector that will be used. The interaction between the energy of the injected DEF spray and the energy of the exhaust will determine the penetration distance of the spray. Figure 15.20 shows an example of spray droplet penetration and the mixer position. As observed in the picture on the left, without a mixer, the droplets would penetrate through the exhaust flow and impinge on the exhaust pipe wall on the opposing side of the injector. Doing this, can lead to issues caused by the DEF impinging on the exhaust pipe wall and locally cooling the surface. Once the exhaust pipe is cooled, the system has the potential to form urea-based deposits. For this reason, a picture on the right shows the position of the mixer placement to ensure that the injected DEF does not impinge on the exhaust pipe wall and instead properly impinges on the 2-stage mixing device.

Mixer placement is not only limited to reducing the potential for impingement on the exhaust pipe, but it also needs to meet the backpressure, velocity, and species uniformity targets. To do this effectively, the engine conditions need to be understood. The primary engine outputs that need to be considered are exhaust mass flow

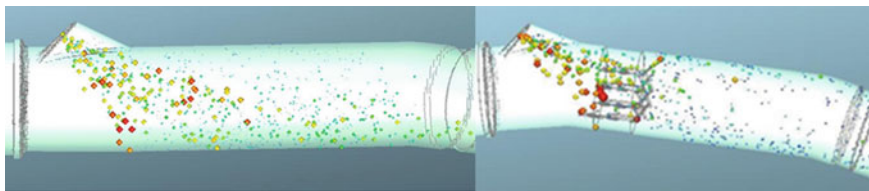


Fig. 15.20 Mixer placement example—2-stage mixer

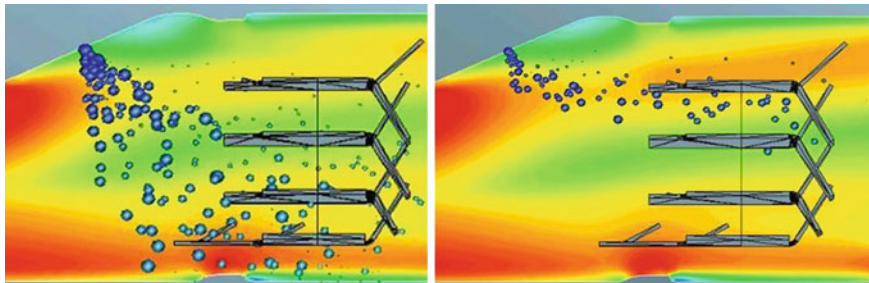


Fig. 15.21 Mixer placement example—2-stage mixer impingement: Low flow (*left*), high flow (*right*)

rate, exhaust gas temperature, and NO_x concentration. Using this information, the CFD model will be accurate and the dosing quantity can be calculated. Additionally, mixer placement cannot be based only on one engine condition. Multiple conditions need to be evaluated in order to fully understand mixer impingement and system performance. Evaluating the system at both low and high mass flow, rate conditions provides valuable information relating to how the injected spray will impinge on the mixer. Figure 15.21 shows the proper configuration for the 2-stage mixer. Under the low flow rate condition (*left*), the droplets penetrate through the gas stream and impinge on the bottom layers of the mixer. During high flow rate conditions (*right*), the droplets still impinge on the mixer. Moving the mixer too far away from the injector increases the risk of the injected spray penetrating through the exhaust and creating the increased potential for DEF pooling on the inside of the exhaust pipe causing urea deposit formation.

15.4 SCR System Mixing Devices: Ford Practical Example

Mixing space limitations in exhaust systems of Ford diesel trucks imposed a difficult set of design constraints. At the same time, fixed injector design parameters (injection pressure, spray angle, droplet size, etc.) and some combinations of exhaust flow and temperature resulted in very short residence times (below 20 ms) for droplet evaporation and urea decomposition.

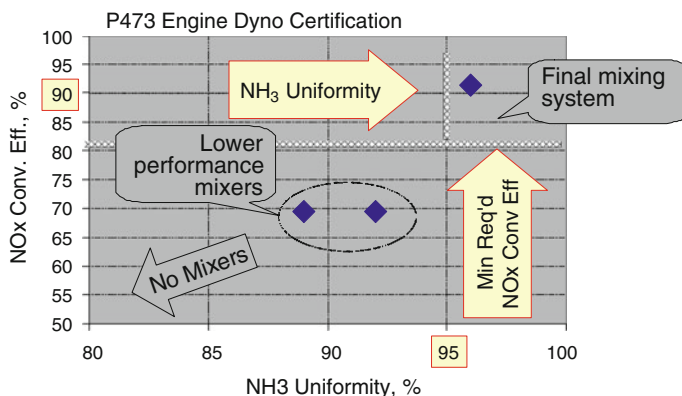


Fig. 15.22 The NO_x conversion efficiency as a function of NH₃ uniformity

To achieve the required NO_x conversion efficiency with these constraints, a single uniformity target for all operating conditions was needed. A series of engine tests was run to determine an effect of mixing uniformity on NO_x emissions. Various mixer designs were tried and produced the data summarized in Fig. 15.22. Here the NO_x conversion efficiency is plotted as a function of mixing uniformity. As the result of the mixer selection process it became possible to meet the NO_x conversion target of 90 % only when uniformity levels were greater than 95 %. To achieve this high level of uniformity, new NH₃ sampling and data analysis methods were developed, as described in the following sections.

To evaluate urea mixing quality, a new test rig was designed and built. The rig allowed collection of 37 ammonia concentration values in about 1 h. The values were collected at the end of the mixing section followed by a short flow-straightening element (Fig. 15.23). A rotating sample probe was designed with a minimal resistance to the gas flow. The data was organized to produce a circular pattern that showed sensitivity to an interaction between the atomized liquid and the gas flow.

The new sampling technique reduced reliance on CFD modeling that, with numerous hardware changes, became more time-consuming and not sufficiently accurate in predicting local gas concentrations. The high-cost engine dynamometer testing was reserved for the rig data validation.

Initial analysis of uniformity was based on the industry-wide uniformity index known as the gamma value. The index is generally expected to take into account local concentration values anywhere within the studied gas flow area. However, when compared to changes in uniformity pattern produced by various mixers, the index was not sufficiently sensitive to certain types of nonuniform distribution resulting in overly optimistic values.

This led to the need to describe uniformity patterns produced by various mixers, and to characterize these patterns in some way. The rotating probe produced data that could be grouped according to the three diameters resulting from rotation of

Fig. 15.23 Rotating sampling probe

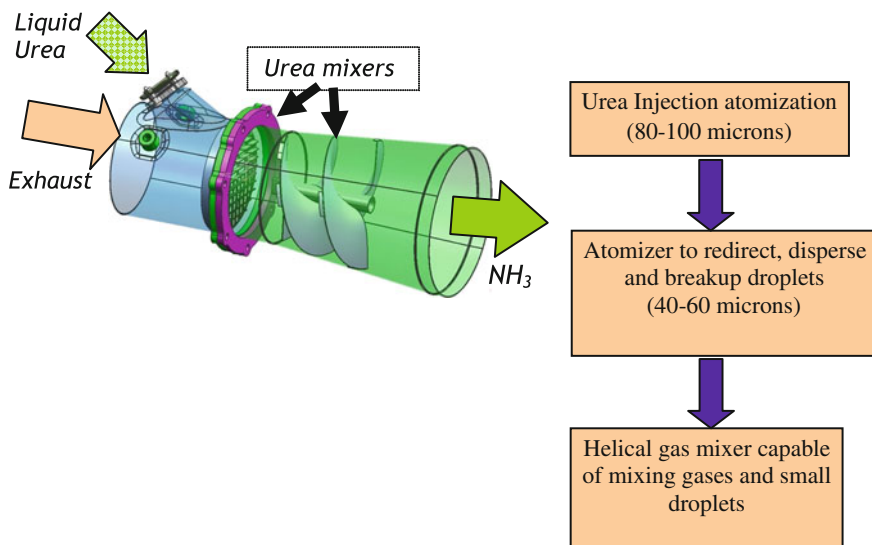
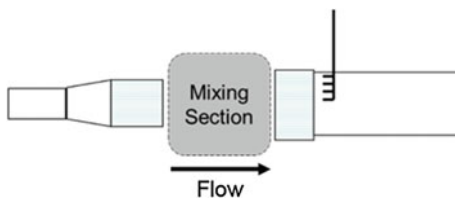


Fig. 15.24 Ford 2-mixer system

probe cell centers. This made it easier to relate uniformity patterns to the round cross-section of the SCR inlet.

The technique was sufficiently sensitive to small changes in uniformity and became a useful tool for continuous improvement of mixing hardware. It allowed:

- Faster comparison of mixing hardware designs and selection of best configurations.
- Fine tuning of mixing hardware within particular mixing section packaging constraints.
- Good correlation of rig uniformity data with engine and vehicle NO_x reduction data.

The uniform mixing (with 95 % gamma or better) was achieved with a 2-mixer approach, using a pre-mixer and a gas mixer, both located downstream of the dosing injector. The spray direction was chosen to form a 45° angle with exhaust flow (Fig. 15.24). The functions of the two mixers were as follows.

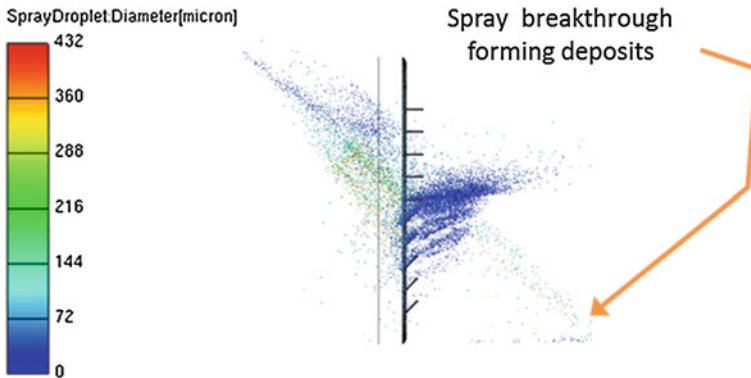


Fig. 15.25 Spray impingement, re-direction and breakthrough

The pre-mixer contained a multitude of spray impingement plates to enable the following:

- (a) Redirect spray to align it with exhaust flow,
- (b) Disperse liquid drops, and
- (c) Facilitate a breakup of urea droplets (secondary atomization).

The width, spacing, and angle of impingement plates were optimized to improve these functions. The angle was adjusted to make the droplets arrive at the center of the main mixer within the variability of the impingement footprint at the mixer entry. The spacing and the width prevented spray breakthrough, so that none of the droplets could pass through the atomizer without being deflected and land at the bottom of the pipe (Fig. 15.25).

The main helically shaped gas mixer (auger mixer) was placed downstream of the atomizer to mix the gaseous fractions and the remaining small drops with exhaust gas. Avoiding reduction in the pipe diameter, allowed achieving the target uniformity levels without exceeding backpressure targets. The helix pitch and the location of the mixer were optimized as a compromise between the space constraints, the uniformity and the backpressure targets.

15.5 Aftertreatment Architecture

The aftertreatment architecture describes the geometry of the decomposition tube, the aftertreatment configuration upstream of the dosing unit, the aftertreatment configuration after the dosing unit (including the mixer), and the catalyst. Figure 15.26 shows the role of aftertreatment architecture in an optimized system design. Like the mixer, the overall geometry of the aftertreatment architecture can either improve system performance or cause system level problems.

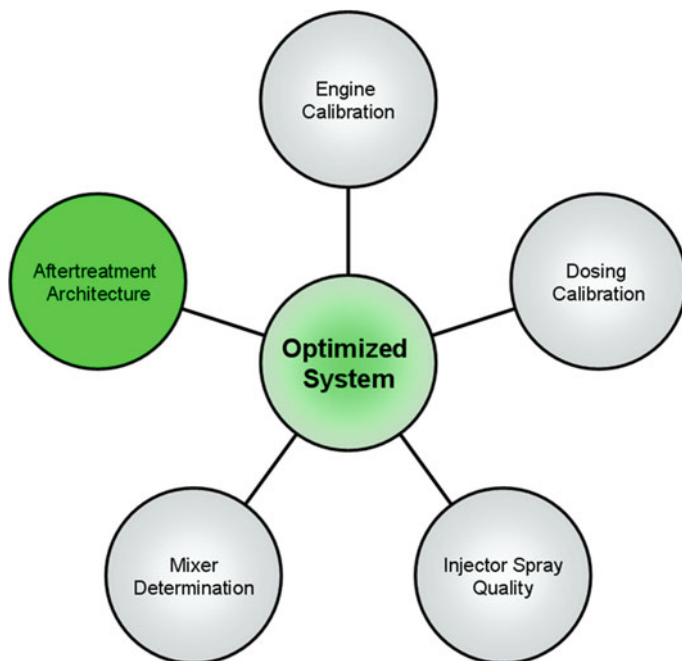


Fig. 15.26 Role of aftertreatment architecture in SCR system optimization

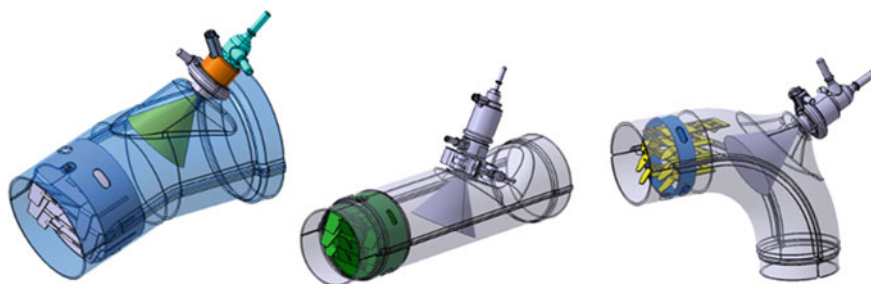


Fig. 15.27 Potential injector mount designs

Because available packaging space and representative duty cycles are not identical between applications, injector mount geometry needs to be optimized based on the targeted application. Figure 15.27 highlights three potential injector mount configurations. The mount on the left is a two-piece stamped design where the injector is recessed from the centerline of the exhaust. This type of configuration has been traditionally utilized in many on-road EPA 2010 compliant applications. Benefits of this configuration include reduced temperature at the outlet of the injector as well as increased distance from the injector to the mixer.

A potential disadvantage of this configuration is an increased potential for exhaust gas recirculation leading to urea deposits in the injector mount housing. The mount geometry in the center is called the inverted mount. The inverted mount moves the injector closer to the centerline of the exhaust gas by placing a V-shape in the exhaust pipe. This type of configuration helps to create flow separation and reduces the potential for deposits in the exhaust mount. Some potential disadvantages include a decreased distance from the injector to the exhaust pipe wall on the opposite side of the injector as well as an increased injector temperature and increased exhaust backpressure. The final design layout is considered an elbow style design. This type of design is prevalent on nonroad applications as well as heavy-duty on-road vehicles. The advantage of an elbow style mount is that the injected DEF is sprayed co-axially into the exhaust stream. This reduces the risk of droplet impingement on the exhaust pipe wall opposing the injector.

After an injector mount geometry and mixer has been determined for an application, the interaction between the pieces needs to be considered and understood. As mentioned in [Sect. 15.4](#), the mixer needs to be placed in a location to achieve the greatest performance at all of the potential operating conditions. [Figure 15.28](#) provides a cross-section of an elbow design with a 2-stage style mixer.

The point of injection defines the distance from the injector outlet to the mixer face (also called the decomposition portion). The distance from the outlet of the mixer to the face of the substrate is called the mixing pipe. Both of these dimensions, as well as the injector mount geometry chosen, has to be evaluated based on the available packaging space for the given application.

For most applications, the ideal aftertreatment geometry and routing will not fit. Because of this, an applications available packaging space needs to be considered when designing the aftertreatment system and integrating the dosing system. Packaging space refers to the allowable area that the aftertreatment fits in. [Figure 15.29](#) provides an example of incorporating aftertreatment design into the available application packaging space for an on-road heavy-duty truck. For this application, there was limited space to incorporate an aftertreatment system consisting of a DOC, dosing system and SCR. To achieve this configuration, an elbow style system was configured to meet the packaging space and performance requirements. A trade-off analysis was performed between temperature loss against system complexity. This trade-off analysis is required in system design because of the chemistry constraints related to temperature. At lower temperatures, reduced DEF decomposition occurs, there is reduced NO_x reduction efficiency due to SCR catalyst washcoat inefficiencies and there is an increased probability of urea deposit formation.

Incomplete decomposition of DEF can lead to deposits within the aftertreatment system. These deposits can have a negative effect on the overall performance of the system as well as the longevity of the application. [Figure 15.30](#) shows the DEF decomposition reactions that occur in the exhaust stream. Along with the primary reactions that produce the NH_3 necessary for reducing NO_x , there is potential for incomplete decomposition leading to deposit formation. The chemical

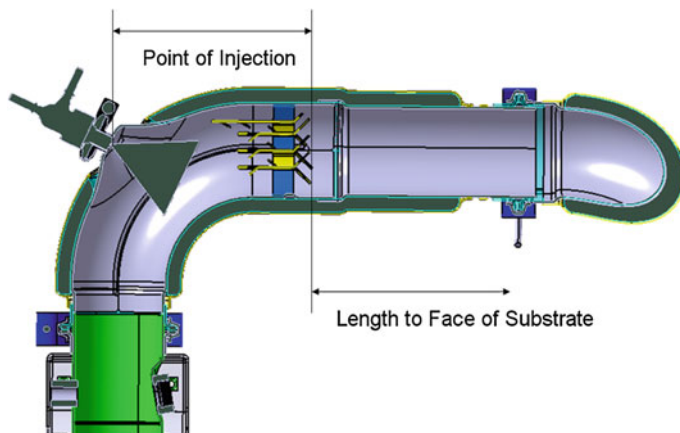


Fig. 15.28 Cross section of elbow style injector mount decomposition tube

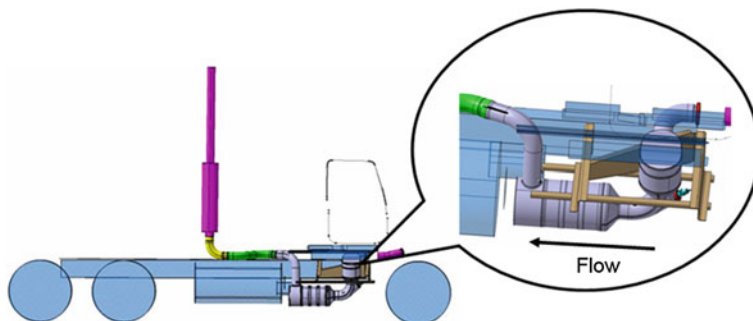


Fig. 15.29 Packaging space considerations

composition of the deposit depends on exhaust conditions and the amount of DEF decomposition that occurs. These deposits can be urea-based or isocyanic acid-based. Urea-based deposits include biuret and ammeline. If the urea makes it through the thermolysis reaction, the isocyanic acid that is created can also form unintended deposit byproducts. Examples of isocyanic acid-based deposits include cyanuric acid, ammelide, and melamine. These deposit formations occur under different conditions and can be mitigated in different ways.

Incomplete DEF decomposition leading to deposit formation is a condition that needs to be avoided and mitigated whenever possible. Multiple approaches can be taken in order to identify and address deposit formation concerns. In the early stages of SCR system development, it is critical that deposit risk is understood. To do this, an applications typical operating conditions and duty cycles need to be understood. For some applications, understanding the typical duty cycle is straightforward. On-road vehicles would fall into this category because

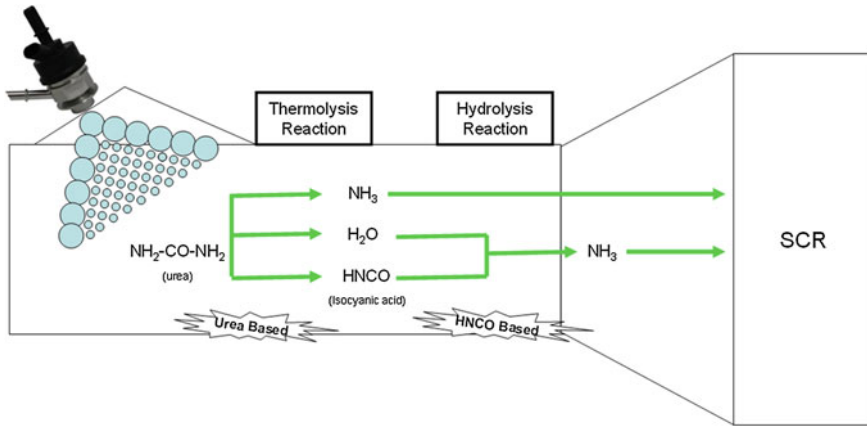


Fig. 15.30 Incomplete DEF decomposition leading to deposit formation

aftertreatment systems typically are designed for one application and that application has a similar daily duty cycle. Complexity comes for nonroad applications. This complexity exists because oftentimes for nonroad applications, there is an engine manufacturer that either provides engines to various machine groups or has loose engine sales. The aftertreatment is then sold with these engines and installed into many different machines. For this reason, nonroad aftertreatment systems traditionally need to be modular in order to adhere to the requirements of the various applications. These applications not only vary by packaging space but also relative duty cycles. With each machine operating differently, the type of deposit mitigation cycle chosen needs to be robust enough to encompass all of the potential uses.

Once a deposit mitigation test cycle has been established and deposit mapping occurs, a deposit mitigation strategy can be implemented. Figure 15.31 shows an example of a reversible deposit and the effect the deposit has on system level backpressure. The test was performed at a steady state test condition where the temperature was held constant at approximately $450\text{ }^\circ\text{C}$ over a 3.6 day period. During the test, depositing was monitored, and it was found that the deposits would meet a point of equilibrium and then decompose. This was observed with an increase in backpressure measured. Because of the adverse effect of backpressure on system performance, an active mitigation strategy would be needed to manage the risk of deposits within the application.

One type of deposit mitigation technique is active deposit sublimation. An active sublimation strategy increases the exhaust gas temperature so that the solid urea deposits turn back into the gaseous phase. Doing this reduces the performance impact caused by the deposits that had occurred in the aftertreatment. Along with an active sublimation strategy, adjusting engine and dosing calibration can also provide a viable deposit mitigation solution. Table 15.2 shows four potential test conditions. Test condition 3 had a $25\text{ }^\circ\text{C}$ increase in temperature and a 20 %

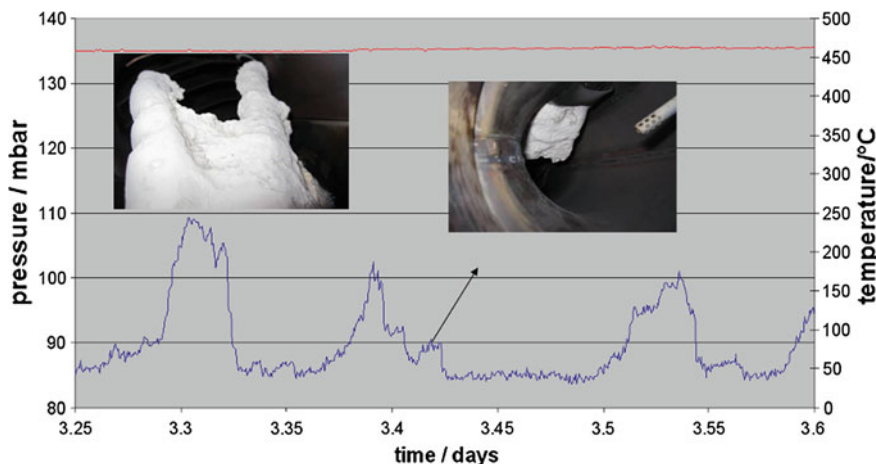


Fig. 15.31 Role of deposit formation on aftertreatment system backpressure

Table 15.2 Deposit mitigation test conditions

Test condition	Exhaust mass flow rate (kg/h)	Temperature (°C)	Dosing rate (g/h)	Decomp tube deposits (g)
1	250	200	150	12.2
2	700	200	1200	19
3	700	225	960	7.3
4	400	500	0	0

reduction in dosing rate in comparison to test condition 2. Figure 15.32 shows a side-by-side comparison of the two mixers after test conditions 2 and 3. The minor calibration modifications between test conditions 2 and 3 reduced the deposit accumulation by 62 %. The fourth test condition increased the exhaust gas temperature, similar to the active sublimation strategy outlined above, which removed all of the deposits that had accumulated.

A systematic approach is necessary for successful implementation of a liquid-based SCR system. Without a systematic approach, the application runs the risk of exceeding established budgets, missing timing, forming deposits, and not meeting NO_x reduction targets. Through these predefined steps, an SCR integration exercise will create a robust system.

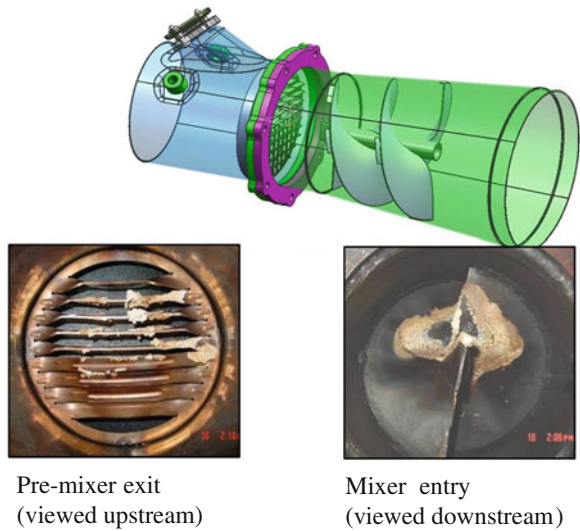
15.6 Deposit Mitigation: Practical Example

Ideally the injected liquid should not come in contact with any surfaces and remain airborne until a complete decomposition of urea into ammonia. However, mixing space constraints and injection design parameters make that impossible.



Fig. 15.32 Impact of calibration modifications on mixer depositing

Fig. 15.33 Deposits formed on both mixers

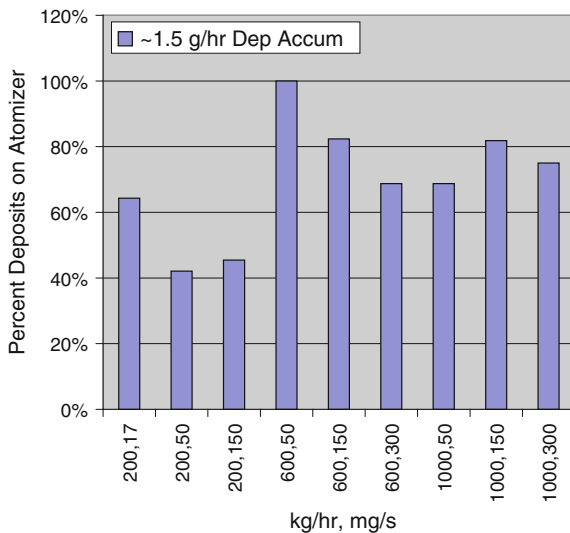


Nevertheless, the contact could be limited to mixer surfaces near the center of the pipe having the highest temperatures. The onset of deposits formation will then be determined by surface temperature, exhaust gas enthalpy, and the dosed quantity [1].

The quantitative measurement of deposits can be based on weighting the mixing section parts before and after a test to record the deposits mass growth rate. Figure 15.33 shows typical deposits formation patterns on the surfaces of both mixers.

The dosing rate restrictions protect the aftertreatment from an excessive deposit accumulation inside the urea mixing section. If remained unchecked, an excessive deposit growth may lead to an increase in the exhaust back pressure and a deterioration of urea mixing quality. Higher back pressures would negatively impact engine performance, and poor mixing would reduce NO_x conversion efficiency of the SCR catalyst.

Fig. 15.34 Deposits collected on the atomizer



At lower exhaust temperatures typical for city driving, deposits could be forming in excess of 2 g/h rate. As exhaust gas and surface temperatures increase, the formation rate drops below 2 g/h, and most deposits form on the pre-mixer (Fig. 15.34). This is preferred, as these surfaces have higher average temperatures, which slows down the deposits growth and makes it easier to burn them off during DPF regeneration events.

In addition to measurements of exhaust gas temperature at various locations, knowing exhaust wall temperatures allows to gain better understanding of deposits formation pattern. For each cross-section of interest the wall temperatures were recorded at four rotational positions, 90° apart.

The wall temperature reduction relative to the gas centerline temperatures at the SCR entry are summarized in Fig. 15.35. The data were collected at deposits rate of 1 g/h for 200, 600, and 1000 kg/h air flow. The wall temperature reduction is much higher (lower wall temperatures) at lower exhaust flows that allow for more droplet residence time resulting in more evaporation of the liquid fraction. The evaporation is also helped by smaller amount of liquid in the mixing section to form the same amount of deposits. The delta_T is increasing with gas temperature at all exhaust flows. The magnitude of the delta_T and the rate of rise as a function of exhaust temperature diminish at higher exhaust flows, where heat content is greater.

All tests described here were conducted at room-temperature ambient conditions. The wall temperatures are lower at cold ambient conditions leading to higher deposits formation rate.

In addition to deposits formation on mixer surfaces, deposits can also form on the injector tip [2]. For recessed injector mounts the gas temperature near the tip is much lower compared to the exhaust centerline temperature, thus the tip deposits

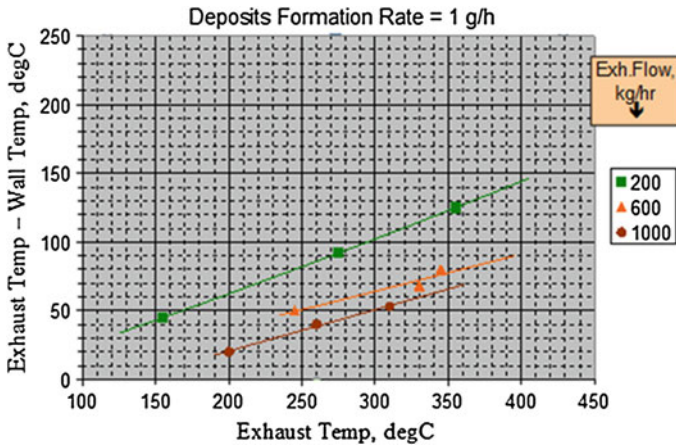
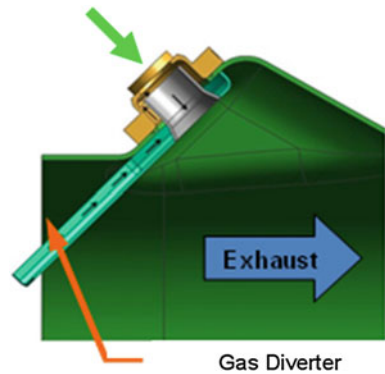


Fig. 15.35 Wall temperature reduction at SCR entry

Fig. 15.36 Deposits tip protection



composition is mostly urea crystals. Consequently, the burn-off temperature for deposits removal does not have to approach DPF regeneration temperature. Still excessive accumulation at the tip threatens to degrade the spray quality and partially block the spray orifices.

To avoid excessive deposits a tip protector can be used (Fig. 15.36). It consists of a gas diverter that directs a small part of exhaust flow to the vicinity of the tip and toward a sleeve. The gas flows around the sleeve outer diameter toward the tip and turns around to create a cylindrical gas shield around the spray. The shield prevents gas recirculation into the recessed area, which would cause the smallest droplets to land on the tip and other surfaces inside the recess cavity. The green arrow represents the location where the injector would be mounted.

The effectiveness of the tip deposits protection is evident from Fig. 15.37. For the case on the left the near-tip temperature (NTT) is 86.6 °C, with the DOC_out temperature at 300 °C (for the gas flow of 200 kg/h and urea dosing at 150 mg/s).

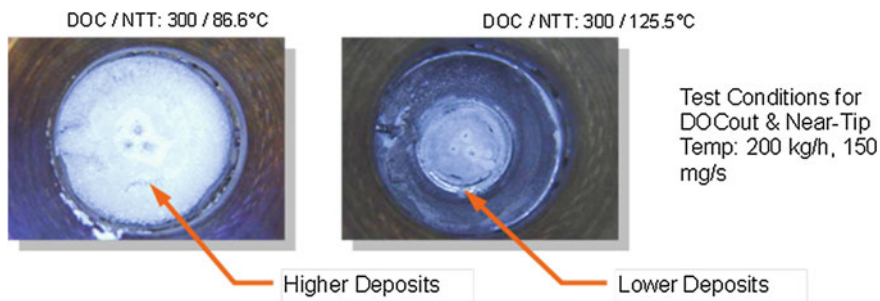


Fig. 15.37 Tip deposits without (*left*) and with (*right*) tip protector

The white deposits are threatening to cover three spray orifices. The photo on the right shows a substantial reduction of deposits, and a higher NTT of 125.5 °C. The higher NTT did not increase the tip internal temperature above the manufacturer specified limit.

15.7 Concluding Remarks

Based on its early adoption into the European market, DEF metered SCR has become the preeminent global NO_x reduction technology. Lessons learned from on-road applications should be incorporated into nonroad applications as well as future high efficiency SCR systems. In order to meet these new system requirements, a structured approach to SCR integration should be taken (as outlined above), which has been proven through many applications that are in production globally and supported by the practical examples provided by Ford Motor Company. By following a structured approach, superior NO_x reduction performance and robust deposit response can be achieved.

References

1. Nishioka et al, "A Study of a New Aftertreatment System (2): Control of Urea Solution Spray for Urea-SCR", SAE Paper 2006-01-0644
2. "Bypass purge for protecting against formation of reductant deposits", US Patent #2010/0107614 A1

Chapter 16

Ammonia Storage and Release in SCR Systems for Mobile Applications

Daniel Peitz, Andreas Bernhard and Oliver Kröcher

16.1 Introduction

The SCR reaction requires ammonia for the reduction of nitrogen oxides. While compressed or liquefied ammonia is used for the supply of ammonia in stationary applications, the odorous ammonia gas had to be replaced in mobile SCR applications by an ammonia precursor compound for the safe storage and reliable release of ammonia in the right quantities and right dynamics. Thus, significant innovation was needed before mobile SCR systems could be realized, even though commercial operation of ammonia SCR systems in coal power plants (>250 MW) started already around 1980 [1]. After the invention of HC-SCR for mobile NO_x sources, to avoid handling NH₃ [2], and the discovery of cyanuric acid as a safe NH₃ storage compound, [3] urea was proposed as a storage material for NH₃ in 1988 [4]. By then, urea was already known to work as an NH₃ precursor for SCR in stationary applications for 3 years [5]. First results on mobile urea-based SCR were publically presented in 1990, already showing NO_x conversions above 90 % from 250 °C at gas hourly space velocities (GHSV) of 12,900 h⁻¹ [6]. The first patented mobile applications of urea solutions for SCR were registered in 1990 [7].

Due to the large-scale production of urea as a bulk commodity, it is readily available in large quantities. Since the involved reactants CO₂ and NH₃ needed for urea synthesis are bulk chemicals that are produced directly from air and natural gas, using the well-known industrial Haber–Bosch process, urea can be produced at a low price [8]. Also, urea is nontoxic, noncorrosive and can easily be handled as aqueous solutions, such as a 32.5 wt % solution with the trade name AdBlue®.

D. Peitz · A. Bernhard · O. Kröcher (✉)
Bioenergy and Catalysis Laboratory, Paul Scherrer Institut, OVGA/112 5232 Villigen PSI,
Switzerland
e-mail: oliver.kroecher@psi.ch

O. Kröcher
École polytechnique fédérale de Lausanne (EPFL), 1015 Lausanne, Switzerland

Usually, urea solution is directly dosed into the main exhaust pipe, where it decomposes due to the elevated temperature and on the SCR catalyst to yield the actual reducing agent NH_3 [9, 10]. These advantages have made urea the most important NH_3 precursor compound used today for the DeNO_x aftertreatment of Diesel exhausts by SCR.

However, some challenges related to the use of urea remain. Urea solution is more difficult to dose and to mix with the exhaust gas than NH_3 gas-urea may decompose incompletely, form deposits and even deactivate the SCR catalyst [11–13]. These issues are subject of ongoing research and will be treated in Sect. 16.2.

Furthermore, the NH_3 storage density of AdBlue[®] solution is only one-third compared to liquefied NH_3 , the freezing point of -11 °C is too high to reliably avoid freezing in many parts of the world [14] and the stability when stored at elevated temperature is limited [15]. Improved NH_3 storage density, freezing and storage stability can be achieved by using alternative NH_3 storage compounds, which will be treated in Sect. 16.3.

16.2 Urea as Ammonia Precursor Compound

16.2.1 Solid Urea

The NH_3 storage density (gravimetric and volumetric) of solid urea is very high, but the dosing is technically challenging. In order to release all the stored NH_3 , urea needs to be contacted with a catalyst, and this is quite difficult to achieve during dynamic operation of a vehicle [16]. In order to dose solid urea, urea is pressed into spherical pellets of defined diameter. The pellets are then dispensed from the storage tank by a star feeder [17] and shot onto a hydrolysis catalyst-coated heated plate using pressurized air [18]. The catalyst-coated plate constituted an external reactor in a bypass flow of the main exhaust for the conversion of solid urea to NH_3 gas [19]. Later modifications of the reactor place the unit in the main exhaust pipe, downstream of an oxidation catalyst, in order to harvest heat from the exhaust gas for the decomposition of the dosed urea, rather than using solely electric heating [20].

Still, the handling and dosing of solid urea in mobile SCR systems remains complicated, as small amounts of solids are hard to dose as dynamically as the NO_x emissions from the engine varies [16]. Handling is made even more difficult by the high deliquescence of solid urea, which easily transforms the single solid urea pellets into larger aggregates of solid urea that no longer pass the solid transfer sections [21].

16.2.2 Urea Solution

In order to simplify the dosage of urea into the main exhaust pipe, urea-water-solutions (UWS) were introduced. A concentration of 32.5 % (by mass) urea in H₂O was chosen for mobile applications as a standardized solution due to the eutectic nature with a melting point of -11 °C. The trade name AdBlue[®] was introduced in many countries, in others the solution became known as Diesel Exhaust Fluid (DEF) or as Aqueous Urea Solution (AUS) [22]. For the exhaust gas aftertreatment of Diesel engines in large ships a more concentrated solution of 40 % urea is used, as the stored urea solution is not exposed to low temperatures in the ship's engine room. As the temperature in many parts of the world falls regularly below -11 °C in winter, the AdBlue[®] tank of vehicles must be equipped with a heating system. Most frequently, the heating system is a combination of electric heating and a heat exchanger drawing off heat from the engine cooling fluid [23]. High-temperature stability of AdBlue[®] is also restricted, as urea in the aqueous solution will start decomposing, thereby building up pressure in the storage tank. AdBlue[®] containments and transport lines are not generally certified to withstand pressures higher than 50 mbar relative to ambient pressure. However, AdBlue[®] in a sealed vessel will build up a pressure of 70 mbar under storage at 40 °C. The shelf life when stored between 30 and 35 °C is reduced to just 6 months [23].

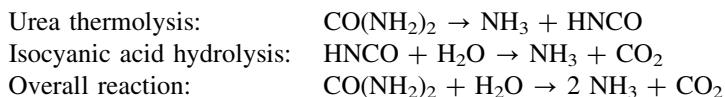
The easy release of NH₃ from the precursor compound clearly becomes a disadvantage for the application of AdBlue[®] in Mediterranean up to tropical areas.

The NH₃ storage potential of AdBlue[®] amounts to 0.201 kg/L (0.184 kg/kg) NH₃/solution [22] compared to solid urea with 0.567 kg/kg (0.749 kg/L solid block or 0.42 kg/L pellets).

Since the commercial introduction of AdBlue[®] in 2004 [24], it has been adopted worldwide for heavy-duty applications of Diesel engines equipped with SCR systems, and is considered the most promising system for the Diesel engine passenger car market [25].

16.2.3 Urea Thermolysis and Evaporation

As urea is the predominant NH₃ precursor compound, its decomposition will be discussed in detail. In general, urea decomposes in the hot exhaust gas via a two-step reaction to yield the actual SCR reducing agent NH₃ [9].



Before these chemical reactions occur, the dosed UWS aerosol is heated up by the surrounding exhaust gas and the contained water evaporates. The exact state of aggregation of urea during decomposition is still uncertain [26, 27]. Two recent theoretical studies [28, 29] relying on experimental data [30–33] point toward urea

evaporation from liquid aerosols and decomposition in the gas phase. However, another recent study supposed the mentioned chemical reactions take place in solid aerosols [34].

Urea thermolysis is usually considered a solely thermal reaction, whereas the intermediate isocyanic acid (HNCO) is stable in the gas phase but hydrolyzes on the SCR catalyst or on a dedicated hydrolysis catalyst [9]. Catalytic reactions will be discussed later; this section is focusing on thermal decomposition.

Back in 1966, Schmidt described a process to thermolyze urea into NH_3 and HNCO gas on an industrial scale [35]. In this process, solid urea was blown into a fluidized bed of inert material, which was heated above 300 °C. The produced HNCO gas was used for melamine synthesis.

HNCO is stable in the gas phase at conditions relevant for SCR [9], but is highly reactive with respect to byproduct formation in the condensed state [36]. Figure 16.1 shows a reaction scheme for urea decomposition, including the two byproducts biuret and cyanuric acid which are formed first [37].

Basic investigations of urea thermolysis, including the formation and decomposition of byproducts, have been performed using thermogravimetric analysis (TGA) and/or differential scanning calorimetry (DSC) [11, 13, 36, 38]. The DSC data consistently show a sharp feature at 133 °C, the melting point of urea. Further features strongly depend on experimental conditions, like the type of sample administration [11, 38].

Typically, solid urea was administrated in a crucible. Inside a crucible, volatile compounds produced within the urea melt have to reach the surface of the liquid, desorb to the gas phase, and finally leave the crucible by gas diffusion and convection. The slow mass transport of gaseous compounds to leave the crucible leads to long residence times of, e.g., the reactive HNCO inside the crucible, resulting in extensive byproduct formation [11]. Since HNCO is consumed during byproduct formation, the observed HNCO concentration in the gas phase is largely reduced compared to the NH_3 concentration below 300 °C [11, 38]. On the other hand, mainly HNCO is observed in the gas phase above 300 °C due to cyanuric acid decomposition [11, 38]. In addition to experiments using a crucible, Lundström et al. [10] performed DSC experiments with cordierite monoliths, impregnated with urea [38]. Due to the large monolith surface, HNCO desorption was faster than cyanuric acid formation, resulting in virtually similar curves for the gas phase concentration of NH_3 and HNCO.

Improving the mass transport further by increasing the space velocity and decreasing the amount of urea on the monolith relative to the gas flow through the channels, allows urea evaporation to be even faster than urea thermolysis [39]. In other words, the urea evaporated in the temperature programmed desorption (TPD) experiments, before the temperature was high enough for urea thermolysis [39]. Urea sublimation under vacuum has been known for decades and gaseous urea exists in monomolecular form [32, 40, 41]. Recent studies have shown that gaseous urea also exists in monomolecular form under atmospheric pressure and that diluted urea vapor is sufficiently stable to be measured by Fourier transform infrared (FTIR) spectroscopy in a gas cell heated to 180 °C [39, 42]. Comparing

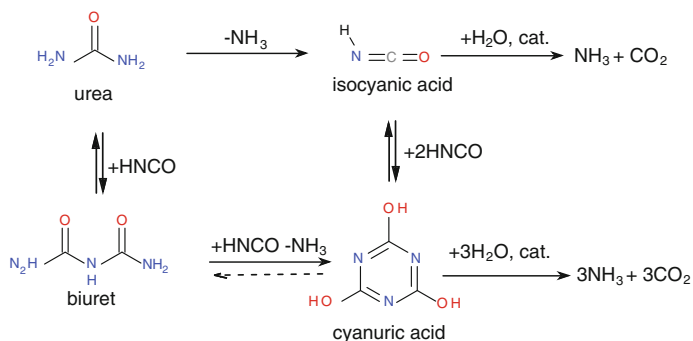


Fig. 16.1 Reaction scheme for urea decomposition, including the two byproducts biuret and cyanuric acid

the saturation vapor pressure of urea [39, 40] with raw NO_x emissions of 200–300 ppm of a modern Diesel engine [14] reveals that a temperature of only about 120°C is sufficient for complete evaporation of the required urea (assuming quantitative urea decomposition and NO_x reduction). Of course, urea-SCR at just 120°C is not feasible due to kinetics, however, one should keep in mind that a significant fraction of the dosed urea may reach the catalyst as urea vapor in addition to NH_3 , HNCO and urea aerosols.

More realistic urea decomposition experiments were performed with single UWS droplets on a quartz fiber [33]. Even contact-free experiments are possible with UWS droplets in an acoustical levitator [43]. Experiments with single UWS droplets also provide information about water evaporation from the UWS droplets as shown in Ref. [33, 43]. These data are a valuable input for modeling work, but real UWS aerosols are much smaller than the droplets used in these studies [33, 43]. It is plausible that, in analogy to the TGA, DSC, and TPD experiments mentioned above [11, 36, 38, 39], smaller aerosols with faster mass transport to the surrounding gas favor the desorption of HNCO and/or urea vapor over byproduct formation inside the aerosols.

16.2.4 Urea Decomposition Byproducts and Catalyst Deactivation

The byproducts biuret and cyanuric acid are observed in the largest quantity at low and moderate temperatures up to about 300°C [36]; however, additional byproducts form in smaller amounts as shown in Fig. 16.2 [11, 36, 37]. Substitution of the OH groups of cyanuric acid by NH_3 yields the more stable triazines ammelide, ammeline, and melamine [36]. Ammelide may also be formed by the reaction of biuret with HNCO , if water is eliminated instead of NH_3 [11]. Melamine may also be produced by trimerization of cyanamide [36] since cyanamide is an intermediate in melamine synthesis [35]. Cyanamide was not observed in a

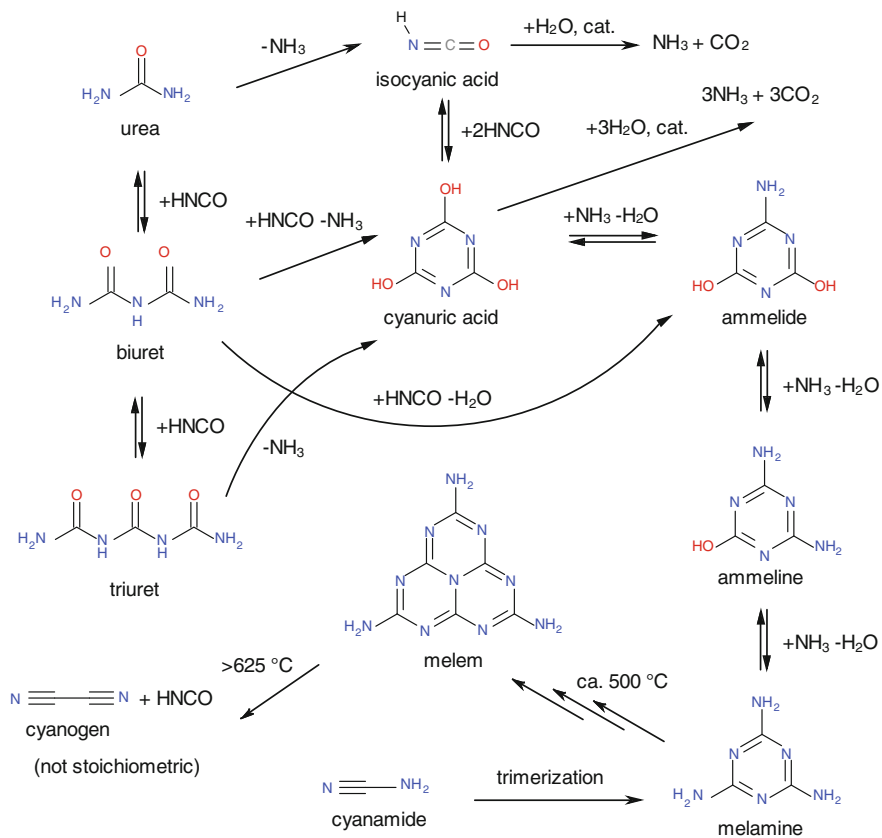


Fig. 16.2 Reaction scheme showing the formation of minor byproducts from urea [11, 36, 37]

prominent study on urea decomposition [36], but it was observed on TiO_2 catalysts in other studies, where cyanamide may have been formed by disproportionation of HCNCO [44, 45]. Melamine is more stable than cyanuric acid; it slowly sublimates rather than decomposes at temperatures around 300°C [36, 37]. At higher temperatures, melamine polymerizes to form melem and melon [11]. Polymeric melamine is water-insoluble and decomposes only above 625°C [11, 13].

Of course, byproduct formation is unwanted in the urea-SCR application. One crucial measure to limit byproduct formation is realizing a high spray quality [13, 46]. In addition, the presence of a catalyst is favorable. Since HCNCO , originating from urea thermolysis, plays a key role in byproduct formation, a catalyst can largely reduce byproduct formation by HCNCO hydrolysis [10, 11, 37]. The best hydrolysis catalyst known for the urea-SCR application is anatase TiO_2 [10, 37, 47–49]. Also, $\text{V}_2\text{O}_5/\text{WO}_3\text{-TiO}_2$ [13, 50] and zeolite-based [10, 11, 51] SCR catalysts provide high hydrolysis activities.

If byproducts form on the catalyst in spite of its hydrolysis activity, or if byproduct-containing aerosols are deposited on the catalyst, even these byproducts can be hydrolyzed catalytically. According to a recent work [37], a temperature around 200 °C is sufficient already to hydrolyze biuret, cyanuric acid, ammelide, ammeline, and melamine on anatase TiO₂. Cyanuric acid, melamine and even melem can be hydrolyzed on Al₂O₃ [52]. Eichelbaum et al. [11] found that urea induces a reversible deactivation of an iron-exchanged Beta catalyst [12]. The SCR reaction at 250 °C was strongly inhibited by cyanuric acid and ammelide, but the activity could be largely restored at 300 °C or completely at 500 °C [12]. In a urea-SCR application, regeneration of the SCR catalyst due to its own hydrolysis activity may often be sufficient. If the urea-induced catalyst deactivation is too fast, this deactivation may be avoided by a dedicated hydrolysis catalyst upstream of the SCR catalyst.

16.2.5 Catalytic Urea Decomposition

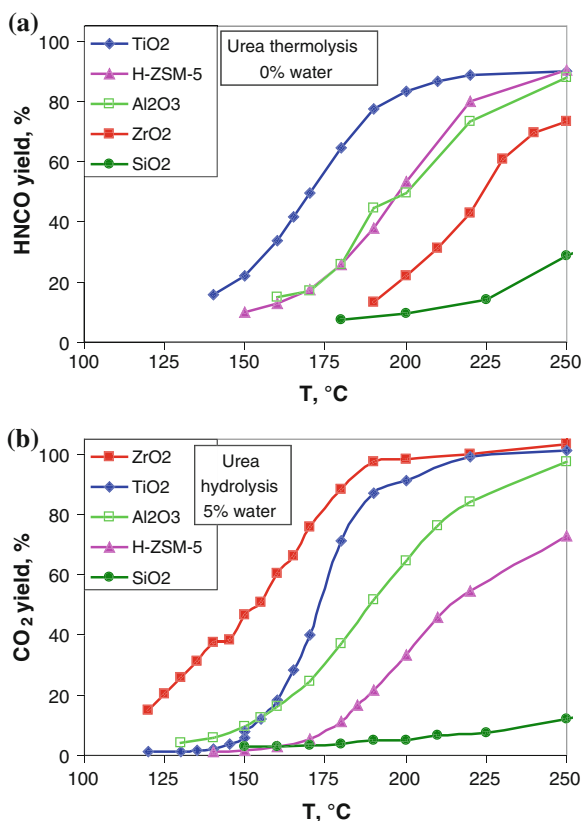
As mentioned above, urea thermolysis into NH₃ and HNCO is usually considered a solely thermal reaction. If urea thermolyzes completely upstream of the catalyst or if urea thermolysis on the catalyst is very fast, catalytic HNCO hydrolysis would be the rate determining step in the overall urea hydrolysis reaction. Catalytic HNCO hydrolysis has been investigated by both experimental and theoretical studies [45, 47–51, 53, 54] and is, therefore, well understood. Pure anatase TiO₂ is the best hydrolysis catalyst, apart from ZrO₂, which is sensitive to sulfur poisoning and consequently not used in urea-SCR applications [54]. The addition of V₂O₅ and/or WO₃ to TiO₂ decreases its hydrolysis activity [50, 54]. Also, zeolite catalysts show lower hydrolysis activity than pure TiO₂ [51, 54]. Still, HNCO hydrolysis on SCR catalysts is faster than the actual SCR reaction, indicating that increasing the size of the SCR catalyst is better than placing a hydrolysis catalyst in front of it [50]. However, in a urea-SCR application, a large fraction of the dosed urea remains intact before it enters the catalyst [9]. Therefore, interaction of molecular urea with catalysts deserves a closer look.

Urea thermolysis is usually thought to be a solely thermal reaction, but there have been some studies pointing toward catalytic urea thermolysis [10, 11, 13, 55]. Previously, Bernhard et al. [37] reported catalytic urea thermolysis as well as hydrolysis under steady-state conditions [42, 56]. Figures 16.3 and 16.4 show a catalyst screening, using the data of Ref. [56]. To reveal differences between the catalysts rather than performing mass transport limited reactions, small amounts of the catalysts (roughly 10 g/L) were coated on cordierite monoliths with a high cell density (600 cps). The space velocity was 91,000 h⁻¹. Urea solution was dosed as a very fine spray, using the setup described in Ref. [57]. In addition to UWS, water-free organic urea solutions were dosed to investigate the thermolysis reaction alone, without subsequent HNCO hydrolysis (Fig. 16.3a).

In the absence of water, urea was catalytically thermolyzed, yielding HNCO with high selectivity (Fig. 16.3a). In the presence of water, urea was efficiently

Fig. 16.3 Catalyst screening for urea decomposition.

Parameters: 100 ppm urea, 10 % O₂ in N₂, total gas flow = 500 L/h at STP, GHSV = 91,000 h⁻¹, active masses: 45 mg anatase TiO₂, 52 mg ZrO₂, 48 mg H-ZSM-5 (H-MFI 27), 64 mg Al₂O₃, 55 mg SiO₂. **a** Water-free experiments with 0.31 % ethanol in the gas phase. **b** Hydrolysis with 5 % water in the gas phase [58]



hydrolyzed as shown in Fig. 16.3b. The order of catalyst activities according to [42, 56] is:

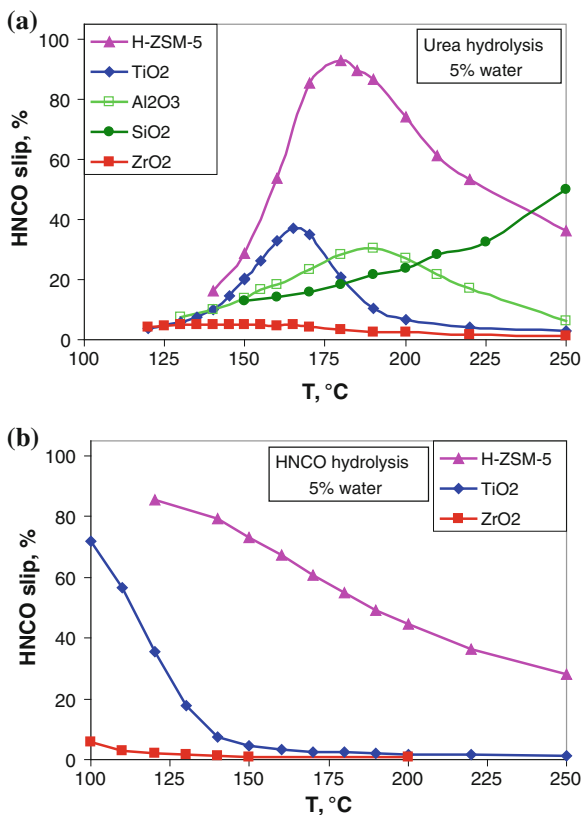
Urea thermolysis: TiO₂ > H-ZSM-5 > Al₂O₃ > ZrO₂ > SiO₂

Urea hydrolysis: ZrO₂ > TiO₂ > Al₂O₃ > H-ZSM-5 > SiO₂

As for HNC O hydrolysis, ZrO₂ was most active for urea hydrolysis, but since ZrO₂ is sensitive to sulfur poisoning [54], TiO₂ is the best for urea-SCR applications.

Figure 16.4a shows the slip of the intermediate HNC O produced during urea hydrolysis. Interestingly, TiO₂, H-ZSM-5 and Al₂O₃ showed significant local maxima in the HNC O slip. Local maxima of the intermediate HNC O are in agreement with the assumed two-step mechanism (urea thermolysis and HNC O hydrolysis). However, pure HNC O hydrolyzed much faster on the same catalysts (Fig. 16.4b). The comparatively slow hydrolysis of the HNC O originating from urea thermolysis indicates that urea strongly inhibits HNC O hydrolysis. Inhibition of HNC O hydrolysis on TiO₂ by NH₃, originating from urea thermolysis, cannot explain the HNC O peak in Fig. 16.4a, because NH₃-inhibition on of HNC O hydrolysis was found to be negligible above 150 °C by Refs. [53, 54].

Fig. 16.4 Urea hydrolysis (a) versus HNCO hydrolysis (b). Parameters: 100 ppm urea or HNCO, 10 % O₂ in N₂, total gas flow = 500 L/h at STP, GHSV = 91,000 h⁻¹, active masses: 45 mg anatase TiO₂, 52 mg ZrO₂, 48 mg H-ZSM-5 (H-MFI 27), 64 mg Al₂O₃, 55 mg SiO₂ [58]



The presented studies [56, 58] will not be the last on catalytic urea decomposition, yet the results already clearly show that urea thermolysis is catalyzed and that catalytic urea hydrolysis is much slower than the hydrolysis of pure HNCO. Taking into account the risk of urea-induced deactivation of the SCR catalyst [12], the ongoing trend for lower exhaust gas temperatures and the good properties of TiO₂ for byproduct decomposition [37], using a dedicated hydrolysis catalyst may be a good option for some urea-SCR applications.

16.3 Alternative Ammonia Precursor Compounds

16.3.1 Cyanuric Acid

Historically, cyanuric acid can be considered one of the first ammonia precursor compounds. As far back as 1977, a Japanese patent mentions the possibility of replacing NH₃ in power plant exhaust gas aftertreatment with inorganic ammonium salts, urea or cyanuric acid granules of 0.1–10 mm diameter [59]. However,

almost one decade later, in 1986, the publication of Perry and Siebers on high NO conversion, when directing a Diesel engine exhaust flow through a heated bed of cyanuric acid, still received much attention [3]. Their intention in using cyanuric acid was to release isocyanic acid upon heating above 330 °C. They believed the evolved HNCO to be the active reactant in reduction of NO [60]. Indeed, they were able to reliably decompose cyanuric acid to HNCO. NO was converted to N₂ in their setup when flowing through a stainless steel beads bed with the produced HNCO. These results led to several patents on the utilization of cyanuric acid in mobile exhaust gas aftertreatment, the process was named RAPRENO_x (RAPid REduction of NO_x) [3, 61, 62]. However, it was later shown that the stainless steel beads used as reactor filling material actually catalyzed the decomposition of HNCO [63], leading to the production of NH₃, which was the actual reducing agent. During this time, first experiments were conducted with solid urea as NH₃ storage compound, and a direct comparison showed urea to be advantageous for multiple applications [64].

16.3.2 Ammonium Formate

In the course of optimizing the low-temperature stability of aqueous urea solution, various anti-freeze additives were tested. For example, typical engine coolant antifreeze additives such as ethanol [65], propylene glycol or methanol [66] were added to aqueous urea. However, the freezing point depression was not very significant (<10 K) and the emission of the additionally introduced hydrocarbons in the exhaust was not acceptable [66]. In contrast, ammonium formate addition to aqueous urea solution caused a depression of the freezing point down to -30 °C, and it could even contribute to the NH₃ storage capacity [67]. Inorganic ammonium salts have already been proposed for application in fossil fuel power plant SCR systems [59], but ammonium formate was only mentioned in previous disclosures concerning the selective non-catalytic reduction (SNCR) of NO_x in these units [68]. The use of ammonium formate as an additive to urea solution has brought the benefit of decreasing the melting point [69], and yet increased the amount of stored NH₃ in the solution [70]. Depending on the application, high NH₃-containing solutions could also be prepared that showed comparable low-temperature stability to AdBlue[®] [71]. The most preferable solutions are named Denoxium-20 or Denoxium-30 with freezing points around -20 and -30 °C, respectively. The NH₃-releasing capacity amounts to 0.207 kg/kg (0.232 kg/L) for Denoxium-30 and to 0.205 kg/kg (0.228 kg/L) for Denoxium-20. Denoxium-20 is only advantageous to Denoxium-30 in so far that it contains less of the more expensive ammonium formate, while containing approximately the same amount of stored NH₃. The melting point of Denoxium-30 is actually not exactly -30 °C—the solution shows a hysteresis of freezing as low as -31 °C and melting as high as -26 °C [72]. Until now, only the Denoxium-30 solution has been commercially employed, either under the name Denoxium[®], or, in Canada, the USA and Mexico, under the name

TerraCairPlus[®], due to a license agreement between Denoxium[®] owner Kemira Oyj with Terra Environmental Technologies Inc [73].

There is already interest in modeling the evaporation of ammonium formate urea solution droplets in the exhaust gas pipe [74]. Ammonium formate will split into ammonia and formic acid in the hot exhaust [70]. While ammonia is the desired product that is consumed in the SCR reaction, formic acid constitutes an undesired emission. In fact, formic acid is the most corrosive halogen-free organic acid, and its corrosive effect on metals is further enhanced by O₂ [75]. The corrosion of steel by formic acid is a function of the acid concentration and the temperature [76], but in contrast to inorganic acids, formic acid does not form a passivating film on the metals during corrosion [77]. In the past, the corrosive effect on various types of steel was investigated (type 304 [78], type 430 [79], SUS 329J1 [80], AISI-316 [81]); however, the experiments did not include corrosion by hot formic acid vapors.

In addition to the immediate corrosive effect of formic acid, there is an additional danger of forming undesired side products from the reaction of formic acid with compounds in the exhaust gas. One possible side reaction is the formation of methanamide by a condensation with NH₃ [82]. Methanamide is considered to be teratogenic [83], though it must be noted that while some animal studies did show teratogenic effects [84], others (with different application doses) did not observe a teratogenic effect [85].

From methanamide hydrogen cyanide (HCN) can also be formed by the removal of another water molecule. As HCN is a very toxic compound, its emissions must be avoided, even though there is no immediate legal regulation on the concentration of HCN in internal combustion engine exhaust gas. The formation of HCN from methanamide will be discussed in more detail later.

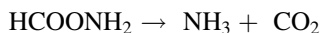
16.3.3 Ammonium Carbamate

In order to avoid freezing issues altogether, solid precursor compounds are a good substitute for solutions of NH₃ precursor compounds. However, the handling of solid NH₃ precursors is more complicated, especially if they also need to be contacted with a decomposition catalyst like solid urea (as discussed in Sect. 16.2.1).

There are, however, also solid substances which do not need a catalyst to yield NH₃, and only need to be heated for NH₃ release. One compound in this category is ammonium carbamate. Ammonium carbamate is the ammonium salt of the instable carbamic acid, and it can be transformed to urea by a condensation of the salt [86]. Another compound which can be decomposed to yield NH₃ without a catalyst is ammonium carbonate [87]. However, ammonium carbonate stores less NH₃ per mass and volume, because it contains an additional molecule of water with respect to ammonium carbamate. In detail, ammonium carbamate stores 0.436 kg NH₃/kg (0.698 kg/L), while ammonium carbonate stores 0.354 kg NH₃/kg (0.531 kg/L).

The decomposition of ammonium carbamate or ammonium carbonate in order to yield NH₃ are both thought to proceed via a two-step reaction. For ammonium

carbamate, the reaction proceeds as shown below via the instable carbamic acid [86].



The decomposition of ammonium carbonate is considered to proceed via the stable ammonium bicarbonate intermediate [87].



In addition, the condensation of ammonium carbamate to yield urea and water can occur as the following side reaction [88].



As all the above reactions are also reversible, the repeated cycling between heating and cooling during the SCR system operation can lead to the presence of all the mentioned compounds in the storage tank. This can become an issue if H_2O condenses during cooling inside the tank, because it can lead to an uncontrolled production of NH_3 from ammonium carbamate and with it a sudden pressure increase in the storage tank [82]. This becomes relevant for the decomposition of ammonium carbonate, because H_2O is released, but commercial ammonium carbonate usually also contains ammonium carbamate as well [89].

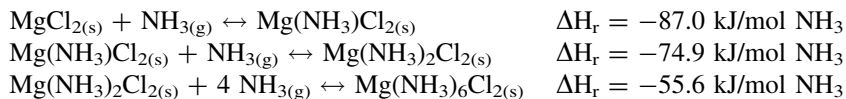
As ammonium carbamate stores more NH_3 , does not produce H_2O during decomposition and needs less heat for decomposition, it is preferred over ammonium carbonate. Despite the difficulties associated with the dynamically controlled decomposition of ammonium carbamate, the system was tested for commercial applications [90, 91]. A light-duty application on a 5.9 L Diesel engine was presented and the use of ammonium carbamate was protected by the name Solid SCR[®] [92].

However, until now, ammonium carbamate does not seem to be commercially applied as NH_3 precursor in mobile or stationary SCR applications.

16.3.4 Metal Ammine Chlorides

A completely different approach in storing NH_3 is the reversible coordination of NH_3 as a ligand to metal atoms [93]. Since the absorption of ammonia as a ligand is exothermic, and its release is endothermic, the idea is to first store NH_3 in metal ammine chlorides, so it can be later released by heating the salt. Salts of particular interest for NH_3 release are $\text{Mg}(\text{NH}_3)_6\text{Cl}_2$, $\text{Ca}(\text{NH}_3)_8\text{Cl}_2$ and $\text{Sr}(\text{NH}_3)_8\text{Cl}_2$, due to the high amount of NH_3 they can store [69]. Even though CaCl_2 and SrCl_2 would be advantageous compared to MgCl_2 because of their higher NH_3 storage capacity,

these compounds are less attractive for practical applications. This is not because of economic considerations, but because of the high NH_3 vapor pressure exhibited by $\text{Ca}(\text{NH}_3)_8\text{Cl}_2$ and $\text{Sr}(\text{NH}_3)_8\text{Cl}_2$. The NH_3 vapor pressure of $\text{Ca}(\text{NH}_3)_8\text{Cl}_2$ at 25 °C is 630 mbar, and that of $\text{Sr}(\text{NH}_3)_8\text{Cl}_2$ is 550 mbar [94], both of which are rather high for handling or even storing in a sealed container, as there would be significant leakage of NH_3 in the case of a container rupture in an accident [95]. The storage and release of NH_3 into or from these salts is proceeding successively, with decreasing enthalpies of adsorption or desorption as the amount of coordinated NH_3 increases. The individual reactions for MgCl_2 are the following:



All reactions are exothermic, but reaction enthalpies are different [96]. Using the Van't Hoff equation, the releasing temperature for NH_3 at a constant reservoir pressure of 1.5 bar can be calculated.

$$\ln P_{\text{NH}_3, \text{eq}} = \frac{-\Delta H_{r,k}}{RT} + \frac{\Delta S_{r,k}}{R}$$

The index k identifies the reaction of the NH_3 absorption or desorption process, R is the gas constant, T the temperature, $\Delta H_{r,k}$ the corresponding desorption enthalpy per mole NH_3 and $\Delta S_{r,k}$ the corresponding desorption entropy of the reaction. The calculated temperatures for release of the last 4 absorbed NH_3 molecules are 150 °C, 298 °C for the second, and 387 °C for the first molecule. From these calculated values, the full release of all six stored NH_3 molecules is impractical because of the high temperatures needed. This reduces the amount of practically stored NH_3 to two-thirds of the theoretical value. Another factor that reduces the amount of stored NH_3 is that a powder, and not a single crystal, is used. Typically void fraction of 45–50 % are present in the storage container, which not only decreases NH_3 -storage capacity but also reduces heat transfer [95]. Since heat transfer is crucial for the dynamic release of NH_3 gas from the salt, the powder is compacted under high pressure [97]. Bulk densities of 97 % of the solid density can be achieved, approaching 93 % of the volumetric NH_3 storage capacity of liquefied NH_3 [95]. As the ammine salt releases NH_3 gas, its density is reduced and NH_3 gas diffusion is not hindered. When the salts are exhausted of NH_3 , they can be recharged with NH_3 . During absorption, the pressurized cylinders are first heated so that the NH_3 evenly distributes within the bulk material [98].

Recently, the Danish company Amminex announced the launch of a production part approval process for exchangeable cylinders filled with metal ammine salts for NH_3 storage, the total investment amounted to 50 million € [99]. Also, the US-based Navistar and French Faurecia invested in Amminex's technology, promising rapid utilization in mobile applications [100]. Interestingly, Amminex is using SrCl_2 rather than MgCl_2 as NH_3 absorbant, because it has the advantage of requiring only 80 °C for the release of seven molecules of NH_3 [101]. This can be achieved by using the engine coolant as heat source. The cartridges filled with

charged $\text{Sr}(\text{NH}_3)_8\text{Cl}_2$ are not classified as dangerous goods, in spite of the 550 mbar of NH_3 vapor pressure present at 25 °C. During the operation, pressures of 6 bar are achieved in the cartridge, so there is a need for robust containers. So far, no comments have been made regarding the possibility of transporting the storage salt during NH_3 dosage onto the SCR catalyst. In this case the SCR catalyst could be deactivated due to its sensitivity toward earth-alkaline metals [102, 103]. In addition to the application as a NH_3 source for SCR, the cartridges are proposed as storage cylinders for NH_3 which will be converted to H_2 and used to power a fuel cell [104].

16.3.5 Methanamide

Analogous to urea being the condensation product of ammonium carbamate, methanamide (formamide) is the condensation product of ammonium formate. At ambient conditions (20 °C, 1 atm), methanamide is a liquid with a vapor pressure of 30 mbar and a melting point of 2 °C [105]. However, if mixed with water, an aqueous 80 % methanamide solution has a melting point of -28 °C, and remains stable at temperatures up to 100 °C [82]. This solution is known as Admide(R) and is also proposed as an NH_3 precursor for mobile applications. In addition to the excellent temperature stability, the solution with 0.30 kg/kg (0.33 kg/L) also stores 50 % more NH_3 than AdBlue® [14]. In contrast to urea, methanamide will molecularly vaporize without decomposition. Admide(R) was further determined to be biodegradable, but was also found to correlate with teratogenic effects in some animal tests [84], though not in all [85]. As the general perception of methanamide was that it indeed causes defects to the unborn child, the introduction of Admide(R) to the automotive market was cancelled [83]. Today's gasoline fuel contains up to 1 % (by volume) of benzene [106] also due to the substitution of lead-based anti-knocking agents, even though benzene is known as a teratogenic substance [107]. Therefore, the handling of Admide(R) solution by trained personnel during the regular service of a vehicle could be an option, considering the great advantages of using the solution.

Under certain conditions, such as overdosage of the reducing agent at low temperature, emissions of molecular methanamide rather than the decomposition products, can occur. Additionally, during decomposition methanamide also yields upon hydrolysis formic acid, which, as previously mentioned, is a corrosive compound. Decomposition of formic acid may either lead to CO and H_2O , or to CO_2 and H_2 . Unfortunately, the preferred latter decomposition reaction products are not the main products, but rather CO and H_2O . Another possible reaction that occurs at very high temperatures during methanamide decomposition is the removal of water to yield HCN. As previously mentioned, there is no immediate legal regulation on the emission of HCN in exhaust gas, but due to the toxicity of the compound it should be avoided.

Currently, the use of Admide(R) as a NH_3 precursor solution is protected by MAN Truck & Bus [108], but seems not to be commercially used.

16.3.6 Guanidinium Salts

In urea, two amine groups are attached to a carbonyl moiety. If the carbonyl is replaced by an imine function, one obtains guanidine. Guanidine is an unstable compound with one of the highest basicities for organic compounds. Both properties are driven by the stabilization of the guanidinium cation by three amine functions connected to the central carbon atom. Due to the symmetric structure, the guanidinium cation is a very stable compound in combination with an anion [109]. For the utilization of guanidinium salts in exhaust gas aftertreatment, small organic anions are preferred which decompose completely to gaseous products. The most promising compounds are therefore guanidinium carbonate, guanidinium hydrogen carbonate, guanidinium formate, and guanidinium oxalate. Besides the preference of CO_2 as decomposition product for the anion, the solubility of the salt in water is also an essential factor, which needs to be observed. Here, the solubility of guanidinium formate, with up to 6.19 kg dissolving in 1 L of water is unrivaled [110]. However, in order to achieve good thermal stability, significantly less salt is dissolved in water. An aqueous 60 % guanidinium formate solution can be stored for several months at a temperature of 60 °C, and can be supercooled to a temperature of -30 °C without freezing [111]. The low amount of water contained in the solution compared to AdBlue[®] is an advantage, because significantly less water needs to be evaporated by the hot exhaust gas [112]. In this solution, again, approximately 1.5 times the amount of NH_3 is stored compared to AdBlue[®]. However, due to the high stability of the compound, its catalytic decomposition below 200 °C is incomplete [14]. The decomposition of guanidinium carbonate and guanidinium bicarbonate is occurring at lower temperatures, but the solubility of the salt is much lower—not even the NH_3 storage capacity of AdBlue[®] is achieved, which makes it largely irrelevant [14].

The decomposition of guanidinium formate is best achieved on a dedicated hydrolysis catalyst, and since higher temperatures than those found in the exhaust gas pipe are needed, the decomposition in a side stream reactor with the possibility of external heating is preferred [14]. The conditions for the catalytic decomposition of guanidinium formate, including the necessary temperature, space velocity and catalyst material, were determined in the framework of a PhD thesis [113].

16.3.7 Catalytic Decomposition of Alternative NH_3 Precursor Compounds

Anatase TiO_2 is an excellent catalyst for HNCN hydrolysis [47, 50, 54] and for urea decomposition [10, 37]. In an early study of alternative ammonia precursor compounds, TiO_2 also showed promising results for the decomposition of guanidinium salts above 300 °C [14]. Interestingly, ZrO_2 , which is even more active for HNCN hydrolysis than TiO_2 , but sensitive to sulfur poisoning [54], showed only low guanidinium hydrolysis activity [14]. Unlike guanidinium formate,

methanamide could also be decomposed fairly well under SCR conditions on a V_2O_5/WO_3-TiO_2 or on a Fe-ZSM5 catalyst around 250 °C [14]. However, depending on the temperature, there were concerns about incomplete decomposition, emission of corrosive formic acid and of toxic CO as well as HCN.

In the course of a recent research project, a novel TiO_2 supported Au catalyst was developed to enable the targeted decomposition of alternative NH_3 precursor compounds without side product formation. Due to the Au deposited (0.5–1.5 % by mass) on the hydrolysis catalyst TiO_2 , formic acid derived side products such as formic acid, CO, methanamide or HCN are efficiently decomposed to CO_2 (and NH_3 if applicable), without any oxidation of the released NH_3 [113].

The Au/ TiO_2 catalyst was also tested concerning its hydrothermal resistivity under authentic operating conditions and its behavior after modeled long-term poisoning by sulfur compounds. In all aging experiments, the catalyst performance even after severe treatment such as hydrothermal aging at up to 850 °C or 200 ppm of SO_2 in the gas feed still maintained acceptable activity for catalytic decomposition of NH_3 precursor compounds [113].

In case of 60 % guanidinium formate solution, temperatures around 250 °C were necessary for quantitative conversion to NH_3 and CO_2 at a gas hourly space velocity (GHSV) of 20,000 h^{-1} . The decomposition was, however, mainly limited by the hydrolysis activity of TiO_2 , as formic acid could be decomposed to CO_2 even at just 130 °C.

An aqueous solution containing 80 % (by mass) methanamide could be converted to NH_3 and CO_2 in a temperature window ranging from 130 to 340 °C at a GHSV of 20,000 h^{-1} on a 1.0 % Au/ TiO_2 catalyst, thereby outperforming state of the art SCR catalysts concerning the light-off temperature [113]. Further increasing of the space velocity in order to shrink the catalyst size, however, will result in higher light-off temperatures. Still, the low temperature requirements for quantitative decomposition enable the direct dosing of the NH_3 precursor solution into the main exhaust pipe. On the other hand, a side stream reactor concept with a very small decomposition catalyst would be feasible to provide a concentrated flow of NH_3 rich gas to the main exhaust gas flux.

Similar to methanamide, ammonium formate decomposition proceeded in a wide temperature window. As ammonium formate does in fact not need to be hydrolyzed, formic acid decomposition is the limiting reaction for the quantitative conversion of the precursor solution to NH_3 and CO_2 . However, if mixtures with urea, such as Denoxium® are being used, the temperature needs to be sufficient to enable urea hydrolysis. Therefore, an in-pipe or side stream system equipped with an Au/ TiO_2 hydrolysis catalyst could in fact be used to provide NH_3 from either AdBlue®, Denoxium® or Admide(R). This would enable the flexibility to ensure efficient NH_3 production, and, consequently, NO_x reduction, even in cold climates or during long refill intervals. Guanidinium formate solution would also be an optional NH_3 precursor solution for a side stream reactor if the reactor could be electrically heated at temperatures below 250 °C, but would not qualify for direct injection into the main exhaust pipe.

The multiple choices for NH_3 precursor solutions, and possibility to even use mixtures thereof, represent valuable advantages for the introduction of a dedicated hydrolysis catalyst based on Au/TiO_2 .

References

1. Cichanowicz JE, Muzio LJ Twenty-Five (2001) Years of SCR Evolution: Implications For US Application And Operation. In: U.S EPA-DOE-EPRI, Chicago
2. Held W, König A (1986) Verfahren und Vorrichtung zur Reduktion von Stickoxiden. DE3,642,018
3. Perry RA, Siebers DL (1986) Rapid reduction of nitrogen oxides in exhaust gas streams. *Nature* 324(6098):657–658
4. Held W, König A, Puppe L (1988) Verfahren zur Reduktion von in Abgasen enthaltenen Stickoxiden mittels eines zeolithhaltigen Katalysators. DE3830045
5. Bowers WE (1988) Reduction of nitrogen-based pollutants through the use of urea solutions containing oxygenated hydrocarbon solvents. US Patent 4,719,092
6. Held W, König A, Richter T et al (1990) Catalytic NO_x Reduction in Net Oxidizing Exhaust Gas. SAE Technical Paper 900496
7. Jacob E (1990) Process and device for selective catalytic NO_x reduction in exhaust gases containing oxygen. EP487,886
8. Fromm D, Lützw D (1979) Moderne Verfahren der Großchemie: Harnstoff. *Chem unserer Zeit* 13(3):78–81
9. Koebel M, Elsener M, Kleemann M (2000) Urea-SCR: a promising technique to reduce NO_x emissions from automotive diesel engines. *Catal Today* 59(3–4):335–345
10. Lundström A, Snelling T, Morsing P et al (2011) Urea Decomposition and HNCO Hydrolysis Studied over Titanium dioxide, Fe-Beta and γ -Alumina. *Appl Catal B* 106:273–279
11. Eichelbaum M, Farrauto RJ, Castaldi MJ (2010) The impact of urea on the performance of metal exchanged zeolites for the selective catalytic reduction of NO_x : Part I. Pyrolysis and hydrolysis of urea over zeolite catalysts. *Appl Catal B* 97(1–2):90–97
12. Eichelbaum M, Siemer AB, Farrauto RJ et al (2010) The impact of urea on the performance of metal-exchanged zeolites for the selective catalytic reduction of NO_x : Part II. Catalytic, FTIR, and NMR studies. *Appl Catal B* 97(1–2):98–107
13. Fang HL, DaCosta HFM (2003) Urea thermolysis and NO_x reduction with and without SCR catalysts. *Appl Catal B* 46:17–34
14. Kröcher O, Elsener M, Jacob E (2009) A model gas study of ammonium formate, methanamide and guanidinium formate as alternative ammonia precursor compounds for the selective catalytic reduction of nitrogen oxides in diesel exhaust gas. *Appl Catal B* 88(1–2):66–82
15. ISO (2008) Diesel engines - NO_x reduction agent AUS 32 - Part 3: Handling, transportation and storage. vol ISO 22241–3
16. Weisweiler W, Buchholz F (2001) Fester Harnstoff als Ammoniakquelle für die katalysierte Stickstoffoxid-Minderung in Dieselabgasen nach dem SCR-Verfahren. *Chem Ing Tech* 73(7):882–887
17. Käfer S, Müller W, Herr A et al (2004) Vorrichtung und Verfahren zur Dosierung und Förderung von trockenem Harnstoff, insbesondere bei der Durchführung des SCR-Verfahrens in Kraftfahrzeugen. DE10,251,498A1
18. Müller W, Herr A, Käfer S et al (2004) SCR using solid urea. In: 3rd Internation Exhaust Gas and Particulate Emissions Forum, Sinsheim

19. Jacob E, Müller W, Herr A et al (2002) Vorrichtung zur Reduktion von Stickoxiden im Abgas von Brennkraftmaschinen. DE10,206,028
20. Dismon H, Lappan R, Nowak M et al (2006) Vorrichtung zur Reduktion von Stickoxiden im Abgas von Brennkraftmaschinen. DE102,006,004,170
21. Berliner JFT (1936) Crystal Urea: Industrial Development and Properties. *Ind Eng Chem* 28(5):517–522
22. ISO (2006) Diesel engines - NO_x reduction agent AUS 32 - Part 1: Quality requirements. vol ISO 22241–1
23. Thompson J, Op De Beeck J, Joubert E et al (2008) Case Studies of Urea SCR Integration on Passenger Cars Monitoring of Urea Inside the Tank During Hot and Cold Environment Test Missions. SAE Technical Paper 2008-01-1181
24. Gabriëllsson PLT (2004) Urea-SCR in Automotive Applications. *Top Catal* 28(1):177–184
25. Granger P, Parvulescu VI (2011) Catalytic NO_x Abatement Systems for Mobile Sources: From Three-Way to Lean Burn after-Treatment Technologies. *Chem Rev* 111:3155–3207
26. Birkhold F, Meingast U, Wassermann P et al (2007) Modeling and simulation of the injection of urea-water-solution for automotive SCR DeNO_x-systems. *Appl Catal B* 70(1–4):119–127
27. Ström H, Lundström A, Andersson B (2009) Choice of urea-spray models in CFD simulations of urea-SCR systems. *Chem Eng J* 150(1):69–82
28. Abu-Ramadan E, Saha K, Li X (2011) Modeling the depleting mechanism of urea-water-solution droplet for automotive selective catalytic reduction systems. *AIChE J* 57(11):3210–3225
29. Lundström A, Waldheim B, Ström H et al (2011) Modelling of urea gas phase thermolysis and theoretical details on urea evaporation. Paper presented at the Proceedings of the Institution of Mechanical Engineers, Part D: Journal of Automobile Engineering
30. Della Gatta G, Ferrq D (1987) Enthalpies of fusion and solid-to-solid transition, entropies of fusion for urea and twelve alkylureas. *Thermochim Acta* 122(1):143–152
31. Emel'yanenko VN, Kabo GJ, Verevkin SP (2005) Measurement and Prediction of Thermochemical Properties: Improved Increments for the Estimation of Enthalpies of Sublimation and Standard Enthalpies of Formation of Alkyl Derivatives of Urea. *J Chem Eng Data* 51(1):79–87
32. Ferro D, Barone G, Della Gatta G et al (1987) Vapour pressures and sublimation enthalpies of urea and some of its derivatives. *J Chem Thermodyn* 19(9):915–923
33. Wang TJ, Baek SW, Lee SY et al (2009) Experimental investigation on evaporation of urea-water-solution droplet for SCR applications. *AIChE J* 55(12):3267–3276
34. Ebrahimian V, Nicolle A, Habchi C (2012) Detailed modeling of the evaporation and thermal decomposition of urea-water solution in SCR systems. *AIChE J* 58:1998–2009
35. Schmidt A (1966) Herstellung von Melamin aus Harnstoff bei Atmosphärendruck. *Chem Ing Tech* 38(11):1140–1144
36. Schaber PA, Colson J, Higgins S et al (2004) Thermal decomposition (pyrolysis) of urea in an open reaction vessel. *Thermochim Acta* 424(1–2):131–142
37. Bernhard AM, Peitz D, Elsener M et al (2012) Hydrolysis and thermolysis of urea and its decomposition byproducts biuret, cyanuric acid and melamine over anatase TiO₂. *Appl Catal B* 115–116:129–137
38. Lundström A, Andersson B, Olsson L (2009) Urea thermolysis studied under flow reactor conditions using DSC and FT-IR. *Chem Eng J* 150 (2–3):544–550
39. Bernhard AM, Czekaj I, Elsener M et al (2011) Evaporation of Urea at Atmospheric Pressure. *J Phys Chem A* 115(12):2581–2589
40. Krasulin AP, Kozyro AA, Kabo GY (1987) Saturation vapor pressure of urea in the temperature range 329–403 K. *J Appl Chem USSR* 60 (1 pt 1):96–99
41. Langer J, Schrader B, Bastian V et al (1995) Infrared-spectra and force-constants of urea in the gaseous-phase. *Fresenius J Anal Chem* 352(5):489–495
42. Bernhard AM, Peitz D, Elsener M et al (2013) Quantification of gaseous urea by FTIR spectroscopy and its application in catalytic urea thermolysis. *Top Catal* 56:130–133

43. Kontin S, Höfler A, Koch R et al (2010) Heat and Mass Transfer accompanied by Crystallisation of single Particles containing Urea-water-solution. In: 23rd Annual Conference on Liquid Atomization and Spray Systems, Brno
44. Bernhard AM, Czekaj I, Elsener M et al (2013) Adsorption and catalytic thermolysis of gaseous urea on anatase TiO₂ studied by HPLC analysis, DRIFT spectroscopy and DFT calculations. *Appl Catal B* 134–135:316–323
45. Hauck P, Jentys A, Lercher JA (2007) On the quantitative aspects of hydrolysis of isocyanic acid on TiO₂. *Catal Today* 127:165–175
46. Dong H, Shuai S, Wang J (2008) Effect of Urea Thermal Decomposition on Diesel NO_x-SCR Aftertreatment Systems. SAE Technical Paper 2008-01-1544
47. Hauck P, Jentys A, Lercher JA (2007) Surface chemistry and kinetics of the hydrolysis of isocyanic acid on anatase. *Appl Catal B* 70(1–4):91–99
48. Piazzesi G, Kröcher O, Elsener M et al (2006) Adsorption and hydrolysis of isocyanic acid on TiO₂. *Appl Catal B* 65(1–2):55–61
49. Czekaj I, Kröcher O (2009) Decomposition of Urea in the SCR Process: Combination of DFT Calculations and Experimental Results on the Catalytic Hydrolysis of Isocyanic Acid on TiO₂ and Al₂O₃. *Top Catal* 52(13):1740–1745
50. Kleemann M, Elsener M, Koebel M et al (2000) Hydrolysis of isocyanic acid on SCR catalysts. *Ind Eng Chem Res* 39(11):4120–4126
51. Piazzesi G, Devadas M, Kröcher O et al (2006) Isocyanic acid hydrolysis over Fe-ZSM5 in urea-SCR. *Catal Commun* 7(8):600–603
52. Zhan Z, Müllner M, Lercher JA (1996) Catalytic hydrolysis of s-triazine compounds over Al₂O₃. *Catal Today* 27(1–2):167–173
53. Czekaj I, Kröcher O, Piazzesi G (2008) DFT calculations, DRIFT spectroscopy and kinetic studies on the hydrolysis of isocyanic acid on the TiO₂-anatase (1 0 1) surface. *J Mol Catal A* 280(1–2):68–80
54. Piazzesi G (2006) The Catalytic Hydrolysis of Isocyanic Acid (HNCO) in the Urea-SCR Process. Dissertation No. 16693, ETH Zurich
55. Larrubia MA, Ramis G, Busca G (2000) An FT-IR study of the adsorption of urea and ammonia over V₂O₅-MoO₃-TiO₂ SCR catalysts. *Appl Catal B* 27(3):L145–L151
56. Bernhard AM, Peitz D, Elsener M et al (2013) Catalytic urea hydrolysis in the selective catalytic reduction of NO_x: Catalyst screening and kinetics on anatase TiO₂ and ZrO₂. *Catal Sci Technol* 3(4):942–951
57. Peitz D, Bernhard A, Elsener M et al (2011) Laboratory test reactor for the investigation of liquid reducing agents in the selective catalytic reduction of NO_x. *Rev Sci Instrum* 82(8):084101
58. Bernhard AM (2012) Urea evaporation and catalytic urea decomposition in the selective catalytic reduction of NO_x. Dissertation No. 20813, ETH Zurich
59. Wada Y, Yamatsuta K (1977) Treating exhaust gases contg. nitrogen oxide(s) - by adding granules of cyanuric acid, urea or ammonium cpd., and an organic cpd. having nitrile gp. JP54,028,771
60. Perry RA (1985) Kinetics of the reactions of NCO radicals with H₂ and NO using laser photolysis–laser induced fluorescence. *J Chem Phys* 82:5485–5488
61. Gardner-Chavis RA, May MP (1990) Catalytic decomposition of cyanuric acid and use of product to reduce nitrogen oxide emissions. US5,087,431
62. Perry RA (1987) System for NO reduction using sublimation of cyanuric acid. US4,800,068
63. Siebers DL, Caton JA (1990) Removal of nitric oxide from exhaust gas with cyanuric acid. *Combust Flame* 79(1):31–46
64. Caton JA, Siebers DL (1989) Comparison of Nitric Oxide Removal by Cyanuric Acid and by Ammonia. *Combust Sci Technol* 65(4–6):277–293
65. Mao FF, Li CG (2000) Urea-Ethanol-Water Solution Properties for Diesel NO_x Control Using Urea. In: Presentations of the 6th Diesel Engine Emissions Reduction (DEER) Workshop, San Diego

66. Lambert C, Montreuil C, Vanderslice J (2003) Application of Organic Freeze-Point Depressants in Aqueous Urea Solutions: Effect on NO_x Reduction. SAE Technical Paper 2003-01-0775
67. Solla A, Westerholm M, Söderström C et al (2005) Effect of Ammonium Formate and Mixtures of Urea and Ammonium Formate on Low Temperature Activity of SCR Systems. SAE Technical Paper 2005-01-1856
68. Lyon RK (1973) Method for the reduction of the concentration of NO in combustion effluents using ammonia. US3,900,554
69. Marko A, Wahl T, Alkemade U et al (1997) Verfahren und Vorrichtung zur selektiven katalytischen NO_x-Reduktion. DE19,728,343
70. Koebel M, Elsener M (1998) Oxidation of Diesel-Generated Volatile Organic Compounds in the Selective Catalytic Reduction Process. *Ind Eng Chem Res* 37(10):3864–3868
71. Nissinen T, Kukkonen J (2004) Catalytic process for reducing nitrogen oxides in flue gases and reducing agent composition. FI2,004,000,057
72. Highfield T (2011) Lower Freezing DEF For Higher NO_x Reduction Attainment. In: Presentations of the Directions in Engine-Efficiency and Emissions Research (DEER) Conference, Detroit
73. Savara A, Li MJ, Sachtler WMH et al (2008) Catalytic reduction of NH₄NO₃ by NO: Effects of solid acids and implications for low temperature DeNO_x processes. *Appl Catal B* 81(3–4):251–257
74. Lee SY, Baek SW (2011) Experimental Study on Evaporation Characteristics of Ammonium Formate-Urea-Water Solution Droplet for Selective Catalytic Reduction Applications. *Ind Eng Chem Res* 50(13):8285–8294
75. Gassen R, Göhr H, Müller N et al (1986) Korrosion in Carbonsäuren Teil II: Das Korrosionsverhalten hochlegierter Stähle, zweier Nickellegierungen und von Titan in Ameisensäure. *Materialwiss Werkstofftech* 17(6):218–225
76. Singh MM, Gupta A (1996) Corrosion behaviour of mild steel in formic acid solutions. *Mater Chem Phys* 46(1):15–22
77. Singh SK, Mukherjee AK, Singh MM (2011) Kinetics of mild steel corrosion in aqueous formic acid solutions. *Can Metall Quart* 50:186–194
78. Sekine I, Chinda A (1984) Comparison of the Corrosion Behavior of Pure Fe, Ni, Cr, and Type 304 Stainless Steel in Formic Acid Solution. *Corrosion* 40:95–100
79. Sekine I, Hatakeyama S, Nakazawa Y (1987) Corrosion behaviour of type 430 stainless steel in formic and acetic acids. *Corros Sci* 27:275–288
80. Sekine I, Momoi K (1988) Corrosion Behavior of SUS 329J1 Stainless Steel in Formic Acid Solution. *Corrosion* 44:136–142
81. Sekine I, Masuko A, Senoo K (1987) Corrosion Behavior of AISI 316 Stainless Steel in Formic and Acetic Acid Solutions. *Corrosion* 43:553–560
82. Kröcher O, Elsener M, Jacob E (2008) Neue Reduktionsmittel für die Low-NO_x-SCR-Technik/New reducing agents for the low-NO_x SCR technology. In: Proceedings of the 5th International Exhaust Gas and Particulate Emissions Forum, Ludwigsburg
83. Kennedy GL (2001) Biological effects of acetamide, formamide, and their mono and dimethyl derivatives: an update. *Crit Rev Toxicol* 31:139–222
84. Dresser TH, Rivera ER, Hoffmann FJ et al (1992) Teratogenic assessment of four solvents using the Frog Embryo Teratogenesis Assay–Xenopus (FETAX). *J Appl Toxicol* 12:49–56
85. Fail PA, George JD, Grizzle TB et al (1998) Formamide and dimethylformamide: reproductive assessment by continuous breeding in mice. *Reprod Toxicol* 12(3):317–332
86. Ramachandran BR, Halpern AM, Glending ED (1998) Kinetics and Mechanism of the Reversible Dissociation of Ammonium Carbamate: Involvement of Carbamic Acid. *J Phys Chem A* 102(22):3934–3941
87. Fulks G, Fisher G, Rahmoeller K et al (2009) A Review of Solid Materials as Alternative Ammonia Sources for Lean NO_x Reduction with SCR. SAE Technical Paper 2009-01-0907
88. Irazoqui HA, Isla MA (1993) Simulation of a Urea Synthesis Reactor - 2. Reactor Model. *Ind Eng Chem Res* 32:2671–2680

89. Sclar CB, Carrison LC (1963) Phase Composition of Commercial “Ammonium Carbonate”. *Science* 140:1205–1207
90. Krüger M, Nisius P, Scholz V et al (2003) A Compact Solid SCR System for NO_x Reduction in Passenger Cars and Light Duty Trucks. *MTZ Worldwide Edition* 2003-06
91. Tatur M, Tomazic D, Lacin F et al (2009) Solid SCR Demonstation Truck Application. In: *Directions in Engine-Efficiency and Emissions Research Conference*, Dearborn
92. Lacin F, Kotrba A, Hayworth G et al (2011) SOLID SCR[®]: Demonstrating an Improved Approach to NO_x Reduction via a Solid Reductant. *SAE Technical Paper* 2011-01-2207
93. Lepinasse E, Spinner B (1994) Cold production through coupling of solid-gas reactors I: Performance analysis. *Int J Refrig* 17(5):309–322
94. Vegge T, Sørensen RZ, Klerke A et al (2008) Indirect Hydrogen Storage in Metal Ammines, Part 4: Chemically Bound Hydrogen Storage. In: *Solid-State Hydrogen Storage: Materials and Chemistry*, Woodhead Publishing Limited, Cambridge, pp 533–564
95. Elmøe TD, Sørensen RZ, Quaade U et al (2006) A high-density ammonia storage/delivery system based on Mg(NH₃)₆Cl₂ for SCR-DeNO_x in vehicles. *Chem Eng Sci* 61(8):2618–2625
96. Liu CY, Aika K-I (2004) Ammonia Absorption on Alkaline Earth Halides as Ammonia Separation and Storage Procedure. *B Chem Soc Jpn* 77:123–131
97. Johannessen T, Christensen CH, Norskov JK et al (2005) High density storage of ammonia. *WO2,006,081,824*
98. Johannessen T, Schmidt H, Svagin J et al (2008) Ammonia Storage and Delivery Systems for Automotive NO_x Aftertreatment. *SAE Technical Paper* 2008-01-1027
99. Johannessen T (2011) Next generation SCR system for fuel-efficient NO_x reduction. In: *IQPC Conference Selective Catalytic Reduction*, Wiesbaden
100. Navistar (2009) Navistar to Invest in Danish Technology Company. <http://media.navistar.com/index.php?s=43&item=343>. Accessed 10 Feb 2014
101. Johannessen T (2010) Compact ammonia storage systems for fuelefficient NO_x emissions reduction. In: *CTI conference on SCR Systems*, Stuttgart
102. Nicosia D, Czekaj I, Kröcher O (2008) Chemical deactivation of V₂O₅/WO₃-TiO₂ SCR catalysts by additives and impurities from fuels, lubrication oils, and urea solution: Part II. Characterization study of the effect of alkali and alkaline earth metals. *Appl Catal B* 77:228–236
103. Tang F, Xu B, Shi H et al (2010) The poisoning effect of Na⁺ and Ca²⁺ ions doped on the V₂O₅/TiO₂ catalysts for selective catalytic reduction of NO by NH₃. *Appl Catal B* 94:71–76
104. Christensen CH, Sørensen RZ, Johannessen T et al (2005) Metal ammine complexes for hydrogen storage. *J Mater Chem* 15:4106–4108
105. Koebel M (1999) Comparative Study on the Use of Various Selective Reducing Agents in Automotive DeNO_x Systems.
106. Smeets PJ, Meng Q, Corthals S et al (2008) Co-ZSM-5 catalysts in the decomposition of N₂O and the SCR of NO with CH₄: Influence of preparation method and cobalt loading. *Appl Catal B* 84(3–4):505–513
107. Gist GL, Burg JR (1997) Benzene - a review of the literature from a health effects perspective. *Toxicol Ind Health* 13(6):661–714
108. Jacob E (2005) Ammoniakvorläufersubstanz und Verfahren zur selektiven katalytischen Reduktion von Stickoxiden in sauerstoffhaltigen Abgasen von Fahrzeugen. *DE102,005,059,250*
109. Günther T, Mertschenk B, Schulz B (2006) Guanidine and derivatives. In: *Ullmann's Encyclopedia of Industrial Chemistry*. Wiley-VCH, Weinheim, pp 175–188
110. Gerhart C (2011) NO_x-Reduzierung im motorischen Abgas mit Guanidinsalzen (NORA), Report No. NAZ-823-08, Bavarian Research Foundation
111. Kröcher O, Elsener M, Glückert U et al (2008) Guanidiniumformiat als neues Reduktionsmittel für die Low-NO_x-SCR-Technik. In: *Proceedings of the 2nd Conference MinNO_x - Minimization of NO_x Emissions Through Exhaust Gas Aftertreatment*, Berlin

112. Koebel M, Strutz EA (2003) Thermal and hydrolytic decomposition of urea for automotive selective catalytic reduction systems: Thermochemical and practical aspects. *Ind Eng Chem Res* 42(10):2093–2100
113. Peitz D (2012) Investigation on the catalytic decomposition of guanidinium formate, ammonium formate and methanamide as NH_3 -precursors for the selective catalytic reduction of NO_x . Dissertation No. 20568, ETH Zurich

Chapter 17

Modeling the Gas Flow Process Inside Exhaust Systems: One Dimensional and Multidimensional Approaches

Gianluca Montenegro and Angelo Onorati

17.1 Introduction

Diesel engines, as a consequence of their use of lean combustion, are the main cause of on-road NO_x emissions. The most promising solution, in terms of efficiency and fuel economy, to the removal of NO_x in oxidizing condition is the use of selective catalytic reduction of NO_x (SCR) [1]. On light and heavy duty vehicles the reducing agent, namely ammonia, is obtained from a water solution of urea (commonly referenced as UWS) directly injected inside the exhaust system. The main challenge, therefore, has become the optimization of the whole process inside the exhaust system, tailoring the best removal efficiency together with a limited ammonia slip and low fuel consumption. A precise injection strategy and an efficient mixing of the ammonia with the gas stream are key factors towards the achievement of high efficiency abatements, and therefore they have become the main object of study by means of numerical simulation tools.

The modeling of SCR systems is a particularly challenging task since it involves different physical phenomena where the evolution of multiphase and multicomponent flows take place. First, a urea/water solution is sprayed into the gas stream. The dispersed multicomponent phase then evaporates and suitably mixes with the gas stream before entering the catalyst. A comprehensive understanding of the underlying flow dynamics is therefore mandatory to design an efficient DeNO_x system which is characterized by a low impact on the engine performances.

From a R&D point of view, the automotive field has experienced a strong application of CFD (Computational Fluid Dynamics) tools for the design and optimization of engines and for the analysis of specific devices. Several

G. Montenegro (✉) · A. Onorati
Politecnico di Milano, via Lambruschini 4, Milan, MI, Italy
e-mail: gianluca.montenegro@polimi.it

A. Onorati
e-mail: angelo.onorati@polimi.it

approaches can be adopted, ranging from the 1D flow assumption to more complex multidimensional models. In particular, 1D codes have shown great flexibility of use, short calculation time, and low costs with respect to more complex multidimensional codes. Their adoption is usually motivated by the need of performing full cycle (several thermodynamic cycles) simulations of the engine coupled to the intake and exhaust system in a short time. As a matter of fact, Diesel exhaust systems are very complex, since they are always equipped with turbochargers, EGR routes, and aftertreatment devices, all of them playing an important role in the determination of the engine global efficiency. These components increase the complexity of the system and therefore the difficulty of a detailed modeling. Despite their flexibility of use and lightness, 1D models lack of predictiveness, since they cannot capture several processes occurring in the exhaust system, such as spray propagation, spray-wall interaction, and mixing processes, unless they resort to extremely simplified models of certain phenomena [2, 3]. The injection of urea/water solution, for example, can be studied in detail resorting to 3D CFD models as well as the formation of liquid film, the spray-gas mixing process, and the evaluation of ammonia distribution at the inlet of the SCR catalyst. In this chapter, it will be described the application of one-dimensional and multi-dimensional models for the study of the fluid dynamics of Diesel engine exhaust systems equipped with SCR systems. The 1D approach will be discussed first to highlight the importance of taking into account the overall engine configuration and the aspects of flow unsteadiness. Multidimensional approaches are usually focused on smaller details, such as the fluid dynamic analysis of the mixer and its interaction with the injected spray, rather than on the whole engine.

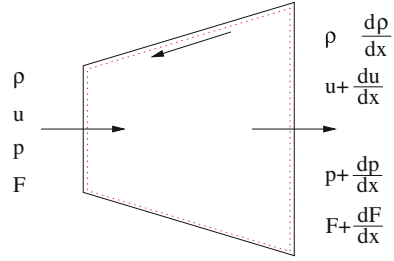
17.2 1D Models for the Prediction of Gas Flows

In the last decades, 1D models have been widely used for multiple purpose in the field of internal combustion engines and several codes are available on the market and in academies, both for commercial and research purposes [4–6]. Historically, different discretization approaches have been followed, but the most common are based on finite difference and finite volume ones, confining the finite element method only to research applications [7]. The finite volume and finite difference approaches are based on the formulation of 1D conservation equation of mass, momentum, and energy for an unsteady and reacting flow. Usually, the level of simplification reached in a 1D model allows to neglect the viscosity of the fluid and to lump the viscous phenomena into a gas-wall friction coefficient [8].

Applying the balance of mass, momentum, and energy to a generic control volume identified by a portion of a pipe with variable cross-section (Fig. 17.1), the conservation equations can be written in the following way:

$$\frac{\partial(\rho F)}{\partial t} + \frac{\partial(\rho u F)}{\partial x} = 0, \quad (17.1)$$

Fig. 17.1 Control volume used to derive the 1D conservation equations



$$\frac{\partial(\rho u F)}{\partial t} + \frac{\partial(\rho u^2 F + p F)}{\partial x} = p \frac{\partial F}{\partial x} x - \frac{2}{D} \rho u |u| f_w F, \tag{17.2}$$

$$\frac{\partial(\rho e_0 F)}{\partial t} + \frac{\partial(\rho e_0 u F + u p F)}{\partial x} = \rho q_{re} F. \tag{17.3}$$

The governing equations can then be written in vectorial form as follows:

$$\frac{\partial \mathbf{W}(x, t)}{\partial t} + \frac{\partial \mathbf{F}(\mathbf{W})}{\partial x} + \mathbf{B}(\mathbf{W}) + \mathbf{C}(\mathbf{W}) = 0 \tag{17.4}$$

$$\mathbf{W}(x, t) = \begin{bmatrix} \rho F \\ \rho u F \\ \rho e_0 F \\ \rho \mathbf{Y} F \end{bmatrix}, \quad \mathbf{F}(\mathbf{W}) = \begin{bmatrix} \rho u F \\ p F + \rho u^2 F \\ \rho u h_0 F \\ \rho \mathbf{Y} F \end{bmatrix}, \quad \mathbf{B}(\mathbf{W}) = \begin{bmatrix} 0 \\ -p \frac{dF}{dx} \\ 0 \\ 0 \end{bmatrix}, \tag{17.5}$$

$$\mathbf{C}(\mathbf{W}) = \begin{bmatrix} 0 \\ \rho G F \\ -\rho(q + q_{re} + q_{ev}) F \\ -\rho \dot{\mathbf{Y}} F \end{bmatrix},$$

where \mathbf{W} is the vector of the conserved variables, \mathbf{F} is the vector of the fluxes of the conserved variables and vector \mathbf{B} takes into account the effect of the cross-section variation. Vector \mathbf{C} accounts for the contributions of: (i) the heat exchanged between the gas and the pipes (q); (ii) the heat generated by the homogeneous reactions occurring in the exhaust line (q_{re}); and (iii) the friction between the gas and the walls (G). The system of equations is then closed by the state equation of the gas, which is treated as a mixture of perfect gases whose specific heat capacity is a function of both chemical composition and temperature [9]. The composition of the gas can then be tracked solving the conservation equation for each chemical component present in the gas phase. The vector Y in Eq. (17.5) refers to the mass fraction of each species composing the gas and allows to transport along the ducts all the information related to the chemical composition of the mixture. In these models, an arbitrary number of chemical species can be considered, depending on the particular chemical process that one wants to simulate. In any case, the gas composition can be assigned as a boundary condition, if

the modeling is focused only onto a single device of the exhaust system, or eventually assigned by a specific combustion model in the case the simulation involves the complete engine configuration (intake system, cylinders, and exhaust system). For the modeling of exhaust systems of Diesel engines a typical gas composition that can be taken into account may be O_2 , N_2 , Ar, CO_2 , H_2 , CO, NO, C_xH_y , NH_3 , HCNCO (isocyanic acid), $NH_2-CO-NH_2$ (urea) plus two phases of water, $H_2O_{(l)}$, and $H_2O_{(g)}$:

$$\mathbf{Y} = \begin{bmatrix} Y_1 \\ Y_2 \\ \vdots \\ Y_{N_s} \end{bmatrix} \sum_{j=1}^{N_s} Y_j = 1. \quad (17.6)$$

The source term $\dot{\mathbf{Y}}$ in \mathbf{C} (Eq. 17.5) expresses the production/destruction rate of the j th specie during the transport, due to reactions in the exhaust manifold (gas-phase reactions) and in the chemical converters (solid phase reactions). In the set of conservation equations, water appears into two phases, gaseous and liquid. The liquid phase can be considered as a property advected with the gas, in the same way the gaseous species are transported. This assumption can only be accepted if the size of the liquid water droplets is very small, which is rarely the case when urea–water solution is injected in the gas stream.

The system of Eq. (17.4) is a partial derivative hyperbolic system, whose numerical solution is achieved using shock-capturing numerical methods [10–13]. These methods are characterized by second-order accuracy and therefore they give rise to spurious oscillation when high gradients are present in the solution field. To suppress the occurrence of numerical instabilities, flux limiting techniques, or gradient limiters are used [8].

17.2.1 Modeling the Thermal Aspects

An accurate prediction of the chemical behavior of aftertreatment devices, can be achieved throughout a correct prediction of the heat fluxes along the exhaust system. This aspect is also important for a correct prediction of the back pressure which, in the end, affects the volumetric efficiency of the engine determining an increase of fuel consumption. In particular, to simulate engine driving cycles with cold start, in which the thermal transient of the exhaust system affects the performance of the catalytic converters, the correct estimation of the heat loss is vital. Also from a point of view of optimization, the estimation of the heat loss becomes important, especially in those cases where the improvement of the manifold insulation is tailored, in order to achieve an higher gas temperature at the inlet of the catalytic devices [3, 14]. The prediction of the thermal transient of the exhaust system can be carried out by considering the heat transferred between the gas and the walls in the energy balance of the gas, as a source term in Eq. (17.6), and

solving a coupled Fourier equation applied to the pipe walls, whose thermal balance can be expressed by:

$$\int_{V_w} \rho_w c_{p,w} \frac{\partial T_w}{\partial t} = \int_{V_w} \text{div}(\lambda \text{grad } T) dV + \int_{V_w} S_{e,c} dV. \quad (17.7)$$

Since the heat flux given by the temperature gradient between the wall and the gas bulk has been imposed as a boundary condition, Eq. (17.7) can be reduced to the following expression:

$$T_w^{n+1} = T_w^n + \frac{\Delta t}{\rho_w c_{p,w} V_w} (Q_r + Q_h + Q_\lambda^{\text{ax}} + Q_\lambda^r + S_{e,c}), \quad (17.8)$$

where T_w^{n+1} and T_w^n are, respectively, the wall temperatures at the new and old time step, while Q_r is the heat flux due to radiative heat transfer, Q_h is the convective heat flux between the gas and the walls, Q_λ^{ax} and Q_λ^r are, respectively, the conductive heat in the axial direction inside the wall and in the radial direction, when layers of different materials are considered. The source term $S_{e,c}$ accounts for the heat released by eventual chemical reactions or condensation and evaporation processes occurring in the proximity of the pipe walls. The quantities $c_{p,w}$, ρ_w , and V_w are, respectively, the wall specific heat capacity, the wall density and the volume of material related to the single computational cell. The Fourier equation can be applied to each layer of material, in order to consider the effects of different material properties on the global heat flux with the surrounding air (e.g., insulating materials, metallic shells, air gaps, or wash-coat layers). Several correlations can be used to model the heat transfer between the gas and the walls, however, the most general correlation appears to be the one proposed by Churchill, since its range of validity for the Reynolds and Prandtl number are those typical of the flow regimes inside exhaust systems of internal combustion engines [14, 15]:

$$\text{Nu} = \sqrt[10]{\text{Nu}_l^{10} + \left(\frac{e^{(2200-\text{Re})/365}}{\text{Nu}_l^2} + \frac{1}{\text{Nu}_l^2} \right)^{-5}}, \quad (17.9)$$

where

$$\text{Nu}_l = \text{Nu}_0 + \frac{0.079(f/2)^{\frac{1}{2}} \text{Re}^{\frac{5}{8}} \text{Pr}^{\frac{1}{4}}}{1 + \text{Pr}^{\frac{4}{5}}}, \quad (17.10)$$

$$\text{Nu}_0 = 4.8, \quad (17.11)$$

$$\text{Nu}_l = \begin{cases} 2.97 & \text{square flow section,} \\ 3.675 & \text{circular flow section,} \\ 3.0 & \text{triangular flow section.} \end{cases} \quad (17.12)$$

This correlation is valid for $0 < \text{Pr} < 10$ and for $0 < \text{Re} < 10^6$, therefore, considering that inside I.C. engine exhaust systems the Prandtl number is usually lower than 1 and Re is that typical of fully turbulent flow regimes, this correlation can be applied to the study of exhaust gas flows. The friction coefficient f that appears in Eq. (17.10) is given by the Churchill correlation as well [16]:

$$f = 2 \left[\left(\frac{8}{\text{Re}} \right)^{12} + \frac{1}{(A + B)^{\frac{3}{2}}} \right]^{\frac{1}{12}}, \quad (17.13)$$

where

$$A = \left[2.2088 + 2.457 \ln \left(\frac{\varepsilon}{d} + \frac{42.683}{\text{Re}^{0.9}} \right) \right]^{16}, \quad (17.14)$$

$$B = \left(\frac{37.530}{\text{Re}} \right)^{16}. \quad (17.15)$$

The same correlation for the friction coefficient is also used to define the source term of the momentum conservation (Eq. 17.2).

17.2.1.1 Effect of Moisture Condensation and Evaporation

The prediction of the thermal transient of the exhaust systems, especially in the case of cold start, can be further improved by modeling the formation of a liquid film layer due to the condensation, and its subsequent evaporation, of the water vapor contained in the exhaust gas (usually around 7–8 % of mass fraction). From the analysis of the temperature history gauged by thermocouples along the exhaust system, it has been pointed out the presence of a plateau due to the insulation effect produced by the evaporation of the liquid film layer [17–19]. This effect is negligible in the hot part of the exhaust line close to the engine head, but becomes important in the low temperature part and in particular inside of catalysts and Diesel particulate filter substrates, due to the high specific surface per unit volume. To predict the effect of the moisture condensation and evaporation, it is necessary to consider the mass transfer of water to the walls during the condensation and the migration of water vapor from the walls to the exhaust gas during the evaporation. Condensation is the cause for the increase of the wall temperature during the first seconds of operating conditions, while the evaporation becomes responsible of an insulation effect due to the latent heat of evaporation taken from the gas. The latent heats of evaporation and condensation ($\Delta h_{e,c}$) in the model can be taken into account in the source term $S_{e,c}$ of the Fourier equation (Eq. 17.8). The rate of phase change (evaporation or condensation) \dot{Y} in Eq. (17.6) can be expressed by the following equation [17]:

$$\dot{Y}_{\text{H}_2\text{O}} = \rho k_{\text{m,H}_2\text{O}} S \left(\frac{1}{\rho v_{\text{sat}}} - C_{\text{s,H}_2\text{O}} \right), \quad (17.16)$$

in which the specific volume of the saturated water vapor v_{sat} has been determined as a function of the wall temperature on the basis of tabulated values:

$$v_{\text{sat}} = e^{1.325 \cdot 10^{-4} T_w^2 - 0.06 T_w + 5.175}. \quad (17.17)$$

The above expression is valid only for $20 \text{ }^\circ\text{C} < T_w < 120 \text{ }^\circ\text{C}$. In the temperature range considered for the evaluation of the saturated water vapor's specific volume, a constant value of 2,370.1 kJ/kg can be assumed for the latent heat with good accuracy. The source term for the thermal balance of the pipe walls is therefore:

$$S_{\text{e,c}} = \dot{Y}_{\text{H}_2\text{O}} \Delta h_{\text{e,c}}. \quad (17.18)$$

17.2.1.2 Water Dragging Model

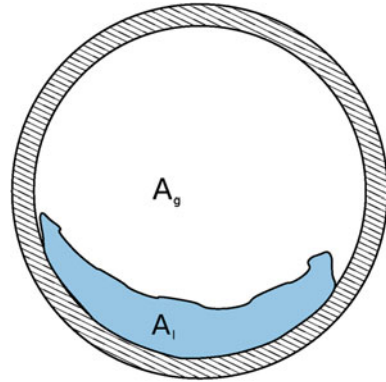
The water mass in direct contact with the gas stream inside the pipe is dragged in the direction of the flow by the friction between the water surface and the gas. The theory of multiphase flow is very complex and far from the complexity degree of a 1D model. The two phase flow inside the monolith can therefore be reduced to a stratified layer flow, where the two phases are moving with different velocities. The reasons of the water motion can be: (i) motion caused by the friction between the gas and the water and (ii) effect of the gravity if the pipe is not horizontal. The mass of dragged liquid is determined by applying the mass and momentum conservation to the two phases, the liquid water and the exhaust gas, calculating the contact surface on the basis of the water layer thickness [20, 21]. Referring to Fig. 17.2 and assuming that the two phases are confined in the two regions A_1 and A_g , respectively, for liquid and gas, the velocity of the liquid can be calculated by the following equation:

$$\frac{\tau_1 S_1}{A_1} - \frac{\tau_g S_g}{A_g} - \tau_i S_i \left(\frac{1}{A_1} + \frac{1}{A_g} \right) + (\rho_1 - \rho_g) g \sin \beta = 0, \quad (17.19)$$

where

$$\begin{aligned} \tau_1 &= \frac{1}{2} f_i \rho_1 |v_1| v_1, \\ \tau_g &= \frac{1}{2} f_g \rho_g |v_g| v_g, \\ \tau_i &= \frac{1}{2} f_i \rho_g |v_g - v_1| (v_g - v_1). \end{aligned} \quad (17.20)$$

Fig. 17.2 Example of the distribution of the two phases in a channel section



The terms f_l , $f_{g, i}$ are, respectively, the friction terms for the liquid-wall, gas-wall, and gas-liquid interface, while β is the inclination angle of the pipe with respect to an horizontal line. Once the liquid velocity v_l has been calculated, the new value of the liquid mass in each calculation node can be determined resorting to an upwind finite difference calculation technique.

17.2.1.3 Urea-Water Solution Injection

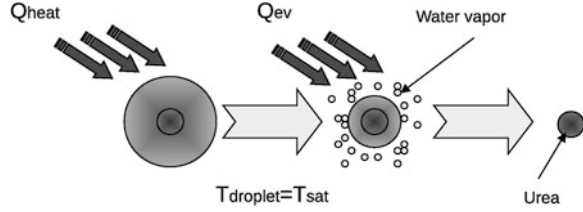
Another important aspect that can be considered in 1D models is the injection of water urea solution. The approach must be very simple but at the same time should be able to account for the main effects of the injection of liquid droplets. As anticipated in Sect. 17.2.1.2, the conservation equations for each chemical species may account for the liquid phase of water. The assumption is arguable, since droplets exchange momentum with the gas stream and they have also inertia. However, to model the impact of liquid droplets on the gas-phase heat balance and the release of urea, it may be acceptable.

Once injected, the number of droplets is fixed and advected with the gas stream. The injected spray does not exchange, for simplicity sake, momentum with the exhaust gas; however, since the temperature gradient between the droplet and the gas is high, the droplet undergoes a heating process until it reaches the saturation temperature. This phase can be divided into two steps (summarized in Fig. 17.3):

- the droplet is heated until the saturation temperature is reached,
- the water contained in the droplet evaporates until its mass fraction becomes null. In this process, the evaporation rate depends on the heat made available by the gas stream.

During the heat up phase the energy balance of the droplet states that its energy variation is given by the heat transferred to the droplet by convection:

Fig. 17.3 Schematic of the heat up and evaporation process of a water urea solution droplet modeled in 1D



$$\frac{4}{3}\pi R_p^3 \rho_p c_{pr} \frac{dT_p}{dt} = (4\pi R_p^2) k \frac{T_g - T_p}{2r_p} \text{Nu}_l, \quad (17.21)$$

where R_p , T_p , ρ_p e c_{pr} are respectively the diameter, the temperature, the density, and the specific heat of the droplet. T_g is the gas temperature and k is the thermal conductivity of the gas. The heat exchanged between the gas and the droplet can be expressed as:

$$q = h_p A_{s,p} (T_g - T_p), \quad (17.22)$$

where h_p is the convective heat exchange coefficient given by the following relation:

$$h_p = \frac{k \text{Nu}_l}{2r_p}, \quad (17.23)$$

and $A_{s,p}$ is the surface of the droplet:

$$A_{s,p} = 4\pi R_p^2. \quad (17.24)$$

The Nusselt number Nu_l in Eq. (17.23) is described by the following relation [22, 23]:

$$\text{Nu}_l = 2.0 + 0.6 \text{Re}^{\frac{1}{2}} \text{Pr}^{\frac{1}{3}}, \quad (17.25)$$

where the Reynolds number, Re , is referred to the droplet velocity and diameter. Properties of viscosity, specific heat capacity, and conductivity are evaluated as functions of the average temperature defined as follows:

$$\hat{T} = \frac{T_g + 2T_p}{3}, \quad (17.26)$$

Solving the energy balance of the droplet (Eq. 17.21) with respect to the droplet temperature, the following equation can be obtained:

$$\frac{dT_p}{dt} = \frac{3}{2} \frac{k \text{Nu}_l}{R_p^2 \rho_p c_{pr}} (T_g - T_p). \quad (17.27)$$

This approach is supported by the assumption that the number of injected droplets does not change and that the mean droplet diameter is also transported as

a property along the gas stream. When water is up to the saturation temperature, the evaporation process is dominant and the whole heat exchanged between the gas and the droplets is used to evaporate the liquid. The rate of evaporation is therefore proportional to the energy made available by the gas through convection:

$$\dot{m}_{\text{H}_2\text{O}} = \frac{\rho_{\text{vp}} c_{\text{pr}} D_{\text{H}_2\text{O}} \frac{T_{\text{g}} - T_{\text{p}}}{2R_{\text{p}}} \text{Nu}_{\text{II}}}{\Delta h_{\text{fg}}} A_{\text{s,p}}, \quad (17.28)$$

where ρ_{vp} is the density of the liquid vapor, $D_{\text{H}_2\text{O}}$ is the diffusion coefficient of gaseous water in air, Δh_{fg} is the latent heat of evaporation. The Nusselt coefficient Nu_{II} is defined in a different way, with respect to the Nu_{I} , since it accounts for reduction of the evaporation rate due to the presence of a vapor layer over the droplet surface:

$$\text{Nu}_{\text{II}} = \left(2.0 + 0.6 \text{Re}^{\frac{1}{2}} \text{Pr}^{\frac{1}{3}}\right) \frac{\ln(1 + B_{\text{p}})}{B_{\text{p}}}, \quad (17.29)$$

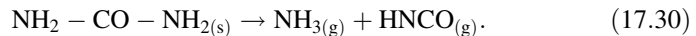
where B_{p} is the Spalding transfer number [24], which is driven by the gradient of concentration between the saturated vapor and the gas stream.

17.2.2 Thermal and Hydrolytic Decomposition of Urea

In mobile applications, the SCR technique involves the atomization of aqueous solution of urea in the hot part of the exhaust system upstream the SCR catalyst. The urea injected undergoes two different chemical processes to produce the ammonia necessary to sustain the SCR reaction: thermal decomposition and hydrolysis.

17.2.2.1 Thermal Decomposition of Urea

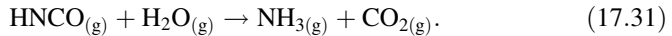
When a solution of urea is injected into the exhaust system, the first process that takes place is the evaporation of the water contained in each droplet. After the water evaporation, the urea is thermolyzed by the surrounding hot gas, producing gaseous ammonia and isocyanic acid according to the following reaction:



This mechanism, however, can be considered as a single-step reaction only if the heating is carried out fast. A slow heating of the urea will produce side reactions, due to the high reactivity of isocyanic acid, with the production of undesirable chemical products such as biuret, triuret, and cyanuric acid [25]. Usually, the reaction is supposed to occur without any side effect and is endothermic (+185.5 kJ at standard conditions).

17.2.2.2 Hydrolysis of Isocyanic Acid

The step following the thermal decomposition of urea is the catalyzed hydrolysis of the isocyanic acid formed in the previous reaction. The isocyanic acid is hydrolyzed by the water contained in the gas stream according to the following reaction:



This reaction completes the process of urea decomposition, transforming the isocyanic acid into further ammonia delivered to the SCR reactor. The reaction enthalpy of hydrolysis indicates that the reaction is exothermic, bringing a heat generation of 95.9 kJ per mole. This aspect is important, since it can be a consistent contribution to the heat request of reaction 17.30, reducing to less than half the heat required by the thermal decomposition. The global process, therefore, can be seen as the reaction:



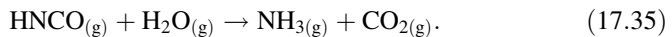
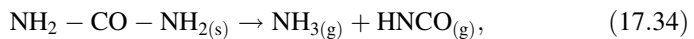
in which the heat required is 89.6 kJ per mole.

17.2.3 Kinetic Model

The chemical reactions can be modeled by means of the source term $\dot{\mathbf{Y}}$ of Eq. (17.6), which expresses the rate of change of the transported chemical species:

$$\dot{\mathbf{Y}} = \begin{bmatrix} Y_1 \\ Y_2 \\ \vdots \\ Y_{N_s} \end{bmatrix} \propto \begin{bmatrix} \frac{dC_1}{dr} \\ \frac{dC_2}{dr} \\ \vdots \\ \frac{dC_{N_s}}{dr} \end{bmatrix}. \quad (17.33)$$

The model for the urea decomposition considers the following reactions:



The rate of reaction (17.34) can be considered as first order with respect to the concentration of urea [26]:

$$r_1 = -k_1 C_{\text{CO}(\text{NH}_2)_2}. \quad (17.36)$$

The same consideration applies to the calculation of the reaction rate of Eq. (17.35), which is assumed to be a function of the concentration of water and isocyanic acid:

$$r_2 = k_2 C_{\text{HNCO}} C_{\text{H}_2\text{O}}. \quad (17.37)$$

The rate of change of the species taken into account by the model is therefore given by the following equations:

$$\frac{dC_{\text{CO}(\text{NH}_2)_2}}{dt} = -k_1 C_{\text{CO}(\text{NH}_2)_2}, \quad (17.38)$$

$$\frac{dC_{\text{HNCO}}}{dt} = k_1 C_{\text{CO}(\text{NH}_2)_2} - k_2 C_{\text{HNCO}} C_{\text{H}_2\text{O}}. \quad (17.39)$$

The reaction scheme presented above, according to experimental measurements available in the literature [26], is characterized by different values of the kinetic constants k_i , depending whether they occur onto a catalyzed bed or not. Focusing on the urea thermal decomposition process, experiments [26] have shown that reaction (17.38) is very rapid and is not affected by the presence of a catalyzed bed of typical SCR systems, whereas the hydrolysis of isocyanic acid occurs only at high temperature levels. According to this analysis, the values of the kinetic constants that can be used for the simulation of urea thermal decomposition are:

$$k_1 = 4.9 \times 10^3 e^{\frac{-5505}{RT}}, \quad (17.40)$$

$$k_2 = 2.5 \times 10^5 e^{\frac{-14861}{RT}}, \quad (17.41)$$

An example of the application of a 1D model for the simulation of thermal decomposition of urea can be found in Montenegro and Onorati [2]. Usually, the solver is optimized just for the gas dynamics and not for the stability of the reaction mechanism. As a matter of fact, the reaction mechanisms may be quite stiff and therefore require very small time steps. The problem can be overcome adopting a smaller time step also for the CFD, however this strategy may be not convenient when several seconds of real time need to be simulated. Hence, stable ordinary differential equation (ODE) solvers [22] are adopted in order to handle the reaction mechanism. In particular, given a time step Δt_{CFD} for the gas dynamics, whose choice for explicit methods is ruled by the CFL criterion [27], the integration of the chemistry is performed following subcycles of integration to solve the ODE system per each gas dynamic time step:

$$\frac{dY_i}{dt} = \dot{Y}_i = \omega_i, \quad (17.42)$$

where ω_i expresses the rate of change, due to heterogeneous reactions, of the i th chemical component:

$$\omega_i = \frac{Y_i^{t+\Delta t} - Y_i^t}{\Delta t}. \quad (17.43)$$

It has been demonstrated that the measurements of Y_{im} could be reproduced numerically with fairly good agreement using the kinetic constants determined experimentally on the test rig [2].

In Figs. 17.4 and 17.5, it is shown a comparison between the measured and calculated gas composition downstream of a thermal reactor as a function of temperature at two different space velocities, namely 32,000 and 65,000 h^{-1} . The feeding gas has been assigned with a fixed composition according to the measurements in [26]: 250 ppm of urea, 5 % O_2 , 2 % H_2O , and 93 % N_2 . Due to thermal decomposition, the quantity of ammonia at the reactor outlet increases with the catalyst temperature. The reaction scheme included in the 1D model has shown a good reliability, since it is capable of predicting the composition trend at the thermal reactor outlet at different gas temperature levels. Moreover, the influence of the space velocity variation can be captured correctly. The presented model can, therefore, be applied to a 1D model of an engine coupled to the intake and exhaust systems. The liquid phase injected in the system can be tracked as a scalar quantity representing the amount of water injected during a time step. Assuming a typical number of droplets on the basis of modeling experience in the field of liquid sprays, it is possible to estimate the amount of evaporated water and urea by means of heat transfer correlations. The advantage of this approach is that the unsteadiness of the process is fully captured, allowing to account for contributions such as temperature discontinuities and heat losses on the thermal decomposition of urea. An example of application on a real engine geometry, comprehensive of the chemistry occurring also in the catalysts, can highlight the importance of a whole engine simulation. The test case considered is an heavy duty 4.0 L four cylinder diesel engine running at full load at 1,000 rpm. Figure 17.6 shows a 1D schematic of that engine where three different reacting regions have been highlighted, namely the thermolizer, the hydrolyzer, and the SCR catalyst.

The results presented in Fig. 17.7 show the concentration profile of the main chemical species considered, along a typical Diesel engine exhaust system, in which the three reacting regions have been supposed at a fixed temperature of 523 K. In particular, it can be noticed the abatement of the nitrogen oxide only inside the SCR reactor, with the consequent decrease of ammonia. This conversion efficiency is low because of the lack of NH_3 , that is completely exploited in this reactor. The ammonia, as can be seen, is produced mainly by the thermal decomposition of urea. In this operating condition the engine presents no ammonia slip at the tailpipe outlet, but a non-negligible quantity of isocyanic acid and urea would be discharged in the atmosphere. These results point out that a 1D computational model can be a useful tool to optimize the urea injection strategy, in order to reduce both the NO_x emission and the slip of dangerous substances like HNCN and ammonia. On balance, the 1D approximation has the main limit of needing the definition of several tuning factors, such as friction factors, heat exchange coefficients, and so on. These aspects are mainly related to the assumption of uniform distribution of thermal and fluid dynamic quantities. A correct prediction of the heat flux between the gas and the external ambient can be assessed only with an accurate resolution of the near-wall temperature gradient, as well as the flow resistance needs to be estimated resolving the near-wall velocity gradient. All these aspects are modeled in 1D codes resorting to empirical correlation. If we consider SCR systems, flow resistance and heat losses are not the

Fig. 17.4 Comparison between calculated and measured HNCO, urea, and NH_3 concentration at the outlet of the thermolysis reactor as a function of the gas temperature with a space velocity of $65,000 \text{ h}^{-1}$

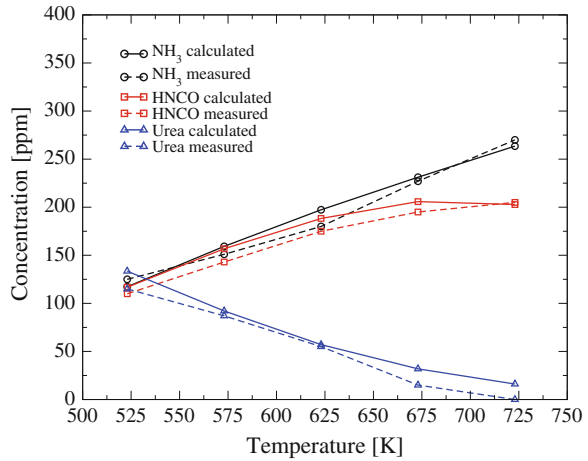
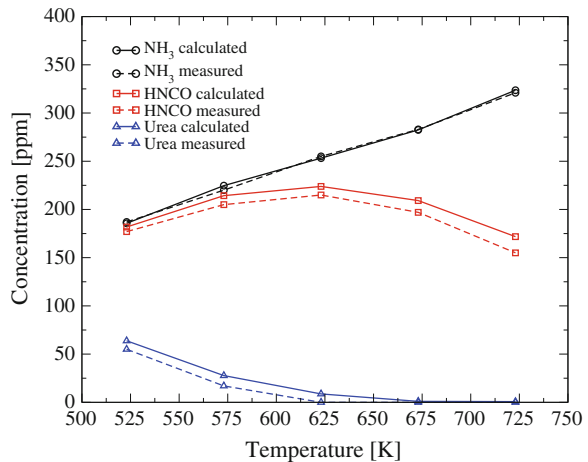


Fig. 17.5 Comparison between calculated and measured HNCO, urea, and NH_3 concentration at the outlet of the thermolysis reactor as a function of the gas temperature with a space velocity of $32,000 \text{ h}^{-1}$



only aspects that matter during the design phase. As a matter of fact, the injection of UWS sprays requires usually the adoption of a mixing device, whose main role is to provide a distribution of reducing agent as much uniform as possible over the catalyst inlet section. This requirement is demanded by the one to one molar ratio between nitrogen oxides and ammonia of the standard SCR reaction. Since the NO_x is uniformly distributed along the surface, its abatement is ensured by an equivalent distribution of ammonia. The lower is the uniformity of the reducing agent, the lower will be the catalyst efficiency. A 1D model is not able to capture the distribution on the flow area of a chemical specie and the mixing process of the reducing agent with the gas stream cannot be determined, unless further tuning parameters are introduced. For this reasons a finer optimization of an SCR system

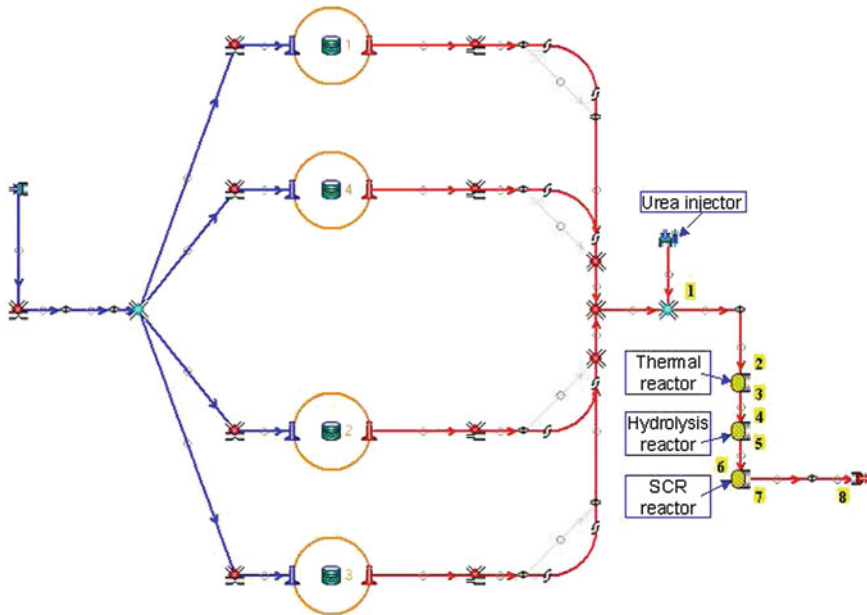


Fig. 17.6 Schematic of the 4.0 L heavy duty Diesel engine used for the simulation of the complete SCR system under unsteady flow condition

cannot be performed resorting exclusively to a 1D analysis, but requires the aid of a deeper investigation of specific aspects, such as the gas-spray interaction and mixing, which can only be carried out resorting to multidimensional codes.

17.3 Multidimensional Models

17.3.1 Governing Equations

When gradients and field non uniformities along the flow section become guiding factors of specific phenomena, such as gas mixing and spray evolution, the modeling of these effects is regarded as fundamental to perform an accurate prediction. In this scenario, the adoption 3D CFD codes represents the only feasible way to follow. Among all the models available, the most used are based on the finite volume approach for the discretization of partial derivative equations. This formulation allows to express the set of equations in a conservative way for any arbitrary mesh shape, without limiting the choice of the grid typology to be used. Defining an arbitrary control volume, the integration of the conservation equation can be generally expressed in the following form:

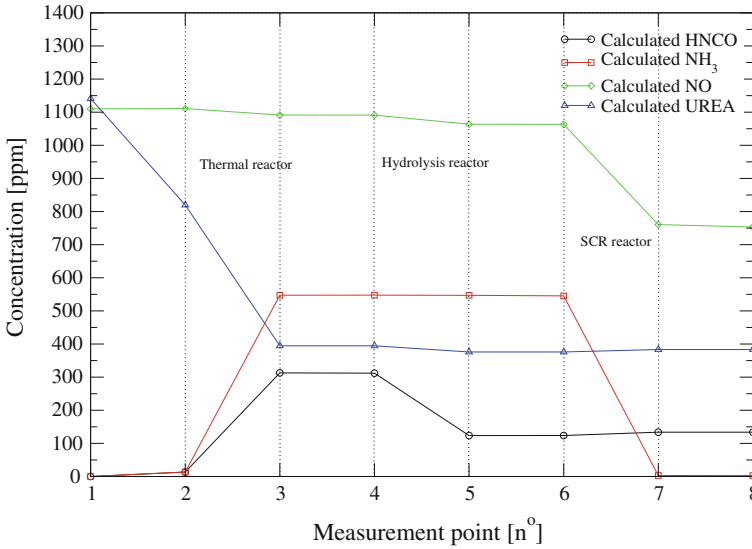


Fig. 17.7 NH₃, HNCO, urea, and NO concentrations tracked along the exhaust system with reactors at 523 K

$$\int_V \frac{\partial(\rho\phi)}{\partial t} dV + \int_S \rho\phi\mathbf{U} \cdot \mathbf{n}dS = \int_S Q_S(\phi) \cdot \mathbf{n}dS + \int_V Q_V(\phi)dV \quad (17.44)$$

where the variable ϕ represents a generic conserved variable and \mathbf{Q}_S and Q_V are surface and volume source terms, respectively. Performing the integral operation and assuming ϕ as the gas density ρ , Eq. (17.44) leads to the multidimensional conservation equation of mass:

$$\frac{\partial\rho}{\partial t} + \nabla \cdot (\rho\mathbf{U}) = \dot{Q}. \quad (17.45)$$

This represents the overall mass conservation without referring to the chemical composition of the gas. The source term of Eq. (17.45) takes into account the mass exchange between the liquid and the gas phase. Since the liquid phase can be present into two different forms, droplets coming from the injection of the water solution and liquid film deposited onto the walls, two distinct terms have been included in this equation:

$$\dot{Q} = \dot{Q}^{\text{Spray}} + \dot{Q}^{\text{WallFilm}}. \quad (17.46)$$

The exhaust gas of an internal combustion engine is usually composed by multiple chemical components (O₂, CO₂, NO_x, and other compounds) each of them is advected along the gas stream. Despite no diffusion of mass is considered in Eq. (17.45), a single component may diffuse due to gradients in the composition.

In particular, gradients in chemical composition are present at interfaces between liquid and gas and also inside the gas, whenever the concentration of a single component changes. These are typically originated by the opening of the exhaust valve at the end of each combustion process. For this reason, additional equations are solved for every chemical component:

$$\frac{\partial}{\partial t}(\rho Y_i) + \nabla \cdot (\rho \mathbf{U} Y_i) = -\nabla \cdot (\rho \Gamma_k \nabla Y_k) + \dot{Q}_k^{\text{Chemistry}} + \dot{Q}_k^{\text{Spray}} + \dot{Q}_k^{\text{WallFilm}}. \quad (17.47)$$

This equation accounts for the presence of convection, diffusion, and source terms due to the occurrence of chemical reactions and to the presence of an evaporating wall film and liquid spray. The mass diffusion coefficient Γ is determined assuming the Fick's law of binary diffusion of a single component into a multicomponent mixture. The momentum equation can be derived from Eq. (17.44) assuming that the quantity ϕ represents a vectorial quantity \mathbf{U} :

$$\frac{\partial}{\partial t}(\rho \mathbf{U}) + \nabla \cdot (\rho \mathbf{U} \mathbf{U}) = -\nabla p + \nabla \cdot \tau + \rho \mathbf{f} + \zeta. \quad (17.48)$$

The term τ is the viscous stress tensor and can be expressed in a complete form as:

$$\tau = \mu [\nabla \mathbf{U} + (\nabla \mathbf{U})^T] - \frac{2}{3} \mu \nabla \mathbf{U} \cdot \mathbf{I}. \quad (17.49)$$

The other two terms \mathbf{f} and ζ account for body forces, such as gravity, and the momentum exchange between the gas and the liquid spray, respectively.

The last conservation equation that can be formulated to completely define the thermo-fluid dynamic state of a fluid is the conservation equation of energy. The total internal energy is a quantity that well represents the thermodynamic state of the fluid:

$$E = U(p, T, \omega_k) + E_k = U + \frac{1}{2} \mathbf{U} \cdot \mathbf{U}, \quad (17.50)$$

With regard to energy conservation equation, we must consider the two types of fluxes, namely the convective and the diffusive (thermal conductivity of the fluid):

$$\mathbf{F}_C = \rho E \mathbf{U}, \quad \mathbf{F}_D = -k \nabla T. \quad (17.51)$$

The volume source terms are the work of the volume forces f_e plus the heat sources (radiation, reactions or electrical resistance) given by:

$$Q_V = \rho \mathbf{f}_e \cdot \mathbf{U} + q_H. \quad (17.52)$$

The surface sources \mathbf{Q}_S are the result of the work done on the fluid by the internal shear stress acting on the surface of the control volume:

$$\mathbf{Q}_S = \sigma \cdot \mathbf{U} = -p \mathbf{U} + \tau \cdot \mathbf{U}. \quad (17.53)$$

Considering all this contributions, the final formulation of the energy conservation equation becomes the following:

$$\frac{\partial \rho E}{\partial t} + \nabla \cdot (\rho E \mathbf{U}) = \nabla \cdot (k \nabla T) + \nabla \cdot (\boldsymbol{\sigma} \cdot \mathbf{U}) + \rho \mathbf{f}_e \cdot \mathbf{U} + q_H. \quad (17.54)$$

17.3.1.1 Modeling the Turbulence

The Navier–Stokes equations do not require assumptions about the particular type of flow taken into account; however, a comprehensive simulation of a turbulent flow would require a space and time discretization capable of resolving the Kolmogorov microscale and the time characteristic associated with it [28]. This approach is extremely onerous from the computational point of view, since the microscale scales with the inverse of $\text{Re}^{\frac{3}{4}}$ [29, 30]. The direct solution of the Navier–Stokes equations is therefore not the suitable approach for the majority of the problems encountered in practice. For this reason, a modeling of the turbulent phenomena is needed to achieve accurate results and to reduce the computational cost of simulations. In practice, the quantities can be expressed as a mean value, plus a fluctuation due to randomness of the process considered. By performing a suitable averaging process, the Reynolds averaged Navier–Stokes (RANS) equations can be obtained, in which the average of the fluctuating component gives rise to additional term in Eqs. (17.47), (17.49), and (17.54):

$$\frac{\partial \rho}{\partial t} + \nabla \cdot (\rho \mathbf{U}) = \dot{\Omega}^{\text{Spray}} + \dot{\Omega}^{\text{WallFilm}}, \quad (17.55)$$

$$\frac{\partial}{\partial t} (\rho \mathbf{u}) + \nabla \cdot (\rho \mathbf{U} \mathbf{U}) = -\nabla p + \nabla \cdot \boldsymbol{\tau}' + \rho \mathbf{f} + \boldsymbol{\xi}, \quad (17.56)$$

$$\frac{\partial \rho E}{\partial t} + \nabla \cdot (\rho E \mathbf{U}) = \nabla \cdot (k \nabla T) + \nabla \cdot (\boldsymbol{\tau}' \cdot \mathbf{U}) + \rho \mathbf{f}_e \cdot \mathbf{U} + q_H, \quad (17.57)$$

where

$$\boldsymbol{\tau}' = \boldsymbol{\tau}(\mu) + \boldsymbol{\tau}_{\text{turb}}(\mu_t), \quad (17.58)$$

$$k' = k(\mu) + k_{\text{turb}}(\mu_t), \quad (17.59)$$

$$\Gamma' = \Gamma(\mu) + \Gamma_{\text{turb}}(\mu_t). \quad (17.60)$$

The additional introduction of turbulent viscosity to the stress tensor in Eq. (17.60) is called the Reynold's stress tensor, while in the energy equation the fluctuating component increases the thermal diffusivity by a turbulent contribution (k_{turb}). The same correction appears in the conservation equations of chemical species, where the presence of a diffusion associated to fluctuations is introduced.

In particular, the conservation equation of the i -th chemical specie becomes the following:

$$\frac{\partial}{\partial t}(\rho Y_k) + \nabla \cdot (\rho \mathbf{U} Y_k) = -\nabla \cdot \left[\rho \left(\Gamma_k + \frac{\mu_t}{Sc_t} \right) \nabla Y_k \right] + \dot{Q}_k^{\text{Chemistry}} + \dot{Q}_k^{\text{Spray}} + \dot{Q}_k^{\text{WallFilm}}, \quad (17.61)$$

where Sc_t is the turbulent Schmidt number defined as:

$$Sc_t = \frac{\mu_t}{\rho \Gamma_t}. \quad (17.62)$$

Determining the value of the turbulent viscosity μ_t is the main scope of the turbulence model. In the classical k - ε turbulence model, two transport equations are solved for the turbulent kinetic energy (k) and its dissipation rate (ε) to calculate the turbulent viscosity:

$$\mu_t = \rho C_\mu \frac{k^2}{\varepsilon}, \quad (17.63)$$

where C_μ is a k - ε model parameter whose value is typically given as 0.09. The two transport equations are also characterized by the presence of constants which depend on the model and on the phenomena taken into account. The main drawback is that the dissipation rate of kinetic turbulent energy is constant for all the length scales. This is not very well representative of the reality and requires the adoption of particular functions to express the turbulence destruction near the walls, the so-called wall functions. These are used to express the gradient of the velocity when the mesh resolution is not adequately refined in the proximity of the walls. An improved formulation of the k - ε model (the RNG k - ε) adopts an expression for the source term of ε which is function of the strain rate [31]. This makes the model suitable for low Reynolds calculation and theoretically does not require the adoption of wall functions. The main drawback of this family of turbulence models, including also those based on a different formulation of the dissipation rate, such as the k - ω [32], is that turbulence is treated as an isotropic property of the flow. Flows inside of exhaust systems equipped with turbochargers and eventual mixers, to encourage the mixing between the injected reducing agent (ammonia or urea) and the gas stream, are characterized by strong swirl components. This highlights that turbulence may be an anisotropic property of the flow, which can be taken into account only resorting to the transport of the Reynolds stress tensor (Reynolds Stress Model) [33].

Particular care must be paid to the choice of the differencing scheme used for the solution of the governing equations. The choice is not univocal, since a trade-off between accuracy and computational cost exists. A first-order approximation for the convection term is the most stable approach, however if the target is the prediction of the mixing efficiency between ammonia and exhaust gas stream, then the solution will be affected by a significant amount of artificial viscosity, comparable to the turbulent one [33]. This issue can be overcome resorting to more

refined calculation grids, which on the other end may lead to excessively long calculation time. The alternative is to adopt accurate differencing schemes, based on linear interpolation, along with TVD smoothing techniques to prevent the occurrence of spurious oscillations [28–30].

17.3.2 Modeling the UWS Injection

Since in SCR systems the urea/water solution is injected in the gas stream, additional submodels are needed to simulate the interaction between the liquid droplets and the exhaust gas. The most straightforward approach used in CFD for the simulation of spray injection is the Eulerian–Lagrangian method, which allows for detailed descriptions of individual droplets during their trajectories and their interaction with the continuous phase [24, 34]. The other possible way of modeling this aspect is the Eulerian–Eulerian approach. In this framework both the liquid and the gas phase are modeled with the same strategy, resorting to an Eulerian approach [35, 36]. The detailed resolution of the interaction between gas and liquid is much more accurate, however the computational effort is significantly higher, since it requires to discretize the injector hole and each single droplet, leading to very refined computational meshes. This main constraint is removed with the Eulerian–Lagrangian approach, where specific submodels are used to simulate the interaction between the liquid jet and the surrounding gas. The droplets injected in the gas are tracked with a Lagrangian approach and their motion is coupled to continuous phase motion via Newton’s second law.

17.3.2.1 Spray Evolution

The spray droplets are described by stochastic particles which are usually referred as *parcels* [37]. Each parcel represents a class of identical, noninteracting droplets, and they are tracked through the physical space in a Lagrangian manner according to the mass, momentum, and energy exchange with the gas (Eulerian) phase. Additional phenomenological models are required to describe the various physical processes taking place in the subgrid length scales such as atomization, breakup, evaporation, heat transfer, turbulent dispersion, and collision. Spray atomization and breakup can be considered as the same process [38], atomization models are rarely used for simulation of urea/water solutions. Moreover, the low injection pressure used in injection systems (typically 6–9 bar) suggests that the droplet breakup occurs mainly due to the aerodynamic interaction between the droplet and the gas stream. For this reason, the droplet distribution can be imposed according to a certain random distribution of droplet diameters. A Rosin–Rammler law can be imposed to represent the distribution of droplet diameters at the injection point, assuming a known average diameter at the injection pressure typical of these systems [39]:

$$d_p = d \left[-\ln(1 - \xi)^{\frac{1}{n}} \right], \quad (17.64)$$

where d is the average diameter, ξ is a random number and $n = 1.21$ [39]. The secondary breakup, which accounts for the aerodynamic interaction between the liquid and the surrounding gas, can be modeled resorting to the WAVE model [38]. In this model the wavelength and growth rate leading to breakup are determined by a linear instability analysis performed on a cylindrical liquid jet of fixed radius, which penetrates through a circular orifice into a stationary incompressible gas environment. Liquid breakup can be described by postulating that new droplets are formed from a parent droplet with a radius proportional to the wavelength of the fastest growing or the most probable unstable surface wave.

Spray evaporation and heat transfer with the surrounding gas phase must be considered along with turbulent dispersion and droplet collisions [40].

Another important aspect that must be taken into account is how the spray interacts with the rigid walls present in the system. This is particularly important in SCR systems, since they are usually confined in limited space due to compactness requirements, therefore offering little space for spray penetration. The interaction between the spray parcels and the liquid film is modeled by the approach proposed by Stanton et al. [41]. The droplet impingement regimes are determined by the parameters describing the approaching droplets, the wall surface conditions, and the gas boundary layer characteristics in the near-wall region. The collision of a droplet with a liquid surface may result in sticking, spreading, bouncing, and splashing [42], as summarized in Fig. 17.8. The impingement regimes are identified by the Weber number We :

$$We = \frac{\rho \left(\vec{V}_p \vec{n}_w \right) d_0}{\sigma}, \quad (17.65)$$

where \vec{V}_p is the relative velocity between the droplet and the wall and \vec{n}_w is the face normal of the impinging wall. The following transition criteria are used:

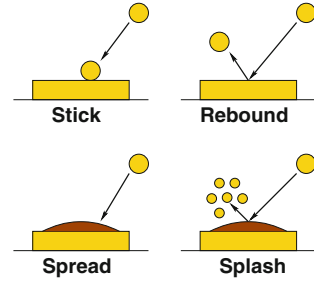
- $We < 5$: stick
- $5 < We < 10$: rebound
- $10 < We < We_s$: spread
- $We > We_s$: splash

We_s represents the splashing threshold and is given by [43, 44]:

$$We_s = (18)^2 d_0 \left(\frac{\rho}{\sigma} \right)^{1/2} \left(\frac{\mu}{\rho} \right)^{1/4} f^{3/4}, \quad (17.66)$$

where ρ , σ , μ , d_0 , and f are the droplet density, surface tension, dynamic viscosity, diameter at wall incidence, and frequency of droplet impingement on the film. The impact frequency is calculated in each boundary surface for each time step as:

Fig. 17.8 Impingement regimes identified in the spray-wall impingement model



$$f = \frac{1}{\sum_i N_{d,i}/\Delta t}, \quad (17.67)$$

where $N_{d,i}$ is the number of droplets contained in a single parcel and Δt is the time step. A detailed description of the correlations used for momentum and mass exchange between the droplets and the liquid film in the rebound and splash regimes can be found in [34, 43]. The splashing process is modeled by introducing three new droplets in the mesh for each impinging droplet.

17.3.2.2 Droplet Continuity Equation

The effect of evaporation of the liquid droplet is the only term that appears in the mass balance of a single liquid droplet. Its variation in time can then be expressed as:

$$\frac{dm_d}{dt} = \dot{m}_d, \quad (17.68)$$

where \dot{m}_d is the evaporation rate, calculated as a function of the droplet diameter D , of the liquid density ρ_v , of the mass diffusion coefficient Γ , and of the Sherwood number Sh :

$$\dot{m}_d = -\pi D \Gamma \rho_v Sh \ln \left(1 + \frac{X_{v,s} - X_{v,\infty}}{1 - X_{v,s}} \right). \quad (17.69)$$

The Sherwood number can be evaluated resorting to the formula proposed by Ranz-Marshall [45]:

$$Sh = 2 + 0.6 Re^{1/2} Sc^{1/3}. \quad (17.70)$$

The terms appearing as argument of the logarithm in Eq. (17.69) are the molar fractions of the species in the gas phase at a sufficiently far distance $X_{v,\infty}$ and the molar fractions at saturation. These terms are also used in a more compact form and referenced as the Spalding number B :

$$B = \frac{X_{v,s} - X_{v,\infty}}{1 - X_{v,s}}. \quad (17.71)$$

These correlations are valid only for evaporating droplets; different expressions must be considered when boiling occurs. In this case, the evaporation rate is governed by the rate of transfer between the droplet at temperature T_d and the gas at the temperature T needed to realize the phase change:

$$\frac{dm_d}{dt} = -\frac{\pi D \lambda_t \text{Nu}}{c_{p,v}} \ln \left(\frac{c_{p,v}}{\hat{H}_v} (T - T_d) + 1 \right), \quad (17.72)$$

where the Nusselt number is evaluated according to the following equation:

$$\text{Nu} = 2 + 0.6 \text{Re}^{1/2} \text{Pr}^{1/3}. \quad (17.73)$$

17.3.2.3 Droplet Motion Equation

From the Newton's law, the motion equation of the droplet can be stated as follows:

$$m_d \frac{d\mathbf{u}_d}{dt} = \mathbf{F}, \quad (17.74)$$

where \mathbf{u}_d is the droplet velocity and \mathbf{F} is the resultant of the forces acting on it, namely the drag force and the gravity [39]:

$$\mathbf{F} = -\frac{\pi D^2}{8} \rho C_D |\mathbf{u}_d - \mathbf{u}| (\mathbf{u}_d - \mathbf{u}) + m_d \mathbf{g}. \quad (17.75)$$

Other forces can be considered in order to take into account the lift resulting from the velocity gradient around the droplet or the virtual mass effect. However, in SCR simulations they can be neglected, since their contribution is usually from 2 to 3 order of magnitudes lower than the others [39]. A typical expression for the determination of the drag coefficient C_D is:

$$C_D = \begin{cases} \frac{24}{\text{Re}_d} \left(1 + \frac{1}{6} \text{Re}_d^{2/3} \right) & \text{Re}_d < 1000, \\ 0.424 & \text{Re}_d > 1000, \end{cases} \quad (17.76)$$

where Re_d is the Reynolds number of the droplet evaluated on the basis of the droplet-gas relative velocity:

$$\text{Re}_d = \frac{\rho |\mathbf{u}_d - \mathbf{u}| D}{\mu}. \quad (17.77)$$

Alternative formulations can also take into account the effect of high volumetric fraction of liquid θ , which is a case typical of injections at low pressure [46]:

$$C_D = \begin{cases} \frac{24}{\text{Re}_d} \left(\theta^{-2.65} + \frac{1}{6} \text{Re}_d^{2/3} \theta^{-1.78} \right) & \text{Re}_d < 1000 \\ 0.424 & \text{Re}_d > 1000. \end{cases} \quad (17.78)$$

Furthermore, due to the interaction with the surrounding gas, the shape of the droplet can change and consequently also its drag coefficient. This aspect can be accounted for correcting the drag coefficient, according to what is proposed in several publications [47, 48] (Fig. 17.9).

17.3.2.4 Droplet Energy Equation

The energy balance of the droplet can be expressed referring to its sensible enthalpy H_d . The variation of the droplet sensible enthalpy is given by the convective heat exchanged with the surrounding gas and by the heat of evaporation required during the phase change:

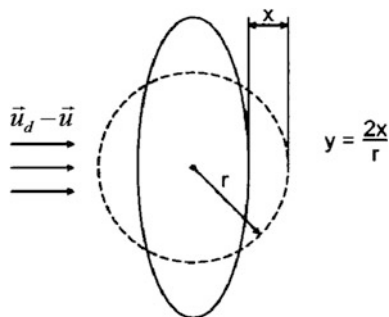
$$m_d \frac{dH_d}{dt} = \dot{m}_d H_v(T_d) + \pi D \lambda_t \text{Nu}(T - T_d) f. \quad (17.79)$$

The corrective coefficient f takes into account the contemporary occurrence of heat and mass transfer. The Nusselt number is determined according to Eq. (17.73). By combining Eqs. (17.68) and (17.79), it is possible to determine the temperature of the droplet. In this process iterative procedures are usually adopted to determine unknown quantities, moreover the properties of the saturated vapor around the droplet are evaluated resorting to the one-third rule (Eq. 17.26).

17.3.2.5 Modeling the Urea/Water Solution

In this analysis, particular care must be paid to the way the urea–water solution is modeled. Several works have been published on the modeling of UWS injection, each of them resorting to specific simplifications of the problem [49–53]. The main source of uncertainty is the lack of characterization of urea–water solutions at various temperature levels. Additionally, the environment temperature at which UWS is injected is quite often critical for two reasons: the gas temperature is higher than the boiling temperature of the UWS droplet; the pipe wall temperature is higher than the boiling temperature of the droplet. These two conditions make the modeling of the UWS evaporation the major challenge in the simulation of SCR systems. By reviewing the literature in the field of UWS injection, it is found that the state of aggregation of urea is not clear during the evaporation of UWS. As a matter of fact, it can be varied among solid, molten and gas phases, depending on

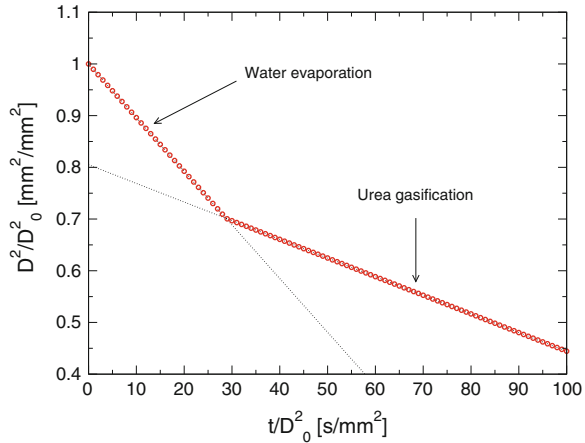
Fig. 17.9 Droplet deformation due to the interaction with the surrounding gas



the local thermophysical conditions. In particular, the high gas temperature can be a source of a strong deviation from the so-called D^2 -law of the droplet [54].

This is caused by the fact that the concentration of the two components in the solution changes during the evaporation, leading to possible high concentration of urea, which may result in formation of solid components. The result is a formation of a solid crust around the droplet which, due to the boiling of the inner liquid core, will cause a sudden explosion of the droplet when the inner pressure increases above a threshold level. Following the trajectory of a single UWS droplet, the history of the events taking places on its surface or inside its core can be determined. Considering that the melting point of urea is known to be around 406 K, at ambient temperature of 373 K only the water fraction evaporates from UWS droplet. At 423 K urea near droplet surface is expected to melt and thermally decomposes into ammonia and isocyanic acid. However, experimental observation reported that a vigorous gas evolution from molten urea commences at 425 K [51, 54]. Solidification can be observed after the complete depletion of liquid component from UWS. The deposits produced may be composed only by solidified urea, because the first urea-derived species, biuret, begins to be generated from the reaction of isocyanic acid with intact urea at 433 K. It has been demonstrated that modeling the radial distribution of temperature and urea concentration inside the droplet is not beneficial in terms of computational effort. Moreover, the comparison with rapid mixing models, in which temperature and concentration are assumed uniform over the droplet, does not show a significant improvement of accuracy [51]. When the temperature of the droplet is below the melting point of urea, the evaporation rate of urea can be modeled resorting to correlations available in the literature, which basically exploit the vapor pressure of solid urea [55]. Among all the proposed formulations, Bernhard et al. [56] characterized the vapor pressure extending the range of temperature above urea melting point, preserving a good matching of the formulation proposed by Krasulin [57]. In Fig. 17.10 it is shown the typical change of slope due to the initial evaporation of water and then to the gasification of urea followed by its immediate decomposition. Despite the different formulation of the vapor pressure, what emerges by the characterization of the UWS droplet is the low evaporation rate of urea if compared to water. This

Fig. 17.10 Two phases of the D^2 -law during evaporation of a UWS droplet at ambient temperature of 423 K [54]



aspect, combined with the need of having compact mixing devices, results in a frequent formation of liquid film with a higher concentration of urea than the injected liquid.

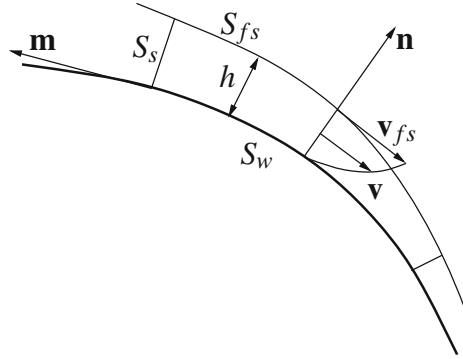
17.3.3 Modeling the Formation of Liquid Film

Once the trajectory of each single droplet is known, it is possible to evaluate its interaction with the walls included in the calculation domain. The definition of the impingement regimes presented in the previous section allows to know the net amount of mass that will form a liquid film over the walls. The interaction between spray and the wall can be realized defining specific solution fields on the surfaces where the formation of liquid film is likely to occur. These allow to define scalar and vectorial fields for the solution of the conservation equations of mass, momentum and energy [43, 58, 59]. The coupling between spray and wall film models can be realized resorting to the definition of a finite area field [60], over which the integration of the differential operations can be performed in a similar way to the finite volume approach. Within this framework, a schematic representation of a thin liquid film on a curved surface can be represented as in Fig. 17.11, where it is possible to identify a curved wall surface S_w , with its normal \mathbf{n} , a free surface of the liquid film S_{fs} , a liquid film of thickness h and an assumed velocity profile \mathbf{v} , varying from zero at the wall to the free surface velocity \mathbf{v}_{fs} .

In order to derive the governing equations for the liquid film, the following assumptions regarding the wall film behavior can be made:

- the film is thin enough for the boundary layer approximation to apply, i.e., the spatial gradients of the dependent variables tangential to the surface are negligible compared to those in the normal direction;

Fig. 17.11 Schematic representation of a thin liquid film



- film motion is caused by the spatial variation in the tangential direction of the total pressure p_L , shear at the wall and film interface, tangential momentum sources provided by incoming droplets, and body forces (e.g., gravity acceleration);
- under boundary layer approximations, local liquid pressure p_L within the film can be taken to be constant across the film depth;
- liquid pressure p_L consists of the following components: pressure of the surrounding gas p_g ; droplet impact pressure p_d ; capillary (or Laplace) pressure p_σ ; and hydrostatic pressure p_h . Thus, the liquid film is locally subject to the following pressure:

$$p_L = p_g + p_d + p_\sigma + p_h. \tag{17.80}$$

- the tangential momentum lost by the incident droplets provides a source of tangential momentum to the wall film;
- the mass flux due to incident droplets may be represented by a spatially smoothly varying function, so that conventional differential operations apply.

Using the above-mentioned modeling assumptions, the general liquid film governing equations can be derived in the following way:

$$\int_{S_w} \frac{\partial h}{\partial t} dS + \oint_{\partial S_w} h \mathbf{m} \cdot \bar{\mathbf{v}} dL = \int_{S_w} \frac{\dot{m}_S}{\rho_L} dS + \int_{S_w} \frac{\dot{m}_V}{\rho_L} dS, \tag{17.81}$$

where h is the local liquid film height, $\bar{\mathbf{v}}$ is the height average liquid film velocity tangential to the surface, ∂S_w is the boundary line of the surface S_w , \mathbf{m} is the unit normal vector to the line ∂S_w , which is at the same time tangential to the surface S_w , ρ_L is the liquid film density, \dot{m}_S is the mass source surface density, and \dot{m}_V is the mass evaporating from the film. Referring to the single face area, the film continuity equation can be expressed as a function of the film thickness, since the assumption of incompressible fluid is valid:

$$\frac{\partial h}{\partial t} + \nabla \cdot (h \mathbf{U}_f) = S_M + S_V. \tag{17.82}$$

The last term S_V accounts for film evaporation under both dynamic and thermal effects [58]. Since the impinging liquid spray is multicomponent (water and urea in our case), species tracking must be considered in the film. A set N_S-1 of conservation equations must be solved, where N_S is the number of chemical components considered:

$$\frac{\partial hY_{f,k}}{\partial t} + \nabla \cdot (h\mathbf{U}_f Y_{f,k}) = S_{M,k} + S_{V,k}, \quad (17.83)$$

where $Y_{f,k}$ indicates the mass fraction of the k -th specie. The two terms $S_{M,k}$ and $S_{V,k}$, are the amount of the k -th species entering the film due to the spray impact and leaving the film due to evaporation, respectively. Similarly, the liquid film momentum equation can be formulated:

$$\frac{\partial h\mathbf{U}_f}{\partial t} + \nabla \cdot (h\mathbf{U}_f \mathbf{U}_f) = -\frac{1}{\rho_f} \nabla (hp_f) + \tau_g - \tau_w + h\mathbf{g} + \mathbf{S}_U, \quad (17.84)$$

where τ_{fs} is the tangential viscous force at the free surface, τ_w is the tangential viscous force at the wall, \mathbf{g}_t is the tangential component of gravity acceleration, $\nabla_s p_L$ is the surface gradient of the pressure and \mathbf{S}_v is the tangential component of the momentum source from incoming droplets. In SCR systems the urea–water solution is usually injected in the gas stream without undergoing a heating process, so its temperature is close to the ambient one. Because of this, the impinging jet is heated by the gas stream and then by the contact with the pipe walls or with the mixer blades. In compact systems, typical of automotive applications, the droplet heat up before the impact with rigid walls is not enough to get all the liquid component evaporated. The process is therefore completed after the impact with the walls and is governed by two phenomena: the heating of the liquid film and the cooling of pipe walls due to the impingement of a colder liquid. This interaction can be taken into account solving for the energy balance of the liquid and the walls. The energy equation of the liquid film is expressed once again as a function of the sensible enthalpy:

$$\frac{\partial hH_{s,f}}{\partial t} + \nabla \cdot (h\mathbf{u}_f H_{s,f}) = j_g - j_w + S_H, \quad (17.85)$$

where the source terms are the contribution due to: the heat flux exchanged with the gas (j_g), the heat flux due to conduction between the liquid and the pipe walls (j_w), and the enthalpy associated with the net mass of the droplet entering the liquid film (S_H). The film-gas heat flux terms accounts for the contribution of the temperature gradient (j_s) with the addition of the heat flux required by the evaporation ($S_V h_{v,f}$):

$$j_g = \frac{\lambda_{t,l}}{\rho_f} \frac{\partial T}{\partial n} \Big|_{z=h} + S_V h_{v,f} = j_s + S_V h_{v,f}. \quad (17.86)$$

The conductive heat flux is determined by assuming a parabolic profile of the temperature within the liquid film [58]:

$$j_w = 3 \frac{\lambda_{t,l}(T_f - T_w)}{\rho_f h} - \frac{1}{2} j_g. \quad (17.87)$$

The energy balance of the pipe walls takes into account the conduction heat that occurs inside the material and is coupled to the liquid film energy balance by means of the j_w term. Once the thermal properties of the walls are known, the balance can be expressed referring to the temperature of the material:

$$\rho_w c_w \frac{\partial T_w}{\partial t} - \lambda_{t,w} \nabla^2 T_w = \frac{j_w/g \rho_f}{\delta}. \quad (17.88)$$

This variation depends on the thermal capacity of the pipe wall material, and in general is very limited if only a narrow time interval is modeled. For steady-state simulation the thermal capacity can be reduced by an arbitrary factor, in order to speed up the thermal transient. However, if pulsating injection is modeled, this strategy cannot be adopted and the time interval to model must be large, in order to observe a significant temperature variation. The coupling with the solid wall balance can be realized resorting to fluid structure interaction approaches, where proper algorithms for coupling the solution matrices must be adopted, or resorting to the definition of a finite area field representing the wall temperature. The heat flux between the liquid film and the pipe walls is calculated resorting to the heat conduction theory. In particular, inside SCR systems it may happen that the wall temperature is much higher than the liquid film temperature (especially when a liquid spray is approaching a dry surface), resulting in what is called the Leidenfrost regime. In this condition, a vapor cushion is formed between the film and the wall, causing a drop in the heat exchange coefficient. The calculation of the heat flux must therefore be corrected in order to take into account this particular phenomenon [61]. However, this correction may not be enough for the prediction of the liquid film dynamics, since it affects mainly the thermal balance. A correction of the momentum exchange between the liquid layer and the pipe walls must be accounted for, in order to reproduce the reduced friction coefficient caused by the vapor gap.

17.3.4 Discretization of Source Terms and Equations

Referring to the liquid film continuity Eq. (17.82), the source term related to the arrival of droplets can be determined as:

$$S_M = \frac{4\pi\rho_d}{3A\rho_f\Delta t} \sum_{i=1}^{N_d} r_i^3, \quad (17.89)$$

where the amount of mass considered is given by the net number of droplets designated to remain in the liquid film. The term S_V is related to the evaporation

rate of each component of the liquid film. It can be expressed in two different ways on the basis of the flow regime:

- when dynamic effects are prevailing (high flow stream velocity):

$$S_{V,k} = \frac{|\tau_g|}{\rho_f |\mathbf{u}_\infty - \mathbf{u}_s|} \left((B_k + 1)^{1/Sc_k} - 1 \right); \quad (17.90)$$

- when thermal effects are prevailing (high gas temperature):

$$S_{V,k} = \frac{j_s}{\rho_f c_p (T_\infty - T_s)} \left((B_k + 1)^{1/Le_k} - 1 \right). \quad (17.91)$$

Once again, the ∞ subscript indicates the gas condition at far field from the liquid film, whereas the condition s refers to quantities evaluated at the film surface using the one-third rule. The specific heat capacity c_p is evaluated with the one-third rule, whereas Le indicates the Lewis number defined as the ratio between the thermal diffusivity and the molecular diffusivity. This number can be also expressed as the ratio between Prandtl and Schmidt numbers:

$$Le = \frac{Sc}{Pr}. \quad (17.92)$$

All these equations are valid for evaporating liquid film regimes. When boiling occurs an additional term, evaluated on the basis of the first principle of thermodynamics, needs to be added. The overall evaporation rate can be derived from the evaporation rate of each single component:

$$S_V = \sum_{k=1}^{N_{f,c}} S_{V,k}. \quad (17.93)$$

The source term in the film momentum equation is considered to account for the interaction between the impinging spray and the pre-existent liquid film. This is particularly important in SCR systems, since the spray axis is always angled with respect to the normal direction of the pipe and mixer walls. For this reason, the contribution to the film momentum can be decomposed into two components: one normal to the wall surface and the other one tangential (\underline{t}), laying on the same plane of the face representing the wall. The former can be included in the film pressure equation, since it acts as an increase of pressure due to the canceling of the momentum in that direction. The latter, instead, is considered in the momentum equation as follows (S_U):

$$\mathbf{S}_U = \frac{4\pi\rho_d}{3A\rho_f\Delta t} \sum_{i=1}^{N_d} r_i^3 (\mathbf{u}_i \cdot \underline{t}) \underline{t}. \quad (17.94)$$

Concerning the film energy conservation equation, the contribution of the sensible heat of the impinging droplet depends on the temperature of the droplet itself:

$$S_H = \frac{4\pi\rho_d}{3A\rho_f\Delta t} \sum_{i=1}^{N_d} r_i^3 \hat{H}_{d,i}, \quad (17.95)$$

where $\hat{H}_{d,i}$ is the specific sensible enthalpy of the droplet.

From a numerical point of view, it is convenient to write the liquid film governing equations in a general surface integral form as:

$$\frac{d}{dt} \int_S h\Phi \, dS + \oint_{\partial S} h\mathbf{m} \cdot \bar{\mathbf{v}}\Phi \, dL = \int_S s_\Phi \, dS, \quad (17.96)$$

where Φ represents a generic scalar or vectorial quantity and s_Φ is the source term. This surface transport equation (Eq. 17.96) is discretized using the Finite Area Method (FAM) on a surface unstructured mesh consisting of arbitrary polygonal control areas. Figure 17.12 shows a sample polygonal control area S_P around the computational point P located in its centroid, the edge e , the edge length L_e , the edge unit bi-normal vector \mathbf{m}_e , and the centroid N of the neighboring control area sharing the edge e . The bi-normal \mathbf{m}_e is perpendicular to the edge normal \mathbf{n}_e and to the edge vector \mathbf{e} . Applying a second-order collocated FAM, Eq. 17.96 can be discretized on the control area S_P (see Fig. 17.12) as follows:

$$\frac{d(h_P\Phi_P S_P)}{dt} + \sum_e h_e \mathbf{m}_e \cdot \mathbf{v}_e L_e \Phi_e = (s_\Phi)_P S_P, \quad (17.97)$$

where the subscripts P and e represent the face-center and the edge-center values. The edge-center value of the dependent variable Φ is calculated using the following linear interpolation formula:

$$\Phi_e = (\mathbf{T}_e)^T \cdot [e_x \mathbf{T}_P \cdot \Phi_P + (1 - e_x) \mathbf{T}_N \cdot \Phi_N], \quad (17.98)$$

where e_x is the interpolation factor, which is calculated as the ratio of the geodetic distances $e\bar{N}$ and $\bar{P}e\bar{N}$ (Fig. 17.12):

$$e_x = \frac{e\bar{N}}{\bar{P}e\bar{N}}, \quad (17.99)$$

and T_P , T_N , and T_e are the tensors of transformation from the global Cartesian coordinate system to the edge-based local coordinate system defined in Fig. 17.13. Dependent variables in the convection term in Eq. (17.97) can be discretized using interpolation methods which locally blend linear and upwind interpolation schemes in order to preserve boundedness. The temporal discretization is performed by using the first-order accurate Euler implicit scheme [28].

Liquid film governing equations are solved using the segregated solution procedure, where the two equations are separately solved and coupling is recovered through the iterative procedure.

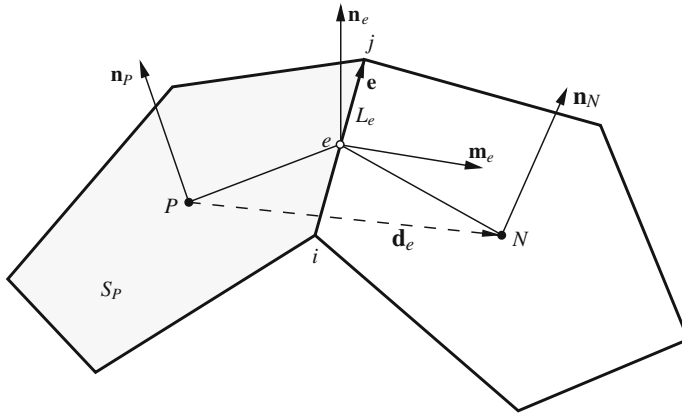


Fig. 17.12 Polygonal control area

17.3.5 Examples of CFD Application

All the submodels presented in the previous subsections have been implemented in an open source CFD code, OpenFOAM[®] [62], in order to show the potentialities of a CFD analysis of the exhaust system equipped with urea injection device. Most often, the prediction of a CFD calculation may be erroneously considered as the truth of what is happening at a certain scale level. Unfortunately, this misinterpretation may lead to wrong considerations in the case the prediction exactly matches some experimental results (obtained directly or indirectly), hence one may assume that it tells the truth, or in the case it does not match exactly the experimental measurement, hence judging that the model does not capture the physics correctly. Considerations drawn from the analysis of the calculated results, must be seen at the light of captured trend instead of exact value matching. In first place, every model for the simulation of a complex process, such as the injection of a multicomponent liquid phase into a hot gas stream, is based on simplifications, otherwise the fully detailed modeling of the phenomena would be much more expensive than the experimental testing of several prototypes. In second place, the experimental measure is usually carried out indirectly, hence hiding the effects that other phenomena may introduce in the overall process. In particular, the quality of the mixing between the ammonia, generated by the thermal decomposition of the injected urea, and the gas stream is indirectly measured by the abatement efficiency of the SCR catalyst, because of the 1 to 1 molar ratio between ammonia and nitrogen oxides. This direct correlation neglects the eventual impact of solid deposit formation during the operating conditions, or the deposition of liquid droplets onto the catalyst surface.

Additionally, CFD simulations are carried out considering steady-state simulation of both the UWS injection and mixing devices, imposing steady-state boundary conditions corresponding to averaged mass flow and temperature values.

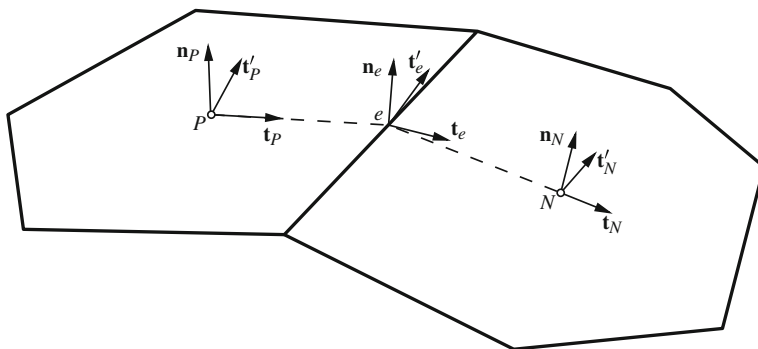


Fig. 17.13 Edge-based local coordinate system

This is obviously far from what happens inside of an exhaust system, when the IC engine is mounted on the test bench. The pulsating flow coming from the cylinders, together with discontinuities in the gas composition and temperature, may affect the global mixing efficiency. For this reason, an important perspective of simulation can be sought in the usage of time varying boundary conditions or in the adoption of hybrid models in which 1D and 3D codes are fully integrated [63]. In this section, the applications of a CFD model to simple test cases is presented, in order to highlight the aspects that can be investigated. In particular, in order to compare the calculation results with similar calculations performed with a different CFD tool, the test case modeled by Strom [39], has been analyzed. The case chosen for the comparison is the one with the highest volumetric flow (100 m/s) at the highest gas temperature (573 K), in order to easily highlight the behavior of gas stream and droplets. In Fig. 17.14a, b the droplet diameter and temperature are displayed, respectively. It is shown that the droplets with the smallest diameter are easily dragged by the gas stream, as they remain confined in the upper region of the pipe, whereas the droplets with larger diameter preserve their momentum, showing a lower deviation from the injection direction. The small droplets, instead, are characterized by a velocity close to that of the gas stream (Fig. 17.15) and are heated up more quickly.

The quicker heat up of the smallest droplets leads to an evaporation of the water fraction of each droplet. This is visible in Fig. 17.16a, b, where the droplets with the largest diameter show a negligible evaporation of both water and urea. As the droplet size decreases, the quicker heat up leads to an almost complete evaporation of the water fraction. Since the droplet temperature is lower than the urea thermal decomposition threshold, the evaporation of urea is very limited, hence the fraction of urea tends to unity. As previously described, the urea fraction of each single droplet evaporates with a rate close to the solid urea sublimation. The gaseous urea is then thermally decomposed with the rate described in Eq. (17.36). The integration of the chemistry has been performed resorting to an ODE solver based on the SIBS algorithm [64] according to what has been described in the section

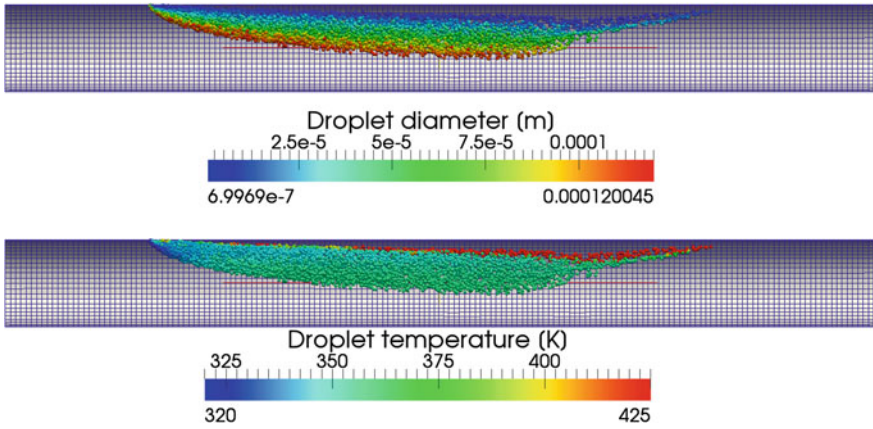


Fig. 17.14 UWS spray: droplet diameter and temperature distribution

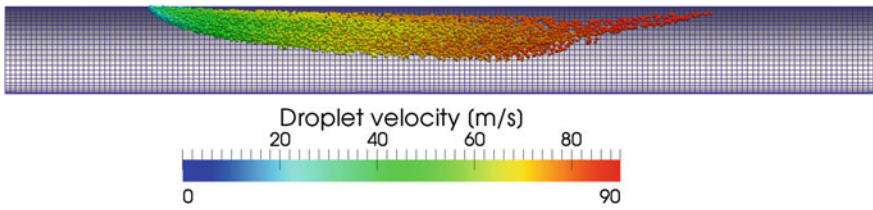


Fig. 17.15 UWS spray: droplet velocity distribution

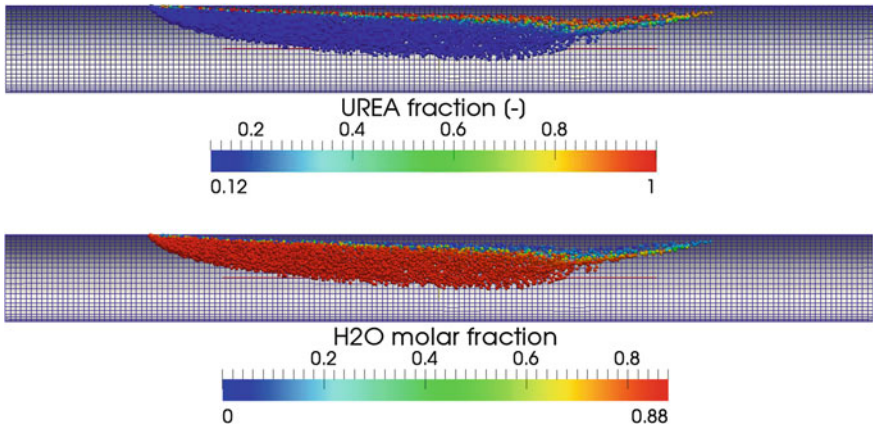


Fig. 17.16 UWS spray: urea and water molar fraction inside the droplets

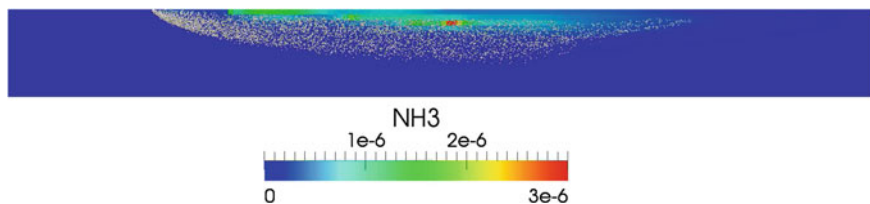


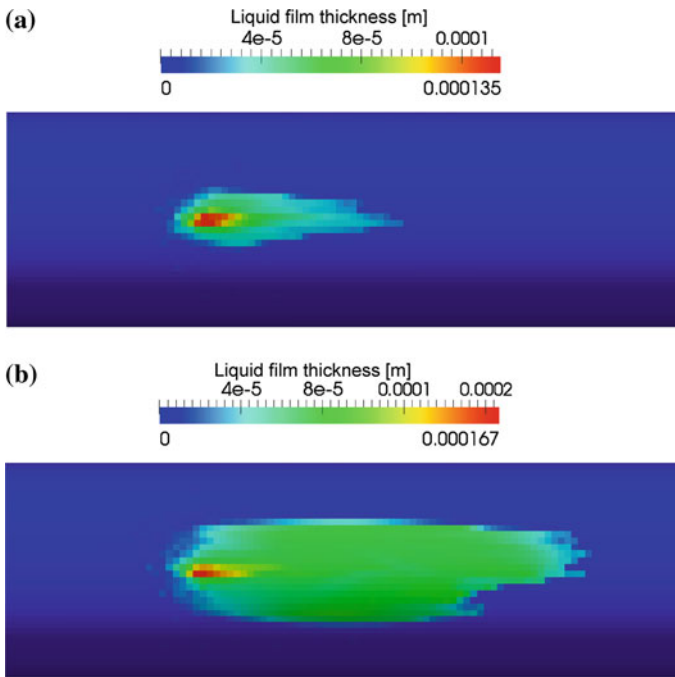
Fig. 17.17 Ammonia mass fraction in the gas stream

relative to 1D models. In Fig. 17.17, it is displayed the gaseous mass fraction of ammonia resulting from the thermal decomposition of the evaporated urea. As can be seen, the ammonia produced is confined in the upper region of the pipe, as a consequence that only the small droplets are likely to evaporate quickly. This aspect suggests that at high flow conditions the presence of the mixer is fundamental to have a uniform distribution of ammonia at the inlet of the catalyst.

Considering that the test case modeled has a length of 1 meter, it is evident that, even considering the most favorable condition for complete evaporation, namely high mass flow rate and gas temperature, the length required for complete evaporation is not enough. This consideration indicates that in real engine applications the space available to complete evaporation is usually not sufficient due to compactness issues. This justifies the adoption of a mixer, placed either upstream or downstream of the injection point, as a device to increase the turbulence intensity in the gas stream, so that the droplet-gas mass transfer and the gaseous species mixing are enhanced. As a secondary effect, the presence of the mixer favors the wall-droplet interaction, in order to generate smaller droplets when the impact occurs and to improve the evaporation rate by the formation of a liquid film. Therefore, in real applications an important role is played by the liquid film layer formed onto the pipe surface and on the mixer blades. The validation of liquid film models is very difficult to be performed, since in the literature there are few works about this topic with a detailed experimental characterization [65]. In particular, the approach presented has been validated for the case of a single component liquid spray designed for port fueled spark ignition engines [66]. In this section it is presented a simple test case which shows the dynamics of the interaction between the UWS spray and the pipe walls, highlighting the contribution to the evaporated urea coming from the spray and from the liquid film. To reproduce realistic operating conditions, the spray injection is directed with an angle of 45° with respect to the pipe axis. The operating conditions are summarized in Table 17.1. In particular, a null mean flow condition was taken into account in order to facilitate the analysis of the results. After the injection, the UWS spray reaches the pipe wall opposite to the injection section, where the formation of the liquid film layer occurs. Assuming this instant as the time 0, Fig. 17.18a, b show the evolution of the liquid film thickness during the first 15 ms. In particular, the liquid layer is spread along the pipe axis due to the momentum of the impinging

Table 17.1 Initial conditions test in the calculations

Injection pressure (bar)	8.52
Injection velocity (m/s)	37.701
Injection temperature (K)	300
Gas temperatures (K)	550
Wall temperature (K)	550
Wall heat specific capacity (J/m ³ K)	3,532,500
Wall heat conductivity (W/mK)	18
Wall thickness (m)	0.002
Pipe diameter (m)	0.05

**Fig. 17.18** Liquid film thickness during the UWS injection: **a** 0 ms, **b** 15 ms

liquid droplets. The highest film section is reached in the region where the incident spray impacts on the film.

When the droplet enters the liquid film, it brings a momentum source but also a contribution to the energy balance of the film itself. In Fig. 17.19a, b it is shown the temperature of the liquid film at two different times. The coldest region lays in the point where the cold spray core reaches the wall. The temperature of the spray remains close to the injection temperature, due to the short space and time available to realize a significant heat up of the droplet. The peripheral regions of the liquid film are characterized by a low layer thickness, ending up in a quicker

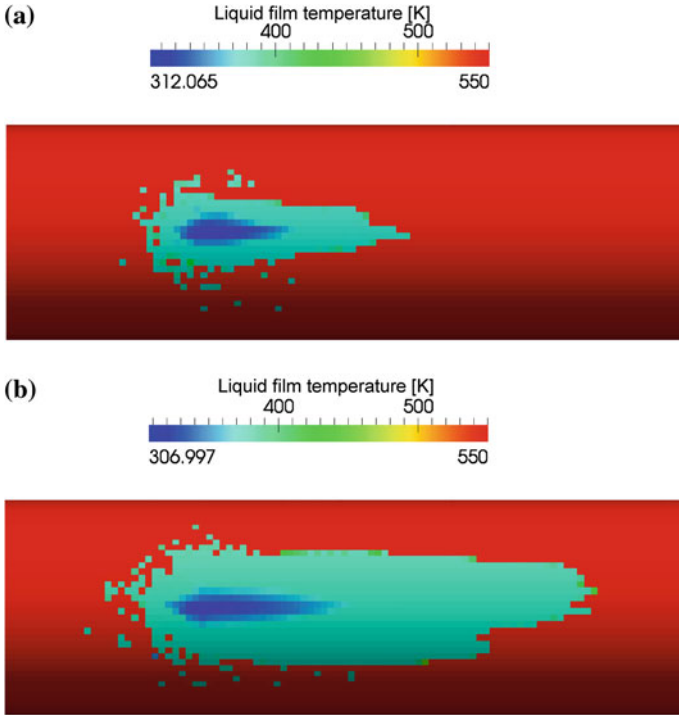
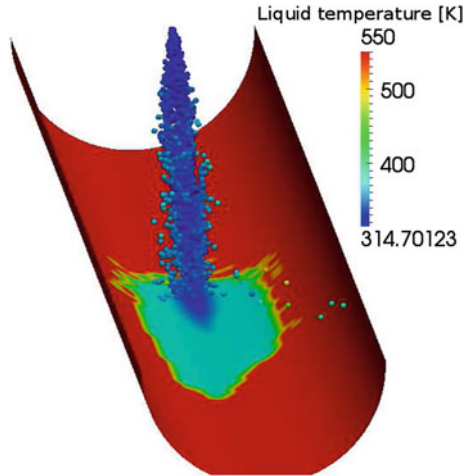


Fig. 17.19 Liquid film temperature at two different times: **a** 5 ms, **b** 20 ms

Fig. 17.20 Visualization of the temperature level of the liquid fraction inside the computational domain after 20 ms: spray and wall film



heating due to the heat exchanged with the surrounding gas and the pipe walls. A narrow spray cone angle (14 deg) has been imposed, in order to have a high impact frequency, resulting in an impact regime confined within the splash and spread

regimes. The formation of liquid film is therefore immediate and the average temperature at which the droplets hit the wall surface is around 320 K, meaning that there is an increase of temperature of about 20 K (mainly determined by the small droplets). Figure 17.20 shows the temperature of the liquid fraction in the calculation domain, namely the spray and the liquid film. The size of the droplets is not scaled with the diameter, they have all the same size, in order to highlight the temperature at which the impact occurs. It can be seen that the spray core is the portion at the lowest temperature, while the particles at higher temperature are those characterized by a small diameter, as a result either of the injection model or of the splashing regimes occurring. The wall temperature, assuming for simplicity sake that the pipe is adiabatic with respect the external environment, shows a consistent cooling in the region where the liquid jet core hits the wall surface (Fig. 17.21a, b). Considering the limited time simulated, the effect of wall thermal conductivity can be neglected, since it is characterized by a higher characteristic time. The portion of the surface covered by the dragged liquid film remains at a higher temperature, since the liquid has been heated by the wall during its path along the pipe and therefore the cooling effect is weaker than in the region where the impingement occurs. Moreover, in all these observations it has to be considered that the film is heated also by the surrounding air via convection. The combination of all the effects results in the determination of the evaporation rate, which shows that the main contribution to the production of water and urea in gaseous phase is the evaporation of the liquid film. As shown in Fig. 17.22a, b, where the thermal decomposition of urea has not been modeled, after 15 ms it is evident that both gaseous water and urea are produced by the evaporation of the liquid film, whereas the contribution of the spray is almost negligible, especially for urea. Additionally, the two figures show how the profile of the two species is identical with different values of mass fractions, due to the lower evaporation rate of urea. Referring to a real engine configuration (Fig. 17.23), it appears evident how limited is the space available to the spray to completely evaporate. Following the trajectory of the UWS droplets, once again it can be noted that the smallest droplets are strongly deflected from the direction of the nozzle axis. These droplets then undergo a heating process, ending their trajectory by hitting the mixer walls. The large diameter droplets, instead, hit the mixer walls in the lower region due to the weaker deflection caused by their higher inertia. Figure 17.23 shows also the difference between the urea produced by the spray and by the liquid film. In particular, the yellow cloud represents the urea evaporated from the liquid film, whereas the red one represents the portion coming from the spray. Both the clouds have been plotted thresholding the two fields with the same minimum value. Once again, the result indicates that the major contribution to the urea, hence ammonia, production comes from the liquid film. The small contribution of the spray is mainly due to the small droplets that are recirculated by the vortexes originated at the sharp edges of the geometry. These droplets remain trapped in the recirculation vortex and therefore have enough time to heat up and evaporate.

The final purpose of the UWS injection and its mixing with the gas stream is the need of having an homogeneous distribution of ammonia at the catalyst inlet. As

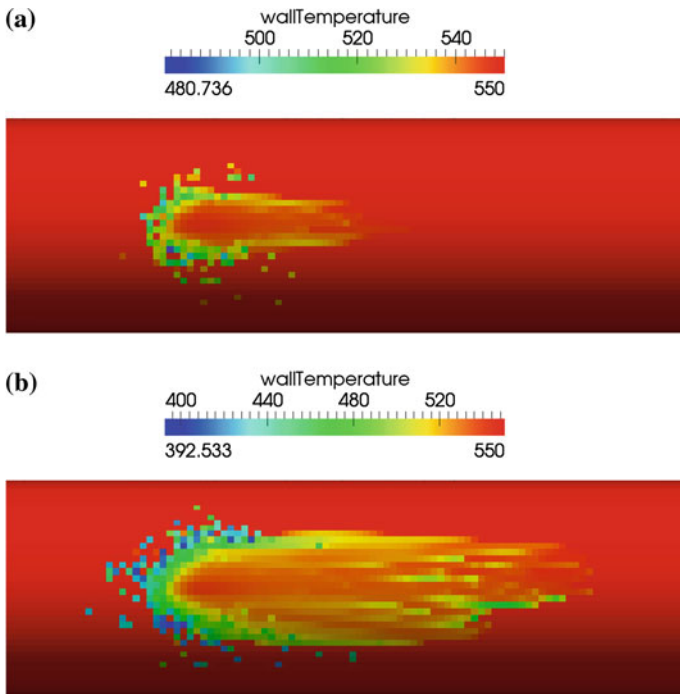


Fig. 17.21 Wall temperature during UWS the injection: a 0 ms, b 15 ms

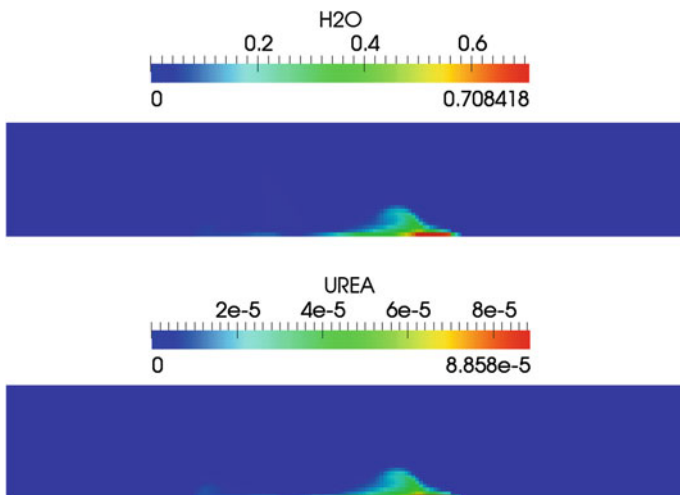


Fig. 17.22 Evaporated mass fraction of water and urea during the UWS injection

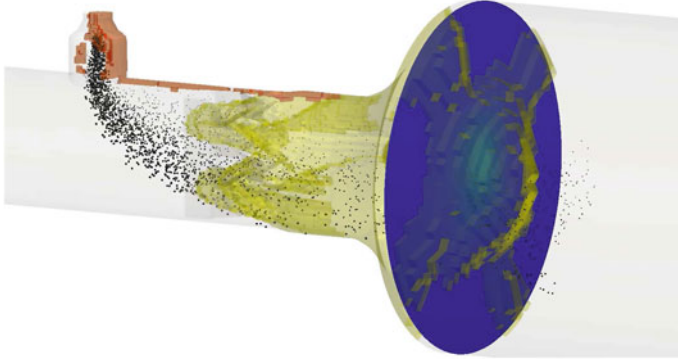


Fig. 17.23 Distinction between urea produced by the evaporation of the spray and by the evaporation of the liquid film

anticipated, the 1 to 1 molar ratio between ammonia and nitrogen oxide, required by the standard SCR reaction, implies that regions in the gas stream, where the concentration of ammonia is low, keep their content of nitrogen oxides. This fact correlates the catalyst efficiency to the degree of uniformity of the reducing agent, namely ammonia. This strong link facilitates the optimization of the SCR systems, since it is enough to estimate how uniform is the distribution of ammonia at the catalyst inlet to know if the system can operate efficiently or not. The level of ammonia distribution uniformity can be determined by the CFD analysis, resorting to different definitions a uniformity index. The most used formulation of the uniformity index is based on the probing and averaging of the mass fraction of ammonia along a surface at the inlet of the catalyst [67, 68]:

$$UI = 1 - \frac{\sum_i |Y_{NH_3,i} - \bar{Y}_{NH_3}| A_i}{2 \sum_i Y_{NH_3,i} A_i}, \quad (17.100)$$

where $Y_{NH_3,i}$ indicates the local value of the mass fraction of ammonia at the face center of a sample surface upstream of the catalyst, while \bar{Y}_{NH_3} is the average value of the ammonia mass fraction over the sampling surface. In case of ammonia equally distributed over the sampling surface, the index would reach the unity, whereas a peak of ammonia localized in a small portion of the sampling surface would lead to values close to zero. The calculation of this index must be performed over a planar surface parallel to the one representing the catalyst inlet, requiring that the mesh of the domain is oriented accordingly and possibly hexahedral. In case the mesh contains tetrahedral elements, and consequently does not allow for the definition of such surface, surface cutting techniques together with field interpolation must be adopted.

References

1. P. Forzatti. Present status and perspectives in de-NO_x catalysis. *Applied Catalysis*, 222:221–236, 2001.
2. G. Montenegro and A. Onorati. 1d thermo-fluid dynamic modelling of de-nox scr systems for diesel engine exhaust gas after-treatment. *Int. J. of Vehicle Design*, 41(No.1/2/3/4):285–306, 2006.
3. G. Montenegro and A. Onorati. 1d thermo-fluid dynamic modeling of reacting flows inside three-way catalytic converters. *SAE International Journal of Engines*, 2(1):1–16, 2009.
4. A. Onorati, G. Ferrari, G. D’Errico, and G. Montenegro. The prediction of 1d unsteady flows in the exhaust system of a si engine including chemical reactions in the gas and solid phase. *SAE Technical Paper, SAE Transactions J. Engines*, pages 01–0003, 2002.
5. J. Wurzenberger, G. Auzinger, R. Heinzle, and R. Wanker. 1d modelling of reactive fluid dynamics, cold start behavior of exhaust systems. *SAE Technical Paper*, 2006-01-1544, 2006.
6. T. Morel, J. Silvestri, K. Goerg, and R. Jebasinski. Modeling of engine exhaust acoustics. *SAE Technical Paper*, 1999-01-1665, 1999.
7. A. Onorati, M. Perotti, and S. Rebay. Modelling one-dimensional unsteady flows in ducts: Symmetric finite difference schemes versus galerkin discontinuous finite element methods. *International Journal of Mechanical Sciences*, 39(11):1213–1236, 1997.
8. D. E. Winterbone and R. J. Pearson. *Theory of engine manifold design*. Professional Engineering Publishing, London, 2000.
9. A. Burcat and B. Ruscic. Third Millennium Ideal Gas and Condensed Phase Thermochemical Database for Combustion with Updates from Active Thermochemical Tables. *Report TAE960*, 2005.
10. R. W. MacCormack. A numerical method for solving the equations of compressible viscous flow. *AIAA*, 81-0110, 1981.
11. P. D. Lax and B. Wendroff. Systems of conservation laws. *Comm. Pure Appl. Math.*, 13:217–237, 1960.
12. M. Chapman, J. M. Novak, and R. A. Stein. Numerical modeling of inlet and exhaust flows in multi-cylinder internal combustion engines. *ASME Winter Annual Meeting*, 1982.
13. G. Montenegro, A. Della Torre, A. Onorati, R. Fairbrother, and A. Dolinar. Development and application of 3d generic cells to the acoustic modelling of exhaust systems. *SAE 2011 Noise and Vibration Conference and Exhibition*, 2011-01-1526, 2011.
14. E. Jean, V. Leroy, G. Montenegro, A. Onorati, and Laurell. M. Impact of ultra low thermal inertia manifolds on emission performance. *SAE Technical Paper*, 2007-01-0935, 2007.
15. S. W. Churchill. Comprehensive Correlating Equations for Heat, Mass and Momentum Transfer in Fully Developed Flow in Smooth Tubes. *Ind. Eng. Chem. Fundam.*, 16:109–116, 1977.
16. S. W. Churchill. Friction-Factor Equation Spans all Fluid Flow Regimes. *Chem. Eng.*, pages 91–92, 1977.
17. R. J. Clarkson and S. F. Benjamin. Modelling the Effect of Moisture on Catalyst Warm-Up. *IMEchE*, 1995.
18. S. H. Chan and D. L. Hoang. Chemical Reactions in the Exhaust System of a Cold-Start Engine. *Chem. Eng. Technol.*, 8:727–730, 2000.
19. S. Heller and G. Wachtmeister. Analysis and modeling of heat transfer in the si engine exhaust system during warm-up. *SAE Technical Paper*, 2007-01-1092, 2007.
20. S.M. Ghiaasiaan. *Two-Phase Flow, Boiling, and Condensation: In Conventional and Miniature Systems*. Cambridge University Press, 2007.
21. Y. Taitel and A.E. Dukler. A model for predicting flow regime transitions in horizontal and near horizontal gas-liquid flow. *AIChE Journal*, 22(1):JANUARY, 1976, 1976. cited By (since 1996) 282.

22. Christopher Depcik, Bram van Leer, and Dennis Assanis. The numerical simulation of variable-property reacting-gas dynamics: New insights and validation. *Numerical Heat Transfer, Part A: Applications*, 47(1):27–56, 2004.
23. V.I. Terekhov and M.A. Pakhomov. The numerical modeling of the tube turbulent gas-drop flow with phase changes. *International Journal of Thermal Sciences*, 43(6):595–610, 2004.
24. C. Baumgarten. *Mixture Formation in Internal Combustion Engines*. Heat and Mass Transfer. Springer, 2006.
25. M. Koebel, M. Elsner, and G. Madia. Reaction Pathways in the Selective Catalytic Reduction Process with NO and NO₂ at Low Temperature. *Ind. Eng. Chem. Res.*, 40:52–59, 2001.
26. S. D. Yim, S. J. Kim, J. H. Baik, I. S. Nam, Y. S. Mok, Lee J. H., Cho B. K., and S. H. Oh. Decomposition of Urea into NH₃ for the SCR process. *Ind. Eng. Chem. Res.*, 43:4856–4863, 2004.
27. R.J. LeVeque. *Finite Volume Methods for Hyperbolic Problems*. Cambridge Texts in Applied Mathematics. Cambridge University Press, 2002.
28. J.H. Ferziger and M. Perić. *Computational Methods for Fluid Dynamics*. Springer, 2002.
29. C. Hirsch. *Numerical Computation of Internal and External Flows: The Fundamentals of Computational Fluid Dynamics*. Number v. 1 in Butterworth Heinemann. Elsevier Science, 2007.
30. H. K. Versteeg and W. Malalasekera. *An Introduction to Computational Fluid Dynamics: the Finite Volume Method*. Addison-Wesley, Longman, 1995.
31. V. Yakhot, S. A. Orszag, S. Thangam, T. B. Gatski, and C. G. Speziale. Development of turbulence models for shear flows by a double expansion technique. *Physics of Fluids A: Fluid Dynamics*, 4(7):1510–1520, 1992.
32. F. R. Menter. Two-equation eddy-viscosity turbulence models for engineering applications. *AIAA Journal*, 32(8):1598–1605, 1994.
33. S. Fischer, R. Bitto, T. Lauer, and C. et al. Krenn. Impact of the turbulence model and numerical approach on the prediction of the ammonia homogenization in an automotive scr system. *SAE Int. J. Engines*, 5(3):1443–1458, 2012.
34. G. Stiesch. *Modeling Engine Spray and Combustion Processes*. Springer, 2003.
35. M. Boileau, S. Pascaud, E. Riber, B. Cuenot, L.Y.M. Gicquel, T.J. Poinsot, and M. Cazalens. Investigation of two-fluid methods for large eddy simulation of spray combustion in gas turbines. *Flow, Turbulence and Combustion*, 80:291–321, 2008.
36. S Hoyas, J.M. Pastor, D. Khuong-Anh, J. M. Momp-Laborda, and F. Ravet. Evaluation of the eulerian-lagrangian spray atomisation (elsa) in spray simulations. *Int. J. Vehicle Systems Modelling And Testing.*, 6(3/4), 2011.
37. F. V. Bracco. Modeling of Engine Sprays. *SAE Paper*, 850394, 1985.
38. R. D. Reitz. Modeling Atomization Processes In High Pressure Vaporizing Sprays. *Atomization and Spray Technology*, Vol. 3:pp. 309–337, 1987.
39. Henrik Stram, Andreas Lundstram, and Bengt Andersson. Choice of urea-spray models in cfd simulations of urea-scr systems. *Chemical Engineering Journal*, 150(1):69–82, 2009.
40. G. D’Errico, D. Ettorre, and T. Lucchini. Simplified and Detailed Chemistry Modeling of Constant-Volume Diesel Combustion Experiments. *SAE Paper*, 2008-01-0954, 2008.
41. D. Stanton, A. Lippert, R. D. Reitz, and C. J. Rutland. Influence of Spray-Wall Interaction and Fuel Films on Cold Starting in Direct Injection Diesel Engines. *SAE Paper*, 982584, 1998.
42. A. V. Kolpakov et al. Calculation of the Rebound Condition for Colliding Drops of Sharply Different Sizes. *Kolloidn. Zh.*, Vol. 47, 1985.
43. D.Stanton and C. J. Rutland. Modeling fuel film formation and wall interaction in diesel engines. *SAE Paper 960628*, 1996.
44. A. L. Yarin and D. A. Weiss. Impact of Drops on Solid Surfaces: Self-Similar Capillary Waves, and Splashing as a new Type of Kinematic Discontinuity. *Journal of Fluid Mechanics*, Vol. 283, 1995.
45. W. E. Ranz and W. R. Marshall. Evaporation from drops. *Chem. Eng. Prog.*, 48:141–146, 1952.

46. P. J. O'Rourke. Statistical Properties and Numerical Implementation of a Model for Droplet Dispersion in a Turbulent Gas. *Journal of Computational Physics*, Vol. 83:345–360, 1989.
47. R. J. Haywood, M. Rensizbulut, and G. D. Raithby. Numerical solution of deforming evaporating droplets at intermediate reynolds numbers. *Numerical Heat Transfer, Part A: Applications*, 26(3):253–272, 1994.
48. B.T Helenbrook and C.F Edwards. Quasi-steady deformation and drag of uncontaminated liquid drops. *International Journal of Multiphase Flow*, 28(10):1631–1657, 2002.
49. S. Kontin, A. Höfler, R. Koch, and H.-J. Bauer. Heat and mass transfer accompanied by crystallisation of single particles containing urea-water-solution. In *ILASS-Europe 2010 23rd Annual Conference on Liquid Atomization and Spray Systems*, Brno, Czech republic, September 2012.
50. A Lundström, B Waldheim, H Ström, and B Westerberg. Modelling of urea gas phase thermolysis and theoretical details on urea evaporation. *Proceedings of the Institution of Mechanical Engineers, Part D: Journal of Automobile Engineering*, 225(10):1392–1398, 2011.
51. Felix Birkhold, Ulrich Meingast, Peter Wassermann, and Olaf Deutschmann. Modeling and simulation of the injection of urea-water-solution for automotive scr denox-systems. *Applied Catalysis B: Environmental*, 70(14):119–127, 2007. Papers presented at the 4th International Conference on Environmental Catalysis (4th ICEC)Heidelberg, Germany, June 05 08, 2005.
52. J. W. Kiedaisch and S. P. Gravante. Calibration of cfd spray model parameters using detailed experimental spray characterization data. In *ICLASS 2009, 11th Triennial International Conference on Liquid Atomization and Spray Systems*, Vail, Colorado, US, July 2009.
53. D.T. Ryddner and M.F. Trujillo. A fully resolved uws droplet simulation. In *ILASS-Americas, 24th Annual Conference on Liquid Atomization and Spray Systems*, San Antonio, Texas, US, May 2012.
54. Tae Joong Wang, Seung Wook Baek, Seung Yeol Lee, Dae Hwan Kang, and Gwon Koo Yeo. Experimental investigation on evaporation of urea-water-solution droplet for scr applications. *AIChE Journal*, 55(12):3267–3276, 2009.
55. A Lundstrm, B Waldheim, H Strm, and B Westerberg. Modelling of urea gas phase thermolysis and theoretical details on urea evaporation. *Proceedings of the Institution of Mechanical Engineers, Part D: Journal of Automobile Engineering*, 225(10):1392–1398, 2011.
56. Andreas M. Bernhard, Izabela Czekaj, Martin Elsener, Alexander Wokaun, and Oliver Kröcher. Evaporation of urea at atmospheric pressure. *The Journal of Physical Chemistry A*, 115(12):2581–2589, 2011.
57. A. A. Kozyro, A. P. Krasulin, V. V. Simirskii, and V. S. Markovnik. Thermodynamic properties of tetramethylurea. *Russ. J. Phys. Chem. (Engl. Transl.)*, 62(10):895–897, 1988.
58. H. Foucart, C. Habchi, J. F. Le Coz, and T. Baritaud. Development of a three-dimensional model of wall fuel liquid film for internal combustion engines. *SAE Paper 980133*, 1998.
59. M. Trujillo and C. F. Lee. Modeling film dynamics in spray impingement. *Journal of Fluids Engineering*, 2003.
60. Ž. Tukovic and H. Jasak. Simulation of free-rising bubble with soluble surfactant using moving mesh finite volume/area method. In *6th International Conference on CFD in Oil & Gas, Metallurgical and Process Industries*. SINTEF/NTNU, June 2008.
61. F. Birkhold, U. Meingast, P. Wassermann, and O. Deutschmann. Analysis of the injection of urea-water-solution for automotive scr denox-systems: Modeling of two-phase flow and spray/wall-interaction. *SAE Technical Papers*, 2006. cited By (since 1996)24.
62. H.G. Weller, G. Tabor, H. Jasak, and C. Fureby. A tensorial approach to computational continuum mechanics using object-oriented techniques. *Computers in Physics*, 12(6):620, 1998.
63. G. Montenegro, A. Onorati, F. Piscaglia, and G. D'Errico. Integrated 1D-MultiD Fluid Dynamic Models for the Simulation of I.C.E. Intake and Exhaust Systems. *SAE Technical Paper*, 2007-01-0495, 2007.

64. W.H. Press. *Numerical Recipes: The Art of Scientific Computing*. Cambridge University Press, 2007.
65. J. F. Le Coz, C. Catalano, and T. Baritaud. Application of laser induced fluorescence for measuring the thickness of liquid films on transparent walls. In *7th Int. Symposium on application of laser techniques to fluid mechanics*, 1997.
66. T. Lucchini, G. D'Errico, G. M. Brusiani, F. and Bianchi, Z. Tukovic, and H. Jasak. Multi-dimensional modeling of the air/fuel mixture formation process in a pfi engine for motorcycle applications. *SAE Technical Paper*, 2009-24-0015, 2009.
67. H. Weltens, H. Bressler, F. Terres, H. Neumaier, H. Neumaier, and D. Rammoser. Optimisation of catalytic converter gas flow distribution by cfd prediction. *SAE Technical Paper*, 930780, 1993.
68. Thomas L. McKinley, Andrew G. Alleyne, and Chia-Fon Lee. Mixture non-uniformity in scr systems: Modeling and uniformity index requirements for steady-state and transient operation. *SAE International Journal of Fuels and Lubricants*, 3(1):486–499, 2010.

Part VII
Integrated Systems

Chapter 18

Dual-Layer Ammonia Slip Catalysts for Automotive SCR Exhaust Gas Aftertreatment: An Experimental and Modeling Study

Isabella Nova, Massimo Colombo, Enrico Tronconi,
Volker Schmeißer, Brigitte Bandl-Konrad
and Lisa Zimmermann

Nomenclature

C_i	Gas-phase concentration of species i [mol/m ³ gas]
E_j	Rate parameter for T-dependence of reaction j [K]
k_j°	Logarithm of rate constant of reaction j at Tref [–]
$k_{\text{ads-PGM}}$	Rate constant for NH ₃ adsorption [1/s]
K_{NN}	Rate parameter in (Eq. 18.18) [m ³ /mol]
K_{NO}	Rate parameter in (Eq. 18.19) [m ³ /mol]
K_{NHNOOX}	Rate parameter in (Eq. 18.20) [m ³ /mol]
$K_{\text{NO}_2\text{-PGM}}$	Rate parameter in (Eq. 18.21) [m ³ /mol]
$K_{\text{NO}_2}^{\text{eq}}$	equilibrium constant of reaction (R4) [1/bar ^{0.5}]
P_{O_2}	Partial pressure of O ₂ [bar]
Q	Flow rate [m ³ /s]
R	Ideal gas constant [J/mol K]
r_k	Rate of reaction k ($\frac{\text{mol}}{\text{m}^3_{\text{cat}}\text{s}}$)
T	Temperature [K]
Tref	Reference temperature [K]

I. Nova · M. Colombo · E. Tronconi (✉)
Dipartimento di Energia, Laboratorio di Catalisi e Processi Catalitici Politecnico di Milano,
Piazza Leonardo da Vinci 32 I-20133 Milano, MI, Italy
e-mail: enrico.tronconi@polimi.it

V. Schmeißer · B. Bandl-Konrad
Daimler AG, 019-G206 RD/RPE 70546 Stuttgart, Germany

L. Zimmermann
Daimler AG, 019-D121 TP/PME 70546 Stuttgart, Germany

Greek Symbols

α	Rate parameter in (Eq. 18.2) [–]
θ_j^{PGM}	Surface coverage of adsorbed species j on PGM catalyst [–]
θ_j^{SCR}	Surface coverage of adsorbed species j on SCR catalyst [–]

18.1 Introduction

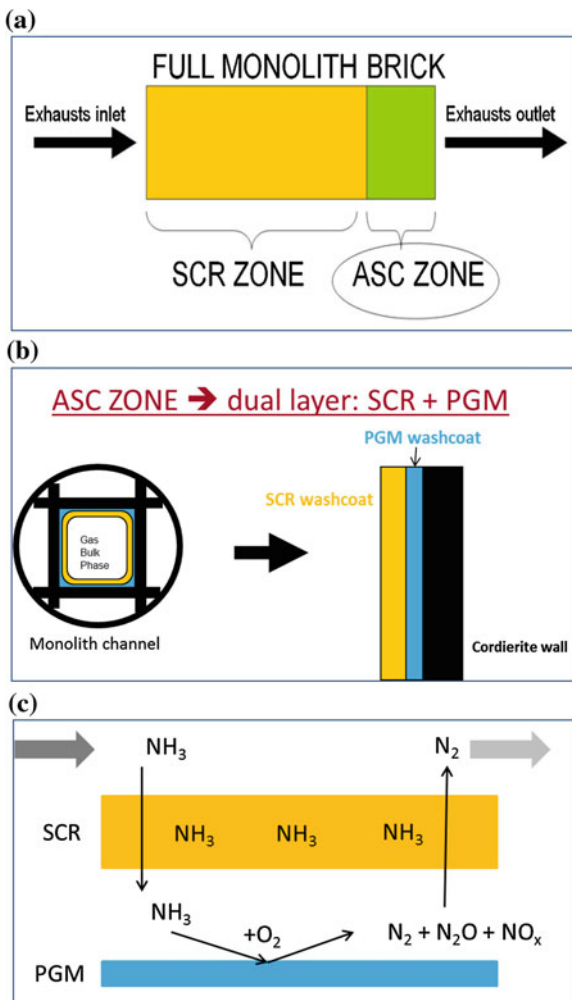
To reduce NO_x emissions from lean exhaust gas (e.g., Diesel exhausts) selective catalytic reduction by NH₃ (NH₃-SCR) has become an established process for passenger cars as well as for heavy duty vehicles [1].

The reducing agent, NH₃, is adsorbed onto the SCR and then consumed by NO_x reduction reactions. The amount of ammonia fed to the reactor must be controlled depending on the operating conditions in order to maintain a high level of NH₃ adsorption and NO_x conversion of the SCR on the one hand. On the other hand, NH₃ emissions from the aftertreatment system into the environment are not desired and have to be avoided. In order to reduce as much as possible the amount of released ammonia, the addition of another catalytic device downstream the SCR one can be an efficient and reliable solution. Furthermore, to maintain the system as compact as possible, one solution is to add an ammonia oxidation functionality directly in the rear part of an SCR monolith (Fig. 18.1a). In this way, an NH₃ slip catalyst (ASC) is added after the SCR to oxidize NH₃ leaving the SCR brick [2].

For a high NH₃ oxidation activity of the ASC, precious metals (e.g., Platinum) can be recommended as catalysts [3]. However, this class of catalysts shows a bad selectivity to N₂, i.e., the desired product. As a solution, the combination of a precious metal containing component with an SCR one presents advantages regarding both NH₃ conversion and selectivity properties of the resulting ASC catalyst [2, 4]. This combination may be realized in a dual-layer architecture, where the bottom layer contains a platinum-based catalyst which oxidizes ammonia, while the upper layer consists of an SCR catalyst (Fig. 18.1b) [4]. The N₂ selectivity in this case is increased, as NO_x being formed in the lower oxidation layer must diffuse through the SCR layer above where it can be selectively reduced (Fig. 18.1c). Such an SCR-ASC system enables minimal NH₃ breakthrough at increased NO_x conversion of the aftertreatment system.

The positive interaction of an oxidation catalyst with an SCR one for ASC applications was also presented by Kamasamudram et al. [5]. In their detailed study, these authors investigated an ASC catalyst that combined the high oxidation activity of a PGM-based component with a zeolite-based SCR component, without specifying however the spatial arrangement of the two components. Also in this case, the resulting ASC catalyst exhibited high activity in the NH₃ oxidation and high selectivity to N₂. Furthermore, the analysis of experimental data pointed out that the overall ASC behavior resulted from the superposition of the chemistries of the two components.

Fig. 18.1 Dual-layer ASC concept **a** configuration of exhaust line including SCR and ASC catalyst bricks **b** Washcoat arrangement in ASC zone **c** reaction scheme over dual-layer ASC catalyst



At such a high degree of complexity of modern exhaust after treatment systems, modeling and simulation of the catalyst performances play an important role as part of the total system simulation in the automotive development process. The processes occurring on the SCR catalysts are already well understood and modeled [6–12], whereas this is not the case for the ASC, for which only a few literature surveys exist [2, 3, 13–15]. Scheuer et al. [3] presented a mechanistic kinetic model for ammonia oxidation over a PGM catalyst. Such a model was derived from previous literature works [16, 17] and includes the following reactions: NH₃, O₂ and NO adsorption/desorption from the catalytic sites, NH₃ activation and N₂, NO and N₂O formation, with the last three species being the main NH₃ oxidation products. The model consists thus of seven reactions that are assumed to proceed

over two different catalytic sites, identified as hollow and on top Pt sites. The same model was then extended in [2] in order to include also the oxidation of NO to NO₂, a process well known to occur on Pt-based catalysts. In the same chapter the PGM model was coupled with a kinetic model of an SCR catalyst and used to simulate the behavior of a dual-layer NH₃-slip catalyst under typical automotive Diesel exhaust conditions.

The functionality of a dual layer ASC catalyst has been investigated and also mathematically described in our labs [18, 19] in order to enable the simulation of vehicle tailpipe emissions. However, this dual-layer setup required a dedicated investigation of the single washcoat layer processes and an appropriate structure of the mathematical model in order to describe such synergetic effects.

The present contribution reviews and further extends the development of a chemically consistent mathematic model of such dual-layer ASC converters performed in [18–20]. A preliminary step involved the catalytic activity study and the kinetic modeling of the SCR component of the ASC system [6], namely a state-of-the-art Fe-zeolite SCR catalyst. The developed SCR kinetic model considered, besides the well-known NO/NO₂/NH₃ SCR reactions (e.g., Standard-, Fast- and NO₂-SCR) also the N₂O reactivity with NO_x and NH₃, an important feature in order to accurately reproduce high-T operation of SCR converters based on Fe-zeolite catalysts. Then, the PGM component of the ASC was studied under typical automotive conditions (e.g., at low temperatures and in presence of NO_x, including NO₂) and in the powdered form, in order to gain intrinsic kinetic information and develop a consistent kinetic model, which was validated against data collected over a single-layered PGM monolith [18, 19]. The potential interactions of the chemistries associated with the PGM and SCR active phases were further analyzed by means of two different reactor configurations involving either the sequential use of the two catalysts or their intimate mixing [18].

Finally, the SCR and PGM kinetics were implemented in a mathematical model of dual-layer monolithic catalysts, specifically developed for SCR + PGM NH₃ slip catalysts [20] and validated against experimental data collected over the full dual-layer ASC monolith catalyst [19].

18.2 Methods

The dual-layer ASC system herein studied consisted of commercial state-of-the-art PGM and SCR catalysts: the PGM catalyst was a Pt/Al₂O₃-based system, while an Fe-zeolite was used as the NH₃-SCR catalyst component. The original ASC monolith was a dual-layer system with an SCR layer coated on top of a PGM one. For the present study, in addition to the dual-layer monolith, the SCR and PGM catalysts were supplied both in the form of precursor powders of the monolith washcoat and in the form of single washcoated monoliths (400 CPSI, wall thickness = 5 mils).

18.2.1 Experimental

Powdered catalysts—Kinetic runs over the powdered catalysts were carried out in a flow-microreactor consisting of a quartz tube (6 mm i.d.) placed in an electric oven. Three different reactors were prepared for the present study: one was loaded only with the PGM catalyst, two were loaded with both SCR and PGM ones. In this latter case two different configurations were studied, named in the following as “Double Bed” and “Mechanical Mixture” configuration. In the case of the Double Bed (DB) configuration two consecutive catalyst beds were loaded in the microreactor, where the SCR catalytic bed was followed by a PGM bed. By contrast, the Mechanical Mixture (MM) configuration involved the intimate mixing of the two powders into a single catalytic layer. The amount of PGM catalyst loaded in the reactor in case of both “Double Bed” and “Mechanical mixture” was equal to that loaded in the case of runs over the PGM catalyst only, while the relative proportions of the two catalysts were representatives of typical SCR/PGM wash-coat load ratios in dual-layer ASC monoliths.

The reactor outlet was directly connected to a quadrupole mass spectrometer (Balzers QMS 200) and to a UV-analyzer (ABB LIMAS 11HW) in parallel. NH_3 , NO , NO_2 , N_2O , O_2 and He were dosed from bottled calibrated gas mixtures by mass flow controllers, while water vapor was added by means of a saturator. The catalyst temperature was measured by a K-type thermocouple directly immersed in the catalytic bed.

The catalysts were conditioned in a T-ramp at $5\text{ }^\circ\text{C}/\text{min}$ up to $600\text{ }^\circ\text{C}$ in $8\text{ }\%$ O_2 v/v, and $8\text{ }\%$ H_2O v/v and keeping them at $600\text{ }^\circ\text{C}$ for 5 h. Kinetic runs included transient and isothermal steady-state experiments in the $150\text{--}550\text{ }^\circ\text{C}$ temperature range. Typical feed concentrations of NO_x and NH_3 ranged between 0 and 1000 ppm, always in the presence of O_2 ($8\text{ }\%$ v/v), H_2O ($8\text{ }\%$ v/v) and balance He. A detailed description of the experimental equipment and procedures can be found elsewhere [21].

Monolith catalysts—Different core monolith samples (6 cm^3 volume, 400 CPSI, wall thickness = 5 mils) were tested, either coated only with the individual SCR and the PGM components, or coated with the SCR layer on top of the PGM one. The latter monolith represents the real configuration of the studied dual-layer ASC system.

Isothermal steady-state and transient tests were performed within the $150\text{--}550\text{ }^\circ\text{C}$ T-range over core drilled monolith samples of cylindrical shape. The catalyst temperature was monitored by two thermocouples placed, respectively, at the monolith inlet and outlet. The feed section of the rig for monolith tests consisted of a set of mass flow controllers to dose N_2 , NH_3 , NO , NO_2 , CO_2 and O_2 , while H_2O was added to the feed stream by means of a vaporizer through a heated pipeline. The following analytical equipment was used: NH_3 was detected by microwave process analysis (Mipan), NO_x by Chemiluminescence techniques using a modified low-temperature NO_2 converter (CLD Ecophysics) and N_2O by means of a nondispersive infrared analyzer (NDIR). NH_3 was removed before the

CLD by means of an NH_3 gas scrubber. The catalyst conditioning procedure was the same as for the powder samples. Typical feed concentrations of NO_x , and NH_3 were 0–500 ppm, with $\text{O}_2 = 8\% \text{ v/v}$, $\text{CO}_2 = 8\% \text{ v/v}$, $\text{H}_2\text{O} = 8\% \text{ v/v}$ and balance N_2 . The space velocity, in this case referred to the monolith volume, was set to $100,000 \text{ h}^{-1}$. Further experiments based on a DOE-plan were carried out in a synthetic gas reactor over the dual layer coated ASC monolith samples. The DOE schedule was designed to assess the main influence of parameters such as temperature, space velocity, the NH_3/NO_x ratio and the NO_2/NO_x ratio.

A detailed description of the experimental equipment and procedures can be found elsewhere [21].

18.2.2 Modeling

Packed-bed micro-reactor model (powdered catalyst)—For both the SCR and the PGM components of the ASC, experimental data collected over the powdered catalysts have been analyzed according to a heterogeneous one-dimensional plug-flow dynamic reactor model that assumes the catalytic bed to be isothermal and isobaric [22].

Tables 18.1 and 18.2 report the list of reaction steps included in the SCR and in the PGM kinetic models, respectively, to fully describe the $\text{NH}_3\text{-NO}_x/\text{O}_2$ reacting system in the whole T-range. The corresponding rate expressions are also reported.

The parameters included in the rate equations were estimated by global multiresponse nonlinear regressions based on the least squares method. For this purpose the BURENL routine, developed by Prof. Guido Buzzi-Ferraris, has been used [23, 24].

PGM/SCR “Double Bed” simulations were carried out through the sequential implementation of SCR and PGM kinetics within the just described reactor model. Due to the arrangement of the two catalytic beds (SCR catalyst followed by the PGM catalyst), the output of the SCR layer simulation was used as input data for the simulation with the PGM model. By contrast, the simulation of the data collected over the SCR/PGM “Mechanical Mixture” configuration called for a dedicated model accounting for the simultaneous presence of two active phases in different amounts. Again, a heterogeneous one-dimensional plug-flow dynamic reactor model has been employed, assuming the catalytic bed to be isothermal and isobaric, with a homogeneous, perfectly mixed distribution of the two active phases [18].

Monolith reactor model—For validation purposes, the kinetic models of the SCR catalyst [6] and of the PGM catalyst [18] were used to simulate catalytic activity runs over honeycomb monoliths coated with the SCR and the PGM component, respectively, of the studied ASC system. In the case of the SCR catalyst, the kinetics were implemented in a heterogeneous dynamic $1\text{D} + 1\text{D}$ model of a single monolith channel, accounting both for external (gas–solid) and internal (intra-porous) mass transfer resistances [12, 25, 26]. Model simulations

Table 18.1 Kinetic scheme and rate expressions for the SCR component

R.1	$\text{NH}_3 + * \rightarrow \text{NH}_3^*$	NH_3 adsorption	$r_{\text{Ads}} = k_{\text{Ads}} C_{\text{NH}_3} (1 - \theta_{\text{NH}_3} - \theta_{\text{Nitr}})$	Eq. (18.1)
R.2	$\text{NH}_3^* \rightarrow \text{NH}_3 + *$	NH_3 desorption	$r_{\text{Des}} = \exp[k_{\text{Des}}^0 - E_{\text{Des}} \left(\frac{1000}{T} - \alpha\theta_{\text{NH}_3} - \frac{1000}{473}\right)] \cdot \theta_{\text{NH}_3}$	Eq. (18.2)
R.3	$2\text{NH}_3^* + 3/2\text{O}_2 \rightarrow \text{N}_2 + 3\text{H}_2\text{O}$	NH_3 oxidation to N_2	$r_{\text{Des}} = \exp[k_{\text{ox}}^0 - E_{\text{ox}} \left(\frac{1000}{T} - \frac{1000}{473}\right)] \theta_{\text{NH}_3} (1 + \gamma \cdot C_{\text{NO}})$	Eq. (18.3)
R.4	$\text{NH}_3^* + 5/4\text{O}_2 \rightarrow \text{NO} + 3/2\text{H}_2\text{O}$	NH_3 oxidation to NO	$r_{\text{oxb}} = \exp(k_{\text{oxb}}^0 - E_{\text{oxb}} \left(\frac{1000}{T} - \frac{1000}{473}\right)) \theta_{\text{NH}_3}$	Eq. (18.4)
R.5	$\text{NO} + 1/2\text{O}_2 \leftrightarrow \text{NO}_2$	NO oxidation to NO_2	$r_{\text{NO-ox}} = \exp(k_{\text{NO-ox}}^0 - E_{\text{NO-ox}} \left(\frac{1000}{T} - \frac{1000}{473}\right)) \frac{\left(\frac{C_{\text{NO}} \sqrt{P_{\text{O}_2}} - C_{\text{NO}_2}}{K_{\text{O}_2}}\right)}{1 + K_{\text{O}_2} C_{\text{O}_2}}$	Eq. (18.5)
R.6	$\text{NH}_3^* + \text{NO} + 1/4\text{O}_2 \rightarrow \text{N}_2 + 3/2\text{H}_2\text{O}$	Standard SCR (Low T)	$r_{\text{No}} = \exp(k_{\text{Std}}^0 - E_{\text{No}} \left(\frac{1000}{T} - \frac{1000}{473}\right)) C_{\text{NO}} \theta_{\text{NH}_3} (1 - \sigma_{\text{NH}_3})$	Eq. (18.6)
R.7	$\text{S1} + \text{NH}_3 \rightleftharpoons \text{S1}[\text{NH}_3]$	Adsorption/desorption of inhibiting NH_3 onto S1 red-ox sites	$r_{\text{Ads/Des-S1}} = \exp\left(k_{\text{Ads-S1}}^0 - E_{\text{Ads-S1}} \left(\frac{1000}{T} - \frac{1000}{473}\right)\right) C_{\text{NH}_3} (1 - \sigma_{\text{NH}_3}) - \exp\left(k_{\text{Des-S1}}^0 - E_{\text{Des-S1}} \left(\frac{1000}{T} - \frac{1000}{473}\right)\right) \sigma_{\text{NH}_3}$	Eq. (18.7)
R.8	$\text{NH}_3 + \text{NO} + 1/4\text{O}_2 \rightarrow \text{N}_2 + 3/2\text{H}_2\text{O}$	Standard SCR (High T)	$r_{\text{L}} = \exp[k_{\text{L}}^0 - E_{\text{L}} \left(\frac{1000}{T} - \frac{1000}{823}\right)] C_{\text{NO}} C_{\text{NH}_3}$	Eq. (18.8)
R.9	$2\text{NO}_2 + 2\text{NH}_3^* \rightarrow \text{NH}_4\text{NO}_3^* + \text{N}_2 + \text{H}_2\text{O}$	Ammonium nitrate build-up	$r_{\text{Amm}} = \frac{\exp(k_{\text{amm}}^0 - E_{\text{amm}} \left(\frac{1000}{T} - \frac{1000}{473}\right)) \theta_{\text{NH}_3} C_{\text{NO}_2}^2}{1 + K_{\text{amm}} \theta_{\text{Nitr}}}$	Eq. (18.9)
R.10	$\text{NH}_4\text{NO}_3^* \rightarrow (\text{NH}_3 + \text{HNO}_3) \rightarrow \text{NH}_4\text{NO}_3(\text{s})$	Ammonium nitrate dissociation/sublimation	$r_{\text{Nitr}} = \exp(k_{\text{Nitr}}^0 - E_{\text{Nitr}} \left(\frac{1000}{T} - \frac{1000}{473}\right)) \theta_{\text{Nitr}}$	Eq. (18.10)
R.11	$2\text{NH}_3^* + 2\text{NO}_2 \rightarrow \text{N}_2\text{O} + \text{N}_2 + 3\text{H}_2\text{O}$	N_2O formation	$r_{\text{N}_2\text{O}} = \exp(k_{\text{N}_2\text{O}}^0 - E_{\text{N}_2\text{O}} \left(\frac{1000}{T} - \frac{1000}{473}\right)) \theta_{\text{NH}_3} C_{\text{NO}_2}$	Eq. (18.11)
R.12	$\text{NH}_3^* + 3/4\text{NO}_2 \rightarrow 7/8\text{N}_2 + 3/2\text{H}_2\text{O}$	NO_2 -SCR	$r_{\text{N}_2\text{O}} = \exp(k_{\text{N}_2\text{O}}^0 - E_{\text{N}_2\text{O}} \left(\frac{1000}{T} - \frac{1000}{473}\right)) \theta_{\text{NH}_3} C_{\text{NO}_2}$	Eq. (18.12)
R.13	$2\text{NH}_3^* + \text{NO} + \text{NO}_2 \rightarrow 2\text{N}_2 + 3\text{H}_2\text{O}$	Fast SCR	$r_{\text{Fast}} = \exp(k_{\text{Fast}}^0 - E_{\text{Fast}} \left(\frac{1000}{T} - \frac{1000}{473}\right)) \theta_{\text{NH}_3} C_{\text{NO}_2} C_{\text{NO}}$	Eq. (18.13)
R.14	$\text{N}_2\text{O} + \text{NO} \rightarrow \text{N}_2 + \text{NO}_2$	N_2O reduction by NO	$r_{\text{N}_2\text{O}DC} = \exp(k_{\text{N}_2\text{O}DC}^0 - E_{\text{N}_2\text{O}DC} \left(\frac{1000}{T} - \frac{1000}{473}\right)) C_{\text{N}_2\text{O}} \cdot \left(\frac{C_{\text{NO}}}{C_{\text{NO}+e}}\right)$	Eq. (18.14)
R.15	$\text{NH}_3^* + 3/2 \text{N}_2\text{O} \rightarrow 2\text{N}_2 + 3/2\text{H}_2\text{O}$	N_2O -SCR with NH_3	$r_{\text{N}_2\text{O}R} = \exp(k_{\text{N}_2\text{O}R}^0 - E_{\text{N}_2\text{O}R} \left(\frac{1000}{T} - \frac{1000}{473}\right)) \theta_{\text{NH}_3} C_{\text{N}_2\text{O}}$	Eq. (18.15)

Table 18.2 Kinetic scheme and rate expressions for the PGM component (from Ref. [18])

R.16	$\text{NH}_3 + * \rightarrow \text{NH}_3^*$	NH ₃ adsorption	$r_{ads} = k_{ads-PGM} C_{\text{NH}_3} \left(1 - \theta_{\text{NH}_3}^{\text{PGM}} \right)$	Eq. (18.16)
R.17	$\text{NH}_3^* \rightarrow \text{NH}_3 + *$	NH ₃ desorption	$r_{des} = \exp \left[k_{des-PGM}^0 - E_{des-PGM} \left(\frac{1000}{T} - \frac{1000}{473} \right) \right] \cdot \theta_{\text{NH}_3}^{\text{PGM}}$	Eq. (18.17)
R.18	$\text{NO} + 1/2\text{O}_2 \leftrightarrow \text{NO}_2$	NO oxidation to NO ²	$r_{\text{NOox}} = \exp \left(k_{\text{NOox-PGM}}^0 - E_{\text{NOox-PGM}} \left(\frac{1000}{T} - \frac{1000}{473} \right) \right) \cdot \left(\frac{C_{\text{NO}} \sqrt{P_{\text{O}_2}}}{1 + K_{\text{NO}_2-\text{PGM}} \cdot C_{\text{NO}_2}} \right)$	Eq. (18.21)
R.19	$2\text{NH}_3^* + 3/2\text{O}_2 \rightarrow \text{N}_2 + 3\text{H}_2\text{O}$	NH ₃ oxidation to N ₂	$r_{\text{NN}} = \frac{\exp \left(k_{\text{NN}}^0 - E_{\text{NN}} \left(\frac{1000}{T} - \frac{1000}{473} \right) \right) \cdot \theta_{\text{NH}_3}^{\text{PGM}}}{(1 + K_{\text{NO}} \cdot C_{\text{NO}_2})}$	Eq. (18.18)
R.20	$2\text{NH}_3^* + 5/2\text{O}_2 \rightarrow 2\text{NO} + 3\text{H}_2\text{O}$	NH ₃ oxidation to NO	$r_{\text{NO}} = \frac{\exp \left(k_{\text{NO}}^0 - E_{\text{NO}} \left(\frac{1000}{T} - \frac{1000}{473} \right) \right) \cdot \theta_{\text{NH}_3}^{\text{PGM}}}{(1 + K_{\text{NO}} \cdot C_{\text{NO}_2})}$	Eq. (18.19)
R.21	$\text{NH}_3^* + \text{NO} + 3/4\text{O}_2 \rightarrow \text{N}_2\text{O} + 3/2\text{H}_2\text{O}$	Non selective standard SCR	$r_{\text{NHNOX}} = \frac{\exp \left(k_{\text{NHNOX}}^0 - E_{\text{NHNOX}} \left(\frac{1000}{T} - \frac{1000}{473} \right) \right) \cdot \theta_{\text{NH}_3}^{\text{PGM}} \cdot C_{\text{NO}}}{(1 + K_{\text{NHNOX}} \cdot C_{\text{NO}_2})}$	Eq. (18.20)
R.22	$2\text{NH}_3^* + 2\text{NO}_2 \rightarrow \text{N}_2 + \text{N}_2\text{O} + 3\text{H}_2\text{O}$	NH ₃ /NO ₂ to N ₂ and N ₂ O	$r_{\text{NHNOO}} = \exp \left(k_{\text{NHNOO}}^0 - E_{\text{NHNOO}} \left(\frac{1000}{T} - \frac{1000}{473} \right) \right) \cdot \theta_{\text{NH}_3}^{\text{PGM}} \cdot C_{\text{NO}_2}$	Eq. (18.22)
R.23	$8\text{NH}_3^* + 6\text{NO}_2 \rightarrow 7\text{N}_2 + 12\text{H}_2\text{O}$	NO ₂ -SCR to N ₂	$r_{\text{NOO}} = \exp \left(k_{\text{NOO}}^0 - E_{\text{NOO}} \left(\frac{1000}{T} - \frac{1000}{473} \right) \right) \cdot \theta_{\text{NH}_3}^{\text{PGM}} \cdot C_{\text{NO}_2}$	Eq. (18.23)

were then systematically compared with experimental data collected over core monolith samples coated with the Fe-zeolite SCR catalyst. The data set for kinetics validation covered the whole $\text{NH}_3/\text{NO}/\text{NO}_2/\text{N}_2\text{O}$ SCR reacting system. The temperature varied between 150 and 550 °C, including both steady-state and transient runs.

A similar approach was used to validate the PGM kinetics: data were collected over a PGM coated monolith and systematically compared with predictive model simulations. However, a different reactor model was used in this case. Indeed, simulation analysis of PGM coated monolith catalysts [20] pointed out that the extremely high reaction rates over this catalytic system result in full mass transfer control above 250 °C. For this reason, we assumed that in the case of washcoated monolith samples only the PGM washcoat surface was effectively active, thus we treated the PGM layer as a surface. The kinetics developed over the powdered PGM catalyst were thus referred to the catalyst surface and directly included in the PGM monolith model.

The same approach for the PGM phase modeling was adopted in the development of the mathematical model of Dual-Layer ASC monolith catalysts [20]. Such a model, named LSM (Layer + Surface Model), was based on the mathematical model for SCR monolithic converters [12, 25, 26]. As detailed in the following, the PGM reactivity was directly included in the mentioned SCR converter model by simply modifying the inner boundary condition for the diffusion–reaction equations within the SCR layer, i.e., the boundary condition at the interface with the PGM phase. It is worth emphasizing that the LSM model reduces to the PGM monolith model when the SCR layer thickness approaches zero.

18.3 Derivation and Validation of the SCR Model

18.3.1 Reaction Network and Kinetic Scheme Over the SCR Component

A systematic kinetic investigation of the full $\text{NO}/\text{NO}_2/\text{N}_2\text{O}-\text{NH}_3$ SCR reacting system was performed over a commercial Fe-promoted zeolite catalyst in the form of powder in a representative temperature range (150–550 °C) at high space velocities. The reacting systems typical of real SCR operating conditions have been addressed separately according to a strategy of increasing complexity, and analyzing for each of them the effects of T, space velocity, reactant feed concentrations, and NO_2/NO_x feed ratio [6].

Ammonia adsorption/desorption—The interaction of NH_3 with the catalyst surface is obviously important for SCR applications, as it is well known that the DeNO_x performances and the dynamics of SCR converters are governed by the reactivity of adsorbed NH_3 . The adsorption–desorption behavior of NH_3 (R.1–R.2 in Table 18.1) was first studied performing isothermal NH_3 feed

concentration step changes (TRM) at different temperatures (150, 200 °C) and with different NH₃ feed concentration (500, 1000 ppm) followed by a Temperature Programmed Desorption (TPD) experiments with different heating rate (15, 20 °C/min).

The results, herein not reported for brevity, indicated that the catalyst adsorb significant amounts of ammonia, which is strongly bonded to the catalyst surface and can be removed completely only by increasing the temperature up to 500 °C. The increase in the adsorption temperature resulted in the decrease of the amount of ammonia adsorbed on the catalyst surface.

NH₃/O₂, NO/O₂, NO₂/O₂—To investigate the catalyst activity in the NH₃ oxidation (R.3 and R.4) and in the reversible NO oxidation reaction (R.5), steady-state runs were performed in the 150–550 °C T-range feeding to the reactor 500 ppm of either NH₃, NO or NO₂ together with O₂ (8 % v/v), H₂O (8 % v/v) and balance helium. NH₃ started to be significantly oxidized at temperatures greater than 300 °C, giving N₂ as the main product. Traces of NO were also detected above 450 °C.

NO oxidation reached a maximum of 10 % NO conversion around 450 °C, while at higher temperatures thermodynamic equilibrium was approached. Finally, the inverse of NO oxidation, namely NO₂ decomposition to NO, was found to become significant only at temperatures greater than 350 °C.

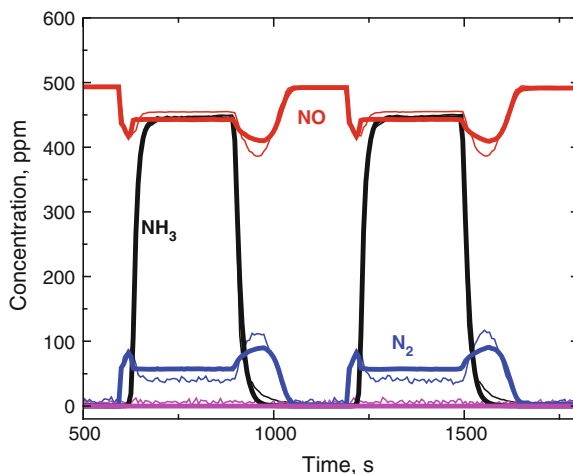
NH₃/NO/O₂—The reactivity of ammonia and NO was first investigated during slow temperature ramps while continuously feeding to the reactor 500 ppm of both NH₃ and NO in flowing O₂ and H₂O. The data indicate a growing consumption of NH₃ and NO, with corresponding evolution of N₂, with increasing temperature in the whole investigated temperature range: the outlet species concentrations were initially consistent with the stoichiometry of the Standard SCR reaction (R.6 or R.8 in Table 18.1), i.e., with an equimolar NO/NH₃ consumption ratio, but above 220 °C a greater conversion of NH₃ with respect to NO was observed.

This effect is likely due to the onset of NH₃ oxidation, which seems to be enhanced when also NO is fed to the reactor. Indeed, dedicated experiments at the same conditions but in the absence of NO indicated that the temperature threshold for NH₃ oxidation was around 300 °C in this case, i.e., at least 50–80 °C higher than the threshold temperature observed in the presence of NO.

Similar findings have been reported by other authors for other Fe-zeolite catalysts [10, 11, 27]. Such a peculiar behavior, i.e., the extra ammonia consumption in the presence of NO, is commonly associated with the possible formation of NO_x surface species with a higher oxidation state with respect to NO, such as nitrites and nitrates, which thus would require more ammonia to be reduced to nitrogen. However, more work is needed to fully elucidate these aspects.

The reactivity of ammonia and NO was then investigated by transient runs performed under isothermal conditions. Figure 18.2 (thin lines) shows for instance a run where ammonia was fed and removed from the reactor every 300 s in a stepwise manner while continuously feeding NO, oxygen, and water at 250 °C. It is evident that each time ammonia was fed to the reactor, the NO signal initially decreased, passed through a minimum, and then approached steady state, and the N₂ trace followed that of NO as a mirror image; meanwhile the ammonia signal,

Fig. 18.2 Transient experiments with steps feed of NH_3 every 300 s at 250 °C over SCR crushed monolith powder. $\text{NH}_3 = 500$ ppm, $\text{NO} = 500$ ppm, $\text{H}_2\text{O} = 3\%$, $\text{O}_2 = 2\%$ v/v, He carrier gas, $Q = 327 \text{ cm}^3/\text{min}$. *Thin lines:* measured concentrations of NH_3 , NO , N_2 at reactor outlet. *Thick lines:* kinetic fit



after a dead time, rose up approaching steady state. At ammonia shut-off the NH_3 signal quickly dropped to zero, while the NO concentration initially decreased and passed through a minimum before recovering its feed value; the minimum in the NO concentration corresponded to a maximum for the nitrogen production, before it gradually decreased to zero. The same qualitative behavior was observed in many experiments, run for example at different temperatures, in the range 175–300 °C, varying space velocity and oxygen feed content.

If we plot the evolution of NO conversion as a function of the ammonia surface concentration during the ammonia start-up and shut off transients of these tests, a hysteresis behavior becomes apparent: during the ammonia feed transient, the NO conversion initially increases up to a certain ammonia surface concentration and then decreases for higher values. Interestingly, the mean NO conversion during the ammonia shut off transient resulted higher than during the feed transient, and also indicates the existence of an optimal ammonia surface concentration, which is however different from that of the start-up transient.

Such transient features have been observed over different Fe-zeolite systems [6, 27–29] and V based SCR catalysts [30], and have been explained invoking an inhibiting effect of ammonia on the Standard SCR reaction [30, 31]. They can be rationalized in fact according to a classic Langmuir-Hinshelwood (LH) mechanism, i.e., invoking a competition between NO and NH_3 for adsorption onto the same catalytic site. During the NH_3 shutdown transients the SCR rate was enhanced as soon as both gaseous and adsorbed NH_3 concentrations became lower than at steady state: this suggests that the incremented DeNOx efficiency may have resulted from improved adsorption of NO onto the catalyst active sites due to the reduced gaseous or surface NH_3 concentration. In order to take into account the ammonia inhibition effect, a new rate expression for the Standard SCR reaction was developed [6].

$\text{NH}_3/\text{NO}-\text{NO}_2/\text{O}_2$ —The $\text{NH}_3/\text{NO}-\text{NO}_2/\text{O}_2$ SCR reactivity was studied keeping a constant feed concentration of 500 ppm of total NO_x , 500 ppm of NH_3 , O_2

(8 %, v/v), H₂O (8 %, v/v) and balance helium. Steady-state activity data were collected in the 150–550 °C T-range changing the NO₂/NO_x feed ratio from 0 up to 1. Symbols in Fig. 18.3 represent the measured steady-state NO_x conversions (a), NH₃ conversions (b) and N₂-selectivity ($=C_{N_2}/(C_{N_2} + C_{N_2O})$) (c) plotted versus the NO₂/NO_x feed ratio at different temperatures.

It is evident that the DeNO_x performance of the system is worse for the limiting situations where either NO or NO₂ are the only NO_x species present in the reacting system together with NH₃ (NO₂/NO_x = 0 or 1). In the whole temperature range the highest DeNO_x activity was observed when equimolar amounts of NO and NO₂ were fed to the reactor (NO₂/NO_x = 0.5), associated with the occurrence of the Fast SCR reaction which is well known to be extremely active over Fe-zeolites. Furthermore, the selectivity to N₂ decreased below 100 % only when a large excess of NO₂ was present in the feed stream.

The behavior observed in Fig. 18.3 is typical of Fe zeolite catalysts: indeed, the Fe zeolite SCR activity strongly depends on the NO₂ feed content, reaching the highest NO_x conversion always in the case of the optimal 1/1 NO/NO₂ feed ratio. This is not the case for Cu zeolites [32], which are very active in the Standard SCR reaction already at low temperatures, so that a lower benefit is granted by the Fast SCR reaction, or for the vanadium-based catalysts [33], whose activity exhibits a broader dependence on the NO₂ content of the feed stream.

Of course the production of N₂O is strictly related to the catalyst as well. For the present Fe zeolite catalyst, significant N₂O formation was detected only when an excess of NO₂ (>50 %) was present in the NO_x feed mixture, while the opposite was found in the case of a Cu zeolite, where N₂O production was observed also in parallel with the occurrence of the Standard SCR reaction, so in the absence of NO₂ feed.

To take into account the NO₂ reactivity, R.9–R.13 have been included in the kinetic scheme, in line with previous findings [6, 12, 26, 28].

N₂O/NO_x/NH₃—It is well known in the literature that Fe-zeolites are active both in the catalytic decomposition of N₂O to N₂ and in the SCR of N₂O by ammonia [34, 35]. Accordingly, a study dedicated to the analysis of these reactions was performed in our labs.

First, the pure N₂O decomposition was investigated at steady state in the 150–550 °C T-range feeding to the reactor 500 ppm of N₂O together with O₂ (8 %, v/v) and H₂O (8 %, v/v): it was found that the Fe zeolite catalyst was indeed able to decompose N₂O to N₂ but only above 500 °C and to a limited extent (roughly 10 %). A completely different situation was obtained when together with N₂O, mixtures of NO_x in different NO/NO₂ proportions were fed to the reactor. Figure 18.4 (symbols) shows data from a run with NO/NO₂ = 1/1: N₂O started to be converted above 400 °C giving again N₂ as the only product and reaching a maximum conversion of about 55 % at 550 °C. The presence of NO_x in the feed stream significantly enhanced the N₂O decomposition activity, according to a well-known “catalytic” effect [34, 35], which may be explained invoking the reaction between N₂O and NO to give N₂ and NO₂ (R.14) and the subsequent decomposition of NO₂ to NO and O₂ (R.5 reverse).

Fig. 18.3 Effect of the NO_2/NO_x feed ratio on the steady-state SCR activity over powder catalyst.

$Q = 250 \text{ cm}^3/\text{min}$ (STP),
 $\text{NH}_3 = 500 \text{ ppm}$,
 $\text{NO}_x = 500 \text{ ppm}$,
 $\text{H}_2\text{O} = 8 \text{ \% v/v}$, $\text{O}_2 = 8 \text{ \% v/v}$. $\text{NO}_2/\text{NO}_x = 0, 0.25, 0.5, 0.75, 1$. **a** NO_x conversion **b** NH_3 conversion **c** N_2 selectivity. *Symbols*: experimental. *Solid lines*: kinetic fit

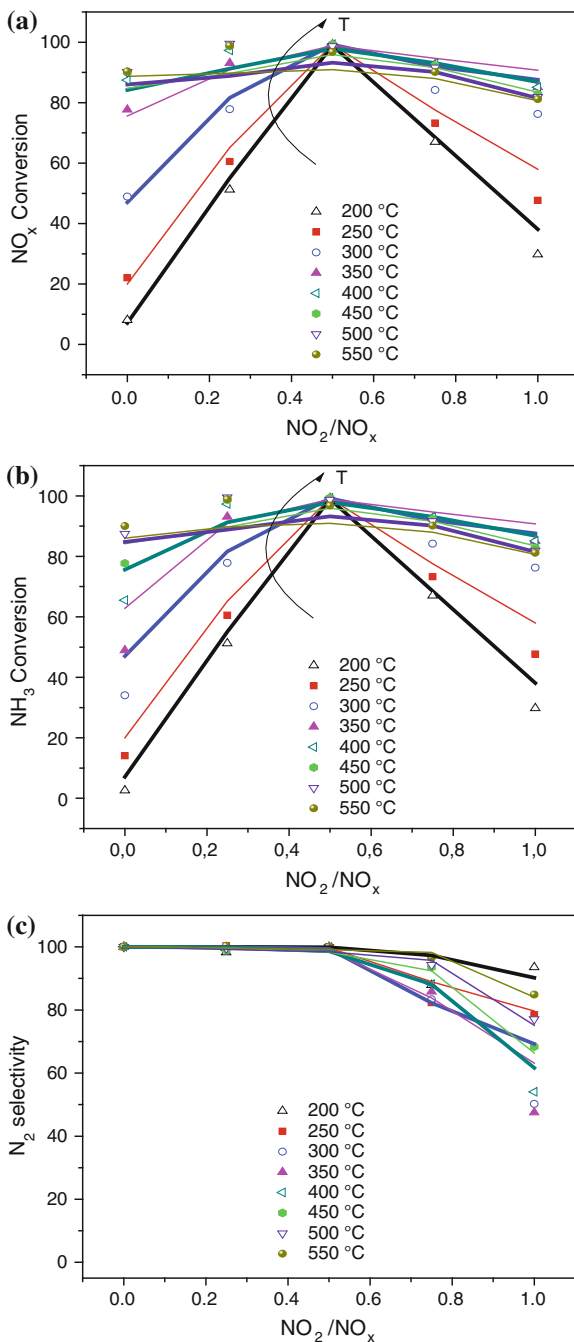
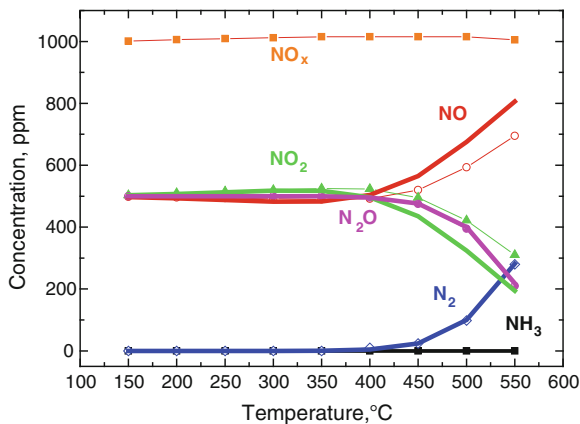


Fig. 18.4 NO_x assisted decomposition of N₂O as a function of temperature over SCR powder catalyst: Q = 250 cm³/min (STP), N₂O = 500 ppm; NO = NO₂ = 500 ppm; H₂O = 8 % v/v, O₂ = 8 % v/v [4]. Symbols: experimental. Solid lines: kinetic fit



The reactivity of N₂O with NH₃ (R.15 in Table 18.1) was studied in steady-state runs. NH₃ and N₂O started to be converted already at 300 °C with corresponding N₂ evolution, resulting both from the reaction between ammonia and N₂O and from ammonia oxidation.

18.3.2 Kinetic Fit

The reactions prevailing in the analyzed reacting systems depending on T and feed composition were used to define the kinetic scheme reported in Table 18.1.

In the case of the Standard SCR reaction (R.6 or R.8), a dual-site Mars-Van Krevelen rate expression assuming that NH₃ blocks the red-ox sites for NO activation was adopted in line with previous work performed over both vanadium-based [30, 36] and Fe-zeolite catalysts [12], in order to explain the observed inhibiting effect of NH₃ on such a reaction at low temperatures. The model has been then extended to include also the SCR reactivity in the presence of excess NO₂ and particularly to describe also the reactivity of N₂O (R.14 and R.15).

The parameters of the rate expressions (Eq. 18.1–18.15) for reactions (R.1–R.15) were estimated by multiresponse nonlinear regression of the transient microreactor runs, as detailed below. Notice that the rate equations do not include dependences on O₂ and H₂O, since the feed concentrations of both such species were kept constant at 8 % v/v.

As evident from the thick lines in Figs. 18.2, 18.3, and 18.4 that represent the model fit, a good agreement between experimental results and model predictions was obtained in all cases. In particular, the model could nicely reproduce the transient features evident in the standard SCR reaction at low T, predicting the differences observed in the deNO_x activity at similar ammonia coverages (Fig. 18.2); also, a reasonably good match between experimental and kinetic fit can be noticed for all runs collected varying the NO₂/NO_x feed ratio between 0

and 1 and covering the 150–550 °C. Eventually, the model was able to describe with a sufficient degree of accuracy also the N_2O decomposition/reactivity observed over the Fe-zeolite catalyst.

18.3.3 Model Validation

The SCR kinetic model was then validated at different scales. First, catalytic activity runs were carried out over a small core monolith sample in a lab rig and data compared with model simulations generated by incorporating the SCR kinetics into the transient 1D + 1D mathematical model of SCR monolith converters.

For all the tests performed in the 150–550 °C T-range and varying the NO_2/NO_x feed ratio from 0 to 1, a fairly good match between predictive model simulations and experimental data was observed. Figure 18.5a shows the validation map for NO_x conversions (absolute error between experimental and simulated percentage conversions at steady-state conditions) plotted as a function of temperature and NO_2/NO_x feed ratio. It clearly appears that model deviations were in the range of $\pm 5\%$ over the whole investigated field [6].

The SCR model was further validated by simulating transient runs performed over small core monoliths. In analogy to the TRM runs over the powdered catalyst, 750 ppm of NH_3 were fed to the core monolith sample in a stepwise manner while continuously flowing NO_x (500 ppm), O_2 (8 % v/v), H_2O (8 % v/v) and balance N_2 at a constant temperature in the range 200–350 °C.

Figure 18.5b shows the results of one experiment performed at 250 °C by feeding and removing the NH_3 feed flow every 300 s for $\text{NO}_2/\text{NO}_x = 0.25$ feed ratio: the figure compares the measured (thin lines) and simulated (thick lines) outlet concentration profiles of NH_3 , NO and NO_2 during such tests [6]. It can be noticed that a clear maximum in the DeNO $_x$ activity was still present at NH_3 feed as already observed on the powdered catalyst. Notably, the simulation obtained by the dual site kinetic model showed the same qualitative behavior.

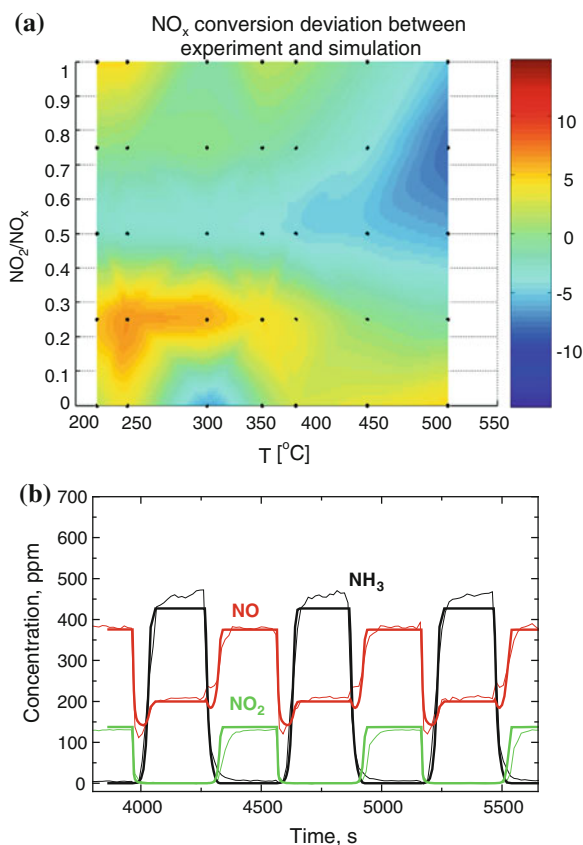
The model was further validated simulating the N_2O decomposition/reactivity onto core monolith samples: simulation results were in fairly good agreement with both the N_2O and the NH_3 concentration traces.

18.4 Derivation and Validation of the PGM Catalyst Model

18.4.1 Reaction Network and Kinetic Scheme Over the PGM Component

Like for the SCR component, the reacting systems prevailing over the PGM component of the Ammonia Slip catalyst under typical NH_3 -SCR operating conditions have been addressed according to an order of increasing complexity,

Fig. 18.5 a Absolute deviations between experimental NO_x conversions and model simulation for steady-state runs over the monolith SCR catalyst as a function of temperature and NO₂/NO_x. GHSV = 100,000 h⁻¹, NH₃ = 500 ppm, NO_x = 500 ppm, H₂O = 8 % v/v, O₂ = 8 % v/v [4]. **b** Concentration step change experiments for the NH₃-NO-NO₂-O₂ reacting system over the SCR monolith catalyst: T = 250 °C, GHSV = 100,000 h⁻¹, NH₃ = 500 ppm, NO_x = 500 ppm (NO₂/NO_x = 0.25) H₂O = 8 % v/v, O₂ = 8 % v/v. NH₃ pulse length = 300 s. *Thin lines* experimental. *Thick lines* model simulation



analyzing for each of them the effects of T, space velocity, reactant concentrations, and NO₂/NO_x feed ratio.

Ammonia adsorption/desorption—First of all, the ammonia adsorption and desorption properties of the PGM catalyst have been investigated by transient runs, involving a concentration step-change run at 150 °C, stepwise feeding 500 or 1,000 ppm of NH₃ in the presence of water (8 % v/v) and balance helium, followed by NH₃ shut off and by a temperature ramp in order to complete ammonia desorption (TPD).

Data, not reported, indicated that ammonia does not appreciably adsorb onto the PGM catalyst. However, literature reviews on the ammonia oxidation mechanism over PGM catalysts unanimously consider the adsorption of both reactant molecules (NH₃ and O₂) [16], with ammonia adsorbing in on-top position on Pt [17]. Indeed, the lack of a detectable storage capacity for ammonia during our runs is not sufficient to rule out the adsorption of the same species on the catalyst surface; accordingly, notwithstanding the experimental evidence, ammonia adsorption/desorption steps were included in the developed kinetic model (R.16 and R.17 in Table 18.2).

Ammonia adsorption was assumed to occur on Pt sites as a nonactivated and molecular process, while the desorption process was regarded as T-dependent according to the Arrhenius law (Eqs. 18.16 and 18.17, respectively, in Table 18.2).

NO–O₂—The behavior of the PGM catalyst in the presence of NO and O₂ was investigated feeding to the reactor NO (500 ppm), O₂ (8 % v/v), H₂O (8 % v/v), and balance helium in the 150–550 °C temperature range. NO started to be converted at 150 °C giving NO₂ as the only reaction product and reaching a maximum consumption of about 300 ppm at about 350 °C, in line with the occurrence of R.18 (Table 18.2). Below 400 °C the NO conversion was kinetically limited, while above such a T the NO and NO₂ concentrations approached thermodynamic equilibrium, resulting in a decrease in NO conversion as the temperature was further incremented.

An interesting feature of NO oxidation over the investigated PGM catalytic system was highlighted during catalyst heat up transients: between 175 and 250 °C, after the catalyst temperature was increased, NO suddenly achieved a certain conversion with a consequent evolution of NO₂; however, although the temperature was kept constant and a steady-state behavior was expected, the NO signal started slowly but surely to rise again: correspondingly the amount of NO₂ released decreased. According to the literature on noble metal systems similar to the present PGM catalyst [37], the slow decrease in NO oxidation activity has to be ascribed to the strongly oxidizing nature of NO₂ and the consequent formation of noble metal oxides/chemisorbed oxygen on the catalyst surface, which reduces the catalyst activity. The transient with decreasing NO conversion would be thus the result of the NO₂ formed during the reaction, which oxidizes the Pt catalyst.

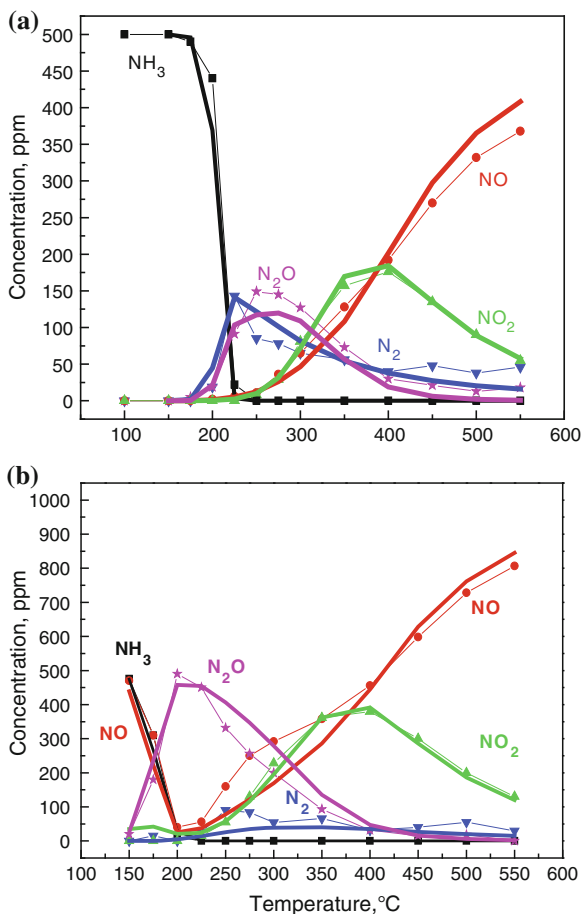
In line both with the literature evidence and with the collected data, a consistent reaction rate was adopted (Eq. 18.18), which takes into account both the thermodynamic equilibrium constraints and the aforementioned inhibiting effect of NO₂.

NH₃–O₂—Feeding only ammonia and oxygen to the reactor, NH₃ oxidation is expected to proceed, as widely reported in the literature [3, 16, 17, 38]. In the cited chapters N₂, N₂O and NO_x were identified as main oxidation products, the selectivity being a function of the noble metal and of the catalyst temperature.

Figure 18.6a, symbols, shows the results of a steady-state run performed over the PGM catalyst. The feed stream consisted of 500 ppm of ammonia in the presence of water (8 % v/v), oxygen (8 % v/v) and balance helium.

A steep light-off of the ammonia conversion was observed between 200 and 225 °C, with NH₃ reaching 100 % conversion already at 225 °C. In the same T-window the evolution of reaction products started, showing a significant change of products selectivity with increasing temperature. N₂ was the first species to be produced, reaching a maximum concentration of about 150 ppm at 225 °C. Further increasing the catalyst temperature resulted then in the progressive drop of the N₂ production. N₂O formation also exhibited a maximum, centered around 250 °C. Above 250 °C the NO_x concentration started to monotonically increase.

Fig. 18.6 NH_3 oxidation over PGM powdered catalyst:
a $\text{NH}_3 = 500$ ppm;
 $\text{H}_2\text{O} = 8\%$ v/v; $\text{O}_2 = 8\%$ v/v; carrier gas = He.
b $\text{NH}_3 = 500$ ppm;
 $\text{NO} = 500$ ppm, $\text{H}_2\text{O} = 8\%$ v/v; $\text{O}_2 = 8\%$ v/v; carrier gas = He. *Symbols and thin lines: experimental. Solid lines: kinetic fit [18]*



Correspondingly, a progressive reduction of both N_2 and N_2O concentrations was observed.

In line with the previous literature indications [3, 16, 17, 38], species outlet concentrations are consistent with the stoichiometry of several global reactions, which proceed in parallel and prevail at different temperature levels: ammonia is oxidized to nitrogen and NO (R.19 and R.20 in Table 18.2), NO can then react with ammonia and oxygen according to the nonselective Standard SCR reaction (R.21 in Table 18.2), or it can be oxidized to NO_2 (R.18 in Table 18.2). Notice that the direct oxidation of NH_3 to N_2O is not present in the kinetic scheme, as it results from the sum of the oxidation of NH_3 to NO (R.20) and of the subsequent reactivity between NH_3 and NO (R.21).

The effect of the ammonia feed concentration (from 250 up to 1000 ppm) was also investigated: it was found that the catalyst activity was not severely affected, complete conversion being always achieved below 250 °C. By contrast, a slight

effect was observed on the selectivity, with a higher production of N_2O in the intermediate T-range as the ammonia concentration increased.

NH_3 - NO - O_2 —The effect of NO on NH_3 oxidation was studied in steady-state runs where NO (100–250–500 ppm) was fed to the reactor together with 500 ppm of NH_3 , 8 % v/v O_2 , 8 % v/v H_2O , and balance helium.

Figure 18.6b, symbols, shows the results for the experiment run with 500 ppm of NO . The addition of NO to the reactant mixture significantly affected both the NH_3 conversion activity and the products distribution. NH_3 consumption reached 100 % already at 200 °C in the presence of NO (Fig. 18.6b), with a drop of about 50 °C of the reaction light-off in comparison with the NH_3 - O_2 reacting system (Fig. 18.6a). At low T, the main reaction product was N_2O . Above 200–250 °C, N_2O started decreasing, while a modest production of N_2 was visible together with the evolution of considerable amounts of NO and NO_2 .

Growing NO feed contents resulted below 275 °C in a progressive decrease in the N_2 yield, while the N_2O yield showed an opposite trend. In line with several literature indications, [3, 16, 17, 38], the enhanced N_2O production in the presence of NO was attributed to the occurrence of the nonselective Standard-SCR reaction (R.21 in Table 18.2). A different behavior was observed at high temperatures, above 400 °C, with the N_2 and N_2O concentrations not significantly affected by NO addition. Finally, the trend of NO_x concentration as a function of temperature highlights that NO was consumed at low temperatures (150–225 °C T-range) and produced at higher ones, up to 550 °C, where the NO_x yield exceeded 90 % independently of the NO feed content. Summarizing, the analysis of N_2 and NO_x concentrations as a function of temperature pointed out that N_2O production was highly enhanced below 275 °C in the presence of NO .

In line with the results above, reactions R.19–21 were included in the kinetic scheme to describe the NH_3 - O_2 and the NH_3 - NO - O_2 reactivities. We adopted first-order kinetics with respect to the NH_3 surface coverage, and a negative dependence on the NO_2 concentration, in line with the inhibiting effect played by NO_2 , as described in the following.

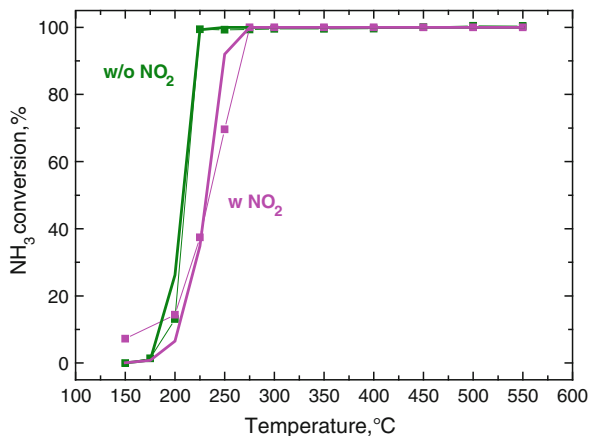
NH_3 - NO_2 - O_2 — NO_2 is commonly present in the feed to SCR converters due to the inclusion of an upstream preoxidation catalyst in the configuration of after-treatment systems. In addition, under unfavorable operative conditions NO_2 might undergo an incomplete selective reduction by NH_3 ; therefore, it could also represent a possible side product at the outlet of SCR converters.

Hence, being NO_2 a likely component of the ASC feed stream, the investigation of the NH_3/NO_2 reacting system was included in the work for the sake of completeness.

Figure 18.7 (symbols) shows the ammonia conversions measured feeding to the reactor 500 ppm of NH_3 and 500 ppm of NO_2 while flowing oxygen (8 % v/v), water (8 % v/v), and balance helium. Experimental results are also compared with those obtained in the absence of NO_2 in the feed stream.

The addition of NO_2 to the feed resulted first in a reduced conversion of NH_3 in the 200–275 °C temperature range. Complete conversion of NH_3 was indeed approached at 225 °C in the absence of NO_2 , while total conversion was achieved

Fig. 18.7 NH_3 conversions over PGM powdered catalyst: $\text{NH}_3 = 500$ ppm; $\text{NO}_2 = 500$ ppm, $\text{H}_2\text{O} = 8\%$ v/v; $\text{O}_2 = 8\%$ v/v; carrier gas = He. Symbols and thin lines: experimental. Solid lines: kinetic fit [18]



only at 275 °C when feeding also 500 ppm of NO_2 . Above this temperature complete ammonia conversion was approached for all reacting mixtures. The N_2 yield was also influenced by the presence of NO_2 (data not shown): the addition of 100 ppm of NO_2 adversely affected N_2 formation, with a decrease of the maximum yield from about 60 % down to about 40 %. However, nitrogen evolution was enhanced in the presence of greater concentrations of NO_2 , with a shift of the maximum yield to higher temperatures with greater NO_2 feed contents. Above 300 °C almost the same yield was obtained both in the presence and in the absence of NO_2 . The formation of N_2O showed instead a progressive decrease with increasing NO_2 feed content: a maximum yield of about 30 % at 300 °C was recorded in the presence of 500 ppm of NO_2 , against a maximum of about 60 % in the absence of NO_2 . At high temperatures ($T > 400$ °C), in analogy with what observed for the N_2 yield, the amount of produced N_2O seemed to be independent of NO_2 .

From the analysis of NH_3 conversion and product yields we speculate that NH_3 oxidation was inhibited by NO_2 , specifically in the low-T region ($T < 275$ °C), resulting in a decrease of the NH_3 conversion with increasing NO_2 feed contents. Despite experimental evidences, a detailed mechanistic study of this phenomenon was not in the scope of this study. On the other hand, in addition to the inhibited NH_3 oxidation reactions, the NO_x consumption observed in the low-T range justified the introduction of two additional reactions describing the reactivity between NH_3 and NO_2 with simultaneous formation of N_2O and of N_2 (R.22 in Table 18.2) or of N_2 only (R.23 in Table 18.2). Second-order kinetics in ammonia surface coverage and NO_2 gas phase concentration were adopted for both reactions (R.22) and (R.23).

$\text{NH}_3\text{-NO-NO}_2\text{-O}_2$ —Eventually, the complete $\text{NH}_3/\text{NO}/\text{NO}_2\text{-O}_2$ reacting system was also investigated in steady-state experiments where 500 ppm of NH_3 were fed to the reactor together with 150–250–500 ppm of NO_x ($\text{NO}_2/\text{NO}_x = 0.5$), 8 % v/v O_2 , 8 % v/v H_2O and balance helium. The addition of increasing amounts of NO_x reduced the catalyst activity in the 200–250 °C temperature region. The N_2

concentration was barely affected by the NO_x feed content over the whole T -range, while the highest N₂O concentration were recorded either in the absence of NO_x or in the presence of the highest NO_x feed content (500 ppm), with a maximum centered around 250 °C.

In summary, it seems that in the low- T region ($T < 275$ °C) the inhibiting role of NO₂ on the NH₃ oxidation activity prevails on the activity enhancement provoked by a larger amount of NO in the feed mixture. Furthermore, there was no evidence of additional reactions with respect to those identified during the investigation of NH₃-O₂, NH₃/NO/O₂ and NH₃/NO₂/O₂ subsystems.

18.4.2 Model Fit

The prevailing reactions identified in the analyzed reacting systems were used to define the kinetic scheme in Table 18.2. The rate parameters of (Eq. 18.18) were independently estimated from NO oxidation tests, while a global multiresponse nonlinear regression on the whole set of runs involving NH₃ provided estimates of the remaining rate parameters in (Eqs. 18.16–18.23).

Kinetic fit results are represented by solid lines in Figs. 18.6 and 18.7. The model provides a fairly good description of the data over the whole 150–550 °C T -range. The onset of NH₃ conversion upon varying the concentrations of ammonia, NO_x and the NO₂/NO_x feed ratio is indeed well captured in all the experiments, and so is the evolution of the product concentrations as a function of the catalyst temperature.

18.4.3 Model Validation

In analogy with what done for the SCR component of the ASC, the kinetics developed over the powdered PGM catalyst were validated against data collected over a core monolith sample coated only with the PGM component of the ASC.

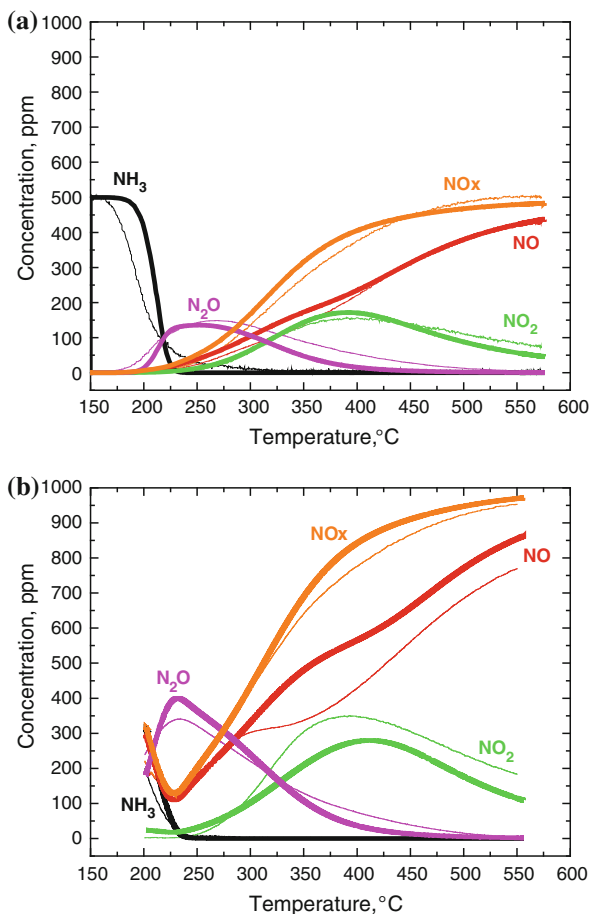
Kinetic data were collected according both to steady-state and transient test protocols. A wide range of operating conditions were covered in terms of temperature (150–550 °C T -window) and feed compositions (NO_x/NH₃ = 0–1 with NO₂/NO_x between 0 and 1). As an example, Fig. 18.8a, b compare experimental results (thin lines) and predictive model simulations (thick lines) for NH₃ conversion and product concentrations obtained during a NH₃ oxidation run (Fig. 18.8a) and an NH₃ oxidation test run in the presence of NO (Fig. 18.8b). Focusing on the ammonia oxidation experimental data (Fig. 18.8a, thin lines), it can be noticed that, in line with what we saw over the powdered catalyst (Fig. 18.8a), NH₃ conversion started above 160–175 °C and rapidly increased up to 80 % already at 200 °C, before approaching 100 % at 350 °C. NH₃ conversion is associated with production of N₂ (not detected by the analyzers), N₂O and NO_x,

Fig. 18.8 NH_3 oxidation on PGM monolith catalyst:

a $\text{NH}_3 = 500$ ppm;
 $\text{H}_2\text{O} = 8\%$ v/v; $\text{O}_2 = 8\%$ v/v;
 $\text{CO}_2 = 8\%$ v/v,
 $\text{GHSV} = 60000\text{ h}^{-1}$.

b $\text{NH}_3 = \text{NO} = 500$ ppm;
 $\text{H}_2\text{O} = 8\%$ v/v; $\text{O}_2 = 8\%$ v/v;
 $\text{CO}_2 = 8\%$ v/v,
 $\text{GHSV} = 60000\text{ h}^{-1}$.

Symbols and thin lines: experimental.
 Solid lines: kinetic fit [19]



with the main product being a function of monolith temperature: N_2O shows a maximum concentration value at 275 °C, while NO_x become the main oxidation product above 350 °.

The same qualitative trend was also shown by the model simulations (thick lines in Fig. 18.8a). From the quantitative point of view the model slightly overestimates the light-off temperature of NH_3 concentration in the 150–200 °C T -range. Above 250 °C the model overestimates the concentration N_2O , while an almost perfect match between experiments and simulations is observed in terms of NO_x concentration, at least up to 450 °C. Above this temperature the model slightly underestimates the NO_x production. Notwithstanding the discussed deviations, the qualitative agreement between experiments and purely predictive model simulations was regarded as satisfactory.

The effect of NO addition to the feed stream was then investigated: thin lines in Fig. 18.8b show that high NH_3 conversion (about 60 %) was recorded already at

200 °C, with complete consumption of the same species above 250 °C. NO consumption was also evident below 300 °C, where the NO concentration was below 250 ppm, i.e., the inlet concentration value. By contrast, at higher temperatures the same species became the main product. Below 300 °C the main reaction product was N₂O with concentrations up to 350 ppm. Model simulations (Fig. 18.8b, thick lines) showed a good agreement with experimental data at low T, while a general underestimation of NO_x production was observed in the high-*T* range.

In summary, validation runs over the PGM monolith catalyst pointed out a satisfactory agreement between predictive model simulations and experimental data above 300 °C for all the investigated feed compositions, whereas slight, but still acceptable, deviations were recorded at lower temperatures mainly in terms of NH₃ conversion.

18.5 Analysis and Modeling of SCR/PGM Interactions

18.5.1 Experimental Study of SCR/PGM Interactions

As discussed in the “Methods” section, the dual-layer ASC configuration involves the presence of a PGM catalytic layer beneath the SCR coating. A microflow reactor loaded with powder is inherently unsuitable for reproducing the real ASC system configuration: in particular, no arrangement of catalytic beds exists which can effectively simulate the NO_x backdiffusion and reaction with the ammonia preadsorbed on the SCR catalyst. Accordingly, the fundamental study performed over SCR-PGM combined systems, to be reported below, does not claim to faithfully simulate the real ASC system behavior. The aim of this investigation was rather to elucidate experimentally the interactions between the SCR and the PGM catalytic chemistries in relation to limiting (sequential vs. parallel) arrangements of the two catalysts. Two catalytic bed layouts have been in fact designed to achieve these goals: (i) a double bed configuration, with the first bed and the second bed consisting of the SCR catalyst and of the PGM catalyst, respectively, provides information on the sequential combination of the respective catalytic activities; (ii) a single bed configuration, wherein the reactor is loaded with a Mechanical Mixture of the two catalyst powders, can provide experimental evidence of local, parallel interactions between the catalysts.

Like for the PGM catalyst, both the “Double Bed” and “Mechanical Mixture” configurations were studied by means of steady-state activity runs addressing the main SCR reacting systems, namely NH₃/O₂, NH₃/NO/O₂, NH₃/NO₂/O₂ and NH₃/NO–NO₂/O₂.

NH₃–O₂—Fig. 18.9 compares data collected over the SCR catalyst only, over the PGM catalyst only, and over the two SCR/PGM combined systems. The analysis is based on NH₃, N₂, NO_x and N₂O concentrations measured when feeding 500 ppm of NH₃, 8 % v/v O₂, 8 % v/v H₂O, and balance helium.

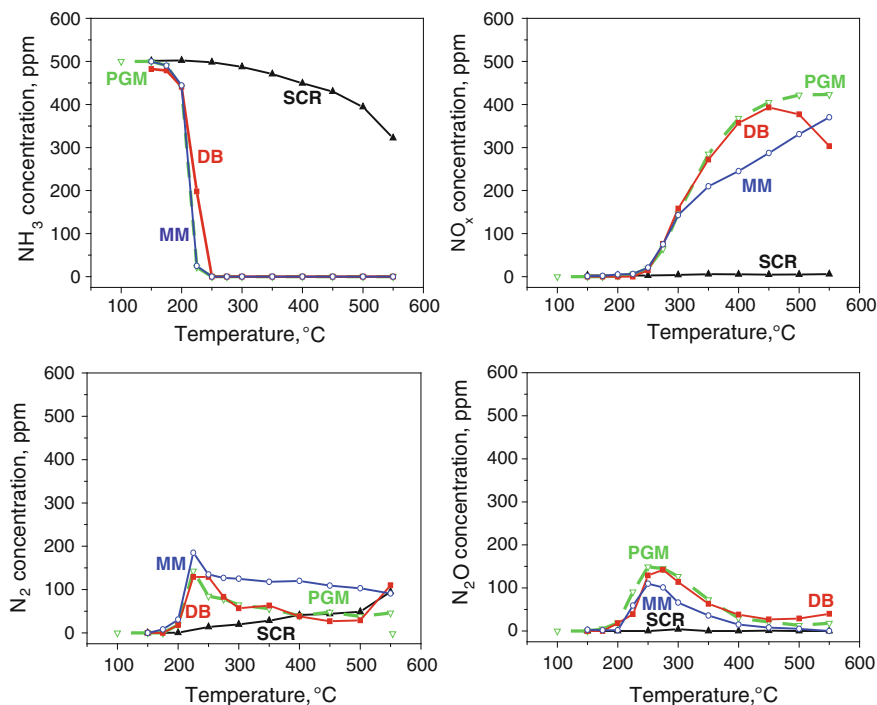


Fig. 18.9 NH_3 oxidation, comparison of different reactor configurations: $\text{NH}_3 = 500$ ppm; $\text{H}_2\text{O} = 8\%$ v/v; $\text{O}_2 = 8\%$ v/v; carrier gas = He [18]

In Fig. 18.9 it is clearly apparent that the composition and configuration of the catalyst bed dramatically affects both the activity and the products selectivity of ammonia oxidation. The SCR catalyst shows the weakest oxidation performance by far, resulting in incomplete ammonia oxidation with almost total selectivity to N_2 at all temperatures, as well established in the literature for Fe-zeolite SCR catalysts [3, 16, 17, 38]. By contrast, the PGM catalyst exhibits the highest activity, with NH_3 conversion above 90 % already at 200 °C. However, the same catalyst is also the one associated with the highest yield of NO_x in the high T-range.

When the SCR catalyst is followed by the PGM one (“Double Bed,” DB, configuration), the overall activity appears strengthened due to the presence of the PGM catalyst: NH_3 conversion and product yields are indeed almost overlapped with those of the PGM-only catalyst below 300 °C, with some deviations only in terms of N_2 concentration. However, on moving to higher temperatures the contribution of the upstream SCR layer starts to become significant, as pointed out by the increase of N_2 concentration above 500 °C and the corresponding decrease of the NO_x yield. This trend is related to the partial selective conversion of NH_3 to N_2 in the upstream SCR catalyst bed. As a result, a smaller amount of unreacted ammonia is available for the oxidation to NO occurring in the following PGM bed.

The best compromise between activity and selectivity is obtained with the PGM/SCR mechanical mixture: complete NH_3 conversion was indeed obtained already at 275 °C, with N_2 concentration above 100ppm over the whole 150–550 °C T -range. Correspondingly, lower NO_x and N_2O yields compared with the PGM-only catalyst and the double bed configuration were measured between 300 and 500 °C.

The direct comparison between the two combined systems (Double Bed versus Mechanical Mixture) clearly shows that the mechanical mixture of SCR and PGM powders entails the occurrence of interactions between the activities of the two catalysts, as the SCR reaction products can react over the PGM catalyst and vice versa. Such an interaction is not possible in the Double Bed configuration, wherein the two catalysts are segregated. A similar picture was observed by Long et al. [39] who studied a noble metal-promoted Fe-ZSM-5 for Selective Catalytic Oxidation of NH_3 . Long et al. [39] attributed the reduced N_2O and NO_x production to the SCR features of the combined catalyst: N_2O and NO generated by oxidation over the noble metal can be indeed further reduced to N_2 by unreacted ammonia, thus improving simultaneously ammonia conversion and N_2 selectivity.

$\text{NH}_3\text{-NO}_x\text{-O}_2$ —The combined SCR/PGM systems were comparatively analyzed in terms of steady-state activity and product yields in the case of a feed mixture consisting of 750 ppm of NH_3 , 250 ppm of NO_x , 8 % v/v O_2 , 8 % v/v H_2O and balance helium.

It was found that for all NO_2/NO_x feed ratios no significant differences between “Double Bed” and “Mechanical Mixture” configurations were apparent in terms of NH_3 conversion. By contrast, the different arrangement of the two catalysts played a role in determining the product yields.

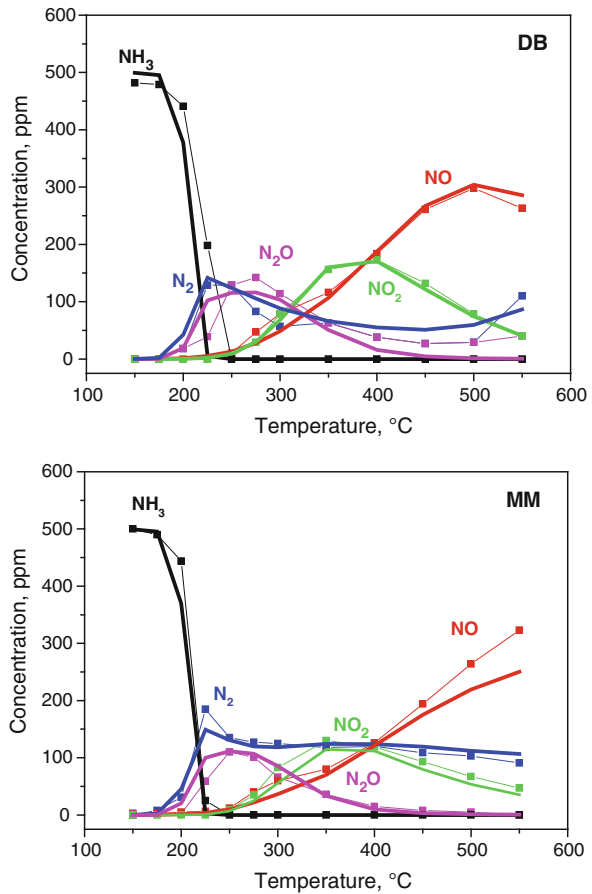
In terms of N_2 formation the picture was more complicated and varied depending on the NO_2/NO_x feed ratio. For $\text{NO}_2/\text{NO}_x = 0$ a greater N_2 concentration was recorded over the Mechanical Mixture below 350 °C, while at higher temperatures the Double Bed configuration prevailed. A constantly higher N_2 yield over the same catalytic system was also recorded in the case of $\text{NO}_2/\text{NO}_x = 1$, while for a feed mixture characterized by $\text{NO}_2/\text{NO}_x = 0.5$ a better N_2 yield was observed only above 350 °C.

The N_2O production resulted to be a function of the NO_2/NO_x ratio, too. When NO was the only source of NO_x the mechanical mixture exhibited a lower N_2O formation in the whole 150–550 °C T -range in comparison with the Double Bed configuration. The latter system however showed lower N_2O yields when NO_2 was also present in the feed stream.

18.5.2 Predictive Simulations of the SCR/PGM Combined Systems

Experimental data collected over both Double Bed and Mechanical Mixture configurations were systematically compared with predictive model simulations, as shown for example by thick lines in Fig. 18.10 for the ammonia oxidations

Fig. 18.10 NH_3 oxidation on Double Bed and Mechanical Mixture (SCR + PGM): $\text{NH}_3 = 500$ ppm; $\text{H}_2\text{O} = 8\%$ v/v; $\text{O}_2 = 8\%$ v/v; carrier gas = He. Symbols: experimental results; lines: model simulations [18]



tests. The simulations were generated simply assuming superposition of the SCR and PGM kinetics independently determined over the two-powdered catalyst components of the ASC system.

A good match between experimental data (symbols) and simulations (thick lines) is evident in terms both of ammonia conversion and of NO_x yield, while some deviations are present between 275 and 500 °C in terms of N_2 and N_2O concentration. Similar results were obtained analyzing the effect of NO_2/NO_x , emphasizing that the overall performance of combined SCR + PGM systems results from a simple superposition of the respective catalytic chemistries, which however provides different overall behaviors depending on the relative spatial distribution of the two catalyst components.

18.6 Modeling of Dual-Layer Monolith ASC

18.6.1 Development of a Dual-Layer Monolith Model

In principle, a rigorous approach to modeling of dual-layer monolith reactors requires modeling of coupled reaction and diffusion phenomena in both catalytic layers. However, this approach is computationally demanding: a simplified and faster model was thus developed in Colombo et al. [20].

We first assessed the impact of internal diffusion limitations in the PGM layer. For this purpose a simulation study was performed progressively increasing the PGM washcoat thickness, from 10 μm up to 71 μm . From the analysis of NH_3 concentration profiles a dramatic impact of diffusional limitations was apparent: indeed only the surface of this layer is effectively active due to the extremely high reactions rates of the PGM catalyst. For this reason, we developed a Layer + Surface Model (LSM) of dual-layer ASC where we treat the PGM layer as a surface, while we retain the rigorous description of coupled reaction/diffusion in the SCR layer, based on the previous 1D + 1D model of SCR monolithic converters [12, 25, 26]. Indeed, avoiding the description of diffusion phenomena in the PGM layer enables the direct inclusion of the PGM reactivity in the SCR converter model by simply modifying the inner boundary conditions of the species differential mass balances in the SCR layer, i.e., those now at the interface with the PGM phase. Treating the PGM layer as a surface thus enabled a simple extension of the 1D + 1D SCR converter model to simulate dual-layer catalytic systems too.

With the developed model we then studied the effect of PGM layer addition beneath the SCR one, in order to verify the need for the description of coupled reaction/diffusion phenomena in the SCR layer. For SCR-only systems this is something still under debate in the literature: most of the available models of SCR converters avoid indeed the description of intralayer C-profiles. Such 1D models provide however good simulation results, due to the fact that intralayer SCR concentration gradients are often not significant. On the opposite, in the case of dual-layer ASC systems the addition of the PGM phase beneath the SCR one leads to the onset of quite significant concentration gradients across the SCR layer, as shown, e.g., by the simulation results in Fig. 18.11. The figure shows the spatial and temporal evolution of the SCR intralayer NO concentration field in a simulated test in which first at 150 °C, 300 ppm of NO, 5 % v/v O_2 , and 5 % v/v H_2O were fed to the reactor; then, NH_3 was added and steady-state conditions approached; finally, the temperature was raised up to 500 °C. The NO concentration is plotted against the monolith axial and radial coordinates, where the zero value of the axial coordinate indicates the gas inlet, while the zero value of the radial coordinate indicates either the SCR/wall or SCR/PGM interface; negative values of the radial coordinate indicate a position inside the SCR washcoat layer.

The spatial distribution of NO is shown for three different temperatures, namely 150, 250, and 500 °C, for both the SCR-only and the dual-layer configuration. For the case of the SCR-only system, a significant NO conversion can be noticed only

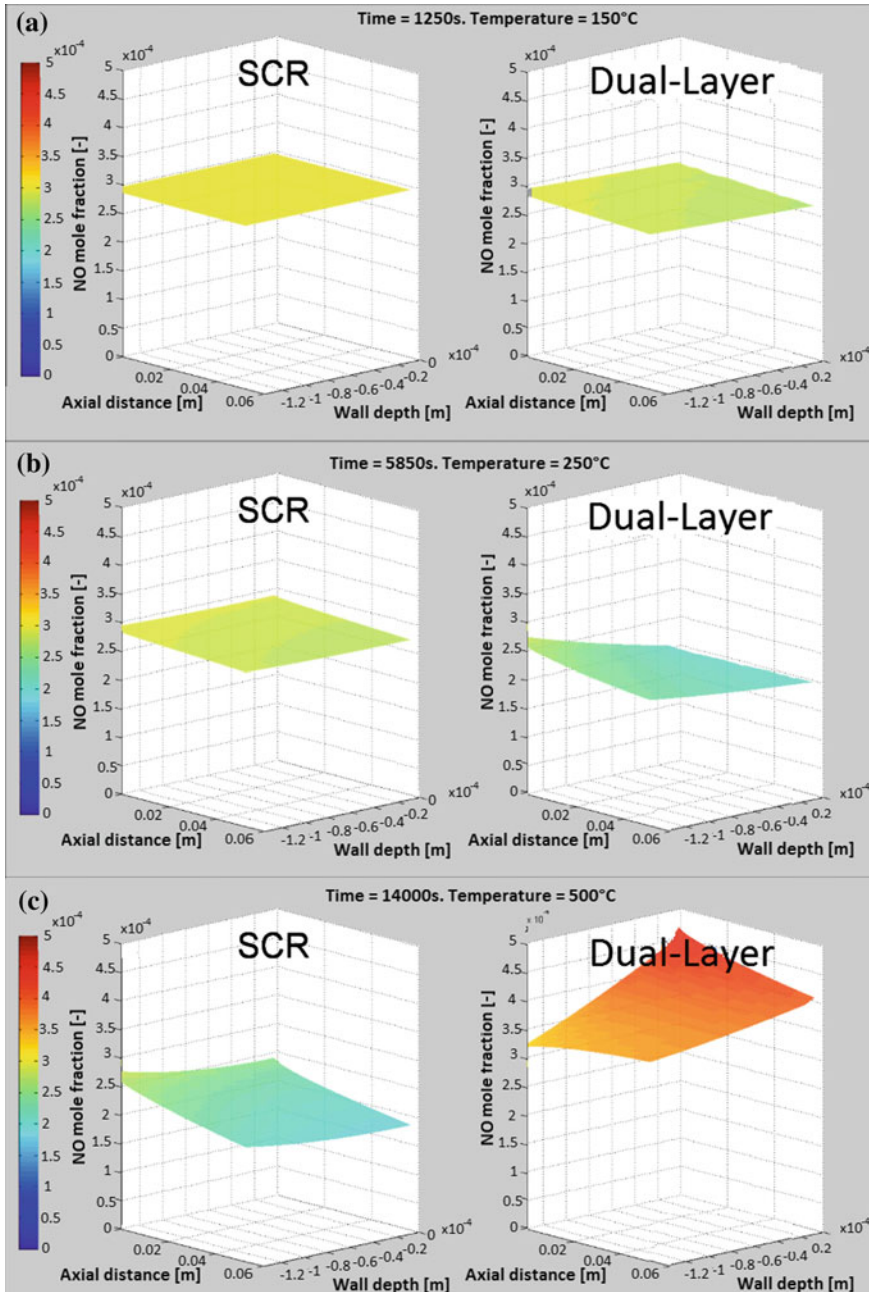


Fig. 18.11 Comparison of intra-layer NO concentration profile in SCR-only and in dual-layer configurations. Simulated conditions: $\text{NH}_3 = \text{NO} = 300 \text{ ppm}$, $\text{O}_2 = 5 \text{ \% v/v}$, $\text{H}_2\text{O} = 5 \text{ \% v/v}$, $\text{GHSV} = 300000 \text{ h}^{-1}$, $T = 150 \text{ }^\circ\text{C}$ a, $250 \text{ }^\circ\text{C}$ b, $500 \text{ }^\circ\text{C}$, c [20]

at 500 °C, but still associated with modest radial concentration gradients. Remarkably, the situation changed dramatically when also the PGM layer was present. As soon as the temperature was increased, NO started being significantly converted and a steep radial concentration profile became evident at 250 °C. However, on further increasing the catalyst temperature the situation changed, being NO a product of NH₃ oxidation over the PGM layer. The analysis of Fig. 18.11 shows in fact that at 500 °C the NO concentration gradient across the SCR layer was reversed with respect to a lower temperature (e.g., 250 °C): the NO concentration was indeed maximum at the SCR/PGM interface, where NO was produced by NH₃ oxidation, and then decreased across the SCR layer toward the SCR/gas interface, since NO diffuses back in the SCR layer and is converted over the SCR catalyst by the Standard SCR reaction with NH₃. Furthermore, the same layer acts as a diffusive barrier for PGM reactants and products. These observations emphasize the need of the rigorous description of coupled reaction/diffusion phenomena within the SCR layer of dual-layer ammonia slip catalysts.

18.6.2 Validation of the Dual-Layer Monolith ASC Model

After independently validating the SCR and the PGM kinetics, the same rate expressions and rate parameters were incorporated into the full Dual-Layer NH₃ slip monolith converter model specifically developed according to the Layer + Surface (LSM) approach. Furthermore, all the relevant geometrical and morphological properties of the monolith sample were also included in the same model, which was then validated against experimental data collected over the Dual-Layer core monolith sample. Figure 18.12 presents a direct comparison between experimental data (dots) and predictive model simulations (solid lines) for all the analyzed reacting systems. The simulation results were obtained after a modest adjustment of five PGM rate parameters, mainly the ones accounting for the inhibition effect of NO₂ on the NH₃ and NO oxidation reactions. A generally good agreement was observed both in terms of NH₃ conversion and products yields, with the most evident deviations recorded in the cases of NO₂/NO_x of 0.5 and 1. In the first case, a good agreement between experimental data and predictive simulation was evident at temperatures as high as 300 °C, while further increasing the catalyst temperature resulted in the underestimation of the N₂ yield and a corresponding overestimation of the NO_x yield. In the case of NO₂/NO_x = 1, the model predicted again a lower N₂ yield in comparison with experiments. A corresponding overestimation of the NO_x and N₂O yields was observed in this case.

The model was then validated against DOE data covering an extensive range of operating conditions, in terms of T, space velocities and ammonia to NO_x feed ratio.

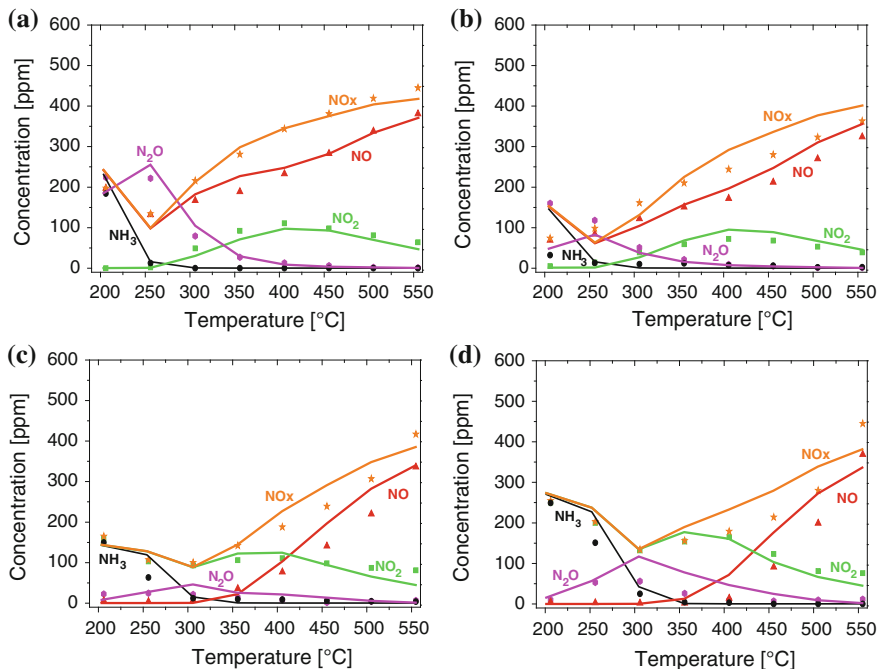


Fig. 18.12 NH_3/NO_x reacting system on ASC dual-layer monolith: $\text{NH}_3 = 500$ ppm; $\text{NO}_x = 500$ ppm; $\text{H}_2\text{O} = 8\%$ v/v; $\text{O}_2 = 8\%$ v/v; $\text{CO}_2 = 8\%$ v/v, $\text{GHSV} = 100,000 \text{ h}^{-1}$ (N_2 amount calculated from N-balance). **a** $\text{NO}_2/\text{NO}_x = 0.25$; **b** $\text{NO}_2/\text{NO}_x = 0.5$; **c** $\text{NO}_2/\text{NO}_x = 0.75$; **d** $\text{NO}_2/\text{NO}_x = 1$. Symbols experimental results; lines model simulations [19]

Figure 18.13 shows the comparison of measured versus simulated data throughout the full DOE range for NH_3 , NO , NO_2 , and N_2O . NH_3 shows the best agreement between simulation and measurement; while for NO and NO_2 one data point presented a high deviation. This data point corresponds to a space velocity of $15,000 \text{ h}^{-1}$, a temperature of $450 \text{ }^\circ\text{C}$, and an NO_2/NO_x ratio of 0% . Taking the comparison of simulated data versus measured data into account (e.g., $\text{SV} = 275,000 \text{ h}^{-1}$, $T = 350 \text{ }^\circ\text{C}$, $\text{NO}_2/\text{NO}_x = 0\%$ or $\text{SV} = 150,000 \text{ h}^{-1}$, $T = 500 \text{ }^\circ\text{C}$, $\text{NO}_2/\text{NO}_x = 0\%$) the measured data seem not to be in line with the received measured data under similar operating conditions. Hence, the measurement of this operation point is regarded as an outlier.

The highest deviations between measurement and simulation over the full data range are observed for N_2O . However, a systematic trend of over or underestimation of N_2O by the model cannot be detected.

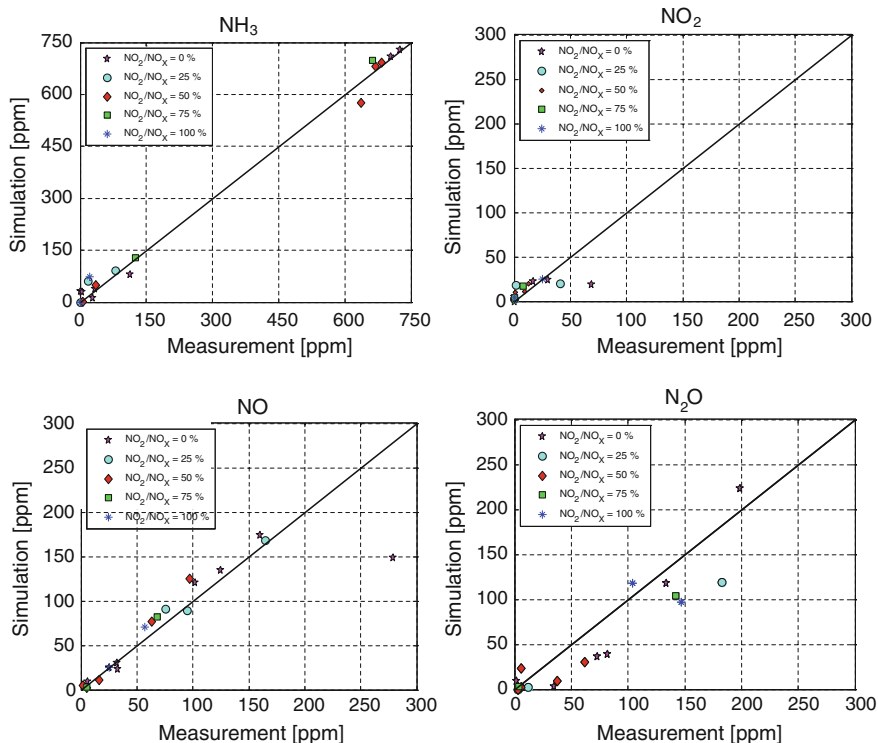


Fig. 18.13 DOE experiments on ASC dual-layer monolith: NH_3 , NO , NO_2 , N_2O measured versus simulated concentrations [19]

18.7 Conclusions

In this chapter a dual-layer washcoated (PGM + SCR) ASC catalyst has been systematically investigated and modeled. First, the individual single washcoat functionalities have been analyzed experimentally, with the catalysts in the powder form. Further, mechanical mixtures of the same powdered washcoats have been investigated in order to assess possible synergistic effects of the dual layer configuration. Kinetic models for the single washcoats have been developed considering all relevant reactions and effects, and fitted to the experimental data to estimate the related kinetic parameters. A first model validation was carried out comparing predictive simulations with data collected over monolith samples coated with the single catalytic phases. Finally, data measured over the real dual layer ASC configuration have been used for successful validation of the dual layer model developed in this work.

This work has clearly pointed out that the dual layer architecture exhibits an increased N_2 selectivity compared to a PGM-only washcoat. The investigated ASC configuration with both washcoats combines in fact the high NH_3 conversion

activity of the PGM layer with the NO_x reduction functionality and high N₂ selectivity of the SCR layer. With such an ASC brick placed behind an NH₃-SCR system, minimal NH₃ breakthrough at increased NO_x conversion of the after-treatment system is possible. Modeling of these catalysts not only helps in understanding such synergetic effects but is required for an efficient development of modern exhaust aftertreatment systems and of their operation strategies.

References

1. Johnson TV (2011) Diesel Emissions in Review. SAE Technical Paper 2011-01-0304
2. Scheuer A, Hauptmann W, Drochner A, Gieshoff J, Vogel H, Votsmeier M (2012) Dual layer automotive ammonia oxidation catalysts: Experiments and computer simulation. *Appl Catal, B* 111–112:445–455
3. Scheuer A, Votsmeier M, Schuler A, Gieshoff J, Drochner A, Vogel H (2009) NH₃-Slip Catalysts: Experiments Versus Mechanistic Modelling. *Top Catal* 52 (13):1847–1851
4. Scheuer A, Votsmeier M, Gieshoff J, Drochner A, Vogel H Design of Dual-Layer Catalysts for NH₃ Oxidation in Automotive Exhaust. In: 6th International Conference on Environmental Catalysis, Beijing, China, 2010.
5. Kamasamudram K, Yezerets A, Chen X, Currier NW, Castagnola M, Chen H-Y (2011). SAE Technical Paper 2011-01-1314
6. Colombo M, Nova I, Tronconi E, Schmeißer V, Bandl-Konrad B, Zimmermann L (2011) NO/NO₂/N₂O–NH₃ SCR reactions over a commercial Fe-zeolite catalyst for diesel exhaust aftertreatment: Intrinsic kinetics and monolith converter modelling. *Appl Catal, B* 111–112:106–118
7. Iwasaki M, Yamazaki K, Shinjoh H (2009) Transient reaction analysis and steady-state kinetic study of selective catalytic reduction of NO and NO + NO₂ by NH₃ over Fe/ZSM-5. *Appl Catal, A* 366 (1):84–92
8. Markatou P, Dai J, Johansson A, Klink W, Castagnola M, Watling TC, Tutuianu M Fe-Zeolite SCR Model Development, Validation and Application. SAE Technical Paper 2011-01-1304
9. Olsson L, Sjövall H, Blint RJ (2009) Detailed kinetic modeling of NO_x adsorption and NO oxidation over Cu-ZSM-5. *Appl Catal, B* 87 (3–4):200–210
10. Schuler A, Votsmeier M, Kiwic P, Gieshoff J, Hauptmann W, Drochner A, Vogel H (2009) NH₃-SCR on Fe zeolite catalysts—From model setup to NH₃ dosing. *Chem Eng J* 154 (1–3):333–340
11. Sjövall H, Blint RJ, Gopinath A, Olsson L (2010) A Kinetic Model for the Selective Catalytic Reduction of NO_x with NH₃ over an Fe-zeolite Catalyst. *Ind Eng Chem Res* 49 (1):39–52
12. Chatterjee D, Burkhardt T, Weibel M, Nova I, Grossale A, Tronconi E (2007) Numerical simulation of zeolite and V-based SCR catalytic converters. SAE Technical Paper 2007-01-1136
13. Scheuer A, Drochner A, Gieshoff J, Vogel H, Votsmeier M (2012) Runtime efficient simulation of monolith catalysts with a dual-layer washcoat. *Catal Today* 188 (1):70–79
14. Scheuer A, Hirsch O, Hayes R, Vogel H, Votsmeier M (2011) Efficient simulation of an ammonia oxidation reactor using a solution mapping approach. *Catal Today* 175 (1):141–146
15. Votsmeier M, Scheuer A, Drochner A, Vogel H, Gieshoff J (2010) Simulation of automotive NH₃ oxidation catalysts based on pre-computed rate data from mechanistic surface kinetics. *Catal Today* 151 (3–4):271–277
16. Kraehnert R, Baerns M (2008) Kinetics of ammonia oxidation over Pt foil studied in a micro-structured quartz-reactor. *Chem Eng J* 137 (2):361–375

17. Rebrov EV, de Croon MHJM, Schouten JC (2002) Development of the kinetic model of platinum catalyzed ammonia oxidation in a microreactor. *Chem Eng J* 90 (1–2):61–76
18. Colombo M, Nova I, Tronconi E, Schmeißer V, Bandl-Konrad B Experimental and modeling study of a dual-layer (SCR + PGM) NH₃ slip monolith catalyst (ASC) for automotive SCR aftertreatment systems. Part 1. Kinetics for the PGM component and analysis of SCR/PGM interactions *Appl Catal, B*. 142–143 (2013) 861–876
19. Colombo M, Nova I, Tronconi E, Schmeißer V, Bandl-Konrad B, Zimmermann LR (2013) Experimental and modeling study of a dual-layer (SCR + PGM) NH₃ slip monolith catalyst (ASC) for automotive SCR after treatment systems. Part 2. Validation of PGM kinetics and modeling of the dual-layer ASC monolith. *Appl Catal, B* 142–143 (0):337–343
20. Colombo M, Nova I, Tronconi E (2012) A simplified approach to modeling of dual-layer ammonia slip catalysts. *Chem Eng Sci* 75 (0):75–83
21. Ciardelli C, Nova I, Tronconi E, Ascherfeld M, Fabinski W (2007) Combined use of a mass-spectrometer and a UV analyzer in the dynamic study of NH₃-SCR for diesel exhaust aftertreatment. *Top Catal* 42–43 (1–4):161–164
22. Ciardelli C, Nova I, Tronconi E, Konrad B, Chatterjee D, Ecke K, Weibel M (2004) SCR-DeNO(x) for diesel engine exhaust aftertreatment: unsteady-state kinetic study and monolith reactor modelling. *Chem Eng Sci* 59 (22–23):5301–5309
23. Buzzi-Ferraris G, Donati G. *Chemical Engineering Science* 29 (1974):154–158
24. Villa P, Forzatti P, Buzzi-Ferraris G, Garone G, Pasquon I (1985) Synthesis of alcohols from carbon oxides and hydrogen. 1. Kinetics of the low-pressure methanol synthesis. *Ind Eng Chem Process Des Dev* 24 (1):12–19
25. Chatterjee D, Burkhardt T, Bandl-Konrad B, Braun T, Tronconi E, Nova I, Ciardelli C (2005) Numerical simulation of ammonia SCR catalytic converters: model development and application. SAE Technical Paper 2005-01-0965
26. Chatterjee D, Burkhardt T, Weibel M, Tronconi E, Nova I, Ciardelli C (2006) Numerical simulation of NO/NO₂/NH₃ reactions on SCR catalytic converters: Model development and applications. SAE Technical Paper 2006-01-0468
27. Kamasamudram K, Currier NW, Chen X, Yezerets A (2010) Overview of the practically important behaviors of zeolite-based urea-SCR catalysts, using compact experimental protocol. *Catal Today* 151 (3–4):212–222
28. Nova I, Colombo M, Tronconi E, Schmeisser V, Weibel M (2011) The NH₃ Inhibition Effect in the Standard SCR Reaction over a Commercial Fe-zeolite Catalyst for Diesel Exhaust Aftertreatment: An Experimental and Modeling Study. *SAE International Journal of Engines* 4 (1):1822–1838
29. Wallin M, Karlsson C-J, Skoglundh M, Palmqvist A (2003) Selective catalytic reduction of NO_x with NH₃ over zeolite H-ZSM-5: influence of transient ammonia supply. *J Catal* 218 (2):354–364
30. Nova I, Ciardelli C, Tronconi E, Chatterjee D, Bandl-Konrad B (2006) NH₃-SCR of NO over a V-based catalyst: Low-T redox kinetics with NH₃ inhibition. *AIChE J* 52 (9):3222–3233
31. Sobalik Z, Jisa K, Jirglova H, Bemauer B (2007) Simultaneous FTIR/UV-Vis study of reactions over metallo-zeolites Approach to quantitative in situ studies. *Catal Today* 126 (1–2):73–80
32. Colombo M, Nova I, Tronconi E (2010) A comparative study of the NH₃-SCR reactions over a Cu-zeolite and a Fe-zeolite catalyst. *Catal Today* 151 (3–4):223–230
33. Ciardelli C, Nova I, Tronconi E, Chatterjee D, Bandl-Konrad B, Weibel M, Krutzsch B (2007) Reactivity of NO/NO₂-NH₃ SCR system for diesel exhaust aftertreatment: Identification of the reaction network as a function of temperature and NO₂ feed content. *Appl Catal, B* 70 (1–4):80–90
34. Kaucký D, Sobalík Z, Schwarze M, Vondrová A, Wichterlová B (2006) Effect of FeH-zeolite structure and Al-Lewis sites on N₂O decomposition and NO/NO₂-assisted reaction. *J Catal* 238 (2):293–300

35. Pérez-Ramírez J, Kapteijn F, Mul G, Moulijn JA (2002) NO-Assisted N₂O Decomposition over Fe-Based Catalysts: Effects of Gas-Phase Composition and Catalyst Constitution. *J Catal* 208 (1):211–223
36. Tronconi E, Nova I, Ciardelli C, Chatterjee D, Bandl-Konrad B, Burkhardt T (2005) Modelling of an SCR catalytic converter for diesel exhaust after treatment: Dynamic effects at low temperature. *Catal Today* 105 (3–4):529–536
37. Bhatia D, McCabe RW, Harold MP, Balakotaiah V (2009) Experimental and kinetic study of NO oxidation on model Pt catalysts. *J Catal* 266 (1):106–119
38. Li Y, Armor JN (1997) Selective NH₃ oxidation to N₂ in a wet stream. *Appl Catal, B* 13 (2):131–139
39. Long RQ, Yang RT (2002) Noble Metal (Pt, Rh, Pd) Promoted Fe-ZSM-5 for Selective Catalytic Oxidation of Ammonia to N₂ at Low Temperatures. *Catal Lett* 78 (1):353–357

Chapter 19

NSR–SCR Combined Systems: Production and Use of Ammonia

Fabien Can, Xavier Courtois and Daniel Duprez

19.1 Introduction

Beside the NH_3 /urea SCR process, the NO_x reduction from lean burn exhaust gas can be achieved using the cycled NO_x -Storage Reduction or NSR system (also called Lean NO_x -trap (LNT) system). In Europe, the NH_3 –SCR technology could be quickly implemented on heavier cars, as it is already the case for trucks, while the NSR system is rather envisaged to be implemented in light passenger car.

However, ammonia may be produced during the regeneration step of NSR catalyst, by the direct reaction ($\text{NO}_x + \text{H}_2$) or/and the isocyanate route. Ammonia emission is proscribed but this undesirable product is also a very efficient NO_x reductant, available in the exhaust gas. Then, logically, the addition of a NH_3 –SCR catalyst to the NSR catalyst was proposed in order to increase the global NO_x abatement and the N_2 selectivity. Ammonia is produced during the brief regeneration period of the NSR catalyst, and it has to be firstly stored on the SCR catalytic bed. During the next lean period, this stored NH_3 can react with NO_x passing through the NO_x -trap, via the NH_3 –SCR reaction.

Then, the addition of a NH_3 –SCR material to the NSR catalyst is a possible way to increase the global NO_x abatement and maximize the N_2 selectivity, together with the prevention of the ammonia slip. A schematic view of the process is presented in Fig. 19.1.

This work reports firstly recent results about the production of ammonia during the NSR process, and then an overview of the recent advances in NO_x abatement in excess of oxygen using the NO_x storage-reduction (NSR)—Selective Catalytic Reduction (SCR) combined systems. With this aim, zeolites are the main studied SCR materials. In addition, studies about the NH_3 storage and the mechanism in NO_x reduction over zeolite are presented.

F. Can (✉) · X. Courtois · D. Duprez
UMR 7285, IC2MP, Université de Poitiers, CNRS, 4 rue Michel Brunet,
86022 Poitiers Cedex, France
e-mail: fabien.can@univ-poitiers.fr

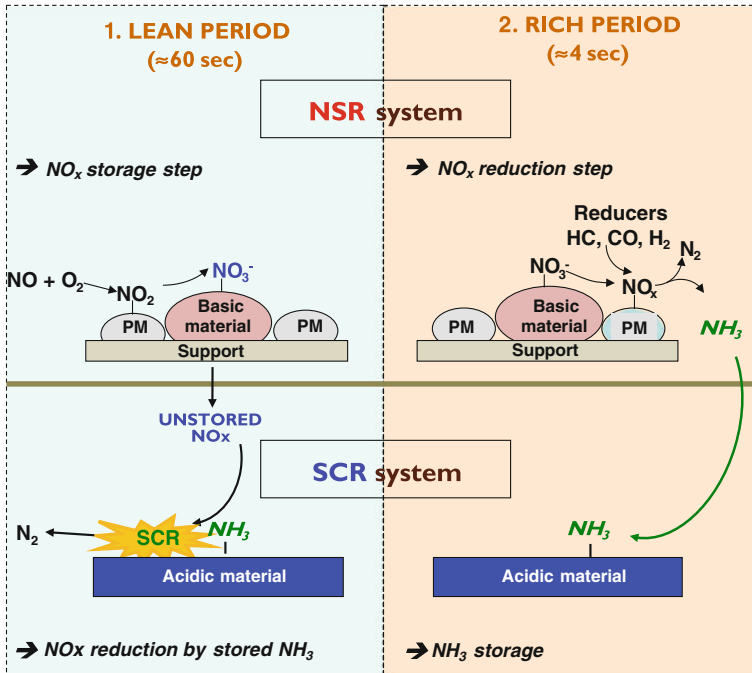


Fig. 19.1 Schematic view of the NSR + SCR combined process

19.2 NH_3 Emission from NSR Catalysts

19.2.1 The NSR Process

The NO_x storage-reduction (NSR) process is largely studied since the beginning of the 1990s [1–5]. Model NO_x -trap catalysts usually contain a noble metal (Pt) allowing the NO oxidation into NO_2 , and a basic phase (Ba oxide/carbonate) in order to trap NO_2 as nitrite/nitrate intermediates. Both precious metals and storage phase are usually supported on a modified alumina support [6]. Other frequent components are rhodium which is known to favor the NO_x reduction into N_2 in stoichiometric/rich media, and cerium-based oxides due to their redox behavior, the NO_x storage capacity and the sulfur resistance [7, 8]. Among other possible basic storage phases, potassium is the more frequently proposed [9, 10].

The NSR catalyst operates in fast lean/rich transients. During the lean steps of approximately 1 min, the gas phase is constituted by the standard exhaust gas from the lean burn engine. NO is then oxidized into NO_2 over the precious metals and further trapped as nitrite/nitrate on the basic components of the catalyst. The “saturated” trap is then regenerated during short incursions in rich media for few seconds in order to reduce the stored NO_x into N_2 . In fact, the rich phases are

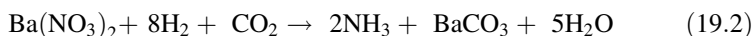
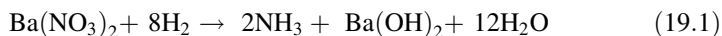
generated by injecting pulses of fuel, immediately transformed into HC, CO and H₂ on a pre-catalyst (usually a Diesel Oxidation Catalyst implemented before the NSR system). These rich pulses induce exothermic reactions which favor the nitrate desorption and reduction into nitrogen. These steps correspond to the ideal operating mode of the NSR system.

The nature of the reductants in the rich mixture directly impacts the NO_x conversion and the selectivity of the NSR reaction. On usual NSR model catalysts, namely Pt/(BaO)/Al₂O₃, hydrogen is reported to be the more efficient agent compared with CO or propene [11–13]. This higher efficiency of H₂ was evidenced by Szailer et al. [11] at very low temperature (150), and in the 150–350 °C temperature range by Nova et al. [12]. Nevertheless, undesirable by-products can also be emitted during the regeneration, such as N₂O and ammonia. As an introduction to the NSR + SCR combined system, the following section focuses on the ammonia formation and emission over NSR catalysts.

19.2.2 Ammonia Formation Pathways

Ammonia is reported to be produced only during the rich phases of the NSR process, even in the presence of usual reductant(s) such as H₂, CO or propene during the lean phases [14, 15]. However, note that significant ammonia emission can be observed during the NO_x reduction in lean condition using ethanol as reductant [16].

During the regeneration of the NO_x trap, two major routes are commonly admitted for the ammonia formation. The first one is the direct reaction of stored NO_x with hydrogen, as described in reaction (19.1) [13, 17]. This route was proposed over Pt–Ba/Al₂O₃ material, when H₂ is used as the reductant [18]. Artioli et al. [19] observed that, depending on the gas feed composition, ammonia is emitted together with CO₂ consumption, as reported in reaction (19.2).



The catalyst temperature is an important parameter which impacts both the NO_x adsorption/desorption equilibrium and reduction rate. Ideally, the NO_x reduction rate has to be higher than the NO_x desorption rate in order to limit the NO_x slip during the rich pulses. During these reduction phases, a part of the introduced reductants also reacts with remaining oxygen from the gas phase or stored on the catalyst. As a consequence, an exothermic phenomenon is generally detected during the rich pulses, which lead to additional releases of unreduced NO_x. In fact, it was showed that when the regeneration of the catalyst is carried out in the presence of NO in the feed stream, ammonia can be directly formed according to reaction (19.3) in the reactor zone where the trap is already regenerated [20].

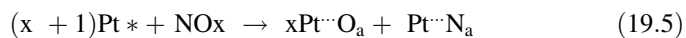


However, it is shown in this work that ammonia is observed after N_2 formation, when hydrogen begins to be emitted. This point is more detailed in [Sect. 19.2.3](#).

The direct ammonia formation mechanism (reactions [19.1](#) and [19.3](#)), when only H_2 is used as reductant, was studied in Ref. [[11](#)]. Authors proposed that hydrogen reacts firstly with the platinum surface on which oxygen species (O_a), resulting from the reduction of NO_2 , remain adsorbed (reaction [19.4](#)).



The produced H_2O is supposed to destabilize the adsorbed nitrates which are suggested to be decomposed on the free Pt surface. The dissociation of NOx species on platinum can thereafter leads to the recombination of N_a atoms to form N_2 (reactions [19.5](#) and [19.6](#)), or to the reaction of these N_a atoms with H_2 to form NH_x and, finally, NH_3 .



In this step way, the initial role of H_2 is the reduction of the platinum surface to allow the NOx dissociative adsorption [[21](#)].

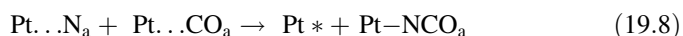
Clayton et al. [[22](#)] also suggested that the ammonia formation mechanism includes the activation of H_2 on Pt sites. They proposed that adsorbed nitrates are decomposed into NOx and released in the gas phase, due to hydrogen spill-over from the noble metal to the alumina support. NOx species are readily reduced to ammonia due to high local H/N ratio.

The second way to obtain ammonia during the NSR regeneration is the “isocyanate route” [[23](#)]. This intermediate reaction is observed when a carbon source is present in the reaction mixture, especially CO [[11](#)]. However, CO can also be produced in situ, for instance by the reverse water gas shift (RWGS) reaction between H_2 and CO_2 , the later being always present in large amounts in a real exhaust gas (see also the influence of the WGS equilibrium [Sect. 19.2.3](#)).

At low temperature ($T < 150 \text{ }^\circ\text{C}$), the first reaction is still the removal of adsorbed oxygen atoms from the Pt particles ($\text{Pt}\cdots\text{O}_a$), leading to CO_2 production (reaction [19.7](#)).



The obtained free Pt sites become available for the NOx dissociative adsorption and the CO adsorption. Then, formation of adsorbed NCO species is possible according to reaction [19.8](#).

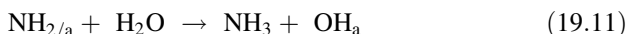
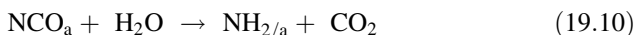


–NCO species generated on the Pt particles migrate to the oxide components of the catalyst, usually alumina. Therefore, –NCO and CO₂ formation occur at the expense of the reduction of the adsorbed NO_x, while N₂ is not produced.

At higher temperatures ($T > 300$ °C) these –NCO species are able to react with the stored NO_x. This reaction route eventually leads to the consumption of both nitrate and NCO adsorbed species according reaction 19.9.



In real exhaust gas, water is present with a large extent and it is reported that N₂ formation is significantly enhanced by adding water to the NCO-covered catalysts [10]. Adding water leads to a new reaction route for the –NCO reactivity, i.e., the hydrolysis of –NCO species to NH₃ and CO₂ (reactions 19.10 and 19.11).



To conclude, ammonia can be formed only during the regeneration steps of the NO_x-trap, even if ammonia release can also occur during the subsequent lean phase. Two pathways are described: the direct reaction of H₂ with the stored NO_x or with NO_x present in the gas phase, and via the hydrolysis of isocyanates species. Hydrogen is reported as a more efficient reductant than CO, leading to a higher emission of ammonia [11, 12].

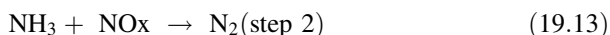
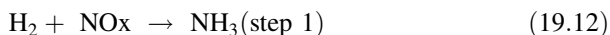
19.2.3 Influencing Parameters/Ammonia Reactivity

Numerous parameters were studied and reported as influencing the ammonia emissions from the NSR catalyst.

Dispersions of the catalyst components were reported to strongly modify the NH₃ emission, For instance, Castoldi et al. have observed that ammonia emission occurs during the NO_x-trap regeneration when barium loading ranges from 16 to 30 wt. % [18]. At lower barium loading (i.e., 5–16 wt. %), authors have reported that the reduction of stored NO_x is initially fully selective into nitrogen.

Bhatia et al. [24] have modeled the effect of the platinum dispersion of a model Pt/BaO/Al₂O₃ sample, also taking into account the influence of the temperature. This study indicates that at high temperature ($T \geq 300$ °C), highest amounts of NH₃ are produced over low dispersed catalyst (3.2 % platinum dispersion). On the contrary, it was observed that ammonia formation is enhanced at low temperature ($T \leq 200$ °C) with the highly dispersed catalyst (50 % dispersion) [24]. The effect of noble metal dispersion on ammonia production is explained by the variation of the average distance—or proximity—between the stored NO_x and the platinum sites. Proximity between storage sites and reaction sites is known to affect the stored NO_x transport process [25].

As presented in Sect. 19.2.2, two main routes are proposed to produce N_2 when H_2 is the reductant: (i) the direct route, from the reduction of stored NO_x by H_2 and (ii) the sequential route through NH_3 intermediate formation [22, 26], which can be simply described following reactions (19.12–19.13).



This two-step mechanism was evidenced in Refs. [27] and [34] over a model Pt–Ba/ Al_2O_3 catalyst. As a consequence, when the amount of introduced hydrogen is too low to reduce all the stored NO_x , incomplete regeneration of the catalyst is observed. Such an incomplete regeneration obviously results in a decrease of the storage capacity for the subsequent lean periods. Beside, the reaction of the stored NO_x with hydrogen results in the formation of negligible amounts of N_2O and NH_3 , nitrogen being the only product detected at the reactor exit. It induces that no ammonia is observed as long as hydrogen is fully consumed. It is especially true for temperature higher than 300 °C, as confirmed by different works [12, 28, 29].

In opposition, the NO_x reduction selectivity is strongly affected by ammonia emission since hydrogen is not fully converted during the pulses. In Table 19.1 are reported some results from the literature in which the hydrogen concentration measurement at the reactor outlet is available. Table 19.1 shows that, whatever the NO_x conversion rate, ammonia is released when hydrogen is not fully consumed during the regeneration step of the NO_x -trap catalyst.

An illustration of these observations is shown in Fig. 19.2. This figure reports the influence of the catalytic mass and the hydrogen concentration in the rich pulses at 400 °C. It allows following the evolution of the reactions along the catalytic bed. The increase of the catalytic weight clearly shows that the in situ produced ammonia during the NO_x reduction on the first part of the catalyst is able to react with the downstream stored NO_x to give N_2 since there is no more available hydrogen [28]. On the contrary, if hydrogen remains, all the catalytic bed works identically.

In agreement with Nova et al. [31], this Fig. 19.2 also strongly suggests that (i) nitrogen formation occurs via a two step pathway and (ii) the stored NO_x react preferentially with the introduced hydrogen to form NH_3 (step 1), whenever H_2 is present in the gas phase. NH_3 further reacts with stored NO_x downstream to form N_2 , preferentially in a hydrogen free environment (step 2) [28, 34]. The selectivity toward NH_3 formation is then governed by the relative rate constants of NH_3 formation and NH_3 consumption. In this dual-step mechanism, step 1 rate is higher than the step 2 one [17, 32], even though the characteristic reaction times for NH_3 formation and consumption are lower than the characteristic diffusion times of stored NO_x .

As previously mentioned, the presence of H_2O and CO_2 in the gas mixture directly impacts ammonia formation mechanism. According to reaction (19.14), the Water Gas Shift (WGS) and the reverse reaction (Reverse WGS, RWGS) can

Table 19.1 Examples of data from the literature about the correlation between the ammonia emission and the presence of unconverted hydrogen during storage/reduction cycled experiments

Ref.	Lietti et al. [32]	Pereda–Ayo et al. [27]	Castoldi et al. [18]	Bhatia et al. [24]	Kočí et al. [13]	Nova et al. [12]	Arioli et al. [19]	Choi et al. [30]
Catalyst	Pt–Ba/Al	Pt–Ba/Al monolith	Pt–Ba/Al	Pt–Ba/Al	Industrial	Pt–Ba/Al	Pt–Ba/Al	Industrial
T (°C)	100	260	350	370	250	200	350	200
H ₂ inlet	2000 ppm	0.85 %	2000 ppm	1500 ppm	3.3 %	2000 ppm	4000 ppm	3.4 %
H ₂ outlet	80 ppm	Traces	600–150 ppm	700 ppm	0.5 %	300 ppm	1000 ppm	1.4 %
NH ₃ outlet	400 ppm	300 ppm	150–400 ppm	330 ppm	2200 ppm	180 ppm	500 ppm	120 ppm

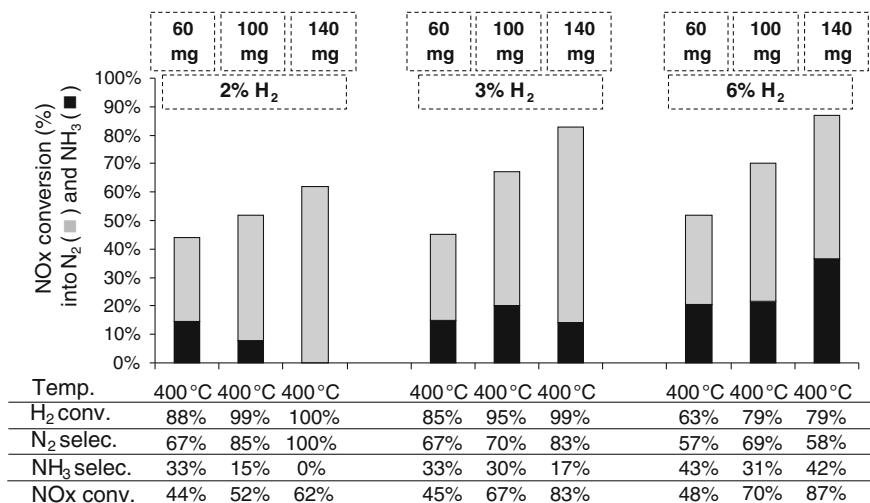


Fig. 19.2 Pt/Ba/Al₂O₃ catalyst: NOx conversion at 400 °C under cycling lean (60 s, 500 ppm NO, 10 % O₂, 10 % H₂O, 10 % CO₂)/rich (3 s, H₂, 10 % H₂O, 10 % CO₂) condition. NOx conversion (%) into N₂ (■) and into NH₃ (■) and related data. Influence of both the H₂ concentration in the rich pulses (1–6 %) and the catalyst mass (60, 100, and 140 mg), from [28]

also occur, leading to the presence of both CO and H₂ in gas phase, even if the initial reductant in the rich mixture is H₂ or CO alone.



It was demonstrated that the presence of water or carbon dioxide in the gas mixture has a negative effect on the storage step of the NSR process [33, 34]. However, their impacts on the reduction step using H₂ as reductant are significantly different. Due to the involvement of water in the (R)WGS reaction, the absence of few percents of H₂O in the gas mixture leads to a small decrease of the NOx removal efficiency because a larger part of the introduced hydrogen is transformed into CO, a less efficient reductant. In the same time, the ammonia selectivity increases due to the possible formation of isocyanate species. In opposition, the absence of CO₂ leads to an increase in NOx conversion [34], with a little ammonia formation. The isocyanate is then impossible since there is no carbon source in the gas mixture. However, ammonia emission can still be observed, indicating that the direct route occurs. Note that hydrocarbons (such as propene) are also possible reductants leading to isocyanates via oximes intermediates [35]. Isocyanates lead to amines (or amides) that are very good reductants of NOx [35, 36].

The nature of the basic storage phase also affects the ammonia formation. For instance, the comparison of usual Pt–Ba/Al₂O₃ catalyst with Pt–K/Al₂O₃ sample (with similar molar amount of basic element, i.e., Ba or K) evidences a higher N₂ selectivity during the reduction step with H₂ for the NOx stored over the K phase [17]. Authors report a similar reactivity for the H₂ + nitrate and NH₃ + nitrate

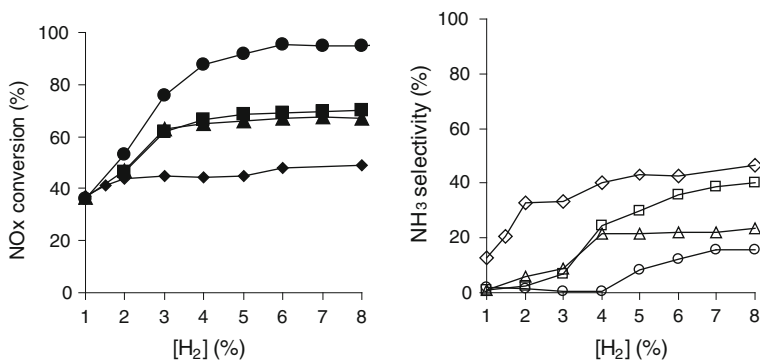


Fig. 19.3 NO_x conversion rate (*full symbols*) and NH₃ selectivity (*open symbols*) measured at 400 °C depending on hydrogen concentration in the rich pulses for Pt/20Ba/Al (◆, ◇), Pt/20BaMn/Al (■, □), Pt/20BaCe1/Al (▲, △) and Pt/20BaMnCe0.5/Al (●, ○) [29]

reactions. In fact, on Pt–K/Al₂O₃, the onset for the direct H₂ + nitrate reaction leading to ammonia (step 1, reaction 19.13) occurs at temperature very close to the threshold for the NH₃ + nitrate reaction (step 2, reaction 19.14), leading to the desired N₂ compound. Finally, this study shows again that the ammonia emission strongly depends on the balance between the ammonia production and the ammonia reaction with the stored NO_x.

The nature of the support, especially in terms of redox properties, obviously significantly impacts this equilibrium between formation and reactivity of NH₃ during the regeneration step of the NSR process. It is possible to increase the reaction rate between the in situ produced ammonia and the remaining stored NO_x. For instance, addition of manganese to a Pt/BaO/Al₂O₃ model material (Pt/Ba(Mn)/Al catalyst) allows an improvement of the NO_x reduction by ammonia, especially at 400 °C, even if the introduced hydrogen is not fully converted [28]. Same trends were obtained with addition of ceria, and more interestingly, further improvements were obtained with the simultaneous Mn and Ce addition to model Pt/BaO/Al₂O₃ catalyst [29]. A synergetic effect was highlighted between Mn and Ce with a significant decrease in ammonia emission in the 200–400 °C temperature range, correlated with a synergetic effect concerning the oxygen storage capacity. The influence of the Mn and Ce addition on the NO_x conversion rate and the NH₃ selectivity at 400 °C are presented in Fig. 19.3 depending on hydrogen concentration in the rich pulses. The increase of the NO_x conversion together with the decrease of the ammonia selectivity was partially attributed to an enhancement of the reactivity between the in situ produced ammonia and the stored NO_x.

In addition to the enhancement of the NO_x + NH₃ reaction rate, the selective ammonia oxidation into nitrogen via the available oxygen was also proposed to occur [22]. Then, this reaction was proposed to explain the low NH₃ emission obtained with the catalysts exhibiting high oxygen storage capacities (OSC), even with very large hydrogen excess (Fig. 19.3), [37]. However, the OSC/oxygen mobility is not the only parameter to explain the activity enhancement. It was showed over Pt/Ce_xZr_{1-x}O₂

catalysts that the NH_3 yield is decreased with the increase of the cerium content, but not with the OSC [38]. This aspect is not totally explained yet.

19.2.4 Conclusion

Finally, significant ammonia emissions are possible at the NSR catalyst outlet. Two pathways are described, the direct route with H_2 and the isocyanate route with CO. However, the ammonia formation is especially favored in the presence of hydrogen, which can be produced in situ or upstream the NSR catalyst. Whatever the ammonia production pathway, ammonia emission strongly depends on the balance between the ammonia formation rate and the ammonia reactivity (with NO_x or oxygen from the support). Ammonia emission is particularly linked to the presence of unconsumed hydrogen. In addition, Ce-based oxides are proved to enhance the ammonia reactivity in the NSR catalyst.

19.3 Coupling of NO_x Trap and NH_3 -SCR Catalysts

19.3.1 Emergence and Development of the NSR-SCR Coupling Concept

The concept of adding a NH_3 adsorbing materials to a NO_x reduction catalyst was patented by Toyota in 1998 for applications on gasoline engines [39]. In the claimed configuration, a Cu-ZSM-5 catalyst is added to the three way catalyst (TWC) with the engine working in cycling conditions. In rich conditions, NO_x can be reduced to N_2 and NH_3 which can be stored on the zeolitic materials. When the engine turns to lean conditions, NO_x is no longer reduced on the TW catalyst. Ammonia is in part oxidized (to N_2) or desorbed. It may then react with NO passing through the TW monolith. This initial system was improved by introducing a small, auxiliary engine working in rich conditions and able to produce ammonia needed for reduction of the NO_x issued from the main engine [40]. Exhaust pipes are arranged to receive a TWC catalyst and a NH_3 adsorbing materials. In a further patent, Toyota claimed a new embodiment of the concept in which a group of cylinders are working in rich conditions while the others are working in lean conditions [41]. TW catalysts and NH_3 adsorbing and oxidizing catalysts (NH_3 -AO) are interconnected to receive alternatively the gases issued from the first and second groups of cylinders. The patent claims a wide range of NH_3 -AO catalysts: zeolites, silica-alumina, titania doped with Cu, Fe, Cr, ... This last system was finally improved by replacing the TW catalyst by a NO_x -trap materials (named NO_x -occluding and reducing catalyst, NH_3 -OR in the patent) [42]. In this configuration, the system is very close to the NSR-SCR coupling for

NO_x after-treatment. Several systems associating NSR and SCR catalysts were further claimed in Toyota patents [43, 44].

A system including an ammonia-generating catalyst coupled with the NO_x-trap or a TW catalyst was claimed by Daimler–Chrysler in 2002 under the name of “smart catalytic converter” [45]. In the lean operating phases, the nitrogen oxides are intermediately stored in the nitrogen oxide adsorption catalyst. In the rich operating phases, ammonia is generated by the ammonia-generating catalyst from the nitrogen oxides contained in the exhaust gas. The generated ammonia then causes a nitrogen oxide reduction in the nitrogen oxide adsorption catalyst. The mechanism by which ammonia is generated is obviously not detailed. The patent merely supposes that ammonia can be formed by reaction of NO_x with reductants in excess (especially H₂) during the rich operating phases. The materials catalyzing the reaction between NO and ammonia are not fully described. It is suggested that the SCR reaction can occur on the NO_x adsorbing catalyst. Commercially, the system was implemented on the Mercedes E320 Bluetec vehicle in 2007.

The coupling between a NO_x-trap sample and a NH₃–SCR catalyst, located downstream the first one or in a double layer on the monolith, was patented by Ford in 2004 [46]. In this patent application, ammonia is generated during the rich spike of the NSR catalyst cycle. It is stored on the SCR catalyst and further used to reduce NO_x during the lean phase. Depending on the temperature, a significant fraction of the nitrogen oxides may not be trapped and passes through the NSR catalyst: the SCR catalyst having stored ammonia helps at converting the NO_x not stored on the NSR catalyst. The Ford patent claims a NSR catalyst composed of noble metals deposited on a NO_x-trap materials (alkali, alkali earth metals,...) while the SCR catalyst would be made of zeolite, silica–alumina, or titania promoted by Cu, Fe, or Ce. This system was further detailed in a patent in 2008 [47]. Chigapov et al. from Ford Germany recently published a patent in which special compositions of the LNT catalyst (based on rare-earth and earth alkaline oxides) and of the SCR catalyst (Cu–Ce zeolites) were claimed for a better use in LNT–SCR coupling [48]. The coupling between a NSR and a SCR catalyst was also claimed by Engelhardt [49]. A more general system in which the SCR catalyst could be coupled to NSR and oxidation catalysts and associated with a soot filter was patented by BASF [50]. In this patent, the claimed SCR catalyst is composed of silver tungstate Ag₂WO₄ supported on alumina. Other BASF patents were published in 2010 and 2011 to cover the specific case of NSR–SCR coupling systems [51, 52]. A NSR–SCR coupling system was also depicted by Johnsson–Matthey [53]. Indeed, recently Twigg et al. suggest the development of a multicomponent diesel catalyst known as “four-way catalysts” (FWCs) [54]. SCR and/or NO_x-trapping components will be incorporated into catalysed filters from diesel cars in order to be cost-effective, weight effective, and space-effective. Finally, in the last 10 years, great efforts were made at Eaton Corporation to propose a viable technology with different configurations. No less than six patents were published by this Company claiming both depollution systems and catalysts for each configuration [55–60]. The systems may include two LNT bricks in parallel with optimization (i) of thermal changes during working and desulfation and (ii) of rhodium usage in the LNT catalyst.

Table 19.2 Effect of the addition of mordenites to Pt catalysts (2 % Pt/Al₂O₃ or 2 % Pt/CeO₂) for NO_x conversion in cycled conditions (physical mixture of 80 part of MOR–20 and 20 part of Pt catalyst)

Catalyst	NO _x conversion at various temperatures				
	200 °C	250 °C	300 °C	350 °C	400 °C
NSR alone	22.0	77.2	94.9	95.3	96.5
Pt/Al ₂ O ₃ + MOR	19.6	28.4	27.1	14.5	5.4
Pt/CeO ₂ + MOR	41.8	75.7	68.6	47.5	32.8
<i>Conv. to N₂</i>	28.6	38.5	49.0	41.8	18.4

Comparison with a NSR catalyst alone (2 wt.% Pt/75 % alumina–21 wt.% BaCO₃–2 wt.% K₂CO₃). From Ref. [61] selectivities are not detailed in this reference

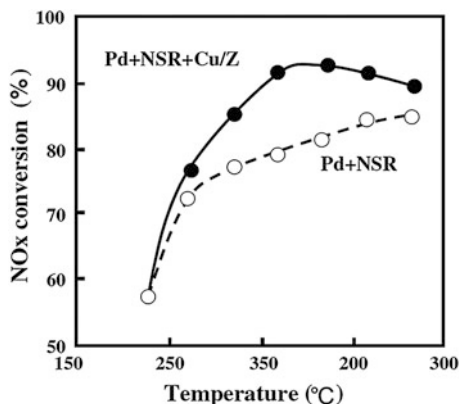
19.3.2 Coupling of Pt Catalysts with Zeolites

Addition of nonpromoted zeolites to a NSR catalyst was investigated by Nakasutji et al. [61]. They showed that mordenites with a SiO₂/Al₂O₃ molar ratio of 10 or 20 were able to store significant amount of ammonia during the NO_x-trap/reduction process and to improve NO_x conversion. Preliminary experiments were carried out in a rich gas (400 ppm NO + 1 % H₂) and in simplified lean/rich cycles (lean: 2000 ppm NO + 8 % O₂; rich: 2 % H₂). They revealed that Pt/Al₂O₃ (without Ba) was able to produce ammonia during the rich phase (NO/H₂ mixture) and that MOR–10 or 20 could store ammonia in similar conditions. In spite of these reactive and adsorptive properties, the physical mixture composed of 20 parts Pt/Al₂O₃ and 80 parts of MOR–20 is much less efficient for NO_x conversion than a standard NSR catalyst (Table 19.2). This is due to the very poor NO_x-trap properties of the Pt–Al₂O₃: as there is no NO_x trapped on the Pt catalyst, no ammonia could be produced during the rich phase. By contrast, the conversion is much higher when Pt/Al₂O₃ is replaced by Pt/CeO₂ which possesses significant NO_x-trap capacity. Ammonia stored on the mordenite contributes for 50, 45, and 30 % of NO_x conversion at 200, 300, and 400 °C, respectively. Unfortunately, relatively large amounts of N₂O are produced at 200–300 °C, which limits the conversion to N₂.

19.3.3 Coupling of Pt(RhPd)/BaO/Al₂O₃ with Cu–Zeolite Catalysts

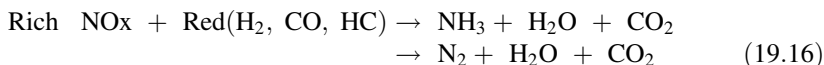
The NSR–SCR coupling was studied by Shinjoh et al. who used Cu–ZMS5 as the SCR catalyst [62]. A three-bed reactor was developed comprising successively: a 2.4 % Pd/γ–Al₂O₃ catalyst (simulating the Diesel Oxidation Catalyst), the NSR catalyst (1.6 % Pt–0.16 % Rh/BaO/Al₂O₃) and the SCR catalyst (5 % Cu–ZMS–5). The catalyst performances were compared in lean/rich cycled conditions (3 min each). A significant beneficial effect of adding Cu–ZMS5 to the Pd + NSR

Fig. 19.4 Effect of Cu-ZSM-5 added to the Pd + NSR catalyst. *Lean gas* 230 ppm NO, 6.5 vol % O₂, 9.6 vol % CO₂, 3 vol % H₂O balanced N₂, *Rich gas* 230 ppm NO, 0.4 vol % O₂, 3,900 ppmC with C₃H₆ as HC, 9.6 vol % CO₂, 3 vol % H₂O balanced N₂

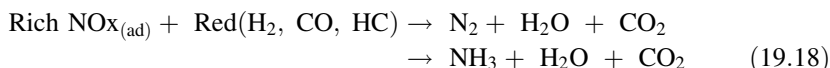


catalyst was observed between 230 and 310 °C. The increase of conversion can amount to +15 % when Cu-ZSM-5 is added (Fig. 19.4).

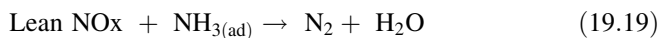
The role of each catalyst was detailed by Shinjoh et al. The **Pd catalyst** allows the NO oxidation into NO₂ in the lean phase (reaction 19.15) and significantly increases the NH₃ formation during the rich phase (reaction 19.16):



A third role of the Pd catalyst is to catalyze partial oxidation of propylene in reducing conditions, C₃H₆ being then partially transformed into H₂ and CO. The **NSR catalyst** stores the NO_x during the lean phase (reaction 19.17) and forms N₂ or NH₃ during the rich phase (reaction 19.18).



Finally, the **SCR catalyst** stores ammonia during the rich phase (reaction 19.20) and allows the reaction of adsorbed ammonia with NO not converted in the lean phase (reaction 19.19).



The effect of Cu-ZSM-5 (5 % Cu) addition on the performances of Pt-Rh/BaO/Al₂O₃ (Pt-RhBa) catalyst was also investigated by Corbos et al. [63, 64]. The catalytic system was tested in periodic cycling conditions (100 s lean/10 s rich) between 200 and 400 °C in three configurations: NSR catalyst alone, physical

Table 19.3 Effect of adding a SCR catalyst (Cu/ZSM-5) to a NSR catalyst (Pt–Rh/Ba) in cycling conditions: 100 s lean (500 ppm NO + 0.13 % CO/H₂ + 167 ppm C₃H₆ + 1 % CO₂ + 10 % O₂ in He) and 10 s rich (100 ppm NO + 8.53 % CO/H₂ + 1 % CO₂ in He)

Reductant	Catalyst	NO _x removal		
		250 °C	300 °C	400 °C
CO/H ₂ mixture	Pt–Rh/Ba (NSR alone)	39	50	39
	CuZSM-5	11	13	–
	Pt–Rh/Ba + CuZSM-5 (2 beds)	46	61	37
	Pt–Rh/Ba + CuZSM-5 (phys. mix.)	86	79	38
Pure CO (6.4 %)	Pt–Rh/Ba (NSR alone)	39	43	36
	Pt–Rh/Ba + CuZSM-5 (2 beds)	39	58	42
	Pt–Rh/Ba + CuZSM-5 (phys. mix.)	54	66	45
Pure H ₂ (6.4 %)	Pt–Rh/Ba (NSR alone)	47	54	48
	Pt–Rh/Ba + CuZSM-5 (2 beds)	67	73	42
	Pt–Rh/Ba + CuZSM-5 (phys. mix.)	68	77	45
Pure H ₂ (2.14 %)	Pt–Rh/Ba + CuZSM-5 (2 beds)	62	60	–
	Pt–Rh/Ba + CuZSM-5 (phys. mix.)	67	61	–

The gas mixture CO/H₂ contains 75 % CO and 25 % H₂

mixture of NSR + CuZSM-5 or dual bed catalyst (CuZSM-5 downstream NSR). The results are shown in Table 19.3.

While Cu–ZSM-5 is almost inactive in NO_x abatement in NSR cycling conditions, addition of this catalyst to Pt–Rh/Ba improves the performance of the NSR catalyst at 250 and 300 °C. At 400 °C, there is virtually no improvement when Cu–ZSM-5 is added to the NSR catalyst. At this temperature, ammonia is either not produced or not stored on the SCR catalyst. Interestingly, the physical mixture of Pt–Rh/Ba and CuZSM-5 gives better performances than the dual bed system. Corbos et al. concluded that a close proximity of the NSR catalyst with the NH₃–SCR catalyst was required for a better production and use of ammonia produced during the rich phase. The greatest effect of Cu–ZSM-5 is observed in the presence of H₂ in the reductant mixture, independently of the catalyst configuration (physical mixture or two beds). This is in line with H₂ giving the highest yield of ammonia in NSR cycling conditions. However, a cooperative effect between H₂ and CO can be observed at low temperature on the physical mixture, the reductant efficiency being in the following order: CO/H₂ mixture > H₂ alone > CO alone. However, most experiments were carried out in the absence of water in the synthetic gas. Adding 1 % H₂O in the gas mixture did not cause great difference in NO_x removal over the NSR catalyst alone while a slight decrease in activity of the NSR–SCR catalyst combination was observed. Another critical point is the process selectivity: residual NH₃ is a criterion of the NSR–SCR efficiency (ammonia slip cannot be accepted) while N₂O formation is a good criterion of the reduction selectivity (N₂O is a powerful greenhouse effect gas). Figure 19.5 shows the NH₃ and N₂O concentration after the NSR catalyst and in the NSR–SCR configuration.

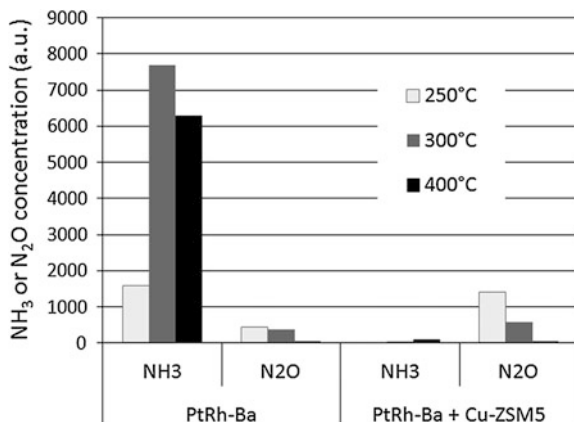


Fig. 19.5 Selectivity to NH₃ and N₂O of the NSR catalyst alone and in the NSR–SCR dual bed configuration. Gas compositions during lean and rich phases are detailed in Table 19.3

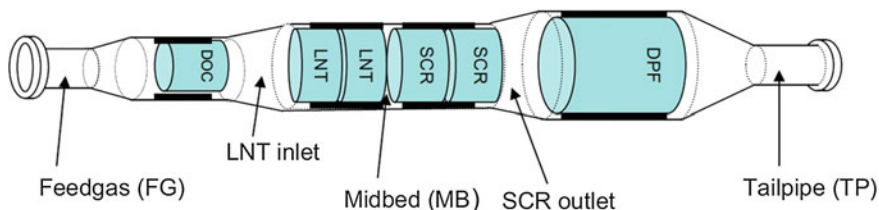


Fig. 19.6 System used in the vehicle tests [67]

A similar system (Pt–Rh NSR + Cu–zeolite) was recently investigated by McCabe et al. [65–67] of Ford Motor Company. Figure 19.6 shows the implementation of the catalysts in the exhaust line for the engine tests.

Using a CO + H₂ + C₃H₆ mixture as the reductant in cycling experiments, NO_x conversion was higher than with ammonia alone. Wang et al. concluded that propylene was an efficient reductant in the NSR–SCR combination. The results of a representative engine test over a high-emitting engine (called LR3) are given in Table 19.4. Though the SCR catalyst shows a non-negligible activity in converting NMHC (nonmethane HC) and CO, the greatest effect can be observed on the NO_x conversion. Only the LNT + SCR configuration allows to reach a good level of NO_x abatement.

Separate experiments proved that Cu–zeolite was a good catalyst for NO_x reduction, both by ammonia and alkenes. High resistance to deactivation by hydrocarbon and sulfur was obtained with a new generation of Cu–zeolite (Cu–CHA) which shows higher performances than the catalyst of the first generation composed of Fe–BEA [66, 67]. The NSR–SCR system is more efficient than the NSR catalyst alone up to 425 °C. Above this temperature, the SCR catalyst has no effect and it is advantageous to increase the loading of the NSR catalyst. However, such high temperatures are rarely encountered with normal diesel engine operation.

Table 19.4 Emission results from FTP test (Federal test procedure) over the LR3 engine (code location: see Fig. 19.6)

Emissions	Before DOC (FG) g/mile	After LNT (MB) g/mile	Tailpipe (TP) g/mile	DOC + LNT efficiency (%) (FG-MB)	SCR efficiency (%) (MB-TP)	Overall efficiency (%) (FG-TP)
NMHC	2.33	0.23	0.07	90	69	97
CO	6.42	0.30	0.21	95	30	97
NOx	1.02	0.25	0.07	78	74	93

Efficiency (%) represents the percentage of pollutant abatement (NMHC, CO, or NOx) at different stages of the exhaust pipe. From Ref. [67]

Table 19.5 NOx conversion, N₂, NH₃ and N₂O formation (expressed in N atoms) over the NSR catalyst alone and in the NSR + SCR configuration

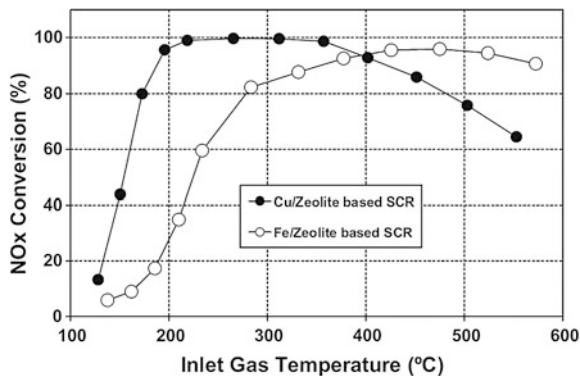
T (°C)	NSR alone				NSR + Cu-ZSM-5 (left) and NSR + Cu-BEA (right)							
	NO conv (%)	N ₂ form (%)	NH ₃ form (%)	N ₂ O form (%)	NO conv (%)	N ₂ form (%)	NH ₃ form (%)	N ₂ O form (%)	NO conv (%)	N ₂ form (%)	NH ₃ form (%)	N ₂ O form (%)
200	40.9	9.8	28.8	2.3	74.5	63.5	70.8	48.7	1.7	12.8	2.0	2.0
250	47.3	27.1	19.5	0.7	73.6	77.3	72.2	73.0	0.2	1.8	1.2	2.5
300	50.0	32.4	17.2	0.4	72.3	71.4	71.6	70.3	0.1	0.3	0.6	0.8
400	39.1	29.4	9.4	0.3	50.9	52.5	50.4	51.7	<0.1	0.1	0.5	0.7

Lean gas 750 ppm NO + 9.5 %O₂ (balance in Ar). *Rich gas* 750 ppm NO + 4 % H₂ (balance in Ar). Cycles: 150 s lean/20 s rich. Space velocity: 28,600 h⁻¹ for NSR and 90,000 h⁻¹ for SCR (1.4 % Cu/ZSM-5 or 2.1 % Cu/BEA). From Ref. [68]

The efficiency of Cu-BEA and Cu-ZSM-5 as SCR catalyst coupled with Pt/BaO/Al₂O₃ was compared by De La Torre et al. in a very recent paper [68]. Both zeolites lead to very active co-catalysts in promoting the NOx reduction by the NSR catalyst alone. The optimal Cu loading is obtained for 1.4 % Cu in ZSM-5 and 2.1 % Cu in BEA (Table 19.5). Cu-ZSM-5 and Cu-BEA can increase the NOx conversion by 20–30 % in the 200–300 °C temperature range. A significant formation of ammonia is observed on the NSR catalyst alone which is used for the SCR reaction (a part of NH₃ being oxidized by O₂). Cu-ZSM-5 and Cu-BEA have very similar effects so that activity per Cu ions appears higher over Cu-ZSM-5.

The two zeolite catalysts were characterized by De La Torre et al. [68]. Total acidity is higher over BEA but ZSM-5 shows a higher number of strong acid sites desorbing ammonia beyond 220 °C. In the optimized catalysts (1.4 % Cu-ZSM-5 and 2.1 % Cu-BEA), all the copper remains in the Cu²⁺ state. Increasing Cu loading leads to H₂/Cu < 1 in TPR experiments, which confirms the formation of Cu⁺ and may be Cu⁰ species. Reduced species of copper appear to be less active and less selective to N₂ (higher formation of N₂O).

Fig. 19.7 NO_x conversion in NH₃–SCR over zeolite catalysts after hydrothermal ageing for 64 h at 670 °C. Reaction conditions: 350 ppm NO, 350 ppm NH₃, 14 % O₂, space velocity: 30,000 h⁻¹. From Ref. [67]



19.3.4 Coupling of Pt(RhPd)/BaO/Al₂O₃ with Fe–Zeolite Catalysts

Systems coupling NSR with Fe–zeolite SCR catalysts were studied by many authors, in particular the Group of Forzatti in Milano [69–71], the Group of Daimler AG [72–75] and others [76–78]. Fe–zeolite are generally found less active in SCR than Cu–zeolite catalysts at low temperatures (Fig. 19.7) but they would be more selective to N₂. However, depending on the nature of the zeolite, contrasted results were obtained: for instance, Cu–ZSM-5 was shown to be slightly more selective than Fe–ZSM-5 when washcoated in dual layer monolith/NSR/SCR [79].

Kinetic studies and specific experiments with designed reactants coupled to FTIR or DRIFT were mainly employed by Forzatti and coworkers to get detailed information about the behavior of each catalyst configuration (Pt–Ba/Al₂O₃ alone, Fe–ZSM-5 alone or Pt–Ba/Al₂O₃ + Fe–ZSM-5). As expected, NO_x is mainly stored on the basic NSR catalyst while ammonia formed upon the rich phase is mainly stored on the acidic SCR catalyst. Gaseous NO_x slipped from the LNT catalyst during the lean phase reacts with NH₃ stored on Fe–ZSM-5 to give N₂. This classical view of the NSR–SCR system can lead to different performances depending on the proximity of the NSR and SCR catalysts (physical mixture vs. dual bed) and on the presence or not of CO₂ and H₂O in the gas mixture. Tables 19.6 and 19.7 summarize the result of Castoldi et al. [71]. Prolonged rich and lean phases (40 min each) were carried out with intermediary He purges to have a clearer analysis of the compounds stored and formed during each phase. Adding the SCR catalyst has a significant positive effect on the NO_x removal, in the presence and in the absence of CO₂ and water in the gas mixture. This effect is slightly more marked when both catalysts are physically mixed, which is in line with the results of Corbos et al. [63]. However, though the dual bed system seems less effective for NO_x removal, it leads to a higher selectivity to N₂ in rich phase, when there is no CO₂ and H₂O and in both phases (lean and rich) in the presence of CO₂ and H₂O.

Table 19.6 Quantitative analysis of lean/rich experiments performed over the NSR, NSR + SCR physical mixture and NSR/SCR dual bed configurations in the absence of CO₂ and H₂O

Amounts ($\mu\text{mol/gcat}$)	NSR alone	NSR + SCR (phys. mix)	NSR + SCR (dual bed)
NOx removed(a)	429	512	472
NOx stored(a)	429	434	423
N ₂ (lean)	0	78	49
N ₂ (rich)	193	51	209
NH ₃ slip	57	70	14

Experimental conditions: T = 250 °C; lean phase NO (1,000 ppm) in O₂ (3 % v/v) + He; rich phase H₂ (2,000 ppm) in He; catalyst weight 60 mg LNT (or 60 mg NSR + 60 mg SCR); total flow rate 100 Ncm³ /min mol/gcat refers to NSR Pt–Ba/Al₂O₃ weight. From Ref. [71]

The results of Tables 19.6 and 19.7 were obtained at 250 °C. In the physical mixture, the amount of removed NOx decreases with the temperature in the absence of CO₂ and H₂O while it is almost constant with CO₂ and H₂O. At 350 °C, there is virtually no difference when there is CO₂ + H₂O or not in the gases. In the dual bed, the amount of removed NOx tends to increase with temperature in every cases (with CO₂ + H₂O or not).

The effect of the reactor configuration (dual bed vs. physical mixture) seems to strongly depends on the temperature: in a preliminary study carried out at 200 °C, Bonzi et al. showed that NOx conversion was significantly higher in the physical mixture configuration, with 390, 610, and 980 μmol NOx removed/g respectively after the NSR catalyst alone, after the NSR–SCR dual bed and after the physical mixture [69]. A comparison with the results of Tables 19.6 and 19.7 shows that the differences between the three configurations are more marked at 200 °C than at 250 °C.

Following their patent publication (see Sect. 19.4.1), the Group of Daimler AG essentially worked at rationalizing the concept of smart catalytic converter by modeling the NSR–SCR dual bed [73, 74]. It was shown that a good adjustment of the NSR and SCR catalyst volume as well as a good balance between rich and lean cycle lengths are a prerequisite to an optimal operation of the system. An example of the modeling results, taken from Ref. [72], is given in Table 19.8. The model shows that increasing the SCR–to–NSR volume ratio (keeping constant the total volume) leads to a slight increase of the percent of NOx removal and to an increase of the amount of reacted ammonia (100 % in the second configuration of Table 19.8). The same model (COMSOL package) was used to optimize the lean/rich cycle duration.

Another modeling of the reactor volume was performed by Seo et al. [80] with a special insight to the formation of N₂O. In the NSR–SCR coupling, it is important to minimize (or annihilate) both ammonia and N₂O in the aftertreatment exhaust gas. This means that ammonia should be used to reduce NOx (or be oxidized to N₂) while N₂O, if formed, should be destroyed in the catalytic system. The NSR catalyst was composed of Pt/Pd/Rh/Ba/Ce/Zr on Al₂O₃ (relative

Table 19.7 Same results with 0.1 % CO₂ and 1 % H₂O in the gas mixture (*lean and rich*)

Amounts (μmol/ gcat)	NSR alone	NSR + SCR (phys. mix)	NSR + SCR (dual bed)
NOx removed(a)	272	323	396
NOx stored(a)	272	307	272
N ₂ (<i>lean</i>)	0	16	123
N ₂ (<i>rich</i>)	93	21	135
NH ₃ slip	117	7	0

Other conditions are given in Table 19.6. From Ref. [71]

Table 19.8 NOx removal efficiency and percentage of ammonia used to reduce NOx in a smart catalytic converter based on Pt–Ba–NSR and Fe–zeolite SCR catalyst

Catalyst configuration Respective volumes	% NOx removed on the NSR unit	% NOx removed on the SCR unit	NH ₃ reacted/ NH ₃ adsorbed
2 V of NSR + 1 V of SCR	55	7	0.3
1 V of NSR + 2 V of SCR	48	15	1.0

Reaction conditions: 240 °C, 165 s *lean* (500 ppm NO + 8 % O₂ + 8 % CO₂ + 8 % H₂O), 7 s *rich* (500 ppm NO + 1.6 % O₂ + 1.4 % H₂ + 0.3 % C₃H₆ + 4.2 % CO + 11.5 % CO₂ + 8 % H₂O). From Ref. [72]

weight– %: 3.3/0.72/0.31/12.56/7.97/4.49) while the SCR catalyst was a Fe–TMI zeolite (1.8 % Fe). Although it is not the best configuration in terms of NOx abatement, the system with an equal volume of NSR and SCR catalysts shows the best result in terms of ammonia and N₂O slip. A similar configuration was adopted by Pereda–Ayo to study the NSR (Pt–Ba–Al₂O₃)–SCR (Fe–BEA zeolite) coupling [78]. Nine values of nine parameters (81 experiments) were chosen to construct the abacus for predicting optimal performances. Very critical points are the temperature, the duration of lean-rich cycles and the concentration of H₂ in the respective lean and rich phase. It was shown that there is an optimum value of H₂ concentration (3 % in the conditions of Ref. [78]) to get the highest NOx conversion and the complete use of the ammonia produced in the NSR catalyst (no NH₃ slip). The specific role of H₂ concentration was also investigated by Lindholm et al. [76] who showed that the optimum H₂ concentration depended on the process temperature. A higher hydrogen concentration enhances the NOx removal efficiency at lower temperatures while this concentration should be reduced at higher temperatures to avoid an excess of ammonia leading to inhibition of the SCR reaction. Lindholm also showed that the NO₂/NO ratio was a critical factor in the NSR–SCR coupling. There is a clear benefit when NO₂ is present in the feed at low temperatures. Model studies were recently performed by Kota et al. who investigated the effect of exhaust pipe architecture (several sequential bricks LNT/SCR), the effect of the lean/rich cycle duration and the possible role of nonuniform noble metal loading [81]. The juxtaposition of two sequences of LNT/SCR bricks has a positive effect on NOx conversion while nonuniform metal loading has only a minor effect.

On the other hand, the lean/rich cycle duration has an important effect on the catalyst performance: reducing the cycle duration by a factor 2 can improve the NO_x conversion by about 15–20 %.

19.3.5 Other Systems Including Tungsten-Based Catalysts

Sullivan and Keane have proposed a system in which both NSR and SCR components are included in the same materials [82]. Ba–ZSM-5 (4.3 % Ba), Fe–ZSM-5 (0.8 % Fe) and Ba–Fe–ZSM-5 were studied to evaluate the benefit of the concept. Oxygen is required to desorb NO_x previously adsorbed on the catalyst, while gaseous ammonia is able to react with this stored NO_x. Interestingly, Sullivan and Keane showed that N₂O was produced in the NH₃(g)/NO(a) reaction on Ba–ZSM-5 and Fe–ZSM-5, but to a lesser extent on the composite FeBa–ZSM-5 catalyst.

Corbos et al. investigate the coupling of Pt–Rh/Ba/Al₂O₃ with different potential SCR catalysts (Co/Al₂O₃, CuZSM-5, Ag/Al₂O₃) [64]. As expected (and already found in a previous work [63]), addition of Cu–ZSM-5 gave the highest performances. Excellent performances were also obtained with Co/Al₂O₃ while addition of Ag/Al₂O₃ had no significant influence. The negative effect of water on the global performances of Pt–Rh/Ba/Al₂O₃ + Cu–ZSM-5 was ascribed to an inhibition of the reactions occurring on Cu–ZSM-5.

Berland et al. also studied the combination of a model NSR catalyst (1 % Pt/10 % BaO/Al₂O₃, denoted as Pt/Ba–Al) with oxides-based SCR samples [84]. WO₃ supported over ceria-zirconia oxides (WO₃/Ce–Zr) were studied as the active NH₃–SCR catalysts. The effect of the composition of the ceria-zirconia mixed oxides was studied with a constant WO₃ loading (10 wt.% of W, added by impregnation). It is demonstrated that Pt/Ba–Al NSR catalyst can release important amount of ammonia, until over 50 % of selectivity at 300 °C (Fig. 19.8a). SCR materials WO₃/Ce–Zr, with different Ce–Zr ratio, were associated downstream to the Pt/Ba–Al NSR catalyst. In the NSR + SCR combined system, the DeNO_x efficiency is strongly improved. An enhancement of 24 points in NO_x conversion was obtained at 300 °C for the better SCR sample (WO₃/Ce–Zr_(20–80)) (Fig. 19.8b) [83].

The acidic, basic, and redox properties of the SCR catalysts were investigated. In fact, it is reported in Ref. [85] that the redox properties are the key factors controlling the reactivity of the catalysts at low temperature, whereas at high temperature the acid properties are expected to play a major role in the SCR reaction. The addition of well-dispersed surface WO₃ to CeO₂–ZrO₂ oxide led to an important NH₃ storage capacity (acidity) not present on the host support. In the same time, the addition of tungsten trioxide strongly decreased the oxygen mobility, the NO to NO₂ oxidation activity and NO_x storage capacity of ceria-zirconia oxides. The NO_x selective catalytic reduction with ammonia (NH₃–SCR) and the NH₃ selective catalytic oxidation with oxygen (NH₃–SCO) behaviors of these SCR samples have been also studied [83]. All WO₃/Ce–Zr materials are active for reducing effectively the NO_x. These solids can reduce more than 80 %

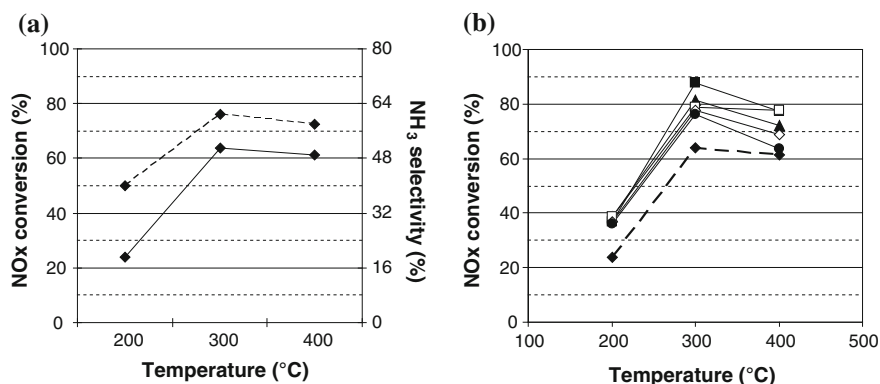


Fig. 19.8 **a** NO_x conversion (—) and NH₃ selectivity (–) over NSR Pt/Ba–Al model catalyst. **b** NO_x conversion in NSR + SCR (NSR:SCR = 60:120) combined system, from [83]: (◆): Pt/Ba–Al; (■): Pt/Ba–Al + WO₃/Ce–Zr(20–80); (▲): Pt/Ba–Al + WO₃/Ce–Zr(40–60); (□): Pt/Ba–Al + WO₃/Ce–Zr(58–42); (◇): Pt/Ba–Al + WO₃/Ce–Zr(70–30); (●): Pt/Ba–Al + WO₃/CeO₂. *Lean* (60 s): 500 ppm NO + 10 % O₂ + 10 % CO₂ + 10 % H₂O, *Rich* (3 s): 3 % H₂ + 10 % CO₂ + 10 % H₂O

of NO_x in NH₃–SCR conditions including CO₂ and H₂O in feed gas. A strong oxidation of ammonia was also reported in the absence of NO_x with nearly 80 % of ammonia oxidized only into nitrogen.

Placed downstream to a model Pt/Ba–Al NSR catalyst, it was demonstrated that the NH₃ reactivity is temperature-dependent. At low temperature (200 °C), all the emitted ammonia from the NSR catalyst reacts (Fig. 19.8c), but according only to the standard NH₃–SCR (see Sect. 19.4.1). At higher temperature, fast NH₃–SCR is then favored due to the NO oxidation into NO₂ over the upstream NSR bed. Besides, at 300 and 400 °C, a part of the stored ammonia is converted into N₂ via the SCO reaction (Fig. 19.9b). In addition, some NH₃ is released, especially for lower Zr contents in WO₃/Ce–Zr materials (WO₃/Ce–Zr_(58–42) and WO₃/Ce–Zr_(70–30)). This result implies competitions between the NH₃–SCR and the NH₃–SCO reactions together with the formulation of WO₃/Ce–Zr SCR samples (Fig. 19.9a and b). It also puts in evidence a lack of strong acid sites in order to store NH₃ at high temperature.

Finally, the work of Kim et al. about the HC–SCR and NH₃–SCR coupling system should be mentioned [86]. Although this study is out of the scope of the present chapter, it obeys to the same principle: the first bed (composed of Ag/Al₂O₃) is active in NO_x reduction by hydrocarbons or alcohols but it produces also ammonia and HCN which can be used in the second bed (CuCoY or Pd/Al₂O₃) in order to reduce the unconverted NO_x by ammonia.

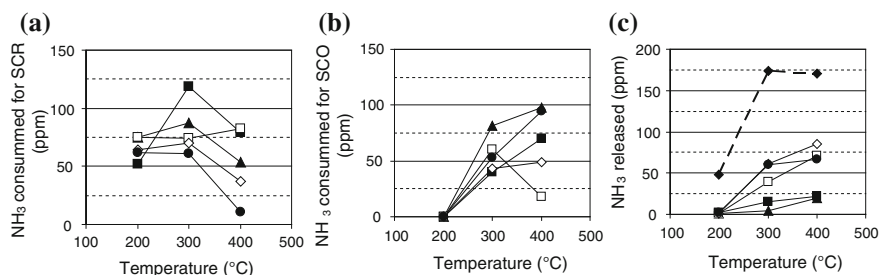


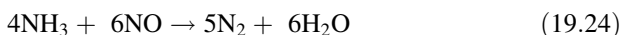
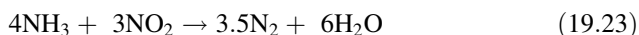
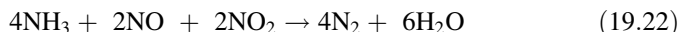
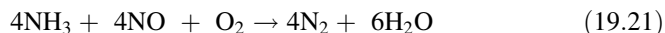
Fig. 19.9 Ammonia consumption (ppm) on WO₃/Ce-Zr SCR catalyst in NSR + SCR (NSR:SCR = 60:120) combined system for (a) NH₃-SCR (b) NH₃ SCO and (c) unconverted NH₃ [83]. (◆): Pt/Ba-Al; (■): Pt/Ba-Al + WO₃/Ce-Zr(20-80); (▲): Pt/Ba-Al + WO₃/Ce-Zr(40-60); (□): Pt/Ba-Al + WO₃/Ce-Zr(58-42); (◇): Pt/Ba-Al + WO₃/Ce-Zr(70-30); (●): Pt/Ba-Al + WO₃/CeO₂, *Lean* (60 s): 500 ppm NO + 10 % O₂ + 10 % CO₂ + 10 % H₂O, *Rich* (3 s): 3 % H₂ + 10 % CO₂ + 10 % H₂O

19.4 Selective Catalytic Reduction of NO_x by Ammonia (NH₃-SCR)

As illustrated previously, materials associated downstream to the NSR catalysts are usually metal-exchanged zeolites [87], or more recently acidic ceria-zirconia based oxides as NH₃-SCR catalysts [83]. These samples have to be active in NO_x reduction by NH₃ together with a high ammonia storage capacity. Thus, zeolite type structure was largely studied in the coupling NSR + SCR system. More specifically, iron and copper are the main exchanged metal in zeolites. Among the possible zeolites, ZSM-5 is one of the most studied materials in the academic literature, even if it is not the more appropriate structure.

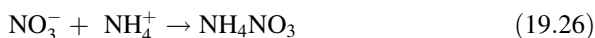
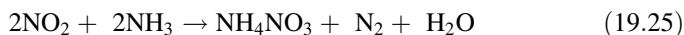
19.4.1 Mechanistic Aspects of the SCR Reaction

The reaction pathway of the NO_x selective catalytic reduction with ammonia (NH₃-SCR) is described by the following reactions (reactions 19.21–19.24):

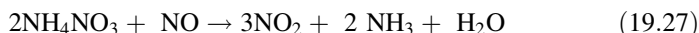


These reactions are usually denoted as “standard” (19.21), “fast” (19.22), “NO₂-SCR” (19.23) and finally “slow” (19.24) SCR reactions [31, 88–91]. It is

usually established in the literature that SCR of NO_x with NH₃ occurs through an Eley–Rideal type mechanism [92–97], in which adsorbed ammonia reacts with weakly adsorbed NO or NO₂ in the gas phase. Nevertheless, some studies suggest a reaction following a Langmuir–Hinshelwood mechanism [98–100]. However, it is currently received that SCR chemistry over metal-exchanged zeolite firstly requires the NO oxidation into NO₂, which is claimed to be the rate-determining step of the SCR mechanism [101]. For this reaction, metal-exchanged zeolites present largely higher activity than transition metal free zeolites [102]. It is also clearly evidenced that the NO₂/NO ratio is a key parameter for the SCR activity [88, 89, 103–105]. Indeed, fast SCR (reaction 19.22) and NO₂–SCR (reaction 19.23) reactions are much faster than the standard NO–SCR reaction (reaction 19.21). Note that in a NSR + SCR coupling system, the high oxidation activity of the Pt(RhPd)/BaO/Al₂O₃ NSR formulation also provides NO₂ by the oxidation of NO. Transition metal centers on zeolite are not only involved in the NO oxidation. For instance, it is suggested that iron species also promote the SCR reaction over zeolite framework in the case of the Fe-exchanged ZSM-5 materials [106]. Especially, transition metal sites are claimed to promote the formation of reactive nitrates on the catalyst surface in the presence of gaseous NO₂ [107]. In fact, the formation of intermediate Feⁿ⁺–NO species (*n* = 2, 3), Fe²⁺(NO)₂ complexes, and NO⁺ are reported [108]. Nitrosyl ion (NO⁺) may be produced by N₂O₄ disproportionation, which is firstly formed by NO₂ dimerization. NO⁺ can further react with H₂O to produce HNO₂. HNO₂ can then react with ammonia to produce ammonium nitrite (NH₄NO₂), which decomposes quickly below 100 °C, leading to the SCR products, N₂ and H₂O [109]. Ammonium nitrate can also be formed according to reactions 19.25–19.26:

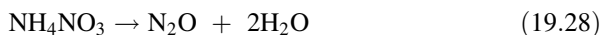


In this later process, NH₃ is activated on zeolitic Brønsted acid sites, giving NH₄⁺ ions [110]. This point is discussed below (Sect. 19.4.2). Ammonium nitrate thereafter decomposes into NO₂ and NH₃, as reported in reaction 19.27:

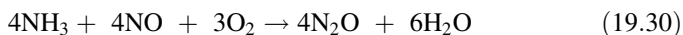
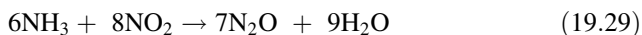


The combination of reactions (19.25) and (19.27) leads to the “fast” SCR, as reported above (reaction 19.22) [111].

However, if transition metal exchanged zeolites are active materials in NH₃–SCR, N₂O emission can be also observed. N₂O emission constitutes one of the main drawbacks of this system. For instance, Wilken et al. [112] reports a maximum N₂O production at 200 °C over Cu–Beta zeolite. Mechanism of N₂O emission is proposed to proceed through the decomposition of ammonium nitrates (reaction 19.28):



Fast SCR conditions, and more especially high NO_2 concentrations, are also proposed to favor the N_2O formation at low temperature (i.e., $T \leq 350$ °C) [113] (reaction 19.29). Mechanism involving NO (reaction 19.30) is proposed to occur at higher temperature (i.e., $T \geq 350$ °C) [114].



Finally, over Fe/MFI, and generally on zeolite, it is reported in the literature that N_2 formation requires one nitrogen atom from a molecule of NO_x , and a second nitrogen atom from ammonia molecule [115]. This observation is consistent with SCR reactions described in reactions 19.21–19.23.

19.4.2 Effect of Zeolite Framework

In the NH_3 –SCR mechanism, ammonia is firstly adsorbed and activated as NH_4^+ ions on the Brønsted acid sites of the zeolite framework. Acidic properties are then a crucial factor that determines the SCR activity. Since zeolite acidity is affected by the Si/Al ratio, high Al contents in the framework are favorable to achieve high NO_x conversions. Indeed, the Brønsted acid sites of the zeolite structure originate from aluminum centers [113, 116]. Besides, it appears that zeolite with small average pore diameter, as encountered in MFI, MOR, BEA, or FER materials, are the more active for NH_3 –SCR reaction. In opposition, molecular sieves having larger pore size, including Y, USY, or MCM–41 structures, exhibit lower activities. It is proposed in the literature that the formation of an active complex $[\text{NH}_4^+_x][\text{NO}]$ (with $x = 1, 2$) during SCR is facilitated in small pores, without effect of reactant surface mobility [117, 118]. A second hypothesis to explain the differences observed with the pore size is the formation of higher concentrations of 3H-NH_4^+ compound (NH_4^+ bonded to three hydrogen atoms) in small pore size support [119]. 3H-NH_4^+ compound is also reported as an intermediate for the formation of the active $[\text{NH}_4^+_x][\text{NO}]$ complex during the NH_3 –SCR reaction. In addition, the zeolite channels size can also influence the H–bonding with framework oxygen atoms [118]. For instance, FeY and FeMCM–41, with large pore sizes, show lower activities for NH_3 –SCR than FeZSM-5.

Nevertheless, it is also proposed that the active sites for the NO SCR by ammonia over HZSM-5 are highly acidic extra–framework alumina. In opposition, for NO_2 reduction reaction, both framework and extra-framework alumina sites are suggested to be active sites [120].

On the basis of these results, it appears that the activity of zeolite materials is associated with two main properties [121]:

1. A shape selectivity effect, due to the molecular sieving properties associated with the well defined crystal pore size, in which a part of the catalytic active sites are located;
2. A strong Brønsted acidity of bridging Si–(OH)–Al sites, generated by the presence of aluminum inside the silicate framework.

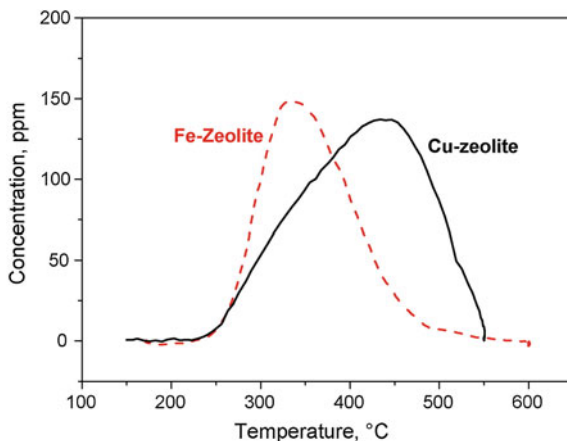
19.4.3 Role of Acidic Sites

The role of the acidic sites was studied by Brandenberger et al. [122] using different Fe–ZSM-5 samples at equal exchange degree but different Brønsted acidities. This study reveals that the acidity of the catalyst is not a crucial factor to achieve high activity for NO SCR with NH₃. Brønsted acidity may not be required for the adsorption or activation of the ammonia molecule, but it is necessary to bind and disperse the transition metal ions. The form in which ammonia is adsorbed on the support is consequently not crucial. These observations are confirmed by Schwidder et al. [123]. Indeed, high reaction rates for the NH₃–SCR can be achieved with nonacidic catalysts. A promoting effect of acidity is noted for the catalysts that contain the iron in the most favorable structure (i.e., oligomeric Fe oxo clusters).

In fact, FTIR characterization of the ZSM-5 acidic properties shows that two types of hydroxyl groups are mainly detected, giving bands at 3,720 and 3,605 cm⁻¹ [124]. Thermal activation temperature strongly affects acidic properties. By increasing the temperature, dehydroxylation of the zeolite is observed above 400 °C. It induces a decrease of the number of Brønsted acid sites, while an increase in strong Lewis acid sites is observed. The dehydration at high temperature irreversibly removes the more acidic hydroxyl groups. Dealumination of zeolitic framework is also reported to modify acidity. Ammonia adsorption and temperature programmed desorption over ZSM-5 (Si/Al = 11.8) are studied in Ref. [125]. Three different states of chemisorbed ammonia are distinguished, which show desorption peaks at around 80, 180, and 430 °C. The distribution of chemisorbed ammonia is also reported to depend on the catalyst pre-treatment or deactivation. Recently, it was proposed that adsorption of ammonia on Brønsted acid sites goes through co-adsorption of up to four ammonia molecules on one active site at low temperatures. In addition, only a fraction of the aluminum framework is evidenced to be able to bind ammonia as ammonium ion [126]. Consequently, the support can act mainly as a reservoir for ammonia molecules, which then migrate to the active sites in order to undergo the reaction with NO_x.

In a comparative study of the NH₃–SCR reactions over a Cu–zeolite and a Fe–zeolite catalyst, Colombo et al. [127] observed that iron zeolite catalyst stores a lower amount of strongly bonded ammonia than copper zeolite (Fig. 19.10). In addition, authors claim a greater activity in the ammonia oxidation reaction for the copper zeolite, together with a less sensitivity to the NO₂/NO_x ratio for the DeNO_x

Fig. 19.10 Ammonia TPD over Cu- and Fe-zeolite: $Q = 71 \text{ cm}^3/\text{min}$ (STP), $\text{H}_2\text{O} = 3 \%$, $\text{O}_2 = 0 \%$, $T \text{ ramp} = 15 \text{ K/min}$. (Solid line) Cu-zeolite. (Dashed line) Fe-zeolite [127]



activity. Besides, N_2O is detected over Cu-zeolite even with negligible NO_2 feed content, whereas over iron zeolite, N_2O formation occurs only in excess of NO_2 .

19.4.4 Active Sites and Performances of Cu-Zeolite, Fe-Zeolite, and Other Systems in NH_3 -SCR

Although the identity and nuclearity of active sites is still in debate, Cu-zeolite binuclear species are clearly reported as active sites. Nevertheless, it seems that the nature of the copper active site is strongly influenced by the reaction temperature and by the properties of the used zeolite. Indeed, over FAU zeolite, $[\text{CuOCu}]^{2+}$ dimer species are proposed to catalyze NH_3 -SCR reaction at low temperature ($T \leq 300 \text{ }^\circ\text{C}$) [128]. For NO decomposition, Moretti et al. [129, 130] also proposed that the main active sites over ZSM-5 (silica to alumina ratio from 66 to 80) consist of dimeric Cu species strongly anchored to “next-nearest-neighbor” framework AlO_4^- species. On the opposite, Cu^{2+} is suggested to become active at higher temperature ($T \geq 350 \text{ }^\circ\text{C}$) over NaY [131, 132].

At temperatures below $250 \text{ }^\circ\text{C}$, Sjövall et al. [133] observed a beneficial effect of oxygen on the activity, contrary to higher temperatures. Ammonia slip is also affected by temperature. For instance, equal amounts of nitrogen oxides and ammonia are required at $175 \text{ }^\circ\text{C}$. In fact, over Cu-ZSM-5 the NO_x conversion is achieved by the reaction between NO_2 and adsorbed NH_3 . At higher temperature, ammonia oxidation occurs. However, if exposing the catalyst to equimolecular amounts of NO and NO_2 increases the NO_x conversion, N_2O formation is furthermore observed.

Unfortunately, Cu-ZSM-5 catalyst suffers from thermal and water deactivation leading to segregation of extra-framework copper ions, and/or to the sintering of CuO-like species. To improve the durability or the low-temperature activity,

Seo et al. studied the effect of ZrO_2 addition on DeNO_x performance of a SCR Cu–ZSM-5 catalyst [134]. It is reported that incorporation of the appropriate amount of ZrO_2 (2 wt.%) increases the acid strength of acidic sites of catalyst which improved by 10–20 % the NO_x conversion in the 200–300 °C temperature range, as well as the durability of Cu–ZSM-5 catalyst. Recently Kwak [135] reports that Cu^{2+} ion-exchanged SSZ-13 (Cu–SSZ-13 with Chabazite (CHA) structure, containing small radius (3.8 Å) eight-membered ring pores), is more active and selective in reducing NO with NH_3 compared to Cu–ZSM-5 and Cu–beta. For instance, after hydrothermal treatment at 800 °C for 16 h, Cu–SSZ-13 was found to show nearly no change in NO_x reduction activity, while Cu–ZSM-5 and Cu–Beta were found to lose NO_x reduction activity. In the same time, no significant rearrangement of nuclearity of copper active sites, of structural zeolite framework is observed on Cu–SSZ-13 compare to Cu–ZSM-5 after hydrothermal ageing.

In Fe/ZSM-5 (Fe/Al = 1), EXAFS characterization reveals the presence of diferric (hydr)oxo-bridged binuclear clusters, located at the ion-exchange positions of the zeolite, and compensating one or two lattice charges [136, 137]. For Fe/Al = 0.8, iron is predominantly present as large hematite particles, although a minor fraction of binuclear species might be present as well [136]. Small Fe_xO_y clusters like Fe_4O_4 , isolated Fe^{2+} and Fe^{3+} ions, are also reported as possible active sites in the literature [138–141]. Besides, electron-deficient ferric oxide nanoclusters, isolated iron ions, and possibly oxygen-bridged iron binuclear complexes, may likewise coexist in Fe/MFI catalysts [142]. Finally, a high exchange level (M/Al ratio \approx 1), which can be achieved with the CVD method for instance, confers activity at low temperature for the material. Additionally, a high metal content may lead to extra-framework metal oxide clusters, which can exhibit high activity for NH_3 oxidation [141]. In fact, the activity of Fe–ZSM-5 for SCR of NO by NH_3 is suggested to be catalyzed by different iron active species depending on temperature [143]. At temperatures below 300 °C, the SCR activity was observed to be primarily caused by monomeric iron sites. At higher temperature ($T = 300\text{--}500$ °C), the contribution of dimeric iron species, oligomeric species and partially uncoordinated iron sites become important. Fe–zeolite catalyst can also be sensitive to the NO/NO₂ ratio for NO_x removal via ammonia SCR [144]. The SCR efficiency was greatly enhanced when using pure NO₂.

Other catalytic systems are also studied for the abatement of NO_x by reaction with ammonia, namely vanadium oxide–titania based samples or transition metal oxide–based materials. On these catalysts, ammonia is activated by coordination over Lewis acid sites, and can react with NO from the gas phase or weakly adsorbed NO [102]. Over $\text{V}_2\text{O}_5\text{--}\text{WO}_3(\text{MoO}_3)/\text{TiO}_2$ materials, new relevant contributions appeared in the literature, in particular concerning the reaction mechanism and the role of preoxidation of NO to NO₂. Coordinated ammonia would be oxidized to amide species, which later reacts with NO to form adsorbed nitrosamide species. Nitrosamide species decomposes into nitrogen and water, while oxygen reoxidizes the catalyst surface [96]. Unfortunately, these catalytic systems remain poorly active at low temperature, and temperature higher than 350 °C is needed to achieve high NO_x abatement. In order to increase the low

temperature activity, new formulations based on transition metal oxides are proposed. For instance, Mn and Fe oxides supported on titania and alumina are active in NH_3 -SCR at low temperature (150–250 °C) [145]. However, the main drawback of these catalysts is the limited selectivity of the NO_x conversion into N_2 , with significant production of N_2O . In addition, vanadia-based catalysts are not suitable for high temperature application as it can be the case in automotive exhaust pipe. Indeed, the sublimation of V_2O_5 occurs from 650 °C [113, 118]. Then, new catalytic systems having high efficiency at low temperature, thermally stable up to 800 °C, and with a limited impact of the NO₂/NO_x ratio on the activity, are developed. Amongst these new emerging SCR catalytic systems, acidic zirconia mixed-oxides are described as attractive alternatives [146]. For instance, 50 % NO conversion was attained at 250 °C for the standard SCR process. By applying the “fast” SCR conditions (NO₂/NO_x = 50 %), 97 % of NO_x were reduced to N_2 at only 200 °C [147]. The promotion of acidic zirconia by ceria also increases the NO_x conversion, the selectivity to N_2 and the catalyst durability. These results show that modified acidic zirconia oxides are attractive materials for Diesel after treatment systems [146]. However, Fe or Cu exchanged zeolites, which exhibit high reactivity toward the NO_x SCR by NH_3 , are the more quoted materials for a coupling with a NSR catalyst.

19.5 Conclusion and Perspective

The combination of NO_x trapping materials with NH_3 -SCR catalysts for the NO_x treatment from mobile lean-burn engines has been reported. Particular attention has been paid in the mechanism of ammonia emission and reactivity toward NO_x abatement in NSR process. For the first point, two reaction paths are proposed in the literature. In the presence of hydrogen during the rich pulses of the LNT regeneration, ammonia can be formed by direct reaction with the previously stored NO_x. When CO is used as the reductant agent, water-assisted reaction, by hydrolysis of intermediate isocyanate species, is suggested. In the presence of water and carbon dioxide in the gas mixture, both reaction pathways co-exist due to direct and reverse water gas shift reaction. Ammonia is thereafter involved in the NO_x reduction mechanism, by a sequential route in which NH_3 reacts faster with NO_x to yield N_2 compared with its own formation rate. It is found that both the nature and the content of the basic element as well as the redox properties of the support interfere in NH_3 yield.

Ammonia may likewise be used as reductant for selective catalytic reduction of NO_x species. For this application, metal-exchanged zeolite catalysts offer new opportunities to reduce NO_x emissions from lean-burn engine via the NH_3 -SCR process. Iron-exchanged ZSM-5 has received much attention because of its promising activity and stability in the NH_3 -SCR process. Correlating catalytic activities with the concentration of mononuclear and binuclear Fe species shows that both types of Fe ions and even small metal clusters are active sites for SCR,

but that isolated species are more active. The topology of the zeolite is also an important factor, as well as its stability under hydrothermal conditions. A high exchange level (M/Al ratio ≈ 1) seems to be proscribed creating extra-framework metal oxide clusters, which can be highly active for NH_3 oxidation.

The coupling between a NO_x -trap catalyst and a NH_3 -SCR material located downstream the first one or in a double layer on the monolith, was firstly patented by Ford in 2004. In other recent studies, two main SCR catalysts are usually associated in such system, namely Cu–ZSM-5 and Fe–ZSM-5 catalysts. For instance, it is reported that using Cu–ZSM-5 material, about 15–50 % of supplementary NO_x conversion can be achieved, depending on the working conditions. Whatever the zeolite used, higher performances are reported with H_2 as reductants, since it enhances NH_3 formation in the first NSR catalytic bed. Physical mixture of NSR and SCR catalysts gives better performances than dual bed system. It is concluded that a close proximity of both materials was required for a better use of ammonia produced during the rich pulses.

Furthermore, in almost every case of lean-burn engine after-treatment implementation in the USA and Europe, a Diesel particulate filter (DPF) is required. The NSR + SCR system must be compatible with the DPF working mode. Filter regeneration induces severe exotherms (900–1000 °C) which expose NSR + SCR catalysts to harsh environment. To maintain the durability of this coupled system, the catalysts must exhibit high thermal stability. As a consequence, usual vanadia-based oxides SCR catalysts are not suitable. The stability of metal-exchanged zeolite has to be improved to prevent potential metal migration, or sulfur poisoning. A way is metal-exchanged in small-pore zeolites which shown to be much more hydrothermally stable than the medium-pore zeolite. New acidic zirconia-based oxides seem also attractive for this application.

Finally, the literature essentially focuses on the association of NSR catalyst with usual NH_3 -SCR samples. However, in this coupled NSR + SCR system, ammonia is not directly injected in the feed gas, but produced during the regeneration step of the NSR process. The additional NO_x reduction occurs during the lean phases (in O_2 excess) between NO_x from gas phase and stored ammonia. It makes a prominent difference with the usual NH_3 -SCR technology. The development of specific SCR catalyst is desirable in a near future to achieved DeNOx efficiency and nitrogen yield even higher.

References

1. Takeshima S, Tanaka T, Iguchi S, Araki Y, Hirota S, Oda T, Murakami F (1995) *Exhaust purification device of internal combustion engine*. US Patent 5,437,153 (Aug. 1, 1995)
2. Goto M, Iguchi S, Katoh K, Kihara T (1995) *Exhaust gas purification device for an engine*. US Patent 5,472,673 (Dec.5, 1995)
3. Takahashi N, Shinjoh H, Iijima T, Suzuki T, Yamazaki K, Yokota K, Suzuki H, Miyoshi N, Matsumoto S, Tanizawa T, Tanaka T, Tateishi S, Kasahara K (1996) *The new concept 3-way*

- catalyst for automotive lean-burn engine: NO_x storage and reduction catalyst*. Catal. Today 27:63–69
4. Kobayashi T, Yamada T, Kayano K (1997) Study of NO_x Trap Reaction by Thermodynamic Calculation. SAE Technical Papers 970745:63
 5. Matsumoto S, (2000) *Catalytic reduction of nitrogen oxides in automotive exhaust containing excess oxygen by NO_x storage-reduction catalyst*. Cattech 4:102–109
 6. Roy S, Baiker A (2009) *NO_x Storage-Reduction Catalysis: From Mechanism and Materials Properties to Storage-Reduction Performance*. Chem. Rev.109:4054–4091
 7. Kwak JH, Kim DH, Szanyi J, Peden CHF (2008) *Excellent sulfur resistance of Pt/BaO/CeO₂ lean NO_x trap catalysts*. Applied Catal. B 84:545–551
 8. Corbos EC, Elbouazzaoui S., Courtois X, Bion N, Marecot P, Duprez D (2007) *NO_x storage capacity, SO₂ resistance and regeneration of Pt(Ba)/CeZr model catalysts for NO_x-trap system*. Topics in Catalysis 42–43:9–13
 9. Toops TJ, Smith DB, Epling WS, Parks JE, Partridge WP (2005) *Quantified NO_x adsorption on Pt/K/gamma-Al₂O₃ and the effects of CO₂ and H₂O*. Applied Catal. B 58:255–264
 10. Lesage T, Saussey J, Malo S, Hervieu M, Hedouin C, Blanchard G, Daturi M (2007) *Operando FTIR study of NO_x storage over a Pt/K/Mn/Al₂O₃-CeO₂ catalyst*. Applied Catal. B 72:166–177
 11. Szailer T, Kwak JH, Kim DH, Hanson JC, Peden CHF, Szanyi J (2006) *Reduction of stored NO_x on Pt/Al₂O₃ and Pt/BaO/Al₂O₃ catalysts with H₂ and CO*. J. Catal. 239:51–64
 12. Nova I, Lietti L, Forzatti P, Prinetto F, Ghiotti G (2010) *Experimental investigation of the reduction of NO_x species by CO and H₂ over Pt–Ba/Al₂O₃ lean NO_x trap systems*. Catal. Today 151:330–337
 13. Kočí P, Plát F, Štěpánek J, Bártová Š, Marek M, Kubiček M, Schmeißer V, Chatterjee D, Weibel M (2009) *Global kinetic model for the regeneration of NO_x storage catalyst with CO, H₂ and C₃H₆ in the presence of CO₂ and H₂O*. Catal. Today 147:257–264
 14. Masdrag L, Courtois X, Can F, Rohart E, Blanchard G, Marecot P, Duprez D (2012) *Understanding the role C₃H₆, CO and H₂ on efficiency and selectivity of NO_x Storage 41 Reduction (NSR) process: Activity during the lean period*. Catal. Today 189:70–76
 15. Masdrag L, Courtois X, Can F, Duprez D. *Effect of reducing agents (C₃H₆, CO, H₂) on the NO_x conversion and N₂O–NH₃ selectivities during representative lean/rich cycles over platinum-based model NSR catalyst*. Submitted
 16. Flura A, Can F, Courtois X, Royer S, Duprez D (2012) *Silver supported over high-surface-area zinc aluminate spinel as an active material in low-temperature SCR of NO with ethanol*. Applied Catal. B 126:275–289
 17. Castoldi L, Lietti L, Forzatti P, Morandi S, Ghiotti G, Vindigni F (2010) *The NO_x storage-reduction on PtK/Al₂O₃ Lean NO_x Trap catalyst*. J. Catal. 276:335–350
 18. Castoldi L, Nova I, Lietti L, Forzatti P (2004) *Study of the effect of Ba loading for catalytic activity of Pt–Ba/Al₂O₃ model catalysts*. Catal. Today 96:43–52
 19. Artioli N, Matarrese R, Castoldi L, Lietti L, Forzatti P (2011) *Effect of soot on the storage-reduction performances of PtBa/Al₂O₃ LNT catalyst*. Catal. Today 169:36–44
 20. Pereda-Ayo B, González-Velasco JR, Burch R, Hardacre C, Chansai S (2012) *Regeneration mechanism of a Lean NO_x Trap (LNT) catalyst in the presence of NO investigated using isotope labelling techniques*. J. Catal., 285:177–186
 21. Frank B, Emig G, Renken A (1998) *Kinetics and mechanism of the reduction of nitric oxides by H₂ under lean-burn conditions on a Pt–Mo–Co/α-Al₂O₃ catalyst*. Appl. Catal. B. 19:45–57
 22. Clayton RD, Harold MP, Balakotaiah V (2008) *NO_x storage and reduction with H₂ on Pt/BaO/Al₂O₃ monolith: Spatio-temporal resolution of product distribution*. Appl. Catal. B. 84:616–630
 23. Breen JP, Burch R, Fontaine-Gautrelet C, Hardacre C, Rioche C (2008) *Insight into the key aspects of the regeneration process in the NO_x storage reduction (NSR) reaction probed using fast transient kinetics coupled with isotopically labelled 15NO over Pt and Rh-containing Ba/Al₂O₃ catalysts*. Appl. Catal. B. 81:150–159

24. Bhatia D, Harold MP, Balakotaiah V (2010) *Modeling the effect of Pt dispersion and temperature during anaerobic regeneration of a lean NO_x trap catalyst*. Catal. Today 151:314–329
25. Corbos EC, Courtois X, Can F, Marécot P, Duprez D (2008) *NO_x storage properties of Pt/Ba/Al model catalysts prepared by different methods: Beneficial effects of a N₂ pre-treatment before hydrothermal aging*. Appl. Catal. B. 84:514–523
26. Clayton RD, Harold MP, Balakotaiah V (2008) *Selective catalytic reduction of NO by H₂ in O₂ on Pt/BaO/Al₂O₃ monolith NO_x storage catalysts*. Appl. Catal. B 81:161–181
27. Pereda-Ayo B, Duraiswami D, González-Marcos JA, González-Velasco JR (2011) *Performance of NO_x storage–reduction catalyst in the temperature–reductant concentration domain by response surface methodology*. Chem. Eng. J. 169:58–67
28. Le Phuc N, Courtois X, Can F, Royer S, Marecot P, Duprez D (2011) *NO_x removal efficiency and ammonia selectivity during the NO_x storage-reduction process over Pt/BaO(Fe, Mn, Ce)/Al₂O₃ model catalysts. Part I: Influence of Fe and Mn addition*. Appl. Catal. B 102:353–361
29. Le Phuc N, Courtois X, Can F, Royer S, Marecot P, Duprez D (2011) *NO_x removal efficiency and ammonia selectivity during the NO_x storage-reduction process over Pt/BaO(Fe, Mn, Ce)/Al₂O₃ model catalysts. Part II: Influence of Ce and Mn–Ce addition*. Appl. Catal. B 102:362–371
30. Choi JS, Partridge WP, Pihl JA, Daw CS (2008) *Sulfur and temperature effects on the spatial distribution of reactions inside a lean NO_x trap and resulting changes in global performance*. Catal. Today 136:173–182
31. Nova I, Lietti L, Forzatti P (2008) *Mechanistic aspects of the reduction of stored NO_x over Pt–Ba/Al₂O₃ lean NO_x trap systems*. Catal. Today 136:128–135
32. Lietti L, Nova I, Forzatti P (2008) *Role of ammonia in the reduction by hydrogen of NO_x stored over Pt–Ba/Al₂O₃ lean NO_x trap catalysts*. J. Catal. 257:270–282
33. Lindholm A, Currier NW, Fridell E, Yezerets A, Olsson L (2007) *NO_x storage and reduction over Pt based catalysts with hydrogen as the reducing agent: Influence of H₂O and CO₂*. Appl. Catal. B. 75:78–87
34. Le Phuc N, Courtois X, Can F, Berland S, Royer S, Marecot P, Duprez D (2011) *A study of the ammonia selectivity on Pt/BaO/Al₂O₃ model catalyst during the NO_x storage and reduction process*. Catal. Today 176:424–428
35. Joubert E, Courtois X, Marecot P, Canaff C, Duprez D (2006) *The chemistry of DeNO_x reactions over Pt/Al₂O₃: The oxime route to N₂ or N₂O*. J. Catal. 243: 252–262
36. Chen HY, Voskoboinikov T, Sachtler WMH (1999) *Reaction Intermediates in the Selective Catalytic Reduction of NO_x over Fe/ZSM-5*. J. Catal. 186:91–99
37. Larson RS, Pihl JA, Chakravarthy VK, Toops TJ, Daw CS (2008) *Microkinetic modeling of lean NO_x trap chemistry under reducing conditions*. Catal. Today 136:104–120
38. Le Phuc N, Corbos EC, Courtois X, Can F, Marecot P, Duprez D (2009) *NO_x storage and reduction properties of Pt/CexZr1–xO₂ mixed oxides: Sulfur resistance and regeneration, and ammonia formation*. Appl. Catal. B. 93:12–21
39. Kinugasa Y, Igarashi K, Itou T, Suzuki N, Yaegashi T, Tanaka T (1998) *Device for purifying an exhaust gas of an engine*. US Patent 5782087 (Jul. 21, 1998)
40. Kinugasa Y, Itou T, Hoshi K, Suzuki N, Yaegashi T, Igarashi K (1999) *Device for purifying exhaust gas from engine*. US Patent 5964088 (Oct. 12, 1999)
41. Kinugasa Y, Igarashi K, Itou T, Suzuki N, Yaegashi T, Takeuchi K (2000) *Metho adsorbbed and device for purifying exhaust gas from engine*. US Patent 6047542 (April 11, 2000)
42. Kinugasa Y, Igarashi K, Itou T, Suzuki N, Yaegashi T, Tanaka T, Miyoshi N (2000) *Device for purifying exhaust gas from an internal combustion engine*. US Patent, 6119452 (Sept. 19, 2000)
43. Sakurai K (2011) *Exhaust purifying system for internal combustion engine*. US Patent Appl. 2011/0138783 A1 (June 16, 2011)

44. Sakurai K, Miyashita S, Katumata Y (2011) *Exhaust purifying system for internal combustion engine*. US Patent Appl. 2011/0214417 A1 (Sep. 8, 2011)
45. Guenther J, Konrad B, Krutzsch B, Nolte A, Voigtlaender D, Weibel M, Wenninger G (2002) *Exhaust gas purification process and apparatus with internal generation of ammonia for reducing nitrogen oxide*. US Patent 6338244 B1 (Jan. 15, 2002)
46. Gandhi HS, Cavatalo JV, Hammerle RH, Chen Y (2004) *Catalyst system for NO_x and NH₃ emission*. US Patent Appl. 2004/0076565 A1 (Apr. 22, 2004)
47. Gandhi HS, Cavatalo JV, Hammerle RH, Chen Y (2008) *Catalyst system for NO_x and NH₃ emission*. US Patent 7332135 (Feb. 19, 2008)
48. Chigapov A., Carberry B, Ukropec R, *LNT and SCR catalysts for combined LNT-SCR applications*. Patent EP 2 481 473 A2 and EP 2 481 473 A3 (26 Jan. 2011)
49. Li Y, Deeba M, Dettling JC (2005) *Emissions treatment system with NSR and SCR catalysts*. Patent WO 2005/047663 A3 (26 May 2005)
50. Furbeck H, Koermer G. S, Moini A, Castellano CR (2008) *Catalyst, method for its preparation and system to reduce NO_x in an exhaust gas stream*. Patent WO 2008/036797 A1 (27 March 2008)
51. Wan CZ, Zheng X, Stiebels S, Wendt C, Boorse SR (2010) *Emissions treatment system with ammonia-generating and SCR catalyst*. Patent WO 2010/114873 A3 (7 October 2010)
52. Li Y, Deeba M, Dettling JC, Patchett JA, Roth SA, *Emission treatment system with NSR and SCR catalysts*, Patent US 7919051B2 (5 April 2011)
53. Chen HY, Weigert E, Fedeyko J, Cox J, Andersen P (2010) *Advanced Catalysts for Combined (NAC + SCR) Emission Control Systems*. SAE Technical Paper 2010-01-0302
54. Twigg MV (2011) *Catalytic control of emissions from cars*. Catal. Today 163:33–41
55. Hu H, Stover Th. (2006) *Hybrid catalyst system for exhaust emissions reduction*, Patent WO 2006/008625 A1 (26 Jan. 2006)
56. Hu H, Stover Th. (2007) *Hybrid catalyst system for exhaust emissions reduction*, Patent US 7213395 B2 (8 May 2007)
57. Hu H, Mc Carthy E. Jr, Yan Y (2007) *Thermal management of hybrid LNT/SCR aftertreatment during desulfation*, Patent US 7251929 B2 (7 Aug. 2007)
58. Hu H, Stover Th. (2010) *Hybrid catalyst system for exhaust emissions reduction*, Patent US 7650746 B2 (26 Jan. 2010)
59. Mc Carthy E. Jr, Bailey OH (2011) *LNT-SCR system optimized for thermal gradient*, Patent US 7950226 B2 (31 May 2011)
60. Ginter DM, Mc Carthy E. Jr (2011) *Optimized rhodium usage in LNT-SCR system*, Patent US 8069654 B2 (6 Dec. 2011)
61. T. Nakatsuji, M. Matsubara, J. Rouistenmäki, N. Sato, H. Ohno (2007) *A NO_x reduction system using ammonia-storage selective catalytic reduction in rich/lean excursions*, Appl. Catal. B: Environmental 77: 190–201
62. H. Shinjoh, N. Takahashi, K. Yokota (2007) *Synergic effect of Pd/gamma-alumina and Cu/ZSM-5 on the performance of NO_x storage reduction catalyst*, Topics Catal., 42–43: 215–219
63. E.C. Corbos, M. Haneda, X. Courtois, P. Marecot, D. Duprez (2008) H. Hamada, *Cooperative effect of Pt–Rh/Ba/Al and CuZSM-5 catalysts for NO_x reduction during periodic lean-rich atmosphere*, Catal. Comm., 10: 137–141
64. E.C. Corbos, M. Haneda, X. Courtois, P. Marecot, D. Duprez (2009) H. Hamada, *NO_x abatement for lean-burn engines under lean–rich atmosphere over mixed NSR-SCR catalysts: Influences of the addition of a SCR catalyst and of the operational conditions*, Appl. Catal. A: General, 365: 187–193
65. J. Wang, Y. Ji, Z. He, M. Crocker, M. Dearth, R. W. McCabe (2012) *A non-NH₃ pathway for NO_x conversion in coupled LNT-SCR systems*, Appl. Catal. B: Environmental 111–112: 562–570
66. J. Theis, J. Ura, R. McCabe (2010) *The Effects of Sulfur Poisoning and Desulfation Temperature on the NO_x Conversion of LNT+SCR Systems for Diesel Applications*, SAE

- Technical Papers, 2010-01-300 & SAE Int. J. Fuels Lubr. 3 (2010) 1–15, doi:[10.4271/2010-01-0300](https://doi.org/10.4271/2010-01-0300)
67. L. Xu, R. W. McCabe, *LNT + in situ SCR catalyst system for diesel emissions control*, Catal. Today 184 (2012) 83–94
 68. U. De La Torre, B. Pereda-Ayo, J. R. González-Velasco, *Cu-zeolite NH₃-SCR catalysts for NO_x removal in the combined NSR–SCR technology*, Chem. Eng. J. in press, doi:[10.1016/j.cej.2012.06.092](https://doi.org/10.1016/j.cej.2012.06.092)
 69. Bonzi R, Lietti L, Castoldi L, Forzatti P (2010) *NO_x removal over a double-bed NSR–SCR reactor configuration*. Catal. Today 151:376–385
 70. Forzatti P, Lietti L (2010) *The reduction of NO_x stored on LNT and combined LNT–SCR systems*. Catal. Today 155:131–139
 71. Castoldi L, Bonzi R, Lietti L, Forzatti P, Morandi S, Ghiotti G, Dzwigaj S (2011) 45 *Catalytic behaviour of hybrid LNT/SCR systems: Reactivity and in situ FTIR study*. J. Catal. 282:128–144
 72. Zukerman R, Vradman L, Herskowitz M, Liverts E, Liverts M, Massner A, Weibel M, Brillhac JF, Blakeman PG, Peace LJ (2009) *Modeling and simulation of a smart catalytic converter combining NO_x storage, ammonia production and SCR*. Chem. Eng. J. 155:419–426
 73. Weibel M, Waldbüßer N, Wunsch R, Chatterjee D, Bandl-Konrad B, Krutzsch B (2009) *A Novel Approach to Catalysis for NO_x Reduction in Diesel Exhaust Gas*. Top. Catal. 52:1702–1708
 74. Chatterjee D, Kočí P, Schmeiser V, Marek M, Weibel M (2010) *Modelling of NO_x Storage + SCR Exhaust Gas Aftertreatment System with Internal Generation of Ammonia*. SAE Technical Papers, 2010-01-0887
 75. Chatterjee D, Kočí P, Schmeiser V, Marek M, Weibel M, Krutzsch B (2010) *Modelling of a combined NO_x storage and NH₃-SCR catalytic system for Diesel exhaust gas aftertreatment*. Catal. Today 151:395–409
 76. Lindholm A, Sjövall H, Olsson L (2010) *Reduction of NO_x over a combined NSR and SCR system*. Appl. Catal. B 98:112–121
 77. Seo CK, Kim H, Choi B, Lim MT, Lee CH, Lee CB (2011) *De-NO_x characteristics of a combined system of LNT and SCR catalysts according to hydrothermal aging and sulfur poisoning*. Catal. Today 164:507–514
 78. Pereda-Ayo B, Duraiswami D, González-Velasco JR (2011) *Control of NO_x storage and reduction in NSR bed for designing combined NSR–SCR systems*. Catal. Today 172:66–72
 79. Liu Y, Harold MP, Luss D (2012) *Coupled NO_x storage and reduction and selective catalytic reduction using dual-layer monolithic catalysts*, Appl. Catal. B 121–122:239–251
 80. Seo CK, Kim H, Choi B, Lim MT (2011) *The optimal volume of a combined system of LNT and SCR catalysts*. J. Ind. Eng. Chem. 17:382–385
 81. Kota AS, Luss D, Balakotaiah V (2012), *Modeling Studies on Lean NO_x Reduction by a Sequence of LNT–SCR Bricks*, Ind. Eng. Chem. Res. 51:6686–6696
 82. Sullivan JA, Keane O (2007) *A combination of NO_x trapping materials and urea-SCR catalysts for use in the removal of NO_x from mobile diesel engines*. Appl. Catal. B 70:205–214
 83. Can F, Berland S, Royer S, Courtois X, Duprez D. *Composition dependant performance of CexZr1-xO2 mixed-oxide supported WO3 catalysts for the NSR–SCR coupled process*. submitted
 84. Berland S (2011) PhD thesis, University of Poitiers. <http://www2.ademe.fr/jsp/theses/these.jsp?num=2353&catid=13842>
 85. Lietti L (1996) *Reactivity of V2O5–WO3/TiO2 de-NO_x catalysts by transient methods* Appl. Catal. B 10: 281–297
 86. Kim MK, Kim PS, Cho BK, Nam IS, Oh SH (2012) *Enhanced NO_x reduction and byproduct removal by (HC + OHC)/SCR over multifunctional dual-bed monolith catalyst*. Catal. Today 184:95–106

87. Brandenberger S, Kröcher O, Tissler A, Althoff R (2008) *The State of the Art in Selective Catalytic Reduction of NOx by Ammonia Using Metal-Exchanged Zeolite Catalysts*. Catal. Rev. 50:492–531
88. Koebel M, Madia G, Elsener M (2002) *Selective catalytic reduction of NO and NO2 at low temperatures*. Catal. Today 73:239–247
89. Nova I, Ciardelli C, Tronconi E, Chatterjee D, Bandl-Konrad B (2006) *NH3–NO/NO2 chemistry over V-based catalysts and its role in the mechanism of the Fast SCR reaction*. Catal. Today 114:3–12
90. Forzatti P, Lietti L, Tronconi E (2002) Nitrogen Oxides Removal—Industrial in: I.T. Horvath (Ed.) *Encyclopaedia of Catalysis*, first ed., Wiley, New York, and references therein
91. Kato A, Matsuda S, Kamo T, Nakajima F, Kuroda H, Narita T (1981) *Reaction between nitrogen oxide (NOx) and ammonia on iron oxide-titanium oxide catalyst*. J. Phys. Chem. 85:4099–4102
92. Apostolescu N, Geiger B, Hizbullah K, Jan MT, Kureti S, Reichert D, Schott F, Weisweiler W (2006) *Selective catalytic reduction of nitrogen oxides by ammonia on iron oxide catalysts*. Appl. Catal. B. 62:104–114
93. Luo JY, Hou X, Wijayakoon P, Schmiege SJ, Li W, Epling WS (2011) *Spatially resolving SCR reactions over a Fe/zeolite catalyst*. Appl. Catal. B. 102:110–119
94. Ozkan US, Cai Y, Kumthekar MW (1994) *Investigation of the Reaction Pathways in Selective Catalytic Reduction of NO with NH3 over V2O5 Catalysts: Isotopic Labeling Studies Using 18O2, 15NH3, 15NO, and 15N18O*. J. Catal. 149:390–403
95. Odenbrand CUI, Bahamonde A, Avila P, Blanco J (1994) *Kinetic study of the selective reduction of nitric oxide over vanadia—tungsta—titania/sepiolite catalyst*. Appl. Catal. B. 5:117–131
96. Ramis G, Busca G, Bregani F, Forzatti P (1990) *Fourier transform-infrared study of the adsorption and coadsorption of nitric oxide, nitrogen dioxide and ammonia on vanadia-titania and mechanism of selective catalytic reduction*. Appl. Catal. 64:259–278
97. Kiel JHA, Edelaar ACS, Prins W, van Swaaij WPM (1991) *Performance of silica-supported copper oxide sorbents for SOx/NOx-removal from flue gas: II. Selective catalytic reduction of nitric oxide by ammonia*. Appl. Catal. B. 1:41–60
98. Hsu LY, Teng H (2001) *Catalytic NO reduction with NH3 over carbons modified by acid oxidation and by metal impregnation and its kinetic studies*. Appl. Catal. B. 35:21–30
99. Lobree LJ, Hwang IC, Reimer JA, Bell AT (1999) *Investigations of the State of Fe in H-ZSM-5*. J. Catal. 186:242–253
100. Long RQ, Yang RT (2000) *Characterization of Fe-ZSM-5 Catalyst for Selective Catalytic Reduction of Nitric Oxide by Ammonia*. J. Catal. 194:80–90
101. Wallin M, Karlsson CJ, Skoglundh M, Palmqvist A. (2003) *Selective catalytic reduction of NOx with NH3 over zeolite H-ZSM-5: influence of transient ammonia supply*. J. Catal. 218:354–364
102. Busca G, Larrubia MA, Arrighi L, Ramis G (2005) *Catalytic abatement of NOx: Chemical and mechanistic aspects*, Catal. Today 107–108:139–148
103. Koebel M, Elsener M, Madia G (2001) *Reaction Pathways in the Selective Catalytic Reduction Process with NO and NO2 at Low Temperatures*. Ind. Eng. Chem. Res. 40:52–59
104. Yeom Y, Henao J, Li M., Sachtler WMH, Weitz E (2005) *The role of NO in the mechanism of NOx reduction with ammonia over a BaNa–Y catalyst*. J. Catal. 231:181–193
105. Ciardelli C, Nova I, Tronconi E, Chatterjee D, Burkhardt T, Weibel M (2007) *NH3 SCR of NOx for diesel exhausts aftertreatment: role of NO2 in catalytic mechanism, unsteady kinetics and monolith converter modelling*. Chem. Eng. Sci. 62:5001–5006
106. Devadas M, Kröcher O, Elsener M, Wokaun A, Söger N, Pfeifer M, Demel Y, Mussmann L (2006) *Influence of NO2 on the selective catalytic reduction of NO with ammonia over Fe-ZSM-5*. Appl. Catal. B. 67:187–196

107. Hadjiivanov K, Knözinger H, Tsyntsarski B, Dimitrov L (1999) *Effect of Water on the Reduction of NO_x with Propane on Fe–ZSM-5. An FTIR Mechanistic Study*. Catal. Lett. 62:35–40
108. Lobree LJ, Hwang IC, Reimer JA, Bell AT (1999) *Investigations of the State of Fe in H–ZSM-5*. J. Catal. 186:242–253
109. Veley VH, (1993) *The Conditions of Decomposition of Ammonium Nitrite*, J. Am. Chem. Soc. 83:736–749
110. Romero Sarria F, Saussey J, Gallas JP, Marie O, Daturi M (2005) *In situ and operando IR study of adsorption sites for NH₄⁺ active species in NO_x–SCR via NH₃ using a Y zeolite*. Stud. Surf. Sc. Catal. 158(A):821–828
111. Grossale A, Nova I, Tronconi E, Chatterjee D, Weibel M (2008) *The chemistry of the NO/NO₂–NH₃ “fast” SCR reaction over Fe–ZSM-5 investigated by transient reaction analysis*. J. Catal. 256:312–322
112. Wilken N, Wijayanti K, Kamasamudram K, Currier NW, Vedaiyan R, Yezerets A, Olsson L (2012) *Mechanistic investigation of hydrothermal aging of Cu–Beta for ammonia 48 SCR*, Appl. Catal. B 111–112:58–66
113. Rahkamaa-Tolonen K, Maunula T, Lomma M, Huuhtanen M, Keiski RL (2005) *The effect of NO₂ on the activity of fresh and aged zeolite catalysts in the NH₃–SCR reaction*. Catal. Today 100:217–222
114. Tuenter G, Vanleeuwen WF, Snepvangers LJM (1986) *Kinetics and Mechanism of the NO_x Reduction with NH₃ on V₂O₅–WO₃–TiO₂ Catalyst*. Ind. Eng. Chem. Prod. Res. Dev. 25(4):633–636
115. Sun Q, Gao ZX, Chen HY, Sachtler WMH (2001) *Reduction of NO_x with Ammonia over Fe/MFI: Reaction Mechanism Based on Isotopic Labeling*. J. Catal. 201:88–99
116. Long RQ, Yang RT (2002) *Reaction Mechanism of Selective Catalytic Reduction of NO with NH₃ over Fe–ZSM-5 Catalyst*. J. Catal. 207:224–231
117. Long RQ, Yang RT (2001) *Temperature-Programmed Desorption/Surface Reaction (TPD/TPSR) Study of Fe–Exchanged ZSM-5 for Selective Catalytic Reduction of Nitric Oxide by Ammonia*. J. Catal. 198:20–28
118. Long RQ, Yang RT (1999) *Catalytic Performance of Fe–ZSM-5 Catalysts for Selective Catalytic Reduction of Nitric Oxide by Ammonia*. J. Catal. 188:332–339
119. Eng J, Bartholomew CH (1997) *Kinetic and Mechanistic Study of NO_x Reduction by NH₃ over H–Form Zeolites. II. Semi-Steady-State and In Situ FTIR Studies*. J. Catal. 171:27–44
120. Stevenson SA, Vartuli JC, Sharma SB (2002) *The Effects of Steaming and Sodium Exchange on the Selective Catalytic Reduction of NO and NO₂ by NH₃ over HZSM-5*. J. Catal., 208:106–113
121. Armaroli T, Simon LJ, Digne M, Montanari T, Bevilacqua M, Valtchev V, Patarin J, Busca G (2006) *Effects of crystal size and Si/Al ratio on the surface properties of H–ZSM-5 zeolites*. Appl. Catal. A. 306:78–84
122. Brandenberger S, Kröcher O, Wokaun A, Tissler A, Althoff R (2009) *The role of Brønsted acidity in the selective catalytic reduction of NO with ammonia over Fe–ZSM-5*. J. Catal. 268:297–306
123. Schwidder M, Kumar MS, Bentrup U, Pérez-Ramírez J, Brückner A, Grünert W (2008) *The role of Brønsted acidity in the SCR of NO over Fe-MFI catalysts*. Micro. Meso. Mater. 111:124–133
124. Védrine JC, Auroux A, Bolis V, Dejaifve P, Naccache C, Wierzchowski P, Derouane EG, Nagy JB, Gilson JP, van Hooff JHC, van den Berg JP, Wolthuisen J (1979) *Infrared, microcalorimetric, and electron spin resonance investigations of the acidic properties of the H–ZSM-5 zeolite*. J. Catal. 59:248–262
125. Topsøe NY, Pedersen K, Derouane EG (1981) *Infrared and temperature-programmed desorption study of the acidic properties of ZSM-5-type zeolites*. J. Catal. 70:41–52
126. Brüggemann TC, Vlachos DG, Keil FJ (2011) *Microkinetic modeling of the fast selective catalytic reduction of nitrogen oxide with ammonia on H–ZSM-5 based on first principles*. J. Catal. 283:178–191

127. Colombo M, Nova I, Tronconi E (2010) A comparative study of the NH₃-SCR reactions over a Cu-zeolite and a Fe-zeolite catalyst. *Catal. Today* 151: 223–230
128. Kieger S, Delahay G, Coq B, Neveu B (1999) *Selective Catalytic Reduction of Nitric Oxide by Ammonia over Cu-FAU Catalysts in Oxygen-Rich Atmosphere*. *J. Catal.* 183:267–280
129. Moretti G, Dossi C, Fusi A, Recchia S, Psaro R (1999) *A comparison between Cu-ZSM-5, Cu-S-1 and Cu-mesoporous-silica-alumina as catalysts for NO decomposition*. *Appl. Catal. B20*:67–73
130. Dossi C, Fusi A, Recchia S, Psaro R, Moretti G (1999) *Cu-ZSM-5 (Si/Al=66), Cu-Fe-S-1 (Si/Fe=66) and Cu-S-1 catalysts for NO decomposition: preparation, analytical characterization and catalytic activity*. *Microp. Mesop. Mater.* 30:165–175
131. Mizumoto M, Yamazoe N, Seiyama T (1978) *Catalytic reduction of NO with ammonia over Cu(II) NaY*. *J. Catal.* 55:119–128
132. Iwamoto M, Yahiro H, Tanda K, Mizuno N, Mine Y, Kagawa S (1991) *Removal of Nitrogen Monoxide through a Novel Catalytic Process. I. Decomposition on Excessively Copper-Ion Exchanged ZSM-5 Zeolites*. *J. Phys. Chem.* 95(9):3727–3730
133. Sjövall H, Olsson L, Fridell E, Blint R.J (2006) *Selective catalytic reduction of NO_x with NH₃ over Cu-ZSM-5—The effect of changing the gas composition*. *Appl. Catal. B.* 64:180–188
134. SeO C-K, Choi B, Kim H, Lee C-H, Lee C-B (2012) *Effect of ZrO₂ addition on de-NO_x performance of Cu-ZSM-5 for SCR catalyst*. *Chem Eng. J.* 191:331–340
135. Kwak J.H, Tran D, Burton S.D, Szanyi J, Lee J-H, Peden C (2012) *Effects of hydrothermal aging on NH₃-SCR reaction over Cu/zeolites*. *J. Catal* 287:203–209
136. Marturano P, Drozdová L, Kogelbauer A, Prins R (2000) *Fe/ZSM-5 Prepared by Sublimation of FeCl₃: The Structure of the Fe Species as Determined by IR, 27Al MAS NMR, and EXAFS Spectroscopy*. *J. Catal.* 192:236–247
137. Battistoni AA, Bitter JH, de Groot FMF, Overweg AR, Stephan O, van Bokhoven JA, Kooyman PJ, van der Spek C, Vankó G, Koningsberger DC (2003) *Evolution of Fe species during the synthesis of over-exchanged Fe/ZSM-5 obtained by chemical vapor deposition of FeCl₃*. *J. Catal.* 213:251–271
138. Hensen EJM, Zhu Q, Hendrix MMRM, Overweg AR, Kooyman PJ, Sychev MV, van Santen RA (2004) *Effect of high-temperature treatment on Fe/ZSM-5 prepared by chemical vapor deposition of FeCl₃: I. Physicochemical characterization*. *J. Catal.* 221:560–574
139. Joyner R, Stockenhuber M (1999) *Preparation, Characterization, and Performance of Fe-ZSM-5 Catalysts*. *J. Phys. Chem. B* 103:5963–5976 50
140. Sobalik Z, Vondrova A, Tvaruskova Z, Wichterlova B (2002) *Analysis of the structural parameters controlling the temperature window of the process of SCR-NO_x by low paraffins over metal-exchanged zeolites*. *Catal. Today* 75:347–351
141. Heinrich F, Schmidt C, Löffler E, Grünert W (2000) *A highly active intra-zeolite iron site for the selective catalytic reduction of NO by isobutane*. *Catal. Commun.* 2:317–321
142. Chen HY, El-Malki M, Wang X, van Santen RA, Sachtler WMH (2000) *Identification of active sites and adsorption complexes in Fe/MFI catalysts for NO_x reduction*. *J. Mol. Catal. A: Chem.* 162:159–174
143. Brandenberger S, Kröcher O, Tissler A, Althoff R (2010) *The determination of the activities of different iron species in Fe-ZSM-5 for SCR of NO by NH₃* *Appl. Catal. B;* 95: 348–357
144. Malpartida I, Marie O, Bazin P, Daturi M, Jeandel X (2012) *The NO/NO_x ratio effect on the NH₃-SCR efficiency of a commercial automotive Fe-zeolite catalyst studied by operando IR-MS*. *Appl. Catal. B.* 113–114:52–60
145. Roy S, Viswanath B, Hegde MS, Madras G (2008) *Low-Temperature Selective Catalytic Reduction of NO with NH₃ over Ti_{0.9}MO_{1.02}-δ (M = Cr, Mn, Fe, Co, Cu)*. *J. Phys. Chem. C.* 112:6002–6012
146. Verdier S, Rohart E, Bradshaw H, Harris D et al. (2008) *Acidic Zirconia Materials for Durable NH₃-SCR deNO_x Catalysts*. SAE Technical Paper 2008-01-1022
147. Rohart E, Kröcher O, Casapu M, Marques R, Harris D, Jones C (2011) *Acidic Zirconia Mixed Oxides for NH₃-SCR Catalysts for PC and HD Applications*. SAE Technical Paper 2011-01-1327

Chapter 20

Integration of SCR Functionality into Diesel Particulate Filters

Thorsten Boger

Notation

A_s	Parameter
c_p	Heat capacity
d_c	Collector diameter
d_h	Hydraulic diameter
d_{Pore}	Pore diameter
d_s	Soot particle diameter
D_{BM}	Diffusion coefficient Brownian motion
f_0	Friction factor
h	Heat transfer coefficient
k	Mass transfer coefficient
L_{ch}	Channel length
L_{W}	Effective wall thickness
p	Pressure
Pe	Peclet number
Q	Cumulative heat of reactions
R_j	Source term for reactions involving species j
t	Time
T	Temperature
u	Velocity
y	Volume or mole fraction
X	Soot load or concentration
ε	Porosity
ε_s	Void fraction of soot deposit
η	Viscosity

T. Boger (✉)

Corning Incorporated, Corning, USA

e-mail: BogerT@corning.com

Corning Environmental Technologies, Corning GmbH, Abraham-Lincoln-Str. 30,
65189 Wiesbaden, Germany

η_{BM}	Unit collector efficiency Brownian motion
η_{Int}	Unit collector efficiency interception
λ	Mean free path
κ	Permeability
ρ	Density
ζ	Constant

20.1 Introduction

Most modern diesel engine aftertreatment systems comprise functions to oxidize hydrocarbons and CO, reduce particulate emissions (mass and number), and reduce NO_x enabling compliance with ever tightening regulations. A typical system layout based on SCR as a means to reduce NO_x is shown in Fig. 20.1a. A diesel oxidation catalyst (DOC) is followed by a catalyzed soot filter (CSF) and the SCR catalyst. In most advanced systems targeting high NO_x conversion rates, an ammonia slip catalyst is installed post SCR catalyst. The system shown in Fig. 20.1a is representative of the majority of medium and heavy-duty systems designed to meet EPA 2010 and EU VI regulations as well as for heavier diesel passenger cars [1–5]. In some cases the SCR catalyst is installed upstream of the DPF [6]. For heavier passenger cars certified for advanced regulations similar system configurations with SCR are common, while lighter vehicles use in most cases either engine-based approaches or lean NO_x trap technologies, or combinations thereof. In all systems, the DOC provides primarily for oxidation of HC and CO as well as oxidation of NO to NO₂ to facilitate the low temperature, passive oxidation of soot in the DPF as well as to accelerate the SCR reactions. The DPF is reducing the particulate emissions in mass and number. In most cases, the DPF is coated with a light oxidation function to promote the oxidation of CO to CO₂ during active regenerations as well as to provide for additional NO to NO₂ oxidation, enhancing the passive regeneration of soot by NO₂ [7, 8] and enabling more favorable NO/NO₂ ratios for the downstream SCR component. The SCR catalyst reduces NO_x emissions using ammonia as reducing agent, typically derived from urea. Due to the potential of high temperatures post DPF, originating primarily from uncontrolled soot regenerations, zeolite-based SCR catalysts are often used in this configuration.

Although the configuration shown in Fig. 20.1a has proven to provide good functionality, there long has been a desire to combine some of the aftertreatment functionalities into fewer, multifunctional components. Integration of the SCR function or at least part of it into the DPF, as shown in Fig. 20.1b, is one such example. This desire for integration of SCR functionality is driven by several factors. One common theme is the objective of reducing the total packaging volume consumed by aftertreatment components, which has been growing significantly since the introduction of EU 4/IV and EPA 2007 regulations. Another

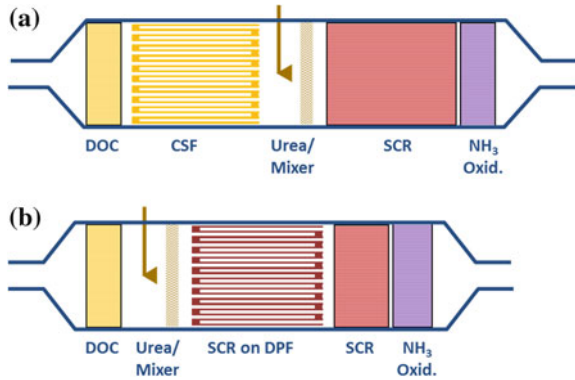


Fig. 20.1 Examples of diesel aftertreatment systems. **a** Conventional DOC-CSF-SCR system; **b** System with SCR integration into DPF

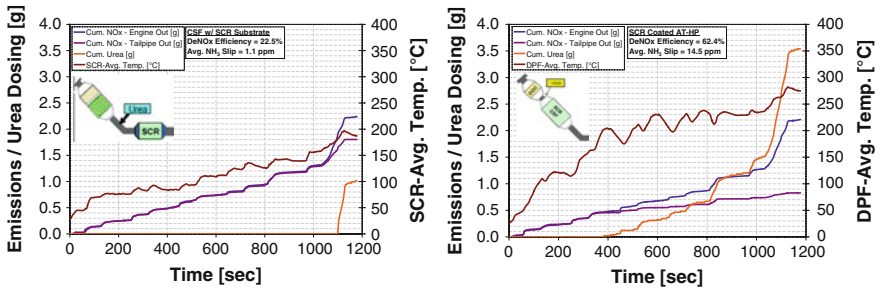


Fig. 20.2 Comparison of NO_x emissions and SCR temperatures for a light-duty diesel application with (left) a CSF + SCR and (right) SCR integrated DPF system [9]

driver of significance, especially considering future light-duty regulations and engines with lower exhaust temperatures, is the need to move the SCR components closer to the engine enabling higher operating temperatures and deNO_x efficiencies. An example demonstrating this benefit is shown in Fig. 20.2 [9]. In this example, the conventional system allows for urea dosing and deNO_x not until the very end of the emission cycle. The system with the SCR catalyst integrated into the close coupled filter, on the other hand, enables urea dosing already fairly early in the cycle, providing for significantly higher deNO_x efficiencies.

As common with all components that are designed to provide multiple functionalities we need to understand the trade-offs and compromises that have to be made to enable an optimized component and system. Objective of this contribution is to provide some of the basic considerations and fundamentals relevant to the combination of SCR catalysis and soot filtration. Since the general catalysis and function of the SCR catalyst is similar to the use in flow-through systems described in separate chapters of this book, the focus of this chapter will be on phenomena

that are introduced by the use of a particulate filter as substrate for the SCR catalyst. Examples of such phenomena are the impact of the accumulated soot and ash on the SCR reactions and vice versa, the pressure drop behavior of coated filters, the differences in the thermal robustness requirements compared to flow-through catalysts and, last but not least, the reduction of particulate emissions via filtration as additional emission relevant functionality of the integrated component.

20.2 Diesel Particulate Filter Technologies

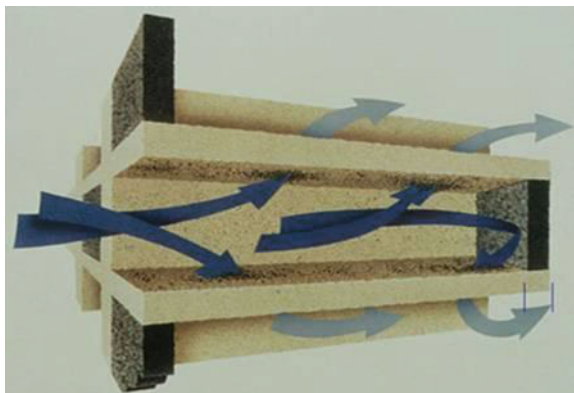
Although diesel particulate filters (DPF) were first introduced in the 1980s, their widespread use started with the first introductions in some EU4 passenger cars in the early 2000s time frame, i.e., [10–13], followed by the introduction for heavy-duty systems in compliance with US EPA 2007 regulations, i.e., [14, 15]. Since the introduction of the EU5 regulation, DPFs have essentially become the standard in all light-duty applications designed to meet this regulation. For heavy duty, DPFs are used in most systems certified to meet US EPA 2007 and 2010 regulations. The introduction of the new EUVI heavy-duty standard is expected to lead to the same result, with DPFs being installed on all engines certified to this regulation. In the non-road sector, we currently find a mix of systems relying entirely on DOC and SCR as well as systems that use a DPF as well [16].

In the following sections particulate filter technologies will be discussed in general and with respect to the unique needs for SCR integration. Since coating technologies for filters are somewhat different from those used for flow-through substrates and have a significant impact on the performance of the composite filter-catalyst component, some general discussion will be dedicated to this topic as well.

20.2.1 Diesel Particulate Filter Designs and Materials

Although a number of designs have been proposed over the years the dominating filter design used by the majority of applications is the wall-flow filter shown schematically in Fig. 20.3. The filter is made of an extruded honeycomb structure with walls made of a porous refractory ceramic. The channels are plugged in a checkerboard pattern at alternate ends. This results in a pattern that force the exhaust flow from the inlet channels, through the porous walls into the outlet channels. On the path through the porous wall particulates are removed by filtration.

Different refractory ceramics are used for the filter matrix. Most common are cordierite-, aluminum titanate-, and silicon carbide-based products [15, 17–21]. Typical physical properties for these materials are provided in Table 20.1. All materials can withstand very high temperatures. Key differences between these

Fig. 20.3 Wall-flow diesel particulate filter design**Table 20.1** Physical properties of common diesel particulate filter materials [18]

	Aluminum titanate composition	Cordierite composition	Silicon carbide
Intrinsic material density, g/cm ³	3.40	2.51	3.24
Specific intrinsic heat capacity, J/(g K) (500 °C)	1.06	1.11	1.12
Volumetric heat capacity ^a ; J/(cm ³ K) (500 °C)	3.60	2.79	3.63
Coefficient of thermal expansion; 10 ⁻⁷ / °C	~ 10 ^b	~ 6 ^c	~ 45 ^b
Thermal conductivity; W/mK (500 °C)	~ 1	~ 1	~ 12

^a Based on the material. Does not include porosity

^b Measured between 25 and 1000 °C

^c Measured between 25 and 800 °C

materials are (1) the thermal expansion, which is very low for the two oxides, cordierite and aluminum titanate, (2) the thermal conductivity, which is low for the oxides and higher for SiC and (3) the elastic modulus, which is low for the oxides providing robustness under thermal gradients.

In general, similar processes are used to manufacture the different filter technologies. The raw materials are batched and adjusted for their rheological properties enabling extrusion of the honeycomb matrix. This is followed by drying and high temperature firing. Materials such as cordierite and aluminum titanate are available in extruded, monolithic shapes up to very large diameters, enabled by their low thermal expansion and ability to withstand thermal stresses. SiC products have higher thermal expansion and require the use of segmenting techniques in which small extrudates are assembled, cemented, and contoured into the final filter product. In the final filter product, these segment seams typically reduce the available volume and area for filtration by ~5–8 % compared to a monolithic design. Another process step required for all materials is the plugging of the alternate channels.

Depending on the specific application, filter products with different levels of porosity and pore size are available. Porosities in the range of 40 % to roughly

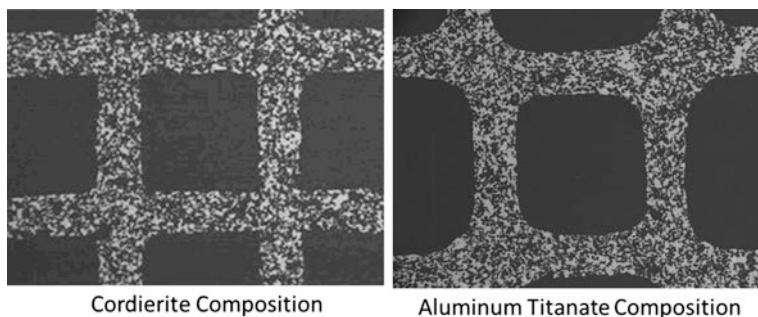


Fig. 20.4 SEM of honeycomb wall of high porosity cordierite (*left*) and aluminum titanate filters (*right*)

65 % are currently used for diesel particulate filters. As will be discussed later, most favorable for SCR integrated filter applications are filters with high porosity of 55 % or more. Figure 20.4 shows examples of SEM images taken from high porosity cordierite and aluminum titanate filter samples. An important feature that can be seen from these images is the excellent connectivity of the pores.

The pore size of diesel particulate filters is significantly larger compared to substrates used for flow-through catalysts. Most common are mean pore sizes in the range of 10–25 μm , compared to 2–5 μm for common flow-through substrates. The choice of pore size is determined by the trade-off between filtration and pressure drop. With respect to filtration, smaller pore sizes enable higher filtration efficiencies. This has to be balanced by the negative effect of small pore sizes on the wall permeability and ease of washcoating. Filters designed for integrated SCR applications typically have mean pore sizes in the medium to upper end of the given range (15–25 μm), mostly driven by the challenge to achieve high catalyst loads.

With respect to the cell design, square cells dominate. Common cell densities are between 200 and 350 cpsi, with the 200 cpsi dominating in heavy duty and the 300–350 cpsi dominating light-duty applications. The difference in cell density is primarily determined by the anticipated soot load in use, with higher cell densities being favorable if higher soot loads are anticipated.

The web thickness of filters is typically in the range of 8–18 mils (1 mil = 1/1000 inch or 25.4 μm), with 10–13 mil being most common. Especially in light-duty applications, filters with asymmetric cell design for increased specific ash storage have become widely used [22]. In these filters the cross-section of the inlet channels is increased by moving the cell webs toward the outlet channels. An example of a filter with such an asymmetric design is shown in Fig. 20.5 in comparison to a standard cell design filter. Various commercialized designs with asymmetric cell structures are available, e.g., ACT[®] (asymmetric cell technology), Octosquare, etc.

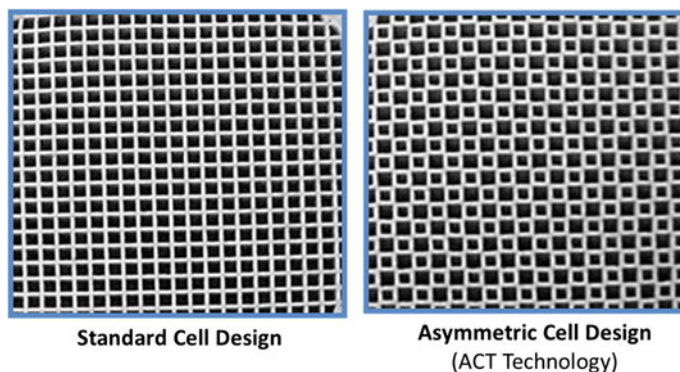


Fig. 20.5 Picture of a diesel particulate filter with standard (*left*) and asymmetric (*right*) cell design

20.2.2 Catalyst Coatings for Diesel Particulate Filters

In flow-through catalysts the active phase is typically coated onto the geometric surface area of the ceramic substrate material in form of a washcoat layer. An example is shown in Fig. 20.6(left). The substrates used to facilitate this approach typically have low porosity of $\sim 25\text{--}35\%$ and small pores of $2\text{--}5\ \mu\text{m}$. Flow is along the channels, low pressure drop, good mass transfer and catalyst performance is achieved by optimizing the web thickness, cell density, and coating layer thickness [23].

In filter applications the exhaust flow is from the inlet to the outlet channels across the filter walls, enabling effective filtration of particulates. This key difference in flow leads to different preferences with respect to the deposition and location of the catalyst coating. It has been observed that due to the small size of catalyst particles (e.g., zeolite crystals), being typically in the range of $\leq 1\text{--}5\ \mu\text{m}$, an on-wall coated catalyst layer deposited analogous to flow-through substrates can have very low permeability, resulting in high pressure drop. It is therefore more favorable to deposit the catalyst uniformly within the porous wall space, utilizing so-called in-wall coating technologies. To enable reasonable catalyst loadings with this method the above-mentioned high porosity filter technologies are used for SCR applications. An example of a zeolite coated filter is shown in Fig. 20.6(right).

From a high level, methods for coating filters are comparable to substrates. First, a slurry is prepared with the catalyst particles dispersed. The coating step can be done by immersion, waterfall, or vacuum assisted methods. Since the coating is done on plugged filters, requiring the slurries to flow from one channel to the corresponding opposite channel the properties of the slurries have to be adjusted, to facilitate the penetration of the slurry into the wall and prevent on-wall deposition. Examples of important parameters used to adjust the slurry properties are the solids load, the particle size, and the pH. The differences between open flow-through substrates and plugged filters also need to be considered during the blow

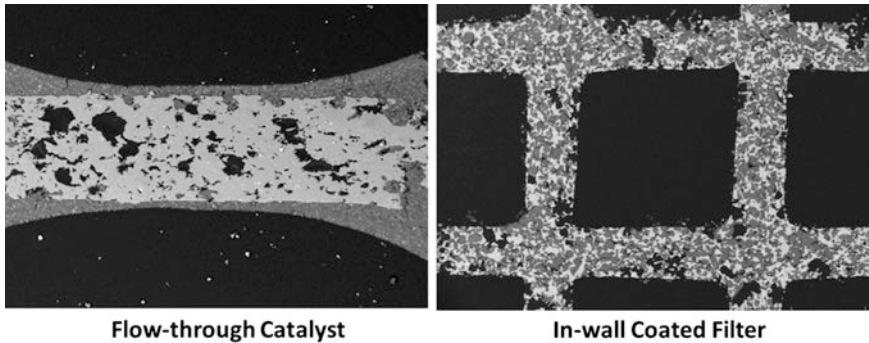


Fig. 20.6 Picture of an on-wall coated flow-through substrate (*left*) and an in-wall coated filter (*right*). Zeolite catalyst: *gray*; substrate/filter material: *white*; open pores: *black*

out step, during which excess slurry is removed. Final process steps are drying and calcining.

Comparing the maximum catalyst loadings on filters versus flow-through substrates, we find that filters are typically limited to about 65–85 % of what could be applied to a substrate, depending on the filter and coating technology. While for substrates the limit is usually determined by the adhesion of a thick layer of washcoat and the catalyst utilization, for filters it is primarily the available pore space for in-wall coatings and the associated increase in pressure drop when high washcoat loadings are applied. The latter effect will be further discussed in the next section.

20.3 Performance Considerations for SCR Integrated Diesel Particulate Filters

The performance of SCR integrated filters is characterized by the deNO_x performance, analogous to catalysts based on flow-through substrates, combined with the additional requirements for the filter component, such as pressure drop, filtration, and thermal robustness under regeneration conditions. In addition, we have to consider the presence of soot and ash within the component and their influence on all the performance aspects including the reactions. In the following sections, each of these characteristics will be discussed in terms of basic fundamentals and design aspects.

20.3.1 Pressure Drop and Permeability

The pressure drop of a filter is an application critical parameter of significant practical relevance, impacting engine power and fuel consumption. In this section,

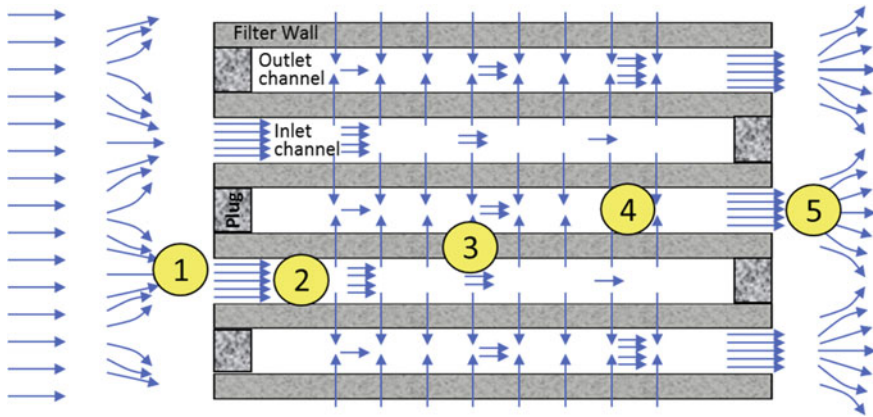


Fig. 20.7 Pressure drop contributions in wall-flow particulate filters

a brief description of the most relevant factors will be provided. There is a rich literature describing the modeling of the pressure drop of particulate filters in more detail. Examples are Refs. [24–26] and references therein.

The pressure drop of particulate filters is composed of five primary contributions, shown in Fig. 20.7. The inlet and outlet effects, shown as (1) and (5) in Fig. 20.7, are due to the contraction and acceleration as the gas enters the inlet channels and the expansion and deceleration of the gas as it exits the channels, respectively. Compared to flow-through substrates where inlet and outlet effects typically are less than 10 % of the total pressure loss, these pressure losses are larger in case of filters since only one half of the channels is open on each end. In addition, the open frontal area of filter honeycombs is often lower. For clean filters inlet and outlet effects can contribute as much as 30–40 % of the total pressure drop, especially at high flow rates. The turbulent entrance effects as result of the developing flow inside channels is typically lumped into these contributions. The inlet and outlet contributions are described by terms proportional to the kinetic energy, with the proportionality constant ζ_j .

$$\Delta p_j^{i/o} = \zeta_j \cdot \rho_j \cdot (u_j^{i/o})^2$$

The index j represents filter inlet or outlet, and i/o indicates the condition at the inlet or outlet of the filter. Correlations for ζ are empirical and typically include the open frontal area as variable. Examples are provided in Refs. [27, 28]. In general the outlet effects roughly are two times larger than the inlet effects.

For the frictional losses along the inlet and outlet channels (Fig. 20.7, index 2 and 4) existence of a laminar flow profile is generally assumed within the channels. The pressure drop along the channels can therefore be described analogous to flow-through substrates.

$$\Delta p_j^{\text{ch}} = 2 \cdot f_0 \cdot \eta \cdot \frac{L_{\text{ch}}}{d_h^2} \cdot u_j^{\text{ch,eff}}$$

The index j again represents the inlet and outlet channels. η , L_{ch} , and d_h represent the viscosity, effective channel length, and hydraulic diameter, respectively. The friction factor f_0 is equal to 14.2 for a square channel. With respect to the velocity to be used it has to be considered that at the inlet side (region of inlet plugs), all the flow is in the inlet channels, whereas the opposite is true on the outlet side (region of outlet plugs), with all the gas flow exiting via the outlet channels. Hence, the local flow rate in the inlet and outlet channels varies along the length, which has to be considered in the choice for $u_j^{\text{ch,eff}}$. To illustrate this, examples for the simulated axial velocity profiles in the inlet and outlet channel as well as across the filter wall are shown in Fig. 20.8. The different lines represent the velocity profiles at different time steps during a soot loading process. Initially no soot is present and the wall permeability is high. The resulting axial velocity profiles are nonlinear. As soot is accumulated the effective wall permeability is reduced and the resistance across the wall and soot layer starts to dominate. This yields to an almost uniform wall-flow velocity and linear velocity profiles along the inlet and outlet channels.

The last contribution to pressure drop comes from the resistance to flow across the filter wall (index 3 in Fig. 20.7), from the inlet to the outlet channels. It is worth noting that this is the only contribution which is determined by the porous microstructure of the filter. In general the pressure drop across the wall can be described by Darcy's law.

$$\Delta p^w = \eta \cdot \left(\frac{\Delta L_w}{\kappa} \right)_{\text{eff}} \cdot u^w$$

with ΔL_w as effective thickness, κ as permeability, and u^w as wall-flow velocity. It should be mentioned that in some references a second-order term (Forchheimer term) is considered as well. However, under most practical terms this term is small and can be neglected. The permeability of a clean wall is in general a function of the porosity, the pore size distribution, and the general morphology of the porous wall, considering for example the connectivity of the pore network. The simplest approaches to estimate the permeability are based on correlations utilizing the porosity and mean pore size only, as described for example in [29, 30].

$$\kappa_w = \frac{3}{200} \cdot \varepsilon \cdot \hat{d}_{\text{pore}}^2$$

Here, κ_w is the wall permeability, ε the porosity and \hat{d}_{pore} the mean pore diameter. These correlations can provide reasonable estimates for the permeability of clean, uncoated filter walls. Typical permeabilities are in the range of $\kappa_w = 1\text{--}6 \times 10^{-12} \text{ m}^2$. Coating of the porous filter wall with a catalyst changes the microstructure. The catalyst particles consume some of the pore space and change the effective microstructure. In addition, since the coating process has

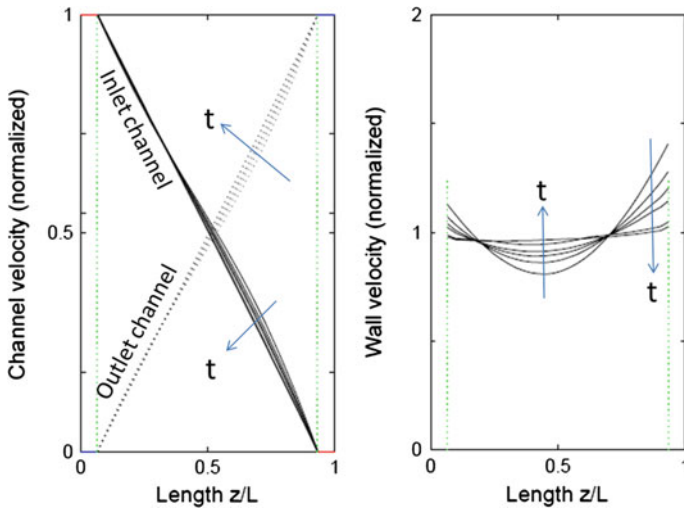


Fig. 20.8 Axial channel flow velocity (*left*) and wall-flow velocity (*right*) distribution at different time steps during soot loading of an initially clean DPF under steady-state flow conditions. The progression in time t is indicated by *arrows*

some directionality the use of bulk properties is less effective. In general, we observe a decrease in clean permeability that can often be described empirically by a power law or exponential function. A useful variable capturing the effect of coating in such a correlation is the ratio between the volume of the coating applied and the total pore volume available. This does, however, require the knowledge of the washcoat packing density, which is not easily accessible. In Fig. 20.9 are examples for the pressure drop and permeability as function of washcoat loading for two different filter designs. Both have the same microstructure and comparable web thickness, but Design 1 has a higher cell density than Design 2. For both designs we can distinguish two distinct regions. For low washcoat loadings the pressure drop is independent of the washcoat loading. In this region the permeability is high enough that the resistance to flow across the wall is not limiting; the microstructure has no significant impact on the pressure drop. The pressure drop observed is determined primarily by the filter geometry and design, as can be seen by comparing the two designs. At higher washcoat loadings, the pressure drop increases corresponding to the decrease in permeability. In this range we also observe that the Design 2, favorable for lower washcoat loadings, shows higher sensitivity and beyond a certain loading level even exceeds the pressure drop of Design 1. This is explained by lower washcoat capacity and surface area of this design.

The collection and deposition of soot also changes the permeability of the filter wall and can lead to a significant increase in pressure drop. Examples are shown in Fig. 20.10. Here, we have to distinguish between the effect of soot deposited inside the porous microstructure (deep bed filtration) and soot deposited onto the channel

Fig. 20.9 Examples for the pressure drop and permeability of wall-flow particulate filter as function of the washcoat load. Data are for filters with two different cell designs

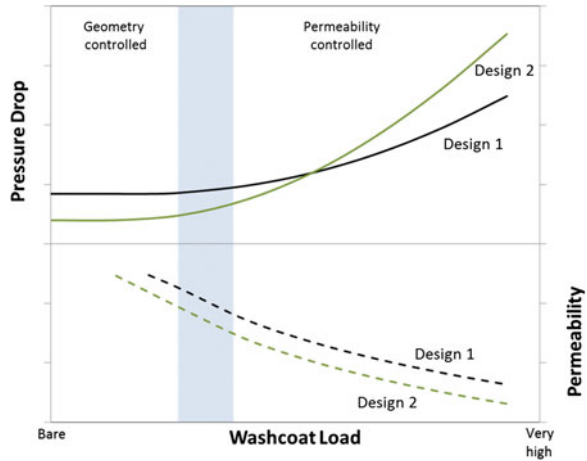
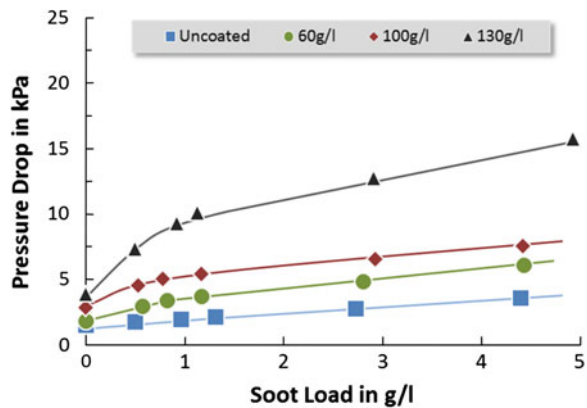


Fig. 20.10 Examples for the pressure drop of wall-flow particulate filter as function of the soot load. Lab pressure drop on 2'' samples with Printex U soot. Filter with Fe-ZSM-5 model coating



walls in form of a soot layer or soot cake. Soot deposited inside the microstructure can significantly reduce the wall permeability. Figure 20.11 illustrates this process showing how soot is deposited and accumulated in a synthetic microstructure, resulting in a decrease in effective permeability. This effect is observed already at low soot loads and is the result of the change in effective microstructure due to the deposition of soot combined with high local velocities inside the pore structure (for example, at pore necks, see Fig. 20.11). The latter amplify the effect of areas with increased resistance to flow. Advanced filter technologies with highly engineered microstructures address this effect and minimize the negative impact of soot deposited inside the microstructure. The effect of catalyst coating on the clean permeability was described above.

The effect of washcoating on the soot-loaded permeability can be even more significant. This can be seen from the comparison of the examples shown in Fig. 20.10. The difference in clean pressure drop is significantly smaller than the

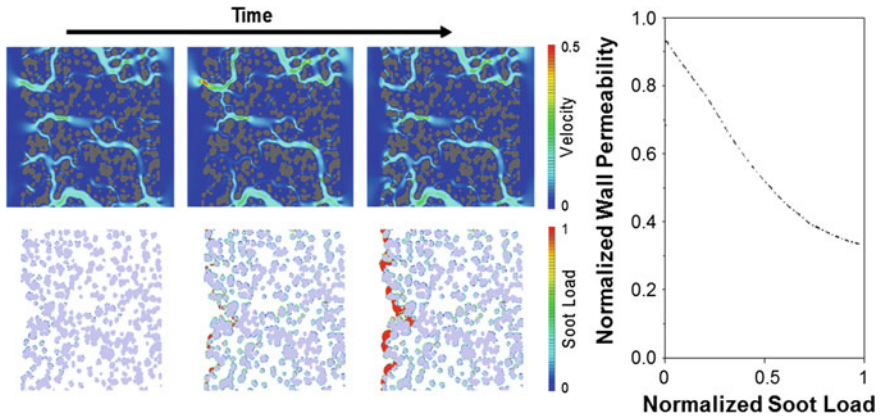


Fig. 20.11 Accumulation of soot inside the microstructure (*left*) and effect on permeability (*right*). Simulation results for a synthetic 2D microstructure with 64 % porosity and 18 μm mean pore size

difference in soot-loaded pressure drop. One explanation for this is that catalyst particles can deposit in the area of pore necks further restricting the flow.

Once a soot cake has formed on the wall surface, the further change in effective permeability of the wall/soot composite is determined to a large extent by growth of the low permeability soot layer. The soot permeability can be reasonably well described using the correlations provided for example in Refs. [29, 31, 32], with the Happel correlation being one example:

$$\kappa_{s,0} = \frac{3 - \frac{9}{2} \cdot (1 - \varepsilon_s)^{1/3} + \frac{9}{2} \cdot (1 - \varepsilon_s)^{5/3} - 3 \cdot (1 - \varepsilon_s)^2}{18 \cdot (1 - \varepsilon_s) \cdot (3 + 2 \cdot (1 - \varepsilon_s)^{5/3})} \cdot d_s^2$$

This correlation should be combined with the Stokes–Cunningham correction, which considers slip as continuum laws for drag breakdown for very small particles under certain operating conditions.

$$\kappa_s = \kappa_{s,0} \cdot \left[1 + \frac{2 \cdot \lambda}{d_s} \cdot \left(1.257 + 0.4 \cdot \exp\left(-1.1 \cdot \frac{d_s}{2 \cdot \lambda}\right) \right) \right]$$

In these correlations, ε_s is the void fraction of the soot deposit, d_s the soot particle size, and λ the mean free path of the fluid. Soot deposits are typically very low in density (50–150 g/l), equivalent to soot void fractions of $\sim 92\text{--}98\%$, and have particles with an electrical mobility diameter in the range of 50–150 nm. As a result, the permeability of the soot layer is in the range of 10^{-14} m^2 , more than two orders of magnitudes lower than the permeability of a clean wall.

Another parameter that needs to be considered with respect to pressure drop is the effect of ash. Particulate filters not only remove soot particles from the exhaust but also inorganic ash particles. These inorganic ash particles cannot be removed

during thermal regeneration but continue to accumulate over life. As a result, the volume and surface area available in the inlet channels decreases and the pressure drop increases. This has to be considered during the design and sizing of the filter. More details related to this consideration can be found for example in Refs. [28, 33].

To summarize the above details on pressure drop, the following generic design guidance may be used for SCR integration into a filter. With respect to cell design higher cell densities provide for larger filtration areas and lower wall-flow velocities. This can be beneficial for high soot loads or filters with very low coated permeability, but comes at the penalty of higher frictional losses in the absence of soot or low coating levels. With respect to the web thickness, thinner is in most cases favorable, but one has to ensure sufficient total pore volume for the catalyst coating (with the total pore volume being the product of porosity and wall volume). In addition, the mechanical strength of the filter component is a strong function of the web thickness. For the microstructure, higher porosities and larger pore sizes are favorable for higher permeabilities and coating capacity. This has to be traded off with the effect these variables have on mechanical strength, thermal robustness, and filtration.

20.3.2 Filtration

Intrinsically, the removal of particles is the primary emission functionality of the filter component. Particles found in diesel exhaust are typically in the range of 30–150 nm (described by their electrical mobility diameter). The filtration of these very small particles occurs based on different mechanisms. The most relevant ones are deposition due to Brownian motion, interception, and, to a lesser extent, inertia effects. This is shown schematically in Fig. 20.12. The filtration based on Brownian motion is related to the random movement or diffusion of small particles relative to the fluid stream lines. Once a particle gets close enough to a solid surface it can deposit and is removed from the fluid stream. Interception occurs when a particle's trajectory passes within one particle radius of the collecting body. In such a case, the particle traveling along that stream line gets in contact with the body and may be collected there. Deposition as a result of inertia is relevant for large, heavy particles only, which do not follow the fluid stream lines. In Fig. 20.13 an example is provided, showing the filtration efficiency as function of the particle size. The “V-shape” of the filtration efficiency curve with very high efficiencies for very small and very large particles is due to the transition between the different collection mechanisms. Very small particles are collected with high efficiency as a result of their significant Brownian motion. This effect decreases as the particles become larger. Very large particles are collected due to their inertia or, more relevant, as a result of them intercepting with the filter media. The efficiency of these mechanisms decreases as they become smaller. In the intermediate range typically between 80 and 200 nm, a minimum in filtration efficiency

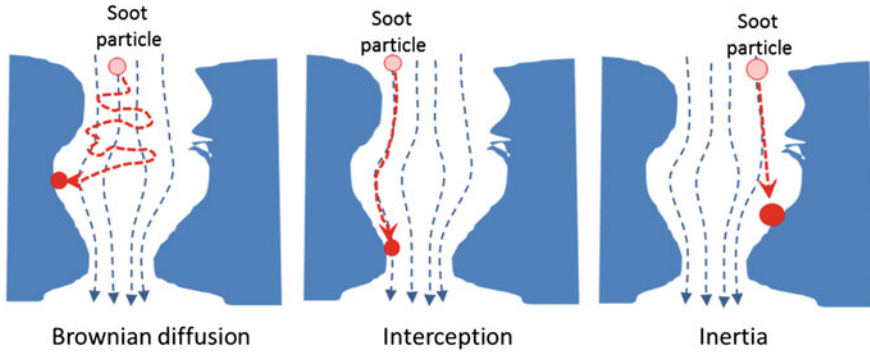
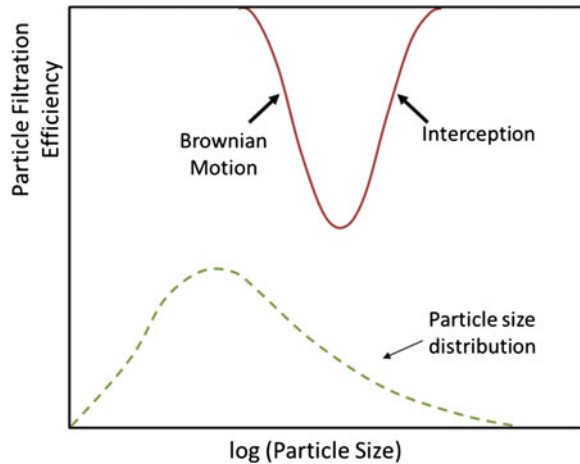


Fig. 20.12 Filtration mechanisms relevant for diesel particulate filters

Fig. 20.13 Filtration efficiency as function of the particle size



is observed, resulting from the transition between the mechanisms. In the following paragraphs only brief descriptions of the physics describing these mechanisms will be provided. More exhaustive information can be found for example in [29–32, 34, 35] and the references therein.

Most models represent the porous filter wall as assemblage of unit collectors, onto which the soot particles are deposited. The size and number of the unit collectors can be derived from the mean pore size and porosity, for example, by assuming spherical shape.

$$d_c = \frac{3}{2} \cdot \frac{1 - \varepsilon}{\varepsilon} \cdot \hat{d}_{\text{pore}}$$

For these unit collectors the efficiency can be determined using established correlations, as given for example in [29–32, 34, 35]. For Brownian motion the unit collector efficiency η_{BM} can be described by [35]

$$\eta_{\text{BM}} = 4 \cdot \frac{A_s^{1/3}}{\text{Pe}_i^{2/3}} \cdot (1 - \varepsilon)^{2/3}$$

With A_s being a parameter [35], primarily dependent on the porosity ε and Pe_i being the Peclet number. The Peclet number is proportional to the fluid velocity and the ratio between collector diameter d_c and diffusion coefficient for Brownian motion D_{BM} .

$$\text{Pe}_i = \frac{u_w}{\varepsilon} \cdot \frac{d_c}{D_{\text{BM},i}}$$

The particle size and temperature dependence of this collection mechanism is introduced via the Brownian diffusion coefficient, $D_{\text{BM}} \sim (T/d_s^2)$.

The collection of particles by interception can be described by [35]

$$\eta_{\text{Int}} = 1.5 \cdot N_r^2 \frac{[g(\varepsilon)]^3}{(1 + N_r)^s}$$

where $g(\varepsilon)$ and the power s are functions of the porosity and $N_r = d_s/d_c$, providing the dependence on soot particle and collector size. Examples for how the clean filtration efficiency changes with pore size and porosity are shown in Fig. 20.14 for some reference conditions. The strong effect of the pore size can be seen as well as the counterintuitive effect of porosity, which is based on the increase in residence time for the particles within the wall. To assess the sensitivity of other filter design parameters such as web thickness, cell density, size, etc., on the clean filtration efficiency a simple characteristic parameter has been introduced in [36].

As soot is accumulated within the porous filter (see also Fig. 20.11), the filtration efficiency increases [30, 34–36]. The soot accumulated acts as a very efficient filtration medium due to its very small collector size and the fact that it is deposited in the areas of flow through the porous wall. Filtration efficiencies close to 100 % across the entire size spectrum are reached at very low soot loads. This is of significant practical relevance since in use a diesel particulate filter is rarely free of soot.

The effect of catalyst coating on filtration efficiency is not easy to generalize and depends on the type of coating applied, the uniformity, as well as the washcoat loading. An effect often observed in laboratory experiments with filters having high washcoat loadings as common for SCR integration is shown schematically in Fig. 20.15. The initial or clean filtration efficiency decreases as washcoat is added (Fig. 20.15b). This is explained by the shorter residence time within the partially filled pore space and more flow being directed through larger pores, which remain less filled with coating. The evolution of filtration as soot is loaded, on the other hand, is accelerated and very high filtration efficiencies are observed already at

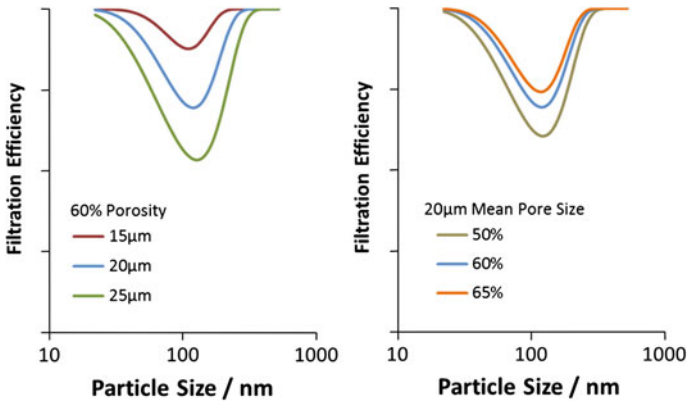


Fig. 20.14 Filtration efficiency as function of the mean pore size (*left*) and porosity (*right*). *Note* particle size is shown as electrical mobility diameter

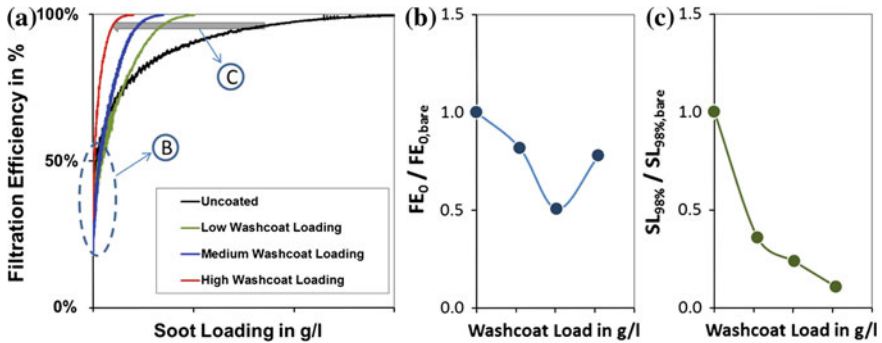
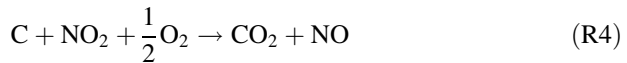


Fig. 20.15 Effect of washcoat loading on the filtration behavior. **a** FE versus soot load; **b** effect of washcoat on clean FE relative to uncoated; **c** effect of washcoat on soot load to reach 98 % FE relative to uncoated. *Note* Testing done at high space velocity to amplify effect

significantly lower soot loads (Fig. 20.15c). This is explained by the reduced pore volume that needs to be filled by soot to form an effective soot cake. With respect to practical applications, where commonly some soot is present, this can result in an observed improvement in filtration efficiency with coating, especially when significant quantities of SCR catalyst are applied.

20.3.3 Filter Regeneration, Thermal Management, and Durability

As described above, the accumulation of soot within the filter results in an increase in backpressure. This has negative impact on the power available and the fuel economy. To maintain the filter pressure drop within certain acceptable limits the soot has to be oxidized, which is commonly described as regenerating the filter. The interval after which the filter has to be regenerated is determined by the rate at which soot is accumulated and the maximum soot load that can be tolerated. For typical EU5 passenger cars the regeneration interval is typically in the range of 250–1500 km, depending on the engine raw emissions and the operating profile. City driving generally results in shorter intervals while highway driving enables longer intervals. Oxidation of soot is typically achieved by using either oxygen or nitrogen dioxide as oxidant [37–41].



While oxygen is abundantly available, the temperatures required to achieve appreciable reaction rates are >550 °C and rarely achieved under typical operation of diesel engines in light-duty and heavy-duty vehicles. Active measures are required to elevate the exhaust temperature to an appropriate level and this process is therefore called active regeneration. Examples for such measures applied to the engine controls are changes to the fuel injection timing, addition of late injections, intake air throttling, increase in load, etc. [42–45]. Typical duration of an active regeneration is 10–20 min, depending on the driving profile and conditions (transients, flow rate, temperature, etc.). Different approaches are used to monitor the accumulated soot mass and initiate active regenerations periodically. Examples of such monitoring and control strategies are provided in [42, 46–49]. Both open as well as closed loop methods are used. Open loop methods are either based on simple distance or time triggers or more advanced models, considering the engine-out soot emissions as function of the engine operation as well as the simultaneous oxidation of soot. Due to the lack of direct sensors, most closed loop strategies are based on a pressure drop measurement across the particulate filter. The signal combined with the calibrated correlation between pressure drop and soot load is then used to estimate the actual quantity of soot. In all cases an active regeneration request is triggered once a target soot load is observed.

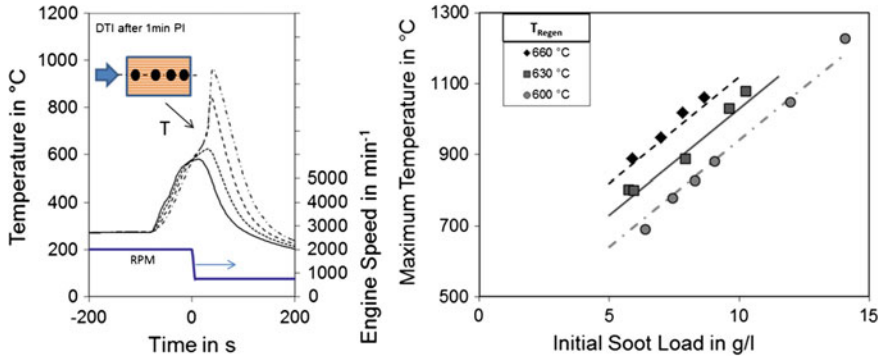


Fig. 20.16 Example of temperatures within an oxidation catalyst (Pt/Pd) coated DPF during a worst-case regeneration. *Left* temperatures at different axial locations; *right* maximum temperature as function of initial soot load and regeneration temperature

Typical exhaust gas temperatures during active regenerations are in the range of 550–650 °C, with most advanced strategies using lower temperatures during the initial phase of the regeneration and higher temperatures toward the end, i.e., [42, 45]. Such a staged or phased approach is essential to manage the heat release under the highly transient operating conditions observed on a vehicle. An example of a critical condition that can be observed is the case where a regeneration is just initiated, the soot oxidation has started, and then the engine changes to an idle operating mode. During engine idling, the exhaust flow rate is very low and the exhaust contains very high levels of oxygen. The abundance of oxygen results in the continuation of the soot oxidation, yet the low flow rate is insufficient to convectively remove the heat released [45]. As a result, the temperature within the filter can increase significantly. Examples of such a worst-case regeneration are shown in Fig. 20.16. The left diagram shows the transient evolution in local temperatures along the centerline of the filter, showing the rapid increase after the engine changed to an idle condition ($t = 0$ s). The right diagram shows examples for the dependence of the maximum temperature on the initial soot load as well as the exhaust (regeneration) temperature at start of the regeneration, before the change to engine idle. It should be mentioned that the temperatures observed are highly dependent on the conditions and the data shown are just examples for one set of parameters.

One important difference between typical DPF systems with oxidation catalyst coatings (containing Pt, Pd) and integrated SCR catalyst coatings is shown in Fig. 20.17 [9]. The heat release observed during a worst-case regeneration at a given soot load and condition is significantly higher for the oxidation coatings compared to integrated SCR technologies. This is a result of the effective catalysis of the oxidation of any CO formed during the soot oxidation (reaction R1 above). SCR catalysts show a significantly lower activity for such a CO oxidation and a

Fig. 20.17 Comparison maximum temperatures during worst-case regeneration conditions with different filter technologies. Adapted from [9]

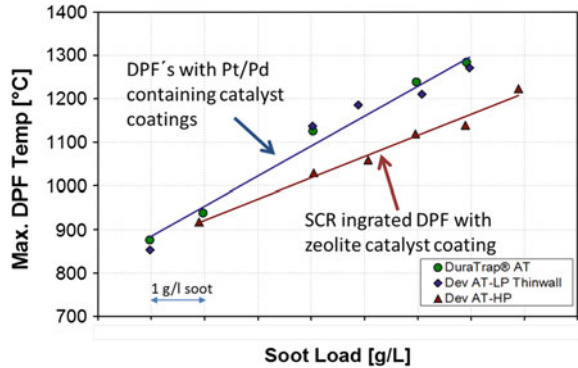
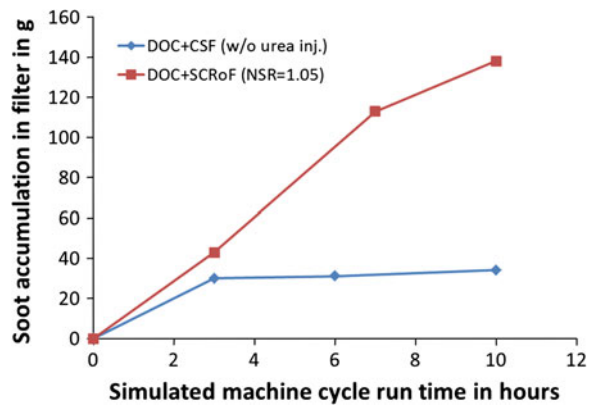


Fig. 20.18 Comparison of the soot load evolution of a DOC + CSF system versus a DOC + SCR on Filter (SCRoF) system under a transient engine operation. Data taken from [50]



significant fraction of the soot remains partially oxidized to CO, releasing less heat per mass of soot burned.

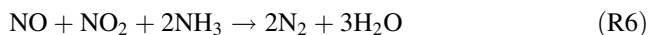
The oxidation of soot by NO₂ mentioned above occurs already at much lower temperatures of 300–550 °C, a range that can be observed during normal operation especially for heavy-duty applications. Since no active measure is required, this regeneration mechanism is called passive. For passive regeneration one limiting factor is the availability of NO₂. Most NO_x emitted by a diesel engine is in the form of NO. Typically, only a small fraction of 5–10 % is NO₂. To overcome this limitation some NO is oxidized to NO₂ over an upstream oxidation catalyst. In the case of oxidation catalyst coated filters, some of the NO₂ consumed by the soot oxidation is re-oxidized inside the filter wall and can be “recycled” via diffusion, further enhancing the passive regeneration rates. In case of SCR catalyst coated filters this latter mechanism does not occur. In addition, competition for NO₂ exists between the soot oxidation and the SCR reactions. This is shown in Fig. 20.18, taken from Ref. [50], in which the soot build up of a DOC + CSF is compared with a DOC + SCR on filter system. The CSF had a platinum containing coating and one can clearly see that a stable, low soot load is established after a short time

(balance point). For the SCR coated filter, this is not the case or would be expected at much higher soot loads. For light-duty applications, which typically do not rely on passive soot oxidation, this lower passive regeneration rate is not of major concern. For heavy-duty applications, however, this is of disadvantage and can result in penalties in fuel economy due to the higher operational soot and pressure drop levels as well as the need for more frequent active regenerations.

20.3.4 DeNO_x Efficiency

The general catalysis of SCR catalysts applied to filter substrates is identical to the more conventional flow-through substrates. Differences exist with respect to the flow pattern, which includes flow across the catalyst coated porous wall in addition to the flow along the channels. Hence, transport of the reactive species occurs not only by diffusion from the gas bulk to the catalyst (as for flow-through catalysts) but also by means of a convective flow-through the catalyzed wall. The same is obviously true with respect to the heat transfer. For conventional flow-through catalysts, some effect of cell density can be observed, primarily at higher temperatures where mass transfer becomes limiting [23]. For filters, the range of cell densities used is significantly smaller ranging typically only from 200 to 350 cpsi and no significant effect has been reported so far.

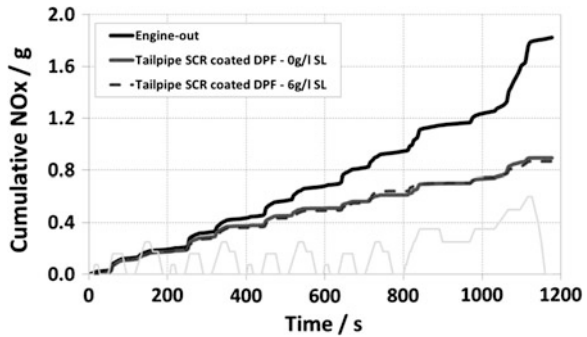
The presence of soot accumulated in close proximity to the catalyst is another difference of filters with integrated SCR functionality leading to competition for NO₂. The NO₂ entering the filter can either react with accumulated soot according to the passive soot oxidation reactions mentioned above, (R3)–(R5), or the NO₂ can react within the SCR reaction system promoting, for example, the rate of deNO_x via the fast SCR route, (R6).



Under most application conditions the rate of the SCR reactions exceeds the rate of the soot oxidation. This is especially true under low to medium temperatures as commonly found in light-duty emission cycles. Under these conditions, no difference in deNO_x efficiency was observed between clean filters and filters loaded with 6–8 g/l of soot [51, 52], see Fig. 20.19. This was also shown in Ref. [53] under laboratory test conditions with a NO₂/NO_x ratio of 0. In the same study, either no effect of the presence of 5 g/l soot or a slightly reduced activity was reported for NO₂/NO_x = 0.5 and temperatures above 200 °C. At a high NO₂/NO_x ratio of 1 a beneficial effect of soot was shown for temperatures below 275–300 °C [53]. This could be explained by some consumption of NO₂ reacting with soot according to (R3)–(R5) and changing the SCR reaction pathways toward the faster reactions involving NO and NO₂.

The amount of ammonia stored in the filter is of relevance to transient operation and cold start conditions. In [53], it was shown that despite its high surface area the

Fig. 20.19 Example of DeNO_x efficiency over NEDC with a clean and a soot-loaded filter with integrated SCR catalyst, adapted from [51]. *Gray line at the bottom indicates the vehicle velocity*



soot stored in the filter adds no or only a negligible ammonia storage capacity. As mentioned above, over the life of the filter ash also accumulates within the inlet channels. The ash can deposit on the walls as well as in the rear of the filter in form of a plug. The ash plug in the rear of the filter can affect the deNO_x efficiency since the wall-flow region with intimate contact between gas and catalyst is reduced and in the region of the ash plug mass transfer occurs by diffusion from the outlet channel to the wall only.

With respect to aging one has to distinguish between thermal aging and poisoning. Poisoning can be expected to be similar to flow-through catalysts with the additional potential for accumulated ash interacting with catalyst. With respect to the ash it should be mentioned that we typically do not see any significant ash quantities penetrating into the pore structure. Hence, if the coating is located inside the pores (or the outlet channel) the ash and catalyst will be spatially separated. The thermal exposure during active regenerations and the above-described worst-case conditions are significantly different from the conditions typically experienced by a standard flow-through SCR catalyst. This needs to be considered with respect to the selection of the catalyst, the selection of the filter technology and the durability evaluations. Typical durability testing with filters is done by performing a large number of regenerations and then test for filtration and deNO_x performance. Most severe are repeated worst-case regenerations, for example, under the above described drop to idle conditions. Under these conditions, local peak temperatures inside the filter can be in the range of 1000 °C and more. The number of worst-case regenerations that should be used in these durability tests depends on the application. In [54], it was shown for several test vehicles that under normal operating conditions only a small fraction of regenerations actually lead to severe conditions. In general, the conditions are expected to be more severe in passenger car applications compared to heavy-duty applications, since the former experience often a more transient driving profile with higher soot loads as well as more frequent idling events. Figure 20.20 shows examples [51] for several zeolite coated filter samples exposed to a larger number of worst-case regenerations with peak temperatures in the range of 1100 °C. Similar data can be found in other references, for example [52]. The data demonstrate that advanced filter and

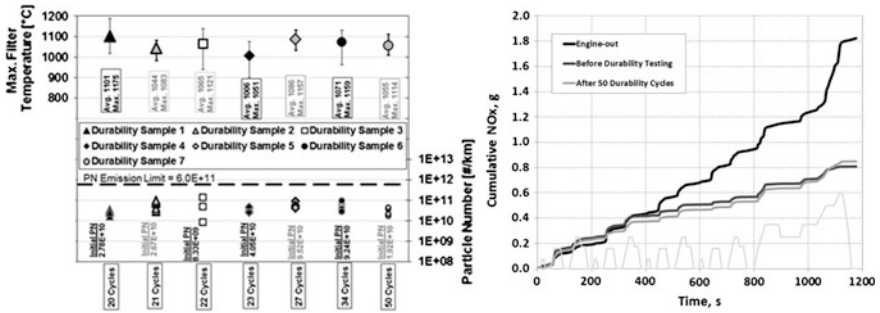


Fig. 20.20 Examples of durability test results over repeated worst-case regenerations with zeolite SCR catalyst coated high porosity aluminum titanate filter [51]

catalyst technologies can maintain low particulate emissions over such harsh conditions as well as maintain good deNO_x activity. To understand the limited effect on catalyst activity shown in this example, it has to be mentioned that the temperature distribution within the filter during these extreme regenerations is highly nonuniform. The peak temperatures are observed in small regions, typically in the back of the filter, and for very short durations only [54]. As a result, the catalyst primarily deactivates locally with larger portions of the filter being aged at significantly milder conditions.

20.4 Modeling of SCR Integrated Particulate Filters

The modeling of particulate filter components has been described in a large number of publications. Examples are Refs. [36, 55–62]. In general, one has to distinguish between simple 0D models, treating the entire filter as one uniform body, and more detailed 1D up to 3D models. For pressure drop and filtration simulations, simple and fast 0D models are often sufficient and provide for an efficient engineering tool. The correlations that are used in these models have been described in the above sections. For some control algorithms, 0D models have been used to simulate the thermal behavior and the reactions occurring inside the filter, e.g., [45]. However, for a better understanding of the phenomena occurring inside the filter and more quantitative description 1D models, assuming uniform flow, temperature, and concentrations in the radial direction, have proven useful yet still efficient. Higher dimensional models are required to consider radial nonuniformities in flow, temperature, or soot loading. Since these models are computationally more expensive their use is typically limited to cases where the additional information is critical. We will limit the discussion to 1D models. In Fig. 20.21 a schematic of a filter with the relevant terms is shown. Due to the design of the filter, one has to distinguish between three axial regions, the two plug zones and the center of the filter representing the main part, and three phases, the

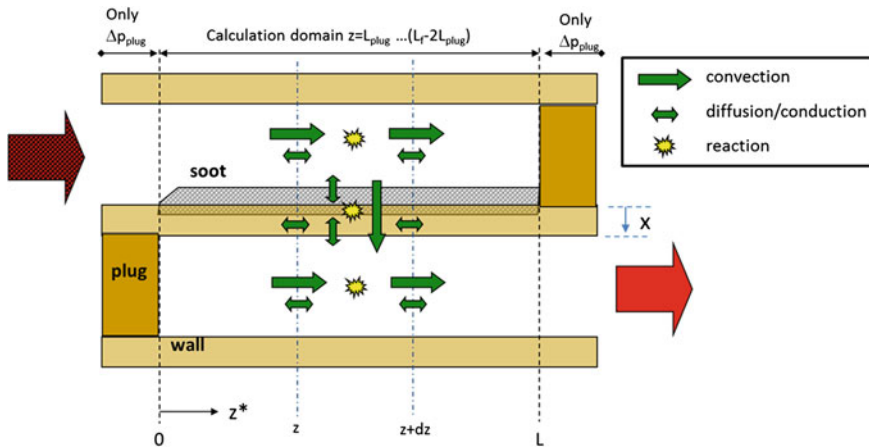


Fig. 20.21 Schematic of filter model

gas phase in the inlet and outlet channel and the wall (solid) phase. The latter phase also includes the soot deposited. The inlet and outlet plug regions can be described analogous to flow-through catalysts and will not be further discussed here. In the main filter region, the gas phase in the inlet and outlet channels is typically treated as locally uniform across the channel and the equations for conservation of mass, momentum, and energy apply. In the inlet channel, we further have to consider for the accumulation of soot (and ash) and the resulting change in the open channel area. The resistance of the flow across the soot layer is best considered in the equations describing the flow across the wall. The wall phase can be either treated as uniform from inlet channel to outlet channel surface or changes across the wall (x -direction in Fig. 20.21) can be considered. Convective flow within the wall in axial direction (z -direction) can typically be neglected, enabling the use of simpler 1D + 1D models, i.e., [36, 62]. The resistance to flow across the wall is described as Darcy flow by the local effective permeability, for which the correlations described in a previous section can be used. Although considered in some references, we have found that the contribution from the second-order term for wall-flow is typically small and can often be neglected. With respect to the source terms do conventional Sh- and Nu-numbers for square channels describe the diffusive/conductive mass and heat transfer between the gas and wall phases reasonably well. Reactions are considered where they occur, i.e., homogeneous gas phase reactions within the respective gas balance and catalyzed reactions within the wall phase equations. Soot oxidation is considered within the wall phase equations only. A summary of model equations for the example of a 1D description of the filter as described in Ref. [56] is provided in Table 20.2 with the notation adapted and the corresponding species equations added. Unlike the equations in [56] the effect of soot on the energy storage and axial thermal conductivity is neglected, since these contributions are

Table 20.2 Model equations (ID) for a wall-flow filter adapted from [56] and with species conservation equations being added

Conservation of mass	Inlet channel	$0 = -\frac{\partial}{\partial z}(d_f^2 \rho_{g,i} u_i) - 4d_f \rho_{g,w} u_w$
	Outlet channel	$0 = -\frac{\partial}{\partial z}(d_o^2 \rho_{g,o} u_o) + 4d_o \rho_{g,w} u_w$
Conservation of gas species	Inlet channel	$0 = -\frac{\partial(u_{g,i,j})}{\partial z} - \frac{4}{d_i} u_w y_{g,i,j} + \frac{4}{d_i} k_{i,j} (y_{w,j} - y_{g,i,j}) + R_{i,j}$
	Wall	$\epsilon \frac{\partial y_{w,j}}{\partial t} = \frac{4}{d_o} (k_{i,j} + u_w) (y_{g,i,j} - y_{w,j}) + \frac{4}{d_i} k_{o,j} (y_{g,o,j} - y_{w,j}) + R_{w,j}$
	Outlet channel	$0 = -\frac{\partial(u_{g,o,j})}{\partial z} + \frac{4}{d_o} u_w y_{w,j} + \frac{4}{d_o} k_{o,j} (y_{w,j} - y_{g,o,j}) + R_{o,j}$
Conservation soot	Wall	$\frac{dX_s}{dt} = -\frac{4}{d_i} y_{i,s} \rho_s u_w + R_{w,s}$
Conservation of energy	Inlet channel	$0 = -c_{pg,i} \rho_{g,i} u_i \frac{\partial T_{g,i}}{\partial z} + \frac{4d}{d_i} h_1 (T_w - T_{g,i})$
	Wall	$c_{p,w} \rho_w L_w \frac{\partial T_w}{\partial t} = h_i (T_{g,i} - T_w) + h_o (T_{g,o} - T_w)$ $+ \rho_{g,w} u_w (c_{pg,i} T_{g,i} - c_{pg,w} T_w) + \lambda_w L_w \frac{\partial^2 T_w}{\partial z^2} + Q$
	Outlet channel	$0 = -c_{pg,o} \rho_{g,o} u_o \frac{\partial T_{g,o}}{\partial z} + \frac{4}{d_o} (h_o + c_{pg,w} \rho_{g,w} u_w) (T_w - T_{g,o})$
Conservation of momentum	Inlet channel	$0 = -\frac{\partial p_i}{\partial z} - \frac{\partial}{\partial z}(\rho_{g,i} u_i^2) - \frac{2\phi_i \mu_i}{d_i}$
	Wall	$0 = -(P_i - P_o) - \mu_w \left(\frac{L_w}{K_w} + \frac{d}{2K_s} \ln \left(\frac{d}{d_i} \right) \right) u_w$
	Outlet channel	$0 = -\frac{\partial p_o}{\partial z} - \frac{\partial}{\partial z}(\rho_{g,o} v_o^2) - \frac{2\phi_o \mu_o}{d_o^2}$

Note The contribution from soot on energy storage and thermal conductivity considered in [56] were neglected

typically small compared to the contributions of the filter solid. In the equations d is the channel diameter, ρ the density, u the velocity, c_p the heat capacity, T the temperature, h and k the heat and mass transfer coefficients, λ the thermal conductivity, μ the viscosity, L_w the wall thickness, κ the permeability, and f_o the friction factor. The indices i and o denote the values for the inlet and outlet channels, respectively, and w and s the wall and soot phase. The model neglects thermal conductivity and axial diffusion in the gas phase and treats the gas phase in both channels as quasi-steady-state. For soot a common assumption is that it is retained within the wall with high filtration efficiency and in the equations of Table 20.2 an ideal filtration efficiency of 100 % is assumed. R_j represents the sum of all reactions involving species j and Q is the cumulative heat release upon all reactions occurring. As initial conditions the values at $t = 0$ s are used. Prior to the simulation it might be required to initiate the axial flow field. A boundary condition is that at $z/L = 0$ the mass flow is equal to the exhaust flow for the inlet channel, whereas it is zero in the outlet channel. The opposite is true for the outlet, $z/L = 1$, where the mass flow in the inlet channel equals zero and is equal to the exhaust flow rate in the outlet channel. The pressure boundary condition is defined at the outlet and is equal to the ambient pressure plus the pressure drop across any components downstream of the filter.

20.5 Application Examples

In this section, some of the published studies related to SCR integration into the particulate filter will be discussed. The discussion is separated into light-duty passenger car applications and heavy-duty or non-road applications.

20.5.1 Light Duty

The advantage of a more compact, packaging space reduced system is discussed in Refs. [63–66]. The systems used in these studies were all for heavier vehicles targeting primarily certification for US regulations. Lee et al. [63] discuss the potential and limitations of a system with Cu/Zeolite-based SCR catalyst integrated into the DPF for a pick up truck equipped with a 4.9 l prototype light-duty diesel engine. Filters with 200 and 300 cpsi were used. The observed NO_x reduction for the integrated SCR/DPF technology was found to be comparable with that of the standard Cu-based flow-through SCR technology when tested over cold start FTP and US06. These results were found to be independent of the level of soot loading in the filter (tested up to 5 g/l). The authors did observe degradation in deNO_x performance after experiments with active regenerations. Authors from the same group [9] report on an additional study in which they repeated up to 300 soot loading and regeneration cycles to simulate 120 k miles of operation. Regeneration was initiated at 4 g/l soot and a target temperature of 625 °C. The

deNO_x efficiency of the aged systems decreased when compared to the fresh performance. The level of change depended on the technology and aging. The pressure drop of the integrated system was found to be higher compared to a conventional DPF plus SCR system. The maximum temperatures observed during worst-case drop to idle regenerations were about 100 °C lower compared to a CSF. The main benefit of the integrated system referenced is the reduced packaging volume. Cavataio et al. [65] discuss laboratory results obtained with different catalyst and filter technologies. In the laboratory tests, the coated filters showed comparable deNO_x performance as conventional flow-through technologies. The higher backpressure was mentioned as a concern and area for improvement. In [66], the same group reports on promising results with integrated SCR on filter systems tested on a Land Rover with a 2.7 l V6 diesel engine. The system had both an SCR coated filter as well as a conventional SCR component. Placing the conventional SCR component upstream of the coated filter was found to be more favorable.

References [9, 51, 52, 67–69] discuss the advantage of integrated SCR-filter systems with respect to improved emissions performance in cold start cycles as result of the closer coupled location. Harth [67] reports on data of SCR integrated filter systems tested under light-duty conditions. The closer coupled location of the integrated system enables significantly lower NO_x emissions over the NEDC compared to a conventional DPF plus SCR system. Excellent stability, comparable to a conventional system is shown over simulated 180,000 km with active regenerations every 800 km. Excellent stability under repeated regeneration conditions expected for light-duty systems is also shown in Refs. [51, 70]. Stiebels [52] and Boorse [68] show data on the sensitivity to NO₂/NO ratio entering the coated filter, with higher deNO_x efficiencies at higher NO₂/NO_x ratios. In [69], the sensitivity with respect to the NO₂ ratio was reported to be low for the Cu-zeolite catalyst used. Ballinger et al. [71] show data for cordierite and SiC filters demonstrating comparable performance under hot test cycle conditions. Unfortunately no cold start cycle data were reported where a benefit of the lower thermal mass and lower thermal conductivity cordierite filter could be expected. The authors also show data comparing the pressure drop of zeolite coated filters with conventional oxidation catalyst coated filters (CSF); at low soot loads roughly 30 and 130 % higher values are shown for the SCR catalyst coated cordierite and SiC filters, respectively.

A commercial application has been reported by Volkswagen for some EU6 vehicle applications of their new 1.6 and 2.0 l TDI engines [72]. The system comprises a close coupled DOC followed in short distance by an SCR catalyst coated DPF. In addition, a slip catalyst with combined SCR and oxidation functionality is installed downstream of the DPF. The urea injection is located in-between the DOC and DPF components and a static mixer is used to improve distribution and evaporation within the limited space. Due to the high temperatures that can occur in this very close coupled position, a water-cooled urea injector was selected and the supply lines for the aqueous urea solution are made of highly temperature resistant materials.

20.5.2 Heavy Duty

The reduction in overall aftertreatment packaging volume as well as the potential for improved deNO_x functionality as result of an increased SCR catalyst volume are the key features discussed in publications related to heavy-duty systems. In [73], Oladipo et al. demonstrate good conversion efficiency of SCR catalyst coated filters over several heavy-duty emission cycles. The performance, however, was slightly less compared to flow-through catalysts with the same catalyst. The authors observed that, with respect to the washcoat technologies considered, the effect on pressure drop is more relevant than the effect on conversion. Some of the technologies had pressure drop comparable to a reference CSF. The authors did observe some negative effect of soot on deNO_x efficiency. Naseri et al. [74] discuss the concept of replacing the oxidation catalyst coated filter in a DOC + CSF + SCR system by an SCR catalyst coated filter to enable higher overall deNO_x conversions. The total component volume as well as the flow-through SCR components were kept the same. The testing was done on a US 2007 heavy-duty engine. In case of the integrated SCR-filter system, the engine was operated without EGR at high engine out NO_x emissions of 5 g/(hp h). The conventional system was tested at the same high NO_x as well as at a level of 1–1.5 g/(hp h). At equal operating conditions, the system with integrated SCR-filter component provided better deNO_x efficiency enabling operation at higher engine-out NO_x and improved fuel economy. The authors also report that the integrated SCR-filter system demonstrated better passive regeneration capability under higher engine out NO_x conditions as compared to the CSF system under lower engine out NO_x. Tan et al. [75] report on a system consisting of two DOC's followed by a flow-through SCR component and then an SCR coated filter. In addition, a reference system with CSF in the same rear position was tested. The pressure drop results show a 48 and 52 % higher pressure drop for the SCR integrated filter compared to the CSF when tested clean and at 5.2 g/l soot, respectively. These values resulted in 9 and 18 % higher system pressure drop, respectively, but were still within the design targets for the system. The soot regeneration efficiency of the SCR coated filter was found to be slightly lower but was recovered by minor adjustments to the strategy. The emission tests showed the potential for an SCR volume reduction of 51 and 44 % for the US06 and HD FTP emission cycle. The opportunity for downsizing the aftertreatment equipment is also discussed in Refs. [76, 77] targeting EU VI heavy duty applications. The authors report high NO_x conversion efficiencies as well as particle number emissions over WHTC and WHSC below EUVI limit. Results from some limited heavy-duty vehicle tests showed sufficient passive soot burn on highway but some build up and increase in pressure drop in urban driving. The aftertreatment volume and mass reduction potential reported in [77] was 52 and 48 %, respectively.

Tang et al. [50] report on experiments of a heavy-duty aftertreatment system comprising a DOC followed by a DPF with integrated SCR functionality and an ammonia slip catalyst. The size of the DPF was 12'' diameter and 12'' in length

and the ratio of filter volume to engine displacement was 2.4. The system was designed for passive operation of the DPF and testing was done under steady state conditions as well as over the NRTC. A high deNO_x efficiency was observed with values of 87 and 90 % for operation at the C20 and A100 conditions, respectively. For the hot NRTC with a soot-free filter an efficiency of 92.6 % is reported, which was increased even further to 95.5 % when 6.2 g/l soot was present. This enhancement was explained by the consumption of some of the NO₂ under the conditions of a high cycle cumulative NO₂/NO_x ratio of ~ 68 %. The authors also discuss the reduced passive soot oxidation compared to a conventional CSF system and discuss solutions how this could be compensated. The authors demonstrate that if the ammonia dosing is reduced from a ratio of 1.05 to 0.5, intentionally accepting a reduction in deNO_x, the soot accumulation could be significantly reduced, with the balance point and steady state pressure drop being reduced by almost 50 % to a value roughly equal to the condition with no ammonia being dosed. Another approach proposed is to calibrate the engine to operation at higher NO_x/PM ratios.

20.6 Summary

The integration and combination of the SCR and filter functionality into one component offer some attractive features. The packaging space as well as the number of components required for the aftertreatment can be reduced. It should be mentioned that this reduction in components and size often does not lead to a reduction in system pressure drop since the effect of catalyst coating on the pressure drop is more expressed for filters than for flow-through substrates. Another advantage, attractive especially for applications with low temperatures or cold start challenges, is the potential to move the SCR function closer to the engine. This enables higher temperatures and the potential for higher deNO_x efficiencies. The benefits come at the cost of increased complexity. Examples being the competition for NO₂ by the SCR reactions and the passive soot oxidation or the trade-off that has to be made when choosing the ideal pore size, balancing between the ease to coat with high loadings, and the filtration efficiency. In addition, the thermally rougher conditions observed in filters impose more challenging requirements with respect to the thermal stability of SCR catalyst technologies.

Overall, we do expect the introduction of SCR integrated filter systems in a number of passenger car applications. The tremendous progress made in the area of catalyst and filter technologies, as well as on the system integration, are key enablers. For passenger car applications, the main benefit is the potential for higher deNO_x efficiencies during cold start emission cycles. The main disadvantage of reduced passive soot oxidation is less of a concern.

For heavy-duty systems, the situation is less clear although significant research and development work have been performed over the past years. The benefit with

respect to low temperature deNO_x performance is less expressed and often outweighed by the disadvantage of reduced passive soot oxidation, leading to penalties in fuel consumption. The benefit of reduced packaging space or higher system deNO_x efficiency at given packaging volume might be an opportunity for some truck or non-road applications designed to meet advanced regulations.

References

1. Charlton S (2010) Meeting the US Heavy-Duty EPA 2010 Standards with Increased Customer Value. Paper presented at the SAE International Heavy-Duty Diesel Emission Symposium, 2010
2. Signer M (2012) Meeting Euro VI and EPA10 Legislation without EGR. Paper presented at the SAE Heavy Duty Diesel Emissions Control Symposium, 2012
3. Herrmann H-O (2009) Der Daimler Weg zur Erfüllung der EPA'10 Gesetzgebung. Proceedings of the MTZ-Konferenz On-/Off –Highway Engines, Friedrichshafen, 2009
4. Reuss T, Bauder R, Weiss U, Macher A, Lörch H, Pamio G-Z (2012) The New, Second-Generation Audi 3.0 V6 TDI EU6 – Powerful and Economical. Proceedings of the 21st Aachener Kolloquium Fahrzeug- und Motorentechnik, Aachen, 2012
5. Enderle C, Binz R, Vent G, Stotz M (2009) BlueTEC Technology in the New E-Class to Fulfil Future EU6 Emission Limits. Proceedings of the 18. Aachener Kolloquium Fahrzeug- und Motorentechnik, Aachen, 2009
6. Miao Y, Chen L-D, He Y, Kuo T-W (2007) Study of SCR cold start by energy method. Chemical Engineering Journal 155: 260–265.
7. Darcy P, Da Costa P, Mellottee H, Trichard J-M, Djega-Mariadassou G (2007) Kinetics of catalyzed and non-catalyzed oxidation of soot from a diesel engine. Catalysis Today 119: 252–256
8. Jeguirim M, Tschamber V, Ehrburger P (1997) Catalytic effect of Platinum on the kinetics of carbon oxidation by NO₂ and O₂. Applied Catalysis B: Environmental 76: 235–240
9. Warkins J, Heibel A, George S, Golomb N, Warren C (2011) Light Duty Filters. Paper presented at the SAE Light Duty Diesel Emissions Control Symposium, Ann Arbor, MI, 2011
10. Salvat O, Marez P, Belot G (2000) Passenger car serial application of a particulate filter system on a common rail direct injection diesel engine. SAE Technical Paper 2000-01-0473
11. Lörch H, Pamio Z G, Gomm S, Gruber M (2004) Audi's DPF solution: the advanced catalyzed soot filter. Proceedings of the 3. International Exhaust Gas and Particulate Emissions Forum, Sinsheim, 2004
12. Kercher L, Rose D, Boger T, Cutler W A, Dorenkamp R, Duesterdiek T (2006) Application of a New Filter Material in Volkswagen's Diesel Particulate Filter Systems. Proceedings of the 3rd Emission Control Conference, Dresden, 2006
13. Adelman B, Karkkainen A, Berke P, Rodgers D, Heibel A, Parker T, Pickles D, Tao T, Zink U (2006) Development and Application of a US-EPA '07 Particulate Filter System for a 7.6 l I-6 Medium Duty Truck Engine. Proceedings of the 15th Aachen Kolloquium Fahrzeug- und Motorentechnik, Aachen, 2006
14. Puetz W, Tindall T (2005) EPA 2007 for Heavy Duty Engines – Requirements and Technology. Proceedings of the 14th Aachener Kolloquium Fahrzeug- und Motorentechnik, Aachen, 2005
15. Heibel A K, Zink U (2007) Technical Paths to Emission Regulation Compliance of Commercial Vehicles in the Next Decade based upon Solutions for EPA 2007 and EU V. MTZ Vol. 68(8): 19–25
16. Bülte H, Schiffgens H-J, Broll P, Schraml S (2009) Exhaust Aftertreatment Concepts for Engines in Mobile Machinery According the Legislation of US Tier 4 and EU Step IV

- Technologies and Applications. Proceedings of the 18. Aachener Kolloquium Fahrzeug- und Motorentechnik, Aachen, 2009
17. Boger T, He S, Collins T A, Heibel A K, Beall D, Remy C (2011) A Next Generation Cordierite Diesel Particle Filter with Significantly Reduced Pressure Drop. *SAE Int. J. Engines* **4**(1): 902–912
 18. Boger T, Rose D, Cutler W A, Heibel A K, Tennent D L (2005) Untersuchung der Eigenschaften neuer Dieselpartikelfilter. *MTZ* Vol. **66**(9): 660–669
 19. Boger T, Jamison J A, Warkins J L, Golomb N A, Warren C J Heibel A K (2010) Next Generation Aluminum-Titanate Material to Meet Upcoming EU6 Emissions Legislation Requirements. Proceedings of the 19. Aachener Kolloquium Fahrzeug- und Motorentechnik, Aachen, 2010
 20. Mizutani T, Ito M, Masukawa N, Ichikawa S, Yuuki K, Kurachi H, Toyoshima T, Ito T, Lappas I, Schaefer-Sindlinger A, Vogt C D (2006) The study for structural design of the segmented SiC-DPF. *SAE Technical Paper* 2006-01-1527
 21. Ohno K, Shimato K, Taokam N, Santae H, Ninomiya T, Komori T, Salvat O (2000) Characterization of SiC-DPF for Passenger Car. *SAE Technical Paper* 2000-01-0185
 22. Young D M, Hickman D L, Bhatia G, Gunasekaran N (2004) Ash storage concept for diesel particulate filters. *SAE Technical Paper* 2004-01-0948
 23. Nova I, Bounechada D, Maestri R, Tronconi E, Heibel A K, Collins T A, Boger T (2011) Influence of the Substrate Properties on the Performances of NH₃-SCR Monolithic Catalysts for the Aftertreatment of Diesel Exhaust: An Experimental and Modeling Study. *Ind. Eng. Chem. Res.*, **50** (1): 299–309
 24. Konstandopoulos A G, Johnson J H (1989) Wall-flow diesel particulate filters – Their pressure drop and collection efficiency. *SAE Technical Paper* 890405
 25. Konstandopoulos A G (2003) Flow resistance descriptors for diesel particulate filters: Definitions, measurements and testing. *SAE Technical Paper* 2003-01-0846
 26. Mansoudi M, Heibel A, Then P M (2000) Predicting pressure drop of wall-flow diesel particulate filters – Theory and experiment. *SAE Technical Paper* 2000-01-0184
 27. Konstandopoulos A G, Skaperdas E, Masoudi M (2001) Inertial contributions to the pressure drop of diesel particulate filters. *SAE Technical Paper* 2001-01-0909
 28. Gaiser G, Mucha P (2004) Prediction of pressure drop in diesel particulate filters considering ash deposit and partial regenerations. *SAE Technical Paper* 2004-01-0158
 29. Tien C, Ramarao B V (2007) *Granular Filtration of Aerosols and Hydrosols*. Elsevier
 30. Schermerhorn A P, Khodosevich K, Joshi A, Boger T (2012) Detailed Simulation of Exhaust Flow and Deposition of Soot Particles in Porous Particulate Filter Walls. *FILTRATION* **12**(4): 246–256
 31. Konstandopoulos A G, Kostoglou M, Vlachos N, Kladopoulou E (2005) Progress in Diesel Particulate Filter Simulation. *SAE Technical Paper* 2005-01-0946
 32. Tandon P, Rosner D E (1995) Translational Brownian Diffusion Coefficient of Large (Multiparticle) Suspended Aggregates. *Ind. Eng. Chem. Res.* **34**: 3265–3277
 33. Heibel A K, Bhargava R (2007) Advanced Diesel Particulate Filter Design for Lifetime Pressure Drop Solution in Light Duty Applications. *SAE Technical Paper* 2007-01-0042
 34. Bollerhoff T, Markomanolakis I, Koltsakis G (2012) Filtration and regeneration modeling for particulate filters with inhomogeneous wall structure. *Catalysis Today* **188**: 24–31
 35. Tandon P, Heibel A, Whitmore J, Kekre N, Chithapragda K (2010) Measurement and Prediction of Filtration Efficiency Evolution of Soot Loaded Diesel Particulate Filters. *Chem. Eng. Sci.* **65**: 4751–4760
 36. Zhong D, He S, Tandon P, Moreno M, Boger T (2012) Measurement and Prediction of Filtration Efficiency Evolution of Soot Loaded Diesel Particulate Filters. *SAE Technical Paper* 2012-01-0363
 37. Messerer A, Niessner R, Pöschl U (2006) Comprehensive kinetic characterization of the oxidation and gasification of model and real diesel soot by nitrogen oxides and oxygen under engine exhaust conditions: Measurement, Langmuir-Hinshelwood, and Arrhenius parameters. *Carbon* **44**: 307–324

38. Neeft J P A, Nijhuis T X, Smakman E, Makkee M, Moulijn J A (1997) Kinetics of the oxidation of diesel soot. *Fuel* **76**(12): 1129–1136
39. Yezerets A, Currier N W, Kim D H, Eadler H A, Epling W S, Peden C H F (2005) Differential kinetic analysis of diesel particulate matter (soot) oxidation by oxygen using a step-response technique. *Applied Catalysis B: Environmental* **61**: 120–129
40. Jacquot F, Logie V, Brilhac J F, Gilot P (2002) Kinetics of the oxidation of carbon black by NO₂ – Influence of the presence of water and oxygen. *Carbon* **40**: 335–343
41. Stanmore B R, Brilhac J F, Gilot P (2001) The oxidation of soot: A review of experiments, mechanisms and models. *Carbon* **39**: 2247–2268
42. Mercury D (2007) GMPT Approach to After-treatment Calibration Control. Proceedings of the SAE TopTec “Optimizing Powertrain: Future Improvements through Control Symposium”, Turin June 12-14, 2007
43. Dollmeyer T A, Vittorio D A, Grana T A, Katzenmeyer J R, Charlton S J (2007) Meeting the US 2007 Heavy-Duty Diesel Emission Standards - Designing for the Customer. SAE Technical Paper 2007-01-4170
44. Becker C, Reinsch B, Strobel M, Frisse H-P, Fritsch A (2008) Particulate Filter Made of Cordierite - Design and Regeneration Management. *MTZ* **69**(6): 20–26
45. Boger T, Rose D, Tilgner I-C, Heibel A K (2009) Regeneration Strategies for an Enhanced Thermal Management of Oxide Diesel Particulate Filter. *SAE Int. J. Fuels Lubr.* 1(1):162–172. doi:[10.4271/2008-01-0328](https://doi.org/10.4271/2008-01-0328).
46. Rose D, Boger T (2009) Different Approaches to Soot Estimation as Key Requirement for DPF Applications. SAE Technical Paper 2009-01-1262
47. Mandel R, Meißner R, Wenninger G, Fekete N (2010) Anwendung eines echtzeitfähigen chemo-physikalischen Modells zur gegendruckbasierten DPF-Rußbelastungserkennung. Proceedings of the 8. FAD Konferenz, Dresden, 2010
48. Meißner R, Mandel R, Wenninger G, Fekete N, Krusch B, Kern M (2008) Auswirkungen der Dieselrußoxidation auf die gegendruckbasierte DPF-Rußbelastungserkennung. Proceedings of the 6. FAD Konferenz, Dresden, 2008
49. Zelenka P, Yoo S-B, Kim W, Lee K-M (2006) Challenges and solutions of diesel particulate filter applications. Proceedings of the 18th Int. AVL “Engine & Environment” Conference, Graz, 2006
50. Tang W, Youngren D, SantaMaria M, Kumar S (2013) On-Engine Investigation of SCR on Filters (SCRoF) for HDD Passive Applications. *SAE Int. J. Engines Vol.* **6**(2). doi:[10.4271/2013-01-1066](https://doi.org/10.4271/2013-01-1066)
51. George S, Warkins J, Golomb N, Warren C, Heibel K, Rose D (2012) A New Generation High Porosity DuraTrap[®] AT for Integration of DeNOx Functionalities. Proceedings of the 21st Aachener Kolloquium Fahrzeug- und Motorentechnik, Aachen, 2012
52. Stiebels S (2011) Reducing Emissions with Smart Catalyst Technologies. Paper presented at the SAE Light Duty Diesel Emissions Control Symposium, Ann Arbor, MI, 2011
53. Schrade F, Brammer M, Schaeffner J, Langeheinecke K, Kraemer L (2012) Physico-Chemical Modeling of an Integrated SCR on DPF (SCR/DPF) System. *SAE Int. J. Engines Vol.* **5**(3). doi:[10.4271/2012-01-1083](https://doi.org/10.4271/2012-01-1083)
54. Rose D, Pittner A, Jaskula C, Boger T, Glasson T, DaCosta V M (2007) On Road Durability and Field Experience Obtained with an Aluminum Titanate Diesel Particulate Filter. SAE Technical Paper 2007-01-1269
55. Bisset E J (1984) Mathematical model of the thermal regeneration of wall-flow monolith diesel particulate filter. *Chem.Eng.Sci.* **39**: 1233–1244
56. Watling T C, Ravenscroft M R, Avery G (2012) Development, validation and application of a model for an SCR catalyst coated diesel particulate filter. *Catalysis Today* **188**: 32–41
57. Konstandopoulos A G, Kostoglou M, Housiada P (2003) Multichannel simulation of regeneration of in honeycomb monolithic diesel particulate filters. *Chem.Eng.Sci.* **58**: 3273–3283
58. Haralampous O A, Koltsakis G (2004) Oxygen diffusion modeling in diesel particulate filter regeneration. *AIChE Journal* **50**(9): 2008–2019

59. Konstandopoulos A G, Kostoglou M, Vlachos N, Kladopoulou E (2005) Progress in diesel particulate filter simulation. SAE Technical Paper 2005-01-0946
60. Schejbal M, Štěpánek J, Marek M, Kočí P, Kubíček M (2010) Modeling of soot oxidation by NO₂ in various types of diesel particulate filters. *Fuel* **89**: 2365–2375
61. Dardiotis C K, Haralampous O A, Koltsakis G (2008) Catalytic oxidation in wall-flow reactors with zoned coating. *Chemical Engineering Science* **63**: 1142–1153
62. Schejbal M, Marek M, Kubíček M, Kočí P (2009) Modeling of diesel filters for particulates removal. *Chemical Engineering Journal* **154**: 219–230
63. Lee J H, Paratore M J, Brown D B (2009) Evaluation of Cu-Based SCR/DPF Technology for Diesel Exhaust Emission Control. *SAE Int. J. Fuels Lubr.* Volume 1 (1): 96–101
64. He Y, Brown D B, Lu S, Paratore M J, Li J (2009) Opportunities and Challenges for Blended 2-Way SCR/DPF Aftertreatment Technologies. SAE Technical Paper 2009-01-0274
65. Cavataio G, Girard J W, Lambert C K (2009) Cu/Zelite SCR on High Porosity Filters: Laboratory and Engine Performance Evaluations. SAE Technical Paper 2009-01-0897
66. Guo G, Warner J, Cavataio G, Dobson D, Badillo E, Lambert C (2010) The Development of Advanced Urea-SCR Systems for Tier 2 Bin 5 and Beyond Diesel Vehicles. SAE Technical Paper 2010-01-1183
67. Harth K (2012) Compact catalytic converter systems for future emissions standards. *MTZ* Vol. **73**(9): 10–14
68. Boorse S, Dieterle M, Voss K, Stiebels s, Wendt C, Neubauer T (2010) Two in one: SCR on Filter. Paper presented at the DEER Conference, 2010
69. Dieterle M, Boorse S, Voss K, Stiebels S, Wendt C, Neubauer T (2010) Two in one: SCR on Filter. Proceedings of the 3rd MinNOx Conference, Berlin, 2010
70. Grisstede I, Franschek S, Seyler M, Hoyer R, Noack H, Basso S, Müller W (2012) Robust NOx After Treatment Systems for Diesel Pass-Cars Beyond EU6. Proceedings of the 21. Aachener Kolloquium Fahrzeug- und Motorentechnik, Aachen, 2012
71. Ballinger T, Cox J, Konduru M, De D, Manning W, Andersen P (2009) Evaluation of SCR Catalyst Technology on Diesel Particulate Filters. *SAE Int. J. Fuels Lubr.*, Vol. **2**(1): 369–374
72. Neußer H-J, Kahrstedt J, Jelden H, Dorenkamp R, Düsterdiek T (2013) The EU6 Engines based on the Modular Diesel System of Volkswagen – Innovative Exhaust Gas Purification Near the Engine for Further Minimization of NOx and CO₂. Proceedings of the 34. Internationales Wiener Motorensymposium, Vienna, 2013
73. Oladipo B, Bailey O, Price K, Balzan N, Kaul S (2008) Simplification of Diesel Emission Control System Packaging Using SCR Coated on DPF. Paper presented at the 14th DEER Conference, 2008
74. Naseri M, Chatterjee S, Castagnola M, Chen H-Y, Fedeyko J, Hess H, Li, J (2011) Development of SCR on Diesel Particulate Filter System for Heavy Duty Applications. *SAE Int. J. Engines*, Vol. **4**(1): 1798–1809
75. Tan J, Solbrig C, Schmiege S J (2011) The Development of Advanced 2-Way SCR/DPF Systems to Meet Future Heavy-Duty Diesel Emissions. SAE Technical Paper 2011-01-1140
76. Döring A, Emmerling G, Rothe D (2012) Downsizing of the EUVI exhaust aftertreatment components to fit into the Euro III silencer. Proceedings of the 33. Internationales Wiener Motorensymposium, Vienna, 2012
77. Emmerling G, Döring A, Rothe D (2012) “SCR on DPF” for commercial vehicles – advantages and risks. Proceedings of the 6th Emission Control Conference, Dresden, 2012

Part VIII
Case Histories

Chapter 21

Development of the 2010 Ford Diesel Truck Catalyst System

Christine Lambert and Giovanni Cavataio

Acronyms

CARB	California Air Resources Board
CHA	Chabazite
DEF	Diesel exhaust fluid
DIN	<i>Deutsches Institut für Normung</i> , the German Institute for Standardization
DOC	Diesel oxidation catalyst
DOE	Department of Energy (U.S.)
DPF	Diesel particulate filter
EGR	Exhaust gas recirculation
FTP-75	Federal test procedure for light-duty vehicles
GVW	Gross vehicle weight
HC	Hydrocarbon
HD	Heavy-duty (>14,000 lbs GVW and incomplete vehicles)
J1	Job 1, first vehicle produced in a new model year
J2	Job 2, first vehicle produced with a significant change in a given model year
LD	Light-duty (<8,500 lbs GVW)
LHDDE	Light heavy-duty diesel engine, a federal category for MD vehicles
LEV	Low emission vehicle program (CARB)
LNT	Lean NO _x trap
MD	Medium-duty (>8,500 lbs and <14,000 lbs GVW)
OEM	Original equipment manufacturer
PFI	Port fuel injection
SCR	Selective catalytic reduction
SiC	Silicon carbide
ULSD	Ultra Low sulfur Diesel
USCAR	United States Council for Automotive Research

C. Lambert (✉) · G. Cavataio
Ford Motor Co., Dearborn, MI, USA
e-mail: clamber9@ford.com

21.1 Introduction

The choice to pursue Selective Catalytic Reduction (SCR) using aqueous urea as a NO_x reductant for lean NO_x control on diesel vehicles was not an easy one. It was difficult to imagine an infrastructure for delivery of aqueous urea to diesel vehicles. In the 1990s, SCR technology was best known for its use in stationary source control of NO_x . There were published studies on its potential effectiveness for diesel vehicle NO_x control at steady state, most notably by Degussa [13], Volkswagen [23], and Hug Engineering [25]. Earlier, interesting work was also being done at the Paul Scherrer Institute in Switzerland [28]. Ford applied urea SCR to a light-duty truck and tested it with success on transient cycles [42]. The SCR catalysts available at that time included vanadia/titania, and base metal/zeolite formulations using copper or iron, usually using ZSM-5. It was unknown if these catalyst types would ever be durable enough for a vehicle application, not only hydrothermally but with diesel fuel sulfur contents on the order of 500 ppm, or approximately 50 times the current diesel sulfur level in the U.S. and Europe today. There was also uncertainty about integration of particulate traps into SCR systems, low temperature/high space velocity applications, and aqueous urea handling issues, including freeze point and replenishment.

A technology was going to be needed to control NO_x under lean conditions to 90+ % reduction levels to meet future emission standards or diesels could not be sold in the U.S. Ford continued research on urea SCR systems [18, 31, 36, 37, 46] when the industry as a whole was primarily focused on the main competing technology of lean NO_x adsorbers. Starting with the 2007MY, the introduction of ultra low sulfur diesel (ULSD) fuel into the U.S. market enabled the use of particulate filters and lean NO_x catalysts on diesel vehicles. In particular, commercially important trucks falling in the medium-duty vehicle (MDV) weight classes of Class 2b (8,501–10,000 lbs) and Class 3 (10,001–14,000 lbs) had the option to certify as a complete chassis to LEVII NO_x standards. By 2010, an infrastructure for aqueous urea delivery to vehicles was expected to develop sufficiently for diesel trucks to use SCR systems. In 2005, Ford began a multiyear advanced development of the SCR system for diesel trucks >8,500 lbs slated for a 2010 launch. Several key issues involving the catalyst system were identified and overcome. The timeline of 10–15 years from research system concept to production is not unusual and reflects the difficult challenges associated with new technology development for a vehicle application at the required durability and cost. The overall impact of medium-duty diesels with urea SCR was 10+ % lower CO_2 at light to moderate loads, 6–7 % lower CO_2 at high loads, and greater use of base metals and lower cost precious metals via Cu-SCR catalysts and Pd-rich diesel oxidation catalysts (DOC). The launch of urea SCR systems on Ford diesel trucks was a success in terms of NO_x and greenhouse gas emissions saved and the first widespread use of a base metal/zeolite catalyst for automotive exhaust gas aftertreatment.

Table 21.1 2007 standards for light-duty (LD) and heavy-duty (HD) diesel vehicles

	NMOG/NMHC	CO	NOx	PM
LD Tier 1 diesel (100 k mi) ^a	0.31–0.56 g/mi	4.2–7.3 g/mi	0.97–1.53 g/mi	0.10–0.12 g/mi
LD Tier 2 Bin 5 (120 k mi)	0.090 g/mi	4.2 g/mi	0.07 g/mi	0.01 g/mi
HD 2004 MY	0.5 g/hp-hr	15.5 g/hp-hr ^b	2.0 g/hp-hr	0.10 g/hp-hr
HD 2007 MY	0.14 g/hp-hr ^c	15.5 g/hp-hr ^b	0.20 g/hp-hr ^c	0.01 g/hp-hr

^a Tier 1 standards vary according to vehicle weight

^b HD CO standard is carried over from 1998 MY

^c 2007 NMHC and NOx standards to be phased in from 2007 to 2010

21.2 Early Research at Ford on Lean NOx Control for Diesel Vehicles

Early research work at Ford on lean NOx control focused on three main catalytic technologies for active NOx reduction on diesels: SCR with diesel fuel (hydrocarbon (HC) SCR), SCR with aqueous urea (urea SCR), and lean NOx traps (LNTs). HC SCR used diesel fuel injected over a Pt-containing catalyst. Urea SCR used a solution of 32.5 wt% urea in water (eutectic) injected over a base metal/zeolite catalyst. LNTs contained precious metal and were similar in formulation to a gasoline three-way catalyst (TWC) with NOx adsorbing materials added. LNTs required rich conditions to decompose the NOx stored within and were known to be especially vulnerable to sulfur, requiring high temperature, rich conditions to recover. The goal for these technologies was 90+ % NOx reduction to meet light duty Tier 2 standards and heavy-duty standards beyond 2007 (Table 21.1).

An important consideration was the operating temperature window of each potential catalyst technology as well as the fuel economy impact. These are summarized in Figs. 21.1 and 21.2. The performance data are for slightly aged catalysts at 30,000 h⁻¹, and the shaded areas indicate typical exhaust gas temperatures on two light-duty vehicle certification cycles: the three phase city driving cycle (FTP-75), and the high speed, fast transient cycle known as US06. A typical HC SCR curve for diesel fuel and a Pt catalyst had overall low NOx conversion in a narrow temperature window. Urea SCR using a Cu/beta catalyst had the widest operating window for >90 % NOx conversion. LNT (Ba type) had a narrower window shifted to higher temperatures. Therefore, the LNT must be heated by at least 100 °C to give high efficiency on that test cycle. Note that LNT efficiency fell off drastically above 400 °C.

The expected performance curves for LNT and Urea SCR versus fuel penalty are shown in Fig. 21.2 for the LD FTP-75. The NOx conversions were optimistic projections for the best formulations available in 2003 without any type of cold start strategy. It was assumed that the NOx catalyst is located downstream of a DOC, and similar engine out conditions were used for each technology. A penalty of 3 % was included for all systems to account for the increased backpressure and periodic regeneration of a soot filter. An equivalent fuel penalty for use of urea

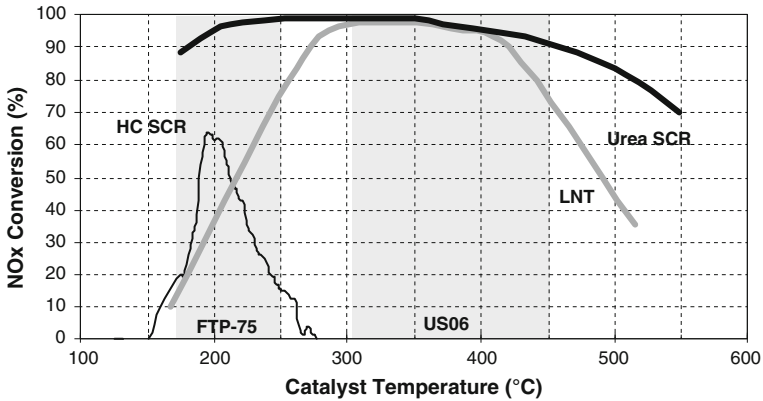
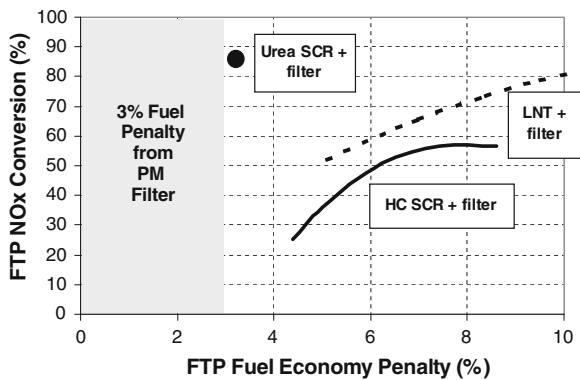


Fig. 21.1 Typical performance curves for slightly aged catalysts on LD test cycles. Typical underfloor temperature ranges for light-duty vehicles are shown for reference (see shaded areas). Space velocity was about $30,000 \text{ h}^{-1}$, as measured at standard conditions, corresponding to a catalyst volume of about equal to the engine swept volume [34]. Copyright © SAE International. Reprinted with permission from 2004-01-1292

Fig. 21.2 Estimated fuel penalties of lean NOx reduction technologies versus NOx conversion for the LD FTP-75 [34]. Copyright © SAE International. Reprinted with permission from 2004-01-1292



based on the energy required for manufacture was estimated to be approximately 0.2 %. This was insignificant compared to the 7 % penalty projected for LNT to achieve 80 % NOx conversion.

In summary, it was found that urea SCR had the most potential to provide the 90+ % NOx conversion required for 2007+ NOx standards with the following technical advantages: wider operating temperature window, greater durability, lower fuel economy penalty, lower HC emissions, lower greenhouse gas emissions, lower system cost, and lower usage cost. The applicability of urea SCR for transient use was further demonstrated on a series of prototype diesel vehicles [31, 46]. Most notably, Ford completed a 120,000 mi aging assessment on a 6,000 lbs light duty truck aimed at Tier 2 Bin 5 emission standards [37]. This study is described below.

21.3 Ford's Research Program on a Prototype Light-Duty Diesel Truck

From 2001 to 2005, Ford participated in the U.S. Department of Energy's Ultra-Clean Transportation Fuels Program with the goal to develop an exhaust emission control system for light-duty diesel trucks that provided high efficiency particulate matter (PM) and NO_x reduction to meet Tier 2 Bin 5 emission standards (0.01 g/mi PM, 0.07 g/mi NO_x). Very low sulfur diesel fuel enabled low PM emissions, reduced the fuel economy penalty associated with the emission control system, and increased the long-term durability of the system. The project team included an emission control technology developer and diesel engine manufacturer (Ford), a fuel and catalyst technology developer (ExxonMobil Research and Engineering), exhaust gas catalyst manufacturers, and an outside research facility (FEV). The program focused on the design options for urea SCR catalyst systems that included a particulate filter, development of robust catalysts, NO_x and ammonia sensor development, urea dosing and mixing, efficient filter regeneration, and the business case for urea infrastructure.

21.3.1 SCR System Design

Integration of NO_x and particulate control was a challenge. If a particulate filter was located upstream of the SCR catalyst, it could take full advantage of heat produced by the engine to oxidize HC, CO, and soot. However, the SCR catalyst took longer to heat up and could be more susceptible to damage by large exotherms generated in the filter. It was thought to be advantageous to reverse the order of the components to achieve higher SCR catalyst temperatures and convert more NO_x earlier in the test cycle. A DOC close to the engine was required to oxidize HC and CO, followed by urea injection and SCR. An oxidation function after urea injection would be detrimental to the SCR process. This configuration would require additional heat to regenerate the filter, resulting in a potentially higher fuel economy penalty.

Light-duty FTP-75 cycle NO_x conversions for two possible configurations (System A = Catalyzed Filter + SCR and System B = DOC + SCR + Filter) were estimated as shown in Fig. 21.3. Neither system by itself was predicted to meet the 90 % NO_x conversion target for a light-duty diesel to meet Tier 2 emissions. More rapid heating of the SCR catalyst was needed to reach higher activity sooner. It was assumed an extra 50 °C could be added to the system during the first 30 s of the cycle.

System B with rapid warm up was predicted to reach the target of 90 % NO_x conversion on the FTP-75. The filter was now located in the coldest position furthest away from the engine. However, a filter can accumulate soot at any temperature and needed to be brought up to higher temperatures for soot oxidation only every 500 mi or so. The SCR catalyst, on the other hand, needed to be heated up at every cold start to its operating window. The DOC + SCR + Filter system

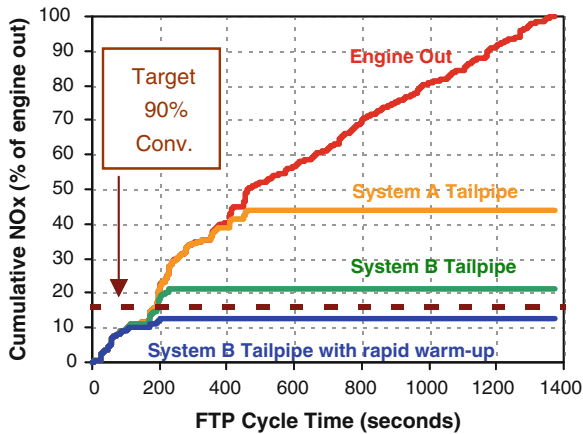


Fig. 21.3 Predicted system efficiencies on the U.S. light duty FTP-75 emissions test. System A is Catalyzed Filter + SCR and System B is DOC + SCR + Filter [32]. Copyright © SAE International. Reprinted with permission from 2002-01-1868

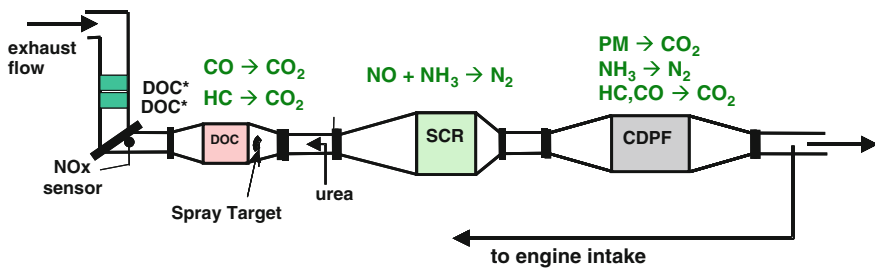


Fig. 21.4 Prototype truck exhaust system design and functionality [37]

configuration and how to regenerate the filter in this configuration was later patented by Ford [21, 47]. The catalyst layout for the vehicle used in Ford’s DOE contract work looked like Fig. 21.4. Besides the catalysts, exhaust gas sensors and a spray target for urea injection were designed to control the stoichiometry between urea and NOx and also improve the uniformity of the urea spray in the short pipe distance available.

21.3.2 DOC Development for SCR Systems

The DOC provided several functions for the urea SCR and filter system: oxidation of HC and CO to meet tailpipe emissions, exotherm generation during cold start and filter regeneration, and NO oxidation for improved, durable SCR performance. Typical curves for HC and CO oxidation for an aged Pt DOC are shown in Fig. 21.5

Fig. 21.5 Light-off behavior of an early Pt DOC formulation for CO, HC and, NOx after aging

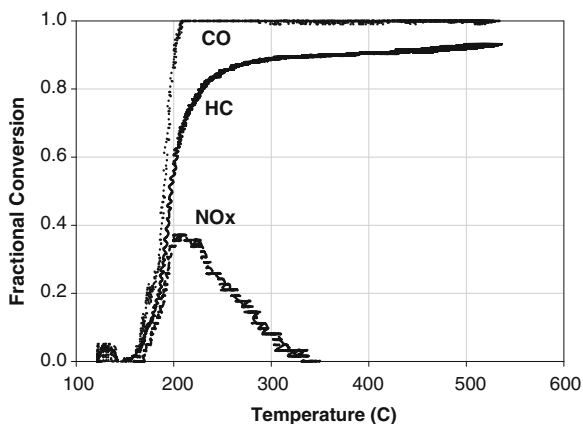
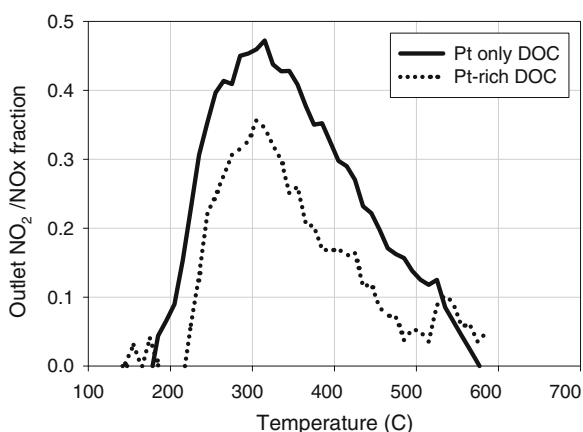


Fig. 21.6 NO oxidation performance of Pt-only DOC versus Pt-rich DOC. Both samples were hydrothermally aged for the equivalent of 120,000 mi

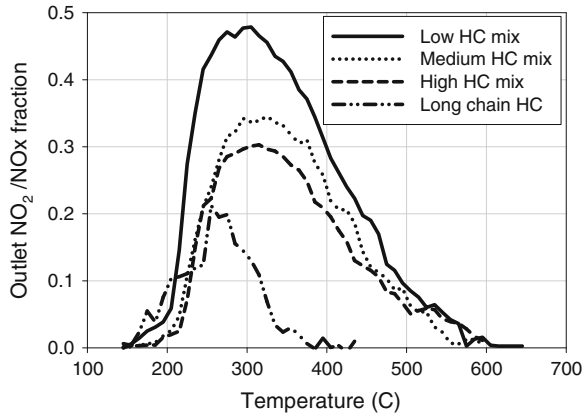


using a pulsating flame combusting reactor or “pulsator” [24]. There was some NO_x conversion during a narrow temperature window just ahead of peak HC conversion due to HC reducing NO_x under partial oxidation conditions, ending at about 300 °C. The catalyst had been hydrothermally aged for 120,000 mi equivalent.

It was known that NO₂ could benefit SCR performance at low temperatures [29]. Peak NO oxidation was found to be about 30–40 % in the laboratory pulsator after hydrothermal aging as shown in Fig. 21.6 for a Pt-only and a Pt-rich catalyst. The Pt-only catalyst was selected as the main DOC for the urea SCR system because of its superior NO oxidation performance.

Further testing was conducted to study the effects of hydrocarbon concentration on NO oxidation. These parameters were important because strategies to warm the SCR catalyst or regenerate the filter could result in high levels of hydrocarbons (HC) entering the DOC. It was found that high HC levels, especially long-chain HC, suppressed the oxidation of NO to NO₂ as shown in Fig. 21.7. At temperatures

Fig. 21.7 Effect of hydrocarbon concentration on NO oxidation



below 350 °C, where the impact on SCR performance is the most significant, the overall oxidation of NO is small. This meant that NO oxidation would be variable in real exhaust gas conditions.

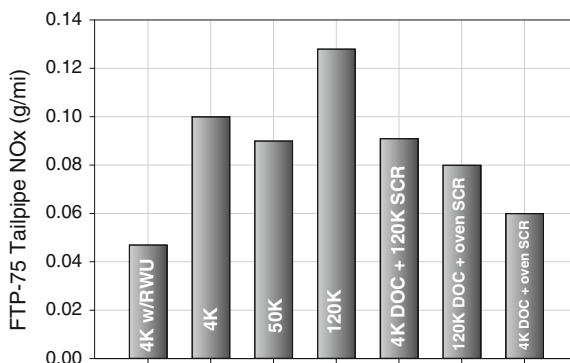
21.3.3 SCR Catalyst Formulations

The main options for SCR catalysts included vanadia/titania, Fe supported on zeolite, and Cu supported on zeolite. Vanadia catalysts, while durable to sulfur, were not suitable for integration into a system with a periodically regenerating particulate filter due to the thermal instability of the anatase titania support material at temperatures above 550 °C and the relatively low melting point of V₂O₅ at 690 °C [43]. Further research focused on Fe and Cu formulations, mainly containing beta zeolite. To some extent, the presence of NO₂ improved low temperature SCR performance, enhanced NO_x conversion at higher space velocity, and provided more robustness. On the other hand, higher NO₂ levels in the feed above 50 % were detrimental to low temperature NO_x conversion and produced large amounts of N₂O. It was also found that Fe was more sensitive to the incoming NO₂/NO_x ratio than Cu. Therefore, Cu/beta was selected as the prime SCR catalyst formulation due to its long-term thermal stability up to filter regeneration temperatures and its lower dependence on feed NO₂.

21.3.4 Vehicle System Results

Tailpipe emissions data were collected on a 6,000 lbs Ford light duty truck equipped with a midsized diesel engine [37]. The exhaust system consisted of an NO_x sensor, Pt-only oxidation catalyst, aqueous urea injection, base metal/zeolite

Fig. 21.8 Aging summary for FTP-75 weighted NO_x on prototype 6,000 lbs light duty diesel truck [36, 37]. Data are multitest averages at each aging condition. The first data taken at 4,000 mi had an active rapid warm up strategy; the remaining data do not



(Cu/beta) catalyst, and catalyzed diesel particulate filter (DPF). Injection of urea against the exhaust flow onto a spray target was used to enhance the distribution of urea in the exhaust gas [30]. An improved exhaust gas recirculation (EGR) system consisting of both high pressure and low pressure EGR was used. The fuel economy penalty for NO_x control was less than 1 % for rapidly warming the catalysts during cold start. Nearly complete regeneration of a filter could be achieved within 10 min, or less time than one FTP-75 cycle. The fresh system achieved over 90 % NO_x conversion on the cold start FTP-75 test cycle.

The tailpipe NO_x data was measured as a progression of aging (Fig. 21.8). The data were averages of multiple tests for each aging condition. At 4,000 mi, emissions were below Tier 2 Bin 5 levels at approximately 0.045 g/mi NO_x and 0.001 g/mi PM. HC and CO emissions were also below Tier 2 Bin 5 levels. Unfortunately, rapid warm up control was lost on the prototype engine, resulting in a doubling of the tailpipe NO_x to 0.1 g/mi. The exhaust system was aged successfully for 120,000 mi on the engine dynamometer using a transient aging cycle, a Ford corporate drive cycle that incorporated both city and highway driving modes [38], with a total aging time of about 2,500 engine hours. The filter was actively regenerated a total of 643 times, with each regeneration typically lasting 10 min, including 6 min with the SCR at high temperature (over 600 °C). In all, the SCR system spent approximately 64 h at high temperature during the durability phase, matching the projected lab aging time. At 50,000 mi, the emissions were similar to 4,000 mi and very little aging had occurred. At 120,000 mi, some SCR aging was evident. Overall FTP-75 NO_x conversion was 74 % conversion with 0.128 g/mi at the tailpipe, exceeding the Tier 2 Bin 5 standard at 120,000 mi of 0.07 g/mi NO_x. This result was improved by using a fresh DOC upstream of the dynamometer-aged SCR (0.091 g/mi); therefore, the durability of the DOC did have a significant impact on SCR performance. During the year that the dynamometer aging took place, further improvements were made to Cu/beta-type SCR catalysts. An improved SCR catalyst was oven-aged for 64 h and tested with the dyno aged DOC, resulting in 0.08 g/mi NO_x. Substituting the fresh DOC into the system gave even lower NO_x at 0.06 g/mi NO_x. Again, the importance of DOC durability for long-term NO_x reduction was shown.

Table 21.2 California diesel emission standards for 8,500–14,000 lbs. (Chassis certified at 120,000 mi, all emissions in g/mi)

Year	Weight (GVW) (lbs)	Category	NMOG	CO	NOx	PM	HCHO
2003	8,501–10,000	ULEV ^a	0.197	8.1	1	0.06	0.021
	10,001–14,000	ULEV	0.257	10.3	1.5	0.06	0.026
2004–2010	8,501–10,000	ULEV II	0.143	6.4	0.2	0.06	0.016
	10,001–14,000	ULEV II	0.167	7.3	0.4	0.06	0.021

^a For simplicity, only California ULEV is shown in the table; LEV and SULEV also were available (California *LEV* Low Emission Vehicle, *ULEV* Ultra Low Emission Vehicle, *SULEV* Super Ultra Low Emission Vehicle)

21.4 Migration of Research into a Production Vehicle Program

21.4.1 Vehicle Program Needs for Lean NOx Control

In 2005, when the Ford-DOE project was ending, a key decision was made that determined the NOx aftertreatment needs for future diesel trucks. Up until then, diesel aftertreatment in the U.S. had consisted of low-cost metal oxide catalysts for some control of soluble organics to meet particulate standards [15, 22]. The high sulfur in the fuel prohibited the use of filters, precious metal catalysts, or lean NOx control. The introduction of ULSD fuel into the market in 2007 enabled the launch of filters and higher precious metal DOCs to meet tighter standards for PM and non-methane hydrocarbons (NMHC). The story for implementation of lean NOx control is slightly different.

Historically, medium-duty vehicles weighing between 8,500 and 19,500 lbs fell under the “light heavy-duty diesel engine (LHDDE)” federal category and were certified on an engine dynamometer. Beginning with the 2004 model year (MY), Federal Tier 2 and California LEV II standards were adopted, with a multiyear phase-in. Medium-duty vehicles between 8,500 and 14,000 lbs had the option to certify as a complete vehicle using the chassis FTP-75 cycle. Tier 2/LEVII phase-in was to be completed by 2010. Ford made the decision to continue to certify LHDDEs on an engine dynamometer until 2010, and then certify trucks <14,000 lbs as a complete chassis thereafter. While the Ford-DOE program had focused on the light-duty vehicle category (<8,500 lbs), this key decision allowed for the same system options to be applied to the production program because the same test cycle, the FTP-75, was going to be used for certification, and the NOx conversion requirements were similar, falling around 80 % for the cycle. The drop in NOx standards can be seen in Table 21.2, where California LEV versus LEVII can be compared for the two weight classes considered to be medium-duty. For a GVW of 8,501–10,000 lbs, the tailpipe NOx requirement went down from 1 to 0.2 g/mi, and for 10,001–14,000 lbs, NOx standards were reduced from 1.5 to 0.4 g/mi.

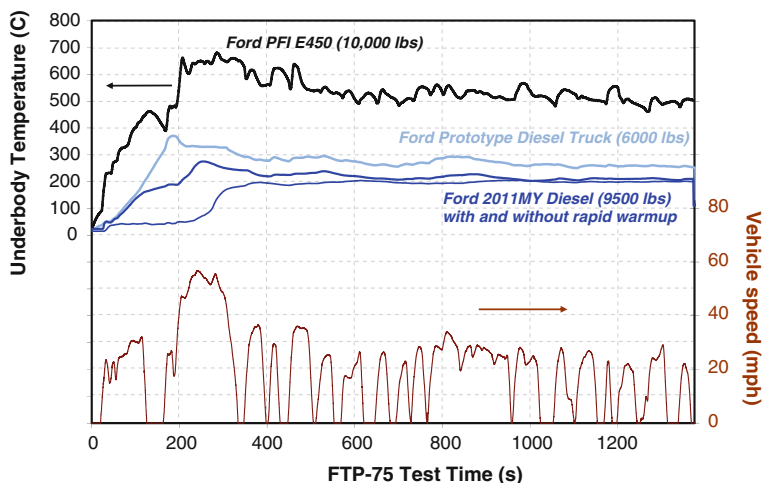


Fig. 21.9 Comparison of underbody exhaust gas temperatures (SCR catalyst location) for a 2011MY diesel truck at 9,500 lbs compared to a prototype truck at 6,000 lbs and a gasoline PFI E450 van at 10,000 lbs. Data are for the first two phases (bags) of the FTP-75, and the effectiveness of rapid warm up is shown for the 9,500 lbs truck

21.4.2 Catalyst and System Design Options

Similar catalyst design options were available for the production program as there were a few years earlier for the research program: DOC + DPF + SCR and DOC + SCR + DPF. The system carried design constraints such as packaging space, backpressure, conversion efficiency targets, and lower exhaust gas temperatures due to the much higher power/weight ratio of medium-duty truck compared to light duty. The underbody exhaust gas temperatures on these larger trucks were especially challenging at a typical operating level of 200 °C. This was about 50 °C lower than the light duty truck and roughly 300 °C lower than a comparable weight gasoline vehicle (Fig. 21.9). Cold start was another problem. The SCR system did not warm up to 200 °C until almost 400 s into the test cycle, and it became apparent that rapid heating would be needed to achieve NO_x conversion within less than 200 s in order to meet the cycle NO_x conversion target of 85–90 %.

Due to packaging constraints, not even a DOC could be close-coupled to the engine; all catalysts would be located underbody. It was decided to proceed with the DOC + SCR + DPF configuration in order to meet the NO_x performance target to 85+ % conversion on the FTP-75. Even with rapid warm up, the overall system performance presented a huge challenge. A schematic of the final system includes two DOC bricks, DEF injection (DEF = diesel exhaust fluid, a trade name for automotive grade aqueous urea), a twist mixer, two SCR bricks, and a diesel particulate filter (Fig. 21.10). The DOC and SCR substrates were cordierite and the

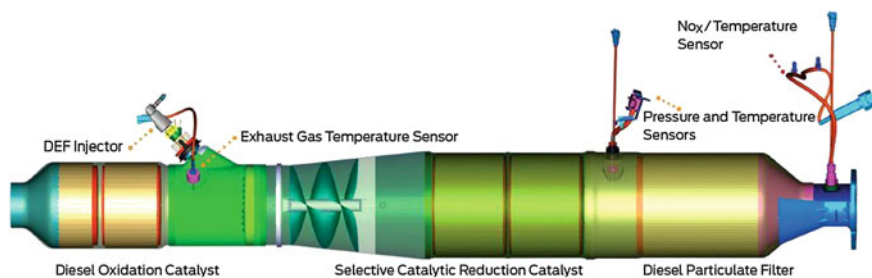
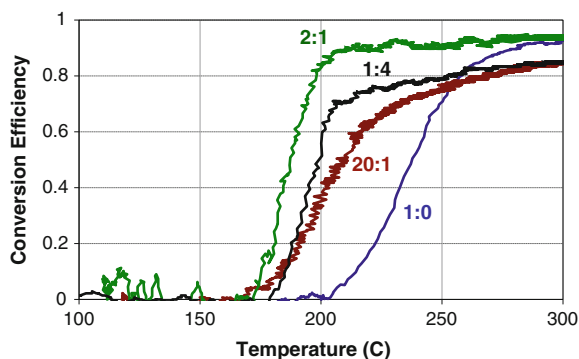


Fig. 21.10 2011MY medium-duty diesel exhaust system [16]

Fig. 21.11 HC light-off performance of DOC technology at $50,000 \text{ h}^{-1}$ according to the Pt:Pd ratio at similar overall metal loadings [39]



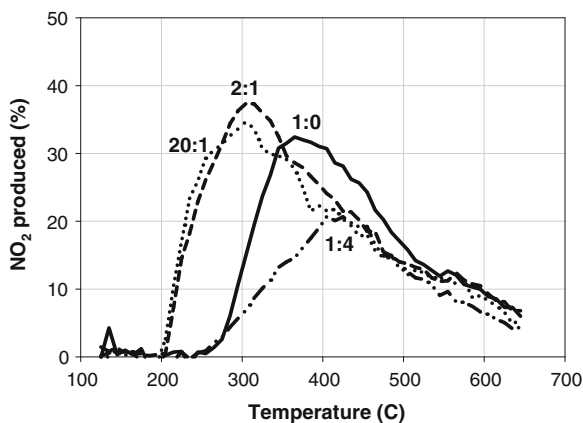
filter was SiC (silicon carbide). The sensor set included a post DOC temperature sensor for rapid warm up and filter regeneration control, pressure and temperature sensors around the filter, and a tailpipe NO_x sensor. A feed gas NO_x model was used to estimate the amount of urea needed for stoichiometric, transient injection.

21.5 Development Challenges Associated with SCR Catalyst Systems

21.5.1 Thermal Stability of the DOC

Historically, Pd was less expensive than Pt, often at 25–30 % of the cost per troy oz [27]. It became desirable to discover if a Pd DOC could be made to work in a diesel exhaust system with urea SCR and filter. The light-off of HC was tested after aging several DOCs. It was found that some addition of Pd to Pt had a stabilizing effect for HC oxidation during cold start (Fig. 21.11). The best ratio for performance was 2:1 Pt:Pd, and this ratio was used for the launch of DOC+SCR+DPF on diesel trucks in the spring of 2010. Further work revealed that

Fig. 21.12 NO oxidation behavior of DOCs as a function of the Pt:Pd ratio at similar overall metal loadings, at $50,000 \text{ h}^{-1}$ [39]



the 1:4 ratio at the same overall metal loading as the 2:1 was almost as good for HC and presented significant cost savings. The 1:4 Pt:Pd ratio was adopted later in the fall of 2010. There was a tradeoff made, mainly in NO oxidation activity. At 20:1 and 2:1, Pd-stabilized Pt and improved NO oxidation but had no inherent activity itself, so the migration to the 1:4 ratio essentially removed any chance for NO oxidation on an aged DOC at typical exhaust temperatures of 200–300 °C. This was deemed acceptable by the program due to the selection of relatively NO₂-insensitive Cu-SCR catalyst and little or no expectation for passive soot oxidation in the DOC + SCR + DPF configuration (Fig. 21.12).

21.5.2 Thermal Stability of the SCR Catalyst

Due to the location of the SCR system upstream of the filter and repeated, potentially variable exposure to high temperature exhaust conditions during filter regenerations, there was a need to develop thermally robust SCR catalysts. A detailed comparison was made early on in the program to better understand the operating temperature range and thermal durability differences between Cu/beta, Fe/beta, and vanadium-containing NO_x reduction catalysts. The catalysts were aged as cores under hydrothermal conditions at a relatively mild 670 °C for 64 h to represent 120,000 mi. It was concluded from the findings presented in Fig. 21.13 that the thermal durability requirements under filter regeneration events significantly deactivated the vanadium-containing catalyst [4]. As a result, vanadium-containing catalysts were deemed inappropriate for U.S. diesel applications.

At a hydrothermal aging temperature of 670 °C, minor deactivation in NO_x reduction with NH₃ was observed for the leading Cu/zeolite and Fe/zeolite catalysts in 2006. For these early generations using beta zeolites, the never-to-exceed temperature for Cu was established to be only 775 °C while Fe was determined to be as high as 925 °C. Under standard SCR reaction conditions (NO_x = NO),

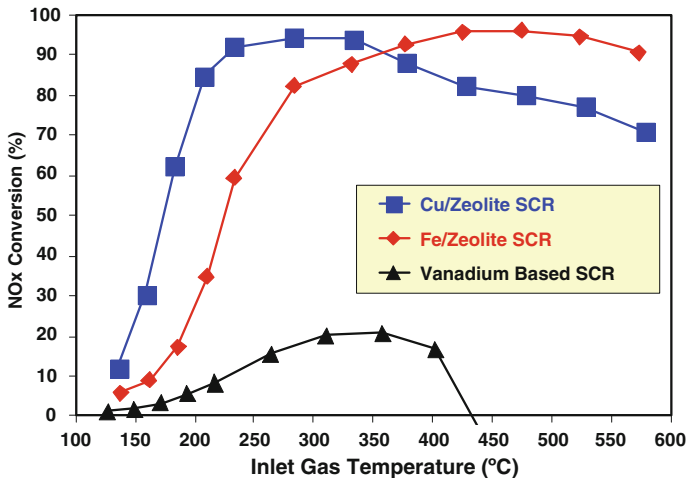


Fig. 21.13 NO_x Conversion over Cu-, Fe-, and vanadium-based SCR formulations as a function of temperature (30 kh⁻¹). Catalyst samples were aged for 64 h at 670 °C under flowing gas with oxygen and water [4]. Copyright © SAE International. Reprinted with permission from 2007-01-1575

Cu/beta was found to have higher NO_x conversion at temperatures below approximately 350 °C. Unfortunately, the Fe/zeolite formulations required higher NO₂/NO_x ratios in order to achieve adequate low temperature NO_x conversion. As a result, no beta zeolite catalysts were satisfactory for both low temperature NO_x activity and high temperature thermal durability. The next generation of Cu/zeolite formulations tested under SCR reactions involved the use of chabazite (CHA) zeolite. This class of small pore zeolite showed remarkable hydrothermal stability [3, 5]. Among the dozens of Cu/zeolite formulations tested in prior years, no formulation was able to withstanding exposure up to 900 °C while maintaining stable NO_x performance at 200 °C. Under the 1 h/900 °C aging condition, the 2007 SCR catalyst retained 90 % NO_x conversion at 200 °C (Fig. 21.14).

Based on these encouraging results, a more severe time-at-temperature aging study was undertaken with the 2007 Cu/CHA SCR formulation defined above. The aging and evaluation helped determine the full robustness map of this promising new SCR formulation and also provided valuable characterization for the upcoming on board diagnostics (OBD) compliance requirements where monitoring of the SCR function was expected. The aging time was varied from 1 to 256 h while the aging temperature was varied from 670 to 1100 °C [6]. Initially, SCR catalyst performance metrics such as NO_x conversion, NH₃ oxidation, NH₃ storage capacity, and BET surface area were within normal limits. However, these features degraded with high temperatures and longer aging times. Upon completion of a full time-at-temperature durability study, performance criteria were established to help determine the risk of SCR failure. Simple mathematical equations were developed

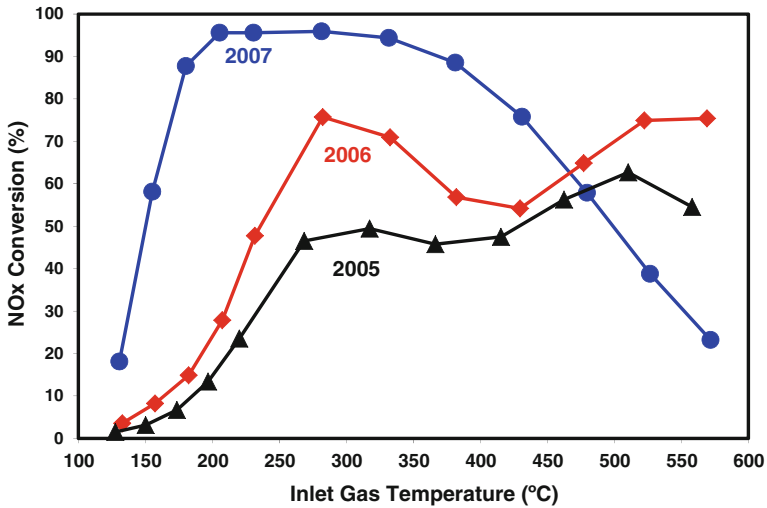


Fig. 21.14 NOx conversion of best in class SCR catalyst formulations from 2005 to 2007 after hydrothermal aging for 1 h at 900 °C [5]. Copyright © SAE International. Reprinted with permission from 2008-01-1025

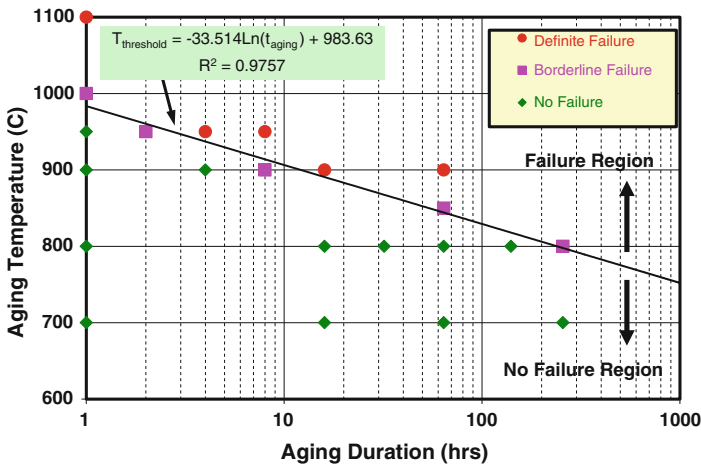


Fig. 21.15 The threshold aging temperature as a function aging duration for the established criteria used to indicate Cu/CHA SCR failures [6]. Copyright © SAE International. Reprinted with permission from 2009-01-1282

that related the threshold temperature to the threshold aging time (Fig. 21.15). Failure was defined as <80 % NOx conversion between 200 and 400 °C, <100 % NH₃ conversion at 500 °C, <600 mg/L NH₃ storage capacity, and <70 % of initial surface area.

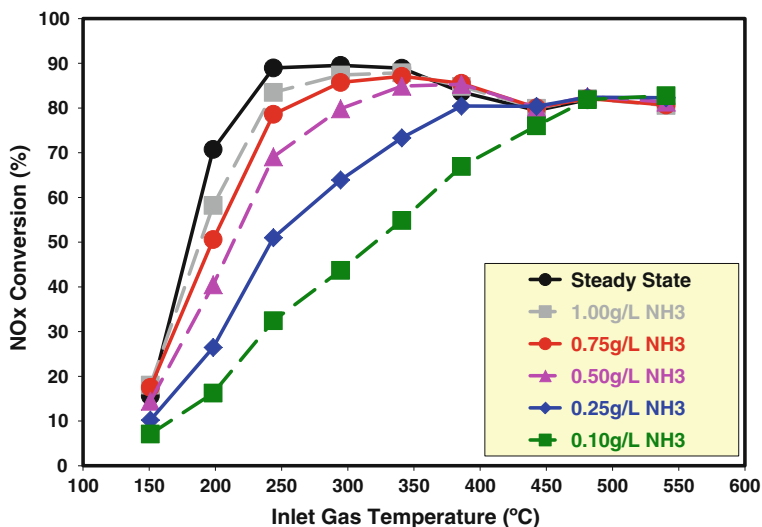


Fig. 21.16 NO_x conversion over the Cu/Beta SCR formulation as a function of temperature and NH₃ exposure (30,000 h⁻¹, 5 % H₂O, 5 % CO₂, 14 % O₂, 350 ppm NO, 350 ppm NH₃, balance N₂) [4]. Copyright © SAE International. Reprinted with permission from 2007-01-1575

21.5.3 Ammonia Storage Management

Steady-state conditions with an ammonia-saturated SCR catalyst did not adequately represent the challenges of NH₃ management on transient vehicle applications. Zeolite-containing SCR catalysts were known to adsorb large amounts of NH₃ below 450 °C and the risk of slip became greater in systems with an actively regenerating filter due to the necessary high temperature excursions that could cause NH₃ to be desorbed. The impact of ammonia storage levels on NO_x conversion was studied with a Cu/beta catalyst (Fig. 21.16). It was found that low temperature NO_x conversion was a strong function of the amount of ammonia stored on the catalyst [4]. Generally, higher NH₃ storage levels resulted in higher NO_x conversion with the saturation NH₃ level having the highest NO_x conversion.

The NO_x conversion dependency as a function of NH₃ exposure was studied with a Cu/CHA catalyst using a feed composition consisting of equimolar levels of NO and NH₃ (Fig. 21.17). With NO already flowing, a step function of 350 ppm NH₃ was introduced at Point 1 and passed over the SCR catalyst. NO_x conversion, NH₃ conversion, NH₃ slip, and N₂O formation were then monitored for the next 3,600 s. During the transition from Point 1 to Point 2, part of the feed gas NH₃ reduced feed gas NO and part of it adsorbed on the catalyst. The NO_x conversion increased as the NH₃ storage level on the catalyst increased. At Point 2, the catalyst began slipping NH₃, and this point was defined as the threshold storage capacity (TSC). Point 3 was the NO_x conversion at TSC, while Point 4 was the

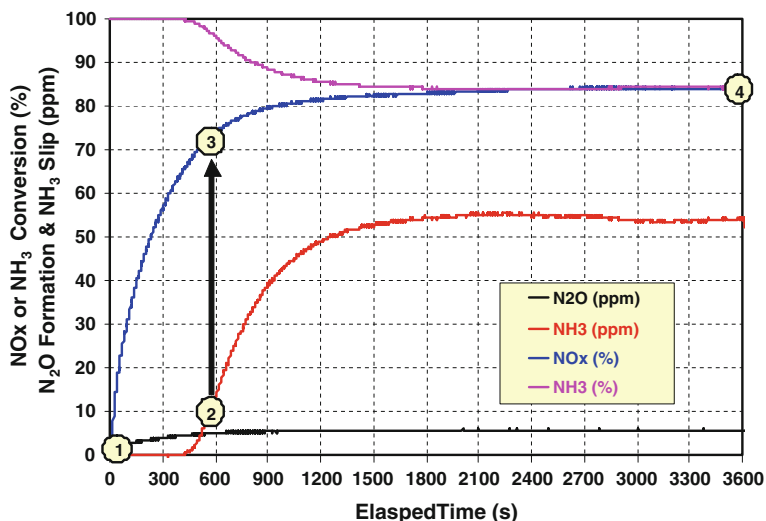


Fig. 21.17 NOx conversion dependence on NH₃ storage exposure time over a Cu/chabazite SCR catalyst at 205 °C while flowing equimolar levels of NO and NH₃ (30,000 h⁻¹, 5 % H₂O, 5 % CO₂, 14 % O₂, 350 ppm NO, 350 ppm NH₃, balance N₂)

maximum NOx conversion possible but with high levels of NH₃ slip and obviously not desired. This characterization procedure was then repeated for the wide range of temperatures for implementation into the vehicle level calibration using urea injection.

The initial NOx conversion, the TSC NOx conversion, the steady-state saturated NOx conversion of Cu/CHA as a function of catalyst temperature using only NO was summarized (Fig. 21.18). The initial NOx conversion represented the SCR catalyst performance after the cumulative NH₃ exposure of only 100 mg/L. The TSC NOx conversion represented the peak performance of the SCR catalyst with no more than 10 ppm NH₃ slip. The steady-state NOx conversion was determined after waiting 1 h at each temperature for conditions to stabilize and represented the best possible NOx conversion with unrestricted NH₃ slip. For high performance at low temperature, one needs to adjust the NH₃ storage level on the SCR catalyst somewhere at or just below the TSC level. Note that performance at temperatures >450 °C was independent of the cumulative NH₃ exposure level since this was beyond the temperature window for NH₃ adsorption.

The fundamental concepts learned in the laboratory were applied to the production vehicle program through the urea dosing controls [49], without the need for a downstream ammonia oxidation catalyst.

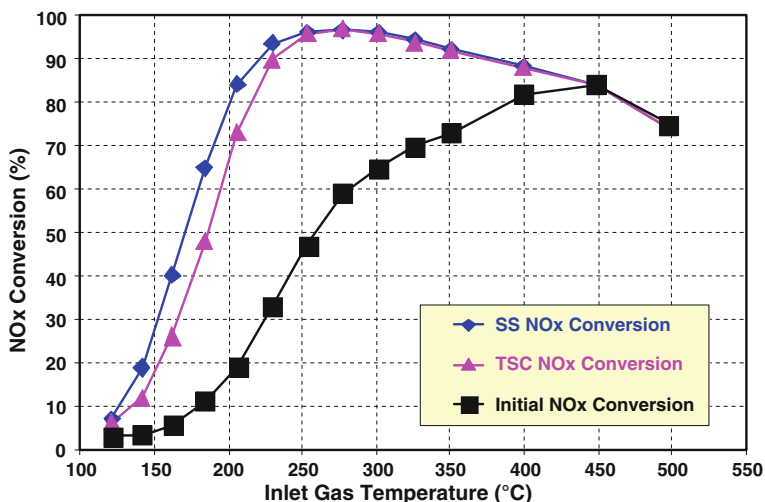


Fig. 21.18 Summary of steady-state NO_x conversion, TSC NO_x conversion, and initial NO_x conversion (100 mg/L NH₃ exposure level) as a function of inlet gas temperature (30,000 h⁻¹, 5 % H₂O, 5 % CO₂, 14 % O₂, 350 ppm NO, 350 ppm NH₃, balance N₂)

21.5.4 HC Poisoning/Coking of Zeolitic SCR Catalysts

Zeolite-based SCR catalysts adsorbed NH₃ for the desired purpose of NO_x reduction. However, zeolites were also well known for adsorbing HC present in combustion gases. HC and NH₃ competed for the storage sites and could have a detrimental effect on the NO_x conversion. The HC impact was found to depend on the hydrocarbon type, geometry, and quantity, as well as the exhaust temperature. At low temperatures less than about 300 °C, HC were physically adsorbed and blocked the zeolite's molecular channels leading to the interior cages holding the ion-exchanged metal such as Cu or Fe, thereby inhibiting the SCR reaction. At temperatures greater than about 300 °C, coke was formed by reaction of HC on the acidic zeolite surface. Additionally, large amounts of adsorbed HC and/or coke not only blocked active sites but also presented an exotherm risk when oxidized. HC inhibition and storage were studied carefully for SCR systems under diesel vehicle conditions in order to assess the risk of applying such a large amount of zeolite to an exhaust system which had never been done before.

The inhibition of SCR reactions by HC were studied in the laboratory flow reactor at temperatures around 200–300 °C typical of diesel vehicles over the FTP-75 drive cycle. From an analytical speciation of HC during a typical diesel cold start event, reasonable surrogates for laboratory testing were determined to be propylene (for olefins), benzene (for aromatics), and n-decane (for paraffins). As described earlier, the initial Cu and Fe SCR catalysts contained beta zeolite. Laboratory evaluations demonstrated that co-feeding any of the three hydrocarbon types had a

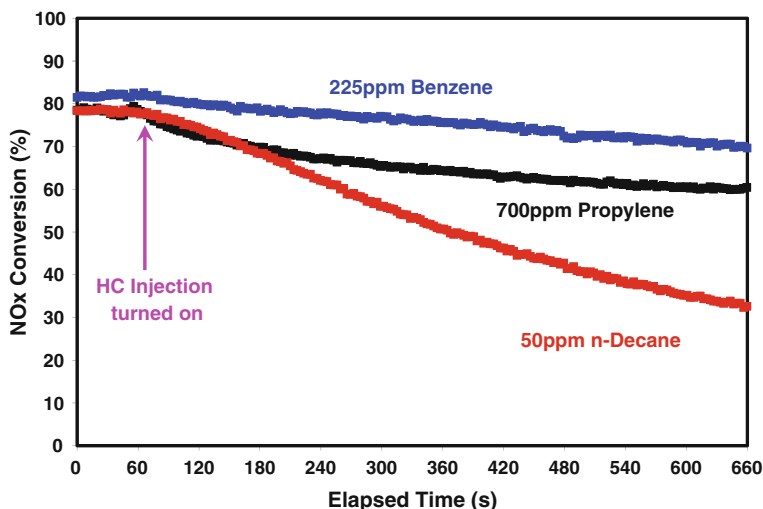


Fig. 21.19 NOx conversion at 200 °C as a function of HC type and elapsed time for a typical Cu/beta SCR catalyst at 30,000 h⁻¹ [4]. Copyright © SAE International. Reprinted with permission from 2007-01-1575

negative impact on NOx conversion [4]. Figure 21.19 shows the results for the Cu/beta at 200 °C. Approximately 80 % NOx conversion was achieved in the absence of HC, but once HC injection was turned on, the NOx conversion steadily declined in the presence of all three HC species tested. Normal decane was the most detrimental, followed by propylene and benzene. For 300 °C, propylene had the most significant impact on NOx conversion followed by n-decane and benzene (not shown). However, compared to 200 °C, the decline in performance at 300 °C was immediate when each HC was introduced rather than the steady decline in NOx conversion observed for the 200 °C case. Fe/beta also suffered a negative impact on NOx conversion by HC, although benzene had the least impact for Cu/beta formulation but the most significant impact on Fe/beta. When HC was turned off, NOx conversion recovered at a rate similar to the inhibition rate.

In addition to HC inhibition effects, large pore zeolites such as beta can also lead to a large build up of stored HC at low exhaust temperatures such as 200 °C [19]. There was a concern that low temperature modes such as repeated cold start events and extend idles slipped abundant HC past the upstream DOC and allowed for excessive HC storage within the SCR catalyst. This stored HC could burn when the exhaust temperature was ramped up such as during active filter regeneration and create a major risk for the exhaust system. A sharp decrease in vehicle NOx conversion with low mileage prototype vehicles prompted further investigation. It was speculated that a rapid oxidation of a potentially large amount of stored HC within the SCR catalyst could damage it. A postmortem analysis revealed that not only was there zeolite damage but portions of the cordierite SCR monolith were melted. Laboratory experiments were devised that exposed SCR catalysts to diesel vapor.

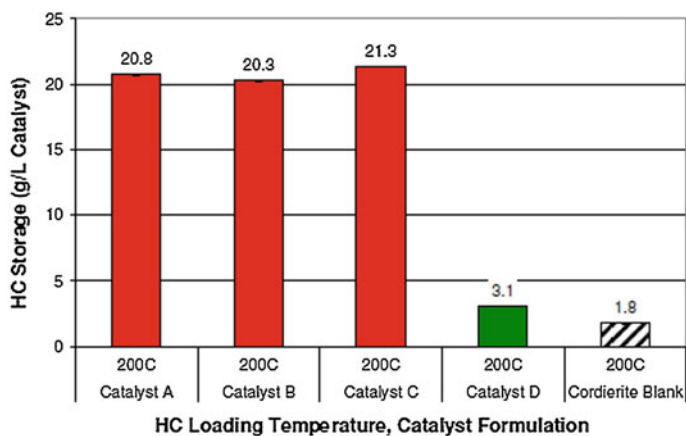


Fig. 21.20 HC storage after exposure to diesel fuel vapor at low temperature for zeolite-based SCR formulations [19]. Catalysts A, B, and C contain beta zeolite while Catalyst D was Cu/CHA. Copyright © SAE International. Reprinted with permission from 2008-01-0767

The beta type zeolites (Catalyst A, B, and D) could store 20 g/L of diesel fuel vapor at 200 °C. Subsequently, the catalyst temperature was ramped up to simulate filter regeneration. A rapid temperature rise confirmed the ability of the base metal zeolites to oxidize HC rapidly to generate extreme temperatures near 1,000 °C. In many cases, the oxidation of the HC was so rapid that all the oxygen in the feed gas was consumed. To put this in perspective, filter regeneration was initiated when the soot accumulation reached a level of about 6–7 g/L in order to have a controlled burn. The SCR catalyst might contain about three times that amount, and often accumulated HC quickly depending on the engine operating condition, resulting in failures at less than 100 mi.

Next, laboratory protocols were developed to screen improved SCR formulations for the HC storage/exotherm failure mode. The improved catalysts were as a result of program requirements communicated to catalyst suppliers. Small pore chabazite (CHA) zeolite catalysts containing Cu became available. Cu/CHA, designated as Catalyst D in Figs. 21.20 and 21.21, significantly reduced the risk of this failure mode. In Fig. 21.20, the apparent hydrocarbon storage was lowered from 20 to 3 g/L, effectively the same amount as an uncoated cordierite monolith. As expected, the small pore zeolite had no significant exotherm for the subsequent rapid temperature rise experiment (Fig. 21.21).

Furthermore, the new generation of small pore CHA zeolite catalyst formulations was reexamined to determine tolerance to inhibition by propylene, benzene, and n-decane [44]. The results indicated that the negative NO_x conversion impact due to benzene and n-decane were largely eliminated and only a modest impact from propylene remained. Now Ford had a catalyst for SCR that not only reduced the risk the HC storage/exotherm that could damage the cordierite substrate, but was also more thermally robust to 900 °C that further mitigated risk of failure.

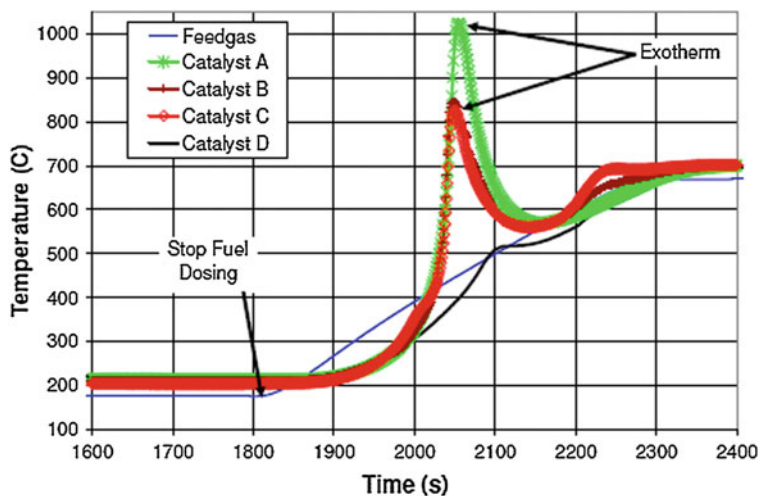


Fig. 21.21 During temperature programmed oxidation (TPO), HC storage resulted in significant exotherms over beta zeolite SCR catalysts (Catalysts A, B and C) compared to the Cu/CHA SCR catalyst (Catalyst D) [19]. During TPO, the space velocity was $15,000 \text{ h}^{-1}$ and there were no HCs, 10 % O_2 , 5 % H_2O , 5 % CO_2 , and balance N_2 . Copyright © SAE International. Reprinted with permission from 2008-01-0767

Based on these findings, work continued with small pore zeolite catalysts for application onto particulate filters. Results indicated additional tolerance to soot and coke deposition due to diesel fuel exposure [7].

21.5.5 Precious Metal Poisoning

Diesel aftertreatment systems configured with a DOC upstream of urea SCR catalyst run the risk of precious metal contamination. During active DPF regeneration events, the DOC bed temperature can reach up to $850 \text{ }^\circ\text{C}$. Under these conditions, precious metal (especially Pt) can be volatilized and then deposited on a downstream SCR catalyst. A diesel aftertreatment system consisting of a DOC, urea-based SCR catalyst and DPF was aged and evaluated on a 6.4 liter diesel engine dynamometer [26]. The SCR catalyst system consisted of Fe/beta followed by Cu/beta. After approximately 400 h of engine operation at varied exhaust flow rates and temperatures, a decline in NO_x conversion was observed. A subsequent detailed investigation revealed that the Cu catalyst was not deactivated but the front half of the Fe catalyst showed severe deactivation. The deactivated portion of the catalyst showed high activity of NH_3 conversion to NO_x and N_2O formation. The cause of the deactivation was suspected to be the presence of trace Pt contamination below the detection limit of 0.002 wt % (20 ppm) by a conventional

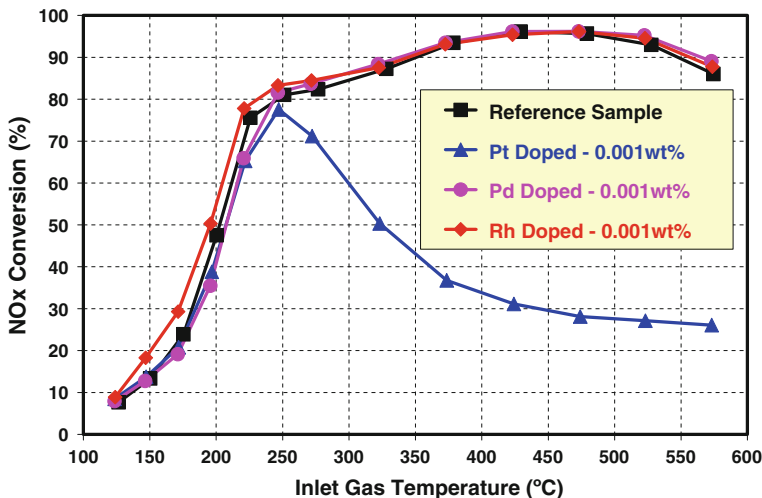


Fig. 21.22 NO_x conversion of de-greened Fe/beta formulations after contamination with various precious metals [8]. Standard SCR evaluation conditions were used (30,000 h⁻¹, 5 % H₂O, 5 % CO₂, 14 % O₂, 350 ppm NO, 350 ppm NH₃, balance N₂). Copyright © SAE International. Reprinted with permission from 2009-01-0627

X-ray fluorescence (XRF) method. At first, an in-house probe reaction method was used to detect the presence of Pt within the SCR catalyst. The reaction system measured the conversion of ethylene to ethane at room temperature, allowing for detection of Pt metal below 0.001 wt % (10 ppm). The presence of Fe, Cu, or Ni did not interfere with the ethylene hydrogenation technique.

In order to duplicate what the Pt poisoning phenomenon found during dyno aging, a laboratory technique was developed that caused sublimation of Pt from an upstream DOC onto a downstream Fe catalyst by exposing the DOC to 850 °C for 16 h with a lean gas composition [8]. This precious metal volatilization method was employed to screen various Pt/Pd-based DOCs for low precious metal contamination risk over a downstream SCR. A correlation was developed that showed a reduction in SCR catalyst contamination as the Pt:Pd ratio decreased. A Pd-only DOC showed no impact to NO_x conversion and no increase in N₂O formation, while a Pt-rich DOC showed the most impact negative impact. In addition to lower risk of contamination, DOC formulations with higher Pd content demonstrated enhanced CO and HC light-off stability after the hydrothermal 850 °C lean exposure. The higher Pd content served to stabilize Pt in the DOC formulations, resulting in less Pt vaporization. The vaporization of Pd from the DOC formulations was determined to be very low. To study the relative impact of the precious metal type, an incipient wetness technique was used to purposely dope 0.001 wt % Pt, Pd, or Rh on the Fe formulation. The results shown in Fig. 21.22 indicate that Pt had the most adverse affect on the NO_x conversion while Pd and Rh had no impact with the 0.001 wt % level.

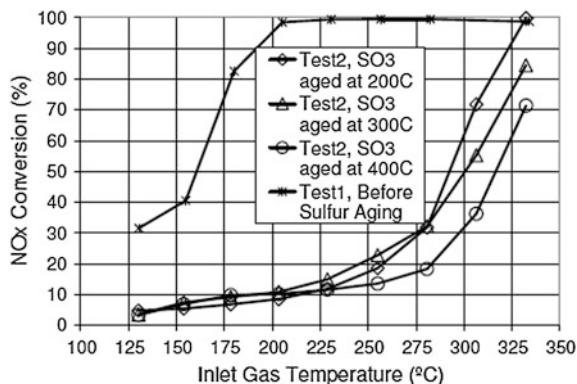


Fig. 21.23 NOx conversion of baseline Cu catalyst sample compared to samples tested after poisoning with SO₃ at 200 °C, 300 °C, and 400 °C formulations [11]. Standard SCR evaluation conditions were used (30,000 h⁻¹, 4.5 % H₂O, 5 % CO₂, 14 % O₂, 350 ppm NO, 350 ppm NH₃, balance N₂). Copyright © SAE International. Reprinted with permission from 2009-01-0898

21.5.6 Sulfur Effects on Catalysts

It was known that Cu/beta SCR catalysts, unlike vanadia/titania, were affected by sulfur poisoning [10]. The catalysts could be regenerated by routinely decomposing the sulfates at higher temperatures (>650 °C) under lean gas such as encountered during an active filter regeneration event. Sulfur poisoning continued to be a concern for the duration between regeneration events even with 15 ppm ULSD fuel. Most studies on sulfur poisoning of base metal zeolite SCR catalysts were based on SO₂ as the poisoning agent. DOCs that were purposely designed to enhance NO oxidation to NO₂ will likely also oxidize a portion of the SO₂ to SO₃. The type and amount of Pt in the DOC influenced this oxidation function, while Pd was neutral. The relative impact of SO₂ poisoning compared to SO₃ poisoning was studied to determine the implications of Pt/Pd DOC design on the sulfur poisoning of the downstream Cu/CHA SCR catalyst [11]. Figure 21.23 shows the NOx activity of the Cu/zeolite samples before and after sulfur poisoning by SO₃ at 200, 300, and 400 °C. The low temperature NOx activities were significantly decreased for all the samples after being exposed to 40 ppm SO₃ for 1.5 h (ca. 500 sulfur equivalent vehicle miles assuming 350 ppm sulfur fuel) regardless of the poisoning temperatures. The SCR catalyst needed to provide better than 90 % NOx conversion in the 200–300 °C temperature range for typical diesel trucks over the FTP-75 cycle. Notice that SO₃ poisoning reduced the NOx conversion at 200 °C from 95 to 10 %, regardless of the poisoning temperature. For the complimentary poisoning study with SO₂, the worst case involved an NOx conversion drop from 95 to 70 % (200 °C SO₂ poisoning condition). Temperature programmed oxidation (TPO) experiments indicated that the SO₃ poisoned samples stored much higher levels of sulfur compared to the SO₂ poisoned samples. Most of the sulfur

released (as SO_2) at 450 and 650 °C. Finally, exposure to lean high temperature gas conditions over 700 °C was adequate enough to regenerate all the poisoned samples and return the NO_x conversion to the baseline level. This meant that the sulfur impact could be managed by lean filter regenerations and Pd-rich DOCs.

21.5.7 Urea Injection/Mixing

It was known that urea mixing was important during the research program between Ford and DOE. Bad mixing gave performance like a poor or degraded SCR catalyst because it effectively used less of the catalyst for NO_x conversion. A spray target for aqueous urea was designed by FEV and used in conjunction with spray against the exhaust flow direction [30]. An elongated entrance cone with a shallow angle into the SCR catalyst also aided the distribution of the urea/water droplets and improved NO_x conversion. For the production program, it was decided to adopt the shallow entrance cone but design a new mixer system that would allow for injection of urea in the exhaust flow direction for greater injector robustness. It also had to fit within the medium-duty exhaust package. Several mixer designs were compared for spray uniformity. The best mixer design was the combination of a so-called flap mixer followed by an auger-like “twist” or helical mixer [41]. The flap mixer improved spray dispersion and increased the breakup of droplets. The helical mixer, installed in the entrance cone to the SCR catalyst, forced exhaust gases and entrained droplets to follow a longer path that increased the time for droplet evaporation. Uniformity of reductant at the front face of the SCR catalyst approached 95 % or more. The new mixing system was put into production in 2010 when urea SCR was launched on Ford diesel trucks.

21.5.8 Urea Specifications and Refill

The final barrier for implementing SCR commercially on diesel trucks was the infrastructure for delivery of the appropriate concentration and purity of aqueous urea. First, the business case for urea infrastructure was explored through collaboration between Ford, ExxonMobil, and DOE. A co-fueled urea/diesel concept [1, 9, 20] useable to -20 °F was improved in reliability and durability and demonstrated to DOE and EPA as a viable long-term solution [35]. Heaters were designed for use in the urea tank and delivery system to prevent freeze and avoid a “winter grade” urea with potential for catalyst contamination due to additives like glycols [33]. A study of the economics of an aqueous urea infrastructure for light-duty service stations in the U.S. found that the long-term cost of bottled aqueous urea for vehicle use could be approximately \$3.66/gal, while co-fueled urea could be as low as \$1.50/gal in mass use [35]. However, co-fueling required a capital

investment in excess of \$25,000 for a new dispenser and urea tank that exceeded what a small business owner with one diesel pump could likely afford.

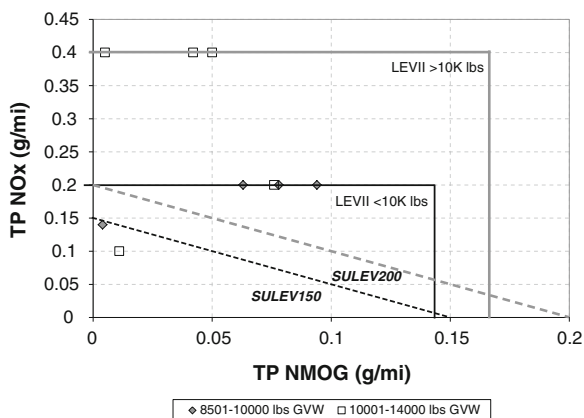
Other feasibility/proof-of-concept studies were completed at about the same time for light duty diesel urea infrastructure with similar results [48]. The next step was to obtain cooperation between OEMs and suppliers and form a working group to define specifications. This group, operating through USCAR, developed a trade name for aqueous urea and defined specifications that were largely based on the DIN specification in Europe for AdBlue[®] [12]. Aqueous urea is now sold in bottles, drums, totes, and bulk dispensers under the name “Diesel Exhaust Fluid” or “DEF.” Costs for DEF in 2012 are running at about \$2.89/gal in bulk and up to \$4.40/gal in 2.5 gal bottles, within the range of the prior business case study. A diesel driver can now go to multiple websites, such as <http://www.dieselexhaustfluid.com/>, and find places to buy DEF. What was once considered a major hurdle is now commonplace.

21.6 Environmental Impact of Medium-Duty Diesels: Current and Future

21.6.1 *NOx Emissions*

The LEVII medium-duty vehicle standards for NO_x represented 70–80 % reduction from past LEV standards. Average medium-duty diesel truck sales from 2010 to 2012 were about 175,000 per year according to the R.L. Polk automotive sales database, roughly split 50/50 between Class 2b (8,501–10,000 lbs GVW) and Class 3 (10,001–14,000 lbs GVW). Assuming an average mileage of 12,000 mi/yr and an NO_x reduction of about 1 g/mi, there was an estimated 2,100 metric tons of NO_x per year not emitted by these trucks after 2010. Future standards offer even further potential reductions. Comparison of current LEVII and future LEVIII medium-duty vehicle standards can be found in Fig. 21.24. Certification data from all 2012MY diesel trucks meeting LEVII are included for reference [14]. All of these trucks use urea SCR except for one (Dodge Ram with lean NO_x adsorber). It is important to note that LEVIII standards will consist of combined NMOG + NO_x, giving more room for OEMs to vary the NO_x/HC tradeoff for best efficiency and cost effectiveness. SULEV150 means 150 mg/mi (0.150 g/mi) NMOG + NO_x and SULEV200 means 200 mg/mi (0.200 g/mi) NMOG + NO_x, and these are the lowest certification levels anticipated for Class 2b and 3. LEVIII will require 150,000 mi of durability while LEVII required 120,000 mi. Evidence exists for the ability for urea SCR to meet these future standards by the current certification of at least one OEM shown in Fig. 21.24.

Fig. 21.24 Progression from LEV to LEVIII (SULEV150/200) emission standards for medium-duty vehicles



21.6.2 Greenhouse Gas Footprint (CO_2 , CH_4 , N_2O)

The majority of 2010+ medium-duty diesel trucks use urea SCR. Comparison of Class 2b/Class 3 peak torque brake specific CO_2 for medium-duty vehicles show a reduction of about 50 g/kWh, or roughly 6–7 % [50]. At light to moderate loads the CO_2 advantage for SCR-equipped diesel is >10 %. The methane contribution of these trucks is small at approximately 25 mg/mi, and is virtually unchanged over the catalyst system. It is known that nitrous oxide (N_2O), a powerful greenhouse gas, can be created in exhaust gas catalysts, including gasoline TWCs [45]. The global warming potential of N_2O is approximately 298 times that of CO_2 on a mass basis [17], so even the creation of a small amount of N_2O is of concern. Following the medium-duty guidelines recently set by the U.S. E.P.A. (United States Environmental Protection Agency), the reported N_2O value for a particular vehicle line is a weighted composite with 55 % city (FTP-75) weighting and 45 % highway (HWFET) weighting, similar to the current approach for CO_2 reporting. The potential sources of N_2O were compared in the laboratory flow reactor and on the system level with a production diesel truck at 9,500 lbs [40]. It was found that the interactions of HC with NO_x on the DOC and NO_2 with NH_3 within the SCR catalyst were the predominant mechanisms for N_2O formation. The composite N_2O mass emission was calculated to be approximately 43 mg/mi, resulting in an equivalent CO_2 penalty of about 2 %, similar to the 1–3 % penalty estimated for the global light-duty vehicle fleet [2]. The formation of N_2O was minimized through the use of low-loaded, Pd-rich DOCs and Cu/CHA SCR catalysts.

21.6.3 Use of Base Metals, Pd Rich Catalysts

The catalyst evolution for Ford's U.S. medium-duty diesel trucks included a migration from low or no precious metal DOCs to Pt-rich DOCs, and finally to

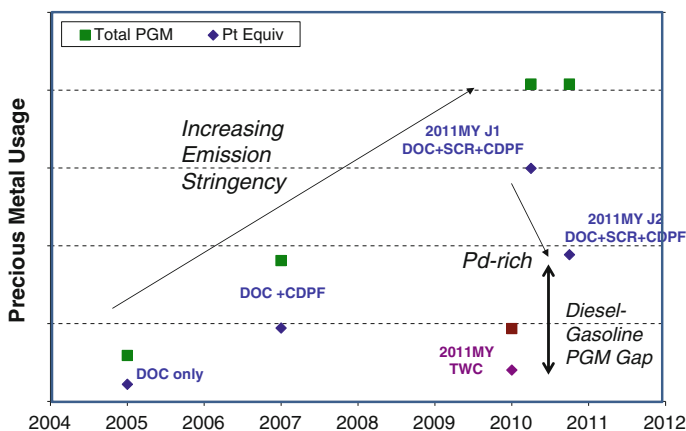


Fig. 21.25 Precious metal usage on Ford super duty trucks

today's Pd-rich DOCs. This migration toward and then away from Pt took place over the course of only 5 years as new emission requirements phased in and new catalyst technology became available through work at Ford and its suppliers. In addition, the lean NO_x technology of urea SCR used low-cost Cu instead of precious metals. The extensive use of Cu was enabled by the development of small pore zeolites for automotive applications that met the low temperature performance requirements and had high temperature durability. To gain perspective on the overall precious metal usage of diesel trucks, it was important to compare to a similar truck with a gasoline engine and a TWC system. Had diesels closed the gap with gasoline PGM (Pt group metal) use? The total precious metal usage of Ford's diesel trucks had crept up due to the addition of DPFs and the need for robust active regenerations, plus the desire for low temperature SCR performance improvement via NO₂ generation. Between 2005 and 2010, the precious metal usage had roughly quadrupled with increasing emissions stringency (Fig. 21.25). The "Job 1" or J1 (first truck produced) for the 2011MY (MY = model year) was in April 2010 with the launch of urea SCR and catalyzed DPF. Pt equivalency was calculated by applying the cost ratio between other precious metals and Pt and it increased proportional to the overall PGM. Later in the 2011MY (J2), Ford introduced Pd-rich DOCs (Nov 2010), causing a significant drop in equivalent Pt, although the overall precious metal use stayed the same. This was accomplished by replacing the DOCs with 2:1 Pt:Pd by DOCs at 1:4 Pt:Pd. However, the Pt equivalence is still much higher than a similar gasoline-powered truck with a Pd-Rh TWC meeting the same LEVII emission standards. Future model years will include overall PGM reductions for diesels. It is also important to note that there are other costs associated with catalyst systems including substrates, washcoats, canning, etc., that are not taken into consideration here. Diesel catalyst systems are considerably larger than gasoline catalyst systems.

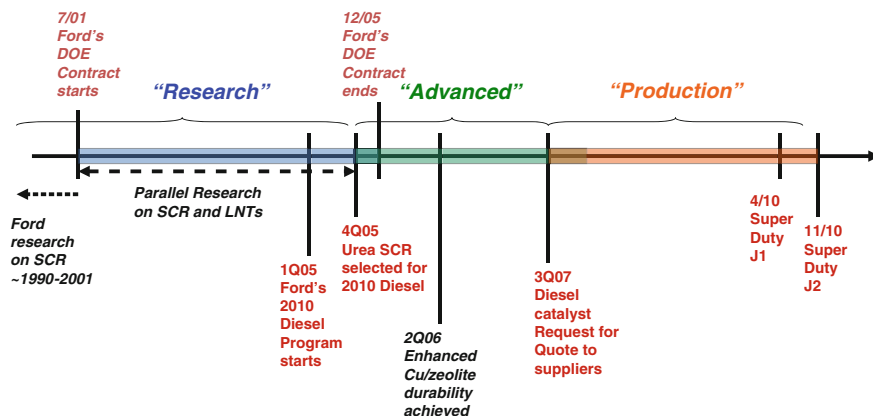


Fig. 21.26 Timeline from research to production program for the 2010 Ford diesel truck catalyst system. J1 = Job 1 (first vehicle produced, urea SCR introduced in 2011MY); J2 = Job 2 (significant change in production, Pd-rich DOCs introduced)

21.7 Conclusion

Diesel aftertreatment systems operate within a window of constraints including cost, fuel economy, and emissions. These constraints determine the range for exhaust temperature, flow rate, and mass flux of chemical species that becomes the basis for the catalyst system design (size, formulation, etc.). Designing a catalyst system for high efficiency that will go on a large Class 2b/3 diesel truck known for its toughness and durability was formidable. Early research into urea SCR systems suggested that the technology had the potential to meet future NO_x emission standards. Ford became a leader in urea SCR technology through early concept studies that proved sound enough to migrate into a production program. Challenges were overcome during the course of the 10+ year catalyst system development that maximized performance and fuel economy of the exhaust system and reduced cost. The location of SCR upstream of the DPF was essential for cold start NO_x performance and better fuel economy. Cu/zeolite was selected as the SCR catalyst over more traditional vanadia/titania and iron/zeolite due to its lower dependence on feed gas NO₂ for low temperature NO_x reduction. DOCs were optimized from Pt to Pd-rich formulations that improved thermal stability, reduced cost, and minimized SCR poisoning by precious metals and SO₃. Risks such as SCR thermal stability and HC storage on the SCR catalyst were minimized by adopting small pore zeolite (CHA) in lieu of the better known beta zeolite. Items associated with the use of an external reductant for lean NO_x control, such as urea injection, urea mixing, ammonia storage by the SCR catalyst, ammonia slip, urea specifications, and urea refill became manageable items once the direction to adopt urea SCR technology was set. There is still more work to do to further reduce cost and robustly meet future LEV_{III} emission standards. However, it is clear that the

launch of urea SCR systems on Ford diesel trucks was a success in terms of NO_x and GHG emissions saved and the first widespread use of a base metal/zeolite catalyst for automotive exhaust gas aftertreatment. A summary of the timeline and important milestones are given in Fig. 21.26.

Acknowledgments The authors acknowledge the input of many team members at Ford, its suppliers, and partners, to this body of work over the last 12 years. Most notably the authors thank Yisun Cheng, Douglas Dobson, James Girard, Gang Guo, Hungwen Jen, Jeong Kim, Cliff Montreuil, Rachel Snow, James Warner, and Scott Williams for their inexhaustible research efforts on how and when diesel catalyst and filters fail and how systems can be improved. Diesel aftertreatment research at Ford would not have gotten very far without the direction of Haren Gandhi, Robert Hammerle, and Richard Baker, and strategic funding by the Department of Energy [DE-FC26-01NT41103] allowed Ford the luxury of studying, in detail, a controversial technology for lean NO_x control that is widely used today. Excellent management by Larry Brouwer allowed a research concept to migrate into a production program. The Vehicle Emissions Research Laboratory at Ford Motor Co. is second to none. Finally, the authors thank essential Ford researchers that worked to develop various aspects of urea SCR systems: Paul Laing, Mike Levin, Michiel van Nieuwstadt, Will Ruona, Paul Tennison, and Devesh Upadhyay.

References

1. Baker RE, Bates B (2000) Automotive vehicle fueling system. US Patent 6,032,703, 7 Mar 2000
2. Becker KH, Lörzer JC, Kurtenback R, Wiesen P, Jensen T, Wallington TJ (1999) Nitrous oxide (N₂O) emissions from vehicles. *Env Sci Tech* 33:4134–4139
3. Bull I, Xue W-M, Burk P, Boorse RS, Jaglowski WM, Koermer GS, Moini A, Patchett JA, Dettling JC, Caudle MT (2009) Copper CHA zeolite catalysts. US Patent 7,601,662, 13 Oct 2009
4. Cavataio G, Girard J, Patterson JE, Montreuil C, Cheng Y, Lambert CK (2007) Laboratory testing of urea-SCR formulations to meet Tier 2 Bin 5 emissions. SAE Technical Paper 2007-01-1575
5. Cavataio G, Jen H-W, Warner JR, Girard JW, Kim JY, Lambert CK (2008) Enhanced durability of a Cu/zeolite based SCR catalyst. SAE Technical Paper 2008-01-1025
6. Cavataio G, Kim JY, Warner JR, Girard JW, Upadhyay D, Lambert CK (2009a) Development of emission transfer functions for predicting the deterioration of a Cu-zeolite SCR catalyst. SAE Technical Paper 2009-01-1282
7. Cavataio G, Warner JR, Girard JW, Ura J, Dobson D, Lambert CK (2009b) Laboratory study of soot, propylene, and diesel fuel impact on zeolite-based SCR filter catalysts. SAE Technical Paper 2009-01-0903
8. Cavataio G, Jen H-W, Girard JW, Dobson D, Warner JR, Lambert CK (2009c) Impact and prevention of ultra-low contamination of platinum group metals on SCR catalysts due to DOC design. SAE Technical Paper 2009-01-0627
9. Channing DA (2002) Fuel and reductant delivery system. US Patent 6,390,147, 21 May 2002
10. Cheng Y, Montreuil C, Cavataio G, Lambert C (2008) Sulfur tolerance and deSO_x studies on diesel SCR catalysts. SAE Technical Paper 2008-01-1023
11. Cheng Y, Montreuil C, Cavataio G, Lambert C (2009) The effects of SO₂ and SO₃ poisoning on Cu/zeolite SCR catalysts. SAE Technical Paper 2009-01-0898
12. Deutsches Institut für Normung E.V. (2005) AUS32 (AdBlue[®]) specifications per DIN 70070. In: <http://din70070.com/>. Accessed 30 Aug 2012

13. Engler B, Koberstein E, Volker H (1986) Catalytically activated diesel particulate traps – New development and applications. SAE Technical Paper 860007
14. Executive Orders Listing (2012) California Environmental Protection Agency Air Resources Board, Sacramento. <http://www.arb.ca.gov/msprog/onroad/cert/cert.php#6>. Accessed 30 Aug 2012
15. Farrauto RJ, Heck RM (1999) Catalytic converters: state of the art and perspectives. *Catal Today* 51:351–360
16. Ford Motor Co. (2011) Diesel engine aftertreatment: How Ford knocks out the NOx. In: Ford Media Technology Fact Sheets. http://media.ford.com/images/10031/SD_Diesel_Aftertreatment.pdf. Accessed 28 Aug 2012
17. Forster P et al. (2007) Changes in atmospheric constituents and in radiative forcing. In: Solomon, S. et al. (Eds.), *Climate Change 2007: The Physical Science Basis. Contribution of Working Group I to the Fourth Assessment Report of the Intergovernmental Panel on Climate Change*. Cambridge University Press, Cambridge
18. Gandhi H, Dobson D, Cavataio G, Guo G, Huang Y, Laing P, Lambert C, Warner J, Williams S (2008) Urea SCR Options for a Tier 2 Light-Duty Diesel Truck. Paper F2008-06-022 presented at FISITA, Munich, Germany, September 2008
19. Girard J, Snow R, Cavataio G, Lambert C (2008) Influence of hydrocarbon storage on the durability of SCR catalysts. SAE Technical Paper 2008-01-0767
20. Grosser RW (2001) Vehicle engine system additive dispenser. US Patent 6,263,924, 24 July 2001
21. Hammerle RH, Lambert CK, Laing PM, Tennison PJ, Ruona WC (2004) Exhaust gas aftertreatment systems, US Patent No. 6,823,663, 30 Nov 2004
22. Heck RM, Farrauto RJ (2001) Automotive exhaust catalysts. *Appl Catal A: Gen* 221:443–457
23. Held W, König A, Richter T, Puppe L (1990) Catalytic NOx reduction in net oxidizing exhaust gas, SAE Technical Paper 900496
24. Hepburn JS, Dobson DA, Hubbard CP, Otto K (1996) The pulse flame combustor revisited. SAE Technical Paper 962118
25. Hug HT, Mayer A, Hartenstein A (1993) Off-highway exhaust gas aftertreatment combining urea-SCR, oxidation catalysis and traps. SAE Technical Paper 930363
26. Jen H-W, Girard JW, Cavataio G, Jagner MJ (2008) Detection, Origin and Effect of Ultra-Low Platinum Contamination on Diesel-SCR Catalysts. SAE Technical Paper 2008-01-2488
27. Kitco Historical Charts for PGMs (2012) Kitco Metals Inc., Montreal. <http://www.kitco.com>, Accessed 29 Aug 2012
28. Koebel M, Elsener M, Marti T (1996) NOx-reduction in diesel exhaust gas with urea and selective catalytic reduction. *Combust Sci Tech* 121:85–102
29. Koebel M, Elsener M, Kleemann M (2000) Urea-SCR: a promising technique to reduce NOx emissions from automotive diesel engines. *Catal Today* 59(3-4):335-345
30. Koehler E, Tomazic D, Adomeit P (2010) Exhaust injector spray target. US Patent 7,788,907, 7 Sept 2010
31. Lambert C, Vanderslice J, Hammerle R, Belaire R (2001) Application of SCR to light-duty diesel vehicles. SAE Technical Paper 2001-01-3623
32. Lambert CK, Laing PM, Hammerle RH (2002) Using diesel aftertreatment models to guide system design for Tier II emission standards. SAE Technical Paper 2002-01-1868
33. Lambert C, Montreuil C, Vanderslice J (2003) Application of organic freeze-point depressants in aqueous urea solutions: Effect on NOx reduction. SAE Technical Paper 2003-01-0775
34. Lambert C, Hammerle R, McGill R, Khair M, Sharp C (2004a) Technical Advantages of Urea SCR for Light-Duty and Heavy-Duty Diesel Vehicle Applications. SAE Technical Paper 2004-01-1292
35. Lambert C et al. (2004b) Urea SCR and DPF system for diesel sport utility vehicle meeting Tier 2 Bin 5. Presented at the 2004 Diesel Engine-Efficiency and Emission Research Conference, Coronado, 2 Sept 2004

36. Lambert C, Cavataio G, Cheng Y, Dobson D, Girard J, Laing P, Patterson J, Williams S (2006a) Urea SCR and DPF system for Tier 2 diesel light-duty trucks. Presented at the 2006 Diesel Engine- Efficiency and Emissions Research Conference, Detroit, 24 Aug 2006
37. Lambert C, Williams S, Carberry B, Koehler E, Tomazic D (2006b) Harnstoff SCR und CDPF system für einen light-duty truck (Urea SCR and CDPF system for a Tier 2 light-duty truck). Paper presented at the 15th Aachener Kolloquium Fahrzeug- und Motorentechnik, Aachen, Germany, October 2006
38. Lambert CK, Cheng Y, Dobson D, Hangas J, Jagner M, Jen H, Warner J (2009) Post mortem of an aged Tier 2 light-duty diesel truck aftertreatment system. SAE Technical Paper 2009-01-2711
39. Lambert C, Cavataio G, Dobson D (2011) Development of the 2011MY Ford Super Duty catalyst system. Presented at the 2011 Directions in Engine-Efficiency and Emissions Research Conference, Detroit, 4 Oct 2011
40. Lambert C, Dobson D, Gierczak C, Ura J, Warner J (2014) Nitrous oxide emissions from a medium-duty diesel truck exhaust system. *Int J Powertrains* 3(1):4–25
41. Levin M, Balestrino S, Kabat DM, Shaikh FZ, Zimmerman BA, Keller J, Cooper SD, Kantebet K (2010) Approach for delivering a liquid reductant into an exhaust flow of a fuel burning engine. US Patent 7,814,745, 19 Oct 2010
42. Luders H, Backes R, Huthwohl G, Ketcher DA, Horrocks RW, Hurley RG, Hammerle RH (1995) An urea lean NO_x catalyst system for light duty diesel vehicles. SAE Technical Paper 952493
43. Madia G, Elsener M, Koebel M, Raimondi F, Wokaun A (2002) Thermal stability of vanadia-tungsta-titania catalysts in the SCR process. *Appl Catal B: Env* 39:181–190
44. Montreuil C, Lambert C, (2008) The effect of hydrocarbon on the selective catalyzed reduction of NO_x over low and high temperature catalyst formulations. SAE Technical Paper 2008-01-1030
45. Odaka M, Koike N, Suzuki H (1998) Deterioration effect of three-way catalyst on nitrous oxide emission. SAE Technical Paper 980676
46. Tennison P, Lambert C, Levin M (2004) NO_x Control Development with Urea SCR on a Diesel Passenger Car. SAE Technical Paper 2004-01-1291
47. Tennison PJ, Laing PM, Lambert CK, Hammerle RH, Ruona WC (2005) Exhaust gas aftertreatment systems, US Patent 6,928,806, 16 Aug 2005
48. TIAX LLC (2004) Light-duty diesel vehicle SCR-urea supply study: Final report. Prepared for the Alliance of Automotive Manufacturers, 23 Nov 2004
49. Upadhyay D, van Nieuwstadt M (2006) Model based analysis and control design of a Urea-SCR deNO_x aftertreatment system. *J Dynamic Sys* 128(3):737–741
50. Wallington TJ, Lambert CK, Ruona WC (2013) Energy policy 54:47–53

Chapter 22

Model-Based Approaches to Exhaust Aftertreatment System Development

Michel Weibel, Volker Schmeißer and Frank Hofmann

Abbreviations and Symbols

Latin Symbols

C	Species concentration (mol/m ³)
E	Activation energy (J)
k_i	Pre-exponential kinetic parameter (mol · K/(m _{pt} ² ·s))
$k_{0,i}$	Pre-exponential kinetic parameter constant (mol · K/(m _{pt} ² ·s))
R	Ideal gas constant (J/(kg K))
SV	Space velocity (1/h)
T	Temperature (K)

Greek Symbols

η	NO _x conversion, DeNO _x performance [-]
θ, θ_{NH_3}	Normalized NH ₃ load [-]

Abbreviations and Indices

a	Activation
AdBlue	DEF (Diesel exhaust fluid)
ASC	Ammonia Slip Catalyst
DOC	Diesel Oxidation Catalyst
out	Catalyst downstream
DPF	Diesel Particle Filter
ECU	Electronic Control Unit
ExACT	Exhaust Aftertreatment Components Toolbox
HC	Hydrocarbons

M. Weibel (✉) · V. Schmeißer · F. Hofmann
Combustion and Emission Control, Group Research and Advanced Engineering Powertrain,
Daimler AG, 019-G206 RD/RPE, 70546 Stuttgart, Germany
e-mail: michel.weibel@daimler.com

HiL	Hardware In the Loop
i	Reaction number
in	Catalyst upstream
inh	Inhibition
j	Parameter number
max	Maximum
NSC	NO _x Storage Catalyst
s	Solid
SiL	Software In the Loop
TWC	Three-Way Catalyst
WHTC	World Harmonized Transient Cycle

22.1 Introduction

One major challenge for car manufacturers since several years is to be compliant with the stringent emission standards for internal combustion engines, especially in Europe and in the US. Besides the treatment of standard pollutants like CO, NO_x, and HC, the emission of CO₂ has gained increasing environmental relevance due to its greenhouse potential. Further reduction in CO₂ emissions for lean-burn engines is, in general, correlated with an increase of NO_x raw emissions and requires improved aftertreatment systems.

The stringent exhaust emission levels in the US as well as future European emission standards considering also Real Driving Emissions represent a huge challenge in the development of efficient exhaust aftertreatment technologies. For lean-burn engines and especially for the diesel engine, proven technologies like the diesel oxidation catalyst (DOC) or the three-way catalyst (TWC) are not capable of reducing the NO_x under lean conditions. Therefore, new catalytic systems have been developed in order to selectively reduce the emissions of NO_x with high efficiency.

In the past years, two major catalytic approaches to NO_x reduction have been developed. The most popular is the SCR technology based on NH₃ as the reducing agent, which is generated from AdBlue injected in the exhaust line. This technology was first introduced on the market for truck application in relation to EURO IV/V emission standards. In the meantime, this technology was also developed for diesel passenger car application [1] and enables high performance in the reduction of NO_x. A second technology, the NO_x storage catalyst, represents an attractive alternative mainly for passenger car application. This technology was developed in the mid-1990s and first published by Toyota for lean-burn gasoline engine application [2]. A further approach consisted in combining both technologies using NH₃ generated on-board over the NSC as the reducing agent for the downstream SCR brick. This technology was developed by Daimler and launched on the US market in 2006 as part of the global emission package BlueTEC [3].

The main common characteristic of all these technologies is the high degree of complexity resulting in strong interaction between the operation of the exhaust line and the management of the engine. Therefore, to reduce the cost and development efforts, modeling and simulation approaches represent an essential step in the development process. Furthermore, since the exhaust system is composed of several catalyst bricks, including generally a DOC, DPF, and SCR or NSC, strong interactions between the devices have to be considered. An optimization of the whole exhaust system is therefore only possible with detailed modeling of the separate bricks and a global approach of the system management.

Looking ahead, Daimler started being active in modeling of exhaust aftertreatment at the end of the 1990s, since appropriate commercial tools or models were not available at that time. Besides having the leading role in corporate research projects of the FVV e.V. on the modeling of NO_x reduction steps (DeNO_x model I–III, [4–6]), Daimler continued its own model development in cooperation with internationally well-known research groups in the field of exhaust aftertreatment. These cooperations led to numerous publications on the understanding of DOC, TWC, NSC, as well as SCR and ASC reaction mechanisms and on the development of corresponding models [7–13]. Based on this, a system simulation tool named *ExACT* was developed at Daimler for supporting and improving the development work on the test bench. *ExACT* includes models for the different exhaust aftertreatment components (filters and catalysts) as well as models for the connecting pipes and for the injection of an additional reducing agent like AdBlue. The simulation tool allows the prediction of emissions for all pollutants under variable conditions. The main objective of the simulation work is to develop control strategies for the whole aftertreatment system and to optimize the design and size of the system.

In the past years, modeling work got more and more important and is now playing a major role in the development procedure of exhaust aftertreatment systems. A global approach using SiL and HiL is currently the most efficient way for developing complex systems including engine and exhaust systems [14]. The following sections describe the simulation methods in the development process and give an outlook on the application of models in the ECU for on-board model-based SCR control.

22.2 Modeling of the Exhaust Gas Aftertreatment System

22.2.1 Total System Simulation

Automotive exhaust aftertreatment systems of modern passenger cars and heavy duty vehicles have complex configurations and operating control management. The systems consist not only of several aftertreatment devices, such as catalysts and particle filters, in addition, dosing systems for fuel or AdBlue, mixers, tubes

and sensors for temperature, pressure, or gas concentrations are installed. All these devices have to be described mathematically in order to simulate the complete aftertreatment system. Furthermore, simulations in the automotive development process require short computational times. Thus the models must not be too complex, but nevertheless have to predict the system behavior within a wide range of operating conditions.

All models should be integrated and connected in a virtual environment that provides a robust tool and is flexible enough to be adapted quickly or coupled with other simulation tools. At Daimler, an exhaust aftertreatment simulation tool called *ExACT* (Exhaust Aftertreatment Components Toolbox) has been developed in-house. It is based on MATLAB/Simulink, while the Fortran-based models themselves are integrated as S-functions.

22.2.2 Model Structure

This chapter focuses on the description of catalytic converters only. To comply with the above-mentioned requirements, a chemically and physically based description of the processes in the catalytic converter is necessary. It is important to model these processes separately so that physical and chemical effects are not mixed. This is a precondition, e.g., to enable scale-up simulations regarding catalyst size or to transfer kinetic parameter sets from one catalyst geometry onto another.

Due to its monolithic structure, the catalyst can be represented by a single monolith channel (Fig. 22.1) if a uniform gas flow distribution over the whole catalyst frontal area is assumed [15–18]. This is nearly the case for the major part of operation, justifying a simplified 1D consideration instead of a 2D model.

Heat exchange with the environment can often be neglected due to the insulating mat between the catalyst and its canning. Otherwise, e.g., during operation without internal exhaust flow (soak time, electric driving), where heat loss can play a role, heat transfer from the channel to its surroundings must be considered. The monolith channel itself can be described mathematically as a plug-flow reactor with basically two phases: the gas phase with laminar axial flow under all relevant conditions and the washcoat layer (or solid) phase at the monolith wall, where heterogeneously catalyzed reactions take place [20, 21]. Homogeneous gas reactions can occur at very high temperatures (>600 °C), but are always of less importance compared to the fast heterogeneously catalyzed reactions. Along the channel, convective mass and heat transport take place in the gas phase, while mass and heat transfer between the gas and the washcoat phase occurs perpendicularly to the axial direction. The latter can be described by a linear driving force approach with transfer coefficients derived from correlations using the dimensionless Nusselt and Sherwood number [15]. The gaseous mass flow rate can be considered constant along the channel, since changes in the total molar amount caused by reaction and accumulation are negligibly small. Inside the washcoat

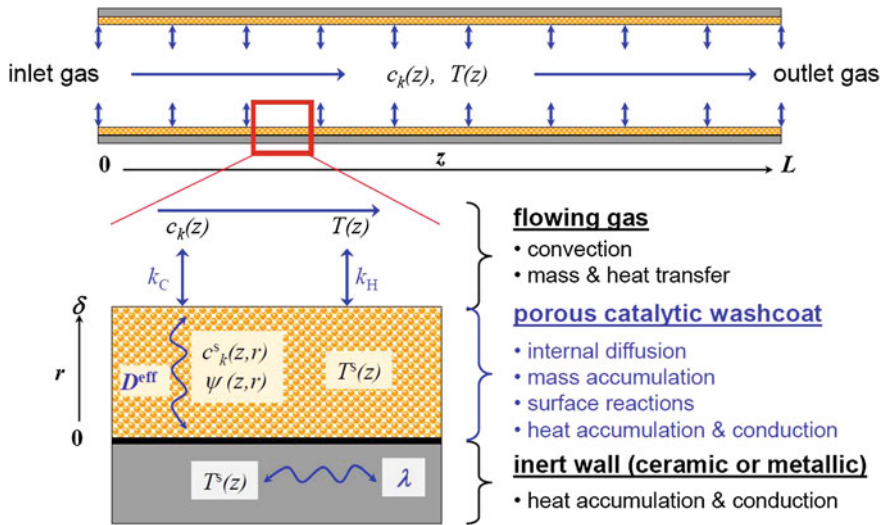


Fig. 22.1 Schematic of a representative single monolith channel [19]

(solid phase), internal diffusion in radial direction, catalytic surface reactions, and mass accumulation occur as well as heat accumulation and heat conduction in both axial and radial directions. To capture radial transport phenomena, the model must be set up in a 1 + 1D structure.

The chemical reactions are commonly described by global reactions and rate formulations of the Langmuir–Hinshelwood type. Such a description requires less computational effort compared to detailed elementary step mechanisms. However, kinetic parameters must be fitted to measurement data in advance. More details on the model equations and the numerical solution of the resulting system can be found elsewhere [15, 16, 20, 22–25].

22.2.3 Kinetics and Parameterization

Global reactions are widely used to describe catalytic converters. Their rate formulations typically consider educt species gas concentration, molar fraction, or partial pressure in the washcoat phase and a kinetic coefficient k_i of each reaction i , which is calculated using an Arrhenius type expression to account for the temperature influence of the reaction rate, cf. Eq. (22.1).

$$k_i = k_{0,i} \cdot \exp\left(\frac{-E_{a,i}}{RT^s}\right) \tag{22.1}$$

Rate formulations can further include inhibition terms in the denominator, accounting for the effect of coverage of active surface sites by adsorbed species, decreasing the activity of the catalyst. These terms are often adopted from [22] and can also consider inhibition by adsorption on separated catalytic active sites. The inhibition coefficients $K_{\text{inh},j}$ are calculated according to Eq. (22.2):

$$K_{\text{inh},j} = K_{\text{inh}0,j} \cdot \exp\left(\frac{E_{\text{inh},j}}{T^s}\right). \quad (22.2)$$

The pre-exponential factors k_i , $K_{\text{inh},j}$ and the activation energies $E_{a,i}$ and $E_{\text{inh},j}$ are kinetic parameters which have to be determined. As they cannot be obtained directly from experimental investigation, they must be adapted iteratively comparing simulation results with measurement data. The measurement data for this purpose must be generated under well-defined conditions for the considered reactions or effects, requiring a precise knowledge of gas concentrations, mass flow, and catalyst temperature. These measurements are usually carried out with synthetic exhaust gas, because the experimental settings can be varied independently over a wide range and are reproducible.

A typical automotive catalyst model contains easily more than ten reactions. Thus, the necessity to adapt 40 or more parameters can end up in a lengthy kinetic parameterization procedure. As the kinetic behavior is affected by the SCR washcoat loading as well as by poisoning or aging of the catalyst, the parameters must be adapted for each state of the catalyst to enable the model to describe the performance of each catalyst condition. An effective and robust way of model parameterization is required to satisfy this demand in the simulation-assisted development process. This includes also the generation of appropriate kinetic data for the considered catalyst. Therefore ongoing efforts are made to improve and speed up the parameterization process. This can be realized by improvements in the applied parameter optimization tool, increasing computational effort (computer clusters) or knowledge of correlations between kinetic parameters and the catalyst status, e.g., the effect of thermal aging on the parameters.

22.3 Simulation Methods in the Development Process

22.3.1 Demands of the Development Process

The modern development process requires results and estimations from simulation at an early stage, prior to the manufacturing of first prototypes. In the context of exhaust aftertreatment they help, for example, to reduce the number of costly test bench runs since they enable an early orientation on promising approaches. Further, the huge diversity in requirements, that originates from different markets, can only be covered effectively in the development process in future by assisting simulations. Exhaust gas aftertreatment simulations have to provide equivalent

information as gained from engine test benches. This is achieved by the application of the models mentioned above. Furthermore, the interaction with the engine and electronic controllers must be considered as well, in order to cover further aspects and tasks of the development process.

22.3.2 The Virtual Testbench Concept

To consider not only the exhaust aftertreatment devices but also other involved parts of the powertrain, the virtual testbench concept has been established. Here, additional devices and their functions are included in the simulation tool, for example, electronic control units (ECUs) or parts thereof. This is realized either by including representative models into the system simulation, or by coupling the simulation with the hardware, being operated in parallel.

22.3.3 Development of an AdBlue[®] Dosing Control Strategy

In this chapter, the application of the virtual testbench as part of the development process is demonstrated. In this case, the virtual testbench represents the SCR system of the aftertreatment of Diesel exhaust, i.e., the SCR catalyst itself and the necessary algorithms for control of the AdBlue dosing into the exhaust stream, cf. Fig. 22.2. These algorithms are coupled with the catalyst model in the same manner as they are implemented in the control unit. However, the injection of AdBlue, its processing, and the generation of NH_3 are not directly modeled. Ideal NH_3 -generation is assumed instead.

22.3.3.1 Tasks

The proceeding during the simulative approach can be divided into three parts with different tasks.

During the first part, data maps required by the dosing control unit are generated. These maps can be easily and systematically generated by simulation.

In the second part of the process, a suitable operation strategy for the SCR catalyst must be developed. This covers the determination of a robust control concept and its mathematical integration into the control unit algorithms. This task can be carried out without using a real testbench and engine.

The third part deals with the optimization of the catalyst configurations, based on the developed dosing strategy.

The content of these three steps will be explained in the following.

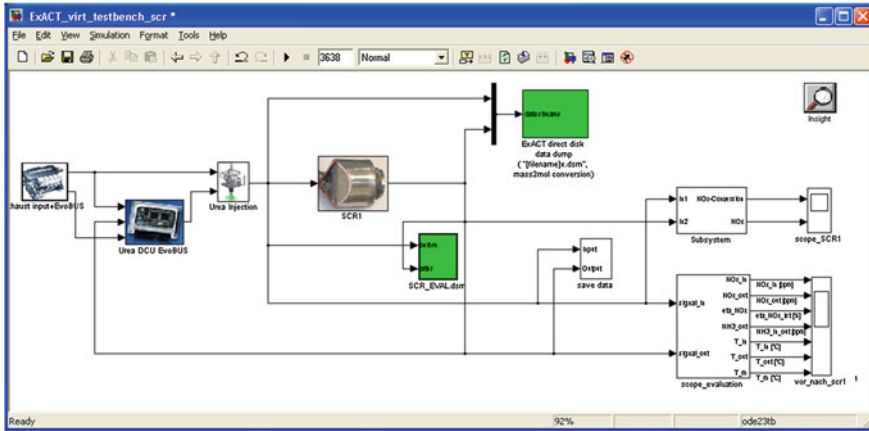
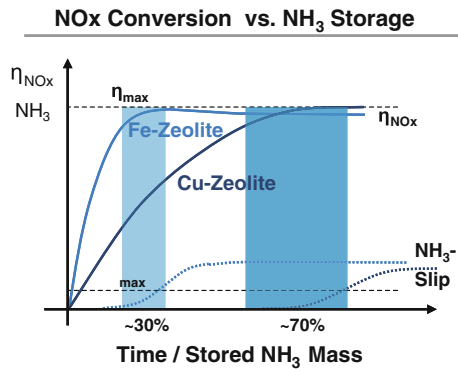


Fig. 22.2 Virtual testbench covering the SCR system

Fig. 22.3 NO_x-conversion (η) and NH₃ slip versus NH₃ load time or mass, comparing the behavior of Fe- and Cu-zeolite SCR catalyst

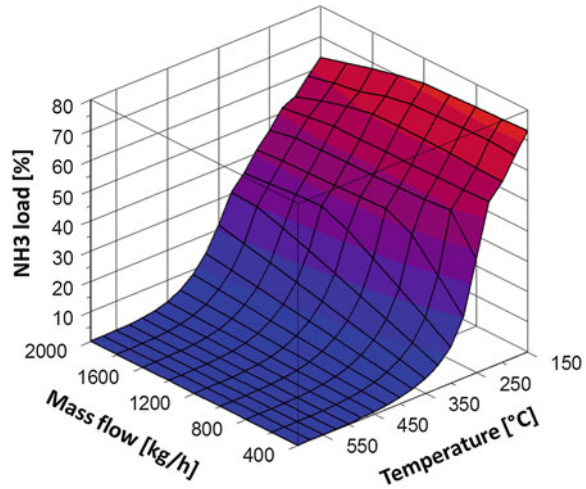


22.3.3.2 First Part: NH₃ Load Maps for the Dosing Control Unit

The SCR catalyst—especially based on Cu-ion exchanged zeolites—requires a high NH₃ load amount to reach high NO_x-conversion efficiency. This is shown schematically in Fig. 22.3, comparing an Fe- and a Cu-based SCR catalyst.

Therefore, the AdBlue dosing rate must be high as long as the catalyst is empty in order to quickly increase load and conversion rate. On the other hand, when the catalyst is filled with NH₃, the dosing rate must be equivalent to the NH₃ consumption, depending on NO_x level in the gas and its conversion. Both storage capacity and NO_x-conversion strongly depend on temperature, and conversion is, in addition, affected strongly by mass flow and NO₂/NO_x-ratio, so that NH₃ load and AdBlue dosing must be adapted according to these operating conditions. Under all conditions, however, NH₃ slip must be avoided. This means that NH₃ emissions in the exhaust gas downstream the SCR brick must be kept below a certain level, e.g., 10 ppm. Hence, a trade-off exists between high NH₃ load of the

Fig. 22.4 Normalized NH_3 load as function of the exhaust gas, mass flow, and temperature



SCR and the risk of NH_3 slip. As a consequence, the ideal state of the catalyst at a certain operating point would be an NH_3 loading amount which provides the maximum possible NO_x -conversion at an NH_3 slip of just below 10 ppm.

This optimization problem is solved iteratively using the virtual testbench. A high number of operation conditions is therefore simulated, varying systematically exhaust mass flow, gas temperature, NO_x level, and NO_2/NO_x -ratio. An optimization algorithm determines the ideal amount of NH_3 load which is acceptable before slip becomes too high. The result of this optimization task is a set of maps providing the ideal level of NH_3 load of the SCR, used by the control unit during operation. A typical NH_3 load map is depicted in Fig. 22.4.

If the ideal NH_3 load is extracted from the maps for a specified driving pattern, the resulting maximum loading level can be plotted versus time, shown schematically as dotted blue line in Fig. 22.5.

22.3.3.3 Second Part: Dosing Control Concept

The next step is the development of the dosing control strategy, based on the ideal NH_3 load. Therefore, the current NH_3 load of the SCR catalyst and the ideal one for the considered operating conditions have to be compared. If the current load is too low, AdBlue dosing must be increased. If the load is too high, dosing must be reduced (cf. Fig. 22.5). For this purpose an estimation model has to be defined, which balances the NH_3 amount entering the catalyst, and the amount being converted by reaction with NO_x and by oxidation with O_2 . The difference is the amount which is stored on the catalyst. For this calculation, the current NH_3 -conversion must be known for each operating point. These conversion values, generated by simulation in the same way as the NH_3 load values described above, are stored in another set of maps (Fig. 22.6).

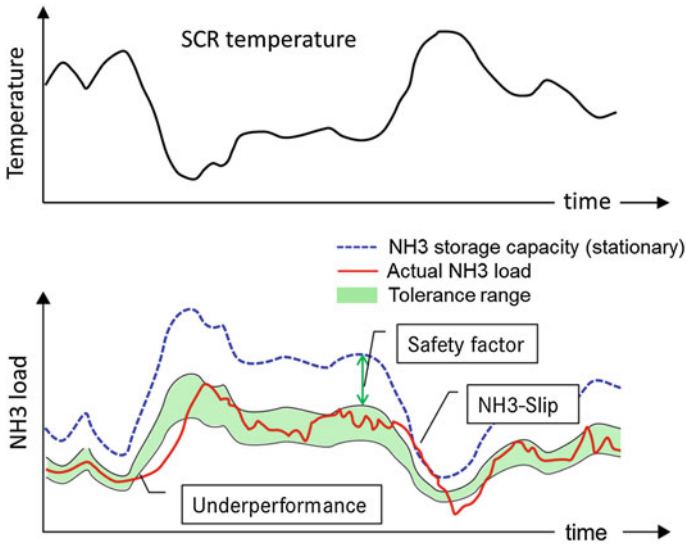
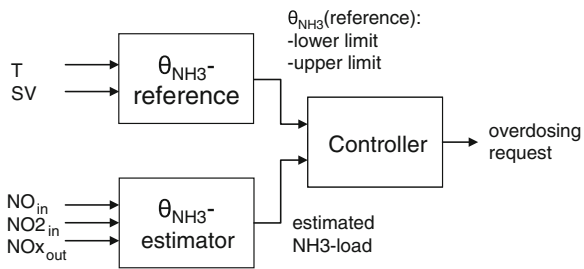


Fig. 22.5 *Top* Time evolution of the SCR catalyst temperature. *Bottom* Schematic diagram of the time evolution of the ideal and actual SCR NH₃ load. In order to avoid NH₃ slip in the case of rapid catalyst heating the tolerance range is well below the SCR steady-state NH₃ load

Fig. 22.6 Scheme of dosing control concept by comparing the ideal (reference) with the actual (estimator) NH₃ load of the SCR catalyst



Further, the manner of over or underdosing in dependence of current and ideal NH₃ load must be defined. Therefore, a range of ideal loading is considered rather than the exact maximum load. This is visualized by the green band in Fig. 22.5. The range is characterized by its width and position relative to the ideal maximum load (blue line). The actual NH₃ load of the SCR (red line) should be inside the ideal range. Although a load near the ideal maximum level should not lead to NH₃ slip above 10 ppm, the safety margin is introduced in the control task, especially for compensation of transient effects. The main transient effect is a sudden rise in exhaust gas temperature, heating up the SCR brick and causing a desorption of the stored NH₃. Assuming a worst-case temperature ramp, the parameters defining the optimal loading range can be determined iteratively by simulation, together with the factors for over and underdosing.

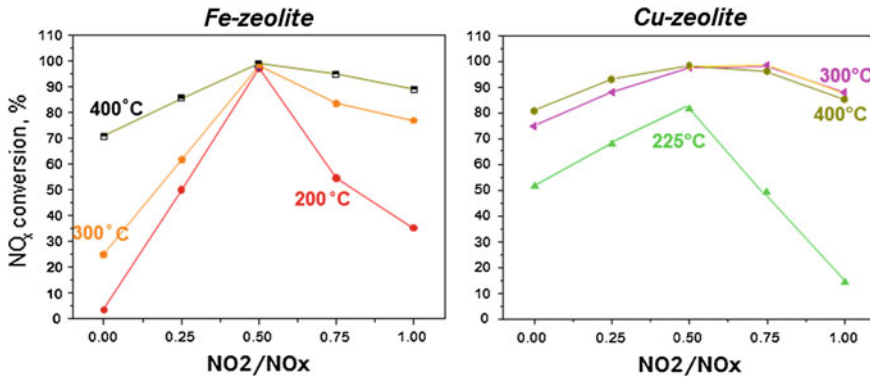


Fig. 22.7 Steady-state NO_x-conversion of Fe- and Cu-SCR catalysts in dependence of the inlet NO₂/NO_x-ratio, according to [26]

22.3.3.4 Third Part: Optimization of the Catalyst Configuration

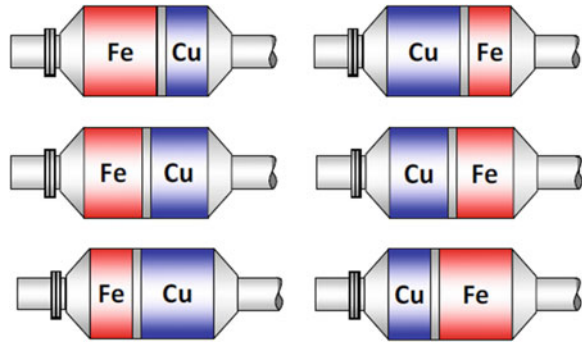
For the NH₃-SCR technology, as a well-established DeNO_x method for purifying lean exhaust gas, different catalyst technologies exist, e.g., Fe- or Cu-exchanged zeolite systems, Vanadia SCR, and nonzeolite catalysts. Each technology shows advantages and disadvantages so that their selection depends on the specifications of application conditions. For the application considered here, Fe- and/or Cu-SCR are the choice.

Fe-SCR catalysts show a very good NO_x-conversion behavior, but this technology requires an NO₂/NO_x-ratio in the exhaust gas close to 50 %. On the contrary, Cu-SCR catalysts are less dependent on the NO₂/NO_x-ratio, thus showing high activity already at low NO₂-fractions, which is mostly the case at lower temperatures. However, Cu-SCR catalysts reveal a much higher NH₃-storage capacity (see Fig. 22.3), thus a higher amount of AdBlue must be provided in advance. These characteristic differences are compared in Fig. 22.7, showing the NO_x-conversion versus NO₂/NO_x-ratio for both technologies.

To overcome these issues, a combination of both technologies can be used for aftertreatment. For example, an Fe-SCR can be used as first part of the SCR system, followed by a Cu-SCR. The Fe-SCR in first position will reach a high activity earlier than a Cu-SCR, because it requires a lower amount of NH₃ load. Further, since an NO₂/NO_x-ratio close to 50 % before SCR is never perfectly matched over the full operation range, either NO or NO₂ will leave the catalyst as the only NO_x species, if NO_x is not fully converted. Now, with an NO₂/NO_x-ratio going either toward zero or one, this is a condition where the Cu-SCR as second brick may be favorable.

The configurations can principally vary in their arrangement (Fe- or Cu-SCR first) and in their length ratios (e.g., 1/2, 1/1, 2/1), as shown schematically in Fig. 22.8.

Fig. 22.8 Possible Fe-Cu-SCR catalyst combinations, varying in order and size



The optimal configuration of the SCR bricks can be determined now by means of simulation and evaluation of driving cycle for each configuration, applying the dosing control strategy described above. Prior to this, the optimal NH_3 load maps used by the dosing control must be determined for each SCR configuration. This is an extensive proceeding for the determination of the best system, but can be executed efficiently with the virtual testbench concept. The single steps in this proceeding are illustrated in Fig. 22.9. After having identified the most promising configurations, their investigation is continued at the engine test bench, called real system validation in Fig. 22.8. Here, it is in general necessary to adapt the maps used by the control unit according to the real behavior of the considered catalysts. This is for example the case, if the simulation with the used set of kinetic parameters does not perfectly match the real behavior of the SCR system. For this adaptation, however, it is not necessary to determine the complete map contents again. It is sufficient to shift the map level relative to dedicated basic points.

22.3.3.5 Results and Conclusion

The results of the driving cycle simulation and the advantage of an Fe-Cu-SCR combination are discussed in the following, respectively, for an Fe only, Cu only, and a 1:2-Fe-Cu system. Figure 22.10 shows their DeNO_x performance in terms of accumulated NO_x mass downstream of the SCR for the cold and hot part of a WHTC. In the cold part of the cycle, Fe only (red) and Cu only (blue) show a comparable DeNO_x performance of ca. 80 %, while the Fe-Cu-combination (violet) reaches more than 83 % conversion. In the hot part, however, the Cu only system (97.4 % NO_x conversion) is clearly better than the Fe only (93.8 %), but again the Fe-Cu-combination exceeds this performance with 98.2 %. Although these differences in conversion seem to be rather small, they can lead to huge differences in the end-of-pipe emissions, as modern aftertreatment systems operate with very high conversion rates.

It is important to point out that the optimal catalyst combination would not have been identified if the appropriate dosing control had not been applied. In other

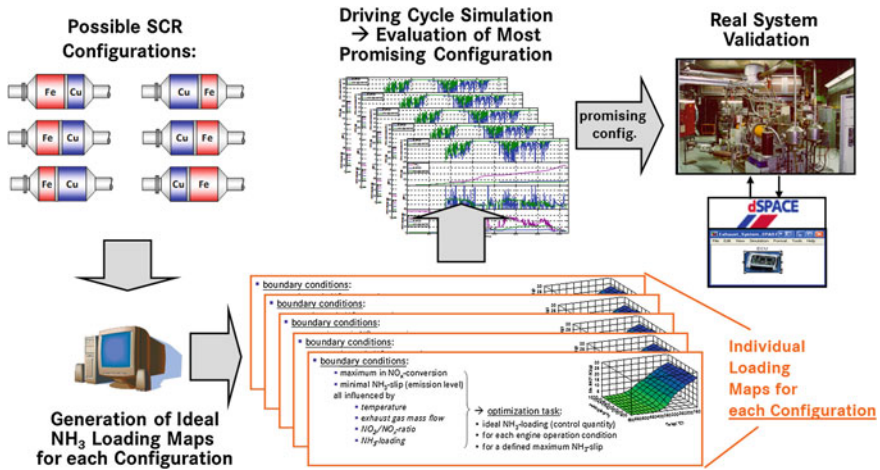


Fig. 22.9 Illustration of the steps during optimization of the SCR catalyst configuration

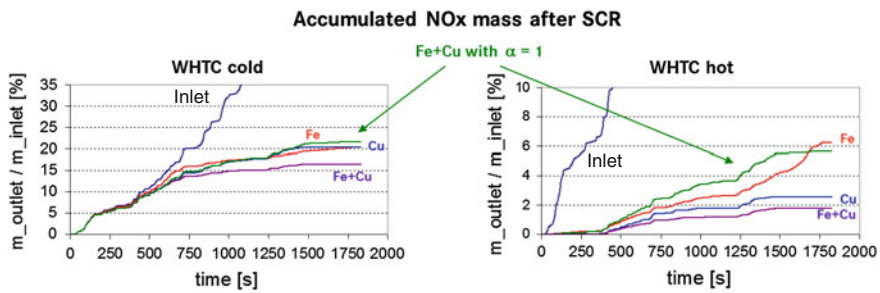


Fig. 22.10 Accumulated NOx mass ahead and after SCR of the Fe only, Cu only and Fe-Cu-combination SCR system during cold and hot WHTC. All data are normalized with the end-of-cycle inlet NOx mass

words, with a simple $\alpha = 1$ dosing strategy or without using the specific NH_3 load maps, the simulation would not predict the best NOx conversion. This can be seen from the DeNOx performance of an Fe-Cu-combination with a simple $\alpha = 1$ dosing strategy, shown as a green curve in Fig. 22.10.

The evolution of the resulting NH_3 load level according to the described AdBlue dosing control strategy is shown representatively for the Fe-Cu-SCR combination during the WHTC hot part in Fig. 22.11 (bottom). The ideal load (thin line) is plotted together with the actual load of the SCR (bold line). The actual load starts from its preloading level and decreases to get below the safety margin during the first few hundred seconds. Due to the steep increase in the ideal load, starting at ca. 250 s, the actual load is too low soon afterwards, so that AdBlue overdosing takes place to increase the actual load. It finally stabilizes within the safety margin (700–1400 s: dosing rate equal to consumption). After

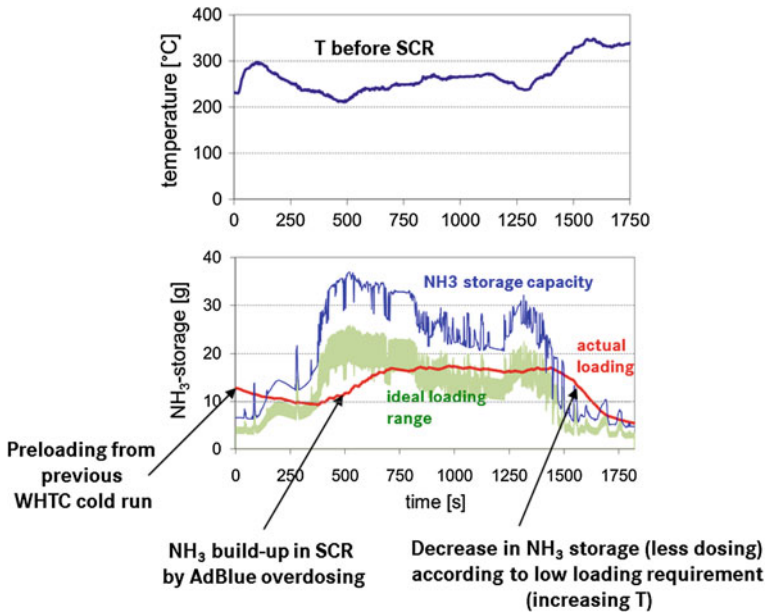


Fig. 22.11 Top gas temperature before SCR catalyst versus time. Bottom actual NH_3 load (red line), ideal loading range (green area), and NH_3 storage capacity (blue line). WHTC hot, Fe-Cu catalyst combination

this period, the ideal loading level drastically decreases due to the exhaust gas temperature rise in front of the SCR (cf. Fig. 22.11, top), so that underdosing takes place and leads to the reduction of the actual NH_3 load. However, it could not be avoided that the actual load exceeds the ideal one in this example, increasing the risk of NH_3 slip. Nevertheless, the slip did not exceed the 10 ppm limit.

This example shows the complexity of the development process already for only one part of the aftertreatment system, consisting of dosing control and SCR catalyst. The simulative approach helps immensely to speed up the development process and to save engine test bench resources. In this regard, the generation of the optimal load maps by simulation plays the major part.

22.4 Outlook: On-board Model-Based SCR Control

A further promising step in using modeling is the development of control strategies based on chemical/physical models which are implemented in the ECU. The model-based approach permits the replacement of the standard maps, which are typically generated by performing comprehensive measurements on the engine test bench. Simplified catalyst models adapted for ECU implementation offer the advantage to be modular, and they can be easily parameterized for different

exhaust configurations. In the case of the SCR technology, the model-based control of the system allows a more accurate control of the AdBlue dosing amount. Since the SCR model describes the chemical reactions inside the catalyst, the dosing strategy can be easily adapted to the requirements of the system and can take into account for changes in the status of the system, e.g., aging over time. Furthermore, the efficiency of the system can be enhanced through the development of dosing control strategies, e.g., based on NH_3 storage, also considering different types of SCR bricks in a serial configuration. Calibration and testing of the models can be done offline and independently of the engine/vehicle configuration, leading thus to substantial gain in the development time and cost.

22.5 Summary

Since exhaust aftertreatment systems have to be more and more efficient, the performance and complexity of the systems increased dramatically over the past years. Especially for the treatment of NO_x emissions from lean-burn engines, two main concepts have been developed. The first one uses SCR catalysts and requires an additional injection of AdBlue. Its efficiency is strongly dependent on current operating conditions, e.g., on the inlet NO_2/NO_x ratio. The second, consisting of a NO_x storage catalyst, requires an active management of the engine operation through periodical rich spikes for regeneration and also for desulfation of the catalyst. If combining both technologies with on-board generation of NH_3 over the NO_x storage catalyst, interactions between both catalytic systems have to be considered. This means that current exhaust aftertreatment systems require an active control management of the catalysts themselves as well as of the engine and its operation mode. Furthermore, the systems have to be configured and calibrated for a large variety of engine/vehicle combinations and markets. All these aspects obviously demonstrate the increasing requirements of the development process, and development cycles are getting shorter. Therefore front loading work using modeling of all components and simulation of the total system is of major importance for the comprehension of the whole system and the development of suitable prototypes and control strategies.

As reported in [Chap. 2](#), all aftertreatment devices have to be described mathematically with high accuracy. Therefore, all chemical reactions and heat transfer phenomena are represented in a chemical and physical form. Since computational time has to be kept short, global reactions and rate formulations based on Langmuir–Hinshelwood type are considered. Moreover, the calibration of the models represents a major step in the modeling work, requiring time and costs and directly affects the accuracy of the simulation of exhaust aftertreatment systems. For the development of control strategies, it is necessary to consider all affected aspects of the powertrain in form of a virtual test bench. The overall simulation tool includes the catalytic parts but also devices like sensors and ECU functions, which interact

with the exhaust aftertreatment system. Thus, as reported in [Chap. 3](#), suitable control strategies of the system can be developed and tested for different exhaust aftertreatment/engine configurations.

As reported in [Chap. 4](#), the models can be adapted for a direct implementation in the ECU of the engine. Such a method allows more accurate dosing strategies (e.g., in the case of the SCR technology) and takes into account the actual state of the catalysts (e.g., aging). Furthermore, the ECU is able to manage the combination of catalytic systems in series with different chemical and physical properties. Since the method is based on chemical reactions and physical properties of the system, it can be easily adapted to different catalyst geometries, different engine/vehicle combinations, and is suitable for all aftertreatment technologies.

Front loading work using simulation is a key phase in the development process of exhaust aftertreatment systems and enables through SiL and HiL methods, considering the whole powertrain, to develop systems with a very high efficiency.

References

1. Mackensen A, Braun T, Duvinage F (2012) Future diesel emission control technologies: The tension between legislation and customer benefits. 4th IAV Conference MinNOx, Berlin, June 12–13, 2012
2. Kato K, Inoue T, Nohira H, Nakanishi K, Iguchi S, Kihara T, Muraki H, Toyota JKK, EP 0 573 672 B1, Priority 27.12.1991 (JP 358125/91)
3. Weibel M, Waldbüßer N, Wunsch R, Chatterjee D, Bandl-Konrad B, Krutzsch B (2009) A Novel Approach to Catalysis for NOx Reduction in Diesel Exhaust Gas. *Topics in Catalysis*, 52, 1702–1708
4. Chatterjee D, Frank E, Warnatz J, Weisweiler W (2001) DeNOx-Modell: Modellierung der selektiven katalysierten NOx-Reduktion. Final Report, FVV e.V. Frankfurt/M., Technical Report, Heft 703
5. Chatterjee D, Inderwildi O, Frank E, Warnatz J, Weisweiler W (2002) DeNOx-Modell II: Modellierung der NOx-Minderung unter Beachtung von Speichereffekten. Final Report, FVV e.V. Frankfurt/M., Technical Report
6. Schmeißer V, Koop J (2008) DeNOx-Modell III: Modellierung und Simulation der NOx-Minderung an Speicherkatalysatoren in sauerstoffreichen Abgasen. Final Report, FVV e.V. Frankfurt/M., Technical Report, Heft 848
7. Guethenke A, Chatterjee D, Weibel M, Krutzsch B, Kočí P, Marek M, Nova I, Tronconi E (2007) Current Status of Modeling Lean Exhaust Aftertreatment Catalysts. *Advances in Chemical Engineering*, 33, 104–211
8. Kočí P, Plát F, Štěpánek J, Bártová ŠŠ, Marek M, Kubíček M, Schmeißer V, Chatterjee D, Weibel M (2009) Global kinetic model for the regeneration of NOx storage catalyst with CO, H2 and C3H6 in the presence of CO2 and H2O. *Catalysis Today*, 147, 257–264
9. Chatterjee D, Kočí P, Schmeißer V, Marek M, Weibel M, Krutzsch B (2010) Modelling of a combined NOx storage and NH3-SCR catalytic system for Diesel exhaust gas aftertreatment. *Catalysis Today*, 151, 395–409
10. Ciardelli C, Nova I, Tronconi E, Konrad B, Chatterjee D, Ecke K, Weibel M (2004) SCR-DeNOx for Diesel engine exhaust aftertreatment: unsteady-state kinetic study and monolith reactor modelling. *Chemical Engineering Science*, 59, 5301–5309

11. Tronconi E, Nova I, Ciardelli C, Chatterjee D, Bandl-Konrad B, Burkhardt T (2005) Modelling of an SCR catalytic converter for Diesel exhaust after treatment: dynamic effects at low temperature. *Catalysis Today*, 105, 529–536
12. Chatterjee D, Burkhardt T, Weibel M, Braun T, Tronconi E, Nova I, Ciardelli C (2006) Numerical Simulation of NO/NO₂/NH₃ Reactions on SCR-Catalytic Converters: Model Development and Applications. SAE Technical Paper 2006-01-0468
13. Colombo M, Nova I, Tronconi E, Schmeißer V, Bandl-Konrad B, Zimmermann L (2012) NO/NO₂/N₂O–NH₃ SCR reactions over a commercial Fe-zeolite catalyst for diesel exhaust aftertreatment: Intrinsic kinetics and monolith converter modelling. *Applied Catalysis B: Environmental*, 111–112, 106–118
14. Krutzsch B, Weibel M, Steiner R, Schmeißer V (2012) System Simulation of Modern Powertrain Concepts. Paper presented at 4th IAV Conference MinNOx, Berlin, 12–13 June, 2012
15. M. Colombo, I. Nova, E. Tronconi, V. Schmeisser, B. Bandl-Konrad, L. Zimmermann (2012) NO/NO₂/N₂O–NH₃ SCR reactions over a commercial Fe-zeolite catalyst for diesel exhaust aftertreatment: Intrinsic kinetics and monolith converter modelling. *Applied catalysis. B, Environmental*, 111–112, 106–118
16. Brinkmeier C (2006) Automotive Three-Way Exhaust Aftertreatment under Transient Conditions—Measurements, Modeling and Simulation. Dissertation, University of Stuttgart.
17. Hayes RE, Liu B, Moxom R, Votsmeier M (2004) The effect of washcoat geometry on mass transfer in monolith reactors. *Chemical Engineering Science*, 59, 3169–3181
18. Scholz CML, Gangwal VR, de Croon MHJM, Schouten JC (2007) Model for NO_x storage/reduction in the presence of CO₂ on a Pt-Ba/γ-Al₂O₃ catalyst. *Journal of Catalysis*, 245, 215–227
19. <http://www.vscht.cz/monolith/>
20. Jiráť J, Kubíček M, Marek M (1999) Mathematical modelling of catalytic monolithic reactors with storage of reaction components on the catalyst surface. *Catalysis Today*, 53, 583–596
21. Tischer S, Deutschmann O (2005) Recent advances in numerical modeling of catalytic monolith reactors. *Catalysis Today*, 105, 407–413
22. Voltz SE, Morgan CR, Liederman D, Jacob SM (1973) Kinetic study of carbon monoxide and propylene oxidation on platinum catalysts. *Industrial & Engineering Chemistry Product Research and Development*, 12(4), 294–301
23. Chatterjee D, Burkhardt T, Weibel M, Nova I, Grossale A, Tronconi, E (2007) Numerical Simulation of Zeolite- and V-Based SCR Catalytic Converters. SAE Technical Paper 2007-01-1136
24. Kočí P, Schejbal M, Trdlička J, Gregor T, Kubíček M, Marek M (2007) Transient behaviour of catalytic monolith with NO_x storage capacity. *Catalysis Today*, 119, 64–72
25. Olsson L, Blint RJ, Fridell E (2005) Global kinetic model for lean NO_x traps. *Industrial & Engineering Chemistry Research*, 44(9), 3021–3032
26. Grossale A, Nova I, Tronconi E, Chatterjee D, Weibel M (2009) NH₃–NO/NO₂ SCR for Diesel Exhausts Aftertreatment: Reactivity, Mechanism and Kinetic Modelling of Commercial Fe- and Cu-Promoted Zeolite Catalysts. *Topics in Catalysis*, 52, 1837–1841

About the Editors

Isabella Nova is Associate Professor of Chemical Engineering at the Department of Energy, Politecnico of Milan, Italy.

Isabella Nova's research work is focused on the study of environmental catalytic processes, including Selective Catalytic Reduction of NO_x by NH₃ and Diesel Particulate filters for the removal of soot, and on new processes for the production of clean energy, such as the photocatalytic water splitting.

She has co-authored over 100 publications on national and international journals in the fields of Chemical Reaction Engineering and Heterogeneous Catalysis, and has three national and international patents.

Enrico Tronconi is Full Professor of Chemical Engineering at Politecnico di Milano, Italy.

His main research interests are in the area of Catalytic Reaction Engineering, with emphasis on industrial chemical processes for energy conversion and for environmental protection. His most recent work is focused on DeNO_x aftertreatment technologies for vehicles, as well as on fundamental and engineering aspects concerning the development of novel structured catalysts and reactors.

Enrico Tronconi has authored or co-authored over 180 scientific publications in international journals and is the inventor of 10 patents.

Index

A

Acid

- Bronsted, 154, 324, 332, 333
- cyanuric, 477, 485, 488–490, 493, 516
- isocianic, HCNO, 68, 427, 487–490, 510, 516, 517
- Lewis, 162, 278, 392, 393, 611, 613
- nitric, HNO₃, 268, 304, 314, 327, 342
- nitrous, HONO or HNO₂, 314, 327

Activation energies, 153, 154, 190, 223–224, 325, 397, 696

Active sites, 17, 124, 125, 132, 139, 142, 143, 152, 154, 159, 181–183, 190, 191, 193, 198, 203–206, 208, 210, 227, 242, 293, 362, 610–614, 676, 696

AdBlue, 11, 68, 73, 74, 92, 426, 427, 429, 431, 432, 434, 441, 442, 446, 448, 485–487, 494, 498–500, 692, 693, 697–699, 701, 703, 705

Adsorption

/desorption, 104, 108, 110, 190, 244, 249, 251, 275–282, 286, 303, 306, 307, 358, 362, 371, 376, 381, 392, 393, 401, 419, 427, 441, 497, 555, 559, 561, 568, 589

enthalpy, 497

heat, 108, 110, 360

isotherm, 18, 101, 358

model, 23

Ageing

hydrothermal, 84, 111, 124, 127, 130, 132, 136, 138, 500, 665

thermal, 25, 82, 83, 89, 644

Air-to-fuel ratios, 97

Alkali metals, 87, 92

Alkaline earth metals, 88, 89

Alumina, 17, 78, 113, 128, 159, 186, 306, 590, 598, 614

Ammonia slip catalyst (ASC), 11, 49, 418, 553, 554, 556, 575, 583, 693

Ammonia, 3, 13, 19, 22, 27, 58, 73, 104, 158, 207, 261, 277, 280, 291, 303, 304, 314, 357, 358, 361, 362, 364, 376, 381, 393, 425, 426, 428, 430, 434, 438, 441–443, 446, 448, 460, 485, 546, 563, 578, 587, 592, 597, 611, 673

adsorption/desorption, 244, 251, 279, 306, 371, 376, 393, 555, 568, 589

blocking, 71, 259, 293, 338, 349

gaseous, 3, 9, 13, 26, 54, 98, 150, 261

inhibition, 110, 244, 284, 288, 291, 293, 302, 325, 338, 396

oxidation, 14, 100, 102, 104, 106, 108, 115, 126, 134, 202, 221, 223, 266, 277, 313, 318, 349, 381, 554, 568, 572, 581, 613

slip, 3, 11, 20, 48, 104, 172, 267, 362, 420, 436, 437, 441, 448, 460, 519, 567, 612, 624

storage, 18, 22, 25

Ammonium

carbamate, 68, 150, 495, 496, 498

formate, 13, 68, 494, 500

hydrogen sulfate, 43

sulfate, 18, 43, 45, 82, 85, 162

Anatase, 71, 83, 490, 491, 499, 666

Aqueous urea solution, AUS, 66, 68, 150, 427, 487, 494, 649

Arrhenius, 222, 223, 393, 428, 569, 695

Arsenic, 91

B

Back pressure, 13, 22, 480

Bulk mass transfer, 561

C

- Calibration, 7, 22, 134, 274, 385, 386, 397, 430, 456, 706
- Canning, 39, 41, 55, 56, 685
- Carbon monoxide (CO), 3, 10, 14, 15, 23, 97, 198, 498
- Carrier, 68, 190, 248, 274
- Catalyst
 - composition, 78, 98
 - deactivation, 113, 124, 130, 132, 134, 491
 - extruded honeycomb, 273
 - formulations, 16, 42, 316, 353, 385, 430, 666
 - performance, 3, 15, 18, 97, 343, 500, 629, 672, 675
 - regeneration, 232, 587, 624
 - sintering, 134, 196
- Cell
 - density, 41, 42, 69, 79, 491, 628, 633, 638, 643
 - shape, 42
- Chemical kinetic control, 421, 518
- Clusters, 113, 126, 152, 182, 194, 613
- Coating, 69, 385, 626, 629, 632, 642
- Cold start, 3, 6, 8, 20–22, 26, 150, 512, 643, 649, 651, 661, 669, 686
- Combustion, 3, 8, 17, 66, 97, 127, 149, 169, 230, 247, 459, 495, 507, 508, 510, 522, 676, 692
- Configuration, 7, 21, 127, 385, 471, 474, 476, 544, 553, 557, 558, 575, 577, 578, 583, 600, 601, 603–605, 624, 663, 702, 705, 706
- Control
 - ammonia storage distribution, 442, 448
 - closed-loop, 22, 75
 - feedback, 22, 441
 - feed-forward, 58, 441
 - open-loop, 13, 56, 75, 441
 - strategy, 58, 76, 697, 699, 703
 - unit, 697–698
- Copper (Cu), 3, 16, 27, 125, 130, 153, 206, 207, 242, 362, 366, 608
- Cordierite, 80, 114, 491, 649, 677
- Coverage
 - ammonia, 101, 293, 358, 360, 364, 373, 374, 378, 428, 430, 437, 439, 442, 566
 - surface, 193, 235, 343, 571, 696
- Cycle
 - driving, 203, 415, 510, 661, 702
 - test, 5, 11
 - transient, 8, 11, 13, 22, 65, 420, 659, 660, 661

D

- Deactivation
 - hydrothermal, 124, 126, 128
 - Decomposition
 - NO₂, 315, 321, 335
 - Diesel Exhaust Fluid (DEF), 7, 11, 455, 487, 669
 - Diesel oxidation catalyst (DOC), 9, 14, 48, 98, 133, 150, 444, 598, 624, 663, 681, 692
 - Diesel particulate filter (DPF), 5, 11, 48, 69, 98, 123, 124, 403, 444, 512, 615, 626, 628–630, 638, 667, 679, 685
 - Diffusion
 - bulk, 643
 - inter, 389
 - intra, 241, 400, 401
 - film, 386, 388
 - limitations, 325, 336, 343, 345, 408
 - pore, 79
 - regime, 248
 - Dimensioning, 76
 - Discretization, 508
 - DPF + SCR, 11, 48, 403
 - Droplet
 - continuity equation, 528, 535
 - motion equation, 529
 - Durability, 3, 13, 15, 16, 69, 71, 92, 98, 111, 143, 244, 312, 613, 644, 663, 671, 685
 - Dynamic
 - behavior, 56, 248, 249, 307, 400
 - test, 24, 276, 285, 302
- E**
- Effectiveness factor, 386, 437, 482, 660, 669
 - Efficiency, 6
 - Eley-Rideal, 291, 293, 330, 369, 396
 - Emission
 - heavy trucks, 6, 41, 66
 - off-road vehicles, 477
 - passenger cars, 6
 - real world driving, 5, 441
 - regulations, 3, 36, 45, 97, 124, 140, 150, 425, 456
 - Energy
 - activation, 104, 182, 223, 225, 306, 325, 331, 345, 358, 428
 - apparent, 223, 325
 - Engine
 - diesel gasoline, 3, 6, 8, 9, 34, 39, 58, 65, 81, 92, 124, 127, 163, 171, 230, 425, 487, 508, 519, 596, 601, 640, 666

heavy duty, 171, 650
light duty, 625
low speed, 34, 46
medium speed, 34, 42, 45, 47
Exhaust gas recirculation (EGR), 3, 5, 26,
476, 667

F

Factor
cross-sensitivity, 431, 433, 434, 437, 438
effectiveness, 386, 437, 482, 660, 669
Federal test procedure (FTP), 9, 602
Film
diffusion, 79
liquid, 507, 512, 522, 532, 534, 536,
541, 544
Filter
catalyzed soot (CSF), 624
diesel particulate (DPF), 5, 48, 66, 82, 98,
123, 124, 512, 615, 626, 628, 638,
667, 669, 685
flow through, 638
Fit, 565
kinetic, 293, 563, 566, 572, 573
Flow, 48, 53, 99, 111, 237, 250, 312, 385, 387,
401, 416, 429, 508, 512, 519, 536,
541, 557, 626, 629, 632, 640, 643,
646, 694
Framework, 104, 111, 119, 125, 132,
142, 261, 610
Fuel
bio, 91–92
heavy oil, 34, 46

G

Genetic algorithm (GA), 430
Genset, 40
Geometric surface area, 629

H

Heat
adsorption, 108, 358, 359
condensation, 511, 512
evaporation, 22, 512, 516, 530
transfer, 527, 643, 694, 705
Honeycomb, 42, 273, 558, 626
Hydraulic diameter, 388, 404, 632

Hydrocarbon (HC), 3, 5, 10, 14, 16, 17,
24, 90, 97, 111, 132, 198,
661, 676
Hydrogen, 164, 238, 495, 499, 589, 590,
592, 595
Hysteresis, 334, 494, 563

I

Impregnation, 151, 152, 160, 606
Incipient wetness, 680
Infrared spectroscopy, 183, 185, 186, 250
Inhibition
Ammonia, 288, 337, 339, 348, 563, 605
NO oxidation, 325
Water, 330
Ion
Cu, 125, 127, 143, 153, 207,
244, 251, 698
Exchange, 128, 138, 142, 151, 152, 613
Fe, 152, 203, 244, 614
NH₄⁺, 125, 154, 238, 609, 614
Iron (Fe), 3, 199, 608, 611, 613
Isotherm
Freundlich, 279
Langmuir, 18, 279
Temkin, 358
Temkin modified, 279

K

Kalman filter, 429, 433
Kinetic
analysis, 193, 243, 276, 285, 302, 553
fit, 565, 566
global, 241, 303, 343, 348, 351, 361, 364,
369, 371, 553
regime, 344
test, 275

L

Langmuir-Hinshelwood, 326, 563, 603,
695
Layer
dual, 345, 347, 351, 352, 417, 556,
558, 603
multi, 386, 420
Layout, 11, 46, 73, 476, 623, 624, 664
Lead, 91

- Lean
 NO_x trap, LNT, 4, 23, 27, 150, 252, 624
 LNT + SCR, 24, 25, 601
- M**
 Marine, 45
 Mars-van Krevelen, 261, 304, 566
 Mass transfer
 inter, 387, 558
 intra, 387, 558
 Mechanical mixture, 553, 557, 558, 575, 577
 Mixing, 13, 48, 52, 134, 250, 461, 467, 470, 471, 480, 508, 520, 521, 531, 544, 682
- Model
 OD, 645
 1D + 1D, 553, 558, 567, 579, 646
 3D, 508, 539, 645
 computational fluid dynamics (CFD), 643, 507
 control-oriented, 425–427, 429, 460, 442
 global, 343, 348, 349, 364, 369, 553
 mathematical, 387, 400, 553, 556, 561, 567
 mechanistic, 329
 multidimensional, 508, 522
 on board, 39
 validation, 403, 558, 561, 567, 573
 water dragging, 513
- Moisture, 167, 199, 512
- Monolith, 68, 69, 73, 79, 100, 264, 312, 343, 345, 348, 349, 353, 400, 407, 488, 491, 513, 553, 556, 558, 561, 567, 573, 575, 581, 596, 615
- N**
 Nitrate, 18, 23, 107, 110, 248, 251, 254–256, 258–264, 266, 268, 303, 308, 313, 314, 318, 326, 341, 366, 374, 562, 590, 609
 Nitric oxide (NO), 288, 331
 Nitrite, 107, 162, 241, 250, 258, 308, 326, 328, 329, 332, 337, 343, 378
 Nitrogen dioxide (NO₂), 3, 10, 15, 640
 Nitrous oxide or dinitrogen monoxide (N₂O), 18, 684
- O**
 Oil
 fuel, 3, 5, 7, 8, 26, 659–661
 Onboard
 generation, 311, 692, 705
 model, 693, 704
- Oxidation
 ammonia, 18, 202, 208, 262, 266, 282, 316, 318, 320, 364
 NO, 15, 14, 101, 154, 204, 205, 227, 315, 329, 365, 562, 681
- Oxide
 metal, 126, 155, 158, 165, 193, 197, 330, 569, 613
 mixed, 156, 158, 196, 197, 208, 210, 247
 supported metal, 158
- Oxygen storage capacity (OSC), 595
- P**
 Palladium (Pd), 3, 26
 Passive NO_x adsorber (PNA), 9, 21, 27
 Permeability, 628, 632, 634, 635, 646
 Platinum-group metals (PGM), 42, 82, 97, 414, 418, 553, 555, 557, 558, 569, 575, 579, 581, 685
 Platinum (Pt), 3, 14, 26, 169, 418, 590, 591
- Poisoning
 chemical, 134, 140
 hydrocarbon, 17, 27, 90, 132
 sulfur, 16, 85, 133, 161, 171, 353, 681
- Pore
 diffusion, 17
 distribution, 391, 394
 porosity, 391, 627, 638
 size, 79, 171, 391, 610, 627, 632, 651
- Pressure drop, 41, 69, 404, 628, 630, 633, 640, 650
- R**
 Rail, 8, 39
- Ratio
 NH₃/NO_x, 100, 558
 NO₂/NO_x, 107, 323, 324, 564, 568, 573, 577, 611, 614, 649, 672, 698, 701, 705
- Reaction
 mechanism, 124, 181, 205, 275, 426, 518
 order, 325, 517, 587
 rate, 69, 71, 81, 131, 152, 183, 193, 196, 203, 243, 373, 388, 392, 428, 569, 595
- Reactor
 bench-scale, 99, 312
 CSTR, 429
 flow micro, 99
- Redox
 cycle, 154, 209, 228, 242, 289, 304, 308

- mechanism, 163, 190, 290, 333, 341
- site, 126, 132, 240, 288
- state, 251
- Regulations or legislation
 - EU, 36, 624
 - heavy duty, 4
 - Japan, 3, 4, 6
 - light duty, 5
 - off road/off highway, 34
 - US, 3, 7, 26, 124
 - vehicles, 624
- S**
- SCR
 - enhanced, 24, 248, 266, 268, 321, 563, 613
 - fast, 10, 14, 157, 182, 203–205, 247, 248, 256, 259, 261, 264, 268, 300, 308, 312, 314, 320, 321, 324, 338, 340, 345, 396, 609
 - H₂, 163, 172
 - HC, 66, 135, 198, 207, 607, 661, 676, 678
 - NO₂, 3, 26, 27, 100, 107, 262, 294, 300, 303, 308, 321, 322, 324, 341, 374, 381, 609
 - standard, 10, 99, 101, 104, 182, 203–205, 288, 304, 307, 313, 315, 317, 319, 321, 324, 325, 333, 520, 546, 671
- SCR filter (SCRF), 403, 407, 410, 415, 416
- Sensor
 - ammonia, 22, 425, 444, 663
 - lambda
 - NOx, 13, 22, 58, 429, 431, 434, 437, 444, 448, 663, 666
- Sherwood number, 388, 528
- Site
 - active, 17, 124, 126, 132, 139, 142, 143, 158, 181, 182, 193, 203–206, 208, 293, 612
 - dual, 202, 279, 567
 - isolated, 195, 199, 201–204, 210
 - multi, 393
 - oligomeric, 203, 331
 - single, 202, 392, 393
- Soot, 14, 66, 82, 404, 409, 411, 625, 635, 636, 639, 641, 643, 650
- Spray, 52, 54, 73, 456, 461, 464, 465, 471, 482, 490, 507, 508, 523, 526, 534, 541, 544, 664
- Stationary applications, 55, 65, 277, 278, 280, 425, 485
- Storage
 - ammonia, 18, 22, 25
 - nitrates, 110
 - NO_x reduction, NSR, 15, 101
 - water, 358, 362
- Substrates, 18, 55, 80, 420, 629, 631
- Sulfur
 - oxides, 42
 - poisoning, 16, 85, 133, 161, 171, 353, 681
- Supports, 125, 127, 139, 156, 166, 193, 291, 329
- Surface
 - area, 69, 79, 83, 111, 113, 125, 131, 132, 155–157, 166, 181, 196, 197, 343, 629, 633, 636, 643, 673
 - coverage, 193, 235, 343, 571, 696
- T**
- Test
 - bench, 49, 65, 402, 539, 553, 693, 696, 702, 704, 705
 - protocol, 108
- Thermal
 - ageing, 25, 82, 83, 89, 111, 644
 - management, 8, 9, 640
- Three way catalyst, (TWC), 23, 25, 596, 692
- Titania, TiO₂, 13, 65, 79, 98, 123, 160, 184, 195, 197, 278, 294, 358, 596, 597, 613, 659, 660, 681
- Turbulence, 53, 54, 524, 525
- U**
- Urea
 - control, 13, 425, 442
 - dosing, 12, 38–40, 46, 50, 51, 54, 56, 58, 65, 67, 73, 425, 426, 437, 443, 625, 663
 - hydrolysis, 13, 491, 492, 500
 - injection, 9, 13, 22, 68, 73, 74, 293, 375, 425, 442, 449, 519, 538, 649, 663, 664, 666, 675, 682, 686
 - mixer, 13, 26, 669
 - solid, 73, 486, 531
 - solution, 11, 12, 14, 41, 50, 66, 68, 73, 134, 150, 426, 486, 487, 491, 494, 514, 649
 - tank, 12, 39, 66, 73, 682, 683
- V**
- Vanadia, V₂O₅, 3, 15, 16, 27, 65, 67–69, 74, 78, 80, 83, 98, 123, 193, 196, 198, 294, 311, 312, 332, 348, 358, 378, 394, 614, 615, 666, 686, 701

W

Wall

flow, 385, 386, 403, 407, 416, 419, 626,
632, 636, 644, 646

thickness, 69, 80, 405, 407, 541, 557

Washcoat

deposition, 79, 629

distribution, 99

thickness, 78, 80, 335, 343, 579

Window

operating, 98, 118, 661, 663

temperature, 119, 151, 166, 171, 247, 345,
352, 500, 661, 662, 665, 675

Z

Zeolite

BEA, 17, 98, 111, 234, 605

CHA, 111, 115, 138, 357, 678

ferrierite, 125

MFI, 166, 610

SAPO-34, 98, 153

small pore, 17, 124, 135–143, 678, 686

SZZ-13

Y, 125, 166

ZSM-5, 98, 111